Victor N. Cassar-Pullicino
A. Mark Davies   *Editors*

Measurements in Musculoskeletal Radiology

Springer

Medical Radiology

Diagnostic Imaging

Series Editors

Hans-Ulrich Kauczor

Paul M. Parizel

Wilfred C. G. Peh

For further volumes:
http://www.springer.com/series/4354

VCP providing illumination while AMD attempts to restore power

Victor N. Cassar-Pullicino
A. Mark Davies
Editors

Measurements in Musculoskeletal Radiology

Springer

Editors
Victor N. Cassar-Pullicino
Department of Radiology
Robert Jones and Agnes Hunt
Orthopaedic Hospital NHS
Foundation Trust
Oswestry, UK

A. Mark Davies
Department of Radiology
Royal Orthopaedic Hospital NHS
Foundation Trust
Birmingham, UK

This book is dedicated to Wendy Pullicino

Preface

From the birth of imaging with Roentgen to the latest molecular imaging, there has always been a desire to obtain measurements that can be compared with further observation over time or with other cases. In their first edition of the *Atlas of Roentgenographic Measurement*, Lusted and Keats stated that "The interpretation of a roentgenogram remains an art ………. To this interpretation the objective evidence of the roentgenographic measurement can make an important contribution". This remains as true today as when first published almost 60 years ago. The difference now is that our knowledge of what is normal or abnormal and pathology in general has expanded almost exponentially hand-in-hand with equally dramatic advances in imaging techniques using both ionising radiation (e.g. CT and PET) and non-ionising modalities (e.g. US and MRI).

It is true to say that way back in the early 1980s, as radiologists in training, we were at best lukewarm to the concepts of measurement and their role in musculoskeletal disorders. Increasingly over the years as advances in imaging and musculoskeletal diseases have continuously evolved, we have often quoted Lord Kelvin's wise words; "To measure is to know" and "If you cannot measure it, you cannot improve it". However if a measured parameter is deemed important in science, research and clinical practice, it is imperative to realise that its value rests entirely on the adequacy, precision and accuracy of its measurement. The purpose for which the measure is intended must be clearly understood and the inferences that can be drawn need to be examined in an objective and critical manner before any conclusions are reached. All too often measurements are introduced and employed without examining their validity, which requires that rigorous steps are put in place to understand the meaning and usefulness of the measured values. The main aim of this book is to critically and clearly bring this knowledge under one roof.

As our understanding of disease processes and the sophistication of imaging techniques have improved with time, there is a need to continuously update radiologists, orthopaedic surgeons and the other allied healthcare professionals working in this field. To this end this book takes a trident approach. The first five chapters are devoted to the differing imaging techniques highlighting the strengths and weaknesses when employed to measurement. There are then 12 chapters dealing with the major anatomical areas where the relevant distilled knowledge and data are presented critically in a template format. The final four chapters are devoted to the wide range of imaging that can be applied in varied disease states.

Oswestry, UK   Victor N. Cassar-Pullicino
Birmingham, UK   A. Mark Davies

Contents

Part III   Measurements in Disease States

Contributors

Christian E. Althoff Interventional Radiology Section, Charité University Hospital—Campus Mitte, Berlin, Germany

Ali Attieh Radiologia— Department of Health Science, Università di Genova, Ospedale Policlinico San Martino, Genova, Italy

Antonio Barile Department of Radiology, University of L'Aquila, L'Aquila, Italy

Andrea Baur-Melnyk Department of Clinical Radiology, University of Munich-Grosshadern, Munich, Germany

Matthias Bollow Department of Radiology, Augusta Hospital Bochum, Bochum, Germany

R. Botchu Department of Musculoskeletal Radiology, The Royal Orthopaedic Hospital, Northfield, Birmingham, UK

Nathalie Boutry Department of Musculoskeletal Radiology, Centre Hospitalier Universitaire de Lille, Hôpital Roger Salengro, CHRU de Lille, Lille Cedex, France

Victor N. Cassar-Pullicino Department of Radiology, Robert Jones and Agnes Hunt Orthopaedic Hospital NHS Foundation Trust, Oswestry, UK

Anne Cotten Department of Musculoskeletal Radiology, Centre Hospitalier Universitaire de Lille, Hôpital Roger Salengro, CHRU de Lille, Lille Cedex, France

A. Mark Davies Department of Radiology, Royal Orthopaedic Hospital NHS Foundation Trust, Birmingham, UK

Xavier Demondion Department of Musculoskeletal Radiology, Centre Hospitalier Universitaire de Lille, Hôpital Roger Salengro, CHRU de Lille, Lille Cedex, France

Department of Anatomy, Faculty of Medicine, Centre Hospitalier Universitaire de Lille, Hôpital Roger Salengro, CHRU de Lille, Lille Cedex, France

Hassan Douis University Hospital Birmingham, Birmingham B15 2TH, UK

Jean-Luc Drapé Sorbonne Paris Centre, Radiologie B, Hospital Cochin, University Paris Descartes, Paris, France

David A. Elias Department of Diagnostic Imaging, King's College Hospital, London, UK

Maria Vittoria Di Fabio Department of Radiology, University of L'Aquila, L'Aquila, Italy

J. Farrant The Royal Free Hospital, London, UK

Tobias Geith Department of Clinical Radiology, University of Munich-Grosshadern, Munich, Germany

Andrew J. Grainger Leeds Teaching Hospitals, Leeds, UK

Kay-Geert A. Hermann Musculoskeletal Radiology Section, Arthritis Imaging Research Group, Department of Radiology, Charité University Hospital—Campus Mitte, Berlin, Germany

Richard Hodgson Centre for Imaging Science, University of Manchester, Manchester, UK

Eric Hughes Department of Radiology, Robert Jones and Agnes Hunt Orthopaedic Hospital, Oswestry, UK

K. Johnson Birmingham Children's Hospital, Birmingham, UK

Anne Grethe Jurik Department of Radiology, Aarhus University Hospital, Aarhus, Denmark

Department of Clinical Medicine, Aarhus University, Aarhus, Denmark

Franz Kainberger CIR—Computational Imaging Research Lab, Department of Biomedical Imaging and Image-Guided Therapy, Medical University of Vienna, Vienna, Austria

Apostolos H. Karantanas Department of Radiology, Robert Jones and Agnes Hunt Orthopaedic Hospital, Oswestry, UK

G.M.M.J. Kerkhoffs Department of Orthopaedic Surgery, Suite G7-153, Academic Medical Center Amsterdam, Amsterdam, The Netherlands

Chadi Khalil Department of Musculoskeletal Radiology, Centre Hospitalier Universitaire de Lille, Hôpital Roger Salengro, CHRU de Lille, Lille Cedex, France

Andrea Klauser Department of Radiology, Rheuma- und Sportbildgebung, Medical University Innsbruck, Innsbruck, Austria

Georg Langs CIR—Computational Imaging Research Lab, Department of Biomedical Imaging and Image-Guided Therapy, Medical University of Vienna, Vienna, Austria

Thomas M. Link Department of Radiology and Biomedical Imaging, University of California, San Francisco, San Francisco, CA, USA

Eva Llopis Hospital Universitario de la Ribera, Alzira, Valencia, Spain

M. Maas Department of Radiology, Suite G1-211, Academic Medical Center, Amsterdam, The Netherlands

Fabio Martino Department of Radiology, ASL BARI, Bari, Italy

Gianluigi Martino Radiology Department of the P.O., "Di Venere" - ASL BARI, Bari, Italy

Carlo Martinoli Radiologia— Department of Health Science, Università di Genova, Ospedale Policlinico San Martino, Genova, Italy

C. Miller Birmingham Children's Hospital, Birmingham, UK

S. Mohan Birmingham Children's Hospital, Birmingham, UK

C.M. Nusman Department of Radiology, Suite G1-211, Academic Medical Center, Amsterdam, The Netherlands

Philip James O'Connor Leeds Teaching Hospitals Trust, The University of Leeds, Leeds, UK

Mario Padrón Clinica Cemtro, Madrid, Spain

Philipp Peloschek Radiology Centre Vienna, Vienna, Austria

R.R. van Rijn Department of Radiology, Suite C2-423.1, Academic Medical Center Amsterdam, Amsterdam, The Netherlands

Andrew Roberts Children's Unit Robert Jones and Agnes Hunt Orthopaedic Hospital, Oswestry, UK

Clare Roche Department of Radiology, University College Hospital Galway (UCHG), Galway, Republic of Ireland

Eugenie Sánchez Clinica Cemtro, Madrid, Spain

Jaspreet Singh Department of Radiology, Robert Jones & Agnes Hunt Orthopaedic Hospital, Oswestry, UK

Michele Solarino University of Bari, Bari, Italy

P.A.A. Struijs Department of Orthopaedic Surgery, Suite G7-152, Academic Medical Center Amsterdam, Amsterdam, The Netherlands

Alberto Tagliafico Radiologia— Department of Health Science, Università di Genova, Ospedale Policlinico San Martino, Genova, Italy

Nicolas Theumann Department of Radiology, Clinique Bois-Cerf, Lausanne, Switzerland

Prudencia N.M. Tyrrell Department of Radiology, Robert Jones & Agnes Hunt Orthopaedic Hospital, Oswestry, UK

Filip M. Vanhoenacker Department of Radiology, University Hospital Antwerp, Antwerp University, Edegem, Belgium

Department of Radiology, AZ Sint-Maarten, Duffel-Mechelen, Duffel, Belgium

Department of Radiology, University Hospital Ghent, Ghent, Belgium

Koenraad L. Verstraete Department of Radiology, University Hospital Ghent, Ghent, Belgium

Reinhard Windhager Department of Orthopaedic & Trauma Surgery, Medical University of Vienna, Vienna, Austria

Richard W. Whitehouse Department of Clinical Radiology, Manchester Royal Infirmary, Manchester, UK

Naomi Winn Department of Radiology, Robert Jones and Agnes Hunt Orthopaedic Hospital NHS Foundation Trust, Oswestry, UK

Part I

Measurement Techniques

The Radiograph

1

Eric Hughes, Prudencia N. M. Tyrrell,
and Victor N. Cassar-Pullicino

Contents

E. Hughes, H.D.C.R. (✉) • P. N. M. Tyrrell, M.D.
V. N. Cassar-Pullicino, M.D.
Department of Radiology, Robert Jones and Agnes
Hunt Orthopaedic Hospital NHS Foundation Trust,
Oswestry, UK
e-mail: eric.hughes@rjah.nhs.uk

1.1 Introduction

Radiographs have been used in diagnosis for over 100 years. Despite the many technical advances in imaging, they retain an important role in the diagnostic workup of many ailments particularly in bone and joint pathology. They are often used in imaging follow-up of disease states to evaluate progression, monitor treatment or assess metalwork or implants following surgery. It is possible from the radiographs to make measurements which aid in diagnosis or subsequent management of a condition. Sometimes, these measurements are crude representing an observation such as the presence of prevertebral soft tissue swelling in a patient with a history of cervical spine injury where that observation signals a very high probability of either bone or soft tissue injury. On other occasions, precise measurements may be required such as in leg length evaluation which may determine the degree and extent of surgical intervention if indeed any. They also are often used for measuring distances and angles in musculoskeletal work to assist in the planning of management including surgery. There are inherent advantages in using radiographs for such measurements, but there are also certain limitations often related to technical factors of which clinicians and radiologists need to be aware. This chapter addresses the general role of radiography in measurements undertaken in musculoskeletal work. The specific role of radiography in measurements of different anatomical and pathological states is made in the relevant chapters.

1.2 Advantages of Radiographs

Radiographs are cheap and readily available. Standardisation of the radiograph is possible such that they can be directly compared both within a department and between different departments. Thus, they are reproducible and in this context can be used in research. The conventional radiograph can be used to monitor progress of a condition such as rheumatoid arthritis by documenting joint space narrowing and number of erosions. It can be used to monitor healing of bone injury documenting new bone formation and progressive consolidation or otherwise. It can be used to monitor the effect of therapy or response to treatment such as may be seen with effective antibiotic treatment in osteomyelitis or appropriate biochemical or endocrine treatment in osteomalacia. Serial lateral radiographs of the thoracic and lumbar spine are used in the monitoring of osteoporosis. Grading systems have developed and employed radiographic appearances to denote severity of disease which is used in therapeutic decision making, e.g. trauma and avascular necrosis. The earliest changes of disease processes, however, may not be seen on radiographs, such as avascular necrosis, and other imaging modalities such as magnetic resonance imaging may need to be employed. Once the radiographic features are detectable, then the radiograph may be used for disease monitoring in some instances. Many surgical instrumentation procedures are monitored over time with periodic radiographs. This is perhaps most commonly seen in patients who are being followed up post arthroplasty. Monitoring of disease with serial or sequential radiographs provides objective evidence as a guide to decision-making for operative or nonoperative treatment. In the examples given above, eyeballing the radiograph to assess status can be adequate. However, there will be many instances where accurate measurements are required in order to determine planning of corrective surgery, for example, in children with unequal leg lengths. Accurate measurements are also required to facilitate evidence-based studies. This can be seen in patients with spinal infection where the disc has been destroyed with associ-

ated loss of vertebral body height. Should vertebral body collapse with kyphotic deformity progress to a particular level, then surgery with instrumentation may be necessary to stabilise the spine and prevent further deformity. Such objective evidence with measurement of the degree of angulation facilitates evidence-based outcomes of treatment.

Assessment of bone age and potential for growth in the immature skeleton is important in treatment planning. This can be done using a number of indices. The Greulich and Pyle atlas of hand radiographs (Greulich and Pyle 1959), or the Sauvegrain method of bone age estimation on elbow radiographs (Sauvegrain et al. 1962) between the approximate ages of 11 and 16 years, are just two of a number of methods available. All methods of estimating skeletal age involve comparing radiographs of the patient with standards in an atlas. This estimation is only moderately accurate. In the Tanner and Whitehouse method (Tanner et al. 1975), 20 indicators on hand and wrist radiographs are assessed and given a score, yielding a total score from 0 to 100. The Risser sign relates to the degree of ossification of the iliac apophysis (Risser 1958). This is a commonly used marker of skeletal maturation especially in the treatment of scoliosis. A bone age estimation in isolation is meaningless. The measurement needs to be compared with the chronological age and ideally the rate of annual growth in standing height assessed.

One particular advantage of plain radiographs, not readily available with other imaging modalities, is the facility to obtain dynamic views in, for example, flexion and extension. This allows a rapid evaluation of stability. Abnormal movement can be detected by eyeballing the radiograph or discrete measurements can be obtained if necessary. Stress views, e.g. at the knee or ankle, can be used for the evaluation of ligamentous integrity.

Radiographs are good for providing both an informal and formal assessment of measurement, but there are a number of technical issues which need special consideration when highly accurate measurements are required. These are addressed in detail below.

1.3 Limitation of Radiographs for Measurement

Despite the many advantages of radiographs for use as a measuring tool in orthopaedic and musculoskeletal work, there are a number of limitations. To understand the nature of these limitations and how they may be overcome, it is helpful to reflect on how X-rays are produced. Although many departments are now using some form of digital radiography, basic principles of both film and digital imaging are covered. In line with commonly used terminology, this text refers to focus film or object film distances, and use of the term film in this instance can refer to a film cassette, computerised radiography plate or a direct digital radiography detector plate.

Fig. 1.1 X-ray tube simplified representation

Basic Principles of X-ray Production

A focused beam of electrons is accelerated between the cathode and anode of an X-ray tube striking the anode at high speed within a small area to produce what is as close to a point source of X-rays as is possible within the efficiency limitations of the system (Fig. 1.1).

The resultant X-rays are emitted in all directions but are contained within the housing of the X-ray tube with the exception of a small window which, with the addition of adjustable lead slats, can result in a directed divergent adjustable beam of X-ray. The portion of the beam which is passed through the object without being deflected forms the shadow image on a film or an image receptor plate. Scattered radiation reaches the film in a random way and does not contribute to the useful image. This scattered radiation may need to be reduced by the use of a lead-slatted grid.

In order to reduce the amount of radiation required to form the image and reduce the radiation dose to the patient, the use of film has been supplemented by the use of intensifying screens which convert each X-ray photon into several light photons. It is therefore the light emitted by the intensifying screens which forms the majority of the image on the film. Conventional film screen cassettes produce an analogue image recorded on film

and developed using a photographic process. These are viewed on a lightbox. All the information is in the hardcopy image only and the image cannot be manipulated. Within PACS digital systems, a similar effect is generated by the use of mathematical algorithms. In the technique of computed radiography (CR), a photostimulable phosphor contained within a cassette is exposed in the same way as conventional film and then removed to be read remotely by a laser mechanism. Direct digital radiography (DDR) uses solid-state detectors to record the latent image, but this is linked directly to the readout device, therefore requiring much higher costs for replacing the X-ray imaging hardware. Digital radiographs, whether produced by CR or DDR, can be manipulated, contrast enhanced and edges sharpened, and with appropriate software, measurements can be readily obtained.

MRI, CT and nuclear medicine are digital imaging techniques where the information contained in the image is stored in numerical form and thus can be manipulated in order to enhance contrast resolution. Spatial resolution can also be controlled by altering pre-imaging parameters. This technological advancement has been slower in conventional radiography, and there are at present a number of options for recording and thus measuring from the radiographic image.

1.4   Technical Limitations of Radiographs for Measurement

These fall into three categories:

1. Resolution—contrast and spatial
2. Magnification
3. Distortion

Resolution: Contrast and Spatial

The resolving capability of a particular radiographic material or fluorescent screen image is a measurement of the degree of fine detail which can be recorded. It is related to the unsharpness characteristics of the material as it is a measure of the ability to differentiate between adjacent positional detail. Resolution is often expressed as the number of lines per millimetre that can be seen as separate elements of an image. Spatial resolution is high for detailed conventional radiography as compared to CT where the degree of spatial resolution is limited by the field of view and matrix size employed.

The attenuation of the X-ray beam is inversely proportional to the square of the atomic number of the object/tissue being imaged. Therefore, the higher the atomic number, e.g. cortical bone, the greater will be the attenuation of the X-ray beam, and the lower the atomic number, the less the beam is attenuated as it passes through the tissue. In conventional radiography, tissues with a wide difference in density, such as cortical bone and soft tissue, can be readily appreciated. Tissues with a narrower difference in density such as fat and muscle can be differentiated but will require optimum viewing conditions to appreciate. Tissues with potentially a very narrow difference in density such as muscle and a non-metallic foreign body such as glass will require close attention by the radiographer to exposure factors (kilovoltage (kVp) and milliampere seconds (mAs)) and optimum viewing conditions for the reporting radiologist. The kilovoltage used is a major determinant of contrast resolution. In conventional radiography, contrast can be altered by adjustment of exposure parameters and is very much less than that which can be achieved with computed axial tomography (CT). Radiography is excellent for the evaluation of bone detail, whereas the soft tissue detail is poor. A large knee joint effusion is seen as distension of the suprapatellar pouch, but it can be extremely difficult if not impossible to identify if the joint distension is due to serous fluid from an arthritic process, due to pus from an infected joint or due to blood following trauma. If a haemarthrosis occurs in association with a fracture, then a fluid-fluid level due to layering of different density materials may be identified on a horizontal shoot-through radiograph.

Contrast and image sharpness have both subjective and objective connotations. Subject contrast is mainly influenced by kilovoltage and scattered radiation. The degree of scatter can be reduced by the use of grids.

Image sharpness is affected by the geometry of the equipment including the size of the focal spot and the relative distance between the focal spot, the subject and the film. The degree of geometric unsharpness can be controlled in several ways:

1. By using a smaller focal spot.
2. By decreasing the object to film distance.
3. By increasing the focus to object distance. In practice, this is equivalent to increasing the focus to film distance.

Focus Size

The production of X-rays is an inefficient system with approximately 98% of the energy used being produced as heat. With temperatures of the tube anode reaching close to 3000 °C during exposure, there is a need to dissipate heat effectively from the anode. This is achieved by use of a rotating angled anode and the ability of the operator to select one of two electron distribution areas on the anode referred to as the broad or the fine focus. Modern imaging units have an effective fine focus of the order of 0.4–0.6 mms and a broad focus of the order of 1.0–1.5 mms. The use

of an X-ray source of a finite size leads to penumbra effect which diffuses the edge of an object rendering it less distinct than if a point source was used (Fig. 1.2). At an operational focus to film distance of 100 cm or more, the effective width of the penumbra is minimal, but the smaller the value of the focus to film distance, the greater the penumbra effect.

Another cause of slight unsharpness of an object image when using film is the parallax effect. Radiographic film is made up of two separate emulsion coatings separated by a film base. X-irradiation or light striking the film will form two images. These can only be directly superimposed when viewed at the same angle as that at which the image forming radiation fell onto the film. Any slight offset between the two images is known as the parallax effect. Movement of the patient during the exposure and also the duration of the exposure itself may contribute to slight variations in image sharpness.

The use of intensifying screens can also be used to improve detail of the image. An intensifying screen consists of crystals suspended within a binding material. Faster screens which require a reduced number of photons to form the image have larger crystals which emit light when struck by an X-ray photon. The larger crystals limit the ability of the resultant image to resolve smaller structures. Slower intensifying screens which are designed to provide high detail have smaller crystals and a dye within the screen to limit the diffusion of light within the binder. This enables such a system to resolve between smaller structures.

For CR or DDR systems, the resolution of the system is dependent on the physical limitations of the plate reader (CR) or the photostimulable material used (DDR) to collect the image. Generally, digital systems are inferior to film in resolution, but this reduction in image quality is overridden by the flexibility offered by PACS software systems.

Some radiographic measurements are dependent on both spatial and contrast resolution. Exposure factors are very important here, and this is particularly in relation to measurements such as cortical thickness, joint space, size of erosions and prosthetic-bone-cement interfaces.
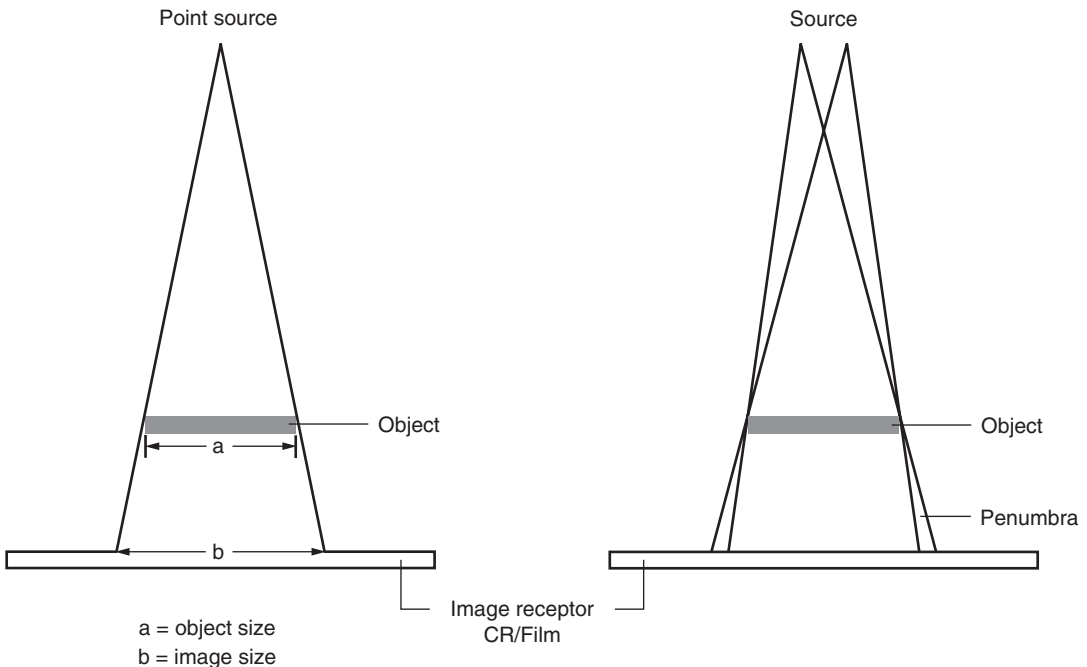
Fig. 1.2 Penumbral effects (see text)

Distortion

Image distortion results from the oblique projection of the image and can be produced in one of two ways:

1. Radiography using an angled beam (Fig. 1.3)
2. Radiography of an object not parallel to the film (Fig. 1.4)

Such image distortion can interfere with measurement, for example, in evaluation of the joint space where there may be a degree of flexion (deformity or positional). In a routine radiograph of the knee joint, the tibial condylar region slopes downwards by approximately 15° posteriorly, and therefore, in the standard anteroposterior view of the knee joint, the tibial plateau is not seen tangentially. Tibial plateau/condylar fractures can be overlooked on this account. An AP projection with 15° caudal angulation produces a tangential view of the plateau and facilitates observation of depressed fractures. Objects can also be angled in relation to the film in more than

one plane and can therefore be distorted in more than one plane, e.g. scoliosis and kyphosis.

Magnification

The X-ray beam diverges from the focus of the X-ray tube in straight lines so that the cross-sectional area of the beam increases with increasing distance from the X-ray source (Fig. 1.5). Therefore, the radiographic shadow image is always larger than the original subject and hence subject to a degree of magnification. The degree of magnification is calculated by the focus to film distance divided by the focus to object distance. The actual size can then be calculated:

Actual size = image size/magnification.

Within an imaging department, there are factors which will affect magnification:

1. Different manufacturer equipment and models will have different tabletop to film distance.

a = object size
b = image size

Fig. 1.3 Distortion, angled beam (see text)

a = object size
b = image size
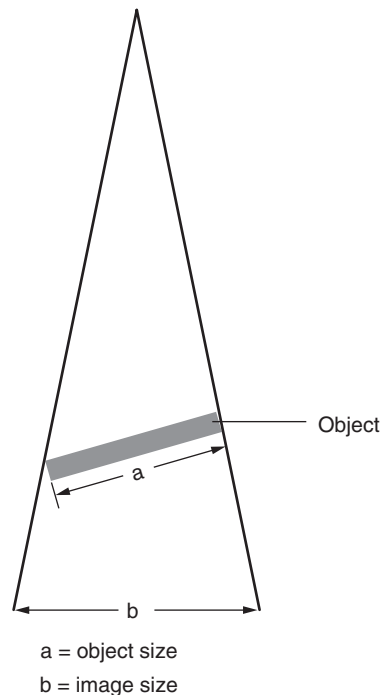
Fig. 1.4 Distortion, object not parallel to the film (see text)

This will contribute to the total object to film distance.

2. Physical size of the patient.
3. Departmental standard focus to film distance and the radiographer adherence to the standard. It must not be assumed that the presence of a standard guarantees that each image will be undertaken at the correct distance. It will vary between X-ray rooms in the same department.

Measurements taken direct from a radiograph are always subject to a degree of magnification. Even with radiography where the object imaged is in direct contact with the film, for example, weight-bearing views of the feet, there will always be a degree of magnification involved because the object imaged always has some thickness. The user must be aware that if taking a measurement from an uncalibrated image, they will not know the extent of magnification to which the object has been subjected. Many methods exist to calibrate an image. The favoured method is using a spherical object (as this is not subject to projectional distortion) of a known size placed at the same object to film distance as the object to be measured, e.g. in planning prosthetic requirement. The magnification to which the calibrating sphere has been subjected is calculated by magnification equalling measured size divided by actual size. In certain situations where direct measurements are required, such as for leg lengths, a measuring ruler can be placed beside the patient and radiographed beside the leg such that any magnification incurred will relate to both the image structure and the ruler measure facilitating a more accurate measurement. For PACS systems, plate (and therefore pixel size) is known and it may appear that there is increased accuracy in using measurement systems inbuilt within the PACS software. These systems however are not calibrated and some assume a magnification factor in the order of 10%. PACS imaging is subject to the same physical factors which affect radiographic film imaging.

Accurate measurements of joint space can be very important when trying to measure rate of disease progression in arthritis and particularly when this is part of a trial to evaluate the effect of

a = object size
b = image size
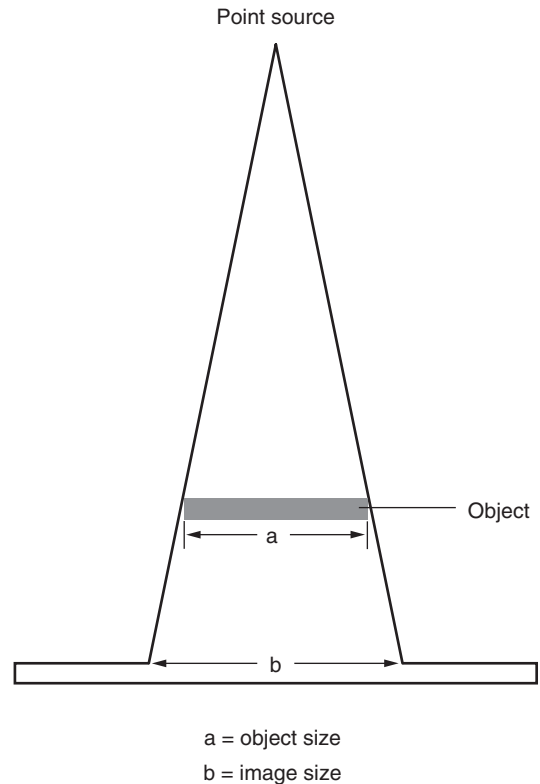
Fig. 1.5 Magnification effects (see text)

disease modifying drugs in arthritis. The use of the semi-flexed anteroposterior view, using a horizontal X-ray beam to produce a beam tangential to the tibial plateau and using fluoroscopy to achieve reproducible alignment, has been valuable (Buckland-Wright 1995). Microfocal radiography has been shown to improve reproducibility of joint space width measurement compared to standard radiography. The chief advantage of microfocal radiography is its spatial resolution, of the order of 10–100 μm, as compared to 300–1000 μm for standard radiography. The first longitudinal study of rates of joint space narrowing measured using microfocal radiography was carried out by Ward and Buckland-Wright (2008) which showed a lowered variability of the rate of joint space narrowing but the high cost and low availability of microfocal equipment remains a barrier to its more widespread use.

1.5 Anatomical Determinants

Anatomical features in certain areas of the body are associated with difficulties in obtaining accurate radiographic assessment and measurement. Such areas include:

1. The patellofemoral joint. Knee flexion to varying degrees has been advocated for the assessment of patellofemoral joint alignment. The conventional radiographic technique of a skyline view in 45° flexion with the X-ray beam angled 30° towards the floor (Merchant's view) (Merchant et al. 1974) has been largely superseded by CT or MR assessment in varying degrees of flexion (10–30°), as at 45° the patella is forced into the intercondylar notch even when prone to subluxation or maltracking (Walker et al. 1993).
2. The hip joint when evaluating for SUFE. An X-ray image is a two-dimensional view of a three-dimensional object. By taking two views at right angles to each other, a three-dimensional image can be built up visually. However, the axial or Z projection is not obtainable, and thus, measurements that might be valuable in this plane cannot be obtained. The angle of slip in SUFE is well seen on axial CT or MR images.
3. Weight-bearing views. These are more accurate for the depiction of joint space narrowing especially in arthritic states. It is important that when comparative assessments are made that like is compared with like, i.e. weight bearing with weight bearing.
4. Dynamic views. A linear measurement in orthopaedics is taken between two bone points of interest. At rest, this measurement can be within the normal range implying that the stabilising soft tissue structures are intact. Dynamic views unmask the loss of soft tissue integrity by showing differing measurement between the same bone points which lies outside the normal range, as may be found, for example, following a spinal injury, or in cases of instability arising in other conditions such as rheumatoid arthritis (Fig. 1.6).

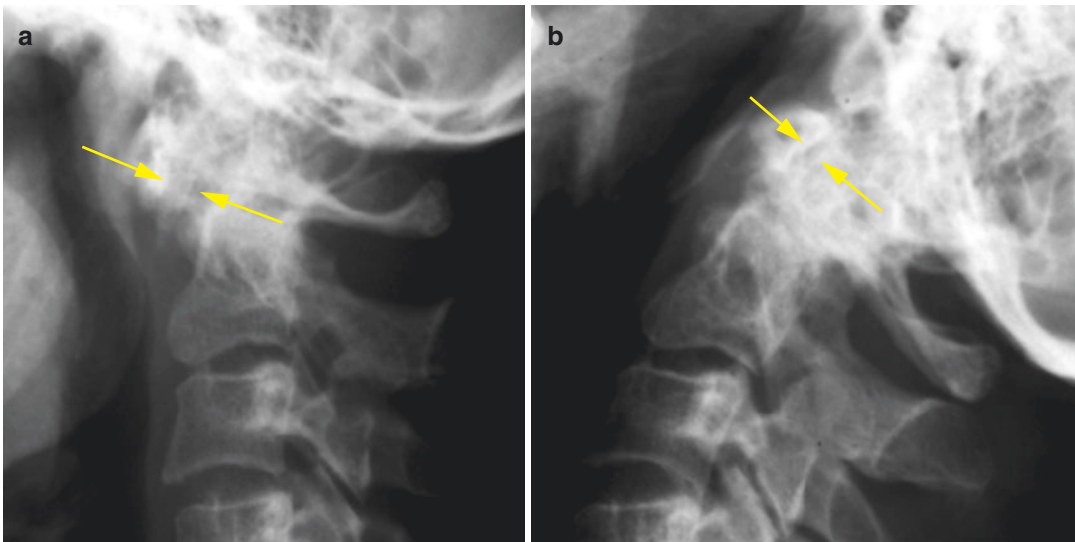**Fig. 1.6** (**a**, **b**) Lateral radiographs of the cervical spine in (**a**) flexion and (**b**) extension in a patient with rheumatoid arthritis. Note the abnormal movement at the atlanto-axial junction (arrows), with marked widening in flexion indicating anterior atlanto-axial instability

1.6   Orthopaedic Templating

Orthopaedic templating is an important element of pre-surgical planning for arthroplasty surgery where the appropriate size of implant to be used must be determined prior to surgery.

This has traditionally been undertaken using acetate templates provided by implant companies which were placed over conventional X-ray images. The acetates enabled the selection of the appropriate-sized implant with measurements in theatre contributing to the final choice of implant. These acetates assume a standard magnification for all radiographs of a particular joint, e.g. 10% for hip images.

With the advent of PACS, the overlay of an acetate template is no longer possible. A number of commercial software packages have been developed which will work within or separate to PACS enabling the user to assess the size of implant required. For accuracy, the magnification of the image must be calculated. This can either be by assessing the magnification of an object of a known size (e.g. a metallic ball) or by calculating the magnification by measurement of the focus to film distance and the object to film distance.

For the use of an object of a known size, accurate calibration relies on the placement of the object at the same distance from the film as the anatomical feature to be measured, in this case the head of femur. Such systems are therefore reliant on the careful placement of the calibrating object.

There is evidence to suggest (Franken et al. 2010) that more accuracy can be gained by measurement of the focus to film and object to film distances and calculating the magnification in this way. This can be achieved using callipers or commercially available products.

Some PACS systems will make an assumption in relation to magnification if no calibration is supplied, and care must be taken to ensure that where accurate measurement is required, e.g. the provision of custom implants, these are only taken using calibrated images.

Many companies are now developing the functionality of the software packages beyond orthopaedic templating to enable the determination of angles and the ability to aid surgical planning by estimating the appropriate size required for:

1. Plates
2. Nails
3. Screws

Many packages now offer the ability to determine osteotomy planning and specific paediatric planning and may prove to be more reliable than conventional methodology (Hankemeier et al. 2006).

Where CT images are available, orthopaedic templating is also available using 3D information. It is anticipated that the use of such software packages will grow in direct relation to the increasing use of PACS systems.

1.7   The Role of the Radiograph Related to Other Imaging Techniques

As outlined earlier in this chapter, radiographs have many advantages as a technique for measurement of various parameters in musculoskeletal conditions. There are limitations however which are largely related to contrast (largely related to the soft tissues) and also to image sharpness which can lead to blurring of image margins and hence a reduction in accuracy of the measurement. The advantages of other specific imaging modalities will be addressed in later chapters. Ultrasound is particularly good for superficial soft tissue measurements. CT with its superb contrast resolution particularly cross-sectional assessment of bone structures facilitates measurement in all imaging planes including the Z projection. MR with its particular soft tissue contrast allows evaluation of both soft tissue and marrow measurements again in all three imaging planes and indeed also in oblique planes as required. Conventional radiography however is readily available in most departments, is universal and can be reproduced at minimal relative cost. This ensures that it will remain as a mainstay in both diagnostic and evaluation processes for some time. However, even with the advent of PACS, care must be taken as regards calibration and ensuring accuracy of measurement techniques.

References

Buckland-Wright C (1995) Protocols for precise radio anatomical positioning of the tibiofemoral and patellofemoral compartments of the knee. Osteoarthr Cartil 3(Suppl A):71–80

Franken M, Grimm B, Heyligers I (2010) A comparison of four systems for calibration when templating for total hip replacement with digital radiography. J Bone Joint Surg (Br) 92-B:136–141

Greulich W, Pyle S (1959) Radiographic atlas of the skeletal development of the hand and wrist. Stanford University Press, Stanford, CA

Hankemeier S, Gosling T, Richter M, Hufner T, Hochhausen C, Krettek C (2006) Computer-assisted analysis of lower limb geometry: higher intraobserver reliability compared to conventional method. Comput Aided Surg 11(2):81–86

Merchant AC, Mercer RL, Jacobsen RH, Cool CR (1974) Roentgenographic analysis of patellofemoral congruence. J Bone Joint Surg Am 56:1391–1396

Risser JC (1958) The iliac apophysis: an invaluable sign in the management of scoliosis. Clin Orthop 11:111

Sauvegrain J, Nahm H, Bronstein N (1962) Etude de la maturation asseuse du coude. Ann Radiol 5:542

Tanner J, Whitehouse R, Marshall W et al (1975) Assessment of skeletal maturity and prediction of adult height (TW2 method). Academic, London

Walker C, Cassar-Pullicino VN, Vaisha R, McCall IW (1993) The patello-femoral joint—a critical appraisal of its geometric assessment utilising conventional axial radiography and computed arthrotomography. Br J Radiol 66(789):755–761

Ward RJ, Buckland-Wright JC (2008) Rates of medial tibiofemoral joint space narrowing in osteoarthritis studies consistent despite methodological differences. Osteoarthr Cartil 16(3):330–336

Computed Tomography

2

Richard W. Whitehouse

Contents

2.1 Introduction

Measurements relevant to the musculoskeletal system that can be made on CT include distances and angles from the scout view, distances, angles and CT numbers from individual axial sections and more complex three-dimensional distances and angles from separate axial sections or reformatted images. Volumes can be estimated from the measured dimensions of the tissue in question or by summing the product of cross-sectional area measurements and slice spacing. CT number measurement gives rise to tissue density estimation, the accuracy of which can be improved by dual-energy scan techniques.

The use of computed tomography for distance and angle measurements has both advantages and limitations compared with plain film radiography, ultrasound and magnetic resonance imaging. Because X-rays travel in straight lines, the location of points defined by axial CT images should not be distorted in the X or Y directions, unlike MR images where image distortion by magnetic field variations occurs. The geometric magnification that occurs in conventional radiography does affect the CT scout view, as described below. Point location in the Y-axis (along the direction of table travel) may be less accurate on axial images, due to the slice thickness, but multislice spiral scanners are

R. W. Whitehouse
Department of Clinical Radiology,
Manchester Royal Infirmary,
Oxford Road, Manchester M13 9WL, UK
e-mail: richard.whitehouse@cmmc.nhs.uk

capable of isometric (X, Y and Z plane) resolution so that measurements between points located on different axial slices should be of comparable accuracy to in-plane measurement. CT utilises ionising radiation, the minimum number of axial sections and lowest mA and kV settings that can produce acceptable images should routinely be used.

There is little recent literature confirming the in vitro accuracy of CT length and angle measurements, with most of the early studies published in the German literature. This chapter is therefore illustrated with in vitro scans depicting measurements that have been compared with the results of calliper and protractor measurements of the scanned objects.

2.2   Scout View Measurements

The scout view is generated by smooth, uniform velocity movement of the scanner table through the scanner aperture, whilst a thinly collimated fan beam of X-rays from the stationary tube is projected across the aperture to the detectors. The data acquired from the detectors at each point in time forms one line across the final image, the location of which within the image is directly related to the table location at that point in time. Consequently, measurements along the long axis of the scanner are potentially as accurate as the table location, which is calibrated to an error of less than 0.5 mm. Measurement across the image is, however, distorted by the fan beam geometry, with objects closer to the X-ray tube being magnified in this direction relative to those nearer the detectors. The image is calibrated to give accurate measurement across the image at the gantry isocentre; consequently table height adjustment to bring the structure being measured as close to the isocentre as possible is necessary for the most accurate result. Figure 2.1 illustrates the effect of altering table height on scout view measurements, using a femur as a test object. Small metallic markers were placed on the top of the femoral head, on the top of the femoral neck, on the lesser trochanter and on the back of each femoral condyle. These can be seen in Fig. 2.1a. Figure 2.1b–d shows the scout view appearances with the table as low as possible (closest to the
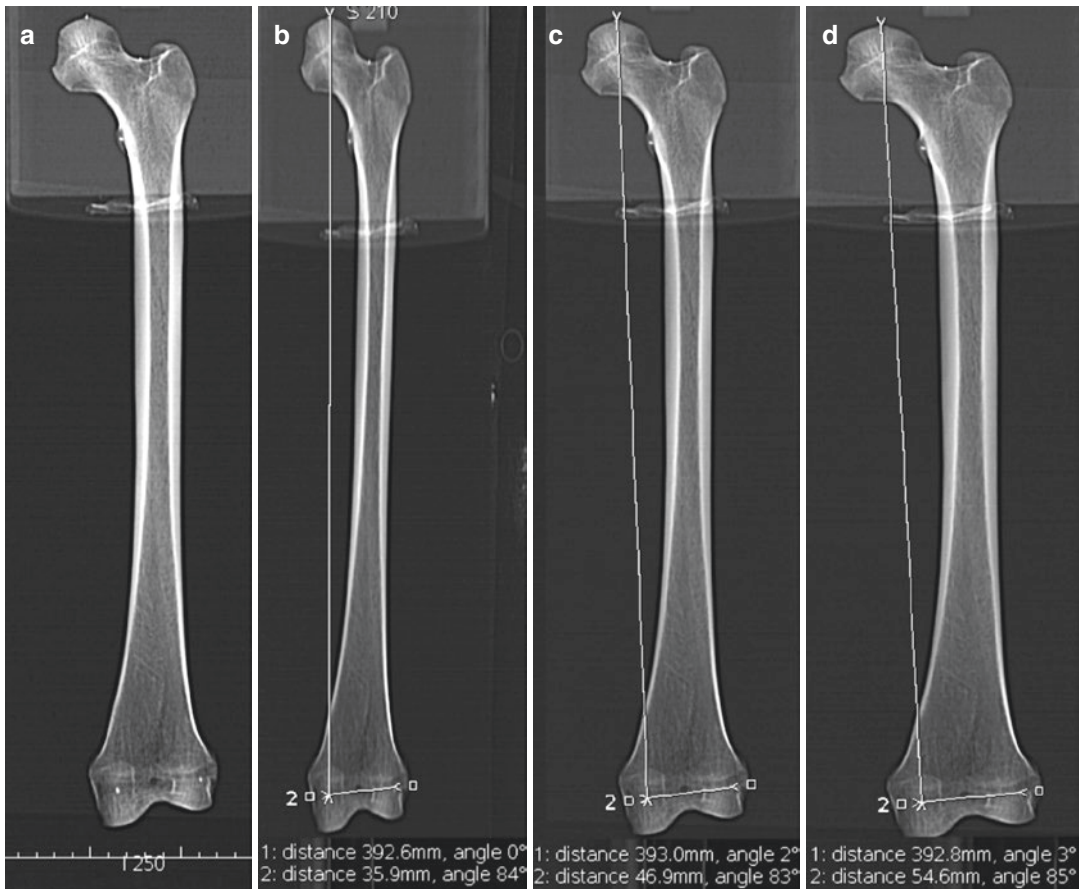
Fig. 2.1   Scout view (scan projection radiographs) of a dry femur at various table heights, demonstrating distortion across the image by geometric magnification. (**a**) With the femur at the isocentre. Note small metal markers are present on the head, neck and condyles for measurements. The apparent length of the bone is not altered in any of the subsequent views. (**b**) Table at its lowest setting. (**c**) Table adjusted to put the femur at the isocentre. The apparent width between the condyle markers is the same as that measured on the specimen. (**d**) Table at its highest setting. The apparent width of the bone is increased

detectors), at the isocentre, and as high as possible (close to the tube). The length of the femur, between the top of the head and the marker on the medial femoral condyle, is not significantly different between these scans, and results of 392.6, 393 and 392.8 mm are all within a reasonable measurement error of the 392 mm distance measured with callipers on the femur. The measurement between the condyle markers varies from 35.9, through 46.9 to 54.6 mm with the different table heights, compared with a calliper measurement of 47 mm, confirming the accuracy of measurement at the isocentre but showing errors of −23% to +16% at the other positions. Angles measured from scout views will have composite errors, from distortion by magnification across the image and also a projection error if the points being measured represent structures at different heights from the tabletop (i.e. if the plane of the measurement points is not perpendicular to the centre of the fan-beam).

Scout views are equivalent to digital radiography, using highly efficient solid-state X-ray detectors on modern multislice scanners. Consequently, a satisfactory image can be achieved at lower radiation doses than required for conventional radiography. When used for lower limb length measurement, further effective dose reduction can be achieved with the use of gonad protection.

2.3   Axial Plane Measurements

On a single axial CT image, distance and angle measurements are standard scanner console or workstation functions. As Fig. 2.2 demonstrates, angles measured from a scanned protractor are within 1° of the expected measurement. Similarly, distances are within 1 mm of the expected distance as measured on the scanned set square. The precisions of such measurements are dependent upon the reproducibility of the placement of measurement points. The scanned image is accurate to the resolution of the scanner (two to three line pairs per millimetre on a small field of view), but the reproducibility of placement of points from which measurements might be taken will be influenced by partial volume averaging, mislocation of the slice and inter- and intra-operator variations.

Fig. 2.2 CT scan of a plastic protractor and a set square. Radiodense markers were placed at fixed points on these objects and measurements between them made on the scanner workstation. All distances were within 0.5 mm and angles within 0.7° of expected
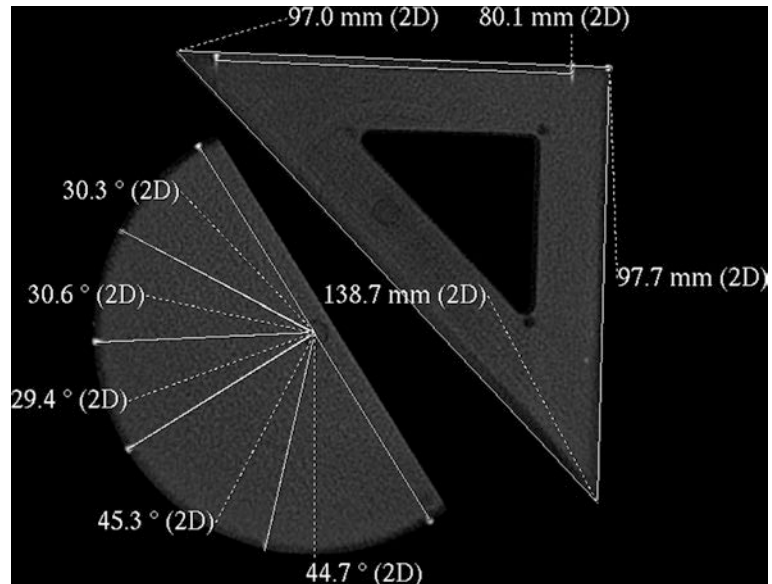
2.4 Three-Dimensional Measurements

When measuring between points on different sections, three-dimensional geometrical calculations are required. If a complete dataset is acquired, with all sections between the two measurement points being available, then a reformatted image on the workstation, angled to include both points, can be used to make the measurement, using the workstation software (Fig. 2.3). If only selected sections are performed (to reduce X-ray exposure to the patient), then the locations in space for each point can be identified as X, Y and Z Cartesian coordinates, from which the distance between the points can be calculated (a visual representation

of this is shown in Fig. 2.4). Similar calculations can be derived for angle measurements between points on separate slices. When applied to a dry skull, linear distances between fixed points, measured as coordinates, were accurate to within 5% when slice thicknesses of 3 mm or less were used but exceeded this error for thicker sections (Togashi et al. 2002).

Measurement of the bone torsion usually relies on measuring planes through defined points at each end of the bone and then calculating the angle between the two planes. A plane is defined by three points in space, but only two points are used for each plane in these estimations, as the plane is assumed to be parallel to the Z-axis of the image dataset. This assumption is only valid if
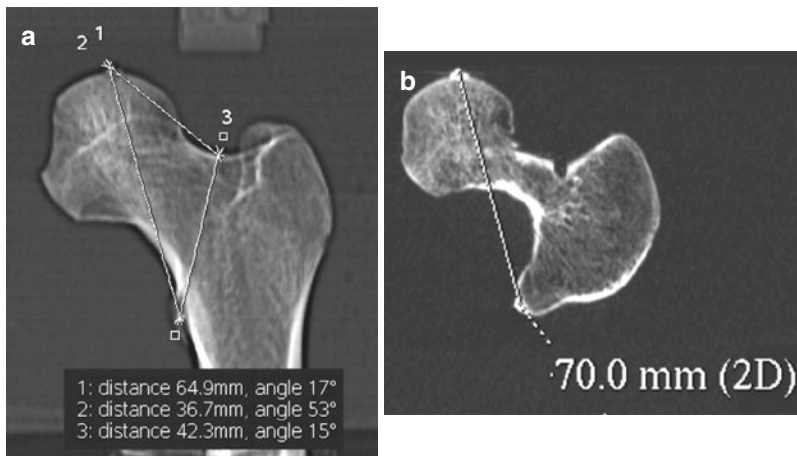
Fig. 2.3 (**a**) Scout view of the upper femur, at the isocentre. The measurement number 1 is between the metal markers on the top of the femoral head and the lesser trochanter, estimated at 64.9 mm on the scout view. These markers were not in the same plane relative to the tabletop; consequently, this distance is foreshortened on the

scout view. (**b**) Coronal oblique reconstruction from axial 0.6-mm-thick contiguous sections to pass through both the metal markers described in (**a**). The distance between them now measures 70 mm, identical to that measured with callipers on the specimen

Fig. 2.4 Composite image demonstrating the relationship between sections containing measurement points, the scout view and the X, Y and Z axes of the dataset
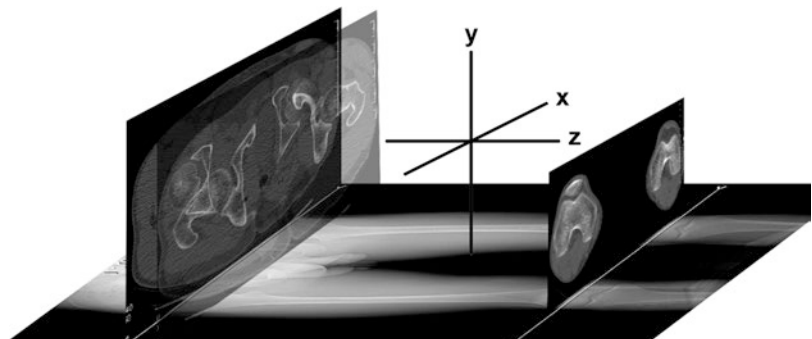
the long axis of the bone being measured is aligned along the *Z*-axis (direction of table travel). The two points defining each plane may not be on the same axial section. Consequently, superimposition of the axial images (Fig. 2.5) (or transfer of the *x,y* coordinates of one point to the image containing the second point (Fig. 2.6)) is used to measure the angle between these points and the horizontal. This angle is then compared to the angle for the second plane to give the total torsion. Such measurements in vitro have shown high precision and accuracy, with some authors claiming that little error is introduced when the long axis of the bone is deviated from the *Z*-axis of the dataset by up to 15° (Dähnert and Bernd
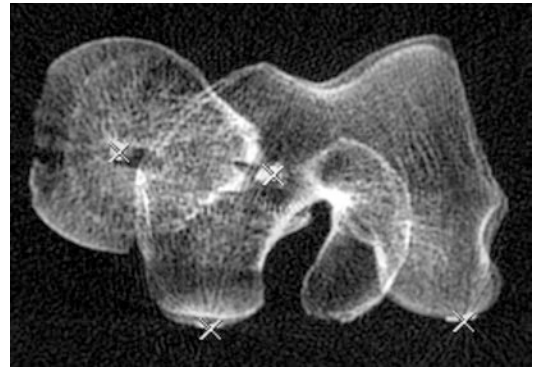
Fig. 2.5 Overlaid image of the axial sections that contain metal markers on the femoral head, neck and condyles. Planes between the relevant pairs of markers can now be drawn and the angle between them measured
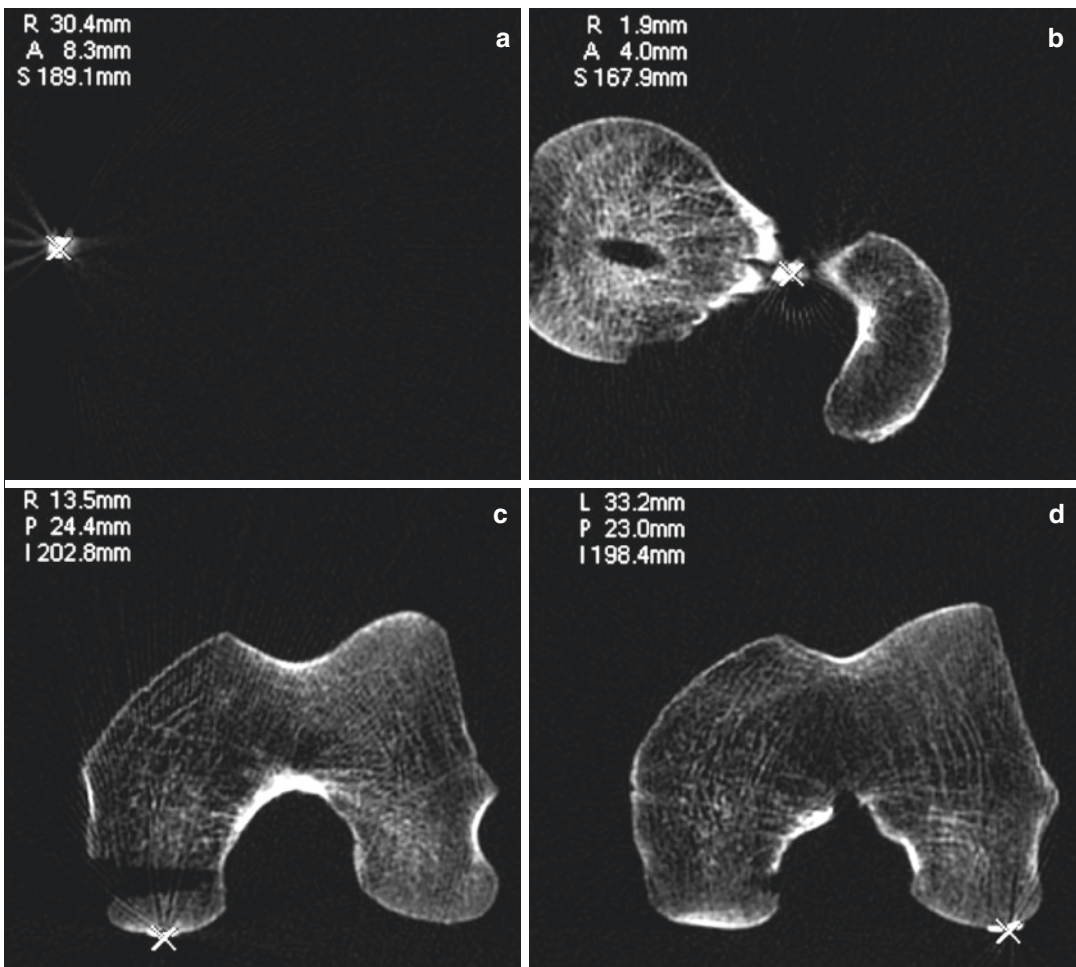
Fig. 2.6 (**a**–**d**) Axial sections through the metal markers on the femoral head (**a**), neck (**b**), medial (**c**) and lateral (**d**) posterior condylar surfaces. For each section, the scanner has identified the point location by reference to the scanner baseline isocentre, in millimetres to the right, left, anterior, posterior, superior or inferior. These relative locations in space allow geometric calculation of the planes, distances and angles between them. These same images are superimposed in Fig. 2.5

1986). Results of such measurements will, how-
ever, vary with the definition of the anatomical
points used and may be influenced by flexion or
varus deformity of the bone (Starker et al. 1998).

One study of femoral anteversion, using three-
dimensional surface reconstructions of the femur
from full CT image datasets, found them to be
less reproducible than selected slice techniques
when the femoral alignment was abnormal
(flexed, adducted and internally rotated to simu-
late cerebral palsy), though the three-dimensional
technique was more accurate (14% of measure-
ments falling within 5° of actual, compared with
3% of 2D measurements) (Davids et al. 2003).

Three-dimensional surface reconstructions
from MDCT data give a clear visual representa-
tion of the structure being assessed and make it
easier to identify and correct for abnormal posi-
tioning. This is relevant, for example, in assess-
ment of acetabular retro- or anteversion, where
the measurement is influenced by pelvic tilting.
Using 3D bone surface reconstruction of the pel-
vis, the pelvic tilt can be identified and the image
rotated to correct it, with subsequent measure-
ments of acetabular version being made in the
true pelvic axial plane (Dandachli et al. 2009).
The standardised pelvic plane joins the anterior
superior ischial spines and the pubic tubercles
(Fig. 2.7a), with the axial plane being perpendic-
ular to this (Fig. 2.7b, c). Radiation dose reduc-
tion could be achieved by identifying the ASIS
locations from limited low-dose sections through
this level, rather than scanning the entire pelvis.

Assessment of the shape of the femoral head and
neck is also currently in vogue, for the demonstra-
tion of bony deformities that cause cam impinge-
ment. Simple measurements of the alpha angle are
influenced by the orientation of the plane of section
chosen through the femoral head and neck. Using a
MDCT 3D reconstruction of the proximal femur
allows a full assessment of the location, size and
"true" alpha angle of a cam deformity to be mea-
sured (Beaulé et al. 2005; Audenaert et al. 2011).

Three-dimensional surface reconstructions of
the hips can also be used to identify the acetabu-
lar margin over the femoral head, to estimate
femoral head coverage in dysplasia (Dandachli
et al. 2008).
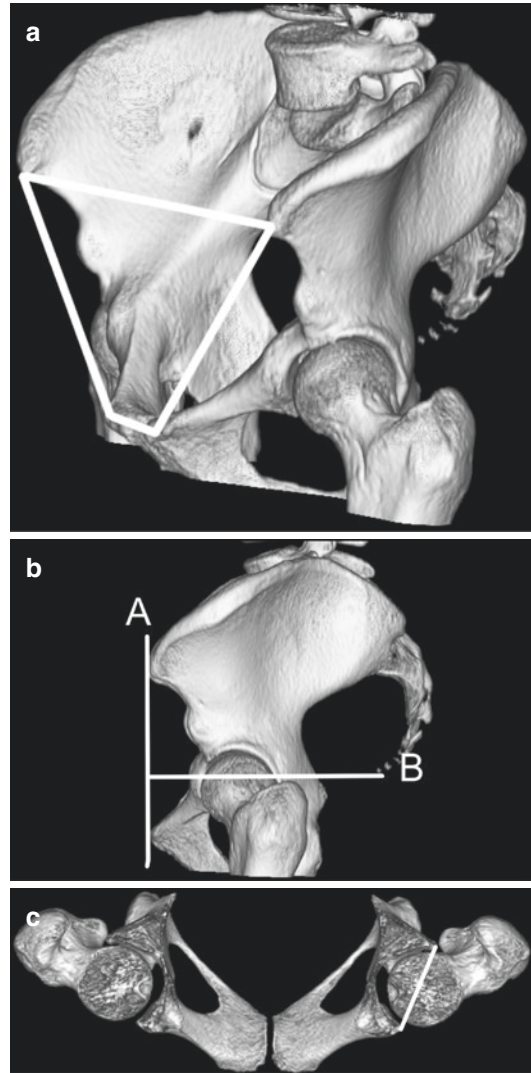
Fig. 2.7 (**a**) Automated 3D surface reconstruction of the
pelvis from MDCT dataset. The white lines join the ante-
rior superior iliac spines and pubic tubercles. (**b**) The
image is then rotated until the plane defined by these lines
is vertical (line "A") to correct pelvic tilt, the true axial
plane (line "B") is perpendicular to this. (**c**) Axial plane
measurements, (such as acetabular version) are then made
in the true transaxial plane

Three-dimensional surface reconstructions of
malunited fractures can also be manipulated on a
workstation, with virtual correction of the deformity
used to make custom jigs that fit onto the bone during
surgery to identify the optimum osteotomy location
and then fits the cut ends of the bone to allow accurate
correction of the deformity (Murase et al. 2008).

Comparisons with Other Techniques (Linear Measurements)

Femoral anteversion has been measured clinically and by using plain radiography, CT, MR and ultrasound (Günther et al. 1996). CT is currently accepted as the standard for this measurement but has the limitation of a relatively high ionising radiation dose. Ultrasound measurement identifies surface locations on the bone; consequently, the absolute results obtained may differ from CT (Miller et al. 1993), where measurement points may be intra-osseous. Relative imprecision of ultrasound localisation of measurement points has been described, both as acceptable (Günther et al. 1996; Aamodt et al. 1995) and unacceptable in an earlier study using a static ultrasound scanner (Berman et al. 1987), for this measurement method. MR can achieve results similar to CT (Günther et al. 1996) and has the advantage of not using ionising radiation. This may therefore become the standard, particularly for measurement in children.

2.5 CT Volume Measurements

The approximate volume of structures with spherical or near spherical shapes can be estimated from measurement of the diameter of the structure in three orthogonal planes, averaging the result and calculating a volume using the formula for a sphere:

$$\text{Volume} = 4/3\pi \left(d/2\right)^3$$

π = pi
d = diameter

For irregular-shaped structures, where the boundaries are clearly defined by a steep CT number gradient (such as pulmonary nodules), then image analysis software packages are now available that will identify the lesion boundaries and calculate its volume automatically, from a summation of the contained pixel numbers and the voxel volume represented by each pixel. Similar manual methods have been used for decades, tracing the outline of the structure on each section, summating the areas obtained and multiplying by the slice spacing. Such manual methods have errors introduced by the window level, size and shape of the structure being measured and the surrounding tissue contrast (Schultz and Lackner 1980). The ratio of the Z-axis diameter of the structure being measured to the section thickness of the measurement slices will also influence volume estimation, in part due to partial volume averaging effects (Schultz and Felix 1978). Using low-dose 3-mm-thick sections applied to the orbits, resulting in on average ten contiguous sections through the structure of interest, we have achieved inter-observer precision of 1.3% and accuracy error of 1.5% for volume measurement (McGurk et al. 1992). Such methods have been applied to muscle volume measurement, for example, in the paraspinal muscles (Fig. 2.8) (Keller et al. 2003) and thighs (Rådegran and Saltin 2000). Measurement of fat and lean soft tissue areas can also be used to estimate body composition (Müller et al. 2002). In vivo measurements in animals (sheep) using just two sections through the hip and loin gave a correlation with dissection adipose mass of 0.79 (Lambe et al. 2006).

Estimation of lung volume from 3D MDCT volume reconstructions has been used to assess the impact of spinal scoliosis surgery (Gollogly et al. 2004a, b), with the degree of scoliosis also quantified three dimensionally (Dubousset et al. 2003). With the thin axial sections routinely produced by MDCT, high-resolution 3D images can be constructed with commercially available software, and the enclosed volume represented by the image (Fig. 2.9) can be automatically calculated.
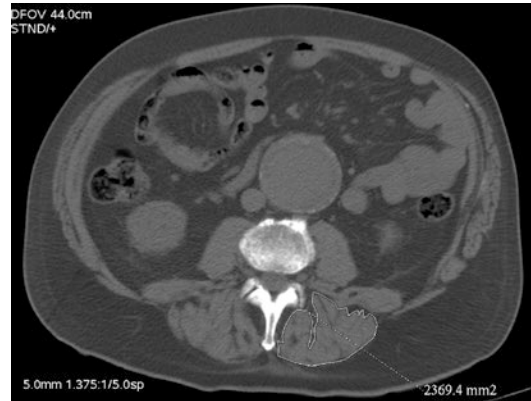
Fig. 2.8 Axial CT section through the mid-abdomen. A region of interest has been drawn around the left paraspinal musculature and its cross-sectional area measured
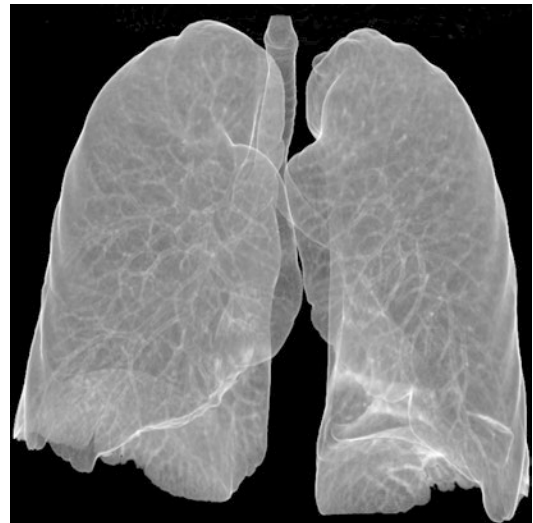
Fig. 2.9 Automated 3D reconstruction of the lungs from MDCT dataset. Commercially available software can measure the lung volume using similar image segmentation

As the lung/soft tissue and the bone/soft tissue interfaces are both high-contrast boundaries, a low-dose CT technique would be appropriate for this.

Semiautomated methods of lymph node volume and linear dimension measurements from MDCT data have been shown to be more precise and better predictors of disease involvement in lymphoma than manual measurements (Buerke et al. 2010).

2.6   CT Number Measurements

The CT number of a pixel in a CT image is an approximation to the Hounsfield value but requires calibration against a reference material to give an accurate Hounsfield unit measurement from an individual scan, as scanner calibration may drift with time and room temperature and may also vary with patient size. The Hounsfield value is a measure of the average voxel X-ray attenuation, compared to the attenuation of water, according to the formula:

$$\mathrm{HU}_{(s)} = \left(\mu_{(s)} - \mu_{(w)} \, / \, \mu_{(w)}\right) \times 1000$$

$\mathrm{HU}_{(s)}$ = Hounsfield unit value of substance filling the voxel
$\mu_{(s)}$ = linear attenuation coefficient of substance filling the voxel
$\mu_{(w)}$ = linear attenuation coefficient of water

Although this appears to calibrate Hounsfield unit measurements against water, the linear attenuation coefficients of different materials vary with X-ray photon energy. Consequently, the HU value of materials with higher average atomic numbers than water increase with reducing X-ray energy, and vice versa. Consequently, to use Hounsfield measurements to estimate the concentration or density of a known material, the scan is calibrated against that material, or an equivalent material of similar average atomic number.

Calibration against material within the patient can have limited application. Hepatic haemangiomas largely contain blood and consequently have CT numbers close to that of the patients' aorta (Whitehouse 1991).

Single Energy Quantitative Computed Tomography (SEQCT)

This technique is most often used to estimate vertebral trabecular bone mineral density. The patient is scanned whilst lying on a reference phantom which contains a water, or water equivalent, reference material and usually several different known concentrations of a bone mineral

equivalent material, dissolved or suspended within water equivalent materials. A calibration curve of CT number against mineral concentration is produced from the reference materials, from which the CT number of a region of interest in the vertebral trabecular bone can be converted into a mineral density equivalent. With care and experience, measurements with a precision error (reproducibility) of better than 1% can be achieved.

Dual-Energy Quantitative Computed Tomography

SEQCT is precise but lacks accuracy, as (for vertebral mineral densitometry) the presence of variable amounts of marrow fat cannot be accommodated for. The linear attenuation coefficients for the three materials in a vertebra (bone, red marrow and yellow marrow) are widely different and also change in different directions with changing scanner kVp. Theoretically, scanning the vertebra at two different kVp values can be used to estimate the proportions of each by solving the simultaneous equations below:

$$V_b + V_r + V_y = 1.$$

$$\mathrm{HU}_b(l) \times V_b + \mathrm{HU}_r(l) \times V_r + \mathrm{HU}_y(l) \times V_y = \mathrm{HU}_v(1).$$

$$\mathrm{HU}_b(h) \times V_b + \mathrm{HU}_r(h) \times V_r + \mathrm{HU}_y(h) \times V_y = \mathrm{HU}_v(h).$$

where
V_b, V_r and V_y are the volume proportions of bone, red marrow and yellow marrow, respectively.

$\mathrm{HU}_b(l)$, $\mathrm{HU}_r(l)$, $\mathrm{HU}_y(l)$ and $\mathrm{HU}_v(l)$ are the Hounsfield unit values for bone, red marrow, yellow marrow and the vertebral region of interest at the low kVp scan.

$\mathrm{HU}_b(h)$, $\mathrm{HU}_r(h)$, $\mathrm{HU}_y(h)$ and $\mathrm{HU}_v(h)$ are the Hounsfield unit values for bone, red marrow, yellow marrow and the vertebral region of interest at the high kVp scan.

HU_b, HU_r and HU_y are measured from materials in the reference phantom, and HU_v is measured in the vertebra, at each scan energy, respectively. V_b, V_r and V_y are the unknowns.

Reference materials for red and yellow marrow (and even bone) are somewhat unsatisfactory. Large errors can occur if the materials do not show the same X-ray energy-dependent change in attenuation as the material being measured. A sophisticated method of overcoming this limitation of reference material was described by Nickoloff, who used the reference phantom calibration curve to estimate the effective X-ray energy of the scan and then used published linear attenuation coefficient data to calculate the expected Hounsfield unit values of the materials, rather than measuring them from a phantom (Nickoloff et al. 1988).

Dual-energy QCT has not been widely used, as it increases the patient radiation dose, is in practice of little advantage over SEQCT and has a considerable poorer precision. The error in SEQCT bone mineral estimation attributable to marrow fat is in the range of 5–15% and has a significant age dependency. Consequently, if age-related reference data is used, the error is relatively small (Glüer and Genant 1989). A further improvement in the accuracy of SEQCT for bone mineral estimation is achieved by lowering the kVp, on those scanners with this facility. At 80 kVp (instead of the more usual 120–140 kVp), the CT number for mineral is markedly increased, whilst the reduction in CT number for fat is less great. Consequently, the CT number for a mixture of the two has a greater dependence upon the mineral concentration. DEQCT has been used to estimate liver iron in patients with haemochromatosis and haemosiderosis from repeated transfusion. There may be a recrudescence of interest with the development of a dual X-ray source CT scanner that acquires both energies almost simultaneously and can produce separate high and low atomic number material images directly.

Comparisons with Other Measurements (Density Measurements)

Currently, the accepted standard technique for bone mineral density measurement is dual-energy X-ray absorptiometry (DXA). This method utilises low-dose X-rays, filtered to produce alternating high- and low-energy X-ray beams and scanned across the region of interest. Results of these scans give an estimate of the total mineral in the scan path, per unit area of the projection; thus trabecular and cortical bone (plus any soft tissue calcification, facet joint osteoarthosis) that lies in the same part of the projected image is included in the result. Despite these limitations, DXA is a very precise measurement method; uses lower X-ray doses than QCT; can provide measurements in the spine, hip, whole body or selected regions; and is cheaper. Consequently, it was adopted by the WHO within its definition of osteoporosis (Miller 2006). QCT has the advantage of measuring trabecular bone separately from cortex and other calcifications and being a true volumetric density is not influenced by patient size.

Conclusions

Computed tomography produces images of excellent dimensional stability. When submillimetre section thickness is used, clearly defined anatomical points can be located in all three dimensions and measurements between them made with high accuracy. The limitation, as with all measurement, is largely in the anatomical definition and precision of point placement. Care to ensure that slice location is correct, that the patient does not move between slice acquisitions and that appropriate consideration of the three-dimensional geometry is allowed for in the measurement technique should optimise the result. Steps to minimise X-ray dose to the patient should be routinely employed—low mA, low kV scans and the use of low mA scout views to place the minimum number of axial sections required for the measurement. Lead gonad protection can also be used for the scout views and high-density (bismuth) protectors can also reduce radiation dose to selected superficial structures on axial sections, without significantly impairing image quality (Hohl et al. 2006).

References

Aamodt A, Terjesen T, Eine J, Kvistad KA (1995) Femoral anteversion measured by ultrasound and CT: a comparative study. Skelet Radiol 24:105–109

Audenaert EA, Baelde N, Huysse W, Vigneron L, Pattyn C (2011) Development of a three-dimensional detection method of cam deformities in femoroacetabular impingement. Skelet Radiol 40:921–927

Beaulé PE, Zaragoza E, Motamedi K, Copelan N, Dorey FJ (2005) Three-dimensional computed tomography of the hip in the assessment of femoroacetabular impingement. J Orthop Res 23:1286–1292

Berman L, Mitchell R, Katz D (1987) Ultrasound assessment of femoral anteversion. A comparison with computerised tomography. J Bone Joint Surg Br 69:268–270

Buerke B, Puesken M, Müter S, Weckesser M, Gerss J, Heindel W, Wessling J (2010) Measurement accuracy and reproducibility of semiautomated metric and volumetric lymph node analysis in MDCT. Am J Roentgenol 195:979–985

Dähnert W, Bernd W (1986) Computertomographische Bestimmung des Torsionswinkels am Humerus. Z Orthop Ihre Grenzgeb 124:46–49

Dandachli W, Kanna V, Richards R, Shah Z, Hall-Craggs M, Witt J (2008) Analysis of cover of the femoral head in normal and dysplastic hips: new CT-based technique. J Bone Joint Surg Br 90-11:1428–1434

Dandachli W, Ul Islam S, Liu M, Richards R, Hall-Craggs M, Witt J (2009) Three-dimensional CT analysis to determine acetabular retroversion and the implications for the management of femoro-acetabular impingement. J Bone Joint Surg Br 91-8:1031–1036

Davids JR, Marshall AD, Blocker ER, Frick SL, Blackhurst DW, Skewes E (2003) Femoral anteversion in children with cerebral palsy. Assessment with two and three-dimensional computed tomography scans. J Bone Joint Surg Am 85-A:481–488

Dubousset J, Wicart P, Pomero V, Barois A, Estournet B (2003) Spinal penetration index: new three-dimensional quantified reference for lordoscoliosis and other spinal deformities. J Orthop Sci 8:41–49

Glüer CC, Genant HK (1989) Impact of marrow fat on accuracy of quantitative CT. J Comput Assist Tomogr 13:1023–1035

Gollogly S, Smith JT, Campbell RM (2004a) Determining lung volume with three dimensional reconstructions of CT scan data. A pilot study to evaluate the effects of expansion thoracoplasty on children with severe spinal deformities. J Pediatr Orthop 24:323–328

Gollogly S, Smith JT, White SK, Firth S, White K (2004b) The volume of lung parenchyma as a function of age: a review of 1050 normal CT scans of the chest with three-dimensional volumetric reconstruction of the pulmonary system. Spine 29:2061–2066

Günther KP, Kessler S, Tomczak R, Pfeifer P, Puhl W (1996) (femoral anteversion: significance of clinical methods and imaging techniques in the diagnosis in children and adolescents). Title in original lang. Femorale Antetorsion: Stellenwert klinischer und bildgebender Untersuchungsverfahren bei Kindern und Jugendlichen. Z Orthop Ihre Grenzgeb 134:295–301

Hohl C, Wildberger JE, Süss C, Thomas C, Mühlenbruch G, Schmidt T, Honnef D, Günther RW, Mahnken AH (2006) Radiation dose reduction to breast and thyroid during MDCT: effectiveness of an in-plane bismuth shield. Acta Radiol 47:562–567

Keller A, Gunderson R, Reikerås O, Brox JI (2003) Reliability of computed tomography measurements of paraspinal muscle cross-sectional area and density in patients with chronic low back pain. Spine 28:1455–1460

Lambe NR, Conington J, McLean KA, Navajas EA, Fisher AV, Bünger L (2006) In vivo prediction of internal fat weight in Scottish blackface lambs, using computer tomography. J Anim Breed Genet 123:105–113

McGurk M, Whitehouse RW, Taylor PM, Swinson B (1992) Orbital volume measured by a low-dose CT scanning technique. Dentomaxillofac Radiol 21:70–72

Miller PD (2006) Guidelines for the diagnosis of osteoporosis: T-scores vs fractures. Rev Endocr Metab Disord 7:75–89

Miller F, Merlo M, Liang Y, Kupcha P, Jamison J, Harcke HT (1993) Femoral version and neck shaft angle. J Pediatr Orthop 13:382–388

Müller MJ, Bosy-Westphal A, Kutzner D, Heller M (2002) Metabolically active components of fat-free mass and resting energy expenditure in humans: recent lessons from imaging technologies. Obes Rev 3:113–122

Murase T, Oka K, Moritomo H, Goto A, Yoshikawa H, Sugamoto K (2008) Three-dimensional corrective osteotomy of malunited fractures of the upper extremity with use of a computer simulation system. J Bone Joint Surg Am 90-A:2375–2389

Nickoloff EL, Feldman F, Atherton JV (1988) Bone mineral assessment: new dual energy approach. Radiology 168:223–228

Rådegran G, Saltin B (2000) Human femoral artery diameter in relation to knee extensor muscle mass, peak blood flow, and oxygen uptake. Am J Physiol Heart Circ Physiol 278:H162–H167

Schultz E, Felix R (1978) Phantommessungen zum räumlichen Auflösungsvermögen und zum Partial-Volume-Effect bei der Computertomographie. Rofo 129:673–678

Schultz E, Lackner K (1980) Die Bestimmung des Volumens von Organen mit der Computertomographie. I. Die Ermittlung von Organquerschnittsflächen unter Berücksichtigung der dabei auftretenden Fehlermöglichkeiten. Rofo 132:672–675

Starker M, Hanusek S, Rittmeister M, Thoma W (1998) Validierung computertomographisch gemessener Antetorisonswinkel am Femur. Z Orthop Ihre Grenzgeb 136:420–427

Togashi K, Kitaura H, Yonetsu K, Yoshida N, Nakamura T (2002) Three-dimensional cephalometry using helical computer tomography: measurement error caused by head inclination. Angle Orthod 72:513–520

Whitehouse RW (1991) Computed tomography attenuation measurements for the characterization of hepatic haemangiomas. Br J Radiol 64:1019–1022

Ultrasound

3

Carlo Martinoli, Ali Attieh, and Alberto Tagliafico

Contents

C. Martinoli, M.D. (✉) • A. Attieh, M.D.
A. Tagliafico, M.D.
Radiologia— Department of Health Science,
Università di Genova, Ospedale Policlinico San
Martino, Genova, Italy
e-mail: carlo.martinoli@libero.it

3.1   Introduction

Measurement is one of the key parameters of US examination and represents an essential part for a correct interpretation of ultrasound (US) images and for distinguishing normal from pathologic conditions. In the musculoskeletal system, US measurements involve calculation of linear distance, area, or volume. Distance measures are the most commonly used by far. They are usually obtained on the freezed image frame by moving a visible cursor on the screen via a track ball: the process may take a couple of seconds. The precision of distance measurements reached by current technology and high frequency broadband transducers is very high, and, in the best circumstances, spot reflectors measuring 0.1 mm in size can be resolved as separate structures. Area measurements are used in more specific settings. Because most of area measurements relate to round/oval structures, built-in systems that produce an ellipse on the screen can give results quickly by adjusting size and shape on the structure to be evaluated with the track ball. On the other hand, freehand area measurements need a steady hand: it may be difficult to draw on the screen a trace that perfectly overlaps the structure of interest. However, positive and negative errors produced by the caliper spots that deviate from the intended position on either side of the outline, at the end, tend to balance. Automated recognition algorithms have recently been introduced to

Fig. 3.1 Longitudinal extended field-of-view 12–5 MHz US image of the posterior ankle in a patient with chronic Achilles tendon rupture and substantial retraction of the tendon ends (*arrows*). The length of the gap exceeds the transducer width but can be effectively measured by means of the extended field-of-view technique
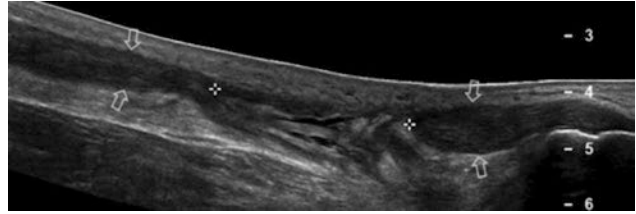
make precise tracing around a given structure without wasting time. If implemented in the equipment software, volume algorithms usually refer to ellipsoid structures or recall obstetrical shapes. In general, these systems do not perfectly fit for use in the musculoskeletal system, where skeletal muscles have variable conformation. The advent of 3D and 4D ultrasound is opening new perspectives in this field. One of the main drawbacks of linear array transducers is the limited extension of the field of view that makes measurements of elongated structures in the musculoskeletal system impractical. Thus, spatial relationships and sizes in the US images often must be synthesized in the mind of the sonologist from multiple real-time images that display only portions of the relevant anatomy (Lin et al. 1999). With extended field-of-view systems, however, geometric measurements can be obtained effectively from lesions larger than the field of view of the transducer with <5% error (Fig. 3.1) (Fornage et al. 2000).

The aim of this chapter is to discuss technical aspects of US measurement of tendons, muscles, nerves, joints, and soft-tissue masses and to determine under what circumstances these measurements are used in the musculoskeletal system.

3.2   **Tendons**

One of the most common applications of muscu-
loskeletal US is the investigation of tendons
(Martinoli et al. 1999, 2002). Nevertheless, lim-
ited data are available in literature regarding
reproducibility of tendon measurements and
observer variability in obtaining these measures
(Ying et al. 2003; O'Connor et al. 2004). This
may be in part related to intrinsic factors, such as
the existence of wide range variation of tendon
size depending on gender, side dominance, and
effects of sports exercise (Koivunen-Niemelä and
Parkkola 1995; Ying et al. 2003). On the other

hand, technical factors, including lack of ade-
quate standardization of probe positioning, dif-
ferences in pressure applied with the probe and
angles of incidence of the US beam as well as
absence of clearly defined landmarks around ten-
dons, contribute to make difficult obtaining com-
parable images and reproducible measurements.
Based on recent studies, interobserver variation
was found to be a greater source of error than
intraobserver variation when measuring tendons
(O'Connor et al. 2004). In general terms, this
would support the use of the same observer if
longitudinal studies of tendon size have to be
undertaken.

3.3   Tendinosis and Partial Tears

The degenerative process in tendons, which is commonly known as "tendinosis," has imaging characteristics that may be used alone or in combination to help in distinguishing this process from normal states or other more severe tendon abnormalities such as complete tears. Among them, an increased size of the affected tendon in the zone of abnormality is virtually pathognomonic of the degenerative process that produces an increase in the glycoprotein matrix, tenocyte, and fibroblast proliferation with the formation of disorganized collagen (Martinoli et al. 2002). Measurement of thickness and determination of increased size is thus an important component of tendon assessment, reflecting both status and severity of tendinopathy (Archambault et al. 1998). In the degenerative setting, the abnormal tendon may thicken circumferentially, leading to a parallel increase in size of the two axial diameters (AP and LL) or may enlarge selectively along the surface-to-depth axis (AP). This "vertical" swelling most often occurs close to bone insertions (e.g., lateral epicondylitis, jumper's knee, etc.). As a rule, it would be, therefore, recommended to calculate the tendon size in the zone of maximum thickening by considering the cross-sectional area (given by calculation of the two axial diameters or by tracing methods provided by the built-in software of the equipment). In alternative, the examiner should take the only AP diameter, which is expression of the tendon thickness. When measuring this parameter, the screen calipers should be placed systematically on the short axis of the tendon to obtain more reliable calculation, because the longitudinal plane may overestimate the tendon thickness due to partial volume averaging artifact and some obliquity in the course of tendons (Fig. 3.2) (Fornage 1986; Ying et al. 2003). If the increased tendon volume is mild (grade I tendinopathy), it may be recognized in a more confident way by comparing the affected tendon with the contralateral one (if this latter is healthy). In tendinosis, measurement accuracy would have potential implications not only to identify mild disorder but also to follow-up tendon changes and evaluate the effects of conservative measures with time. On the other hand, high values of tendon thickness have also been proposed to correctly predict tendinosis and partial tears, at least in the Achilles tendon (Hartgerink et al.
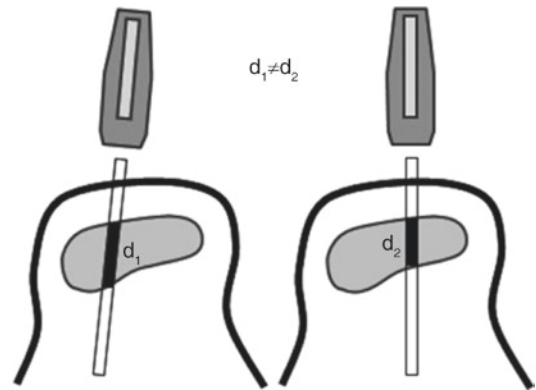

Fig. 3.2 Tendon thickness measurement. Schematic drawings illustrate possible sources of inaccuracy when placing the probe over the long axis of the tendon. Slight tilting of the probe or some obliquity of the tendon relative to the skin may cause calculation errors of tendon diameter (*d*) and poor reliability

2001). Softening (tenomalacia) is another feature of tendons affected by degenerative changes and partial tears (Koury and Cardinal 2009). Under certain circumstances, probe compression may be useful in distinguishing between effusion and synovial hypertrophy filling a partial-thickness tear (soft) from residual intact tendon fibers (stiff). In the absence of a tear, an increased tendon compressibility may be encountered in abnormally thickened tendons as a result of deranged intratendinous structure (Koury and Cardinal 2009). Compressibility can be visually assessed on gray-scale imaging applying graded compression with the probe on the abnormal tendon. This evaluation should be performed in a relaxed state, without applying any tension to the tendon fibers. More recently, sonoelastography, a relatively new technique that is able to assess the elastic properties of tissues, can offer better quantitative analysis of tendon compressibility (strain) expressed in pressure units, commonly kilopascals (kPa), or as a strain ratio (Klauser et al. 2010). Initial application of sonoelastography in lateral epicondylitis and Achilles tendinopathies showed promising results (De Zordo et al. 2009, 2010; Drakonaki et al. 2009). In most cases, however, this modality should be viewed as emerging rather than an established tool of assessment. A standardized protocol for image acquisition, range of values, and limitations need to be defined in this setting. Further clinical evaluation is also mandatory.

3.4   Complete Tears

When findings noted at clinical examination are inconclusive or equivocal for a diagnosis of acute tendon rupture, further evaluation with US aids to distinguish complete tears from less severe pathologic conditions. In complete tendon tears, US is able to provide detailed information on the position of the tendon ends and measurement of the gap between them. When the gap is less than the width of the transducer array, both tendon ends can be easily demonstrated in the same image frame. In the instance of significant retraction and longer gaps, the examiner can use extended field-of-view algorithms to improve the presentation of the US information for the referring physician. Alternatively, the position of the tendon ends can be related to definite landmarks (e.g., bone, joint level, etc.) that are palpable or can be readily identified by the orthopedic surgeon. One of the main advantages of US over MR imaging to image tendons consists of its ability to perform dynamic scans during active and passive joint motion. In daily practice, dynamic scanning is particularly helpful to distinguish partial from complete tears, especially if there is no fluid filling the gap and the tendon ends are curled up thus mimicking a degenerated but continuous tendon. In the Achilles tendon, for instance, the gap between the tendon ends should be recorded not only in the resting position (static technique) but also when the foot is moved into as much plantar flexion as pain allows (dynamic technique). When the tendon ends closely appose or the dynamic gap is measured as less than 5 mm, there may be indication for conservative (cast immobilization) treatment without additional risk of re-rupture compared with patients who undergo operative treatment (Webb and Bannister 1999; Kotnis et al. 2006). Although a limited number of trials have assessed the reliability and accuracy of US measurements in tendon rupture compared with surgical measures, there is general consensus on the assumption that US is an accurate means to predict the size of a tear and calculate the amount of tendon retraction on long-axis planes. However, the accu-racy of tendon gap measurement may be influenced by a variety of factors, including patient positioning and the status of the tendon ends. It is well-known, for instance, that proper patient's positioning is critical to image the rotator cuff with US. The modified Crass (Middleton) maneuver is routinely obtained for this purpose by asking the patient to extend the patient's arm posteriorly, placing the palm of the hand on the superior aspect of the iliac wing with the elbow flexed, directed posteriorly and toward midline, so that the supraspinatus tendon is moved away from underneath the acromion (Crass et al. 1988; Middleton 1992). This position helps to confirm rupture and to identify the location of the injury but it inherently creates greater tension across full-thickness supraspinatus tears, thus resulting in overestimation of tear size compared with surgical findings (Ferri et al. 2005). Conversely, the Crass position, which is obtained with a higher degree of internal rotation by keeping the shoulder extended, adducted, and internally rotated with the elbow flexed, the palm facing out, and the fingers pointing toward the contralateral scapula, causes less stretching on the tendon fibers (Crass et al. 1987; Ferri et al. 2005). As this latter position mimics the adducted shoulder position at the time of surgery, it was found to reflect more precisely the true size of the tears (Ferri et al. 2005).

In tendon gap measurement, another limitation of US may be related to the status of the tendon ends, particularly in cases of rupture of tendons invested by synovial sheath, when they are retracted, frayed, and irregular. Acutely, hemorrhage and debris often distend the tenosynovial sheath and may make depiction of the tendon ends unclear. In these cases, some overestimation of tendon retraction should also be expected due to irregular shrinking, wavy retraction of the proximal tendon fibers, and action of the muscle. If defining the site of the tendon stumps is important to plan reconstructive surgery and US is reliable to provide this information, one should be aware that the end-to-end gap measurement provided by US may be slightly overestimated compared to surgery.

3.5　Muscles

Accurate estimation of the volume of individual muscles or muscle groups assumes clinical relevance in specific specialized settings, such as rehabilitation medicine for monitoring the effects of disuse and immobilization, sports medicine for assessing muscle building programs and adaptations in response to training and physiotherapy, as well as pediatrics for children and adolescents with muscle dystrophies or disabili-

ties secondary to cerebral palsy. Estimation of the muscle volume is a complex task which requires stereological methods based on systematic sectioning the muscle with equidistant parallel planes along a known distance and the application of a mathematical formula (Walton et al. 1997). US and MR imaging may be equally used to obtain the required number of axial parallel sections through the muscle for volume calculation (Fig. 3.3). Using these methods, recent studies performed with current generation machines

Fig. 3.3 Muscle volume assessment. The length (*l*) of the tibialis anterior muscle is taken as the distance between the proximal origin and the distal myotendinous junction over a straight line. A number (five in this example) of axial planes ($a_1 … a_5$) are taken along the length of the muscle with a constant interscan distance. The volume of the muscular portion between every two consecutive scans is calculated with mathematical algorithms. Then, the volume of the entire muscle is calculated by summing up all of the interscan muscle volumes
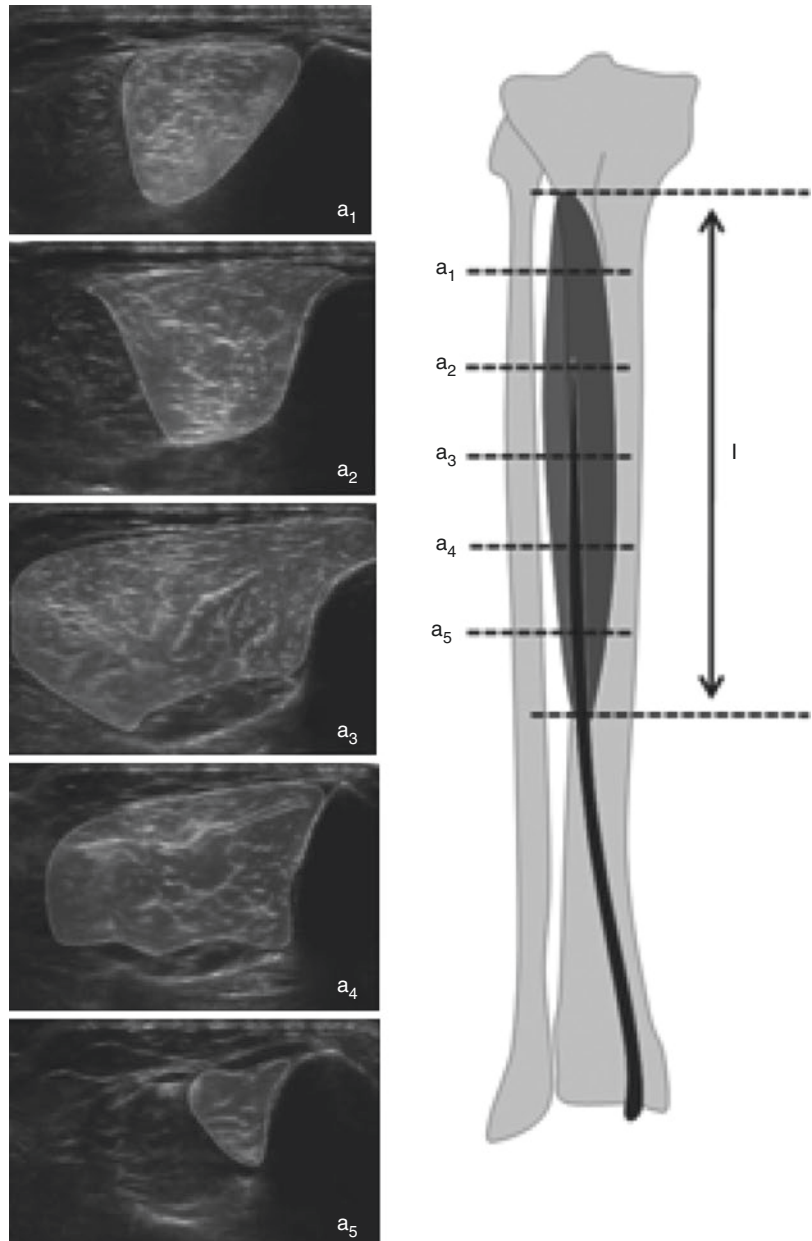
concluded that US can provide accurate and reproducible measurements of muscle volume. Using unrestrained free-hand technique, however, US is not unbiased, requires external markers and has certain disadvantages compared with MR imaging-based measurements. Main limitations include: some underestimation of the muscle volume (error ≈7%); dependency upon the orientation of the probe; restricted use to superficial and relatively small muscles only (Esformes et al. 2002). In addition, US methods are more time consuming than MR imaging measurements (Esformes et al. 2002). With introduction of three-dimensional systems, the validity and reliability of US-based volume measurements is expected to improve (Delcker et al. 1999), even if some limitation related to the attenuation of the US beam for evaluating deep-seated structures and a too small acquisition field of view seems to be difficult to overcome.

Given the complexity of volume calculation with US, a widely used alternative and quicker way to estimate the muscle bulk and compare it with the opposite side relies on measuring either the muscle thickness or the CSA by the ellipse formula (Dupont et al. 2001; Koury et al. 2008). These methods are more practical but are also more subjective and, in themselves, do not perfectly correlate with true volume assessment. They serve as indicators of either muscle disuse/atrophy or hypertrophy when values are compared with the opposite side (Fig. 3.4). On the other hand, these methods have several potential source of errors, such as the need to match scan landmarks precisely, to use identical probe orientation when comparing the two sides, and to avoid any pressure on the underlying tissues (a generous amount of contact gel should be used!). As regard this latter point, the flattening-related error related to probe pressure would be greater for thickness measurements than for CSA measurements, since the reduction in one dimension would be presumably compensated by bulging in another dimension and the volume of the muscle would remain constant (Dupont et al. 2001). Apart from these considerations, US has proved to be a reliable means to measure both muscle thickness and CSA with a test-retest correlation of 0.98–0.99 (Reeves et al. 2004) and a 0.90–
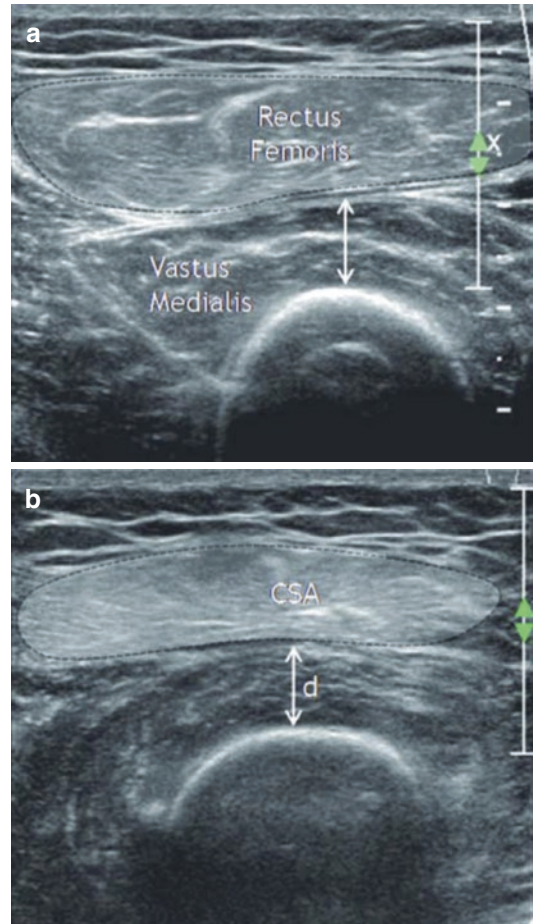

Fig. 3.4 Muscle size measurement. Transverse 12–5 MHz US images over the right (**a**) and left (**b**) anterior thighs in a patient with left femoral nerve injury. Atrophy of the left rectus femoris muscle is recognized by comparing its cross-sectional area (CSA) with that of the contralateral muscle. On a deeper plane, the thickness measurement (*d*) is used to estimate the size of the vastus intermedius: a milder degree of atrophy corresponding to a reduced thickness is observed in the left muscle

0.99 correlation with MR imaging (Walton et al. 1997; Dupont et al. 2001; Reeves et al. 2004; Koury et al. 2008). Although some studies have used US to determine muscle thickness in healthy subjects (Arts et al. 2007), the established normal values are dependent on site of measurement, subject's position, activity, and body mass. In addition, the influence of age and gender is different for each muscle group and should be taken into account when evaluating US images of muscles of individual patients (Pillen et al. 2008).

On longitudinal US images, skeletal muscles show a typical pennate pattern: this is related to multiple hyperechoic parallel linear echoes due to fibroadipose septa of the perimysium that surround muscle fibers forming oblique angles with the myotendinous junction (Fornage et al. 1983). In the past, US has been suggested as a means to measure the angles (θ) of the pennate pattern (angle of fascicular insertion into the aponeurosis) in an attempt to better quantify echotextural changes in diseased muscles (Rutheford and Jones 1992). A direct correlation was found between pennation angles and muscle fiber length (Bleakney and Maffulli 2002), whereas these angles decrease with parallel increase of fatty atrophy and decrease of muscle CSA (Narici and Cerretelli 1998; Meyer et al. 2004). However, US measurements of the angles of the pennate pat-tern may be unpractical at certain sites, and clear depiction of the orientation of fibroadipose septa may be hardly appreciated when muscle atrophy is severe (Strobel et al. 2005). This is the reason for which subjective analog scales, such as the Goutallier' scale, are still preferred to assess fatty changes in muscle echotexture (Koury et al. 2008). Recently, quantitative sonoelastography was found to be feasible for measuring dynamic viscoelastic properties of human skeletal muscles. Investigations into the dynamic viscoelastic properties of healthy skeletal muscles revealed that voluntarily contracted muscles exhibit considerable increases in both shear modulus and viscosity estimates as compared to the relaxed state (Hoyt et al. 2008). Further validation of these systems is still needed to establish their ultimate value in the diagnostic work-up.

3.6   Nerves

In the last years, US is being used more and more frequently to evaluate peripheral nerves, thus influencing the diagnosis and clinical care in a variety of settings of orthopedic, neurologic, neurophysiologic, and anesthesiologic interest. A large number of studies have provided evidence that measurements of the nerve CSA can discriminate between normal and pathologic states in a variety of neuropathies (Duncan et al. 1999; Yesildag et al. 2004; Cartwright et al. 2008). Nevertheless, there are many discrepancies in literature concerning nerve measurements and related cutoff values between normal and pathologic states. These inconsistencies derive from methodological differences in design and technology, measurement errors, and difference in the sample population among research papers (Thoirs et al. 2008). The extent to which these factors may affect the diagnosis is, for large part, undefined, but it is such to possibly influence the data used for reference. In absence of substantiated reference values, the data available in the literature on nerve US may not find validation in the clinical practice, possibly confounding the diagnostic thinking and, with time, weakening the overall acceptance of the technique by the referring physicians. Although initial attempts to introduce protocols for measurement and normal reference values have been made, much work should still be done on this matter (Alemán et al. 2008; Padua and Martinoli 2008; Cartwright et al. 2008).

3.7 Nerve Compression Syndromes

In nerve entrapment syndromes, the measurement that has to be taken on a nerve is essentially the nerve CSA (for large nerves, such as the median, the ulnar, and the tibial) or the maximum cross-sectional diameter (for small nerves, such as the radial, the peroneal, the divisional branches of the ulnar), when the nerve size is too small for a reliable calculation of the area. Even if measurements obtained at specific levels—for instance, the pisiform bone for the median nerve at the carpal tunnel—are a valuable means to obtain better standardization, the nerve cross-sectional area should be sampled, in logical terms, at the site where the nerve is maximally enlarged, and the histopathologic changes are, therefore, maximal: in general, this occurs just ahead the compressing structure as the result of intraneural changes related to vasocongestion and edema. In the carpal tunnel, for instance, daily experience suggests that the point of maximum enlargement of the median nerve corresponds to the proximal boundary of the retinaculum, a position located slight cranially to the pisiform. We believe that definition of a level of measurement could be still matter of debate to establish whether selection of an extrinsic landmark or evaluation of the nerve shape in itself is the most sensitive way to identify disease. Two methods are used to measure the nerve CSA: the indirect method, based on calculation of the nerve diameters by calipers and application of the ellipse formula (transverse diameter x anteroposterior diameter x $\pi/4$) and the direct method, based on manual tracing and automated calculation of the area (Yesildag et al. 2004; Duncan et al. 1999). Both methods can be used depending on the examiner's preference and the equipment software available. In fact, no significant differences were found between the mean values of the CSA of the median nerve calculated by the two methods ($P < 0.314$; Alemán et al. 2008; $p = 0.08$; Yesildag et al. 2004), with a high degree of correlation (0.97 in patients with carpal tunnel syndrome and 0.84 in controls; Yesildag et al. 2004).

Similarly, a high reproducibility was observed in CSA measurements performed by experienced and inexperienced observers after a short learning period (Alemán et al. 2008). Either using the direct or the indirect method, the CSA measurement should be obtained from the outer margin of hypoechoic fascicles: the echogenic rim surrounding the fascicles (often visible in the ulnar nerve at the cubital tunnel) reflects the outer epineurial sheath and has to be excluded because it may not be clearly distinguishable from the external perineural fat (Fig. 3.5) (Yesildag et al. 2004). Even if the nerve margin used for CSA measurement has not been specified in many research studies, most of available data seem referring to the hypoechoic portion of the nerve. At certain osteofibrous tunnels, the joint position may significantly affect CSA measurement. This typically occurs at the elbow, where the ulnar nerve diameter was found to be smaller in full flexion than in elbow extension secondary to the length changes required to accommodate the nerve along a curved path during flexion of the elbow joint (Yoon et al. 2007; Thoirs et al. 2008). Probe positioning is another factor potentially affecting the variability of CSA measurements as the US beam should be always directed perpendicularly to the long axis of the nerve to be examined (even if the nerve assumes a curved course or an oblique course from surface to depth). The optimal probe orientation for measurements can be defined dynamically by tilting the probe over the nerve or inducing slight changes in the joint position. When setting cutoff values for nerve CSA, gender, weight, body mass index, and race should also be taken into account as possible confounders (Thoirs et al. 2008). The results of all the above variables considered as a whole are responsible of the lack of consensus still existing on the optimal cutoff value for median nerve at the wrist and the ulnar nerve at the elbow. More specifically, diagnostic cutoff values for carpal tunnel syndrome have ranged from 9 to 13 mm^2 with most studies choosing a mark of >10 or 11 mm^2 (Hobson-Webb et al. 2012). In the cubital tunnel syndrome, the exact diagnostic cutoff values also vary between institutions, but an ulnar
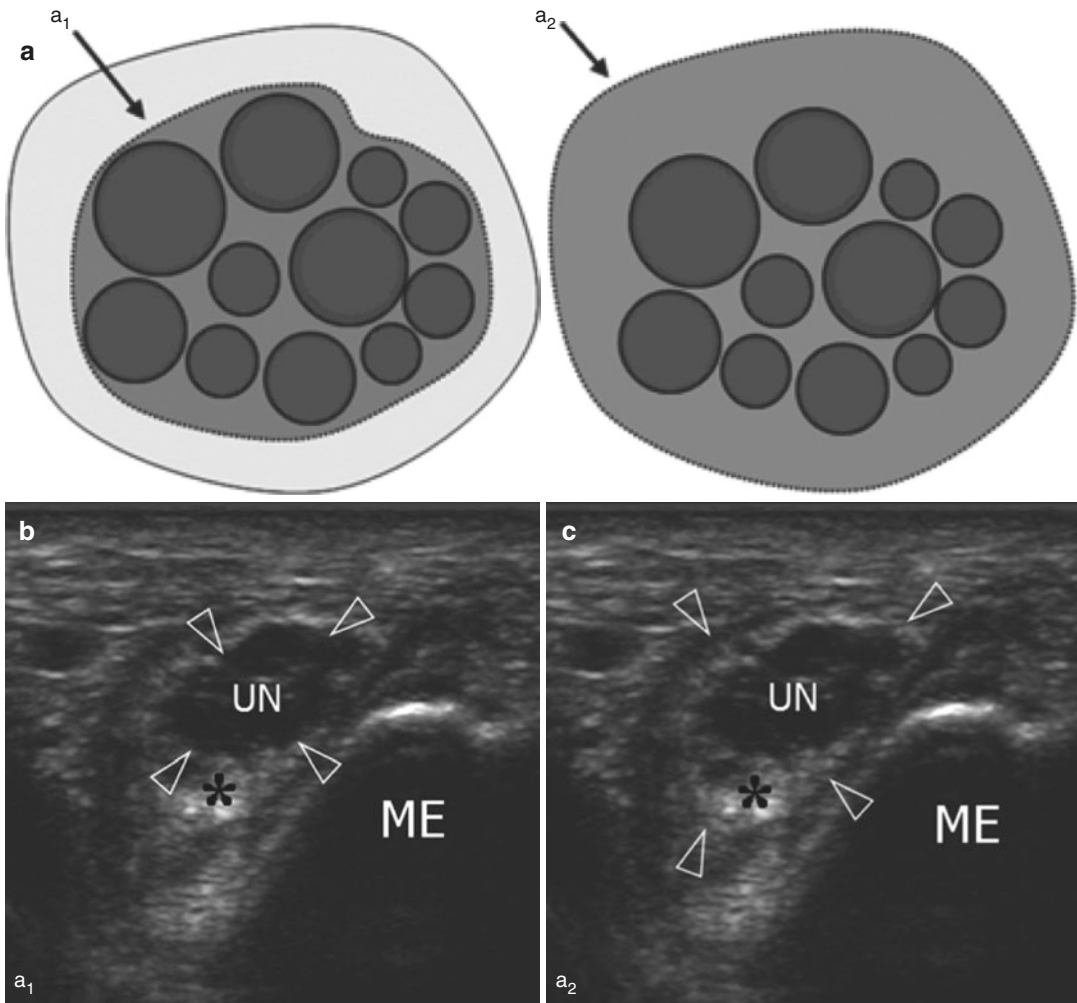
Fig. 3.5 Nerve cross-sectional area. (**a**) Schematic drawing illustrates two modalities to calculate the nerve CSA by tracing the boundary of the hypoechoic fascicles (a_1) or the outer margin of the hyperechoic epineurium (a_2). (**b**, **c**) Short-axis 17–5 MHz US images of the ulnar nerve (UN) at the elbow demonstrate a central cluster of fascicles forming a well-delimited hypoechoic complex surrounded by an undefined echogenic envelope (*asterisk*). Arrowheads indicate the points for caliper positioning to calculate a_1 and a_2

nerve CSA >10 mm^2 is a generally accepted mark (Beckman et al. 2011). In lieu of using absolute cutoff values, a wrist-to-forearm ratio of median nerve CSA has been recently introduced (Hobson-Webb et al. 2008). To calculate this ratio, the CSA is determined at the level of the distal wrist crease and 12 cm proximally in the forearm. These authors found an upper normal limit of wrist-to-forearm ratio of 1.4 to have 100% sensitivity for detecting carpal tunnel syndrome with no false positives in the control group (Hobson-Webb et al. 2008). Other authors have proposed the pronator quadratus muscle as the level for the second CSA measurement. A difference (ΔCSA) between the largest CSA of the median nerve obtained at the level of the carpal tunnel and at the proximal third of the pronator quadratus is then calculated (Klauser et al. 2009). A ΔCSA threshold of 2 mm^2 proved to have a sensitivity and specificity as high as 99% and 100%, respectively, for the diagnosis of carpal tunnel syndrome (Klauser et al. 2009). In the

occurrence of a bifid median nerve, the same method can be used by summing the CSAs of the radial and ulnar branches of the nerve (Klauser et al. 2011). After doing that, a ΔCSA threshold of 4 mm^2 between the carpal tunnel level and the proximal third of the pronator quadratus provided sensitivity and specificity as high as 92.5% and 94.6%, respectively, for the diagnosis of compressive neuropahty (Klauser et al. 2011). One-to-one comparison of values with the opposite side used as control has been also suggested as an alternative option for objective assessment of the nerve size (Thoirs et al. 2008). This seems particularly promising in mild initial entrapments, when electrophysiology is positive, but the CSA is within or at the limits of the normal range. In these cases, a difference in the CSA between right and left sides might increase the examiner's confidence that a mild compression exists.

3.8 Nerve Injuries

When a nerve has been injured, the goal of surgical repair is generally to approximate the ends of the injured nerve to restore function in muscles. If the nerve ends cannot be brought together (gap >5 mm), then a nerve graft may be necessary. Assessing the exact location of the nerve ends and measuring the gap in between them on longitudinal scans is crucial in a preoperative setting for selection of the adequate treatment. In fact, direct visualization of the nerve ends may be impaired at surgical exploration following retraction of the proximal stump and presence of surrounding scar tissue and hematoma (Peer et al. 2001). In general, this information can be more accurately achieved by US rather than by MR imaging because, in the acute setting, edema and hemorrhage lead to a high T2-weighted signal intensity that may be similar to the hyperintense signal of the nerve ends. After interruption, regenerating axonal sprouts and nerve sheath cells grow randomly at the lesion site in an attempt to restore the nerve continuity. This process usually gives off a terminal (stump) neu-

roma. The neuroma may involve the two ends or, more commonly, the proximal end of the severed nerve. When measuring the gap, the examiner should be aware that the neuroma needs to be excised at repair after a nerve injury. For this reason, the measurement should be also performed by adding the neuroma/s' length to the actual gap length, starting measurement at the base of neuroma, where the normal CSA and fascicular appearance of the nerve bundle is preserved (Fig. 3.6). In order to avoid harvesting of sensory nerves and formation of neuromas, recent surgical therapies have been developed using the implantation of coil-reinforced hydrogel tubes between the nerve ends which impose directionality to the regenerating nerve axons and reduce the incidence of neuromas (Battiston et al. 2005; Katayama et al. 2006). Once the tube is in place, the regenerating nerve fibers grow from the proximal nerve stump, through the graft, into the distal nerve segment (Belkas et al. 2006). In these cases, the surgeon needs not only to know the end-to-end distance-free of neuromas but also the cross-sectional diameter of the nerve ends to select the appropriate size of the tube.

Fig. 3.6 Nerve gap measurement. Longitudinal 12–5 MHz US scan over a transected ulnar nerve at the middle third of the arm. Note the proximal (*white arrows*) and the distal (*open arrows*) nerve stumps ending in two hypoechoic neuromas (N). The gap is measured by a straight line joining the tips of the neuromas (d_1). The distance between the junctions of the neuromas with the normal nerve tissue (d_2) should be also taken
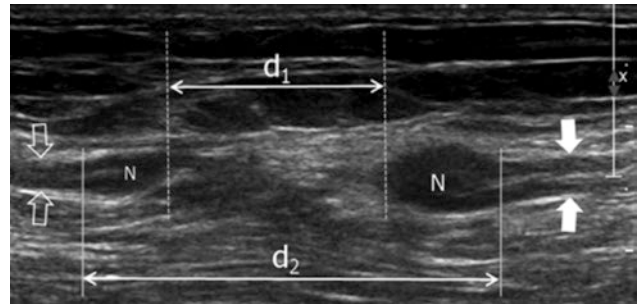
3.9   Joints

The indications for joint US are growing up due to the progressive refinement of technology and the fact that both radiologists and clinicians are increasingly aware of the potential of US in this field (Bianchi et al. 2002). Regarding joint measures, US can be used to better quantify synovitis, to help the diagnosis of joint instability and ligament tears as well as to assess the articular cartilage damage in degenerative and inflammatory disorders.

3.10 Synovitis

Absolute measurements of normal joints have not been universally agreed, because of wide variation in the normal, intrinsic anatomic complexity and inability of US to examine large part of the joint surfaces due to problem of access. Nevertheless, many attempts have been made and especially in the rheumatologic literature or as part of training programs of the EULAR/OMERACT groups to standardize measurements and quantify the amount of joint distension by effusion and synovitis at any individual location. Many variables may interfere while measuring joint distension with US, including joint size, joint positioning, number and accessibility of the recesses, selection of appropriate landmarks, and a variety of local intra- and extraarticular features. These factors have limited the value of gray-scale US as a means for quantification of findings. Until now, the thickness of the joint space measured at the level of the joint line or at any recess of the joint cavity has been regarded as the established measure for diagnosing joint distension and synovitis (McNally 2008). Depending on the joint, the thickness measurement may reflect the space occupied by effusion or the combination of effusion plus hypertrophic synovium and capsular structures. An example is given by the anterior recess of the hip joint, a pouch formed by a combination of anterior and posterior capsular layers between the femoral neck and the iliopsoas muscle. In the pediatric age group, the parietal layers of this recess are closely apposed and the thickness of the total capsule (anterior femoral neck-to-posterior iliopsoas muscle distance) measures 4.9 mm ±1 mm in normal states, whereas the difference between both hips should not exceed 1 mm (Robben et al. 1999). In the past, hip synovitis was diagnosed with a thickness of the total capsule more than the cutoff value of 5 mm (Robben et al. 1999). With improving transducer technology, the ability to discriminate the effusion from surrounding capsular layers has led to measure the effusion directly as a separate element (Rohrschneider et al. 1996). With this latter measurement, that is more reliable and accurate, a 2 mm threshold is

now used to distinguish pathologic from physiologic effusions (Rohrschneider et al. 1996). In adult patients with arthritis, much of the reference data available did not yet reach full validation and consensus regarding technical parameters and standard examination technique. In the ventral aspect of the metacarpo-phalangeal joint (MCPJ), for instance, a standard measurement has been proposed using the distance between the subchondral bone of the metacarpal head and the volar plate, but variation was found to be quite wide (Schmidt et al. 2004). In addition, this measurement does not include the proximal recess where early and prominent thickening may occur (McNally 2008). For these reasons, some authors suggest to measure at the point of maximal joint distension (bone-to-capsule distance) irrespective of its location and compare the result with the normal value known for that location (McNally 2008). However, the normal reference values vary with the area of the joint being examined and too mild changes (1 mm) in joint thickness are already considered significant to suggest synovitis. This exposes the system to inaccuracies for minor sampling errors. Similar considerations are valid for the carpal joints and the proximal interphalangeal joint (PIPJ) in patients with arthritis. In the last years, the problems posed by absolute measurements to assess synovitis have been, at least in part, overcome by development of semiquantitative systems, in which volume grading is based on analog scales (e.g., mild, moderate, severe) (Szkudlarek et al. 2004). On the other hand, the advent of three-dimensional (volume) US seems very promising to open new perspectives in terms of automated volume calculation of the joint space. Following acquisition with volumetric probes, data can be displayed with multiplanar (MPR) or maximum intensity projection (MIP) reconstruction algorithms. With MPR, each plane is oriented within the volume dataset by parallel or rotational shifting around any of the three spatial axes. Using MIP algorithms, the area of interest (i.e., a joint recess) may be represented as a solid shape and its volume measured in cc/mm^3. At the same time, these systems are able to provide automated calculation of the percentage of blood flow sig-

nals in the joint volume using color/power Doppler systems. This percentage can be expressed as the area occupied by color signal. Other measurements can calculate the mean intensity of the color signals in the joint space as well as a ratio of the amount and intensity of color signals in the same joint space. In addition, the ability to store serial volume datasets of a joint space with time would allow better comparison of findings in longitudinal studies, providing new insights into assessment of the patient outcome and reinforcing the role of ultrasound to evaluate the results of treatment. This seems par-

ticularly relevant in the light of establishment of high-cost therapies based on anti-TNFα drugs. Some loss of spatial resolution and worsening of image quality is expected using current 3D probe types in which the US beam is swept throughout the tissue volume along the z-axis by tilting the scanhead with a mechanized drive. As technology progresses, the forthcoming introduction of high-frequency matrix probes capable of isotropic-voxel volumetric acquisition would be able to provide more reliable and accurate quantification measurements.

3.11   Instability

The diagnosis of joint instability basically relies on plain films. In some instances, however, the complex anatomy of joints and surrounding structures may make detection of subluxation and dislocation difficult to be diagnosed on standard radiographs. Static and dynamic US scanning can contribute to detect occult positional joint abnormalities by measuring the width of the joint space or the abnormal relationship of adjacent bones in a variety of clinical settings, such as posterior shoulder dislocation and mild acromioclavicular joint instability (Bianchi et al. 1994; Heers and Hedtmann 2005). In addition, dynamic US may indirectly suggest ligament rupture by demonstrating the instability that the ligament injury causes (Fig. 3.7). This may be particularly useful when static examination of the ligament is equivocal in case of subtle injuries or when the ligament is difficult to be directly imaged. An example of "stress sonography" is given by the assessment of the laxity of the ulnohumeral joint that occurs secondary to the injury of the anterior band of the ulnar collateral ligament. The width of the ulnohumeral joint space at the level of the anterior band is measured on the longitudinal plane while in neutral position and during application of valgus stress (De Smet et al. 2002; Nazarian et al. 2003). Measurement of changes in joint width with stressing allows quantitation of the degree of laxity of the joint and can give indirect confirmation of both complete ligament tears and partial tears in which the ligament is continuous but lax. Comparison with the noninjured opposite elbow should be obtained to compare the amount of joint widening that occurs during valgus stressing. Joint width measurements are more confidently performed when the bony edges facing the joint space are sharp and not smooth to avoid ambiguous caliper positioning.
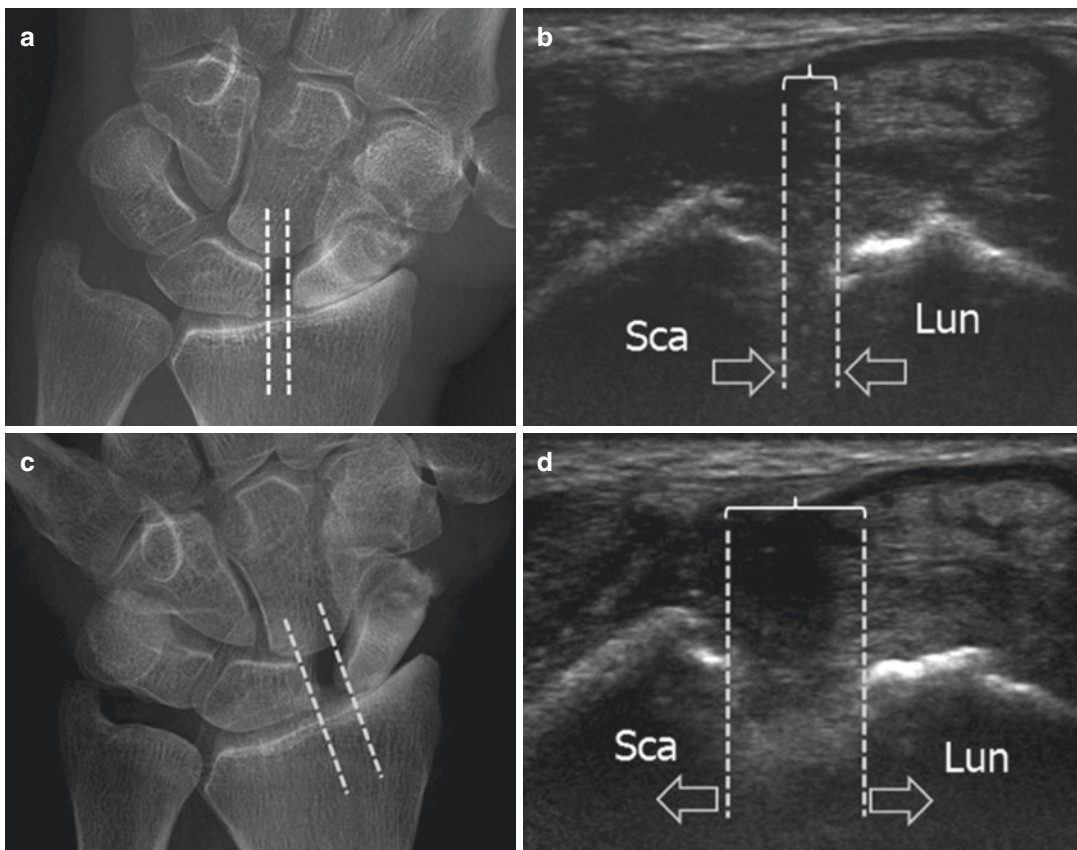

Fig. 3.7 Joint instability (SLAC wrist). (**a**, **c**) AP radiographs of the wrist and (**b**, **d**) corresponding 17–5 MHz US images over the dorsal aspect of the scapholunate joint obtained during (**a**, **b**) radial (*converging arrows*) and (**c**, **d**) ulnar (*diverging arrows*) deviation of the wrist demonstrate widening of the scapholunate distance (distance between the vertical bars) while in ulnar deviation. This can be considered an indirect sign of ligament tear

3.12   Osteoarthritis and Cartilage

Generally speaking, hyaline cartilage thickness measurement is an important marker of structural joint damage in osteoarthritis and inflammatory arthritis. In spite of important limitations related to the fact that large part of the articular cartilage is hidden by bone surfaces and cannot be explored with US, this technique has proved able to provide accurate measurements of its thickness at clinically relevant sites, such as the femoral condyles and the femoral trochlea (Mathiesen et al. 2004; Lee et al. 2008; Naredo et al. 2009). The cartilage thickness should be measured perpendicular to the bone-cartilage interface at a given reference point (Naredo et al. 2009). The measurement is easy to take because the cartilage

appears as a homogeneous anechoic band overlying the subchondral bone, delimited by two clearcut echoes formed at the interface with bone and soft tissues. In a cadaveric model, US demonstrated good reproducibility in knee measurements with 0.75–0.90 interobserver and 0.69–0.83 intraobserver correlation coefficients (Naredo et al. 2009). In addition, the thickness measurement highly (0.82) correlated with that by MR imaging over corresponding area (Østergaard et al. 1995). In patients with osteoarthritis, thickness measurement combined with other indexes, such as echogenicity and sharpness of margins, can be considered good predictors of articular cartilage damage (Grassi et al. 1999).

3.13   Soft-Tissue Masses

Characterization remains a major issue in the management of soft-tissue tumors. Excepting for some benign histotypes (e.g., superficial lipomas, AVM, neurogenic tumors, etc.) and tumorlike lesions (e.g., ganglia, synovial chondromatosis, elastofibroma dorsi, etc.), it is widely accepted that gray-scale US and Doppler techniques play a limited role in providing differentiation between benign and malignant lesions and staging soft-tissue neoplasms (Colleran et al. 2011). Nevertheless, US has proved to be an appropriate modality for monitoring the effects of chemotherapy in patients with high-grade soft-tissue sarcomas or bone sarcoma extending to the soft tissues (Van der Woude and Vanderschueren 1999). For this purpose, the tumor diameters are conventionally measured on the three spatial axes and the amount of intratumor blood flow graded on a semiquantitative scale (Adler et al. 1999). Complete disappearance of intratumor blood flow signals and a decreased tumor size after chemotherapy would be indicative of a favorable response (Van der Woude and Vanderschueren 1999). Of course, US is feasible in these measurements only when the mass does not exceed the field of view of the probe. In the instance of too large or deep-seated tumors, MR imaging is more accurate and represents the modality of choice. As technology progresses, three-dimensional US seems opening perspectives to measure the tumor volume more precisely and quantify the amount of intratumor color voxels and their intensity with greater accuracy than using 2D systems (Fig. 3.8). In particular, automated acquisition with volumetric probes seems reducing system variability when comparing data one-to-one between baseline and after treatment. Although there are only a few papers in the literature about objective quantification of fractional moving blood in the musculoskeletal system using microbubble-based contrast agents, their

introduction seems providing the advantage of a higher sensitivity over conventional Doppler systems to assess the tumor neovasculature (Gay et al. 2012). Compared to gadolinium, ultrasonic contrast media do not pass through the interstitial area and can be assessed with a temporal resolution higher than theoretically possible with MR imaging. The examination is performed with iv bolus injection of contrast medium and continuous imaging with very low mechanical index (MI = 0.06–0.1). This technique maximizes contrast and spatial resolution and enables evaluation of the microvasculature (perfusion imaging). The region of the neoplasm with the greatest vascularization density is targeted with a ROI, and data are expressed in an intensity-time curve (Fig. 3.9). Parameters of evaluation of the curve include peak intensity, time-to-peak, initial slope, mean transit time, and area under the curve. Based on recent studies, this latter parameter resulted to be the most discriminating measure to differentiate benign from malignant histotypes (Gay et al. 2012). The results of sonoelastography in the evaluation of musculoskeletal tissue tumors are still preliminary and need validation on the large scale. The physical basis of this modality essentially depends on deformation of the target lesion compared to the background tissue: softer masses deform to a higher extent when compressed and show a high strain relative to the background. Conversely, hard tissues tend to deform less and have a lower degree of strain. The strain differences can be used to generate a visual elastogram based on a color scale or can be semiquantitatively assessed with the strain ratio measurement (Kumm and Szabunio 2010). This value is based on determining the average strain measured in a lesion and comparing it to the average strain of an adjacent area of fatty tissue (Fig. 3.10). The ratio value increases as a function of the relative stiffness of the target lesion and tends to increase in fibrotic masses and possibly with malignant histotypes.
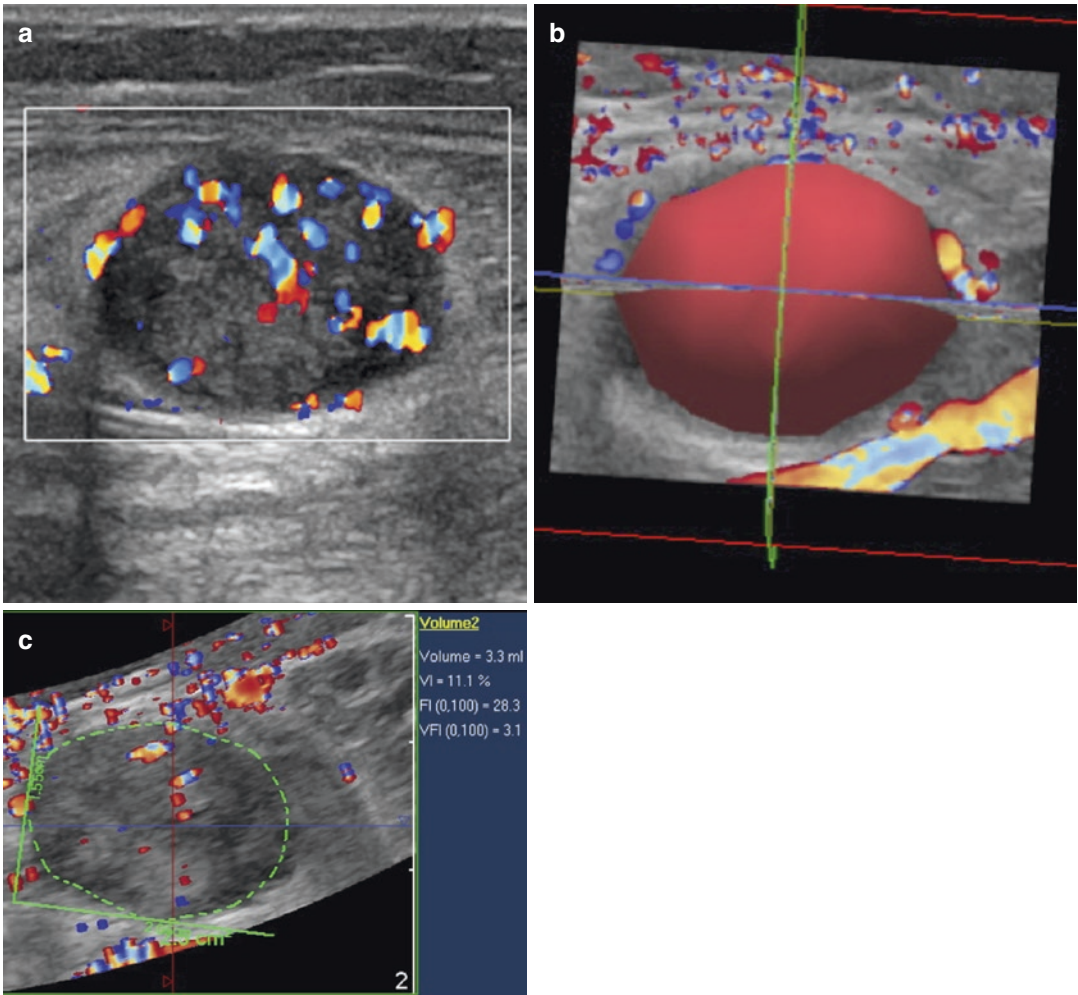
Fig. 3.8 Volume US. (**a**) 12–5 MHz color Doppler US image shows an oval solid hypoechoic mass with hypervascular pattern. (**b**) Three-dimensional rendering of the mass as a *red solid*. Volumetric acquisition allows auto-mated calculation of the tumor volume (3.3 mL). (**c**) Measurement of the amount (11.1%) and intensity (28.3 [0,100]) of intratumor color flow signals is also obtained. Histopathological diagnosis was schwannoma

Fig. 3.9 Ultrasonic contrast media. Intensity-time curve of microbubble contrast agent obtained in the same nodule shown at Fig. 3.8. The ROI has been adjusted to the tumor size. Some of the parameters of evaluation of the curve are illustrated, including *AT* arrival time, *TTP* time-to-peak, *AUC* area under the curve, *PI* peak intensity
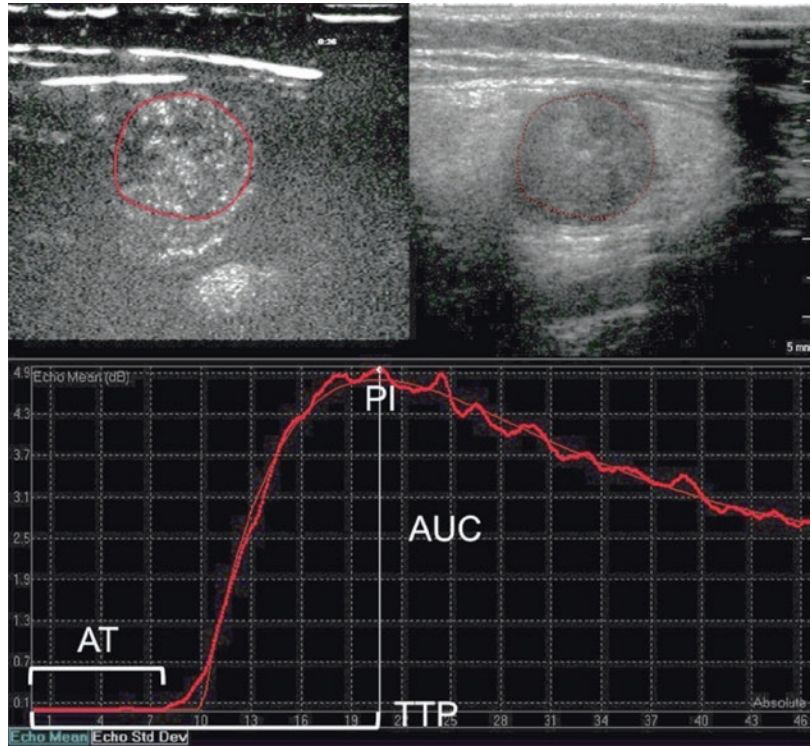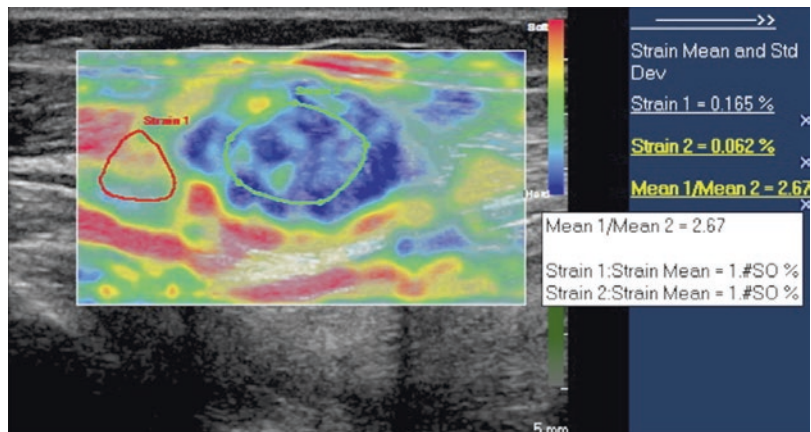

Fig. 3.10 Sonoelasto-gram. Strain ratio assessment in a *blue*-coded soft-tissue mass. Two ROI are placed within a soft-tissue tumor (*green circle*) and in the adjacent fat (*red circle*) at the same level of depth. Strain ratio measurement shows the mass 2.67 times stiffer than fat

References

Adler RS, Bell DS, Bamber JC et al (1999) Evaluation of soft-tissue masses using segment color Doppler velocity images; preliminary experience. Am J Roentgenol 172:781–788

Alemán L, Berná JD, Reus M et al (2008) Reproducibility of sonographic measurements of the median nerve. J Ultrasound Med 27:193–197

Archambault JM, Wiley JP, Bray RC (1998) Can sonography predict the outcome in patients with achillodynia? J Clin Ultrasound 26:335–339

Arts IM, Pillen S, Overeem S et al (2007) Rise and fall of skeletal muscle size over the entire life span. Am J Geriatr Soc 55:1150–1152

Battiston B, Geuna S, Ferrero M et al (2005) Nerve repair by means of tubulization: literature review and personal clinical experience comparing biological and synthetic conduits for sensory nerve repair. Microsurgery 25:258–267

Beckman R, Visser LH, Wl V (2011) Ultrasonography in ulnar neuropathy at the elbow: a critical review. Muscle Nerve 43:627–635

Belkas JS, Munro CA, Shoichetb MS et al (2006) Peripheral nerve regeneration through a synthetic hydrogel nerve tube. Restor Neurol Neurosci 23:19–29

Bianchi S, Zwass A, Abdelwahab I (1994) Sonographic evaluation of posterior instability and dislocation of the shoulder: prospective study. J Ultrasound Med 13:389–393

Bianchi S, Martinoli C, Bianchi-Zamorani M et al (2002) Ultrasound of the joints. Eur Radiol 12:56–61

Bleakney R, Maffulli N (2002) Ultrasound changes to intramuscular architecture of the quadriceps following intramedullary nailing. J Sports Med Phys Fitness 42:120–125

Cartwright MS, Passmore LV, Yoon JS et al (2008) Cross-sectional area: reference values for nerve ultrasonography. Muscle Nerve 37:566–571

Colleran G, Madewell J, Foran P et al (2011) Imaging of soft-tissue and osseous sarcomas of the extremities. Semin Ultrasound CT MR 32:442–455

Crass JR, Craig EV, Feinberg SB (1987) The hyperextended internal rotation view in rotator cuff ultrasonography. J Clin Ultrasound 15:416–420

Crass JR, Craig EV, Feinberg SB (1988) Ultrasonography of rotator cuff tears: a review of 500 diagnostic studies. J Clin Ultrasound 16:313–327

De Smet AA, Winter TC, Best TM et al (2002) Dynamic sonography with valgus stress to assess elbow ulnar collateral ligament injury in baseball pitchers. Skelet Radiol 31:671–676

De Zordo T, Lill SR, Fink C et al (2009) Real-time sonoelastography of lateral epicondylitis: comparison of findings between patients and healthy volunteers. AJR Am J Roentgenol 193:180–185

De Zordo T, Cheem R, Smekal V et al (2010) Real-time sonoelastography: findings in patients with symptomatic Achilles tendons and comparison to healthy volunteers. Ultraschall Med 31:394–400

Delcker A, Walker F, Caress J et al (1999) In vitro measurement of muscle volume with 3-dimensional ultrasound: technical note. Eur J Ultrasound 9:185–190

Drakonaki EE, Allen GM, Wilson DJ (2009) Real-time ultrasound elastography of the normal Achilles tendon: reproducibility and pattern description. Clin Radiol 64:1196–1202

Duncan I, Sullivan P, Lomas F (1999) Sonography in the diagnosis of carpal tunnel syndrome. Am J Roentgenol 173:681–684

Dupont AC, Sauerbrei EE, Fenton PV et al (2001) Real-time sonography to estimate muscle thickness: comparison with MRI and CT. J Clin Ultrasound 29:230–236

Esformes JI, Narici MV, Maganaris CN (2002) Measurement of human muscle volume using ultrasonography. Eur J Appl Physiol 87:90–92

Ferri M, Finlay K, Popowich T et al (2005) Sonography of full-thickness supraspinatus tears: comparison of patient positioning technique with surgical correlation. Am J Roentgenol 184:180–184

Fornage BD (1986) Achilles tendon: US examination. Radiology 159:759–764

Fornage BD, Touche DH, Segal P et al (1983) Ultrasonography in the evaluation of muscular trauma. J Ultrasound Med 2:549–554

Fornage BD, Atkinson EN, Nock LF et al (2000) US with extended field of view: phantom-tested accuracy of distance measurements. Radiology 214:579–584

Gay F, Pierucci F, Zimmerman V et al (2012) Contrast-enhanced ultrasonography of peripheral soft-tissue tumors: feasibility study and preliminary results. Diagn Interv Imaging 93:37–46

Grassi W, Lamanna G, Farina A et al (1999) Sonographic imaging of normal and osteoarthritic cartilage. Semin Arthritis Rheum 28:398–403

Hartgerink P, Fessel DP, Jacobson JA et al (2001) Full- versus partial-thickness Achilles tendon tears: sonographic accuracy and characterization in 26 cases with surgical correlation. Radiology 220:406–412

Heers G, Hedtmann A (2005) Correlation of ultrasonographic findings to Tossy's and Rockwood's classification of acromioclavicular joint injuries. Ultrasound Med Biol 31:725–732

Hobson-Webb LD, Massey JM, Juel VC, Sanders DB (2008) The ultrasonographic wrist-to-forearm median nerve area ratio in carpal tunnel syndrome. Clin Neurophysiol 119:1353–1357

Hobson-Webb LD, Padua L, Martinoli C (2012) Ultrasonography in the diagnosis of peripheral nerve disease. Expert Opin Med Diagn 6:457–471

Hoyt K, Kneezel T, Castaneda B, Parker KJ (2008) Quantitative sonoelastography for the in vivo assessment of skeletal muscle viscoelasticity. Phys Med Biol 7:4063–4080

Katayama Y, Montenegro R, Freier T et al (2006) Coil-reinforced hydrogel tubes promote nerve regeneration equivalent to that of nerve autografts. Biomaterials 27:505–518

Klauser AS, Halpern EJ, Zordo D et al (2009) Carpal tunnel syndrome assessment ith US: value of additional

cross-sectional area measurements of the median nerve in patients versus healthy volunteers. Radiology 250:171–177

Klauser AS, Faschingbauer R, Jaschke WR (2010) Is sonoelastography of value in assessing tendons? Semin Musculoskeletal Radiol 14:323–333

Klauser AS, Halpern EJ, Faschingbauer R et al (2011) Bifid median nerve in carpal tunnel syndrome: assessment with US cross-sectional area measurement. Radiology 259:808–815

Koivunen-Niemelä T, Parkkola K (1995) Anatomy of the Achilles tendon (tendo calcaneus) with respect to tendon thickness measurements. Surg Radiol Anat 17:263–268

Kotnis R, Saronjini D, Handley R et al (2006) Dynamic ultrasound as a selection tool for reducing Achilles tendon reruptures. Am J Sports Med 34:1395–1400

Koury V, Cardinal E (2009) "Tenomalacia": a new sonographic sign of tendinopathy? Eur Radiol 19:144–146

Koury V, Cardinal E, Brassard P (2008) Atrophy and fatty infiltration of the supraspinatus muscle: sonography versus MRI. Am J Roentgenol 190:1105–1111

Kumm TR, Szabunio MM (2010) Elastography for the characterization of breast lesions: initial clinical experience. Cancer Control 17:156–161

Lee CL, Huang MH, Chai CY et al (2008) The validity of *in vivo* ultrasonographic grading of osteoarthritic femoral condylar cartilage: a comparison with *in vitro* ultrasonographic and histologic gradings. Osteoarthr Cartil 16:352–358

Lin EC, Middleton WD, Teefey SA (1999) Extended field of view sonography in musculoskeletal imaging. J Ultrasound Med 18:147–152

Martinvoli C, Bianchi S, Derchi LE (1999) Tendon and nerve sonography. Rad Clin North Am 37(4):691–711

Martinoli C, Bianchi S, Dahmane M et al (2002) Ultrasound of tendons and nerves. Eur Radiol 12:44–55

Mathiesen O, Konradsen L, Torp-Pedersen S et al (2004) Ultrasonography and articular cartilage defects in the knee: an in vitro evaluation of the accuracy of cartilage thickness and defect size assessment. Knee Surg Sports Traumatol Arthrosc 12:440–443

McNally EG (2008) Ultrasound of the small joints of the hands and feet: current status. Skelet Radiol 37:99–103

Meyer DC, Hoppeler H, von Rechenberg B et al (2004) A pathomechanical concept explains muscle loss and fatty muscular changes following surgical tendon release. J Orthop Res 22:1004–1007

Middleton WD (1992) Ultrasonography of the shoulder. Radiol Clin N Am 30:927–940

Naredo E, Acebes C, Möller I et al (2009) Ultrasound validity in the measurement of knee cartilage thickness. Ann Rheum Dis 68:1322–1327

Narici M, Cerretelli P (1998) Changes in human muscle architecture in disuse-atrophy evaluated by ultrasound imaging. J Gravit Physiol 5:73–74

Nazarian L, McShane JM, Ciccotti MG et al (2003) Dynamic US of the anterior band of the ulnar collateral ligament of the elbow in asymptomatic major league baseball pitchers. Radiology 227:149–154

O'Connor PJ, Grainger AJ, Morgan SR et al (2004) Ultrasound assessment of tendons in asymotomatic

volunteers: a study of reproducibility. Eur Radiol 14:1968–1973

Østergaard M, Court-Payen M, Gideon P et al (1995) Ultrasonography in arthritis of the knee. A comparison with MR imaging. Acta Radiol 36:19–26

Padua L, Martinoli C (2008) From square to cube: ultrasound as a natural complement of neurophysiology. Clin Neurophysiol 119:1217–1218

Peer S, Bodner G, Meirer R et al (2001) Examination of postoperative peripheral nerve lesions with high-resolution sonography. Am J Roentgenol 177:415–419

Pillen S, Arts IM, Zwarts MJ (2008) Muscle ultrasound in neuromuscular disorders. Muscle Nerve 37:679–693

Reeves ND, Maganaris CN, Narici MV (2004) Ultrasonographic assessment of human skeletal muscle size. Eur J Appl Physiol 91:116–118

Robben SGF, Lequin MH, Diepstraten AFM et al (1999) Anterior joint capsule of the normal hip and in children with transient synovitis: US study with anatomic and histologic correlation. Radiology 210:499–507

Rohrschneider WK, Fuchs G, Tröger J (1996) Ultrasonographic evaluation of the anterior recess in the normal hip: a prospective study on 166 asymptomatic children. Pediatr Radiol 26:629–634

Rutheford OM, Jones DA (1992) Measurement of fibre pennation using ultrasound in the human quadriceps in vivo. Eur J Appl Physiol Occup Physiol 65:433–437

Schmidt WA, Schmidt H, Schicke B et al (2004) Standard reference values for musculoskeletal ultrasonography. Ann Rheum Dis 63:988–994

Strobel K, Hodler J, Meyer DC et al (2005) Fatty atrophy of supraspinatus and infraspinatus muscles: accuracy of US. Radiology 237:584–589

Szkudlarek M, Narvestad E, Klarlund M et al (2004) Ultrasonography of the metacarpophalangeal joints in rheumatoid arthritis: comparison with magnetic resonance imaging, conventional radiography, and clinical examination. Arthritis Rheum 44:2103–2112

Thoirs K, Williams MA, Cert G et al (2008) Ultrasonographic measurements of the ulnar nerve at the elbow. J Ultrasound Med 27:737–743

Van der Woude HJ, Vanderschueren G (1999) Ultrasound in musculoskeletal tumors with emphasis on its role in tumor follow-up. Radiol Clin N Am 37:753–766

Walton JM, Roberts N, Whitehouse GH (1997) Measurement of the quadriceps femoris muscle using magnetic resonance and ultrasound imaging. Br J Sports Med 31:59–64

Webb JM, Bannister GC (1999) Percutaneous repair of the ruptured tendo Achillis. J Bone Joint Surg Br 81:877–880

Yesildag A, Kutluhan S, Sengul N et al (2004) The role of ultasonographic measurements of the median nerve in the diagnomsis of carpal tunnel syndrome. Clin Radiol 59:910–915

Ying M, Yeung E, Brian L et al (2003) Sonographic evaluation of the size of Achilles tendon: the effect of exercise and dominance of the ankle. Ultrasound Med Biol 29:637–642

Yoon JS, Kim BJ, Kim SJ et al (2007) Ultrasonographic measurements in cubital tunnel syndrome. Muscle Nerve 36:853–855

Magnetic Resonance Imaging

4

Filip M. Vanhoenacker and Koenraad L. Verstraete

Contents

F. M. Vanhoenacker, M.D., Ph.D. (✉)
Department of Radiology, University Hospital
Antwerp, Antwerp University,
Wilrijkstraat 10, 2650 Edegem, Belgium

Department of Radiology, AZ Sint-Maarten,
Duffel-Mechelen, Rooienberg 25,
2570 Duffel, Belgium

Department of Radiology, University Hospital Ghent,
De Pintelaan, 185, 9000 Ghent, Belgium
e-mail: filip.vanhoenacker@telenet.be

K. L. Verstraete, M.D., Ph.D.
Department of Radiology, University Hospital Ghent,
De Pintelaan, 185, 9000 Ghent, Belgium

4.1   Introduction

In the past, textbooks dedicated to measurements in musculoskeletal imaging have been almost exclusively dedicated to roentgenographic measurements (Keats and Lusted 1985). They focused particularly on static measurements, whereas dynamic and functional aspects were often disregarded. Moreover, quantitative evaluation of soft tissues was not included.

Since the introduction of MRI in imaging of the musculoskeletal system, quantification of musculoskeletal disorders has evolved from a pure static assessment to a more functional evaluation.

The purpose of this chapter is to give a short overview of the capabilities of magnetic resonance imaging in measurement techniques of the musculoskeletal system.

For didactical reasons, we will focus in the first section on the classic orthopedic measurement techniques, which have been adapted to MRI, followed by a short discussion on new applications of MRI in the morphologic evaluation of the musculoskeletal system.

In the last section of this chapter, functional applications of MRI will be discussed.

4.2 (Modified) Static Orthopedic Measurements on MRI

Evaluation of Lesion Size

Evaluation of the size of a lesion has always been an important issue in imaging, because it may influence the therapeutic strategy and the patient's prognosis. The prototype is the size of a bone or soft tissue tumor. Compared to conventional radiography, the size of the tumor can be assessed very precisely in the three imaging planes on MRI. Although high-quality isotropic reformations (MPR) can be obtained with current "state-of-the-art" multidetector CT technology as well, MRI allows more accurate evaluation of both bone and soft tissue involvement, due to its higher-contrast resolution (Figs. 4.1 and 4.2). For comparison of the lesion size on follow-up studies, it is—however—of utmost importance to use the same MRI parameters (such as field of view, matrix, scaling angulation, etc.). Most modern MR equipments have pre-installed software to copy identical image parameters for follow-up studies.
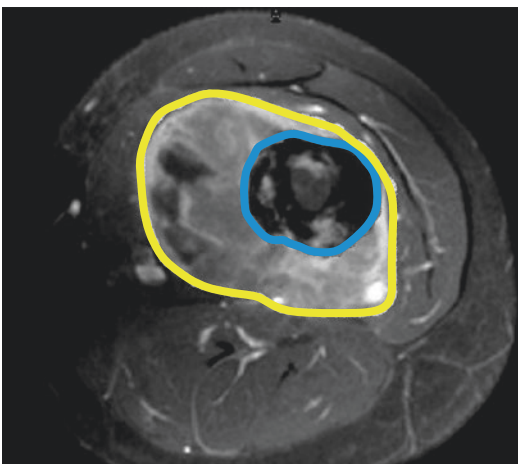

Fig. 4.1 Ewing's sarcoma. Axial fat-suppressed T2-weighted MR image demonstrating the size of both the bone (*blue*) and soft tissue components (*yellow*) of the lesion

Evaluation of Positional Abnormalities

Relative positional abnormalities of bones as a consequence of an underlying pathology have been traditionally evaluated by standard radiography, but these measurements can be performed by MRI as well.

Most of these topographic measurements will be discussed separately in the regional anatomic sections of the book.

The current chapter will deal with some illustrative examples.

Anterior Tibial Translation as Secondary Sign of Anterior Cruciate Ligament Rupture

Anterior translation of the tibia with respect to the femur can occur when the anterior cruciate ligament of the knee is disrupted.

A quick and easy method of assessing tibial translation is to measure it directly. A tangent is drawn at the most posterior point of the lateral femoral condyle to form the baseline from which the tibial translation will be measured (Chan et al. 1994). The section midway between the cortex adjacent to the posterior cruciate ligament and the most lateral section containing the femoral condyle is used. A distance of greater than 5 mm separating the posterior margin of the tibial plateau from this line indicates anterior tibial translation (Fig. 4.3a).

The big advantage of MRI, compared to other imaging modalities, is that—due to its high-contrast resolution—direct visualization of underlying pathology is possible (e.g., ACL rupture, Fig. 4.3b). Furthermore, other associated bone (e.g., secondary bone bruise associated with ACL rupture, Fig. 4.3a) or soft tissue injuries (e.g., medial collateral ligament rupture) can be evaluated at once.

Patellar Maltracking

Another clinical indication in which traditional static orthopedic measurements techniques can be performed on MRI is patellar maltracking. Patients with chronic instability may suffer from patello-femoral dysplasia with one or more of the following
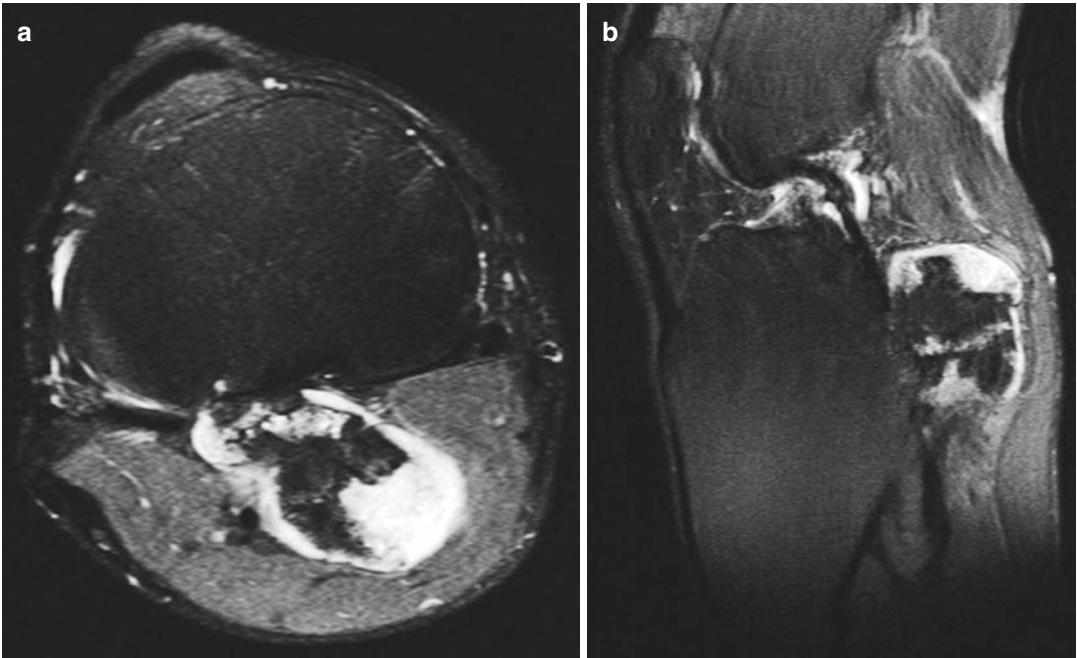
Fig. 4.2 (**a**, **b**) Cartilaginous exostosis of the tibia in a patient with hereditary multiple exostoses syndrome. (**a**) Axial fat-suppressed T2-weighted MR image. (**b**) Sagittal fat-suppressed T2-weighted MR image. The size of both the bony exostosis and the overlying cartilage cap (high signal intensity areas) can be appreciated very precisely
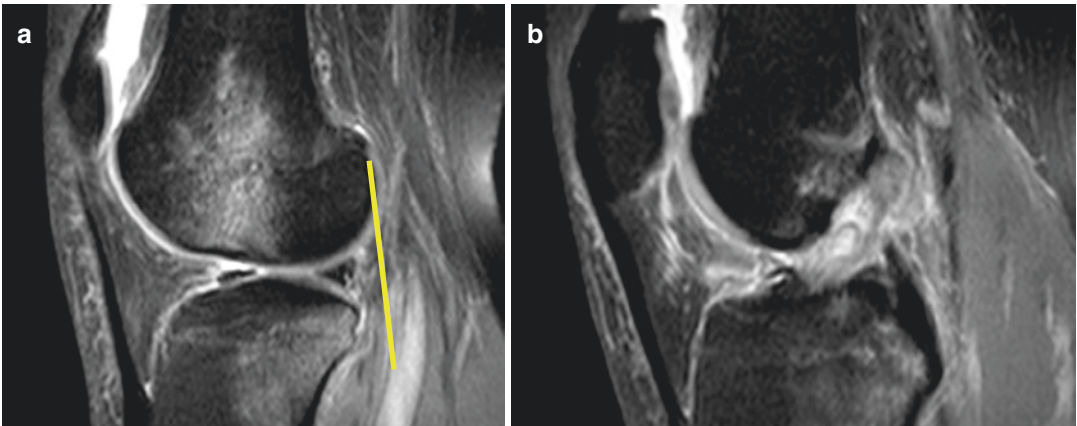

Fig. 4.3 (**a**, **b**) Anterior tibial translation as a secondary sign of anterior cruciate ligament (ACL) rupture. (**a**) Sagittal fat-suppressed T2-weighted MR image. A line drawn tangential to the lateral femoral condyle passes more than 5 mm from the posterior tibial margin. Note also bone marrow edema at the posterolateral aspect of the tibia and at the midportion of the lateral femoral condyle, due to bone impaction as result of the anterior subluxation of the tibia relative to the femur (**b**). Midsagittal fat-suppressed T2-weighted MR image shows complete disruption of the ACL

anatomical positional abnormalities: a high riding patella (patella alta), a flat trochlear groove, and a laterally positioned tibial tubercle (Ostlere 2007).

MRI may identify and quantify these anatomical abnormalities, similar to other imaging modalities such as plain radiography or CT.

The degree of patella alta is assessed on sagittal images by calculating the ratio of the minimum length of the posterior surface of the patellar tendon divided by the maximum length of the patella (Fig. 4.4). This ratio should be under 1.3–1.5 (Miller et al. 1996; Shabshin et al. 2004).

The relative position of the tibial tubercle is assessed on MRI by measurement of the tibial tubercle-trochlear groove (TT-TG) distance. This is the distance between the position of the trochlear groove and the tibial tubercle in the sagittal plane. In practice two slices are selected on an axial scan, one at the level of the trochlear groove and one at the level of the attachment of the patellar tendon at the tubercle. The two slices are superimposed. A baseline is drawn along the back of the femoral condyles. Two lines are drawn perpendicular to this baseline, one through the tibial tubercle and one through the deepest point of the trochlear groove. The TT-TG is the distance between these two lines (Fig. 4.5). The upper limit of this distance is 1.7–1.8 cm.

Grading of Spondylolisthesis

The word spondylolisthesis is derived from the Greek words *spondylo* meaning spine and *listhesis* meaning to slip or slide. Spondylolisthesis is a descriptive term referring to slippage (usually forward) of a vertebra and the spine above it relative to the vertebra below.

The most common types of spondylolisthesis are due to aging (degenerative spondylolisthesis) or due to a bony defect (isthmic spondylolisthesis).

Degenerative Spondylolisthesis

Degenerative spondylolisthesis, due to osteoarthritis of the facet joints, is by far the most common cause of spinal segments slipping on top of each other. Typically, as continued degeneration weakens the facet joints, the L4 vertebral body
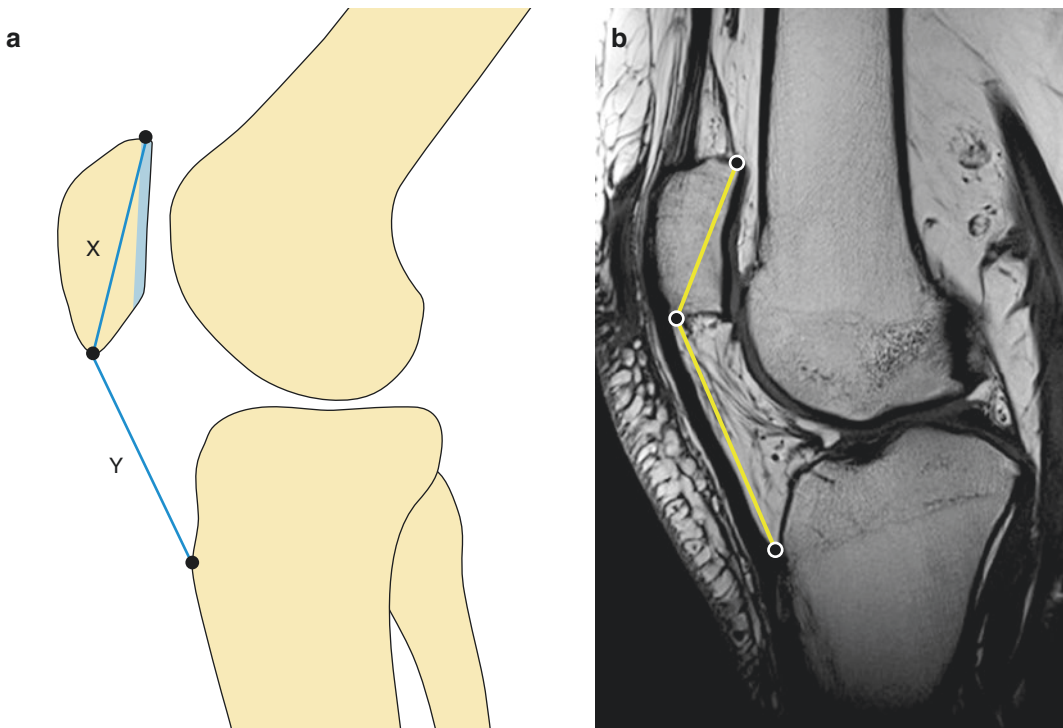

Fig. 4.4 Diagram illustrating the position of the patella (**a**). X = the maximum length of the patella, Y = the minimum length of the posterior surface of the patellar tendon. This Y/X ratio should be under 1.3–1.5. Note the abnormal ratio on the MR sagittal image (**b**)
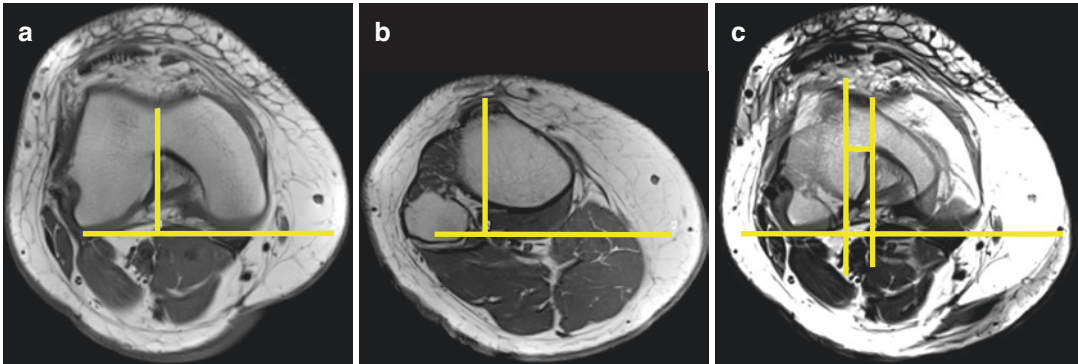
Fig. 4.5 Diagrams illustrating the TT-TG distance estimation. Two MR slices are selected on an axial scan, one at the level of the trochlear groove (**a**) and one at the level of the attachment of the patellar tendon at the tubercle (**b**). The two slices are superimposed (**c**). A baseline is drawn along the back of the femoral condyles. Two lines are drawn perpendicular to this baseline, one through the tibial tubercle and one through the deepest point of the trochlear groove. The TT-TG is the distance between these two lines

slips forward on the L5 vertebral body. Since the L4–L5 segment has substantial flexion-extension-type movement, this area is most likely to slip. The next most likely level is L3–L4 and rarely L5–S1.

Isthmic Spondylolisthesis

Isthmic spondylolisthesis is due to a specific bony defect in the spine called spondylolysis. Spondylolysis is a defect in a specific region called the pars interarticularis. A pars defect is most commonly the result of repetitive microtrauma during childhood. Some sports are thought to make children more susceptible to developing spondylolysis, including gymnastics, diving, and football. The level L5–S1 is most commonly affected.

Grading of spondylolisthesis usually occurs on a lateral plain radiograph, according to the Meyerding classification (Fig. 4.6). This measurement can be applied on a sagittal MR image as well. A disadvantage of MRI compared to plain films is that MRI is usually performed in the supine position, ignoring the effect of axial loading of a standing radiograph. To overcome this problem, MR techniques for upright, weight-bearing, dynamic-kinetic MRI of the spine have been developed (Jinkins 2003).

Another indirect measurement, which is helpful to distinguish degenerative spondylolisthesis from isthmic spondylolisthesis (Ulmer et al. 1994), evaluates the position of the spinous processes on a lateral plain radiograph or on a sagittal MR image (Malghem et al. 2011) (Fig. 4.7).

A disadvantage of MRI, compared to CT, is that direct visualization of the defect in the pars interarticularis in case of an isthmic spondylolisthesis is much more difficult to demonstrate on MRI than on CT (Leone et al. 2011).

Volumetric Measurements

Volumetric assessment of cartilage is a typical example, in which clinical MR imaging may be useful.

Many imaging methods are available to assess articulate cartilage. Conventional radiography can be used to detect gross loss of cartilage evident as narrowing of the distance between the bony components of the joint, but it does not image cartilage directly. Secondary changes such as osteophyte formation can be seen, but conventional radiography is insensitive to early chondral damage. Conventional arthrography, CT arthrography, or MR arthrography are more invasive techniques providing information limited to the contour of the cartilage surface.

MR imaging offers a noninvasive means of assessing the status and degree of degenerative cartilage and the adjacent bone and allows measurement of the effectiveness of treatment.
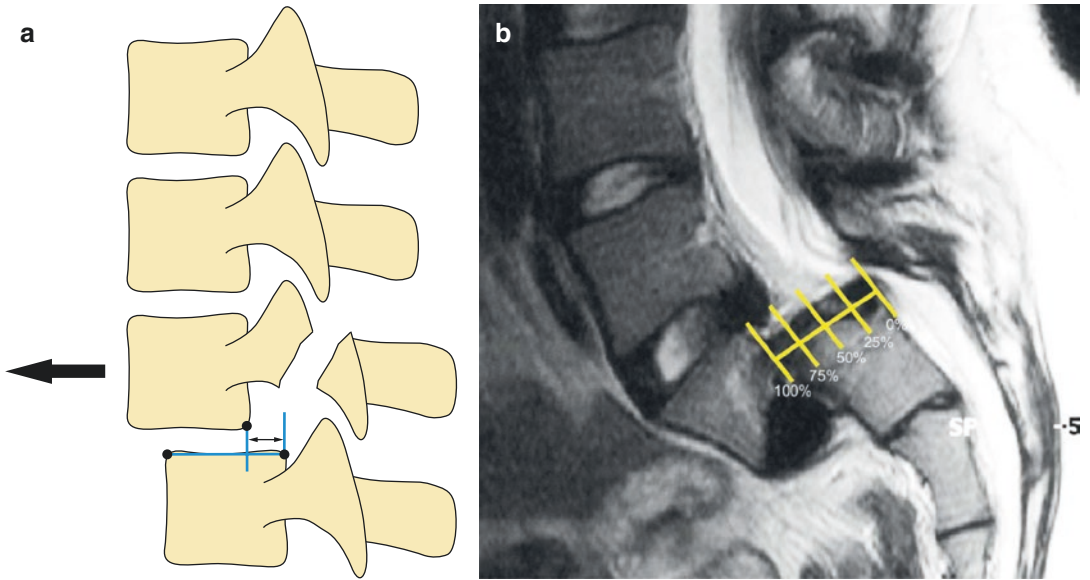
Fig. 4.6 Diagram of the grading of spondylolisthesis (**a**) and a sagittal MR image (**b**) (Meyerding). The two *arrows* on the diagram, one indicating vertebral body width and the other indicating the amount of slippage that has occurred, represent the measurements needed. The ratio of amount of slippage to vertebral body width is obtained as a percentage. Grade 1 is a ratio of 0–25%, grade 2 is 25–50%, grade 3 is 50–75%, and grade 4 is 75–100%. Note the 100% slip on the MR image (**b**) at the L5/S1 level
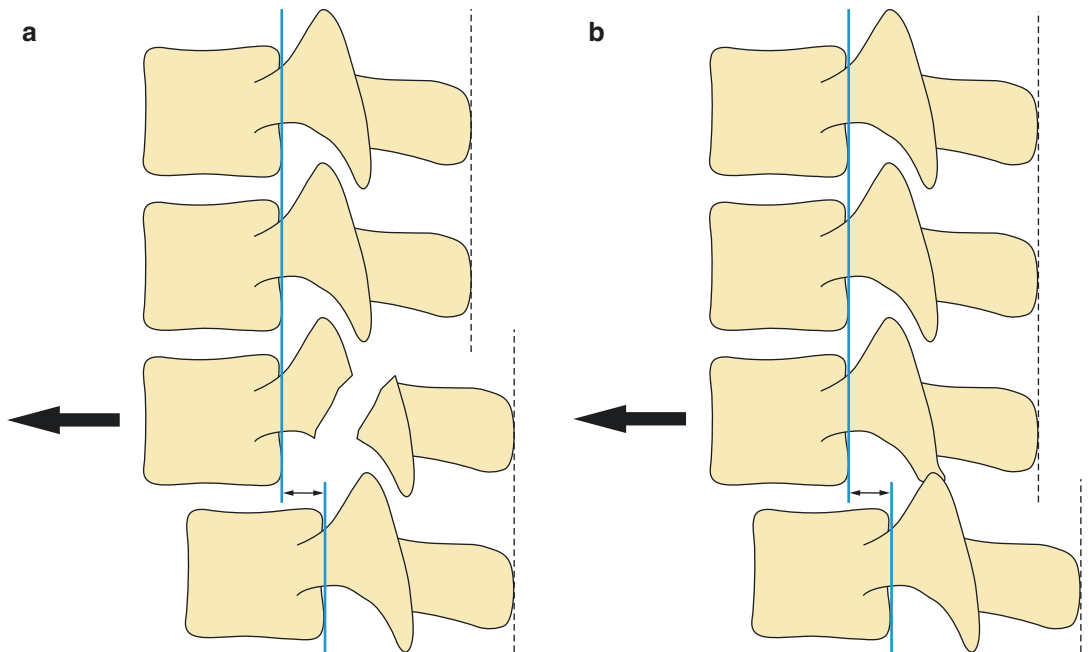
Fig. 4.7 (**a**, **b**) Measurement technique for differentiation of isthmic versus degenerative spondylolisthesis on a lateral plain film or sagittal MR image. (**a**) In isthmic spondylolysis, there is anterior slippage of the vertebral body due to lysis of the pars interarticularis, whereas the spinous process remains in line with the underlying vertebra. The anteroposterior diameter of the spinal canal is increased. (**b**) In degenerative spondylolysis, the spinous process slips anteriorly along with the vertebral body, resulting in a step-off of the spinous process with the underlying vertebra

An ideal MR imaging study for cartilage should provide accurate assessment of cartilage thickness and volume, demonstrate morphological changes of the cartilage surface, demonstrate internal cartilage signal changes, allow evaluation of subchondral bone, and allow evaluation of the underlying cartilage physiology (Gold et al. 2005).

Three-dimensional spoiled gradient-recalled echo imaging with fat suppression (3D-SPGR) is the standard technique for evaluation of cartilage volume and thickness measurements (Cicuttini et al. 2000), but does not highlight surface defects with fluid and does not evaluate other joint structures such as ligaments or menisci (Gold et al. 2005).

A combination of a variety of advanced steady-state free precession (SSFP)-based imaging techniques with high-field MR imaging shows promise in creating cartilage thickness maps and volume measurements at improved resolution of the images, yielding greater accuracy of the measurements than current 3D-SPGR sequences (Gold et al. 2005; Huysse and Verstraete 2007; Horng et al. 2011).

Figure 4.8 represents an illustration of a cartilage thickness map of the femoral condyle, displaying thickness of cartilage in a 3D image.

Physiological MR imaging of articular cartilage will be discussed in the section on functional imaging.
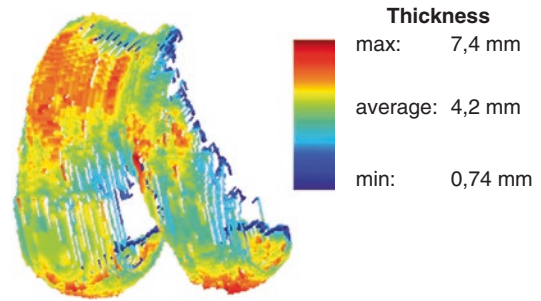

Fig. 4.8 Cartilage thickness map of femoral condyle, displaying thickness of cartilage in a 3D image with a color-encoded thickness scale. This image was created by semiautomated segmentation and extraction of high signal intensity voxels of cartilage from a thin-section volume acquisition (fat-suppressed 3D-SPGR MR image) using selective water excitation (we) (FLASH-3Dwe; 128 slices of 1 mm) (reprinted with permission from Huysse and Verstraete 2007)

4.3   Other Morphologic Measurements of Bone and Soft Tissue

Grading Fat Infiltration in Muscles

Computed tomography and MRI of muscular trophicity have been performed for neuromuscular diseases and in spine disorders. The areas of muscular CT hypodensity observed seem to correspond to fat content, which does not necessarily mean that there is a muscular atrophy. Moreover, the pattern on CT scan is often not of specific diagnostic value (Schwarz et al. 1988).

MRI and CT have also been used to evaluate fatty infiltration associated with rotator cuff tear (Goutallier et al. 1994; Zanetti et al. 1998). The assessment of fatty atrophy of the muscle of the rotator cuff is particularly important for the prognosis of surgical treatment. The clinical outcome of a rotator cuff repair is significantly correlated with the degree of fatty muscle degeneration of the rotator cuff muscle (Schaefer et al. 2002).

MRI is much more sensitive than CT in detecting minor fatty changes semiquantitatively. A parasagittal T1-weighted turbo spin-echo sequence is most suitable for grading of fatty changes within the supraspinatus tendon (Fig. 4.9). Five stages of grading have been proposed (Goutallier et al. 1994; Vanhoenacker et al. 2007):

Stage 0: Normal muscle; no fat infiltration.
Stage 1: The muscle contains some fatty streaks.
Stage 2: Important fatty infiltration, but still more muscle than fat.
Stage 3: There is as much fat as muscle.
Stage 4: There is more fat than muscle.

Grading Muscle Atrophy

Another important factor influencing the outcome of rotator cuff repair is the grade of muscle atrophy.

Quantitative volumetric assessment of cross-sectional areas is not very practical in routine clinical practice.
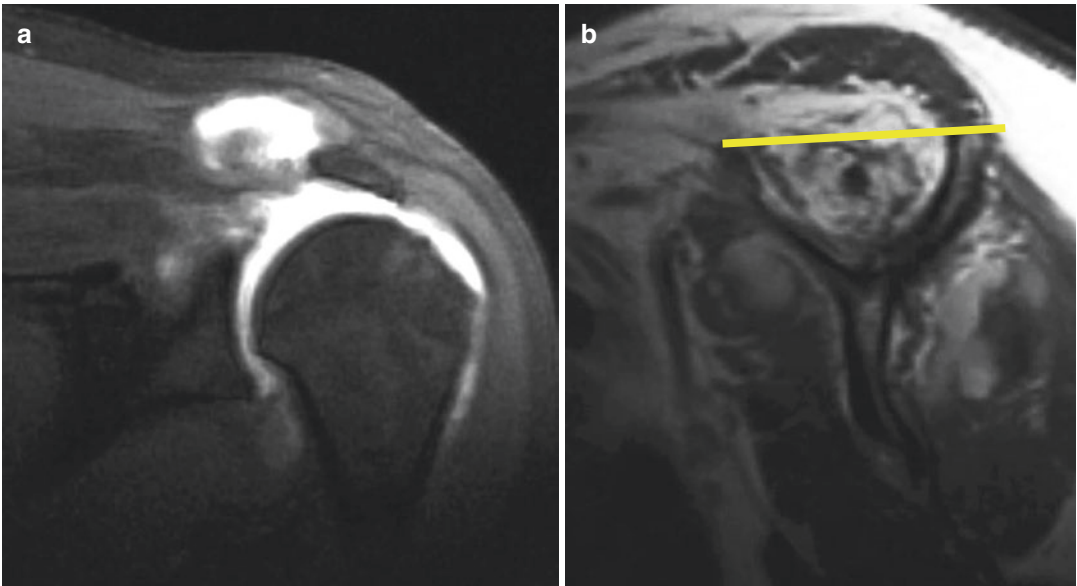
Fig. 4.9 (**a**, **b**) Grading of fatty changes within the supraspinatus muscle associated with a rotator cuff tear. (**a**) Coronal fat-suppressed T1-weighted MR arthrogram showing a full-thickness tear of the supraspinatus. (**b**) Parasagittal T1-weighted MR image demonstrating important fatty infiltration stage 3 within the supraspinatus muscle belly. Note also a positive tangent sign with grade 2 muscle atrophy (see also Fig. 4.10)

An example of a very quick semiquantitative assessment of muscle atrophy in rotator cuff disease has been presented by Zanetti et al. (1998), on parasagittal T1-weighted turbo spin-echo MR sequences. A tangent line is drawn through the superior borders of the scapular spine and the superior margin of the coracoid. The tangent sign is abnormal when the supraspinatus muscle does not cross the tangent. Three grades of muscle atrophy may be distinguished (Figs. 4.9b and 4.10).
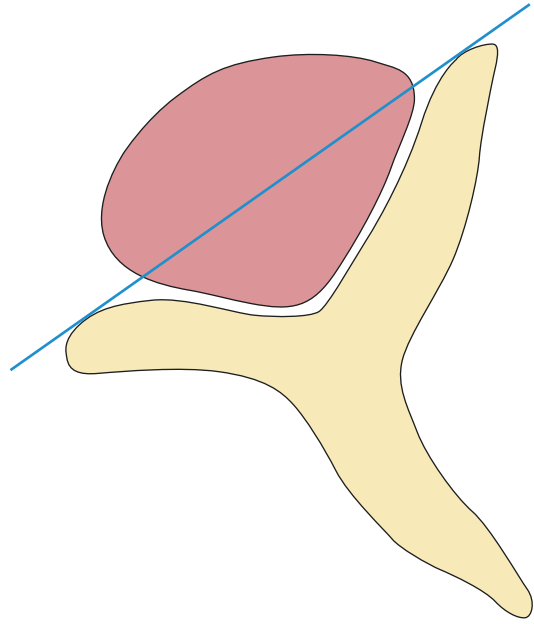

Fig. 4.10 Schematic line drawing of the tangent line

4.4   Functional Measurements

Dynamic Contrast-Enhanced MRI

Basic Principles

Dynamic contrast-enhanced MRI is a method of physiological imaging, based on fast or ultrafast imaging, with the possibility of following the early enhancement kinetics of a water-soluble contrast agent after intravenous bolus injection (0.2 mL/kg at an injection rate of 5 mL/s).

A sufficiently high temporal resolution and serial imaging of at least one image per 3.5–7 s is required for this type of imaging.

This technique provides clinically useful information, by depicting tissue vascularization and perfusion, capillary permeability, and composition of interstitial space (Verstraete et al. 1994).

Imaging is performed during and immediately after bolus injection to study the initial distribution of the contrast agent in the capillaries and into the interstitial space of the tissues.

During the first pass of the contrast agent through the capillaries, a net unidirectional, fast diffusion occurs into the extravascular tissue, due to the high concentration gradient between the intravascular and interstitial space, accounting for approximately 50% of the circulating contrast agent in normal tissues (Verstraete and Bloem 2006).

After the first pass, the diffusion rate immediately drops because the concentration of the recirculating contrast has decreased owing to further dilution in the blood and partial accumulation in the interstitial space. The length of the time interval between the end of the first pass and the equilibrium phase, with equal concentrations of contrast medium in plasma and interstitial space, depends on the size of the interstitial space.

After the equilibrium phase, the contrast medium is progressively washed out from the interstitial space as the arterial concentration decreases. Only in highly vascular lesions with a small interstitial space does early washout occur within the first minutes after bolus injection (Verstraete and Bloem 2006).

The factors determining contrast kinetics are summarized in Fig. 4.11.

Imaging Evaluation

Evaluation of a series of images obtained with dynamic contrast-enhanced MRI can be performed by different postprocessing techniques, quantitatively and/or qualitatively.

The region-of-interest method is the most used quantitative method in clinical practice (Verstraete et al. 1995). In this method, signal intensities in a determined ROI are measured and plotted against time in a time-intensity curve (TIC). The TICs provide a graphic display of the early pharmokinetics of the contrast agent during and immediately after the first pass. From these curves, quantitative information can be derived. An example of a TIC and quantitative parameters is summarized in Fig. 4.12.

Other quantitative postprocessing methods, used by other investigators, are first-pass images (Verstraete and Bloem 2006) and discrete signal processing (Reddick et al. 1994).

Indications

Dynamic contrast-enhanced MRI has been used in various clinical applications, such as:

1. Musculoskeletal tumors

   (a) Differentiation of benign from malignant musculoskeletal tumors (Geirnaerdt et al. 2000; Van Rijswijk et al. 2004; Verstraete et al. 2017)
   (b) Tissue characterization by narrowing down the differential diagnosis (Verstraete and Bloem 2006; Verstraete et al. 2017)
   (c) Identification of areas of viable tumor before biopsy (Verstraete and Bloem 2006)
   (d) Differentiation of tumor from surrounding edema (Lang et al. 1995)
   (e) Monitoring of chemotherapy (Verstraete and Bloem 2006; Verstraete et al. 2017)
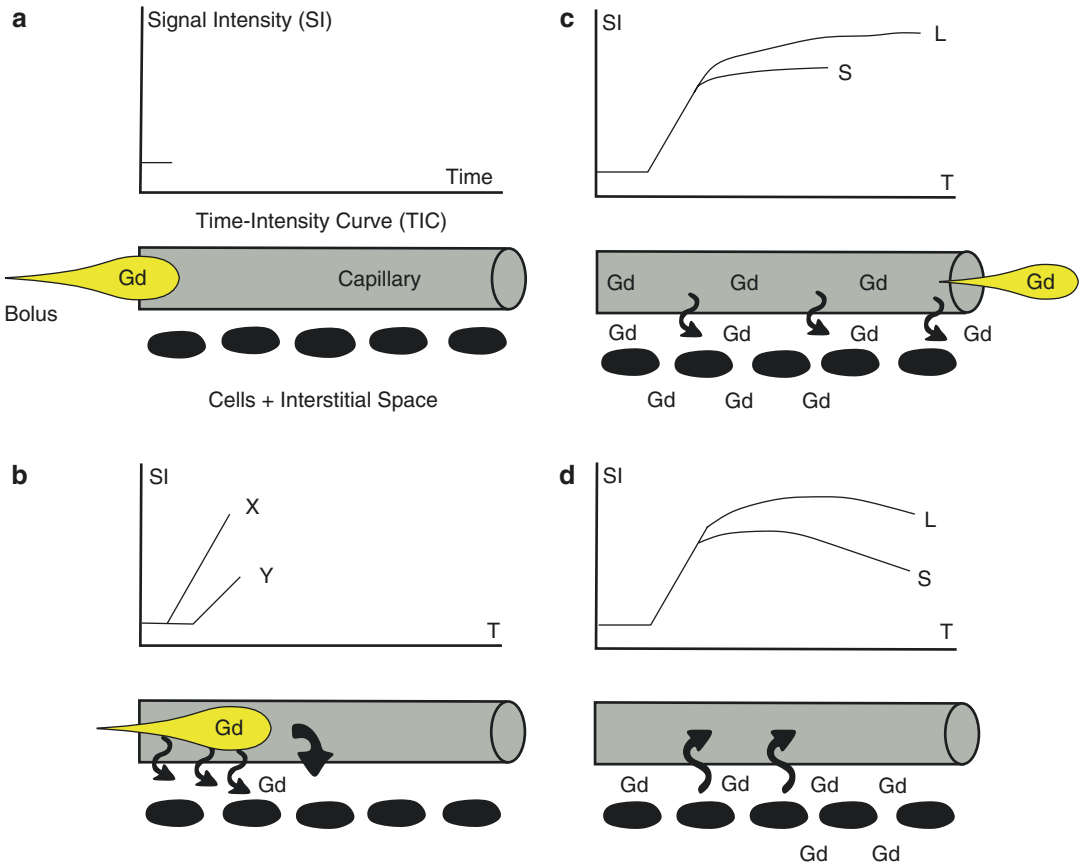   (f) Detection of residual or recurrent tumor (Verstraete and Bloem 2006; Verstraete et al. 2017)

Fig. 4.11 (**a–d**) Factors determining early tissue enhancement. The *lower parts* of **a–d** show what occurs at the level of the capillary and the interstitial space after intravenous bolus injection; the *upper parts* graphically display the changes in signal intensity (*SI*) in a time-intensity curve. (**a**) The time interval between the intravenous bolus injection and arrival of the bolus in the capillary is determined by the injection rate, the heart rate, the localization of the lesion, and the local capillary resistance (tissue perfusion). (**b**) The enhancement rate during the first pass of the contrast agent is determined by number of vessels (tissue vascularization), local capillary resistance (tissue perfusion), and capillary permeability. Tissues with high vascularization, perfusion, and capillary permeability (*X*) will enhance earlier and faster than tissues with a lower number of vessels, higher capillary resistance, and lower capillary permeability (*Y*). (**c**) After the first pass of the bolus, the SI increases further until the concentration of the gadolinium (*Gd*) contrast medium in the blood and the interstitial space of the tissues are equal. In tissues with a small (*S*) interstitial space, this equilibrium is reached earlier than in tissues with a larger (*L*) interstitial space. (**d**) After the arterial concentration of the contrast medium decreases, the SI drops, while the Gd is progressively washed out from the interstitial space. This progress occurs faster in tissues with a small (*S*) interstitial space than in tissues with a large (*L*) interstitial space (reprinted with permission from Verstraete and Bloem 2006)

2. Early detection of avascular necrosis and transient osteoporosis (Tsukamoto et al. 1992; Malizos et al. 2004)
3. Viability of vascularized grafts (Bey et al. 2001)
4. Evaluation of rheumatoid arthritis and inflammatory sacroiliitis (Konig et al. 1990; Huang et al. 2000; Bollow et al. 1995; Gaspersic et al. 2008)
5. Evaluation of carpal tunnel syndrome (Sugimoto et al. 1994)
6. Differentiation between benign vertebral compression fracture and pathologic fracture (Chen et al. 2002; Biffar et al. 2010)

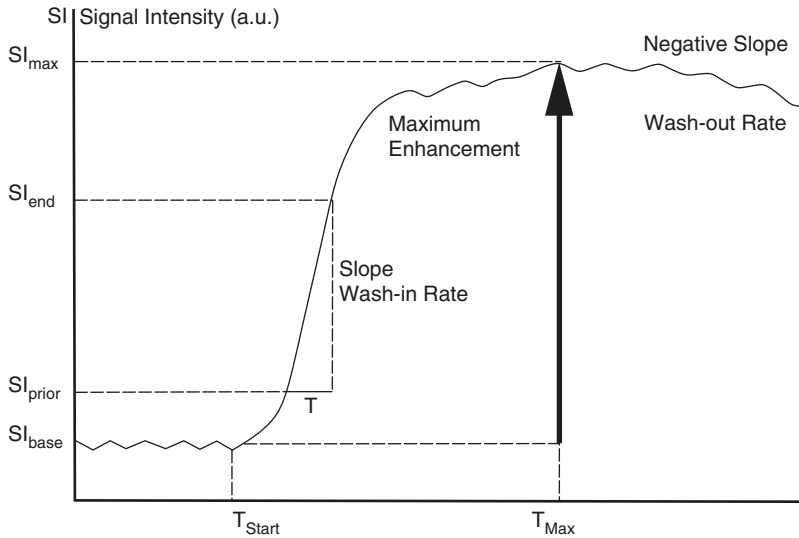More coverage is found in the appropriate chapters in the book.

Fig. 4.12 Time-intensity curve (TIC). In a TIC, the temporal change of the signal intensity in a region of interest (ROI; or pixel) is plotted against time. At T_{start}, when the bolus enters the ROI, the signal intensity rises above the baseline signal intensity (SI_{base}). The steepest slope represents the highest enhancement rate during the first pass (wash-in rate) and is mainly determined by tissue vascularization, perfusion, and capillary permeability. At T_{max}, the time of maximum enhancement, capillary and interstitial concentrations reach equilibrium. The time period between the end of the first pass and the maximum enhancement is mainly determined by the volume of the interstitial space. The washout rate can be calculated from the negative slop of the curve (*a.u.* arbitary units, *T* time interval between SI_{end} and SI_{prior}) (reprinted with permission from Verstraete and Bloem 2006)

Chemical Shift Imaging

Basic Principles

The MR signal in a normal MR image originates from two types of hydrogen nuclei: protons in water molecules and protons in fat molecules (Dixon 1984). These protons have a different molecular environment leading to a slightly different MR frequency, due to the so-called "chemical shift" effect.

The Dixon method uses this frequency difference to separate the individual contribution of water and fat. This makes it possible to quantify the fat signal fraction (Dixon 1984).

Indications and Its Alternatives

The use of quantitative chemical shift imaging (QCSI) has been known for years. QCSI has been described in hematological disorders (Rosen et al. 1988), in Gaucher's disease (Johnson et al. 1992), and in detecting response to treatment in Gaucher's disease (Rosenthal et al. 1995).

The mean fat fraction in the healthy volunteers is 0.37 (SD 0.08) (Maas et al. 2001).

In Gaucher's disease, there seems to be a clear relationship between a low-fat fraction measured with QCSI and the occurrence of bone complications, such as avascular necrosis, osteopenia, localized or diffuse bone destruction, and fracture (Maas et al. 2002a, b). A fat fraction <0.23 is considered a serious risk factor for the development of bone complications.

An increase of fat fraction of 10% results in a decrease of the relative risk for bone complications by 85%.

Dixon QCSI is also a sensitive technique for monitoring of treatment response of the bone marrow compartment to enzyme replacement therapy (Hollak et al. 2001; Maas et al. 2011) (Fig. 4.13).

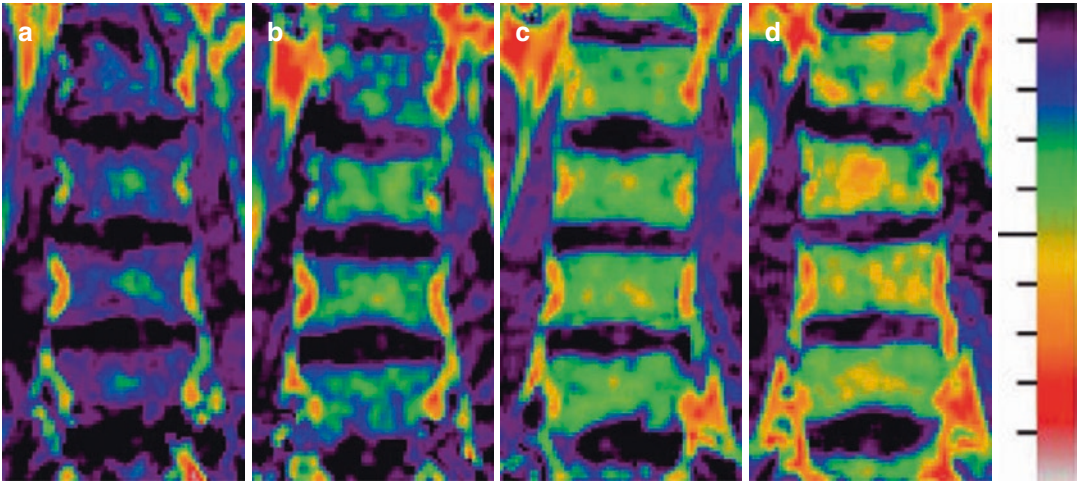Bone marrow response is detectable within the first year of onset of treatment.

Fig. 4.13 (**a–d**) Example of quantitative chemical shift imaging in Gaucher's disease. 50-year-old female patient before therapy and follow-up every 2 years. Response to therapy is clearly noted by means of altered fat fraction. Fat fraction $a = 0.22$, $b = 0.34$, $c = 0.41$, $d = 0.53$ (Courtesy of M. Maas, Amsterdam)

Although the QCSI technique has been shown to be a robust technique, there are some limitations.

This technique is not included in the standard packages of sequences of commercially available MR systems. Moreover, a physicist is required for implementation of this technique, and extensive expertise is required for interpretation. For all the above mentioned reasons, this technique is currently not available in most MR centers.

Therefore, several semiquantitative visual scoring systems have been developed for monitoring of bone marrow infiltration (Maas et al. 2002a, b; Poll et al. 2001; Rosenthal et al. 1992; Vlieger et al. 2002).

As a result, several visual scoring systems have been described in the literature (Maas et al. 2002a, b). Most of these scoring systems, however, do not evaluate axial bone marrow and have not been compared to state-of-the-art QCSI.

In our opinion, the bone marrow score (BMS) technique, developed by Maas et al. (2003), is the most useful technique that can be regarded as the second best technique for semiquantitative evaluation of bone marrow involvement by GD.

The BMB in Gaucher's disease shows a significant correlation with QCSI fat fraction ($\rho = -0.78$, $p < 0.0001$). In longitudinal measurements BMB is able to detect response to therapy; however QCSI is more sensitive.

The MRI technique is based on the evaluation of both the spine (axial bone marrow) and femora (peripheral bone marrow). Sagittal T1- and T2-weighted MR images of the lumbar spine and coronal T1- and T2-MR images of both femora (from femoral head to distal femora) suffice as routine sequences.

The method of bone marrow scoring (BMB score) and interpretation is extensively summarized in Tables 4.1 and 4.2. Both the lumbar spine and femoral score are added up, which lead to a total score of maximum of 16 (femora, eight; lumbar spine, eight).

A higher BMB score signifies more severe bone marrow involvement (Maas et al. 2003).

For follow-up analysis, a decrease of three points was defined as good response within 95% confidence limits by Maas et al. (2003).

Diffusion-Weighted Imaging (DWI) in MSK Imaging

Basic Principles

This technique is based on the tissue-depending signal attenuation caused by incoherent thermal motion of water molecules (Brownian motion).

Table 4.1 BMB score of the femora (modified from Maas 2003)

	BMB score
A. Signal intensity[a]	
T2-WI hyperintense	2
T2-WI slightly hyperintense	1
T2-WI isointense	0
T2-WI slightly hypointense	1
T2-WI hypointense	2
T2-WI mixed type	3
T1-WI slightly hyperintense or isointense	0
T1-WI intensity slightly hypointense	1
T1-WI intensity hypointense	2
B. Sites of involvement	
Diaphysis	1
Proximal epiphysis/apophysis	2
Distal epiphysis	3

[a]Determined in relation to signal intensity of subcutaneous fat

Table 4.2 BMB score of the lumbar spine (modified from Maas 2003)

	BMB score
A. Signal intensity[a]	
T2-WI hyperintense	2
T2-WI slightly hyperintense	1
T2-WI isointense	0
T2-WI slightly hypointense	1
T2-WI hypointense	2
T1-WI slightly hyperintense	0
T1-WI isointense	1
T1-WI slightly hypointense	2
T1-WI hypointense	3
B. Infiltration pattern	
Patchy infiltration	1
Diffuse infiltration	2
Absence of fat in basivertebral vein region	1

[a]Determined in relation to signal intensity of nondiseased intervertebral disk

Changes of the motion of water molecules in biological tissue can be detected in various pathologic conditions. Initially, DWI was successfully applied in acute stroke, which can be detected by DWI within minutes after its onset (Le Bihan et al. 1986).

Imaging Techniques

Standard diffusion-weighted SE and TSE pulse sequences are seriously affected by motion artifacts. Images suitable for clinical use can be obtained either by adding a correction technique such as the navigator echo or by using new developed SE-based sequence (*k*-space spin-echo or the line scan diffusion imaging sequences).

Application of DW-EPI sequences to the bone marrow seriously restricts the image quality due to susceptibility artifacts. This problem is partially solved by the multi-shot DW-EPI sequence (Raya et al. 2005). SSFP sequences allow the acquisition of good-quality images in short time, but with the disadvantage of not being appropriate for quantitative DWI. Currently, no generally accepted standard sequence for DWI of the bone marrow has been established (Raya et al. 2005; Khoo et al. 2011).

Indications in Musculoskeletal Radiology

1. *Differential diagnosis of acute osteoporotic and neoplastic vertebral compression fractures* (Baur et al. 1998, 2001b; Dietrich et al. 2009). DWI can distinguish between both types of fractures since the microscopic structure is altered in both cases in a different way. DWI of benign fractures shows iso- or hypointensity in comparison to normal bone marrow because of a higher water mobility in bone marrow edema. Conversely, compression fractures due to malignant tumors lead to hyperintensity related to the high cellularity of tumor tissue. Quantitative analysis of DWI can be achieved by analyzing the ADC value in a region of interest within the abnormal vertebrae. However, there is considerable overlap in ADC values in patients with benign versus metastatic fractures (Khoo et al. 2011).
2. *Degenerative disease processes, such as disk and cartilage degeneration* (Baur and Reiser 2000; Eguchi et al. 2011).
3. *Differential diagnosis of bone neoplasms and soft tissue tumors* (Van Rijswijk et al. 2002). An overlapping spectrum of diagnostic DWI findings between benign and malignant etiologies limits the clinical value of DWI for this indication (Khoo et al. 2011).

4. *Distinction between necrotic and viable tumor tissue and differentiation between post-therapeutic soft tissue changes and tumor recurrence* (Baur et al. 2001a).
5. *Osteoporosis* (Yeung et al. 2004; Tang et al. 2010).
6. *Monitoring of therapy for ankylosing spondylitis* (Gaspersic et al. 2008).

Kinematics

Basic Principles

Kinematics describes the movement of a body without reference to force or mass. With static MRI joint kinematics and the effect of muscular contractions on the position of the joint cannot be assessed. Kinematic MR imaging made it possible to evaluate joint function and the relative alignment of joint structures through a specific range of motion. The technique has been developed in recognition of the fact that certain pathologic conditions are dependent on the specific position of the joint or exist in response to loading or stress (Shellock 1997).

Imaging Techniques

Kinematic MRI has been performed on all types of MR systems, including high field strength tunnel-shaped systems, low or middle field strength open systems, low field strength C-shaped magnet systems, and low field strength dedicated extremity systems (Shellock 1997).

Open MRI systems offer the advantages of allowing greater incremental movements of certain joints and greater comfort for patients during kinematic MRI procedures.

Specific positioning devices are necessary for the performance of kinematic examinations. These devices are used to guide and maintain the joint in a specific imaging plane through a specific range of motion. Positioning devices may also apply resistance to the joint during movement and can incorporate surface coils to facilitate MR imaging (Vandevenne et al. 2010).

Kinematic MRI methods may be divided into four types (Shellock 1997): (1) incremental, passive positioning, (2) motion-triggered cine MR imaging, (3) active movement, and (4) active movement against resistance.

Incremental, Passive Positioning

The incremental, passive positioning technique involves the gradual movement and sequential imaging of the joint through a specific range of motion. Gradient-echo pulse sequences are usually used for this purpose.

Motion-Triggered Cine MR Imaging

Motion-triggered cine MR imaging, proposed by Melchert et al. (1992), follows the principle used in electrocardiographic (ECG)-triggered cine MRI studies of the heart. The periodically performed joint movements are represented by an electric signal, which is used to trigger the MR scanner. A pneumatic pressure transducer, commonly applied for respiratory monitoring, is placed on the joint. The cyclic pressure alterations are registered by the sensor during joint motion and are transformed by an active differentiator to an ECG-like signal, comparable to that used in standard cine MR imaging of the heart. Gradient-echo sequences are used in a multiple-slice, multiple-phase technique. The patient is instructed to repeat the joint movement in a similar extent throughout the imaging acquisition cycle, which may last for two to several minutes. The major disadvantage of this method is the dependence on patient compliance (Muhle et al. 1999).

Active Movement

The active movement technique is performed with ultrafast gradient-echo pulse sequences or echo planar imaging in a single-slice, multiple-phase technique. Acquisition times of one image per second or less are required for this form of imaging (Shellock 1997; Muhle et al. 1999). The main advantage of this technique is it is less dependent on patient cooperation and compliance.

Active Movement Against Resistance

The active movement against resistance method is similar to the active movement technique with respect to MRI requirements. This form of kinematic MRI imposes a resistive load to stress the joint during dynamic motion (Shellock 1997).

Indications

Kinematic MRI has been applied to evaluate many joints such as the temporomandibular joint (Iwasaki et al. 2010), the knee and patellofemoral joint (Muhle et al. 1999; McNally et al. 2000; Shin et al. 2009; wrist (Fulmer et al. 1989; Bergey et al. 1989; Moritomo et al. 2006), ankle (Shellock 1997), shoulder (Sans et al. 1996), hip (Scheys et al. 2011), and spine (Jinkins and Dworkin 2003; Jayakumar et al. 2006; Takasaki et al. 2011).

Relaxometry

Basic Principles

MR imaging is characterized by excitation of water molecules and relaxation of the molecules back to an equilibrium state. The exponential time constants describing this relaxation are referred to as T1 and T2 relaxation times and are constant for a given tissue at a given MR field strength. Changes in these relaxations times can be due to tissue pathology or the effect of the presence of contrast agents in the tissues.

Indications

Cartilage Imaging: T2 Relaxation Time Mapping of Cartilage

The T2 relaxation time of articular cartilage is a function of the water content and collagen ultrastructure of the tissue. Measurement of the spatial distribution of the T2 relaxation time may reveal areas of increased or decreased water content, correlating with cartilage damage. An image of the T2 relaxation time is generated with either a color or a grayscale map representing the relaxation map (Dardzinski et al. 1997; Gold et al. 2005).

Aging is associated with a symptomatic increase in T2 relaxation times in the transitional zone of cartilage (Mosher et al. 2000). Focal increases in T2 relaxation times within cartilage have been associated with matrix damage, particularly loss of collagen integrity.

Muscle Imaging: T2 Mapping of Muscle

Muscle activation increases T2 signal intensity on MRI, leading to recruitment images that demonstrate spatial patterns and intensity of muscle activation. These T2 activation maps are useful for visualizing and quantifying various aspects of muscle function. Activity-dependent changes in T2 result from an increase in the T2 relaxation time of muscle water.

The mechanism of increased T2 signal results from osmotically driven shifts of muscle water that increase the volume of the intracellular space and from intracellular acidification resulting from the end products of metabolism. Although the spatial resolution of magnetic resonance imaging is still insufficient to map territories of individual motor units, it is possible to demonstrate nonuniform activation between subregions or compartments of muscle. T2 mapping of muscle is promising for demonstrating aberrant muscle activation patterns in pathology and positive adaptation to exercise or rehabilitative intervention (Patten et al. 2003).

Spectroscopy

Basic Principles and Indications

Osteoporosis

MR-detectable bone marrow signal is composed mainly of water and lipids, and these two key components may be measured accurately by hydrogen 1 (^{1}H) magnetic resonance (MR) spectroscopy (De Bisschop et al. 1993). In vivo proton MR spectroscopy studies have shown both a linear increase in vertebral marrow fat content with aging and a higher fat concentration in males than females of similar age groups (Schellinger et al. 2000; Kugel et al. 2001).

Histomorphometric studies on bone biopsy samples have shown that marrow fat is increased in osteoporosis (Verma et al. 2002; Yeung et al. 2005) and showed that hydrogen 1 (^{1}H) magnetic resonance (MR) spectroscopy may be applied to the noninvasive assessment of marrow lipids (Li et al. 2011). Subjects with osteoporosis and osteopenia have significantly higher marrow fat

content compared to age-matched subjects with normal bone density. There is a clear relationship between marrow fat and bone density as measured by dual-energy X-ray absorptiometry (DXA). The increase in marrow fat seen in subjects with osteoporosis or osteopenia is the result of a preferential increase in saturated lipids compared to unsaturated lipids.

Characterization of Bone and Soft Tissue Tumors

Hydrogen 1 (^{1}H) magnetic resonance (MR) spectroscopy in combination with dynamic contrast material-enhanced MR imaging can reliably differentiate between benign and malignant musculoskeletal tumors by revealing the absence or presence of water-soluble choline metabolites (Wang et al. 2004). Choline and its derivates are thought to represent important constituents in the phospholipid metabolism of cell membranes (Miller 1991). In vivo, the choline peak (resonance at 3.2 ppm) is composed of choline, phosphocholine, phosphatidylcholine, and glycerophosphocholine. Elevation is thought to represent increased membrane phospholipid biosynthesis and also to be an active marker for cellular proliferation (Negendank 1992). In malignant tumors, cellular areas may contain more choline-containing components. Dynamic contrast-enhanced MR imaging may be used for sampling cellular areas for MR spectroscopy. Indeed, according to Van der Woude et al. (1998), the early enhanced regions represent areas of high biologic activities, such as cellularity, cell turnover time, and neovascularity.

In a series of 210 patients, Wang et al. (2011) found an overall diagnostic accuracy of 73.3% of hydrogen 1 (^{1}H) magnetic resonance (MR) spectroscopy in characterization of musculoskeletal bone and soft tissue neoplasms. The diagnostic accuracy was higher for smaller lesions (less than 4 cm) and for solid nonsclerotic lesions.

False-positive results were seen in benign lesions, due to hypercellular and hypervascular areas, such as in perineuroma, giant cell tumor, and an abscess. These lesions may show a high choline peak. A false-negative result was seen in a malignant parosteal osteosarcoma. The lower proton amounts and susceptibility effects in this densely ossified tumor may account for the false-negative choline uptake.

Assessment of Lipid Content of Muscles

Proton MR spectroscopy has been used to assess the lipid content in different metabolic disorders, such as congenital lipodystrophy (Szczepaniak et al. 1999) and acquired generalized lipoatrophy (Brechtel et al. 2000), and other causes of muscular hypo- or hypertrophy (Brechtel et al. 2009).

Routine assessment of the apparent lipid content of rotator cuff muscles is feasible with proton MR spectroscopy and provides the possibility to quantify fatty atrophy of the supraspinatus muscle more accurately than the semiquantitative assessment of fatty atrophy by CT or MRI (Pfirrmann et al. 2004). Proton MR spectroscopy is able to depict fatty muscle changes before they become visible on T1-weighted MR images.

References

Baur A, Reiser MF (2000) Diffusion-weighted imaging of the musculoskeletal system in humans. Skelet Radiol 29:555–562

Baur A, Stäbler A, Brüning R et al (1998) Diffusion-weighted MR imaging of bone marrow: differentiation of benign versus pathologic compression fractures. Radiology 207:349–356

Baur A, Huber A, Arbogast S et al (2001a) Diffusion-weighted imaging of tumor recurrences and post-therapeutic soft-tissue changes in humans. Eur Radiol 11:828–833

Baur A, Huber A, Ertl-Wagner B et al (2001b) Diagnostic value of increased diffusion weighting of a steady-state free precession sequence for differentiating acute benign osteoporotic fractures from pathologic vertebral compression fractures. Am J Neuroradiol 22:366–372

Bergey PD, Zlatkin MB, Dalinka M, Osterman AL, Machek J, Dolinar J (1989) Dynamic MR imaging of the wrist: early results with a specially designed positioning device. Radiology 173:26

Bey E, Paranque A, Pharaboz C, Cariou JL (2001) Postoperative monitoring of free fibular grafts by dynamic magnetic resonance imaging. Preliminary results in three cases of mandibular reconstruction. Ann Chir Plast Esthet 46(1):10–17

Biffar A, Sourbron S, Dietrich O et al (2010) Combined diffusion-weighted and dynamic contrast-enhanced imaging of patients with acute osteoporotic vertebral fractures. Eur J Radiol 76:298–303. Erratum in: Eur J Radiol 77:528

Bollow M, Braun J, Hamm B et al (1995) Early sacroiliitis in patients with spondyloarthropathy—evaluation with dynamic gadolinium-enhanced MR-imaging. Radiology 194:529–536

Brechtel K, Jacob S, Machann J et al (2000) Acquired generalized lipoatrophy (AGL): highly selective MR lipid imaging and localized (1)H-MRS. J Magn Reson Imaging 12:306–310

Brechtel K, Machann J, Pick M, Schaefer JF, Claussen CD, Schick F (2009) Changes in muscular lipids in unilateral isolated hypertrophy of gastrocnemius muscle can be revealed by 1H MR spectroscopy. Korean J Radiol 10:581–586

Chan WP, Peterfy C, Fritz RC et al (1994) MR diagnosis of complete tears of the anterior cruciate ligament of the knee: importance of anterior subluxation of the tibia. Am J Roentgenol 162:355–360

Chen WT, Shih TT, Chen RC et al (2002) Blood perfusion of vertebral lesions evaluated with gadolinium-enhanced dynamic MRI: in comparison with compression fracture and metastasis. J Magn Reson Imaging 15:308–314

Cicuttini F, Forbes A, Asbeutah A, Moriis K, Stuckey S (2000) Comparison and reproducibility of fast and conventional spoiled gradient-echo magnetic resonance sequences in the determination of knee cartilage volume. J Orthoped Res 18:580–584

Dardzinski BJ, Mosher TJ, Li S, Van Slyke MA, Smith MB (1997) Spatial variation of T2 in human articular cartilage. Radiology 205:546–550

De Bisschop E, Luypaert R, Louis O, Osteaux M (1993) Fat fraction of lumbar bone marrow using in vivo proton nuclear magnetic resonance spectroscopy. Bone 14:133–136

Dietrich O, Biffar A, Reiser MF, Baur-Melnyk A (2009) Diffusion-weighted imaging of bone marrow. Semin Musculoskelet Radiol 13:134–144

Dixon WT (1984) Simple proton spectroscopic imaging. Radiology 153:189–194

Eguchi Y, Ohtori S, Yamashita M et al (2011) Diffusion-weighted magnetic resonance imaging of symptomatic nerve root of patients with lumbar disk herniation. Neuroradiology 53:633–641

Fulmer JM, Harms SE, Flamig DP, Guerdon G, Machek J, Dolinar J (1989) High resolution cine MR imaging of the wrist. Radiology 173:26

Gaspersic N, Sersa I, Jevtic V, Tomsic M, Praprotnik S (2008) Monitoring ankylosing spondylitis therapy by dynamic contrast-enhanced and diffusion-weighted magnetic resonance imaging. Skelet Radiol 37:123–131

Geirnaerdt MJA, Hogendoorn PCW, Bloem JL, Taminiau AHM, van der Woude HJ (2000) Cartilaginous Tumors: fast contrast-enhanced MR imaging. Radiology 214:539–546

Gold GE, Hargreaves BA, Reeder SB, Vasanawala SS, Beaulieu CF (2005) Controversies in protocol selection in the imaging of articular cartilage. Sem Musculoskelet Radiol 9:161–172

Goutallier D, Postel JM, Bernageau J, Lavau L, Voisin MC (1994) Fatty muscle degeneration in cuff ruptures: pre- and postoperative evaluation by CT-scan. Clin Orthop 304:78–83

Hollak C, Maas M, Akkerman EM et al (2001) Dixon quantitative chemical shift imaging is a sensitive tool for the evaluation of bone marrow responses to individualized doses of enzyme supplementation therapy in type 1 Gaucher disease. Blood Cells Mol Dis 27:1005–1012

Horng A, Raya J, Zscharn M et al (2011) Locoregional deformation pattern of the patellar cartilage after different loading typeschigh-resolution 3D-MRI volumetry at 3 T in-vivo. Rofo 183:432–440

Huang J, Stewart N, Crabbe J et al (2000) A 1-year follow-up study of dynamic magnetic resonance imaging in early rheumatoid arthritis reveals synovitis to be increased in shared epitope-positive patients and predictive erosions at 1 year. Rheumatology 39:407–416

Huysse WCJ, Verstraete KL (2007) Cartilage trauma. In: Vanhoenacker FM, Maas M, Gielen L (eds) Imaging of orthopedic sports injuries. Springer, Berlin, pp 41–60

Iwasaki H, Kubo H, Harada M, Nishitani H (2010) Temporomandibular joint and 3.0 T pseudodynamic magnetic resonance imaging. Part 1: evaluation of condylar and disc dysfunction. Dentomaxillofac Radiol 39:475–485

Jayakumar P, Nnadi C, Saifuddin A, Macweeney E, Casey A (2006) Dynamic degenerative lumbar spondylolisthesis: diagnosis with axial loaded magnetic resonance imaging. Spine 31:E298–E301

Jinkins JR, Dworkin J (2003) Proceedings of the State-of-the-Art Symposium on Diagnostic and Interventional Radiology of the Spine, Antwerp, September 7, 2002 (Part two). Upright, weight-bearing, dynamic-

kinetic MRI of the spine: pMRI/kMRI. JBR-BTR 86(5):286–293

Johnson LA, Hoppel BE, Gerard EL et al (1992) Quantitative chemical shift imaging of the vertebral bone marrow in patients with Gaucher disease. Radiology 182:451–455

Keats TE, Lusted LB (1985) Atlas of Roentgenographic measurement, 5th edn. Year Book Medical, Chicago

Khoo MM, Tyler PA, Saifuddin A, Padhani AR (2011) Diffusion-weighted imaging (DWI) in musculoskeletal MRI: a critical review. Skeletal Radiol 40(6):665–681. https://doi.org/10.1007/s00256-011-1106-6

Konig H, Sieper J, Wolf KJ (1990) Rheumatoid arthritis—evaluation of hypervascular and fibrous pannus with dynamic MR imaging enhanced with Gd-DTPA. Radiology 176:473–477

Kugel H, Jung C, Schulte O, Heindel W (2001) Age- and sex-specific differences in the 1H spectrum of vertebral bone marrow. J Magn Reson Imaging 13:263–268

Lang P, Honda G, Roberts T et al (1995) Musculoskeletal neoplasm: perineoplastic edema versus tumor on dynamic postcontrast MR images with spatial mapping of instantaneous enhancement rates. Radiology 197:831–839

Le Bihan D, Breton LD et al (1986) MR imaging of intravoxel incoherent motions: applications to diffusion and perfusion in neurologic disorders. Radiology 161:401–407

Leone A, Cianfoni A, Cerase A, Magarelli N, Bonomo L (2011) Lumbar spondylolysis: a review. Skelet Radiol 40:683–700

Li X, Kuo D, Schafer AL, Porzig A, Link TM, Black D, Schwartz AV (2011) Quantification of vertebral bone marrow fat content using 3 tesla MR spectroscopy: reproducibility, vertebral variation, and applications in osteoporosis. J Magn Reson Imaging 33:974–979

Maas M, Akkerman EM, Venema HW et al (2001) Dixon quantitative chemical shift MRI for bone marrow evaluation in the lumbar spine: a reproducibility study in healthy volunteers. J Comput Assist Tomogr 25:691–697

Maas M, Hollak CE, Akkerman EM, Aerts JM, Stoker J, den Heeten GJ (2002a) Quantification of skeletal involvement in adults with type 1 Gaucher's disease: fat fraction measured by Dixon quantitative chemical shift imaging as a valid parameter. AJR Am J Roentgenol 179:961–965

Maas M, Poll LW, Terk MR (2002b) Imaging and quantifying skeletal involvement in Gaucher disease. Br J Radiol 75(Suppl 1):A13–A24

Maas M, van Kuijk C, Stoker J, Hollak CE, Akkerman EM, Aerts JF, den Heeten GJ (2003) Quantification of bone involvement in Gaucher disease: MR imaging bone marrow burden score as an alternative to Dixon quantitative chemical shift MR imaging—initial experience. Radiology 229(2):554–561

Maas M, Kuijper M, Akkerman EM (2011) From Gaucher's disease to metabolic radiology: translational radiological research and clinical practice. Semin Musculoskelet Radiol 15:301–306

Malghem J, Maldague B, Vande Berg B, Lecouvet F (2011) Imagerie de l'appareil musculo-squelettique. Sauramps Médical, Montpellier, 363 pp

Malizos KN, Zibis AH, Dailiana Z, Hantes M, Karahalios T, Karantanas AH (2004) MR imaging findings in transient osteoporosis of the hip. Eur J Radiol 50:238–244

McNally EG, Ostlere SJ, Pal C et al (2000) Assessment of patellar maltracking using combined static and dynamic MRI. Eur Radiol 10:1051–1055

Melchert UH, Schröder C, Brossman J, Muhle C (1992) Motion-triggered cine MR imaging of active joint movement. Magn Reson Imaging 10:457–460

Miller BL (1991) A review of chemical issues in 1-H NMR spectroscopy: n-acetyl-L-aspartate, creatine and choline. NMR Biomed 4:47–52

Miller TT, Staron RB, Feldman F (1996) Patellar height on sagittal MR imaging of the knee. AJR Am J Roentgenol 167:339–341

Moritomo H, Murase T, Goto A, Oka K, Sugamoto K, Yoshikawa H (2006) In vivo three-dimensional kinematics of the midcarpal joint of the wrist. J Bone Joint Surg Am 88:611–621

Mosher TJ, Dardzinski BJ, Smith MB (2000) Human articular cartilage: influence of aging and early symptomatic degeneration on the spatial variation of T2-preliminary findings at 3 T. Radiology 214:259–266

Muhle C, Brossmann J, Heller M (1999) Kinematic CT and MR imaging of the patellofemoral joint. Eur Radiol 9:508–519

Negendank W (1992) Studies of human tumors by MRS: a review. NMR Biomed 5:303–324

Ostlere S (2007) Imaging of anterior knee pain and maltracking. In: Vanhoenacker FM, Maas M, Gielen L (eds) Imaging of orthopedic sports injuries. Springer, Berlin, pp 307–319

Patten C, Meyer RA, Fleckenstein JL (2003) T2 mapping of muscle. Semin Musculoskelet Radiol 7:297–305

Pfirrmann CWA, Schmid MR, Zanetti M, Jost B, Gerber C, Hodler J (2004) Assessment of fat content in supraspinatus muscle with proton MR spectroscopy in asymptomatic volunteers and patients with supraspinatus tendon lesions. Radiology 232:709–715

Poll LW, Koch J-A, vom Dahl S et al (2001) Magnetic resonance imaging of bone marrow changes in Gaucher disease during enzyme replacement therapy: first German long-term results. Skelet Radiol 30:496–503

Raya JG, Dietrich O, Reiser MF, Bauer-Melnyk A (2005) Techniques for diffusion-weighted imaging of bone marrow. Eur J Radiol 55:64–73

Reddick WE, Langston JW, Meyer WH et al (1994) Discrete signal-processing of dynamic contrast-enhanced MR-imaging—statistical validation and preliminary clinical-application. J Magn Reson Imaging 4:397–404

Rosen BR, Fleming DM, Kushner DC et al (1988) Hematological bone marrow disorders: quantitative chemical shift MR imaging. Radiology 169:799–804

Rosenthal DI, Barton NW, Mckusick KA et al (1992) Quantitative imaging of Gaucher disease. Radiology 185:841–845

Rosenthal DI, Doppelt SH, Mankin HJ et al (1995) Enzyme replacement therapy for Gaucher disease: skeletal responses to macrophage-targeted glucocerebroside. Pediatrics 96:629–637

Sans N, Richardi G, Railhac JJ et al (1996) Kinematic MR imaging of the shoulder: normal patterns. AJR Am J Roentgenol 167:1517–1522

Schaefer O, Winterer J, Lohrmann C, Lauwenberger J, Reichelt A, Langer M (2002) Magnetic resonance imaging for supraspinatus muscle atrophy after cuff repair. Clin Orthop 403:93–99

Schellinger D, Lin CS, Fertikh D et al (2000) Normal lumbar vertebrae: anatomic, age, and sex variance in subjects at proton MR spectroscopy-initial experience. Radiology 215:910–916

Scheys L, Desloovere K, Spaepen A, Suetens P, Jonkers I (2011) Calculating gait kinematics using MR-based kinematic models. Gait Posture 33:158–164

Schwarz MS, Swash M, Ingram DA, Graham RD (1988) Patterns of selective involvement of thigh muscles in neuromuscular disease. Muscle Nerve 11:1240

Shabshin N, Schweitzer ME, Morrison WB et al (2004) MRI criteria for patella alta and baja. Skelet Radiol 33:445–450

Shellock FG (1997) Kinematic magnetic resonance imaging. Sem Musculoskel Radiol 1:143–173

Shin CS, Carpenter RD, Majumdar S, Ma CB (2009) Three-dimensional in vivo patellofemoral kinematics and contact area of anterior cruciate ligament-deficient and -reconstructed subjects using magnetic resonance imaging. Arthroscopy 25:1214–1223

Sugimoto H, Miyaji N, Ohsawa T (1994) Carpal-tunnel syndrome-evaluation of median nerve circulation with dynamic contrast-enhanced MR-imaging. Radiology 190:459–466

Szczepaniak LS, Babcock EE, Schick F et al (1999) Measurement of intracellular triglyceride stores by H spectroscopy: validation in vivo. Am J Phys 276:E977–E989

Takasaki H, Hall T, Oshiro S, Kaneko S, Ikemoto Y, Jull G (2011) Normal kinematics of the upper cervical spine during the flexion-rotation test—in vivo measurements using magnetic resonance imaging. Man Ther 16:167–171

Tang GY, Lv ZW, Tang RB, Liu Y, Peng YF, Li W, Cheng YS (2010) Evaluation of MR spectroscopy and diffusion-weighted MRI in detecting bone marrow changes in postmenopausal women with osteoporosis. Clin Radiol 65(5):377–381. https://doi.org/10.1016/j.crad.2009.12.011

Tsukamoto H, Kang YS, Jones LC et al (1992) Evaluation of marrow perfusion in the femoral head by dynamic magnetic resonance imaging—effect of venous occlusion in a dog model. Investig Radiol 27:275–281

Ulmer JL, Elster AD, Mathews VP, King JC (1994) Distinction between degenerative and isthmic spondylolisthesis on sagittal MR images: the importance of increased anteroposterior diameter of the spinal canal. AJR Am J Roentgenol 163:411–416

Van der Woude HJ, Verstraete KL, Hogendoorn PC, Taminiau AH, Hermans J, Bloem JL (1998) Musculoskeletal tumors; does fast dynamic contrast-enhanced subtraction MR imaging contribute to the characterization? Radiology 208:821–828

Van Rijswijk CS, Kunz P, Hogendoorn PC, Taminiau AH, Doornbos J, Bloem JL (2002) Diffusion-weighted MRI in the characterization of soft-tissue tumors. J Magn Reson Imaging 15:302–307

Van Rijswijk CSP, Geirnaert MJA, Hogendoorn PCW, Taminiau AHM, van Coevorden F, Zwinderman AH, Pope TL, Bloem JL (2004) Soft-tissue tumors: value of static and dynamic gadopentetate dimeglumine-enhanced MR imaging in prediction of malignancy. Radiology 233:493–502

Vandevenne J, Pearle A, Lang P, Pauly KB, Bergman G (2010) Clinical feasibility of a magnetic resonance tracking system to guide the position of the scan plane during physiologic joint motion. Radiol Med 115:133–140

Vanhoenacker FM, Van der Woude HJ, Vanhoenacker PK, De Praeter G (2007) MR arthrography of the rotator cuff. JBR-BTR 90:338–344

Verma S, Rajaratnam JH, Denton J, Hoyland JA, Byers RJ (2002) Adipocytic proportion of bone marrow is inversely related to bone formation in osteoporosis. J Clin Pathol 55:693–698

Verstraete KL, Bloem JL (2006) Dynamic contrast-enhanced magnetic resonance imaging. In: De Schepper AM, Vanhoenacker F, Gielen J, Parizel PM (eds) Imaging of soft tissue tumors, 3rd edn. Spinger, Berlin, pp 73–91

Verstraete KL, Dedeene Y, Roels H, Dierick A, Uyttendaele D, Kunnen M (1994) Benign and malignant musculoskeletal lesions-dynamic contrast-enhanced MR-imaging-parametric first-pass images depict tissue vascularization and perfusion. Radiology 192:835–843

Verstraete KL, Dutoit JC, Drapé JL, Bloem JL (2017) Magnetic resonance imaging: advanced imaging techniques. In: Vanhoenacker FM, Parizel PM, Gielen JL (eds) Imaging of soft tissue tumors, 4th edn. Spinger, Berlin, pp 85–113

Verstraete KL, Vanzieleghem B, De Deene Y et al (1995) Static, dynamic and first-pass MRI of musculoskeletal lesions using gadodiamide injection. Acta Radiol 36:27–36

Vlieger EJ, Maas M, Akkerman EM et al (2002) Vertebra disc ratio as a parameter for bone marrow involvement and its application in Gaucher disease. J Comput Assist Tomogr 26:843–848

Wang CK, Li CW, Hsieh TJ, Chien SH, Liu GC, Tsai KB (2004) Characterization of bone and soft-tissue tumors with in vivo ^{1}H MR spectroscopy: initial results. Radiology 232:599–605

Wang CK, Li CW, Hsieh TJ et al (2011) In vivo (1) H MRS for musculoskeletal lesion characterization: which factors affect diagnostic accuracy? NMR Biomed 25:359–368. https://doi.org/10.1002/nbm.1758

Yeung DK, Wong SY, Griffith JF, Lau EM (2004) Bone marrow diffusion in osteoporosis: evaluation with quantitative MR diffusion imaging. J Magn Reson Imaging 19(2):222–228

Yeung DKW, Griffith JF, Antonio GE, Lee FKH, Woo J, Leung PC (2005) Osteoporosis is associated with increased marrow fat content and decreased marrow fat unsaturation: a proton MR spectroscopy study. J Magn Reson Imaging 22:279–285

Zanetti M, Gerber C, Hodler J (1998) Quantitative assessment of the muscles of the rotator cuff with magnetic resonance imaging. Investig Radiol 33:163–170

Computer-Assisted Quantification

5

Philipp Peloschek, Georg Langs,
Reinhard Windhager, and Franz Kainberger

Contents

P. Peloschek
Radiology Center Vienna, Vienna, Austria
e-mail: ph@radiology-center.com

G. Langs • F. Kainberger (✉)
CIR—Computational Imaging Research Lab,
Department of Biomedical Imaging and Image-
Guided Therapy, Medical University of Vienna,
Vienna, Austria
e-mail: georg.langs@meduniwien.ac.at;
franz.kainberger@meduniwien.ac.at

R. Windhager
Department of Orthopaedic & Trauma Surgery,
Medical University of Vienna, Vienna, Austria
e-mail: reinhard.windhager@meduniwien.ac.at

5.1   Introduction

Computer-aided image analysis and decision support has become an indispensable part of treatment planning in orthopaedic surgery and in osteology. The first use of computers for image interpretation probably was for a musculoskeletal application and was published by Lodwick who developed a computer diagnostic model for the pattern analysis of osteolytic bone tumours in 1963 (Lodwick et al. 1963). The next important step forward was, after quantitative computed tomography, the development of dual X-ray absorptiometry (DXA, the abbreviation DEXA should not be used) in 1987 (Wahner et al. 1994). With this technique, the image is not in the centre of the radiology report but is used as a guidance tool for generating measurable quantification parameters of the bone density, the trabecular architecture, and the body composition with the impact of expressing trends. A more detailed analysis of bone structure in the form of a "virtual biopsy" is possible with micro-CT systems and, for in vivo investigations, with high-resolution peripheral quantitative computed tomography (HRpqCT) (Rügsegger et al. 1996). Semiautomated and later fully automated measurements of the skeleton is a further application which bases on contour finding techniques and was developed for orthopaedic treatment planning and skeletal age assessment (Niethard 1999). Parallel to these applications for radiogra-

phy and computed tomography, quantification schemes of MR data were established for the biochemical imaging of cartilage, for the perfusion of the synovial tissue in arthritis, and for the chemical shift imaging to measure the fat fraction in the bone marrow of patients with skeletal storage diseases (Kubassova 2007; Maas et al. 2011; Reiser et al. 1989; Trattnig et al. 2012). Many of these skeletal and soft tissue applications have been designed towards better patient's and social outcomes, with important research in the field of maxillofacial surgery for designing individual prosthetic devices with and without 3D printing and for automated steering of implant positioning (Ploder et al. 1995; Windhager et al. 1996).

Computer assistance has been shown to support the detection of disease patterns, to quantify changes over time in virtually all fields of musculoskeletal imaging, thus improving the use of imaging biomarkers in measuring treatment (Angwin et al. 2004; Gnudi et al. 2004; Herring and Dawant 2001; Mazzuca et al. 2003, 2004; Rubin et al. 2005; Sharp et al. 2000; Soo et al. 2005). These imaging biomarkers have considerable impact on decision-making for treatment monitoring and drug and device development and in many cases are used as a surrogate endpoint in clinical studies.

There is general agreement that computer-assisted imaging is not replacing but supporting the radiologist's or other physician's diagnosis. Despite deep learning systems can match or surpass the human's decision, errors are still possible. Therefore, as a ground rule, every form of computer-assisted imaging needs a signed report. In imaging informatics, the number of publications per year is steadily increasing with stepwise improvements of the applications that have to be correlated with the physician's diagnosis. In some cases, as in DXA or in preoperative endo-prosthesis planning, the automated quantification yields more precise results than the human interpretation, but most computer-assisted applications are still inferior to subjective assessment. The development of computer-assisted quantification of musculoskeletal diseases is oriented towards fully automated applications, i.e. measuring with not more than one mouse click, data exchange among PACS, post-processing and RIS systems, and data interpretation for physicians, other healthcare professionals, and patients.

The direction of this interdisciplinary research field goes beyond semiautomatic approaches, where constant guidance by a technician or physician is needed, towards fully automatic approaches that provide the clinician with a measurement result that only has to be reviewed. Basing on the underlying method, the musculoskeletal applications of computer-assisted quantification schemes may be divided into predominantly contour finding, segmentation and pattern analysis, and diagnosis-oriented techniques. The aim of this review is to present, beyond the routinely used MR sequences or PET-CT, a synoptic view on the various techniques and applications with a focus on clinical and potential clinical applications. Computer vision is, together with web search, self-driving vehicles and natural language processing part of artificial intelligence (AI) in imaging. Imaging informatics is currently on the move from traditional predefined engineered parameters to deep learning, so in this chapter, both existing applications basing on old technology and new, nondeterministic options are presented.

5.2 Techniques of Computer Vision

Computer vision is used in medical imaging as a complement to the human visual system to improve the precision and consistency, accuracy, and speed of radiological image interpretation. From a clinician's viewpoint, there are three relevant methods:

1. Model-based approaches, for which the computer learns a certain amount of a priori knowledge or certain assumptions are made about the shape or appearance of an object to be measured, before the actual application is performed
2. Registration-based approaches that find correspondences between different images, or volumes, and enable the user to measure and compare different structures
3. Classifier-dependent methods that focus on the classification or recognition of structures, textures, or pathologies

The borders between these groups are rather loose, and application of these methods is more complementary than exclusive. An example includes recent publications that formulate the segmentation or detection of anatomic structures, which has been a traditional domain of model-based approaches, as a classification task (Hong et al. 2006).

Model-Based Approaches

Model-based computer vision applications derive generally valid functions from the input of, e.g. a training set of bone shapes. This "training" is based on a set of annotated examples provided to the algorithm, which then derives a statistical model for the shape and texture of a certain structure. A parametric description of the plausible bone shapes is obtained. The model can be used for the automatic detection and segmentation of the learned structure (e.g. a proximal phalanx on a hand radiograph). In addition, the model can be used to define pathological features by comparing

the observation with the training population. Models rely on a priori knowledge that is acquired during the training phase. This phase is usually supervised by a human expert, although, more recently, weakly supervised models (i.e. the training images are restricted to images depicting the structure to be studied, but no additional annotations are provided by human experts) have achieved increasing levels of quality. Since they make the assessment of far more complex structures feasible than supervised training would allow with reasonable cost, this type of model can be expected to have a strong influence on the field of automatic quantification methods in medical imaging (Cootes et al. 2001; Langs et al. 2005). Examples of model-based approaches include active shape models (ASMs) or active appearance models (AAMs), which capture the shape and texture variation of a specific structure or object (Cootes et al. 2001; Donner et al. 2006). Geodesic active contours are another line of approaches that are also capable to incorporate a priori knowledge (Caselles et al. 1993). These types of models utilize the learned a priori knowledge to provide a robust segmentation (Leventon et al. 2000).

The medical fields in which model-based methods, and, in particular, active appearance models, are used are widespread: the segmentation of cardiac MRIs, the diaphragm in CT data, the vertebral morphometry in dual X-ray absorptiometry data, and in registration in functional heart imaging (Beichel et al. 2005; Stegmann et al. 2003; Roberts et al. 2006; Langs et al. 2006).

Registration Techniques and Their Applications

Image registration techniques establish correspondences across different images or volumes of medical data. That is, after registering two volumes, each point in one volume has a unique corresponding point in the other volume (the same applies to 2D images). Registration can be performed on data pairs stemming from the same modality and the same patient as, for example, in the compensation for tissue deformations when

contrast has to be detected in subtractive radiology. Registration can also be performed between pairs of different modalities. This is important if, for example, the high resolution of a CT scan needs to be merged with the soft tissue information from MRI. By registering the data, a new source of information emerges, since—for every point—data from both modalities is available, making analysis of differences and similarities possible. The registration of different modalities from many different individuals is employed for anatomic atlas building (Thompson et al. 2000).

Classifiers

Classifiers are algorithms that assign one of several possible classes to a certain example pattern. Classifiers are trained on several examples for which classes are known. After the training, the classifier is performed automatically and, given a new example, with an unknown class. There are a number of applications that use classifiers in the detection of pathology, i.e. for the differentiation between healthy and diseased as a classifier (Gefen et al. (2003).

Degrees of Computer Assistance for Measurements in Radiology

The use of digital techniques for the acquisition and processing of medical images has substantially increased in recent years. Hence, the possibilities to increase speed, enhance sensitivity or specificity, and reduce observer variability of well-circumscribed tasks in radiological reporting with computer assistance became a wide and emerging field of biomedical imaging research.

Computer Assistance for Measurements in Radiology
A nomenclature of four degrees may be proposed by means of a practical example, the assessment of the mechanical axes of the femur and the tibia:

1. Line drawing based on the mechanical axes of the femur and tibia with consecutive, standardized, manual angle measurement on the printed radiograph without computer assistance. This is the prototype of a standardized measurement in musculoskeletal radiology: widespread, easy to use, but limited by some inherent drawbacks.
2. Computer-assisted angle measurement on digital total leg radiographs. The inherent problems of interreader error with this method were not addressed by computer-assisted measurement software, as the measurements were performed by radiologists (in a digital manner).
3. Fully automatic approaches do not require manual interaction with the anatomic landmarks, such as the manual identification or marking of points contours, nor do the radiographs have to be cropped, rotated, or centred for the measurement procedure. The only interaction acceptable is, e.g. to define a region of interest. The axes are then measured autonomously by the algorithm, and measurement results are provided in a printable report. Thus, this method can be used by an assistant without the need for detailed instructions and allows the batch processing of large amounts of data to reduce the impact of computation time on the time required for the whole procedure.
4. Autonomous image analysis is the ultimate solution, where images are analysed by PACS-integrated and computer-assisted measurement software and results are put in the DICOM format. No user interaction is required to obtain the results. In any case, results must be confirmed by a certified radiologist because of the medicolegal issues.

The resultant quantitative information on radiographs can be fully exploited in an objective and reproducible way without the need for additional human resources (Roberts et al. 2006; Binkley et al. 2005; Genant 1997; Rea et al. 2001; Sailer et al. 2005).

Segmentation

A concise nominal definition of the object of interest is a prerequisite for the segmentation process and later analysis, assuming that a "correct" segmentation of the object in the image is possible at all. Anatomic variations emphasize the importance of a concise nominal definition of the object of interest, especially if low-contrast or overlapping structures complicate a "correct" segmentation.

The concise nominal definition of shapes was achieved in some clinical applications: e.g. in rheumatoid arthritis, joint space width and erosions are measured, while in osteoporosis, the shape of vertebral bodies and femoral heads are assessed quantitatively by more or less automated segmentation of these shapes (Angwin et al. 2004; Genant 1997; Bruynesteyn et al. 2004; Conrozier et al. 2004; Dacre and Huskisson 1989; Sharp 2004; van der Heijde 2000).

Segmentation is the isolation of an object of interest from the background, and the goal of segmentation is to define which part of the image data corresponds to the actual object. Automatic segmentation is desirable, but due to limitations imposed by image acquisition, pathological abnormalities, or anatomical variation, fully automatic segmentation is difficult to obtain in many cases. Approaches that use manual segmentation have proven to be time-consuming and inaccurate due to interreader variations. Interactive procedures, where manual interaction is combined with computational segmentation, are the methods of choice in many fields of medical image segmentation where low-contrast, overlapping, or touching objects and abnormal shapes are common. Thus, the computation effort supports precision, while the operator steers the segmentation, based on his/her opinion, to optimize accuracy. Thus, if "correct" segmentation is feasible, errors must be attributable to disagreement among radiologists and perceptual inaccuracy. Interactive segmentation should not be confused with manual processing, which has been shown to be susceptible to subjective results and inefficient operation.

An example of an interactive method is the coarse initial delineation of the object of interest, which, in turn, initializes the computational method. The initial curve or surface is optimized with a function-balancing shape and image properties. Initialization can be accomplished by drawing an initial curve freely, by adjusting predefined templates to the object, or by placing a starting point and control points close to the object's boundary (Beard et al. 1994; Brinkley 1993; Buck et al. 1995; Hinshaw et al. 1995; Kass et al. 1987; Neumann and Lorenz 1999; Vehkomäki et al. 1997). In the last case, initial points are used by the algorithm to begin the search for a globally optimal delineation of the contour. This strategy is also used by Live Wire and Live Lane, the Intelligent Scissors, and the Magic Crayon (Beard et al. 1994; Falcao et al. 1998, 2000). Graph cuts follow a similar interaction strategy, by letting the user define a small number of seed points on the object and on the background (Boykov and Kolmogorov 2004). Based on this annotation, an estimate of the object border is detected by the algorithm, and refinements can be performed by defining additional seed points.

In the Live Wire and Intelligent Scissors methods, a cost function that is dependent on local image information and image intensity statistics is defined for each pixel of an image. The cost function is based on a weighted combination of image-derived features, such as gradient magnitude or direction, with parameter values initialized from prior knowledge, and this function is dynamically updated based on the contour parts accepted by the user. The user dynamically provides local information that indicates the desired outcome, guiding the computational effort in a process of progressive refinement of the segmentation result.

For instance, in the Live Wire paradigm, the contour is displayed in real time by retrieving the shortest paths to the initial point by means of the cost function while moving the mouse cursor around, so that the user can dynamically evaluate the result and simply change the mouse position

to obtain a better delineation. The contour is accepted when the user clicks the mouse button, and this position becomes the starting point for a new boundary segment. The software ideally provides the expert with a tool that supports manual segmentation but, at the same time, accelerates this tedious process, provides immediate feedback, and produces repeatable results. Interactive definition of shapes is a highly effective strategy to exploit the synergy between a human operator who is superior in object recognition and an algorithm that is better in reproducible object delineation. Accuracy and precision of results are dependent on the anatomical complexity of the object of interest. As suggested above, the results of such a segmentation may be used:

1. Directly to evaluate distances (e.g. joint space width), shapes, or axes in different anatomic regions (Angwin et al. 2004; Mazzuca et al. 2004; Sailer et al. 2005)
2. Indirectly, if used for the training of algorithms, which then perform image analysis autonomously

Fully Automatic or Autonomous Approaches

These approaches do not require human interaction during application. Many of these methods are still in the early stages of clinical testing, but they are soon expected to reach a reliability level sufficient to be used in a clinical setting. The abovementioned semiautomatic segmentation can serve as a training annotation by an expert and does not have to be performed after a supervised learning phase during which the algorithm incorporates the anatomic a priori knowledge. From this point on, the algorithm is able to detect objects of interest (e.g. a bone); segment them (e.g. delineate the bone contour), even with ambiguous image content because of its model of anatomic appearance and shape; and, finally, use the model to perform measurements between predefined landmarks on the structures. These landmarks are defined reliably by the model, after training, and after their definition on a single prototype shape. Functional complexity and computation time are the defining characteristics of each method, and steps that are time-consuming or cumbersome for the user increase functional complexity and, thus, are indirectly correlated to the clinical acceptance of the system. Efficient interaction must be achieved by keeping the operation of the system as simple and operator independent as possible.

Deep Learning

Deep learning is a form of machine learning, and with its potential to allow rapid and scalable systems, it is more and more applied in radiology. With the traditional form, the machine is trained to analyse features and patterns from training sets. An early and widely used form was the artificial neural networks (ANN). With deep learning, no definition of features and no correlation to a standard are necessary, so that the cumbersome and in part inefficient training can be saved, if a powerful computer is used. Convolutional neural networks (CNNs) are the most prevalent deep learning architecture typologies in medical imaging today (Paul et al. 2016). A typical CNN comprises a series of layers that successively map image inputs to desired endpoints while learning increasingly higher-level imaging features (Hosny et al. 2018). A deep learning access for segmentation is characterized by fully CNNs. Another form is U-net which has been specifically designed for medical images, so that with a single deep learning system, the segmentation across multiple modalities and tissues is possible. With CNNs and other forms of AI, unsupervised classification is also possible. With AI, the process of image acquisition and reporting can also be supported. With its expanding capabilities, machine learning is an increasingly important part of research at the interface of computer science and medicine (Langs et al. 2018).

5.3   Applications

Geometric Measurements and Customized Treatment

Applications in this form are the assessment of limb and spine alignment for orthopaedic treatment planning, volume measurements of bone and soft tissue tumours, skeletal age assessment, and 3D devices for teaching anatomy.

Assessment of Limb and Spine Alignment, Surgical Planning, and Simulations

Today, computer-assisted techniques are available for all steps of correction procedures of malalignment, and many of them are indispensable for standardization and documentation. Computer-assisted measurements base on semiautomated or fully automated contour finding software with automated measurements of distances, angles, or volumes. The surgery can be planned by calculating the relevant parameters for designing the procedure and by virtually positioning a prosthesis in the bone. A simulation of the operation is possible with 3D images or with 3D printing. Image-guided surgery with navigation systems can today be regarded as a standard. The surgeon uses tracking devices for navigating the procedure to achieve a higher accuracy of hardware placement and a reliable documentation.

Lower limb axis lengths and angles (Fig. 5.1), especially associated with leg-length discrepancy, and spinal parameters can be precisely measured and calculated (Sailer et al. 2005). With 3D reconstruction, rotational abnormalities of lower limbs, scoliosis, and other spine deformities can be displayed and quantified (Wade et al. 2013). For lower limb alignment, several indices have been described (Krackow et al. 1990; Odenbring et al. 1993; Shearman et al. 1998; Tetsworth and Paley 1994). The very low radiation exposure of some of these systems, used in musculoskeletal and dental radiology, may result in insufficient spatial resolution of the images (Krug et al. 2014).

Templating is a process wherein the surgeon plans the size and the positioning of a device and quantify the degree of limb deformity in paediatrics, after trauma or prior to spine surgery. For preoperative planning, several dedicated software solutions are available on the market with huge libraries of prostheses for joint replacement. The contours of a given endoprosthesis, which has been registered from the real model by the industrial providers, are positioned within the image display of the patient's joint (Fig. 5.2). The contours of the implant are automatically aligned to anatomic landmarks, and the relevant distance and angle measurements are calculated. The systems are used for planning hip and knee surgery as well as many other applications. Such systems may also be used for perioperative osteotomy planning for the dysplastic hip, and on long-leg radiographs as well, as for osteophyte quantification (Sailer et al. 2005; Conn et al. 2002; Haddad et al. 2001; Hadler et al. 1978; Hefti 1995).

A simulation of the surgical procedure can be done with these templating software products. For improving the intuitive approach of surgery, additional 3D reconstructions for performing a virtual surgical planning can be used. Three-dimensional printing allows to generate a real model of the bone in the form of 3D templates, so that customized devices with optimized fitting can be generated and the surgical procedure be simulated (Ballard et al., 2018). Applications for printing prostheses and other devices are under development (Liacouras et al. 2017).

Volume Calculations

Volume calculations of bone and soft tissue tumours are, in contrast to other oncologic applications of computer-assisted imaging, difficult due to the great varieties of form and structure with inhomogeneous architecture and sometimes unsharp borders. In an animal model, volumetric treatment response assessment of osteolytic bone metastases with automated segmentation was shown to be superior to unidimensional measurements (Bretschi et al. 2014). In a clinical study about semiautomated volumetry of chordomas, however, the significantly longer investigation

Fig. 5.1 A 70-year-old female after total knee endoprosthesis. A standing anteroposterior radiograph of the lower extremity for assessment of limb length and angular inequality. Measurement was done in this case with a commercially available software
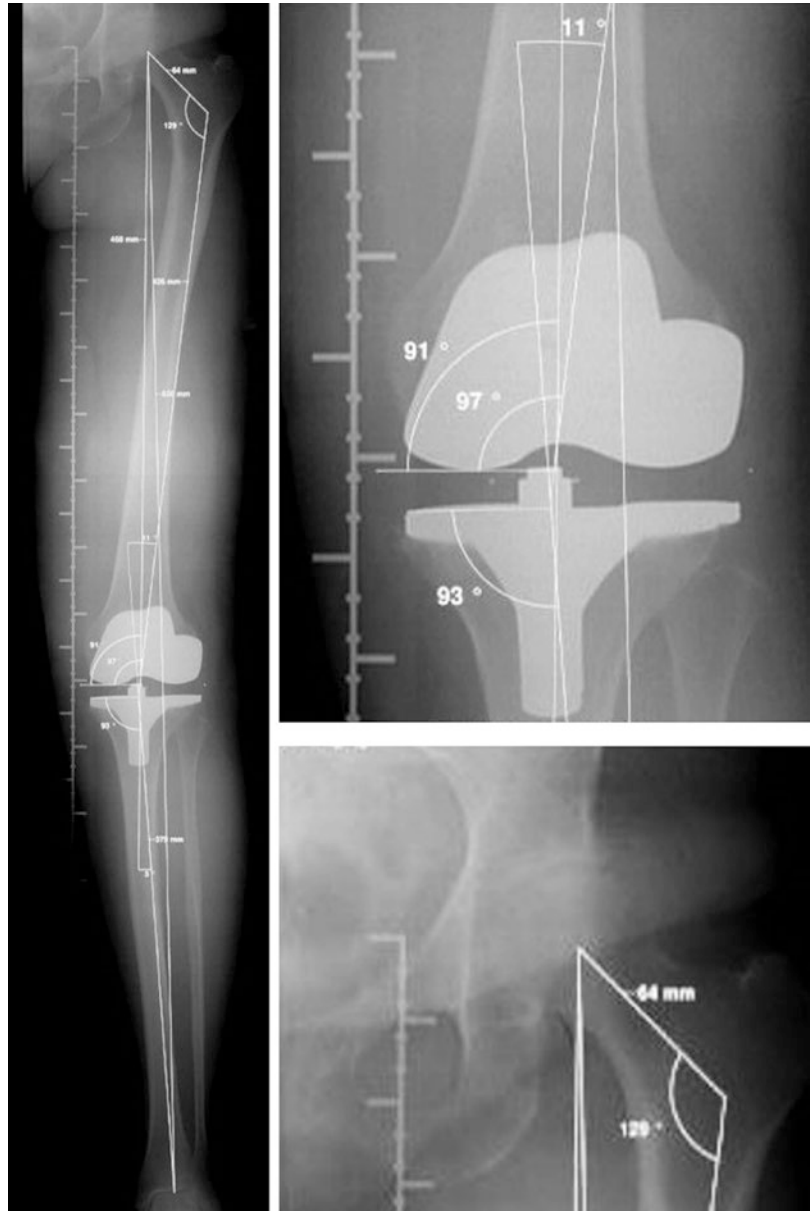
time compared to visual quantification was mentioned (Fenerty et al. 2016).

Skeletal Age Assessment

Radiographic bone age assessment (BAA) is used for evaluation paediatric endocrine and metabolic disorders, for treatment planning in paediatric oncology, and for forensic purposes. Research on computer-assisted technique dates back to the 1980s, but the systems were time-consuming and the contour finding algorithms

inaccurate. Automated artificial intelligence (AI) deep learning algorithms were developed to perform BAA using convolutional neural networks, and it could be shown that radiologists perform better if they are supported with this system (Tajmir et al. 2018; Larson et al. 2018).

Anatomy

For teaching purposes, virtual or 3D printed models are used with increasing frequency and bone models are, besides those from large vessels

| Measurement Tools Information | Original Image | Image After Pre-Planning |

Hip Parameter Measurements

Leg length changes = 3 mm
Offset changes = 3 mm
Pre-reduction =
Post-reduction =
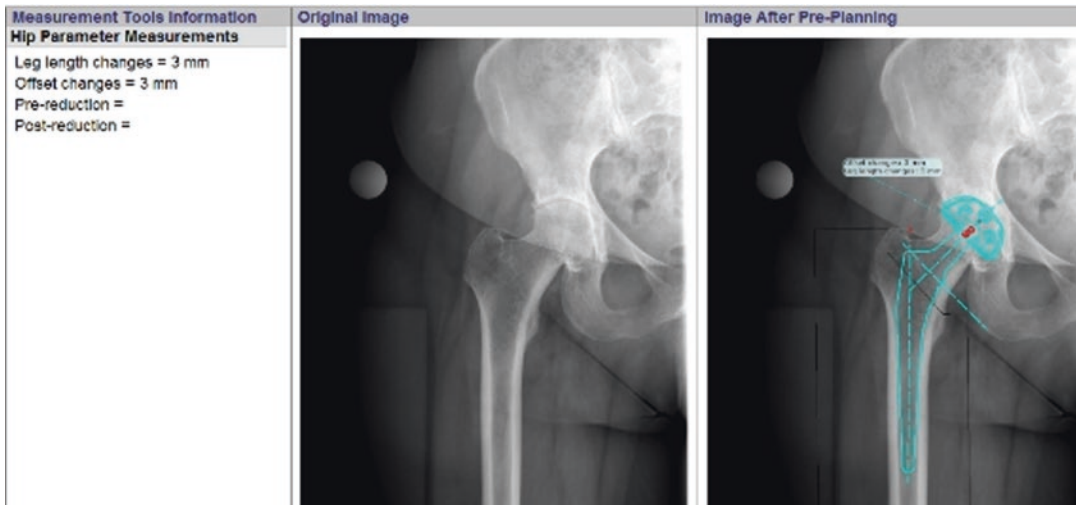
Fig 5.2 A 59-year-old female with hip osteoarthritis. Planning of total hip arthroplasty by selecting the appropriate prosthesis template from a digital library and by fully automated positioning of template

or the heart, the prototype of such teaching materials. In terms of quantification, the differentiation between normal and abnormal findings as well as the degree of abnormalities is an important learning objective.

Three-dimensional statistical shape models can be used for research to assess the anatomy and anatomical variances of CT data sets of bones. After a 3D segmentation, such models can be calculated, and the variations of each surface point can be displayed and the differences classified. This technique has been applied for analysing the shape of vertebra, femora, the wrist and the distal radius, the pelvis, and others (van de Giessen et al. 2012; Baumbach et al. 2017).

Bone Tissue Analysis

What is still called bone densitometry is in fact much more than the calculation of density values that are in most cases derived from dual-energy X-ray beam attenuation and expressed with T- and Z-scores. Today, bone tissue analysis also includes architectural components, and attempts have been made to quantify the vessel wall calcifications for the risk assessment of cardiovascular diseases. Bone tissue analysis may be referred to bone mineral density or to bone architecture;

both are calculated from the attenuation of the X-ray beams.

Bone Mineral Density

Bone mineral density (BMD) measurements, in this context also referred to as areal bone mineral density (aBMD), are generally performed with DXA which, according to the recommendations by the International Society of Clinical Densitometry (ISCD), is the first-line imaging modality in many forms of osteoporosis and related diseases. The indications and comments on the measurement techniques are listed in detail in the current version of the ISCD position paper (International Society of Clinical Densitometry 2015). An additional indication for DXA, established after 2015, is cystic fibrosis in children and in adults under 50 years. Limitations of the computer-assisted calculation of the scores may occur during the data analysis process with the semiautomated contour finding and during the physician's data interpretation, if other reasons for a higher or lower calcium content in the region of investigation are not considered (Guglielmi and Bazzocchi 2017).

Besides DXA, the BMD may be calculated with a dedicated CT software named CTXA Hip (Cann et al. 2014). The latter uses three-dimensional QCT data sets to generate bone projection images, and with the software, bone

voxels can be classified as "cortical" or "trabecular" based on a user-defined threshold. For these two compartments, the area BMD, volumetric BMD, mass, area, and volume are calculated. With this, a similar information as with DXA is yielded with the additional advantage of estimating the BMD for the cortex and for the trabecular bone separately. From the CTXA Hip areal BMD measurements, T-scores may derived by using conversion equations (Khoo et al. 2009).

The BMD may be indirectly assessed with quantitative ultrasound (QUS). With this technique, the speed of sound (SOS) or the broadband ultrasound attenuation (BUA) at the heel is measured (theoretically the tibia, patella, and other peripheral skeletal sites may also be investigated). A composite parameter of SOS and BUA may be used clinically. According to the recent version of the ISCD position paper, validated heel QUS devices predict fractures in postmenopausal women (vertebral, hip, and overall fracture risk) and in men 65 and older (hip and non-vertebral fractures). Discordant results between heel QUS and DXA of the hip are often observed and may be due to methodological error or the different involvement of these sites in osteoporosis because the sensitivity of QUS is high with severe bone loss.

Bone Architecture

For bone architecture quantification, several software products, mainly for use of CT image data sets, are available: with DXA, the trabecular bone score (TBS) can be calculated (Fig. 5.3). It is a textural measurement derived from lumbar DXA images and basis on the observation that the vertically oriented trabeculae dominate in relation to the transverse trabeculae with the progression of osteoporosis. This index of bone microarchitecture provides additional information to that obtained from standard BMD measurement. The combination of BMD and the TBS Z-score is a better predictor of fracture risk than T- and Z-scores alone. Further, it is independent from osteophytes and is a better indicator of bone strength than a bone density T-score. It is of specific value in postmenopausal women with type 2 diabetes mellitus and in hyperparathyroidism and related diseases.

Prediction of hip fractures in osteoporosis can be done with DXA or with CT by calculating parameters of the architecture of the femoral neck, i.e. hip structural analysis (HS), hip axis length (HAL), neck shaft angle (NSA), cross-sectional moment of inertia (CSMI), femoral cross-sectional area (CSA), outer diameter (OD), section modules (SM), buckling ratio (BR), and femoral strength index (FSI). The HAL is associated with hip fracture risk in postmenopausal women. It has been reported to be independent from bone densitometry and FRAX (fracture risk assessment tool) in predicting a hip fracture, but hip geometry parameters are still under validation and should not be used to assess hip fracture risk or to initiate treatment (Cann et al. 2014; Leslie et al. 2016).

High-resolution peripheral quantitative computed tomography (HRpqCT) is a technique for the analysis of the bone architecture at the distal radius, the wrist, and the distal tibia in patients. It has the potential to perform "virtual biopsies" (Patsch et al. 2011). As a clinical routine indication, HRpqCT can be performed in patients with or suspected with hyperparathyroidism (Bilezikian et al. 2014). Micro-CT is a research application for the structural analysis of the bone with a spatial resolution between 1 and 40 micrometres. Two main types are available: for analysing the bone and soft tissue of living animals with a 12 cm bore warranting the quantitative analysis to scan rats and mice and, depending on the size and the tube generator of the unit, for bone biopsy probes or larger specimens. HRpqCT and micro-CT offer enormous research possibilities in osteology and anthropology (Dall'Ara et al. 2012; Fischer et al. 2015; Valentinitsch et al. 2013; Weber et al. 2011). The computer-assisted quantification in all these systems bases on automated threshold segmentation, so that the total, trabecular, and cortical bones are separated and quantified in vivo. With a spatial resolution of 1–82 mm, the assessment of cross-sectional bone geometry and of volumetric bone mineral density (vBMD) is possible. The vBMD can be differentiated as total and trabecular bone mineral density (expressed in mg hydroxyapatite $(HA)/cm^3$) and correlated with the cortical thickness and other parameters of bone geometry
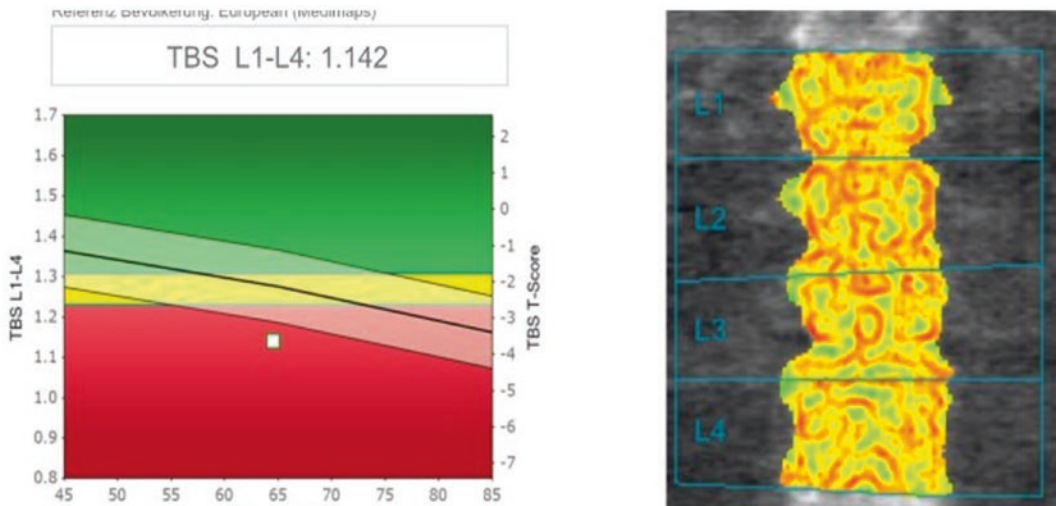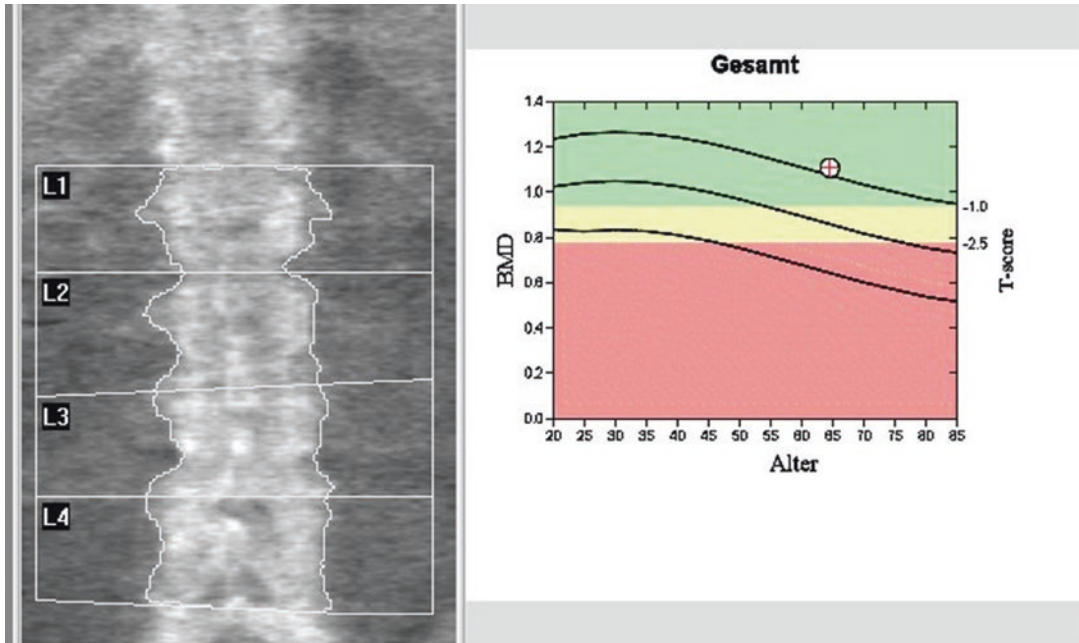
Fig. 5.3 A 64-year-old female with breast cancer after treatment. T-score of +0.5 and Z-score of +2.3 indicate normal BMD. The trabecular bone Z-score, however, is with -1.5 significantly lower

(Aeberli et al. 2010; Fouque-Aubert et al. 2010). Among the various parameters is one of the most relevant the bone volume/tissue volume (BV/TV, %) for assessing the bone surface area per tissue volume which is the percentage of the number of bone voxels in the volume of interest (VOI) divided by the total number of voxels in the VOI. Others are the trabecular thickness (Tb.Th, mm) and some subforms of it and the connectivity density (ConnD, mm^3), cortical thickness

(CTh, μm), trabecular number (TbN, mm^{-1}), and distribution of trabecular separation (TbSpSD, μm). Three-dimensional volume reconstruction is often based on the Feldkamp algorithm (Feldkamp et al. 1989).

With CT-based nonlinear finite element method (FEM), the vertebral compressive strength can be predicted accurately ex vivo and in vivo. It is an advanced computer technique of structural stress analysis developed in engineering mechan-

ics and has been used for many years to study the biomechanical effects on the human bone. CT-based FEM seems to be promising in analysing femoral strength and in predicting proximal femoral fracture location (Cody et al. 1999; Keyak et al. 2001). With FEM, a given structure is divided into many small elements, and mechanical properties are defined for each of them mathematically. Under specific loading conditions, their strength is then estimated. A subform is micro-FEM in which binary images of the bone structure are converted into isotropic bone elements to simulate mechanical properties. With micro-FEM cortical and trabecular bone can be differentiated (van Rietbergen and Ito 2015).

Quantitative CT (QCT) of the lumbar spine for measuring bone mineral density with an in-scan calibration phantom or with a comparable form of calibration has been replaced by DXA and is only recommended under certain circumstances in the majority of guidelines about osteoporosis. Apart from these recommendations in guidelines in recent research, the limitations of areal bone mineral density are mentioned as there is growing evidence for use of 3D techniques in routine CT with the potential to from areal aBMD (expressed in mm^2) to volumetric vBMD measurements (expressed in mm^3) (Johannesdottir et al. 2018). The next steps in this concept towards 3D assessment are voxel-based morphometry (VBM) and statistical shape and intensity modelling (Li et al. 2007; Bredbenneer et al. 2014). VBM is an application for the identification of bone regions where the vBMD is associated with certain biomechanical parameters.

A specific technique used mainly by anatomists for quantifying the subchondral bone calcification is CT osteoabsorptiometry (CT-OAM) (Müller-Gerbl 1998). With this method a surface representation of the 3D density distribution in the joints of living subjects can be generated.

With MRI, high-resolution 3D sequences have been used to segment the trabecular bone from surrounding tissues and analyse the architecture of the calcaneus, the knee and the hip. With seven Tesla units, this application has been boosted, and the volume of the bone and marrow can be calculated in a reproducible way (Chang et al. 2013).

Quantification of Body Composition

Body composition is a term used in physiology with specific reference to physical fitness for describing the percentages of fat, water and muscle, and additionally of bone in the human body. For quantifying the fat content and the leanness of an individual, DXA, bioimpedance analysis (BIA), CT, and MRI may be used. The computer-assisted quantification schemes of all these methods rely on assumptions mainly influenced by the individual's phenotype and the hydrogen content. DXA is regarded as the gold standard, and BIA, because of its easy instrumentation, portability of the equipment, and low costs, is most widely used. The indications for body composition are continuously increasing with most of them being not yet fully adopted in official guidelines. They mainly refer to diseases associated with obesity, anorexia, or other problems of nutrition, especially bariatric surgery for obesity, drug or dietary therapy with significant weight reduction (> about 10%) in obesity, muscle weakness or poor mobility, antiretroviral therapy and increased risk of lipoatrophy in HIV, and transgender individuals. Along with the continuous refinement of body composition parameters, DXA is on the way to become part of digital anthropometry, as clinical nutrition applications include morphologic phenotyping across lifespan. Another indication for body composition measurement is in sports medicine the relative energy deficiency in sport (RED-S). It is due to overtraining and poor nutrition with impact on bone health and muscle loss; the female athlete triad (with amenorrhoea/oligomenorrhoea, eating disorders, and low bone mass) is a subform of this condition (Brunet 2005). Quantification of posttraumatic muscle atrophy and bone loss of an extremity is another possible indication in sports medicine.

With DXA the fat fraction is estimated from the attenuation values that differ significantly from bone and lean mass. These three compartments can be fully automated differentiated with high precision. With the term lean mass, the muscle and water fractions are summarized, as they cannot be discriminated because of similar attenuation values. By using correlation coefficients in the calculations, the estimation of the fat, the lean
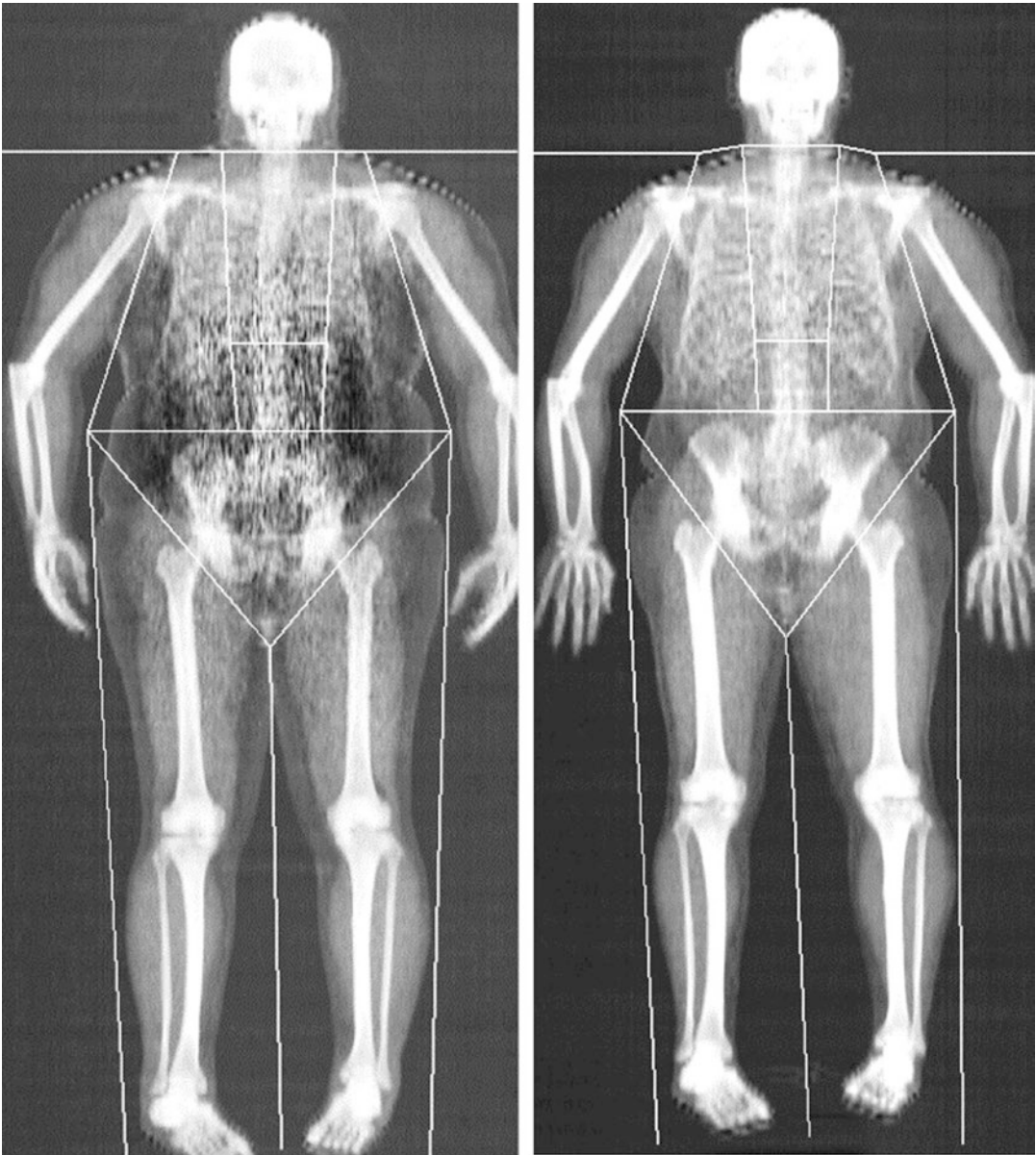
Fig 5.4 A 55-year-old male prior (left) and 6 months after (*right*) bariatric surgery (omega-loop gastric bypass). Loss of total body weight from 132 kg before surgery to 93 kg after 6 months. Body composition analysis showed that this difference of 39 kg consisted of a fat loss of 23 kg

(11.6 % of fat mass) and a loss of lean mass which is related to muscle of 16 kg. These measurements show a success of surgery but no success of postsurgical rehabilitation with relevant muscle atrophy

mass, and the bone mass can be performed with the best possible precision and accuracy among all non-invasive techniques for body composition measurement (Fig. 5.4) (Shepherd et al. 2017). An important issue is the differentiation between subcutaneous and visceral adipose tissue (VAT).

DXA-VAT measurements can be used in the same way as VAT measured with CT. These parameters may be used as phenotype descriptors, mainly for the assessment of the relationship between osteoporosis and sarcopenia. Together with functional parameters like muscle strength,

such morphologic phenotyping might have the potential to predict quality of life and mortality.

With BIA, the electrical impedance of an electric current through body tissue is measured for calculating total body water, fat-free body mass and, by differentiating the sum from body weight, body fat.

CT and MRI are used for measuring body composition by segmenting the fat and muscle due to their characteristic density values. Only with these modalities, the subcompartments of fat and muscle can be quantified: visceral adipose tissue (VAT), subcutaneous adipose tissue (SAT), interstitial adipose tissue (IAT), and total adipose tissue (TAT). For computer-assisted quantification, geometric models of the adipose tissue have been described (Shen et al. 2003). Because of the limited availability of CT and MRI, they are not widely used for body composition measurement, but indications for certain groups of patients as in oncology may emerge. For such routine CT and MRI studies, whole body adipose tissue and muscle volume can be estimated from a preselected level of CT or MRI slices (abdomen or mid-thigh) by assuming a linear relationship between cross-sectional area and whole body composition.

Quantitative magnetic resonance, QMR, is a dedicated system which may be used for measuring the differences between hydrogen properties in organic and anorganic tissue. Studies have shown high precision, but further research is necessary for improving the accuracy of this observer-independent and fast method (Gallagher et al. 2010).

US anthropometry has been developed to quantify the subcutaneous tissue. The investigator visually identifies the tissue boundaries and measures the thickness with a caliper (Wagner 2013). Software products to aid this process and improve precision and accuracy are emerging.

Fracture Assessment

Besides bone mineral density and bone architecture analysis for predicting the risk of fractures in osteoporosis, other computer-assisted tools have been developed for the detection and quantification of fractures.

For the vertebral fracture assessment (VFA) with DXA, Genant's semiquantitative assessment is the current standard (Genant 1997). A further development was an algorithmically based qualitative diagnosis method (ABQ) which is not used in clinical routine (Ferrar et al. 2005; Jiang et al. 2004). According to this study, the main limitation of VFA is the difficulty in differentiating a true fracture from a non-fracture deformity if only relying on shape assessment. For computer-assisted quantification, active appearance models (AAMs) with an almost fully automatic analysis of the shape and appearance of vertebrae have been developed (Roberts et al. 2006). The spine is modelled by a sequence of overlapping triplets of vertebrae to extract the shape contour around each vertebra. The algorithms then locate all vertebral endplates automatically. In normal vertebrae, the results were comparable to manual segmentation, but the results worsened with increasing fracture grade and stayed comparable to manual assessment in approximately 80% of cases. Thus, a considerable amount (20%) of manual correction, mainly for advanced fractures, is still required.

Spine radiographs may be checked semiautomatically for grading the degree of vertebral deformity (Engelke et al. 2010). Comparing DXA to spine radiographs, the DXA scans have a better contrast resolution with a reduction of signal loss due to overprojection of lung vessels, the diaphragm, or other extravertebral structures. Further, with DXA the X-ray beam is directed more orthogonally to the vertebrae than with radiography. Due to the low radiation dose, however, the contours of the vertebrae may be blurred. Practical experience with this technique shows that some vertebral fractures may be overlooked that are detected with spine radiographs and vice versa.

Vertebral fracture assessment with CT has been published by using semiautomated and fully automated morphometry or finite element analysis (Burns et al. 2016; Glinkowski and Narloch 2017; Nakashima et al. 2018).

For other than vertebral or hip fractures, the detection and assessment can be improved by using unfolding of the bony surface. A clinical application is available for skull fractures which can be detected with higher sensitivity compared to two-dimensional CT (Ringl et al. 2010). The same principle has been applied for rib fractures (Ringl et al. 2015). With skull fractures, the same principle of computer-assisted diagnosis and recently with a deep learning architecture can be applied for dural haematoma (Ringl et al. 2013; Arbabshirani et al. 2018).

Quantification of Synovitis

Attempts to quantify synovitis have been directed towards the volume of the synovium or parts of it, the degree of perfusion and vascularization, on joint space narrowing due to hyaline cartilage destruction, and on erosions. Rheumatoid arthritis (RA) and related diseases have been of great interest in this field of research; other focussed diseases are osteoarthritis and gout, the latter being regarded as a form of biochemical imaging.

Perfusion Imaging

For dynamic contrast-enhanced magnetic resonance imaging (DCE-MRI) and MR perfusion imaging, post-processing might be useful to quantify the flow rate of contrast media, thus calculating the severity of local inflammation in the synovium (Axelsen et al. 2014). The precision of positioning of the regions of interest is, however, low and standardization is difficult. With a voxel-by-voxel analysis of enhancing voxels, data which are automatically normalized to baseline images are quantified. Principally, with such software for the analysis of tumour or synovitis perfusion in dynamic-enhanced MR, parameters such as slope, maximum enhancement, wash-in and wash-out rate, volume of interstitial space, and transfer constants between blood plasma and interstitial space are calculated. The limitation of this technique is the low intra- and interobserver rates in positioning the regions of interest.

Joint Space Narrowing Measurements

Joint space narrowing measurements have been applied for the metacarpophalangeal joints of the fingers as they can be displayed on radiographs in a standardized form and because this feature is a relevant biomarker. Many attempts to use computer assistance for radiographic evaluation of joint space have been published concerning rheumatoid arthritis, partly inspired by the OMERACT initiative (www.omeract.org). Highly reproducible results have been published for several computer-assisted methods, and the results were consistent with traditional scoring methods. It has been shown that a metacarpophalangeal joint of about 2 mm in width, which is symmetric and sharply outlined and has no overlying structures, can be measured with good reproducibility, but that fully automated methods for measuring joint space have failed frequently in diseased joints with overlapping structures and less sharply outlined edges (Figs. 5.5 and 5.6) (Angwin et al. 2004; Sharp et al. 2000; Sharp 2004; Duryea et al. 2002, 2007; Peloschek et al. 2007). Since then, the techniques of automated analysis of joint space narrowing measurements on radiographs have been refined (Okino et al. 2018).

Erosions

Erosions are due to artefacts in the form of overlying structures on radiographs or partial volume effects on cross-sectional images difficult to be detected automatically. Another problem is the discrimination of various concavities of the bone, so-called pseudoerosions, from true inflammatory erosions. In one application, the model landmarks used during the model-based contour search serve as position references, enabling follow-up monitoring of specific locations on the bone (Langs et al. 2005). A semiautomated technique with a freely available Live Wire-based program was published with excellent intraobserver reliability and inter-occasion reliability (intra-class correlation coefficients) for erosion and synovial volumes (Bird et al. 2003a, b, 2004, 2005). In this work, interreader agreement for wrist MRI studies was considerably higher compared to
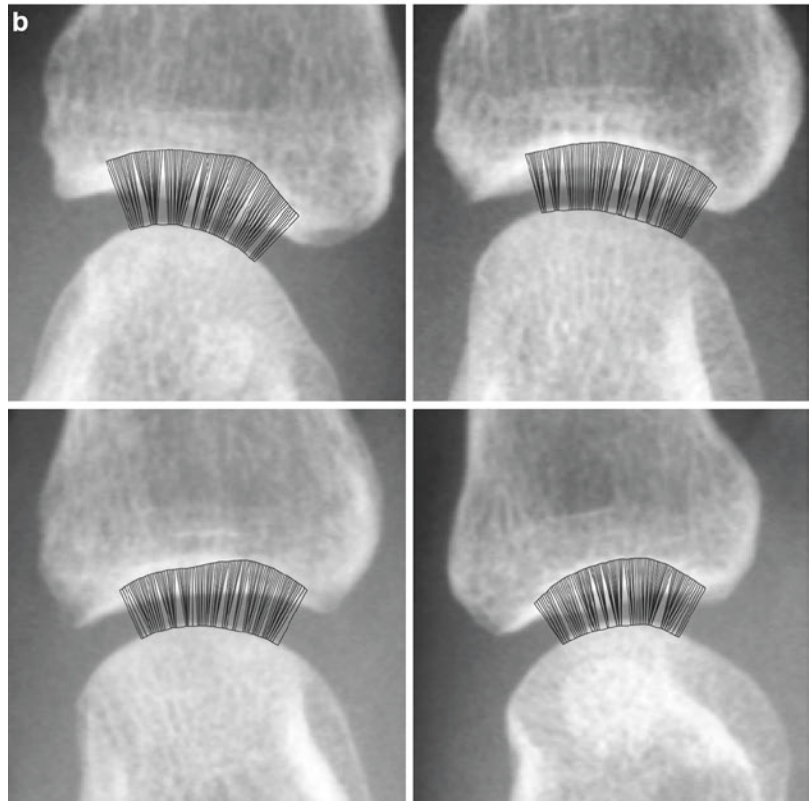
the MCP joint studies, limiting the usefulness of erosion volume measurements in this joint with this approach. With a new computer vision technique, the erosion volume can be calculated independent of erosion shape (Figueiredo et al. 2018).

Biochemical Imaging of Collagen and Fat

Biochemical imaging is a term which in musculoskeletal imaging mainly refers to the analysis and quantification of hyaline cartilage with high-

Fig. 5.6 (**a** and **b**)
Model landmarks are
positioned in the form of
supervised learning as in
this case the greatest
joint space width is not
the contour on the
radiograph but the
sclerotic line beneath it
outlined by a sclerotic
structure which
represents the deepest
point of a shallow
groove on the base of
the proximal phalanx
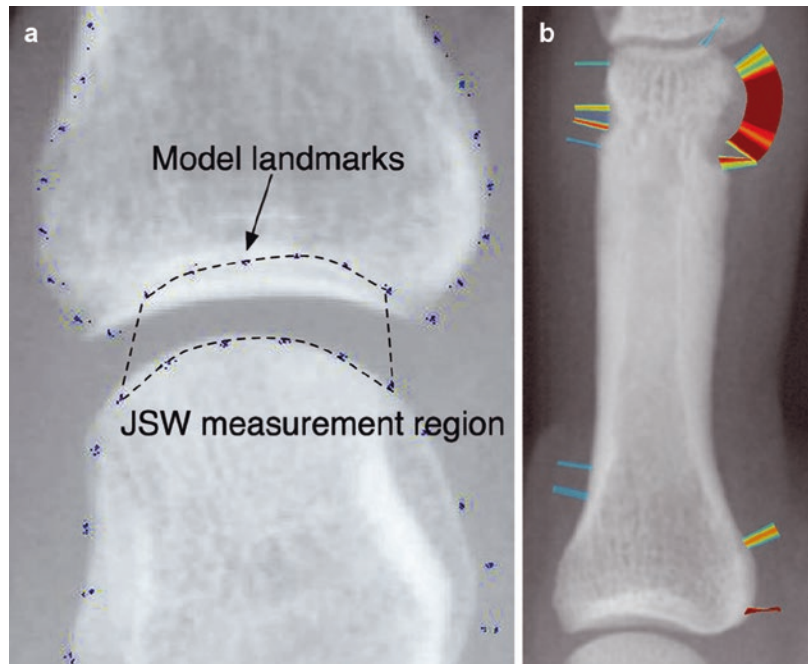
resolution MRI (Welsch et al. 2008). The definition may be extended to other applications of chemical analysis of tissue components which include the quantification of collagen tissue, of calcifications, of monosodium urate deposits, and of fat and bone marrow oedema. The techniques mainly rely on MR and PET, and conclusions may be drawn about the urate and glucose metabolism of tissue.

Cartilage

For the hyaline cartilage, the use of T2 maps and T1rho imaging potentially gives information on early cartilage damage by measuring glucosaminoglycane (GAG) content reduction in cartilage of large joints (i.e. knee) but also in small joints (ankle, wrist). Duryea et al. published a semiautomatic method ("hybrid approach") to segment the cartilage on knee MR images on a slice-by-slice basis and provided the reader with automated image processing tools to reduce the time consumption of the procedure (Duryea et al. 2007). Millington et al. recently described a method for quantitative and topographical evaluation of articular cartilage using high-reso-

lution ankle MRI (Millington et al. 2007). Texture analysis can be used for quantifying the amount of heterogeneity of the spatial distribution of pixels. The technique bases on a grey-level co-occurrence matrix (GLCM) for tabulating the frequency of combinations of pixel intensities and for calculating contrast, orderliness, and statistical attributes (Li et al. 2009). For osteoarthritis, this technique has been shown to be a reliable biomarker in detecting early extracellular matrix changes (Joseph et al. 2011). For analysing the validity of automated segmentation of knee cartilage, deep learning models were developed with efficacy and precision in quickly generating accurate segmentations (Norman et al. 2018; Liu et al. 2018).

For quantifying the fat fraction in the bone marrow, quantitative chemical shift imaging (QCSI) is used in patients with skeletal storage disorders such as Gaucher's disease, where the bone marrow is replaced by Gaucher cells (glucocerebroside-loaded macrophages). This fat fraction quantification is important to assess the disease status and therapy response.

Calcifications

Calcifications have been, because of the principally ease way of mainly cutoff-based segmentation, a major target of computer-assisted quantification. With respect to bone diseases, the correlation of osteoporosis and atherosclerosis is of interest. With DXA, an automated technique for abdominal aortic calcification (AAC) has been developed which bases on the analysis of lateral vertebral fracture assessment (VFA) images (Elmasria et al. 2016). An AAC score at the level between the first and the fourth lumbar vertebra or more than 3 is associated with an increased risk of cardiovascular disease which is independent from other risk factors for this disease. With HRpqCT, the simultaneous assessment of arterial calcifications, bone density, and bone microarchitecture is possible, and associations between bone and cardiovascular diseases can be evaluated (Patsch et al. 2014).

Monosodium Urate (MSU) Deposits in Gout

Cartilage, uric acid, fluids, and fatty tissue have characteristic Hounsfield values. With dual-source CT and a dedicated post-processing software, the amount of MSU and of bone marrow oedema lesions (BMEL) can be estimated. A precise anatomic allocation of MSU deposits within or adjacent to collagen fibrils is possible. Certain anatomic structures, however, may show similar colour encoding after post-processing, because the calculated values are not unique for a tissue. In such a way, the skin and nails with high keratin concentration, inadequate signal-to-noise ratio, or metallic artefacts may appear with the same encoding. BMEL can be located and quantified with a "virtual noncalcium technique" by subtracting calcium from cancellous bone (Pache et al. 2010).

Bone Marrow Oedema

Bone marrow oedema on coronal STIR and enhancement on T1w Gd-enhanced MR images were quantitatively evaluated using a computer-assisted method for texture analysis based on greyscale threshold values (Mayerhoefer et al. 2004, 2005). In this study, the high inter- and intraobserver variability inherent to manual measuring and segmenting of tissue abnormalities on MR images was reduced (Fig. 5.7). Threshold calculation to create a basis for segmenting healthy bone marrow from the bone marrow with abnormal signal intensity through the greyscale value distribution was performed for every examination of a patient on three images with large areas of healthy bone marrow. More recently, an atlas-based segmentation technique was used to locate and delineate the carpal bones. Basing on this, the extent of BME within each bone was quantified by identifying image intensity value characteristic of BME by fuzzy clustering and measuring the fraction of voxels with these characteristic intensities within each bone (Aizenberg et al. 2018).

Glucose Metabolism

With PET/CT, PET/MR, and dedicated preclinical units, the normal and abnormal glucose metabolism and other forms of tracer accumulation may be exactly located. PET depicts biological targets and can be used for the detection of inflammation at molecular and cellular levels. Multiple PET tracers have been investigated for their utility in imaging RA by using markers of cell proliferation; by targeting macrophages, B cells, or endothelial cells; and by using bone markers (Narayan et al. 2017). Macrophage-targeting PET tracers, such as 11C-(R)-PK11195 (1-(2-chlorophenyl)-N-methyl-N-(1-methylpropyl)-3-isoquinoline carboxamide) for visualizing macrophage activity especially in clinically quiescent phases of RA (Gent et al. 2015). Segmentation is done mainly with threshold techniques.
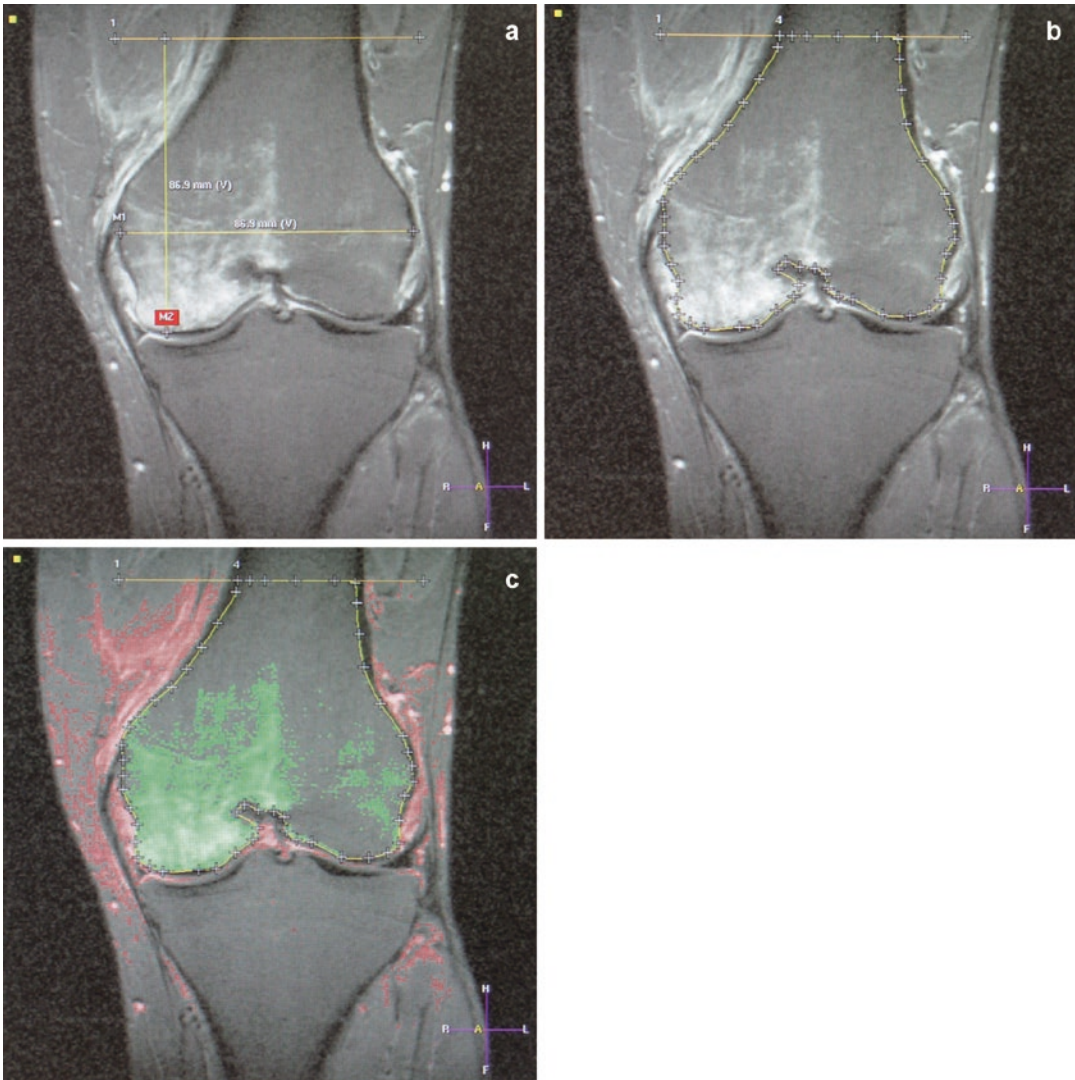
Fig. 5.7 (**a–c**) These figures illustrate the image analysis concept published by Mayerhoefer et al. (2004): 1. Coronal STIR images depict definition of total volume of investigation (TVI). (**a**) Maximal width of femoral condyles is determined through line M1. Length of M1 is then used as maximal height of TVI by drawing line M2, starting at most caudal point of condyles. Line orthogonal to M2 is then drawn (*1*) and remains in constant position for all slices to separate TVI from adjacent diaphysis. (**b**) Coronal STIR image depicts manual definition of remaining borders of TVI. (**c**) Coronal STIR image depicts colour demarcation of bone marrow oedema. Pixels with signal intensity lower than that of previously calculated threshold value are coloured *green* if inside TVI and *red* if outside TVI. *Green* areas represent bone marrow oedema of femoral condyles

5.4   Referring and Reporting

Communication of radiologists and radiologic technicians with their partners, i.e. the referring physicians, other healthcare providers, and last not least the patients and their relatives, is a crucial part of imaging. As computer-assisted imaging is not replacing but supporting the radiologist's diagnosis, the results of quantification have to be embedded in a report. Communicating the degree of findings should be an indispensable part of referrals to and of reports from radiology. In the RSNA Radlex reporting initiative (http://www.radlex.org/) for a radiology-specific ontology, a detailed wording for quantification is provided. With digital referrals or structured reports, mandatory entry fields for attributing the clinical diagnosis and the radiologic findings should be part of the software.

The referral diagnosis is traditionally not quantified. Adding an attribute to it concerning the severity and the degree of pretest probability in the form of "mild inflammatory back pain, suspected ankylosing spondylitis" is a simple but enormously efficient way of improving the communication at the interface between referrers and radiologists.

In the field of musculoskeletal imaging, this has been realized with so-called report generators which are provided by DXA and digital templating manufacturers, within the software of skeletal age assessment or in web applications. Many of these systems provide the referrers with graphics to display the calculations, classifications, risk estimates, and trending. For generating a so-called structured report, an important prerequisite is that in the radiologic community, the basic structure is defined by scientific societies and by following a certain workflow in establishing the templates. As computer-assisted quantification should support but not replace the radiologist's diagnosis, the process of reporting must be semiautomated with the option of editing the machine-generated text. A preliminary report should be generated which includes numeric and qualitative assessments of osteoporosis as well as data from prior studies if available. Further editing can also be performed with computer assistance as it was described for a voice recognition dictation system (Iv et al. 2011; England and Colletti 2018).

For DXA reporting, standards for a structured report have been established by the International Society for Clinical Densitometry and by the Canadian Association of Radiologists (Lewiecki et al. 2016; Siminoski et al. 2005). The automated transmission of the measurements has been shown to be significantly more reliable and quicker than with manual reporting if the manual data input into the DXA machine has been done correctly by the technicians (Tsai et al. 2016; Wachsmann et al. 2018; Binkley et al. 2018). Further, with such structured reports, a reduction of variability, amelioration of errors, and improvement of clarity were shown (Allin et al. 2016).

Other musculoskeletal reports are more complex to be structured so that the literature on this topic is scarce. New applications are natural language processing and other forms of machine learning with initially promising results as it has been shown for lumbar spine imaging (Tan et al. 2018).

Eventually, the reports should contain a "diagnostic impact", i.e. that the impression section contains relevant information for the patient's and the social outcomes. In other terms, we should follow the recommendations of P4 medicine for creating effective, predictive, personalized, preventive, and participatory models to treat patients (Herold et al. 2016). This means that the numeric data in the reports should be processed with respect to the consequences and explained in a patient-friendly form. An example is to include the results of DXA in the FRAX or another fracture risk assessment tool or the idea to add cooking recipes in the radiology report for patients with low bone mass or osteoporosis if appropriate.

5.5   Conclusion: Towards More Validated Imaging Biomarkers and Digital Anthropometry

The demands on more efficiency and efficacy of imaging are steadily increasing, and reports have to contain more detailed information with shorter turnaround times but be produced with insufficient resources. With AI, the radiologists' work can be supported and quantification be specified. It may be expected that the radiologist's job description will be changed in a way we only can guess: the core of our daily work, the reporting process will be done by the computers. After having applied a profound error management with cross-checks to other healthcare documents and available data sets, the computers will prepare a multimedia report with estimations of the future trend of a disease, prognostic impact, and suggestions for prevention and treatment. The radiologist's role perhaps will be to approve that the relevant information has been extracted and compiled in a diagnosis and to manage all matters arising from it: personalization with predictive impact, communication and counselling, and approving new imaging features and definitions of new diseases. Handling effectively the huge amount of information condensed in such a computer-assisted radiology report seems to be the outline of our future job profile. A short-term prognosis, however, is easy as AI is still in its infancy so that traditional reporting and patient care can be expected to change slowly and gradually.

Imaging biomarkers are a crucial part of quantitative imaging. Broadly defined, these are all imaging findings which represent normal processes, abnormal processes, or therapeutic responses to such processes and which are attributed with a precise quantification and clear dimension of their meaning. As such, a close correlation exists between the development of AI tools and of imaging biomarkers. In musculoskeletal imaging, only joint space narrowing and the slowing of progression of arthritis as surrogate imaging biomarker have been accepted by the US Food and Drug Administration (FDA) and the European Medicines Agency (EMA). Another is osteoporotic fractures which have been approved by the FDA. The other imaging features presented in this chapter are in the process of biomarker definition. With the now appearing new machine learning techniques, the diversity of findings in musculoskeletal imaging can be quantified with higher precision and all steps of the imaging workflow be more standardized.

References

Aeberli D, Eser P, Bonel H, Widmer J, Caliezi G, Varisco PA, Möller B, Villiger PM (2010) Reduced trabecular bone mineral density and cortical thickness accompanied by increased outer bone circumference in metacarpal bone of rheumatoid arthritis patients: a cross-sectional study. Arthritis Res Ther 12:R119

Aizenberg E, Roex EAH, Nieuwenhuis WP, Mangnus L, van der Helm-van Mil AHM, Reijnierse M, Bloem JL, Lelieveldt BPF, Stoel BC (2018) Automatic quantification of bone marrow edema on MRI of the wrist in patients with early arthritis: a feasibility study. Magn Reson Med 79:1127–1134

Allin S, Bleakney R, Zhang J, Munce S, Cheung AM, Jaglal S (2016) Evaluation of automated fracture risk assessment based on the Canadian Association of Radiologists and Osteoporosis Canada Assessment Tool. J Clin Densitom 19:332–339

Angwin J, Lloyd A, Heald G, Nepom G, Binks M, James MF (2004) Radiographic hand joint space width assessed by computer is a sensitive measure of change in early rheumatoid arthritis. J Rheumatol 31:1050–1061

Arbabshirani MR, Fornwalt BR, Mongelluzzo GJ, Suever JD, Geise BD, Patel AA, Moore GJ (2018) Advanced machine learning in action: identification of intracranial hemorrhage on computed tomography scans of the head with clinical workflow integration. npj Digit Med 1:9

Axelsen MB, Ejbjerg BJ, Hetland ML, Skjødt H, Majgaard O, Lauridsen UB, Hørslev-Petersen K, Boesen M, Kubassova O, Bliddal H, Østergaard M (2014) Differentiation between early rheumatoid arthritis patients and healthy persons by conventional and dynamic contrast-enhanced magnetic resonance imaging. Scand J Rheumatol 43:109–118

Ballard DH, Trace AP, Ali S, Hodgdon T, Zygmont ME, DeBenedectis CM, Smith SE, Richardson ML, Patel MJ, Decker SJ, Lenchik L (2018) Clinical applications of 3D printing: primer for radiologists. Acad Radiol 25:52–65

Baumbach SF, Binder J, Synek A, Mück FG, Chevalier Y, Euler E, Langs G, Fischer L (2017) Analysis of the three-dimensional anatomical variance of the distal radius using 3D shape models. BMC Med Imaging 17:23

Beard DV, Eberly D, Hemminger B, Pizer SM (1994) Interacting with image hierarchies for fast and accurate object segmentation. In: SPIE Conf. on Medical Imaging, Bellingham, WA, pp 10–17

Bredbenner TL, Mason RL, Havill LM, Orwoll ES, Nicolella DP, The Osteoporotic Fractures in Men (MrOS) Study (2014) Fracture risk predictions based on statistical shape and density modeling of the proximal femur. J Bone Miner Res 29:2090–2100

Beichel R, Bischof H, Leberl F, Sonka M (2005) Robust active appearance models and their application to medical image analysis. IEEE Trans Med Imaging 24:1151–1169

Bilezikian JP, Brandi ML, Eastell R, Silverberg SJ, Udelsman R, Marcocci C, Potts JT (2014) Guidelines for the management of asymptomatic primary hyperparathyroidism: summary statement from the Fourth International Workshop. J Clin Endocrinol Metab 99:3561–3569

Binkley N, Krueger D, Gangnon R, Genant HK, Drezner MK (2005) Lateral vertebral assessment: a valuable technique to detect clinically significant vertebral fractures. Osteoporos Int 16:1513–1518

Binkley N, Krueger D, Siglinsky E, Shives E, Buehring B, Hansen KE (2018) An interpretation template reduces DXA reporting errors. J Clin Densitom 21:28

Bird P, Lassere M, Shnier R, Edmonds J (2003a) Computerized measurement of magnetic resonance imaging erosion volumes in patients with rheumatoid arthritis: a comparison with existing magnetic resonance imaging scoring systems and standard clinical outcome measures. Arthritis Rheum 48:614–624

Bird P, Ejbjerg B, McQueen F, Ostergaard M, Lassere M, Edmonds J (2003b) OMERACT Rheumatoid Arthritis Magnetic Resonance Imaging Studies. Exercise 5: an international multicenter reliability study using computerized MRI erosion volume measurements. J Rheumatol 30:1380–1384

Bird P, Lassere M, Shnier R, Edmonds J (2004) Magnetic resonance imaging computerized assessment in rheumatoid arthritis: comment on the article by Goldbach-Mansky et al. Arthritis Rheum 50:1011–1012

Bird P, Joshua F, Lassere M, Shnier R, Edmonds J (2005) Training and calibration improve inter-reader reliability of joint damage assessment using magnetic resonance image scoring and computerized erosion volume measurement. J Rheumatol 32:1452–1458

Burns JE, Yao J, Muñoz H, Summers RM (2016) Automated detection, localization, and classification of traumatic vertebral body fractures in the thoracic and lumbar spine at CT. Radiology 278:64–73

Boykov Y, Kolmogorov V (2004) An experimental comparison of min-cut/max-flow algorithms for energy minimization in vision. IEEE Trans Pattern Anal Mach Intell 26:1124–1137

Bresnihan B, Newmark R, Robbins S, Genant HK (2004) Effects of anakinra monotherapy on joint damage in patients with rheumatoid arthritis. Extension of a 24-week randomized, placebo-controlled trial. J Rheumatol 31:1103–1111

Bretschi M, Franzle A, Merz M, Hillengass J, Semmler W, Bendl R, Bauerle T (2014) Acad Radiol 21: 1177–1118

Brinkley JF (1993) A flexible, generic model for anatomic shape: application to interactive two-dimensional medical image segmentation and matching. Comput Biomed Res 26:121–142

Brunet M (2005) Female athlete triad. Clin Sports Med 24:623–636

Bruynesteyn K, van der Heijde D, Boers M, van der Linden S, Lassere M, van der Vleuten C (2004) The Sharp/van der Heijde method out-performed the Larsen/Scott method on the individual patient level in

assessing radiographs in early rheumatoid arthritis. J Clin Epidemiol 57:502–512

Buck TA, Ehricke HH, Strasser W, Thurfjel L (1995) 3D segmentation of medical structures by integration of ray-casting with anatomic knowledge. Comput Graph 19:441–449

Cann CE, Adams JE, Brown JK, Brett AD (2014) CTXA hip--an extension of classical DXA measurements using quantitative CT. PLoS One 17:e91904

Caselles V, Catté F, Coll B, Dibos F (1993) A geometric model for active contours in image processing. Numer Math 66:1–1

Chang G, Xia D, Sherman O, Strauss E, Jazrawi L, Recht MP, Regatte RR (2013) High resolution morphologic imaging and T2 mapping of cartilage at 7 Tesla: comparison of cartilage repair patients and healthy controls. MAGMA 26:539–548

Conn KS, Clarke MT, Hallett JP (2002) A simple guide to determine the magnification of radiographs and to improve the accuracy of preoperative templating. J Bone Joint Surg Br 84:269–272

Conrozier T, Favret H, Mathieu P et al (2004) Influence of the quality of tibial plateau lignment on the reproducibility of computer joint space measurement from Lyon schuss radiographic views of the knee in patients with knee osteoarthritis. Osteoarthritis Cartilage 12:765–770

Cody DD, Gross GJ, Hou FJ, Spencer HJ, Goldstein SA, Fyhrie DP (1999) Femoral strength is better predicted by finite element models than QCT and DXA. J Biomech 32:1013–1020

Cootes T, Edwards GJ, Taylor CJ (2001) Active appearance models. IEEE Trans Image Process 23:681–685

Dacre JE, Huskisson EC (1989) The automatic assessment of knee radiographs in osteoarthritis using digital image analysis. Br J Rheumatol 28:506–510

Dall'Ara E, Pahr D, Varga P, Kainberger F, Zysset P (2012) QCT-based finite element models predict human vertebral strength in vitro significantly better than simulated DEXA. Osteoporos Int 23:563–572

Donner R, Reiter M, Langs G, Peloschek P, Bischof H (2006) Fast active appearance model search using canonical correlation analysis. IEEE Trans Pattern Anal Mach Intell 28:1690–1694

Duryea J, Zaim S, Wolfe F (2002) Neural network based automated algorithm to identify joint locations on hand/wrist radiographs for arthritis assessment. Med Phys 29:403–411

Duryea J, Neumann G, Brem MH et al (2007) Novel fast semi-automated software to segment cartilage for knee MR acquisitions. Osteoarthritis Cartilage 15:487–492

Elmasria K, Hicksa Y, Yanga X, Sunb X, Pettitc R, Evans W (2016) Automatic detection and quantification of abdominal aortic calcification in dual energy X-ray absorptiometry. Procedia Comput Sci 96:1011–1021

Engelke K, Stampa B, Steiger P, Fuerst T, Genant HK (2010) quantitative morphometry on spinal x-rays: initial evaluation of a new workflow tool for measuring vertebral body height in fractured vertebrae. J Bone Miner Res 25(Suppl 1)

England JR, Colletti PM (2018) Automated reporting of DXA studies using a custom-built computer program. Clin Nucl Med 43:474–475

Falcao A, Udupa J, Samarasekra S, Sharma S, Hirsch B, Lotufo R (1998) User-steered image segmentation paradigms—live wire and live lane. Graph Models Image Process 60:233–260

Falcao AX, Udupa JK, Miyazawa FK (2000) An ultra-fast user-steered image segmentation paradigm: live wire on the fly. IEEE Trans Med Imaging 19:55–62

Feldkamp LA, Goldstein SA, Parfitt AM, Jesion G, Kleerekoper M (1989) The direct examination of three-dimensional bone architecture in vitro by computed tomography. J Bone Miner Res 4:3–11

Fenerty KE, Patronas NJ, Heery CR, Gulley JL, Folio LR (2016) Resources required for semi-automatic volumetric measurements in metastatic chordoma: is potentially improved tumor burden assessment worth the time burden? J Digit Imaging 29:357–364

Ferrar L, Jiang G, Adams J, Eastell R (2005) Identification of vertebral fractures: an update. Osteoporos Int 16:717–728

Figueiredo CP, Kleyer A, Simon D, Stemmler F, d'Oliveira I, Weissenfels A, Museyko O, Friedberger A, Hueber AJ, Haschka J, Englbrecht M, Pereira RMR, Rech J, Schett G, Engelke K (2018) Methods for segmentation of rheumatoid arthritis bone erosions in high-resolution peripheral quantitative computed tomography (HR-pQCT). Semin Arthritis Rheum 47:611–618

Fischer L, Valentinitsch A, DiFranco MD, Schueller-Weidekamm C, Kienzl D, Resch H, Gross T, Weber M, Jaksch P, Klepetko W, Zweytick B, Pietschmann P, Kainberger F, Langs G, Patsch JM (2015) High-resolution peripheral quantitative CT imaging: cortical porosity, poor trabecular bone microarchitecture, and low bone strength in lung transplant recipients. Radiology 274:473–481

Fouque-Aubert A, Boutroy S, Marotte H, Vilayphiou N, Bacchetta J, Miossec P, Delmas PD, Chapurlat RD (2010) Assessment of hand bone loss in rheumatoid arthritis by high-resolution peripheral quantitative CT. Ann Rheum Dis 69:1671–1676

Gallagher D, Thornton JC, He Q, Wang J, Yu W, Bradstreet TE, Burke J, Heymsfield SB, Rivas VM, Kaufman R (2010) Quantitative magnetic resonance fat measurements in humans correlate with established methods but are biased. Obesity (Silver Spring) 18(10):2047–2054

Gefen S, Tretiak OJ, Piccoli CW et al (2003) ROC analysis of ultrasound tissue characterization classifiers for breast cancer diagnosis. IEEE Trans Med Imaging 22:170–177

Genant HK (1997) Assessment of vertebral fractures in osteoporosis research. J Rheumatol 24:1212–1214

Gent YY et al (2015) Subclinical synovitis detected by macrophage PET, but not MRI, is related to short-term flare of clinical disease activity in early RA patients: an exploratory study. Arthritis Res Ther 17:266

Glinkowski WM, Narloch J (2017) CT-scout based, semi-automated vertebral morphometry after digital image enhancement. Eur J Radiol 94:195–200

Gnudi S, Malavolta N, Testi D, Viceconti M (2004) Differences in proximal femur geometry distinguish vertebral from femoral neck fractures in osteoporotic women. Br J Radiol 77:219–223

Guglielmi G, Bazzocchi A (2017) Bone mineral densitometry pitfalls. In: Peh W (ed) Pitfalls in musculoskeletal radiology. Springer, New York, pp 893–924

Haddad FS, Garbuz DS, Duncan CP (2001) Osteotomies around the hip: radiographic planning and postoperative evaluation. Instr Course Lect 50:253–261

Hadler NM, Gillings DB, Imbus HR et al (1978) Hand structure and function in an industrial setting. Arthritis Rheum 21:210–220

Hefti F (1995) Spherical assessment of the hip on standard AP radiographs: a simple method for the measurement of the contact area between acetabulum and femoral head and of acetabular orientation. J Pediatr Orthop 15:797–805

Herold CJ, Lewin JS, Wibmer AG, Thrall JH, Krestin GP, Dixon AK, Schoenberg SO, Geckle RJ, Muellner A, Hricak H (2016) Imaging in the Age of Precision Medicine: Summary of the Proceedings of the 10th Biannual Symposium of the International Society for Strategic Studies in Radiology. Radiology 279:226–238

Herring JL, Dawant BM (2001) Automatic lumbar vertebral identification using surface-based registration. J Biomed Inform 34:74–84

Hinshaw KP, Altman RB, Brinkley JF (1995) Shape-based models for interactive segmentation of medical images. In: SPIE Conf. on Medical Imaging: Bellingham, WA, pp 771–780

Hong W, Georgescu B, Zhou XS, Krishnan S, Ma Y, Comaniciu D (2006) Database-guided simultaneous multi-slice 3D segmentation for volumetric data. In: ECCV 2006. Springer, Berlin, pp 397–409

Hosny A, Parmar C, Quackenbush J, Schwartz LH, Aerts HJWL (2018) Artificial intelligence in radiology. Nat Rev Cancer 18:500–510

International Society of Clinical Densitometry (2015) Official Positions 2015 Adult & Pediatric. ISCD, Middletown

Iv M, Patel MR, Santos A, Kang YS (2011) Informatics in radiology: use of a macro scripting editor to facilitate transfer of dual-energy X-ray absorptiometry reports into an existing departmental voice recognition dictation system. Radiographics 31:1181–1189

Jiang G, Eastell R, Barrington NA, Ferrar L (2004) Comparison of methods for the visual identification of prevalent vertebral fracture in osteoporosis. Osteoporos Int 15:887–896

Johannesdottir F, Allaire B, Bouxsein ML (2018) Fracture prediction by computed tomography and finite element analysis: current and future perspectives. Curr Osteoporos Rep 16:411–422

Joseph GB, Baum T, Carballido-Gamio J, Nardo L, Virayavanich W, Alizai H, Lynch JA, McCulloch CE, Majumdar S, Link TM (2011) Texture analysis of cartilage T2 maps: individuals with risk factors for OA have higher and more heterogeneous knee cartilage MR T2 compared to normal controls—data from the osteoarthritis initiative. Arthritis Res Ther 13:R153

Kass M, Witkin A, Terzopoulos D (1987) Snakes: active contour models. Int J Comput Vision 1:321–331

Keyak JH, Rossi SA, Jones KA, Les CM, Skinner HB (2001) Prediction of fracture location in the proximal femur using finite element models. Med Eng Phys 23:657–664

Keystone EC, Kavanaugh AF, Sharp JT et al (2004) Radiographic, clinical, and functional outcomes of treatment with adalimumab (a human anti-tumor necrosis factor monoclonal antibody) in patients with active rheumatoid arthritis receiving concomitant methotrexate therapy: a randomized, placebo-controlled, 52-week trial. Arthritis Rheum 50:1400–1411

Khoo BCC, Brown JK, Cann CE, Zhu K, Henzell S et al (2009) Comparison of QCT-derived and DXA-derived areal bone mineral density and T scores. Osteoporos Int 20:1539–1545

Kubassova O (2007) Automatic segmentation of blood vessels from dynamic MRI datasets. Med Image Comput Comput Assist Interv 10:593–600

Krackow KA, Pepe CL, Galloway EJ (1990) A mathematical analysis of the effect of flexion and rotation on apparent varus/valgus alignment at the knee. Orthopedics 13:861–868

Krug KB, Weber C, Schwabe H, Sinzig NM, Wein B, Müller D, Wegmann K, Peters S, Sendler V, Ewen K, Hellmich M, Maintz D (2014) Comparison of image quality using a X-ray stereotactical whole-body system and a direct flat-panel X-ray device in examinations of the pelvis and knee. Rofo 186:67–76

Langs G, Peloschek P, Bischof H (2005) Optimal sub-shape models by minimum description length. CVPR 2005: 310–315

Langs G, Peloschek P, Bischof H, Kainberger F (2006) Automatic detection of erosions in rheumatoid arthritis assessment. In: MICCAI Joint Disease Workshop, pp 33–40

Langs G, Röhrich S, Hofmanninger J, Prayer F, Pan J, Herold C, Prosch H (2018) Machine learning: from radiomics to discovery and routine. Radiologe Epub ahead of print

Larson DB, Chen MC, Lungren MP, Halabi SS, Stence NV, Langlotz CP (2018) Performance of a deep-learning neural network model in assessing skeletal maturity on pediatric hand radiographs. Radiology 287:313–322

Leslie WD, Lix LM, Morin SN, Johansson H, Odén A, McCloskey EV, Kanis JA (2016) Adjusting hip fracture probability in men and women using hip axis length: the Manitoba Bone Density Database. Clin Densitom 19:326–331

Leventon M, Grimson W, Faugeras O (2000) Statistical shape influence in Geodesic active contours. In: Proceedings of IEEE CVPR00, pp 316–322

Lewiecki EM, Binkley N, Morgan SL, Shuhart CR, Camargos BM, Carey JJ, Gordon CM, Jankowski LG, Lee JK, Leslie WD, International Society for Clinical

Densitometry (2016) Best practices for dual-energy X-ray absorptiometry measurement and reporting: International Society for Clinical Densitometry Guidance. J Clin Densitom 19(2):127–140

Li W, Kezele I, Collins DL, Zijdenbos A, Keyak J, Kornak J, Koyama A, Saeed I, Leblanc A, Harris T, Lu Y, Lang T (2007) Voxel-based modeling and quantification of the proximal femur using inter-subject registration of quantitative CT images. Bone 41:888–895

Li X, Pai A, Blumenkrantz G, Carballido-Gamio J, Link T, Ma B, Ries M, Majumdar S (2009) Spatial distribution and relationship of T1rho and T2 relaxation times in knee cartilage with osteoarthritis. Magn Reson Med 61:1310–1318

Liacouras PC, Sahajwalla D, Beachler MD, Sleeman T, Ho VB, Lichtenberger JP (2017) Using computed tomography and 3D printing to construct custom prosthetics attachments and devices. 3D Print Med 3:3–7

Liu F, Zhou Z, Samsonov A, Blankenbaker D, Larison W, Kanarek A, Lian K, Kambhampati S, Kijowski R (2018) Deep learning approach for evaluating knee mr images: achieving high diagnostic performance for cartilage lesion detection. Radiology Epub ahead of print

Lodwick GS, Haun CL, Smith WE, Keller RF, Robertson ED (1963) Computer diagnosis of primary bone tumors: a preliminary report. Radiology 80:273–275

Maas M, Kuijper M, Akkerman EM (2011) From Gaucher's disease to metabolic radiology: translational radiological research and clinical practice. Semin Musculoskelet Radiol 15:301–316

Müller-Gerbl M (1998) The subchondral bone plate. Adv Anat Embryol Cell Biol, 141:III–XI, 1–134

Mayerhoefer ME, Breitenseher M, Hofmann S et al (2004) Computer-assisted quantitative analysis of bone marrow edema of the knee: initial experience with a new method. AJR Am J Roentgenol 182:1399–1403

Mayerhoefer ME, Breitenseher MJ, Kramer J, Aigner N, Norden C, Hofmann S (2005) STIR vs. T1-weighted fat-suppressed gadolinium-enhanced MRI of bone marrow edema of the knee: computer-assisted quantitative comparison and influence of injected contrast media volume and acquisition parameters. J Magn Reson Imaging 22:788–793

Mazzuca SA, Brandt KD, Buckwalter KA (2003) Detection of radiographic joint space narrowing in subjects with knee osteoarthritis: longitudinal comparison of the metatarsophalangeal and semiflexed anteroposterior views. Arthritis Rheum 48:385–390

Mazzuca SA, Brandt KD, Buckwalter KA, Lequesne M (2004) Pitfalls in the accurate measurement of joint space narrowing in semiflexed, anteroposterior radiographic imaging of the knee. Arthritis Rheum 50:2508–2515

Millington SA, Li B, Tang J et al (2007) Quantitative and topographical evaluation of ankle articular cartilage using high resolution MRI. J Orthop Res 25:143–151

Nakashima D, Kanchiku T, Nishida N, Ito S, Ohgi J, Suzuki H, Imajo Y, Funaba M, Chen X, Taguchi T (2018) Finite element analysis of compression fractures at the thoracolumbar junction using models constructed from medical images. Exp Ther Med 15:3225–3230

Narayan N, Owen DR, Taylor PC (2017) Advances in positron emission tomography for the imaging of rheumatoid arthritis. Rheumatology (Oxford) 56:1837–1846

Neumann A, Lorenz C (1999) Statistical shape model based segmentation of medical images. Comput Med Imaging Graph 22:133–143

Niethard FU (1999) Computer-assisted orthopedic surgery (CAOS) in hip joint prosthetics. Z Orthop Ihre Grenzgeb 137:99–100

Norman B, Pedoia V, Majumdar S (2018) Use of 2D U-net convolutional neural networks for automated cartilage and meniscus segmentation of knee MR imaging data to determine relaxometry and morphometry. Radiology 288:177–185

Odenbring S, Berggren AM, Peil L (1993) Roentgenographic assessment of the hip-knee-ankle axis in medial gonarthrosis. A study of reproducibility. Clin Orthop Relat Res:195–196

Okino T, Kamishima T, Lee Sutherland K, Fukae J, Narita A, Ichikawa S, Tanimura K (2018) Radiographic temporal subtraction analysis can detect finger joint space narrowing progression in rheumatoid arthritis with clinical low disease activity. Acta Radiol 59:460–467

Pache G et al (2010) Dual-energy CT virtual noncalcium technique: detecting posttraumatic bone marrow lesions–feasibility study. Radiology 256:617–624

Patsch JM, Burghardt AJ, Kazakia G, Majumdar S (2011) Noninvasive imaging of bone microarchitecture. Ann N Y Acad Sci 1240:77–87

Patsch JM, Zulliger MA, Vilayphou N, Samelson EJ, Cejka D, Diarra D, Berzaczy G, Burghardt AJ, Link TM, Weber M, Loewe C (2014) Quantification of lower leg arterial calcifications by high-resolution peripheral quantitative computed tomography. Bone 58:42–47

Paul R et al (2016) Deep feature transfer learning in combination with traditional features predicts survival among patients with lung adenocarcinoma. Tomography 2:388–395

Peloschek P, Langs G, Weber M, Sailer J, Reisegger M, Imhof H, Bischof H, Kainberger F (2007) An automatic model-based system for joint space measurements on hand radiographs: initial experience. Radiology 245:855–862

Ploder O, Wagner A, Enislidis G, Ewers R (1995) Computer-assisted intraoperative visualization of dental implants. Augmented reality in medicine. Radiologe 35:569–572

Rea JA, Chen MB, Li J et al (2001) Vertebral morphometry: a comparison of long-term precision of morphometric X-ray absorptiometry and morphometric radiography in normal and osteoporotic subjects. Osteoporos Int 12:158–166

Reiser MF, Bongartz GP, Erlemann R, Schneider M, Pauly T, Sittek H, Peters PE (1989) Gadolinium-DTPA in rheumatoid arthritis and related diseases: first results

with dynamic magnetic resonance imaging. Skeletal Radiol 18:591–597

Ringl H, Schernthaner RE, Schueller G, Balassy C, Kienzl D, Botosaneanu A, Weber M, Czerny C, Hajdu S, Mang T, Herold CJ, Schima W (2010) The skull unfolded: a cranial CT visualization algorithm for fast and easy detection of skull fractures. Radiology 255:553–562

Ringl H, Stiassny F, Schima W, Toepker M, Czerny C, Schueller G, Asenbaum U, Furtner J, Hajdu S, Serles W, Weber M, Herold CJ (2013) Intracranial hematomas at a glance: Advanced Visualization for Fast and Easy Detection. Radiology 267:522–530

Ringl H, Lazar M, Töpker M, Woitek R, Prosch H, Asenbaum U, Balassy C, Toth D, Weber M, Hajdu S, Soza G, Wimmer A, Mang T (2015) The ribs unfolded—a CT visualization algorithm for fast detection of rib fractures: effect on sensitivity and specificity in trauma patients. Eur Radiol 25:1865–1874

Roberts M, Cootes TF, Adams JE (2006) Vertebral morphometry: semiautomatic determination of detailed shape from dual-energy X-ray absorptiometry images using active appearance models. Invest Radiol 41:849–859

Rubin GD, Lyo JK, Paik DS et al (2005) Pulmonary nodules on multi-detector row CT scans: performance comparison of radiologists and computer-aided detection. Radiology 234:274–283

Rügsegger P, Koller B, Müller R (1996) A microtomographic system for the nondestructive evaluation of bone architecture. Calcif Tissue Int 58:24–29

Sailer J, Scharitzer M, Peloschek P, Giurea A, Imhof H, Grampp S (2005) Quantification of axial alignment of the lower extremity on conventional and digital total leg radiographs. Eur Radiol 15:170–173

Castro FJ, Pollo C, Meuli R et al (2006) A cross validation study of deep brain stimulation targeting: from experts to atlas-based, segmentation-based and automatic registration algorithms. IEEE Trans Med Imaging 25:1440–1450

Sharp JT (2004) Measurement of structural abnormalities in arthritis using radiographic images. Radiol Clin North Am 42:109–119

Sharp JT, Gardner JC, Bennett EM (2000) Computer-based methods for measuring joint space and estimating erosion volume in the fi and wrist joints of patients with rheumatoid arthritis. Arthritis Rheum 43:1378–1386

Shearman CM, Brandser EA, Kathol MH, Clark WA, Callaghan JJ (1998) An easy linear estimation of the mechanical axis on long-leg radiographs. AJR Am J Roentgenol 170:1220–1222

Shen W, Wang Z, Tang H, Heshka S, Punyanitya M, Zhu S, Lei J, Heymsfield SB (2003) Volume estimates by imaging methods: model comparisons with visible woman as the reference. Obes Res 11:217–225

Shepherd JA, Ng BK, Sommer MJ, Heymsfield SB (2017) Body composition by DXA. Bone 104:101–105

Siminoski K, Leslie WD, Frame H, Hodsman A, Josse RG, Khan A, Lentle BC, Lévesque J, Lyons DJ, Tarulli

G, Brown JP, Canadian Association of Radiologists (2005) Recommendations for bone mineral density reporting in Canada. Can Assoc Radiol J 56:178–188

Soo MS, Rosen EL, Xia JQ, Ghate S, Baker JA (2005) Computer-aided detection of amorphous calcifications. Am J Roentgenol 184:887–892

Stegmann MB, Ersboll BK, Larsen R (2003) FAME—a flexible appearance modeling environment. IEEE Trans Med Imaging 22:1319–1331

Tajmir SH, Lee H, Shailam R, Gale HI, Nguyen JC, Westra SJ, Lim R, Yune S, Gee MS, Do S (2018) Artificial intelligence-assisted interpretation of bone age radiographs improves accuracy and decreases variability. Skeletal Radiol Epub ahead of print

Tan WK, Hassanpour S, Heagerty PJ, Rundell SD, Suri P, Huhdanpaa HT, James K, Carrell DS, Langlotz CP, Organ NL, Meier EN, Sherman KJ, Kallmes DF, Luetmer PH, Griffith B, Nerenz DR, Jarvik JG (2018) Comparison of natural language processing rules-based and machine-learning systems to identify lumbar spine imaging findings related to low back pain. Acad Radiol Epub ahead of print

Tetsworth K, Paley D (1994) Malalignment and degenerative arthropathy. Orthop Clin North Am 25:367–377

Thompson PM, Woods RP, Mega MS, Toga AW (2000) Mathematical/computational challenges in creating deformable and probabilistic atlases of the human brain. Hum Brain Mapp 9:81–92

Trattnig S, Zbýň Š, Schmitt B, Friedrich K, Juras V, Szomolanyi P, Bogner W (2012) Advanced MR methods at ultra-high field (7 Tesla) for clinical musculoskeletal applications. Eur Radiol 22:2338–2346

Tsai IT, Tsai MY, Wu MT, Chen CK (2016) Development of an automated bone mineral density software application: facilitation radiologic reporting and improvement of accuracy. J Digit Imaging 29:380–387

Valentinitsch A, Patsch JM, Burghardt AJ, Link TM, Majumdar S, Fischer L, Schueller-Weidekamm C, Resch H, Kainberger F, Langs G (2013) Computational identification and quantification of trabecular microarchitecture classes by 3-D texture analysis-based clustering. Bone 54:133–140

van de Giessen M, Foumani M, Vos FM, Strackee SD, Maas M, Van Vliet LJ, Grimbergen CA, Streekstra GJ (2012) A 4D statistical model of wrist bone motion patterns. IEEE Trans Med Imaging 31:613–625

van der Heijde DM (2000) Radiographic imaging: the 'gold standard' for assessment of disease progression in rheumatoid arthritis. Rheumatology (Oxford) 39(Suppl 1):9–16

van Rietbergen B, Ito K (2015) A survey of micro-finite element analysis for clinical assessment of bone strength: the first decade. J Biomech 48:832–841

Vehkomäki T, Gerig G, Székely G (1997) A user-guided tool for efficient segmentation of medical data. In: Troccaz J, Grimson E (eds) Virtual reality and robotics in medicine and medical robotics and computer-assisted surgery (CVRMed-MRCAS'97). Springer, Berlin, pp 685–694

Wachsmann J, Blain K, Thompson M, Cherian S, Oz OK, Browning T (2018) Electronic medical record integration for streamlined DXA reporting. J Digit Imaging 31:159–166

Wade R, Yang H, McKenna C, Faria R, Gummerson N, Woolacott N (2013) A systematic review of the clinical effectiveness of EOS 2D/3D X-ray imaging system. Eur Spine J. 22(2):296–304

Wahner HW, Steiger P, von Stetten E (1994) Instruments and measurement techniques. In: Wahner HW, Fogelman I (eds) The evaluation of osteoporosis: dual energy X-ray absorptiometry in clinical practice. Martin Dunitz, London, pp 14–34

Wagner DR (2013) Ultrasound as a tool to assess body fat. J Obes 280713

Weber GW, Bookstein FL, Strait DS (2011) Virtual anthropology meets biomechanics. J Biomech 17: 1429–1432

Welsch GH, Mamisch TC, Hughes T, Zilkens C, Quirbach S, Scheffler K, Kraff O, Schweitzer ME, Szomolanyi P, Trattnig S (2008) In vivo biochemical 7.0 Tesla magnetic resonance: preliminary results of dGEMRIC, zonal T2, and T2* mapping of articular cartilage. Invest Radiol 43(9):619–626

Windhager R, Karner J, Kutschera HP, Polterauer P, Salzer-Kuntschik M, Kotz R (1996) Limb salvage in periacetabular sarcomas: review of 21 consecutive cases. Clin Orthop Relat Res 31:265–276

Part II

Measurements at Anatomical Sites

Cervical Spine

6

Clare Roche

Contents

C. Roche, M.D., M.B., B.C.H., B.A.O., M.R.C.P.I.
Department of Radiology, University College
Hospital Galway (UCHG),
Newcastle Road, Galway, Republic of Ireland
e-mail: clare.roche@hse.ie

6.1   Lines, Landmarks and Concepts
(Roche and Carty 2001)

At birth, the cervical spine measures 3.7 cm in length and grows to its adult state by adding a further 9 cm. It almost doubles in length by the age of 6 and gains an additional 3.5 cm during the growth spurt at puberty to reach its adult length of 12–13 cm. There are a number of important lines and landmarks used in measuring the cervical spine at both the paediatric and adult stages of development. Due to different anatomical and pathological significance, these cervical spine parameters are best presented by separating the craniocervical junction from the subaxial portion.

The craniocervical junction is defined as the anatomical region between the basiocciput and the C2/C3 interspace. Many measurements have evolved to assess the craniocervical junction and in particular to help determine if there is vertical migration of the dens and instability. These measurements will be presented and their strengths and weaknesses identified. The normal range for each of these measurements, variability of normal anatomy and challenges in identifying the osseous landmarks produce inherent limitations. The imaging modality used, (lateral radiograph, MDCT and MRI) also has a bearing on the reliability and accuracy of the employed measurement. Depiction of the basion, opisthion and rostrum of the odontoid peg is not always possible on lateral radiographs posing difficulties and challenges. For these reasons a wide spectrum of measuring methods have evolved all enjoying strengths marred with inherent weaknesses.

Precise measurement technique and careful analysis are especially important in paediatric spinal trauma (Roche and Carty 2001). As the paediatric ligaments are more lax in children, they enjoy a greater normal range of measurements. In addition due to incomplete ossification, the measurement points are different in children. There are three developmental variants in which measurement aids in differentiating true pathology from normal variants, namely, C1 pseudospread, C2/C3 pseudosubluxation and C3 pseudofracture.

In C1 pseudospread, the atlas exhibits a C1/C2 offset of up to 6 mm on the odontoid view in young children (up to age 7) due to the advanced C1 differential growth rate that can take place compared with C2 (Sussex et al. 1983). This needs to be differentiated from a true Jefferson's fracture producing an offset where an offset of >2 mm on each side is deemed abnormal. The rule of Spence is useful in this regard where a tear of the alar ligament can confidently be suspected if the total combined right and left C1/C2 offset is 7 mm or more (Fig. 6.1) (Spence et al. 1970). However, as this measurement was derived from direct measurement of cadaveric specimens, Heller et al. (1993) warned that overestimation of displacement takes place on radiographic assessment due to magnification artefact, and if the total displacement is <8.1 mm on open-mouth radiographs, the transverse ligament is usually intact. This can be also assessed on coronal reformatted CT images through the centres of the lateral masses. Vertical lines are first drawn at a tangent to both the lateral outlines of C1 and C2 bilaterally, and then the transverse offset between the lines is measured and added together as a total lateral mass displacement (Fig. 6.1).

In C2/C3 pseudosubluxation, the anterior and posterior vertebral lines are distorted at this level as the C2 vertebral body can lie up to 3 mm anterior to C3. The spinolaminal line however is not disturbed. In differentiating C2/C3 pseudosubluxation from a hangman's fracture dislocation, one can employ Swischuk's posterior cervical line drawn by joining the C1 to C3 spinolaminal interface. This line should intersect the C2 spinolaminal interface or lie anterior to it within a 2 mm distance in pseudosubluxation, while a distance >2 mm indicates underlying traumatic disruption (Fig. 6.2).

The higher fulcrum location at the C2/C3 level in the paediatric spine promotes pseudosubluxation as well as morphological features of a pseudofracture at the anterosuperior corner of C3 vertebra due to a delay in ossification. In vertebral pseudofracture the discrepancy between the anterior and posterior vertebral body height is 3 mm or less, while a difference >3 mm is taken as indicative of true vertebral body fracture.

Craniocervical measurement techniques in suspected trauma to the upper cervical spine have been standardised by the Spine Trauma Study Group which produced a consensus statement as a means of producing consistent measurements that can guide therapeutic management (Bono et al. 2007). Although on the one hand the authors based their measurement techniques on an extensive review of the literature up to 2007, they stressed that as the accuracy and reproducibility of many of the parameters had not been reported, validation was still awaited. Odontoid fractures
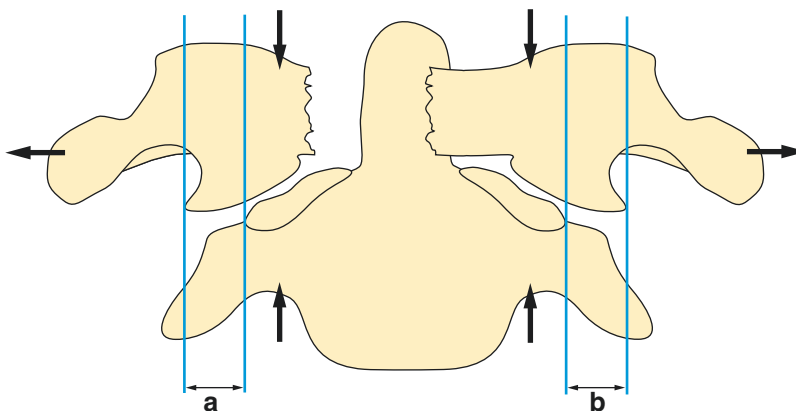
Fig. 6.1 C1/C2 offset. Vertical lines are first drawn at a tangent to both the lateral articular outlines of C1 and C2 bilaterally, and then the transverse offset between the lines is measured and added together as a total lateral mass dis-placement A + B. 'Pseudospread' of C1 on C2 on the odontoid peg view is a normal variant in children below age of 7 and can measure up to 6 mm
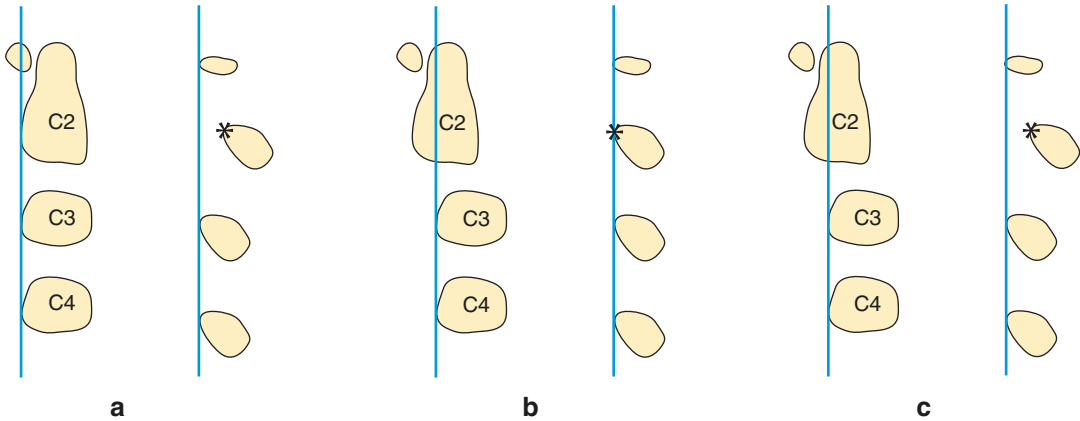
Fig. 6.2 C2/C3 pseudosubluxation: in children up to 16 years, the C2 vertebral body can lie up to 3 mm anterior to C3, as a normal variant. In differentiating C2/C3 pseudosubluxation from a hangman's fracture dislocation, Swischuk's posterior cervical line is helpful. In pseudosubluxation a line drawn connecting the anterior cortices of the spinous processes of C1and C3 should intersect (**b**) or come within 2 mm of the anterior cortex of spinous process of C2 (**c**). A distance >2 mm indicates underlying traumatic disruption. Note that when the posterior cervical line is drawn in the absence of pseudosubluxation (**a**), it should also be within 2 mm of the anterior cortex of the C2 spinous process

require two measurements for optimal healing prognostication: sagittal displacement and angulation as measured on lateral radiographs or CT midsagittal reconstructed images. Fractures displaced by >5–6 mm are regarded as at a high risk of non-union. Sagittal fracture displacement is determined by drawing tangents to the anterior aspects of the odontoid peg and C2 body, respectively, and then the transverse line between them at the level of the fracture determines the displacement (Fig. 6.3). Odontoid fracture angulation is determined by drawing tangent lines to the posterior aspects of the odontoid peg and the posterior body of C2 and calculating the subtended angle between the two lines (Fig. 6.4). In C2/C3 traumatic spondylolisthesis, due to the so-called hangman's fracture, translation and angulation are also helpful determinants in management. C2/C3 angulation can be assessed either by the endplate method (Fig. 6.5) or the posterior vertebral body line method (Fig. 6.6), while translation is the transverse distance between the two posterior vertebral body lines (Fig. 6.7).

Craniocervical measurements based on a number of craniometric lines are very useful in the assessment of instability in the adult rheumatoid cervical spine. Anterior and posterior instability can result in abnormal C1/C2 measurements which are enhanced on flexion and extension
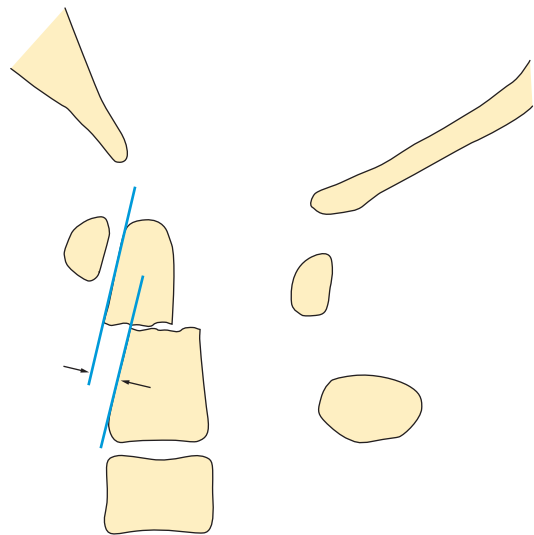
Fig. 6.3 Odontoid fractures: sagittal displacement and angulation as measured on lateral radiographs or CT midsagittal reconstructed images. Fractures displaced by >5–6 mm are regarded as at a high risk of non-union. Sagittal fracture displacement is determined by drawing tangents to the anterior aspects of the odontoid peg and C2 body, respectively, and then the transverse line between them at the level of the fracture determines the displacement (*arrows*)

views. In the assessment of vertical atlantoaxial subluxation, Riew et al. (2001) assessed the reliability of radiographic criteria employing eight measurement methods on 131 adult cervical
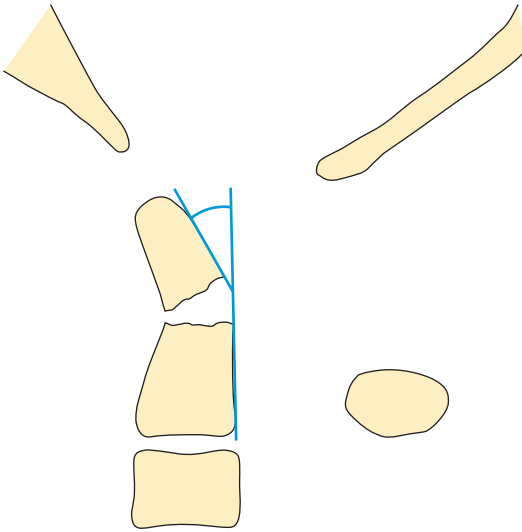
Fig. 6.4 Odontoid Fracture Angulation: odontoid fracture angulation is determined by drawing tangent lines to the posterior aspects of the odontoid peg and the posterior body of C2 and calculating the subtended angle between the two lines
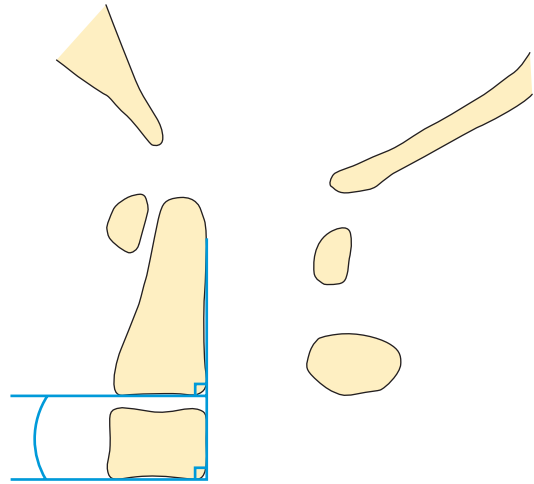
Fig. 6.6 C2/C3 angulation: posterior vertebral body line method. Lines are drawn tangential to posterior cortex of bodies of C2 and C3. Perpendicular lines at right angles are then extended anteriorly and the angle between them is measured
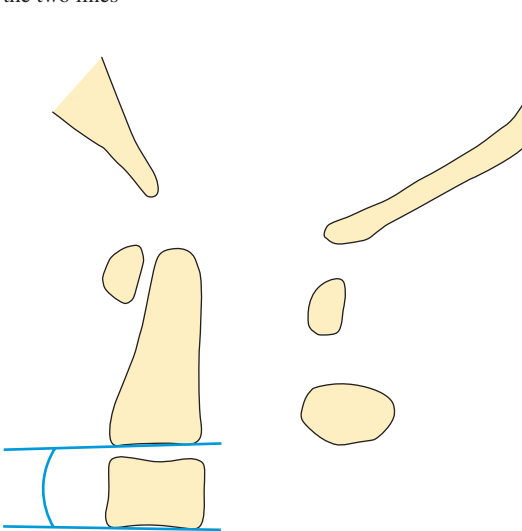
Fig. 6.5 C2/C3 angulation: endplate method. In traumatic C2/C3 spondylolisthesis due to the so-called hangman's fracture, translation and angulation are helpful determinants in management. C2/C3 angulation can be assessed by the endplate method where the angle between lines drawn tangential to the inferior endplate of C2 and C3 is measured
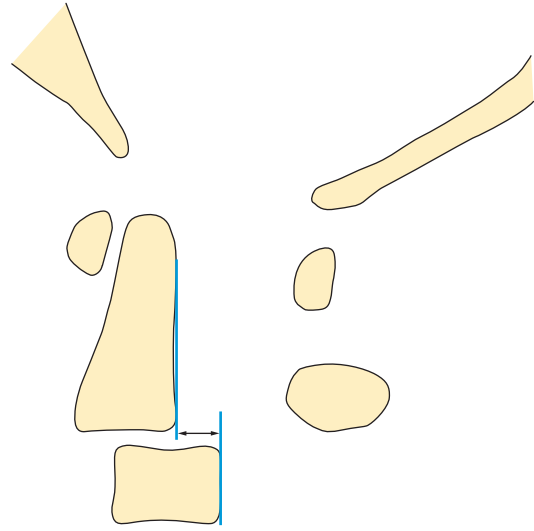
Fig. 6.7 C2/C3 fracture: translation. Translation is the degree of forward subluxation of C2 on C3, shown by the arrowhead line between the posterior cortex of C2 and C3

spine radiographs in patients with rheumatoid arthritis and found that none of these methods are more than 90% sensitive or specific. They compared the measurement findings with tomography, CT sagittal reformats and MRI as the gold

standards. There were 67 with basilar invagination. As the odontoid was correctly identified in only 23 of 67 radiographs, they recommended combining various measurements to enhance the diagnostic accuracy. For this reason methods that do not require accurate visualisation of the tip of the odontoid peg were recommended, namely, the Clark station, Ranawat criterion and Redlund
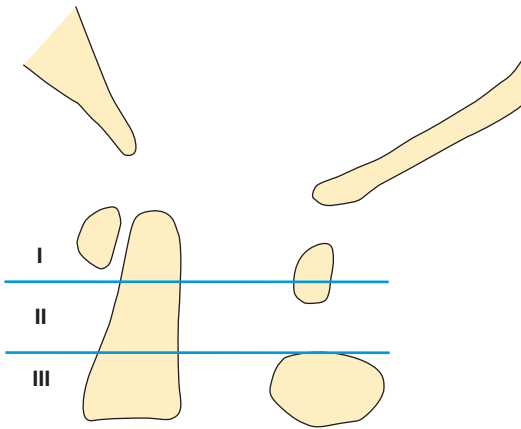
Fig. 6.8 Clark Station method of assessing basilar invagination: The Clark Station defines the location of C1 in relation to C2. The C2 vertebra is divided into three equal parts in the sagittal plane, labelled I, II and III in diagram. If C1 anterior arch is level with the middle third (level II) or caudal third (level III) then basilar invagination is present

Fig. 6.9 X-line method for evaluation of atlanto-occipital relationship. A line is drawn from the basion 'B' (anterior margin of the foramen magnum) to the most anterior part of the C2 spine laminar junction 'C2SL'. This line should run tangential to the posterosuperior aspect of odontoid peg. A second line is drawn from the opisthion 'O' (posterior margin of foramen magnum) to the posteroinferior corner of the body of C2. This line should pass just anterior to the posterior arch of C1

and Johnell criterion. The Clark station defines the location of C1 in relation to the C2 vertebra which is divided into three equal parts in the sagittal plane (Fig. 6.8). If the C1 anterior arch is level with the middle third (station 2) or caudal third (station 3), basilar invagination is present (Riew et al. 2001). It is therefore important to be familiar with more than one method as the underlying pathological state can give rise to difficulties in identifying the required anatomical landmarks needed for accurate assessment. Using MRI, Dvorak et al. (1989) also determined another parameter they called the **cranial migration distance (CMD)** by measuring the perpendicular distance between McRae's line and the posteroinferior corner of C2. This is normally **38.7 mm (SD 2.9 mm, range 33–46 mm)** and is declared abnormal if **<31.5 mm** which carries a high incidence of myelopathy. There was a good correlation between the cranial migration distance and the values from the Redlund-Johnell and Ranawat methods of measurement.

In the evaluation of atlanto-occipital relationships on the cross-table lateral radiograph, difficulties are not uncommonly encountered as landmarks may be indistinct, and magnification errors render the measured values spuriously

beyond the normal range. Lee et al. (1987) validated the measurement methods performed on cross-table lateral radiographs in AOD. The Powers ratio was accurate (>1) in 33%, while both the direct measurement of the condylar gap (>2 mm in adults, >5 mm in children) and the basion-dens interval (>10 mm in adults, >12 mm in children) were accurate in 50% of cases. They devised an X-line method which was the most accurate in 75% of cases of AOD. In the X-line method, two intersecting lines are drawn often referred to as Lee's lines (Fig. 6.9). The first line from the basion to the most anterior point of the C2 spinolaminar junction should pass across the supero-posterior aspect of the peg of C2, while the second line from the opisthion to the posteroinferior corner of the body of C2 should pass just anterior to the posterior portion of the C1 ring (Lee et al. 1987). However, in a later study comparing the X-line method with the Harris line (BDI, BAI) criteria for AOD, the X-line method performed poorly compared with the Rule of 12's or Harris criteria (BDI and BAI) (Harris et al. 1994). In a blinded study, Dziurzynski et al. (2005) compared radiographic with

CT-based methods of measuring five criteria for AOD, namely, the Powers ratio, X-line method, basion-dens interval, condylar gap and Harris method. They concluded that the sensitivity, specificity, positive and negative predictive values of these methods improve when CT is used because the anatomical landmarks are better visualised. They were optimally visualised in 99.75% on CT compared to 39–84% on radiographs (Dziurzynski et al. 2005). The Wackenheim line is also useful in the assessment of craniocervical relationships. This line is drawn down the posterior surface of the clivus as seen on the lateral radiograph or CT sagittal reformatted image. Its inferior extension should normally barely touch the posterior aspect of the rostral outline of the odontoid peg as it lies ventral to the line (Fig. 6.10). This normal relationship depicted in the cervical spine in the neutral position is not altered in flexion or extension views. This relationship is disrupted in both vertical migration and atlanto-occipital dissociation (Fig. 6.11) (Thiebaut et al. 1961). It is important to remember that the value of the measurement methods for AOD assessment is predominantly applied to the most common anterior AO dislocation. The performance is unreliable in the rarer posterior AO dislocation and in AO distraction separation. The **Wackenheim angle** between the clivus and the spinal canal is normally >150°, while **Boogaard's angle** measured between the clivus line and McRae's line is normally <135°.

It is essential to realise that the craniocervical measurement values and ranges differ when measured on plain radiographs and CT. This is because of the magnification effect in radiography and the limitations of accuracy in depicting the anatomical radiographic landmarks. Using MDCT and MPR, Rojas et al. studied 200 patients measuring the basion-axial interval (BAI), basion-dens interval (BDI), Powers ratio, atlantodental interval (ADI) and atlanto-occipital interval (AOI) and compared the measurements with established values from plain radiographs. In 95% the BDI measured <8.5 mm on MDCT compared with 12 mm on
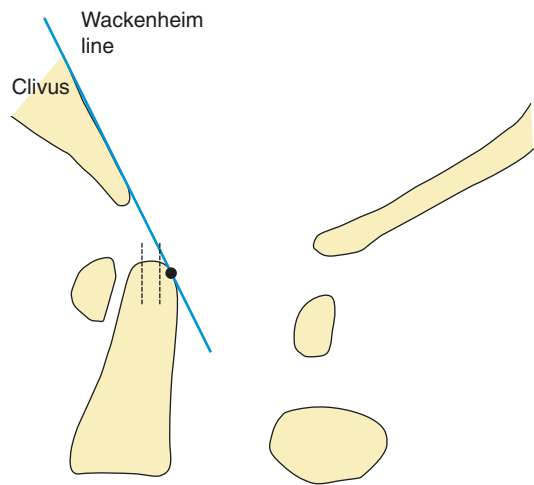
Fig. 6.10 Wackenheim clivus line—normal position. A line drawn along the posterior aspect of the clivus should barely intersect or be tangential to the posterior aspect of odontoid tip. This relationship is maintained in neutral flexion and extension positions
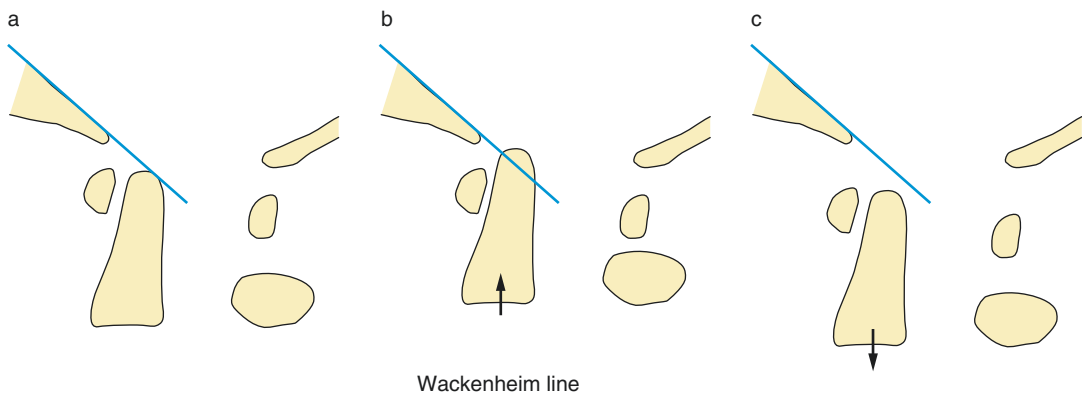
Fig. 6.11 Wackenheim clivus line in: **a** = normal, **b** = vertical migration, **c** = atlanto-occipital dissociation
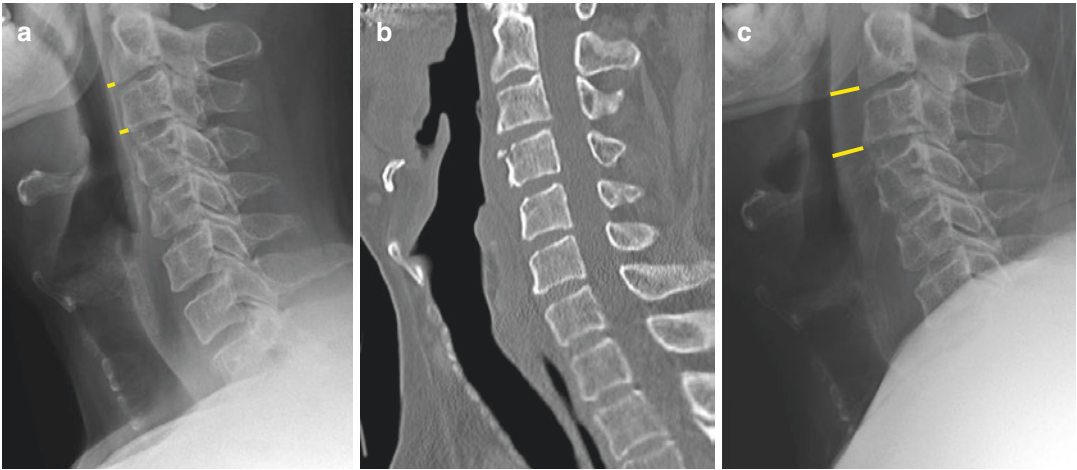
Fig. 6.12 Prevertebral soft tissue space (PVSTS). Pre-injury normal radiographic measurement of PVSTS (**a**), followed by a fracture of C4 as shown on sagittal MDCT (**b**), resulting in widened PVSTS radiographic measurements (**c**)

radiographs, the ADI < 2 mm compared with 3 mm on radiographs and the AOI ranged between 0.5 and 1.4 mm. There are no recorded AO condylar gap measurements in adults although there is general agreement this should not be >2 mm, while in the paediatric population studies indicate it should be <5 mm. The BAI was difficult on CT, and no change noted in Powers ratio values (Rojas et al. 2007, 2009).

An important clue to the presence of cervical spine trauma can be obtained by careful analysis of the thickness and appearance of the prevertebral soft tissue space (PVSTS) made along lines perpendicular to the contact point with the airway. Postural changes of the neck alter the measurements recorded. Penning looked at radiographs done in flexion and extension and showed a maximal difference of <1 mm compared with the neutral position. It is more common to detect a pathologically widened PVSTS in the C2/C3 levels irrespective of the level of injury as the tissues in the higher cervical spine are more lax. The C4 and C5 levels have a wide range of variability with all imaging modalities due to the presence of the larynx and oesophagus and should not be employed in the assessment of PVSTS. Increased thickness and contour alterations are good indicators of injury although it is important to remember that significant injury can be present despite a normal PVSTS. Increased

thickness can also be due to infection, haemorrhage, neoplasia and fluid collection. There is variation between paediatric and adult measurements and these also vary in their respective normal range depending on the imaging modality used. It is inappropriate to adopt the normal radiographic range of PVSTS from C1 to C7 to CT images, as measurements on CT have no magnification factors and the expected normal ranges are less. Furthermore radiographic measurements are calculated from the inferior/superior borders of the vertebral bodies, while those based on sagittal MDCT reformatted images are taken from the vertebral midpoint anteriorly (Fig. 6.12). A preset CT soft tissue window setting is crucial to ensure uniformity of measurement (WW 500 HU, WL-10 HU) (Rojas et al. 2007, 2009). The results using radiographic or MDCT methods show a wide range of normal PVSTS values, which is why one needs to focus on the upper limits of the range when assessing the measurement with reference values.

Measurement techniques used in both the diagnosis and quantification of lower cervical spine injury have also been standardised by the Spine Trauma Study Group (Bono et al. 2006) primarily focusing on kyphosis (Cobb angle and posterior vertebral body tangent methods), vertebral body translation, vertebral body height loss, facet fracture fragment size and percentage facet
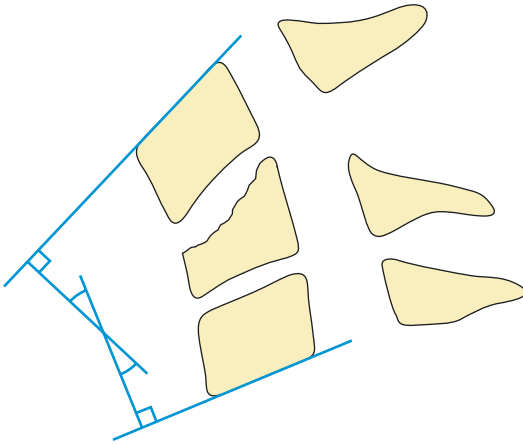
Fig. 6.13 Cobb measurement of sagittal cervical angulation. A line is drawn along the superior endplate of the next cranial unaffected vertebra. Another line is drawn along the inferior endplate of the next most caudal unaffected vertebra. The Cobb angle is the angle between the perpendicular of the two lines

Fig. 6.14 Posterior vertebral body tangent method of assessing kyphosis: A line is drawn along the posterior body of the fractured vertebra and a second line is drawn along the posterior cortex of the next most cranial unaffected level. The angle between the two lines is the angle of kyphosis

Fig. 6.15 Cervical translation: The amount of cervical translation is measured at the level of the inferior endplate of the dislocated vertebral body by measuring the transverse distance between two lines drawn tangential to the posterior aspect of the vertebral bodies

subluxation. In the Cobb measurement of sagittal cervical angulation, a superior endplate line through the next cranial unaffected vertebra is drawn along with an inferior endplate line through the next most caudal unaffected vertebra. The Cobb angle is the angle between the two lines (Fig. 6.13). The posterior vertebral body tangent method of assessing kyphosis relies on drawing two posterior vertebral body lines at the fractured and next most cranial unaffected level and determining the angle in between them (Fig. 6.14). Cervical translation accompanying dislocation is measured at the level of the inferior endplate of the dislocated (upper) vertebral body (Fig. 6.15), by measuring the transverse distance between two lines drawn tangential to the posterior vertebral bodies. Translation is an indicator of instability with 2 mm considered by some as the critical threshold, although most agree that 3.5 mm of translation is usually associated with mechanical instability. Postfracture vertebral loss of height requires firstly measurement of the anterior and posterior heights of the two unaffected vertebrae cranial and caudal to the injured level with an averaging of both measurements. This is then followed by measuring the anterior and posterior heights at the fractured level, divided by the respective averaged intact anterior

and posterior heights and multiplied by 100 (Fig. 6.16) (Frobin et al. 2002). Facet fracture results in a fragment of variable size and a concomitant reduction of intact articular facet surface apposition which could have a bearing on insta-
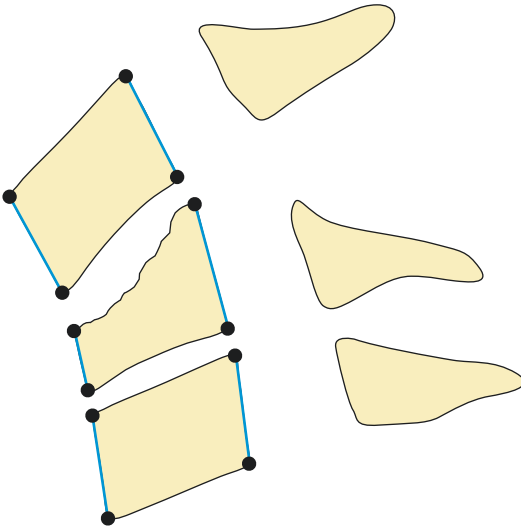
Fig. 6.16 Measurement of postfracture loss of vertebral body height: The anterior and posterior vertebral body heights of the two unaffected vertebrae cranial and caudal to the fractured vertebra are measured and both measurements (anterior height and posterior height) are averaged. The anterior and posterior vertebral body height at the affected level are then measured. These are divided by the respective averaged intact anterior and posterior heights and multiplied by 100 to calculate percentage loss of height

Fig. 6.17 Assessment of intact articular facet apposition following facet fracture: *A* = line drawn along intact facet articular surface is measured in mm. *B* = line drawn along residual intact articular surface of the fractured facet is measured in mm. *B* is divided by *A* and multiplied by 100 to give a percentage measurement of residual facet apposition

bility. The measurement can be done on lateral radiographs or parasagittal CT reconstructions (Fig. 6.17). A line is drawn along the intact articular surface and measured in mm (A), followed by a line measurement of the residual intact articular surface of the fractured articular surface (B). The latter (B) is divided by the former (A) measurement and multiplied by 100. Using a similar technique residual articular apposition following facet subluxation without fracture can be measured as (B/A × 100), where A represents total articular surface as measured along the inferior articular surface of the superior level, and B is the distance of contacting articular surface (Fig. 6.18). In a reproducibility and interobserver reliability study of these radiographic and CT-based measurements on 30 cases of cervical spinal injury, Bono et al. (2011) found that the translation and kyphosis had satisfactory reliability, while the results for vertebral body height loss and facet joint apposition were unreliable (Bono et al. 2006). The endplate method was bet-

ter and more reliable than the posterior vertebral body tangent method in determining kyphosis.

The canal dimensions of the cervical spine, especially its sagittal diameter, have attracted considerable attention with a number of imaging methods used in the assessment in both symptomatic and asymptomatic populations. A number of studies have confirmed that the diameter of the cervical canal varies with location, decreasing in width from C1 to C7, while the spinal cord area increases making lower levels at increased risk for myelopathy or injury. In the normal adult, the AP canal diameter at C3 is equal or >19 mm, while the transverse diameter is 27 mm. Regardless of vertebral size, e.g. dwarf dysplasias, the cord will always attain its intended adult size even if the cervical spinal canal is congenitally narrow due to the dysplasia. The average AP diameter of the spinal cord is 7.7 mm and its width 13.2 mm (Dimeglio 2011).

In 1956 Wolfe et al. established the normal values of the sagittal cervical canal diameter on
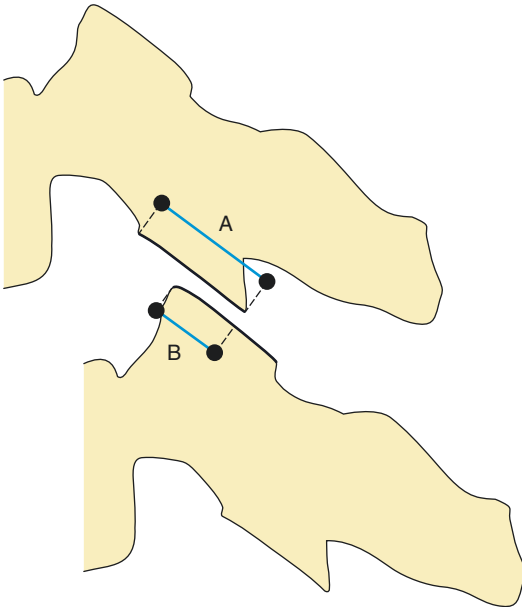
Fig. 6.18 Assessment of residual articular apposition following facet subluxation: *A* = measurement of total articular surface along inferior articular surface of superior facet. *B* = measurement of residual contacting articular surface. *B* is divided by *A* and multiplied by 100 to give percentage residual facet articular apposition

Fig. 6.19 Torg-Pavlov ratio: ratio of vertebral canal to vertebral body = distance from midpoint of posterior aspect of vertebral body to nearest point on corresponding spinolaminar line (**a**), divided by anteroposterior width of vertebral body, measured at its midpoint (**b**)

lateral radiographs taken with a FTD of 72 in. of 200 randomly selected asymptomatic cases. The average AP diameter at C1 was 22 mm, 20 mm at C2 and 17 mm at C3–C7. Since then studies on the subaxial cervical spine have shown that the AP dimension should normally be >15 mm and spinal stenosis is declared if <13 mm. In 1986 the Torg-Pavlov ratio was introduced as the canal/body ratio with measurement of both numerator and denominator taken from the mid-vertebral body (Fig. 6.19). If the ratio was <0.80 significant spinal stenosis was declared. This was employed in screening sport athletes until it was shown to carry a low predictive value. Using this method Herzog et al. (1991) found that 49% of 80 asymptomatic professional football players had ratios <0.80 at least at one cervical level. They indicated a low predictive value of 12% in determining spinal stenosis. This was due to the larger vertebral body dimensions in athletes which lowered the ratio measurement resulting in high false positive rate of 88%. CT also has been employed in the assessment of bony canal dimen-

sions in the sagittal and transverse plane, but as in radiography these osseous dimensions underestimate the true functional space for the cord as they do not include the intraspinal soft tissues. Employing 1.5 T MRI on healthy asymptomatic volunteers, normative cervical spinal canal and spinal cord dimensions have been recently established in a multicentre study (Ulbrich et al. 2014). The midsagittal diameters were measured producing a range of values at C1 (10.7–19.7 mm), C3 (9.4–17.2 mm) and C6 (9.2–16.8 mm) levels on 140 healthy white volunteers. Measurements employed a line drawn from the midpoint between the superior and inferior endplates of the vertebral bodies from C3 to C6, perpendicular to the anterior surface of the spinal cord, to the midpoint of the level's spinous process. Using midsagittal TSE T2 and VIBE sequences, they concluded that the dimensions of the cervical spinal canal and cord in healthy individuals vary with age, sex, height and vertebral level. The diameter and the area of the spinal canal decrease from C1 to C6 in all the height subgroups. The spinal cord behaves in a similar fashion in its AP diameter measurements, but the area of the spinal

cord remains virtually the same from C1 to C6. This is because the cord alters its shape from circular at C1 to ellipsoid at C6 becoming broader at lower cervical levels. Importantly at all spinal levels, the individual's factors of height, age and gender play a statistically significant influence on the spinal measurements. This means that the provision of valid normal values as reference standards for spinal canal and cord dimensions require allied definition to location, height, etc. In earlier studies, namely, by Sherman et al. (1990) on MRI-based measurements of the normal cervical cord, it was amply evident that there is no single value for assessing spinal cord dimensions. The spinal cord at each level should be compared with the normal reference range specific to that level. The average AP and transverse cord diameters were measured at C2 (8.8 mm × 12.4 mm), C4 (8.7 mm × 14mm) and C7 (7.4 mm × 11.4 mm) with the normal cervical enlargement at C4-C6. The average spinal cord area at C4 in Sherman's study was **121.8 mm²**, while the average area in a Japanese study (Ishikawa et al. 2003) was found to be significantly less at **94.6 mm².** This is likely to reflect racial differences and not just use of different pulse sequences. However, the cord dimensions are influenced by pulse sequences with the T1 images yielding almost the same values as actual cord measurements in a cadaveric spinal cord model (Suzuki and Shimamura 1994). In Dvorak et al.'s study, the mean diameter of the spinal cord in normal individuals was **7.7 mm (SD, 0.58; range, 6.5-9 mm)** which covers the range reported by Sherman et al. (1990).

Cervical spondylosis is the commonest cause of tetraparesis in adults resulting from a decrease in the space available for the cord. Imaging plays a role in identifying the extrinsic pressure from the spondylotic processes. In addition there are four factors that are important determinants of myelopathy, namely, the AP diameter of the spinal canal, dynamic cord compression, dynamic alteration of the cord's intrinsic morphology and its vascular supply. As discussed previously an AP diameter of the canal <13 mm denotes congenital stenosis. Flattening of the cord is associated with myelopathy with Penning et al. (1986) showing that when the transverse area of the cord is <60mm², cord compression symptoms developed. Ono et al. (1997) proposed an AP cord/compression ratio which is calculated by dividing the AP diameter of the cord by the transverse diameter. Those with an AP ratio of <0.40 have worse neurological deficit. Furthermore postoperative assessment by Ogino et al. (1983) showed that an AP ratio > 0.40 or a transverse diameter increased to >40 mm indicated a strong likelihood of recovery of cord function. Dynamic cord compression occurs in flexion and extension, and this can increase the degree of compression or cause it in these positions in the absence of compression on the static neutral neck position (Bernhardt et al. 1993). Dvorak et al. recommend functional MRI in flexion in an effort to determine the cord's diameter in a subluxed position. If the cord diameter in flexion is 6 mm, this is the minimum AP diameter beyond which there is an increased incidence of myelopathy (Dvorak et al. 1989).

6.2   Basilar Invagination: Method of Chamberlain
(Chamberlain 1939)

Definition

Distance from tip of odontoid process to Chamberlain's line—a line drawn from the posterior margin of the hard palate to the posterior margin of the foramen magnum (Fig. 6.20).

Indications

To detect basilar invagination or protrusion of the odontoid process into the foramen magnum. Occurs in rheumatoid arthritis, Paget's disease, osteomalacia, rickets and congenital disorders such as Chiari malformation, atlanto-occipital fusion, hypoplasia of atlas, Klippel-Feil syndrome, osteogenesis imperfecta, achondroplasia, spondyloepiphyseal dysplasia, Morquio's syndrome, chondro-osteodystrophy and cleidocranial dysostosis.
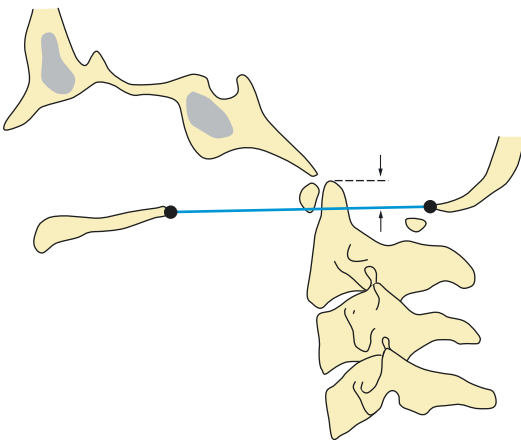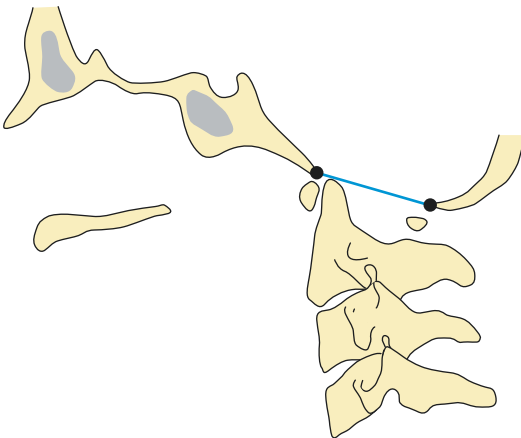

Fig. 6.20 Basilar invagination—method of Chamberlain. Perpendicular distance from tip of Odontoid process (*dotted line*) to Chamberlain's line: Chamberlain's line is represented by the horizontal blue line in the diagram, a line drawn from the posterior margin of the hard palate to the posterior margin of the foramen magnum. In most normal subjects, the odontoid tip lies less than 3.3 mm above Chamberlain's line

Measurement

Radiography	Normal—odontoid tip +/− 3.3 mm from Chamberlain's line
	Abnormal—6.6 mm or greater indicates basilar invagination
MRI	Mean 1.2 mm below Chamberlain's line, median 1.5 mm and SD 3 mm
CT	Mean 1.4 mm below Chamberlain's line, median 1.2 mm and SD 2.4 mm

Techniques

Radiography	Central ray perpendicular to lateral skull
	Target-film distance 36 in.
CT	Reformatted midline sagittal images
MRI	Sagittal T1-weighted turbo spin-echo (TSE) sequence. TR 390, TE echo time 10, slice thickness 5 mm and interslice gap 1 mm. FOV 400 mm. Flip angle 50

Full Description of Technique

Radiography: Perpendicular distance from tip of odontoid process to Chamberlain's line (line connecting posterior aspect of the hard palate to posterior aspect of the foramen magnum).

CT/MRI: Midsagittal image used for analysis. Perpendicular distance from tip of odontoid process to Chamberlain's line (line connecting posterior aspect of the hard palate to posterior aspect of the foramen magnum).

Reproducibility/Variation

Radiography: Normal—odontoid tip +/− 3.3 mm from Chamberlain's line. Abnormal— 6.6 mm or greater indicates basilar invagination. This is based on 102 normal skull radiographs (Poppel et al. 1953).

CT: Mean 1.4 mm, median 1.2 mm and SD 2.4 mm. This is based on measurements done in 150 adults (Cronin et al. 2009).

MRI: Mean 1.2 mm, median 1.5 and SD 3 mm. This is based on 200 brain MRI studies in adult Europeans (Cronin et al. 2007).

Clinical Relevance/Implications

Basilar invagination can cause impingement on the medulla and result in neurological problems and even sudden death (estimated to occur in up to 10% of patients with basilar invagination due to rheumatoid arthritis).

Analysis/Validation of Reference Data

Analysis from a plain lateral radiograph is not 100% sensitive (Riew et al. 2001). Sometimes it is not easy to see the tip of the odontoid peg. In about 50% of normal subjects, the tip of the odontoid process is at or below Chamberlain's line. Using CT the mean position of the odontoid process was 1.4 mm below Chamberlain's line (median1.2 mm, SD 2.4 mm). There is no difference between male and female values or between CT and MRI measurements. Chamberlain's line is in practice more difficult to use than McGregor's line.

Conclusion

In most normal subjects, the odontoid tip lies less than 3.3 mm above Chamberlain's line, and basilar invagination is present when it lies >3 mm.

6.3   Basilar Invagination: Method of McGregor

Definition

Distance from tip of odontoid process to McGregor's line; a line drawn from the posterior margin of the hard palate to the lowest point on the midline occipital curve (Fig. 6.21).

Indications

To detect basilar invagination or protrusion of the odontoid into the foramen magnum. Occurs in rheumatoid arthritis, Paget's disease, osteomalacia, rickets and congenital disorders such as Chiari malformation, atlanto-occipital fusion, hypoplasia of atlas, Klippel-Feil syndrome, osteogenesis imperfecta, achondroplasia, spondyloepiphyseal dysplasia, Morquio's syndrome, chondroosteodystrophy and cleidocranial dysostosis.
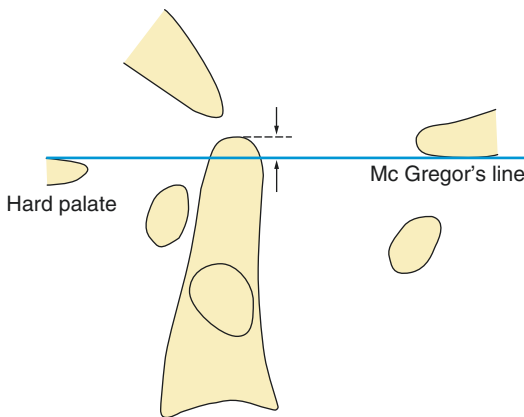
Fig. 6.21 Basilar invagination—method of McGregor. Perpendicular distance from tip of odontoid process (*dotted line*) to McGregor's line (*blue line*) should not exceed 4.5 mm. McGregor's line is drawn from the posterior margin of the hard palate to the most caudal point on the midline occipital curve

Measurement

Radiography: Odontoid tip from McGregor's line.

   Male adults: Mean 3.3 mm, SD 3.81, 90% tolerance −7.4 to +8.0

   Female adults: Mean 3.67 mm, SD 1.69, 90% tolerance −2.4 to +9.7

CT: Mean position 0.8 mm below McGregor's line (median 0.9 mm, SD 3 mm)

MRI: Mean position 0.9 mm below McGregor's line (median 1.1 mm, SD 3 mm)

Techniques

Radiography: Central ray perpendicular to lateral skull.

Target-film distance 72 in.

CT: Midline sagittal reformatted MDCT images using bone window settings.

MRI: Sagittal T1-weighted turbo spin-echo (TSE) sequence. TR 390, TE echo time 10, slice thickness 5 mm and interslicegap 1 mm. FOV 400 mm. Flip angle 50.

Full Description of Technique

Radiography: Perpendicular distance from tip of odontoid process to McGregor's line (line connecting posterior aspect of the hard palate to the lowest point on the midline occipital curve.

CT/MRI: Midsagittal image used for analysis. Perpendicular distance from tip of the odontoid process to McGregor's line.

6.4 Basilar Invagination: Method of McRae

Definition

The odontoid tip should lie below McRae's line (a line connecting the anterior and posterior margins of the foramen magnum). A perpendicular line drawn from apex of odontoid should intersect McRae's line in its ventral quarter (Fig. 6.22).

Indications

To detect basilar invagination or protrusion of the odontoid into the foramen magnum. Occurs in rheumatoid arthritis, Paget's disease, osteomalacia, rickets and congenital disorders such as Chiari malformation, atlanto-occipital fusion, hypoplasia of atlas, Klippel-Feil syndrome, osteogenesis imperfecta, achondroplasia, spondyloepiphyseal dysplasia, Morquio's syndrome, chondroosteo-dystrophy and cleidocranial dysostosis.

Fig. 6.22 Basilar invagination—method of McRae. Odontoid tip should lie below McRae's line—a line drawn between the anterior and posterior margins of the foramen magnum (*blue line* in diagram). In addition, a perpendicular line drawn from the apex of the odontoid to McRae's line should intersect it in its ventral quarter

Measurement

Radiography: Odontoid tip should lie below McRae's line (a line connecting the anterior and posterior margins of the foramen magnum).
MRI: Odontoid tip 4.6 mm below McRae's line, median 4.8 and SD 2.6.

Techniques

Radiography: Central ray perpendicular to lateral skull.
CT: Midline sagittal reformatted images on bone settings.
MRI: Sagittal T1-weighted turbo spin-echo (TSE) sequence. TR 390, TE echo time 10, slice thickness 5 mm and interslice gap 1 mm. FOV 400 mm. Flip angle 50.

Full Description of Technique

Radiography: Perpendicular distance from tip of odontoid process to McRae's line (line connecting anterior margin to posterior margin of the foramen magnum).
CT/MRI: Midsagittal image used for analysis. Perpendicular distance from tip of the odontoid process to McRae's line.

Reproducibility/Variation

Radiography: Odontoid tip should lie below McRae's line. A line drawn from the apex of the odontoid should intersect the ventral quarter of McRae's line. Based on 26 normal skull radiographs (Poppel et al. 1953).

However, it can be difficult to identify anterior and posterior margins of the foramen magnum on plain radiographs. A midline sagittal CT reformatted image is more reliable.
MRI: 4.6 mm, median 4.8 and SD 2.6 below McRae's line. Based on 200 brain MRI studies in adult Europeans. CT measurements based on 150 normal adult patients (Cronin et al. 2009).

Clinical Relevance/Implications

Basilar invagination can cause impingement on the medulla and result in neurological problems and even sudden death (estimated to occur in up to 10% of patients with basilar invagination due to rheumatoid arthritis).

Analysis/Validation of Reference Data

It can be difficult to identify the anterior and posterior margins of the foramen magnum on plain radiographs. Using CT reformatted sagittal midline images, the mean position of the odontoid process of C2 is normally 5 mm (median 5 mm, SD 1.8 mm) below McRae's line. There is no significant difference between males and females or between these CT values from those on MRI.

Conclusion

It can be difficult to identify McRae's line in practice. McGregor's line is easier to identify and is a more useful measurement for basilar invagination.

6.5   Basilar Invagination: Method of Ranawat (Weinstein 2001)

Definition

The distance between the centre of the pedicles of C2 and a line drawn in the transverse axis of C1 (Fig. 6.23).

Indications

To detect basilar invagination. Particularly useful if hard palate cannot be visualised on the film, also if the odontoid is poorly visualised, for example, due to erosion in rheumatoid arthritis.
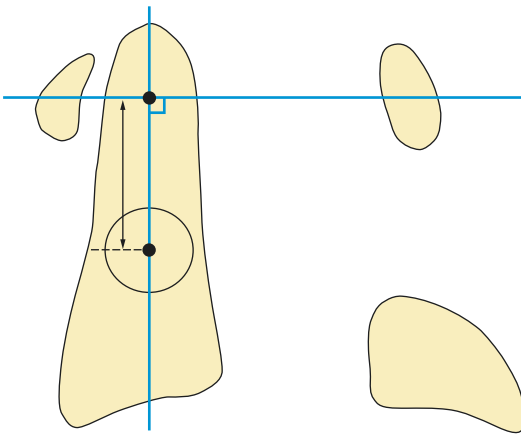
Fig. 6.23 Basilar invagination—method of Ranawat. A line is drawn connecting the centre of the anterior arch of the first cervical vertebra with its posterior ring (*horizontal blue line*). The centre of the sclerotic ring of the second cervical vertebra, representing the pedicle is marked. The perpendicular distance between the centre of the pedicle of C2 and the perpendicular line drawn in the transverse axis of C1 is measured. A distance of <15 mm in men and <13 mm in women suggests basilar invagination

Measurement

Men:
    Average 17 mm (SD 2 mm)
Women:
    Average 15 mm (SD 2 mm)
    A distance <15 mm in men and <13 mm in women suggests the presence of basilar invagination, and an MRI needs to be done for further assessment.

Techniques

Radiography: Standard lateral cervical spine radiograph.

Full Description of Technique

Twenty-six normal individuals and 33 patients with rheumatoid arthritis were analysed. Using this method standard lateral cervical spine radiographs are first obtained.

The distance between the centre of the pedicles of C2 and the transverse axis of C1 is measured.

Reproducibility/Variation

Limited studies regarding validation.

Clinical Relevance/Implications

Useful for detecting basilar invagination when the hard palate cannot be visualised—if the hard palate cannot be visualised, Chamberlain's and McGregor's lines cannot be used to assess for basilar invagination.

Analysis/Validation of Reference Data

Limited validation data available. The study by Riew et al. (2001) who examined eight plain film diagnostic methods of basilar invagination showed that no single plain radiographic assessment method was 100% reliable. They recommended that measurements be made according to the methods described by Ranawat et al. (1979), Redlund-Johnell and Pettersson (1984) and Clark et al.

However, 6% of cases with basilar invagination in RA patients would still be missed. If any of these three methods suggest basilar invagination or are equivocal, a CT and MRI should be performed.

Conclusion

Useful for detecting basilar invagination when odontoid peg is poorly visualised or eroded.

6.6 Basilar Invagination: Method of Bull (Bull et al. 1955)

Definition

The angle between a line drawn along the plane of the hard palate and a line drawn along the horizontal plane of C1 should not exceed 13° (Fig. 6.24).

Indications

To detect basilar invagination or protrusion of the odontoid into the foramen magnum. Occurs in rheumatoid arthritis, Paget's disease, osteomalacia, rickets and congenital disorders such as Chiari malformation, atlanto-occipital fusion, hypoplasia of atlas, Klippel-Feil syndrome, osteogenesis imperfecta, achondroplasia, spondyloepiphyseal dysplasia, Morquio's syndrome, chondroosteodystrophy and cleidocranial dysostosis.

Measurement

Radiography: Angle of Bull more than 13° indicates odontoid process position is abnormal.
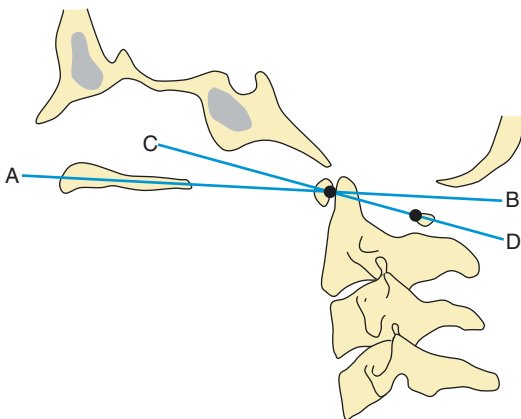
Fig. 6.24 Basilar invagination—method of Bull. Angle between a line drawn along plane of hard palate (**a**, **b**) and a line drawn along horizontal plane of C1 (**c**, **d**) should be <13°

Technique

Radiography: Central ray perpendicular to lateral skull.
Patient prone. Chin in neutral position.

Full Description of Technique

Radiography: A line is drawn along the plane of the hard palate and a line is drawn along the horizontal plane of C1. Angle >13° means the position of the odontoid is abnormal.

Reproducibility/Variation

Radiography: Not useful in everyday practice since the measurements were made from radiographs obtained with patient prone. Based on 120 normal skull radiographs.

Clinical Relevance/Implications

Basilar invagination can cause impingement on the medulla and result in neurological problems and even sudden death (estimated to occur in up to 10% of patients with basilar invagination due to rheumatoid arthritis).

Analysis/Validation of Reference Data

Very limited validated data.

Conclusion

Not useful in everyday practice.
Varies considerably with flexion and extension.

6.7 Basilar Invagination: Method of Redlund-Johnell (Roche et al. 2002a, b)

Definition

The distance between McGregor's line and the lower endplate of C2 (Fig. 6.25).

Indications

To detect basilar invagination or protrusion of the odontoid into the foramen magnum. Occurs in rheumatoid arthritis, Paget's disease, osteomalacia, rickets and congenital disorders such as Chiari malformation, atlanto-occipital fusion, hypoplasia of atlas, Klippel-Feil syndrome, osteogenesis imperfecta, achondroplasia, spondyloepiphyseal dysplasia, Morquio's syndrome, chondroosteo-dystrophy and cleidocranial dysostosis.

Measurement

Males: 41.6 mm (SD 4 mm).
Females: 37.1 mm (SD 4.3 mm).
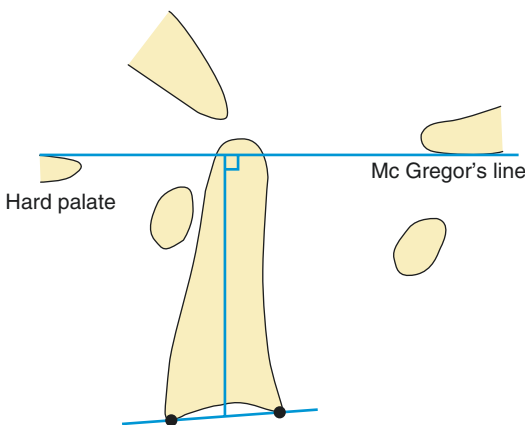
Fig. 6.25 Basilar Invagination—method of Redlund-Johnell. The distance between McGregor's line (*blue line* drawn between the posterior margin of the hard palate and the lowest point of midline occipital curve) and the midpoint of the inferior margin of C2. A measurement of <34 mm for men and <29 mm for women is considered abnormal

Techniques

Radiography: Standard lateral cervical spine radiographs.
CT/MRI in the sagittal plane.

Full Description of Technique

Standard lateral cervical spine radiographs were taken of 200 normal adults, 100 female and 100 male. The distance between McGregor's line and the inferior endplate of C2 was measured.

Reproducibility/Variation

Limited information but the study by Riew et al. (2001) supported its use as one of three most reliable methods.

Clinical Relevance/Implications

Useful in patients in whom the tip of the odontoid is eroded or difficult to see, i.e. especially useful in rheumatoid arthritis patients.

Analysis/Validation of Reference Data

Limited but deemed useful in certain clinical situations. A measurement <34 mm in men and <29 mm in women indicates basilar invagination.

Conclusion

Useful measurement in patients in whom the odontoid is poorly visualised.

6.8 Foramen Magnum in Children and Adult

Definition

Measurements of the anteroposterior diameter of the foramen magnum were made on a line drawn between the lower margin of the occipital bone and the basion (anterior margin of foramen magnum) (Fig. 6.26).

Indications

To help identify abnormalities of craniocervical junction, which can be congenital or acquired.

Measurement

Average anteroposterior diameter 30–35 mm in children.
Average anteroposterior diameter 34.78 +/− 2.19 mm in adults.
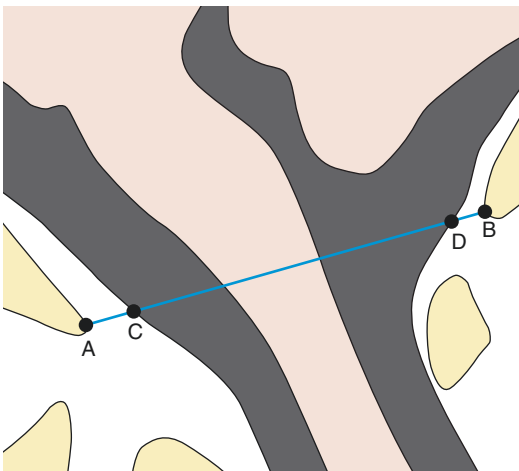
Fig. 6.26 Foramen magnum in children and adults. AP diameter of the foramen magnum is the distance between the basion 'A' and opisthion 'B'. Average diameter in children is 30–35 mm. Average diameter in adults is 34.78 +/− 2.19 mm. AP diameter of the subarachnoid canal at the level of the foramen magnum is the distance between 'C' and 'D'. The average diameter in adults is 28 mm

Techniques

Radiography: Midsagittal pneumotomogram.
CT: Midsagittal reformat.
MRI: Midsagittal image.

Full Description of Technique

Measurements were obtained from a midsagittal pneumotomogram and are reported by Martinez-Lozano (2001).
    Original data taken from Schmeltzer et al. (1971). 200 subjects.
    Measurements using CT, taken from normal CT examinations in 100 adults are reported by Kanodia and Parihar (2012).
    Measurements using MRI (1.5 T) in 40 healthy adults are reported by Damiani and Borelli (2012).

Reproducibility/Variation

Limited available data.

Clinical Relevance/Implications

May be useful in congenital or acquired disorders of craniovertebral junction, if applied to plain radiographs. Pneumotomography is no longer performed.

Analysis/Validation of Reference Data

Limited data.

Conclusion

Pneumotomography has been replaced by MRI in sagittal plane as it depicts both the bony landmarks and subarachnoid space.

6.9 Atlanto-Occipital Joint Space in Children and Adults

Definition

The atlanto-occipital joint space or interval (AOI) is defined as the distance between the top of the C1 facet and the bottom of the corresponding occipital condyle (Fig. 6.27).

Indications

Useful in suspected atlanto-occipital dislocation.

Measurement

Radiography: 100 normal children

Point 1: 2.22 +/− 0.70SD range 1.0–3.5
Point 2: 2.63 +/− 1.02SD range 1.0–5.0
Point 3: 2.52 +/− 0.95SD range 1.0–5.0
Point 4: 2.13 +/− 0.70SD range 1.0–4.0
Point 5: 1.96 +/− 0.65SD range 1.0–4.0
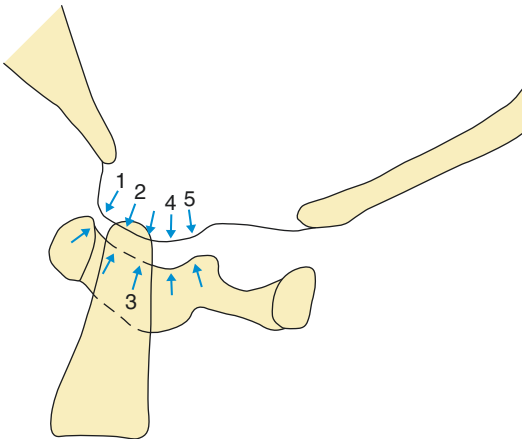
Fig. 6.27 Atlanto-occipital joint space in children and adults. The space between the occipital condyle and corresponding upper margin of C1 facet should not exceed 5.0 mm in radiographs of children. On CT the space should not exceed 1.8 mm in adults.

CT: 200 normal adults
Mean 1.0 mm, range 0.5–1.8 mm.

Techniques

Radiography: Lateral skull radiographs in 100 normal subjects.
CT: Parasagittal reformatted images in 200 adults.

Full Description of Technique

Lateral skull radiographs, taken with a film—focus distance of 40 in. 100 normal children aged 1–15 years, 63 boys and 37 girls.

The bony landmarks of the occipital condyles and the top of the C1 facets were traced on to transparent film, and the joint space was measured at five evenly spaced points, using a hand lens micrometre.

CT measurements done on parasagittal MDCT reformatted images. The AOI is calculated by drawing a line perpendicular to the articular surfaces of the occipital condyle and the lateral mass of C1. The line is drawn at the centre of the articulation by correlating the coronal and sagittal reformatted images.

Reproducibility/Variation

Generally accepted as reliable and used in practice with limited studies validating the AOI value.

Clinical Relevance/Implications

Useful in suspected atlanto-occipital dislocation. This is usually a fatal injury but some children survive. Atlanto-occipital dislocation needs to be recognised early to improve outcome.

Measurements of the atlanto-occipital joint (Kaufman et al. 1987)

Measurement position	Measurable (%)	Mean ± SD	Range
Normal subjects (n = 100)			
1	65 (77)	2.22 ± 0.70	1.0–3.5
2	64 (76)	2.63 ± 1.02	1.0–5.0
3	58 (69)	2.52 ± 0.95	1.0–5.0
4	63 (75)	2.13 ± 0.70	1.0–4.0
5	60 (71)	1.96 ± 0.65	1.0–4.0
Atlanto-occipital distraction injury (n = 8)			
1	8 (100)	6.44 ± 1.43	4.5–8.0
2	8 (100)	8.12 ± 2.20	5.5–11.0
3	6 (75)	7.50 ± 1.70	5.0–9.5
4	6 (75)	7.67 ± 2.09	5.0–10.0
5	3 (38)	6.33 ± 3.01	3.5–9.5

Analysis/Validation of Reference Data

Measurements obtained in the 100 normal children were compared to measurements obtained in eight children who had suffered atlanto-occipital distraction injury.

Conclusion

In children, the atlanto-occipital joint space on plain radiograph should not exceed 5.0 mm.

In adults the atlanto-occipital joint space on CT should not exceed 1.8 mm.

6.10 Powers Ratio
(Powers et al. 1979)

Definition

The Powers Ratio is used to confirm a normal relationship between occiput and C1 (Fig. 6.28).

Indications

To detect anterior atlanto-occipital dislocation following trauma.

Measurement

The ratio BC/OA is used to detect anterior atlanto-occipital dislocation. A ratio of less than 1 is normal. Ratio of equal to or greater than 1 implies anterior atlanto-occipital dislocation.

Techniques

Radiography: Lateral cervical spine radiographs. Central ray perpendicular to the plane of the film
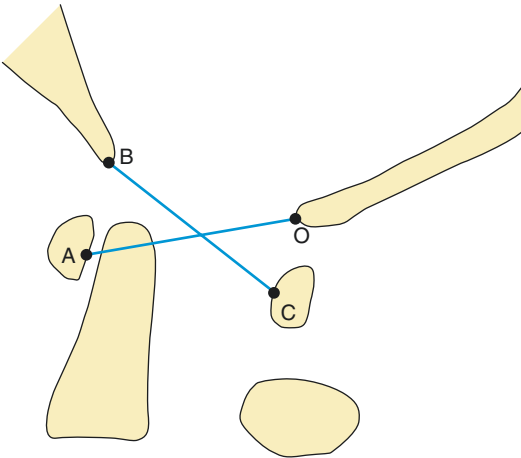
Fig. 6.28 Powers ratio. B is the basion at the anterior margin of the foramen magnum. O is the opisthion at the posterior margin of the foramen magnum. A is the posterior cortex of the anterior arch of the atlas (C1). C is the anterior cortex of the posterior arch of the atlas (C1). The ratio of the two interval lines BC/OA should be less than 1 in normal subjects

and centred over the midcervical spine. Film to focus distance not relevant, since the measurement is a ratio.
CT: Midline sagittal reformatted image.
MRI: Sagittal images.

Full Description of Technique

Lateral radiographs of the cervical spines of 100 adults and 50 children were analysed and compared with four cases of proven anterior atlanto-axial subluxation.

B is the basion at the anterior margin of the foramen magnum.
O is the opisthion at the posterior margin of the foramen magnum.
A is the posterior cortex of the anterior arch of the atlas (C1).
C is the anterior cortex of the posterior arch of the atlas (C1).

The ratio of the two interval lines BC/OA should be less than 1 in normal subjects.

Reproducibility/Variation

Unknown.
The bony landmarks required to assess Powers ratio are often not clearly seen, especially the opisthion (posterior margin of foramen magnum).
Lee et al. (1987) found Powers ratio to be accurate in 33% of cases of atlanto-occipital dislocations.

Clinical Relevance/Implications

Anterior atlanto-occipital dislocation is a severe injury and is usually fatal. Commonest cause is road traffic accidents. The injury is also reported following falls, direct trauma and forceps delivery. Younger children are at particular risk because of relatively small occipital condyles and

relative horizontal orientation of the atlanto-occipital joint. If the victim survives to reach hospital, it is important to recognize this injury at an early stage to prevent death or disability. It is usually associated with marked prevertebral soft tissue swelling.

Analysis/Validation of Reference Data

One hundred fifty normal subjects compared to a small sample of four patients with proven atlanto-occipital dislocation. It is essential to realise that the ratio is normal and therefore unreliable when the dislocation is posterior instead of anterior and in instances of vertical atlanto-occcipital distraction injury.

Conclusion

Atlanto-occipital dislocation is a rare but very serious injury. Recognition of the abnormal atlanto-occipital relationship can be helped by using Powers ratio. Sometimes difficult to identify the bony landmarks required.

6.11   Basion-Dens Interval

Definition

The distance between the inferoposterior tip of the basion (anterior margin of the foramen magnum) and the superior tip of the odontoid process (Fig. 6.29).

Indications

To detect atlanto-occipital dislocation.

Measurement

The distance from the basion to the tip of the odontoid (BDI) ranges from 2 to 15 mm (mean 7.5 +/− 4.3 mm 2SD).

In 95% cases, the distance is less than 12 mm.

Techniques

Radiography: Supine lateral cervical spine radiograph taken with a film-focus distance of 40 in. centred on the occipitocervical junction. CT: Midsagittal reconstruction is recommended.
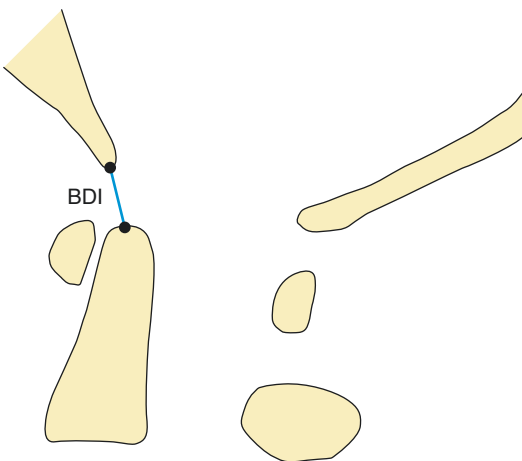
Fig. 6.29 Basion-Dens interval. The basion-dens interval (BDI) is the distance between the basion and the tip of the odontoid. In 95% adults, this measures less than 12 mm on a lateral cervical spine radiograph

Full Description of Technique

Four hundred adult subjects, cleared clinically and radiologically of cervical spine injury. Lateral cervical spine radiographs were analysed. The distance between the basion and the tip of the odontoid process was measured.

Reproducibility/Variation

The basion-dens interval was measurable in 374 of the 400 adults. In the others, the bony landmarks could not be clearly identified.

Cannot be applied to children because of variable ossification of the odontoid.

Clinical Relevance/Implications

Simple and useful measurement. Atlanto-occipital dislocation is a rare and usually fatal injury, commoner in children. If patients survive to reach hospital, it is important to recognise the injury to prevent further neurological injury.

Analysis/Validation of Reference Data

It was only possible to measure the basion-dens interval in 94% of subjects. Good sample size of 374 adults. Deliganis et al. (2000) and Fisher et al. (2001) also concluded that both BDI and BAI measurements are the most useful parameters of AOD. However, there are no interobserver and intraobserver studies.

Conclusion

Simple measurement provided anatomical landmarks are visible. A value greater than 12 mm is very suggestive of AO dissociation.

6.12 Basion: Axial Interval

Definition

The basion-axial interval (BAI) is defined as the distance (either anterior or posterior) between the basion and the rostral extension of a line drawn along the posterior cortical margin of the body of the axis (C2) to just beyond the foramen magnum (Fig. 6.30).

Indications

To detect anterior atlanto-occipital dislocation.

Measurement

In normal subjects the distance from the basion to the posterior axial line (PAL) should be less than 12 mm.

In 80% of subjects, the basion lies within 0–6 mm of the posterior axial line.
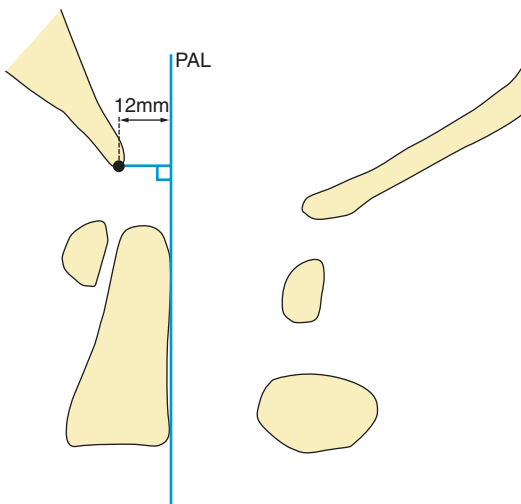
Fig. 6.30 Basion-axial interval. The perpendicular distance between the basion (inferior tip of clivus, anterior margin of foramen magnum) and the posterior axial line (superior continuation of a line drawn along the posterior cortex of the body of C2) is measured. This distance should be less than 12 mm

Techniques

Radiography: Horizontal beam lateral cervical radiographs. Film-focus distance 40 in.
CT/MRI in the midsagittal plane.

Full Description of Technique

Four hundred adult subjects and 50 children aged 1–14 years, cleared clinically and radiologically of cervical spine injury. Lateral cervical spine radiographs taken with a film-focus distance of 40 in. The perpendicular distance between the basion (inferior tip of clivus, anterior margin of foramen magnum) and the posterior axial line (superior continuation of a line drawn along the posterior cortex of the body of C2) is measured.

If the posterior cortex of C2 measured less than 1 mm thick, the line was drawn over it. If the thickness of the posterior cortex of C2 measured more than 1 mm, the line was drawn along the midplane between the anterior and posterior margins. The distance between the basion and this line is the basion-axial interval.

Reproducibility/Variation

Harris et al. (1994) found that after complete ossification and fusion of the dens >13 years of age, both the BDI and BAI measured 12 mm normally. However, <12 years of age, the BDI was unreliable due to incomplete ossification, but the BAI in such normal patients did not exceed 12 mm. The normal range of BAI in reality extends from 12 mm anterior to 4 mm posterior to the posterior axial line while the BDI normally does not exceed 12 mm. This is important as the BAI has to cope with the limits that are exceeded in both anterior as well as posterior AO dislocation. The BAI is not useful on MDCT. When MPR images from MDCT are used the BAI assessment is difficult to obtain reliably. There is a lot of variation in drawing the PAL due to the irregular contour of the posterior C2 cortex, which leads to significant intraobserver and interobserver variation. In addition obtaining a

perfect midline sagittal image is not easy and different sagittal views are used by different observers.

Clinical Relevance/Implications

Atlanto-occipital dislocation is a rare and usually fatal injury. Survivors are often left with severe neurological defects. The injury occurs more commonly in children. It is important to recognise this injury if the patient survives to reach the hospital to help prevent further neurological damage.

Analysis/Validation of Reference Data

Harris et al. (1994) performed two complimentary studies using lateral radiographic assessment of BDI and BAI. The first was on a large cohort of normal subjects, 400 adults and 50 children. The BAI and BDI did not exceed 12 mm in 98% and 95%, respectively, in adults.

In the second study, 37 patients' lateral radiographs with suspected atlanto-occipital dislocation were retrospectively analysed—31 were subsequently proven to have complete (23) or incomplete (8) dislocation.

Conclusion

Useful measurement, provided the relevant anatomical landmarks, can be visualised. It can be used in association with the basion-dens interval.

Recommended cut-off value for the basion-axial interval is 12 mm anterior to posterior axial line and no greater than 4 mm posterior to posterior axial line.

6.13 C1 Bony Landmarks on CT
(Naderi et al. 2003)

Definition

Computed tomographic measurements of C1 AP diameter, C1 transverse diameter, facet diameter, distance between anterior tubercle and anterior aspect of C1 lateral mass on the lateral view (Fig. 6.31).

Indications

Can be helpful prior to surgical procedures, e.g. C1 laminectomy or C1/C2 fusion.
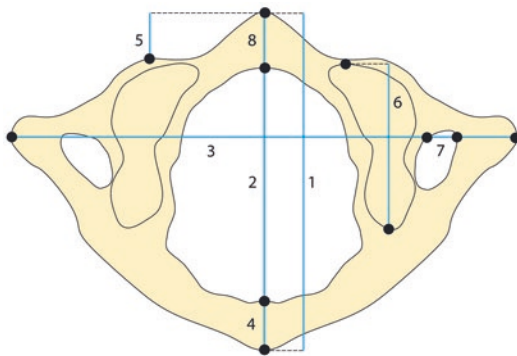
Fig. 6.31 C1 bony landmarks on CT. The measured parameters. (*1*) outer AP diameter of C1, (*2*) inner AP diameter of C1, (*3*) outer transverse diameter of C1, (*4*) distance between midline and vertebral artery groove on the outer cortex of C1 posterior arch, (*5*) distance between C1 anterior tubercle and lateral mass in lateral view, (*6*) AP diameter of C1 superior facet, (*7*) distance between outer margin of transverse foramen and outer margin of lateral mass and (*8*) AP diameter of superior surface of C1 anterior arch

Measurement

1. Outer AP diameter of C1: 43.3548 mm (SD 2.3741 mm) 2. Inner AP diameter of C1: 30.6774 mm (SD 2.4548 mm)
3. Outer transverse diameter of C1: 74.9677 mm (SD 5.5286 mm)
4. Distance between C1 anterior tubercle and lateral mass in lateral view: 4.9032 mm (SD 1.3749 mm)
5. AP diameter of superior articular facet: 19.9355 mm (SD 1.9989 mm).
   AP diameter of anterior arch: 6.2258 mm (SD 1.0555 mm)

Technique

CT: Axial plane, with sagittal reformatting.

Full Description of Technique

Axial thin slice CT through C1 vertebra, reviewed on bone window settings.

1. Outer AP diameter of C1 is measured from the most anterior cortex of the anterior arch to the most posterior cortex of the posterior arch.
2. Inner AP diameter of C1 is measured from the inner cortex of the anterior arch to the inner cortex of the posterior arch.
3. Outer transverse diameter of C1 is measured from the most lateral point of the transverse processes.
4. Distance between C1 anterior tubercle and lateral mass in lateral view.
5. AP diameter of superior articular facet.

AP diameter of anterior arch is measured from the anterior to posterior cortex of anterior arch.

Reproducibility/Variation

Study involved 31 cadavers. CT measurements were obtained and compared with anatomical measurements for each C1 vertebra examined.

Good correlation between CT and anatomical measurements.

Clinical Relevance/Implications

May be useful in preoperative planning for patients undergoing surgery at C1 level.

Analysis/Validation of Reference Data

CT of anatomical specimens compared with accurate measurements of same specimens, good reproducibility.

Conclusion

An anatomical study, measuring C1 specimens from 31 cadavers. May be useful for preoperative planning.

6.14 Anterior Atlantoaxial Interval

Definition

The distance between the posteroinferior margin of the anterior arch of the atlas and the anterior surface of the odontoid process (Fig. 6.32).

Indications

Suspected anterior atlantoaxial subluxation, which can occur due to trauma, arthritis (including rheumatoid arthritis, ankylosing spondylitis, psoriatic arthritis), odontoid hypoplasia, some skeletal dysplasias and Down's syndrome.
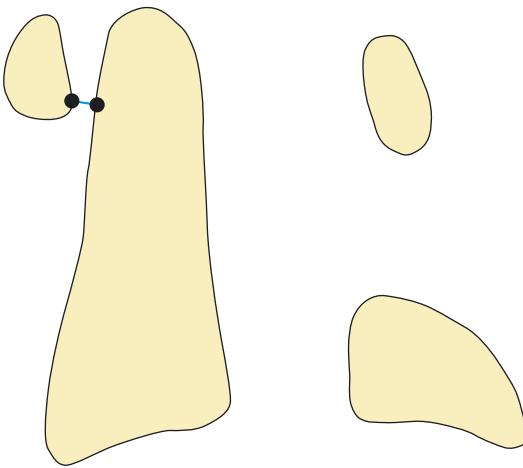
Fig. 6.32 Anterior atlantoaxial interval and anterior atlantoaxial distance in children. Anterior atlantoaxial interval is the distance between the posteroinferior margin of the anterior arch of the atlas (C1) and the anterior surface of the Odontoid process

Measurement

Lateral cervical spine radiograph:

Adult male: $2.052-(0.0192 \times$ age in years$)$ +/− 1.0 mm.

Adult female: $1.238-(0.0074 \times$ age in years$)$ +/− 0.9 mm.

95% of normal adults will have an atlas-odontoid distance of between 0.4 and 2.0 mm in neutral position.

CT: In 95% of normal adults, the anterior atlanto-axial interval is less than 2 mm.

Techniques

Radiography: Lateral cervical spine radiographs. Target-film distance 72 in.
CT: Midsagittal reformatted image.

Full Description of Technique

Radiography: 25 adult male and 25 adult female subjects, aged 20–80 years. Lateral cervical spine radiograph at a target-film distance of 72 in. Central ray perpendicular to the plane of the film, centred at the level of thyroid cartilage.
CT: Two hundred patients without cervical spine injury, aged 20–40 years.
MDCT. Sixteen slice scanner using 1 mm thick slices and multiplanar reconstructions.

Reproducibility/Variation

Unknown.

Clinical Relevance/Implications

Useful in detecting atlantoaxial subluxation which can cause cervical cord impingement.

Analysis/Validation of Reference Data

Limited data. Not possible in very young children before ossification is present.

Conclusion

Useful measurement but needs to be taken in conjunction with the posterior interval measurement.

6.15 Anterior Atlantoaxial Distance in Children

Definition

The anterior atlantoaxial distance (AAAD) or anterior atlantodental interval (AADI) is the distance between the posterior aspect of the anterior arch of C1 and the anterior aspect of the odontoid in the anteroposterior direction.

Indications

To determine if there is anterior atlantoaxial subluxation.

Measurement (Wang et al. 2001)

Male children

   0–60 months: median 2.02 mm (SD 0.40)
   61–120 months: median 2.16 mm (SD 0.57)
   121–180 months: median 2.19 (SD 0.67)

Female children

   0–60 months: median 2.16 mm (SD 0.96)
   61–120 months: median 1.91 mm (SD 0.51)
   121–180 months: median 1.83 (SD 0.64)

Measurement (Locke et al. 1966)

Anterior atlantoaxial distance in children average = 2.0 mm; 99% of children will have an anterior atlantoaxial distance of between 1 and 4 mm. Maximum distance found in a normal child was 5 mm.

Techniques

Radiography: Lateral cervical spine radiographs, film-to-focal-spot distance approximately 183 cm. CT: Midsagittal reformatted images.

Full Description of Technique

50 boys and 46 girls who had serial cervical spine radiographs taken as part of the Cleveland Study of Normal Growth and Development, compiled between 1927 and 1942.

Lateral radiographs of the cervical spine were taken at the ages of 3, 6, 9, 12, 18, 24, 30, 36, 42, 48, 54 and 60 months and then annually until the age of 17 years.

Film-to-focal-spot distance of approximately 183 cm.

The outline of the cervical spine on each radiograph was traced onto a transparent sheet. Vertical lines were placed along the most anterior and posterior point of the vertebral bodies, along the most anterior point of the posterior arches, along the posterior portion of the anterior arch of C1 and along the anterior aspect of the odontoid. Horizontal lines were placed along the most superior and inferior portions of the vertebral bodies. Images were entered into a computer using a Summasketch Plus digitizing pad (Summagraphics, GTCO CalComp, Scottsdale, Arizona). The images were analysed with the use of a custom-designed software programme (Wang et al. 2001).

Two hundred children aged 3–15 years were analysed by Locke et al. (1966). Lateral radiographs were taken in neutral, flexion and extension positions at target-film distances of 72 in. (patient sitting) and 40 in. (patient supine).

Reproducibility/Variation

Limited published data.

Clinical Relevance/Implications

Increased atlantoaxial distance can indicate anterior atlantoaxial subluxation. This can occur due to trauma, with rupture of alar ligaments. It can also occur due to inflammatory arthropathies such as rheumatoid arthritis and following infections in the head and neck.

Analysis/Validation of Reference Data

Computer programme analysis of tracings of the cervical spine was done to obtain the measurements. This is a unique study, made from the same dataset that Greulich and Pyle used to chart bone age.

Conclusion

A useful measurement to help determine if there is anterior atlantoaxial subluxation.

6.16   Dens Tilt Angle (Bohrer et al. 1985)

Definition

The dens tilt angle (DTA) is defined as the angle enclosed by the intersection of tangents from the anterior cortex of the odontoid and the posterior cortex of the body of C2 (Fig. 6.33).

Virtually all subjects have a posterior slanting or tilting of the dens.

Indications

May help to identify injury to odontoid peg.

Measurement

The range of values of dens tilt angle is up to 35° (mean 17.43, standard deviation 6.11).

98% have an angle greater than 6°.

Techniques

Radiography: 175 patients. Lateral radiographs in flexion, extension and neutral.
CT/MRI: Midsagittal images.

Full Description of Technique

175 adult, 94 male and 81 female patients, aged 16–84 years, without subsequent clinical or radiological evidence of neck injury.

Lateral radiographs taken in neutral, flexion and extension. Radiographic technique not described. The dens tilt angle was measured for each patient.

Reproducibility/Variation

No mention of how measurements were made or how many observers. There is no identified

Fig. 6.33 Dens tilt angle and predens space angle. *PDA* (predens angle) is formed by lines *AC* and *BD*. *DTA* (dens tilt angle) is formed by lines tangent to upper anterior portion of the dens and the posterior body of C2

relationship between the predens angle and the dens tilt angle.

Clinical Relevance/Implications

Probably not that useful a measurement in clinical practice. Study serves to emphasise the wide variation in normal subjects. Virtually every person has some degree of posterior tilt or slant of the anterior cortex of the odontoid. This may reflect the complex embryology of the odontoid and its propensity for wide anatomic variation. A posteriorly slanted odontoid on its own is not a sign of a fractured odontoid, and additional studies should be used to confirm or refute the diagnosis.

Analysis/Validation of Reference Data

Unknown.

Conclusion

Serves to emphasise the wide variability in normal subjects. A tilted odontoid, on its own, should not be taken to be as a sign of acute or remote fracture.

6.17   Predens Space Angle

Definition

The predens space angle (PDA) is defined as the angle enclosed in the intersection of tangents from the posterior cortex of the anterior arch of the atlas and the anterior cortex of the articulating part of the odontoid (Fig. 6.33).

Indications

It can help to identify injury to atlantoaxial and alar ligaments.

Measurement

0–13° (mean 5.57 ° SD 4.13) in neutral position. 0–18° (mean 9.27 ° SD 5.06) in flexion.

92% of cases have angles >3° in flexion.

Techniques

Radiography: 175 patients. Lateral radiographs in flexion, extension and neutral.
CT/MRI: Midsagittal images.

Full Description of Technique

175 adult, 94 male and 81 female patients, aged 16–84 years, without subsequent clinical or radiological evidence of neck injury.

Lateral radiographs taken in neutral, flexion and extension. Radiographic technique not described. The predens angle (PDA) was measured in the flexion and neutral position for each patient.

Reproducibility/Variation

No mention of how measurements were made or how many observers.

Clinical Relevance/Implications

Probably not that useful a measurement in clinical practice. Study serves to emphasise the wide variation in normal subjects.

Analysis/Validation of Reference Data

Unknown.

Conclusion

Limited clinical use.

6.18   Odontoid Dimensions
(McManners 1983)

Definition

Measurement of the vertical height and sagittal depth of the odontoid peg on plain radiographs (Fig. 6.34).

Indications

To assess for odontoid hypoplasia.

Measurement

Odontoid vertical height:

   18.04 mm +/− 0.14 (males)
   16.88 mm +/− 0.10 (females)
   17.4 mm (overall mean)
   9–23 mm (range)

Odontoid sagittal depth:

   12.3 mm (males)
   11.8 mm (females)
   12.0 mm (overall mean)
   9–16 mm (range)

Techniques

Radiography: Film-focus distance of 100 cm. As the embryological base of the dens lies within the body of C2, the exact point of the junction cannot be determined once the ossification centres have fused. For this paper, the anatomical junction of the body and dens has been used for the purposes of measuring. This point can be readily identified on the lateral film by the superimposed shadows of the superior articular processes.
CT/MRI. Usually landmarks more readily appreciated.

Full Description of Technique

From a randomised series of 500 adult patients (217 male and 283 female), aged 25–90, average measurements of the normal adult odontoid peg in the vertical and sagittal planes, as seen on a standard lateral radiograph of the cervical spine, were obtained. Film-focus distance of 100 cm. As the embryological base of the dens lies within the body of C2, the exact point of the junction cannot be determined once the ossification centres have fused. For this paper, the anatomical junction of the body and dens has been used for the purposes of measuring; this point can be read-
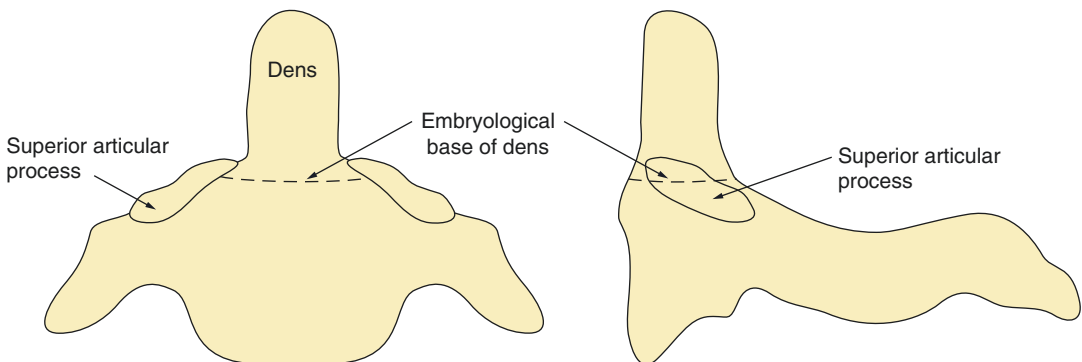
Fig. 6.34 Odontoid dimensions. Odontoid vertical height is measured from tip of odontoid to the anatomical junction of odontoid with C2. Anatomical junction of the body of C2 and the odontoid is represented by hatched line on diagram. This can be readily identified on lateral radiograph by the superimposed shadows of the superior articular processes. Odontoid sagittal depth is the distance between anterior and posterior margin of the odontoid

ily identified on the lateral film by the superimposed shadows of the superior articular processes.

Reproducibility /Variation

Unknown how measurements were made. Single observer. Large population studied = 500 patients.

Clinical Relevance/Implications

Odontoid hypoplasia is taken as a vertical height of 11.9 mm or less.

In odontoid hypoplasia the attachments for the alar and apical ligaments are missing, and the hypoplastic odontoid process cannot act as a restraining structure within the ring of the atlas. The hypoplastic odontoid may slide underneath the transverse ligament resulting in atlantoaxial subluxation.

Analysis/Validation of Reference Data

Unknown.

Conclusion

Odontoid hypoplasia is taken as a vertical height of **11.9 mm** or less.

6.19 Posterior Atlantoaxial Relationship (Lovelock and Schuster 1991)

Definition

The relationship between the height of the posterior arch of C1 at the spinolaminar line (SLL) and the interspinous distance between C1 and C2 during maximal flexion (FID) (Fig. 6.35).

Indications

To detect posterior ligamentous disruption between C1 and C2.

Measurement

Ratio of flexion interspinous distance (FID) between C1 and C2 to height of posterior arch of C1 at spinolaminar line (SLL):

FID mean 9.86 mm (range 4–20 mm)
SLL mean 12.0 mm
FID/SLL mean 0.82, +/− 0.28
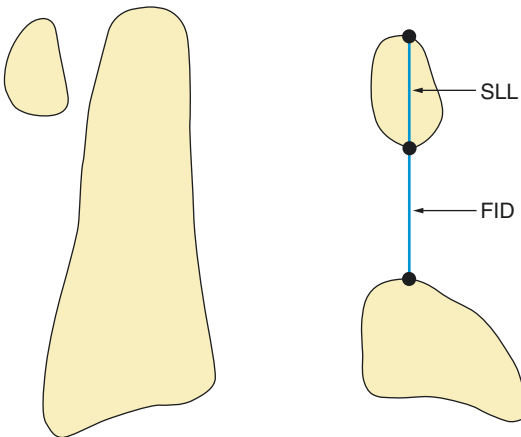
Fig. 6.35 Posterior atlantoaxial relationship. FID and SLL measurements. The height of the posterior arch of C1 is measured at the level of the spinolaminar line (SLL). The flexion interspinous distance (FID) is measured as the distance between the spinous processes of C1 and C2 at the level of the spinolaminar line. The ratio of FID/SLL should be less than 2

FID/SLL range 0.29–1.82

If the FID/SLL ratio is >2, it is deemed abnormal due to ligamentous insufficiency.

Techniques

Radiography: Lateral cervical spine radiographs taken during maximal cervical spine flexion.
CT/MRI: Midsagittal images.

Full Description of Technique

100 healthy adult volunteers, 56 men and 44 women, aged 20–69 years. Subjects were asked to flex their necks to limit of tolerance. Lateral cervical spine radiographs were taken. Focus film distance not given.

The height of the posterior arch of C1 was measured at the level of the spinolaminar line (SLL).

The interspinous distance was measured as the distance between the spinous processes of C1 and C2 measured at the level of the spinolaminar line (FID).

The ratio of FID/SLL was calculated.

Reproducibility/Variation

Although there was variation in the individual measurements of FID and SLL between individuals and gender, the ratio remained constant. In no case was the FID/SLL ratio greater than 2. No change with advancing years.

May be difficult to apply, for instance, in patients with congenital anomalies of posterior arch of C1.

Clinical Relevance/Implications

Can be used to detect ligamentous injury. Ratio method, therefore film-focus distance irrelevant.

Analysis/Validation of Reference Data

Reasonable sample size of 100 healthy adult volunteers.

Conclusion

Useful measurement when analysing cervical spine radiographs in trauma. Injuries of the upper cervical spine are often missed. This method uses a ratio; therefore, measurements are not affected by magnification distortion. The ratio FID/SLL is reasonably constant and should be less than 2.

6.20 Interspinous Distance

Definition

The C1–C2 interspinous distance is measured on a true lateral view. The Sun ratio is also assessed on the lateral view by direct measurement. These two measurements are useful in the detection of craniocervical distraction injuries (Fig. 6.36).

The interspinous distance (ISD) in the subaxial portion of the cervical spine is measured on the AP view from the centre of the spinous process above to the centre of the spinous process below. An abnormal measurement is seen in posterior ligamentous injury usually with anterior dislocation (Fig. 6.37).
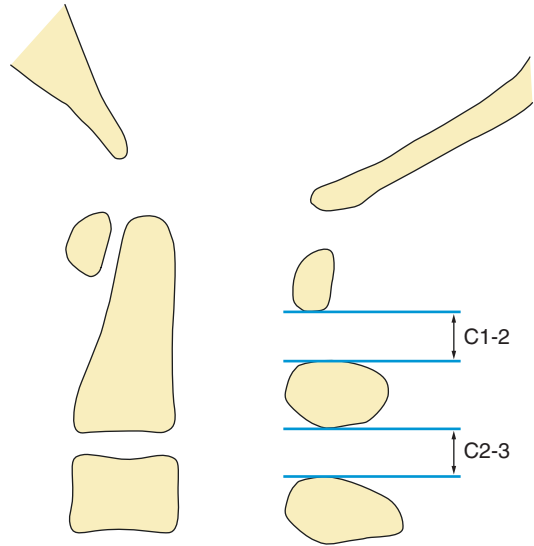
Fig. 6.36 Interspinous distance. The C1–C2 interspinous distance on a lateral radiograph is normally <10 mm. Sun ratio of C1–C2 ISD to C2–C3 ISD should be <2.5

Measurement

There are three measurements:

1. The C1–C2 interspinous distance is normally <10 mm.

Fig. 6.37 Interspinous distance. The interspinous distance on an AP radiograph may be measured from the centre of the spinous process above to the centre of the spinous process below (**a**). For increased accuracy the measurement can be done between the cranial ends of the 'teardrops' at the confluence of the inner cortices (**b**). The normal interspinous distance (ISD) on the AP view is <1.5 times the ISD above and <1.5 times the ISD below. No interspinous distance should be more than 50% wider than the one immediately above and below it
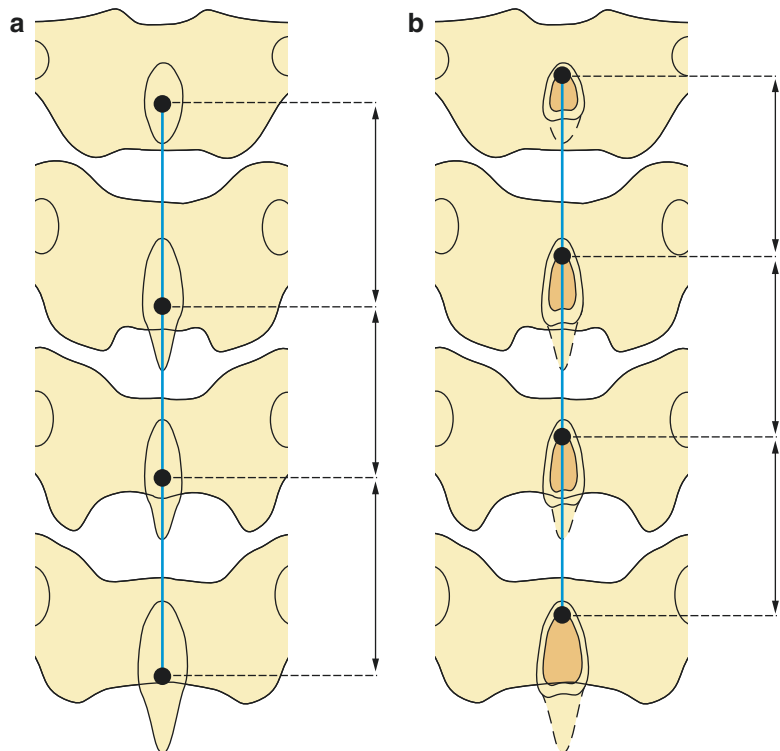
2. Sun ratio of C1–C2 ISD to C2–C3 ISD should be <2.5.
3. The normal interspinous distance (ISD) on the AP view is <1.5 times the ISD above and <1.5 times the ISD below.

Indications

To detect cervical injury.

Technique

Radiography: Lateral and anteroposterior cervical radiograph.
Film-focus distance immaterial.

Full Description of Technique

Routine lateral views must be done with meticulous technique.

In Naidich et al.'s study, anteroposterior cervical spine radiographs, taken in the supine position, in 500 normal subjects were analysed and compared with anteroposterior radiographs obtained in 14 patients with documented anterior cervical dislocations. The interspinous distances were measured from the C3–C4 interval through the C7–T1 interval. The distance was measured from the centre of the spinous process above to the centre of the spinous process below. The measurements can be done for increased accuracy between the cranial ends of the 'tear drops' at the confluence of the inner cortices and not the outer cortices.

Although widening of the interspinous space had been well known as a sign of spinal injury, validated and practical methods were lacking until 2010. In Eubanks et al.'s (2010) study, the ISD measurements were taken from the flexion-extension lateral views of 156 skeletally mature asymptomatic subjects providing normal reference data that can be used quantitatively. In addition radiographic measurements were done on 12 cadaveric cervical spines before and after C4–C5 posterior ligamentous disruption. Of the two

distances measured, the interlaminar values were more reliable than the true ISD measurements because there were difficulties in identification of the tips of some of the spinous processes (Fig. 6.38). The authors normalised the measured cervical ISD's to the AP width of the C4 vertebral endplate as well as calculating the changes in flexion/extension distances. Flexion-extension radiographs have poor sensitivity to disco-ligamentous soft tissue injury but are highly specific. They introduced two simple 'rule of thumb' criteria for abnormal ISD widening (based on interlaminar measurements) on flexion lateral radiographs:

1. When >30% relative to an adjacent level (>40% at C1–C2 and C2–C3).
2. When >50% of the anteroposterior width of the C4 vertebral body (>30% for C2–C3).

Reproducibility/Variation

Very large study of 500 normal subjects in Naidich's study examined the C3–C4 to C7–T1 levels compared with 14 patients with anterior cervical dislocation. In every case of anterior dislocation, the affected interspinous distance was found to be at least 2.1 times > than the one below
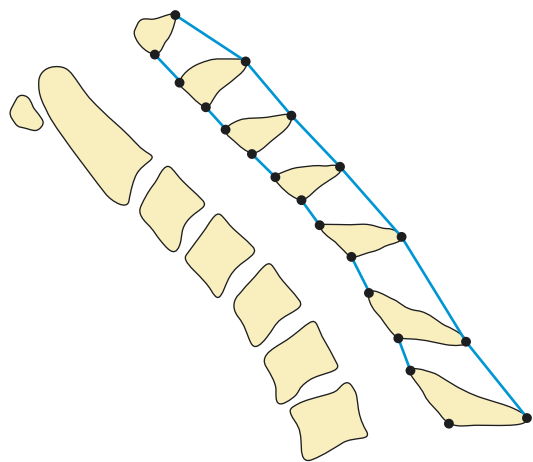
Fig. 6.38 Interspinous distance. On lateral radiographs the interlaminar distance is more reliable than the interspinous distance, because there may be difficulty in identifying the tips of some of the spinous processes

and above. The use of the ratio has the added advantage of eliminating the effect of magnification.

Clinical Relevance/Implications

In occipital to C2 paediatric cervical spine injuries, Sun et al. (2000) showed that the tectorial membrane is the critical stabilising ligamentous structure. The radiographic Sun ratio in the upper cervical spine is important as a ratio equal to or >2.5 signifies injury to the tectorial membrane which is a potentially unstable injury. This was shown to be 87% (95% CI 0.42–0.99) sensitive and 100% (95% CI 0.94–1.0) specific when correlated with MRI evidence of injury to the tectorial membrane.

The C1–C2 ISD (Fig. 6.37) should normally be <10 mm, but in the paediatric age group due to the large head, a supine cross-table lateral view can result in flexed position of the upper cervical spine producing a widened C1–C2 ISD in keeping with pseudosubluxation.

The ISD ratio in the subaxial cervical spine is a useful sign only of anterior cervical dislocation and not posterior dislocation. Particularly useful in patients in whom the lower cervical spine/cervicothoracic junction cannot be visualised on the initial lateral cervical radiograph because of overlying shoulders. Put succinctly, no interspinous space should be 50% wider than the one immediately above and below it. If it is, it indicates anterior cervical dislocation, and if there is no rotation, it usually has underlying bilateral facet dislocation.

Analysis/Validation of Reference Data

Although small in number, Sun et al.'s study is novel and correlates the MRI spectrum of AO injury in 23 patients with the cross-table lateral radiographic measurement of the posterior C1–C2 ISD. The other traditional craniocervical measurements were also performed radiographically or on CT reconstructions, namely, BDI, BAI, Powers ratio, AO joint distance, etc. The bone landmarks for Sun et al.'s C1–C2:C2–C3 ratio are always well seen radiographically unlike the landmarks for the other measurements. The ratio in all the patients with normal MR appearances was <2.5 (mean 1.41+/− 0.45 2SD). The ratio in all the ten patients with abnormal MR appearances but intact tectorial membrane was also <2.5. In the eight patients with MR evidence of ruptured tectorial membrane, the ratio was 2.5 or > (3.1+/−0.71 2SD) and statistically greater than the other two groups' values ($p < 0.005$). Four of these eight patients also had AO dissociation. The interobserver agreement was excellent (Pearson correlation coefficient of 0.96).

Large sample in Naidich's study of 500 patients with normal cervical spines and 14 patients with anterior cervical dislocations. Importantly the criteria for anterior dislocation require that *both* the ISD measurements above and below are less than the widened ISD at the injured level. In differentiating voluntary flexion from anterior dislocation, the ISD at one level may exceed 1.5 times the ISD on either side of it but not on both sides. There was no false positive or false negative diagnosis in Naidich's study. However, caution needs to be exercised as this measurement may be misleading in the presence of spinous process fractures. Pennecot et al. (1984) applied the ratio to normal children's cervical spines and found there was a significant correlation with the conclusions found by Naidich et al. (1977).

The ISD is also measured on the lateral radiograph either from the tips of the spinous processes and more reliably as the interlaminar distances as shown in Eubanks et al.'s study, in the assessment of post-traumatic from the cranio-caudal tips of the spinolaminal line (Fig. 6.39).

Conclusion

The C1–C2 and Sun ratio ISD values are very useful in suspecting the presence of upper cervical injury. In the lower cervical spine, these measurements are used in a trauma setting when assessing the AP view. In most patients this measurement will be unnecessary because anterior cervical dislocation will be readily apparent on the lateral radiograph. However, if the lower cervical spine is not visualised on the initial lateral radiograph, a widened interspinous distance should alert the radiologist to the possibility of anterior dislocation, and further investigation should be undertaken, usually by CT.

Fig. 6.39 Cervical spinal canal sagittal dimensions. The sagittal spinal canal diameter is measured from the middle of the posterior surface of the vertebral body to the nearest point of the corresponding spinolaminar line

6.21 Cervical Spinal Canal Sagittal Dimensions

Definition

The conventional method measures the sagittal diameter of the cervical spinal canal at mid-vertebral body level (Fig. 6.39).

The vertebral body ratio method compares the sagittal diameter of the cervical spinal canal with the sagittal diameter of the corresponding vertebral body (Pavlov).

Indications

To assess for congenital or acquired spinal canal stenosis.

Measurement

Cervical spinal canal sagittal dimensions; conventional and vertebral body ratio method, measured using plain radiographs (Pavlov et al. 1987).

Conventional method (males):

C3: 19.24 mm +/− 0.188
C4: 18.56 mm +/− 0.195
C5: 18.71 mm +/− 0.183
C6: 19.3 mm +/− 0.193

Conventional method (females):

C3: 17.19 mm +/− 0.151
C4: 16.92 mm +/− 0.134
C5: 17.04 mm +/− 0.138
C6: 17.52 mm +/− 0.144

Vertebral body ratio method (males):

C3: 1.008 +/− 0.118
C4: 0.973 +/− 0.110
C5: 0.975 +/− 0.091
C6: 0.978 +/− 0.104

Vertebral body ratio method (females):

C3: 1.018 +/− 0.106
C4: 1.011 +/− 0.071
C5: 1.016 +/− 0.057
C6: 1.016 +/− 0.078

Average AP diameter of cervical spinal canal (Wolfe)

C1: 22 mm
C2: 20 mm
C3–C7: 17 mm

Measurement

Cervical spinal canal sagittal dimensions, measured using CT (Matsura et al. 1989):

C3: 15.2 mm +/− 1.9
C4: 15.1 mm +/− 1.6
C5: 14.7 mm +/− 1.5
C6: 14.4 mm +/− 1.4
C7: 14.6 mm +/− 1.5

Measurement

Cervical spinal canal sagittal dimensions; measurement using MRI (Ulbrich et al. 2014)

C1: 10.7–19.7 mm
C3: 9.4–17.2 mm
C6: 9.2–16.8 mm

Techniques

Radiography: Routine lateral radiographs of 74 patients (49 male and 25 female) aged 15–38 years, without spinal abnormalities, fractures, dislocations or neurological symptoms (Pavlov).
(Wolfe): Lateral radiographs taken with a FTD of 72 in. 200 asymptomatic cases.
CT: 100 control subjects (47 males and 53 females aged 18–36) GE 8800 CT scanner, high-resolution, 1.5 mm thin section images in the axial, coronal and sagittal planes.

MRI: 140 healthy Caucasian volunteers (Ulbrich et al. 2014).

Full Description of Technique

Plain radiographs: (Pavlov) Routine lateral radiographs of 74 patients (49 male and 25 female) aged 15–38 years, without spinal abnormalities, fractures, dislocations or neurological symptoms.

Cervical spinal measurements were determined with two different methods:

1. The sagittal spinal canal diameter is measured from the middle of the posterior surface of the vertebral body to the nearest point of the corresponding spinolaminar line.
2. The 'ratio method' compares the sagittal spinal canal diameter, measured as described in (1) with the sagittal diameter of the corresponding vertebral body, measured at its midpoint.

Plain radiographs (Wolfe): lateral radiographs taken with a FTD of 72 in. 200 asymptomatic cases.

In CT: (Matsura) 100 control subjects (47 males and 53 females aged 18–36) who were being investigated for non-traumatic neurological or orthopaedic disorders and whose plain cervical spinal radiographs were deemed normal.

GE 8800 CT scanner, high-resolution, 1.5 mm thin section images in the axial, coronal and sagittal planes. Images enlarged and transferred to copy paper. An X-360 planimeter, which is a highly accurate architectural drafting instrument, was used to obtain linear and area measurements.

All sagittal diameters were measured using sagittal reconstruction to minimise the potential for gantry-angle distortion. Transverse diameters and area measurements were obtained from sagittal images.

MRI: 140 adult Caucasian volunteers. Midsagittal TSE T2 and VIBE sequences. Sagittal diameter measured as a line drawn from the midpoint between superior and inferior endplates of the vertebral bodies, perpendicular to the anterior surface of the spinal cord, to the midpoint of the corresponding spinous process.

Reproducibility/Variation

Plain radiographic study (Pavlov et al. 1987): Unknown what the inter or intraobserver variability is.

CT study (Matsura et al. 1989): 15 group members were randomly selected for independent measurement by two of the investigators. Measurements were found to be highly reliable: sagittal diameter, $r = 0.96$ ($p < 0.001$), transverse diameter, $r = 0.97$ ($p < 0.001$) and cross-sectional area $r = 0.97$ ($p < 0.001$).

Clinical Relevance/Implications

The ratio method of diagnosing cervical spinal canal stenosis is independent of magnification factors caused by differences in target distance, object to film distance or body habitus.

There is normally an approximately one-to-one relationship between the sagittal diameter of the spinal canal and vertebral body regardless of sex. A spinal canal/vertebral body ratio of less than 0.82 indicates significant spinal stenosis.

Analysis/Validation of Reference Data

Using direct measurements of 469 skeletal specimens, Lee et al. (1987) reported an average sagittal canal diameter in the cervical spine between C3 and C7 of 14.1+/−1.6 mm. Males have significantly larger diameters than females at all levels when measured radiographically, but this is not due to a true difference and is related to other factors that affect magnification from wider shoulders, etc.

The assumption here is that the canal-to-body ratio is an accurate and reliable determinant of the true diameter of the canal of the cervical spine. However, both the diameter of the canal and the vertebral body are variable. On lateral radiographs, the sagittal diameter of the cervical

spinal canal is constant from C4 to C7 (range 15–25 mm, average 17 mm), and measurements <14 are regarded critical. The diameter of the vertebral bodies gradually enlarge from C4 to C7.The midsagittal cervical canal diameter is largest in whites, followed by Afro-Caribbean and then Asian populations. From radiological measurements, Murone 1974 showed that the Japanese dimension is narrower by 2.25 mm compared with the dimension in the European adult. The relationship of the radiographic canal-to-body ratio with the true diameter of the cervical canal as measured by CT was assessed from C3 to C6 by Blackley et al. (1999) and found to be of limited value. This is probably explained by the common unrelated anatomical variations seen in any cervical vertebra.

Herzog et al. (1991) evaluated athletes to assess the risk from spinal stenosis and indicated that the ratio relies on both the spinal canal size and the vertebral body size. Their athletes had significantly larger vertebral bodies which resulted in low Torg ratios with inaccu-

rate reflection of the true spinal canal dimensions. Herzog et al. (1991) recommended that if the Torg ratio is <0.80, an MRI is done to assess the space available for the cord (SAC). The sagittal diameter of the spinal cord is uniformly constant from C3 to C7 averaging 7 mm with an increase at the C3 and C5 levels (Prasad et al. 2003). The SAC is determined by subtracting the sagittal diameter of the spinal cord from the sagittal diameter of the spinal canal. This is measured with the head in the neutral position, i.e. the orbitomeatal line perpendicular to the horizontal plane.

Conclusion

Useful measurements when assessing patients for spinal stenosis.

Vertebral body ratio is a practical tool, which eliminates error due to magnification distortion.

6.22   Paediatric Sagittal Diameter of Cervical Spinal Canal

Definition

The sagittal diameter of the spinal canal is measured from the midpoint of each vertebral body to the closest point of the corresponding spinolaminar line on lateral cervical spine radiographs.

Indications

To detect spinal canal stenosis or pathological widening.

Sagittal diameter of the cervical spinal canal in children from 3 to 14 years of age (Markuske (1977). Sagittal diameter measurements of the bony cervical spinal canal in children. Pediatr Radiol 6:129–131. Used by permission)

midpoint of the posterior cortex of the vertebral body to the closest point of the corresponding spinolaminar line, using a caliper device.

Reproducibility/Variation

Unknown.

Clinical Relevance/Implications

Useful reference ranges for detection of spinal stenosis.

Measurements show that the spinal canal diameter increases with increasing age and body height.

Sagittal diameter reduces from the foramen magnum to C3 level then remains fairly constant.

Age (years)	3–6		7–10		11–14	
	40		40		40	
Number	Mean ± SD	90% CI	Mean ± SD	90% CI	Mean ± SD	90% CI
Level						
C1	19.9 ± 1.3	17.8–22.0	20.6 ± 1.3	18.5–22.7	21.3 ± 1.4	19.0–23.6
C2	17.9 ± 1.3	15.8–20.0	18.8 ± 1.0	17.2–20.4	19.4 ± 1.1	17.6–21.2
C3	16.0 ± 1.3	13.9–18.1	17.2 ± 1.0	15.6–18.8	17.8 ± 1.0	16.2–19.4
C4	15.8 ± 1.3	13.7–17.9	16.9 ± 0.9	15.4–18.4	17.3 ± 0.9	15.8–18.8
C5	15.7 ± 1.3	13.6–17.8	16.7 ± 0.9	15.2–18.2	17.0 ± 0.9	15.5–18.5
C6	15.6 ± 1.2	13.6–17.6	16.4 ± 0.9	14.9–17.9	16.7 ± 0.9	15.2–18.2
C7	15.3 ± 1.1	13.5–17.1	16.0 ± 0.9	14.5–17.5	16.2 ± 0.9	14.7–17.7

All measurements are in millimetres. *SD* standard deviation, *CI* confidence interval

Techniques

Radiography: Lateral projection, film-focus distance 60 in.

Full Description of Technique

The subjects were 120 children aged 3–14 years. FFD was 150 cm and there was no correction for magnification. Measurements were made from lateral cervical spine radiographs of children. The sagittal diameter was measured from the

Analysis/Validation of Reference Data

Most studies show that regardless of age, the sagittal diameter either gradually decreases from C1 to C7 or diminishes from C1 to C3 and then remains unchanged from C4 to C7. However, at ages below 11 years, Yousefzadeh et al. (1982) showed that the canal slightly widens in the lower cervical canal in 30% of normal children. Markuske et al. also demonstrated that the sagittal diameter of the bony cervical spinal canal varied according to height. For example, at the level of C4, the

diameter was 15 mm at a height of 91–100 cm, 15.6 mm at 101–110 cm, 16.5 mm at 111–120 cm, 16.9 mm at 121–130 cm and 17.0 mm at 131–140 cm.

Conclusion

Useful to have a range of normal values to help detect abnormal stenosis or widening of the cervical spinal canal.

6.23 Paediatric Sagittal Diameter of Cervical Spinal Canal (in Infants under 1 Year)

Definition

The sagittal diameter of the spinal canal is measured from the posterior border of the vertebral body to the posterior end of the laminae (distance *a*) and subtracting the height (*c*) of the laminae (Fig. 6.40).

Indications

To detect spinal canal stenosis or pathological widening.

Measurement

C2: Mean 12.5 mm, SD 0.7 mm
C3: Mean 11.5 mm, SD 0.7 mm
C4: Mean 11.5 mm, SD 0.7 mm
C5: Mean 12.2 mm, SD 0.7 mm
C6: Mean 12.6 mm, SD 0.7 mm
C7: Mean 12.1 mm, SD 0.7 mm

Techniques

Radiography: Lateral projection, film-focus distance 90 cm.

Fig. 6.40 Paediatric sagittal diameter of cervical spinal canal (in infants under 1 year). Cervical spinal canal sagittal diameter in infants. *A* = distance from posterior border of vertebral body to tip of the spinous process; *B* = thickness of the spinous process; *C* = height of the spinous process. Since in infants under 1 year of age *B* = *C* (based on Naik study of postmortem cases), the sagittal diameter of the cervical spinal canal can be taken as measurement *A* minus measurement *C*

Full Description of Technique

Twenty-five postmortem specimens of normal cervical spines of infants under 12 months of age were studied. Lateral radiographs were obtained at a FFD of 90 cm with no correction for magnification.

Reproducibility/Variation

Unknown.

Clinical Relevance/Implications

Small sample size. Useful reference ranges for detection of spinal stenosis.

Analysis/Validation of Reference Data

In infancy it is not possible to define the osseous landmark of the anterior spinous process margin as it is cartilaginous and not visible. Naik (1970) showed that in infancy the height of the spinous process at its base is equal to its sagittal thickness. The internal sagittal diameter can be calculated as shown in the diagram.

Conclusion

Useful to have a range of normal values to help detect abnormal stenosis or widening of the cervical spinal canal.

6.24   Width of Cervical Vertebrae

Definition

The width of the vertebral body measured from the anterior to posterior cortex at the level of the midpoint of the posterior aspect of each vertebral body (Fig. 6.41).

Indications

To help determine if a cervical vertebra is abnormally widened, as can occur due to fracture, or narrowed as can occur with congenital anomalies.
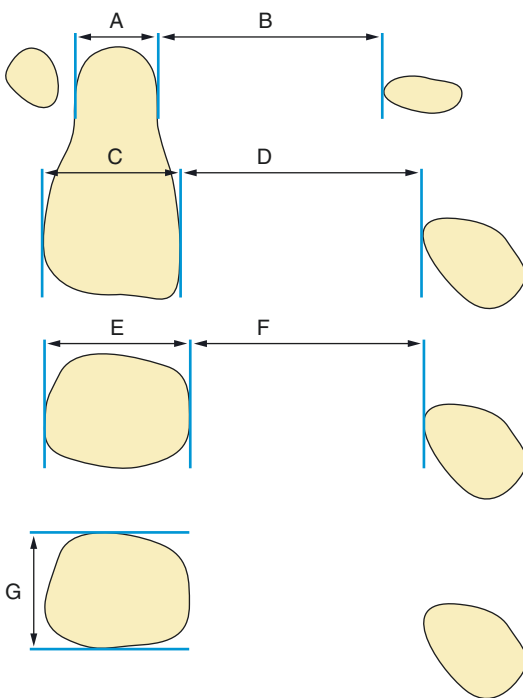
Fig. 6.41 Width of cervical vertebrae in children. A = width of the dens, B = sagittal diameter of the canal at the first cervical level, C = width of the second cervical vertebra, D = sagittal diameter of the canal at the second cervical level, and E = sagittal diameter of the third cervical vertebral body. F = sagittal diameter of the canal at the third cervical level and G = height of the fourth cervical vertebra

Measurement

Width of cervical vertebrae (in mm) in male children:

At C2 level:

   0–60 months: median 10.41 (SD 0.61)
   61–120 months: median 12.88 (SD 0.82)
   121–180 months: median 14.52 (SD 0.98)

At C3 level:

   0–60 months: median 10.36 (SD 0.62)
   61–120 months: median 12.93 (SD 0.84)
   121–180 months: median 14.53 (SD 0.97)

At C4 level:

   0–60 months: median 10.37 (SD 0.62)
   61–120 months: median 12.76 (SD 1.18)
   121–180 months: median 14.10 (SD 1.18)

At C5 level:

   0–60 months: median 10.57 (SD 0.66)
   61–120 months: median 12.57 (SD 0.95)
   121–180 months: median 13.94 (SD 1.60)

Measurement

Width of cervical vertebrae (in mm) in female children:

At C2 level:

   0–60 months: median 9.79 (SD 0.70)
   61–120 months: median 12.49 (SD 0.84)
   121–180 months: median 14.30 (SD 1.02)

At C3 level:

   0–60 months: median 9.74 (SD 0.65)
   61–120 months: median 12.26 (SD 0.91)
   121–180 months: median 13.86 (SD 0.95)

At C4 level:

   0–60 months: median 9.68 (SD 0.69)
   61–120 months: median 12.11 (SD 0.92)
   121–180 months: median 13.38 (SD 1.08)

At C5 level:

   0–60 months: median 10.05 (SD0.74)
   61–120 months: median 12.03 (SD 1.24)
   121–180 months: median 13.64 (SD 1.17)

Techniques

Radiography: Lateral radiograph of cervical spine, film-to-focal-spot distance of approximately 183 cm.

Full Description of Technique

50 boys and 46 girls who had serial cervical spine radiographs taken as part of the Cleveland Study of Normal Growth and Development, compiled between 1927 and 1942.

Lateral radiographs of the cervical spine were taken at the ages of 3, 6, 9, 12, 18, 24, 30, 36, 42, 48, 54 and 60 months and then annually until the age of 17 years.

Film-to-focal-spot distance of approximately 183 cm.

The outline of the cervical spine on each radiograph was traced onto a transparent sheet. Vertical lines were placed along the most anterior and posterior point of the vertebral bodies, along the most anterior point of the posterior arches, along the posterior portion of the anterior arch of C1 and along the anterior aspect of the odontoid. Horizontal lines were placed along the most superior and inferior portions of the vertebral bodies. Images were entered into a computer using a Summasketch Plus digitizing pad (Summagraphics, GTCO CalComp, Scottsdale, Arizona). The images were analysed with the use of a custom-designed software programme.

Reproducibility/Variation

A unique radiographic record of growth of the cervical spine.

It would not be possible to replicate this study nowadays because of radiation safety concerns.

Clinical Relevance/Implications

Can help to determine if there is abnormal widening of the vertebral body, for example, due to trauma or tumour.

Analysis/Validation of Reference Data

This study could not be replicated because of radiation protection concerns.

Conclusion

It is a unique dataset acquired over time, from the same archive that the Greulich and Pyle data on bone age norms were derived.

6.25 Vertical Height of Cervical Vertebrae

Definition

The vertical height of each vertebra measured at both the anterior and posterior portions of the vertebral body. The average of the anterior and posterior heights for each vertebra is used to calculate the height of individual vertebrae. The height of C2 was measured from the inferior aspect of the vertebral body to the tip of the odontoid process (Fig. 6.41).

Indications

To help determine if there is vertebral collapse, due to trauma, for example.

Measurement

Vertical height of cervical vertebrae (in mm) in male children:

At C2 level:

  0–60 months: median 18.79 (SD 5.03)
  61–120 months: median 27.54 (SD 3.26)
  121–180 months: median 33.65 (SD 3.71)

At C3 level:

  0–60 months: median 5.52 (SD 1.18)
  61–120 months: median 7.82 (SD 1.29)
  121–180 months: median 11.51 (SD 2.45)

At C4 level:

  0–60 months: median 5.41 (SD 1.24)
  61–120 months: median 7.77 (SD 1.15)
  121–180 months: median 10.98 (SD 2.12)

At C5 level:

  0–60 months: median 5.47 (SD 1.19)
  61–120 months: median 7.53 (SD 0.99)
  121–180 months: median 10.51 (SD 2.10)

Measurement

Vertical height of cervical vertebrae (in mm) in female children:

At C2 level:

  0–60 months: median 18.92 (SD 5.49)
  61–120 months: median 27.48 (SD 3.09)
  121–180 months: median 34.28 (SD 3.75)

At C3 level:

  0–60 months: median 5.84 (SD 1.18)
  61–120 months: median 8.09 (SD 1.20)
  121–180 months: median 11.56 (SD 2.69)

At C4 level:

  0–60 months: median 5.70 (SD 1.17)
  61–120 months: median 8.01 (SD 1.24)
  121–180 months: median 11.27 (SD 2.43)

At C5 level:

  0–60 months: median 5.74 (SD 1.12)
  61–120 months: median 7.69 (SD 1.10)
  121–180 months: median 10.79 (SD 2.16)

Techniques

Radiography: Lateral radiographs of the cervical spine. Film-to-focal-spot distance of approximately 183 cm.
CT/MRI: Midsagittal images.

Full Description of Technique

50 boys and 46 girls who had serial cervical spine radiographs taken as part of the Cleveland Study of Normal Growth and Development, compiled between 1927 and 1942.

Lateral radiographs of the cervical spine were taken at the ages of 3, 6, 9, 12, 18, 24, 30, 36, 42, 48, 54 and 60 months and then annually until the age of 17 years.

Film-to-focal-spot distance of approximately 183 cm.

The outline of the cervical spine on each radiograph was traced onto a transparent sheet. Vertical lines were placed along the most anterior and posterior point of the vertebral bodies, along the most anterior point of the posterior arches, along the posterior portion of the anterior arch of C1 and along the anterior aspect of the odontoid. Horizontal lines were placed along the most superior and inferior portions of the vertebral bodies. Images were entered into a computer using a Summasketch Plus digitizing pad (Summagraphics, GTCO CalComp, Scottsdale, Arizona). The images were analysed with the use of a custom-designed software programme.

Reproducibility/Variation

This study is unique and could not be replicated because of radiation protection concerns. The radiographs were obtained over time in a cohort of healthy children. The same database was used for compiling the Greulich and Pyle data on bone age assessment.

Clinical Relevance/Implications

Reduced vertebral body height can occur due to congenital anomaly of the vertebral body or can be acquired, for example, due to trauma or other conditions such as osteomyelitis or Langerhans cell histiocytosis, for example.

Analysis/Validation of Reference Data

A computerized programme analysed the data once the cervical vertebral shapes were traced onto transparent sheets.

Conclusion

Useful and unique series of longitudinal measurements of the growth and development of the paediatric cervical spinal canal.

6.26 Cervical Spinal Canal Transverse Dimensions

Definition

Transverse diameter is the widest diameter of the cervical spinal canal, measured from the axial plane.

Indications

To assess for congenital or acquired spinal canal stenosis.

Measurement

C3: 25.1 mm +/− 1.5
C4: 25.3 mm +/− 2.0
C5: 25.1 mm +/− 1.7
C6: 25.3 mm +/− 1.7
C7: 24.4 mm +/− 1.9

Technique

CT: 100 control subjects (47 males and 53 females aged 18–36) GE 8800 CT scanner, high-resolution, 1.5 mm thin section images in the axial, coronal and sagittal planes.

Full Description of Technique

CT: 100 control subjects (47 males and 53 females aged 18–36) who were being investigated for non-traumatic neurological or orthopaedic disorders and whose plain cervical spinal radiographs were deemed normal.

GE 8800 CT scanner, high-resolution, 1.5 mm thin section images in the axial, coronal and sagittal planes. Images enlarged and transferred to copy paper. An X-360 planimeter, which is a highly accurate architectural drafting instrument, was used to obtain linear and area measurements.

All sagittal diameters were measured using sagittal reconstruction to minimise the potential for gantry-angle distortion. Transverse diameters and area measurements were obtained from axial images.

Reproducibility/Variation

CT study (Pavlov et al. 1987): 15 group members were randomly selected for independent measurement by two of the investigators. Measurements were found to be highly reliable: sagittal diameter, $r = 0.96$ (p <0.001), transverse diameter, $r = 0.97$ (p <0.001) and cross-sectional area $r = 0.97$ (p <0.001).

Clinical Relevance/Implications

The ratio of sagittal to transverse diameter of the spinal canal gives some indication of its shape. The smaller the sagittal to transverse diameter of the cervical spine, the greater the predisposition to spinal cord injury.

In practice, transverse spinal canal diameter is not routinely used.

Analysis/Validation of Reference Data

CT study (Pavlov et al. 1987): 15 group members were randomly selected for independent measurement by two of the investigators. Measurements were found to be highly reliable: sagittal diameter, $r = 0.96$ ($p < 0.001$), transverse diameter, $r = 0.97$ ($p < 0.001$) and cross-sectional area $r = 0.97$ ($p < 0.001$).

Conclusion

The ratio of sagittal to transverse diameter of the spinal canal gives some indication of its shape. The smaller the sagittal to transverse diameter of the cervical spine, the greater the predisposition to spinal cord injury.

In practice, transverse spinal canal diameter is not routinely used.

6.27 Cervical Spinal Canal Cross-Sectional Area

Definition

Transverse area of cervical spinal canal.

Indications

To detect spinal stenosis.

Measurement

CT: Cross-sectional area of cervical spinal canal on CT in 100 normal adults:

C3: 320 mm^2, (SD 35)
C4: 270 mm^2 (SD 43)
C5: 264 mm^2 (SD 37)
C6: 272 mm^2 (SD 38)
C7: 280 mm^2 (SD 47)

MRI: Transverse area of cervical spinal canal on MRI in 96 normal adults:

C3: 246.9 mm^2, (SD 30.3)
C4: 236.1 mm^2, (SD 29.0)
C5: 238.8 mm^2, (SD 30.6)
C6: 248.5 mm^2, (SD 30.1)
C7: 254.8 mm^2, (SD 32.7)

Techniques

CT: GE 8800 CT scanner, high-resolution, 1.5 mm thin section images in the axial, coronal and sagittal planes.
MRI: T1-weighted sequences. 0.5 T MRI, cervical coil, pulse sequence TR 500, TE 20–30 ms, 192 × 192 matrix, 10 mm section thickness, and FOV 25 cm.

Full Description of Technique

CT: 100 control subjects (47 males and 53 females aged 18–36) who were being investigated for non-traumatic neurological or orthopaedic disorders and whose plain cervical spinal radiographs were deemed normal.

GE 8800 CT scanner, high-resolution, 1.5 mm thin section images in the axial, coronal and sagittal planes. Images enlarged and transferred to copy paper. An X-360 planimeter, which is a highly accurate architectural drafting instrument, was used to obtain linear and area measurements.

All sagittal diameters were measured using sagittal reconstruction to minimise the potential for gantry-angle distortion. Transverse diameters and area measurements were obtained from axial images.
MRI: 92 normal adults (54 males and 42 females). T1-weighted sequences. 0.5 T MRI, cervical coil, pulse sequence TR 500, TE 20–30 ms, 192 × 192 matrix, 10 mm section thickness, and FOV 25 cm.

Axial images were angled parallel with each disc and vertebral body from C2 to C7, perpendicular to the long axis of the spinal canal.

The area of the spinal canal was measured along the inner border line of low signal intensity, which included ligaments as well as the bone.

Areas measured five times in each slice using a computer-linked digitizer.

Mean of the middle three measurements in each area was taken.

Reproducibility/Variation

CT study: 15 group members were randomly selected for independent measurement by two of the investigators. Measurements were found to be highly reliable: sagittal diameter, $r = 0.96$

(p <0.001); transverse diameter, $r = 0.97$ (p <0.001) and cross-sectional area $r = 0.97$ (p <0.001).

MR study: The reliability of the measurements was confirmed by measuring 20 normal adults twice by two independent observers.

(p <0.001) and cross-sectional area $r = 0.97$ (p <0.001).

MR study: The reliability of the measurements was confirmed by measuring 20 normal adults twice by two independent observers.

Clinical Relevance/Implications

Can be used to detect spinal canal stenosis, which can be congenital or acquired. Transverse area is more reliable than canal diameter alone.

Conclusion

Not practical in day-to-day practice.

Measurements on MRI give smaller cross-sectional areas than those obtained at CT.

Analysis/Validation of Reference Data

CT study: 15 group members were randomly selected for independent measurement by two of the investigators. Measurements were found to be highly reliable: sagittal diameter, $r = 0.96$ (p <0.001), transverse diameter, $r = 0.97$

6.28 Flexion-Extension Motion

Definition

Altered angular and linear dimensions with dynamic movements. Full flexion to full extension angular ranges of motion (ROM) from C2 to C7 (Holmes et al. 1994).

Interspinous distance defined as the distance between the midpoints of each spinous process at the posterior margin of the spinal canal (Knopp et al. 2001).

Subluxation defined as the distance from the posterior margin of one vertebral body to the posterior margin of the next caudad vertebral body (Knopp et al. 2001).

The degree of angulation between C3 and C7 was defined as the intersecting angle from a line perpendicular to the base of C3 to a line perpendicular to the base of C7 (Knopp et al. 2001).

Measurement

(Holmes et al. 1994):

Average ROM at C2–C3: 7.7° (SD 3.2)
Average ROM at C3–C4: 13.5° (SD 3.4)
Average ROM at C4–C5: 17.9° (SD 3.1)
Average ROM at C5–C6: 15.6° (SD 4.9)
Average ROM at C6–C7: 12.5° (SD4.8)

(Knopp et al. 2001):
Interspinous distance—flexion minus neutral:

C3–4: 1.2 mm, SD 1.7
C4–5: 2.2 mm, SD 1.7
C5–6: 3.5 mm, SD 2.3
C6–7: 4.6 mm, SD 2.4

Interspinous distance—neutral minus extension:

C3–4: 1.5 mm, SD 1.9
C4–5: 2.2 mm, SD1.7
C5–6: 1.9 mm, SD 1.8
C6–7: 1.2 mm, SD 1.8

Vertebral angulation C3–C7:

Flexion minus neutral = mean 14.1°, SD 9.5
Neutral minus extension = mean 24.2°, SD 13.3

Subluxation:

Was less than 2 mm during flexion in all subjects from C3 to C7.
Was greater than 2 mm in one of the subjects at C3–C4 in extension.

Indications

To determine if there is abnormally increased or reduced flexion-extension motion.

Technique

Radiography: 78 normal subjects (Chinese population). Tube-film distance 150 cm. Lateral radiographs taken in maximal voluntary flexion and extension (Holmes et al. 1994).

One hundred male volunteers. Tube-film distance 72 in. Lateral cervical spine radiographs taken in neutral position and during maximal voluntary extension. Flexion radiographs were obtained with the patient supine and asked to flex their neck until forehead rested on a stop, predetermined to provide approximately 30° of flexion (Knopp et al. 2001).

Full Description of Technique

Measurements are taken from lateral radiographs of the cervical spine in maximum flexion and extension. 78 normal subjects (Chinese).

Tube-film distance 1.5 m.

The angular range of motion (ROM) was measured at each level from C2 to C7 by adding the full flexion angle to the full to the full extension angle, giving the maximum angular displacement of the joint under voluntary effort. This was done

by tracing the outline of the lower vertebra (e.g. C5) onto translucent paper over a light box. The four corners of the superior vertebral body (in this case C4) were marked and the tracing was then transferred to the corresponding radiograph of the pair (either full flexion or full extension). The traced outline of the lower vertebra was superimposed on, and aligned with, the same vertebra on the new radiograph and the four corners of the superior vertebral body were again marked, now in their new positions. Four lines were then drawn between the four pairs of points to represent the planes of the superior and inferior margins of the vertebra, both in full flexion and full extension (see diagram). The flexion-extension range of motion is equal to the angles a and b, which are measured using a protractor (Holmes et al. 1994).

One hundred male volunteers, aged 18–40. Tube-film distance 72 in. Lateral cervical spine radiographs taken in neutral position and during maximal voluntary extension. Flexion radiographs were obtained with the patient supine and asked to flex their neck until forehead rested on a stop, predetermined to provide approximately 30° of flexion. For each subject the radiologist measured the interspinous distance, amount of subluxation and degree of angulation between C3 and C7 in each of the three views. Interspinous distance was defined as the distance between the midpoints of each spinous process at the posterior margin of the spinal canal. Subluxation was defined as the distance from the posterior margin of one vertebral body to the posterior margin of the next caudad vertebral body. The degree of angulation between C3 and C7 was defined as the intersecting angle from a line perpendicular to the base of C3 to a line perpendicular to the base of C7 (Knopp et al. 2001).

Reproducibility/Variation

Some errors due to change in appearance of radiographic landmarks between the flexion and extension radiographs can occur.

Intra- and interobserver variability gives a measurement error of +/− 2° (Holmes et al. 1994).

Single observer for this study (Knopp et al. 2001).

Clinical Relevance/Implications

Increased angular range of motion can occur in cervical instability due to ligament rupture following trauma.

Decreased angular range of motion can occur due to a variety of causes including congenital and acquired vertebral fusion, degenerative change and arthropathies.

There is a wide range of normal for angular range of motion and interspinous distance on flexion and extension radiographs in normal subjects, so these measurements may not be very useful clinically.

However, subluxation of greater than 2 mm is a useful sign of abnormality.

Analysis/Validation of Reference Data

Measurements in reference apply to a Chinese population (Holmes et al. 1994).

Conclusion

Useful studies.

6.29   C C0-C3 Rotation

Definition

Rotation at C0/C1 is defined as the degree of angular rotation between the occiput and C1 (Fig. 6.42).

Rotation at C1/C2 is defined as the degree of angular rotation at the atlantoaxial joint.

Indications

Useful when atlantoaxial rotatory fixation is suspected.

Measurement (Pfirrmann 2000)

Rotation at C0/C1:

To the right (from neutral) mean 2.7 °, SD 3.3
To the left (from neutral) mean 3.3 °, SD 3.6

Differences in left-to-right segmental rotation at C0/C1: 3.5 °, SD 8

Rotation at C1/C2:

To the right (from neutral) mean 38.0°, SD 6.5
To the left (from neutral) mean 37.8°, SD 6.4
Differences in left-to-right segmental rotation at C1/C2: 6.3 °, SD 4.4

Rotation at C2/C3:

To the right (from neutral) mean 1.7 °, SD 4.0
To the left (from neutral) mean 2.0 °, SD 4.1
Differences in left-to-right segmental rotation at C2/C3: 3.9 °, SD 2.9

(Roche 2002)
Rotation at C1/C2:

To the right (from neutral) mean 32.4 °, SD 8.2
To the left (from neutral) mean 34.2 °, SD 9.4

Atlantoaxial rotation (right)

Fig. 6.42 Rotation. Axial MR or CT images of mid-C1 and mid-C2 are obtained. From the axial C2 image, a line is drawn in the AP plane bisecting the body and spinous process of C2, and from this a perpendicular line is drawn at a tangent to the posterior body of C2. From the axial C1 image, a line through the midpoints of the foramina transversaria is drawn. The angle between the superimposed lines determines the degree of rotation

Techniques

CT: Dynamic CT in children is the optimal method of assessing rotational C1/C2 relationships. Transaxial images of mid-C1 and mid-C2 are obtained ideally by angling the gantry appropriately. From the axial C2 image, a line is drawn in the AP plane bisecting the body and spinous process of C2, and from this a perpendicular line is drawn at a tangent to the posterior body of C2. From the axial C1 image, a line through the midpoints of the foramina transversaria is drawn. The angle between the superimposed lines determines the degree of rotation (Fig. 6.42).

MR: (Pfirrmann) 50 healthy volunteers. Imaging performed with a 1.0 T scanner (Siemens Impact Expert; Siemens medical systems, Erlangen, Germany).

Axial T1-weighted images (TR 640, TE 12 milliseconds) were obtained with the head in maxi-

mal right and left rotation and in neutral position. Neutral position was verified by an axial localiser sequence. Slices covered the region between skull base and third cervical body (Pfirrmann et al. 2000).

(Roche 2002): 29 subjects, 20 adult aged 19–52 (mean age 37.6) and 9 children aged 5–14 (mean 10.5). Axial T1 images, slice thickness 4 mm. Imaged from occipital to lower border of C3. Subject imaged supine, in neutral position then repeated with maximal head rotation to the right and to the left. Angle of rotation calculated by superimposing anatomical landmarks.

Full Description of Technique

50 healthy volunteers, 31 male and 19 female aged 19–47. Imaging performed with a 1.0 T scanner (Siemens Impact Expert; Siemens medical systems, Erlangen, Germany).

Axial T1-weighted images (TR 640, TE 12 milliseconds) were obtained with the head in maximal right and left rotation and in neutral position. Neutral position was verified by an axial localiser sequence. Slices covered the region between skull base and third cervical body. Additionally coronal T1- and T2-weighted turbo spin-echo images with a slice thickness of 3 and 4 mm were obtained parallel to the dens axis with a field of view of 26 × 180, 3 and 4 acquisitions were averaged.

For determination of the range of motion of C0 to C3 images in maximum right and left rotation were analysed digitally. Lines were drawn through the nasal septum and internal occipital crista for C0, through the foramen of the transverse processes for C1 and C3 and through the middle of the body of C2. Angles to neutral position and differences were calculated to obtain segmental range of motion and left-to-right differences. All measurements were independently performed by two musculoskeletal radiologists to assess correlation coefficients for the interobserver agreement (Pfirrmann).

Twenty-nine healthy volunteers. 20 adult aged 19–52 (mean age 37.6) and 9 children aged 5–14 (mean 10.5). 0.5 T MRI scanner (Philips). Axial T1 images, slice thickness 4 mm. Imaged from occipital to lower border of C3. Subject imaged supine, in neutral position then repeated with maximal head rotation to the right and to the left. Angle of rotation calculated by superimposing anatomical landmarks on tracings of images of each vertebra at each stage of rotation. (Roche)

Reproducibility/Variation

Two observers. Interobserver correlation coefficients for the rotation measurements range from 0.93 to 0.98 (Pfirrmann et al. 2000).

Clinical Relevance/Implications

Reduced C1/C2 rotation occurs in rotatory atlantoaxial subluxation.

Increased rotation at C0/C1 or C1/C2 can occur following trauma due to ligament rupture.

There is often a difference between left and right rotation in normal subjects and a discrepancy should not be considered pathological.

Analysis/Validation of Reference Data

Fifty healthy subjects. Two observers. Interobserver correlation coefficients for the rotation measurements range from 0.93 to 0.98 (Pfirrmann et al. 2000).

Similar range of rotation at C1/C2 confirmed in (Roche 2002)

6.30 Prevertebral Soft Tissue Space (PVSTS)

Definition

The retrocricoid soft tissue thickness is measured on a lateral radiograph from the posterior aspect of the cricoid to the adjacent anterior cortex of C5. The retrotracheal soft tissue thickness is measured from the posterior wall of the tracheal air column to the anterior cortex of C5 (Chen and Bohrer 1999).

The prevertebral soft tissue thickness is measured on a lateral radiograph from the inferior endplate to the posterior aspect of the pharyngeal or tracheal air space (Matar and Doyle 1997) (Fig. 6.43).

Indications

In the setting of acute trauma to alert the radiologist to the possible presence of prevertebral haematoma or oedema. This can be a sign of vertebral injury (Fig. 6.12).

Measurement

Prevertebral soft tissue thickness (radiographs) (Chen and Bohrer 1999):

Retrocricoid thickness (C5 level):

    10.46 mm +/− 2.53 (all)
    10.74 mm +/− 3.33 (male)
    10.31 mm +/− 2.01 (female)

Retrotracheal thickness (C5 level):

    15.46 mm +/− 3.08 (all)
    17.16 mm +/− 4.00 (male)
    14.54 mm +/− 1.95 (female)

C5 diameter:

    19.33 mm +/− 2.80 (all)
    21.47 mm +/− 2.34 (male)
    18.17 mm+/− 2.33 (female)

Retrocricoid/C5 ratio:

    0.5485 +/− 0.1348 (all)
    0.5003 +/− 0.1438 (male)
    0.5746 +/−0.1239 (female)

Retrotracheal/C5 ratio:

    0.8111 +/− 0.1709 (all)
    0.8054 +/− 0.1975 (male)
    0.8141 +/− 0.1577 (female)

Prevertebral soft tissue thickness (radiographs) (Matar and Doyle 1997):

C2/C3 prevertebral soft tissue thickness should be less than 7 mm
C6/C7 prevetebral soft tissue thickness should be less than 21 mm

Fig. 6.43 Measurement of prevertebral soft tissue space (PVSTS). Radiographic measurements of the PVSTS are calculated from the inferior/superior borders of the vertebral bodies. CT measurements of the PVSTS based on reformatted sagittal MDCT are calculated from the vertebral midpoint anteriorly and are measured using a soft tissue window setting

Prevertebral soft tissue thickness (radiographs) (Templeton et al. 1987):

C2:

4.7 mm +/− 1.5 (all)
5.0 mm +/− 1.7 (male)
4.4 mm +/− 1.2 (female)

C3:

5.0 mm+/− 1.5 (all)
5.1 mm+/− 1.5 (male)
4.8 mm+/− 1.4 (female)

C4:

6.4 mm+/−2.0 (all)
6.6 mm+/−2.1 (male)
6.2 mm+/−1.8 (female)

'Considerable overlap between measurements in normal and spine-injured patients. Taking an upper limit of normal of 10 mm at any level from C2 to C4 only 5% of normal patients would be classified as abnormal'

Prevertebral soft tissue thickness (radiographs) (Penning 1981):

C1:

Flexion 5.6 mm, range 2–11 mm
Midposition 4.6 mm, range 1–10 mm
Extension 3.6 mm, range 1–8 mm.

C2:

Flexion 4.1 mm, range 2–6 mm
Midposition 3.2 mm, range 1–5 mm
Extension 3.8 mm, range 2–6 mm

C3:

Flexion 4.2 mm, range 3–7 mm
Midposition 3.4 mm, range 2–7 mm
Extension 4.1 mm, range 3–6 mm

C4:

Flexion 5.8 mm, range 4–7 mm
Midposition 5.1 mm, range 2–7 mm
Extension 6.1 mm, range 4–8 mm

C5:

Flexion 17.1 mm, range 11–22 mm
Midposition 14.9 mm, range 8–20 mm
Extension 15.2 mm, range 10–20 mm

C6:

Flexion 16.3 mm, range 12–20 mm
Midposition 15.1 mm, range 11–20 mm
Extension 13.9 mm, range 7–19 mm

C7:

Flexion 14.7 mm, range 9–20 mm
Midposition 13.9 mm, range 9–20 mm
Extension 11.9 mm, range 7–21 mm

Prevertebral soft tissue thickness (radiographs) (Keats and Sistrom 2001):

Measurements expressed as ratio of width of C5 vertebral body:
Adult male postpharyngeal: 0.3
Adult female postpharyngeal: 0.3
0–1 year: postpharyngeal 1.5, postventricular 2.0
1–2 year: postpharyngeal 0.5, postventricular 1.5
2–3 year: postpharyngeal 0.5, postventricular 1.2
3–6 year: postpharyngeal 0.4, postventricular 1.2
6–14 year: postpharyngeal 0.3, postventricular 1.2

Prevertebral soft tissue thickness (multidetector CT) (Rojas).
Upper limits of normal:

C1: 8.5 mm
C2: 6 mm
C3: 7 mm
C6: 18 mm
C7: 18 mm

Techniques

Radiography: Lateral cervical spine radiograph obtained with patient in the upright position. Tube-film distance 100 cm. The retrocricoid soft tissue thickness was measured, and the retrotracheal soft tissue thickness was measured at C5 level (Chen and Bohrer 1999).

Lateral cervical spine radiograph. Variable tube-film distance between 120 and 150 cm. Prevertebral soft tissues measured from the anterior aspect of the inferior endplate to the posterior aspect of the pharyngeal or tracheal air column (Matar and Doyle 1997).

Lateral cervical spine radiograph. Tube-film distance 102 cm. Retropharyngeal soft tissues were measured at C2, C3 and C4 levels. Distance from posterior aspect of pharyngeal air column to anteroinferior aspect of respective vertebral body was measured (Templeton et al. 1987).

CT: 16 slice MDCT. Midline sagittal image (Rojas).

Full Description of Technique

54 adults (19 male and 35 female) aged 22–75, who had normal findings on lateral cervical radiographs.

Lateral cervical spine radiograph obtained with patient in the upright position. Tube-film distance 100 cm. Calipers were used to make measurements to the nearest millimetre. The diameter of C5 vertebral body was measured at its mid-level. The retrocricoid soft tissue thickness was measured from the most anteroinferior aspect of C5 perpendicular to the soft tissue of the posterior pharyngeal wall to the cricoid. The retrotracheal soft tissue thickness was measured from the same point to posterior wall of the tracheal air column (Chen and Bohrer 1999).

Seventy-five control subjects, aged 15–88, who had cervical radiographs taken for trauma but who subsequently had no clinical or radiological evidence of cervical spine injury. All films taken within 24 h of injury. Radiographic technique variable, with tube-film distance ranging between 120 and 150 cm. Measurements were taken at C2, C3, C6 and C7. Measurements were made directly from the radiograph using a transparent ruler. Distance between the anterior aspect of the relevant inferior endplate and the posterior aspect of the pharyngeal or tracheal air column was measured (Matar and Doyle 1997).

Two hundred thirty-six subjects who were classified as normal had lateral cervical spine radiographs. Tube-film distance 102 cm. Retropharyngeal soft tissues were measured at C2, C3 and C4 levels. Distance from posterior aspect of pharyngeal air column to anteroinferior aspect of respective vertebral body was measured (Templeton et al. 1987).

50 normal adults and 25 normal infants. Postpharyngeal soft tissue, measured at the point where the soft tissues run parallel to the vertebra. Postventricular soft tissue for use in children when the cricoid is not visible. The distance is measured between the posterior commissure of the larynx and the nearest portion of the cervical spine. Retrotracheal soft tissue is measured between the posterior wall of the trachea and the anterior surface of the adjacent cervical vertebra. Postcricoid soft tissue is measured from the posterior surface of the cricoid cartilage and the anterior surface of the adjacent cervical vertebra. C5 diameter is measured from the anterior to posterior surface of the body of C5 at its middle (Keats and Sistrom 2001).

One hundred ninety-two adults aged 20–98 years, 119 male and 73 female. 16 slice MDCT. 16 × 0.75 mm collimation. 1 mm slice thickness. Measurements made on midline sagittal reconstructions. Prevertebral soft tissues measured using soft tissue window settings, from midpoint of anterior vertebral body to the closest point in the air column. Upper limits of normal for C4 and C5 measurements not taken because of variable position of the larynx and oesophagus (Rojas).

Reproducibility/Variation

Calipers were used for measurement. No indication of how many observers were used or if there was inter- or intraobserver variability in the measurements (Chen and Bohrer 1999).

Two independent reviewers made the measurements. At C2 and C3 levels, the two reviewers recorded measurements within 1 mm of each other 95% of the time (correlation coefficients 0.91 and 0.93) and within 2 mm of each other 93% of the time at C6 and C7 (correlation coefficients 0.88 and 0.95) (Matar and Doyle 1997).

Clinical Relevance/Implications

Increased retrocricoid or retrotracheal soft tissue measurement can be an indication of prevertebral haematoma or soft tissue oedema following trauma and should prompt further evaluation to exclude cervical spine injury (Fig. 6.41). Increased prevertebral soft tissue thickness can also occur due to infection, tumour, non-traumatic haemorrhage and foreign bodies.

Analysis/Validation of Reference Data

Small study, 54 adults. The retrotracheal/C5 ratio is useful because it does not require remembering empirical diameters; taking the mean plus one standard deviation then one should take $1 \times$ C5 diameter for the maximum allowed retrotracheal soft tissue thickness (Chen and Bohrer 1999).

In a large study of 236 subjects and measurements are compared to 49 spine-injured patients. No mention is made of how many observers or how measurements were made (Templeton et al. 1987).

Conclusion

Useful measurement for detecting subtle soft tissue signs of cervical spine trauma.

Cannot be used if patient is unconscious or intubated because pooled secretions in the trachea and pressure effects from endotracheal tube can falsely alter the apparent soft tissue thickness.

Large overlap between measurements in normal and spine-injured patients; therefore, false positive and negative cases occur.

6.31 Dural Sac AP Diameter on MR

Definition

The anteroposterior diameter of the cervical dural sac measured using MR imaging (Fig. 6.44).

Indications

To detect spinal stenosis or dural ectasia.

Measurement

(Holsheimer)

    C4: 13.3 mm +/− 1.4 SD
    C5: 13.4 mm +/− 1.5 SD
    C6: 13.4 mm +/− 1.4 SD

(Khanapurkar et al. 2014)

    C1: mean 14.39 mm
    C2: mean 13.82 mm
    C2–C3: mean 12.58 mm
    C3: mean 12 mm
    C3–C4: mean 11.51 mm
    C4: mean 11.54 mm
    C4–C5: mean 11.29 mm
    C5: mean 11.45 mm
    C5–C6: mean 11.15 mm

    C6: mean 11.37 mm
    C6–C7: mean 11.14 mm
    C7: mean 11.7 mm

Technique

MRI: T2 sequences, 5 mm thick slices (Holsheimer).
MRI: T2 sequences (Khanapurkar et al. 2014)

Full Description of Technique

MRI: (Holsheimer) 26 adult volunteers, aged 19–38 years.

Turbo spin-echo T2 (4000/168)-weighted axial images were obtained, using a dedicated spine coil. Slice thickness was 5 mm with a 0.5 mm interslice gap.

MRI: (Khanapurkar et al. 2014) 60 patients without cervical spinal pathology, 30 male and 30 female, age range 25–60.

T2 slices. Measurements made at level of mid-height of vertebral body and at mid-disc level.

Reproducibility/Variation

Unknown.

Clinical Relevance/Implications

Can be used to detect spinal stenosis or dural ectasia. Measurement can easily be made in routine practice.

Analysis/Validation of Reference Data

Limited evidence.

Conclusion

Simple measurement which can be made readily. However, transverse area is a more accurate reflection than single bidimensional diameter alone.

Fig. 6.44 Dural sac/cord diameters on MRI. The AP diameter of thecal sac/cord is measured at the midsagittal plane. The transverse diameter of thecal sac/cord is measured in the mid-coronal plane

6.32 Dural Sac Transverse Diameter on MR

Definition

The transverse diameter of the cervical dural sac measured using MR imaging (Fig. 6.44).

Indications

To detect spinal stenosis or dural ectasia.

Measurement

(Holsheimer)

C4: 20.4 mm +/− 2.0 SD
C5: 20.6 mm +/− 2.0 SD
C6: 20.7 mm +/− 2.1 SD

(Khanapurkar et al. 2014)

C1: mean 20.8 mm
C2: mean 20.19 mm
C2–C3: mean 19.7 mm
C3: mean 19.25 mm
C3–C4: mean 18.97 mm
C4: mean 19.31 mm
C4–C5: mean 19.01 mm
C5: mean 19.64 mm
C5–C6: mean 18.97 mm
C6: mean 18.95 mm
C6–C7: mean 17.95 mm
C7: mean 18.06 mm

Technique

MRI: T2 sequences, 5 mm thick slices.

Full Description of Technique (s)

MRI: (Holsheimer) 26 adult volunteers, aged 19–38 years.

Turbo spin-echo T2 (4000/168)-weighted axial images were obtained, using a dedicated spine coil. Slice thickness was 5 mm with a 0.5 mm interslice gap.
MRI: (Khanapurkar et al. 2014) 60 patients without cervical spinal pathology, 30 male and 30 female, age range 25–60.
T2 slices. Measurements made at level of midheight of vertebral body and at mid-disc level.

Reproducibility/Variation

Good reproducibility between the two MRI studies.

Clinical Relevance/Implications

Can be used to detect spinal stenosis or dural ectasia. Measurement can easily be made in routine practice.

Analysis/Validation of Reference Data

Limited validation with other studies.

Conclusion

Simple measurement which can be made readily. However, transverse area is a more accurate reflection than single bidimensional diameter alone.

6.33 Cervical Dural Tube Transverse Area

Definition

Transverse area of cervical dural tube on MRI in normal adults.

Indications

To detect dural ectasia or canal stenosis.

Measurement

Transverse area of cervical dural tube on MRI in 96 normal adults:

C2–C3: 218.8 mm², (SD 31.4)
C3: 200.8 mm², (SD 25.4)
C3–C4: 192.6 mm², (SD 21.9)
C4: 193.0 mm², (SD 21.6)
C4–C5: 189.8 mm², (SD 20.3)
C5: 188.9 mm², (SD 21.2)
C5–C6: 186.0 mm², (SD 20.3)
C6: 191.7 mm², (SD 24.2)
C6–C7: 186.6 mm², (SD 22.0)
C7: 196.5 mm², (SD 24.4)

Technique

MRI: T1-weighted sequences. 0.5 T MRI, cervical coil, pulse sequence TR 500, TE 20–30 ms, 192 × 192 matrix, 10 mm section thickness, and FOV 25 cm.

Full Description of Technique

MRI: 92 normal adults (54 males and 42 females) T1-weighted sequences. 0.5 T MRI, cervical coil, pulse sequence TR 500, TE 20–30 ms, 192 × 192 matrix, 10 mm section thickness, and FOV 25 cm.

Axial images were angled parallel with each disc and vertebral body from C2 to C7, perpendicular to the long axis of the spinal canal.

Areas measured five times in each slice using a computer-linked digitizer.

Mean of the middle three measurements in each area was taken.

Reproducibility/Variation

The reliability of the measurements was confirmed by measuring 20 normal adults twice by two independent observers.

Clinical Relevance/Implications

Can be used to detect dural ectasia and spinal stenosis.

Analysis/Validation of Reference Data

Limited but measurements seem reliable.

Conclusion

Readily made assessment.

6.34 Adult Spinal Cord on CT Myelography (Thijssen et al. 1979)

Definition

The mean frontal and sagittal diameter of the adult cervical spinal cord measured at CT myelography (Fig. 6.45).

Indications

CT myelography rarely performed nowadays, unless there is a contraindication to MRI.

Measurement

Frontal diameter: (in mm +/− 2SD)

    C1: 10.4 +/− 1.7
    C2: 10.9 +/− 2.2
    C3: 11.3 +/− 2.0
    C4: 11.7 +/− 1.9

    C5: 11.8 +/− 2.7
    C6: 10.5 +/− 2.3
    C7: 9.3 +/− 2.5

Sagittal diameter: (in mm +/− 2SD)

    C1: 7.2 +/− 1.6
    C2: 6.5 +/− 2.0
    C3: 6.2 +/− 2.2
    C4: 6.0 +/− 1.5
    C5: 6.2 +/− 2.3
    C6: 6.4 +/− 2.7
    C7: 6.8 +/− 2.5

Techniques

CT myelography.

Full Description of Technique

Twenty adult patients, without cervical symptoms, who were undergoing lumbar myelography because of suspected herniated lumbar disc. CT scanner used was a Technicare Delta 50-DS with 13 mm slice collimation and gantry angulation perpendicular to the long axis of the spinal column. Patients scanned in supine position. 19 mm of metrizamide (170 mg iodine/mL) instilled in lumbar subarachnoid space. After completion of the myelogram, patient is placed in lateral decubitus position for 1 h to mix the cervical region.

Reproducibility/Variation

Unknown.

Clinical Relevance/Implications

CT myelography not used routinely now. However the values serve as reference values
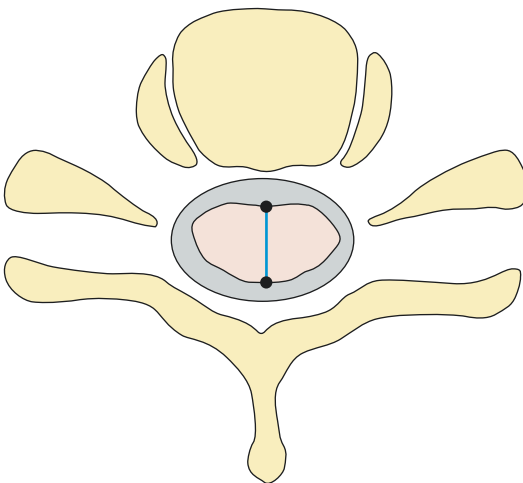
Fig. 6.45 Adult spinal cord on CT myelography/MRI. The sagittal diameter of the spinal cord is measured from the anterior margin to the posterior margin in the midsagittal plane. The transverse (frontal) diameter is the widest diameter from right to left in the coronal plane

which can be applied when evaluating MR of the cervical spine.

Analysis/Validation of Reference Data

Limited.

Conclusion

Can be used as reference values for interpreting MR of cervical spine, particularly when looking for cord atrophy.

6.35 Cervical Spinal Cord AP Diameter on MRI

Definition

Anteroposterior diameter of cervical spinal cord on MRI in normal adults (Fig. 6.46).

Measurement

Cervical spinal cord AP diameter on MRI (Okada et al. 1994):

C3: 7.8 mm +/− 2.4 SD
C3–C4: 7.6 mm +/− 2.8 SD
C4: 7.7 mm +/− 2.6 SD
C4–C5: 7.5 mm +/− 2.8 SD
C5: 7.5 mm +/− 2.4 SD
C5–C6: 7.3 mm +/− 2.4 SD
C6: 7.3 mm +/− 1.9 SD
C6–C7: 7.1 mm +/− 1.7 SD
C7: 7.0 mm +/− 1.6 SD

Cervical spinal cord AP diameter on MRI (Holsheimer et al. 1994):

C4: 7.3 mm +/− 0.6 SD
C5: 6.9 mm +/− 0.6SD
C6: 6.7 mm +/− 0.6SD

Cervical spinal cord AP diameter on MRI (Khanapurkar et al. 2014)

C2–3: mean 7.651 mm
C3–4: mean 7.222 mm
C4–5: mean 7.022 mm
C5–6: mean 6.623 mm
C6–7: mean 6.102 mm

Cervical spinal cord AP diameter on MRI (Sherman)

C1: 9.3 mm (SD 0.9)
C2: 8.8 mm (SD 0.9)
C3: 8.6 mm (SD 0.8)
C4: 8.7 mm (SD 0.9)
C5: 8.3 mm (SD 0.9)
C6: 7.9 mm (SD 0.8)
C7: 7.4 mm (SD 0.9)

Indications

To detect cord oedema or atrophy.

Technique

MRI: T1-weighted sequences. 0.5 T MRI, cervical coil, pulse sequence TR 500, TE 20–30 ms, 192 × 192 matrix, 10 mm section thickness, and FOV 25 cm (Okada et al. 1994).

T2-weighted sequences, 5 mm slice thickness (Holsheimer et al. 1994).

T2-weighted sequences (Khanapurkar et al. 2014).

Fig. 6.46 Adult spinal cord AP diameter on MRI. AP diameter is measured from anterior aspect to posterior aspect of the cord, in the midsagittal plane, perpendicular to long axis of the cord

Full Description of Technique

MRI: 92 normal adults (54 males and 42 females) T1-weighted sequences. 0.5 T MRI, cervical coil, pulse sequence TR 500, TE 20–30 ms, 192 × 192 matrix, 10 mm section thickness, and FOV 25 cm.

Axial images were angled parallel with each disc and vertebral body from C2 to C7, perpendicular to the long axis of the spinal canal.

Diameters measured five times in each slice using a computer-linked digitizer.

Mean of the middle three measurements in each area was taken (Okada et al. 1994).

MRI: 26 adult volunteers, aged 19–38 years. Turbo spin-echo T2 (4000/168)-weighted axial images were obtained, using a dedicated spine coil. Slice thickness was 5 mm with a 0.5 mm interslice gap (Holsheimer et al. 1994).

MRI: 60 healthy subjects, 30 male, 30 female. Aged 25–60. T2 axial images. Measurements taken at the level of the intervertebral disc spaces (Khanapurkar et al. 2014).

MRI: 66 'normal' subjects, aged 19–74 (mean 41). 1.5 T MRI. 5 mm slice thickness, FOV 20 cm. Axial slices (Sherman).

Reproducibility/Variation

The reliability of the measurements was confirmed by measuring 20 normal adults twice by two independent observers (Okada et al. 1994).

Similar measurements obtained in study by Holsheimer et al. (1994), though for all levels the mean was slightly less. This may reflect the different imaging sequences used. On T2 sequence there is more contrast between cord and high-signal CSF, which could affect accuracy of measurements. Also the slice thickness was less in this study, reducing partial volume averaging.

Clinical Relevance/Implications

Can be used to detect cord atrophy or swelling. Transverse area is more reliable than cord diameter alone.

Analysis/Validation of Reference Data

Ninety-six healthy subjects. The reliability of the measurements was confirmed by measuring 20 normal adults twice by two independent observers (Okada et al. 1994).

Conclusion

Cervical spinal cord AP diameter can be readily measured from MR images. The AP diameter is widest at C3 level then reduces sequentially at levels below.

6.36 Cervical Spinal Cord Transverse Diameter on MR

Definition

The transverse diameter of the cervical dural sac measured using MR imaging (Fig. 6.44).

Indications

To detect spinal cord swelling or atrophy.

Measurement

(Holsheimer)

C4: 13.6 mm +/− 1.1 SD
C5: 13.4 mm +/− 1.1 SD
C6: 13.0 mm +/− 1.1 SD

(Khanapurkar et al. 2014)

C2–C3: mean 11.77 mm
C3–C4: mean 12.48 mm
C4–C5: mean 12.93 mm
C5–C6: mean 12.9 mm
C6–C7: mean 11.24 mm

(Sherman)

C1: 11.3 mm (SD 0.9)
C2: 12.4 mm (SD 0.9)
C3: 13.2 mm (SD 1.0)
C4: 14.0 mm (SD 1.1 mm)
C5: 13.9 mm (SD 1.0)
C6: 13.2 mm (SD 1.0)
C7: 11.4 mm (SD1.2)

Technique

MRI T2 sequences, 5 mm thick slices.

Full Description of Technique

MRI: (Holsheimer) 26 adult volunteers, aged 19–38 years.

Turbo spin-echo T2 (4000/168)-weighted axial images were obtained, using a dedicated spine coil. Slice thickness was 5 mm with a 0.5 mm interslice gap.

MRI: (Khanapurkar et al. 2014) 60 patients without cervical spinal pathology, 30 male and 30 female, age range 25–60.

T2 slices. Measurements made at mid-disc level.

MRI: 66 'normal' subjects, aged 19–74 (mean 41). 1.5 T MRI. 5 mm slice thickness, FOV 20 cm. Axial slices (Sherman).

Reproducibility/Variation

Good correlation between studies.

Clinical Relevance/Implications

Can be used to detect spinal cord swelling or atrophy. Measurement can easily be made in routine practice.

Analysis/Validation of Reference Data

Limited.

Conclusion

Simple measurement which can be made readily. However, transverse area is a more accurate reflection than single bidimensional diameter alone.

6.37 Cervical Spinal Cord Transverse Area

Definition

Transverse area of cervical spinal cord on MRI in normal adults (Fig. 6.44).

Indications

To detect cord oedema or atrophy.

Measurement

Transverse area of cervical spinal cord on MRI in 96 normal adults: (Okada)

C2–C3: 79.4 mm², (SD 6.9)
C3: 80.5 mm², (SD 7.1)
C3–C4: 82.9 mm², (SD 6.9)
C4: 84.6 mm², (SD 6.2)
C4–C5: 85.8 mm², (SD 7.2)
C5: 83.2 mm², (SD 6.2)
C5–C6: 81.2 mm², (SD 7.2)
C6: 76.1 mm², (SD 7.3)
C6–C7: 69.3 mm², (SD 8.0)
C7: 60.9 mm², (SD 7.5)

(Sherman)

C1: 105.1 mm² (SD 13.8)
C2: 109.1 mm² (SD 15)
C3: 113.5 mm² (SD 16)
C4: 121.8 mm² (SD 17.5)
C5: 115.4 mm² (SD 15.7)
C6: 104.3mm² (SD 15.0)
C7: 84.4 mm² (SD 15.7)

Technique

MRI T1-weighted sequences. 0.5 T MRI, cervical coil, pulse sequence TR 500, TE 20–30 ms, 192 × 192 matrix, 10 mm section thickness, and FOV 25 cm.
Other.

Full Description of Technique

MRI: 92 normal adults (54 males and 42 females) T1-weighted sequences. 0.5 T MRI, cervical coil, pulse sequence TR 500, TE 20–30 ms, 192 × 192 matrix, 10 mm section thickness, and FOV 25 cm.
Axial images were angled parallel with each disc and vertebral body from C2 to C7, perpendicular to the long axis of the spinal canal.
Areas measured five times in each slice using a computer-linked digitizer.
Mean of the middle three measurements in each area was taken.
MRI: 66 'normal' subjects, aged 19–74 (mean 41). 1.5 T MRI. 5 mm slice thickness, FOV 20 cm. Axial slices (Sherman).

Reproducibility/Variation

The reliability of the measurements was confirmed by measuring 20 normal adults twice by two independent observers.

Clinical Relevance/Implications

Can be used to detect cord atrophy or swelling. Transverse area is more reliable than cord diameter alone.

Analysis/Validation of Reference Data

Ninety-six healthy subjects. The reliability of the measurements was confirmed by measuring 20 normal adults twice by two independent observers.

Conclusion

Cervical spinal cord area measurement is not a routine measurement and is difficult to apply in practice, needing a dedicated computer programme. These are useful reference measurements, however, for research studies where objective assessment of the spinal cord area is required to detect cord atrophy or swelling.

6.38   Ratio of Cervical Spinal Cord Area to Cervical Spinal Canal Area on MRI

Definition

The ratio of cervical spinal cord area to cervical spinal canal area.

Indications

Can help to determine what space is available for the cord in the spinal canal.

Measurement

C3: 33.0 +/− 4.4%
C4: 36.4 +/− 4.1%
C5: 35.5 +/− 4.4%
C6: 30.8 +/− 3.9%
C7: 23.7 +/− 3.4%

Technique

MRI: T1-weighted sequences. 0.5 T MRI, cervical coil, pulse sequence TR 500, TE 20–30 ms, 192 × 192 matrix, 10 mm section thickness, and FOV 25 cm.

Full Description of Technique

MRI: 92 normal adults (54 males and 42 females) T1-weighted sequences. 0.5 T MRI, cervical coil, pulse sequence TR 500, TE 20–30 ms, 192 × 192 matrix, 10 mm section thickness, and FOV 25 cm.

Axial images were angled parallel with each disc and vertebral body from C2 to C7, perpendicular to the long axis of the spinal canal.
Area of spinal cord and spinal canal measured in each slice using a computer-linked digitizer.
Mean of the middle three measurements in each area was taken.

Reproducibility/Variation

The reliability of the measurements was confirmed by measuring 20 normal adults twice by two independent observers.

Clinical Relevance/Implications

Can be used to detect cord atrophy or swelling and also canal stenosis. Transverse area is more reliable than cord or canal diameters alone.

Analysis/Validation of Reference Data

Ninety-six healthy subjects. The reliability of the measurements was confirmed by measuring 20 normal adults twice by two independent observers.

Conclusion

Cervical spinal cord and spinal canal areas are not routinely measured in everyday practice. These measurements require a dedicated computer programme.

6.39 Paediatric Cord/Subarachnoid Space Ratio (Boltshauser and Hoare 1976)

Definition

The ratio of spinal cord to thecal sac diameters in children, measured using air myelography with tomography (Fig. 6.47).

Indications

To assess cord atrophy or cord swelling.

Measurement

Normal range for paediatric cord/subarachnoid space ratio—2 standard deviations to +2 standard deviations:
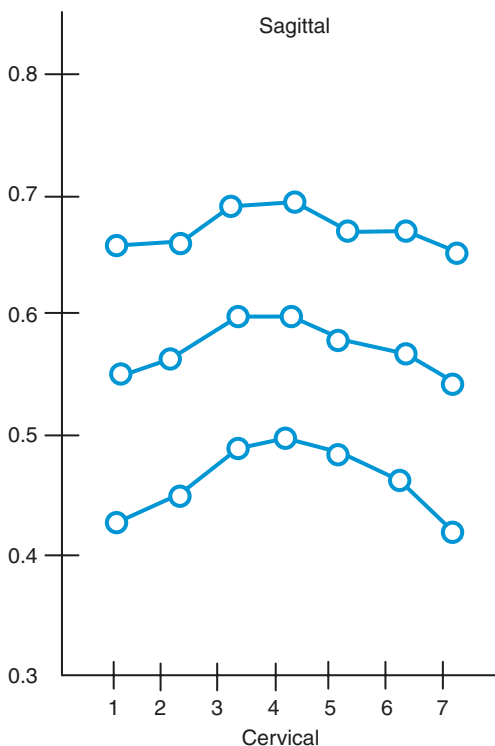
Fig. 6.47 Paediatric cord/subarachnoid space ratio. Mean and two standard deviations of cervical cord/subarachnoid space ratio in sagittal plane

C1: 0.44–0.68
C2: 0.47–0.67
C3: 0.51–0.71
C4: 0.51–0.71
C5: 0.49–0.69
C6: 0.46–0.7
C7: 0.43–0.67

Technique

Air myelography with tomograms.

Full Description of Technique

Based on a study of 110 normal air myelograms in children aged 1 month to 15 years.

One hundred ten normal air myelograms of children were reviewed, and the ratio of the spinal cord width to the subarachnoid space width (cord/SAS ratio) was calculated in the sagittal and transverse planes.

The spinal cord and subarachnoid space are measured in sagittal diameter at mid-vertebral level and in the transverse diameter at interpedicular level. The cord/subarachnoid space (cord/SAS) ratio is calculated.

Reproducibility/Variation

This technique is no longer used and has been superseded by MRI.

Clinical Relevance/Implications

Useful reference values for detecting cord atrophy or oedema.

Analysis/Validation of Reference Data

One hundred ten normal air myelograms of children were reviewed, and the ratio of the spinal cord width to the subarachnoid space width (cord/SAS ratio) was calculated in the

sagittal and transverse planes. This ratio proved to be independent of age and sex. The mean values at different vertebral levels are in close agreement with those previously reported for adults.

Conclusion

The cord/SAS ratio is helpful in evaluating changed cord dimensions, especially that of cord atrophy.

References

Bernhardt M, Hynes RA, Blume HW, White AA III (1993) Current concepts review. Cervical spondylotic myelopathy. J Bone Joint Surg Am 75:119–128

Blackley HR, Plank LD, Robertson PA (1999) Determining the sagittal dimensions of the canal of the cervical spine. The reliability of ratios of anatomical measurements. J Bone Joint Surg (Br) 81-B:110–112

Bohrer SP, Klein A, Martin W III (1985) 'V' shaped pre-dens space. Skelet Radiol 14:111–116

Boltshauser E, Hoare RD (1976) Radiographic measurements of the normal spinal cord in childhood. Neuroradiology 10:235–237

Bono CM, Vaccaro AR, Fehlings M, Fisher C, Dvorak M, Ludwig S, Harrop J (2006) Measurement techniques for lower cervical spine injuries. Spine 31(5):603–609

Bono CM, Vaccaro AR, Fehlings M, Fisher C, Dvorak M, Ludwig S, Harrop S (2007) Measurement techniques for upper cervical spine injuries. Spine 32:593–600

Bono CM, Schoenfeld A, Rampersaud R, Levi A, Grauer J, Arnold P, Fehlings M, Dvorak M, Vaccaro AR (2011) Reproducibility of radiographic measurements for subaxial cervical spine trauma. Spine 36(17):1374–1379

Bull JW, Nixon WL, Pratt RT (1955) The radiological criteria and familial occurrence of primary basilar impression. Brain 78:229–247

Chamberlain WIE (1939) Basilar impression (Platybasia) a bizarre developmental anomaly of the occipital bone and upper cervical spine with striking and misleading neurological manifestations. Yale J Biol Med 11:487

Chen MY, Bohrer SP (1999) Radiographic measurement of prevertebral soft tissue thickness on lateral radiographs of the neck. Skelet Radiol 28(8):444–446

Cronin CG, Lohan DG, Mhuircheartigh JN, Meehan CP, Murphy JM, Roche CJ (2007) MRI evaluation and measurement of the normal odontoid peg position. Clin Radiol 62:897–903

Cronin CG, Lohan DG, Mhuircheartigh JN, Meehan CP, Murphy JM, Roche CJ (2009) CT evaluation of Chamberlain's, McGregor's, and McRae's skull base lines. Clin Radiol 64:64–69

Damiani D, Borelli NS (2012) Morphometry and spatial correlation of the foramen magnum and spinal cord through the magnetic resonance in normal young adults—anatomical and clinical aspects. J Morphol Sci 29(2):87–90

Deliganis AV, Baxter AB, Hanson JA (2000) Radiologic spectrum of craniocervical distraction injuries. Radiographics 20:S237–S250

Dimeglio A (2011) Normal growth of the spine and thorax. In: Akbarnia BA, Yazici M, Thompson GH (eds) The growing spine. Springer, Berlin, p 28

Dvorak J, Grob D, Baumgartner GN, Grauer W, Larsson S (1989) Functional evaluation of the spinal cord by MRI in patients with rheumatoid arthritis and instability of the upper cervical spine. Spine 14:1057–1064

Dziurzynski K, Anderson PA, Bean DB, Choi J, Leverson GE, Marin RL, Resnick DK (2005) A blinded assessment of radiographic criteria for atlanto-occipital dislocation. Spine 30:1427–1432

Eubanks AC, Hipp A, Lador R, Ben-Galim PJ, Reitman CA (2010) Reference data for assessing widening between spinous processes in the cervical spine and the responsiveness of these measures to detecting abnormalities. Spine J 10:230–237

Fisher CG, Sun JC, Dvorak M (2001) Recognition and management of atlanto-occipital dislocation : improving survival from an often fatal condition. Can J Surg 44:412–420

Frobin W, Leivsith G, Biggemann M (2002) Vertebral height, disc height, posteroanterior displacement and dens-atlas gap in the cervical spine: precision measurement protocol and normal data. Clin Biomech 17:423–431

Harris JH Jr, Carson GC, Wagner LK, Kerr N (1994) Radiologic diagnosis of traumatic occipitovertebral dissociation: 2. Comparison of three methods of detecting occipito-vertebral relationships on lateral radiographs of supine subjects. AJR 162:887–892

Heller JG, Viroslav S, Hudson T (1993) Jefferson fractures: the role of magnification artefact in assessing transverse ligament integrity. J Spinal Disord 6:392–396

Herzog RJ, Wiens JJ, Dillingham MF, Sontag MJ (1991) Normal cervical spine morphometry and cervical spinal stenosis in asymptomatic professional football players: plain film radiography, multiplanar computed tomography, and magnetic resonance imaging. Spine 16:178–186

Hinck VC, Hopkins CE, Savara BS (1960) Measurement of the atlanto-dental interval in the adult. Am J Roentgenol Radium Ther Nucl Med 84:945–951

Holmes A, Wang C, Han ZH, Dang GT (1994) The range and nature of flexion-extension motion in the cervical spine. Spine 19(22):2505–2510

Holsheimer J, den Boer JA, Struijk JJ, Rozeboom AR (1994) MR assessment of the normal position of the spinal cord in the spinal canal. Am J Neuroradiol 15:951–959

Ishikawa M et al (2003) Changes of cervical spinal cord and cervical spinal canal with age in asymptomatic subjects. Spinal Cord 41:159–163

Kanodia G, Parihar V (2012) Morphometric analysis of posterior fossa and foramen magnum. J Neurosci Rural Practice 3(3):261–266

Kaufman RA, Carroll CD, Buncher CR (1987) Atlanto-occipital junction: standards for measurement in normal children. Am J Neuroradiol 8:995–999

Keats TE, Sistrom C (2001) Atlas of radiologic measurement, 7th edn. Mosby, St. Louis

Khanapurkar SV, Kulkarni DO, Bahetee BH, Vahane MI (2014) MRI study on spinal canal content in western Maharashtrian population. Int J Med Res Health Sci 3(3):610–614

Knopp R, Parker J, Tashijan J, Ganz W (2001) Defining radiographic criteria for flexion-extension studies of the cervical spine. Ann Emerg Med 38(1):31–35

Lee C, Woodring JH, Goldstein SJ, Daniel TL, Young AB, Tibbs PA (1987) Evaluation of traumatic atlantooc-cipital dislocations. Am J Neuroradiol 8:19–26

Locke GR, Gardner JI, Van Epps EF (1966) Atlas-dens interval (ADI) in children: a survey based on 200 normal cervical spines. Am J Roentgenol Radium Ther Nucl Med 97:135–140

Lovelock JE, Schuster JA (1991) The normal posterior atlanto-axial relationship. Skelet Radiol 20(2):121–123

Markuske H (1977) Sagittal diameter measurements of the bony cervical spinal canal in children. Pediatr Radiol 6:129–131

Martinez-Lozano AG (2001) Radiographic measurements, appendix C. In: Weinstein SL (ed) The paediatric spine, principles and practice, 2nd edn. Lippincott Williams and Wilkins, Philadelphia, pp 965–999

Matar LD, Doyle AJ (1997) Prevertebral soft tissue measurements in cervical spine injury. Australas Radiol 41(3):229–237

Matsura P, Waters RL, Adkins RH, Rothman S, Gurbani N, Sie I (1989) Comparison of computerized tomography parameters of the cervical spine in normal control subjects and spinal cord-injured patients. J Bone Joint Surg Am 71(2):183–188

McManners T (1983) Odontoid hypoplasia. Br J Radiol 56(672):907–910

Monu J, Bohrer SP, Howard G (1987) Some upper cervical spine norms. Spine 12(6):515–519

Murone I (1974) The importance of the sagittal diameters of the cervical spinal canal in relation to spondylosis and myelopathy. J Bone Joint Surg 56-B:30–36

Naderi S, Cakmakci H, Acar F, Arman C, Mertol T, Arda MN (2003) Anatomical and computed tomographic analysis of C1 vertebra. Clin Neurol Neurosurg 105:245–248

Naidich JB, Naidich TP, Garfein C, Liebeskind AL, Hyman RA (1977) The widened interspinous distance: a useful sign of anterior cervical dislocation in the supine frontal projection. Radiology 123:113–116

Naik DR (1970) Cervical spinal canal in normal infants. Clin Radiol 21:323–326

Ogino H, Tada K, Okada K, Yonenobo K, Yamamoto T, Ono K, Namiki H (1983) Canal diameter, anteroposterior compression ratio and spondylotic myelopathy of the cervical spine. Spine 8:1–15

Okada Y, Ikata T, Katoh S, Yamada H (1994) Morphological analysis of the cervical spinal cord, dural tube, and spinal canal by magnetic resonance imaging in normal adults and patients with cervical spondylotic myelopathy. Spine 19(20):2331–2235

Ono K, Ota H, Tada K, Yamamoto T (1997) Cervical myelopathy secondary to multiple spondylotic protrusion: a clinico-pathologic study. Spine 2:109–125

Pavlov H, Torg JS, Robie B, Jahre C (1987) Cervical spinal stenosis: determination with vertebral body ratio method. Radiology 164(3):771–775

Pennecot GF, Gouraud D, Hardy JR, Pouliquen T (1984) Roentgenographical study of the stability of the cervical spine in children. J Pediatr Orthop 4:346–352

Penning L (1981) Prevertebral hematoma in cervical spine injury; incidence and etiologic significance. Am J Roentgenol 136:553–561

Penning L, Wilmink JT, van Woerden HH, Knol E (1986) CT myelographic findings in degenerative disorders of the cervical spine: clinical significance. Am J Roentgenol 146:793–801

Pfirrmann CW, Binkert CA, Zanetti M, Boos N, Hodler J (2000) Functional MR imaging of the craniocervical junction. Correlation with alar ligaments and occipito-atlantoaxial joint morphology: a study in 50 asymptomatic subjects. Schweiz Med Wochenschr 130(18):645–651

Poppel MH, Jacobson HG, Duff BK, Gottlieb C (1953) Basilar impression and platybasia in Paget's disease. Radiology 61:639–644

Powers B, Miller MD, Kramer RS et al (1979) Traumatic atlanto-occipital dislocation. Neurosurgery 4:12–17

Ranawat CS, O'Leary P, Pellici P (1979) Cervical spine fusion in rheumatoid arthritis. J Bone Joint Surg Am 61:1003–1010

Redlund-Johnell I, Pettersson H (1984) Radiographic measurements of the craniovertebral region. Acta Radiol Diagn 25:23–28

Riew KD, Hilibrand AS, Palumbo MA, Sethi N, Bohlman HH (2001) Diagnosing basilar invagination in the rheumatoid patient. The reliability of radiographic criteria. J Bone Joint Surg Am 83-A:194–200

Roche C, Carty H (2001) Spinal trauma in children. Pediatr Radiol 31:677–700

Roche CJ, Eyes BE, Whitehouse GH (2002a) The rheumatoid cervical spine: signs of instability on plain cervical radiographs. Clin Radiol 57:241–249

Roche CJ, King SJ, Dangerfield P, Carty HM (2002b) The Atlanto-axial joint: physiological range of rotation on MRI and CT. Clin Radiol 57:103–108

Rojas CA, Bertozzi JC, Martinez CR, Whitlow J (2007) Reassessment of the craniocervical junction: normal values on CT. Am J Neuroradiol 28:1819–1823

Rojas CA, Vermess D, Bertozzi JC, Whitlow J, Guidi C, Martinez CR (2009) Normal thickness and appearance of the prevertebral soft tissues on multidetector CT. Am J Neuroradiol 30:136–141

Schmeltzer A, Babin E, Wenger JJ (1971) Foramen magnum in children: measurement of the anteroposterior diameter on midsagittal pneumotomograms. Neuroradiology 2:162–163

Sherman JL, Nassaux PY, Citrin CM (1990) Measurements of the normal cervical spinal cord on MR imaging. Am J Neuroradiol 11:369–372

Spence KR Jr, Decker S, Sell KN (1970) Bursting atlantal fracture associated with rupture of the transverse ligament. J Bone Joint Surg Am 52:543–548

Sun PP, Poffenberger GJ, Durham S, Zimmerman RA (2000) Spectrum of occipitoatlantoaxial injury in young patients. J Neurosurg 93:28–39

Sussex RA, Zimmerman RD, Leeds NE (1983) Pseudospread of the atlas: false sign of Jefferson fracture in young children. Am J Roentgenol 140:1079–1082

Suzuki M, Shimamura T (1994) Morphological study of the axial view of the cervical spinal cord by MR images. J Jap Orthop Assoc 68:1–13

Templeton PA, Young JW, Mirvis SE, Buddemeyer EU (1987) The value of retropharyngeal soft-tissue measurements in trauma of the adult cervical spine. Cervical spine soft tissue measurements. Skelet Radiol 16(2):98–104

Thiebaut F, Wackenheim A, Vrousos C (1961) New median sagittal pneumostratigraphical finding concerning the posterior fossa. J Radiol Electrol Med Nucl 42:1–7

Thijssen HOM, Keyser A, Horstink MW, Meijer E (1979) Morphology of the spinal cord on computed myelography. Neuroradiology 18:57–62

Ulbrich EJ, Schraner C, Boesch C, Hodler J, Busato A, Anderson S, Eigenheer S, Zimmermann H, Sturzenegger M (2014) Normative MR cervical spine canal dimensions. Radiology 271:172–182

Wang JC, Nuccion SL, Feighan JE, Cohen B, Dorey FJ, Scoles PV (2001) Growth and development of the paediatric cervical spine documented radiographically. J Bone Joint Surg Am 83-A(8):1212–1218

Weinstein SL (2001) The paediatric spine, principles and practice, 2nd edn. Lippincott Williams and Wilkins, Philadelphia, pp 965–999

Yousefzadeh DK, El-Khoury GY, Smith WL (1982) Normal sagittal diameter and variation in the pediatric cervical spine. Radiology 144:139

Thoracolumbar Spine

7

Naomi Winn, Eva Llopis,
and Victor N. Cassar-Pullicino

Contents

N. Winn • V. N. Cassar-Pullicino
Department of Radiology, Robert Jones and Agnes
Hunt Orthopaedic Hospital NHS Foundation Trust,
Oswestry, UK
e-mail: naomi.winn@rjah.nhs.uk

E. Llopis (✉)
Hospital Universitario de La Ribera,
Alzira, Valencia, Spain
e-mail: ellopis@hospital-ribera.com

7.1 Introduction

The spine is a complex anatomical structure, undergoing huge developmental changes from birth to attain skeletal maturity. At birth the spine is predominantly cartilaginous, with 30% ossification. The primary ossification centres in each vertebra expand to demarcate the parallel growth plates, which then contribute to cranio-caudal growth under normal physiological stresses. Interstitial growth in the physes accounts for circumferential growth (Debnath 2010). By 5 years of age, 65% of the spine is ossified, and the spinal canal capacity has reached up to 95% of its final size. The growth velocity is particularly rapid during the first 5 years of life, then slowing towards puberty. From the age of 5 to puberty, the growth of the thoracolumbar spine is in the order of 15 cm, with 2/3 accounted for by the thoracic spine. By age 10, approximately 11 cm of thoracolumbar growth remains for males and 7 cm for females. At the onset of puberty, there is an average of a further 9.5 cm thoracolumbar growth for males and 6.5 cm for females (Bick and Copel 1950). The rate of growth during puberty remains less than the initial growth from birth to age 5.

In neonates the cervical and lumbar lordosis are relatively underdeveloped, with a predominantly straight spine or mild kyphotic curve above a well-demarcated lumbosacral angle. These primary curves are then followed by the development of secondary curves (lumbar and cervical lordosis) from around age 3 onwards. Cil et al. have shown through radiographic assessment that as a child

grows and an upright posture is attained, the axial loading of the spine contributes to the development of the adult-type sagittal curvature, with a neutral coronal and axial-plane curvature (Cil et al. 2004). As a child grows, there is a significant change in total thoracic kyphosis and lumbar lordosis; however, this is not a linear progression. As childhood advances there is an increase in thoracic kyphosis and lumbar lordosis; however, at the time of the adolescent growth spurt, the kyphosis decreases, and the lumbar lordosis continues to increase. During this growth spurt, anterior vertebral growth exceeds posterior growth, resulting in a decrease in the thoracic kyphosis and an increase in the lordosis. The same trend in sagittal alignment has also been shown in studies quantifying clinical and visual assessment of curvature through a pantograph (Giglio and Volpon 2007). Once skeletal maturity is reached, there is a wide variation in the normal values for thoracic kyphosis and lumbar lordosis. Normal values for lumbar lordosis have been determined between 46°–87° (Legaye et al. 1998) and 35°–90° (Jackson et al. 2000a), with a mean of 61° (Guigui et al. 2003). Physiological thoracic kyphosis ranges between 7°–65° (Guigui et al. 2003) and 33°–71° (Legaye et al. 1998), with a mean of 41° (Guigui et al. 2003).

A study by Shefi et al. has shown that the physiological lumbar lordosis in children and adolescents is formed by wedging of the vertebral bodies and intervertebral discs (Shefi et al. 2013). Dorsal wedging of the bodies and discs increases the lordosis angle, and ventral wedging increases the thoracic kyphosis. The intervertebral discs show increased wedging with age, contributing 14° towards the lordosis angle at age 2–4 compared with 35° from 17 to 20 years. In the 2–4 year-old group, the intervertebral discs contribute 47% of the lordosis angle and the vertebral bodies 53%. In the older group, the relationship changes, and the discs contribute towards 80% of the lordosis and the vertebral bodies only 20%. This study shows that the intervertebral discs and vertebral bodies function together as a disco-vertebral unit in the development of physiological sagittal plane curvature.

Dynamic changes with growth influence both sagittal spinal balance and posture. The orientation of each vertebra to gravity alters with growth. Furthermore it is different before and after the adolescent growth spurt. In addition there are significant gender differences which impact on the normal/abnormal development and treatment of adolescent spinal deformity. Thoracic kyphosis gender differences exist with a mean value of 34+/− 9° in boys compared with 32+/−10° in girls. This gender difference is maximal at the peak of the growth spurt, with girls exhibiting significantly lower thoracic kyphosis values due to the growth spurt starting about 1.4 years earlier in girls. Sagittal parameters including thoracic kyphosis and lumbar lordosis in isolation are of limited value in the assessment of spinal loading as the same value of thoracic kyphosis may have different positions related to gravity. Dubousset introduced the "pelvic vertebra" concept stressing that this transitional area between the spine and hips needs to be taken into consideration in the evaluation of sagittal spinal balance. Global analysis of lumbar-pelvic-femoral balance needs to be done in the erect posture to allow an assessment of the reciprocal contribution of each of these segments in achieving a stable standing position. This is done on spino-pelvic radiographs in the erect posture. Sagittal spinal alignment therefore requires three spinal (cervical lordosis (CL), thoracic kyphosis (TK), lumbar lordosis (LL)) and three pelvic (pelvic incidence (PI), pelvic tilt (PT), sacral slope (SS)) parameters. Mac-Thiong et al. described normal paediatric spino-pelvic parameter values, while Lee et al. provided values in asymptomatic children in stratified age groups (CL 4.8°, TK 33.2°, LL 48.8°, PI 43.9°, SS 34.9°). Mac-Thiong et al. extensively researched sagittal alignment of the spine and pelvis and have shown that PI, PT, LL and TK increase with age through childhood and adolescence before stabilising and are significantly increased at the end of puberty. PI remains constant in adulthood governing the ideal spino-pelvic morphology and does not change in the standing or sitting postures. Sacral slope generally does not change after 3 years of age. The combination of a stable sacral slope and an increase in lordosis is postulated to give rise to a dorsal shift in the C7 plumb line as a child grows, to allow a stable sagittal alignment (Cil et al.

2004). The three pelvic parameters are closely related whereby PI = PT + SS. As the SS is stable, the increase in PI that takes place with growth is therefore due to a PT increase. The sagittal vertical axis (SVA) is defined as the linear horizontal distance between the C7 plumb line which originates in the centre of C7 vertebral body and the posterior corner of the S1 endplate. If the SVA is posterior, it is designated negative, and if it is anterior to the posterior corner of S1, it is designated positive. The spino-pelvic structures are continually adjusting the posture to ensure that the C7 plumb line falls through or within 2 cm anterior or posterior of the posterior corner of S1. The ideal sagittal balance is therefore expected to have a SVA of <5 cm and a PT of <25°, with major sagittal malalignment defined as an SVA > 5 cm.

The growing vertebra responds to loading, with the Hueter-Volkmann law indicating that growth is inversely proportional to the mechanical stress sustained (Castro 2003). No spinal deformity exists in a single plane alone and is a combination of coronal and sagittal deviation. The concept of imbalanced stresses is one theory proposed for the development of adolescent idiopathic scoliosis (AIS). A slight neuromuscular imbalance is further compounded by a growth response of the vertebra to the altered mechanical loading, thus perpetuating any scoliosis. The vertebrae on the convex side of the scoliosis are mechanically loaded to a greater extent than the vertebrae on the concave side and thus undergo less growth, further compounding the curvature through differential growth. In females with AIS, the increased dorsal vertebral inclination is due to the relative anterior vertebral overgrowth. Indeed it is the vertebral height growth that accounts almost exclusively for spinal growth in AIS and not the intervertebral disc height growth in patients between 10 and 20 years of age. The perturbation in normal physiological stresses can lead to altered vertebral development also in spondylolysis. This was first proposed by Farfan et al. in 1978, whereby a chronic spondylolysis gives rise to less pronounced growth of the posterior aspect of L5 vertebral body compared with the anterior aspect and corresponding overgrowth of the pars interarticularis (Farfan et al. 1976).

The lumbar index (see later) is reduced, and this becomes relevant clinically helping to differentiate a chronic spondylolysis from acute traumatic pars fractures.

Quantifying normal variation in the shape of vertebrae is important to be able to appreciate pathology. This has particular importance in assessing vertebral fractures in osteoporosis and trauma (Oei et al. 2013; Black et al. 1991; O'Neill et al. 1994). Studies have shown a normal variance in vertebral morphology, as determined by the vertebral height ratio. Generally, the anterior vertebral height is slightly less than the posterior vertebral height, in particular in the thoracic spine. At T7 the ratio of anterior-posterior vertebral height is 0.860 compared with 0.929 at T12, 0.962 at L1 and 1.037 at L4. The relationship between anterior and posterior vertebral height was studied by Black et al. (Black et al. 1991). A graph has been plotted from their data (Graph 7.1). This shows that the anterior vertebral height is less than the posterior vertebral height in the thoracic spine, with the difference gradually decreasing caudally along the spine to L4. Females have smaller anterior and central vertebral height ratios compared with males, with significant differences in the same values between populations (O'Neill et al. 1994). Thus, vertebral morphological data are population and gender specific (Lau et al. 1996).

The facet joints are paired posteriorly located synovial joints throughout the spine. The width of the articular cartilage is 2.5–4 mm and the cartilage is always thicker at the centre of the joint. The sagittal alignment of the facet joints determines the degree of movement of the joints. In the lumbar spine they usually assume a more coronal orientation from proximal to distal with the sagittally orientated joints allowing a greater range of flexion while preventing significant rotational instability. The facet capsule also has a role in limiting excessive joint motion. The facet joint capsule is normally 1 mm thick and attaches 2 mm from the articular margins. It is increasingly being recognised that the sagittal orientation of the lumbar facet joints is an important determinant for the risk of developing degenerative spondylolisthesis. Patients with narrow facet angles less than 78° have a

2.5 times higher risk of developing degenerative spondylolisthesis. The facet joint angles can be determined from axial CT or MRI images. A coronal reference line passing tangential to the posterior outline of the disk perpendicular to the spinous process at the level of interest is first drawn. Respective facet joint lines are then drawn passing through the anteromedial and posterolateral margins of the joints. This also allows a calculation of the degree of facet joint tropism. Facet joint tropism is the asymmetry between the right and the left facet joint angles when one joint has a predominant sagittal orientation than the other. Asymmetry of the facet joints occurs in 25–32% of individuals. An increased severity of facet joint tropism at the L4–L5 has been associated with a significantly higher risk of developing symptomatic disk herniation at that level. This occurs on the side of the more obliquely orientated facet joint. The normal capacity of a facet joint is not more than 2 mL of joint fluid, which means that larger effusions result from an underlying loss of integrity and abnormal facet joint motion. On T2-weighted MRI images, facet joint effusions with a joint gap greater than 1.5 mm are highly predictive of a degenerative spondylolistheses even if this is not seen on supine MRI. In these circumstances standing lateral flexion/extension radiographs will demonstrate the degenerative spondylolistheses. A facet–fluid index has been developed which is the sum of the facet fluid width divided by the sum of the facet width. There is a positive linear correlation between this facet–fluid index and the anterior percentage spondylolisthesis seen at the L4–L5 level. This positive predictive value of the facet fluid at the L4–L5 level correlates with radiographic instability in the order of 82%.

This chapter explores measurements in the adolescent and adult spine, with reference to their clinical utility.

Graph 7.1 Graph showing the variance of anterior and posterior vertebral heights at different spinal levels
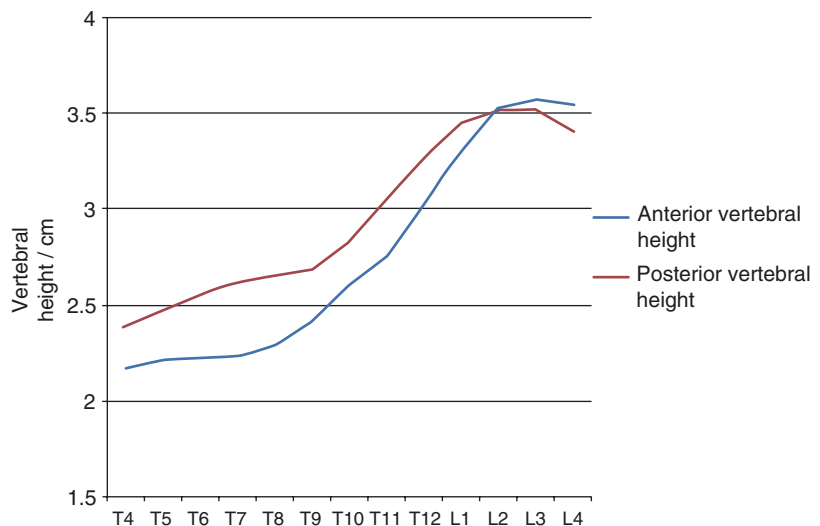
7.2 Lumbar Intervertebral Disc Height

Definition

The cranio-caudal length of the intervertebral disc, measured at either the dorsal or ventral aspect.

Full Description of Technique

On a standing lateral radiograph, the four corners of the vertebra are determined, and the cranio-caudal midpoint is noted. A line bisecting the dorsal and ventral midpoints for two adjacent vertebrae is drawn, and then a further line bisecting the distance between these two lines is drawn and designated as the bisectrix. The disc height is determined by the sum of the distance between the bisectrix and the perpendicular for the anterior (or posterior) vertebral corners as described by Shao et al. (2002) (Fig. 7.1).

Reproducibility/Variation

The disc height is subject to changes in lumbar lordosis and potentially positioning, which can be accounted for using adjustment factors (Frobin et al. 1997).

Clinical Relevance/Implications

Studies have shown that disc height increases from L1–2 caudally to L4–5 and then decreases at L5–S1 or remains static (Pfirrmann et al. 2006; Roberts et al. 1997). In asymptomatic people, disc height increases with age up to the seventh decade and then decreases (Shao et al. 2002; Inoue et al. 1999; Luoma et al. 2001). This is postulated to be secondary to an increase in disc concavity, with resultant increase in disc height as the discal tissue fills the space left by the more pronounced vertebral concavity (Shao et al. 2002).

Fig. 7.1 Lumbar intervertebral disc height: Disc height can be determined both anteriorly and posteriorly by measuring the distance between the bisectrix (*dashed line*) and the corners of the vertebra, shown here as the anterior disc height. The distance from the inferior margin of the cranial vertebra to the bisectrix is added to the distance from the bisectrix to the superior margin of the caudal vertebra to give the total disc height. Usually these two values are equal
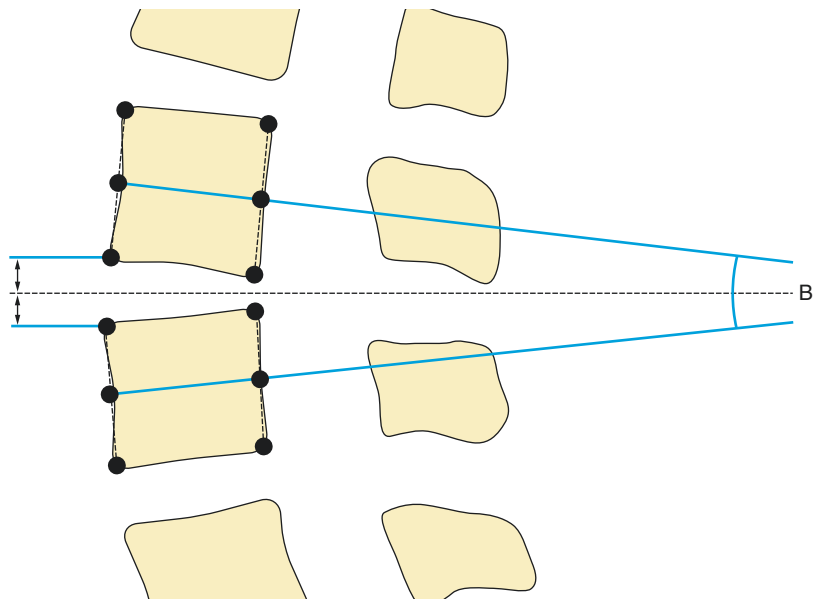
Loss of disc height is known to be associated with disc degeneration, confirmed in studies comparing MRI and radiography (Roberts et al. 1997; Luoma et al. 2001; Tibrewal and Pearcy 1985; Frobin et al. 2001; Amonoo-Kuofi 1991). A study by Luoma et al. demonstrated that early disc degeneration is not necessarily correlated with loss of disc height on radiographs, and a decrease in T2 signal on MRI is a better indicator. MRI can therefore detect disc pathology prior to the radiographic loss of disc height. Surgical discectomy decreases disc height and is associated with disc degeneration. Knowledge of normal disc height, therefore, is necessary to appreciate changes with pathology.

7.3   Interpediculate Distance

Definition

The distance between the narrowest point of the pedicles, as viewed on a frontal radiograph or coronal plane on cross-sectional imaging.

Indications

Knowledge of the normal values for interpediculate distance is necessary to appreciate the differences with pathology which can increase, as in chronic space occupation in the spinal canal, or reduce, as in bone dysplasias. The interpediculate distance should increase normally from L1 to L5.

Full Description of Technique

The anteroposterior radiograph is the current gold standard for this measurement. The original reference values were taken from anteroposterior radiographs and have not been extensively reproduced on cross-sectional imaging modalities. On the radiograph, the narrowest point between the medial edge of the pedicles is determined, and the distance is measured on a perpendicular line between the left and right pedicles (Fig. 7.2).

Reproducibility/Variation

As with all radiographic measurements, there are errors introduced by the magnification factor of the image. Errors are introduced by imprecise assessment of the narrowest point between the pedicles, with no defined reference marker to take this measurement from. Inter and intra-observer variation may also introduce error. In addition poor radiographic technique or rotation due to scoliotic deformity also introduces measurement errors.

In 1956 Schwarz measured the interpediculate distance in children and determined the normal values across the different ages in the growing
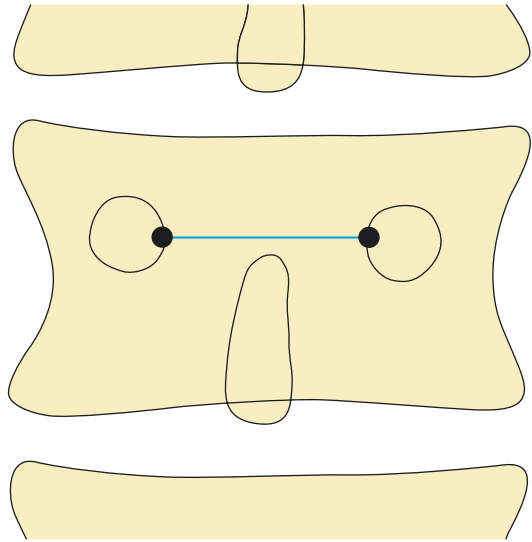
Fig. 7.2 Interpediculate distance: The interpediculate distance is measured on an anteroposterior image as the narrowest point between the medial edge of the pedicles

skeleton (Schwarz 1956). In 1966 Hinck also took the same measurements in a different patient cohort (Hinck et al. 1966). This work was later extended by Larsen in 1981, taking into account the magnification factor of the radiographs (Larsen 1981). The studies all showed a slightly greater distance at all levels between males and females and a gradual increase in value progressing caudally along the lumbar spine. Selected data from Larsen's paper has been plotted as a graph (Larsen 1981) (see Graph 7.2).

Clinical Relevance/Implications

Knowledge of the interpediculate distance in normal subjects is necessary to appreciate abnormalities indicating pathology. For example, usually the interpediculate distance widens progressing caudally along the lumbar spine; however, in achondroplasia, this relationship is reversed with narrowing of the interpediculate distance caudally (Jeong et al. 2006). The interpediculate distance is also affected by the presence of intraspinal tumours, usually widened (Steurer et al. 2011; North American Spine Society 2011). Before the advent of MRI, detecting alteration of the inter-

Graph 7.2 Graph showing the variance of interpediculate distance at different ages across the lumbar levels
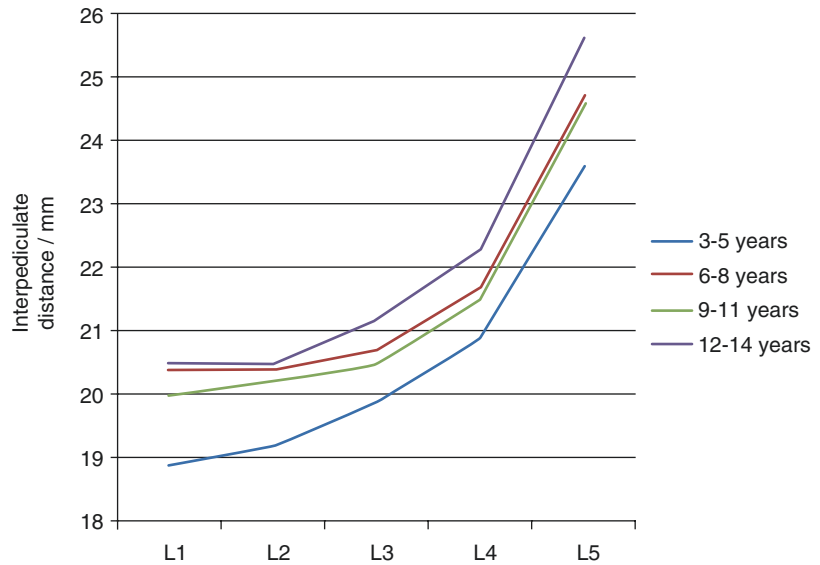
pediculate distance was the mainstay of identifying spinal tumours and remains an important assessment of the radiograph. Occult pathology, such as benign intraspinal tumours or syringomyelia, can present with a scoliosis and assessment of the interpediculate distance is required in the evaluation of scoliosis radiographs. Pathology of the interpediculate distance may also be a feature in spinal dysraphism, and appreciating this radiographic abnormality may be the only feature in occult spinal dysraphism.

7.4   Inter-facetal Distance

Definition

The distance between the inferior articular processes of the facet joints, as measured on the frontal plane.

Indications

Recent studies have shown a relative lack of increase in lumbar facet spacing at L4–5 to be associated with spondylolysis; therefore a knowledge of the normal lumbar inter-facet distance is important to appreciate perturbance in pathology (Zehnder et al. 2009; Ward et al. 2007).

Full Description of Technique

On a frontal radiograph (or equivalent coronal plane on a cross-sectional study), the perpendicular distance between the two inferior articular processes is measured. The distance can be expressed as a ratio compared with the lumbar interpediculate distance or the vertebral width, to standardise for the size of an individual vertebra. Normally the inter-facet distances increase from L1 to L5. When compared with the adjacent inter-facet distance, the ratios in the spondylotic patients are found to be significantly smaller compared with normal (Fig. 7.3).

Reproducibility/Variation

Studies in both adult and paediatric patients have shown a similar trend, with a relative lack of increase in the lumbar facet distance in patients with spondylolysis. The absolute values and ratios have been shown to be different between control and affected groups.
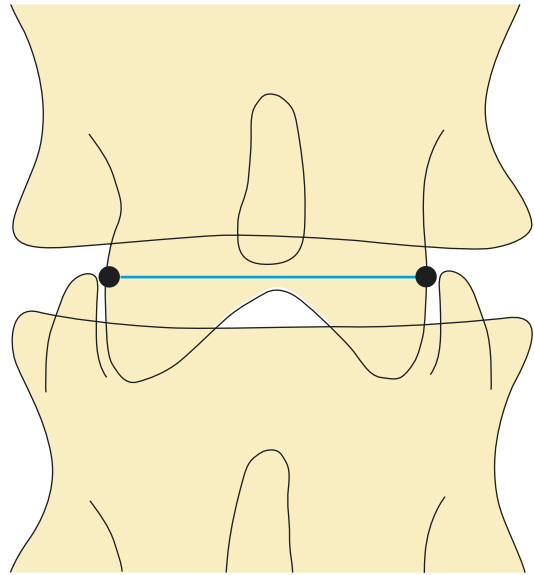
Fig. 7.3 Inter-facetal distance: The inter-facetal distance is the perpendicular measurement between the most lateral point of the two inferior articular processes

Clinical Relevance/Implications

Detection of an abnormal pattern of inter-facet spacing may be useful to help predict if a patient is at risk to develop a spondylolysis. It may also have implications for predicting healing in patients with an established pars defect. Alteration in the orientation of the facet joints is also implicated in the development of a spondylolysis.

Analysis/Validation of Reference Data

The trend has been replicated in both paediatric and adult populations suggesting a genuine finding (Zehnder et al. 2009; Ward et al. 2007); however, this has not been extensively replicated in further studies.

7.5 Lumbar Spinal Stenosis

Definition

A radiological definition of spinal stenosis is narrowing of the spinal canal, which may be associated with clinical symptoms (Steurer et al. 2011). This is distinct from the clinical definition of lower extremity pain, which may occur with low back pain, associated with reduced space for the neural and vascular elements in the lumbar spine (North American Spine Society 2011).

Indications

Lumbar spinal stenosis is the most frequent indication for spinal surgery in the older population. A radiological diagnosis of spinal stenosis which correlates with clinical signs and symptoms can guide surgery and further management.

Multiple different measurements can be made in the assessment of degenerative lumbar spinal stenosis. In general reporting of CT and MRI of the lumbar spine, in practical terms semi-quantitative assessment is acceptable in describing the presence and extent of spinal stenosis. Of the methods available for quantitative assessment, the AP diameter and thecal cross-sectional area are the two more often employed.

1. Anteroposterior Diameter of the Osseous Spinal Canal

Full Description of Technique

This measurement can be made on CT, MRI or CT myelography. On MRI, one described method is to take the midline sagittal image and measure between the posterior aspect of the mid-vertebral body and the anterior aspect of the posterior neural arch (Herzog et al. 1991). This measurement may also be taken in a similar manner from a sagittal CT-reconstructed image.

The anteroposterior diameter of the canal may be measured on both CT and MRI axial images, taking the measurement at the mid-
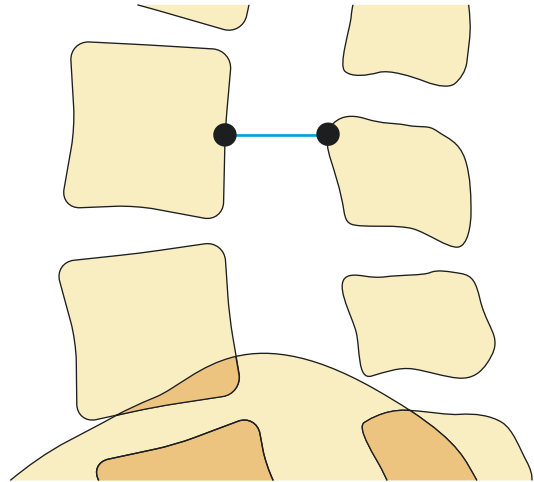
Fig. 7.4 Anteroposterior diameter of the canal: This measurement is taken from a midline sagittal image, at the narrowest portion of the canal and perpendicular to the posterior edge of the vertebral body

body of each vertebra and measuring to the confluence of the lamina (Herzog et al. 1991) (Figs. 7.4 and 7.5).

Reproducibility/Variation

The numerical value for defining stenosis by the anteroposterior canal dimension shows a wide variation between studies. On MRI, this has been defined as 12 mm (Koc et al. 2009), 15 mm (Fukusaki et al. 1998) and the range of values between these (Eisenstein 1977; Guen et al. 2011). Most papers denote relative spinal stenosis being between 10 and 12 mm and absolute spinal stenosis as <10 mm (Kalichman et al. 2009). Some of the first studies using CT showed significant interobserver variation in measuring the midline sagittal diameter of the canal (Beers and Carter 1985). In order to address the difficulties with measurement reproducibility, Herzog proposed using percentage compression of the thecal sac in comparison with the normal mid-sagittal diameter rather than absolute measurements (Herzog et al. 1991). Thus, there is no consensus as the value for relative spinal stenosis, with most authors agreeing that an anteroposterior dimension of <10 mm constitutes absolute spinal stenosis.
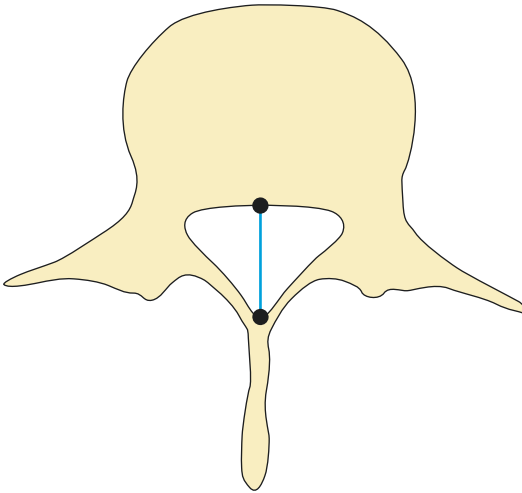
Fig. 7.5 Anteroposterior diameter of the canal: The measurement can also be taken from an axial image, with the measurement taken perpendicular to the posterior margin of the vertebral body and to the confluence of the lamina at the midpoint of the vertebral body

2. Cross-sectional Area of the Thecal Sac

Full Description of Technique

Cross-sectional area of the thecal sac is a further measurement of spinal stenosis and can be made on CT, MRI or CT myelography. At the level of the intervertebral disc, a region of interest is drawn around the thecal sac, and the cross-sectional area can be computed by most commercially available PACS software (Fig. 7.6).

Reproducibility/Variation

Similar to measuring the anteroposterior dimensions of the osseous spinal canal, there is a range of measurements quoted in the literature. Generally, <70 mm^2 is taken to represent severe spinal stenosis (Mamisch et al. 2012; Quint et al. 1988) and >145 mm^2 within normal range (Guen et al. 2011; Quint et al. 1988; Lisai et al. 2001).

3. Ligamentous Inter-facet Distance

Full Description of Technique

This measurement can be made on both CT and MRI. It is the distance between the inner surfaces
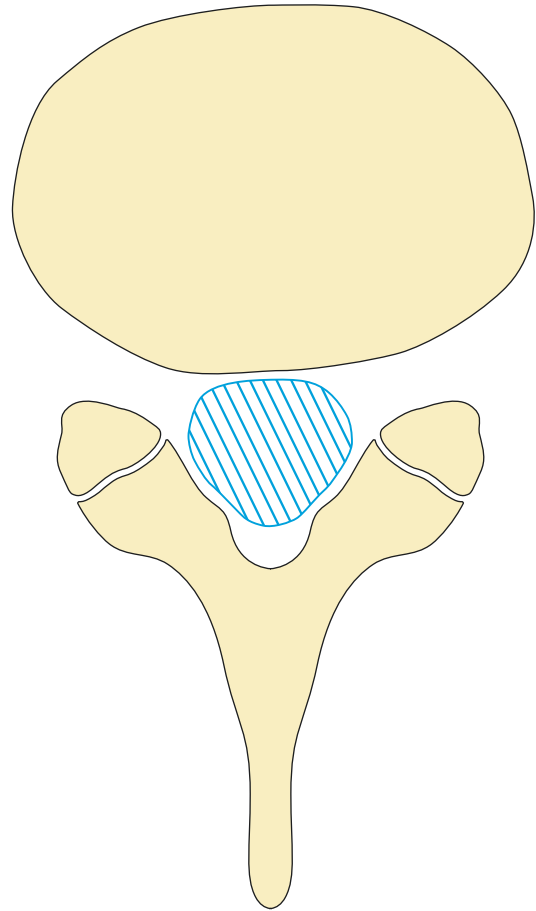
Fig. 7.6 Cross-sectional area of the thecal sac: This is measured at the level of the intervertebral disc by drawing a region of interest around the thecal sac

of the ligamentum flavum on a line connecting the joint space of the facet joints at the level of the intervertebral disc (Fig. 7.7).

Reproducibility/Variation

The measurements in the literature to define stenosis are <10 mm at L2–3, <10 mm at L3–4, <12 mm at L4–5, <13 mm at L5–S1 (Beers and Carter 1985; Wakerley et al. 2011), <16 mm (Ullrich et al. 1980) and <15 mm (Koc et al. 2009). Ligamentous inter-facet distance is quoted in relatively few papers, owing to its poor reproducibility, likely owing to the difficulty in adequately visualising the ligamentum flavum on CT.
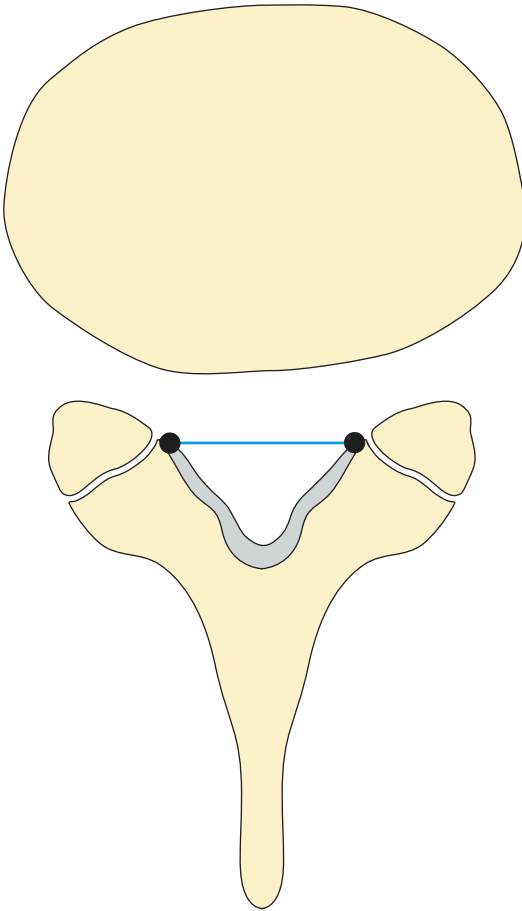
Fig. 7.7 Ligamentous inter-facet distance: This measurement is taken at the level of the facet joint and is the distance between the anterior limits of the ligamenta flava, parallel to the posterior margin of the vertebral body

4. Transverse Diameter of the Spinal Canal

Full Description of Technique

This measurement can be taken at the upper, middle and lower zones of the vertebral bodies and the disc space (Fig. 7.8).

Reproducibility/Variation

<15 mm is taken to represent stenosis (Koc et al. 2009; Ullrich et al. 1980). This measurement is infrequently used in the literature and is not fully validated. Furthermore, one study shows that the transverse diameter of the canal is not consistent between racial groups (Amonoo-Kuofi et al. 1990) and thus not reliable between populations.

Reproducibility/Variation

All of the above described measurements are subject to error in equipment and observer. The interobserver and intra-observer reproducibility for many of the measurements is poor (Steurer et al. 2011), as is the consistency of the defined measurements between the studies. Importantly comparing measurements made between CT and MRI introduces variability, and the two modalities are not always directly comparable. For example, the slice thickness for most standard protocol MRI examinations is 4 mm compared with 1 mm for CT, thereby introducing error from image spatial resolution.

Absolute measurements are unlikely to be consistent between different population groups. For example, between Caucasian and Asian populations, there may be a difference purely secondary to average height and skeletal size (Eisenstein 1977).

Most of the papers regarding spinal measurements date from the 1980s and 1990s with relatively few studies published more recently. A paper in Skeletal Radiology from 2011 proposed that a semi-quantitative scale may be more clinically useful rather than absolute measurements (Guen et al. 2011), hence negating any inaccuracies secondary to measurement error, different modalities and different population groups.

Clinical Relevance/Implications

The degree of constriction of the spinal canal related to patient's symptoms is a controversial topic; radiographic severity is only weakly associated with clinical symptoms and prognosis. Anatomically, there are two separate types: central stenosis, when there is abnormal narrowing of the main spinal canal, and lateral, when there is lateral recess (subarticular stenosis) or foraminal stenosis. Central canal stenosis is found at the intervertebral level and is caused by hypertrophic
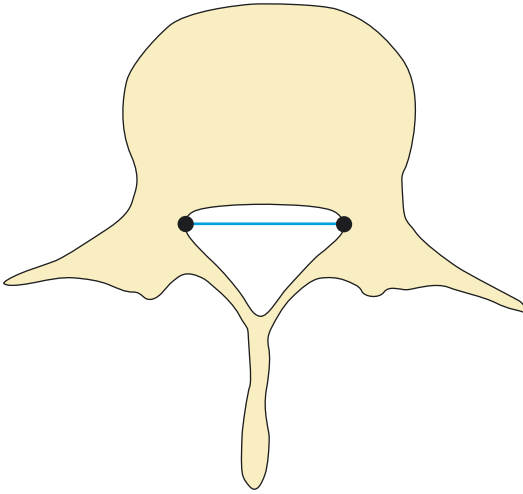
Fig. 7.8 Transverse diameter of the canal: This measurement is taken at the narrowest point of the canal, parallel to the posterior margin of the vertebral body at the midpoint of the vertebral body

facets, ligamentum flavum hypertrophy, disc protrusion or spondylolisthesis. Lateral canal stenosis is another cause of lumbar radicular symptoms, includes nerve root canal or lateral recess, and the intervertebral foramen.

The most accepted measurements are in the midsagittal lumbar canal for absolute stenosis, anteroposterior diameter on myelography or cross-sectional dimension at the level of the intervertebral disc less than 10 mm or 75–80 mm^2 and relative, anteroposterior diameter on myelography between 10 and 12 mm. With dynamic myelographic studies, 10.5 mm anteroposterior diameter is accepted as the lower normal limit. A lateral recess height of 5 mm or more is normal and a height of 2 mm or less is absolutely abnormal, whereas 3–4 mm is suggestive. Unrecognised foraminal stenosis may be the cause of unsuccessful back surgery. Foraminal stenosis is related to the process of lumbar spondylosis and can have two components, transverse stenosis due to the combination of disc space narrowing and overgrowth of structures anterior to the facet joint capsule, and an additional aetiology is craniocaudal or vertical compression from vertebral endplate osteophytes and herniated or bulging disc. MR imaging underestimates root compres-

sion in the lateral recess by up to 26%, so some authors recommend conventional myelography and CT myelography.

Lumbar spinal canal size changes with axial loading and movements. The anatomic relationship of the ligamentum flavum and intervertebral disc to the spinal nerve roots changes too. Lumbar spinal canal size changes with axial loading, decreasing with extension and axial loading and increasing in forward flexion. Therefore if only a supine examination is used, dynamic stenosis might remain undetected. Careful dynamic studies may be required for better evaluation of the central canal and the foramen. Dynamic CT scanning has shown that lumbar flexion increases the size of the central canal by 11% and decreases with extension by 11%. In the foraminal area, a 12% increase occurs with flexion, whereas extension leads to a 15% decrease in the available area. In patients with suspected spinal stenosis, axial loading in extension has shown pathological features not detected in the conventional psoas relaxed examination, and dynamic studies are recommended when the cross-sectional area of the dural sac is smaller than 130 mm^2 or when there is a suspected narrow lateral recess. Dynamic MRI has also been used with axial loading techniques, and although enhancement of the stenosis has been confirmed, it is controversial as to whether this affects clinical decision-making or outcomes.

Lumbar spinal stenosis prevalence increases with age, with an increase in low back pain associated with spinal stenosis (Kalichman et al. 2009). Radiological spinal stenosis is not infrequent in asymptomatic people (Kuittinen et al. 2014), and the imaging appearances do not always correlate with the clinical symptoms. The lack of an accurate definition for lumbar spinal stenosis may explain some of these discrepancies, in particular with reference to inclusion criteria in research trials. A Delphi survey published in 2012 showed that there are no consistent quantitative definitions of spinal stenosis and only partially accepted qualitative criteria (Mamisch et al. 2012). Given the lack of consistency in radiological definition, the North American Spine

Society base their recommendations on both clinical and radiological terms.

5. Epidural Fat

The capacity of the canal can be narrowed by excessive overgrowth of epidural fat, known as epidural lipomatosis. Most cases have been described in patients who have received long-term exogenous steroids for medical management of a chronic disease; however, other cases have been associated with Cushing's disease, hypothyroidism, prolactinoma and morbid obesity (Quint et al. 1988; Lisai et al. 2001; Wakerley et al. 2011; Dumont-Fischer et al. 2002; Fassett and Schmidt 2004; Rajput et al. 2010). Occasionally there is no known predisposing factor—idiopathic epidural lipomatosis. This entity is diagnosed on MRI or CT (on either an axial or sagittal image) when the maximum horizontal thickness of the posterior epidural fat at the site of compression exceeds 7 mm, commonest in the thoracic and lumbar regions (Robertson et al. 1997; Kumar et al. 1996).

7.6   Cobb Angle in Scoliosis

Definition

Cobb originally described measuring angles for the definition of scoliosis in 1948 (Cobb 1948). In order to make this measurement, a number of vertebrae must be defined on the radiograph, as described in Table 7.1.

Indications

The Cobb angle is the accepted standard for diagnosing scoliosis (defined as an angle >10°), monitoring progression of curvature and for therapeutic planning.

Full Description of Technique

The initial evaluation of a patient with suspected spinal deformity is a standing posteroanterior (PA) and full lateral spine film (Fig. 7.9).

Full spine films are obtained using a long cassette 30 × 90°cm or 30× 120°cm at a distance of 180–200 cm. The top of the cassette is placed at the level of the EAC (external auditory canal) and the lower level at the anterior superior iliac crest. Good-quality spinal radiographs will show C7 to the femoral heads and the entire rib cage from right to left. The patient must stand erect barefoot

Table 7.1 Table of definitions in relation to scoliosis measurement

Nomenclature	Definition
End vertebra (cranial and caudal)	Those which are most tilted
Apex	The vertebra most deviated from the centre of the vertebral column, as defined by the central sacral vertical line
Neutral vertebra	One which is not rotated
Stable vertebra	One which is bisected by the central sacral vertical line
Central sacral vertical line	A line perpendicular to a tangent drawn across the iliac crests which bisects the sacrum
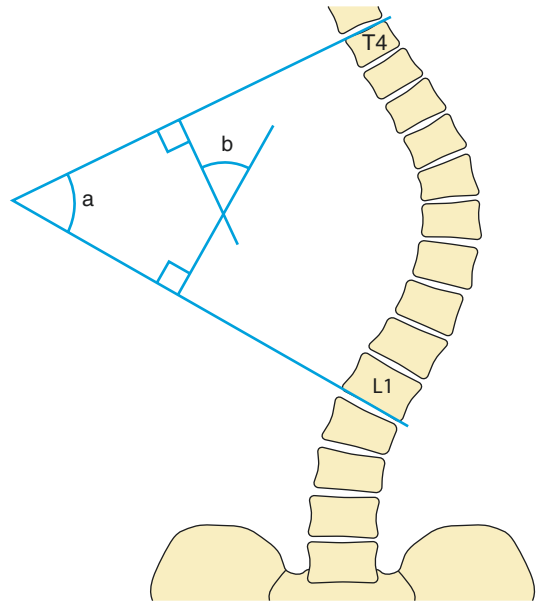
Fig. 7.9 Cobb angle in scoliosis: The Cobb angle is measured by the intersection of the lines parallel to the superior endplate of the superior end vertebra and the inferior endplate of the inferior end vertebra. In this example, T4 is the superior end vertebra, and L1 is the inferior end vertebra. The measurement may also be taken from the angle of intersection of the perpendicular lines, which equates to the same angle if correctly measured; $a = b$

and parallel to the cassette with no rotation, feet and knees together. In the lateral view, the shoulders are flexed 60–80° asymmetrically to allow visualization of the upper thoracic spine. When leg discrepancy has already been diagnosed, the film needs specific blocks beneath the foot on the short side to raise it and make the pelvis level. In the case of impaired patients who cannot tolerate a standing position, the radiograph must be obtained seated. Supine films are limited to patients with congenital scoliosis with complex abnormalities or who cannot be seated.

It is well known that multiple diagnostic radiographic examinations during childhood and adolescence may increase the risk of breast cancer among women with scoliosis. Organ irradiation has a cumulative effect, and the most sensitive organs are the breast, bone marrow and thyroid gland. The breast is especially vulnerable in the formative years, during early breast budding, before the onset of the menarche.

Postero-anterior position reduces the breast dose significantly, a twentieth of the dose of the anteroposterior view. Proper collimation, gonadal shielding and postero-anterior position, as well as minimizing repeat exposures, are essential to reduce radiation.

The Cobb method is the standard method for measuring scoliosis curve magnitude, and treatment guidelines have been established on the basis of its value. Scoliosis is considered to be present when a structural vertebral curve of 10° or greater is measured in the coronal plane radiograph of the erect patient. The management of scoliosis is frequently based on the magnitude of spinal curvature and the extent of the curve progression. Many studies have assumed that the Cobb method provides a reliable measure that allows clinical decisions to be based on differences of 3–5°. Generally, when the angle is mild (up to 20°), careful follow-up is recommended, whereas patients with moderate scoliosis (20–40°) are treated by bracing. Surgical fusion is reserved for severe scoliosis with curves greater than 50°.

The Cobb angle is the angle of intersection of the lines parallel to the superior endplate of the superior end vertebra and the inferior endplate of the inferior end vertebra (Cobb 1948). The measurement may also be taken from the angle of intersection of the perpendicular lines, which equates to the same angle, if correctly measured. The angle may be measured using the tools on commercially available PACS software, using a protractor on printed films or with computer assistance (Greendale et al. 2011; Gstoettner et al. 2007; Wills et al. 2007). Recently, articles have been published detailing how to measure the Cobb angle with a smartphone (Jacquot et al. 2012; Shaw et al. 2012).

Reproducibility/Variation

Multiple factors can affect the measurement of the Cobb angle, ranging from patient-centred factors (biological variance) and equipment (calibration) to the observers (training). The Cobb angle has been shown to vary throughout the day by as much as 5° (Beauchamp et al. 1993) and to differ

by as much as 20° between supine and standing positions (Keenan et al. 2014). Patient positioning between radiographs also has the potential to alter the measured Cobb angle, given the difficulty of obtaining comparable true frontal projections (Göçen and Havitçioglu 2001). Regarding the equipment, the magnification factor between different X-ray rooms may affect the Cobb angle. Variance between modality also has potential to influence the reliability of the measured Cobb angle, for example, between CT and radiography or between MRI and radiography (Malfair et al. 2010). Possibly the factor introducing the greatest measurement error in the Cobb angle is the observer. Multiple studies have shown a large interobserver and intra-observer reliability in measuring the Cobb angle (Gstoettner et al. 2007; Kuklo et al. 2005; Morrissy et al. 1990; Wu et al. 2014). Selection of the end vertebra accounts for some of the poor observer reliability, and this has been shown to improve with pre-determined selection of the end vertebra (Gstoettner et al. 2007; Wills et al. 2007). Computer-assisted measurement may help with reproducibility; however, this technology is not yet reliable enough to replace the input of a trained observer (Wu et al. 2014). Given the difficulties with reproducibility, any measured Cobb angle progression and subsequent surgical decision should be made by the responsible surgeon with the same method and equipment.

Clinical Relevance/Implications

The commonest type of scoliosis is the adolescent idiopathic scoliosis (AIS). A systematic assessment of the radiographs is needed for clinical purposes with documentation of sequential steps which are used in decision-making in the management of scoliosis.

1. Identification of the primary curve: The regional curves are identified by the level and location of the apex; the curve is called thoracic when the apex is found between T2 and T11/T12 intervertebral disc, thoracolumbar when it is located between T12 and L1 and
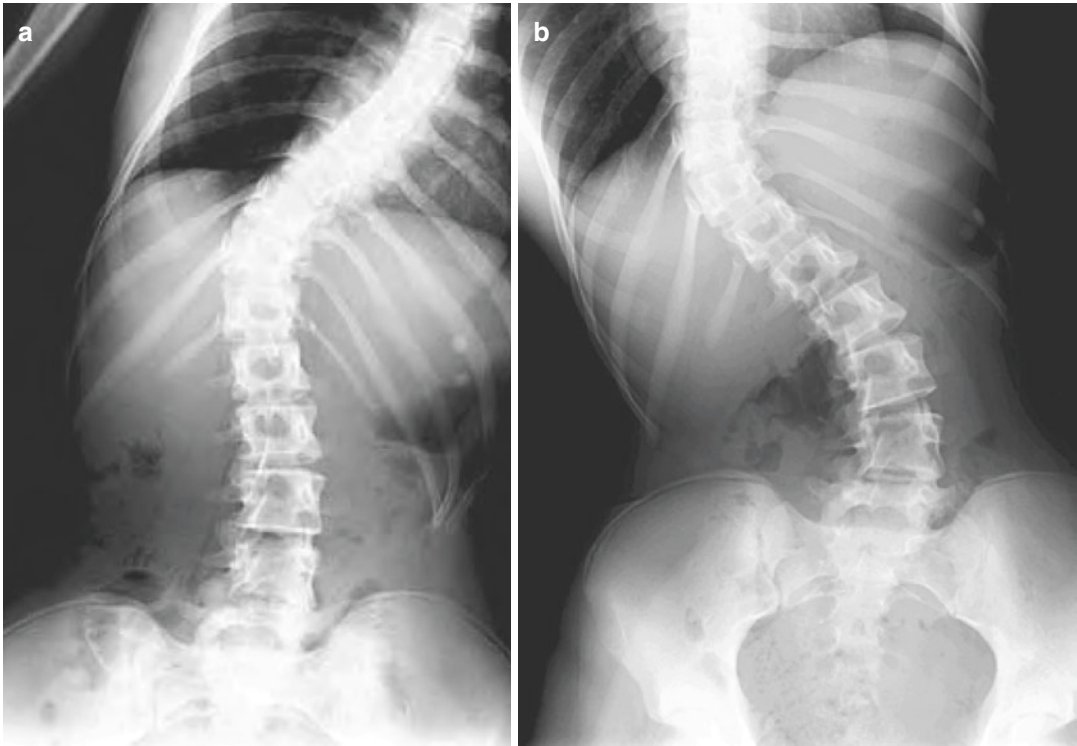
Fig. 7.10 Lateral-bending radiographs: Figure a shows a patient bending to the left. Figure b shows the same patient bending to the right. The thoracic curve does not straighten on bending to the right, making this a fixed or structural curve. The lumbar curve straightens on bending to the left, making this a non-fixed or nonstructural curve

lumbar curve when the apex is between L1 and L2 intervertebral disc to L4.

2. Identification of the main or major curve (largest curve) and minor curves: The minor curves may be structural, i.e. fixed, if they are >25° on the standing PA radiograph and do not bend out to <25° on the side-bending radiographs or if the regional sagittal profile reveals a kyphosis >20° in the standing lateral radiograph (Fig. 7.10).

3. The central sacral line is drawn from the midpoint of S1 upwards measuring its distance to C7 vertebral body in millimetres; alternatively, from C7 vertebral body down to the sacrum can also be measured.

4. Identification of apical vertebra. The apical vertebra is the most deviated from the patient's vertical axis, and one needs to measure the apical translation in proximal thoracic, main thoracic and thoracolumbar/lumbar curves.

5. Shoulder asymmetry, depending on the height of the shoulders, can offer some useful measurements. Shoulder soft tissue shadow measured by the radiographic soft tissue difference can be divided into balanced, i.e. <1 cm, slight 1–2 cm, moderate 2–3 cm or significant >3 cm. The classic radiographic measure has been the T1 tilt angle which is the angle formed between the cephalad endplate of T1 to the horizontal in the coronal plane. However, the best preoperative radiographic prediction of postoperative shoulder balance is the clavicle angle, the angle formed by the tangential apical line connecting the two clavicles (Fig. 7.11).

6. Identification of end, neutral and stable vertebra. End vertebrae are the most tilted vertebrae at the cephalad and caudal end of a curve. The Cobb angle is the angle formed between the superior endplate of the cephalad end vertebra and the inferior endplate of the caudal end

Fig. 7.11 Clavicle angle: The clavicle angle is formed by the intersection of a horizontal line and a line connecting the highest two points of each clavicle. In a non-scoliotic spine, this should be zero

vertebra. The neutral vertebra (NV) is the most cephalad vertebra below the apex of the major curve whose pedicles are symmetrically located within the radiographic silhouette of the vertebral body. The stable vertebra (SV) is the most cephalad vertebra immediately below the end vertebra of the major curve which is most closely bisected by the central sacral line. Curve flexibility views are essential for evaluating the flexibility of a curve to measure the maximal preoperative correction.

Despite the multiple sources of measurement error, the Cobb angle is the accepted standard to define scoliosis, and an increase in the Cobb angle of 5° or more is the definition of curve progression (Cassar-Pullicino and Eisenstein 2002). The Cobb angle may be used to define scoliosis in many aetiologies, including adolescent idiopathic scoliosis and adult onset degenerative scoliosis (Korovessis et al. 1994; Everett and Patel 2007). The Cobb angle also defines structural and nonstructural curves or a curve which forms to compensate for a fixed, structural curve. A structural curve is one which does not reduce to less than 25° on bending views. A nonstructural curve will significantly reduce on bending or supine positioning and therefore has the potential for spontaneous correction following surgical correction of a structural curve (Korovessis et al. 1994).

Adult scoliosis is defined as a lumbar curvature exceeding a Cobb angle of 10° after complete skeletal maturity. Two different types have been described, adolescent scoliosis of the adult—scoliosis during childhood or adolescence that progresses as patient ages—and de novo adult scoliosis, when the deformity develops after skeletal maturity. Studies have proved that adolescent scoliotic curves greater than 50° have a high propensity for progression into adulthood. De novo adult scoliosis is related to progressive disc and posterior osteo-articular-ligamentous degenerative changes. There are important differences from the adolescent deformity, which include pattern of deformity, natural history of progression and development of degenerative changes. Adult scoliosis has some distinct radiographic characteristics. Traditional scoliosis parameters, such as Cobb angle, are less useful in the assessment of adult scoliosis. Adult scoliosis needs assessment over and above the Cobb angle in the coronal plane, with sagittal plane assessment crucial for a global assessment using LL, PT and SVA. Loss of global alignment is important in adult deformity. Sagittal imbalance is significant if the sagittal balance lies anteriorly or posteriorly more than 5 cm from the sacral promontory and coronal imbalance when the C7 plumb line is more than 3 cm either side of central sacral vertical
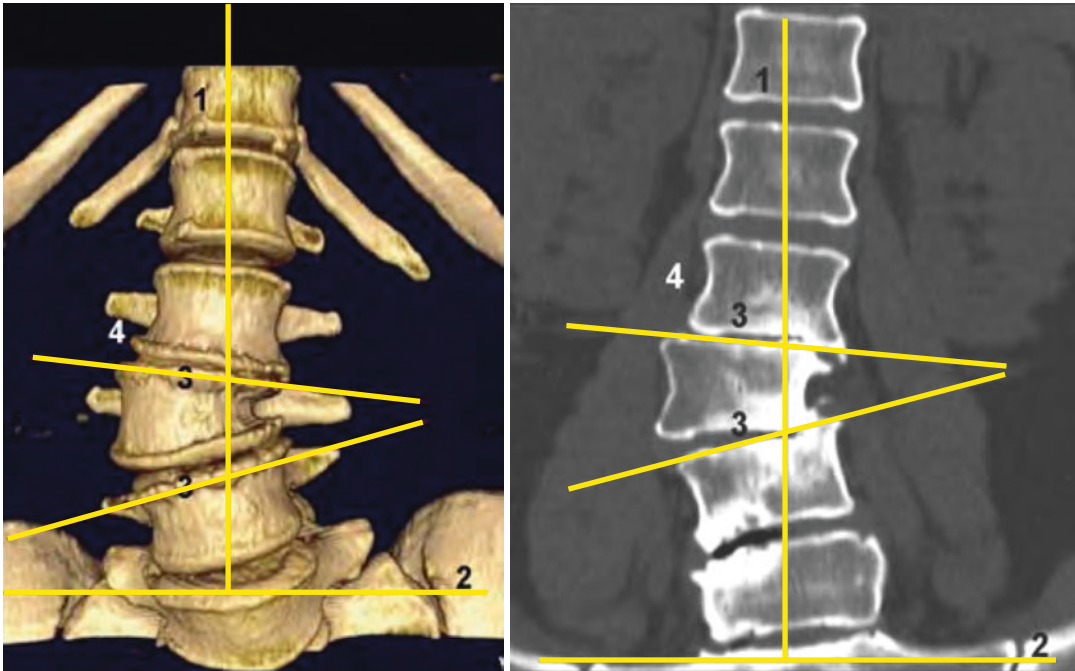
Fig. 7.12 Endplate obliquity: In adult degenerative scoliosis, the measurement of the Cobb angle becomes less useful. Instead, the vertebral endplate obliquity in reference to the horizontal can be measured. A line is drawn across the superior vertebral endplates, and the angle formed with the horizontal can be used to determine the severity of scoliosis. This can be replicated on subsequent radiographs to assess for any disease progression

line. Treatment of fixed sagittal malalignment in adult degenerative scoliosis may need an osteotomy designed to restore global balance such as the pedicle subtraction osteotomy (PSO). There is a relationship between LL and PI, and as the normal LL range is wide and its meaning in isolation of low value, two indices have emerged based on the LL and PI relationship: the **PI-LL index** and the **LL/PI ratio**. Blondel et al. (2012) updated adult scoliosis by adding PI-LL sagittal modification. Sagittal imbalance is immobile in adult scoliosis which leads to compensatory mechanisms to maintain sagittal alignment, which then leads to pelvic retroversion and thoracic kyphosis reduction promoting sagittal malalignment. The normal PI-LL numerical interval is −9 to 9°. A PI-LL mismatch of 11° or more indicates imbalance. It is worth noting however that Schwab found that 33% of patients with a PI-LL mismatch of >11° do not have global imbalance as defined by an SVA >5 cm. In the surgical treatment of scolio-

sis, both the coronal and sagittal deformities need attention. If there is postoperative sagittal imbalance, there is an increased risk of complications due to increased stress on the adjacent non-instrumented segments including flatback, implant failure and proximal junctional kyphosis.

In adults in whom lumbar scoliosis is the principal abnormality, there is rotatory subluxation at L3–L4 and fixed tilt at L4–L5. Rotatory olisthesis is a triaxial deformity consisting of axial rotation on the vertical axis, lateral translation towards the convexity of the curve and anterior translation in the sagittal axis. The most significant radiographic parameters are upper endplate obliquities of L3 and L4, lateral spondylolisthesis between adjacent lumbar vertebra on the frontal plane and vertebral rotation (Fig. 7.12). Ploumis et al. (2006) developed a grading system for lateral rotatory listhesis, based on anteroposterior lumbar spine film and following the Nash and Moe method for verte-

bral rotation grading. Increased lateral translation judged by grading at 5 mm increments is associated with increased intervertebral rotation.

Degenerative lumbar changes are characteristic of adult spinal deformity and are often the cause of presenting clinical symptoms, disc narrowing, facet arthropathy with ligamentum flavum hypertrophy and lateral spondylolisthesis. The radicular leg symptoms on the concavity of the curve could be caused by the traction of neural elements due to rotation and/or translation rather than reduced lateral canal dimensions.

Analysis/Validation of Reference Data

The use of the Cobb angle has been extensively studied and validated, since it was first proposed by Cobb (1948).

Conclusion

Cobb angle measurement is an internationally accepted standard for the assessment of scoliosis while acknowledging the potential for measurement error between different observers, measurement techniques and biological variance.

7.7   Ferguson Angle in Scoliosis

Definition

An alternative measurement of scoliosis, determined by the intersection of the mid-end vertebrae and the apical vertebra.

Full Description of Technique

The centres of the end vertebral bodies are determined using diagonals. The centre of the apical vertebra is best determined in view of morphological deformity by drawing two intersecting lines that bisect the endplates and lateral outlines of the apical vertebral body. The intersection of the diagonals for the superior and inferior end vertebra is determined and also the centre for the apical vertebra (the most deviated from the central sacral line). The Ferguson angle is the angle of intersection of the mid-diagonal point of the two end vertebra and the apical vertebra's centre (Fig. 7.13).

Reproducibility/Variation

The Ferguson angle is not generally used as its reproducibility is limited (Gupta et al. 2007).
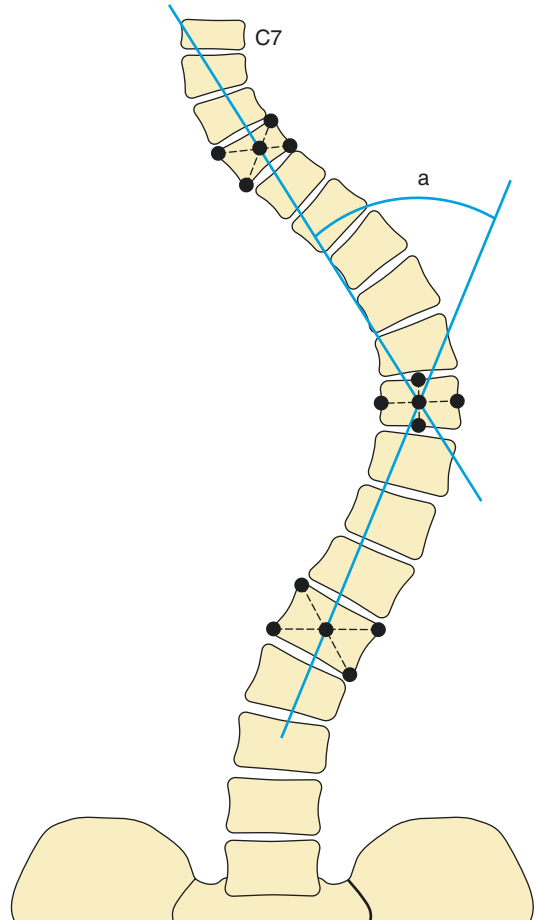
Fig. 7.13   Ferguson angle: The Ferguson angle (*a*) is the angle of intersection of the mid-diagonal point of the two end vertebra and the apical vertebra's centre, determined by the intersection of the perpendicular height and width

7.8   Vertebral Rotation in Scoliosis

Spinal deformity is a 3-D morphological disorder, and its assessment especially before therapeutic decisions are made requires the evaluation of the rotation in the axial plane of the vertebral bodies.

1. Nash and Moe Method

Definition

As scoliosis is a tridimensional deformity, the degree of vertebral rotation needs to be measured. Vertebral rotation is a prognostic factor and is important for planning surgical correction. Several techniques have been described to estimate rotation. The Nash and Moe method grades the rotation by measuring the distance between the pedicle and the lateral side of the vertebral body at the apex in the coronal plane and comparing the convex with the concave side pedicle distance. The degree of rotation of the vertebra away from the neutral position, as viewed from a coronal perspective, is the basis of this method.

Full Description of Technique

The vertebral bodies are viewed on a standing frontal radiograph, and the convex side of the curve is identified. The apical vertebra undergoes the maximal rotational deformity. The half of the vertebra on the convex side is divided into three segments, and the extent of rotation is determined by the position of the convex side pedicle in relation to its position in the segments. In a nonrotated vertebra, the two pedicles are viewed symmetrically. In grade 1, the convex side pedicle migrates within the first segment. In grade 2, the convex pedicle migrates to the second segment. In grade 3 the convex pedicle reaches the middle segment and grade 4 past the midline to the concave side of the vertebral body (Nash and Moe 1969) (Fig. 7.14).

Clinical Relevance/Implications

Nash and Moe studied the radiographic effects of rotating cadaveric vertebra and the relative
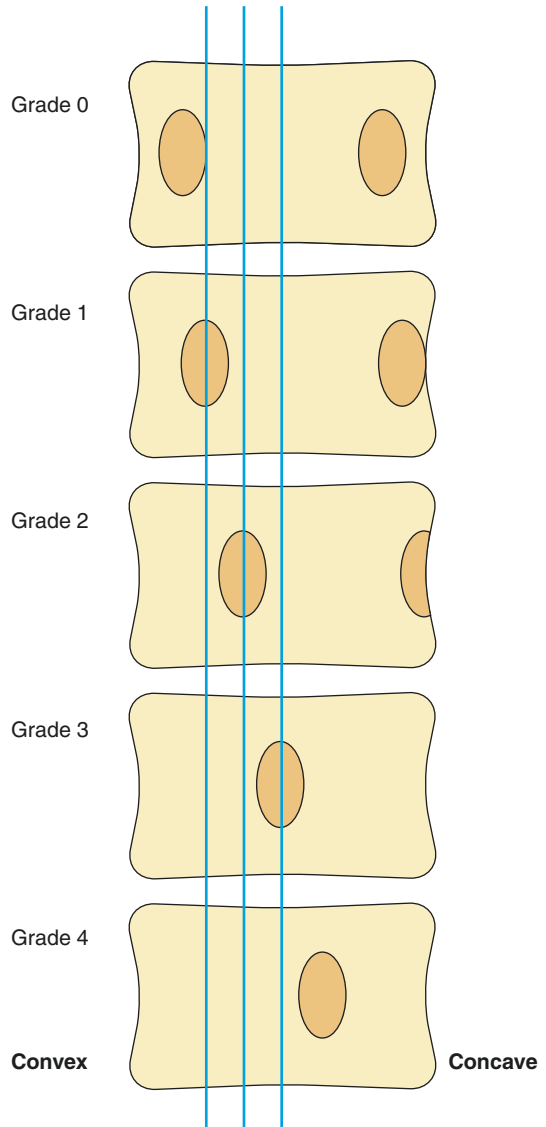
Fig. 7.14 Nash and Moe method of assessing vertebral rotation: The position of the convex side pedicle is viewed in relation to its position against hypothetical segments of the vertebra, as viewed from a frontal radiograph. The half of the vertebra on the convex side is divided into three segments. Grade 0 is a non-rotated vertebra. In Grade 1, the convex side pedicle migrates within the first segment. In Grade 2, the convex pedicle migrates to the second segment. In Grade 3 the convex pedicle reaches the middle segment and in Grade 4, past the midline to the concave side of the vertebral body

positions of the convex pedicles and equated this to degrees of rotation. Regarding the lower thoracic and lumbar vertebra, grade 1 radiographic rotation equates to between 5 and 15°, grade 2 between 15 and 30°, grade 3 20–40° and grade 4

40–50° (Nash and Moe 1969). They found that quantifying rotation according to the convex side pedicle gave a more accurate assessment of rotation compared with the method proposed by Cobb, namely, by comparing the rotation of the spinous process (Cobb 1948).

2. Mehta Rib-Vertebra Angle Difference

Definition

This is a marker of vertebral rotation in infantile scoliosis (children aged less than 3 years) and assesses the relationship of the ribs to the vertebral bodies as a marker of rotation viewed on a frontal radiograph.

Full Description of Technique

In essence Mehta found that differences in the relationship between the rib and vertebral body correlate with infantile scoliosis prognosis. The rib-vertebra angle is calculated by intersecting a line perpendicular to the apical vertebra endplate and a line drawn from the mid head of the rib, and the difference between the concave and the convex angle is the rib-vertebra angle difference (RVAD). It makes it possible to differentiate between progressive scoliosis (>20°) and resolving scoliosis (< 20°).The rib-vertebra angle is the angle formed between the apical thoracic vertebra and its corresponding ribs, with the difference (RVAD) being the subtraction of the smaller from the larger numerical value. A line is drawn along the superior vertebral endplate, the midpoint is determined and a perpendicular line is drawn. Another line is drawn from the midpoint of the head of the rib to the midpoint of the head of the rib neck and extended medially to intersect the line perpendicular to the mid-endplate perpendicular line. This forms the rib-vertebra angle (Mehta 1968) (Fig. 7.15).

Clinical Relevance/Implications

Mehta described a phase 1 and a phase 2 in infantile idiopathic scoliosis. In phase 1 the convex side rib does not overlap the vertebral body on a frontal radiograph, while with phase 2, the convex side rib does overlap the vertebral body. Phase 2 is shown to be a marker of a progressive scoliosis. Within phase 1, the rib-vertebra angle difference values can be a marker for prediction of progressive scoliosis. Mehta showed that the initial rib-vertebra angle difference in resolving curves is smaller than in progressive curves, with a critical difference angle of 20°. An increasing rib-vertebra angle difference on subsequent frontal radiographs at 3 months shows that the curve is progressive, in particular, in those children whose rib-vertebra angle difference at presentation is greater than 20° (Mehta 1968).
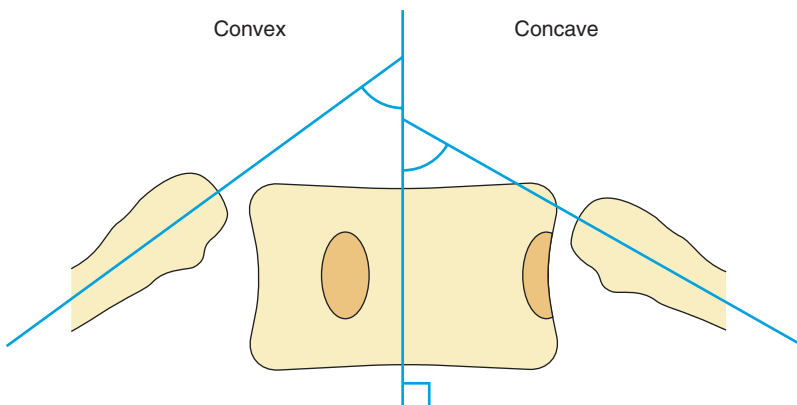
Fig. 7.15 Mehta rib-vertebra angle difference: This is a measure of vertebral rotation in infantile scoliosis. The rib-vertebra angle is calculated by intersecting a line perpendicular to the apical vertebra endplate and a line drawn from the mid head of the rib, and the difference between the concave and the convex angle is the rib-vertebra angle difference. Differences of greater than 20° indicating progressive scoliotic curvature

7.9 Cobb Angle in Kyphosis and Lordosis

Indications

The Cobb angle may also be used to assess kyphosis and lordosis.

Full Description of Technique

The superior endplate of T1 and inferior endplate of T12 are identified and a line drawn along them. The Cobb angle is formed by the angle of intersection of the perpendicular lines (Cobb 1948). In assessing kyphosis, the endplates of T4 and T9 may be chosen to give a more localised assessment or the most tilted vertebra. For lordosis the corresponding endplates of L1 and L5 are used. In common clinical usage, the kyphosis is often measured between T5 and T12 to improve reproducibility (Fig. 7.16).

Reproducibility/Variation

Normal values are quoted between 20 and 40° with an increase with age and a greater kyphosis in females compared with males (Kalichman et al. 2009; Mehta 1968).

The thoracic kyphosis may change with age, spinal disorders and between different populations (Boseker et al. 2000). The angle may also change with positioning; hence it is influenced by radiographic technique. For example, the kyphosis may be different if the radiograph is taken with the patient's arms by their side, holding a support, supine or erect (Boseker et al. 2000) (Fig. 7.17).

With lumbar lordosis, values of 30–80° may be regarded as normal, with the same caveats as for measuring kyphosis. In a normal person, lumbar lordosis is roughly the value for pelvic incidence +9° (North American Spine Society 2011).

Fig. 7.16 Cobb angle in kyphosis: Similar to assessing the Cobb angle in scoliosis, this angle is the intersection of the perpendicular lines drawn along the endplates of the most tilted vertebra. If measured correctly, *a = b*
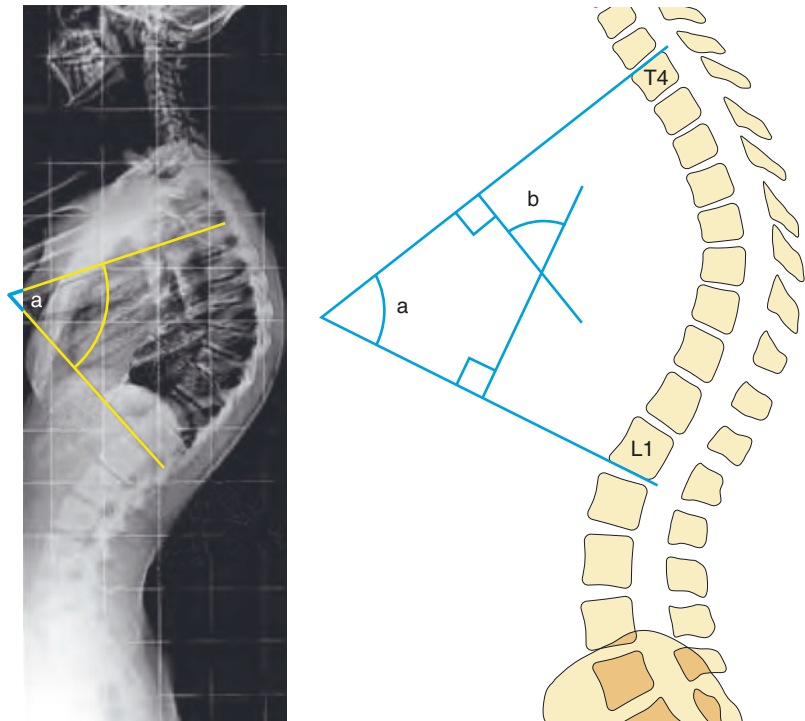
Fig. 7.17 Postural kyphosis: Two radiographs of the same patient taken consecutively. In image a, the patient is standing, showing an exaggerated lumbar lordosis and thoracic kyphosis. In image b, the patient is lying supine on a pad with the thoracic and lumbar curves straightening

Clinical Relevance/Implications

Kyphosis is defined as a posterior convex angulation of the spine, assessed by a lateral radiograph. Unlike scoliosis, where any significant lateral deviation in the coronal plane is abnormal, alignment of the lateral spine has a wide normal range, ranging from 20 to 40°.

Thoracic kyphosis as indicated above is measured using a modified Cobb angle from the upper thoracic spine, T1 through T12. Due to the difficulties in identifying T1 secondary to shoulder interposition, the inferior endplate of T4 is used as the upper limit for thoracic kyphosis. A kyphosis greater than 45–50° is considered to be abnormal.

The thoracolumbar transition angle is defined as the angle formed between the superior endplate of T10 and inferior plate of L2. Normal range is between 0 and 5°.

The vertebral wedging angle is formed by the intersection of superior endplate line and inferior endplate angle of a vertebra. This angle is useful in vertebral fracture sequelae.

A hyperextension lateral radiograph of the spine is taken using a polyurethane plastic wedge placed at the apex of the curvature to assess the flexibility of the kyphosis. In Scheuermann's disease the kyphosis is rigid. It is associated with wedged vertebral bodies that occur during late childhood. The deformity might be progressive and is sometimes painful during its relatively acute phase, although the deformity itself is the most cause for complaint.

Sorensen described specific diagnostic criteria: increased thoracic kyphosis to greater than 45°, wedging of vertebral bodies, disc space narrowing with irregular endplates and Schmorl's nodes. These criteria can also be used in cross-sectional imaging. Scheuermann's disease must be differentiated from postural round back deformity. Round back deformity is referred to a moderate thoracic kyphosis (40–60°), accentuated lumbar lordosis without classic radiographic Scheuermann's changes, normal vertebral bodies contour, no wedging or endplate irregularities. Clinically and radiographically, the spine is flexible and correctable.

Accurately determining the degree of lordosis and kyphosis is important for assessing disease states, progression of disease, and for evaluating surgical outcomes, in particular, with reference to the global sagittal balance.

Analysis/Validation of Reference Data

Difficulties with measuring the Cobb angle in kyphosis and lordosis are similar to those for scoliosis. It may be difficult to determine the vertebral endplates, and hence the line drawn may not be consistent. Determining the upper and lower extent of the kyphosis may also affect the interobserver and intra-observer reliability (Dang et al. 2005). Other methods have been proposed, such as measuring the angle of intersection of the vertebral centroids and radius of curvature to negate some of the difficulties with measuring the Cobb angle (Briggs et al. 2007). However, the use of the Cobb angle to measure kyphosis has been validated with good inter- and intra-observer reliability and remains the current standard (Hong et al. 2010).

7.10   Coronal Balance

This can be determined by the C7 plumb line and the central sacral vertical line. The midpoint of C7 vertebral body on a frontal radiograph is determined by the intersection of the diagonals and a dropped vertical line. A vertical line is then drawn through the mid-sacral point; the horizontal distance between these two points corresponds to the coronal balance. In a normal spine, this should be close to zero (Glassman et al. 2005) (Fig. 7.18).
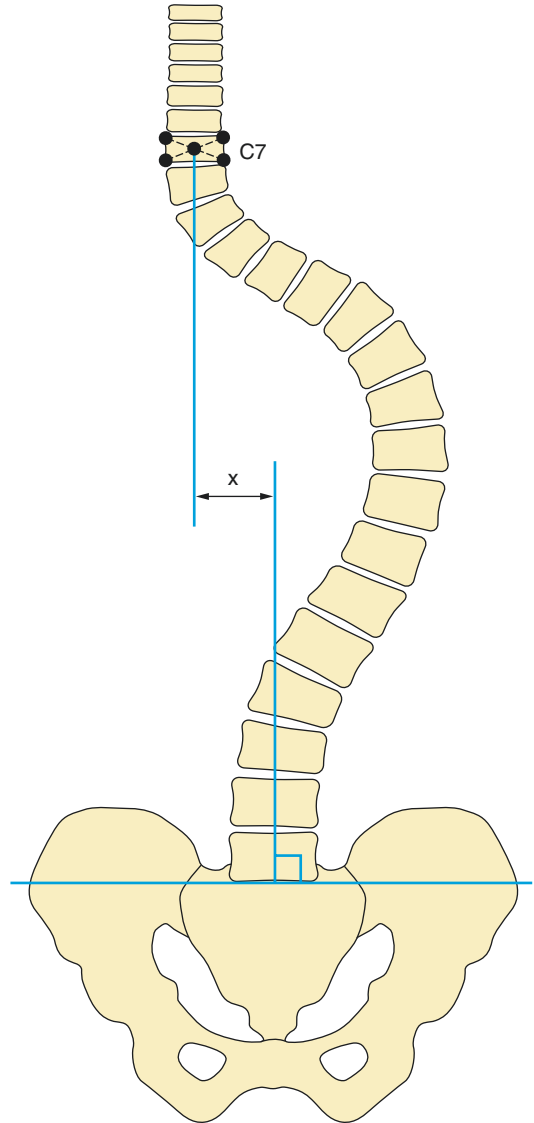
Fig. 7.18 Coronal balance, plumb line: Coronal balance measures the offset of the centre of C7 vertebral body compared with the centre of the sacrum, distance *x*, with vertical plumb lines taken from both points. In a balanced spine, this should be close to zero

7.11 Spino-pelvic Organisation

There are three sacro-pelvic parameters that can be assessed.

1. Pelvic Incidence

Definition

Pelvic incidence was described by Duval-Beaupere as the angle formed by the intersection of the line drawn from the centre of the femoral heads to the middle of the sacral endplate and the line perpendicular to the middle of the sacral endplate (Legaye et al. 1998).

Indications

The pelvic incidence is a morphological constant once skeletal maturity has been reached, determining the relative position of the sacral endplate in relation to the femoral heads. It provides information regarding pelvic compensation for perturbation in sagittal balance, for example, it dictates the ability of the pelvis to retrovert.

Full Description of Technique

The midpoint of the femoral heads is determined by drawing a best fit circle and then bisecting the diameter. If the femoral heads are not overlapped on the radiograph owing to magnification, a line joining the centre of both femoral heads is taken as the midpoint. A line is then drawn along the best fit of the sacral endplate and the midpoint is marked. The pelvic incidence angle is the angle between a line from the midpoint of the femoral heads to the midpoint of the sacral endplate and a line perpendicular to the mid-sacral plate (Fig. 7.19).
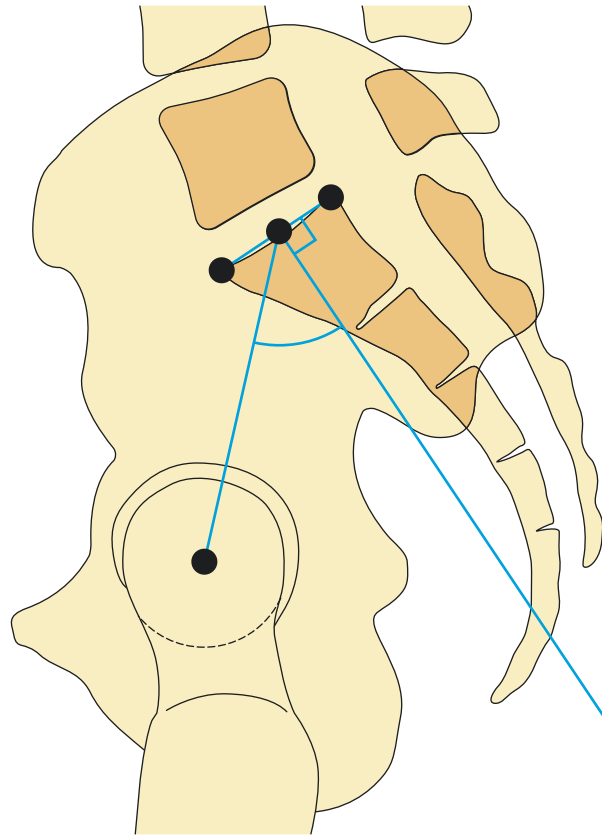
Fig. 7.19 Spino-pelvic organisation: Pelvic incidence an important parameter in spino-pelvic organisation. It is determined from the intersection of a line drawn from the centre of the femoral heads to the middle of the sacral endplate and the line perpendicular to the middle of the sacral endplate. This value is constant following skeletal maturity

Reproducibility/Variation

The lowest normal values are 35° and the highest 85°. The average quoted values are 51.9° and 53° (Roussouly et al. 2005; Boulay et al. 2006a). In the younger age group, 21–40, average pelvic incidence is 52° +/− 10°. For 41–60 yr., it is 53° +/− 8°, and age greater than 60, it is 51° +/− 9° (http://etext.srs.org).

2. Sacral Slope

Definition

Sacral slope (SS) is the orientation of the sacral plate in relation to the horizontal.

Indications

Sacral slope is a positional parameter related to pelvic tilt, describing the position of the pelvis.

Full Description of Technique

A line is drawn along the best fit of the sacral endplate. The horizontal is determined with the aid of PACS software. The sacral slope is the angle between the sacral plate and the horizontal (Fig. 7.20).

Reproducibility/Variation

This is a positional parameter, dependent on pelvic tilt and pelvic incidence. SS values in normal children are 38.2°, in adolescents 39.1° and in adults 41.2°. The SS value is reduced in Scheuermann's disease <32°.

3. Pelvic Tilt

Definition

The pelvic tilt is a further positional parameter which influences positioning of the pelvis. It is the angle between a vertical line and a line from the mid-femoral heads to the centre of the sacral endplate. Negative values of PT are noted when the midpoint of S1 endplate is anterior to the centre of the femoral head axis.

Full Description of Technique

The midpoint of the sacral endplate and femoral heads is determined, as described above. The vertical is determined with the aid of PACS software. The pelvic tilt is the angle between midpoint of the sacral endplate to the mid-femoral heads and the vertical (Fig. 7.20).

Reproducibility/Variation

As with sacral slope, the pelvic tilt is a positional parameter. In an adult population, average pelvic tilt in ages 21–40 years is 13° +/− 7°, ages 41–60 years, it is 14° +/− 6° and ages greater than 60, it is 16° +/−9° (http://etext.srs.org).
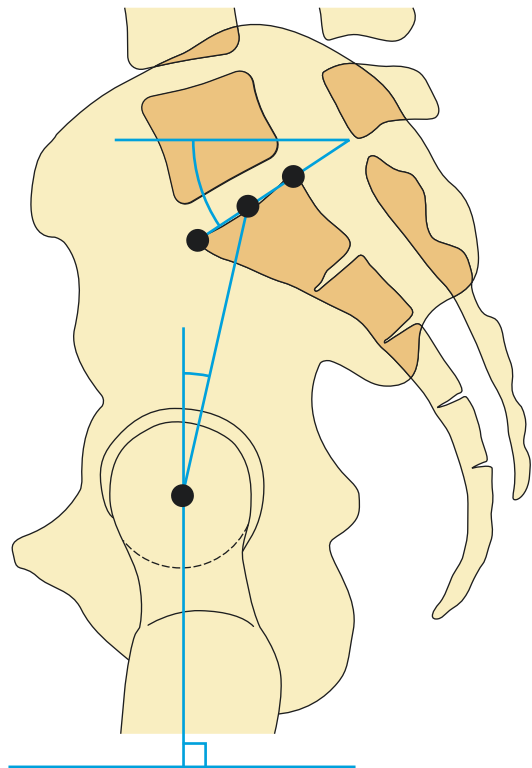
Fig. 7.20 Spino-pelvic organisation: This image shows further important parameters in spino-pelvic organisation—sacral slope and pelvic tilt. The sacral slope is measured as the angle between the horizontal and the sacral endplate. Pelvic tilt is the angle formed by a line joining the mid-femoral heads to the mid-sacral endplate and the vertical. Pelvic incidence (see Fig. 7.19) = pelvic tilt + sacral slope

Clinical Relevance/Implications

The numerical value of pelvic tilt and sacral slope can be summated to equal the value of the pelvic incidence, with the following equation:

Pelvic incidence = pelvic tilt + sacral slope (Roussouly and Pinheiro-Franco 2011) (Fig. 7.20).

PI is generally regarded as the fundamental pelvic parameter for 3-D regulation of sagittal spinal curves. It increases during childhood and adolescence and becomes fixed at skeletal maturity remaining constant thereafter in adulthood. Normally in children the PI is 43.7°, in adolescence 46.9° and in adults 54.7°. The relatively fixed pelvic incidence is a marker of the potential for pelvic compensation in disorders of alignment. Low values of pelvic incidence (<35°) can be seen in Scheuermann's disease, and greater than 85° can be seen in degenerative spondylolisthesis (Labelle et al. 2011). The latter high PI is associated with a reduction of LL which in turn promotes sagittal malalignment which can be judged by the PI-LL modifier or the PT/PI ratio. As compensatory mechanisms are not sufficient, there is usually an anterior C7 tilt.

A lower PI value <44° as seen in Scheuermann's disease (SD) generally equates to a more vertical pelvis and flattened lordosis and less ability to tilt to compensate for any pathology in alignment. An increased TK in SD patients is initially compensated by an increase in LL to maintain neutral sagittal balance. A point is reached when it is no longer possible to increase the LL, and further increases in TK are compensated by a posterior tilt of the pelvis that decreases SS, and as PI is fixed it increases PT. Conversely, a higher pelvic incidence (>62°) equates to a more horizontal pelvis, more pronounced lordosis and generally means more possibility of pelvic tilting/retroversion and therefore compensation for any more proximal disorders in sagittal balance (Boulay et al. 2006a). Pelvic incidence has also been shown by Roussouly et al. to be related to lumbar lordosis, with classification into four different types in healthy volunteers dependent on their pelvic incidence (Roussouly et al. 2003, 2005). He concluded that different types of spino-pelvic complexes lead to different patterns of degenerative disease in the spine. The four proposed types of lumbar alignment based on SS and PI values predict the natural history of lumbar morphology. Blondel et al. showed that patients with a PI-LL mismatch (defined as **PI-LL > 11°**) are more prone to global malalignment, increased risk of pelvic retroversion and severe disability risk. In adult scoliosis LL and TK change significantly and are correlated with pain. High values of PI predispose to degenerative spondylolisthesis (DS), while reduced LL and TK are seen in lumbar spinal stenosis (LSS). DS shows significantly greater PI and SS than normal population and LSS. DS also shows significantly LL than LSS. LSS shows significantly greater PT than DS and normal population. Pelvic retroversion assessed by the PT value is different in DS and LSS. DS shows significantly smaller PT values and greater SS values than LSS. As PT and SS are inversely related (PI = PT + SS), a ratio can be created which denotes pelvis position, whereby the PT/SS ratio should ideally be <1 for ideal alignment without pelvic compensation. The PT/SS ratio is greater in LSS than DS and the normal population suggesting that the pelvis is more retroverted (PT/SS >1) in LSS than DS. Slight differences in pelvic incidence have been shown across different age groups, indicating that this parameter is not entirely fixed. The values of the sagittal spino-pelvic parameters are also useful in postoperative assessment. Hyperkyphosis after a lumbar PSO can have a marked negative effect on SVA reversing the beneficial alignment effect of the surgery. Blondel et al. concluded that a larger PI requires a larger LL for spino-pelvic alignment which is also associated with a higher TK and CK (Blondel et al. 2013).

A paper assessing a cohort from the general population has shown the importance of all the pelvic parameters in association with back pain, with a higher pelvic incidence and sacral slope being associated with severe pain (Jackson et al. 2000b).

Analysis/Validation of Reference Data

The spino-pelvic parameters have been validated in multiple studies (Roussouly et al. 2005; Roussouly and Pinheiro-Franco 2011) (North American Spine Society 2011; http://etext.srs.org; Mac-Thiong et al. 2010).

Accuracy of PI and PT measurements depends on the accurate identification of the coxofemoral joints on the lateral long-cassette standing radiograph and the S1 endplate. Precision and accuracy of PI measurements reported by Duval-Beaupere are 2 and 3°, respectively. Reproducibility for PI measurements on radiographs is 6°, while digital radiographs improve reproducibility and reliability. It is essential that proper S1 endplate positioning takes place when measuring PI and PT. When the femoral heads are not quite superimposed, the centre of the bicoxofemoral axis joining the centre of the two femoral heads is taken as the origin of the measurement point.

7.12 Sagittal Balance

Sagittal balance is the alignment of C7 to the posterior superior aspect of the sacrum. The distance between the vertical line downwards from C7 to the sacrum should range from −2 cm to +2 cm. Positive balance is considered to exist when the line lies anterior to the sacrum and negative balance when the plumb line lies posterior to the sacrum. Adolescents usually have a negative balance.

Sagittal balance describes the alignment of the spine in the anteroposterior dimension and can be quantified by the measurements described below.

1. C7 Plumb Line

Definition

A vertical line dropped from the midpoint of C7 vertebral body (Roussouly et al. 2006).

Indications

This is a marker of global sagittal balance, determined by where the centre of C7 vertebral body lies in relation to the sacrum and hip axis. C7 is chosen as a reference point owing to its relative ease of identification on a lateral spine radiograph.

Full Description of Technique

A vertical plumb line is dropped from the centre of C7 vertebral body. The plumb line position is assessed in relation to the posterior edge of the sacral endplate (Fig. 7.21).

Reproducibility/Variation

In most asymptomatic adults, the C7 plumb line lies behind or at the posterior edge of the sacral endplate and less than 5 cm (North American Spine Society 2011; Roussouly et al. 2006). A study by Roussouly showed that C7 does not directly correlate with the ground reactive forces/centre of gravity for the patient; however, it serves as a surrogate radiographic marker for the centre of gravity and a measure of overall sagittal balance (Roussouly et al. 2006).
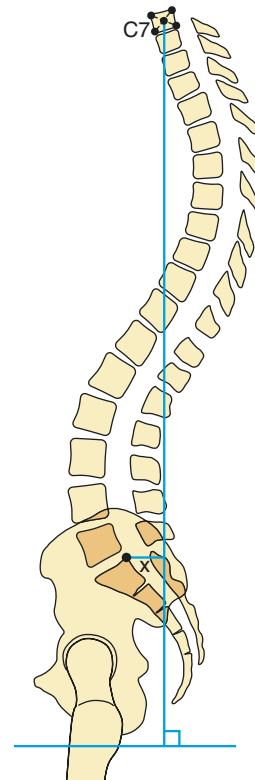
Fig. 7.21 Sagittal balance C7 plumb line: The C7 plumb line is a marker of global sagittal balance, determined by where the centre of C7 vertebral body lies in relation to the posterior edge of the sacral endplate. A vertical plumb line is dropped from the mid C7 vertebral body, and the horizontal distance between this line and the posterior edge of the sacral endplate is measured (x). This is known as the sagittal vertical axis (SVA)

2. Spinosacral Angle

Definition

The angle between the centre of C7 vertebral body and the sacral endplate.

Indications

This angle quantifies the global kyphosis of the whole spine and therefore is a marker of sagittal balance.

Full Description of Technique

Commercially available software can be used to determine these points (Roussouly et al. 2003, 2005) (Fig. 7.22).
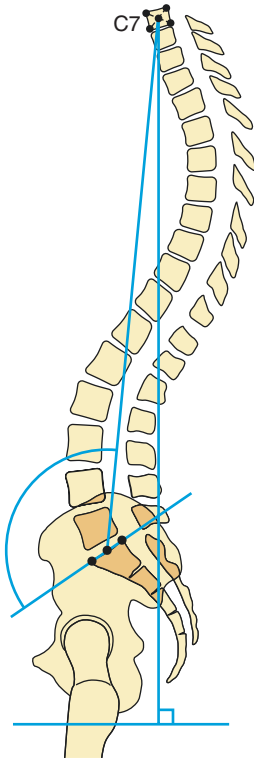
Fig. 7.22 Spinosacral angle: This global measurement of sagittal balance is the angle formed between the sacral endplate and the centre of C7 vertebral body. The centre of C7 vertebra is determined by a line intersecting the midpoint of the diagonals drawn across the vertebral body. A line is then drawn to the mid-sacral endplate and the angle is measured between the C7-sacral endplate intersection and the line across the sacral endplate

Reproducibility/Variation

The mean spinosacral angle is 130.4°, with a slight difference between males and females. (Females = 131.2°, males = 129.5 (Mac-Thiong et al. 2010)). In a balanced spine, the spinosacral angle is proportional to the sacral slope. In pathology with increased kyphosis or loss of lordosis, the angle decreases.

3. Sacral Inclination

Definition

The angle between the line perpendicular to a line along the posterior border of S1 to a line perpendicular to the vertical lateral edge of the radiograph.

4. Spinal Tilt

Definition

The angle between the centre of C7 vertebral body and the centre of the sacral endplate (Mac-Thiong et al. 2010).

Indications

A marker of sagittal balance.

Full Description of Technique

The centre of C7 vertebral body is determined, as described above, and a line is drawn to the centre of the sacral endplate. The spinal tilt is the angle formed between this line and the horizontal, determined as described above. An angle greater than 90° indicates the centre of C7 vertebral body is posterior to the centre of the upper sacral endplate, with the converse being true for values less than 90° (Fig. 7.23).
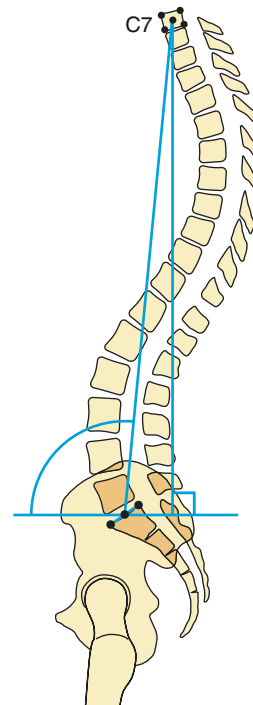
Fig. 7.23 Spinal tilt: This is a further measure of global sagittal balance, formed by a line joining the mid C7 vertebral body to the mid-sacral endplate and the horizontal. The horizontal is identified as perpendicular to the C7 plumb line

Reproducibility/Variation

A prospective study of 709 asymptomatic people showed the mean spinal tilt to be 90.8°, with two standard deviations on either side being 84.1° and 97.5°. The mean value for females is 91.4° and males 90.2° (Mac-Thiong et al. 2010).

5. C7 Translation Ratio

Definition

This ratio determines the relative position of the centre of C7 compared with the hip axis.

Indications

A marker of sagittal balance.

Full Description of Technique

A plumb line is dropped from the centre of C7 vertebral body, and the horizontal distance between this line and the mid-sacral endplate is measured. A vertical line is drawn from the mid-sacral endplate, and the horizontal distance between this line and the mid-femoral point (hip axis) as described previously is determined. The C7 translation ratio is the horizontal distance from C7-mid-sacral endplate divided by the mid-femoral point—mid-sacral endplate (Boulay et al. 2006b) (Fig. 7.24).

Reproducibility/Variation

The mean C7 translation ratio is −1.1 with no difference between males and females. This means that most adults stand with the C7 plumb line in front of the sacral endplate but behind the hip axis. This ratio is perceived to be harder to visualise compared with the global position of C7—sacral endplate, limiting its clinical utility.
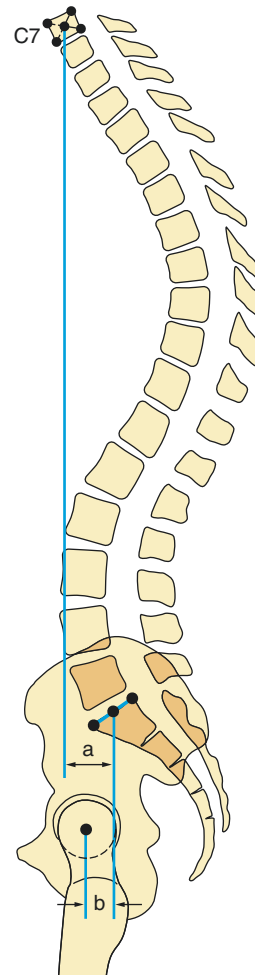
Fig. 7.24 C7 translation ratio: This ratio is defined as *a/b*. In adults, this generally has a negative value, meaning that most adults stand with the C7 plumb line in front of the sacral endplate. The centre of C7 vertebra is determined by a line intersecting the midpoint of the diagonals drawn across the vertebral body, and a plumb line is drawn. A vertical plumb line is also drawn from the mid-sacral endplate. The horizontal distance between the two plumb lines is then measured (a) and divided by the distance between the vertical sacral endplate plumb line and the femoral heads (b) to obtain the ratio

6. T9 Sagittal Offset

Definition

This parameter has been used to define global sagittal balance.

Full Description of Technique

The midpoint of T9 vertebral body is determined, as above, and a line is drawn connecting the mid-femoral axis. The angle between this line and the vertical represents the T9 sagittal offset.

Reproducibility/Variation

The mean for females is −10.5° and for males −10.2° with no significant difference between the genders (Vialle et al. 2005).

Analysis/Validation of Reference Data

The values for sagittal balance have been determined in asymptomatic volunteers (Mac-Thiong et al. 2010; Vialle et al. 2005), with alteration in pathologies (Legaye 2011).

Clinical Relevance/Implications

Sagittal balance is important in the global assessment of patients with spinal disorders, in particular for surgical planning to allow return to normal function and to minimise the risk of adjacent segment disease. Abnormal sagittal balance is associated with a worse perception of quality of life (Harroud et al. 2013). Incomplete restoration of sagittal balance is thought to be responsible for the failure to relieve symptoms in spinal surgery, the so-called "flat-back" deformity. Disturbances in sagittal balance are shown to be related to back pain, in particular in females (Jackson et al. 2000b). In adult patients with scoliosis, restoring sagittal balance is more important for function and reduction in pain compared with coronal balance (Glassman et al. 2005).

In the advanced stages of ankylosing spondylitis with a rigid thoracolumbar kyphosis, there are accompanying severe abnormalities of sagittal balance resulting in a fixed downward gaze. In an attempt to compensate for this, the patient changes their posture, with flexion at the ankles and knees, extension of the hips and retroversion of the pelvis. This tilts the fixed section of the spine backwards, to realign the gaze; however, this position is uncomfortable and inefficient in terms of energy usage. One of the aims of surgical intervention in ankylosing spondylitis is to correct the sagittal imbalance (Debarge et al. 2011; Tokala et al. 2005).

7.13 Spondylolisthesis: Anterior Displacement

Definition

The pathological displacement of one vertebra over another, most commonly at L5–S1.

Indications

An accurate measurement of the displacement of one vertebra over another, either as a numerical value (3 mm or greater) or percentage, is useful to classify the extent of the pathology, to plan surgery and for follow-up.

Full Description of Technique

Deformity results from a translational displacement and from an angular displacement. The percentage of slippage is measured with the classic Meyerding method where grade 1 is slippage of 0 to 25%, grade 2 from 25 to 50%, grade 3 from 50 to 75% and grade 4 greater than 75%. Other angles can be subtended relating the deformity to its severity (Fig. 7.25).

Slip angle is defined as the angle subtended by the inferior endplate of L5 and the line drawn perpendicular to the posterior aspect of S1 vertebral body.

Lumbosacral angle of Dubousset is defined as the angle subtended by the superior endplate of L5 and the line drawn along the posterior aspect of the S1 vertebral body.

Lumbosacral angle is described as the angle subtended by the S1 endplate and the superior endplate of L5.

Progression risk increases in women during the pre-puberty growth spurt. Radiological factors related with slippage progression are type I, dysplastic spondylolisthesis, trapezoidal shape of L5 or round sacrum. Children and adolescents with a slip percentage greater than 30–50% have high rates of progression and need surgical fusion. Slip angle greater than 55° is also associated with progressive deformity.

Meyerding Method

Meyerding's original classification in 1931 does not require absolute measurements. The superior sacral endplate is divided equally into quarters, and the position of L5 in relation to this is noted. In this classification, the precise location of L5 intersecting S1 (e.g. the posterior or anterior corner) is not described (Meyerding 1931) (Figs. 7.25 and 7.26).
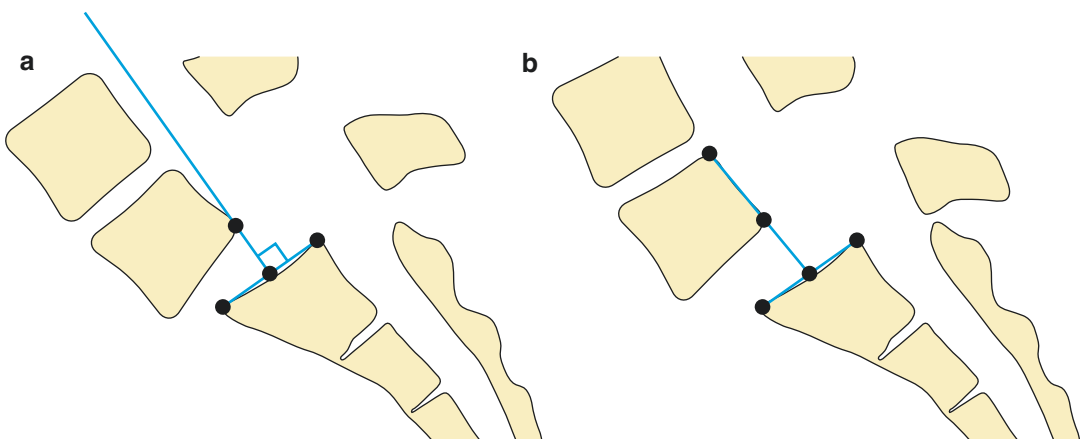
Fig. 7.25 Spondylolisthesis: The degree of olisthesis of L5 on S1 can be measured either in relation to the intersection of a line perpendicular to the sacral endplate and the posterior inferior corner of L5 (**a**) or the intersection of a line drawn along the posterior border of L5 vertebral body and the intersection of the sacral endplate (**b**). The latter (**b**) is the more commonly used method
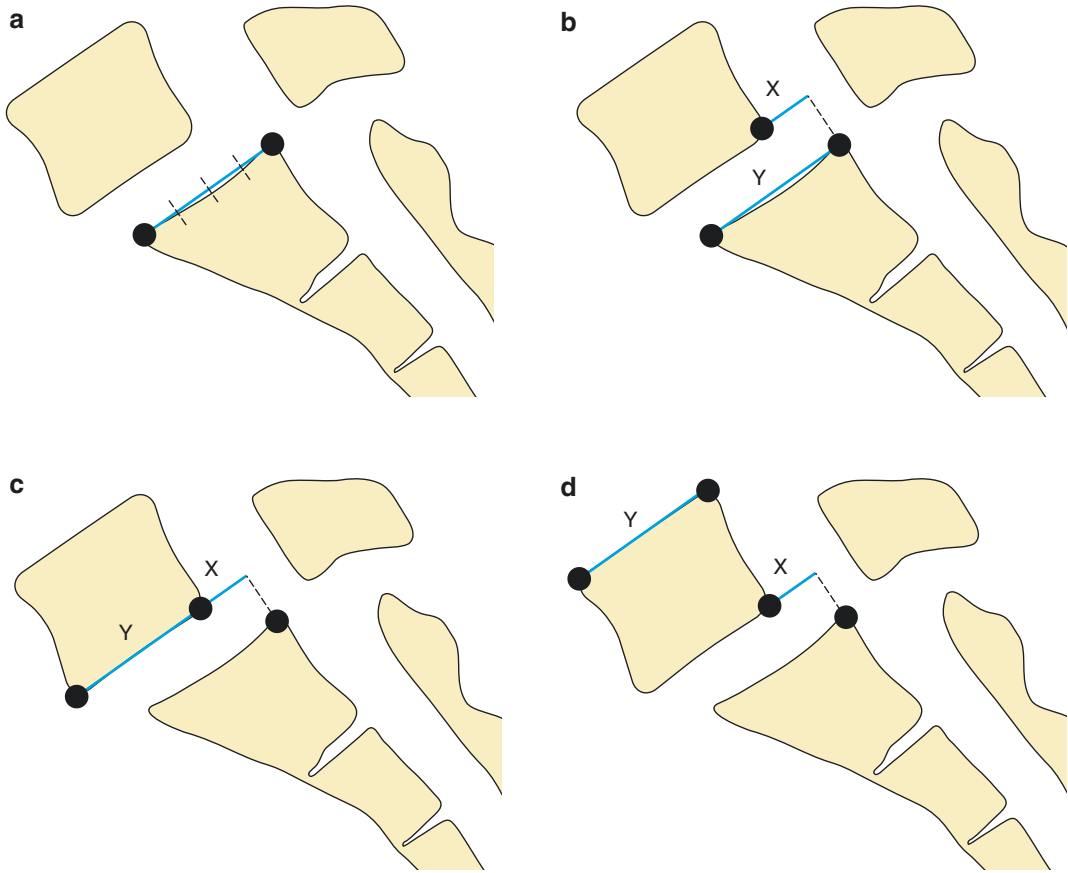
Fig. 7.26 Spondylolisthesis: Multiple different methods can be used for determining the olisthesis of one vertebra over another. (**a**) shows the Meyerding method, whereby the percentage slippage is gauged in reference to quarters of the sacral endplate. For (**b**) the Taillard method, (**c**) the Boxall method and (**d**) the Wright and Bell method, the slip percentage is calculated as $X/Y \times 100$. In the Taillard method, a line is drawn along the sacral endplate (*Y*), and a further line is drawn along the posterior border of the sacrum. The distance (*X*) is then measured between the continuation of a line along the posterior border of the sacrum and the inferior corner of L5 vertebra. In the Boxall method, the measurement of (*X*) is the same as the Taillard method; however, (*Y*) is taken as the length of the inferior L5 endplate. In the Wright and Bell method, (*X*) is measured also as above, but (*Y*) is the distance of the superior endplate of L5

Many different methods using a slip percentage value for measuring the anterior displacement of one vertebra over another (Capasso et al. 1992) have been subsequently described following Meyerding's proposal. One method involves drawing a line across the superior endplate of S1 and then taking a line perpendicular to this, intersecting the posterior inferior corner of L5. The displacement of L5 on S1 is then measured along the sacral endplate. Another method (Taillard) also involves drawing a line along the superior endplate of S1 and then intersecting this with a line drawn along the posterior border of L5. The displacement is then measured in relation to the superior sacral endplate (Fig. 7.25).

Taillard Method

In the method proposed by Taillard, the anterior displacement of the vertebra above is measured as a percentage to the width of the endplate of the

vertebra below (Taillard 1954). This is more accurate and is especially useful in monitoring progression on follow-up (Fig. 7.26).

Other methods take the displacement percentage in relation to L5 vertebral body (both the inferior and superior endplates) rather than S1.

Boxall Method

In this method the distance from the posterior outline of the inferior endplate of L5 to the posterior tip of S1 endplate is divided by the distance of the inferior L5 endplate × 100 (Boxall et al. 1979) (Fig. 7.26).

Wright and Bell Method

In this method the distance between the posterior outline of the inferior endplate of L5 to the posterior tip of S1 endplate is divided by the distance of the superior L5 endplate x 100 (Wright and Bell 1991) (Fig. 7.26).

Neutral radiographs provide some indirect signs indicative of spinal instability, such as traction spur, horizontally-oriented osteophyte or intervertebral vacuum phenomena.

Although dynamic radiographic techniques are the only techniques that can demonstrate abnormal movements, they are debatable and have poor clinical correlation. The reliability of assessing intervertebral displacement with plain radiographs is questionable because of the lack of standardised techniques, measurements and different postures of the patients. Measurements can be made directly from resting or flexion-extension radiographs. Sagittal plane displacement greater than 4.5 mm or 15% of the anteroposterior diameter of the vertebral body on a static lateral radiograph should be considered potentially unstable.

Reproducibility/Variation

As for all other measurements, the values are affected by inter- and intra-observer variation and are not necessarily equivalent between the different modalities. For example, on radiographs the anatomy may be hard to define, while on MRI, the image resolution and slice thickness may adversely affect accurate measurement.

Clinical Relevance/Implications

The treatment of spondylolisthesis requires knowledge of the aetiology (e.g. spondylotic or degenerative) and also the extent of displacement, either through an absolute measurement or percentage.

Analysis/Validation of Reference Data

The two most commonly used measurements are influenced by the lumbosacral angle, with significant differences in the percentage displacement using the two first described methods, reported in the paper by Bourassa-Moreau. The authors conclude that neither method is superior to the other; however, the measuring technique must be accurately described in studies requiring spondylolisthesis measurement (Bourassa-Moreau et al. 2010).

7.14 Spondylolisthesis: Altered Spinal Geometry

Alterations due to progressive mechanical forces on a growing spine take place in spondylolisthesis. This affects the displaced vertebral body's morphology and its angular relationships with the vertebrae above and below. In addition there is an anterior shift of the spine's centre of gravity which increases with the degree of anterior displacement. This is counterbalanced by an increased lordosis and a straightened pelvic orientation. In combination there is a summation of these effects producing a global impact on the spino-pelvic sagittal balance which can be of several types. Evaluation of these changes using angular measurements forms the basis of identifying surgical candidates.

1. Lumbar Index

In the presence of a spondylolisthesis in a growing spine, morphological changes to the vertebral bodies involved in the olisthesis are commonly present. For example, in spondylolisthesis at the L5/S1 level, it is common to have the postero-inferior corner of the L5 vertebral body displaced posteriorly, which introduces errors in measurements if one uses a measurement that relies on the inferior endplate of L5 as a reference point. For these reasons, in the calculation of displacement percentage, McCarty et al. described taking the superior border of L5 to be more accurate compared with the inferior border (McCarty et al. 2009). To mitigate for this, Wiltse proposed a way of defining the location of the postero-inferior corner of L5. A first perpendicular line defines the AP width of the superior endplate with the anterior vertebral body line, and this measurement is then drawn as a second perpendicular line along the inferior endplate of L5 (Fig. 7.27). The measurements are also affected by hypoplasia of L5 (Niggemann et al. 2012) and doming of the sacrum (Mac-Thiong et al. 2007). The whole of the posterior portion of the L5 vertebral body may be hypoplastic and wedged posteriorly. This is likely if the anterior slip is >30%.

The anterior vertebral body height is significantly greater than the posterior height (Fig. 7.28).

The **lumbar index** is calculated by dividing the posterior height by the anterior height and multiplied by 100. A lumbar index of 90% is normal, while in spondylolisthesis it averages around 70% (Fig. 7.28).
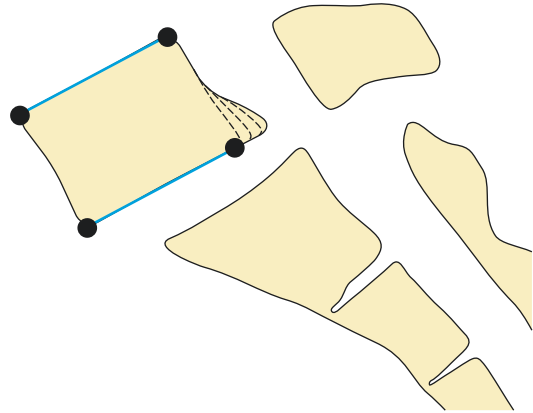
Fig. 7.27 Defining the posterior border of L5 in L5/S1 spondylolisthesis: Altered morphology of the vertebral body in spondylolisthesis can adversely affect measurements. Wiltse proposed this method for assessing the potential inferior border of L5, prior to any morphological changes secondary to the olisthesis. The length of the superior endplate is measured, and then the same distance is measured along the inferior endplate. This is then taken to represent the inferior corner of the vertebra, negating the effects of any alteration in shape owing to altered morphology
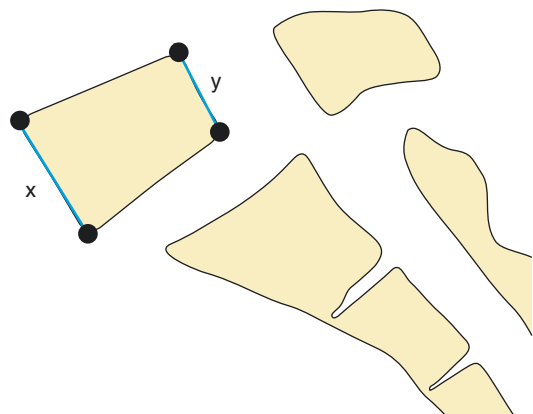
Fig. 7.28 Lumbar index: This is measured as $Y/X \times 100$, with X being the anterior height of the vertebral body and Y being the posterior height. The lumbar index is decreased in long-standing spondylolisthesis owing to hypoplasia of the posterior aspect of L5 vertebral body

2. Lumbar Lordosis

The centre of gravity shifts anteriorly directly proportional to the degree of anterior vertebral displacement in spondylolisthesis. The spine above the olisthesis responds by increasing the lumbar lordosis in accordance with the degree of slip in an attempt to restore the centre of gravity. The normal lumbar lordosis is 35° (range 25–45°). Using the method employed by Wiltse (1983), this is measured by drawing perpendiculars to lines passing through the upper endplate of L1 and superior endplate of L5 in an L5/S1 spondylolisthesis and the superior endplate of L4 in an L4/L5 spondylolisthesis (Fig. 7.29).

3. Sacral Inclination

Due to the anterior shift of the centre of gravity, the sacral inclination decreases with increasing anterior displacement, in an attempt to compensate for this by straightening the pelvis. Sacral inclination (sacral tilt) is determined on the lateral coned radiograph of L5/S1 by drawing a tangent to the posterior outline of S1 and measuring the angle it subtends with a vertical plumb line. Normally the angle is 52° (range 44–60°). Surgical intervention is offered when the angle is <35° (Fig. 7.30).
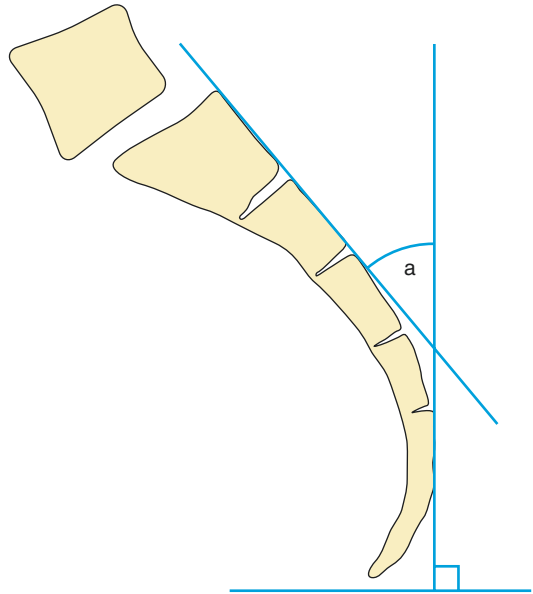
Fig. 7.30 Sacral inclination in spondylolisthesis: Spinal geometry is perturbed in spondylolisthesis, with alterations in sacral inclination to rectify sagittal balance. The angle of sacral inclination (**a**) is measured between the vertical perpendicular and the posterior border of the sacrum. Normally this is 50°

Fig. 7.29 Measuring lordosis in L5–S1 spondylolisthesis: This angle is measured from the intersection of perpendiculars passing through the superior endplate of L1 and the superior endplate of L5 in an L5–S1 spondylolisthesis
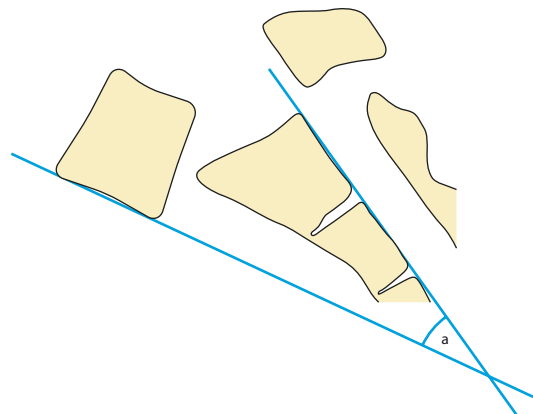
Fig. 7.31 Sagittal rotation in L5–S1 spondylolisthesis: In spondylolisthesis this angle of sagittal rotation (**a**) shows the relationship of L5 and S1. It is measured by calculating the angle between the posterior S1 tangent to the anterior L5 tangent. Normally this is 30°

4. Sagittal Rotation

Sagittal rotation or slip angle increases with increasing rotational displacement of the displaced vertebra. It is measured by calculating the angle between the posterior S1 tangent and the anterior L5 tangent. Normally it is 32 ° in adolescents (range 23–41°) (Fig. 7.31).

5. Ferguson Angle in Spondylolisthesis

This angle is calculated by measuring the angle between the tangential line passing through the superior endplate of S1 and the horizontal line and normally should be 35°.

6. Sagittal Balance (Fig. 7.32)

Besides the abnormal sacro-pelvic morphology and orientation described above, spondylolisthesis also disturbs the global sagittal balance of the spine. Patients with spondylolisthesis can have different variations of how they adapt their posture. This is important as in spondylolisthesis sagittal balance has been shown to have an important influence on surgical outcomes. The Spinal Disorders Study Group has proposed a classification of spino-pelvic organisation and sagittal spino-pelvic balance in spondylolisthesis, to try and bring order to a heterogeneous group of pathologies (Labelle et al. 2011). The degree of slip is determined from a lateral radiograph and classified into low grade (<50%) or high grade (>50%). The global sagittal
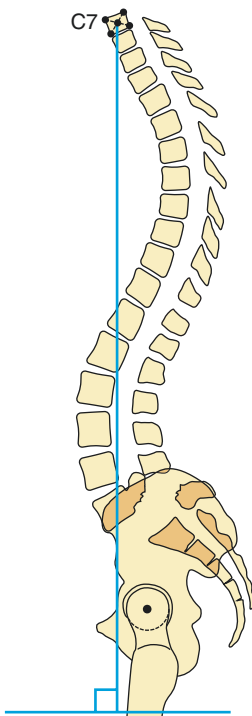
Fig. 7.32 L5–S1 spondylolisthesis and a balanced spine: High-grade spondylolisthesis with compensatory balanced spine and the C7 plumb line falling just anterior to the femoral heads. The midpoint of C7 vertebral body is determined, and a vertical line dropped. The position of this plumb line is then assessed in relation to the centre of the femoral heads
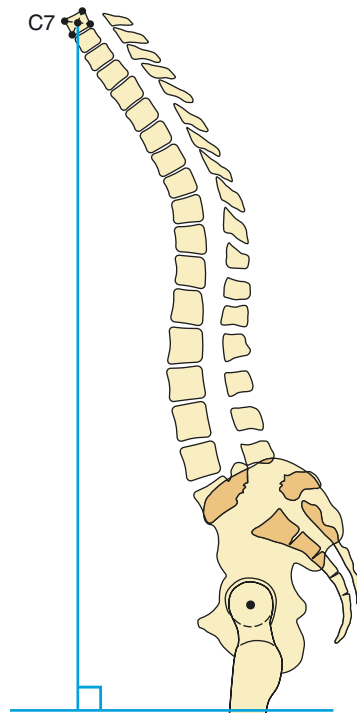
Fig. 7.33 L5–S1 spondylolisthesis and an unbalanced spine: High-grade spondylolisthesis with unbalanced spine and the C7 plumb line falling markedly anterior to the femoral heads, measured as described previously

balance is then determined by assessing the pelvic incidence, sacral slope, pelvic tilt and the C7 plumb line. In low-grade spondylolisthesis, three types of sacro-pelvic balance have been identified.

Type 1—"nutcracker" type, low pelvic incidence (<45°)

Type 2—normal pelvic incidence (45°–60°)

Type 3—"shear" type, high pelvic incidence (>60°)

In high-grade spondylolisthesis, there are also three different subtypes, determined by whether the patient has a balanced or unbalanced sacro-pelvic organisation and the position of the C7 plumb line. This gives rise to:

Type 4—balanced pelvis

Type 5—retroverted pelvis with balanced spine (Fig. 7.32)

Type 6—retroverted pelvis with unbalanced spine (Fig. 7.33)

The presence of multiple patterns of sacro-pelvic morphology and balance suggests that the underlying biomechanical aetiology of the spondylolisthesis may be different between patients, and this should be taken into consideration with any proposed surgical management. Surgical decision-making ideally should account for the different spino-pelvic organisations, with the optimal surgical procedure for each of the 6 types still to be fully validated in the surgical literature.

7.15   Skeletal Maturity

Skeletal maturity assessment for the purposes of assessing the residual growth potential of the vertebral bodies is an important parameter in deciding therapeutic options for spinal deformity, especially in adolescent idiopathic scoliosis. Radiographic assessment of the vertebral bodies directly is useful, whereby incorporation of the endplate apophysis with the vertebral body indicates maturity. Bone age assessment using hand radiographs is also a useful additional tool, but it is the assessment of the degree of ossification and state of fusion of the iliac apophysis that is favoured as a parameter of growth potential by spinal surgeons.

Risser Index

Definition

The Risser index is a measure of the extent of ossification of the iliac apophysis (Risser 1958).

Indications

Knowledge of the degree of skeletal maturity is useful in the management of adolescent idiopathic scoliosis.

Full Description of Technique

The assessment is taken from an anteroposterior image of the pelvis, with visualisation of the entire pelvis (Bitan et al. 2005) (Fig. 7.34).

The original method is more widely used in North America compared with the French variation, which is mainly used in France and Europe. See Table 7.2 for a comparison between the two methods.

Table 7.2 Table showing the differences between the two Risser methods of grading skeletal maturity as assessed by the iliac apophysis

Risser stage	Original method	French method
0	No ossification	No ossification
1	Ossification within first quarter	Ossification within the first third
2	Ossification extending into second quarter	Ossification extending into the second third
3	Ossification into the third quarter	Ossification of the entire apophysis
4	Ossification into the fourth quarter to the completion of the apophyseal line excursion	Start of fusion of the apophysis to the ilium posterior-medially
5	Fusion of the apophysis	Complete fusion of the apophysis to the ilium
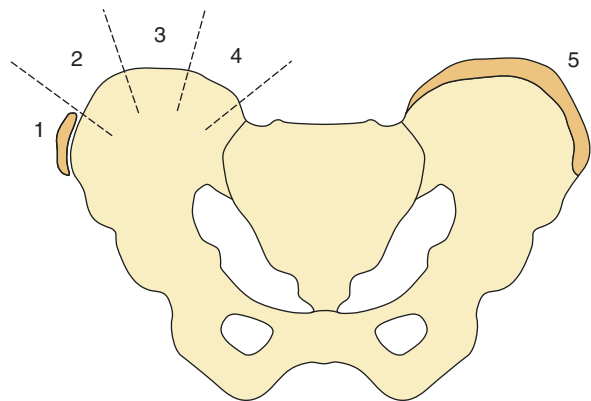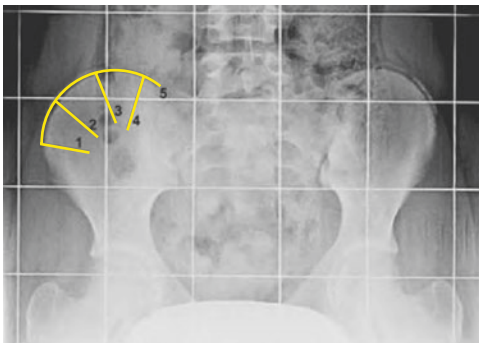
Fig. 7.34   Risser index: This illustration shows the original method described by Risser for determining skeletal maturity. Stage 0, no ossification. Stage 1, ossification within first quarter. Stage 2, ossification extending into second quarter. Stage 3, ossification into the third quarter. Stage 4, ossification into the fourth quarter to completion of the apophyseal line excursion. Stage 5, fusion of the apophysis

Reproducibility/Variation

Assessment of the Risser stage has been shown to have good interobserver and intra-observer reliability (Yang et al. 2014). The accuracy is improved by a review of the whole pelvic image, rather than the ilium alone, likely owing to the combined assessment of other ossification centres, such as the greater trochanter (Reem et al. 2009). Other authors have shown improved accuracy with the inclusion of yet more ossification centre, such as the ribs (Hoppenfeld et al. 2004).

Clinical Relevance/Implications

The Risser assessment is an indicative measure of the residual growth potential of the vertebral bodies. Curves tend to progress during the growth spurt and cease at skeletal maturity, so during the growth spurt period progress must be closely followed up. Treatment decisions are taken depending on the curve, rate of progression and skeletal age. Large curves tend to progress after skeletal maturity has ended. There are several methods for evaluating skeletal maturity; some are used together in order to provide a more accurate evaluation of skeletal age. Skeletal age is determined by comparing a patient's left-hand radiograph with the populational standard, most frequently using the Greulich and Pyle method.

Risser was the first to document the coincidental development and ossification of vertebral apophyseal endplate growth and the excursion of ossification of the iliac apophysis. Ossification starts at the anterior superior iliac spine and progresses to the posterior superior iliac spine and ends with the complete fusion of the iliac crest. Stages are divided into quarters and are correlated with the curve magnitude progression.

The ossification of the iliac apophysis correlates with skeletal maturity (Biondi et al. 1985). The Cobb angle in adolescent idiopathic scoliosis has been shown to progress in line with growth and to cease progression once skeletal maturity is reached. Therefore, accurately determining the state of skeletal maturity is a useful parameter in the management of adolescent idiopathic scoliosis.

Conclusion

Knowledge of spinal measurements is a valuable tool for determining normality and therefore any disturbances in pathology.

References

Amonoo-Kuofi HS (1991) Morphometric changes in the heights and anteroposterior diameters of the lumbar intervertebral discs with age. J Anat 175:159–168

Amonoo-Kuofi HS, Patel PJ, Fatani JA (1990) Transverse diameter of the lumbar spinal canal in normal adult Saudis. Acta Anat (Basel) 137(2):124–128

Beauchamp M, Labelle H, Grimard G, Stanciu C, Poitras B, Dansereau J (1993) Diurnal variation of cobb angle measurement in adolescent idiopathic scoliosis. Spine (Phila Pa 1976) 18(12):1581–1583

Beers G, Carter A (1985) Interobserver discrepancies in distance measurements from lumbar spine CT scans. Am J Roentgenol 144:395–398

Bick EM, Copel JW (1950) Longitudinal growth of the human vertebra: a contribution to human ostegeny. J Bone Jt Surg. 32:803–814

Biondi J, Weiner DS, Bethem D, Reed JF III (1985) Correlation of Risser sign and bone age determination in adolescent idiopathic scoliosis. J Pediatr Orthop 5(6):697–701

Bitan FD, Veliskakis KP, Campbell BC (2005) Differences in the Risser grading systems in the United States and France. Clin Orthop Relat Res 436:190–195

Black D, Cummings S, Stone K, Hudes E, Palermo L, Steiger P (1991) A new approach to defining normal vertebral dimensions. J Bone Miner Res 6:883–892

Blondel B, Schwab F, Bess S, Ames C, Mummaneni PV, Hart R et al (2013) Posterior global malalignment after osteotomy for sagittal plane deformity. Spine (Phila Pa 1976) 38(7):E394–E401

Boseker EH, Moe JH, Winter RB, Koop SE (2000) Determination of "normal" thoracic kyphosis: a roentgenographic study of 121 "normal" children. J Pediatr Orthop 20(6):796–798

Boulay C, Tardieu C, Hecquet J, Benaim C, Mouilleseaux B, Marty C et al (2006a) Sagittal alignment of spine and pelvis regulated by pelvic incidence: standard values and prediction of lordosis. Eur Spine J 15(4):415–422

Boulay C, Tardieu C, Hecquet J, Benaim C, Mouilleseaux B, Marty C et al (2006b) Sagittal alignment of spine and pelvis regulated by pelvic incidence: standard values and prediction of lordosis. Eur Spine J 15(4):415–422

Bourassa-Moreau E, Mac-Thiong J, Labelle H (2010) Redefining the technique for the radiologic measurement of slip in spondylolisthesis. Spine (Phila Pa 1976) 35(14):1401–1405

Boxall D, Bradford DS, Winter RB, Moe JH (1979) Management of severe spondylolisthesis in children and adolescents. J Bone Joint Surg Am 61(4):479–495

Briggs AM, Wrigley TV, Tully EA, Adams PE, Greig AM, Bennell KL (2007) Radiographic measures of thoracic kyphosis in osteoporosis: cobb and vertebral centroid angles. Skelet Radiol 36(8):761–767

Capasso G, Maffulli N, Testa V (1992) Inter- and intra-tester reliability of radiographic measurements of spondylolisthesis. Acta Orthop Belg 58(2):188–192

Cassar-Pullicino VN, Eisenstein SM (2002) Imaging in scoliosis: what, why and how? Clin Radiol 57(7):543–562

Castro FP (2003) Adolescent idiopathic scoliosis, bracing, and the Hueter-Volkmann principle. Spine J 3:180–185

Cil A, Yazici M, Uzumcugil A, Kandemir U (2004) The evolution of sagittal segmental alignment of the spine during childhood. Spine (Phila Pa 1976) 30(1):93–100

Cobb JR (1948) Outline for the study of scoliosis. AAOS Instr Course Lect 5:261–275

Dang NR, Moreau MJ, Hill DL, Mahood JK, Raso J (2005) Intra-observer reproducibility and interobserver reliability of the radiographic parameters in the spinal deformity study group? AIS radiographic measurement manual. Spine (Phila Pa 1976) 30(9):1064–1069

Debarge R, Demey G, Roussouly P (2011) Sagittal balance analysis after pedicle subtraction osteotomy in ankylosing spondylitis. Eur Spine J 20(Suppl 5):619–625

Debnath UK (2010) Current concepts in the management of early-onset idiopathic scoliosis. Ped Health 4:343–354

Dumont-Fischer D, Rat A-C, Saidenberg-Kermanac'h N, Laurent S, Cohen R, Boissier M-C (2002) Spinal epidural lipomatosis revealing endogenous Cushing's syndrome. Jt Bone Spine 69(2):222–225

Eisenstein S (1977) The morphometry and pathological anatomy of the lumbar spine in south African negroes and caucasoids with specific reference to spinal stenosis. J Bone Joint Surg Br 59:173–180

Everett CR, Patel RK (2007) A systematic literature review of nonsurgical treatment in adult scoliosis. Spine (Phila Pa 1976) 32(19):130–134

Farfan HF, Osteria V, Lamy C (1976) The mechanical etiology of spondylolysis and spondylolisthesis. Clin Orthop Relat Res:40–55

Fassett DR, Schmidt MH (2004) Spinal epidural lipomatosis: a review of its causes and recommendations for treatment. Neurosurg Focus 16(4):E11

Frobin W, Brinckmann P, Biggemann M, Tillotson M, Burton K (1997) Precison measurement of disc height, vertebral height and sagittal plane displacement from lateral radiographic views of the lumbar spine. Clin Biomech 12

Frobin W, Brinckmann P, Kramer M, Hartwig E (2001) Height of lumbar discs measured from radiographs compared with degeneration and height classified from MR images. Eur Radiol:263–269

Fukusaki M, Kobayashi I, Hara T, Sumikawa K (1998) Symptoms of spinal stenosis do not improve after epidural steroid injection. Clin J Pain 14(2):148–151

Giglio CA, Volpon JB (2007) Development and evaluation of thoracic kyphosis and lumbar lordosis during growth. J Child Orthop 1(3):187–193

Glassman SD, Berven S, Bridwell K, Horton W, Dimar JR (2005) Correlation of radiographic parameters and clinical symptoms in adult scoliosis. Spine (Phila Pa 1976) 30(6):682–688

Göçen S, Havitçioglu H (2001) Effect of rotation on frontal plane deformity in idiopathic scoliosis. Orthopedics 24(3):265–268

Greendale GA, Nili NS, Huang M-H, Seeger L, Karlamangla AS (2011) The reliability and validity of three non-radiological measures of thoracic kyphosis and their relations to the standing radiological Cobb angle. Osteoporos Int 22(6):1897–1905

Gstoettner M, Sekyra K, Walochnik N, Winter P, Wachter R, Bach CM (2007) Inter- and intraobserver reliability assessment of the Cobb angle: manual versus digital measurement tools. Eur Spine J 16(10):1587–1592

Guen YL, Joon WL, Hee SC, Kyoung-Jin O, Heung SK (2011) A new grading system of lumbar central canal stenosis on MRI: an easy and reliable method. Skelet Radiol 40:1033–1039

Guigui P, Levassor N, Rillardon L, Wodecki P, Cardinne L (2003) Physiological value of pelvic and spinal parameters of sagittal balance: analysis of 250 healthy volunteers. Rev Chir Orthop Reparatrice Appar Mot 89:496–506

Gupta MC, Wijesekera S, Sossan A, Martin L, Vogel LC, Boakes JL et al (2007) Reliability of radiographic parameters in neuromuscular scoliosis. Spine (Phila Pa 1976) 32(6):691–695

Harroud A, Labelle H, Joncas J, Mac-Thiong J-M (2013) Global sagittal alignment and health-related quality of life in lumbosacral spondylolisthesis. Eur Spine J 22(4):849–856

Herzog RJ, Kaiser JA, Saal JA, Saal JS (1991) The importance of posterior epidural fat pad in lumbar central canal stenosis. Spine (Phila Pa 1976) 16(6 Suppl):S227–S233

Hinck V, Clark W, Hopkins C (1966) Normal interpedicular distances (minimum and maximum) in children and adults. Am J Roentgenol 97:141–153

Hong JY, Suh SW, Modi HN, Hur CY, Song HR, Park JH (2010) Reliability analysis for radiographic measures of lumbar lordosis in adult scoliosis: a case-control study comparing 6 methods. Eur Spine J 19(9):1551–1557

Hoppenfeld S, Lonner B, Murthy V, Gu Y (2004) The rib epiphysis and other growth centers as indicators of the end of spinal growth. Spine (Phila Pa 1976) 29(1):47–50

http://etext.srs.org/

Inoue H, Ohmori K, Miyasaka K, Hosoe H (1999) Radiographic evaluation of the lumbosacral disc height. Skelet Radiol 28(11):638–643

Jackson RP, Kanemura T, Kawakami N, Hales C (2000a) Lumbopelvic lordosis and pelvic balance on repeated standing lateral radiographs of adult volunteers and untreated patients with constant low back pain. Spine (Phila Pa 1976) 25:575–586

Jackson RP, Kanemura T, Kawakami N, Hales C (2000b) Lumbopelvic lordosis and pelvic balance on repeated standing lateral radiographs of adult volunteers and untreated patients with constant low back pain. Spine (Phila Pa 1976) 25(5):575–586

Jacquot F, Charpentier A, Khelifi S, Gastambide D, Rigal R, Sautet A (2012) Measuring the cobb angle with the iPhone in kyphoses: a reliability study. Int Orthop 36(8):1655–1660

Jeong S-T, Song H-R, Keny SM, Telang SS, Suh S-W, Hong S-J (2006) MRI study of the lumbar spine in achondroplasia. A morphometric analysis for the evaluation of stenosis of the canal. J Bone Joint Surg Br 88(9):1192–1196

Kalichman L, Cole R, Kim DH, Li L, Suri P, Guermazi A et al (2009) Spinal stenosis prevalence and association with symptoms: the Framingham study. Spine J 9(7):545–550

Keenan BE, Izatt MT, Askin GN, Labrom RD, Pearcy MJ, Adam CJ (2014) Supine to standing cobb angle change in idiopathic scoliosis: the effect of endplate pre-selection. Scoliosis 9:16

Koc Z, Ozcakir S, Sivrioglu K, Gurbet A, Kucukoglu S (2009) Effectiveness of physical therapy and epidural steroid injections in lumbar spinal stenosis. Spine (Phila Pa 1976) 34:985–989

Korovessis P, Piperos G, Sidiropoulos P, Dimas A (1994) Adult idiopathic lumbar scoliosis. A formula for prediction of progression and review of the literature. Spine (Phila Pa 1976) 19(17):1926–1932

Kuittinen P, Sipola P, Saari T, Aalto TJ, Sinikallio S, Savolainen S et al (2014) Visually assessed severity of lumbar spinal canal stenosis is paradoxically associated with leg pain and objective walking ability. BMC Musculoskelet Disord 15:348

Kuklo TR, Potter BK, O'Brien MF, Schroeder TM, Lenke LG, Polly DW (2005) Reliability analysis for digital adolescent idiopathic scoliosis measurements. J Spinal Disord Tech 18:152–159

Kumar K, Nath RK, Nair CP, Tchang SP (1996) Symptomatic epidural lipomatosis secondary to obesity. Case report J Neurosurg 85(2):348–350

Labelle H, Mac-Thiong J-M, Roussouly P (2011) Spino-pelvic sagittal balance of spondylolisthesis: a review and classification. Eur Spine J 20(Suppl 5):641–646

Larsen J (1981) The lumbar spinal canal in children. Part II: the interpedicular distance and its relation to the sagittal diameter and transverse pedicular width. Eur J Radiol:312–321

Lau EM, Chan HH, Woo J, Lin F, Black D, Nevitt M et al (1996) Normal ranges for vertebral height ratios and prevalence of vertebral fracture in Hong Kong Chinese: a comparison with American Caucasians. J Bone Miner Res 11:1364–1368

Legaye J (2011) Analysis of the dynamic sagittal balance of the lumbo-pelvi-femoral complex. Biomech Appl. (Figure 1): ISBN 978-953-307-969-1

Legaye J, Duval-Beaupère G, Hecquet J, Marty C (1998) Pelvic incidence: a fundamental pelvic parameter for three-dimensional regulation of spinal sagittal curves. Eur Spine J 7:99–103

Lisai P, Doria C, Crissantu L, Meloni GB, Conti M, Achene A (2001) Cauda equina syndrome secondary to idiopathic spinal epidural lipomatosis. Spine (Phila Pa 1976) 26(3):307–309

Luoma K, Vehmas T, Riihimäki H, Raininko R (2001) Disc height and signal intensity of the nucleus pulposus on magnetic resonance imaging as indicators of lumbar disc degeneration. Spine (Phila Pa 1976) 26(6):680–686

Mac-Thiong J-M, Labelle H, Parent S, Poitras B, Jodoin A, Ouellet J et al (2007) Assessment of sacral doming in lumbosacral spondylolisthesis. Spine (Phila Pa 1976) 32:1888–1895

Mac-Thiong J-M, Roussouly P, Berthonnaud E, Guigui P (2010) Sagittal parameters of global spinal balance: normative values from a prospective cohort of seven hundred nine Caucasian asymptomatic adults. Spine (Phila Pa 1976) 35(22):E1193–E1198

Malfair D, Flemming AK, Dvorak MF, Munk PL, Vertinsky AT, Heran MK et al (2010) Radiographic evaluation of scoliosis: review. Am J Roentgenol 194:S8–22

Mamisch N, Brumann M, Hodler J, Held U, Brunner F, Steurer J (2012) Radiologic criteria for the diagnosis of spinal stenosis. Radiology 264(1):174–179

McCarty ME, Mehlman CT, Tamai J, Do TT, Crawford AH, Klein G (2009) Spondylolisthesis: intraobserver and interobserver reliability with regard to the measurement of slip percentage. J Pediatr Orthop 29(7):755–759

Mehta H (1968) The rib-vertebra angle in the early diagnosis between resolving and progressive infantile scoliosis. J Bone Jt Surg 54B(2):230–244

Meyerding HW (1931) Spondylolisthesis. J Bone Jt Surg 13(1):39–48

Morrissy RT, Goldsmith GS, Hall EC, Kehl D, Cowie GH (1990) Measurement of the cobb angle on radiographs of patients who have scoliosis. Evaluation of intrinsic error. J Bone Joint Surg Am 72(3):320–327

Nash C, Moe J (1969) A study of vertebral rotation. J Bone Jt Surg. 2:223–229

Niggemann P, Kuchta J, Grosskurth D, Beyer HK, Hoeffer J, Delank KS (2012) Spondylolysis and isthmic spondylolisthesis: impact of vertebral hypoplasia on the use of the Meyerding classification. Br J Radiol 85(1012):358–362

North American Spine Society (2011) Evidence-based clinical guidelines for multidisciplinary spine care diagnosis and treatment of degenerative lumbar spinal stenosis. https://www.spine.org/Portals/0/Documents/ResearchClinicalCare/Guidelines/LumbarStenosis.pdf

O'Neill TW, Varlow J, Felsenberg D, Johnell O, Weber K, Marchant F et al (1994) Variation in vertebral height ratios in population studies. European vertebral osteoporosis study group. J Bone Miner Res 9:1895–1907

Oei L, Rivadeneira F, Ly F, Breda SJ, Zillikens MC, Hofman A et al (2013) Review of radiological scoring methods of osteoporotic vertebral fractures for clinical and research settings. Eur Radiol 23:476–486

Pfirrmann CW, Metzdorf A, Elfering A, Hodler J, Boos N (2006) Effect of aging and degeneration on disc volume and shape: a quantitative study in asymptomatic volunteers. J Orthop Res 24(5):1086–1094

Ploumis A, Transfeldt EE, Gilbert TJ, Mehbod AA, Dykes DC, Perra JE (2006) Degenerative lumbar scoliosis: radiographic correlation of lateral rotatory olisthesis with neural canal dimensions. Spine (Phila Pa 1976) 31(20):2353–2358

Quint DJ, Boulos RS, Sanders WP, Mehta BA, Patel SC, Tiel RL (1988) Epidural lipomatosis. Radiology 169(2):485–490

Rajput D, Srivastava AK, Kumar R (2010) Spinal epidural lipomatosis: an unusual cause of relapsing and remitting paraparesis. J Pediatr Neurosci India: Medknow Publications 5(2):150–152

Reem J, Carney J, Stanley M, Cassidy J (2009) Risser sign inter-rater and intra-rater agreement: is the Risser sign reliable? Skelet Radiol 38(4):371–375

Risser JC (1958) The iliac apophysis; an invaluable sign in the management of scoliosis. Clin Orthop 11:111–119

Roberts N, Gratin C, Whitehouse GH (1997) MRI analysis of lumbar intervertebral disc height in young and older populations. J Magn Reson Imaging 7:880–886

Robertson SC, Traynelis VC, Follett KA, Menezes AH (1997) Idiopathic spinal epidural lipomatosis. [review] [41 refs]. Neurosurgery 41(1):68–74

Roussouly P, Pinheiro-Franco JL (2011) Biomechanical analysis of the spino-pelvic organization and adaptation in pathology. Eur Spine J 20(Suppl 5):609–618

Roussouly P, Berthonnaud E, Dimnet J (2003) Geometrical and mechanical analysis of lumbar lordosis in an asymptomatic population: proposed classification. Rev Chir Orthop Reparatrice Appar Mot 89:632–639

Roussouly P, Gollogly S, Berthonnaud E, Dimnet J (2005) Classification of the normal variation in the sagittal alignment of the human lumbar spine and pelvis in the standing position. Spine (Phila Pa 1976) 30(3):346–353

Roussouly P, Gollogly S, Noseda O, Berthonnaud E, Dimnet J (2006) The vertical projection of the sum of the ground reactive forces of a standing patient is not the same as the C7 plumb line: a radiographic study of the sagittal alignment of 153 asymptomatic volunteers. Spine (Phila Pa 1976) 31(11):E320–E325

Schwarz G (1956) The width of the spinal canal in the growing vertebra with special reference to the sacrum. Am J Roentgenol 76(3):476–481

Shao Z, Rompe G, Schiltenwolf M (2002) Radiographic changes in the lumbar intervertebral discs and lumbar vertebrae with age. Spine (Phila Pa 1976) 27(3):263–268

Shaw M, Adam CJ, Izatt MT, Licina P, Askin GN (2012) Use of the iPhone for cobb angle measurement in scoliosis. Eur Spine J 21(6):1062–1068

Shefi S, Soudack M, Konen E, Been E (2013) Development of the lumbar lordotic curvature in children from age 2 to 20 years. Spine (Phila Pa 1976) 38(10):E602–E608

Steurer J, Roner S, Gnannt R, Hodler J (2011) Quantitative radiologic criteria for the diagnosis of lumbar spinal stenosis: a systematic literature review. BMC Musculoskelet Disord 12(1):175

Taillard W (1954) Spondylolisthesis in children and adolescents. Acta Orthop Scand 24(2):115–144

Tibrewal SB, Pearcy MJ (1985) Lumbar intervertebral disc heights in normal subjects and patients with disc herniation. Spine (Phila Pa 1976) 10:452–454

Tokala DP, Mukerjee KB, Grevitt MP, Freeman BJC, Webb JK (2005) Factors affecting correction of sagittal balance in ankylosing spondylitis. J Bone Jt Surgery Br 87-B(SUPP III):236

Ullrich CG, Binet EF, Sanecki MG, Kieffer SA (1980) Quantitative assessment of the lumbar spinal canal by computed tomography. Radiology 134:137–143

Vialle R, Levassor N, Rillardon L, Templier A, Skalli W, Guigui P (2005) Radiographic analysis of the sagittal alignment and balance of the spine in asymptomatic subjects. J Bone Joint Surg Am 87(2):260–267

Wakerley B, Kent L, Jackson M (2011) Progressive epidural lipomatosis with steroid use in severe refractory asthma. J Asthma 48(3):316–318

Ward CV, Latimer B, Alander DH, Parker J, Ronan JA, Holden AD et al (2007) Radiographic assessment of lumbar facet distance spacing and spondylolysis. Spine (Phila Pa 1976) 32(2):E85–E88

Wills BP, Auerbach JD, Zhu X, Caird MS, Horn BD, Flynn JM et al (2007) Comparison of Cobb angle measurement of scoliosis radiographs with preselected end vertebrae: traditional versus digital acquisition. Spine (Phila Pa 1976) 32(1):98–105

Wiltse LL, Winter B (1983) Terminology and measurement of spondylolisthesis. J Bone Joint Surg Am 768–772

Wright J, Bell D (1991) Lumbosacral joint angles in children. J Pediatr Orthop 11:748–751

Wu W, Liang J, Du Y, Tan X, Xiang X, Wang W et al (2014) Reliability and reproducibility analysis of the cobb angle and assessing sagittal plane by computer-assisted and manual measurement tools. BMC Musculoskelet Disord 15:33

Yang J, Bhandarkar A, Suh S, Hong J, Hwang J, Ham C (2014) Evaluation of accuracy of plain radiography in determining the Risser stage and identification of common sources of errors. J Orthop Surg Res 9(1):101

Zehnder SW, Ward CV, Crow AJ, Alander D, Latimer B (2009) Radiographic assessment of lumbar facet distance spacing and pediatric spondylolysis. Spine (Phila Pa 1976) 34(3):285–290

Shoulder

8

Fabio Martino, Michele Solarino, Antonio Barile,
Maria Vittoria Di Fabio, and Gianluigi Martino

Contents

F. Martino, M.D. (✉)
Department of Radiology, ASL BARI,
70100 Bari, Italy
e-mail: radio23@libero.it

M. Solarino, M.D.
University of Bari, 70100 Bari, Italy
e-mail: michele.solarino@fastwebnet.it

G. Martino, M.D.
Radiology Department of the P.O.,
"Di Venere" - ASL BARI, Bari, Italy
e-mail: gigimartino@hotmail.it

A. Barile, M.D. • M. V. Di Fabio, M.D.
Department of Radiology, University of L'Aquila,
67100 L'Aquila, Italy
e-mail: Antonio.barile@univaq.it;
mavidifabio@libero.it

8.1 Introduction

Over the last 20 years the "*forgotten*" shoulder joint has attracted a lot of orthopaedic attention primarily focused on rotator cuff disease, instability and arthroplasty. New orthopaedic concepts and a better understanding of the relationship between shoulder structure and function have increased the role of, and demand for imaging of the shoulder. With this increased interest, an increased application of imaging methods has evolved to support diagnosis, therapeutic decision making and outcome assessment. Revisiting the conventional radiograph has led to the creation and harnessing of a number of measurements, whose values relate not only to structural relationships but

more importantly to shoulder function. Increasingly these values are sought for before arthroscopic procedures but also prior to carrying out a shoulder replacement, to optimise the choice and ensure accurate placement of the implanted prosthesis. Cross-sectional imaging (CT and MRI) has also been used to provide accurate measurement of important structures such as the glenoid and acromion whose morphology is difficult to ascertain with conventional radiography. As noted by Natsis et al. (2007), these techniques along with ultrasound also provide visualization of the soft tissues of the shoulder, which are increasingly being employed in providing qualitative and quantitative values to aid clinical diagnosis and management.

8.2   Lines and Landmarks

It is essential that there is a clear understanding and agreement concerning the appropriate anatomical landmarks that need to be optimally visualised as a prerequisite to accurate measurement. This is particularly important in a complex anatomical structure like the shoulder girdle. As in the pelvic girdle, it requires a sound anatomical knowledge which needs to be translated into the plan of carrying out the measurement. This is reflected by the high degree of attention to detail that is required in image procurement and optimal use of modalities to minimise the error rate.

Glenohumeral Parameters

The conventional true AP radiograph plays an essential preliminary role in diagnosis and is the mainstay for a number of measurements. Good quality radiographs should allow clear depiction of bony anatomy with specific reference to the acromion, glenoid, coracoid process and humeral head to include the proximal humerus. A true AP view of the glenohumeral joint is essential for measurement purposes. This needs to be acquired using a standard technique to ensure accuracy and reproducibility. The patient's arm is positioned by the side in 0° of abduction, extension and external rotation. The cassette is placed posterior to the symptomatic shoulder and the patient is rotated towards this shoulder by 35° so that the cassette lies parallel to the scapula. The beam is centred perpendicular to the cassette with an FFD of 105 cm which provides a magnification of 110%. This view can be obtained with the patient supine but ideally upright with the arm at rest by the side of the body (Fig. 8.1). A dynamic element can be introduced by employing the **Leclercq's manoeuvre** to the weight bearing arm which is placed in abduction for optimal assessment of the subacromial space. In addition a caudal 20° tilt can also be added to assess the acromial anatomy and relationship to the humerus.

The anatomical interplay of the various humeral and glenoid dimensions dictate the functional performance of the articulation. This

Fig. 8.1 A true AP view of the glenohumeral joint is essential for measurement purposes, done with a 20° caudal tube tilt to assess the acromiohumeral relationship optimally

is particularly relevant in post-traumatic reconstruction and shoulder replacement as emphasised by Ianotti et al. (1992) The articular surface of the humeral head is defined by its size and shape. In turn the size of the articular surface is defined as its radius of curvature and its thickness. The articular surface of the humeral head has a normal posterior and medial offset with respect to the central axis of the humeral shaft. The *posterior humeral offset* is defined as the distance between the axis of the medullary canal and the centre of humeral head in the anteroposterior direction. Normally the humeral head lies **0-4 mm posterior** to the axis of the humeral shaft. The humeral head is normally retroverted approximately by **30°**. The *medial humeral offset* is the distance between the humeral shaft intramedullary axis, and the centre of rotation of the humeral articular surface in the mediolateral direction. Its range is from **7 to 14 mm,** with the humeral head lying an average of **11 mm** medial to the humeral shaft axis (Fig. 8.2). The neck shaft angle is related to the

size of the humeral head, with a range between **30 and 50°**. The larger the head size, the greater is the neck shaft angle. Although it is not easy to define a normal size to the greater tuberosity it is important to establish if it is more prominent

Fig. 8.2 The articular surface of the normal humeral head (c) has a variable posterior and medial offset with respect to the central axis of the humeral shaft (A). The posterior humeral offset is between 0 and 4 mm and the medial humeral offset is between 7 and 14 mm

than normal as it could make contact with the coracoacromial arch. This can happen after trauma or arthroplasty giving rise to cuff impingement. Its location is defined in relation to the superior outline of the humeral head.

The size and shape of the glenoid articular surface is defined by its radius of curvature, linear length and width dimensions. Its length ranges from **30** to **48 mm.** The pear-shaped morphology of the glenoid results from its superior AP width being smaller than its inferior AP width (Fig. 8.3). The range of the superior AP width is **18–30 mm**, compared with the wider inferior AP width of **25–35 mm**. The ratio of these glenoid AP dimensions is **0.80–1.00.** In addition the ratio of the superoinferior length to the lower AP width is **1:0.7**.

The lateral glenoid offset is the location of the joint line, which is defined as the distance between the base of the coracoid process and the surface of the glenoid fossa. This is independent of the size of the individual and is **0–5 mm**. The term *internal glenoid impingement* refers to contact between the nonarticular portions of the
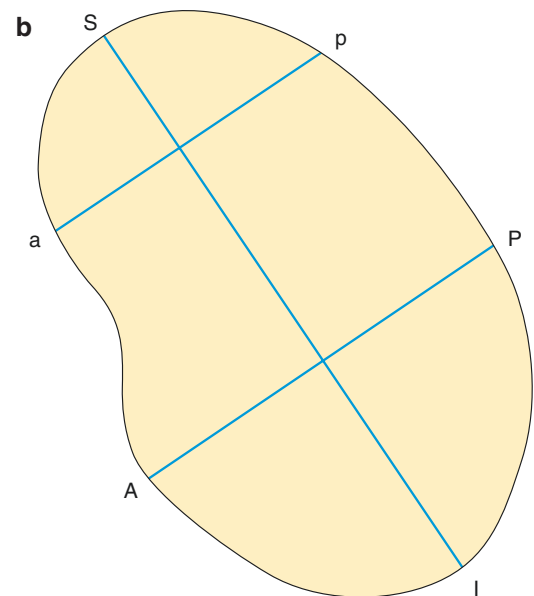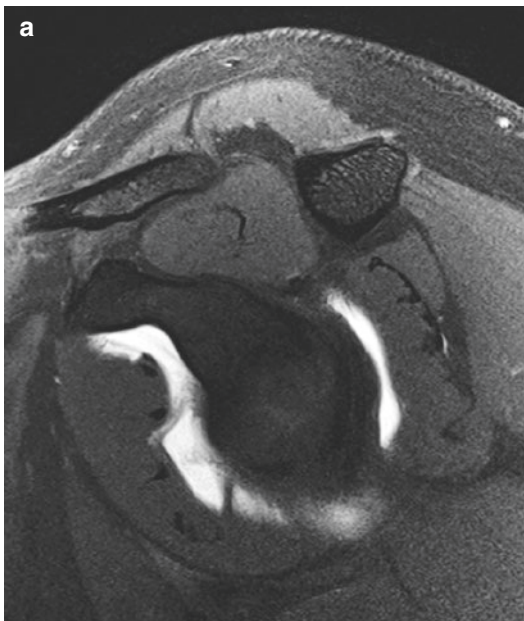
Fig. 8.3 Parasagittal MR arthrogram view through the glenoid showing the characteristic pear shape configuration (**a**). The superior AP width is smaller than the inferior AP width of the glenoid (**b**), but both are shorter than the glenoid length (SI)

proximal humerus and rotator cuff with the gle-
noid rim at the extremes of arm motion. This is
reflected by the correlation of the relative sizes
of the head and glenoid. The pear-shaped gle-
noid and its narrower AP superior width, is pro-
tective as it increases the arc of motion required
before abnormal humeral or cuff contact occurs.

The lateral glenohumeral offset is defined by
the size of the humeral head and the location of
the joint line with relation to the base of the cora-
coid (Fig. 8.4). It plays a critical role in shoulder
function as it dictates the soft tissue tension of
the capsule and the moment arm of the deltoid
and rotator cuff muscles. It exhibits a wide range
of **43–68 mm**. The radius of curvature of the
humeral head also has a wide range of **19–
28 mm**. It is dependent on the size of the humeral
head which in turn varies with the size of the
individual. This means that a wide range of pros-
thetic humeral sizes are required. In contrast as
the lateral glenoid offset is independent of size,
the anatomic data requires a thin glenoid
component.
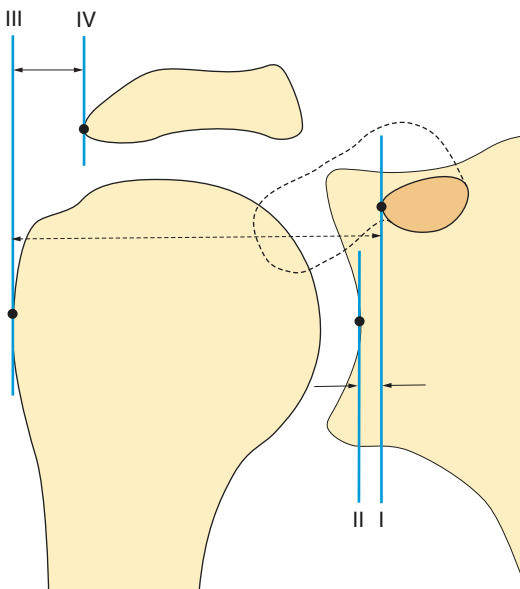
Fig. 8.4 Vertical lines I–IV through the anatomical land-
marks which are respectively the floor of the glenoid cav-
ity, lateral side of the base of the coracoid process, lateral
point of the greater tuberosity and lateral point of
acromion

The radius of curvature of the glenoid is much
greater than that of the humeral head. The gle-
noid subchondral bone is virtually flat, but it is
supplemented at the periphery by the thicker
articular cartilage and the labrum. The labrum
deepens the glenoid by 50%, and the socket by
5 mm in the AP plane and 9 mm in the superoin-
ferior plane. As a result of the adjacent soft tissue
anatomy, the radius of curvature of the glenoid
equals that of the humeral head. Normally there
is good congruency of these glenohumeral
arrangements which allow only a small amount
of translations of 0–2 mm. Excessive translation
in a superior direction occurs as a result of rotator
cuff deficiency and when there is a mismatch in
the humeroglenoid articular surfaces. All of these
measurements in combination provide most of
the structure–function information which needs
to be included in shoulder reconstruction and in
the design and choice of shoulder prosthesis.

The previously described parameters identi-
fied by Ianotti et al. (1992) above on cadaveric
studies have been applied to the true AP radio-
graphic view by Takase et al. (2004) (Figs. 8.4,
8.5 and 8.6):

1. I–II: Distance between joint line and the base
   of coracoid process (Lateral Glenoid offset)
2. I–III: Lateral Glenohumeral offset
3. II–III: Lateral Humeral offset
4. III–IV: Distance between the acromion and
   the greater tuberosity
5. V line: Humeral head diameter
6. α angle: Neck shaft angle
7. VII–VIII: Distance between the greater tuber-
   osity and humeral head
8. Distance between IX and humeral surface:
   Radius of curvature of the humeral head

In the determination of these parameters the
following lines and landmarks are identified and
drawn as follows. Firstly a vertical tangential line
through the most medial arc of the glenoid cavity
is drawn—joint line I. The anatomical landmark
points are then identified: the lateral side of the
base of the coracoid process; the most lateral
point of the greater tuberosity; the most lateral
point of the acromion. Vertical lines II, III, IV

parallel to line I passing through these points are then drawn. From these lines, three distances can be measured as described above (Fig. 8.4). The maximum transverse axis of the humeral head (anatomical neck plane) in the coronal plane (head diameter—V line), is the distance traversing obliquely between the junctional point of the head with the greater tuberosity superiorly and the medial limit of the anatomical neck of the humerus inferiorly. The angle between a line perpendicular to the V line and the humeral shaft axis is the neck shaft angle (α angle). The radius of the curvature of the humeral head is measured by determining the rotational centre (IX) of the humeral head from the point of intersection of perpendicular lines of multiple arcs. The anatomical relationship between the humeral head and greater tuberosity can also be measured, by drawing horizontal two parallel lines (VII, VIII lines) perpendicular to the humeral shaft axis, passing through the greater tuberosity–head junction and the superior part of the humeral head, and then measuring the vertical intervening distance between them (Fig. 8.5). This distance varies with a mean of **6.7 +/−2.0 mm**. It is worth noting at this stage that the humeral head although spherical centrally is elliptical rather than spherical in shape peripherally with a radius which is **2 mm less** in the axial plane than in the coronal plane. The radius of curvature of the glenoid

measured in the coronal plane is an average **2.3+/−0.2 mm** greater than that of the humeral head (Fig. 8.6). The average dimensions of the glenoid are **39+/−3.5 mm** superoinferiorly, while anterosuperiorly due to the pear-shaped configuration the lower diameter is larger measuring **29+/−3.2 mm**, with a ratio with the upper diameter of 1:0.80.

Based on these parameters, Takase et al. (2004) provided average normal radiographic values and standard deviations in men and women.

		Average	Men	Women
1.	I–II (mm)	6.4 +/−1.9	6.5+/−2.0	6.3+/−1.8
2.	I–III (mm)	55.7 +/−5.7	59.9+/−3.6	50.7+/−3.1
3.	II–III (mm)	62.3 +/−6.2	66.5+/−4.1	57.0+/−4.0
4.	III–IV (mm)	16.8 +/−5.9	18.9+/−5.6	14.2+/−5.2
5.	Head diameter (mm)	54.3 +/−5.4	58.2+/−3.1	49.4+/−3.1
6.	α angle (°)	140.4 +/−4.1	141.2+/−3.7	139.5+/−4.4
7.	VII–VIII (mm)	6.7 +/−2.0	7.4+/−1.9	5.7+/−1.7
8.	IX radius of curvature of humeral head (mm)	28.0 +/−3.0	30.1+/−1.9	25.4+/−1.9
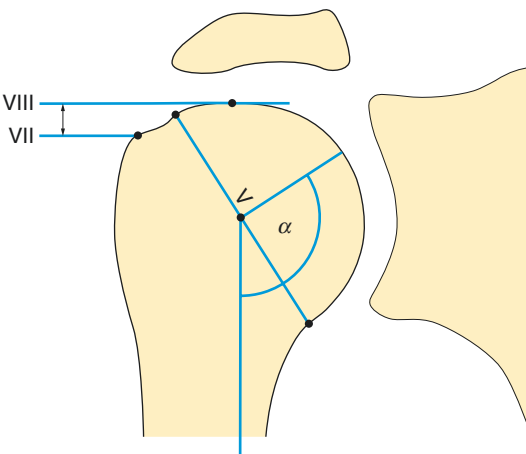
Fig. 8.5 The maximum axis of the humeral head (V line), the neck shaft angle (α) and the intervening distance between lines VII and VIII can be measured
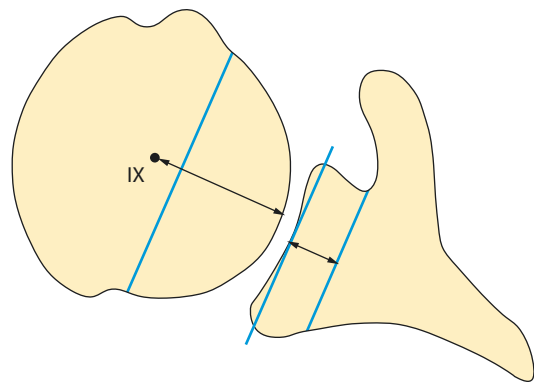
Fig. 8.6 Axial diagram showing the lateral glenoid offset as the distance from the glenoid joint line to the base of the coracoid laterally. The centre of the humeral head (IX) depicts the radius of curvature of the humeral head, while the articular rim is seen to lie off centre

The glenoid orientation is important for proper biomechanical function of the glenohumeral joint. Glenoid inclination abnormalities may be related to rotator cuff tears and superior humeral head migration. A valid and reproducible radiographic technique for measuring glenoid inclination has only recently been described. Maurer et al. (2011) demonstrated one of three measurements (angle beta) to be the most reproducible with inherent resistance to positional variation of the scapula and a good interrater reliability. Beta angle is formed by the intersection of the glenoid fossa line which joins the superior and inferior points of the glenoid, with the supraspinatus fossa line which passes through the sclerotic outline of the floor of the supraspinatus fossa (Fig. 8.7). This assessment is also important before total shoulder arthroplasty. A downward facing of the glenoid component seems to improve the stability of the glenohumeral joint. In these studies a mean value for the **beta angle of 75° with 2 SD** was found. The other two angles (alpha and gamma) were unreliable probably due to variation and normal inconsistency in anatomical landmarks location.

In glenoid version determination, radiography is not reliable due to technical difficulties in obtaining optimal images. When CT or MRI is used, the slices have to be perpendicular to the glenoid cavity and the midpoint image is chosen for determination rather than one from the superior or inferior levels (Fig. 8.7). This introduces a standardised way of obtaining the optimal method of glenoid imaging. If this is not adhered to, as

Bokor et al. (1999) showed, the measured glenoid version value varies by as much as 10° with minor rotation of the scapula in the coronal plane. This is primarily due to differences in the curvature of the vertebral border of the scapula. Altering the vertebral reference point changes the angle measured against the plane of the glenoid. Using these cross-sectional images, the necessary landmarks are easily identified for the appropriate linear and angular measurements to be determined. More recently sphere fitting software has been reported to provide an optimal assessment of glenoid face 3D orientation from which the required version measurements can be determined.

These measurements play an increasingly important role in the accurate reproduction of anatomic relationships at prosthetic arthroplasty and proximal humerus reconstruction, which are essential in ensuring retention of the soft tissue lever arms and joint stability. The latter dictate the postoperative outcome in terms of efficient shoulder function and long term endurance of the replacement. The variations between the parameters are not random but related, and this relationship is useful in a predictive sense. There is interdependence between these measures, with a relationship between the neck shaft angle and humeral head size; neck shaft angle and lateral glenohumeral offset etc., which need to be taken into consideration in preoperative planning to ensure restoration of the muscle power balance, resultant force direction and accurate tension of the soft tissues.
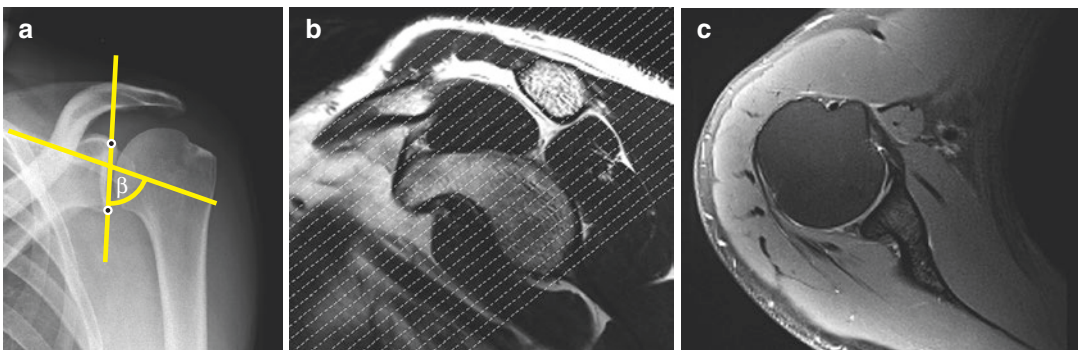
Fig. 8.7 Glenoid inclination reflected by the β angle (**a**). A true axial of the glenoid requires accurate choice of the axial cut at 90° to the glenoid face (**b**) to produce an optimum slice for measuring the glenoid version angle (**c**)

Supraspinatus Outlet Parameters

The interdependence of osseous structures like the acromion, bony glenoid and coracoid process to shoulder function is manifested by the effects structural abnormality has on function of the soft tissues (Natsis et al. 2007) that provide the range of glenohumeral mobility while maintaining stability. With this in mind, it is not surprising that the evolution of measurements of the shoulder have focused on both the identification of osteoarticular structural causes underlying the abnormal anatomical values (e.g. reduced acromiohumeral distance), as well as their effects on soft tissue structures (e.g. rotator cuff—tangent sign, fatty muscle index) which effect their function. Similarly glenoid version has an effect on shoulder mechanics, and abnormalities are associated with glenohumeral instability, rotator cuff tears and adverse outcome of total joint arthroplasty. All the imaging modalities have been employed (US, CT and MRI) for this purpose besides conventional radiography.

The detailed anatomic studies by Neer in the 70s showed that only the anterior portion of the acromion contributes to the supraspinatus outlet. It is important also to understand that the outlet opening is not lateral but orientated anterolaterally perpendicular to the direction of the supraspinatus tendon. It is for these reasons that the outlet view is the best radiographic method to assess the role of the anterior acromion on the supraspinatus outlet (Fig. 8.8). Once again it needs to be emphasised that the correct standard of acquiring the image on which the measurement will be based is crucial. The effects of suboptimal radiographs on the six measurements of the acromion shown by Stehle et al. (2007) are profound. Furthermore in comparing the accuracy of measurements of the size of subacromial spurs obtained from four radiographic views with surgical findings as the gold standard, Kitay et al. (1995) showed that only the supraspinatus outlet view and the AP 20° caudal tilt view correlated accurately with the intraoperative measurements. Similarly in the assessment of acromial shape related to rotator cuff disease, the MR plane also needs to be perpendicular to the supraspinatus tendon (Fig. 8.18).
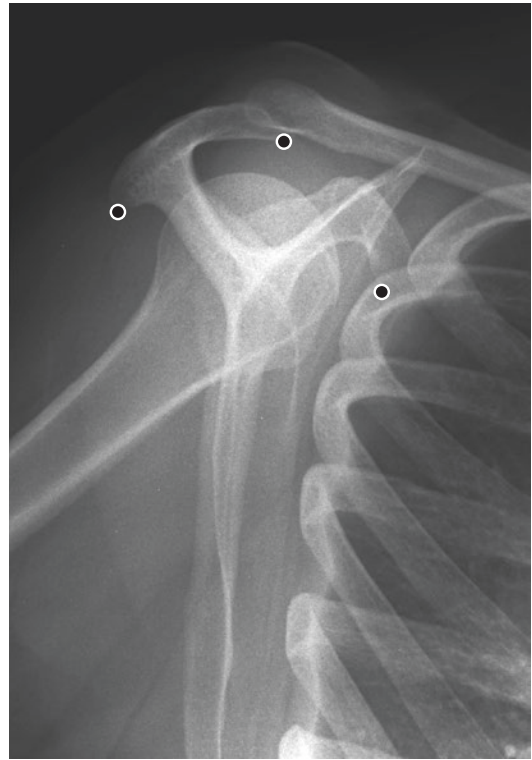
Fig. 8.8 Supraspinatus outlet view with acromial and coracoid process landmarks used for measurements

The measurements of the acromion dimensions and morphology are best assessed on the supraspinatus outlet view (Fig. 8.8). This provides clear depiction of the anterior and posterior outlines of the acromion to allow length assessment as well as measurement of the vertical thickness. Wuh and Snyder (1992) stressed the importance of knowing the thickness of the acromion besides its morphological configuration prior to surgical decompression. They provided these thickness values based on three types of acromion:

Type A	<8 mm
Type B	8–12 mm
Type C	>12 mm

The inferior surface of the acromion is easily assessed on a good quality outlet radiograph which allows depiction of the apex and other important landmarks including the anteroinferior and posteroinferior acromial limits as well as revealing the acromial shape (Fig. 8.9). This view
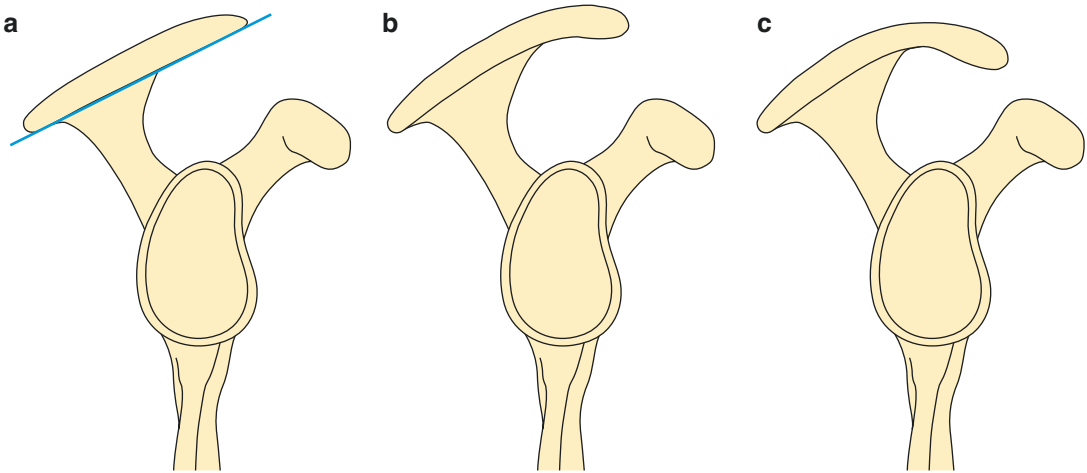
Fig. 8.9 Bigliani Type I—flat (**a**) based on anterior acromial morphology as seen on outlet view, Bigliani Type II—curved (**b**), and Bigliani Type III—hooked (**c**)
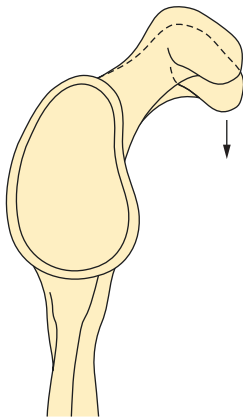
Fig. 8.10 Subcoracoid impingement. The morphology and size of the tip of the coracoid process, its location and craniocaudal relationship to the glenoid are important determinants of subcoracoid impingement. The more inferiorly located, the increased likelihood of impingement

also reveals the coracoid landmarks used in measurements, namely the inferior limit of the tip of the coracoid and inferior curved outline of the coracoid process (Fig. 8.10). There is a direct relationship between an inferiorly located coracoid tip relative to the glenoid and rotator cuff disease as shown by MR arthrography (Porter et al. 2015).

One should resist the temptation of measurement extrapolation, by taking reference values of one modality, and applying them in the assessment of values of the same measurement deter-

mined by another modality. This is an important principle that applies to any musculoskeletal measurement and includes the magnification effect of conventional radiography. It is particularly important in shoulder measurements, e.g. acromiohumeral distance (AHD), as the soft tissue alterations with positional and dynamic muscle engagement, have a significant effect on the osteoarticular relationships used for making the measurements. The AHD measurements in the same patient are always smaller in value when determined by MRI compared with the radiographically determined value. The dynamic engagement of the muscles can also reveal measurement differences which reflect altered osteoarticular relationships secondary to underlying rotator cuff pathology. Using conventional radiography, Deutsch et al. (1996) showed that patients with subacromial impingement demonstrated a greater superior migration of the humeral head during elevation. In this study the authors studied three groups of patients: normal, impingement and rotator cuff tear groups, using sequential AP shoulder radiographs done in increments of 20° abduction from 0 to 120°. They measured the excursion of the humeral head on the glenoid face expressed as the distance that the centre of the head lies below or above the centre of the glenoid (Fig. 8.11). At rest the humeral head normally lies **−0.4 mm** below the glenoid centre.
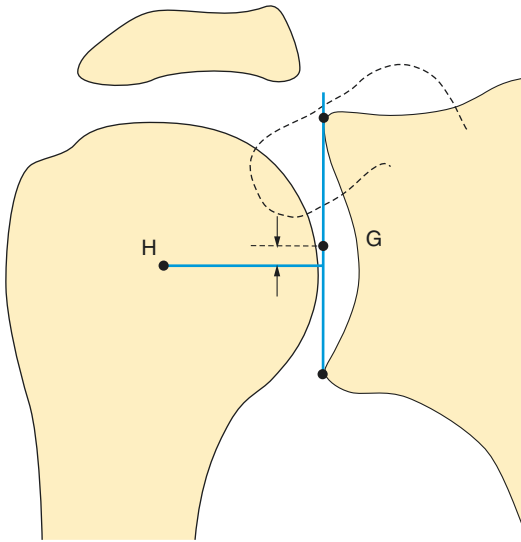
Fig. 8.11 Relationship of the centre of the humeral head (H) to the centre of the glenoid. Normally the head is −0.4 mm inferior to the glenoid centre (G)

They found an average humeral head displacement of **1–2 mm** superiorly in the impingement group compared with **0.7 mm** in the normal shoulders. In the rotator cuff tear patients, the humeral head exhibited a **sharp rise of 1.0 mm at the first 20–40 °** of abduction, and then fell sequentially in the next 100°. This is thought to be due to a muscle imbalance in the impingement and rotator cuff tear groups due to a weakened rotator cuff, promoting superior migration of the humerus. This feature is seen on both the AP and outlet views, which have been shown to show no significant difference in the measurement of acromiohumeral distances. This study stresses the importance of the role that the rotator cuff plays in maintaining the humeral head position in the glenoid.

8.3   Subacromial Space: Radiography

Definition

The width of the space between the inferior surface of the acromion and the head of the humerus is called the subacromial space or acromiohumeral distance. It has been measured on radiographs by several authors, notably Golding (1962), Cotton and Rideout (1964), and Weiner and Macnab (1970). However, all these authors pooled their estimates from normal shoulders without regard to age and gender.

Indications

The acromiohumeral interspace is examined to rule out the suspicion of a rotator cuff tear in patients with clinical symptoms of shoulder impingement syndrome.

Subacromial space width is determined by calculating the shortest distance between the humerus and acromion, which reflects superior migration of the humeral head (Fig. 8.12), as shown by Petersson and Redlund-Johnell (1983, 1984).

The subacromial space is measured on radiographs taken with the arm in zero abduction and slight outward rotation.

Technique:

Radiography: standard shoulder AP view.

Full Description of Technique

The subacromial space is measured on AP radiographic projection of the shoulder. The radiograph is obtained in the upright position, with the patient positioned obliquely by approximately 35–45° so that the plane of the scapula parallels the cassette, providing a tangential view of the glenohumeral joint. The arm of the involved side is held in a neutral position. The beam is centred to the glenohumeral joint and angled 10–15° craniocaudally. To obtain a better tangential view of the subacromial surface it is preferable to have fluoroscopic guidance for optimal radiographic projection execution. The tube-screen distance is around 100 cm, and the kilovoltage is usually 60–65 kV.
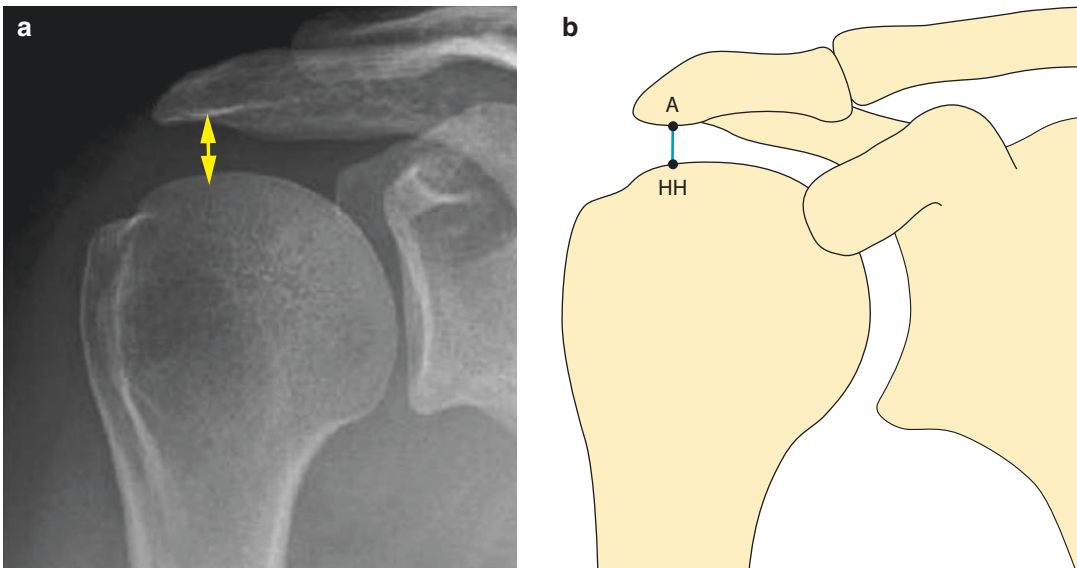
Fig. 8.12 Acromiohumeral distance between (A) the inferior outline of the acromion and (HH) the superior outline of the humeral head

Due to the angulation of the X-ray beam the superimposed anterior and posterior portions of the acromial undersurface appear as a regular cortical profile.

The subacromial space corresponds to the shortest distance between the most cranial point of the subchondral outline of the humeral head (HH) and the inferior dense cortex of the acromion (Fig. 8.12).

As proposed by Leclercq (1950) and remarked by Totty (1988), an additional manouvre, **"Leclercq's Manouvre"**, can be employed when obtaining the AP radiograph by asking the patient to abduct the arm by 20° while holding a weight. This enhances the superior migration of the humeral head, i.e. reducing the subacromial distance further, in the presence of rotator cuff disease. This provides an easy way of assessment by comparison with the previous measurement from the conventional ipsilateral AP radiograph and the contralateral shoulder. When positive there is always a rotator cuff tear.

Normal Acromiohumeral Distance	10.5 mm
Abnormal Acromiohumeral distance	<7 mm

A measurement of <7 mm is indicative of a large rotator cuff tear.

Reproducibility/Variation

Interrater reliability of the subacromial space measurement is consistently high with no significant interrater differences.

The measurement technique reported here has proved to be accurate to within 0.4 mm and 0.5 mm in a rigorous validation study that accurately simulated in vivo testing conditions.

Clinical Relevance/Implications

The subacromial space plays an important part in the pathogenesis of the impingement syndrome. It is not known if specific tendon involvement (supraspinatus or infraspinatus), tear size or muscle degeneration are the most important structural determinants of a reduced acromiohumeral distance.

Saupe et al. (2006) noted that when the acromiohumeral distance is <7 mm, full thickness supraspinatus tears are present in 90% of patients, infraspinatus tendon tears in 67% of patients and subscapularis tendon tears in 43% of the patients. Bey et al. (2007) argued that the size of rotator cuff tendon tears and the degree of fatty infiltration in all rotator muscles show a significant negative correlation with acromiohumeral distance.

Furthermore when the subacromial distance is <7 mm, the chances of a favourable outcome following surgical repair of the tear is poor. The short distance is usually associated with a large tear and profound fatty degeneration of both the supraspinatus and infraspinatus muscles. The number of full thickness tears of the supraspinatus and infraspinatus decrease considerably with a distance of 8–14 mm. There are however some exceptions where despite a measurement of <7 mm the rotator cuff is occasionally found to be intact.

Analysis/Validation of Reference Data

The implications of a reduced subacromial space and its association with rotator cuff disease, tears and fatty infiltration have been validated.

Conclusion

The finding of a narrowed subacromial space is useful in identifying, with high degree of specificity, patients with a rotator cuff tear and/or with rotator cuff muscle degeneration.

8.4 Subacromial Space: Ultrasound

Definition

Sonography of the shoulder is useful in detecting tears of the rotator cuff. In the evaluation of the subacromial space (average 5–10 mm), a 20% reduction compared to the contralateral normal shoulder is considered an US sign of rotator cuff disease.

Indications

Azzoni et al. (2004) noted that in the evaluation of the subacromial space, ultrasound has been proven to be accurate, specific and sensitive in diagnosing rotator cuff lesions.

Technique

Ultrasound-Shoulder along supraspinatus long axis scan (superior coronal section plane).

Full Description of Technique

The examination technique for the rotator cuff always includes static and dynamic components. The shoulder is examined anteriorly and laterally on both axial and sagittal planes with the patient's arm in neutral and then in internally rotated positions; the latter is achieved by placing the patient's wrist against the wall of the patient's back.

In the section in which it is possible to study the supraspinatus tendon in longitudinal axis (superior coronal plane), one can measure the subacromial space placing one point on the inferolateral point of the acromion (A) and another point on the surface of the humeral head (HH) where the measurement is the lowest achievable (Fig. 8.13).

Reproducibility/Variation

The accuracy, specificity and sensitivity of the method have reached levels of 90–95%.

Sonography is certainly useful due to its simplicity of execution and rapidity of use. Measurement of the subacromial space can easily be carried out during routine sonographic evaluation of the shoulder.

Clinical Relevance/Implications

The ultrasound diagnosis provides important information about tendon components, sometimes better than MRI.

Sonography is extremely sensitive in the evaluation of the thickening of the tendon and the presence of fibrosis or micro-calcifications.
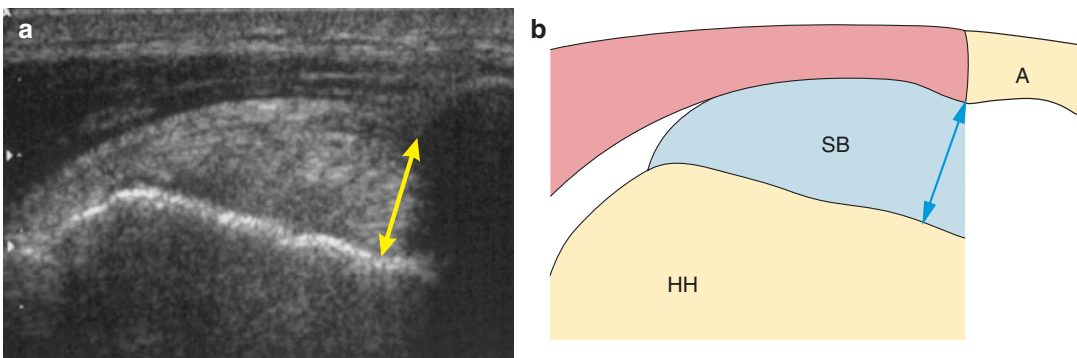
Fig. 8.13 Sonographic measurements of the acromiohumeral distance

Analysis/Validation of Reference Data

The sonographic method for subacromial space measurement has been validated with excellent comparative results with other imaging methods and in cadaveric studies.

Conclusion

Sonography of the rotator cuff is a substantially accurate examination, specific and sensitive in the measurement of subacromial space, but also in the diagnosis of the disease of the rotator cuff of the shoulder.

8.5   Subacromial Space: MRI

Definition

The subacromial space is the width of the anatomic interval between the humeral head and the undersurface of the acromion.

Indications

The subacromial space plays an important role in the pathogenesis of the impingement syndrome. The pain is typically brought about by actions that carry the arm above the head, and therefore the patient is usually examined clinically during active elevation of the shoulder. As indicated by Graichen et al. (1999), on static MRI units the distance is measured only at rest, while Open MR scanners allow the measurements to be made at the points of clinical impingement positions.

Technique

Shoulder MRI: sagittal oblique section plane and coronal if required.

Full Description of Technique

The subacromial space is measured on T1 sequences in the coronal and sagittal oblique planes, in millimetres, between the most caudal point of the acromial undersurface and the most cranial point of the humeral head directly in line with the centre of the humeral head (Fig. 8.14). There is a variation (invariably lower) in the normal range for the subacromial space measured by MRI compared with radiographic measurement in normal individuals. This in part is due to the geometric magnifying effect of radiography. However, as noted by Roberts et al. (2002), there is also a difference in the MR measured acromiohumeral distance
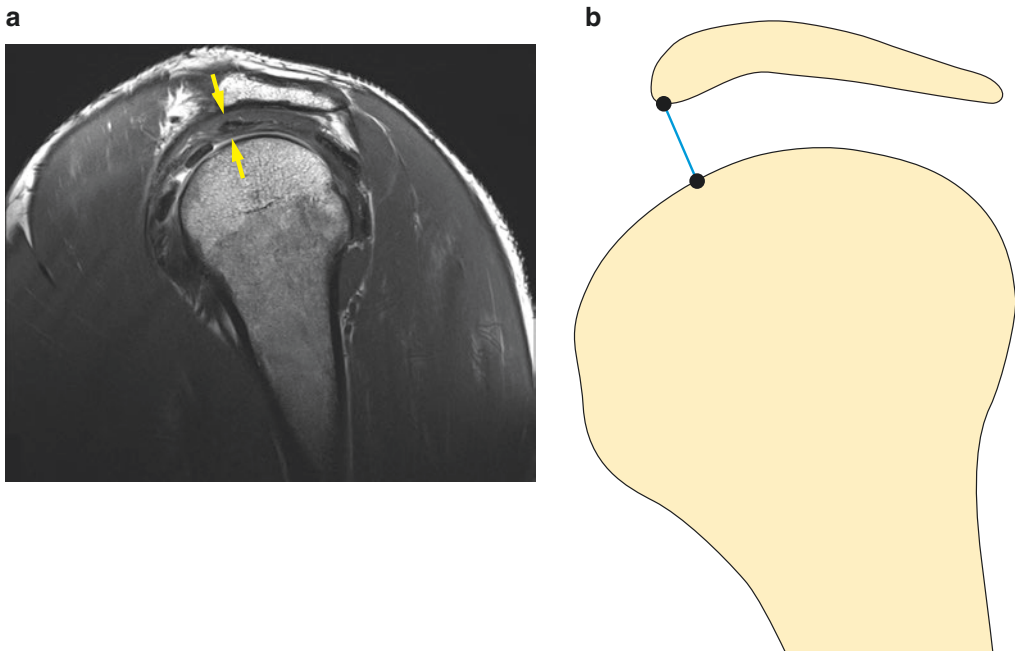
Fig. 8.14 Parasagittal assessment used in determining the acromiohumeral distance on MR imaging (**a**) and in diagrammatic depiction (**b**)

in normal individuals, between the resting state with the arm by the side and on abduction as shown by Open MRI studies with the patient seated.

| Normal acromiohumeral distance on MRI at rest | Mean 6.4 mm |
| Progressive AHD increase as the arm is elevated 90–160° | Mean 7.7–14.2 mm |

This variation in normal individuals is also mirrored by the measurement of the thickness of the rotator cuff, which also exhibits its lowest value at rest with the arm by the side.

In a comparative study measuring the mean acromiohumeral distance between AP radiography and the coronal and parasagittal MR obliques, the MR measurement was found to be consistently **lower by an average of 2.8 mm**. This could be positional or related to different muscle groups acting in the upright as opposed to the supine position. The comparative mean AHD values in one study between conventional AP radiography and sagittal MRI in a clinically heterogeneous group were:

Radiograph	MRI
8.7 mm (1.0–13.7)	5.9 mm (range 1.2–9.8)

Reproducibility/Variation

The limitation of MRI lies in the difficulty to exactly reproduce the same plane and orientation of a specific required section.

Clinical Relevance/Implications

MR imaging studies have focused on describing qualitative morphologic alterations of the rotator cuff (e.g. changes of signal intensity or continuity, intrasubstance fraying of rotator cuff tendons), the soft tissue (e.g. fluid in the subacro-

mial–subdeltoid bursa), and the adjacent bones but the technique has so far not been applied in examining functional deficits of the supraspinatus muscle in patients with impingement syndrome. In normal individuals, interestingly the measurements obtained during dynamic studies of the subacromial space in an Open MR scanner have shown the converse of expected, with an increase of subacromial space dimensions with abduction in the so called "impingement sign positions". However in patients with unilateral impingement, Hebert et al. (2003) demonstrated on MRI, that the acromiohumeral distance decreases as the arm is elevated, and at 80° of arm elevation the distance is significantly smaller in the symptomatic shoulders than in the contralateral side.

Analysis/Validation of Reference Data

Although a number of studies have repeatedly shown that superior migration of the humeral head is associated with late-stage rotator cuff disease, the exact mechanism for its production is still unclear. Dynamic MRI studies have also confirmed a lower limit of MR measurements compared with radiographic measurements of the subacromial space. This is probably related to the kinetic effect of muscle contraction and tension involved in motion.

Conclusion

MRI is the best modality of assessing the presence, role and effect of a reduced acromiohumeral distance on the rotator cuff. Tendon tears and fatty muscle infiltration correlate with a reduced subacromial space. The size of the tear and the degree of fatty infiltration of the infraspinatus muscle have the most pronounced influence on the measured distance Saupe et al. (2006).

8.6 Acromial Angle

Definition

The acromial angle is the angle at the junction of two lines drawn along the inferior surface of the anterior and posterior portions of the acromion. It provides an objective measure of acromial morphology. The average acromial angles are **20°** for patients with an intact rotator cuff and no impingement.

Indications

The angle is useful in identifying patients with a greater likelihood of having a rotator cuff tear and in distinguishing patients with primary impingement from those with instability.

It is useful to orthopaedic surgeons during presurgical planning for an arthroscopic acromioplasty. It provides an indication of how much bone needs to be removed prior to surgery and acts as a measure of success following its removal after surgery.

Technique

Radiography: outlet (arch) radiographs.

Full Description of Technique

Neer's supraspinatus outlet or arch radiograph of the shoulder is obtained in the lateral projection with the standing patient positioned 40° anterior oblique facing the cassette and the central beam coned to the superior half of the scapula. The tube-screen distance is about 183 cm, with a 10 ° caudal tilt of the tube. The acromial angle is determined by drawing a line along the inferior acromial cortex on either side of the apex, resulting in anterior and posterior lines that meet to form an angle.

From the resultant arch radiograph the apex along the undersurface of the acromion is first identified, and from it two lines are drawn along the inferior cortex of the anterior and posterior acromial portions respectively. The apex is usually at the junction of the anterior third with the posterior two thirds of the acromion. The angle formed at the apex by the intersection of these lines is the acromial angle (Fig. 8.15). The following are the average acromial angle values in asymptomatic states and in different clinical shoulder scenarios.

		Impingement	
Normal	20°	Full thickness tear	30°
Instability	20°	Partial tear	25°
		Intact cuff	26°
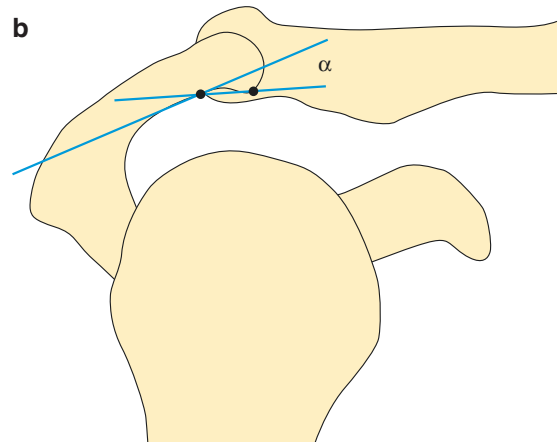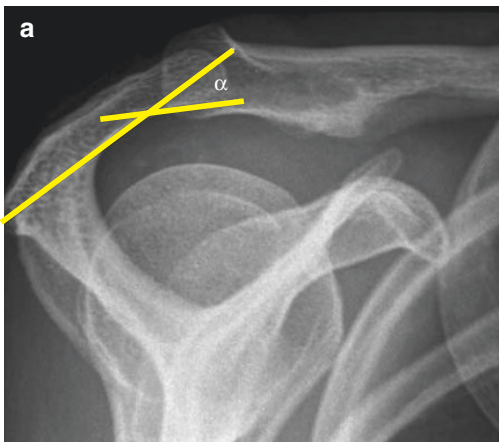
Fig. 8.15 Acromial angle

Note that the acromial angle is greater in patients with impingement and an intact rotator cuff compared with normal individuals and patients with glenohumeral instability.

Reproducibility/Variation

Obtaining a satisfactory arch view for determining the acromial angle is not always easy, as demonstrated by Tuite et al. (1995) who required repeat views with different caudal tube tilt (5–15°) for some patients. There was a good inter-observer variability in Tuite et al.'s study as determined by the intercorrelation coefficient (a test of reproducibility of quantitative measurements). However despite meticulous attention to the measuring technique, the heterogeneity of acromial shapes posed difficulties in drawing the acromial lines resulting in inevitably both intra-observer and inter-observer variations.

Clinical Relevance/Implications

Using the arch radiograph, Bigliani et al. (1986) highlighted the importance of the anterior acromion morphology (Fig. 8.9), classifying the shape into Type 1 (flat), Type 2 (curved) and Type 3 (hooked). However following this concept's introduction, a number of authors reported a wide unacceptable inter-observer variation using both radiographic and MRI means of assessment for a variety of reasons. An objective method was required and the acromial angle was promoted by Toivonen et al. (1995) as the means of determining anterior acromial shape. Using the acromial angle, Tuite et al. (1995) found a statistically significant correlation between the average acromial angle and preoperative diagnosis. A correlation was found between the increasing severity of cuff disease as determined by arthroscopy and the increasing acromial angle ($p < 0.01$).

Arthroscopic acromioplasty decompresses impingement by removing about 4–6 mm of the anterior portion of the acromion. In their study Green et al. (2004) have shown that the risk of detaching the attached anterior deltoid origin is related to the acromial angle. The extent of deltoid detachment is inversely related to the acromial angle, so that when the acromial angle is large (e.g. Type 3 acromion) a smaller % of deltoid origin is detached and vice versa. This risk is especially important in patients treated by acromioplasty with massive rotator cuff tears who functionally are more dependent on the deltoid muscle.

Analysis/Validation of Reference Data

Mallon et al. (1992) were the first to identify anterior and posterior axes of the acromion in their study on cadaveric shoulders. They measured the acromial angle across the centres of the acromion portions and not by drawing lines along the inferior cortical outlines as Tuite et al. (1995) did. In their study Mallon et al. (1992) reported an average acromial angle of 37 ° which is higher than the normal values reported by Tuite et al. (1995). What is interesting however is that both studies failed to identify a single case of the Bigliani Type 1 (0°- flat) acromion!

It is important to note that the acromial angle should not be measured on the scapular Y-view. Haygood et al. (1994) showed that 41% of scapular views were not diagnostic for evaluating acromial shape. The scapular view does not have the caudal tilt to optimally reveal the inferior profile of the acromion.

Conclusion

The acromial angle is an objective and fairly reproducible measurement of the anterior acromial shape. The angle is useful in identifying patients with a greater likelihood of having a rotator cuff tear and in distinguishing patients with primary impingement from those with instability.

8.7 Acromial Tilt Angle

Definition

The acromial tilt angle is a measure of the anterior slope of the acromion. The angle values varied from **31.7 to 33.5°**.

Indications

The acromial tilt angle expresses the reduction in the acromiohumeral distance anteriorly, in the "critical area" crossed by the supraspinatus tendon, due to abnormal anterior slope of the acromion.

Normal	31.7–33.5°

Technique

Radiography: outlet view.

Full Description of Technique

As noted by Prato et al. (1998), the acromial tilt angle can be radiologically evaluated on the outlet view of the shoulder. The measurement

of the angle in relation to the scapula is based on the method described by Aoki et al. (1986) and Kitay et al. (1995) This angle (α) is calculated through the intersection of a line drawn between the anteroinferior point and the posteroinferior point of the acromion and another line drawn between the posteroinferior point of the acromion and the inferior tip of the coracoid process curve (Fig. 8.16).

Reproducibility/Variation

This measurement is an easy, valid and objective tool for diagnosing impingement and makes it possible to express a quantitative judgement on the acromial shape. It enjoys excellent intra-observer and inter-observer levels of agreement.

The measured acromial slope in the method proposed by Aoki et al. (1986) on 130 cadaveric shoulders was done by calculating the alpha angle. They concluded that acromions with a decreased alpha angle (flatter slope) were associated with impingement, degenerative changes, spur formation and pitting on the surface of the greater tuberosity. They also showed that the prevalence of subacromial spurs increased with advancing age and with it an alteration in the alpha angle value.
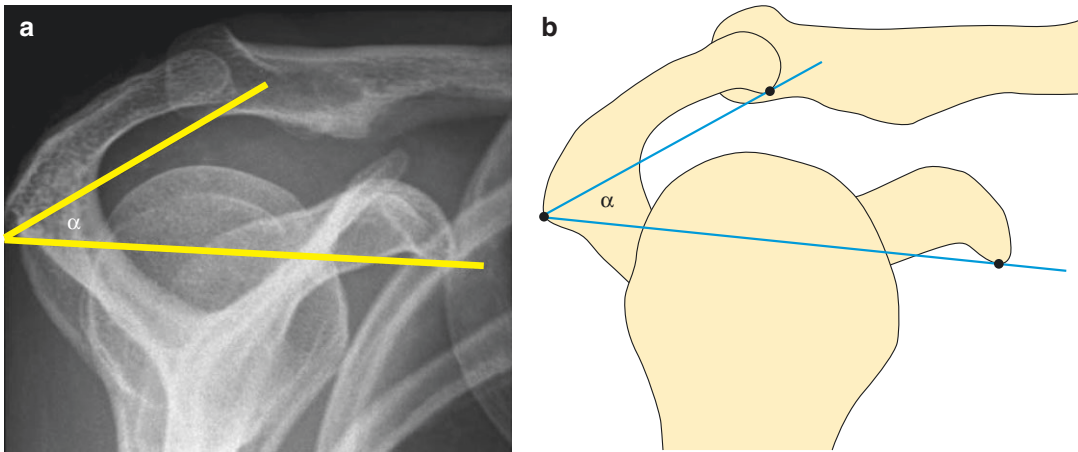
Fig. 8.16 Acromial tilt angle

Clinical Relevance/Implications

There is a statistically significant correlation between the average acromial tilt angle and the preoperative diagnosis.

The acromial tilt angle in patients with impingement is smaller than the angles in patients with instability and patients with trauma.

Analysis/Validation of Reference Data

In a large cadaveric study Zuckerman et al. (1992) found a significantly greater anterior acromial projection and a lower acromial tilt in the presence of a rotator cuff tear than in those speciments with an intact rotator cuff ($p < 0.0001$).

Edelson and Taitz (1992) defined the acromial slope in a similar method, except that they used a horizontal line instead of a line connecting the posteroinferior aspect of the acromion and the inferior aspect of the tip of the coracoid process. They too concluded like Aoki et al. (1986) that the more horizontal the acromial slope is, the bigger the magnitude of the observed degenerative changes. However in in-depth 3D studies with computer spatial graphics, Moses et al. (2006) showed that there was no support that a flatter acromial slope causes impingement and rotator cuff tears, concluding that acromial slope should not be considered as a source of pathological changes. The method employed by them however was not the same, as they relied on an average of multiple points along the undersurface of the acromion, which would not have included a focus of impingement at the anteroinferior tip of the acromion unlike the methods used by Aoki et al. (1986) and Edelson and Taitz (1992).

Conclusion

The angle is useful in identifying patients with a greater likelihood of having a rotator cuff tear and in distinguishing patients with primary impingement from those with instability.

8.8   Intrinsic Acromial Angle

Definition

The intrinsic acromial angle indicates the degree of curvature of the anterior acromion.

Its value ranges from **0 to 17°**.

Indications

The intrinsic acromial angle indicates the degree of mechanical compression on the subacromial space due to abnormal bone shape and causing impingement on rotator cuff.

Normal	0–17°

Techniques

MRI Shoulder: parasagittal oblique plane.

Full Description of Technique

Sagittal oblique MR of the shoulder, with SE T1-weighted sequences, is currently the best technique for identifying and assessing acromial angle, one of the fundamental factors in determining impingement. The acromial slope angle is formed by the intersection of a line joining the anterior and posterior undersurface of the acromion and a line running parallel to the main acromial axis (Fig. 8.17).

Reproducibility/Variation

Fairly reproducible.

Clinical Relevance/Implications

The intrinsic acromial angle, proposed by Di Mario and Fraracci (2005), may be useful to orthopaedic surgeons during presurgical planning for an arthroscopic acromioplasty.
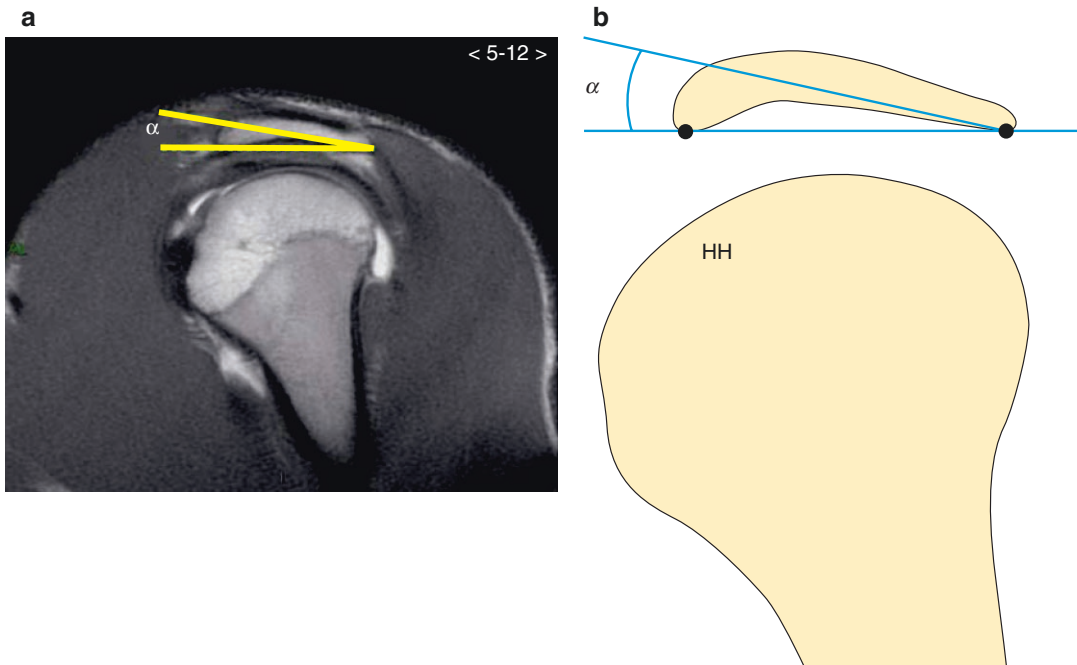
Fig. 8.17   Intrinsic acromial angle (α)

Analysis/Validation of Reference Data

Limited number of references to provide validation**.**

Conclusion

The acromial angle is an objective and fairly reproducible measure of anterior acromial shape. The angle is useful in identifying patients with a greater likelihood of having a rotator cuff tear and in distinguishing patients with primary impingement from those with instability.

8.9 Acromial Shape: MRI

Definition

Mathematical determination of acromial morphology based on MR image assessment. Acromial shape is classified on the appearance of its undersurface. On the basis of dried cadaver scapulae and conventional outlet views Bigliani originally described three morphological types (Fig. 8.9)—**Type 1 flat** (12%), **Type 2 curved** (56%), **Type 3 hooked** (29%)—which was followed by the later addition of **Type 4 inferiorly convex** (3%). The acromial undersurface is assessed by angular measurements based on mathematically dividing it into three equal segments.

Indications

Subacromial outlet impingement can be due to abnormal shape of the anterior acromial undersurface. Type 1 is normal and physiologic. The others are abnormal with Type 3 and to a lesser extent Type 2 acromions being associated with an increased incidence and severity of rotator cuff tears.

Technique

MRI—Parasagittal T2 Oblique views.

Full Description of Technique

The method described here only refers to estimation on MRI. The standard technique of determining the value can also be applied to the radiographic outlet or arch view. This has been covered previously using Toivonen et al.'s method of assessment.

The agreed standard MR sequence chosen is T2 weighted, in the parasagittal plane, perpendicular to the supraspinatus tendon (Fig. 8.18) with a slice thickness of 4 mm. Two slices are used as standard: the first slice (A) 4 mm from the lateral edge of the acromion and the second slice (B), medial to A just lateral to the acromioclavicular joint.

Mathematical assessment of acromial shape based on the MR image through slice B is then done in two steps. Firstly a line is drawn connecting the inferior most points of the acromion's undersurface; its distance is measured and then divided into three equal portions. Using two orthogonal lines to the dividing marks on the line, the inferior acromial surface is then divided into three
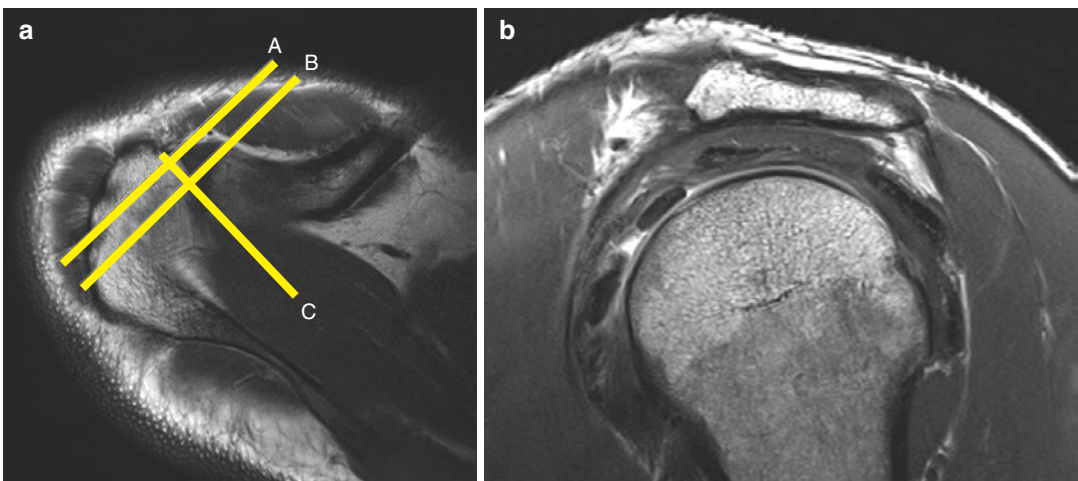
Fig. 8.18 Parasagittal MR slices are taken 4 mm medial to the edge of the acromion (A) and medial to (A) lateral to the acromioclavicular joint (B) perpendicular to the supraspinatus axis (C) to assess acromial morphology (**a**). Parasagittal MR image (**b**) corresponding to the slice at point A

segments of equal length. The angle formed between the anterior third and the posterior two thirds of the acromion is then measured (Fig. 8.19a) and designated as the acromial **a1 angle**.

a1 angle	Type 1	<10°		
	Type 2	11–20°	a2 angle	>10°
	Type 3	>20°		<10°

If the angle a1 measures more than 20°, the second step is taken which measures the second acromial angle **(a2)** between the anterior two thirds and the posterior one third of the acromion (Fig. 8.19b). If this angle (a2) is 10° or less, the acromion is classified as type 3, if it is larger than 10° it is labelled as extreme type 2. Measurements based on the B position are more sensitive to the type 3 acromion, but the arithmetic mean of the angles measured from both A and B positions increases the sensitivity and specificity compared with the outlet radiograph.

Reproducibility/Variation

Outlet or arch radiographs have been shown to show a variable correlation with rotator cuff tears primarily for technical reasons, because minor changes of the angle of the central beam cause different radiographic depiction of acromial shape.

MRI based determination of acromial shape has also been shown to be variable as it is highly dependent on the MR plane and the chosen slice, giving rise to a high inter-observer variability. It is for this reason that this mathematical MR based method is recommended Mayerhoefer et al. (2005), as it uses standardised and reproducible sequences in the choice of image procurement and in calculation.
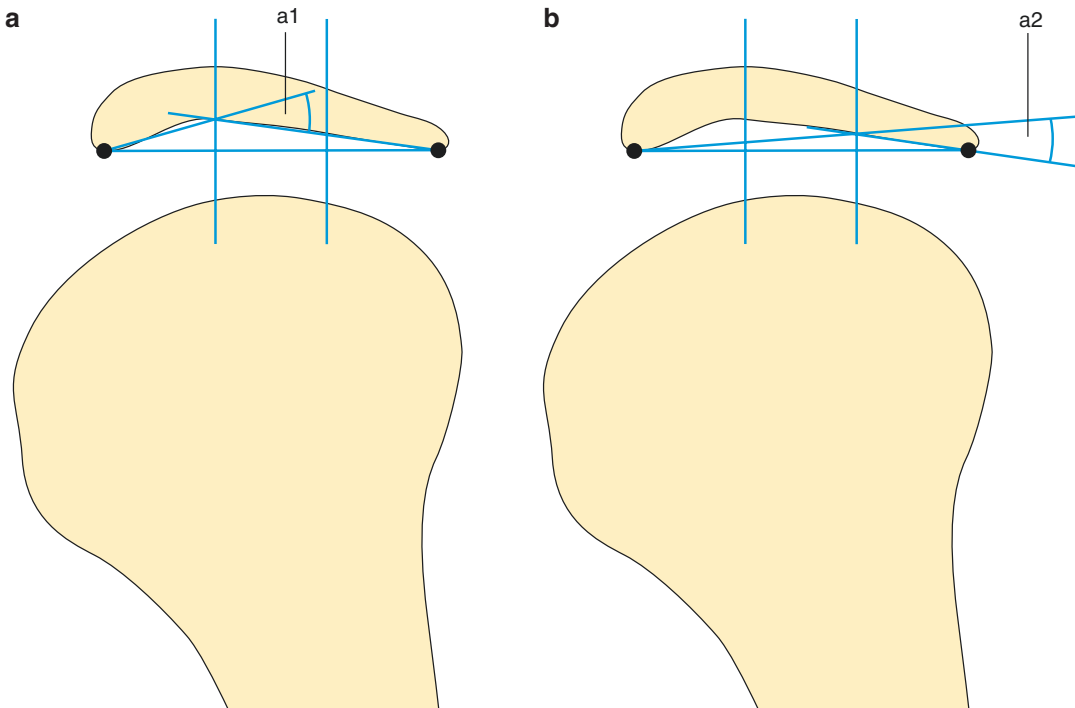
Fig. 8.19 Mathematical estimation of acromial shape based on parasagittal slices taken at position A. The 2 angles are measured a1 (**a**) and a2 (**b**) and respective values indicate and determine the acromial shape

Clinical Relevance/Implications

The B position just lateral to the acromioclavicular joint is a reliable site to obtain the appropriate MRI slice for the mathematical assessment of acromial shape. If this slice depicts a type 3 acromion, the slice located 4 mm from the lateral edge (A) is recommended as this slice has a very high specificity for this type of acromion. This acromial shape has a high correlation with rotator cuff tears.

Analysis/Validation of Reference Data

Since Bigliani's first description of the role of the shape of the acromial undersurface as seen in the sagittal radiographic plane in rotator cuff disease, many authors have confirmed a close correlation of the hooked Type III acromion with rotator cuff disease. There is however poor interobserver reliability and considerable difficulty in standardising the outlet radiograph which in combination create a significant deficiency of its clinical utility. A mathematical based measurement should enhance its role in clinical practice especially in acromioplasty consideration as a form of treatment. The best results from the MRI angular assessments are achieved by the arithmetic calculation of the mean angle by combining the measurement of both the A and B positions. This is superior to the radiographic outlet view assessment. There are no agreed mathematical values for the type 4 acromion.

Conclusion

A simple and reliable method which if done appropriately is accurate in identifying the acromial morphological type.

8.10   Tangent Sign

Definition

The tangent sign provides a quick semi-quantitative evaluation of the effect of a rotator cuff tear on the supraspinatus muscle. A line is drawn through the superior borders of the scapular spine and the superior margin of the coracoid (*the tangent*). The tangent sign is considered present when the supraspinatus muscle does not cross the tangent and is indicative of atrophy of the supraspinatus muscle.

Tendinous rotator cuff tears induce muscle atrophy and fatty infiltration, which are regarded as important factors in influencing the postoperative outcome of rotator cuff repair.

Technique

MRI—Parasagittal T1 oblique.

Full Details of Technique

The patient lies supine in the scanner with the arm placed by the side of the body in a neutral position with the thumb pointing forward. The shoulder is placed in a dedicated receive-only shoulder coil. A single sequence of parasagittal T1 weighted Turbo spin echo MR images parallel to the glenohumeral joint space is obtained. Slice thickness of 5 mm with an interslice gap of 1.5 mm is sufficient. The rotator cuff is examined from the humeral tuberosities to the middle third of the scapula.

The most lateral image which shows the spine of the scapula in contact with the rest of the scapula is the optimal image to choose to make these soft tissue assessments. This position is reproducible and shows the muscle rather than the tendinous components of the rotator cuff. The *tangent line* is drawn from the superior border of the scapular spine to the superior margin of the coracoid. The tangent sign is deemed positive (abnormal) when the tangent does not cross the supraspinatus muscle. Normally it is negative in the asymptomatic individuals (Fig. 8.20).

Clinical Relevance/Implications

The tangent sign is a sign of muscle atrophy with a high positive predictive value. The main limitation is that it is only applicable to the assessment
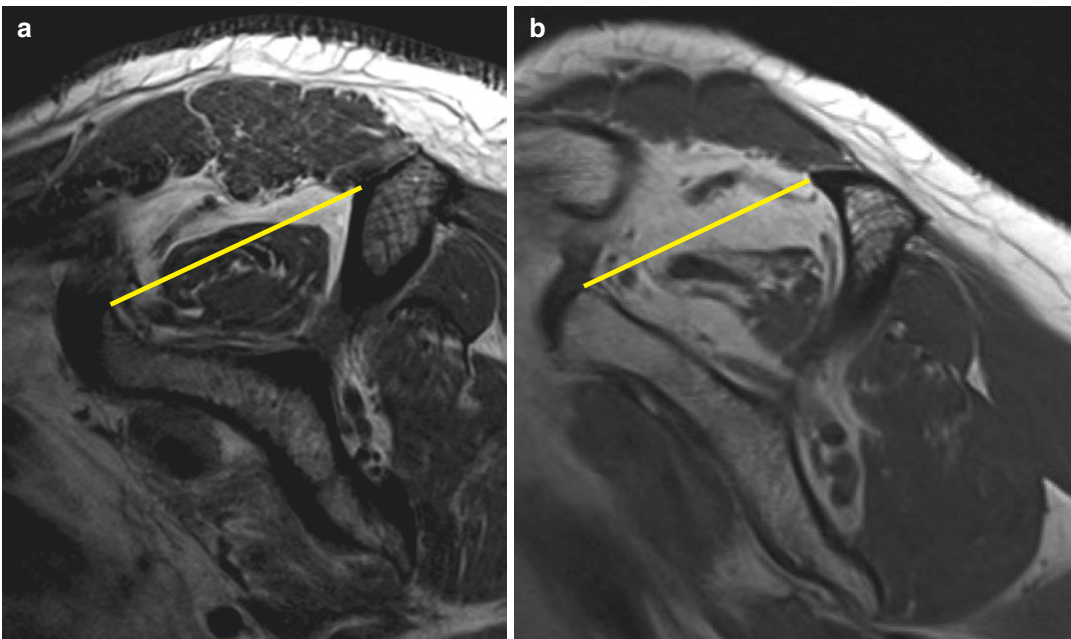
Fig. 8.20 The tangent sign is negative as shown by the line intersecting the supraspinatus muscle on the parasagittal MR view (**a**) and positive in (**b**)

of the supraspinatus muscle. The mean radiographic acromiohumeral distance (AHD) in patients with a positive tangent sign is 6.7 mm compared with 9.7 mm in shoulders exhibiting a negative tangent sign.

Positive tangent sign	AHD mean	6.7 mm
Negative tangent sign	AHD mean	9.7 mm

Reproducibility/Variation

The measurement is easily reproduced with high inter-observer and intra-observer correlation.

Analysis/Validation of Reference Data

True validation studies are difficult to conduct and therefore there is currently limited reference for this. Quantitative values of the individual rotator cuff muscles in asymptomatic and rotator cuff tear patients have however been worked out. The assessment of the supraspinatus muscle is achievable by this method reliably.

Conclusion

A most helpful indicator of muscle atrophy with prognostic value towards a good/bad outcome prediction for surgical repair.

8.11   Fatty Muscle Index

Definition

Rotator cuff tears induce muscular changes which are highlighted by fat deposition. Fatty infiltration can be extensive and is correlated with severe functional impairment. Muscular fatty infiltration is graded in five prognostic stages which are linked with favourable or poor therapeutic outcomes.

Indications

As part of the assessment of rotator cuff tears. This can be done preoperatively but also postoperatively as a method of assessing reversible muscle changes following cuff repair. The more severe the fatty infiltration, the poorer the functional and anatomical outcome.

Technique

CT or MRI. MRI is more accurate.

Full Description of Technique

Axial assessment was first utilised using CT. The imaging planes are through the supraspinatus fossa for the supraspinatus muscle, and the tip of the coracoid process and inferior glenoid margin for the infraspinatus and subscapularis muscles. As remarked by Kasra (2010), the five grades are based on a quantitative assessment:

Grade 0	Normal muscle, no fatty streaks
Grade 1	Muscle contains some fatty streaks
Grade 2	Increased fat deposition but less in volume compared to muscle
Grade 3	Equal quantities of fat and muscle
Grade 4	More fat deposition than muscle

The above Goutallier et al. (1994) grading was then validated for MRI by Fuchs et al. (1999), and employed in comparative studies of the role of fatty infiltration in reducing the acromiohumeral distance (Fig. 8.21).

Clinical Relevance/Implications

It is very important to include the muscle status as a factor in decision making concerning treatment options, prognosis and postoperative expectations concerning functional restoration. Although wrongly referred to as fatty degeneration it is important to note that the amount of fat accumulation in muscle is proportional to the extent of rotator cuff disease. There is an extramuscular and
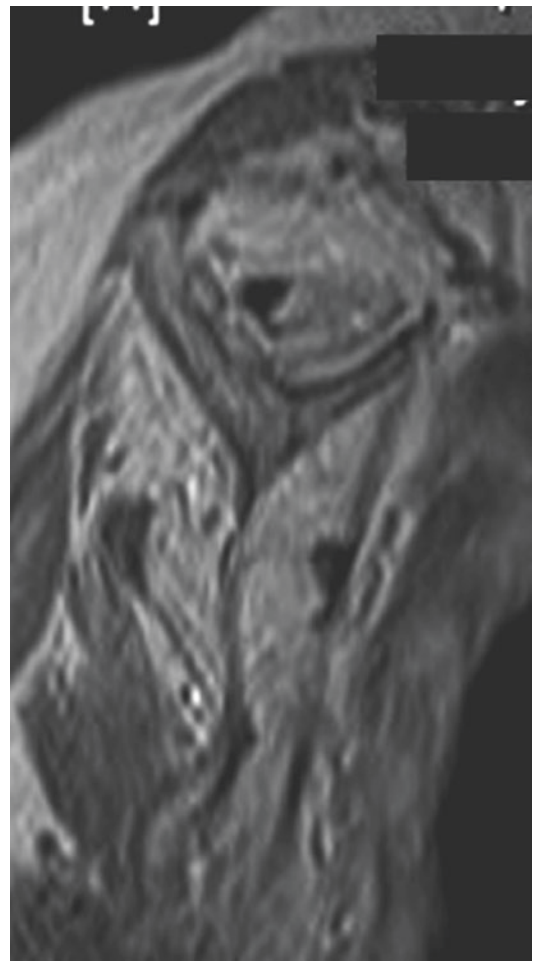
Fig. 8.21 Fatty muscle index involving the three main muscles of the rotator cuff—Grade 4 as seen on parasagittal T1 MR image

intramuscular accumulation of fat which is not degenerative in nature as the muscles are atrophic but retain the property of recovery. There is however a spatial pattern of fatty accumulation in the affected muscle with a higher % fat accumulation in the distal aspects and a milder accumulation proximally. This means that MR assessment on the single parasagittal oblique may underestimate the grade of fatty muscle index. The fatty infiltration of the supraspinatus is global but usually light. Infraspinatus fatty infiltration is usually global if more than 50% of its tendon is torn. It can however also undergo severe fatty infiltration even if the rotator cuff tear does not involve its tendon (supraspinatus and subscapularis tear) which could be due to denervation (see below). Degeneration of the subscapularis can be severe but is always limited to the part of the muscle pertaining to the torn portion of the tendon.

What is not known is whether some or all of these muscle changes are due to denervation secondary to neuronal damage to the suprascapular nerve (e.g. in infraspinatus). A rotator cuff tear may lead to retraction of the myotendinous junction medially, and as the suprascapular nerve is relatively tethered in the notch, give rise to nerve injury. It is then the nerve injury that causes denervation and fatty muscle infiltration. In a recent study comparing the muscle changes following rotator cuff tear and denervation, the net effect of fatty infiltration in rotator cuff musculature was seen to be identical in its spatial distribution, and also found to be histologically identical. If the amount of fat deposition leads to a 2 or more grading, the changes are deemed irreversible and surgical repair of the cuff tear is not carried out.

Reproducibility/Variation

There is limited data but it is fairly good and supportive as a reliable and reproducible assessment tool. It can also be used postoperatively to monitor regeneration. The infraspinatus rarely regenerates which could be due to denervation.

Analysis/Validation of Reference Data

Limited validation related to functional loss and postoperative improvement based on clinical examination with respect to external rotation.

Conclusion

Useful and reliable imaging factor.

8.12 Acromion–Glenoid Angle and Supraspinatus–Glenoid Angle: MRI

Definition

The acromion–glenoid angle (AGA) is the angle between the inferior outline of the acromion and the line tangent to the superior and inferior margins of the glenoid labrum. The mean value is **78.9° +/− 8°**.

The supraspinatus–glenoid angle (SGA) is the angle between a line tangent to the superior and inferior margins of the glenoid labrum and the axis of supraspinatus fossa. The mean value is **88.0° +/− 6.5°**.

Indications

The acromion–glenoid angle (AGA) and the supraspinatus–glenoid angle (SGA) are important in evaluating the relationship between rotator cuff tears and glenoid orientation. A reduced AGA and an increased SGA will result in reduced outlet dimensions for the rotator cuff.

Techniques

MRI Shoulder: oblique coronal section.

Full Description of Technique

The coronal oblique MRI plane is equivalent to the true AP radiographic plane of the shoulder. The measurement of the acromion–glenoid angle and the supraspinatus–glenoid angle are performed on an MR coronal oblique image just posterior to the acromioclavicular joint.

The acromion–glenoid angle (AGA) is determined through the intersection of a line drawn along the inferior acromial cortex (A line) and another line that connects the superior and inferior margins of the glenoid labrum (G line). The supraspinatus–glenoid angle (SGA) is the angle formed by the G line and the axis of supraspinatus fossa (S line) which represents the bed of supraspinatus muscle (Fig. 8.22).

Reproducibility/Variation

MRI is the best technique for identifying acromion–glenoid angle and supraspinatus–glenoid angle, two factors that play a role in rotator cuff disease.

Clinical Relevance/Implications

It is important to realise that there is a predictive association between rotator cuff tears and the orientation of the glenoid relative to the axis of the supraspinatus fossa. An increased SGA promotes

Fig. 8.22 The AGA and SGA estimation seen in diagrammatic format (**a**) on a coronal MR image in a normal patient (**b**) and on a coronal MR image in a patient with a large complete rotator cuff tear of the supraspinatus and abnormal angles (**c**)

upward gliding of the humeral head causing compression of the rotator cuff beneath the coracoacromial arch.

Analysis/Validation of Reference Data

Banas et al. (1995) were the first to report the relationship between rotator cuff tears and the AGA angle which they termed the *lateral acromial angle (LAA).* They defined the LAA as the slope of the acromion relative to the face of the glenoid fossa measured on the coronal MR oblique. As the LAA decreased, rotator cuff disease increased. The LAA was significantly lower in rotator cuff disease patients compared with patients who had an intact rotator cuff ($p < 0.0001$). LAA or AGA values are:

Normal	Mean 78° (70–86°)
Full thickness tear	< 70°

The LAA was found to be an independent significant predictor of cuff disease. All patients with a LAA of 70° or less had a full thickness rotator cuff tear.

Tétrault et al. (2004) confirmed that rotator cuff patients had a lower AGA (**76 +/−7°**) compared with normal (86 +/−10°). They also showed that the

rotator cuff tears were associated with larger SGA (**112 +/−6°**) compared with normal (102 +/−7 °).

Normal AGA	86 +/−10°	RC Tear	76 +/−7°
Normal SGA	102 +/−7°	RC tear	112 +/−6°

In their glenoid version measurement assessment they also discovered that anterior cuff tears occurred in increased glenoid retroversion (−5 +/−4°), while increased anteversion (3 +/−3°) was predictive of posterior cuff tears.

Glenoid version	−5 +/−4°	Anterior cuff tears
Glenoid version	3 +/−3°	Posterior cuff tears

Significant differences were found between patients and controls by Tokgoz et al. (2007) for axial glenoid version and bicipital–humeral distance MRI measurements regarding supraspinatus tears. In their study a relationship was demonstrated between reduced measurements and supraspinatus tears:

– glenoid version (Fig. 8.23a)—average decrease of **2.3°** (**−7.1 +/− 7.8°** patients, **−4.8 +/−5.6°** normal),
– bicipital-humerus distance (Fig. 8.23b)—an average decrease of **2.7 mm** (**12.1 +/− 3.7 mm** in patients, **14.8 +/−4.1 mm** normal).
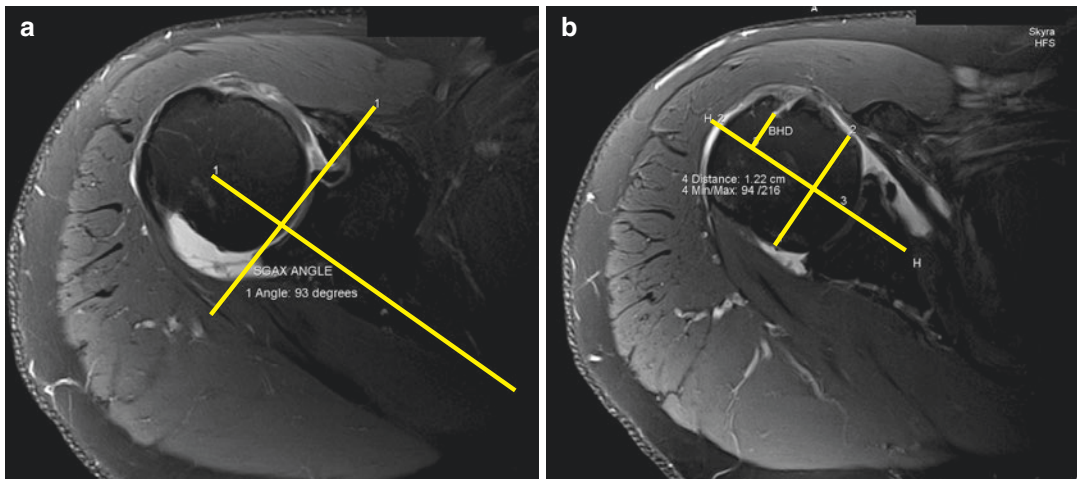
Fig. 8.23 Estimating the SGAX angle (**a**) and the BHD (**b**)

Conclusion

The AGA and SGA represent the space for the supraspinatus tendon outlet. There is a strong association between patients with rotator cuff pathology and predisposing abnormal bone structure evidenced by alterations in AGA and SGA angle measurements. The AGA or LAA is a measurement of the lateral extension of the acromion in the coronal plane. It should be used in association with the other two parameters (described later) which also assess lateral acromial extension, the critical shoulder angle (CSA) and acromial index (AI) to increase the specificity and value of the measurement.

8.13   Critical Shoulder Angle

Definition

The critical shoulder angle (CSA) combines the measurement of inclination of the glenoid and the lateral extension of the acromion and was first introduced by Moor et al. in 2013. The mean CSA is **33.1°** (**26.8–38.6°**) in normal individuals, with only a 1.2° difference between bilateral healthy shoulders. In rotator cuff tears it is increased measuring **38°** (**29.5–43.5°**) and decreased in OA measuring **28.1°** (**18.6–35.8°**).

Indications

Degenerative shoulder pathology ranging from rotator cuff impingement, rotator cuff tears and osteoarthritis. Postoperative assessment following surgery in patients with recurrent rotator cuff symptoms.

Techniques

True AP shoulder radiographs with visible joint space and minimal overlap between posterior and anterior bony rims of the glenoid.

Full Description of Technique

The CSA distance is measured on a true AP radiographic projection of the shoulder. The radiograph is obtained in the upright or supine position with the patient turned outwards approximately 35–45° so that the plane of the scapula parallels the cassette, providing a tangential view of the glenohumeral joint with superimposed anterior and posterior glenoid margins. The arm is placed in a neutral position. The central beam is pointed to glenohumeral joint and angled 10–15° caudally. A tangential view of the subacromial surface can be obtained by fluoroscopic projection. The tube-screen distance is 100 cm and the tube voltage is usually 60–65 kV. Due to the angulation of the central beam, the anterior and posterior rims of the acromion are superimposed and appear as a regular cortical outline.

The first line connecting the superior and inferior osseous margins of the glenoid cavity is first drawn. A second line is then drawn from the inferolateral acromial border to intersect the first line at the inferior glenoid rim (Fig. 8.24) and the subtended angle is the CSA.

Reproducibility/Variation

Quantitative individual scapular anatomical factors play a role in rotator cuff tears. Glenoid inclination is associated with full thickness tears (Hughes et al. 2003) while a large acromial index (high AI) is also found to be associated with rotator cuff tears (Nyffeler et al. 2006). The CSA is a radiological parameter that takes into account both the glenoid inclination and the AI.

There is good interobserver reliability on both CSA estimation done on AP radiographs and MDCT reconstructions. Furthermore there is a very strong inter-method correlation of the CSA measured on radiographs and CT scans (Bouaicha et al. 2014).
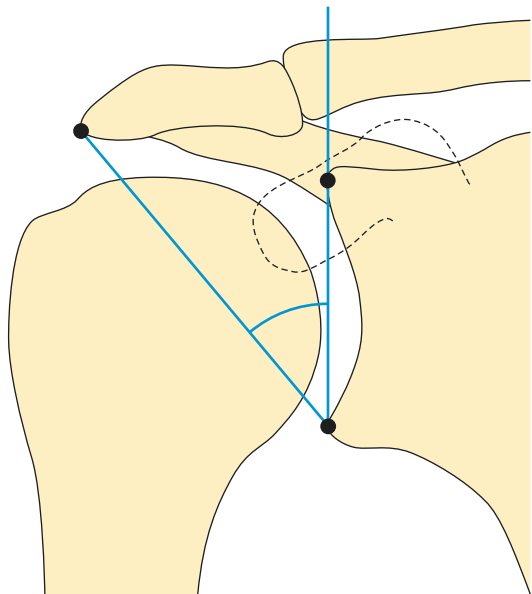
Fig. 8.24   Critical Shoulder Angle

Clinical Relevance/Implications

In Moor et al.'s study (2013) of patients with a CSA >35°, 89% had a rotator cuff tear, while in those with a CSA <30°, 93% were in the OA group.

These findings suggest that individual quantitative anatomical variation is associated with altered shoulder biomechanics with the induction of specific systematic degenerative disorders (Moor et al. 2014a). Viehofer et al. (2016a) have shown that a high CSA destabilises the shoulder joint requiring higher than normal supraspinatus forces to maintain glenohumeral stability during active abduction. Conversely a lower CSA predisposes the glenohumeral joint to high joint reaction forces, overloading and development of OA (Viehofer et al. 2016b).

The high CSA predisposes not only to rotator cuff tears but also to a worse postoperative score after rotator cuff repair. Furthermore as shown by Garcia et al. 2017, a high CSA significantly increased the risk of full thickness rotator cuff retear after rotator cuff repair.

In a more recent article, Heuberer et al. (2017) concluded that the combination of CSA and age could predict different shoulder pathologies in symptomatic patients.

Analysis/Validation of Reference Data

Some authors believe that acromial changes are the consequence and not the cause of rotator cuff tears. This means that the measurements related to changes in the acromion are relevant to rotator cuff tears but not necessarily the primary biomechanical factor predisposing to rotator cuff pathology.

Age is a very important parameter however. The data suggests that in a 65 year old with no OA or rotator cuff tears the CSA is 30–35°. A CSA >35° usually is associated with a rotator cuff tear and an angle <30° with OA (Moor et al. 2014b).

Conclusion

The CSA is a simple highly reproducible measurement which is increasingly used in the assessment of a number of shoulder degenerative pathologies.

8.14 Humeral Neck Shaft Angle

Definition

The humeral neck shaft angle (NSA) is created at the intersection of the line perpendicular to the humeral anatomic neck with the humeral shaft axis. The average angle is **140° (136–144)** for normal subjects.

Indications

The angle is useful in the preoperative assessment of the glenohumeral relationships in proximal humeral fractures and prosthetic shoulder arthroplasty as explicity proven by Lehtinen et al. (2000).

Normal	140° (range 136–144)

Techniques:

Radiography: true AP view of the glenohumeral joint.

Full Description of Technique

The humeral neck shaft angle is measured on a true AP radiographic projection of the shoulder. The radiograph is obtained in the upright or supine position with the patient turned outwards approximately 35–45° so that the plane of the scapula parallels the cassette, providing a tangential view of the glenohumeral joint with superimposed anterior and posterior glenoid margins. The arm of the side under evaluation is in a neutral position. The central beam is pointed to the glenohumeral joint and angled 10–15° caudally. For a better tangential view of the subacromial surface, it is preferable to have fluoroscopic guidance to execute radiographic projection. The tube-screen distance is 100 cm, and the X-ray voltage is usually 60–65 kV.

Due to the angulation of the X-ray beam, the superimposed anterior and posterior portions of the acromial undersurface appear as a regular cortical profile.

The measurement technique consists of drawing a line (L. neck) perpendicular to the plane (P. neck) passing through the anatomic neck of the humerus. A second line (L. shaft) corresponding to the longitudinal axis of the humeral diaphysis is drawn. This is constructed by drawing a line through two points along the proximal humeral medulla which correspond to the midpoints of perpendiculars to the humeral diaphyseal cortex. Humeral neck shaft angle (α) is defined as the obtuse angle between line L Neck and line L Shaft (Fig. 8.25).
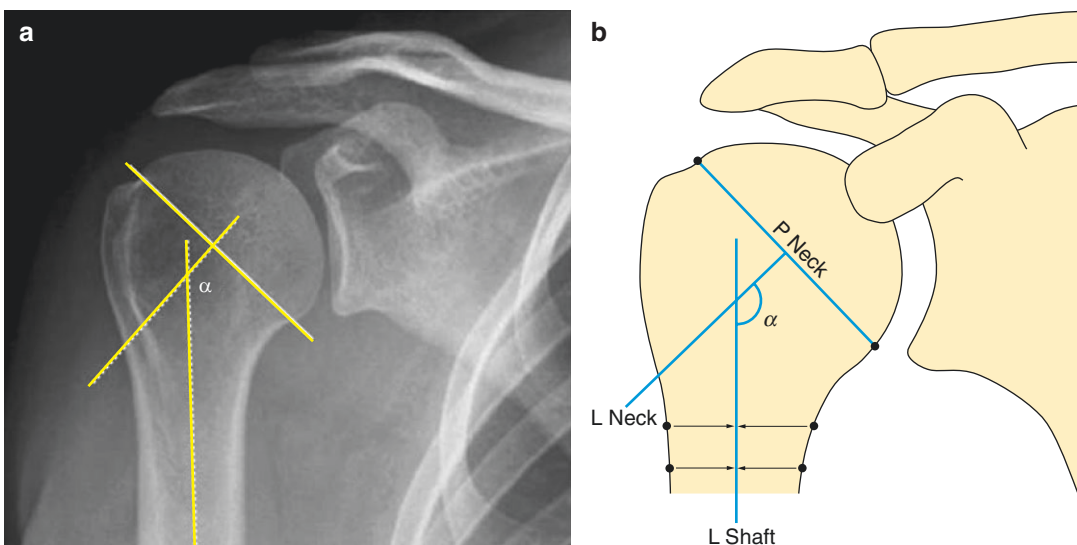
Fig. 8.25 The humeral neck shaft angle (α)

Reproducibility/Variation

Very easy to evaluate the angle on the AP shoulder radiographs with a high reproducibility.

Clinical Relevance/Implications

The humeral neck shaft angle can help surgeons to better adapt a prosthesis to a patient's bony anatomy. It is one of a number of interdependent measurements which are considered in choosing the appropriate prosthesis.

The humeral neck shaft angle as defined by Ianotti et al. (1992) is of a lower value with a mean of 45.0° +/− 5° (range 30–55°). This is because the angle measurement lines employed are different. In Ianotti et al.'s method the angle is measured between the humeral shaft axis

and the anatomical neck plane (V line or P neck line), while in the described method the perpendicular to the V line is used. There is therefore a difference of 90° in the values obtained between the two methods of measuring the humeral NSA.

Analysis/Validation of Reference Data

Validated using experimental and clinical means.

Conclusion

The angle is useful in the preoperative assessment of the glenohumeral relationships and helps orthopaedic surgeons in planning reconstructive and prosthetic shoulder arthroplasty.

8.15 Glenohumeral Joint Space

Definition

The glenohumeral joint space corresponds to the distance between the articular profile of the humeral head and the glenoid fossa. The average width of the glenohumeral space (integral space) in normal subjects is **4.7 mm**.

Indications

The assessment of the glenohumeral joint space, as proposed by Lehtinen et al. in their study (2000), is useful as a quantitative definition of the articular cartilage loss in shoulder involvement by degenerative and inflammatory arthropathies.

Normal	4.7 mm

Technique

Radiography: true AP view glenohumeral joint.

Full Description of Technique

The glenohumeral joint space is measured on a true AP radiographic projection of the shoulder. It is obtained in the upright or supine position, with the patient slightly turned outwards by approximately 20°, providing a tangential view of the glenohumeral joint. The arm is placed in external rotation, palm facing upwards. The central beam is pointed perpendicularly to the glenohumeral joint. To obtain an optimal tangential view of the glenohumeral joint, fluoroscopic guidance may be used. The tube-screen distance is 90–100 cm, and the tube voltage is usually 50–60 kV.

The diameter of the humeral head (line D) is traced joining the two terminal articular carti-lage points of the joint surface projection. The mid-point (point O) of the line D is determined with a ruler. Points a and c being the superior and inferior limits of the glenoid surface, and point b the mid-point. Three lines are traced joining point O with points a, b, c and intersecting the humeral joint surface, respectively, in points A, B, C. The joint width is evaluated from three measurement sites at the glenoid cavity, a-A, b-B and c-C. The joint space at the three sites and the average value, the integral space, is determined (Fig. 8.26).

Reproducibility/Variation

A true AP view is necessary to gauge the degree of joint space narrowing. In the lower extremity, weight bearing radiographs are used to delineate loss of joint space. Although attempts have been made to obtain stress glenohumeral radiographs, these studies have not successfully demonstrated joint space collapse in the absence of other radiographic signs of arthritis.

An axillary radiograph is required to assess the presence of glenoid wear. If glenoid wear is seen, a CT scan is the best study to evaluate the degree of osseous loss. Routine use of MRI scanning is not necessary.

Clinical Relevance/Implications

Diagnosis of osteoarthritis (OA) is made based on history, physical examination, and standard radiographs. A true anteroposterior (AP) view is necessary to gauge the degree of joint space narrowing.

Analysis/Validation of Reference Data

Limited correlative studies available.
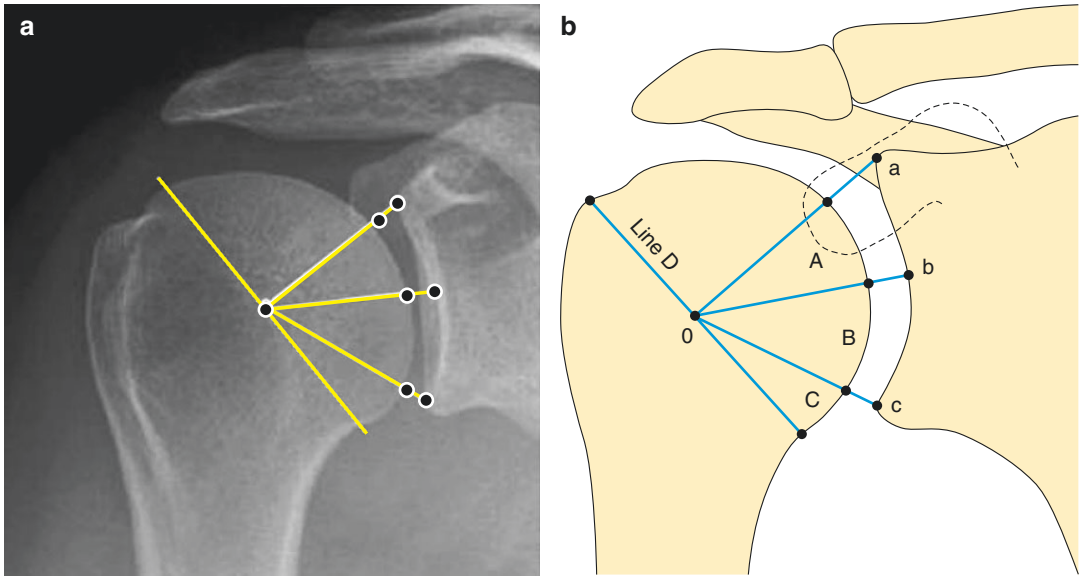
Fig. 8.26 From the centre of the diagonal line, joint space width estimation is done at 3 points: superior, middle, and inferior joint space

Conclusion

The joint space narrowing in the rheumatoid GH joint is a late phenomenon and the existence of rheumatoid involvement in the GH joint should be based on erosions, not on joint space narrowing on the radiograph.

8.16   Lateral Glenohumeral Offset Distance

Definition

The lateral glenohumeral offset distance corresponds to the interval measured between the glenoid cavity and lateral margin of the humeral greater tuberosity. The mean value is of **55.7 +/− 5.7 mm**.

Indications

This parameter is useful for the preoperative assessment of the glenohumeral relationships in planning post-traumatic humeral reconstruction or a prosthesis for shoulder arthroplasty.

Normal	55.7 +/−5.7 mm

Technique

Radiography: true AP view of the glenohumeral joint.

Full Description of Technique

The lateral glenohumeral offset distance is measured on a true AP radiographic projection of the shoulder. The X-ray is obtained in the upright or supine position with the patient turned outwards approximately 35–45° so that the plane of the scapula parallels the cassette, providing a tangential view of the glenohumeral joint with superimposed anterior and posterior glenoid margins. The arm is placed in a neutral position. The central beam is pointed to glenohumeral joint and angled 10–15° caudally. A tangential view of the subacromial surface can be obtained by fluoroscopic guidance prior to executing the radiographic projection. The tube-screen distance is 100 cm, and the tube voltage is usually 60–65 kV. Due to the angulation of the central beam, the anterior and posterior rims of the acromion are superimposed and appear as a regular cortical outline.

The lateral glenohumeral offset distance (Fig. 8.27) is assessed by the interval distance between two vertical lines; the line tangent to the glenoid cavity (line G), (or joint line), and the line parallel to the joint line and tangent to the lateral greater tuberosity border (line GT).
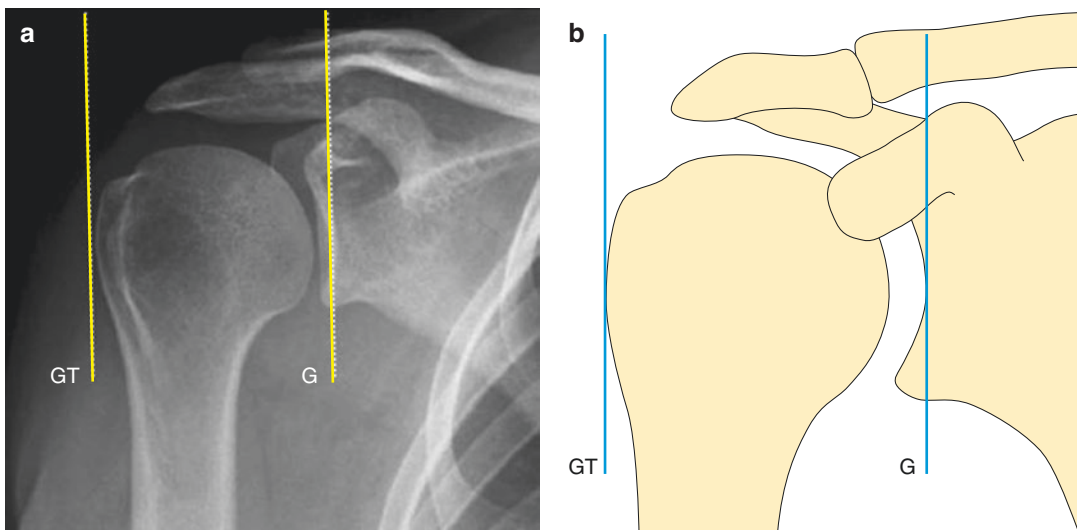
Fig. 8.27   Lateral Glenohumeral Offset

Reproducibility/Variation

Very easy and highly reproducible by evaluation on AP shoulder radiograph.

Clinical Relevance/Implications

The lateral glenohumeral offset distance helps surgeons to optimally choose and place the prosthesis in the patient's bone anatomy.

Analysis/Validation of Reference Data

There are a number of other important measurements which are taken in consideration along with the lateral glenohumeral offset in the planning of total shoulder arthroplasty. There are ethnic variations which account for differences in their reference values from different articles. It is important to remember that the measurements need to be seen as an interrelated group which in combination determine the structural–functional relationships.

Conclusion

This measurement is useful in the preoperative assessment of the glenohumeral relationships aiding the orthopaedic surgeon in planning a prosthetic shoulder arthroplasty.

8.17   Acromial Index

Definition

The acromial index (AI) quantifies the amount of lateral acromial extension relative to the humeral head as described by Nyffeler et al. in 2006. A high acromial index reflects a large lateral extension of the acromion.

Normal value: **0.64 +/− 0.06.**
Full thickness cuff tear: **0.73 +/− 0.06.**
O.A: **0.60 +/− 0.08.**

Indications

The pathogenesis of degenerative shoulder disorders ranging from rotator cuff disease (tears and impingement) and primary osteoarthritis of the glenohumeral joint.

Technique

A true AP radiograph of the shoulder with the glenoid surface perpendicular to the cassette and the humerus held in neutral or internal rotation is essential.

Full Description of Technique

The AI is measured on a true AP radiographic projection of the shoulder. The X-ray is obtained in the upright or supine position with the patient turned outwards approximately 35–45° so that the plane of the scapula parallels the cassette, providing a tangential view of the glenohumeral joint with superimposed anterior and posterior glenoid margins. The arm is placed in a neutral position. The central beam is pointed to glenohumeral joint and angled 10–15° caudally. A tangential view of the subacromial surface can be obtained by fluoroscopic projection. The tube-screen distance is 100 cm and the tube voltage is usually 60–65 kV. Due to the angulation of the central beam, the anterior and posterior rims of the acromion are superimposed and appear as a regular cortical outline.

Three parallel vertical lines are drawn for this measurement and the distances between them are then measured.

The first line passing through the superior and inferior glenoid margins represents the glenoid cavity.

The second line is drawn tangential to the lateral tip of the acromion and the third line at a tangent to the lateral part of the proximal humerus.

The glenoid-acromion distance (GA) is divided by the glenoid-humeral distance (GH) to produce the acromial index (Fig. 8.28).

Reproducibility/Variation

Rotation of the humerus or scapula introduces significant errors in this measurement, and a scrupulous radiographic technique is crucial when obtaining the radiograph to avoid them as shown by Nyffeler.

The interobserver correlation is excellent (coefficient of correlation 0.87).

It is worth noting that as OA is often associated with a flattened humeral head and wear of the bony glenoid, there is a misleading increase in the AI.
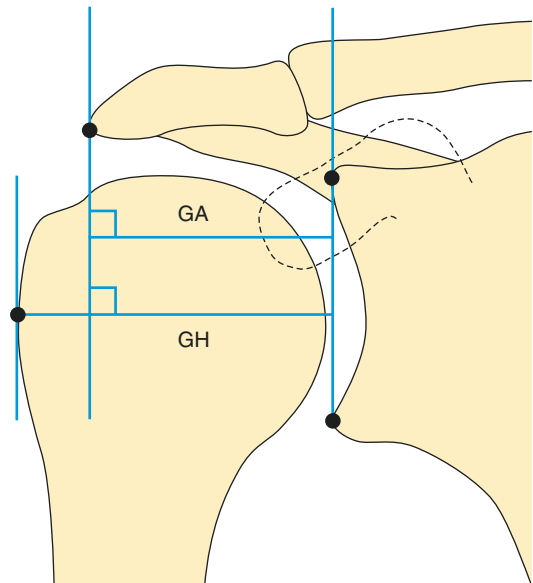
Fig. 8.28 Acromial Index

Clinical Relevance/Implications

Nyffeler et al. found average AI of 0.73 +/− 0.06 in full thickness rotator cuff tears compared with 0.60 +/− 0.08 in patients with OA ($p < 0.0001$) and the control group 0.64 +/− 0.06.

They postulated that a large AI results in a more vertical force vector orientation of the deltoid which will pull the humeral head superiorly, which then requires the supraspinatus tendon to increase its horizontal force required to stabilise the centre of rotation during active abduction.

Analysis/Validation of Reference Data

Nyffeler et al.'s findings were corroborated by Torrens et al. in 2007.

However other studies did not reproduce this difference. Hamid et al. in 2012 found identical

values for AI in all pathological and control groups of 0.690 and no association with rotator cuff disease. This may be due to differences in the radiographic technique of obtaining the true AP of the shoulder.

Conclusion

The acromial index is one of three parameters that assess the degree of acromial lateralisation (LAA and CSA). A high index is associated with rotator cuff tears. It is still not clear if the abnormal acromial morphology is the cause or effect of disease (Wang and Shapiro 1997).

8.18 Joint Line: Coracoid Process Distance

Definition

The joint line–coracoid process distance corresponds to the interval measured between the glenoid cavity and the base of the coracoid process. The mean value is of **6.4 +/− 1.9 mm**.

Indications

This lateral glenoid offset parameter is useful for the preoperative assessment of the glenohumeral relationships in planning for a prosthetic shoulder arthroplasty.

Normal	6.4 +/− 1.9 mm

Technique

Radiography: true AP view of the glenohumeral joint.

Full Description of Technique

The joint line–coracoid process distance is measured on true AP radiographic projection of the shoulder. The radiograph is obtained in the upright or supine position with the patient turned outwards approximately 35–45° so that the plane of the scapula parallels the cassette, providing a tangential view of the glenohumeral joint with superimposed anterior and posterior glenoid margins. The arm of the side under evaluation is in a neutral position. The central beam is pointed to the glenohumeral joint and angled 10–15 °caudally. For a better tangential view of the subacromial surface it is preferable to employ fluoroscopic guidance in the execution of the radiographic projection. The tube-screen distance is about 110 cm, and the tube voltage is usually 60–65 kV.

Due to the angulation of the central beam the superimposed anterior and posterior portions of the acromial undersurface appear as a regular cortical profile.

The joint line–coracoid process distance (Fig. 8.29) is assessed by the interval between the vertical line tangent to glenoid cavity (G line), (or
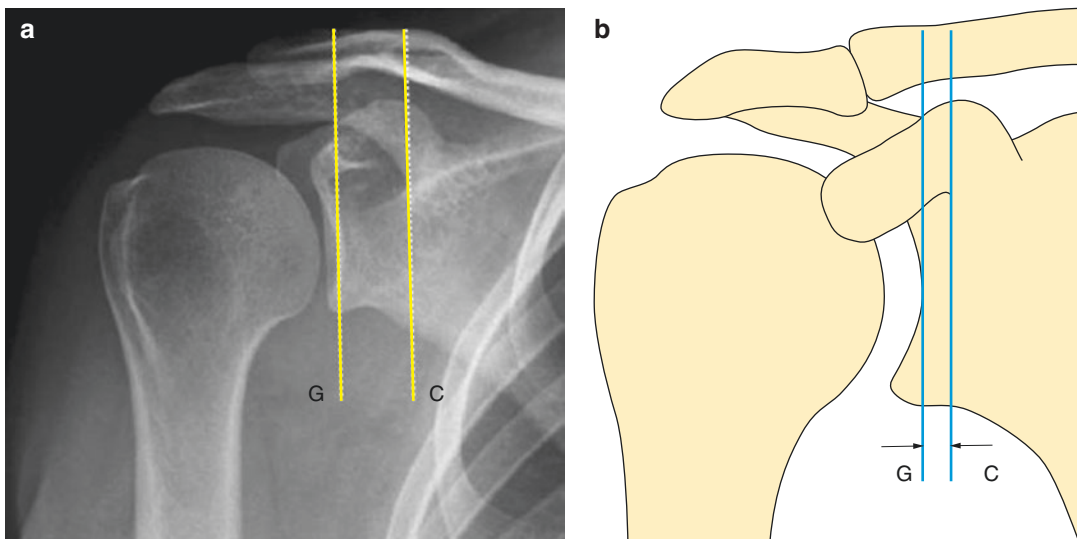
Fig. 8.29 The lateral glenoid offset

joint line), and the line parallel to the joint line and tangent to the lateral coracoid border (C line).

Reproducibility/Variation

Very easy and reproducible by evaluation on the AP radiograph.

Clinical Relevance/Implications

The joint line–coracoid process distance can help surgeons to better adapt prosthesis to a patient's bone anatomy.

Analysis/Validation of Reference Data

A number of studies have shown that this distance is independent of other measurable parameters in the individual.

Conclusion

This measurement is useful in the preoperative assessment of glenohumeral relationships and help orthopaedic surgeons in the optimal planning of a prosthetic shoulder arthroplasty.

8.19 Bicipital Groove Width

Definition

The bicipital groove width of the humerus is the distance between the medial and the lateral lips of the intertubercular sulcus. The mean distance of the top width is of **4.6 mm**.

Indications

It is useful to determine the normal configuration and common anatomic abnormalities of bicipital tendon sulcus.

Normal	4.6 mm

Technique

Radiography: bicipital groove view.

Full Description of Technique

The bicipital groove width of the humerus is measured on a bicipital groove radiographic view of the shoulder as proposed by Cone et al. (1983). The radiograph is obtained with the patient in the supine position with the arm in external rotation. The central beam is directed parallel to the coronal axis of the humerus and angled 15–25° medially. The cassette is held perpendicular to the superior aspect of the shoulder. The width of the bicipital groove is measured in two locations on the bicipital groove view. The top width is determined as the distance between the medial and lateral lips of the intertubercular sulcus along the plane of the intertubercular line (Fig. 8.30). The middle width is measured between the walls of the intertubercular sulcus at a point equating to one-half of the depth of the sulcus.

Reproducibility/Variation

This radiographic view is not easy to perform and the reproducibility is related to the technician experience.

Clinical Relevance/Implications

Radiographic factors useful in the evaluation of the bicipital groove of the proximal humerus are not widely known. This is unfortunate, as abnor-
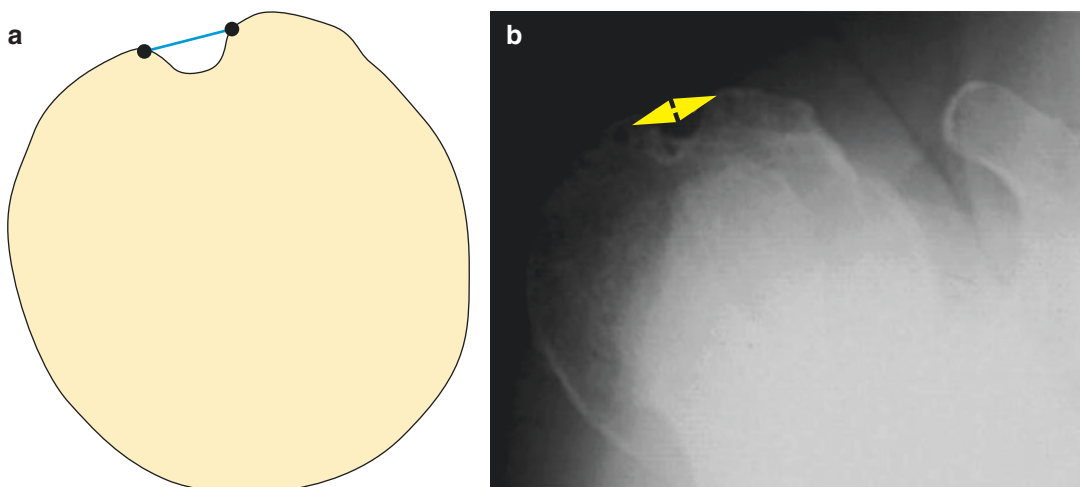
Fig. 8.30 Bicipital groove width

malities of the bicipital tendon and its synovial sheath have been implicated in a variety of causes of shoulder pain and disability.

Analysis/Validation of Reference Data

Insufficient number of references available for validation**.**

Conclusion

Due to the technical difficulty of execution of this projection, today this measurement is generally performed on images obtained from US, CT or MRI.

8.20   Bicipital Groove Medial Wall Angle

Definition

The bicipital groove medial wall angle of the humerus is the angle of intersection between the tangent to the superior margins of the greater and lesser tuberosities and the tangent to the medial wall of the intertubercular sulcus. The normal angle ranges from about **40 to 70°** (average angle of 48°).

Indications

As remarked by Hitchcock and Bechtol (1948), the bicipital groove medial wall angle is useful in the evaluation of the relationship between this angle and the incidence of subluxation or dislocation of the bicipital tendon.

Normal	48° (40–70)

Technique

Radiography: bicipital groove view.
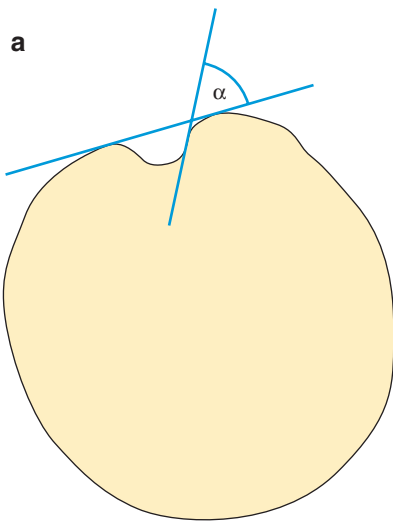
Full Description of Technique

The bicipital groove width of the humerus is measured on bicipital groove radiographic view of the shoulder as proposed by Cone et al. (1983). The radiograph is obtained with the patient in the supine position, and with the arm in external rotation. The central beam is directed parallel to the coronal axis of the humerus and angled 15–25° medially. The cassette is held perpendicular to the superior aspect of the shoulder. A line is drawn tangent to the superior margins of the greater and lesser tuberosities of the humerus. A second line is drawn tangent to the medial wall of the intertubercular sulcus of the bicipital groove. The angle of intersection of these lines is the medial wall angle (Fig. 8.31).

Reproducibility/Variation

This radiographic view is not easy to perform and the reproducibility is related to the technician experience.

Clinical Relevance/Implications

The medial wall angle, presence or absence of bicipital groove spurs, coexisting degenerative
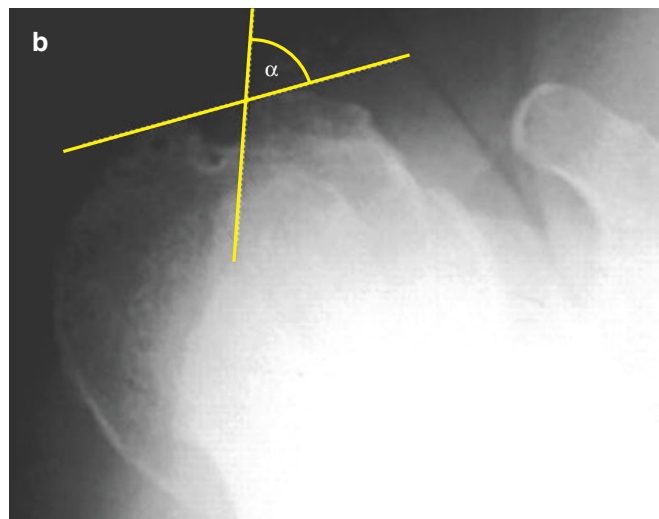
Fig. 8.31 Bicipital groove—medial wall angle

changes in the greater or lesser tuberosity, and the presence or absence of a supratubercular ridge can be determined.

Analysis/Validation of Reference Data

Not possible to validate due to lack of reference evidence.

Conclusion

Due to the technical difficulty of execution of this projection, today this measurement is generally performed with CT or MRI images.

8.21 Coracoclavicular Distance: US

Definition

The coracoclavicular distance is the width between the clavicle and the coracoid process of the scapula assessed during the sonographic investigation of the acromioclavicular joint.

Indications

Ultrasound is useful in detecting coracoclavicular pathologies in cases of trauma, inflammatory and degenerative changes.

Technique

Ultrasound shoulder: anterior sagittal section plane.

Full Description of Technique

The patient is seated in front of the examiner as proposed by Sluming (1995), with the arm in neutral position. The ultrasound evaluation is performed with the US transducer placed on the anterior sagittal plane passing through the coracoid process. The coracoclavicular distance is assessed measuring the shortest distance between the inferior border of the clavicle and the superior border of the coracoid process (Fig. 8.32).

Reproducibility/Variation

Very easy to reproduce having as references the clavicle and the coracoid process.

Clinical Relevance/Implications

This distance is assessed routinely on radiographs of the shoulder as part of the assessment of the acromioclavicular joint. The pathologic findings consist of bone irregularities, soft tissue cyst formation, excessive fluid collection and calcification.

Analysis/Validation of Reference Data

Limited by lack of studies, but there is evidence that the US technique for this measurement is reliable, reproducible and validated. When compared with radiographic assessment of the measurement there was a mean difference of 0.38 mm.

Conclusion

The ultrasound technique described is a reliable, accurate and valid technique for evaluating the coracoclavicular distance and may usefully supplement the routine radiographic examination of the shoulder in patients presenting for radiographic examination of the acromioclavicular joint.
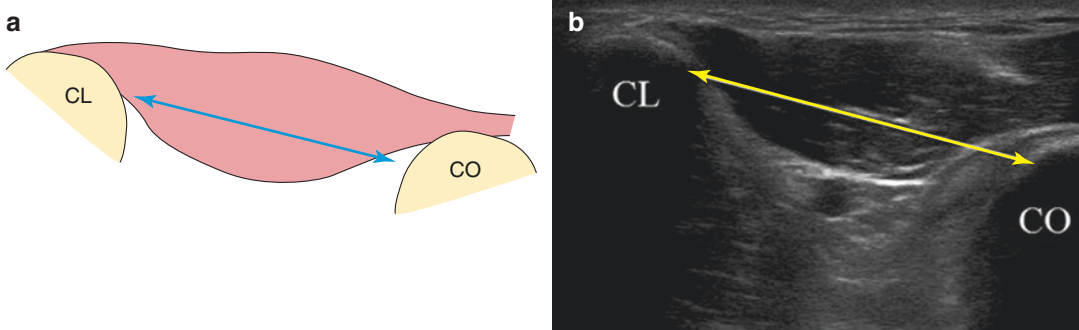
Fig. 8.32 Coracoclavicular distance—US

8.22 Subcoracoid Space: Six Anatomic Measurements

Definition

The subcoracoid space is the distance between the coracoid process and the anterior portion of the humeral head. The articular cartilage of the humeral head, the capsule, the tendinous rotator cuff, the subcoracoid bursa, and the soft tissues over the coracoid tip are the contents of the space.

Indications

It is thought to predispose to rotator cuff tear (subscapularis and long head of biceps) and coracoid impingement syndrome. Impingement producing anterior clinical signs and symptoms occurs predominantly in forward flexion, adduction, and internal rotation (U.S. military parade rest position). Symptoms are presumed to occur when the superficial surface of the upper subscapularis tendon impinges between the coracoid and lesser tuberosity causing stretching of the deep surface of the tendon producing the "*Roller-Wringer effect*" proposed by Lo and Burkhart (2003). This leads to a *TUFF* (tensile undersurface fibre failure) lesion. Importantly subcoracoid impingement is a well-known cause of persistent postoperative pain after rotator cuff repair.

Technique

Using CT or MRI axial images six different anatomic measurements allow assessment of the subcoracoid space.

Full Description of Technique

MRI is preferred to CT as it has no ionising radiation burden, is superior in defining the soft tissue contents of the space and the soft tissue contribution to impingement. Dumontier et al. (1999) showed that the thickened fibrous falx near the

confluence of the coracoacromial ligament and coracobrachialis contributes to the soft tissue impingement. This is seen as soft tissue thickening on the lateral coracoid tip. Different points of the axial images are best suited for optimal assessment of these measurements. CD, CA and CI are best measured from the image that best shows the tip of the coracoid process (Fig. 8.33).

Coracohumeral Distance (CD): is the shortest distance between the tip of the coracoid process and the humeral head. The shortest distance between the articular surface of the humeral head and the posterior surface of the coracoid is measured.

Coracoglenoid Angle (CA): is the angle between the coracoid body and the plane of the glenoid articular surface. Two reference lines are drawn and the angle is formed at their point of intersection; line A from the anterior lip of the glenoid and the most prominent portion of the coracoid tip, and line B running through to the glenoid articular surface.

Coracoid Index (CI): is the perpendicular distance by which the base of the coracoid extends anteriorly past the reference line drawn through to the glenoid articular surface.

Coracoid Overlap (CO): is the perpendicular distance from the maximal anterior projection of
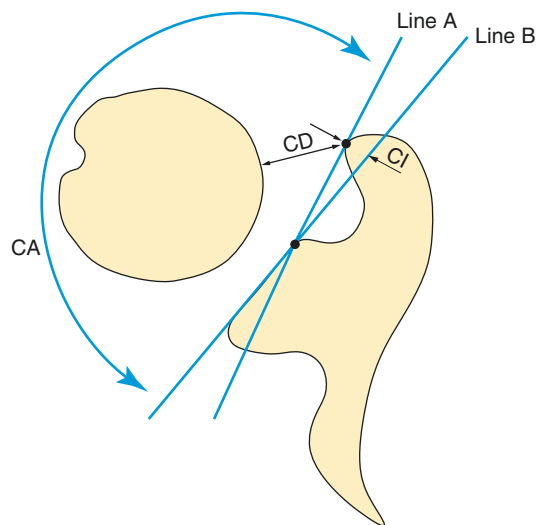
Fig. 8.33 Subcoracoid impingement parameters in the axial plane: CD, CA, CI
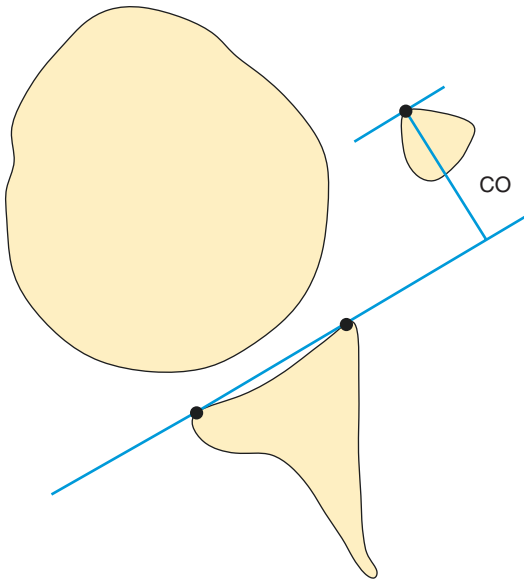
Fig. 8.34 Subcoracoid impingement parameter: CO

the tip of the coracoid process to the reference plane running tangential through the glenoid articular surface (Fig. 8.34).

Centre of Humeral Head to Coracoid Tip Distance (CHCT): is the distance from the centre of the humeral head **to** the tip of the coracoid. The centre of the head is determined by choosing the best- fit plastic circle method.

Centre of Humeral Head to Bicipital Groove Distance (CHBG): is the distance from the centre of the humeral head to the bicipital groove.

Normal values	Men	Women
CD	9.3 mm (SD, 3.3 mm)	7.9 mm (SD 2.5 mm)
CA	146.9° (SD, 9.0)	147.8° (SD, 9.2)
CI	8.7 mm (SD, 5.4 mm)	6.5 mm (SD, 4.2 mm)
CO	12.7 mm (SD, 5.0 mm)	10.3 mm (SD, 4.3 mm)
CHCT	36.4 mm (SD, 10.8 mm)	29.9 mm (SD, 2.7 mm)
CHBG	24.9 mm (SD, 2.3 mm)	21.1 mm (SD, 1.5 mm)

The CD measurement is the commonly used subcoracoid parameter in a clinical context.

Subcoracoid stenosis	CD	<5.5 mm (MR in max internal rotation)
Subscapularis tears	CD	<5 mm+/− 1.7 mm

Reproducibility/Variation

Interestingly the values of most of the anatomical measures (CD, CA, CI, CO) have been studied by static CT and MRI and the results are remarkably similar.

The position of the arm does have the potential of affecting measurements. CD for example is reduced with the arm in flexion, adducted and internally rotated. Gerber et al. (1987) reported that the average CD resting value of 8.7 mm decreased to 6.8 mm in healthy individuals with forward flexion and maximal internal rotation. Using dynamic MR Friedman et al. (1992, 1998) reported an average CD interval of 11 mm in asymptomatic individuals compared with <5.5 mm in symptomatic patients. In a more recent review of static MR, studies by Giaroli et al. showed that when the threshold of 5.5 mm CD distance was applied to their study groups, this value achieved a sensitivity value of only 5.3% but with a specificity of 97.6%. This difference may be due to the different shoulder positions employed in doing the MR examinations which could have affected these measurements. Using static MR of the shoulder obtained routinely in which the humerus is in neutral or external rotation position, Giaroli et al. reported a 79% sensitivity and 59% specificity for coracoid impingement when the CD measured <10.5 mm on axial MR images. In addition the authors identified that CD measurements in females yielded an average of **3 mm less** than in males. Lastly in a study by Richards et al. (2005) looking at the CD distance and subscapularis tears, the mean CD was 5+/−1.7 mm in the tear group compared with 10+/− 1.3 mm in the control group.

Clinical Implications/Relevance

Subcoracoid impingement appears to be a predominantly clinical diagnosis that may be supported but not established by routine MR examination. There does not appear to be any association between pathology in the superior and posterior components of the rotator cuff and the subcoracoid anatomy. There is a possible relationship however with pathology seen in the anterior supraspinatus tendon, subscapularis tendon, pulley lesions and long head of the biceps tendon. The diagnosis of coracoid impingement is controversial. Coracoid impingement often occurs with other joint pathology and is a cause of persistent symptoms after satisfactory subacromial decompression and rotator cuff repair. The possibility of coexistent subacromial and subcoracoid sites of primary external impingement must be considered before treating either as an isolated condition.

Analysis/Validation of Reference Data

The CD, CA, CI and CO have had a number of studies that have validated the normal ranges of the six anatomical measurements. There is still only limited validation concerning the lower ranges and their clinical significance.

Conclusion

Isolated subcoracoid impingement is rare and is usually associated with other conditions such as acromioclavicular arthritis, rotator cuff pathology, and glenohumeral instability. Promising but not fully established role of subcoracoid impingement and the abnormal values pertaining to the diagnosis.

8.23 Glenoid Version Angle: Radiography

Definition

Glenoid version defines the glenoid orientation relative to a perpendicular to the plane of the scapula.

Indications

Glenoid version plays an important role in the stability and loading of the glenohumeral joint. Changes in glenoid version (scapuloglenoid angle) are a predictive parameter in atraumatic shoulder laxity or instability. It is important in shoulder replacement surgery whereby excessive glenoid component version is related to poor outcomes. It is also related to rotator cuff disease (see previous section AGA/SGA angles).

Techniques

Radiography of the shoulder: axillary view.

Full Description of Technique

The glenoid version (scapuloglenoid) angle can be radiologically evaluated on the axillary view of the shoulder. This projection can be obtained with the patient in the horizontal position on the table, with the arm in neutral rotation and in 60° of abduction. The beam is directed to the upper surface of the axilla and meticulous attention to the standard technique is necessary as measurement can be rendered difficult on axillary radiographs even with optimal radiographic technique.

A tangential line is drawn connecting the most lateral aspect of the posterior glenoid to the most medial aspect of the anterior glenoid. An intersecting line is constructed connecting the centre point of the first line at its midpoint and the medial aspect of the scapula. The angle in the posterior medial quadrant is measured and its value is subtracted from 90° to yield the glenoid version angle (Fig. 8.35). A retroverted glenoid has a negative value, while a positive value indicates anteversion.

Normal radiographic value	−9° retroversion	+2° anteversion
(beware as this method is associated with an overestimation mean of 6.4°)		
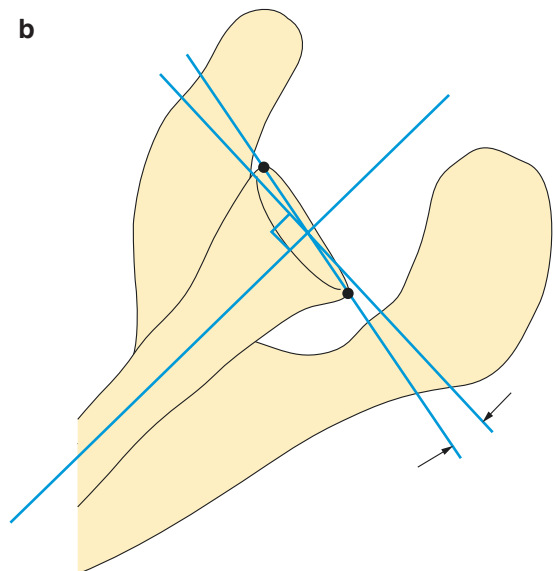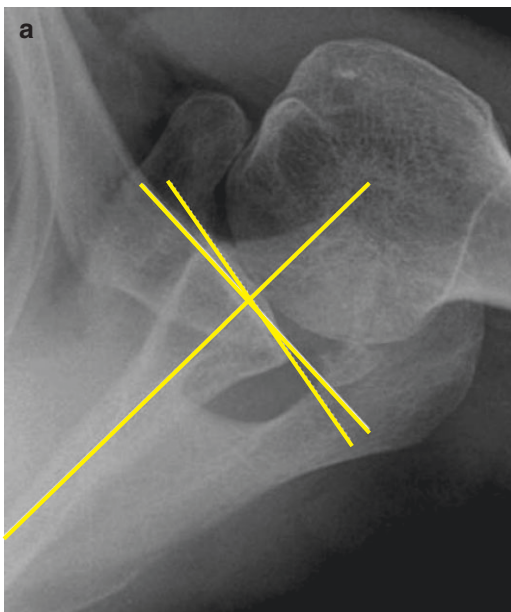
Fig. 8.35 Glenoid version estimation: Radiographic

Reproducibility/Variation

This radiographic view is not easy to obtain in a true lateral plane for measurement purposes and the reproducibility is related to the technician's experience.

Clinical Relevance/Implications

Apparent changes in glenoid version can arise from loss of part of the glenoid rim. Dias et al. (1993) found no difference in apparent glenoid version between normal subjects and recurrent anterior dislocators. Dowdy and O'Driscoll (1994) found only minor variances of radiographic glenoid version among patients with and without recurrence following stabilisation surgery. However, Hirschfelder and Kirsten (1991) found increased glenoid retroversion in both the symptomatic and asymptomatic shoulders of individuals with posterior instability. Grasshoff et al. (1991) found increased anteversion in shoulders with recurrent anterior instability.

Analysis/Validation of Reference Data

The mean glenoid version angle determined on macerated scapular specimens was found to be $-1.1°$ with a range of $-12°$ to $+11°$. In the literature, radiographically determined mean glenoid version values on normal shoulders yielded retroversion values of around $-7.5°$ consistently, compared with the mean value on specimens. Conventional radiography also appears to overestimate retroversion compared with CT and MRI values. Nyffeler et al. (2003) in their study noted that the overestimation is seen in about 86% of cases with a mean difference of $6.5°$ but a maximum of up to $21°$. Not uncommonly the inferior and superior glenoid rims on the axillary view are not perfectly superimposed making measurement difficult. This may also be because conventional axial radiographs superimpose levels of the glenoid that have a different version angle. Randelli and Gambrioli's CT work has shown that the upper portion of the glenoid has a mean value of $-5°$ (range of -2 to $-15°$), the middle portion a mean value of $-2°$ (range -8 to $0°$), and the lower portion a mean value $-7°$ (range -2 to $-15°$). Furthermore, the radiographic measurements are associated with unsatisfactory interobserver reproducibility.

Conclusion

The standard axillary radiographic method of determining glenoid version is inaccurate and not reproducible. It overestimates retroversion when compared with CT and MRI values.

This measurement may be useful in the preoperative assessment of the glenohumeral relationships, may help orthopaedic surgeon in planning surgery in case of shoulder instability and can also assess postoperative status. A more reliable method using CT or MRI is required.

8.24   Glenoid Version Angle: CT

Definition

The glenoid version defines the orientation of the glenoid cavity in relation to a plane perpendicular to the scapular body. In normal shoulders, using CT, the glenoid version angle ranges between **0 and 8°** of retroversion.

Indications

The glenoid version angle assessment can be useful in the definition of glenohumeral instability and also in improving implant alignment in shoulder arthroplasty.

Techniques

C.T. Shoulder: axial scan of the glenohumeral joint.

Full Description of Technique

The CT glenoid version angle assessment is obtained with the patient in the supine position with the shoulder flat in contact with the table and the humerus at rest laterally. It is vitally important that the scapular plane is perpendicular to the scan plane so that in the scout view the glenoid profile appears perpendicular to the planes of the CT slices. To achieve this, the gantry may need to be tilted and the patient propped up by cushions. The shoulder is examined with contiguous 2.5 mm thick scans from the acromion to the glenoid inferior border. For the determination of the glenoid version, the next four slices inferior to the coracoid process are identified, corresponding approximately to the mid-glenoid level, and the scapular axis is drawn connecting the scapular medial margin to the midpoint of the glenoid (Fig. 8.36).

The glenoscapular angle (θ) is measured at the intersection between the line perpendicular to the scapular axis and the line tangent to the anterior and posterior borders of the glenoid. The perpendicular line drawn to the scapular axis line is designated as the neutral version line. If the posterior glenoid margin is seen to incline posterior and medial to this line, the glenoid is deemed retroverted and the measured alpha angle between the line of neutral version and the tangent line passing through the anterior and posterior tips of the glenoid is negative. Vice versa if the anterior margin is medial to the line of neutral version, the glenoid is anteverted and the measured alpha angle is positive.

At mid-glenoid level the following are CT based mean values:
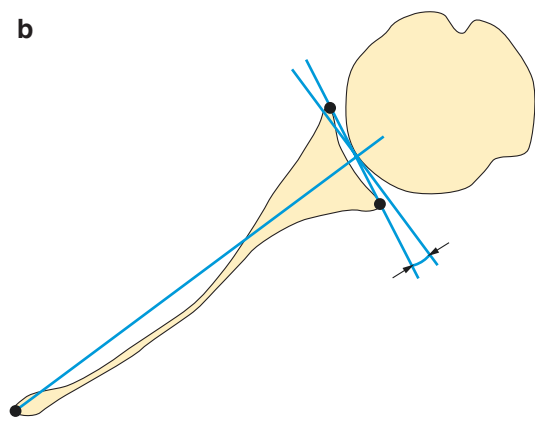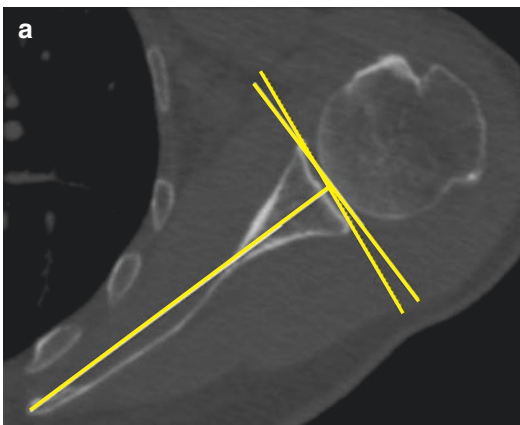
Fig. 8.36   Glenoid version estimation: CT

Normal	0 to −8° retroversion
Posterior instability	> −15° (retroverted)
Anterior instability	> +5° (anteverted)

Reproducibility/Variation

The technique of glenoid version angle CT measurement is both valid and reproducible with regard to the inter-observer and intra-observer variability, thus establishing its accuracy. However it is important to realise that this depends on using the standard mid-glenoid slice for measurement purposes as described by Friedman et al. (1992, 1998).This is because as Randelli and Gambrioli (1986) have shown, the glenoid cavity does not have the same AP orientation varying in version values from superior to inferior.

Normal values	
Superior glenoid version mean	−5° (range −2° to −15°)
Middle glenoid version mean	−2° (range −8° to 0°)
Inferior glenoid version mean	−7° (range −2° to −15°)

Glenoid version measurement is affected by the rotation of the scapula in the coronal plane. Using CT, Bokor et al. (1999) evaluated the effect of scapular rotation in the coronal plane on glenoid version, and found that glenoid version could vary by as much as 10.5° with scapular rotation of just 20°. For this reason the CT scans need to be obtained with the glenoid surface perpendicular to the plane of the CT slices in the scout view. All CT images need to include the vertebral border of the scapula as the axis of the body of the scapula extends posteriorly medial to it. The range of normal values reported in Friedman's CT based study was −12° retroversion to 14° of anteversion. This gives a mean value of 2° of anteversion which has not been reproduced in subsequent studies and probably reflects the fact that the measurements for normal value determination were done retrospectively on CT chest examinations. In all probability the measurements had an error factor due to

the scan slices not being perpendicular to the glenoid as required. In a more recent study Hoenecke et al. (2010) confirmed that in the supine position the direction for the 2D axial CT slice was almost never perpendicular to the scapular body but was angled 35° (+/−19) from the transverse plane relative to the scapular body, supporting Bokor et al. (1999) findings.

Racial differences of statistical significance have been reported with the average glenoid version for black and white patients measured at 0.20 and 2.65° of retroversion, i.e. a difference of about **3°**. There have not been any statistical studies to suggest a gender difference between men and women.

Clinical Relevance/Implications

It is important to evaluate glenoid anteversion and retroversion in cases of shoulder instability.

Analysis/Validation of Reference Data

The reproducibility section above covers the subject explaining and analysing the possible reasons for seemingly a lack of accuracy. More recent studies using 2D CT and MRI have shown a good reproducibility using a single CT slice at midglenoid level for the measurement. However the high level of accuracy required for assessing the "true "glenoid version for the purposes of preoperative planning for total shoulder arthroplasty may not be achieved by the 2D CT technique. Mullaji et al. (1994) showed that the single axial CT slice technique does not necessarily coincide with the site of maximal posterior wear (and increased retroversion) in cases of arthritis. In Hoenecke's study comparing glenoid version measurements using 2D and 3D CT in patients scheduled for total arthroplasty, an average absolute error of 5.1° (range 0–16°) was reported by the 2D CT valuation. On high-resolution 3D CT reconstructions, the location of maximum wear was most commonly postero-inferiorly and was missed on the 2D slices in

52% of cases. This error rate can substantially affect the determination of the degree of correction necessary in arthritic glenoids, promoting postoperative failure risk from joint instability and implant loosening. In Hoenecke' study however, the 2D CT slices were NOT perpendicular to the glenoid and therefore the error is not unexpected for the reasons previously addressed by Bokor et al. (1999). The 3D CT reconstructions are recommended for full preoperative planning for another reason. Correction of severe retroversion in arthritis is usually associated with a reduced volume of glenoid vault bone stock, which increases the risk of peg perforation due to excessive medialisation at the time of placing the glenoid implant to correct the excessive retroversion.

Conclusion

The glenoid version angle is an objective and fairly reproducible measurement of glenoid orientation and shape. The angle is useful in identifying patients with a greater likelihood of having shoulder instability and in the preoperative planning of glenohumeral joint prosthetic replacement.

8.25   Glenoid Version Angle (MRI)

Definition

Glenoid version is the angle that the glenoid centre line makes with the plane of the scapula. The glenoid centre line usually points a few degrees posterior (retroverted to the plane of the scapula. Changing the version of the glenoid articular surface imposes a corresponding change in the humeroscapular positions in which the net humeral joint reaction force will be contained by the effective glenoid arc.

Indications

Glenoid version may be altered by glenoid dysplasia, fractures, arthritis, glenoid osteotomy, and glenoid arthroplasty. Abnormal glenoid version positions the glenoid fossa in an abnormal relationship to the forces generated by the scapulo-humeral muscles. Normalising abnormal glenoid version is often a critical step in glenohumeral reconstruction.

Techniques:

MRI.

Shoulder MRI: axial scan of the glenohumeral joint.

Full Description of Technique

The pear-shaped parasagittal MRI oblique view of the glenoid cavity en face is the starting image on which the glenoid inclination is first determined along its superoinferior axis. A perpendicular line is then drawn to this line at its midpoint which refers to the axis required for the glenoid version measurement (Fig. 8.37). The MRI glenoid version angle is then measured on this axial scan of the glenohumeral joint. A line is drawn connecting through the tip of the anterior and posterior labrum. At the same level a second line passing through the medial border of the scapular body is drawn. Alpha (α) is the angle between these two lines.

90° is subtracted from the angle (α) to determine glenoid version of the shoulder (GV = $\alpha - 90°$).

Reproducibility/Variation

It is very easy on MRI and reproducible but must be mindful of the position arm.
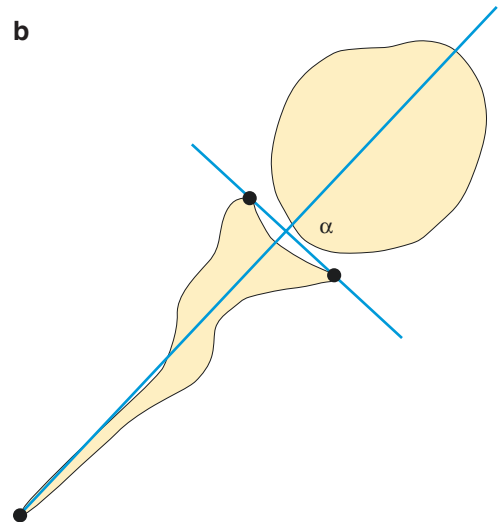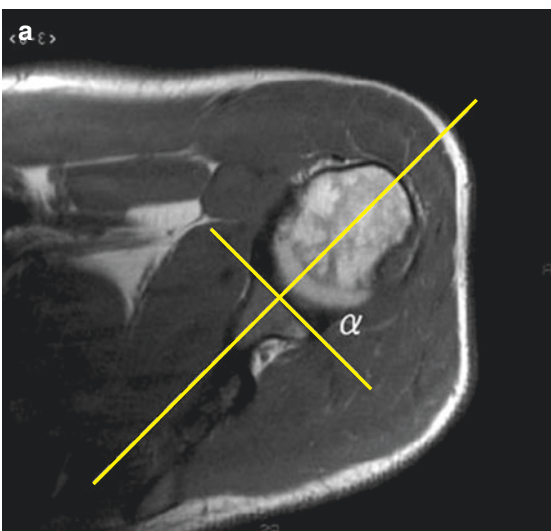
Fig. 8.37   Glenoid version estimation: MRI

Clinical Relevance/Implications

It is important in the evaluation of glenoid ante-version and retroversion in shoulder instability.

Analysis/Validation of Reference Data

Most of the data is available for the measurement using the axial CT method.

Conclusion

This measurement may be useful in the preoperative assessment of the glenohumeral relationships to help in planning surgery in cases of shoulder instability.

8.26 Glenoid Version in Children

In the anatomic work of Gardner and Grey (1953) an axial histological glenohumeral section of a foetus demonstrated a glenoid version of −20°. As argued by Mintzer et al. (1996), after birth the glenoid is maximally retroverted before 2 years of age and becomes less retroverted with growth, indicating a dynamic element similar to that seen in the acetabulum. The appearance of the ossification centres for the upper glenoid and base of the coracoid occurs at the end of the first decade of life when adult glenoid version is reached. Insults to this normal glenoid sequence of progression will result in the persistence of excessive retroversion and potential posterior instability. Brewer et al. (1986) showed posterior instability in adolescents with a mean glenoid version of **−16.9**°.

The same CT and MRI based techniques described above are employed in acquiring the optimal images and carrying out the measurement. The angle in the posterior medial quadrant is measured. 90° is then subtracted from this reading to give the value of glenoid retroversion. A negative value indicates retroversion, while a positive value indicates anteversion.

Normal values with age	Mean glenoid version
Birth–2 years	−6.3°+/− 6.5° (range −23 to 8°)
2–8 years	−4.2°+/− 6.2° (range −23 to 8°)
8–16 years	−1.7°+/− 6.4° (range −16 to 12°)

8.27   Glenoid Defect: Critical Size Measurement

Definition

The critical size of a post-traumatic osseous defect of the glenoid is a reliable prognosticator for ongoing instability, risk of recurrent anterior shoulder dislocation and failure of Bankart repair. Yamamoto et al. (2009) argued that this critical measurement is 20% of the glenoid length.

Indications

The incidence of post-dislocation glenoid defect varies from 8 to 90%. The defect may be predominantly identified as an osseous fragment in 50%, or predominant erosion in 40%. Residual instability following treatment of anterior dislocation is the main indication. The measurement of the glenoid defect is essential for making the appropriate therapeutic decisions and a preoperative requirement.

Repeat studies have shown that the **critical size** of the glenoid defect is **6 mm.** This is equated to the glenoid dimension**s.** When the mean glenoid length is 31.9 +/−2.6 mm and its width is 24.0 +/−2.7 mm, a **6 mm defect** equates to a **19% +/−1% reduction** of glenoid length, and a **25% +/−2% reduction** of its width.

If the size of the defect is calculated as a % of the area of the entire glenoid surface, a 6 mm defect involves about **26% of the glenoid surface**.

Technique

CT—MDCT with both oblique coronal and sagittal reconstructions. The oblique sagittals produce an en face profile which is very informative and is the basis for obtaining the glenoid length and width dimensions. As noted by Griffith (2007), MRI can be used but CT is thought to be more reliable. 3D CT is also increasingly being used and is proving to be the optimum modality of choice among the surgeons.

Full Details of Technique

The whole of the glenoid is imaged and reconstructions carried out. Using bone window settings of the en face oblique sagittal image, based on Griffith's et al. study (2003), the length of the glenoid is measured from the supraglenoid tubercle superiorly to the most inferior point of the glenoid fossa. At its midpoint the maximum width dimensions are calculated. Cross referencing is needed with the axial images to ensure that the most superior point is located for measurement purposes. The width: length ratio is also calculated. The length and width of the defect is then measured as well and expressed as a % of the glenoid dimensions (Fig. 8.38). As noted by Yamamoto et al. (2009, 2010), the **critical size is 20% of glenoid length**, which equates to **25% of glenoid width**.

Simultaneous assessment of the uninjured contralateral glenoid increases the accuracy of the measurement and significance even though there are some inherent small individual measurement variations between both sides in the uninjured state.

Reproduction/Variability

The technique and employed method is robust and reproducible. This has been shown in both experimental and clinical studies.

Clinical Relevance/Implications

The effect of losing the osseous critical size from the glenoid is a main predictor of recurrent dislocation and determinant for surgery with bone graft augmentation. The post traumatic glenoid defect lies anterior rather than anteroinferior in location. This means that it is more meaningful to measure the glenoid length of both the native glenoid and the defect as this is likely to provide a more accurate measurement ratio compared with the width which is affected by the trauma. Comparative assessment can also be done with the contralateral side to obtain an insight of the likely preinjury glenoid dimensions as there is usually only a minor degree of variation. The lateral humeral displacement represents the total depth of the gle-
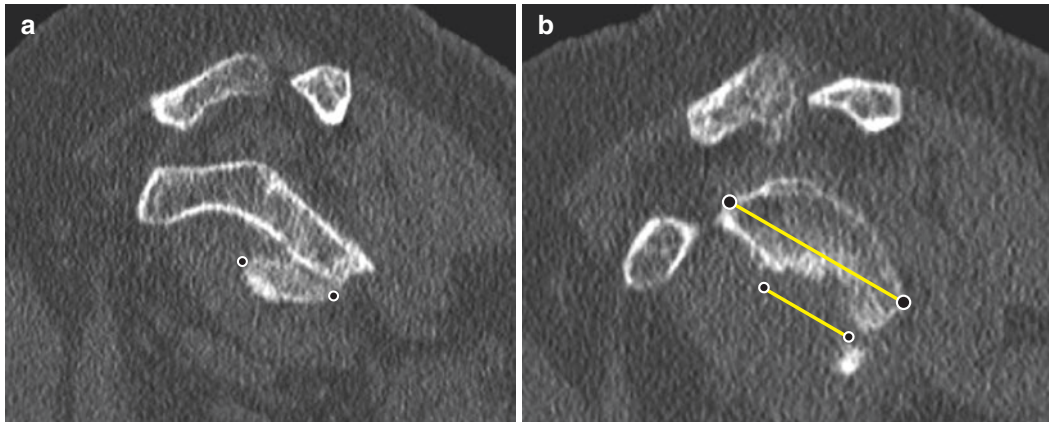
Fig. 8.38 Glenoid critical size estimation of bone defect following anterior dislocation showing a large fracture fragment (Bankart lesion) from anterior glenoid (**a**). Note the large size of the anterior glenoid defect (**b**) relative to the glenoid length

noid socket. This displacement is reduced to 15% (an 85% reduction) as a result of a 6 mm defect.

Analysis/Validation of Reference Data

A small but respectable number of experimental, cadaveric and biomechanical studies support the conclusion that a 20% reduction of glenoid length usually requires open surgical stabilisation with bone grafting. The post procedure CT assessment shows altered measurements which correlate with clinical improvement.

The stability ratio without an osseous defect is	32% +/−6%
The stability ratio with a 6 mm defect equates to	17% +/−5%

From loss of 20% glenoid length**.**

Conclusion

A reliable measurement which is important in the management of patients with anterior dislocation.

References

Aoki M, Ishii S, Usui M (1986) The slope of the acromion and rotator cuff impingement. Orthop Trans 10:228

Azzoni R, Cabitza P, Parrini M (2004) Sonographic evaluation of subacromial space. Ultrasonics 42:683–687

Banas MP, Miller RJ, Totterman S (1995) Relationshio between the lateral acromion angle and rotator cuff disease. J Shoulder Elb Surg 4:454–461

Bey M, Brock S, Beierwaltes W et al (2007) In vivo measurement of subacromial space width during shoulder elevation: technique and preliminary results in patients following unilateral rotator cuff repair. Clin Biomech Aug 22(7):767–773

Bigliani L, Morrison DS, April EW (1986) The morphology of the acromion and its relationship to rotator cuff tears. Orthop Trans 10:228

Bokor DJ, O'Sullivan MD, Hazan GJ (1999) Variability of measurement of glenoid version on computed tomography scan. J Shoulder Elb Surg 8:595–598

Bouaicha S, Ehrmann C, Slankamenac K, Regan WD, Moor BK (2014) Comparison of the critical shoulder angle in radiographs and computed tomography. Skeletal Radiol 43:1053–1056

Brewer BJ, Wubben RC, Carrera GF (1986) Excessive retroversion of the glenoid cavity. J Bone Joint Surg (Am) 68:724–731

Cone RO, Danzig L, Resnick D, Goldman AB (1983) The bicipital groove: radiographic, anatomic, and pathologic study. Am J Roentgenol 141:781–788

Cotton RE, Rideout DF (1964) Tears of the humeral rotator cuff: a radiological and pathological necropsy survey. J Bone Joint Surg 46:314–318

Deutsch A, Altchek DW, Schwartz E, Otis JC, Warren RF (1996) Radiological measurement of superior displacement of the humeral head in the impingement syndrome. J Shoulder Elb Surg 5:186–193

Di Mario M, Fraracci L (2005) MR study of the intrinsic acromial angle in 74 symptomatic patients. Radiol Med 110:273–279

Dias JJ, Mody BS, Finlay DB, Richardson RA (1993) Recurrent anterior glenohumeral joint dislocation and torsion of the humerus. Injury 24:329–332

Dowdy PA, O'Driscoll SW (1994) Recurrent anterior shoulder instability. Am J Sports Med 22(4):489–492

Dumontier C, Sauter A, Gagey O, Apoil A (1999) Rotator interval lesions and their relation to cora-

doid impingement syndrome. J Shoulder Elb Surg 8(2):130–135

Edelson JG, Taitz C (1992) Anatomy of the coracoacromial arch. Relation to degeneration of the acromion. J Bone Joint Surg Br 74:589–594

Friedman RJ, Hawthorne KB, Genez BM (1992) The use of computerized tomography in the measurement of glenoid version. J Bone Joint Surg Am 74:1032–1037

Friedman RJ, Bonutti PM, Genez B (1998) Cine magnetic resonance imaging of the subcoracoid space. Orthopaedics 21:545–548

Fuchs B, Weishaupt D, Zanetti M, Hodler J, Gerber C (1999) Fatty degeneration of the muscles of the rotator cuff: assessment by computed tomography versus magnetic resonance imaging. J Shoulder Elb Surg 8:599–605

Garcia GH, Lui JN, Degen RM, Johnson CC, Wong A, Dines DM, Gulotta LV, Dines JS (2017) Higher critical shoulder angle increases the risk of retear after rotator cuff repair. J Shoulder Elbow Surg 26:241–245

Gardner E, Grey DJ (1953) Prenatal development of the human shoulder and acromioclavicular joint. Am J Anat 92:219–276

Gerber C, Terrier F, Ganz R (1987) The subcoracoid space: an anatomic study. Clin Orthop 215:132–138

Golding C (1962) The shoulder: the forgotten joint. Br J Radiol 35:149–458

Goutallier D, Postel JM, Bernageau J, Lavau L, Voisin MC (1994) Fatty muscle degeneration in cuff ruptures : pre and postoperative evaluation by CT scan. Clin Orthop Rel Res 304:78–83

Graichen H, Bonel H, Stammberger T, Englmeier KH, Reiser M, Eckstein F (1999) Subacromial space width changes during abduction and rotation: a 3-D MR imaging study. Surg Radiol Anat 21:59–64

Grasshoff H, Buhtz C, Gellerich I, Von Knorre C (1991) CT diagnosis in instability of the shoulder joint. ROFO 155(6):523–526

Green A, Griggs S, Labrador D (2004) Anterior acromial anatomy: relevance to arthroscopic acromioplasty. Arthroscopy 20:1050–1054

Griffith JF, Antonio GE, Tong CW, Ming CK (2003) Anterior shoulder dislocation: quantification of glenoid bone loss with CT. Am J Roentgenol 180:1423–1430

Griffith JF, Antonio GE, Yung PSH, Wong EMC, Yu AB, Ahhuja AT, Chan KM (2007) Prevalence, pattern and spectrum of glenoid bone loss in anterior shoulder dislocation: CT analysis of 218 patients. Am J Roentgenol 190:1247–1254

Hamid N, Omid R, Yamaguchi K, Steger-May K, Stobbs G, Keener JD (2012) Relationship of radiographic acromial characteristics and rotator cuff disease: a prospective investigation of clinical, radiographic, and sonographic findings. J Shoulder Elbow Surg 21:1289–1298

Haygood TM, Langlotz CP, Kneeland JB, Ianotti JP, Williams GR, Dalinka MK (1994) Categorisation of acromial shape: interobserver variability with MR imaging and conventional radiography. Am J Roentgenol 162:1377–1382

Hebert LJ, Moffet H, Dufour M, Moisan C (2003) Acromiohumeral distance in a seated position in persons with impingement syndrome. J Magn Reson Imaging 18:72–79

Heuberer PR, Plachel F, Willinger L, Moroder P, Laky B, Pauzenberger L, Lomoschitz F, Anderl W (2017) Critical shoulder angle combined with age predict five shoulder pathologies: a retrospective analysis of 1000 cases. BMC Musculoskelet Disord 18:259

Hirschfelder H, Kirsten U (1991) Biometric analysis of the unstable shoulder. Z Orthop Ihre Grenzgeb 129(6):516–520

Hitchcock HH, Bechtol CO (1948) Painful shoulder. J Bone Joint Surg Am 30:262–273

Hoenecke HR Jr, Hermida JC, Flores-Hernandez C, D'Lima DD (2010) Accuracy of CT-based measurements of glenoid version for total shoulder arthroplasty. J Shoulder Elb Surg 19:166–171

Hughes RE, Bryant CR, Hall JM et al (2003) Glenoid inclination is associated with full-thickness rotator cuff tears. Clin Orthop Relat Res 407:86–91

Ianotti JP, Gabriel JP, Schneck SL, Evans BG, Masra S (1992) Normal glenohumaral relationship: an anatomic study of one hundred and forty shoulders. J Bone Joint Surg 74:491–500

Kasra R (2010) Development of fatty atrophy. J Bone Joint Surg 92:2270–2278

Kitay GS, Ianotti JP, Williams GR, Haygood T, Kneeland JB, Berlin J (1995) Roentgenographic assessment of acromial morphologic condition in rotator cuff impingement syndrome. J Shoulder Elb Surg 4:441–448

Leclercq R (1950) Diagnostic de la rupture du susepineux. Rev Rhum 10:510–515

Lehtinen JT, Lehto MUK, Kaarela K, Kautiainen HJ, Belt EA, Kauppi MJ (2000) Radiographic joint space in rheumatoid glenohumeral joints. A 15-year prospective follow-up study in 74 patients. Rheumatology 39:288–292

Lo IK, Burkhart SS (2003) The etiology and assessment of subscapularis tendon tears: a case for subcoracoid impingement, the roller-wringer effect, and TUFF lesions of the subscapularis. Arthroscopy 19:1142–1150

Mallon WJ, Brown HR, Vogler JB, Martinez S (1992) Radiographic and geometric anatomy of the scapula. Clin Orthop 277:142–154

Maurer A, Fucentese SF, Pfirrmann CWA, Wirth SH, Djahangiri A, Jost B, Gerber C (2011) Assesment of glenoid inclination on routine clinical radiographs and computed tomography examinations of the shoulder. J Shoulder Elb Surg 1:1–8

Mayerhoefer ME, Breitenseher M, Roposch A, Treitl C, Wurnig C (2005) Comparison of MRI and conventional radiography for assessment of acromial shape. Am J Roentgenol 184:671–675

Mintzer CM, Waters PM, Brown DJ (1996) Glenoid version in children. J Pediatr Orthop 16:563–566

Moor BK, Bouaicha S, Rothenfluh DA, Sukthankar A, Gerber C (2013) Is there an association between the individual anatomy of the scapula and the development of rotator cuff tears or osteoarthritis of the glenohumeral joint? Bone Joint J 95-B:935–941

Moor BK, Wieser K, Slankamenac K, Gerber C, Bouaicha S (2014a) Relationship of individual scapular anatomy

and degenerative rotator cuff tears. J Shoulder Elbow Surg 23(4):536–541

Moor BK, Rothlisberger M, Muller DA, Zumstein MA, Bouaicha S, Ehlinger M, Gerber C (2014b) Age, trauma and the critical shoulder angle accurately predict supraspinatus tendon tears. Orthop Traumatol Surg Res 100:489–494

Moses DA, Chang EY, Schweitzer ME (2006) The scapuloacromial angle: a 3D analysis of the acromial slope and its relationship with shoulder impingement. J Magn Res Imaging 24:1371–1377

Mullaji AB, Beddow FH, Lamb GHR (1994) CT measurement of glenoid erosion in arthritis. J Bone Joint Surg (Br) 76-B:384–388

Natsis K, Tsikaras P, Totlis T (2007) Correlation between the four types of acromion and the existence of enthesophytes: a study on 423 dried scapulas and review of the literature. Clin Anat 20:267–272

Nyffeler RW, Jost B, Pfirrmann CWA, Gerber C (2003) Measurement of glenoid version: conventional radiographs versus computed tomography scans. J Shoulder Elb Surg 12(5):493–496

Nyffeler RW, Werner CML, Sukthanakar A, Schmid MR, Gerber C (2006) Association of a large lateral extension of the acromion with rotator cuff tears. J Bone Joint Surg Am 88-A:800–805

Petersson CJ, Redlund-Johnell I (1983) Joint space in normal gleno-humeral radiographs. Acta Orthop Scand 54(2):274–276

Petersson CJ, Redlund-Johnell I (1984) The subacromial space in normal shoulder radiographs. Acta Orthop Scand 55:57–58

Porter NA, Singh J, Tins BJ, Lalam RK, Tyrrell PNM, Cassar-Pullicino VN (2015) A new method for measurement of subcoracoid outlet and its relationship to rotator cuff pathology at MR arthrography. Skeletal Radiol. 44(9):1309–1316

Prato N, Peloso D, Franconeri A, Tegaldo G, Ravera GB, Silvestri E, Derchi LE (1998) The anterior tilt of the acromion: radiographic evaluation and correlation with shoulder diseases. Eur Radiol 8:1639–1646

Randelli M, Gambrioli PL (1986) Glenohumeral osteometry by computed tomography in normal and unstable shoulders. Clin Orthop 208:151–156

Richards DP, Burkhart SS, Campbell SE (2005) Relation between narrowed coracohumeral distance and subscapularis tears. Arthroscopy 21:1223–1228

Roberts CS, Davila JN, Hushek SG, Tilett ED, Corrigan TM (2002) Magnetic resonance imaging analysis of the subacromial space in the impingement sign positions. J Shoulder Elb surg 11:595–599

Saupe N, Pfirrmann CWA, Schmid MR, Jost B, Werner CM, Zanetti M (2006) Association between rotator cuff abnormalities and reduced acromiohumeral distance. AJR 187:376–382

Sluming VA (1995) Technical note: measuring the coracoclavicular distance with ultrasound—a new technique. Br J Radiol 68:189–193

Stehle J, Moore SM, Alaseirlis DA, Debski RF, McMahon PJ (2007) Acromial morphology: effects of suboptimal radiographs. J Shoulder Elb Surg 16:135–142

Takase K, Yamamoto K, Imakiire A, Burkhead WZ Jr (2004) The radiographic study in the relationship of the glenohumeral joint. J Orthop Res 22:298–305

Tétrault P, Krueger A, Zurakowski D, Gerber C (2004) Glenoid version and rotator cuff tears. J Orthop Res 22:202–207

Toivonen DA, Tuite MJ, Orwin JF (1995) Acromial structure and tears of the rotator cuff. J Shoulder Elb Surg 4:376–383

Tokgoz N, Kanatli U et al (2007) The relationship of glenoid and humeral version with supraspinatus tendon tears. Skelet Radiol 36:509–514

Torrens C, Lopez J, Puente I, Caceres E (2007) The influence of the acromial coverage index in rotator cuff rears. J Shoulder Elbow Surg 16:347–351

Totty P, Proust F, Bertrand P, Fouquet B, Rosset P, Alison D, Valat JP, Rouleau P, Laffont J (1988) Rupture de la coiffe des rotateurs. Quantification des signes indirects en radiologie standard et manouevre de Leclercq. J Radiol 69:633–638

Tuite MJ, Toivonen DA, Orwin JF, Wright DH (1995) Acromial angle on radiographs of the shoulder: correlation with the impingement syndrome and rotator cuff tears. Am J Roentgenol 165:609–613

Viehofer AF, Gerber C, Favre P, Bachmann E, Snedeker JG (2016a) A larger critical shoulder angle requires more rotator cuff activity to preserve joint stability. J Orthop Res 34:961–968

Viehofer AF, Snedeker JG, Baumgartner D, Gerber C (2016b) Glenohumeral joint reaction forces increase with critical shoulder angles representative of osteoarthritis—a biomechanical analysis. J Orthop Res 34:1047–1052

Wang JC, Shapiro MS (1997) Changes in acromial morphology with age. J Shoulder Elbow Surg 6:55–59

Weiner DS, Macnab I (1970) Superior migration of the humeral head: a radiological aid in the diagnosis of tears of the rotator cuff. J Bone Joint Surg 52:524–527

Wuh HCK, Snyder SJ (1992) A modified classification of the supraspinatus outlet view based on the configuration and anatomical thickness of the acromion. Orthop Trans 16:767

Yamamoto N, Itoi E, Abe H, Kikuchi K, Seki N, Minagawa H, Tuoheti Y (2009) Effect of an anterior glenoid defect on anterior shoulder instability: a cadaveric study. Am J Sports Med 37:949–954

Yamamoto N, Muraki N, Sperling JW, Steinmann SP, Cofield RH, Itoi E, An KN (2010) Stabilising mechanism in bone grafting of a large glenoid defect. J Bone Joint Surg (Am) 92:2059–2066

Zuckerman JD, Kummer FJ, Cuomo F, Simon J, Rosenblum S, Katz N (1992) The influence of the coraco-acromial arch anatomy on rotator cuff tears. J Shoulder Elbow Surg 1:4–14

Mario Padrón, Eugenie Sánchez,
and Victor N. Cassar-Pullicino

Contents

M. Padrón, M.D. (✉) • E. Sánchez, M.D.
Clinica Cemtro, Avda Ventisquero de la Condesa, 42,
28035 Madrid, Spain
e-mail: mario.padron@clinicacemtro.com

V. N. Cassar-Pullicino
Department of Radiology, Robert Jones and Agnes
Hunt Orthopaedic Hospital NHS Foundation Trust,
Oswestry, UK

9.1　Introduction

The elbow consists of three highly congruent articulations—the radiocapitellar, ulnohumeral and proximal radioulnar joints—and its normal capacity at arthrography is **10–12 mL**. The radiocapitellar and proximal radioulnar joints account for the pivot joint (trochoid) components allowing axial forearm rotation, while the ulnohumeral joint provides a hinge joint (ginglymus) component allowing flexion/extension. The articular geometry is an important determinant of joint stability, but the soft tissues play a paramount role (Jean et al. 2012). The joint capsule which is thick anteriorly and the collateral ligaments aid in providing significant (50%) static joint stability. These ligaments can be assessed and measured by both sonography and MRI. Measurements based on radiographic standard projections are predominantly employed in assessing the traumatised paediatric elbow, although there is a steady increasing interest in adult elbow measurements for the purposes of post-traumatic reconstruction and arthroplasty. Comparison with the contralateral elbow to establish true measurement prior to injury is recommended before surgical planning. Nerve entrapment at various sites at the elbow is well recognised, and the clinical diagnosis can be challenging without the benefit of qualitative and quantitative imaging analysis.

9.2 Anatomical Landmarks

The capitellum and trochlea form the articular surfaces of the distal humerus. The capitellum almost forms a hemispherical surface and exhibits a maximal cartilage thickness anteriorly of **2 mm**. The capitellum is posteriorly devoid of articular cartilage which appears as a pseudodefect in MR images measuring **3.3 mm** (sagittal) × **5.6 mm** (mediolateral). In the sagittal projection, the capitellum is normally rotated by **30°–40°** anteriorly with respect to the long humeral axis (Fig. 9.1). Transversely the articular surface is rotated inwards by **5–7°** (usually increased in supracondylar fractures), while in the frontal plane it lies in **6–8°** of valgus tilt (Fig. 9.2). The distal humeral diametaphysis shows a difference in size between the prominent lateral and the smaller medial supracondylar columns. Although both columns are strong, they are connected by a wafer-thin area of bone which centrally is only **1 mm** thick visible as a component of the teardrop on the lateral view. The medial column deviates from the central long axis of the humerus at approximately twice the angle (**45°**) of the lateral column (**20°**). The trochlea is not a symmetrical

pulley as its medial edge is about **6 mm** longer than its lateral counterpart (Fig. 9.2).

The proximal ulna articulates through its trochlear notch with the trochlea of the humerus. The articular portion of the ulna extends from the coronoid process to the olecranon process. The orientation of the trochlear notch is **30°–40°** posterior to the long axis of the ulna, which corresponds to the 30°–40° of anterior angulation of the distal humerus. On the AP view, the trochlear notch of the proximal ulna is angulated in varus (**2°–6°**) with respect to the ulnar shaft which contributes to the carrying angle (Fig. 9.3). Apart from the normal varus angulation, further important morphological features of the proximal ulna include the "hook angle" and the anterior deviation. The "hook angle" is the angle between the proximal plane of the ulna from the tip of the triceps insertion area and the dorsal plane distal from the triceps insertion area (**95.3° +/− 9.0**). **Anterior angulation** is also referred to as the dorsal apex of the proximal ulna or proximal ulna dorsal angulation (PUDA) which usually measures **6.2° +/− 2.7** (Fig. 9.4). Furthermore, it is important to note that there are distinct gender differences in ulna morphology with a lesser angular measurement range in men. Anatomically
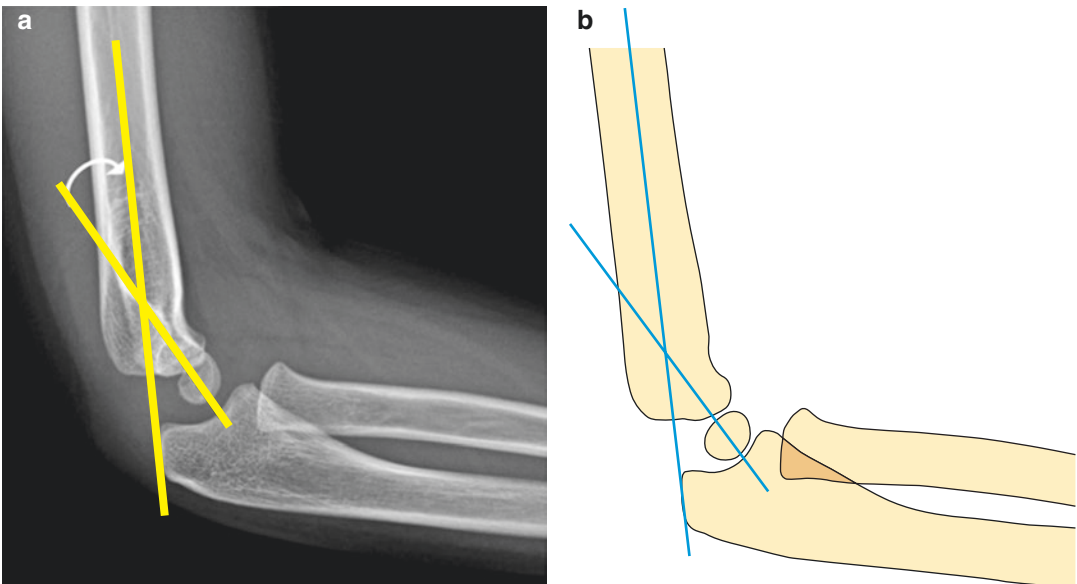
Fig. 9.1 (**a**, **b**) The humero-condylar angle. The capitellum is normally rotated 30–40° anteriorly with respect to the long humeral axis
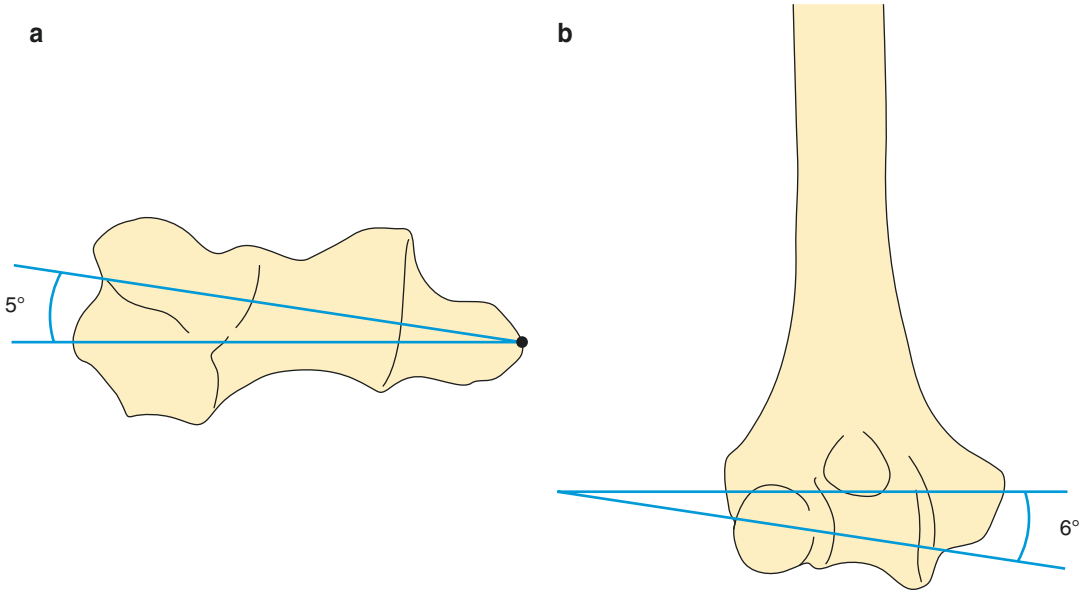
Fig. 9.2 The articular surface is transversely rotated inwards by 5–7° (**a**), with a 6–8° valgus tilt in the frontal plane (**b**)
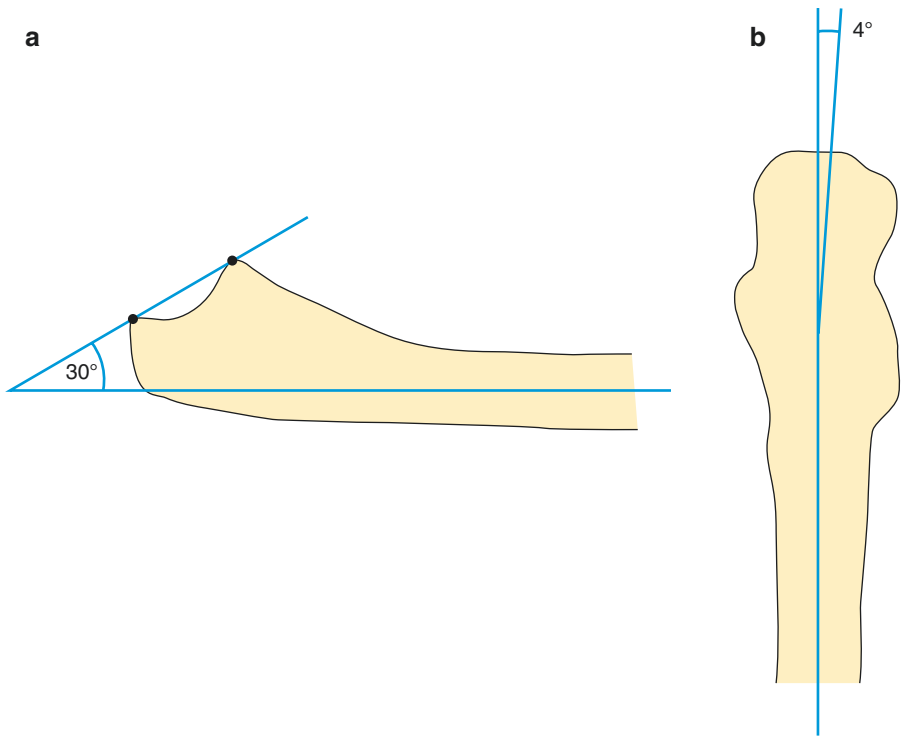
Fig. 9.3 The trochlear notch of the ulna is 30–40° posteriorly orientated to the long axis of the ulna (**a**), with a varus angulation of 4° to the shaft in the frontal plane (**b**)

Fig. 9.4 The head and neck axis of the proximal radius lie 15° laterally angulated with respect to the radial shaft (**a**). Morphological features of the proximal ulna are further depicted by the 'hook angle' (α) and anterior angulation (PUDA) in (**b**)
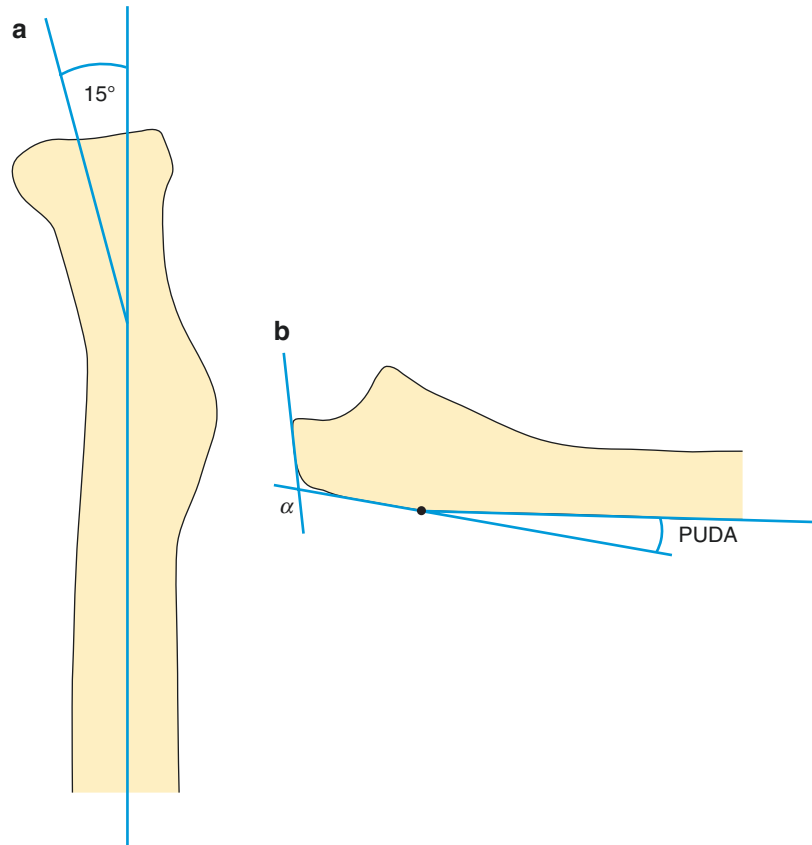
preshaped internal fixation plates have become increasingly available for ulnar fracture reconstruction based on these morphological features. In complex fractures of the ulna especially in cases of Monteggia fracture with radiocapitellar joint instability, measurement of the hook angle and anterior angulation on a radiograph of the contralateral elbow is recommended to choose the appropriate preshaped plate for reconstruction (Puchwein et al. 2012).

In childhood, fractures of the upper extremity account for about 70% of all fractures and of these about 10% involve the elbow. The distal humerus is the most commonly injured site accounting for 86% of fractures around the elbow, and the peak age range is 5–10 years. Physeal injury of the distal humerus however has a peak age of 4–5 in girls and 5–8 in boys, which is much earlier compared with the peak age range of 10–13 for physeal injuries elsewhere in the skeleton. A number of radiographic lines and

angle measurements are employed in the routine evaluation and management of paediatric elbow trauma (Webb and Sherman 1989).

In the paediatric age group, there are six ossification centres around the elbow joint which appear and fuse at different ages (Beaty and Kasser 2009). They appear in a predictable order (*CRITOE*) starting with the capitellum (1–3 years) followed by the radius, internal epicondyle (3–5 years), trochlea (5–7 years), olecranon (7–9 years), and external epicondyle (9–11 years) (Fig. 9.5).

Standard radiographs of the elbow used for measurement purposes include AP and lateral views. The **AP view** should be performed in full elbow extension and full forearm supination. There are three angles measured on the AP radiograph which are used to determine the alignment of the distal humerus: Baumann's, humero-ulnar and metaphyseal-diaphyseal angles. The major radiographic landmark on the
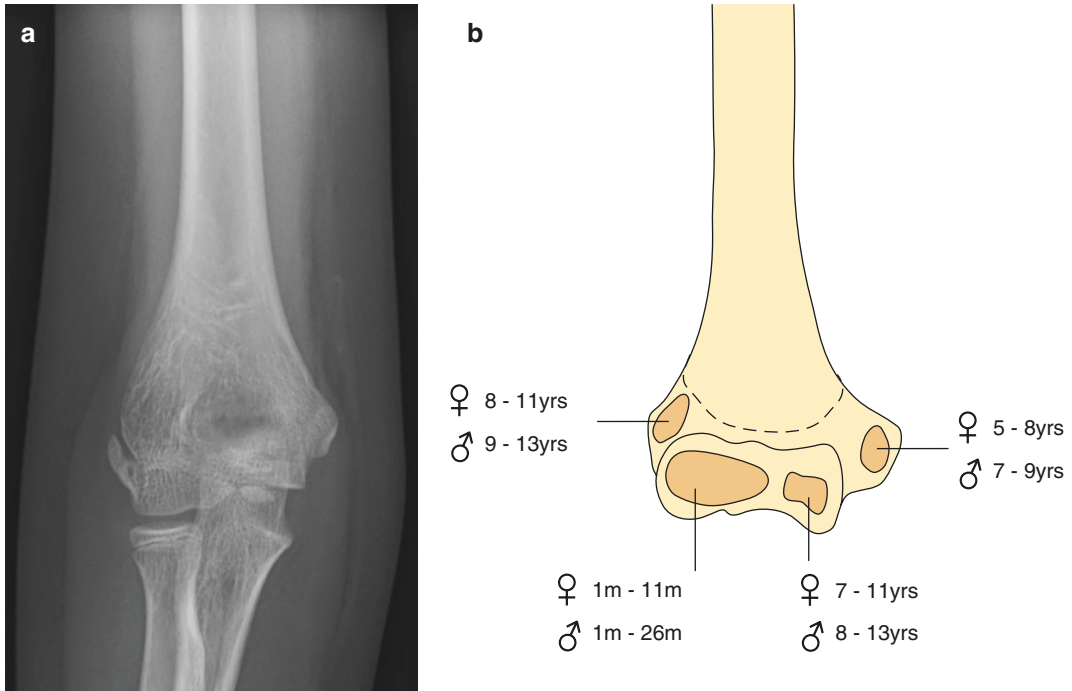
Fig. 9.5 The ossification centres around the elbow (**a**) which appear in sequential order within the epiphysis and apophysis (**b**)

standard AP view is the angulation of the physeal line between the lateral condyle and metaphysis of the distal humerus. The angle subtended by the physeal line and the long axis of the humerus is the Baumann's angle. The Baumann's angle enjoys a good correlation with the clinical carrying angle, but difficulties in its measurement arise in adolescents when the lateral condyle ossification centre commences the normal fusion process in the distal humerus. The humero-ulnar angle is determined by lines longitudinally bisecting the shafts of the humerus and ulna. This angle is regarded as the most accurate in determining the true carrying angle of the elbow as shown by Webb and Sherman (1989). The metaphyseal-diaphyseal angle is formed by the line that longitudinally bisects the shaft of the humerus intersecting with the line that connects the widest points of the metaphysis of the distal humerus. It is the least accurate of the three angles. The **carrying angle** of the elbow is the clinical measurement of varus-valgus angulation of the arm with the elbow fully extended and the forearm fully supinated. Radiographically

various methods in its measurement have evolved by regarding it as the angle between the longitudinal axis of the humerus with either the mid-forearm or the ulna on the AP projection and is normally between **11 and 13°** of valgus. It is due firstly to the fact that the medial trochlear edge is about 6 mm longer than the lateral edge and secondly to the obliquity of the coronoid's superior articular surface which is not orthogonal with the ulnar shaft (Fig. 9.6).

The **lateral view** needs to be a true lateral projection obtained with the elbow flexed by 90° and the forearm in neutral position with the thumbs up position. This is crucial as errors arise if measurements are conducted on inappropriately positioned radiographs. A true lateral view of the joint also needs the beam to be directed distally about 7°. To avoid errors from poor radiographic technique, both the humerus and forearm should be in full contact with the radiographic table. A true lateral radiograph allows a *teardrop* to be formed by the boundaries of the coronoid and olecranon fossae and the capitellum inferiorly (Fig. 9.7). On a true lateral elbow projection, the

Fig. 9.6 AP view of the elbow showing the anatomical landmarks, joint space and 'carrying angle'. Note the lateral angulation of the radial head/neck to the shaft and the varus angulation of the trochlear notch to the ulnar shaft

Fig. 9.7 A true lateral radiograph of the elbow depicting the 'teardrop' which has the thin bony interface formed by the coronoid and olecranon fossae and the capitellum inferiorly

superimposition of the posterior supracondylar ridges is the best means of confirming true laterality. There are three lateral radiographic landmarks: the humero-condylar angle, anterior humeral line and the anterior coronoid line.

The coronoid process is **1.5 cm** in height and **2.5 cm** wide at its base. In an injured elbow with intact ligaments, stability is maintained until about 60% of the coronoid height is lost, but in the presence of an associated fractured radial head, stability is only maintained up to 40% of coronoid height. At surgery, however, coronoid fracture fragments appear larger than anticipated from radiography and CT assessment due to the contribution of the overlying cartilage. At the coronoid tip, the cartilage thickness is maximal, with a mean of **3.00 mm** (range 1.7–4.6 mm). This means that a 2 mm coronoid tip fracture measured

on CT translates into a 5-mm-sized fragment at surgery which has an effect on classification and treatment decisions (Rafehi et al. 2012).

The proximal radius exhibits a normal angulation of **15°** between the neck and shaft, with the neck angulated laterally and mildly anteriorly relative to the radial shaft (Silberstein et al. 1982). The neck orientation and not the shaft of the radius should be used as the reference for measurements employed in assessing radiocapitellar alignment (Fig. 9.4).

In the management of radial head fractures, an estimate of the degree of angulation and displacement is required. The O'Brien classification characterises fractures of the radial head and neck according to the angulation at the fracture site: type 1 is less than 30°, type 2 is between 30 and 60° and type 3 is more than 60° angulation. The exact degree of angulation can only be determined by an AP radiograph with the forearm placed in the position of rotation at the moment of impact. In cases where it is unclear if fracture reduction is required or not, Jeffery (1950) advised obtaining radiographs in various degrees of rotation, and when the radial head forms as nearly a rectangle as possible, the real degree of angulation is determined (Jeffery 1950).

9.3   The Humeral and Ulnar Shaft Lines

Definition

A line is drawn through and parallel to the humeral shaft using the midpoints of two perpendicular lines to the diaphysis. Similarly a line is drawn through and parallel to the ulnar shaft (Yochum and Rowe 1996).

Indications

The lines are a prerequisite for the formation of the elbow axial angles that are altered in fractures of the elbow and other deformities (Morrey 2004).

Technique

AP radiograph.

Full Description of Technique

In the anteroposterior projection, the elbow must be fully extended with no rotation of the humerus (Yochum and Rowe 1996).

Diagram/Illustration

Humeral and ulnar shaft lines (Fig. 9.8).
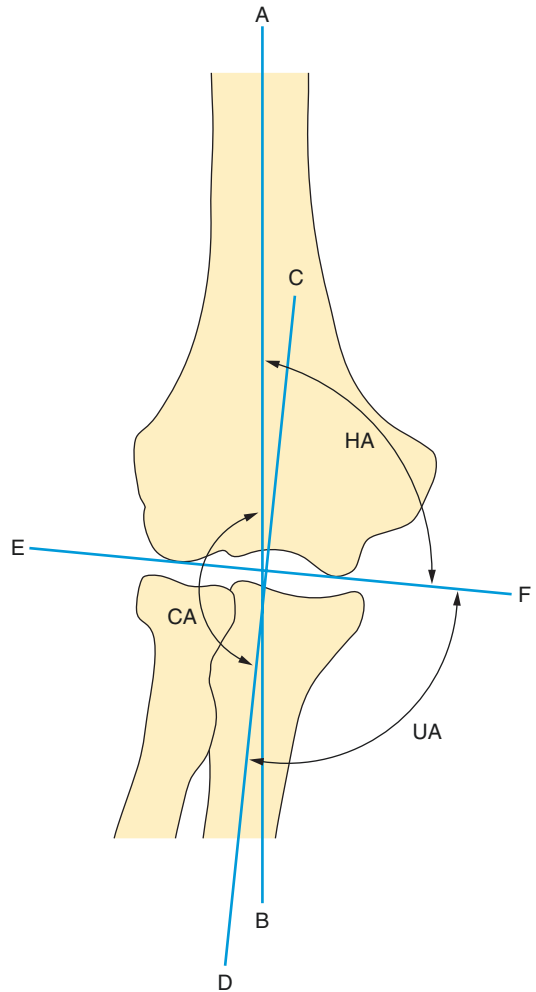
Fig. 9.8 Lines and angles at the elbow. *AB* the humeral shaft line. *EF* the humeral articular line, *CD* the ulnar shaft line, *HA* the humeral angle, *UA* the ulnar angle, *CA* the carrying angle

9.4 The Humeral Articular Line

Definition

A transverse line is drawn tangentially through the most distal articular surfaces of the trochlea and capitellum (Yochum and Rowe 1996).

Indications

This line is altered in condylar and supracondylar fractures of the humerus.

Technique

AP radiograph.

Full Description of Technique

In the anteroposterior projection, the elbow must be fully extended with no rotation at the humerus.

Diagram/Illustration

Humeral articular line (Fig. 9.8).

9.5 The Radiocapitellar Line

Definition

A line is drawn through the centre and parallel to the long axis of the proximal radius and is extended proximally through the elbow joint. This line should pass through the centre of the capitellum in all degrees of flexion of the elbow, although in young children the capitellar ossification centre may have an eccentric position within the largely cartilaginous capitellum. As the radius usually bends in the region of the tuberosity, the line should be drawn through only the most proximal part of the radius rather than along the greater length of the diaphysis (Yochum and Rowe 1996).

Indications

The radiocapitellar line is used to evaluate the relationship of the proximal radius to the capitellum and to determine the presence of radial head subluxation or dislocation (Morrey 2004).

Technique

True lateral radiograph.

Full Description of Technique

The arm should be flexed at 90° with the thumb pointing vertically and the shoulder as close to table level as possible.

Reproducibility/Variation

This line should normally intersect the capitellum on all views. In its drawing only the radial neck should be used to avoid errors. In young children the position of the small ossific nucleus in the relatively large cartilaginous capitellum may vary and lie in an eccentric position.

Clinical Relevance/Implications

As the radiocapitellar line compares the relative positions and relationships of two articulating bones, malalignment is indicative of a dislocation. In children under the age of 2, elbow dislocations are very rare, and transphyseal fractures producing distal humeral epiphyseal separation are often mistaken for elbow dislocation. The radiocapitellar relationships are however undisturbed and appear normal in transphyseal fracture, and the forearm bones are usually displaced medially and not laterally which are two useful clues used to differentiate this injury from elbow dislocation.

Diagram/Illustration

Radiocapitellar line (Fig. 9.9).
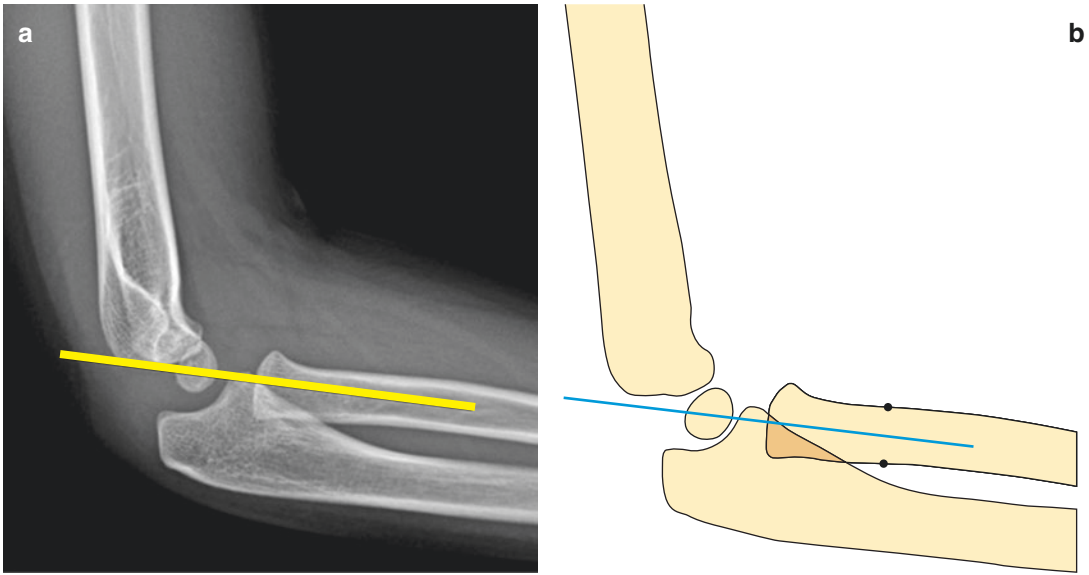
Fig. 9.9 The radiocapitellar line shown on a lateral radiograph (**a**) and diagram (**b**) which normally passes through the centre of the capitellum in any degree of elbow flexion

Analysis/Validation of Reference Data

The reliability of this line has been confirmed in establishing congruent or incongruent elbow relationships, but one cannot stress enough the importance of proper radiographic technique in acquiring the true lateral projection.

Conclusion

Very useful and reliable line in the assessment of osseous relationships at the elbow.

9.6 The Anterior Humeral Line

Definition

On a true lateral radiograph, this is a line drawn along the anterior cortex of the distal metaphysis of the humerus. This line should normally pass through the middle third of the capitellum, reflecting the normal anteversion of the distal humeral metaphysis and capitellum relative to the humeral shaft (John et al. 1996).

Indications

If this line does not pass through the middle third of the capitellum, anterior or posterior displacement or angulation must be suspected secondary to fracture. This line is useful in the detection of supracondylar fractures most of which occur in extension and are associated with posterior displacement or angulation, although posterior displacement of the capitellum may also be seen in lateral condyle fractures. In such circumstances the anterior humeral line passes either through the anterior third of the capitellum or anterior to the capitellum. Caution is needed in young children when the capitellum is still predominantly cartilaginous and the capitellar ossification centre is small.

Technique

A true lateral radiographic projection of the elbow.

Full Description of Technique

The arm should be flexed at 90° with the thumb pointing vertically and the shoulder as close to table level as possible.

Reproducibility/Variation

The age and stage of skeletal development can have an effect on the reliability of this sign. In young children below the age of 2, the ossification centre of the capitellum can be so small that the anterior humeral line can lie anterior to the small capitellar ossification centre in the absence of a fracture. Herman et al. (2009) suggest that the anterior humeral line reliably passes through the middle third of the capitellum in children older than 4 years, while previous authors suggest that the sign is reliable from the age of 2.5 years (Herman et al. 2009).

Clinical Relevance/Implications

The anterior humeral line is very useful in the diagnosis of supracondylar fractures of the humerus as most result in posterior displacement or angulation of the distal fragment. It is seen to usually pass anterior to the middle third of the capitellum in 94% of supracondylar fractures. Posteriorly displaced lateral condylar fractures can also be associated with an abnormal intersection of the capitellum by the drawn anterior humeral line, but this is less useful as these fractures can be subtle with minimal displacement.

This line is not accurate or reliable if the lateral view is not a true lateral projection. Skibo and Reed (1994) showed that if the humerus is not perfectly lateral to the film, the anterior humeral line is not only unreliable but in many instances falsely positive (Skibo and Reed 1994).

Diagram/Illustration

The anterior humeral line (Fig. 9.10).
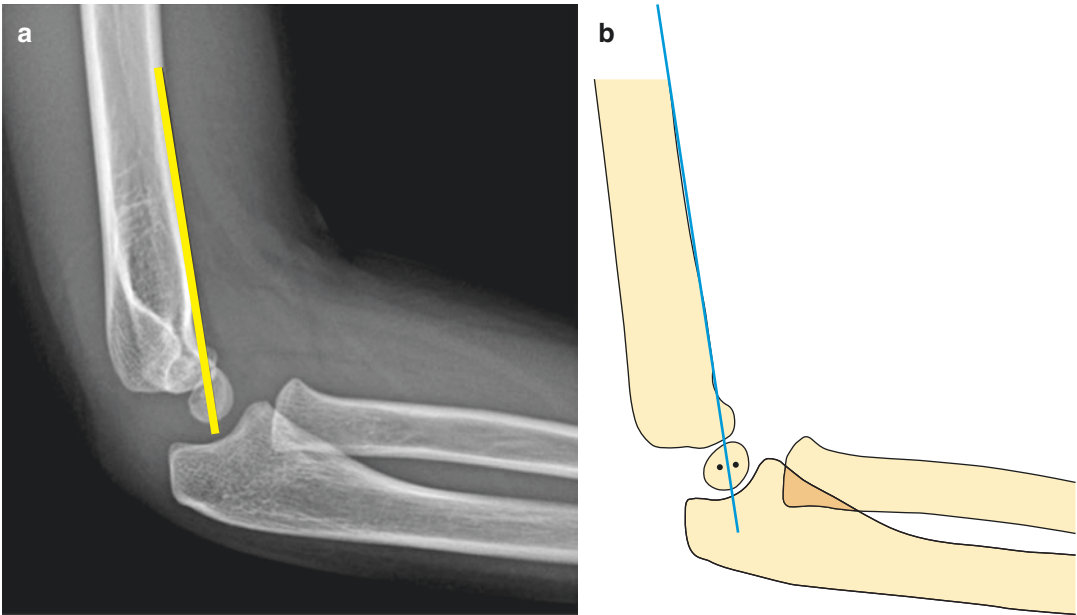
Fig. 9.10 The anterior humeral line normally passes through the middle third of the capitellum (**a**, **b**)

Analysis/Validation of Reference Data

Reliability is very high as long as the radiograph is a true lateral view.

Conclusion

This line along with the radiocapitellar line is employed as part of the routine radiographic assessment of the paediatric elbow following trauma.

9.7 The Anterior Coronoid Line

The anterior coronoid line is drawn along the coronoid and continued proximally towards the anterior outline of the distal humerus. Normally it should just touch the capitellum anteriorly. If there is a fracture resulting in angulation or displacement of the capitellum, this line intersects or lies posterior to the capitellum. It is not as well known as the radiocapitellar and anterior humeral line, but is a helpful parameter in the full assessment of osteoarticular status on the true lateral view (Fig. 9.11).
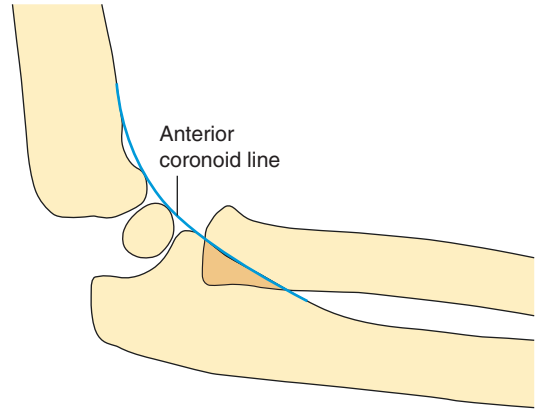
Fig. 9.11 The anterior coronoid line and its normal relationship to the outline of the capitellum

9.8   Carrying Angle

Definition

The carrying angle is formed between the humeral and ulnar shaft lines although the mid-forearm axis can also be used instead of the ulna. This angle is normally between **11 and 14°** in males (164°) and **13 and 16°** (168°) in females.

Indications

This angle can be altered in supracondylar humeral fractures and following ulnar and radius fractures (Ippolito et al. 1990; Arnold and Nasca 1977).

Technique

AP radiograph.

Full Description of Technique

In the anteroposterior projection, the elbow must be fully extended with no rotation at the humerus and with the forearm fully supinated. Measurement of the carrying angle is complicated because of the S shape of the ulna. Two horizontal lines perpendicular to the humeral shaft are used, and the longitudinal line joining the centre of the lines produces the humeral line axis. The drawing of the axis of the forearm differs if the measurement is intended as the HEW angle or the humero-ulnar angle. In the humero-ulnar angle measurement, two horizontal lines are drawn, one across the ulnar segment between the radial head and radial tuberosity and the other at the farthest distal diaphysis segment included on the radiograph. The line joining the centre of these lines represents the forearm axis. The angle of intersection between the two lines forms the carrying angle. In the HEW angle measurement, the forearm axis is dependent on joining the centrepoints of two horizontal lines, one drawn across the width of the radius and ulna just above the level of the radial tuberosity and the other

Humero-ulnar   Humero-elbow-wrist
angle   angle
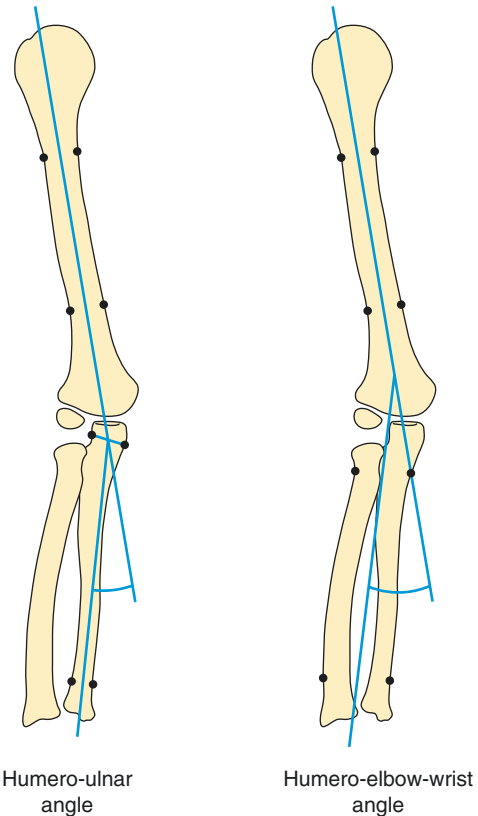
Fig. 9.12 The humero-ulnar and the humero-elbow-wrist angles produce different values of the 'carrying angle'

across the width of the distal radius and ulna metaphysis (Fig. 9.12).

Reproducibility/Variation

A number of articles based on clinical measurements have shown gender differences in the carrying angle indicating that it represents a secondary sex characteristic (Chapleau et al. 2011; Zampagni et al. 2008). In a radiographic study in adults, this was also shown with a significantly greater angle in females (range 10–27° and a mean of 18.47° +/− 4.12°) compared with males (range 5–17° and a mean of 9.29 +/− 2.98°). Beals' (1976) study of the carrying angle in 422 radiographs however showed that the angle increased with age, with a measured angle of **17.8°** with no gender difference (Beals 1976).

Clinical Relevance/Implications

It is wrongly assumed that the Baumann's angle has a constant relationship to the carrying angle. As shown by Mohammad et al. (1999) there is a nonlinear relationship between the two angles beyond 10° of rotation. Increased carrying angle is a risk factor for nontraumatic ulnar neuropathy at the elbow (Mohammad et al. 1999).

Diagram/Illustration

Carrying angle (Figs. 9.8 and 9.12).

Analysis/Validation of Reference Data

There have been a number of methods employed in the estimation of the carrying angle, and the data reported by different authors show considerable differences. These differences are due to different definitions of the angle as well as different methodologies. Some of the radiographic methods are based on drawing the reference lines to include the whole of the long bone shafts, while others based the measurement on angles at the elbow (Chang et al. 2008). Oppenheim et al. (1984) used three radiographic measurements based on the AP radiograph from the upper humerus to the wrist—the humero-ulnar angle, Baumann's angle and the humero-elbow-wrist (HEW) angle. The HEW angle is the most accurate method of approximating the true clinical carrying angle (Oppenheim et al. 1984).

HEW angle	Normal	10° valgus
	Cubitus varus	<5°
	Cubitus valgus	>15 °

The humero-ulnar angle calculated radiographically overestimates the carrying angle because of the curvature of the ulna. This normal curvature makes placement of a line parallel to the proximal ulna and radius arbitrary. The normal value is **13°** in females and **11°** in males. Measurements attempted on radiographs with limited inclusion of the forearm bones tend to underestimate the deformity. Mohammad and Abdelmonem (2010) proposed a simple and perceived reliable method based on the elbow AP view obtained with the elbow in full extension and the forearm in full supination (Mohammad and Abdelmonem 2010). It is measured between a line passing through the midaxis of the lower third of the humerus and a line along the midaxis of the upper third of the forearm between the radius and ulna. The two lines are extended to meet at the midpoint of the trans-epicondylar distance. The forearm midaxis line passes from the midpoint between the radius and ulna in the upper third of the forearm to the midpoint of the trans-epicondylar distance passing through the superior radioulnar joint. The carrying angle also normally progresses into a more varus alignment as the elbow is flexed (Van Roy et al. 2005). The intraobserver variation using the radiographic methods is also a problem. There are only a few reports focusing on the reliability of specific methods which have been published based on biomechanical studies (Morrey and Chao 1976). Furthermore in throwing athletes, it may be greater than 15° due to stress-related adaptive morphological changes (King et al. 1969).

Conclusion

This is probably one of the best known angles in elbow assessment which does carry with it a significant degree of variation, reducing its reliability in clinical practice especially if used in isolation.

9.9 The Humeral Angle

Definition

The angle is formed between the humeral shaft and humeral articular lines and is normally **85°** with a range of **72°–95°**.

Indications

This is abnormal in supracondylar fractures.

Technique

AP radiograph.

Full Description of Technique

In the anteroposterior projection, the elbow must be fully extended with no rotation at the humerus (Yochum and Rowe 1996).

Diagram/Illustration
(see Sect. 9.3, Fig. 9.8)

Humeral angle.

9.10   The Ulnar Angle

Definition

The angle is formed between the ulnar shaft line and humeral articular line and normally measures **84°** with a range of **72°–95°**.

Indications

It is abnormal in ulnar fractures.

Techniques

AP radiograph.

Full Description of Technique

In the anteroposterior projection, the elbow must be fully extended with no rotation at the humerus (Yochum and Rowe 1996).

Diagram (see Sect. 9.3, Fig. 9.8)

Ulnar angle.

9.11 Baumann's Angle

Definition

This is defined by the intersection of a line drawn along the physis of the capitellum and a line along the long axis of the humerus. It normally is about **70°–75°,** but it may vary with gender and should be compared to the opposite elbow, and a deviation of more than 5° is regarded as unacceptable following fracture. Variations of its measurements have evolved which will be addressed separately.

Indications

It is very useful in determining the adequacy of reduction of a supracondylar fracture.

Techniques

AP radiograph.

Full Description of Technique

In the anteroposterior projection, the elbow must be fully extended with no rotation at the humerus and the arm in contact with the cassette. For the purposes of measuring this angle, full extension is not necessary.

Reproducibility/Variation

This angle is consistent when both sides are compared and the radiographic beam is directed perpendicular to the long axis of the humerus. For the measured **Baumann's angle (α)** to be reliable and accurate, the humerus must be parallel to the cassette with the beam directed perpendicular to the cassette as well. Angulation of the tube and rotation of the distal fragment or entire reduced humerus can alter the Baumann's angle projection rendering the measurement inaccurate. Camp et al. (1993) showed that the Baumann's angle varies 6° for every 10° of humeral rotation on the

AP view (Camp et al. 1993). Using Baumann's original measurement technique described as variation 1 (see below) within the age range of 2–13 years, Williamson et al. (1992) found that the angle did not change significantly, there was no significant gender difference, with mean values of **72°** (SD 4°) and 95% of normal elbows were in the 64–81° range. After reduction and fixation, Baumann's angle (α) should be equal to that of the uninjured side usually 70–75°. More than 75° denotes varus malposition.

Baumann's angle (α)	Normal mean value	72° (SD 4°)
	Normal range values	64–81°

Baumann (1929) wrongly believed that the reciprocal angle (**90-α**) equalled the carrying angle, but this variation is also valid for measuring reduction adequacy, and it too is referred to in some textbooks as Baumann's angle (Baumann 1929). Normal Baumann's angles measured by this variation 2 (see below) in the paediatric age group is about **15°** with a range of 9–26° which is why comparison with the contralateral elbow measurement is so important. There was little or no knowledge of the reliability of this measurement before Williamson et al.'s and Silva et al.'s articles. When applied to 35 cases of supracondylar fractures, Silva et al. (2010) showed an excellent interobserver reliability between the five observers in the study (Silva et al. 2010). Similarly excellent values of intraobserver reliability were found for the measurement of the Baumann's angle. Some authors furthermore incorporate the normal articular tilt in the estimation regarding Baumann's angle as 90°-α°-5°.

Clinical Relevance/Implications

Acton and McNally (2001) reviewed the descriptions of the Baumann's angle in established textbooks and discovered three different variations in its measurement technique (Acton and McNally 2001). Variation 1 is the angle between the long axis of the humerus and a line through the physis of the lateral condyle of the distal humerus. They

recommend that this angle be regarded as the *shaft-physeal angle* measured as described by Baumann, between the long axis of the humerus and the inclination of the capitellar physis. Variation 2, also referred to in one of Baumann's articles, is the reciprocal angle to variation 1, between the perpendicular to the long axis of the humerus and a line through the physis of the lateral condyle. Variation 3 is the angle between the line through the physis of the lateral condyle and a line connecting a point on the edge of the trochlea to a point at the lateral limit of the physis of the lateral condyle. This variation 3 is inaccurate and should not be employed as it does not have the humeral axis reference. A deviation of more than 5° using variation 1 method, compared to the contralateral side, should not be accepted.

Diagram/Illustration

Baumann's angle (α) measured as in variation 1 described originally by Baumann, and the reciprocal angle measurement (90-α) developed later as variation 2 (Fig. 9.13).

Analysis/Validation of Reference Data

Correct projection and consistent measurement technique allied to comparative evaluation of the contralateral elbow measurements increase the diagnostic value. Williamson et al. (1992) reported the normal range of Baumann's angle between 64° and 81°, validating the range proposed by Baumann earlier. Interobserver errors of around 8% arise at the extremes of the age range (< 3 and > 9 years) based on difficulties in defining accurately and consistently the physeal line of the capitellum. From age 4 to 9, the period when 80% of supracondylar fractures occur, the measurement is reliable (Skaggs et al. 2004).

Krengel et al. (2012) have recently suggested that visualisation of at least 7 cm of the humeral
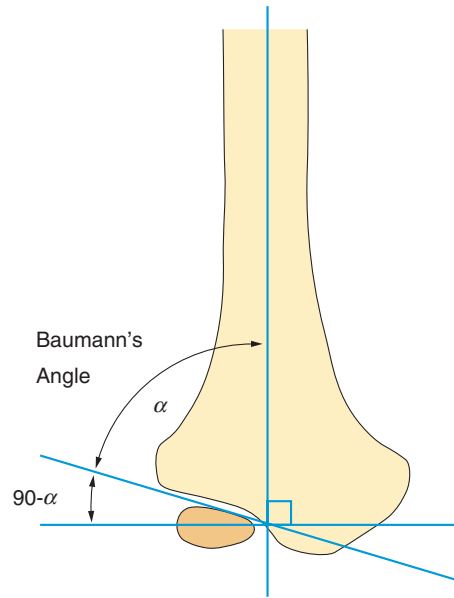
Fig. 9.13 Baumann's angle (α) depicts the humeral 'shaft-physeal' angle as measured in variation 1 or as the reciprocal angle of the perpendicular to the humeral shaft (90-α) in variation 2

shaft improves the reliability of the angle measurement (Krengel et al. 2012). Furthermore using the medial or lateral cortices of the distal humeral diaphysis as the axis rather than the standard central axis as the humeral shaft increased the reproducibility of the measurement.

Silva et al. (2010) proved that the angle is highly reliable with excellent interobserver and intraobserver reliability values ($r = 0.78$, $r = 0.80$, respectively). As in most cases, the Baumann's angle measurements were within 7° of each other; a difference of up to 7° in its measurement should be considered to be within the normal error of the measurement (Ruotolo and Healy 1999).

Conclusion

The angle is a simple, repeatable and reliable measurement used for determining the outcome of paediatric supracondylar fractures.

9.12 Medial Epicondylar Epiphyseal (MEE) Angle

Definition

This was described in 1993 in response to the difficulty sometimes experienced in measuring Baumann's angle, and it is formed by the intersection of the long axis of the humeral shaft and the line formed by the medial epicondylar growth plate. The mean value is **38.2° +/− 4.17°** (Biyani et al. 1993).

Indications

It is very useful in assessing the outcome after reduction of supracondylar fractures.

Techniques

AP radiograph.

Full Description of Technique

In the anteroposterior projection, the elbow must be fully extended with no rotation at the humerus.

Reproducibility/Variation

The MEE angle could be drawn satisfactorily in 96 out of 100 AP radiographs, and the measured angle did not vary significantly from this value in 25 Jones' view radiographs (paired *t* test, *t* = 0.06).

Clinical Relevance/Implications

Good results for reduction can be expected with measurements between **34° and 42°**.

Diagram/Illustration

Medial epicondylar epiphyseal angle (Fig. 9.14).

Analysis/Validation of Reference Data

Limited data. In younger children in whom the medial epicondyle is not yet ossified, a line is drawn along the straight medial and distal border of the distal humeral metaphysis. The MEE was found to be inaccurate in children under 3 years of age due to the rounded configuration of the medial humeral metaphysis.

Conclusion

The MEE angle is useful in assessing the accuracy of reduction following supracondylar fractures with good outcomes.
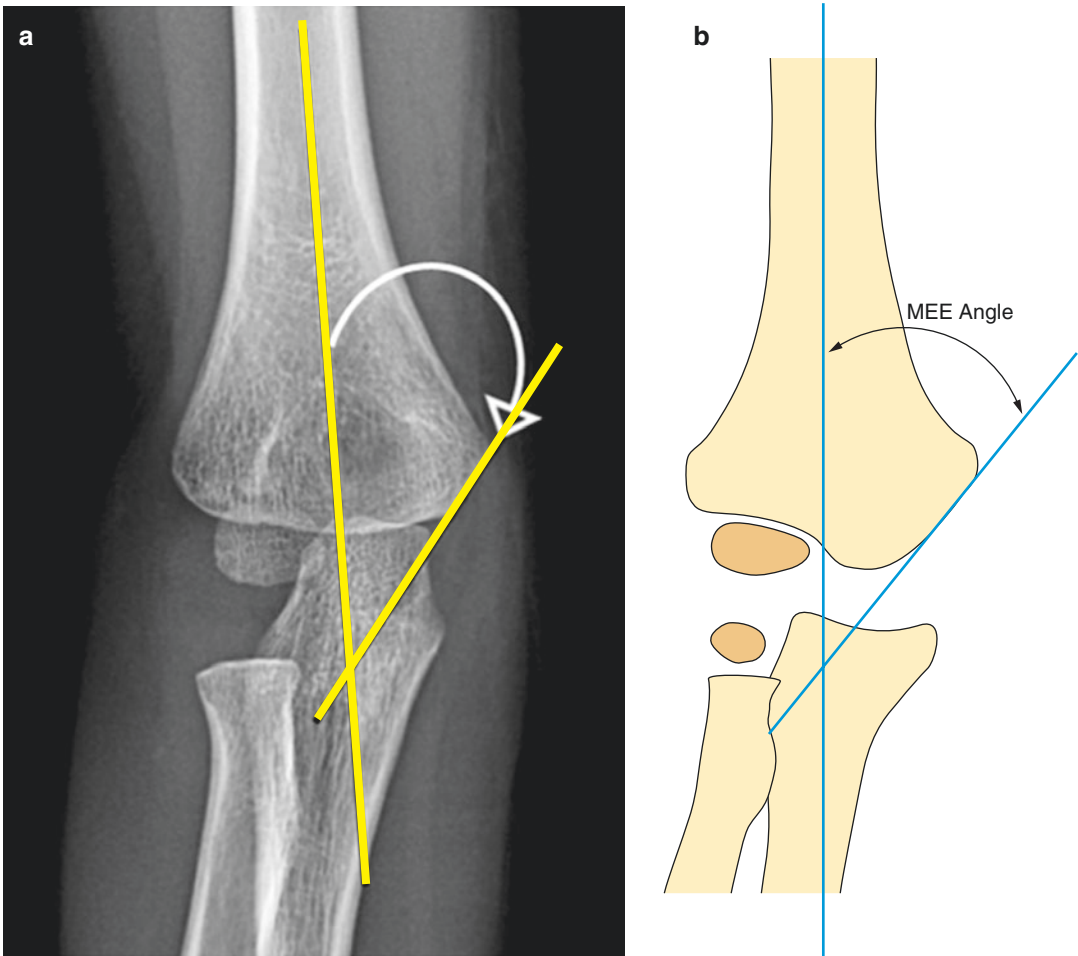
Fig. 9.14 (**a**, **b**) The medial epicondylar epiphyseal angle depicted on an AP radiograph (**a**) and in diagrammatic format (**b**)

9.13 The Humero-Condylar Angle

Definition

This is the angle formed by the shaft of the humerus and the axis of the condyles on the lateral radiograph, and it should be approximately **30°–40°** with a range of 25–45°. In children the distal humerus has an angular appearance, similar to a hockey stick, with an angle of around 145°, being the complementary angle to the humero-condylar angle.

Indications

This angle is helpful in the assessment of the status of the distal humerus following trauma and in the evaluation of the effect of reduction of supracondylar fractures and other deformities (Greenspan 2000).

Technique

True lateral projection.

Full Description of Technique

The arm should be flexed at 90° with the thumb pointing vertically and the shoulder as close to table level as possible.

Reproducibility/Variation

There is probably ethnic and population variation in this measurement as few studies have shown a higher average value and range for this angle. Simanovsky et al.'s study, for example, showed a mean HCA of **41.6°** with a range of 30–70° (Simanovsky et al. 2007).

Clinical Relevance/Implications

The emphasis of the quality of reduction of supracondylar fractures focuses on the coronal and transverse plane. In the sagittal plane, under-reduction leaves the fracture in extension, leading to loss of the normal HCA value of 40°. This leads

to limited elbow flexion outcome on final follow-up. Simanovsky et al. (2007, 2008) emphasised the importance of obtaining a satisfactory reduction of the HCA, as 80% of humeral growth occurs proximally after the age of 6 years leaving limited opportunity for remodelling distally at the fracture site. Due to significant individual variations of HCA, it alone cannot be deemed sufficient in clinically deciding the management and therapeutic decisions of supracondylar fractures, and it is best to obtain the comparative HCA measurement from the contralateral elbow (Simanovsky et al. 2008).

Diagram/Illustration

The humero-condylar angle (Fig. 9.15).

Analysis/Validation of Reference Data

The HCA measurement value does not alter with age, indicating that the distal humeral geometry in the sagittal plane is established very early in growth and remains constant through the ages.

Conclusion

A useful measurement in the paediatric age group but of limited value in isolation.

Fig. 9.15 Lateral view showing the humero-condylar relationship in the growing distal humerus

9.14 Medial Collateral Ligament (MCL) Complex

The medial collateral ligament complex is also known as the ulnar collateral ligament. Three components (anterior, posterior, transverse) make up the medial collateral ligament complex with the anterior bundle being the most discernible. It measures **27.1 +/− 4.3 mm** in length and is **4–5 mm wide** compared with **5-6 mm** at the midportion of the fan-shaped posterior ligament. The anterior bundle is primarily responsible for valgus stability of the elbow attaching to the coronoid process of the ulna adjacent to the sublime tubercle. The posterior component of the medial ligament has a mean length of **24.2 +/− 4.3 mm** and a mean width of **5.3+/−1.1 mm** (Fig. 9.16) (Husarik et al. 2010).

MR-based median ligament thickness of MCL	
Anterior UCL	2.5 mm (range, 0.9–4.3 mm)
Posterior UCL	1.0 mm (range, 0.5–2.2 mm)
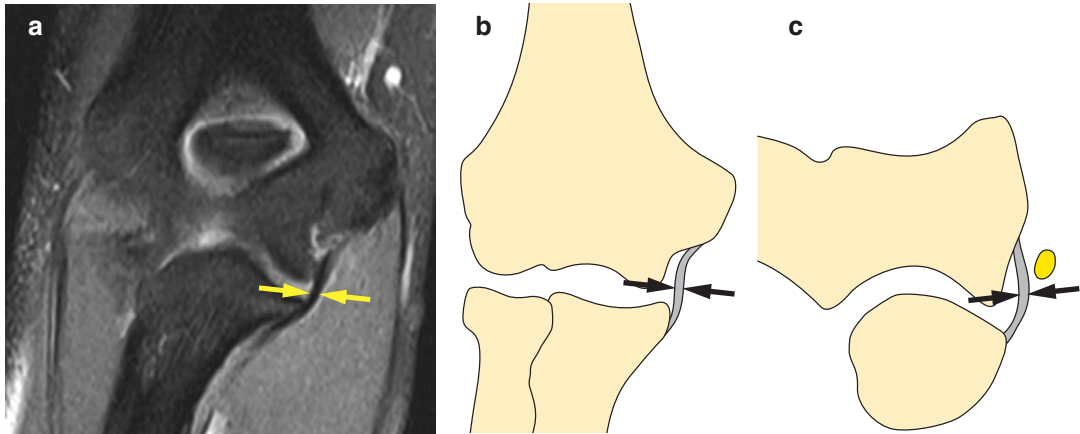
Fig. 9.16 Anterior UCL depicted on a coronal 3-D MRI (True FISP) (**a**) and the schematic diagram (**b**). Posterior UCL depicted schematically transversely lying deep to the ulnar nerve (**c**)

9.15 Lateral Collateral Ligament (LCL) Complex

The LCL is an important stabiliser of the elbow and is the main constraint to posterolateral rotatory instability. It has a Y-shaped structural configuration. Three components (radial collateral, annular, lateral ulnar collateral) make up the lateral collateral ligament complex which provides varus stability to the elbow. The radial collateral ligament measures **20 mm** in length and is **8 mm** wide. The most important component is the lateral ulnar collateral ligament situated posteriorly arising from the lateral epicondyle and traversing obliquely across the radius to insert at the supinator crest of the ulna.

High-resolution sonography using a linear transducer (15–17 MHz) allows the assessment of all the components of the LCL and can distinguish them from the overlying tendinous structures (Gondim Teixera et al. 2011; Stewart et al. 2009). The important lateral ulnar collateral ligament (LUCL) is sonographically usually seen as a clear separate component of the LCL as it courses over the radial head. The mean thickness of the ligament along the longitudinal short axis at this point is **1.2 mm** in women and men. The mean thickness of proximal attachment of the ligament to the humerus is **1.7 mm** in women and

1.6 mm in men. Differences in measurements with regard to gender and hand dominance are not significant. The LUCL can be difficult to differentiate from the radial collateral ligament in its proximal course, and sonography has an advantage over MRI in this aspect.

MRI and MR arthrography have been successfully employed in examining lateral epicondylitis and in determining the status of the LCL. It is not uncommon at MRI to see abnormalities of the LUCL (thin, absent, thickened) in association with MR evidence of lateral epicondylitis. Some authors earlier noted that MRI is not reliable as it does not show a normal LUCL in 50% of cases (Cotton et al. 1997). This however is likely to be due to the sequences and imaging planes used. MR imaging can be difficult in the coronal plane due to the oblique course of the ligament and requires 3-D sequences in an oblique coronal plane to analyse the ligament (Terada et al. 2004). In later studies on asymptomatic volunteers, most of the components of the ligament were noted as distinct structures in a high percentage of elbows and thickness evaluated at their midpoint (Fig. 9.17) (Husarik et al. 2010).

MR-based median ligament thickness of LCL	
LUCL	2.3 mm (range, 1.3–4.8 mm)
RCL	1.9 mm (range, 1.2–4.2 mm)
AL	1.0 mm (range, 0.5–1.5 mm)
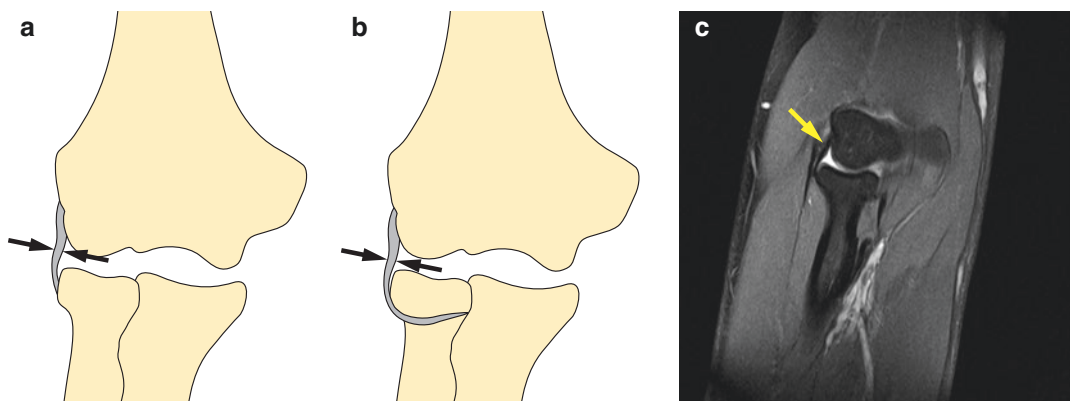
Fig. 9.17 The RCL in the coronal plane (**a**) and the lateral UCL (**b**) which attaches to the supinator crest of the ulna. A coronal MRI 3-D (True FISP) image showing the RCL deep to the common extensor tendon (**c**)

9.16 Joint Space and Plicae

The average radiographic adult joint space is **3 mm**. There are differences in the joint space measurements of the radiocapitellar and ulnohumeral joint space as seen on AP radiography. Furthermore on AP radiographs, the width of the lateral ulnohumeral joint space is greater than the width of the medial ulnohumeral joint space. The medial joint ulnohumeral space is parallel, while the lateral joint space is nonparallel and usually wider laterally (Rowland et al. 2007) (Fig. 9.18). Primary osteoarthritis predominantly involves the radiocapitellar joint and rarely the ulnohumeral articulation. Goodfellow and Bullough (1967) suggested this to be directly related to the different types of movement at these articular surfaces.

Noninvasive analysis of cartilage volume of the elbow using MRI shows that the humerus accounts for 49–60%, the radius for 15–27% and the ulna for 20–29% of the total volume which ranges between **3.90 and 7.17 mL** (mean 5.5 mL +/− 20%) (Springer et al. 1998). The mean cartilage thickness on MRI ranges from an average of **0.9 mm** (proximal ulna) **to 1.4 mm** (capitellum), while the maximal thickness from **2.30 mm** (proximal ulna) to **2.9 mm** (distal ulna). The articular cartilage thickness is not uniform, and in the sites used for potential osteochondral donor sites for treating osteochondritis dissecans, the mean thickness is **1.27 mm** (range 0.78–1.63 mm) (Schub et al. 2013). The trochlear notch of the ulna is normally traversed by a cartilage-free bony ridge at the junction of the olecranon and coronoid process which is about **2-3 mm** wide, but as it is also elevated by **2-3 mm** in relation to the rest of the trochlear notch, it is at the same height as the adjacent articular cartilage. In addition small medial and lateral cortical notches are found at the edges of the trochlear notch which vary in size measuring **3–7 mm** in AP width and **2–3 mm** in depth located peripheral to the bony ridge traversing the trochlear notch. Both the trochlear ridge and notches are optimally measured on sagittal MR images.

A widened joint space could herald ligament insufficiency. Stress radiography of the MCL enables accurate diagnosis of large and complete tears when the increase in joint space width is **0.5 mm** or more in the affected elbow compared with the normal contralateral joint (Rijke et al. 1994). However, it has been shown that the uninjured elbow does also exhibit significant medial ulnohumeral gapping on valgus stress radiography (Lee et al. 1998). This suggests that stress radiography may provide a false positive assessment
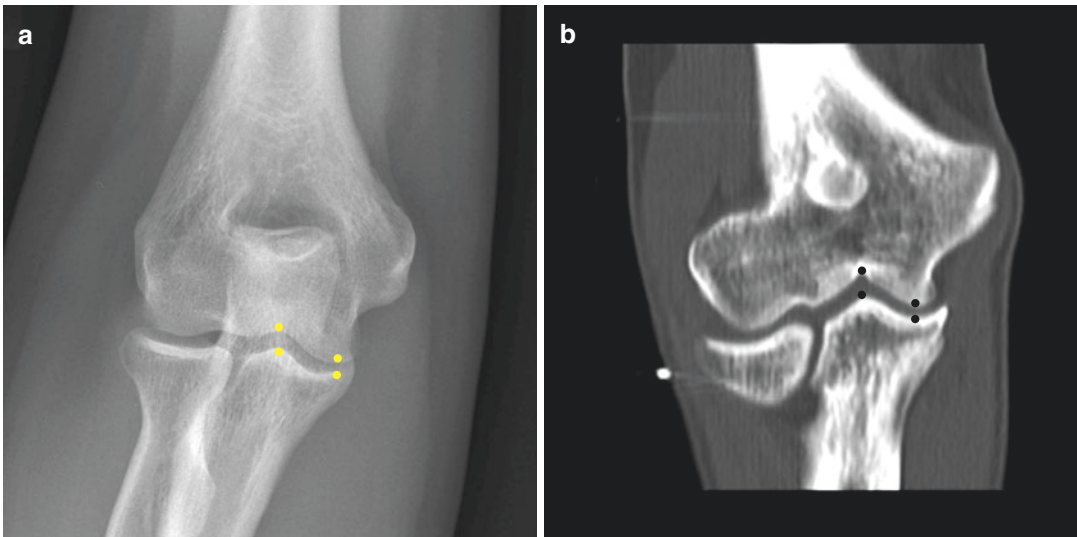
Fig. 9.18 Joint space. Note the normal asymmetrical dimensions of the space at the ulnohumeral joint on an AP radiograph (**a**) and coronal CT (**b**)

Fig. 9.19 Posterior plica depicted schematically (**a**) and in a sagittal MRI 3-D (True FISP) image (**b**). The capitellar pseudodefect is also depicted between the markers
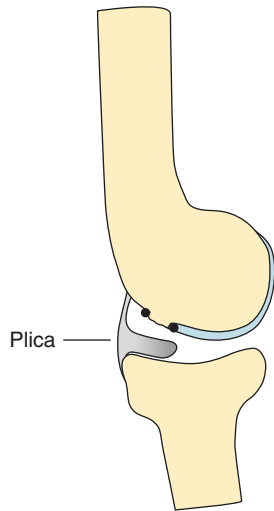
which requires comparative assessment with the contralateral elbow also with stress radiography to minimise it.

Normal plicae are present posterolaterally (98%) and posteriorly (33%) in asymptomatic patients, and these are seen on MRI. The thickness of the average normal plicae is usually **< 3 mm,** and the posterior plicae are normally thinner than the posterolateral plicae (Fig. 9.19).

9.17 Effusion

The nonechogenic space between the capsule and the bone at the level of the trochlea and capitellum can be measured sonographically (Koski 1990). A sonographic distance of more than **2 mm** on the volar aspect of the extended elbow joint between the joint capsule and the bone is a high probability of intra-articular effusion/synovitis. The effusion can also be measured in the olecranon fossa (Konin 2013). Fluid distribution in the elbow joint is affected by joint position due to the dynamics of elbow extension and flexion with resultant imaging implications. Sonographically fluid initially is seen to collect posteriorly and with larger amounts anteriorly. Sonography of the olecranon fossa with the flexed elbow is very sensitive at identifying 1–3 mL of fluid posteriorly in this position (De Maeseneer et al. 1998).

9.18   Nerves: Radial, Median, and Ulnar Dimensions

Entrapment neuropathies due to compression from a host of conditions—bony, ligamentous and tumoral—can affect the radial, median and ulnar nerves at the elbow due to their specific anatomical course, location and the dynamic effects from elbow movements. Both sonography and MRI offer the capability of assessing the detection, cause and effect of nerve compression (Bayrak et al. 2010).

As a result of chronic compression, the dimensions of the nerves alter, and sonographically this is usually highlighted by swelling proximally and narrowing distally from the point of compression. When compared with the normal contralateral side, the cross-sectional area or diameter of the nerve just proximal to the compression site is increased. An ulnar nerve area at the elbow of **7.9 mm²** has been deemed the upper limit of normal (Jacob et al. 2004) although prior studies (Chiou et al. 1998) suggested that the threshold value for cubital tunnel syndrome was an area of 7.5 mm². Care is paramount to ensure that sonographic assessment of the ulnar nerve in the contralateral elbow or in the ipsilateral elbow at different locations is done with the same degree of elbow flexion, as the cross-sectional diameter of the nerve decreases with flexion. MRI plays an important role in the detection of nerve entrapment by assessing the morphological and signal features of the nerves and related pathology directly, as well as secondary signs in the muscles from denervation and atrophy. Quantitative evaluation using T1-weighted spin echo or intermediate-weighted fat-saturated transverse MR images plays a role in the analysis of nerve structure as a possible cause of elbow pain and dysfunction. The nerves are well depicted appearing as smooth round or ovoid structures on axial images (Fig. 9.20). Multiple axial nerve measurements can be carried out within the anatomical range of 2 cm above to 2 cm below the level of the joint space providing the widest and narrowest nerve diameter dimensions before bifurcation (Bodner et al. 2002). The normal median values and related measurement ranges are provided (short and long diameters) below (Husarik et al. 2009).

Radial nerve	1.0 × 1.9 mm (range 0.8–2.0 × 0.9–5.0 mm)
Ulnar nerve	2.4 × 4.0 mm (range 1.0–4.0 × 3.0–7.0 mm)
Median nerve	3.0 × 5.4 mm (range 1.0–5.0 × 3.0–9.0 mm)
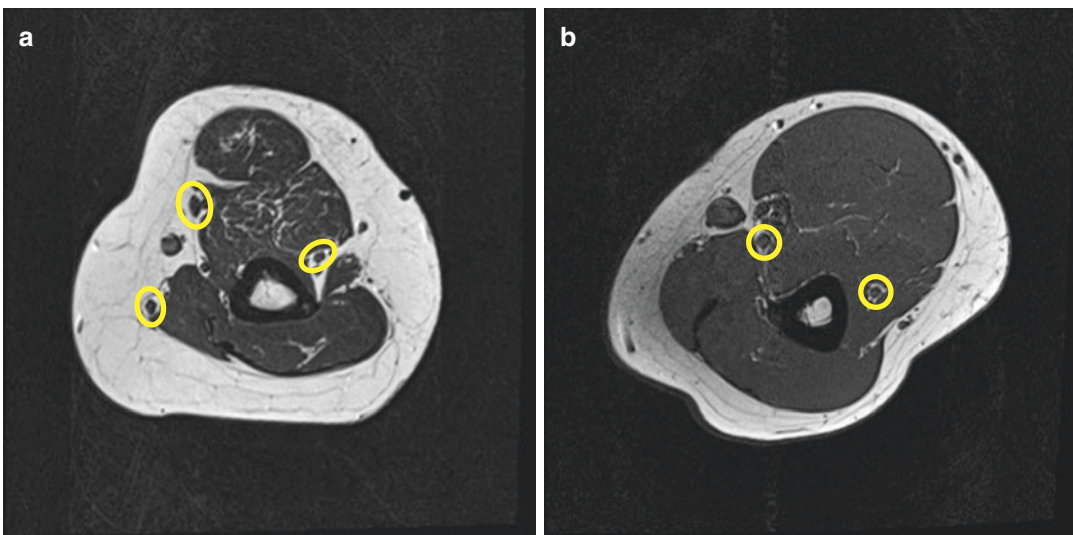
Fig. 9.20 Axial MRI T1 images of the elbow at different levels (**a**, **b**) showing the median, ulnar and radial nerves within the round/oval markers

At 2 cm proximal to the joint space, the radial nerve median dimension is 2.0 × 4.0 mm, while following bifurcation the diameters are smaller with median measurements of 1.1 × 1.7 mm for the superficial radial nerve and 1.0 × 2.0 mm for posterior interosseous nerve, respectively. In patients with posterior interosseous nerve syndrome, the swollen nerve has a mean diameter of 4.2 mm.

The median dimensions of the ulnar nerve decrease from 2.7 × 4.7 mm, 2 cm above the elbow joint space to 2.0 × 3.4 mm below the joint.

The diameter of the median nerve shows little variation with median dimensions of 3.0 × 5.0 mm at 2 cm above the joint space and 2.3 × 5.0 mm at 2 cm distal to it.

There are gender considerations with diameter measurements of the ulnar and median nerves in men being larger particularly proximal to the joint compared with women, but no difference found regarding the radial nerve.

References

Acton JD, McNally MA (2001) Baumann's confusing legacy. Injury 32:41–43

Arnold J, Nasca RJ (1977) Nelson Cl. Supracondylar fractures of the humerus: the role of dynamic factors in prevention of deformity. J Bone Joint Surg Am 59:589–595

Baumann E (1929) Beitrage zur kenntnis dur frackturen am ellbogengelenk. Bruns Beitr Klin Chir 146:1–50

Bayrak AO, Bayrak IK, Turker H, Elmali M, Nural MS (2010) Ultrasonography in patients with ulnar neuropathy at the elbow: comparison of cross-sectional area and swelling ratio with electrophysiological severity. Muscle Nerve 41:661–666

Beals RK (1976) The normal carrying angle of the elbow. A radiographic study of 422 patients. Clin Orthop Relat Res 119:194–196

Beaty JH, Kasser JR (eds) (2009) Rockwood and Wilkins fractures in children, 7th edn. Lippincott Williams & Wilkins, Philadelphia, PA

Biyani AMS, Gupta SPM, Sharma JCMS (1993) Determination of medial epicondylar epiphyseal angle for supracondylar humeral fractures in children. J Pediatr Orthop 13:94–97

Bodner G, Harpf C, Meirer R, Gardetto A, Kovacs P, Gruber H (2002) Ultrasonographic appearance of supinator syndrome. J Ultrasound Med 21:1289–1293

Camp J, Ishizue K, Gomez M, Gelberman R, Akeson W (1993) Alteration of Baumann's angle by humeral position: implications for treatment of supracondylar fractures. J Pediatr Orthop 13:521–525

Chang CW, Wang YC, Chu CH (2008) Increased carrying angle is a risk factor for nontraumatic ulnar neuropathy at the elbow. Clin Orthop Relat Res 466:2190–2195

Chapleau J, Canet F, Petit Y, Laflamme GY, Rouleau DM (2011) Validity of goniometric elbow measurements: comparative study with a radiographic method. Clin Orthop Relat Res 469:3134–3140

Chiou HJ, Chou YH, Cheng SP (1998) Cubital tunnel syndrome: diagnosis by high resolution ultrasonography. J Ultrasound Med 17:643–648

Cotton A, Jacobson J, Brossman J (1997) Collateral ligaments of the elbow: conventional MR imaging and MR arthrography with coronal oblique plane and elbow flexion. Radiology 204:806–812

De Maeseneer M, Jacobson JA, Jaovisidha S, Lenchik L, Ryu KN, Trudell DR, Resnick D (1998) Elbow effusions: distribution of fluid with flexion and extension and imaging implications. Invest Radiol 33:117–125

Gondim Teixera PA, Omoumi P, Trudell DJ, Ward SR, Lecocq S, Blum A, Resnick D (2011) Ultrasound assessment of the lateral collateral ligamentous complex of the elbow : imaging aspects in cadavers and normal volunteers. Eur Radiol 21:1492–1498

Goodfellow JW, Bullough PG (1967) The pattern of ageing of the articular cartilage of the elbow joint. J Bone Joint Surg Br 49:175–181

Greenspan H (2000) Radiologia en Ortopedia. Traumatismos, Codo, Marban, Madrid, p 106–133

Herman MJ, Boardman MJ, Hoover JR, Chafetz RS (2009) Relationship of the anterior humeral line to the capitellar ossific nucleus: variability with age. J Bone Joint Surg Am 91:2188–2193

Husarik DB, Saupe N, Pfirrmann CW, Jost B, Hodler J, Zanetti M (2009) Elbow nerves: MR findings in 60 asymptomatic subjects—normal anatomy, variants and pitfalls. Radiology 252:148–156

Husarik DB, Saupe N, Pfirrmann CW, Jost B, Hodler J, Zanetti M (2010) Ligaments and plicae of the elbow: normal MR imaging variability in 60 asymptomatic patients. Radiology 257:185–194

Ippolito E, Moneta MR, D'Arrigo C (1990) Post-traumatic cubitus varus. Long- term follow up of corrective supracondylar humeral osteotomy in children. J Bone Joint Surgery Am 72:757–765

Jacob D, Creteur V, Courthaliac C (2004) Sonoanatomy of the ulnar nerve in the cubital tunnel: a multicentre trial by the GEL. Eur Radiol 14:1770–1773

Jean IH, Sanchez-Sotelo J, An KN, Morrey BM (2012) The contribution of the coronoid and radial head to the stability of the elbow. J Bone Joint Surg Br 94-B:86–92

Jeffery CC (1950) Fractures of the head of the radius in children. J Bone Joint Surg Br 32:314–324

John SD, Wherry K, Swischuk LE, Phillips WA (1996) Improving detection of pediatric elbow factures by understanding their mechanics. Radiographics 16:1443–1460

King JW, Brelsford HJ, Tullos HS (1969) Analysis of the pitching arm of the professional baseball pitcher. Clin Orthop 67:116–123

Konin GP (2013) US of the elbow: indications, technique, normal anatomy and pathologic conditions. Radiographics 33:E125–E147

Koski JM (1990) Ultrasonography of the elbow joint. Rheumatol Int 10:91–94

Krengel WF III, Wiater BP, Pace JL, Jinguji TM, Bompadre V, Stults JK (2012) Does using the medial or lateral humeral line improve reliability of Baumann angle measurement on plain x-ray? The effect of humeral length visualised on the x-ray. J Pediatr Orthop 32:373–377

Lee GA, Katz SD, Lazarus MD (1998) Elbow valgus stress radiography in an uninjured population. Am J Sports Med 26:425–427

Mohammad OA, Abdelmonem AMH (2010) Radiographic evaluation of the normal elbow carrying angle in adults. J Med Sci 10:40–44

Mohammad S, Rymaszewski LA, Runciman J (1999) The Baumann angle in supracondylar fractures of the distal humerus in children. J Pediatr Orthop 19:65–69

Morrey BF (2004) Traumatologia del codo. Estudio de imagen del codo pediátrico. Chapter 13. Mayo Medical School, Mayo Clinic, Marban, p 157

Morrey BF, Chao EY (1976) Passive motion of the elbow joint. J Bone Joint Surg 58A:501–508

Oppenheim WL, Clader TJ, Smith C, Bayer M (1984) Supracondylar humeral osteotomy for traumatic childhood cubitus varus deformity. Clin Orthop Relat Res 188:34–39

Puchwein P, Schildhauer TA, Schoffman S, Heidari N, Windisch G, Pichler W (2012) Three dimensional morphometry of the proximal ulna: a comparison to currently used anatomically preshaped ulna plates. J Shoulder Elbow Surg 21:1018–1023

Rafehi S, Lalone E, Johnson M, King GJW, Athwal GS (2012) An anatomic study of coronoid cartilage thickness with special reference to fractures. J Shoulder Elbow Surg 21:961–968

Rijke AM, Goitz HT, McCue FC, Andrews JR, Berr SS (1994) Stress radiography of the medial elbow ligaments. Radiology 191:213–216

Rowland AS, Athwal GS, MacDermid JC, King GJW (2007) Lateral ulnohumeral joint space widening is not diagnostic of radial head arthroplasty overstuffing. J Hand Surg 32:637–641

Ruotolo CJ, Healy WA III (1999) Supracondylar and lateral condyle fractures of the humerus. MedGenMed. 1(3):1–10

Schub DL, Frisch NC, Bachmann KR, Winalski C, Saluan PM (2013) Mapping of cartilage depth in the knee and elbow for use in osteochondral autograft procedures. Am J Sports Med 41:903–907

Silberstein MJ, Brodeur AE, Graviss ER (1982) Some vagaries of the radial head and neck. J Bone Joint Surg Am 64:1153–1157

Silva M, Pandarinath R, Farng E, Park S, Caneda C, Fong YJ, Penman A (2010) Inter- and intra-observer reliability of the Baumann angle of the humerus in children with supracondylar fractures. Int Orthop 34:553–557

Simanovsky N, Lamdan R, Mosheiff R, Simanovsky N (2007) Under-reduced supracondylar fracture of the humerus in children:clinical significance at skeletal maturity. J Pediatr Orthop 27:733–738

Simanovsky N, Lamdan R, Hiller N, Simanovsky N (2008) The measurement and standardisation of humerocondylar angle in children. J Pediatr Orth 28:463–465

Skaggs DL, Cluck MW et al (2004) Lateral—entry pin fixation in the management of supracondylar fracture in children. J Bone Joint Surg 86-A:702–707

Skibo L, Reed MH (1994) A criterion for a true lateral radiograph of the elbow in children. Can Assoc Radiol J 45:287–291

Springer V, Graichen H, Stammberger T, Englmeier KH, Reiser M, Eckstein F (1998) Noninvasive analysis of cartilage volume and cartilage thickness in the human elbow joint using MRI. Ann Anat 180:331–338

Stewart B, Harisch S, Oomen G, Wainman B, Popowich T, Moro JK (2009) Sonography of the lateral ulnar collateral ligament of the elbow: study of cadavers and healthy volunteers. Am J Roentgenol 193:1615–1619

Terada N, Yamada H, Toyama Y (2004) The appearance of the lateral ulnar collateral ligament on magnetic resonance imaging. J Shoulder Elbow Surg 13:214–216

Van Roy P, Baeyens D, Fauvart R, Lanssiers R, Clarijs JP (2005) Arthro-kinematics of the elbow: study of the carrying angle. Ergonomics 48:1645–1656

Webb AJ, Sherman FC (1989) Supracondylar fractures of the humerus in children. J Pediatr Orthop 9:315–325

Williamson DM, Coates CJ, Miller RK, Cole WG (1992) Normal characteristics of the Baumann (humerocapitellar) angle: an aid in assessment of supracondylar fractures. J Pediatr Orthop 12:636–639

Yochum TR, Rowe LJ (1996) Essentials of skeletal radiology, 2nd edn. Williams and Wilkins, Baltimore, MD, p 186

Zampagni ML, Casino D, Martelli A, Visani A, Marcacci M (2008) A protocol for clinical evaluation of the carrying angle of the elbow by anatomical landmarks. J Should Elbow Surg 17:106–112

Wrist/Hand

10

Jean-Luc Drapé and Nicolas Theumann

Contents

J.-L. Drapé (✉)
Sorbonne Paris Centre, Radiologie B, Hospital
Cochin, University Paris Descartes,
27 rue du Fg Saint Jacques, Paris, France
e-mail: jean-luc.drape@aphp.fr

N. Theumann (✉)
Department of Radiology, Clinique Bois-Cerf,
1006 Lausanne, Switzerland
e-mail: Nicolas.Theumann@chuv.ch

10.1 Anatomical and Imaging Considerations

The wrist and hand attracted radiological attention ever since the discovery of X-rays. Radiographic measurements have evolved in the assessment of chronic systemic diseases such as rheumatoid arthritis, metabolic bone disease as well as congenital and developmental disorders. Imaging also plays a very important role in traumatic and post-traumatic assessment and this in part relies on measurement assessment Goldfarb et al. (2001). Carpal instability from ligament insufficiency is complex and can arise from traumatic and non-traumatic causes such as rheumatoid disease. To a large extent radiographs are still the most common imaging modality from which measurements are made. They are reliable and with care easily reproduced, minimising the risk of measurement errors on follow-up assessment. The adoption of standard radiographic methods however is crucial as shown by Schuind et al. (1992) and Larsen et al. (1991a, b), and this aspect will be expanded upon in detail in this introduction.

Dynamic radiography has a selected role in identifying instability from loss of osteoligamentous integrity by obtaining views in radial and ulnar deviation, with the clenched fist in the

frontal plane, and in flexion and extension in the lateral projection. Normally the intercarpal distances are unchanged in radial and ulnar deviation. The relationship of the lunate to the articular surfaces of the radius and ulna does however alter. In neutral or radial deviation AP and PA radiographs, the lunate lies 50:50 relative to the ulnar border of the distal radius, coming to lie completely in the lunate fossa of the radius in maximal ulnar deviation (Fig. 10.1). Abnormal lunate translation towards the ulna indicates ulnar translocation. When more than 50% of the lunate lies medial to the radius on the neutral PA view, ulnar translocation is usually the underlying carpal instability due to extrinsic ligament failure. This results in an increased radioscaphoid gap with the trapezium approximating the radial styloid. Simultaneously the centre of the head of the capitate which is regarded as the centre of rotation of the carpus, also moves towards the longitudinal axis of the ulna reducing the carpal–ulnar distance as described by McMurtry et al. (1978). Dividing this distance by the third metacarpal length normally produces a consistent ratio of **0.30 +/−0.03**, which is reduced in ulnar translocation. Lateral flexion and extension views are helpful in assessing carpal instability which aid in differentiating true instability from a normal variant. It is important to realise that comparison with the contralateral asymptomatic side also needs to be taken into consideration before a decision is made to treat a particular abnormality. Gilula and Weeks' "*ligamentous instability*" series compared both wrists by performing PA views in neutral and ulnar/radial deviation, AP view with the clenched fist, routine oblique, 30° off lateral

Fig. 10.1 Neutral PA view (**a**) showing the lunate lying 50:50 relative to the ulnar border of the distal radius. Neutral lateral view (**b**) showing the scaphopisocapitate (SPC) relationship criteria needed for a true lateral view
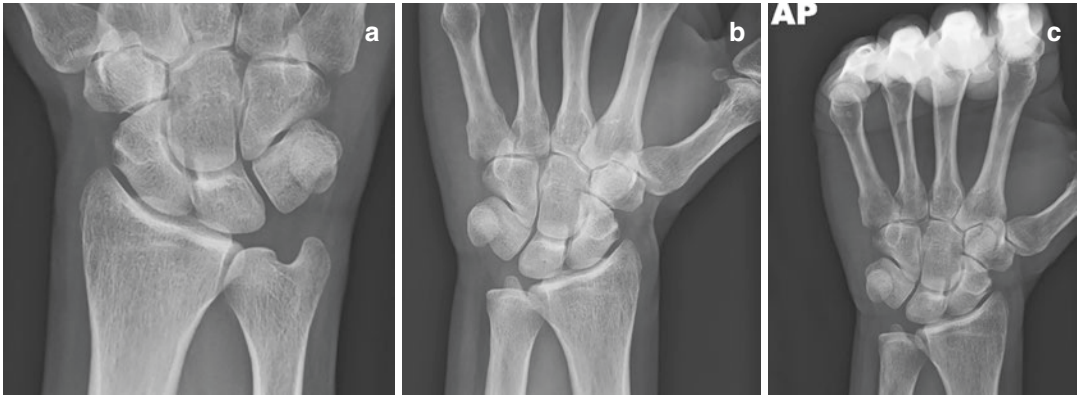
Fig. 10.2 PA view in pronation (**a**), in supination (**b**) and with the clenched fist (**c**). The ulna is shorter compared to the radius in supination and with the fist clenched

oblique, and laterals in neutral and flexion/extension positions.

When obtaining the standard radiographs care needs to be given to the positions of the wrist, arm and forearm as they affect the appearances and location of the osseous landmarks introducing measurement errors. This is well seen in the assessment of ulnar variance which can alter from negative to positive in the same asymptomatic wrist when a PA view is compared with either an AP view or one obtained with the fist clenched (Fig. 10.2). Epner et al. noted that ulnar variance is altered by three factors; forearm rotation, wrist deviation and the X-ray beam incidence angle. When the forearm is supinated the radius moves distally and negative ulnar variance increases as the ulna becomes relatively shorter with respect to the radius. Indeed it can change from positive to negative as the pronated forearm is supinated. With radial deviation of the supinated wrist there is an increased negative ulnar variance, while ulnar deviation decreases the ulnar variance. The X-ray beam needs to be perpendicular to the wrist to avoid further errors. When the X-ray beam is angled distally along the longitudinal axis, the radius appears longer relative to the ulna, thereby increasing the apparent negative ulnar variance.

Meticulous positioning for radiographic technique is therefore essential to provide optimal standard PA and lateral radiographs as a prerequisite to obtaining measurements. The PA view is obtained in a seated patient with the wrist and elbow held at shoulder height on the X-ray table so that they are in one plane, the shoulder abducted with 90° flexion at the elbow. The ulna is perpendicular to the humerus and the forearm is in pronation, the wrist in neutral and the hand palm down on the cassette Bateni et al. (2013). In a correctly positioned PA view the groove of the extensor carpi ulnaris (ECU) lies lateral to the midportion of the ulnar styloid, radial to the fovea and the ulnar styloid itself is seen to extend from the ulnar border of the ulna Jedlinski et al. (1995) (Fig. 10.3). The ulnar groove criterion is inconsistent as the groove may be hypoplastic and not discernible radiographically. The long axis of the third metacarpal and radius are collinear confirming there is no ulnar or radial deviation. In this position the radius and ulna are parallel to each other which is essential as it is the only position that depicts the true length of the radius. The position of the wrist is an important factor in determining ulnar variance as described above. If the PA view is obtained whereby the radius is allowed to cross over the ulna it invariably shortens introducing an error in the ulnar variance assessment. This means that when the forearm is pronated maximally there is an increase in positive ulnar variance while
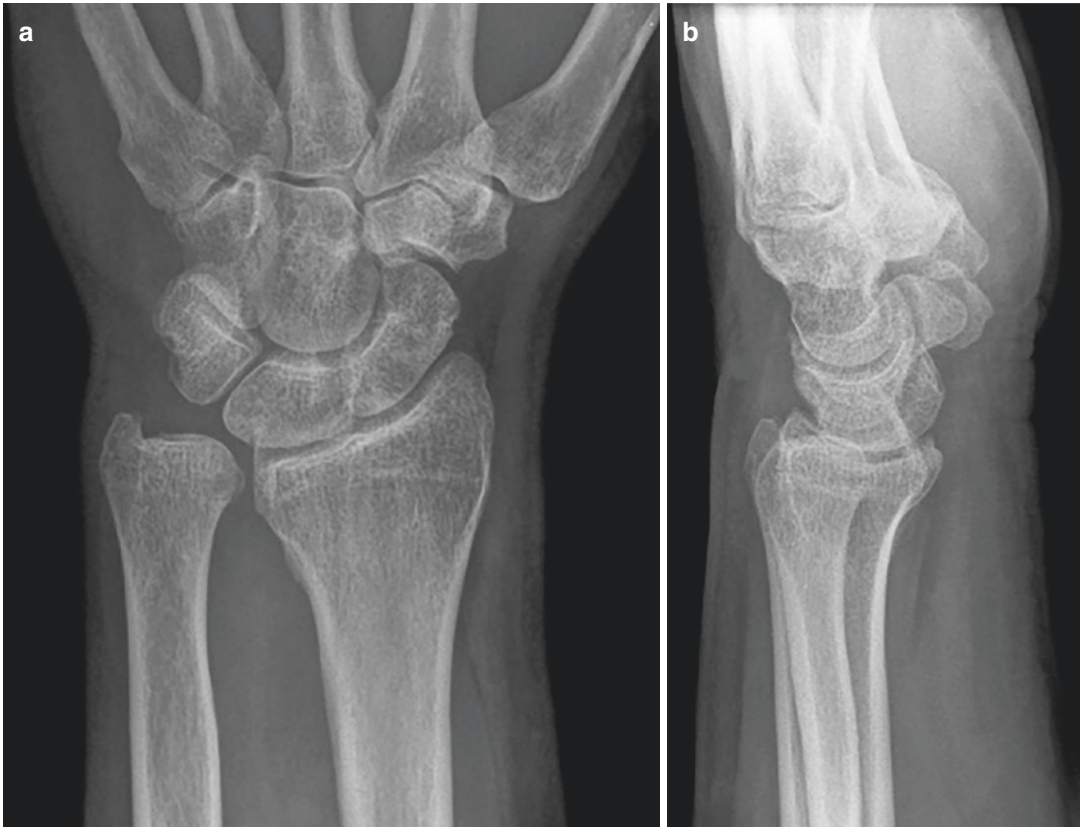
Fig. 10.3 Neutral PA view (**a**) showing the ulnar groove of the ECU lies lateral to the ulnar styloid. The ulnar styloid extends from the medial border of the ulna. The lateral projection (**b**) shows the volar cortex of the pisiform lying anterior to the cortex of the scaphoid which is suboptimal for measurement purposes

maximal forearm supination promotes a decrease in ulnar variance. Essentially the ulnar variance measurements should only be done when the ulnar styloid extends from the ulnar border of the ulna on the neutral PA view. Incidentally it is important to stress that ulnar variance refers to the relative lengths of the radius and ulna on the *wrist radiographs,* and ulnar variance status is likely to be erroneous if attempted from CT and MRI images. The specific position of the wrist required to reliably determine ulnar variance cannot be replicated in MR and CT. In addition the clenched fist can also increase significantly the ulnar variance which returns to normal when the fist is released. In combination, a firm grip with the forearm pronated can cause significant positive ulnar variance not appreciated on a neutral PA view. A negative ulnar variance may be associated with Kienböck's disease and scapholunate dissociation, while a positive ulnar variance is associated with ulnar impaction syndrome and degenerative TFCC tears Cerezal et al. (2002). Preoperatively ulnar variance needs to be measured twice on a pronated forearm with and without a firm grip respectively when surgery is being planned for such causes of ulnar wrist pain.

A reliable and consistent radiographic technique for obtaining optimal lateral projections is also crucial if they are to form the basis of measurements that evaluate carpal congruency, malalignment and instability. Larsen et al.

(1991a, b) recommended a stabilising device to control wrist movements in all directions with the wrist held in zero position. Attention to ensure that there is no ulnar/radial deviation, nor flexion/extension of the wrist (zero position) is essential, as these positions normally and physiologically alter the alignment of the carpal bones (Figs. 10.1 and 10.3). The scaphoid normally foreshortens in volar flexion or radial deviation, and elongates in ulnar deviation or wrist extension. For the lateral view the arm is adducted by the side in a seated patient so that the shoulder, the 90° flexed elbow, the forearm in neutral rotation and wrist are in the same plane. This ensures that this view is truly perpendicular to the PA view. A correctly positioned lateral view shows overlap of the ulna and radius, the ulnar styloid is exactly in the centre of the ulnar head and it should clearly outline the volar edges of the trapezium, scaphoid, pisiform and capitate. However this criterion is not valuable in the presence of dorsal subluxation of the ulnar head. The pisiform should be projected over the distal scaphoid pole. The scaphopisocapitate (SPC) relationship is a reliable criterion of a true lateral (Yang et al. 1997). The volar cortex of the pisiform should lie in the middle third of the interval between the volar aspects of the scaphoid and capitate respectively providing a clear "line of sight" (Fig. 10.4). It is often stated that a true lateral view should show that the radiographic long axes of the third metacarpal, capitate, lunate and radius are coaxial forming a straight line. Sarrafian et al. (1977) however found that this ideal of a common longitudinal axis running through the axes of the third metacarpal, capitate, lunate and radius is observed in only 11% of normal individuals, but the axes are normally usually <10° to this line.

Biomechanically the proximal carpal row is designated as an "intercalated segment", indicating that its position is determined by forces acting on its proximal and distal articulations as no tendons are attached to it. The scaphoid and triquetrum have opposing natural tendencies for volar flexion and dorsiflexion respectively. Therefore in the presence of a scapholunate liga-

Fig. 10.4 Lateral view of the wrist showing acceptable SPC criteria for measurements from a true lateral projection, with the pisiform's volar cortex lying in the middle third of the interval between the volar aspects of the scaphoid and capitate

ment dissociation, the scaphoid volar flexes and the attached triquetrum acts unopposed and pulls the lunate into dorsiflexion producing a DISI (Dorsal Intercalated Segmental Instability). A lunotriquetral tear produces the opposite instability pattern VISI (Volar Intercalated Segmental Instability) as the intact scapholunate ligament pulls the lunate into volar flexion as the scaphoid acts unopposed. Care needs to be exercised in

distinguishing a true DISI from a normal positional dorsal tilt of the lunate which as indicated previously arises when the wrist is normally ulnar deviated or when it is hyperextended. Adaptive DISI is also associated with architectural alteration of the surrounding structures, such as instances of excessive callus from the distal radius.

On the PA view the intercarpal joints should clearly show the subchondral outlines of the respective carpal bones appearing parallel and symmetrical. Three carpal arcs can be defined on the PA view: the first is along the proximal outlines of the scaphoid, lunate and triquetrum; the second along the distal outlines of the same bones; and the third along the proximal capitate and hamate outlines. Normally these arcs are smooth and curvilinearly parallel. The articulation between the capitate and lunate is the baseline joint width all others are compared with. The joint spaces are normally in the order of **2 mm** or <, but the scapholunate and radiocarpal joints are usually wider. The width of the carpometacarpal joints is normally narrower than the midcarpal articulation. The scapholunate space harbours the important scapholunate interosseous ligament. This complex ligament is horseshoe-shaped in the sagittal plane with three distinct anatomical zones that have different histological and biomechanical characteristics; dorsal, proximal (intermediate) and volar components, connecting the respective surfaces of the two bones (Fig. 10.5). Anatomical studies have shown it to be 18 mm long and 1–6 mm thick. The dorsal component is 3 mm thick while the volar component is only 1 mm thick (Berger 1996). The proximal (intermediate) component is mainly fibrocartilage and

shaped like a meniscus appearing triangular on coronal MRI images. On routine MRI it is not possible to consistently visualise all three parts of it but this is improved with MR arthrography and dedicated coils at 3 T producing high resolution images. The average length of the ligament in the dorsopalmar direction seen on MRI is 12.8 +/− 0.3 mm and 13.6 +/− 0.4 mm at MR arthrography Scheck et al. (1997).

There has been considerable controversy focused on the optimal method to measure the radiographic scapholunate distance and the critical cut-off point from normal to abnormal. A widened scapholunate distance is more noticeable in the AP than the PA view Mann et al. (1992a). Cautilli and Wehbe (1991) measured the distance on neutral PA views from the proximal corners of the scaphoid and lunate in 100 normal wrists providing a range of 2.5–5 mm (mean 3.7 mm, SD 0.6 mm). Variation arises using this method because it is difficult to define the corners (especially on the scaphoid aspect) to measure from in a reliable manner (Fig. 10.6). Gilula and Weeks (1978) used the midpoint of the articulation and reported a normal distance up to 2 mm, an abnormal value when >4 mm, and deemed a value between 2 and 4 mm as of uncertain significance. There is now general agreement that the scapholunate interval should be measured at the midpoint of the joint on a PA view following the studies by Kindynis et al. (1990) and Schimmerl-Metz et al. (1999) (Fig. 10.6). It is vital that the wrist is in a truly neutral position because flexion and extension profile the palmar and dorsal portions of the articulation respectively, both of which are wider than the true interface of car-

Fig. 10.5 Diagram of the scapholunate ligament on the axial view (**a**) and sagittal view (**b**). *D* dorsal segment, *V* ventral segment, *P* proximal segment
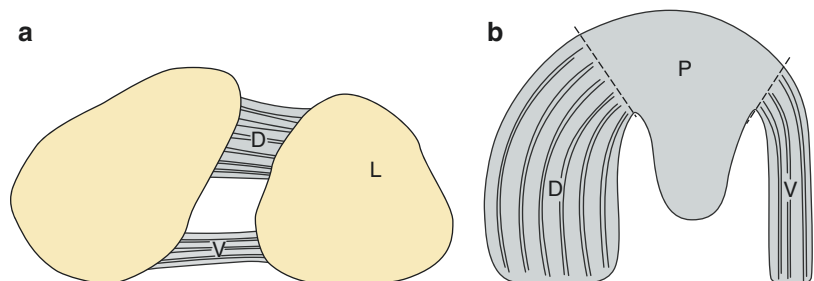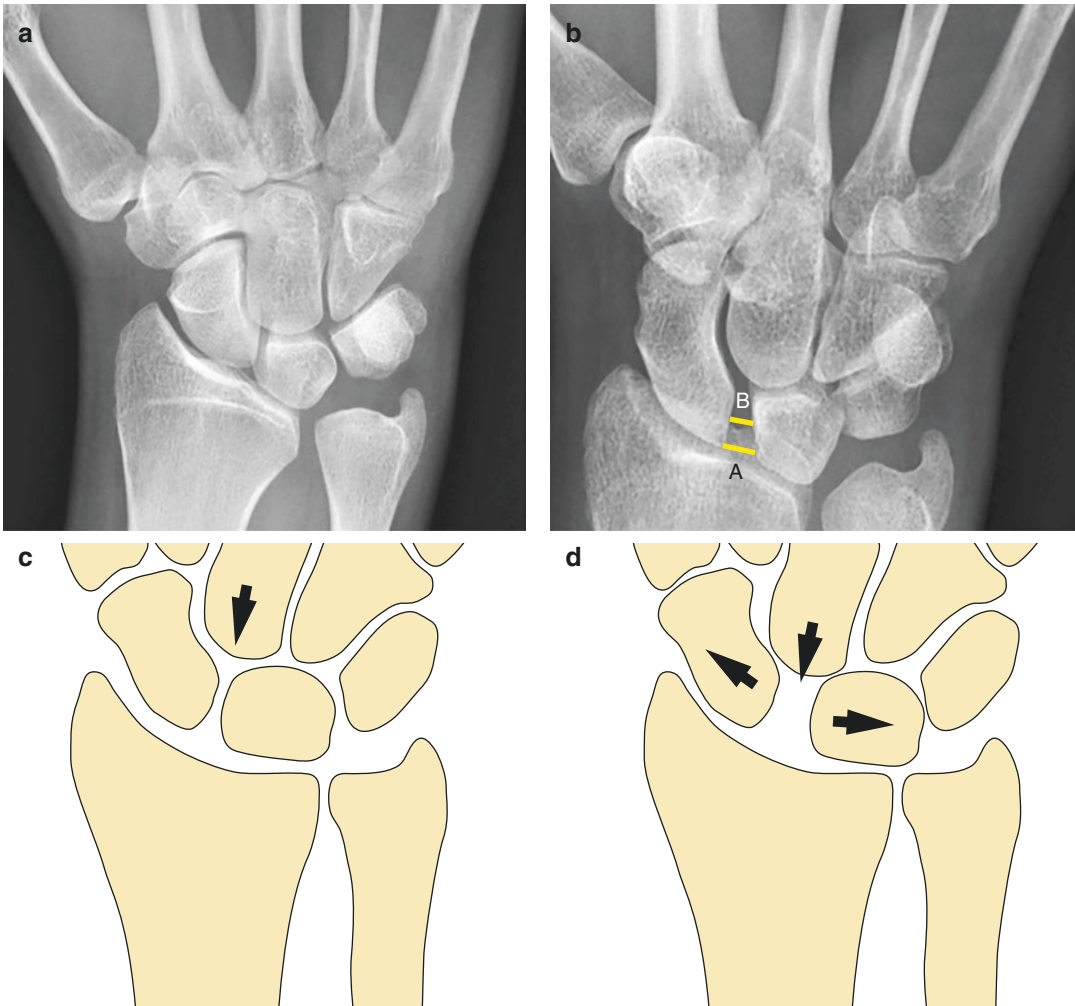
Fig. 10.6 Scapholunate distance variation seen on (**a**) neutral and (**b**) clenched fist PA views, measured using the Cautilli and Wehbe method (A) and at the midpoint of the scapholunate joint (B). Diagrammatic representation of the dynamics involved in altering the scapholunate distance (**c**, **d**) due to the stress manoeuvre with the clenched fist

tilage surfaces of the joint resulting in a falsely wider measurement in the abnormal range. This neutral PA view position is confirmed when (a) the third carpometacarpal joint is seen in clear profile, (b) the third metacarpal and radius are coaxially aligned, and (c) in the absence of ulnar or radial deviation. For accurate measurement the midportion of the flat medial facet of the scaphoid is the commencement point. Kindynis et al. (1990) also suggested optimisation of scapholunate interval visualisation by obtaining a PA position with a 10° tube tilt

from the ulna towards the radius (Fig. 10.7), with the central ray directed in the middle of a line joining the extremity of the radial and ulnar styloid processes, centred on the carpus. Using this method of measurement Pliefke et al. (2008) found a mean scapholunate distance in patients with scapholunate dissociation of 2.9 +/− 0.9 mm compared with 2.2 +/− 0.4 mm in patients with normal arthroscopy. According to their study scapholunate diastasis of **3.5 mm** between the middle of the medial facet of the scaphoid and lunate proves the presence of
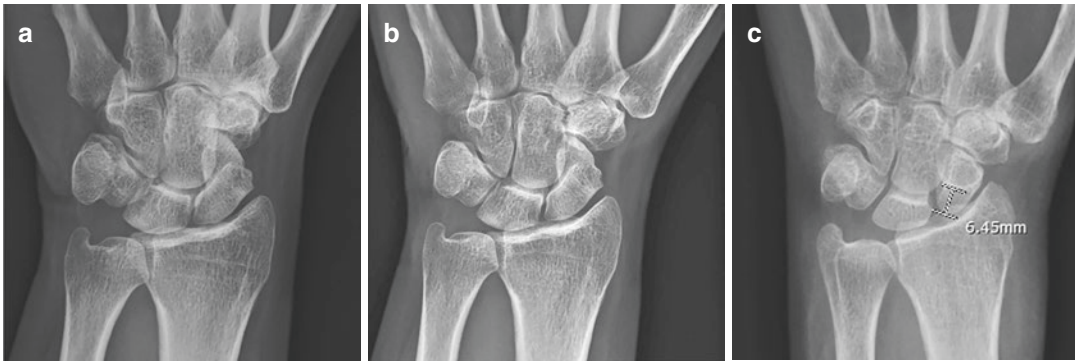
Fig. 10.7 Scapholunate distance seen on a neutral PA view (**a**) and on a 10° tube tilt from the ulna (**b**) towards the radius. Positive scaphoid "cortical ring sign" on neu- tral PA view (**c**) where the distance between the ring out- line and the proximal pole of the scaphoid is <7 mm

dissociation, and measuring the scapholunate angle further increases the diagnostic accu- racy. However in 14 of 36 ligament ruptures in Pliefke et al.'s study, the abnormal diastasis was only appreciated on cineradiography and not on the plain radiographs. This resulted in plain radiographs producing a 57.1% sensitivity and 98.3% specificity, while cineradiography enjoyed 85.7% sensitivity and 95.0% specific- ity. Gilula and Weeks (1978) have also shown that an interval **> 4 mm** is abnormal indicat- ing scapholunate dissociation (rotatory scaph- oid subluxation). Diastasis is increased with the clenched fist position (Fig. 10.6), but this is often limited in its use due to pain. Moneim (1981) showed that a tangential PA view of the wrist produced by elevating the ulnar border of the hand 20° off the table (by flexing the fourth and fifth fingers) also reveals dissociations not seen on the routine views. This is particularly useful when the ancillary AP and clenched fist views cannot be done due to pain. Moneim showed that the tangential view eliminated the bone overlap that is invariably present on the routine PA view. Obermann (1991) optimised obtaining the PA and lateral radiographs using fluoroscopy and found that the standard radio- graphs had a 25% false negative and a 6.5% false positive rate in the diagnosis of carpal instability. A positive scaphoid cortical "ring

sign" is also regarded as pathognomonic of SL dissociation. The distal pole of the scaphoid is projected over the midbody of the flexed scaph- oid which is rendered foreshortened. For a posi- tive sign the distance between the ring outline and the proximal pole of the scaphoid on neu- tral radiographs should be **<7 mm** (Fig. 10.7). A positive ring sign can be observed however on radiographs taken in full radial deviation, and up to 25% of normal radiographs. Needless to say the assessment described above does not apply to the paediatric wrist as due to differ- ential delay in ossification the normal scaph- olunate anatomy seen radiographically appears spuriously widened (Fig. 10.8).

Although the stability of the scapholunate joint is primarily dependent on the scapholunate liga- ment (Fig. 10.9), the extrinsic stabilisers which include the volar carpal ligaments and the dorsal capsular ligaments play an important role Boabighi et al. (1993). Studies have revealed that *static instability* producing radiographic scaphol- unate diastasis requires combined extrinsic liga- ment injury besides a complete tear of the scapholunate ligament. Experimental studies car- ried out by Meade et al. (1990) on serial radio- graphic changes in scapholunate kinematics following sequential sectioning of the portions of the intrinsic and extrinsic ligaments, have shown that significant tears of the scapholunate ligament

Fig. 10.8 PA view in a child showing the normal "widened" appearance of the scapholunate distance

Fig. 10.9 MR arthrography with contrast medium in both the midcarpal and radiocarpal joints depicting intact scapholunate ligament status on a T1 Fatsat coronal sequence

can be present despite normal radiographs, and scapholunate diastasis implies injury not just to the interosseous ligament but also to the dorsal or volar extrinsic ligaments. Interestingly Meade et al. observed an increase in the radioscaphoid interval between maximal radial and ulnar deviation following sectioning of the volar extrinsic ligaments. In the predissection radiographs the difference in radioscaphoid interval measurements between radial and ulnar deviation was normally <0.4 mm. However the radioscaphoid difference increased to 1.60 mm, 1.61 mm, 1.90 mm and 3.12 mm with sequential sectioning of the radioscaphoid ligament, volar portion of the

scapholunate ligament, complete scapholunate ligament and radioscaphocapitate ligament. This also means that if only the interosseous scapholunate ligament is torn there may not be any radiographic diastasis if the extrinsic ligaments are intact. Thus *dynamic instability* can only be demonstrated on stress radiographs or fluoroscopic studies. When the scapholunate ligament fails the triquetrum and lunate dorsiflex (DISI) and the scaphoid flexes (Fig. 10.10). The dorsal tilt of the lunate leads to a scapholunate angle on the lateral radiographs **>60**°. When the lunotriquetral ligament fails the triquetrum dorsiflexes and both the lunate and scaphoid flex (VISI). The scapholunate angle on the lateral radiographs is **<30**°**.**

On the lateral view the longitudinal axis of the main carpal bones (scaphoid, lunate and capitate) can be defined, and intercarpal angles measured to provide an assessment of the spatial relationship of the carpus. The *midscaphoid axis* is not easily determined as the proximal pole is not always well seen. A tangential line drawn volarly joining the most volar edges of the proximal and distal scaphoid poles is almost parallel to the mid-axis and reliable (Fig. 10.11).

Fig. 10.10 Diagram of the middle column of the wrist in the lateral projection in (**a**) DISI and (**b**) VISI. In both instances there is a shift between the long axis of the radius/ulna and the long axis of the capitate/metacarpals. *D* dorsal, *V* ventral aspects
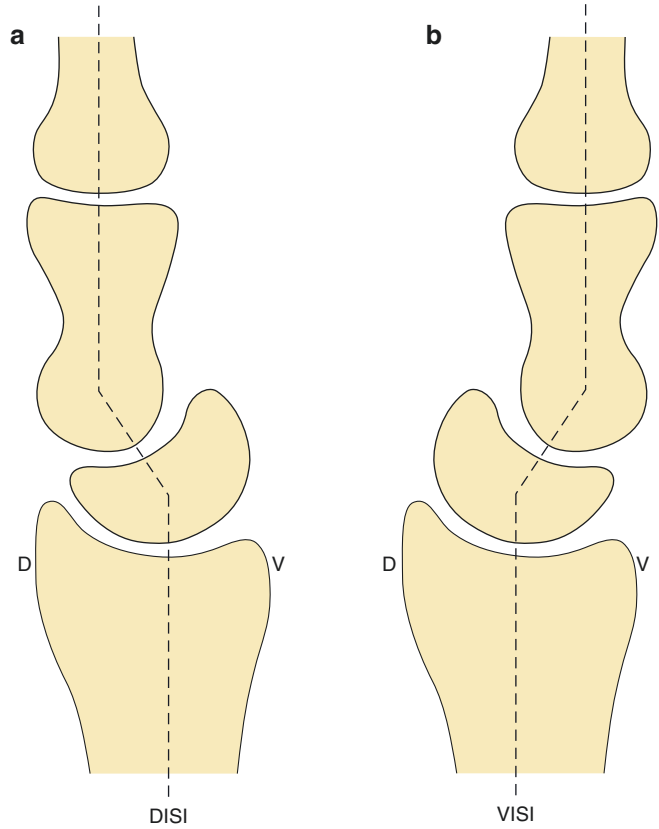
Fig. 10.11 Scaphoid axis. The volar tangential line (ST) is parallel to the scaphoid axis (SA)
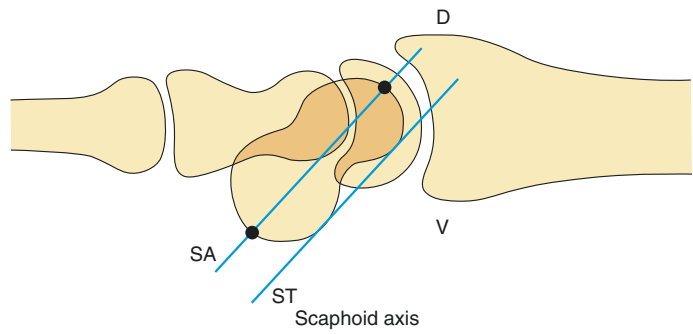
It was shown by Crittenden et al. (1970) that the normal angle subtended between the axes of the scaphoid and radius (radioscaphoid) with the hand held in neutral lateral position is 136° (range 121–153°), while Hudson et al. (1976) recorded a higher normal angle of 150° (Fig. 10.12). Alternately the adjacent angle is regarded as the radioscaphoid angle with a normal value of 44° and a range 27°–59° indicating any measurement >60° as abnormal. The *midlunate axis* is the perpendicular line drawn to the line that joins the distal dorsal and distal volar corners of the lunate dividing the proximal and distal articular surfaces (Fig. 10.13). The radiolunate angle is normally expected to be 0° as the wrist should be coaxial with the axis of the radius (determined by plotting a line through two points through the centre of the distal radius at 2 and 5 cm proximal to the articular surface) passing through the lunate axis, but a normal range exists of −15–+15° (Fig. 10.14). Similarly

the capitolunate angle should normally be 0° with a range of −15–+15° (Fig. 10.15). The subtended scapholunate angle is normally **30–60°** and instability is inferred if it is >60° (Fig. 10.16). As a guide VISI (volar intercalated segmental instability) is denoted by an angle **<30°** where the lunate is tilted volarly due to a lunotriquetral ligament tear, and DISI (dorsal intercalated segmental instability) by an angle **>60°** where the lunate is angulated dorsally due to a complete scapholunate ligament tear. As indicated earlier in scapholunate dissociation the scaphoid is abnormally flexed and the lunate abnormally extended, which results in an increase in the radiolunate angle **>15**. However a DISI pattern can also be seen when the scapholunate ligament is intact in the presence of an unstable scaphoid waist fracture, as the proximal scaphoid pole moves dorsally with the lunate due to the intact ligament as the separated distal pole volar flexes. The *capitate axis* passes

Radioscaphoid angle

Fig. 10.12 Radioscaphoid angle
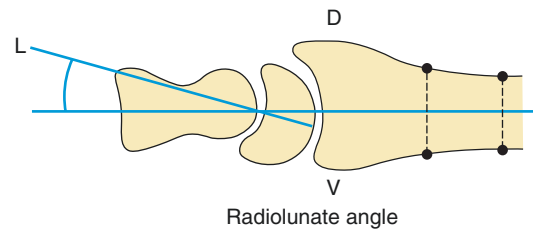
Radiolunate angle

Fig. 10.14 Radiolunate angle. Normal range −15–+15°

Lunate axis

Fig. 10.13 Lunate axis (L)

Capitolunate angle
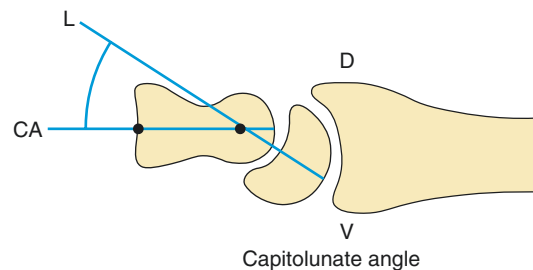
Fig. 10.15 Capitolunate angle. Normal range −15–+15°. Line through the midpoints of the proximal and distal poles of the capitate (CA) intersects with the lunate axis line (L)
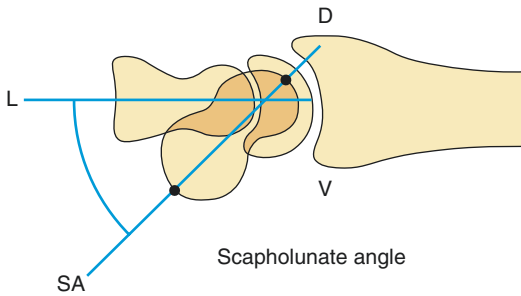
Fig. 10.16 Scapholunate angle. Normal range 30°–60°. Defined by intersection of scaphoid axis (SA) and lunate axis (L) lines
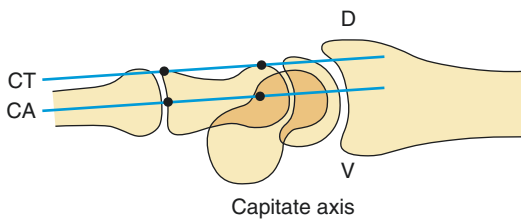
Fig. 10.17 Capitate tangent (CT) line to the dorsal outlines of the capitate is parallel to the capitate axis (CA)

through the midpoint of the convex articular outline of the third metacarpal and the proximal convex outline of the capitate. Alternatively, a tangent to the dorsal contour of the capitate can be used as the axis (Fig. 10.17). The subtended angle with the lunate creates a *capitolunate angle* which normally is **−10°** with a normal range of −15°– +15° (Fig. 10.15). Dorsiflexion of the lunate with a capitolunate angle >15° is suggestive of DISI, and volar flexion of the lunate with a capitolunate angle >15° is suggestive of VISI. Care is needed to minimise errors of measurements done on lateral radiographs as there can be significant observer variability. Larsen et al. (1991a, b) reported a standard deviation of the inter-observer variation which ranged from 2.60° to 18.15°, and an intra-observer variation from 1.89° to 4.66° depending on the angles measured. Nevertheless Larsen et al. also showed that as long as standardised radiography is employed, a difference of **>5°**

between the carpal angles in the same individual between the symptomatic and the asymptomatic wrist is regarded as significant.

The distal radius exhibits three concave surfaces. The scaphoid and lunate fossae articulate with the respective carpal bones with at least half of the lunate surface covered by the radius in the neutral PA projection. This alters in radial and ulnar deviation (Fig. 10.18). The sigmoid notch articulates with the head of the ulna at the distal radioulnar joint (DRUJ). The triangular fibrocartilage (TFC) is attached from the sigmoid notch to the ulnar styloid and this is supported by capsuloligamentous structures forming a triangular complex (TFCC) that also supports the articulation with the lunate and triquetrum (Fig. 10.19). As a result the DRUJ is L-shaped and separate from the radiocarpal joint. The thickness of the TFC is variable 1–5 mm which depends on the station of ulnar variance. Radiographic parameters to assess the distal radial anatomy are used to guide therapeutic planning and postsurgical outcomes usually related to fracture management. These include *radial length, radial inclination, palmar tilt* and articular congruency. Adverse clinical outcomes are associated with altered loading patterns and premature osteoarthritis due to extra-articular malunion parameters. A dorsal tilt >10° (equates to 20° from normal), radial inclination <10° and radial shortening of 6 mm are associated with poor outcomes Mann et al. (1992b); Mann et al. (1992c). The radial assessment can be enhanced if the PA view is done with the central beam directed by 10° proximally for the PA view, and 15° proximally for the lateral view. No difference in measurements are found when comparing this PA view with the standard PA view, but on this modified lateral view the points of measurement are better defined increasing measurement accuracy compared with the conventional lateral view. The main consideration of the articular surface of the ulna concerns the ulnar variance status and the clinical syndromes associated with either a positive or negative ulnar variance (Fig. 10.20). There is also an
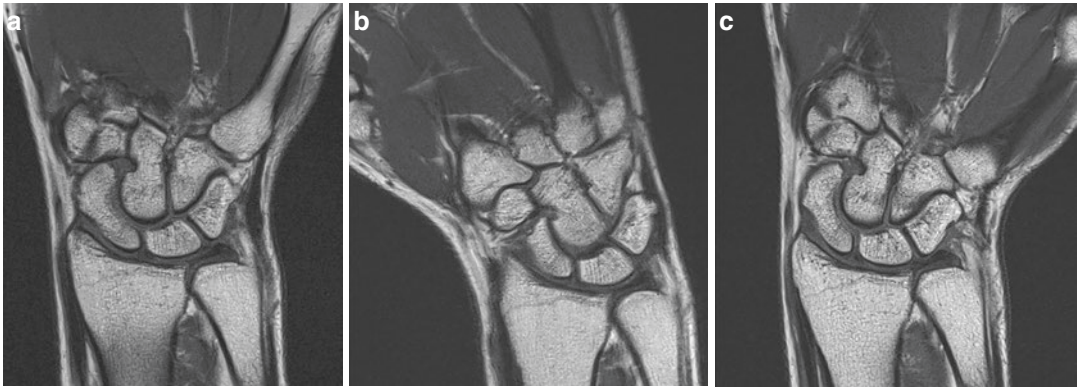
Fig. 10.18 Coronal T1 MR images. Relationship between the radius and lunate in neutral (**a**), radial tilt (**b**), and ulnar tilt (**c**). Note that the lunate locates completely in the lunate notch of the radius in (**c**)
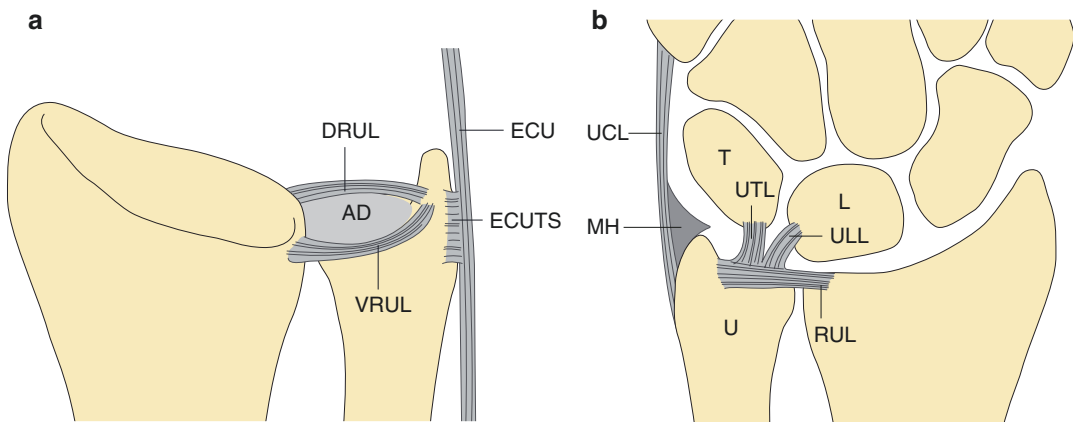
Fig. 10.19 Coronal diagrams (**a**, **b**) showing the triangular fibrocartilage complex (TFCC) which is composed of: -articular disc (AD); radioulnar volar and dorsal ligaments (VRUL,DRUL);ulnotriquetral ligaments (UTL) and ulno-lunate ligaments(ULL) (volar and dorsal); extensor carpi ulnaris tendon sheath (ECUTS); ulnar collateral ligament (UCL) and meniscal homologue (MH)

ulnar styloid index which is partially dependent on the ulnar variance, which plays a role in producing the ulnar styloid impaction syndrome on the triquetrum. Normally the ulnar styloid process is **2–6 mm** long. Garcia-Ellis (1987) proposed the *ulnar styloid process index* (USPI) as a determinant of direct impaction injury by an excessively long ulnar styloid process on the dorsal aspect of the triquetrum. This is calculated by subtracting the degree of ulnar variance from the length of the ulnar styloid process and dividing the difference by the transverse diameter of the ulnar head. The normal USPI range is **0.21 +/− 0.07**, and excess length of the ulnar styloid **>6 mm** produces a greater USPI value promoting ulnar styloid impaction syndrome (Fig. 10.42).

As the articular surface of the radius slopes in a volar and ulnar direction there is a tendency towards a vector migration of the carpus in the same direction. This is counteracted by strong liga-
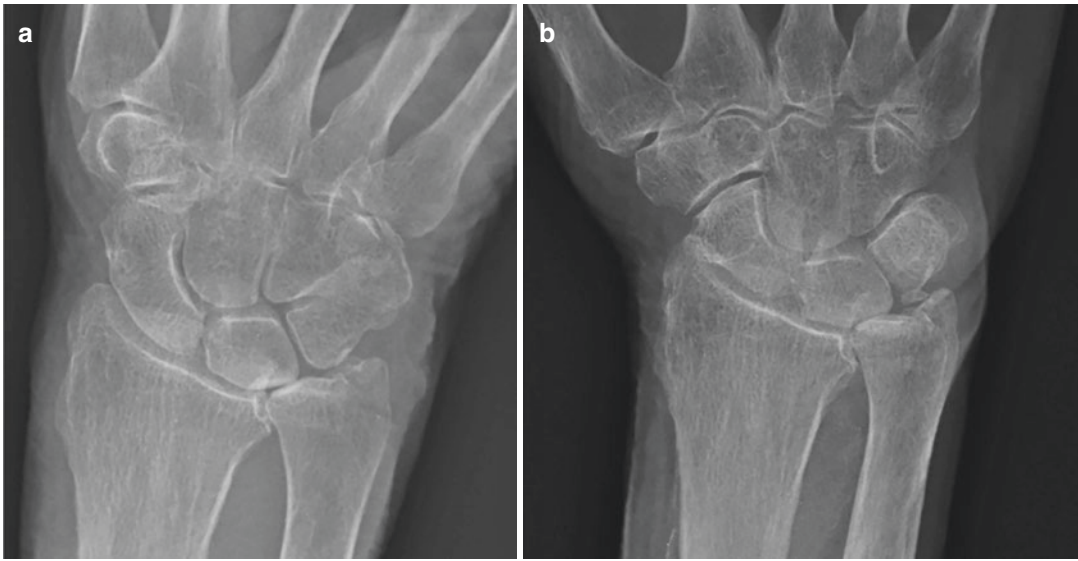
Fig. 10.20 Positive ulnar variance with ulnocarpal impaction (**a**) which is worse in 1 year (**b**)

ments. With the advent of ultrasound and MR arthrography it is possible to visualise and measure wrist and hand ligaments which play an important role in articular stability. Due to their small dimensions and oblique course high spatial resolution is required with ideally a 3 T magnet using an FOV < 10 cm, slices <2 mm and a high matrix (>384X256). 3D GRE are helpful but generate susceptibility artefacts at 3 T. Native axial oblique imaging planes or MPR from an isotropic acquisition can depict the individual ligaments optimally. In the wrist there are intrinsic and extrinsic ligaments. The intrinsic ligaments attach solely to the carpal bones while extrinsic ligaments additionally attach to the forearm bones, tendon sheaths and retinacula. The three main intrinsic ligaments are the scapholunate, lunotriquetral and triangular fibrocartilage complex. The scapholunate has already been covered previously, while the lunotriquetral ligament also exhibits three components—dorsal, volar and proximal with the 2 mm thick volar component being stronger than the 1 mm dorsal component. The extrinsic ligaments are as important as the intrinsic ligaments in maintaining carpal stability. Their main function is to counter the tendency of the carpus to displace in a volar and ulnar direction as dictated anatomically by the slope of the distal radius. As these extrinsic ligaments are only 2–3 mm thick and obliquely orien-

tated in the three imaging planes, they are not completely visualised on standard MRI. Volar extrinsic ligaments include the three main intracapsular extrasynovial ligaments; volar radioscaphocapitate, volar radiotriquetral and volar radioulnar ligaments, as well as the volar ulnolunate and volar ulnotriquetral. The volar radioscaphocapitate and volar radiotriquetral ligaments arise close to one another from the radial styloid and course fairly parallel towards the carpus (Fig. 10.21) allowing them to be visualised distinctly on coronal images especially on MR arthrography with intervening contrast medium from the joint. Smith's study provided MRI based average dimensions for the radioscaphocapitate ligament length of 22.2 +/− 1.4 mm, proximal–distal width of 5.6 +/− 0.8 mm, and a dorsal–volar thickness of 2.2 +/−0.4 mm. As the radiolunotriquetral ligament is curved its length is not possible to measure reliably but its proximal–distal width is 6.9 +/− 1.0 mm, with a dorsal–volar width of 2.3+/− 0.5 mm. Some of these extrinsic ligaments are also incorporated in the triangular fibrocartilaginous complex. The volar ulnolunate, volar ulnotriquetral, and volar distal radioulnar ligaments form part of the TFCC (Fig. 10.19). The volar radioulnar ligament is a thickened peripheral attachment to the TFC disc, while the volar radioulnar ligament attaches to the styloid process and fovea of the ulna. The ulnolu-
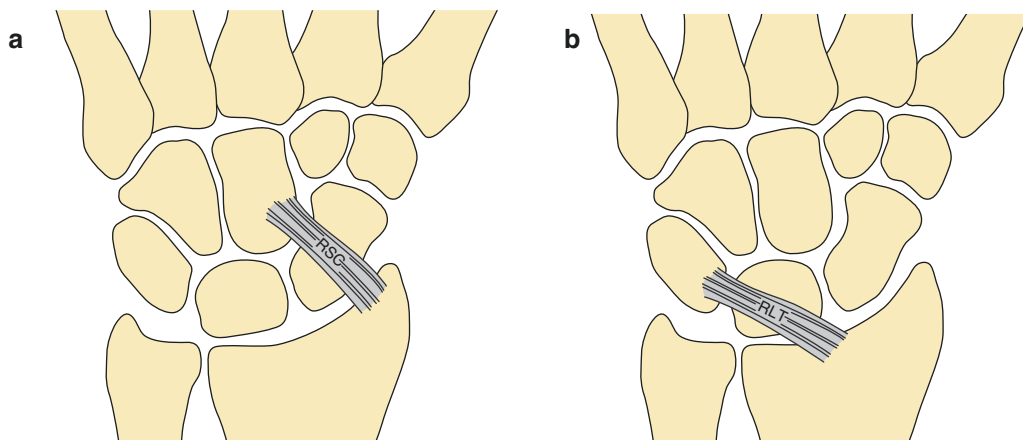
Fig. 10.21 Volar extrinsic ligaments: (**a**) radioscaphocapitate (RSC) and (**b**) radiolunotriquetral (RLT) ligaments

nate ligament arises from the volar radioulnar ligament and extends along the forearm axis to attach onto the lunate. Its average dimensions on MRI are a length of 11.6 +/− 1.5 mm, a mediolateral width of 6.5 +/− 1.2 mm, with a dorsovolar thickness of 2.5 +/− 0.6 mm. Similarly the volar ulnotriquetral ligament arises from the volar radioulnar ligament passing medial to the volar ulnolunate ligament and has a fan-shaped attachment to the triquetral bone. Its average MRI dimensions are 11.4 +/− 0.7 mm long, 4.0 +/− 0.8 mm mediolaterally and 3.7 +/− 0.5 mm dorsovolar thickness Smith (1993b). These two ligaments are also seen on the coronal MR images with joint fluid between them. The volar radioulnar ligament is easy to be seen in all the three MR planes but it is the sagittal images that show best the volar and dorsal radioulnar ligaments with the TFC disc. Dorsal extrinsic ligaments are orientated in the transverse plane and converge towards the triquetrum. They include two main dorsal extrinsic ligaments: the dorsal intercarpal and dorsal radiotriquetral, the latter lying inferior to the former (Fig. 10.22). The dorsal intercarpal ligament also attaches to the scapholunate and lunotriquetral ligaments. They are seen as a v-shaped configuration on coronal MR images both linked to the triquetrum. The dorsal radioulnar ligament is a third dorsal ligament and is like its volar counterpart a thickened periphery of the TFC disc best seen on sagittal images. There is however considerable normal variation in morphology and

morphometry of all of these extrinsic ligaments. Ligament widths show larger individual variation than their lengths. Feipel and Rooze (1998) found that the SD of most of the ligament lengths and widths are in the order of 20% of the average values, but the dorsal and ulnar have a wider variation of 32–57%. This probably explains the differences found in the dimensions of ligaments assessed by MRI in different studies. Smith's early studies produced MR based measurements of the dorsal ligaments with the radiotriquetral ligament exhibiting a mean length of 24.4 +/− SD 2.4 mm, a mean proximal–distal width of 3.4 +/− SD 0.9 mm, and a mean dorsovolar thickness of 2.2 +/− SD 0.4 mm Smith (1993a).

The dorsal intercarpal ligament exhibited a mean proximal–distal width of 4.6 +/− 0.9 mm at its triquetral origin, and 7.5 +/− 1.6 mm at its scaphoid insertion Smith (1993a). Difficulties are encountered in its MR measurements as it is curved in the three planes. From the normative data the dorsal ligaments are symmetrical which can be helpful in assessing ligament integrity by comparing the symptomatic with asymptomatic sides. An in depth coverage is found in the following text in the assessment of specific ligaments.

The contents are presented in a sequential manner addressing first the measurements that can be done on conventional radiography, followed by those performed on advanced imaging incorporating US, CT and MRI.
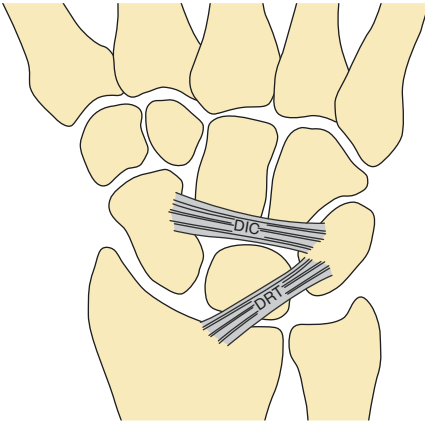
Fig. 10.22 Dorsal extrinsic ligaments: dorsal intercarpal (DIC) and dorsal radiotriquetral (DRT) ligaments

10.2 Conventional Radiography

1. Scapholunate Distance

Definition

Distance of the scapholunate joint space.
Normal Value: 3.7 mm using Cautilli and Wehbe method.

Indications

Scapholunate dissociation in carpal instability.

Technique

Radiography: PA view (elbow flexed 90° and the shoulder is abducted 90°. The elbow must be at shoulder height).

Full Description of Technique

Measurement from the proximal ulnar corner of the scaphoid to the radial corner of the lunate as described by Cautilli and Wehbe (1991).

Reproducibility/Variation

Mean 3.7 ± 0.6 mm.
Range 2.5–5 mm.
Mean 4 mm (men) and 3.6 mm (women).

Clinical Relevance/Implications

As discussed in the introduction of this chapter if the midpoint of the joint is used widening of the scapholunate joint space in **adults > 3 mm** is suggestive of scapholunate dissociation in carpal instability (Figs. 10.6 and 10.7).

In children the normal values are higher due to a large chondral component of the carpal bones and the fact that the scaphoid ossifies eccentrically promoting the false impression of a widened space (Fig. 10.8). Leicht et al. (1996) carried out a study in 79 children by comparing the injured with the uninjured side and produced an age determined range of normal values. The measurements were done using the Cautilli and Wehbe (1991) method from the proximal ulnar most corner of the scaphoid to the radial most corner of the lunate in PA radiographs. In 7-year-olds the median distance was 9 mm compared with 3 mm in 15-year-olds. Kaawach et al. (2001) also provided data on children noting the combined effect of age and gender on values of scapholunate distance. Females exhibit a shorter distance as they achieve adult skeletal maturity earlier reaching the adult range by 11 years of age compared with boys who do so at 12 years. Prior to that there is an age-dependent factor which also needs to be taken into consideration. Kaawach et al.'s study on 85 bone age radiographs showed the following values (upper limits in mm in brackets) with clear age-dependent and gender-dependent variation with excellent inter-observer and intra-observer agreement:

Age	Female	Male
6	7 (9) mm	9 (12) mm
7	6 (8.5) mm	8 (11) mm
8	5.5 (8) mm	7.5 (10.5) mm
9	5 (7.5) mm	6.5 (9.5) mm
10	4.5 (7) mm	6 (9) mm
11	4 (6.5) mm	5 (8) mm
12	3.5 (6) mm	4.5 (7.5) mm

Scapholunate distance Kaawach W, (2001)

Analysis/Validation of Reference Data

Cautilli and Wehbe's study on 100 normal adults was done by taking the measurements from the

proximal aspect of the joint. Measurements provided a normal range of 2.5–5 mm with a mean of 3.7 mm (SD 0.6 mm). A statistically significant difference is demonstrated with respect to sex. This technique does not measure the scapholunate width through the centre of the joint which has difficulties. Increasingly there is adoption of measuring the midpoint distance because of the difference in value based on the different normal craniocaudal variation in dimension. Kindynis et al. (1990) proposed a 10° X-ray tube tilt from the ulna towards the radius to optimise visualisation of the space, concluding that measurements are more reliable using the midpoint distance from the flat medial facet of the scaphoid. However this too has inherent difficulties because of the anatomical variation from dorsal to palmar of the scapholunate space and how it is profiled on PA radiography. It is common to have overlapping bones which makes accurate set up for measurement challenging. On routine PA view of the wrist the scapholunate joint is often not profiled. Obermann used fluoroscopy to optimise the radiographic positioning of radiographs for this purpose and found a false negative rate of 25% and a false positive rate of 6.5%. Moneim showed that a tangential view of the wrist produced by elevating the ulnar border of the hand 20° off the table (e.g. by flexion of the fourth and fifth fingers) better delineates the scapholunate interspace.

AP view of the wrist is preferable and the contralateral wrist may be used as reference in all cases when pathological measurements are suspected. This is important before surgical intervention and especially in patients exhibiting hypermobility which can be associated with a physiological increase in scapholunate distance. Indeed Watson et al. (1993) showed that 12% of the general population exhibit normal hypermobile scaphoid bones due to underlying lax ligaments.

Stress views with a clenched fist in supination may highlight a widening of the scapholunate joint space. The musculotendinous forces in fist clenching drive the capitate's head towards the scapholunate joint, stressing the joint promoting diastasis in the presence of ligament insufficiency (Fig. 10.7). A tangential view with the wrist held in 20° of ulnar deviation can also uncover occult dissociation not seen on the routine PA radiograph. When measured at the midpoint of the scapholunate joint it normally measures 2 mm, and usually remains constant within the normal range in radial and ulnar deviation of the wrist (Kindynis et al. 1990). However the magnification factor also needs to be taken into consideration as it can create an acceptable normal range of up to 3 mm.

Conclusion

The adult measurement needs to be consistently done from the mid-point of the scapholunate interface and a measurement >3.5 mm is suspicious of injury. Contralateral comparison before embarking on surgical intervention is recommended to ensure that there is no underlying ligamentous laxity as the cause for a wide distance.

2. Scapholunate Angle

Definition

Angle between the scaphoid axis and lunate axis.
Normal Value: 50°.

Indications

Carpal instability.

Technique

Radiography: lateral view (arm adducted against the trunk, the elbow flexed 90°, the forearm in neutral rotation (no supination or pronation) and the wrist in neutral position (no radial or ulnar deviation and no palmar flexion or extension)).

Full Description of Technique

Line SA is through the proximal and distal poles of the scaphoid.
Line ST: variant of line SA with the tangent of the volar proximal and distal convexities.
Line L is the line perpendicular to the tangent of the two distal poles of the lunate.

Reproducibility/Variation

Mean: 46°. Range 30–60° (Linscheid) (Line ST method) Linscheid et al. (1972).

Mean: 50 ± 8.2°. Range 30–67° (Yamada 1988) (Line ST method).
Mean: 50.8 ± 6.7°. Range 36–66° (Larsen) (Line ST method).

Clinical Relevance/Implications

The scapholunate angle (Fig. 10.16) is modified in instances of carpal intercalated segmental instability. The angle is increased in the case of traumatic scapholunate dissociation with DISI, while the scapholunate angle is decreased in instances of VISI Linscheid et al. (1972).

Analysis/Validation of Reference Data

The range of angles in normal wrists varies considerably in different studies. Precise positioning of the arm and wrist, use of a support and evaluation using well-defined carpal bone axes are necessary to make accurate wrist measurements. The uninjured wrist in a patient with unilateral wrist trauma can be used as a reference. A difference between the carpal bone angles on lateral radiographs exceeding 5° is considered significant Linscheid (1986).

Conclusion

Useful measurement in instances of DISI and VISI when combined with other measurements.

3. Lunotriquetral Angle

Definition

Angle between the lunate axis and triquetrum axis.
Normal Value: 14°.

Indications

Carpal instability.

Technique

Radiography: lateral view (arm adducted against the trunk, the elbow flexed 90°, the forearm in neutral rotation (no supination or pronation) and the wrist in neutral position (no radial or ulnar deviation and no palmar flexion or extension).

Full Description of Technique

Line T is the line through the proximal and distal poles of the triquetrum.
Line L is the line perpendicular to the tangent of the two distal poles of the lunate.

Reproducibility/Variation

Mean: 14°. Range-3°–31° (Reagan et al. 1984).

Clinical Relevance/Implications

The lunotriquetral angle is decreased or even minus in lunotriquetral dissociation.

Analysis/Validation of Reference Data

The range of angles in normal wrists varies considerably in different studies. Precise positioning of the arm and wrist, use of a support and evaluation using well-defined carpal bone axes are necessary to make accurate wrist measurements. The triquetrum line is more difficult to delineate than the lunate outline. The uninjured wrist in a patient with unilateral wrist trauma can be used as a reference. A difference between the carpal bone angles on lateral radiographs exceeding 5° is considered significant.

Conclusion

Useful but not regularly utilised.

4. Capitolunate Angle

Definition

Angle between the lunate axis and capitate axis.
Normal Value: −10°.

Indications

Carpal instability.

Technique

Radiography: lateral view (arm adducted against the trunk, the elbow flexed 90°, the forearm in neutral rotation (no supination or pronation) and the wrist in neutral position (no radial or ulnar deviation and no palmar flexion or extension)).

Full Description of Technique
(Fig. 10.15)

Line CA is the line through the midpoints of the proximal and distal poles of capitate.
Line CT is the tangent of the dorsal proximal and dorsal margins of the capitate.
Line L is the line perpendicular to the tangent of the two distal poles of the lunate.

Reproducibility/Variation

Range: 0–30° (Gilula).
Mean: −4.5 ± 9.1° (Yamada 1988).
Mean: −10 ± 8° (Nakamura et al. 1989).

Clinical Relevance/Implications

In dorsal intercalated segmental instability (DISI) the capitolunate angle is more volarly flexed than 30°.
In volar intercalated segmental instability (VISI) the capitolunate angle is more dorsiflexed than 30°.

Analysis/Validation of Reference Data

The range of angles in normal wrists varies considerably in different studies. Precise positioning of the arm and wrist, use of a support and evaluation using well-defined carpal bone axes are necessary to make accurate wrist measurements. The uninjured wrist in a patient with unilateral wrist trauma can be used as a reference. A difference between the carpal bone angles on lateral radiographs exceeding 5° is considered significant.

Conclusion

Useful but not routinely relied upon.

5. Carpal Height

Definition

Distance from the base of the third metacarpal to the subchondral sclerotic line of the distal articular surface of the radius.
Normal Value: 33.8 mm.

Indications

Rheumatoid arthritis.
Kienböck's disease.
Scapholunate advanced collapse (SLAC) wrist.
Scaphoid nonunion advanced collapse (SNAC) wrist.

Technique

Radiography: PA view (elbow flexed 90° and the shoulder is abducted 90°. The elbow must be at shoulder height, and the wrist in neutral without ulnar/radial deviation or volar/dorsiflexion) including the third metacarpal. It is important that there is no flexion or extension of the hand as this alters the apparent length of the third metacarpal. The third metacarpal axis is the reference line along which measurements of carpal height are made.

Full Description of Technique
(Fig. 10.23**)**

L2: carpal height.

Reproducibility/Variation

Mean: 33.8 mm.
Median: 32.9 ± 6.1 mm.
Range: 26.4–40.5 mm.
Normal limits: 27.4–40 mm.

Clinical Relevance/Implications

Carpal height is a quantitative aid in assessing carpal collapse. Carpal collapse primarily of the proximal row may occur in Kienböck's disease,
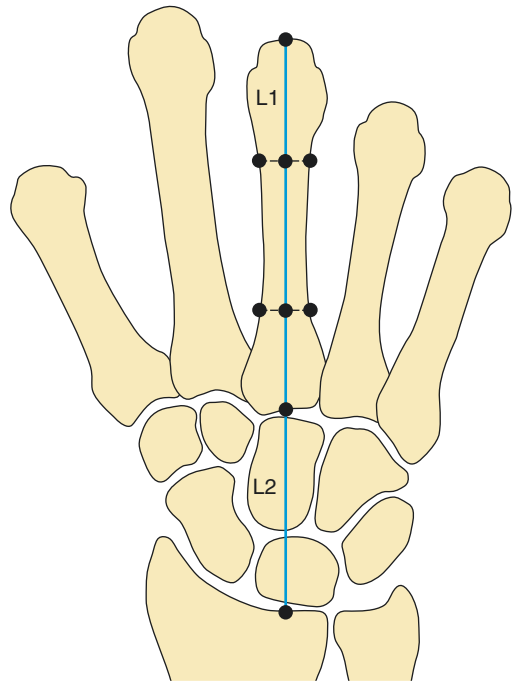
Fig. 10.23 Carpal height and carpal height ratios. Carpal height (L2); length of third metacarpal (L1) and carpal ratio (L2/L1)

SLAC and SNAC wrist. In rheumatoid arthritis the carpal collapse is due to bony loss and/or volar subluxation. Sequential measurements assess progression and severity.

Analysis/Validation of Reference Data

Limited validated data.

Conclusion

Useful in follow-up monitoring in chronic diseases over a long period.

6. Carpal Height Ratio

Definition

Ratio of the carpal height to the length of the third metacarpal.
Normal Value: 0.53.

Indications

Rheumatoid arthritis.
Kienböck's disease.
Scapholunate advanced collapse (SLAC).
Scaphoid nonunion advanced collapse (SNAC) wrist.

Technique

Radiography: PA view (elbow flexed 90° and the shoulder is abducted 90°. The elbow must be at shoulder height) including the third metacarpal. It is important that there is no flexion or extension of the hand as this alters the measured length of the carpus and third metacarpal.

Full Description of Technique
(Fig. 10.23)

This is based on Youm's method Youm et al. (1978).
L1: length of the third metacarpal.

L2: carpal height measured in line with L1, from the base of the third metacarpal to the articular surface of the distal radius.
Carpal height ratio = L2/L1, where the carpal height measured in line with the third metacarpal axis, is divided by the third metacarpal length.

Reproducibility/Variation

Mean: 0.53.
Median: 0.52 ± 9.9.
Range: 0.45–0.61.
Normal limits: 0.46–0.60.

Clinical Relevance/Implications

Carpal collapse of the proximal row may occur in Kienböck's disease, SLAC and SNAC wrist. In rheumatoid arthritis the carpal collapse is due to bony loss and/or volar subluxation. Carpal height ratio allows comparative assessment between individuals Stahelin et al. (1989).

Analysis/Validation of Reference Data

Limited validated data.

Conclusion

Useful in follow-up monitoring in chronic diseases over a long period.

7. Carpal Height Ratio with Capitate Length

Definition

Ratio of the carpal height to the length of capitate. **Normal Value: 1.57**.

Indications

Rheumatoid arthritis.
Kienböck's disease.
Scapholunate advanced collapse (SLAC).
Scaphoid nonunion advanced collapse (SNAC) wrist.

Technique

Radiography: PA view (elbow flexed 90° and the shoulder is abducted 90°. The elbow must be at shoulder height). Does not need to include the full length of the third metacarpal.
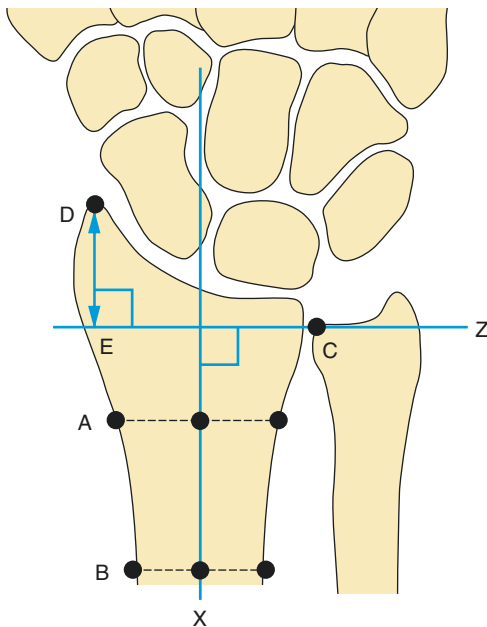
Full Description of Technique
(Fig. 10.24**)**

This employs Natrass' method Natrass et al. (1994).
L2: carpal height.
LC: the longest line between the point at the angular distal cortex of the capitate at the second to third carpometacarpal junction to the proximal cortex of the capitate.
Carpal height ratio = L2/LC, where the carpal height is divided by the capitate length.

Reproducibility/Variation

Mean: 1.57 ± 0.05.
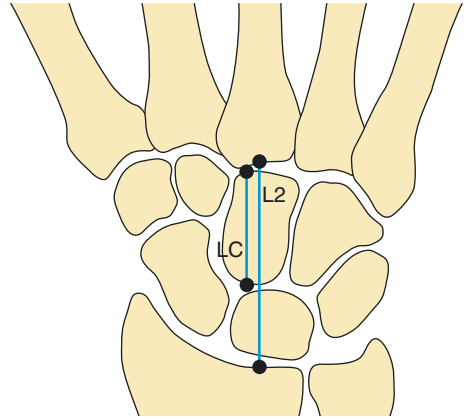
Fig. 10.24 Carpal height ratio with capitate length. Carpal height (L2), capitate height (LC)

Clinical Relevance/Implications

Carpal collapse may occur in Kienböck's disease, SLAC and SNAC wrist. In rheumatoid arthritis the carpal collapse is due to bony loss and/or volar subluxation.

Analysis/Validation of Reference Data

Limited validated data.

Conclusion

Useful in follow-up monitoring in chronic diseases over a long period.

8. Carpal Height Index

Definition

Division of the carpal height ratio of the dominant side by that of the nondominant side.
Normal Value: 1.

Indications

Rheumatoid arthritis.
Kienböck's disease.
Scapholunate advanced collapse (SLAC).
Scaphoid nonunion advanced collapse (SNAC) wrist.

Technique

Radiography: PA view (elbow flexed 90° and the shoulder is abducted 90°. The elbow must be at shoulder height) including the third metacarpal.

Full Description of Technique
(Fig. 10.23**)**

L1: length of the third metacarpal.
L2: carpal height.
Carpal height ratio = L2/L1.
Carpal height index = carpal height ratio dominant side/carpal height ratio nondominant side.

Reproducibility/Variation

Mean: 1 ± 0.015.

Clinical Relevance/Implications

Carpal collapse may occur in Kienböck's disease, SLAC and SNAC wrist. In rheumatoid arthritis the carpal collapse is due to bony loss and/or volar subluxation. This comparative index is superior to the carpal height ratio for the evaluation of unilateral disease. It is preferred being more sensitive in detecting changes in carpal height in a specific hand on follow-up.

Analysis/Validation of Reference Data

Limited validated data.

Conclusion

Useful in follow-up monitoring in chronic diseases over a long period.

9. Carpal Ulnar Translation Index (Pirela-Cruz Method)

Definition

Two types of ulnar translations of the wrist are described:

Type I: ulnar translation of the entire carpus.

Type II: the scaphoid remains in its anatomic position while the other carpal bones shift ulnarward causing a scapholunate gap.

Normal Value: 28 mm.

Indications

Rheumatoid arthritis.

Other synovial arthritides.

Posttraumatic carpal instability.

Technique

Radiography: PA view (elbow flexed 90° and the shoulder is abducted 90°. The elbow must be at shoulder height) including the third metacarpal.

Full Description of Technique
(Fig. 10.25**)**

The relationship of the carpus to the ulna is used as a reference Pirela-Cruz et al. (1993).

Line X: longitudinal axis of the ulna.

Line YR: perpendicular line to X drawn at the level of the third metacarpal.

Line ZD: perpendicular line to X at the level of the dorsal (radiodense) portion of the ulnar fovea.

L2: carpal ulnar distance (distance from line X to the reference point R).

Reproducibility/Variation

Median: 28 ± 6 mm.

Clinical Relevance/Implications

L2 decreases as the carpus drifts ulnarly.
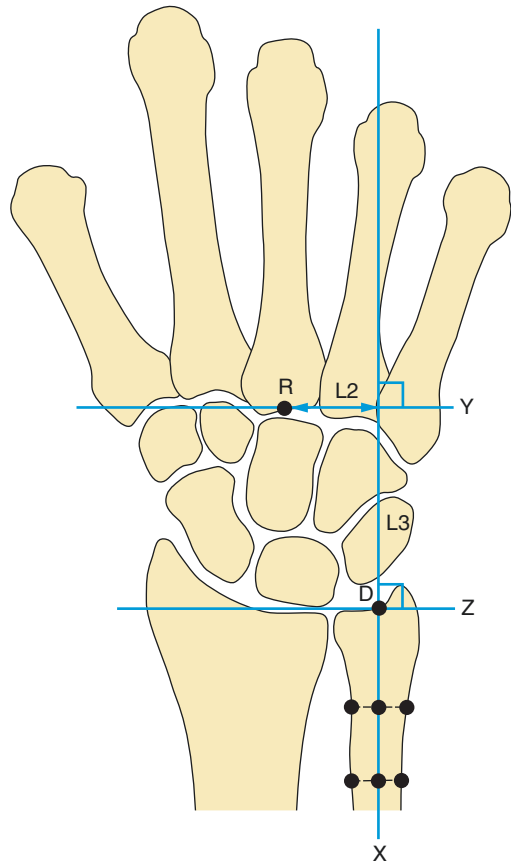
Fig. 10.25   Carpal ulnar translation index. Line X (longitudinal axis of the ulna); Line YR (perpendicular line to X drawn at the base of the third metacarpal); Line ZD (perpendicular line to X drawn at the level of the ulnar fovea); L2 (carpal ulnar distance)

Analysis/Validation of Reference Data

Sensitivity is low and underdiagnosis may occur.

Conclusion

Useful in follow-up monitoring in chronic inflammatory diseases over a long period.

10. Carpal Ulnar Translation Ratio

Definition

Two types of ulnar translations of the wrist are described:
Type I: ulnar translation of the entire carpus.
Type II: the scaphoid remains in its anatomic position while the other carpal bones shift ulnarward causing a scapholunate gap.
Normal value: 0.28.

Indications

Rheumatoid arthritis.
Other synovial arthritides.
Posttraumatic carpal instability.

Technique

Radiography: PA view (elbow flexed 90° and the shoulder is abducted 90°. The elbow must be at shoulder height) including the third metacarpal.

Full Description of Technique (Fig. 10.26)

The relationship of the carpus to the ulna is used as a reference Pirela-Cruz et al. (1993).
Line X: longitudinal axis of the ulna.
L2: carpal–ulnar distance (distance from line X to the reference point R).
L1, third metacarpal length

$$\text{Carpoulnar translation ratio} = \text{ulnometacarpal distance} \left(L2\right) / \text{metacarpal length} \left(L1\right)$$

Reproducibility/Variation

Mean: 0.28 ± 0.06.

Clinical Relevance/Implications

Carpoulnar translation ratio decreases as the carpus drifts ulnarly.

Analysis/Validation of Reference Data

Sensitivity is low and underdiagnosis may occur.

Conclusion

Useful in follow-up monitoring in chronic inflammatory diseases over a long period.
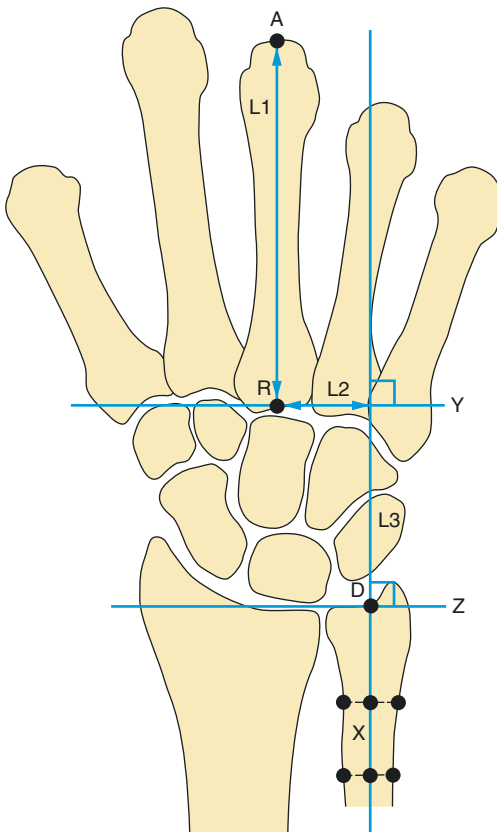
Fig. 10.26 Carpal ulnar translation ratio. Line X (longitudinal axis of the ulna); Line YR (perpendicular line to X drawn at the base of the third metacarpal); Line ZD (perpendicular line to X drawn at the level of the ulnar fovea); L2 (carpal ulnar distance); L1 (length of third metacarpal); Carpal ulnar translation ratio = L2/L1

11. Carpal Ulnar Index Translation Distance (Youm Method)

Definition

Two types of ulnar translations of the wrist are described:
Type I: ulnar translation of the entire carpus.
Type II: the scaphoid remains in its anatomic position while the other carpal bones shift ulnarward causing a scapholunate gap.
Normal Value: 30 mm.

Indications

Rheumatoid arthritis.
Other synovial arthritides.
Posttraumatic carpal instability.

Technique

Radiography: PA view (elbow flexed 90° and the shoulder is abducted 90°. The elbow must be at shoulder height) including the third metacarpal.
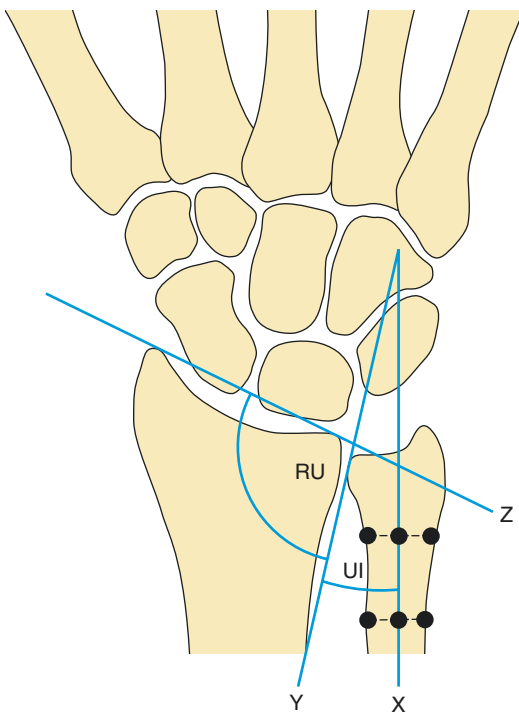
Full Description of Technique
(Fig. 10.27)

The relationship of the carpus to the ulna is used as a reference Youm et al. (1978).
C: centre of the head of the capitate.
Line X: long axis of the ulna.
Carpal ulnar distance L2: perpendicular line measured from C to D.

Reproducibility/Variation

Median: 30 ± 3 mm.

Clinical Relevance/Implications

L2 decreases as the carpus drifts ulnarly.
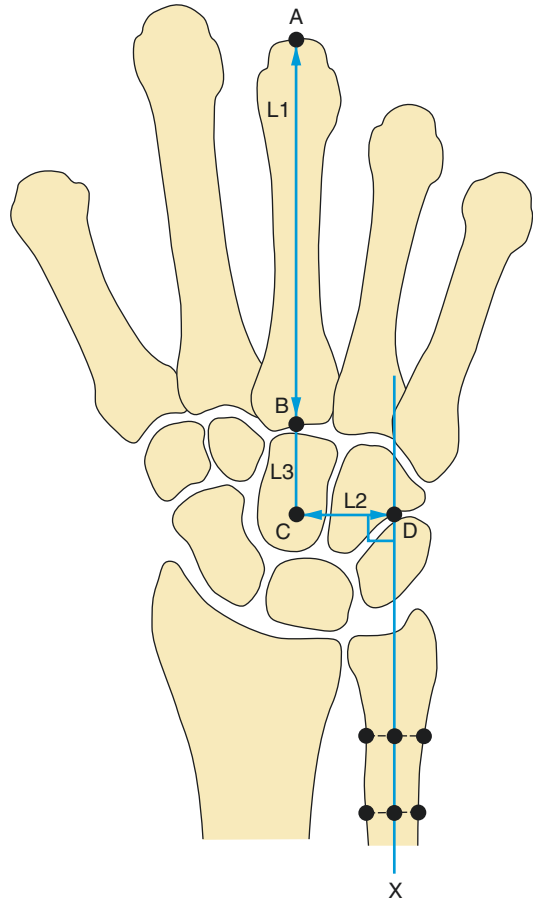
Fig. 10.27 Carpal ulnar index translation ratio (Youm method). Line X (longitudinal axis of the ulna); L1 (length of third metacarpal between points AB); C (centre of the head of the capitate); L2 (distance between C and line X is carpal ulnar index translation or CUTD); Carpal ulnar index translation ratio or CUTR = L2/L1

Analysis/Validation of Reference Data

Sensitivity is low and underdiagnosis may occur.

Conclusion

Useful in follow-up monitoring in chronic inflammatory diseases over a long period.

12. Carpal Ulnar Index Translation Ratio (Youm Method)

Definition

Two types of ulnar translations of the wrist are described:

Type I: ulnar translation of the entire carpus.
Type II: the scaphoid remains in its anatomic position while the other carpal bones shift ulnarward causing a scapholunate gap.

Normal Value: 0.3.

Indications

Rheumatoid arthritis.
Other synovial arthritides.
Posttraumatic carpal instability.

Technique

Radiography: PA view (elbow flexed 90° and the shoulder is abducted 90°. The elbow must be at shoulder height) including the third metacarpal.

Full Description of Technique
(Fig. 10.27**)**

The relationship of the carpus to the ulna is used as a reference Youm et al. (1978).

C: centre of the head of the capitate.
Line X: long axis of the ulna.
Length of the third metacarpal L1: AB.
Carpal ulnar distance L2: perpendicular line measured from C to D is the Carpal Ulnar Index Translation Distance (CUTD).
Carpal ulnar Index Translation Ratio (CUTR) = L2/L1.

Reproducibility/Variation

Mean: 0.3 ± 0.03.

Clinical Relevance/Implications

CUTR increases as the carpus drifts ulnarly.

Analysis/Validation of Reference Data

Sensitivity is low and underdiagnosis may occur.

Conclusion

Useful in follow-up monitoring in chronic inflammatory diseases over a long period.

13. Carpal Ulnar Translation Index (Chamay Method)

Definition

Two types of ulnar translations of the wrist are described:
Type I: ulnar translation of the entire carpus.
Type II: the scaphoid remains in its anatomic position while the other carpal bones shift ulnarward causing a scapholunate gap.
Normal Value: 28 mm.
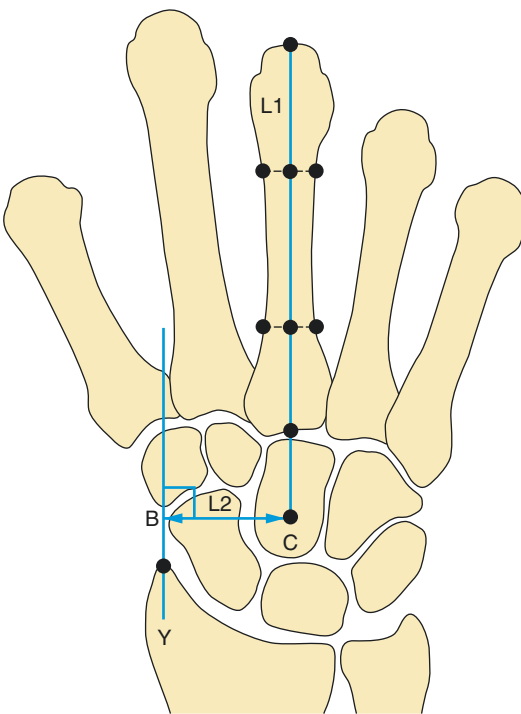
Fig. 10.28 Carpal ulnar translation index (Chamay method) and carpal radial distance ratio. L1 (length of the third metacarpal); line Y (parallel line to the long axis of the radius drawn at the level of the radial styloid); C (centre of the head of the capitate); Carpal ulnar distance (CUD) is L2 (BC distance between C and line Y); carpal radial distance ratio = BC/L1

Indications

Rheumatoid arthritis.
Other synovial arthritides.
Posttraumatic carpal instability.

Technique

Radiography: PA view (elbow flexed 90° and the shoulder is abducted 90°. The elbow must be at shoulder height) including the third metacarpal.

Full Description of Technique
(Fig. 10.28)

The relationship of the carpus to the radius is used as a reference.
C: centre of the head of the capitate.
Line Y: linear reference line drawn proximal to distal through the radial styloid process parallel to the long axis of the radius.
L2: distance measured from C to the point B on a perpendicular line to line Y.
Carpal ulnar translation index = BC.

Reproducibility/Variation

Mean: 28±3 mm.

Clinical Relevance/Implications

Carpal ulnar translation index increases as the carpus drifts ulnarly.

Analysis/Validation of Reference Data

Sensitivity is low and underdiagnosis may occur.

Conclusion

Useful in follow-up monitoring in chronic inflammatory diseases over a long period.

14. Carpal Radial Distance Ratio (Chamay Method)

Definition

Two types of ulnar translations of the wrist are described:

Type I: ulnar translation of the entire carpus.

Type II: the scaphoid remains in its anatomic position while the other carpal bones shift ulnarward causing a scapholunate gap.

Normal value	0.28
Abnormal value	>0.31

Indications

Rheumatoid arthritis.
Other synovial arthritides.
Posttraumatic carpal instability.

Technique

Radiography: PA view (elbow flexed 90° and the shoulder is abducted 90°. The elbow must be at shoulder height) including the third metacarpal.

Full Description of Technique
(Fig. 10.28)

The relationship of the carpus to the radius is used as a reference.

C: centre of the head of the capitate.

Line Y: linear reference line drawn proximal to distal through the radial styloid process parallel to the long axis of the radius.

L2: distance measured from C to the point B on a perpendicular line to line Y.

L1: length of the third metacarpal.

Carpal ulnar translation index = BC.

Carpal radial distance ratio = BC/L1.

Reproducibility/Variation

Mean: 0.28 ± 0.03.

Clinical Relevance/Implications

Carporadial distance ratio increases as the carpus drifts ulnarly.

Analysis/Validation of Reference Data

Sensitivity is low and underdiagnosis may occur.

Conclusion

A value >0.31 is deemed abnormal Chamay et al. (1983).

15. Carpal Ulnar Translation Ratio (Gilula Method)

Definition

Two types of ulnar translations of the wrist are described:
Type I: ulnar translation of the entire carpus.
Type II: the scaphoid remains in its anatomic position while the other carpal bones shift ulnarward causing a scapholunate gap.
Ulnar translocation of the carpus is present if more than 50% of the lunate overhang is ulnar to the lunate fossa.
Normal Value: <50%.

Indications

Rheumatoid arthritis.
Other synovial arthritides.
Posttraumatic carpal instability.

Technique

Radiography: PA view (elbow flexed 90° and the shoulder is abducted 90°. The elbow must be at shoulder height).

Full Description of Technique
(Fig. 10.29**)**

CD: lunate overhang.
AB: lunate width.
Lunate overhang ratio = CD/AB.

Reproducibility/Variation

Limited data

Clinical Relevance/Implications

Ulnar translocation is present if lunate overhang ratio is >50%.

Analysis/Validation of Reference Data

Sensitivity is low and underdiagnosis may occur.

Conclusion

Useful in follow-up monitoring in chronic inflammatory diseases over a long period.

Fig. 10.29   Carpal ulnar translation ratio (Gilula method). AB (lunate width); CD (lunate overhang); CUTR (carpal ulnar translation ratio) = CD/AB

16. Carpal Ulnar Translation Index (Dibenedetto Method)

Definition

Two types of ulnar translations of the wrist are described:
Type I: ulnar translation of the entire carpus.
Type II: the scaphoid remains in its anatomic position while the other carpal bones shift ulnarward causing a scapholunate gap.
Normal Value: 9 mm.

Indications

Rheumatoid arthritis.
Other synovial arthritides.
Posttraumatic carpal instability.
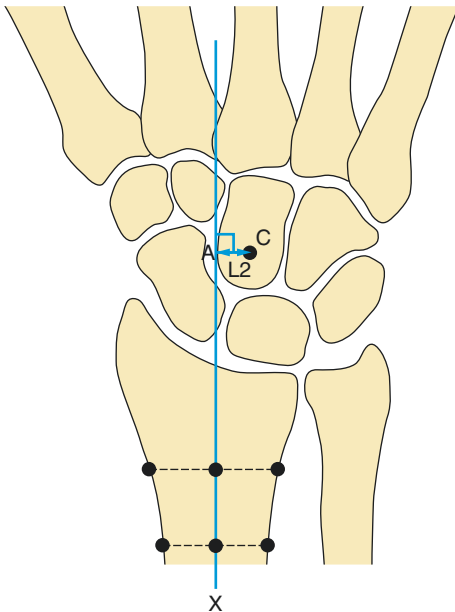
Fig. 10.30 Carpal ulnar translation index (Dibenedetto method). Line X (long axis of the radius); C (centre of the head of the capitate); L2 (perpendicular line to X passing through C); ulnar translation distance = AC

Technique

Radiography: PA view (elbow flexed 90° and the shoulder is abducted 90°. The elbow must be at shoulder height).
The relationship of the carpus to the radius is used as a reference.

Full Description of Technique
(Fig. 10.30**)**

Line X: reference line based on the radius. Bisection of the distal radius 2 and 4 cm proximal to the articular surface of the radius.
C: centre of the head of the capitate.
L2: perpendicular line to X passing through C.
Ulnar translation distance = AC.

Reproducibility/Variation

9±2 mm.

Clinical Relevance/Implications

Ulnar translation distance increases as the carpus drifts ulnarly.

Analysis/Validation of Reference Data

Sensitivity is low and underdiagnosis may occur.

Conclusion

A value >11 mm is deemed abnormal.

17. Radiocapitate Distance Ratio (Dibenedetto Method)

Definition

Two types of ulnar translations of the wrist are described:
Type I: ulnar translation of the entire carpus.
Type II: the scaphoid remains in its anatomic position while the other carpal bones shift ulnarward causing a scapholunate gap.
Normal Value: 0.09.

Indications

Rheumatoid arthritis.
Other synovial arthritides.
Posttraumatic carpal instability.

Technique

Radiography: PA view (elbow flexed 90° and the shoulder is abducted 90°. The elbow must be at shoulder height).
The relationship of the carpus to the radius is used as a reference.

Full Description of Technique
(Fig. 10.31**)**

Line X: reference line based on the radius. Bisection of the distal radius 2 and 4 cm proximal to the articular surface of the radius.
C: centre of the head of the capitate.
L2: perpendicular line to X passing through C.
L1: length of the third metacarpal.
Ulnar translation distance = AC.
Radiocapitate distance ratio (RCDR) = AC/L1.

Reproducibility/Variation

0.09±0.02.

Clinical Relevance/Implications

Radiocapitate distance ratio increases as the carpus drifts ulnarly.
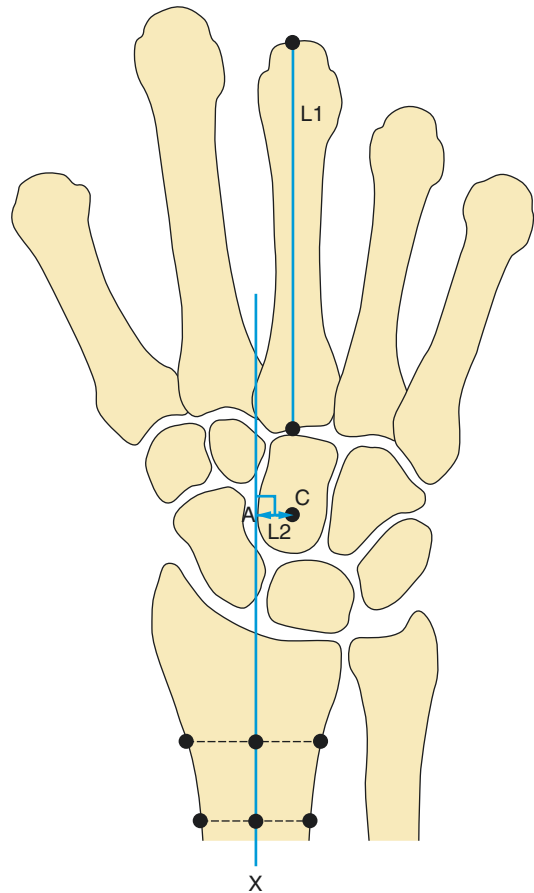
Fig. 10.31 Radiocapitate distance ratio (Dibenedetto method). Line X (long axis of the radius); C (centre of the head of the capitate); L2 (perpendicular line to X passing through C); L1 (length of third metacarpal); RCDR (radiocapitate distance ratio) = AC/L1

Analysis/Validation of Reference Data

Sensitivity is low and underdiagnosis may occur.

Conclusion

A ratio > 0.11 is deemed abnormal.

18. Length of the Third Metacarpal

Definition

Length of the third metacarpal.
Normal Value: 63.2 mm.

Indications

Rheumatoid arthritis.
Other synovial arthritides.
Posttraumatic carpal instability.

Technique

Radiography: PA view (elbow flexed 90° and the shoulder is abducted 90°. The elbow must be at shoulder height) including the full length of the third metacarpal. It is important that there is no flexion or extension of the hand as this will result in foreshortening of the metacarpal and introduce an error in measurement.

Full Description of Technique
(Fig. 10.31)

L1: length of the third metacarpal.

Reproducibility/Variation

Mean: 63.2.
Median: 62.9±4.5.
Range: 53.4–74.0.
Normal limits: 55.3–73.2.

Clinical Relevance/Implications

The length of the third metacarpal is used to normalise many ratios at the wrist.

Analysis/Validation of Reference Data

Wide range of length of the third metacarpal.

Conclusion

Use to normalise many ratios at the wrist.

19. Radial Inclination Angle (Dibenedetto and Matsushita Methods)

Definition

Radial inclination also referred to as radial deviation, ulnar inclination, radial tilt or radial angle. Angulation of the distal radial articular surface in relationship with the long axis of the radius or ulna as seen in the PA or AP view of the wrist. **Normal Value: 22° (range 13–30°).**

Indications

Distal radius fracture.
Madelung deformity.

Technique

Radiography: PA view in neutral position (elbow flexed 90° and the shoulder is abducted 90°. The elbow must be at shoulder height).

Full Description of Technique— Dibenedetto Method (Fig. 10.32)

Line X: line bisecting the distal radial shaft 4 and 8 cm proximal to the radiocarpal joint (AB).
Line Z perpendicular to line X passing through the distal sigmoid notch (C).
Line Y between point C and the radial styloid (D).
Radial inclination angle = angle between line Z and Y.
Variant recommended by **Matsushita** et al. (1992) (Fig. 10.33): line Z is perpendicular to the ulnar long axis (line joining the two midpoints of the ulna at 2 cm and 4 to 5 cm depending on the size of the radiograph).

Reproducibility/Variation

It is important to stress that for consistency the osseous landmark at the ulnar aspect of the radius, passes through the midpoint between the volar and dorsal points of the sigmoid notch.

Radial inclination angle-
Dibenedetto Method
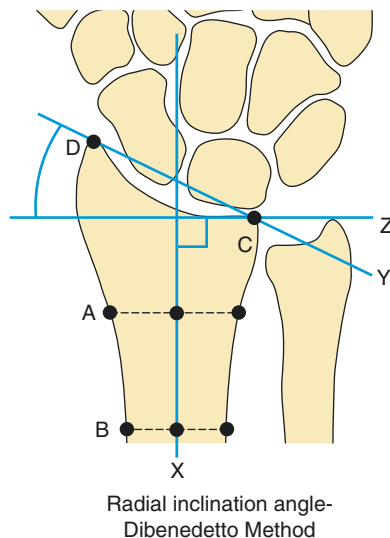
Fig. 10.32 Radial inclination angle (Dibenedetto method). Line X (long axis of the radius); Line Z (perpendicular line passing through the distal sigmoid notch at point C); line Y (line passing through point C and the radial styloid tip at point D); radial inclination angle is the angle between the lines Z and Y

Radial Inclination Angle-
Matsushita Method
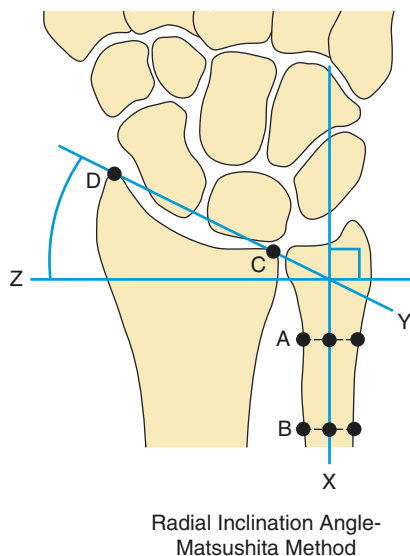
Fig. 10.33 Radial inclination angle (Matsushita method). Line X (long axis of the ulna); Line Y (line passing between point C and the tip of the radial styloid); Line Z (perpendicular line to X drawn at the intersection of X and Y lines); radial inclination angle is the angle between lines Z and Y

Mean: 22 ± 3°.
Mean: 25.4 ± 2.2° (Friberg and Lundstrom 1976).
Mean: 23.8°. Median 23.8 ± 2.6°. Range 12.9–
30.3°. Normal limits 18.8–29.3° (Schuind et al.
1992).
Mean: 25.5±6.2°. Range 15–35° (Warwick et al.
1993).

Clinical Relevance/Implications

This measurement generally is used with confidence between physicians. Loss of radial inclination increases the mechanical load on the lunate. Increased radial inclination increases the risk of injury to the scapholunate ligament. Loss of radial inclination post-fracture of <5° carries a worse outcome.

Radial inclination is difficult to determine in the case of distal radius fracture with intra-articular displacement and comminution. Comparison with contralateral side is required.

Analysis/Validation of Reference Data

Reproducible angle measurement with a narrow standard deviation.

Conclusion

Useful to diagnose a Madelung deformity and to manage fractures of the distal radius.

20. Radial Length (Solgaard Method)

Definition

Radial length also called radial height and length of radial styloid. It is the distance between the radial styloid tip and distal tip of the sigmoid notch. **Normal Value: 12 mm.**

Indications

Distal radius fracture (Colles' fracture).

Technique

Radiography: PA view (elbow flexed 90° and the shoulder is abducted 90°. The elbow must be at shoulder height).

Full Description of Technique
(Fig. 10.34**)**

Line X: line bisecting the distal radial shaft 4 and 8 cm proximal to the radiocarpal joint (AB).
Line Z perpendicular to line X passing through the distal sigmoid notch (C).
Radial length = distance DE.

Reproducibility/Variation

Mean: 12 ± 2.2 mm.
Range: 8–17 mm.

Clinical Relevance/Implications

There are three helpful measurements that assess the distal radius particularly in congenital and
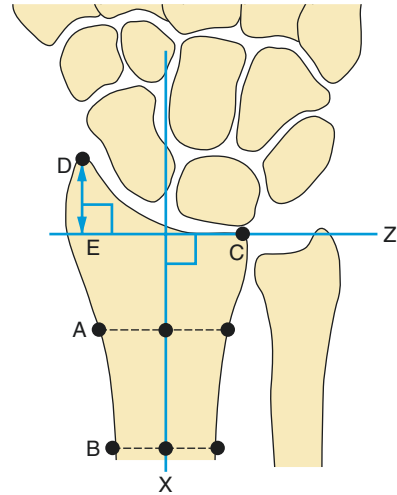
Fig. 10.34 Radial length (Solgaard method). Line X (long axis of the radius); Line Z (perpendicular line to X passing through the distal sigmoid notch at point C; D (tip of the radial styloid); radial length is the distance DE where E is the intersection point between lines Z and a perpendicular line to it drawn from point D

post-traumatic scenarios which include the palmar tilt, radial inclination and radial length. Colles' fracture induces a radial shortening. A loss of radial length (height) is associated with poor outcomes. Measurements <9 mm in adults suggest the presence of an impacted fracture. A comparison with the contralateral normal side is required for a further evaluation.

Conclusion

A loss of radial length is often associated with a loss of the radial tilt in impacted fracture of the distal radius.

21. Radial Length (Mann Method)

Definition

Radial length also called radial height and length of radial styloid. It is the distance between the tip of the radial styloid and the articular surface of the ulnar head.

Normal Value: 13.5 mm (range 11–22 mm).

Indications

Distal radius fracture (Colles' fracture).

Technique

Radiography: PA view (elbow flexed 90° and the shoulder is abducted 90°. The elbow must be at shoulder height).

Full Description of Technique
(Fig. 10.35)

Line X: line bisecting the distal radial shaft 4 and 8 cm proximal to the radiocarpal joint (AB).
Line Z perpendicular to line X passing through most distal aspect of the ulnar articular surface (C).
D: radial styloid.
Radial length = distance DE where E is the intersection point between line Z and its perpendicular line passing through D.

Reproducibility/Variation

Mean: 13.5±3.8 mm.

Clinical Relevance/Implications

The radial shortening in radial fractures needs a contralateral view to determine the pre-existing ulnar variance.

Conclusion

The radial shortening in impacted fracture of the radius is minimised in case of relative lengthening of the ulnar index.

Fig. 10.35 Radial length (Mann method). Line X (long axis of the radius); Line Z (perpendicular line to X passing through the most distal aspect of the ulnar articular surface at point C); D (tip of the radial styloid); radial length is the distance between points D and E where E is the intersection point between line Z and a perpendicular line to it drawn from point D)

22. Palmar Tilt

Definition

Palmar tilt is also called dorsal tilt, dorsal angle, volar tilt, volar angle, volar inclination and palmar slope. It is the angle of intersection between a tangential line across the distal points of the articular radial surface and a perpendicular to the mid-axis of the radius.
Normal Value: 12°.

Indications

Distal radius fracture.

Technique

Radiography: lateral view (arm adducted against the trunk, the elbow flexed 90°, the forearm in neutral rotation (no supination or pronation) and the wrist in neutral position (no radial or ulnar deviation and no palmar flexion or extension)).

Full Description of Technique
(Fig. 10.36**)**

Line Y drawn across the most distal points of the dorsal and ventral rims of the distal radial articular surface.

Line X long axis of the radius: line through the centre of its medullary space at 2 and 5 cm proximal to the radiocarpal joint.
Line Z perpendicular line to the long axis of the radius (line X).
Palmar tilt: angle between line Y and line Z.

Reproducibility/Variation

Mean 12±3.5°. Range 4–23° (Schuind et al. 1992).
Mean: 12.1°. Range 2–20°. Normal limits: 11.3–13° (Mann).
The values are modified if line Y is drawn across the proximal points of the dorsal and ventral rims of the distal radial articular surface: mean 10.8° and range 3–20° and normal limits 10.0–11.6° (Mann).

Clinical Relevance/Implications

Palmar tilt is modified in fractures of the distal radius as in Poteau-Colles fracture and the Goyrand Smith fracture. It represents the sagittal plane inclination of the distal radial articular surface as an initial or residual state following fracture.

Conclusion

A strict lateral view of the wrist is mandatory.

Fig. 10.36   Palmar tilt. Line X (long axis of the radius); Line Z (perpendicular line to X passing through the volar rim of the radius); Line Y (joins the most distal points of the dorsal and ventral rims of the distal radial articular surface); palmar tilt is the angle between lines Y and Z
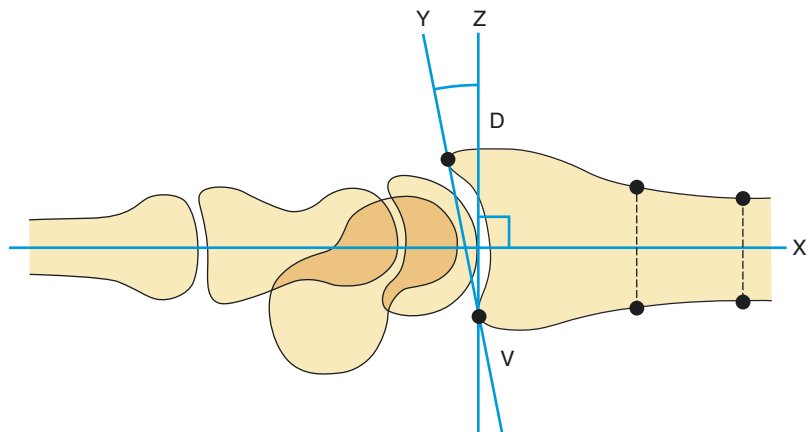
23. Carpal Angle

Definition

Angle of the proximal cortex of the proximal carpal bones.
Normal Value: 130.88°.

Indications

Congenital malformation including Madelung deformity.

Technique

Radiography: PA view (elbow flexed 90° and the shoulder is abducted 90°. The elbow must be at shoulder height).

Full Description of Technique
(Fig. 10.37)

Angle resulting from the intersection of two lines, one tangent to the proximal edges of the lunate and scaphoid (X) and one tangent to the proximal edges of the lunate and triquetrum (Y).

Reproducibility/Variation

Mean 130.88°. Range 124°–139° Harper et al. (1974).

Clinical Relevance/Implications

Increased > 139° in bone dysplasias, Down's syndrome and Pfeiffer syndrome.
Decreased < 124° in Madelung's deformity, Turner's syndrome, multiple exostosis, Hurler's syndrome and Morquois's syndrome.

Analysis/Validation of Reference Data

The carpal angle is altered by positioning of the wrist.
Significant ethnic differences have been found.

Conclusion

cr83

Carpal angle and the radial tilt are increased in Madelung deformity.
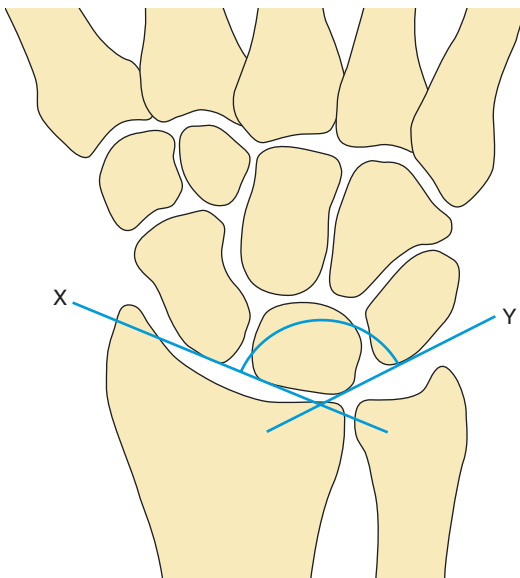
Fig. 10.37 Carpal angle. Line X (tangent line to the proximal edges of the lunate and scaphoid); Line Y (tangent line to the proximal edges of the lunate and triquetrum). Carpal angle is the subtended angle between line X and Y

24. Lunate Fossa Inclination

Definition

Angle of the articular surface of the lunate fossa of the distal radius.
Normal Value: 0–20°.

Indications

Kienböck's disease.

Technique

Radiography: PA view (elbow flexed 90° and the shoulder is abducted 90°. The elbow must be at shoulder height).

Full Description of Technique
(Fig. 10.38**)**

Angle between the sclerotic line of the lunate fossa of the radius and the line perpendicular to the long axis of the distal ulna.
If the lunate fossa is concave, a line is drawn between the radial and the ulnar prominences of the lunate fossa.

If the lunate fossa is flat, the line is simply extended. Line X, long axis of the ulna: line joining the two midpoints of the ulna at 2 cm and 4 to 5 cm (depending on the size of the X-ray film) proximal from the carpal ulnar joint surface.

Reproducibility/Variation

Range 0–20°.

Clinical Relevance/Implications

To correlate lunate collapse to inclination of the distal radius and to evaluate the effect of radial shortening procedures.

Analysis/Validation of Reference Data

Limited validated data.

Conclusion

Lunate fossa inclination must be associated with the analysis of the ulnar index in Kienböck's disease.
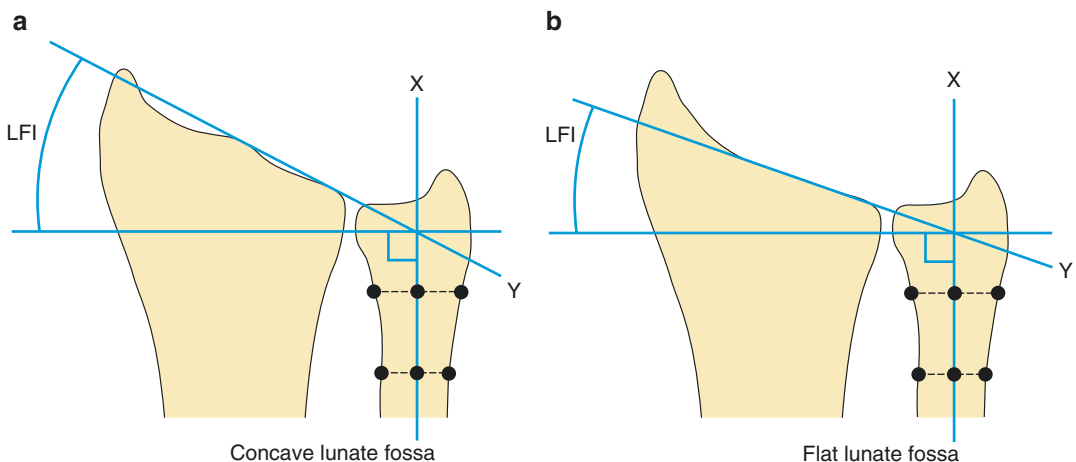
Fig. 10.38 Lunate fossa inclination (LFI). Line X (long axis of the ulna); Line Y (tangent line passing through the sclerotic line of the lunate fossa of the radius); LFI is the angle between line Y and the perpendicular drawn from its intersection point with line X

25. Ulnar Head Inclination Angle

Definition

Angle between the long axis of the ulna and the articular surface of the ulnar head facing the sigmoid notch.
Normal value: 18.6°.

Indications

Congenital disease.
Wrist injuries.

Technique

Radiography: PA view (elbow flexed 90° and the shoulder is abducted 90°. The elbow must be at shoulder height).

Full Description of Technique
(Fig. 10.39**)**

Line X: long axis of the ulna.
Line Y: tangent to the articular surface of the ulnar head facing the sigmoid notch.
Ulnar head inclination (UI) = angle between line X and line Y.

Reproducibility/Variation

Mean 18.6°±4.1.
Range 11–27°.

Clinical Relevance/Implications

The ulnar head inclination is altered by congenital abnormalities.

Analysis/Validation of Reference Data

Comparison with the opposite side is helpful in wrist injuries.

Conclusion

Ulnar head inclination angle >18.6° is deemed abnormal.

Fig. 10.39 Ulnar head inclination and radioulnar angle. Line X (long axis of the ulna); Line Y (tangent to the articular surface of the ulnar head facing the sigmoid notch); Line Z (line drawn between the radial and ulnar limits of the distal radius joint surface); UI (Ulnar inclination) is the angle between the lines X and Y; RU (radioulnar) angle is the intersection of lines Z and Y Tornvall et al. (1974)

26. Radioulnar Angle

Definition

Angle between the line tangent to the ulnar head surface facing the sigmoid notch and the radial inclination.
Normal Value: 100.4°.

Indications

Congenital disease.
Wrist injuries.

Technique

Radiography: PA view (elbow flexed 90° and the shoulder is abducted 90°. The elbow must be at shoulder height).

Full Description of Technique
(Fig. 10.39)

Line Y: tangent to the articular surface of the ulnar head facing the sigmoid notch.
Line Z: line drawn between the radial and ulnar limits of the distal radius joint surface.
Radioulnar angle (RU) = angle between line Z and line Y.

Reproducibility/Variation

Mean 100.4°±4.5.
Range 90–111°.

Clinical Relevance/Implications

The radioulnar angle is altered in malalignments of the distal radioulnar joint.

Analysis/Validation of Reference Data

Comparison with the opposite side may be helpful in case of wrist injuries.

Conclusion

A radioulnar angle <95.9° is deemed abnormal.

27. Ulnar Variance (Gelberman Method)

Definition

Ulnar variance is also called the radioulnar index. It describes the relative positions of the distal articular surfaces of the radius and ulna on a standard neutral PA wrist radiograph.

Normal Value: +0.27 mm (Gelberman et al. 1975**), +0.70 mm (**Friberg and Lundstrom 1976**).**

Indications

Kienböck's disease.
Ulnocarpal impaction syndrome.

Technique

Radiography: PA view (elbow flexed 90° and the shoulder is abducted 90°. The elbow must be at shoulder height).
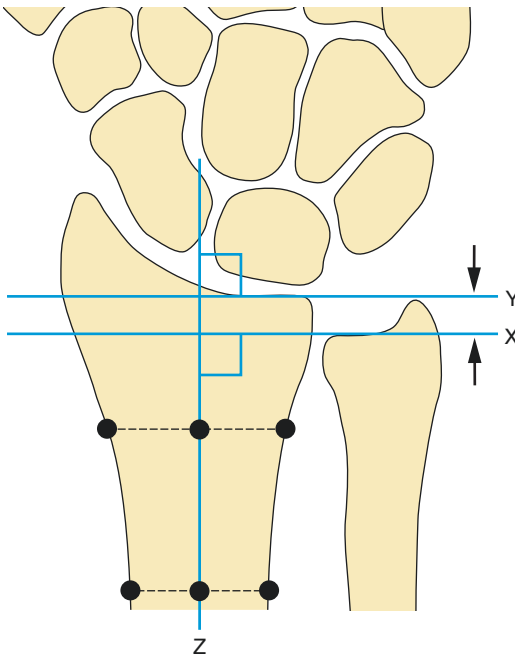
Fig. 10.40 Ulnar variance (Gelberman method). Line Z (long axis of the radius); Line X (perpendicular to line Z passing through the carpal surface of the ulna); Line Y (perpendicular to line Z passing through the lunate fossa of the radius); Ulnar variance is the distance between lines X and Y

Full Description of Technique (Fig. 10.40)

Two lines perpendicular to the mid-radius axis are drawn.
Line X: horizontal line tangent to the carpal surface of the ulna.
Line Y: horizontal line passing through the carpal joint surface of the distal end of the radius towards the ulna. Once again for consistency it is important to use the midpoint between the volar and dorsal limits of the radius at the sigmoid notch for this line to pass through.
Ulnar variance = distance in millimetres between the two lines.

Reproducibility/Variation

Of the various methods of determining ulnar variance the Gelberman method is deemed the most reliable by Steyers and Blair Steyers and Blair (1989).
Mean + 0.27±1.69 mm.
Range (−6.0)–7.0 mm (US blacks) (Gelberman et al. 1975).
Mean + 0.70±1.73 mm.
Range (−5.0)–6.0 mm (US whites) (Friberg and Lundstrom 1976).
Mean + 0.74 +/− 1.46 in neutral rotation, a value which was significantly lower in males than in females (Jung et al. 2001).
Maximum ulnar variance +1.52 +/− 1.56 mm when gripping in pronation, and
Minimum ulnar variance +0.19 +/− 1.43 mm when relaxed in supination (Jung et al. 2001).
Static unloaded radiographs may underestimate ulnar variance in wrists in which power grip and pronation result in significant proximal migration of the radius (Tomiano 2000). The author recommends that preoperative ulnar variance should be measured using both neutral rotation and pronated grip radiographs, before selecting treatment for causes of ulnar wrist pain that are affected by radioulnar length so that dynamic increases in ulnar variance are considered.

Clinical Relevance/Implications

A positive ulnar variance occurs when the distal subchondral outline of the ulna projects distally >2 mm than the adjacent distal radial articular surface. In negative ulnar variance the distal subchondral outline of the ulna is proximal to the distal articular surface of the radius by >2 mm.

Analysis/Validation of Reference Data

Studies comparing ulnar variance require carefully selected age and sex-matched controls, since a positive correlation between ulnar variance and both age and sex has been demonstrated.

Ulnar variance alters the distribution of compressive forces across the wrist. Wrist and forearm position as well as centring of the tube influence the obtained measurements. **Positive** ulnar variance is associated with ulnar impaction syndrome and TFCC tears, while **negative** ulnar variance is associated with increased incidence of Kienböck's disease and scapholunate ligament injury.

Conclusion

An accurate positioning of the wrist and the upper limit is mandatory as the ulnar variance is altered by positioning of the wrist.

28. Ulnar Variance (Palmer Method)

Definition

Ulnar variance is also called radioulnar index. It describes the relative positions of the distal articular surfaces of the radius and ulna on a wrist radiograph.

Normal Value: −0.14 mm (Palmer et al. 1982)**, −0.60 mm** (Kristensen et al. 1986)**, −0.38 mm** (Czitrom et al. 1987)**, +0.20 mm** (Nakamura et al. 1991)**, −0.90 mm** (Schuind et al. 1992)**.**

Indications

Kienböck's disease.
Ulnocarpal impaction syndrome.

Technique

Radiography: The generally accepted standard PA view obtained with the wrist in neutral forearm rotation, elbow flexed 90° and the shoulder is abducted 90°. The elbow must be at shoulder height.

Full Description of Technique

A template of concentric semicircles ranging from 22 to 50 mm is used for measuring ulnar variance.

Reproducibility/Variation

Mean − 0.60±1.38 mm.
Range   (−4.0)–2.0   mm   (Scandinavian) (Kristensen et al. 1986).

Mean − 0.38±1.48 mm.
Range (−5.0)–2.0 mm (N. American) (Czitrom et al. 1987).
Mean + 0.20±1.39 mm.
Range (−4.0)–5.0 mm (Japanese) (Nakamura).
Mean − 0.90±1.5 mm (N. American) (Schuind et al. 1992).

Clinical Relevance/Implications

A positive ulnar variance occurs when the distal cortex of the ulna projects more distally than the adjacent distal radial articular surface by >2 mm. In negative ulnar variance the distal cortex of the ulna is proximal to the distal articular surface of the radius by >2 mm.

Analysis/Validation of Reference Data

Studies comparing ulnar variance require carefully selected age and sex-matched controls, since a positive correlation between ulnar variance and both age and sex has been demonstrated.

Conclusion

An accurate positioning of the wrist and the upper limit is mandatory as the ulnar variance is altered by positioning of the wrist.

29. Ulnar Variance (Kristensen Method)

Definition

Ulnar variance is also called radioulnar index. It describes the relative positions of the distal articular surfaces of the radius and ulna on a wrist radiograph.
Normal Value: −0.84 mm.

Indications

Kienböck's disease.
Ulnocarpal impaction syndrome.

Technique

Radiography: PA view (elbow flexed 90° and the shoulder is abducted 90°. The elbow must be at shoulder height).

Full Description of Technique
(Fig. 10.41**)**

Two parallel lines are outlined (A, B) passing through the axes of the radius and ulna.
A new line (C), parallel to A and B, which strikes the ulnar border of the distal subchondral sclerotic radial line (D) is outlined. A semicircle, the radius being the distance between the point D and the styloid process of the radius (E) is drawn. The centre of the semicircle (X) lies on line C. This semi-circle approximates the distal subchondral sclerotic line of the radius. The ulnar variance is determined as the distance between the most distal part of the ulnar cortical rim and the semicircle.

Reproducibility/Variation

Mean − 0.84±1.23 mm.
Range (−4.0)–3.0 mm (Scandinavian) (Kristensen et al. 1986).

Clinical Relevance/Implications

A positive ulnar variance occurs when the distal cortex of the ulna projects >2 mm distally than the adjacent distal radial articular surface. In negative ulnar variance the distal cortex of the ulna is proximal to the distal articular surface of the radius by >2 mm.

Analysis/Validation of Reference Data

Studies comparing ulnar variance require carefully selected age and sex-matched controls, since a positive correlation between ulnar variance and both age and sex has been demonstrated.

Conclusion

An accurate positioning of the wrist and the upper limit is mandatory as the ulnar variance is altered by positioning of the wrist.
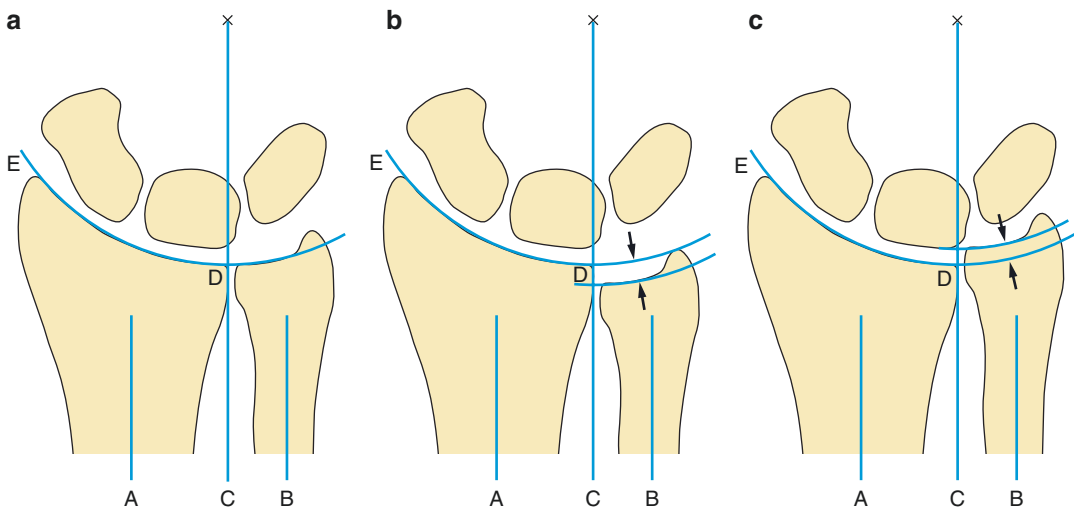
Fig. 10.41 Ulnar variance (Kristensen method). Neutral variance (**a**); negative variance (**b**); positive variance (**c**)

30. Ulnar Styloid Process Index

Definition

A relative index of the length of the ulnar styloid process relative to the other bones in the area.

Indications

Abnormal length of the ulnar styloid process can result in impaction onto the triquetral bone particularly in wrist extension producing chronic wrist pain and promoting dorsal triquetral fractures in acute settings. The chronic ulnar styloid impaction syndrome leads to chondromalacia of the proximal triquetrum, subcortical sclerosis of the styloid process, marrow oedema of the opposing surfaces, synovitis, and lunotriquetral instability Biyani et al. (1990).

Normal value: USPI	−0.21 +/− 0.07 (range 0.05–0.47)

Technique

AP standard wrist radiograph with the forearm in neutral rotation and the elbow flexed at 90°.

Full Description of Technique (Fig. 10.42)

The ulnar styloid process index (USPI) is calculated by measuring a number of distances from the radiograph and expressed through the formula:

$$\text{USPI} = C - B \text{ divided by } A.$$

A is the transverse diameter of the ulnar head, B is the ulnar variance and C is the length of the styloid process (Fig. 10.42). In essence, $C-B$ is the net portion of the styloid process projected forward of the distal articular radial surface after taking into consideration the ulnar variance.

Reproducibility/Variation

As the ulnar styloid is expressed as a ratio to the ulnar head it eliminates differences due to other factors such as age, gender, size and radiographic magnification.

Garcia-Ellis compared the USPI ratio in 76 patients with a fracture of the triquetrum and 100 control patients, and produced the following statistically relevant mean +/− SD data with a $p < 0.0001$.
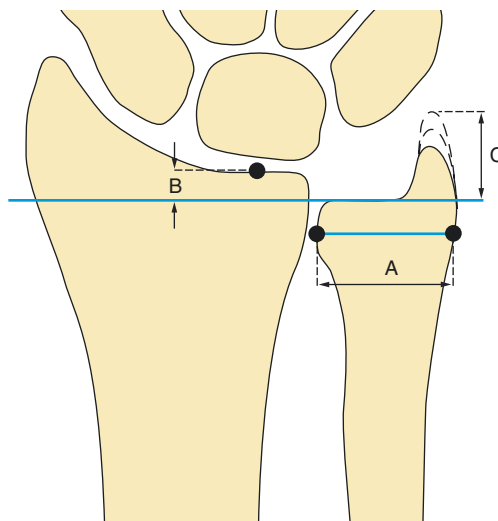
Fig. 10.42 Ulnar styloid process index (USPI). *A* (transverse diameter of the ulnar head); *B* (ulnar variance); *C* (length of the ulnar styloid process); USPI = (*C−B*)/*A*

Normal USPI	−0.21 +/− 0.07 (range 0.05–0.47)
Abnormal USPI	−0.29 +/− 0.12 (range 0.07–0.73)

The presence of complete fragment displacement and multiple fragments off the dorsal triquetrum were associated with higher mean USPI **>0.30 and 0.34** respectively**.**

Clinical Relevance/Implications

In 1979 Levy et al. provided evidence using radiographic views and cadaveric wrist dissection supporting the theory that dorsal triquetral fractures were due to a direct chisel action of the styloid process onto the triquetrum in acute hyperextension wrist injury. Garcia-Ellis' clinical study supported this mechanism as the main cause of injury rather than an avulsive dorsal ligamentous injury.

Analysis/Validation of Reference Data

Ulnar variance needs to be included in the formula as it directly influences the striking impaction potential of the tip of the styloid process on the triquetrum Topper et al. (1997).

Conclusion

In the presence of an elongated styloid process producing an increased USPI there is an increased risk of impaction syndromes and fractures of the triquetrum.

31. Lunate Deformation Quotient

Definition

Quantify deformation of the lunate in Kienböck's disease.
Normal Value: 0.53.

Indications

Kienböck's disease.

Technique

Radiography: lateral view (arm adducted against the trunk, the elbow flexed 90°, the forearm in neutral rotation (no supination or pronation) and the wrist in neutral position (no radial or ulnar deviation and no palmar flexion or extension)).

Full Description of Technique (Fig. 10.43)

The longitudinal height (AB) of the lunate is divided by its greatest dorsopalmar dimension (CD).

Reproducibility/Variation

Limited data

Clinical Relevance/Implications

The ratio is considered as the lunate deformation quotient (LDQ). The LDQ decreases with lunate deformity.

Analysis/Validation of Reference Data

None of these radiographic measurements has proven to be strongly correlated with clinical findings Stahl (1947); Mirabello et al. (1987).

Conclusion

Ratio not routinely relied upon.

Fig. 10.43 Lunate deformation quotient (LDQ). AB (height of lunate); CD (greatest dorsopalmar dimension); LDQ = AB/CD
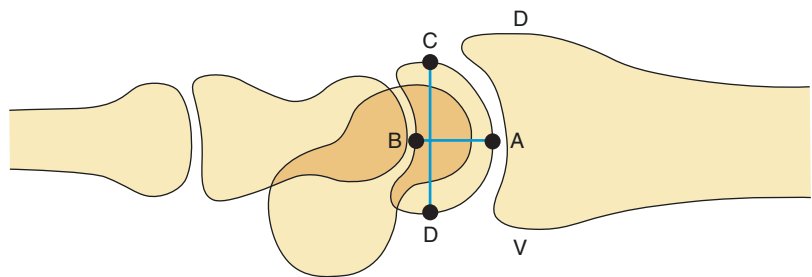
32. Metacarpal Line/Sign

Definition

Tangent line of the heads of the fourth and fifth metacarpals.

Normally the metacarpal line which is tangential to the head of the fourth metacarpal passes distal to the outline of the third metacarpal head.

Indications

Turner's syndrome, pseudohypoparathyroidism.

Technique

Radiography: PA view of the hand (elbow flexed 90° and the shoulder is abducted 90°. The elbow must be at shoulder height).

Full Description of Technique
(Fig. 10.44)

A tangential line is drawn through the distal ends of the fourth and fifth metacarpal heads. Normally the line passes distal to the head of the third metacarpal.

Reproducibility/Variation

Normally the line does not cross the third metacarpal head. A *positive* metacarpal sign is declared when the fourth metacarpal is considered short as the line intersects the third metacarpal.

Clinical Relevance/Implications

A short fourth metacarpal occurs in certain endocrine syndromes, particularly Turner's syndrome and pseudohypoparathyroidism. However it really should be regarded as a sign of growth retardation as it can be associated with other non-endocrine diseases. It can also be found in instances where no underlying cause is discovered and therefore presumed normal.

Analysis/Validation of Reference Data

When all the metacarpals are short, which sometimes occurs in pseudohypoparathyroidism, the metacarpal sign may be negative. Similarly, if there is more shortening in the third metacarpal than in the fourth metacarpal, the sign may be negative.

Conclusion

Useful and routinely relied upon but under diagnosis may occur.
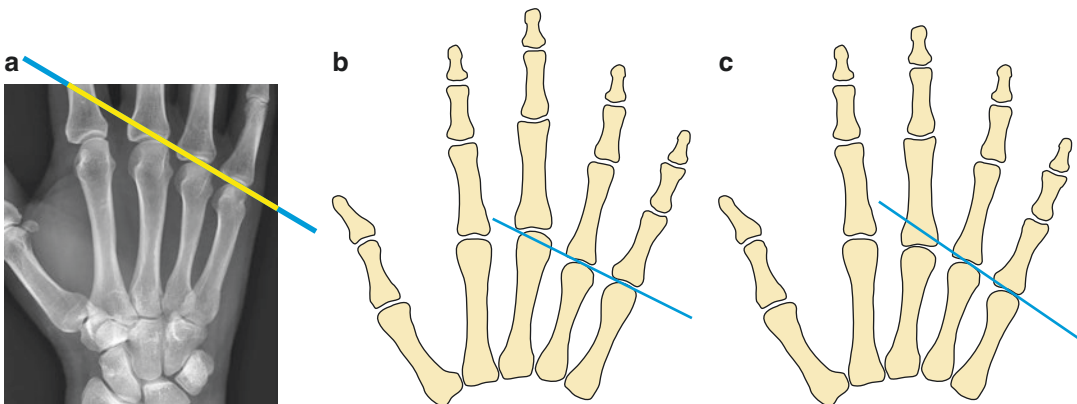
Fig. 10.44 Metacarpal line. Line is drawn as a tangent to the heads of the fourth and fifth metacarpal heads. Normal (**a**) passes through the third metacarpal compared with abnormal (**b**, **c**)

33. Metacarpal and Phalangeal Pattern Profile Analysis

Definition

Normative data on the length of the bones of each finger at various ages (year on year from age 2 to adulthood).

Indications

Skeletal dysplasia.
Turner's syndrome, pseudohypoparathyroidism, hand-foot-genital syndrome.

Technique

Radiography: PA view of the hand (elbow flexed 90° and the shoulder is abducted 90°. The elbow must be at shoulder height).

Full Description of Technique (Fig. 10.45)

Each of the hand bones is measured and compared against the normal for age and sex with the standard charts and graphs produced by Poznanski (1991).

Measurement of Length

For instance at the third finger:

Distal phalanx:	8.7 mm +/− 0.9 (2-year-old) to 20.1 mm +/− 1.2 (adult)
Middle phalanx:	14.1 mm +/− 0.8 (2-year-old) to 31.1 mm +/− 1.8 (adult)
Proximal phalanx:	21.8 mm +/− 1.0 (2-year-old) to 48.5 mm +/− 2.6 (adult)
Metacarpal:	28.6 mm +/− 1.3 (2-year-old) to 69.0 mm +/− 3.8 (adult)

Reproducibility/Variation

The number of standard deviations (Z score) each bone varies from the mean is plotted against the location of the hand. By using the standard deviation units or Z scores, adults and children of either sex are plotted on the same graph.

Clinical Relevance/Implications

A short fourth metacarpal occurs in certain syndromes, particularly Turner's syndrome and pseudohypoparathyroidism.

Analysis/Validation of Reference Data

Relatively subtle changes in alteration of hand bones can be detected with the technique of pattern profile analysis. A very characteristic pattern may be depicted in some syndrome, as hand-foot-genital syndrome. The correlation coefficient, the Pearsonian r between many congenital malformation syndromes, is published and from this table, one can determine which are unique and which are not (Poznanski 1974).

Conclusion

It is beyond the scope of this section to provide all the data that distinguish normal from abnormal measurements of each bone in different age groups. Appropriate referral to the recommended bibliography is recommended.
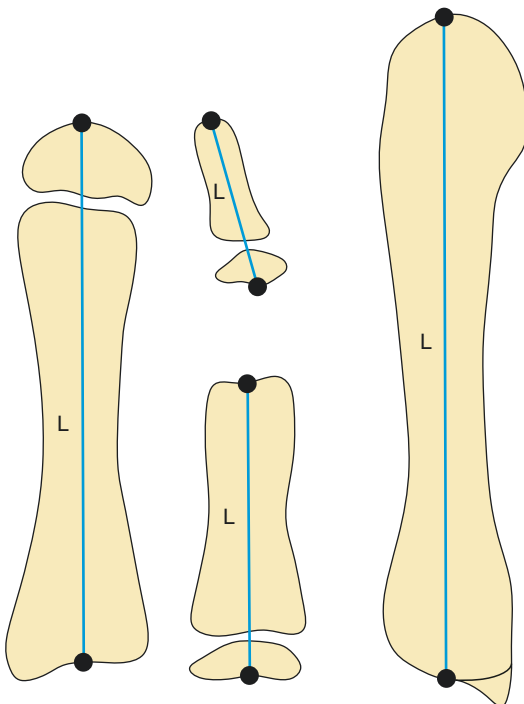
Fig. 10.45 Phalangeal/metacarpal length measurements

34. Radiogrammetry

Definition

Metacarpal morphometry and radiogrammetry are the oldest methods for quantitative assessment of the skeleton.

Indications

Osteoporosis.

Technique

Radiography: PA view of the hand (elbow flexed 90° and the shoulder is abducted 90°. The elbow must be at shoulder height).

Full Description of Technique (Fig. 10.46)

Measurements of the cortex using the Garn method of the second metacarpal are performed at a point halfway between the metacarpal head and the notch at its base excluding the styloid process. At this point measurements are made of the outside diameter of the second metacarpal (O) and the inner diameter of the medullary space at the same level (I). The cortical thickness (C) is the difference between the two values ($C = O-I$).

Measurements

For instance cortical thickness of the second metacarpal according to the age and sex Adams (2010):

1-year-old:	1.46 mm +/− 0.30 (male), 1.47 mm +/− 0.31 (female)
2-year-old:	1.85 mm +/− 0.39 (male), 1.79 mm +/− 0.36 (female)
4-year-old:	2.48 mm +/− 0.37 (male), 2.32 mm +/− 0.35 (female)
16-year-old:	5.29 mm +/− 0.51 (male), 5.08 mm +/− 0.60 (female)
30-year-old:	5.94 mm +/− 0.43 (male), 5.33 mm +/− 0.69 (female)
60-year-old:	5.24 mm +/− 0.62 (male), 4.85 mm +/− 0.68 (female)
80-year-old:	4.89 mm +/− 0.56 (male), 3.30 mm +/− 0.51 (female)
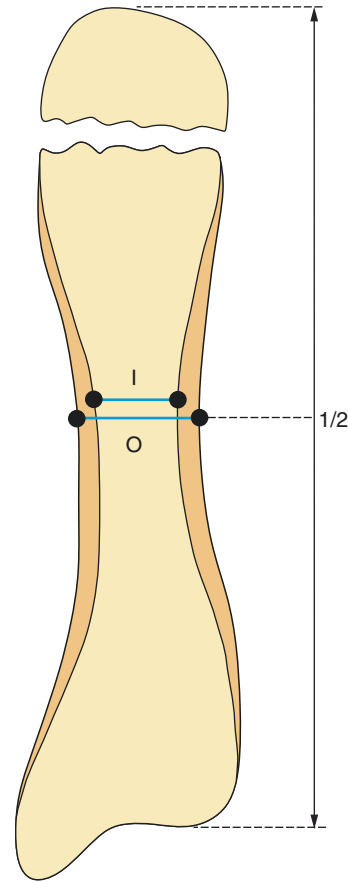
Fig. 10.46 Cortical thickness is determined using the Garn method where the midpoint of the second metacarpal is the point of measurement. The outer diameter (O) is measured and the inner diameter (I) is the subtracted from it

Reproducibility/Variation

More precise if computer based digital assessment is used.

Clinical Relevance/Implications

The thickness of the cortex of the second metacarpal is used as a measure of bone loss. The outside diameter (O) is low when there is a lack of bone apposition, which indicates a failure of growth and is seen in several conditions in children, such as long-standing juvenile rheumatoid arthritis. The inner diameter (I) is increased when there is increased endosteal bone resorption, which occurs in most forms of osteoporosis.

Analysis/Validation of Reference Data

The hand radiograph is useful for measuring bone mass, particularly in children.

Conclusion

This technique is labour intensive and imprecise and has been replaced with the current established methods of bone mineral densitometry. With the application of modern computer visual techniques, metacarpal morphometric analysis has been rejuvenated, with improvement in precision and evidence that the method can be applied to studies in both adults and children. In Digital X-Ray Radiogrammetry (DXR) the cortical thickness of the three middle metacarpal bones in the hand is measured in a digital X-ray image by a computer and through a geometric calculation is converted to bone mineral density. The BMD is corrected for porosity of the bone, estimated by a texture analysis performed on the cortical part of the bone. Like other technologies for estimating the BMD, the outputs are an areal BMD value, a T-score and a Z-score for assessing osteoporosis and risk of bone fracture.

35. Trapezial Tilt

Definition

Radiographic measure of trapezial inclination.

Indications

Trapeziometacarpal (TMC) joint osteoarthritis.

Techniques

2 techniques:

1. Radiograph Robert's view: anteroposterior (AP) radiograph of the hand.

2. Radiograph Kapandji's View: Posteroanterior (PA) Radiograph of the Hand.

Robert's View
Normal measurement.
Mean value: 42° +/−4°.

Full Description of Technique (Fig. 10.47)

The angle is obtained by taking the complement of the angle formed by the intersection of a line tangent to the middle third of the trapezial articular surface parallel to the scaphotrapezial joint and a line parallel to the proximal third of the index metacarpal (90°-α).
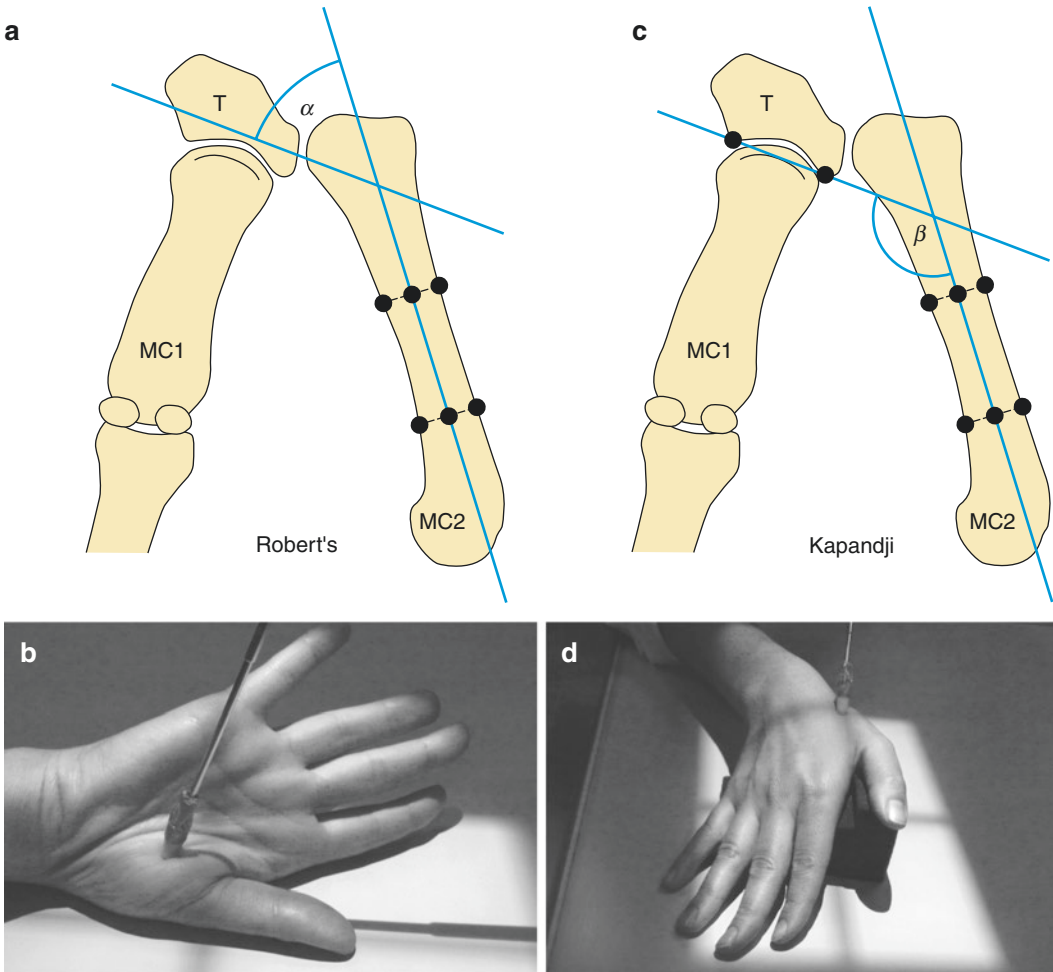
Fig. 10.47 Trapezial tilt angle measurement using the Roberts (**a**) and Kapandji (**b**) methods and the corresponding respective radiographic positions for obtaining them (**c**, **d**)

The view is standardised by checking the overlap of the sesamoid bones on the head of the thumb metacarpal.

The X-ray beam is tilted cranially in order to highlight the TM joint space.

Reproducibility/Variation

Mean: 42° +/−4°.
The trapezial tilt of the left thumb is 3° greater than on the right side (Bettinger 2001).
In early trapeziometacarpal osteoarthritis (Eaton I and II)**:** there is no significant difference in trapezial tilt with normal group.
In more severe osteoarthritis (Eaton III and IV), the angle is increased: 50° +/− 4°.

Kapandji's View
Normal Measurement.
Mean value: 129° +/−6.

Full Description of Technique (Fig. 10.47)

Tilt angle is obtained by taking a line tangent to the trapezial articular surface (with abstraction of osteophytes) and the longitudinal axis of the index metacarpal, on a PA view.

The X-ray beam is tilted caudally in order to highlight the TM joint space.

Reproducibility/Variation

Pathologic: >135°/140° (Kapandji and Kapandji 1993).

Clinical Relevance/Implications

Positive correlation between an increased trapezial tilt and severity of TMC joint osteoarthritis (Eaton 1, 2, 3, 4).
Two anatomic conditions can lead to TM osteoarthritis:

1. Joint instability: recurrent stress or overuse have been hypothesised to lead to progressive ligament instability initiating the degeneration of articular cartilage.
2. Trapezial dysplasia with increased trapezial tilt.

10.3   Advanced Imaging

1. Wrist Bone Density

Definition

Bone mass density.

Indications

To enable BMD assessment using a cost effective technique free of ionising radiation which is particularly suited for preventative studies.

Technique

Quantitative US.

Full Description of Technique

The device used is based on the transmission of ultrasound through the distal end of the proximal phalangeal diaphysis in the proximity of the condyles (region-of-interest, ROI) of the last four fingers of the hand Baroncelli et al. (2001); Drozdzowska and Pluskiewicz (2003); Pluskiewicz et al. (2006). Two 12-mm diameter transducers on a high precision (± 0.02 mm) caliper, which measures the distance between the two probes, are positioned on the lateral and medial surface of each finger. The device calculates the speed of sound (m/s) through the phalanx by measuring the width of the finger (including soft tissues) divided by the time of flight, defined as the time from emitted pulse to received signal considering the signal which reaches a predetermined minimum amplitude value (2 mV) for the first time; thus, the assessed ultrasound velocity is amplitude-dependent. Moreover, the device calculates BTT (µs) as the difference between the time when the first peak of the signal received attains its maximum and the time that would be measured if no bone but only soft tissue is present between the transducers.

Reproducibility/Variation

Measurements performed in nondominant hand (Table 10.1).

Table 10.1 Mean AD-SoS values per 1-year class through the distal end of the first phalanx diaphysis of the last four fingers of the hand in healthy male and female subjects ages 3–21 years Baroncelli et al. (2001)

Age group, (years)	AD-SoS, males (m/s)	AD-SoS, females (m/s)
3	1845.9 ± 25.5	1842.3 ± 23.0
4	1853.7 ± 21.5	1862.1 ± 25.6
5	1880.0 ± 35.2	1882.6 ± 21.9
6	1883.5 ± 35.5	1883.6 ± 27.3
7	1891.5 ± 37.4	1887.5 ± 34.9
8	1924.2 ± 29.4	1907.0 ± 38.6
9	1925.9 ± 38.7	1936.3 ± 38.2
10	1928.4 ± 42.3	1944.6 ± 32.2
11	1949.6 ± 40.6	1957.5 ± 50.1
12	1949.5 ± 45.5	2000.2 ± 72.0[c]
13	1967.8 ± 42.4	2017.6 ± 93.4[d]
14	1981.0 ± 58.0	2034.9 ± 45.3[e]
15	2032.5 ± 43.2[a]	2046.1 ± 41.3
16	2067.7 ± 47.9[b]	2059.1 ± 39.5
17	2091.4 ± 50.5	2079.2 ± 50.9
18	2099.2 ± 43.9	2083.3 ± 39.5
19	2108.4 ± 45.9	2088.6 ± 28.1
20	2115.4 ± 45.9	2094.5 ± 34.4
21	2119.1 ± 38.9	2099.8 ± 46.1

Data expressed as mean ± SD

[a]$p < 0.0001$ in comparison with 1-year younger age group

[b]$p < 0.002$ in comparison with 1-year younger age group

[c]$p < 0.01$ in comparison with males having the same chronologic age

[d]$p < 0.05$ in comparison with males having the same chronologic age

[e]$p < 0.0001$ in comparison with males having the same chronologic age

Clinical Relevance/Implications

Therefore, BTT, unlike AD-SoS, is largely independent of ultrasound attenuation and soft tissue bias, and it depends only on bone properties.

Validation/Analysis

QUS cannot replace DXA, but can screen out patients with normal bone mass. Further and larger studies are needed to examine if QUS may reflect other aspects than bone mass, or if it is possible to improve its sensitivity by supplementing the SOS results with clinical factors DeSchepper et al. (2012).

Conclusion

In conclusion, clinical risk factors for osteoporosis affected AD-SOS measurements to the same extent as axial BMD Z score measurements, but QUS alone cannot replace DXA.

2. Carpal Tunnel-Transverse Carpal Ligament (TCL)-MRI

Definition

Degree of bowing of the transverse carpal ligament (TCL) seen on MRI.

The palmar bowing of the TCL is defined as the perpendicular distance to the TCL from the line drawn between the hook of the hamate and the trapezium at *level 3*.

Indications

The carpal tunnel syndrome (CTS) is the most frequently diagnosed peripheral entrapment neuropathy and is caused by irritation of the median nerve in its osteofibrous canal at wrist level. Any condition that exerts pressure on the nerve can cause this syndrome. Different authors have regarded the palmar bowing of the transverse carpal ligament (TCL) as a risk factor for the manifestation of CTS.

Technique

MRI - axial T1 SE and T2 GE images.

Full Description of Technique
(Fig. 10.48)

The protocol for the MRI: arm wrist position prone with the arm extended over the head, the forearm in pronation, wrist in neutral position and fingers extended using the axial imaging plane from the distal radioulnar joint to the carpometacarpal joint level.

Level 1 is at the distal part of the distal radioulnar joint level where the relative position of the ulnar head to the radial sigmoid notch varies due to difference in ulnar variance. Select a slice that is closest to the distal sigmoid notch.

Level 2 is at the middle of the pisiform, and a slice is selected with the largest pisiform cross-section.

Level 3 is at the level of the hook of the hamate, and the slice with the longest dimension of the hook of hamate is selected.

Level 4 is at the exit of the carpal tunnel.

The palmar bowing of the TCL is defined as the perpendicular distance to the TCL from the line drawn between the hook of the hamate and the trapezium at level 3.

Reproducibility/Variation

Palmar bowing of the TCL At Level 3: hook of the hamate.

Palmar bowing (mm)	
Control	1.29 (0.78)
Mild to moderate CTS	2.58 (0.82)[a]
Severe CTS	2.78 (0.85)[a]
Extreme CTS	2.26 (0.84)[a] $p = 0.0182$[b]

All values are expressed as means (SD). [a]$p < 0.05$ versus control, [b]$p < 0.05$ vs. severe. The p value is not shown if <0.001

TCL transverse carpal ligament; *CTS* clinical carpal tunnel syndrome

Fig. 10.48 Axial T1 MRI sequence depicting the anatomical level at the hook of hamate to enable the measurement of the transverse carpal ligament
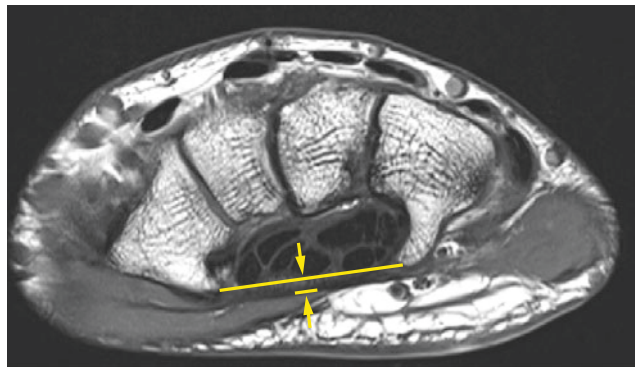
Clinical Relevance/Implications

The aetiology of idiopathic CTS may be attributed to an incompatibility of space between the median nerve and the carpal tunnel. As a result, the intracarpal tunnel pressure increases causing disturbance of circulation to the nerve. Longstanding epineural oedema leads to invasion of fibroblasts and subsequent formation of constricting scar tissue inside the nerve. Swelling of the nerve trunk proximal to the compression site is due to an increase in the amount of endoneurial connective tissue, oedema in the epineurium and endoneurial space, and obstruction of axoplasmic flow.

Analysis/Validation of Reference Data

In our clinical experience, bowing of the transverse carpal ligament is only one of the elements for the diagnosis of carpal tunnel syndrome and should be correlated with median nerve delta diameter with or without EMG studies.

Conclusion

Severity of disease could be judged by evaluating not only longitudinal changes of signal intensity and configuration of the median nerve, but also palmar bowing of the TCL. Increased palmar bowing of the TCL was found to be associated with an increase in the area of the carpal tunnel.

3. Carpal Tunnel: Cross-Sectional Area—MRI

Definition

Cross-sectional area of the carpal tunnel determined by MRI.

Indications

The carpal tunnel syndrome (CTS) is the most frequently diagnosed peripheral entrapment neuropathy and is caused by irritation of the median nerve in its osteofibrous canal at the wrist level. Any condition that exerts pressure on the nerve can cause this syndrome. Different authors have regarded the cross-sectional area of the carpal tunnel as a risk factor for the manifestation of the CTS Uchiyama et al. (2005).

Technique

MRI—axial T1 and T2 GE images.

Full Description of Technique
(Fig. 10.49)

The protocol for the MRI: arm wrist position prone with the arm extended over the head, the forearm in pronation, wrist in neutral position and fingers extended using the axial imaging plane from the distal radioulnar joint to the carpometacarpal joint level.

Level 1 is at the distal part of the distal radioulnar joint level where the relative position of the ulnar head to the radial sigmoid notch varies due to differences in ulnar variance. The slice that is closest to the distal sigmoid notch is selected.

Level 2 is at the middle of the pisiform and the slice with the largest pisiform cross-section is selected.

Level 3 is at the hook of the hamate level and the slice with the longest dimension of the hook of hamate is selected.

Level 4 is at the exit of the carpal tunnel.

The carpal tunnel area at *level 2* is bound anteriorly by the TCL, laterally by the capitotrapezial
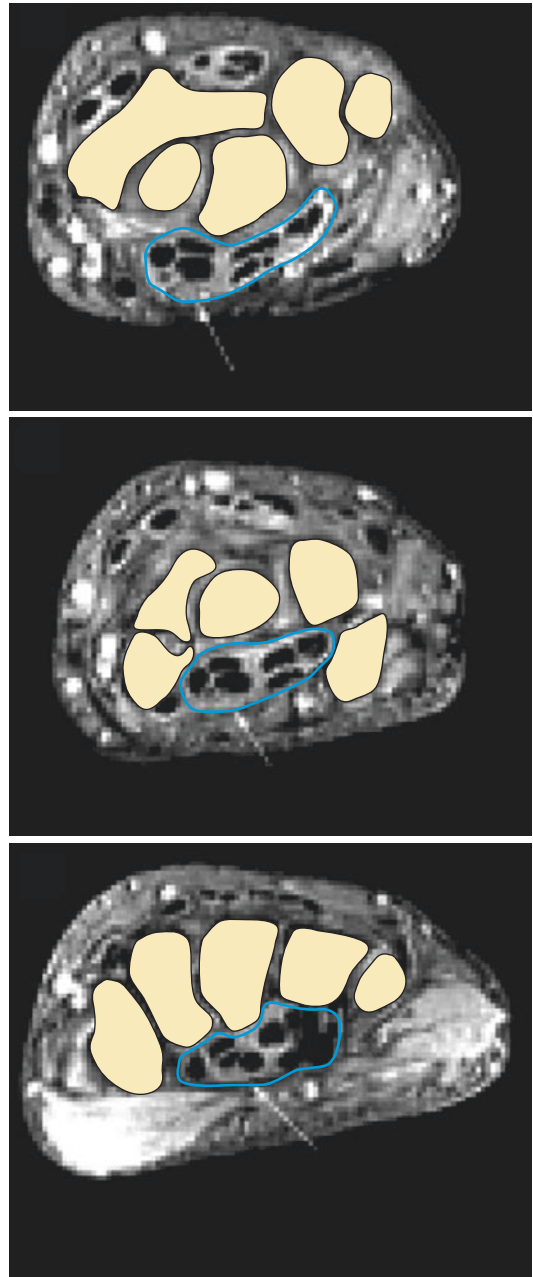
Fig. 10.49 Axial MRI images at three levels in the carpal tunnel which enable cross-sectional area measurements to be made

ligament and the scaphoid, medially by the pisiform, and dorsally by the carpal bones and the intercarpal ligament. At *level 3* it is bound anteriorly by the TCL, laterally by the

capitotrapezial ligament and the scaphoid, medially by the hook of the hamate, and dorsally by the carpal bones and the intercarpal ligaments.

Reproducibility/Variation

Results: cross-sectional area of the carpal tunnel.

	Carpal tunnel area (mm^2)	
	Level 2: Pisiform	Level 3: Hook of the hamate
Control patients	164.6 (16.6)	146.3 (13.1) 136.4 (13.1)[a]
Mild to moderate CTS	183.5 (16.8)[b]	156.8 (15.6) $p = 0.0035$[b]; 136.4 (17.5)[a]
Severe CTS	180.3 (19.3)[b]	153.4 (15.4) $p = 0.0287$[b]; 132.2 (13.0)[a]
Extreme CTS	174.2 (22.1)	150.0 (16.3) 131.1 (15.9)[a]

All values are expressed as means (SD)

[a]Carpal tunnel area in the absence of palmar bowing of the TCL

[b]$p < 0.05$ vs. control. The p value is not shown if <0.001

Clinical Relevance/Implications

There is a significant linear correlation between the area of the carpal tunnel and palmar bowing of the TCL for the CTS groups, but not for the control group. Furthermore, palmar bowing of the TCL does not have a linear correlation with wrist size in either group. These results suggest that increased palmar bowing of the TCL is a characteristic of idiopathic CTS, resulting from an increase in the area of the carpal tunnel. It may be a result of the disease, not a difference in the initial carpal tunnel area, as the carpal tunnel area in the absence of palmar bowing of the TCL of the CTS groups was the same as that of the control group. The increased area of the carpal tunnel could be due to flexor tendons and the median nerve.

Analysis/Validation of Reference Data

There are limited validation studies concerning carpal tunnel area. It should be correlated with median nerve delta cross-sectional area and/or EMG studies. The size of the carpal tunnel area has been measured by MRI and CT, but the results are inconsistent. Some studies showed a larger carpal tunnel area in patients than in controls, but others did not.

Conclusion

There are limited validation studies concerning carpal tunnel area. It should be correlated with median nerve delta cross-sectional area and/or EMG studies.

4. Carpal Tunnel Cross-Sectional Area—US

Definition

Cross-sectional area of the carpal tunnel measured by US.

Indications

The carpal tunnel syndrome (CTS) is the most frequently diagnosed peripheral entrapment neuropathy and is caused by irritation of the median nerve in its osteofibrous canal at the wrist level. Any condition that exerts pressure on the nerve can cause this syndrome. Different authors have regarded the cross-sectional area of the carpal tunnel as a risk factor for the manifestation of the CTS.

Technique

US
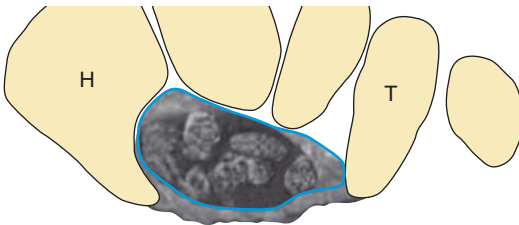
Fig. 10.50 Axial image through the carpus at the level of the hook of hamate demonstrating the cross-sectional area outline in *blue*

Full Description of Technique
(Fig. 10.50**)**

Standard US—using the software available the ultrasonograph is used to display axial images of the carpal tunnel and its contents (flexor tendons and median nerve). For standardisation, the probe is always positioned in the axial plane at the level of the hook of the hamate and the tubercle of the trapezium bone. At that level the borders of the carpal tunnel are identified as follows: the palmar border is formed by a strong, fibrous band known as the flexor retinaculum, the ulnar border by the hook of the hamate, the dorsal border by the distal carpal bones and the radial border by the tubercle of the trapezium bone.

Reproducibility/Variation (Table 10.2)

Limited data

Table 10.2 Parameters of the carpal canal measured at the level of the hook of the hamate

	Ultrasound measurements	Anatomic measurements	Correlation
DPD in mm	9.0 ± 1.1	9.3 ± 1.2	0.92
RUD in mm	20.5 ± 1.5	20.1 ± 1.5	0.81
P in mm	52.9 ± 4.1	54.9 ± 6.0	0.83
A in mm^2	162.4 ± 29.3	168.4 ± 31.2	0.95

DPD dorsopalmar diameter, *RUD* radioulnar diameter, *P* perimeter, *A* area

Clinical Relevance/Implications

The mean cross-sectional area (CSA) at the carpal tunnel level (9.0 mm^2) is smaller than that in patients with carpal tunnel syndrome (CTS) (16.8 mm^2). The mean Delta CSA is smaller in symptomatic wrists (0.25 mm^2) than in CTS- affected wrists (7.4 mm^2). Use of a Delta CSA threshold of 2 mm yield the greatest sensitivity and specificity for the diagnosis of CTS.

Analysis/Validation of Reference Data

There are limited validation studies concerning carpal tunnel area. It should be correlated with median nerve delta cross-sectional area and/or EMG studies Yao and Gai (2009).

Conclusion

Receiver operating characteristic analysis revealed improved accuracy in the diagnosis of carpal tunnel syndrome determined with the Delta CSA compared with the accuracy of the diagnosis determined with the cross-sectional area at the carpal tunnel level.

5. Carpometacarpal Ligaments: MRI

Definition

The normal ligamentous anatomy of the inter-metacarpal (IMC) and common carpometacarpal (CCMC) joints with MRI.

Indications

The anatomy of the tendons and ligaments of and about the second to fifth intermetacarpal (IMC) joints and the common carpometacarpal (CCMC) joints is quite complex and differs from the anatomy of the first ray. Although injuries of the second to fifth IMC joints and CCMC joints are relatively uncommon, their detection is important as they can result in significant functional disability of the hand Theumann et al. (2002b).

Technique (Fig. 10.51)

MRI—axial, sagittal and coronal T1 SE images.

Reproducibility/Variation

Table 10.3.

Clinical Relevance/Implications

The hand and wrist are composed of a series of arches: a longitudinal arch, formed by the
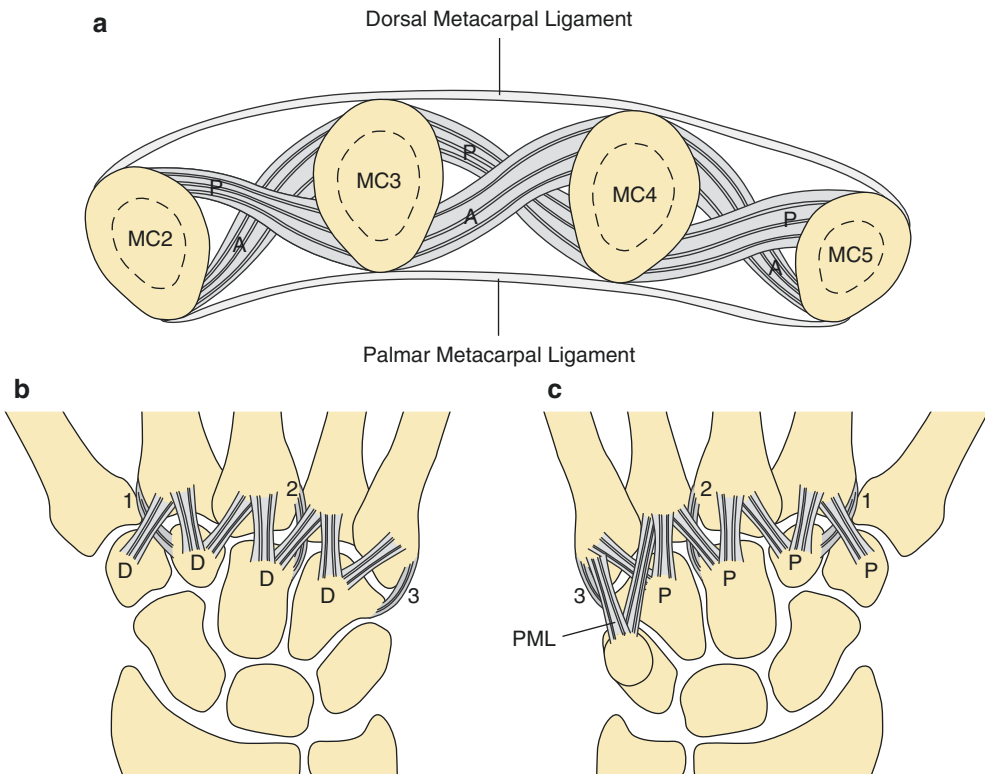
Fig. 10.51 Diagram of the 2nd–5th intermetacarpal joints at the level of the bases of the metacarpals (**a**). Diagram displaying the common metacarpal (CCMC) ligaments (**b**, **c**). The dorsal ligaments (D) span the spaces between the dorsal surface of the second carpal row bones and the dorsal surface of the bases of the 2nd–5th metacarpals (**b**). The palmar CCMC ligaments (P) join the palmar surface of the second carpal row bones and the palmar surface of the bases of the 2nd–5th metacarpals. The pisometacarpal ligament (PML) on the palmar aspect links the distal edge of the pisiform to the base of the 4th and 5th metacarpals (**c**) A,P (anterior and posterior bands of the interosseous ligaments); MC (metacarpal); 1 (radial collateral ligament); 2 (capito-third ligament); 3 (ulnar collateral ligament)

Table 10.3 Intermetacarpal ligament measurements in axial T1-weighted spin echo images

	Second space	Third space	Fourth space
Dorsal metacarpal ligament			
Length (mm)	8.7 ± 1.2 (6–10)	8.6 ± 1.4 (6–10)	11.1 ± 1.8 (10–13)
Width (mm; axial slices)	3 (2–3)	2 (2–3)	2 (1–2)
Thickness (mm)	< 1.0	< 1.0	< 1.0
Palmar metacarpal ligament			
Length (mm)	8.5 ± 1.0 (6–10)	8.4 ± 1.4 (6–10)	10.4 ± 1.8 (8–11)
Width (mm; axial slices)	3 (2–3)	2 (2–3)	2 (1–2)
Thickness (mm)	1.4 ± 0.3 (1–2)	1.4 ± 0.3 (1–2)	1.2 ± 0.3 (1–2)
Interosseous ligament, anterior band			
Length (mm)	7.2 ± 1.0 (6–8)	7.4 ± 1.1 (6–9)	NA
Width (mm; axial slices)	2 (1–2)	2 (1–2)	NA
Thickness (mm)	1.4 ± 0.3 (1–2)	1.4 ± 0.3 (1–2)	NA
Interosseous ligament, posterior band			
Length (mm)	9.0 ± 1.5 (8–10)	8.4 ± 1.4 (7–10)	NA
Width (mm; axial slices)	2 (1–2)	2 (1–2)	NA
Thickness (mm)	1.4 ± 0.3 (1–2)	1.4 ± 0.3 (1–2)	NA

Values are means ± SD (range)

NA not applicable

metacarpals and phalanges, and transverse arches at the distal carpal row and at the metacarpal heads. The longitudinal arch of the hand with the metacarpal bones of the index and middle fingers is referred to as the central fixed unit of the hand. The transverse arch is a mobile structure that facilitates power grip as well as cupping and flattening of the hand. Strong IMC ligaments are instrumental in maintaining these arches, which in turn maintain function.

Injuries to the CCMC joint can result when a large torsional force is applied to the hand. CCMC dislocations most commonly result in dorsal displacement of the metacarpal bases.

Analysis/Validation of Reference Data

Morphology and signal intensity are much more important than measurements in order to diagnose ligamentous lesions of the CMCC joints.

Conclusion

The anatomy of the ligaments and tendinous insertions about the second to fifth IMC and the CCMC joints is well demonstrated by MR imaging and MR arthrography. MR arthrography does not significantly improve the visualisation of these complex structures.

6. Excursion of the Flexor Pollicis Longus Tendon: MRI

Definition

In vivo assessment using MRI.

Indications

The possibility of visualisation and the accurate determination of the FPL-tendon excursions are of use in the reconstruction and the transposition of the FPL-tendon.

Technique

MRI—Coronal T1 SE.

Full Description of Technique

Magnetic resonance imaging (MRI) of the flexor pollicis longus tendon (FPL tendon) with the thumb in different positions allows the in-vivo assessment of its abduction-adduction/flexion excursion.

Measurements can also be performed in different positions of the wrist Ham et al. (1993).

Reproducibility/Variation

The mean excursion amplitudes of the FPL-tendon in seven healthy volunteers were shown to be 2.6 (+/− 0.26), 2.6 (+/− 0.25), and 2.7 (+/− 0.63) cm for neutral position, ulnar, and radial deviation of the wrist, respectively. The contribution of the abduction-neutral position route and the neutral position-adduction/flexion route to the total excursion of the thumb varies for the different positions of the wrist, despite the equal excursion amplitudes.

Clinical Relevance/Implications

The possibility of visualisation and the accurate determination of the FPL-tendon excursions is of use in the reconstruction and the transposition of the FPL-tendon. In addition, the shift of the FPL-tendon can be visualised for different positions of the thumb and the wrist.

Analysis/Validation of Reference Data

These measurements have to be compared, in any doubtful situation, with ultrasound measurements which are more precise and which can show the dynamic movement of the tendon.

Conclusion

Magnetic resonance imaging (MRI) of the flexor pollicis longus tendon (FPL-tendon) with the thumb in different positions allows the in vivo assessment of its abduction-adduction/flexion excursion, but this is much less precise than ultrasound.

7. Thickness of the Extensor Hood of the Fingers: US

Definition

The extensor hood is a fibrous expansion on the dorsum of the proximal phalanx of each digit. The expansion is triangular, with the base wrapped around the dorsal and collateral aspects of the metacarpophalangeal joint. A tendon of extensor digitorum (or extensor pollicis longus to the thumb) blends with the expansion along its central core, separated from the metacarpophalangeal joint by a small bursa. The interossei and lumbrical muscles attach to the expansion, which is further stabilised by links to the deep transverse metacarpal ligament. Each expansion forms a moveable hood that moves distally during flexion of the metacarpophalangeal joint.

Indications

Rupture from trauma or chronic inflammation.

Technique

US—5–13 MHz linear array transducer.

Full Description of Technique (Fig. 10.52)

At sonography, the extensor hood appears as a thin (< 2 mm) echogenic fibrillar structure that overlies the dorsal aspect of the finger Kichouh et al. (2011).

Reproducibility/Variation

At sonography, the extensor hood appears as a thin (< 2 mm) echogenic fibrillar structure that overlies the dorsal aspect of the finger. The sonographer should suspect an injury if the body of the hood, or the central tendon, becomes decentred during flexion. Injuries to the extensor hood rarely occur in the absence of rheumatoid arthritis. Tears usually involve the radial sagittal band with ulnar subluxation.

Clinical Relevance/Implications

A clear understanding of normal sonographic anatomy is required to prevent misdiagnosis and ensure optimal patient care. The anatomy of the wrist and hand is best described by considering the extensor and flexor surfaces separately.

Analysis/Validation of Reference Data

Ultrasound is a valuable tool for the assessment of injuries to the extensor dorsal hood and is an easily available method for the diagnosis of the fine soft tissue components of the dorsal hood region. However it is difficult to satisfactorily assess for the 3rd and 4th MCP joints which should be investigated by MRI to rule out any uncertainty.

Conclusion

Sonography provides a rapid, cheap, noninvasive and dynamic method for examination of the soft tissue structures of the wrist and hand Lee and Healy (2005). Familiarity with the appearance of normal anatomic structures is a prerequisite for reliable interpretation of the resultant sonograms. Assessment of the anatomy of the 3rd and 4th MCP joints requires MRI for completeness.
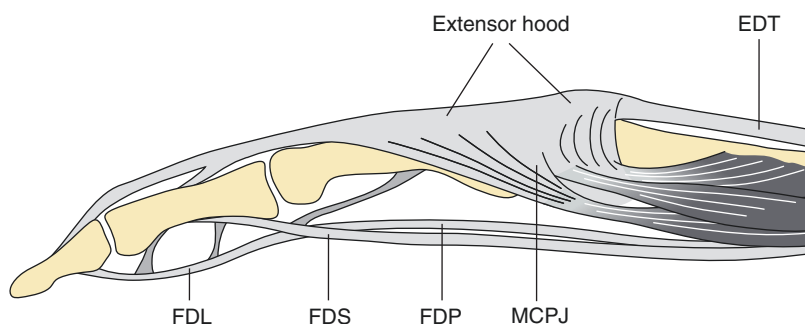
Fig. 10.52 Diagram depicting the extensor hood of the fingers

8. Extrinsic Ligaments of the Wrist: MRI

Definition

Cross-sectional and long axis measurements of the extrinsic carpal ligaments.

Indications

Assessment of carpal stability or instability.

Technique

MRI - Transverse T1 SE after arthrography, hand placed in prone position, with the wrist in neutral position in the centre of the bore.

Full Description of Technique
(Fig. 10.53)

The cross-sectional dimensions of each of the ligaments are measured digitally in at least two orthogonal planes on MR images, chosen to best show the ligaments and their bone attachments. These are measured at the midportion of each ligament and at their bone attachments Kim et al. (1994).

Reproducibility/Variation
(Tables 10.4 and 10.5)

Clinical Relevance/Implications

The ligamentous anatomy of the wrist and the ligamentous integrity are important to carpal stability Theumann et al. (2003). Controversy exists in the literature regarding the terminology applied to individual ligaments of the wrist. The carpal ligaments are divided into two major groups: extrinsic ligaments and intrinsic ligaments. The intrinsic ligaments are ligaments that are entirely within the carpus located between carpal bones. The extrinsic ligaments are those that have an attachment on the carpus and pass out of the carpus. Injuries to the intrinsic and extrinsic ligaments of the wrist are probably more common than appreciated. The identification of ligamentous attachment sites is important to ensure analysis of the entire ligament.
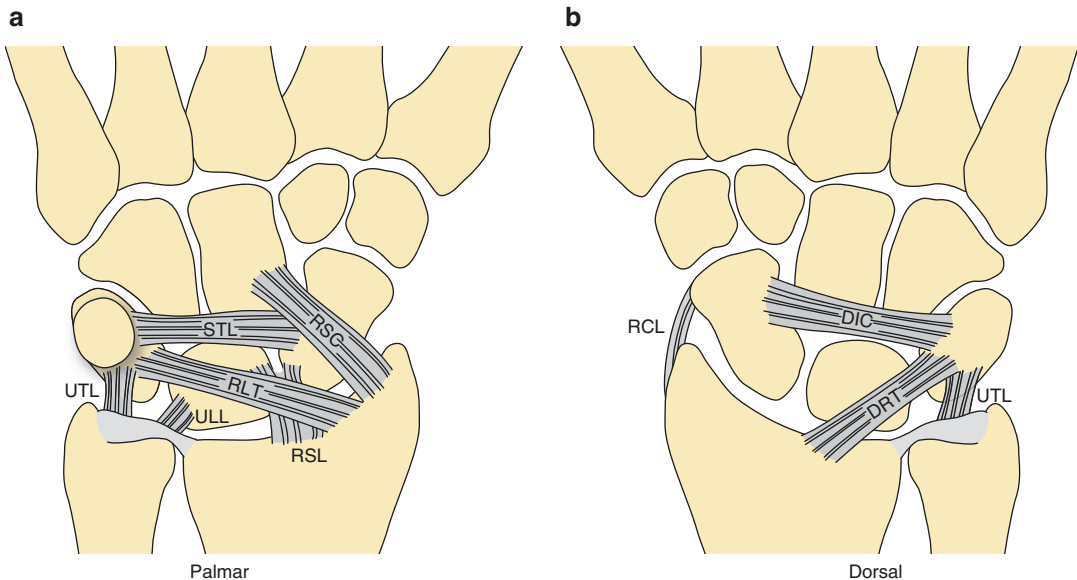
Fig. 10.53 Diagram showing the extrinsic palmar and dorsal carpal ligaments. The palmar ligaments (**a**) include the radioscaphocapitate (RSC); radiolunotriquetral (RLT); radioscapholunate (RSL); ulnotriquetral (UTL); ulnolunate (ULL); scaphotriquetral (STL) ligaments. The dorsal ligaments (**b**) include the dorsal radiotriquetral (DRT); dorsal intercarpal (DIC); ulnotriquetral (UTL); radial collateral (RCL) ligaments

Table 10.4 Measurements of cross-sectional dimensions of ligaments in the optimal plane

Diameter (mm)			
Ligament and its parts	Plane	Long axis	Short axis
RSC			
Radioscaphoid	Sagittal	7.0 (1.5)	2.8 (0.8)
Scaphocapitate	Sagittal	7.3 (1.6)	7.3 (1.6)
RLT			
Radiolunate	Sagittal	8.0 (2.0)	3.1 (0.7)
Lunotriquetral	Sagittal	7.4 (1.4)	3.1 (0.7)
Radioscapholunate	Transverse	2.5 (0.8)	2.2 (0.7)
Palmar ulnotriquetral	Transverse	5.8 (0.8)	3.0 (0.7)
Ulnolunate	Transverse	5.4 (0.8)	2.6 (0.8)
Palmar scaphotriquetral			
Scaphocapitate	Sagittal	7.3 (1.2)	2.6 (0.5)
Capitotriquetral	Sagittal	6.3 (1.2)	2.4 (0.5)
Dorsal scaphotriquetral	Sagittal	7.4 (1.6)	1.6 (0.9)
Dorsal radiotriquetral	Sagittal	5.5 (1.7)	1.7 (0.6)
Dorsal ulnotriquetral	Transverse	6.5 (2.1)	2.1 (0.5)
Radial collateral	Transverse	5.1 (1.2)	1.2 (0.4)

Table 10.5 MR diameter measurements of carpal ligaments and their attachments

Ligament	Radius (mm)	Radioulnar Ligament (mm)	Scaphoid (mm)	Lunate (mm)	Triquetrum (mm)	Capitate (mm)
Transverse plane						
RSC	6.0 ± 1.3	NA	6.8 ± 1.4	NA	NA	8.2 ± 1.7
RLT	6.0 ± 1.3	NA	NA	11.6 ± 1.6	5.5 ± 1.1	NA
Radioscapholunate	2.4 ± 0.6	NA	2.1 ± 0.7	NA	NA	NA
Palmar ulnotriquetral	NA	5.8 ± 0.6	NA	NA	6.5 ± 1.4	NA
Ulnolunate	NA	5.3 ± 0.6	NA	6.0 ± 1.2	NA	NA
Palmar scaphotriquetral	NA	NA	6.9 ± 1.5	NA	5.3 ± 0.6	NA
Dorsal scaphotriquetral	NA	NA	6.2 ± 1.4	9.6 ± 1.1	6.0 ± 1.3	8.3 ± 1.6
Dorsal radiotriquetral	3.9 ± 0.8	NA	NA	NA	5.6 ± 1.0	NA
Dorsal ulnotriquetral	NA	6.0 ± 0.8	NA	NA	7.0 ± 1.1	NA
Radial collateral[a]	5.3 ± 0.8	NA	5.2 ± 0.7	NA	NA	NA
Sagittal plane						
RSC	11.8 ± 2.1	NA	6.8 ± 2.0	NA	NA	7.3 ± 1.6
RLT	11.8 ± 2.1	NA	NA	8.9 ± 1.2	8.1 ± 1.3	NA
Radioscapholunate	2.9 ± 0.6	NA	2.9 ± 0.6	NA	NA	NA
Palmar ulnotriquetral	NA	3.6 ± 0.7	NA	NA	7.2 ± 1.1	NA
Ulnolunate	NA	3.6 ± 0.7	NA	8.6 ± 1.5	NA	NA
Palmar scaphotriquetral	NA	NA	7.5 ± 1.3	NA	6.0 ± 0.8	NA
Dorsal scaphotriquetral	NA	NA	6.1 ± 1.2	3.1 ± 0.8	6.6 ± 1.0	7.6 ± 1.2
Dorsal radiotriquetral	4.0 ± 0.7	NA	NA	NA	6.8 ± 1.2	NA
Dorsal ulnotriquetral	NA	3.6 ± 0.6	NA	NA	6.6 ± 1.3	NA
Radial collateral[a]	3.6 ± 0.8	NA	4.3 ± 0.9	NA	NA	NA

NA not applicable
[a]Measured in transverse and coronal planes

Analysis/Validation of Reference Data

Morphology, attachments and signal intensity are much more important than measurements in order to diagnose extrinsic ligamentous lesions.

Conclusion

MR arthrography allows visualisation of the carpal ligaments. Detailed knowledge of the normal appearance of these ligaments can serve as a baseline for future studies in which MR arthrography is used to characterise wrist instability from ligamentous pathology.

9. Hamatolunate Facet Size

Definition

The hamatolunate facet is an anatomic variant of the midcarpal joint of the wrist consisting of an additional articulation between the hamate and lunate bones.

Indications

Usually only one distal articular facet, articulating with the capitate bone, is present in the lunate bone. In cases with a hamatolunate facet, a second facet in the ulnar side of the lunate bone articulates with the proximal pole of the hamate Pfirrmann et al. (2002). A lunate with this additional facet has been termed a type II lunate, while a type I lunate does not have this additional facet. The reported frequency of a hamatolunate facet has varied between 44 and 73%. This facet has received a great deal of attention by hand surgeons because of its strong association with marked cartilage lesions in the proximal pole of the hamate and with ulnar-sided wrist pain.

Technique

MRI -Coronal T_1 SE.

Full Description of Technique
(Fig. 10.54)

An additional facet at the lunate (type II lunate) is considered only when a concave or straight additional joint surface was present that could be differentiated from the main joint surface. A convex surface is not considered as an additional facet. The size of the facet is measured as displayed (distance y).

Reproducibility/Variation

The mean coronal size of the facet in the lunate is **4.5 mm (range, 2–6 mm).** The size of the facet is usually not uniform throughout all the consecutive coronal sections, and the facet is often larger at the dorsal aspect of the wrist than at the more palmar aspect.
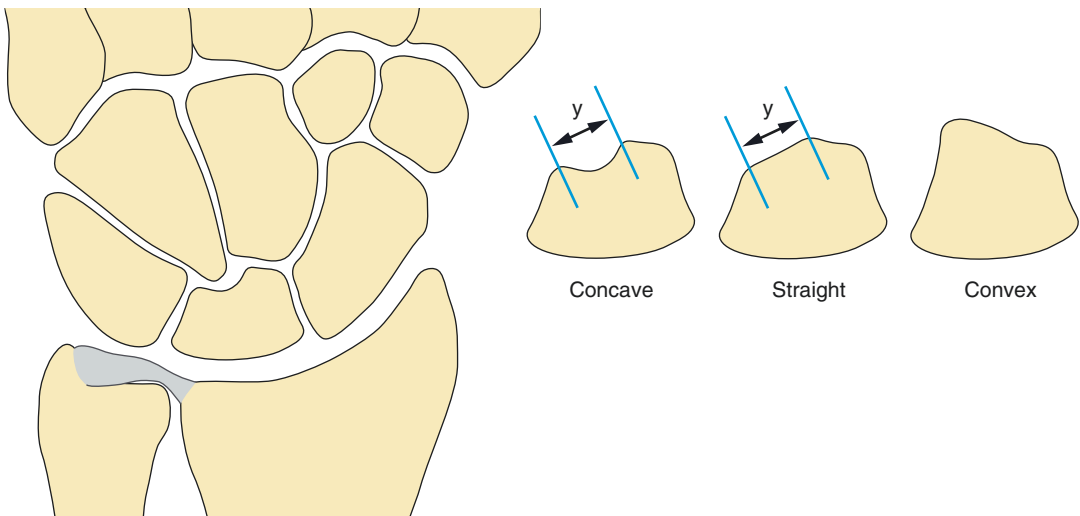
Fig. 10.54 Hamatolunate facet size variants and estimation

Clinical Relevance/Implications

The hamatolunate facet is a very common anatomic variant. The presence of a hamatolunate facet is associated with cartilage damage in the proximal pole of the hamate.

Analysis/Validation of Reference Data

Without a hamatolunate facet joint, osteoarthritis is rarely seen at this site. Primary OA of the ulnar portion of the wrist is most frequently seen at the DRUJ and the second most frequent site is in the ulnolunate joint. Ulnar variance is correlated mostly with OA in the ulnar aspect of the wrist joint.

Conclusion

The hamatolunate facet is a very common anatomic variant. The presence of a hamatolunate facet is associated with cartilage damage in the proximal pole of the hamate.

10. Ligaments and Palmar Plates of the Metacarpophalangeal Joints—MRI

Definition

Measurements of the ligaments and palmar plates of the normal metacarpophalangeal joints of the fingers with MRI Theumann et al. (2002a).

Indications

Imaging of the MCP joints of the fingers is not performed routinely. Palmar plate and collateral ligaments are often sites of injuries and are well depicted with MRI or MR arthrography.

Technique

MRI—axial and sagittal T1 SE +/− arthrography.

Full Description of Technique (Fig. 10.55)

Conventional and arthrographic transverse T1-weighted spin-echo MR images of the joints in flexion allow the most complete analysis for the main collateral ligaments.

Conventional and arthrographic transverse T1-weighted spin-echo MR images of the joints in extension provide the best visualisation of the accessory collateral ligaments.

Transverse and sagittal T1-weighted spin-echo MR images and arthrograms of the joints in either extension or flexion are the best ways to evaluate the palmar plate.

Reproducibility/Variation

Tables 10.6 and 10.7.
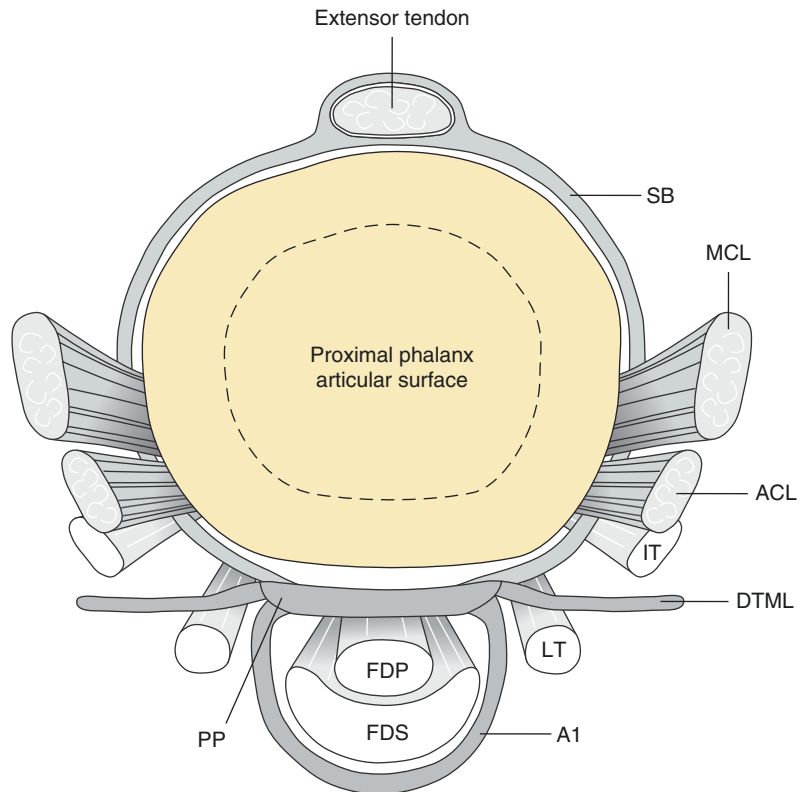
Fig. 10.55 Ligaments and palmar plates of the proximal metacarpophalangeal joints. Palmar plate (PP); Flexor tendons (FDP, FDS); A1 (pulley); Lumbrical tendon (LT); Deep transverse metacarpal ligament (DTML); Interosseous tendon (IT); Accessory collateral ligament (ACL); Main collateral ligament (MCL); Sagittal band (SB)

Table 10.6 MCP joint measurements

Measured structure	Mean (mm)	Range (mm)
Second finger		
Radial main CL	2.0	1.8–2.3
Ulnar main CL	2.0	1.8–2.3
Radial accessory CL	2.0	1.5–2.5
Ulnar accessory CL	1.7	1.3–2.0
PP, longest size in extension	11.0	10.0–12.0
PP, maximal thickness in extension	2.6	2.3–3.3
PP, minimal thickness in extension	1.5	1.0–2.0
Third finger		
Radial main CL	2.7	2.3–3.0
Ulnar main CL	2.1	1.5–3.0
Radial accessory CL	1.5	1.3–2.3
Ulnar accessory CL	1.5	1.0–1.8
PP, longest size in extension	11.9	11.0–13.5
PP, maximal thickness in extension	2.8	2.3–3.5
PP, minimal thickness in extension	1.4	1.3–2.0
Fourth finger		
Radial main CL	2.2	1.8–3.0
Ulnar main CL	2.0	1.5–2.8
Radial accessory CL	1.6	1.3–2.0
Ulnar accessory CL	1.4	1.3–1.5
PP, longest size in extension	11.3	9.8–13.0
PP, maximal thickness in extension	2.4	2.0–2.8
PP, minimal thickness in extension	1.3	1.0–1.8
Fifth finger		
Radial main CL	2.1	1.8–2.5
Ulnar main CL	1.9	1.5–2.3
Radial accessory CL	1.4	1.3–1.5
Ulnar accessory CL	1.3	1.0–1.8
PP, longest size in extension	8.2	7.0–8.8
PP, maximal thickness in extension	2.3	2.0–2.8
PP, minimal thickness in extension	1.1	1.0–1.3

CL collateral ligament

Table 10.7 Correlation between articular structure measurements and presence of cartilaginous lesions

Articular structure	Mean size	Range	SD	Cartilaginous lesions of pisiform bone	Cartilaginous lesions of triquetral bone
Proximal recess	7.8	3–12	2.1	$P = 0.943$	$P = 0.724$
Distal recess	2.3	0–4	1.1	$P = 0.535$	$P = 0.909$
Pisiform bone					
Transverse	8.9	7–10	0.9	$P = 0.822$	$P = 0.743$
Sagittal	9.3	7–10	2.1	$P = 0.886$	$P = 0.775$
Triquetral bone					
Transverse	9.2	7–11	1.1	$P = 0.663$	$P = 0.718$
Sagittal	11.4	10–13	1.2	$P = 0.812$	$P = 0.796$
Pisotriquetral separation					
In flexion	2.0	0–5	1.6	NC	NC
In extension	4.4	2–7	1.8	NC	NC

Significance level was set to $P < 0.05$. All data were calculated with the Spearman rank test. *NC* not calculated

Clinical Relevance/Implications

Although uncommon, injuries of the metacarpo-phalangeal (MCP) joints of the fingers necessitate accurate diagnosis, because the loss of function of even one MCP joint can seriously impair overall hand function. To ensure appropriate treatment, the identification of the damaged structures at the time of injury is essential. Advances in magnetic resonance (MR) imaging technology that improve spatial resolution enable the visualisation of important intra-articular and periarticular struc-tures, even in small joints such as the MCP joints, with standard clinical equipment. Detailed knowl-edge of the normal anatomy remains essential to the analysis of MR images of this area.

The main collateral ligaments have a primary role in stabilising the MCP joint in all modes of joint alignment and especially in flexion.

The accessory collateral ligaments prevent palmar displacement of the proximal phalanx. Conventional and arthrographic transverse T1-weighted spin-echo MR images of the joints in extension provided the best visualisation of these ligaments.

The palmar plate (PP) prevents hyperexten-sion and dorsal subluxation of the MCP joints. Transverse and sagittal T1-weighted spin-echo MR images and arthrograms of the joints in either extension or flexion are the best way to evaluate the PP.

Analysis/Validation of Reference Data

Morphology, attachments and signal intensity are much more important than measurements in order to diagnose extrinsic ligamentous lesions.

Conclusion

Conventional MR imaging and MR arthrography enable accurate visualisation of the important anatomic structures of the MCP joints. MR arthrography enhances visualisation of the intra-articular elements.

11. Cross-Sectional Area of the Median Nerve—MRI/US

Definition

Cross-sectional area of the median nerve in the carpal tunnel.

Indications

Carpal tunnel syndrome.

Technique

MRI	T2-GE images
US	7.5 MHz or > high resolution probe

Full Description of Technique
(Fig. 10.56)

The Protocol for the MRI

Arm wrist position prone with the arm extended over the head, the forearm in pronation, wrist in neutral position and fingers extended using the axial imaging plane from the distal radioulnar joint to the carpometacarpal joint level.

Level 1 is at the distal part of the distal radioulnar joint level where the relative position of the ulnar head to the radial sigmoid notch varies due to difference in ulnar variance. Select a slice as closest to the distal sigmoid notch.

Level 2 is at the middle of the pisiform; select a slice that shows the largest pisiform section.
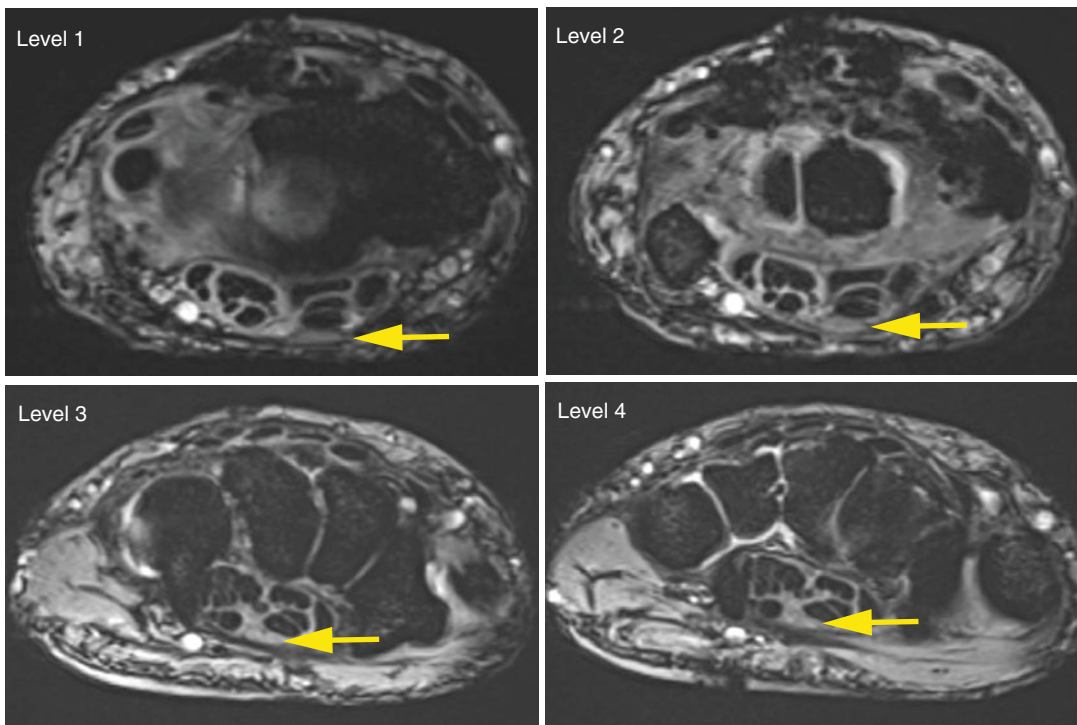
Fig. 10.56 Cross-sectional area measurements of the median nerve (*arrow*) in the carpal tunnel at levels 1–4

Level 3 is at the hook of the hamate level; select a slice with the longest dimension of the hook of hamate.

Level 4 is at the exit of the carpal tunnel.

The signal intensity of the nerve is expressed as a ratio, which is calculated with respect to the signal intensity of the hypothenar muscles at level 4, to avoid variations in signal that are encountered with surface coils.

Thus, a value < 1.0 means a higher intensity than the hypothenar muscle, and vice versa.

The flattening ratio is calculated by dividing the transverse axis of the nerve by its longitudinal axis at the four levels Cudlip et al. (2002).

The Protocol for the US

Standard US-software available at ultrasonography is used to display axial images of the carpal tunnel and its contents (flexor tendons and median nerve) Kamolz et al. (2001). For standardisation, the probe is always positioned at the level of the hook of the hamate and the tubercle of the trapezium bone. At that level the borders of the carpal tunnel are identified as follows; the palmar border is formed by a strong, fibrous band

known as the flexor retinaculum, the ulnar border by the hook of the hamate, the dorsal border by the distal carpal bones and the radial border by the tubercle of the trapezium bone.

Reproducibility/Variation

Ultrasound Measurement of the Median Nerve

Parameters of the median nerve measured at the level of the hook of the hamate Kamolz et al. (2001).

	Ultrasound measurements	Anatomic measurements	Correlation
DPD in mm	1.8 ± 0.2	2.1 ± 0.4	0.89
RUD in mm	6.5 ± 1.1	5.2 ± 1.0	0.77
P in mm	13.8 ± 1.5	14.5 ± 0.1	0.84
A in mm²	9.2 ± 2.4	9.4 ± 2.2	0.91

DPD dorsopalmar diameter, *RUD* radioulnar diameter, *P* perimeter, *A* area

Cross-sectional area, signal intensity ratio and flattening ratio of the median nerve with MRI.

	Level 1: DRUJ	Level 2	Level 3	Level 4
Cross-sectional area (mm²)				
Control (*n* = 36)	9.0 (2.5)	9.1 (2.3)	8.8 (1.8)	8.3 (2.0)
Mild/moderate (*n* = 33)	14.1 (4.8)[a]	14.6 (4.8)[a]	10.8 (3.0)[a]	10.9 (3.2)[a]
Severe (*n* = 50)	17.7 (6.7)[a]	14.6 (5.6)[a]	11.2 (3.3)[a]	11.4 (3.5)[a]
	p = 0.0085[b]			
Extreme (*n* = 22)	19.5 (7.4)[a]	14.8 (5.5)[a]	10.0 (3.1)	10.8 (3.2)[a]
	p = 0.0015[b]			
Signal intensity ratio				
Control	3.31 (1.71)	3.14 (1.79)	3.16 (1.86)	3.47 (1.73)
Mild to moderate	2.08 (1.02)[a]	2.07 (1.02)	2.54 (1.27)	2.50 (1.07)
	p = 0.0038[a]	*p* = 0.008[a]		
Severe	1.45 (1.07)[a]	1.86 (1.40)[a]	2.36 (1.44)	2.36 (1.41)
	p = 0.0093[b]	*p* = 0.026[a]	*p* = 0.0018[a]	
Extreme	1.24 (0.58)[a,b]	1.78 (1.40)	2.43 (1.31)	2.35 (1.06)
	p = 0.0037[a]	*p* = 0.0086[a]		
Flattening ratio				
Control	2.14 (0.41)	2.33 (0.52)	2.63 (0.67)	3.04 (0.70)
Mild to moderate	2.38 (0.61)	2.62 (0.55)[a]	2.76 (0.75)	2.87 (0.55)
	p = 0.0245			
Severe	2.56 (0.49)[a]	2.84 (0.55)[a]	2.53 (0.61)	2.77 (0.74)
Extreme	2.64 (0.42)[a]	2.92 (0.63)[a]	2.62 (0.87)	2.94 (1.19)

All values are expressed as means (SD)
[a]*p* < 0.05 vs. control
[b]*p* < 0.05 vs. mild to moderate. The *p* value is not shown if <0.001. *TCL* transverse carpal ligament

Clinical Relevance/Implications

The aetiology of idiopathic CTS may be attributed to an incompatibility of relative space between the median nerve and carpal tunnel. As a result, the intracarpal tunnel pressure increases causing disturbance of circulation to the nerve. Longstanding epineurial oedema leads to invasion of fibroblasts and subsequent formation of constricting scar tissue inside the nerve. Swelling of the nerve trunk proximal to the compression site is due to an increase in the amount of endoneurial connective tissue, oedema in the epineurium and endoneurial space, and obstruction of axoplasmic flow.

Macroscopic configuration of the median nerve during open carpal tunnel surgery has varied; however, conventionally proximal enlargement of the median nerve, or pseudoneuroma is believed to result from compression in the distal carpal tunnel, indicating a reduction in the size of the nerve or flattening of the nerve at the hook of the hamate level.

Imaging techniques can be used to detect these morphological changes Yao and Gai (2009). Configuration of the median nerve is the parameter most widely investigated not only by MRI, but also by ultrasonography, because delineation of this nerve is easy. Enlargement of the cross-sectional area of the median nerve at the proximal carpal tunnel or at the entrance to the tunnel is found to be of diagnostic value for idiopathic CTS.

The mean cross-sectional area (CSA) at the carpal tunnel level, in healthy volunteers (9.00 m^2) is smaller than that in patients with carpal tunnel syndrome (CTS) (16.8 mm^2). The mean delta cross-sectional area is smaller in asymptomatic wrists (0.25 mm^2) than in CTS-affected wrists (7.4 mm^2). Use of a Delta CSA threshold of 2mm2yield the greatest sensitivity and specificity for the diagnosis of CTS.

Analysis/Validation of Reference Data

Receiver operating characteristic analysis is mandatory to improve accuracy in the diagnosis of carpal tunnel syndrome determined with the Delta CSA compared with the accuracy of the diagnosis determined with the cross-sectional area at the carpal tunnel level.

Conclusion

Receiver operating characteristic analysis revealed improved accuracy in the diagnosis of carpal tunnel syndrome determined with the Delta CSA compared with the accuracy of the diagnosis determined with the cross-sectional area at the carpal tunnel level.

12. Pisotriquetral Joint

Definition

Ulnar Flexor Tendon, Pisohamate Ligament, and Pisometacarpal Ligament measurements.

Indications

Pain and tenderness are common in the palmar and ulnar aspects of the wrist in the area of the pisiform bone.

Technique

MRI—axial, coronal and sagittal T1 SE images.

Full Description of Technique
(Fig. 10.57)

–
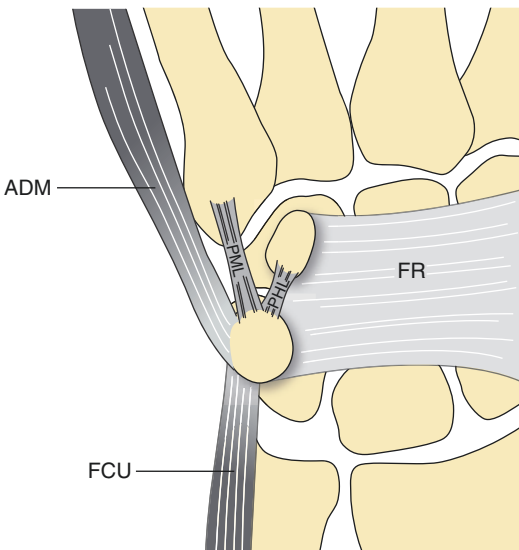
Fig. 10.57 Pisiform soft tissue attachments. Abductor digiti minimi muscle (ADM); Flexor carpi ulnaris tendon (FCU); Pisohamate ligament (PHL); Pisometacarpal ligament (PML); and Flexor retinaculum (FR)

Reproducibility/Variation

Measurements of Ulnar Flexor Tendon, Pisohamate Ligament, and Pisometacarpal Ligament Theumann et al. (2002c).

Anatomic structure and parameter	Mean (mm)	Range (mm)
Ulnar flexon tendon		
Width	8.3	6–12
Thickness	3.2	3–4
Pisohamate ligament		
Length	7.3	5–11
Width	6.6	5–10
Width	6.6	5–10
Thickness	6.2	5–10
Pisometacarpal ligament		
Length	10.2	7–14
Width	3.3	3–4
Thickness	2.9	2–4

Clinical Relevance/Implications

Pain and tenderness are common in the palmar and ulnar aspects of the wrist in the area of the pisiform bone. When chronic, this pain may be due to tendinopathy at the insertion site of the ulnar flexor tendon, to carpal fractures, or to osteoarthritis of the pisotriquetral joint (PTJ). The PTJ is the second most common site of osteoarthritis in the wrist after the scaphotrapezial joint, if the first carpometacarpal joint is excluded. Instability of the PTJ is a recognised complication of osteoarthritis of this joint. Degenerative changes of the PTJ often remain undiagnosed at clinical and radiographic evaluation.

Analysis/Validation of Reference Data

Morphology, attachments and signal characteristics are much more important than measurements in order to diagnose extrinsic ligamentous lesions.

Conclusion

MR imaging and/or MR arthrography allows visualisation of all anatomic structures of the PTJ. MR arthrography improves visualisation of findings related to osteoarthritis.

13. Scapholunate Interval—MRI

Definition

The interval at the level of the midpoint between the scaphoid and lunate articular surfaces.

Indication

Scapholunate interval measurements with MRI.

Indications

Pain and signs suggesting scapholunate dissociation usually following trauma.

Technique

MRI—axial and coronal T1 and T2 GE.

Full Description of Technique (Fig. 10.58)

Scapholunate interval measurements with MRI are based on mid-SL joint image from both the axial and coronal planes.

Reproducibility/Variation

The most consistent and narrowest distance between the scaphoid and lunate is found at midjoint: coronal **1.45 mm** (44% coefficient of variation) and axial **1.00 mm** (22% coefficient of variation).

Clinical Relevance/Implications

Measurement of the apparent SL joint interval in an inappropriate site, as with extended or flexed clenched fist views, may provide inaccurate SL joint interval distance assessments. Regardless of SL joint configuration, the midportion of the SL joint shows only moderate biologic variation and the least absolute measurement variance in width and should be the most precise part of the joint to measure. On magnetic resonance imaging, the normal SL joint interval measures less than **2 mm.**

Analysis/Validation of Reference Data

Many different stress views for the diagnosis of scapholunate instability have been described in the literature, and as covered in the previous sections, radiographic assessment is very sensitive with these techniques in demonstrating diastasis at the scapholunate interface.

Conclusion

Measurement of the apparent SL joint interval is a useful adjunct in the exclusion of scapholunate injury besides direct assessment of the status of the scapholunate ligament The measurement needs to be done at the midpoint of the joint as this carries the best precision due to the least biological variation and least absolute measurement variance in width at this point. Although an interval < 2 mm is expected in normal status, stress radiographic views still are recommended to exclude dynamic SL instability.
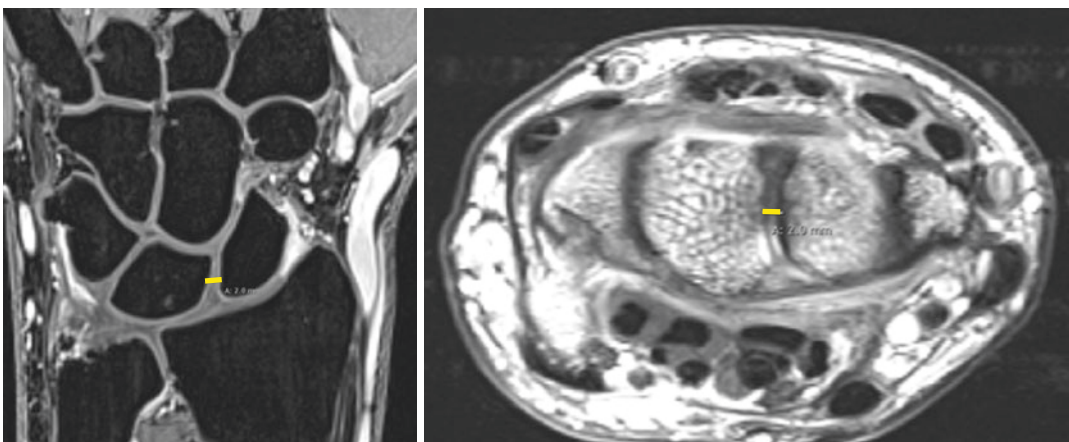
Fig. 10.58 Scapholunate distance measurement on MRI at the midpoint of the joint in coronal and axial planes

14. Torsion Angles of Long Bones of the Fingers-CT

Definition

Using CT it is possible to measure the torsion angles of the long bones of the fingers.

Indications

Rotational dislocation at the fracture site is a complication of long bone fractures of the metacarpals and phalanges. To evaluate such deformities, CT of the articular surfaces of these bones is performed to demonstrate the torsion angles.

Technique

CT—The parameters used are 140 kV and 111 mA, slice thickness 2 mm for the topogram, and 140 kV and 111 mA, slice thickness 1 mm for the tomogram.

Full Description of Technique (Fig. 10.59)

The torsion of the long bone axes is defined as the angle between a tangent positioned parallel to the proximal articular surface (or the "baseline" in the case of the metacarpal arch) and a tangent parallel to the distal articular surface of individual bones. The "baseline" at the proximal ends of the metacarpal bone arch is defined as shown in Fig. 10.59b (bottom line).

The dorsal surfaces of the metacarpal heads are flat, so that the measurements are performed along the dorsal contour as shown in Fig. 10.59b (top line).

The phalangeal bones have an oval shape at the proximal ends and have tiny condyles at the distal ends, so the reference lines are measured along the volar margin as shown in Fig. 10.59c, d.

Outward rotation is referred to as supination, inward rotation as pronation.

Fig. 10.59a Suggested positioning of a patient for measurement.
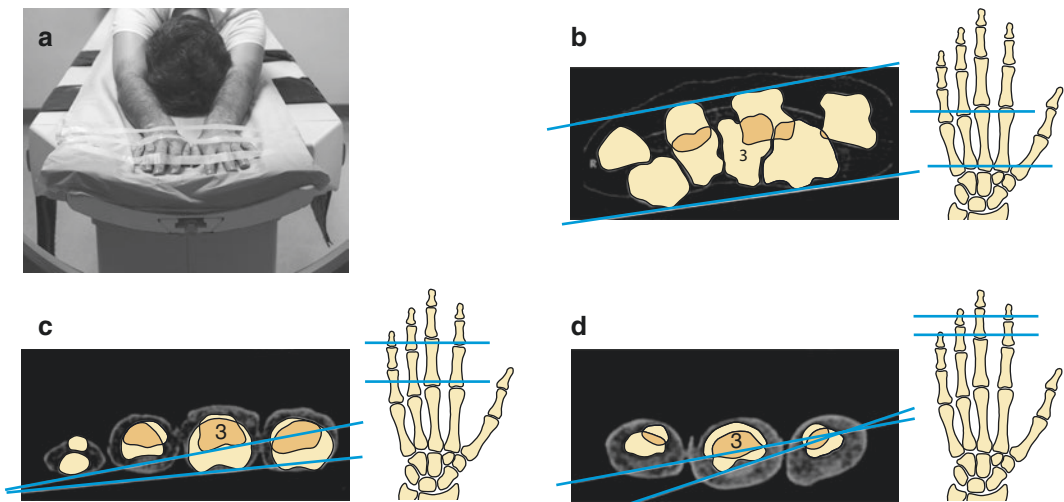
Fig. 10.59 Torsion of finger long bones axes. Recommended positioning in CT gantry (**a**). Measurement of the torsion angle of the 3rd metacarpal (**b**) using superimposed CT images obtained at the metacarpal baseline through the 2nd–5th metacarpals and head of the 3rd metacarpal respectively. The angle between the bottom baseline and the tangent line to the metacarpal head is the torsion angle which is normally 3° supination. Measurement of the torsion angle of the 3rd proximal phalanx (**c**) using superimposed CT sections through the base and head of the proximal phalanx which is normally 5° supination. Measurement of the torsion angle of the 3rd middle phalanx (**d**) using superimposed CT images which is normally 8° supination

Fig. 10.59b Measurement of the torsion angle of the third metacarpal bone. The angle between baseline (*bottom line*) and the tangent to the metacarpal head is 3° supination.

Fig. 10.59c Measurement of the torsion angle of the proximal phalanx of the third finger: torsion angle is 5° supination.

Fig. 59d Measurement of torsion angle of the middle phalanx of the third finger: torsion angle is 8° supination.

Reproducibility/Variation

When the hand is turned with 10° of ulnar deviation and afterwards in 10° of radial abduction, the angles measured vary from 3° (radial abduction), 8° (neutral position) to 13° (ulnar abduction). These findings indicate that only true axial scans through the base of the metacarpals or the joint ends of the finger bones reflect the shape of the articular surface. If the bone axis through the shaft is not identical to the table axis, the joint end is not symmetric as the section passes the two tiny condyles at different places. This demonstrates the requirement for exact positioning.

	II finger	III finger	IV finger	V finger
Metacarpals	p 9°–15°	s 2°–7°	s 4°–10°	s 7°–17°
Proximal phalanges	s 10°–18°	s 4°–11°	Neutral	s 2°–8°
Middle phalanges	s 3°–12°	s 4°–10°	Neutral	p 1°–9°

p pronation, *s* supination Berthold et al. (2001)

Clinical Relevance/Implications

Rotational dislocation at the fracture site is a complication of phalangeal or metacarpal fractures. The consequence of a malrotation is digital overlap on closing the hand Orset et al. (1991). To treat this deformity, the orthopaedic surgeon may perform derotational osteotomies involving metacarpal or phalangeal bones.

Side differences in torsion angles exceeding 3° are strongly suspicious of a malrotation after fracture. These measurements might help to plan derotational osteotomy and assess the results of therapy.

Analysis/Validation of Reference Data

There are limited validation studies.

Conclusion

Side differences in torsion angle exceeding 3° are strongly suspicious of a malrotation after fracture. These measurements might help the planning of a derotational osteotomy and assess the results of therapy, but there are limited validation studies.

15. Flexor Tendon-Phalangeal Distance

Definition

The distance between the flexor tendon and phalanx (TP) is measured at the levels of the A2, A3 and A4 annular pulleys.

Indication

Finger pulley injuries most common in sports related activity such as elite rock climbers.

Techniques

The distance can be assessed by MRI or US. Dynamic ultrasound has the advantage of assessing the TP distance at rest and during active forced flexion of the finger. A high resolution

transducer is required with a multi-D linear array, at least 12 MHz frequency with a gel standoff.

Full Description of Technique (Fig. 10.60)

At dynamic US the transducer is placed on the volar aspect and at rest the three TP measurements are made relating to the positions of the A2, A3 and A4 pulleys (Fig. 10.60a). This is performed from the metacarpal heads to the distal phalanges longitudinally and transversely. This is then repeated by asking the patient to forcibly flex the injured fingertip against the sonographer's finger. The TP distance is assessed at the level of the areas of the pulleys. The A2 pulley arises from the base of the proximal phalanx and covers a 20 mm distance distally towards the PIP joint so measurements need to be done at this location. The A4 TP

Fig. 10.60 Diagrammatic depiction of normal A1–A5 pulley arrangements (**a**), and the varying degrees of bowstringing resulting from pulley injuries which cause increased flexor tendon-phalangeal distances (**b**, **c**)
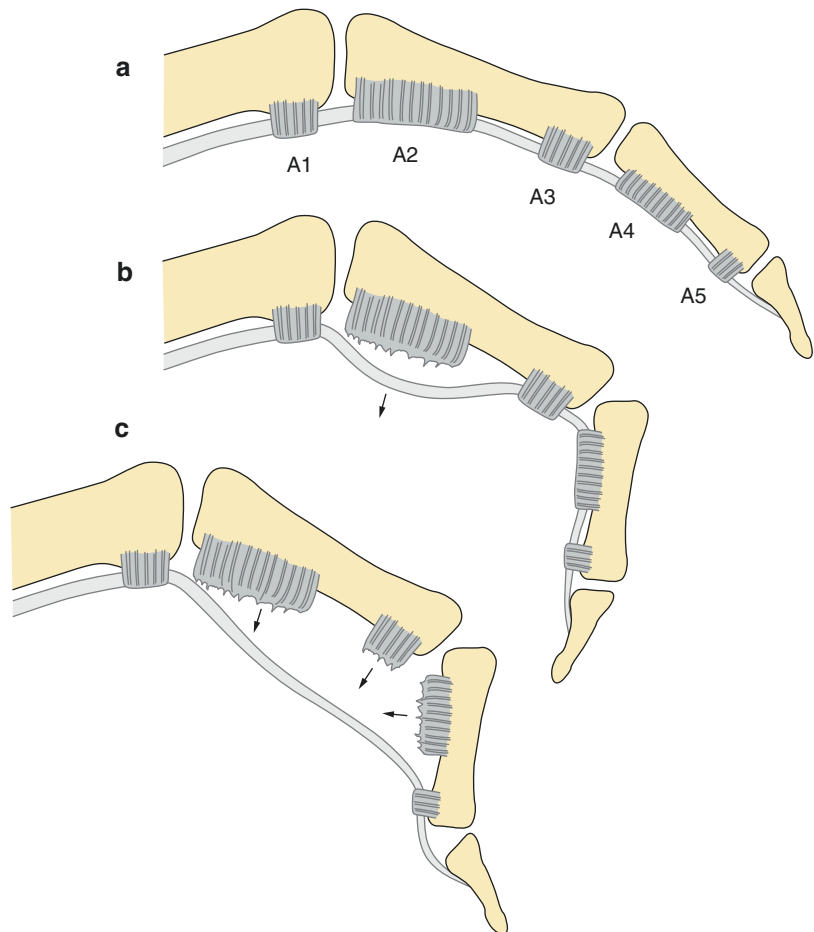
Fig. 10.61 Normal flexor tendon–phalangeal distances seen on sagittal MRI sequences at rest (*top*) and on finger stress (*bottom*)
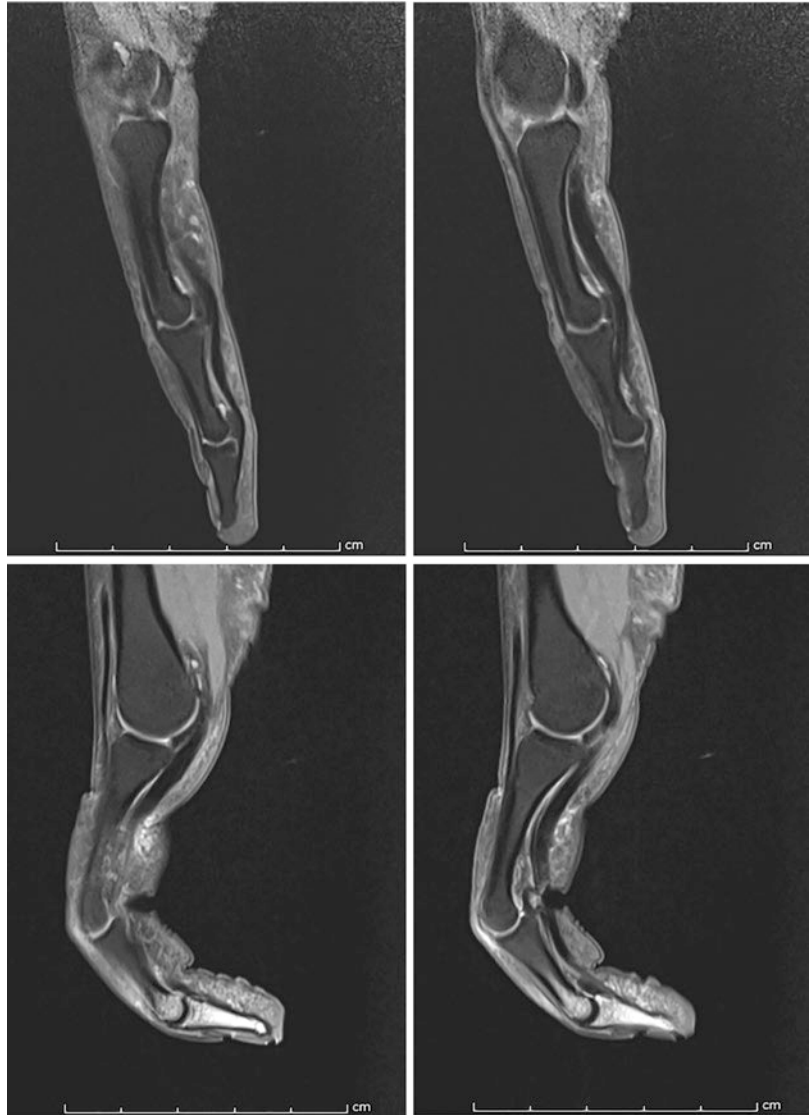
distance is measured at the midportion of the middle phalanx. In the presence of a pulley injury the tendon sheath will bowstring away from the phalanx both at rest but in particular during active forced flexion. There is a recognised sequence of injury to the pulley system whereby the injury commences at the distal part of the A2 pulley, then escalates from a partial to a complete A2 rupture, followed by ruptures of the A3, A4 and rarely the A1 pulleys (Fig. 10.60b, c). Injuries therefore can

be present at one or more of the four pulleys and in particular if an A2 pulley lesion is diagnosed the measurement needs to be done at the A3 pulley to exclude a combined tear.

The "bowstringing" increasing the TP distance can also be indirectly measured on sagittal MR scans done with the hand in the prone position with the fingers first in the extended position and then in forced flexion (Figs. 10.60 and 10.61). Increased TP distances are seen at the proximal

phalanx in an A2 rupture and at the middle phalanx in an A4 rupture. The longitudinal extent of the increased TP distance seen on MR relative to the phalanges aids in further differentiation. If the bowstringing does not extend proximally to reach the base of the proximal phalanx one can confidently declare a partial A2 pulley rupture. When the bowstringing effect extends proximally from the PIP joint beyond the base of the proximal phalanx one can diagnose a complete rupture. When there is a combined A2 + A3 pulley rupture the TP distance is seen to increase from the base of the proximal phalanx extending distally beyond the level of the PIP joint. If the measured increased TP distance occurs longitudinally at the middle phalanx this denotes an A4 pulley rupture (Figs. 10.62 and 10.63).

Reproducibility/Variation

Dynamic US enjoys a high sensitivity in the diagnosis of finger pulley injuries using the indirect

Fig. 10.62 Increased flexor tendon–phalangeal distance seen on sagittal (*top*) and axial (*bottom*) MRI images due to pulley injury
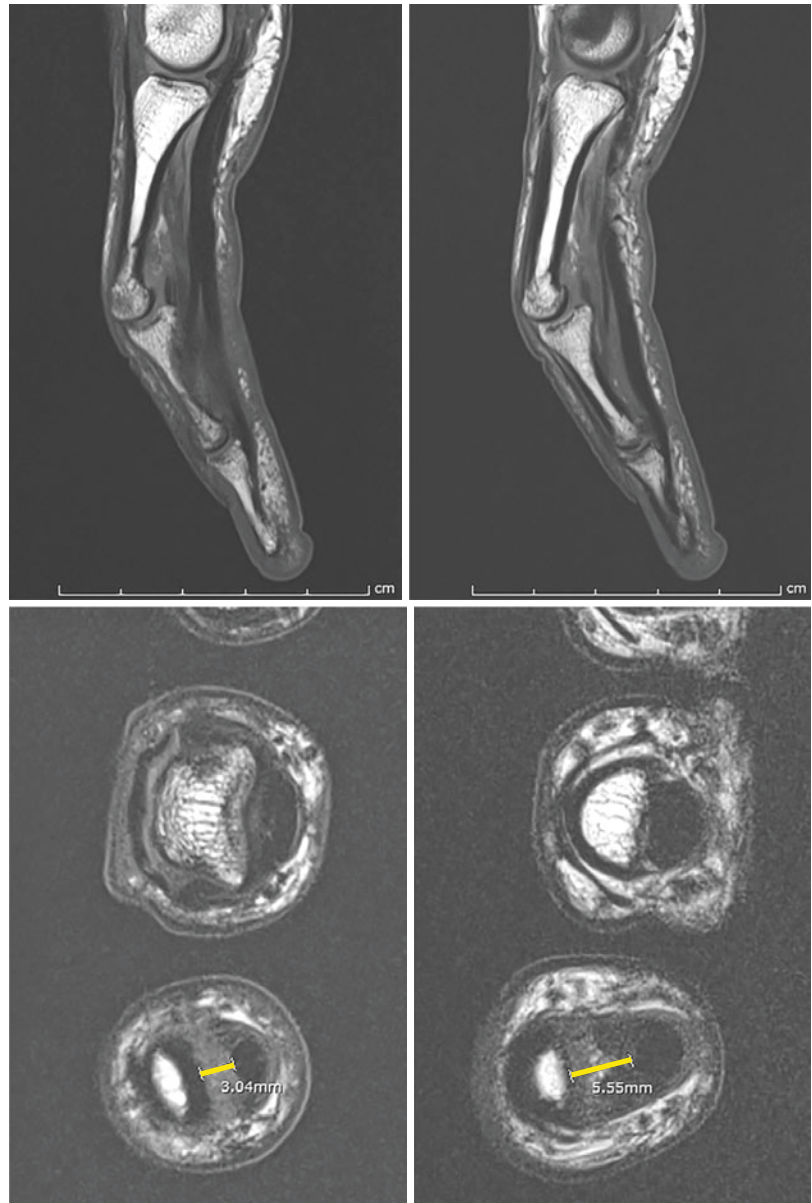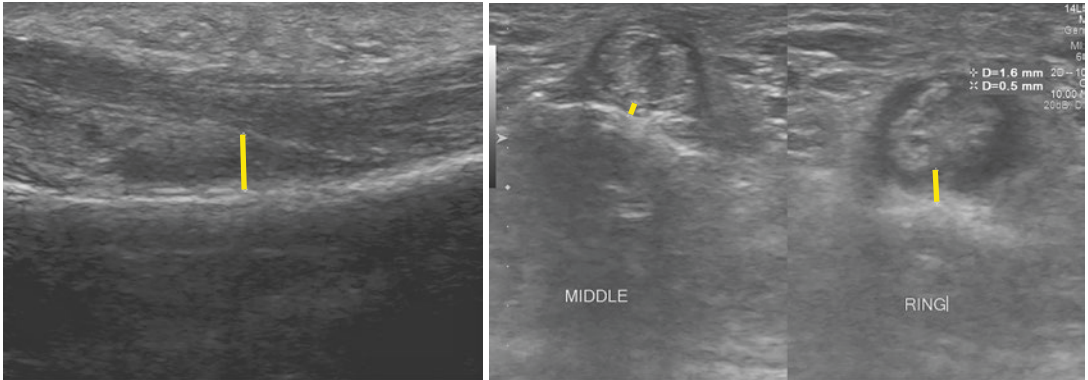
Fig. 10.63 Increased flexor tendon–phalangeal distance measurements due to pulley injury seen by longitudinal and transverse US images

method of TP distance measurements. **Normally the TP distance is < 1 mm**.

If the **TP distance is > 1 mm** in the resting position it suggests a pulley rupture. The measurements during active forced flexion will indicate if this is partial or complete rupture:

A2	<3 mm (partial)
	>3 mm (complete)
A2 + A3	<5 mm (partial)
	>5 mm (complete)
A4	<2.5 mm (partial)
	>2.5 mm (complete)

Other authors have also indicated that the TP distance of 2–5 mm in isolated rupture is seen to increase from 5 to 8 mm in combined complete multiple pulley ruptures.

Clinical Relevance/Implications

The finger pulley system includes annular ligaments (A1–A5) and cruciform ligaments (C1–C3). The A2 and A4 pulleys are the most important as they stabilise the flexor tendons during active flexion avoiding bowstringing. The assessment to exclude pulley rupture and the extent of injury needs to be done in the acute stage for optimal outcomes. Surgical procedures need to be done early to ensure a good functional return.

Analysis/Validation of Reference Data

In the cadaveric study by Gabl et al. (1998) a TP distance >1 mm was indicative of a pulley injury.

Of the 64 elite rock climbers in Klauser et al.'s (2002, 2009) study dynamic US depicted 16 (100%) complete A2 ruptures, 9 (100%) A4 complete ruptures, 6 (86%) of 7 surgically proven complete A2 and A3 pulley ruptures, and 15 (100%) of A2 incomplete ruptures. Correlation with MRI was also done in this study. The sensitivity was 98% and the specificity 100%.

Conclusion

Using the indirect TP distance a diagnosis of a pulley rupture can be made reliably.

References

Adams JE (2010) Radiogrammetry and radiographic absorptiometry. Radiol Clin N Am 48:531–540

Baroncelli GI, Federico G, Bertelloni S, de Terlizzi F, Cadossi R, Saggese G (2001) Bone quality assessment by quantitative ultrasound of proximal phalanxes of the hand in healthy subjects aged 3–21 years. Pediatr Res 49(5):713–718

Bateni CP, Bartolotta RJ, Richardson ML, Mulcahy H, Allan CH (2013) Imaging key wrist ligaments: what the surgeon needs the radiologist to know. Am J Roentgenol 200:1089–1095

Berger RA (1996) The gross and and histologic anatomy of the scapholunate ligament. J Hand Surg Am 21:170–178

Berthold LD, Peter A, Ishaque N, Mauermann F, Bohringer G, Klose KJ (2001) Measurement of torsion angles of long finger bones using computed tomography. Skelet Radiol 30(10):579–583

Bettinger PC (2001) Trapezial Tilt: a radiographic correlation with advanced Trapeziometacarpal joint arthritis. J Hand Surg 26A(4)

Biyani A, Mehara A, Bhan S (1990) Morphological variations of the ulnar styloid process. J Hand Surg (Br) 15:352–354

Boabighi A, Kuhlmann JN, Kenesi C (1993) The distal ligamentous complex of the scaphoid and the scapholunate ligament: an anatomic, histological and biomechanical study. J Hand Surg (Br) 18:65–69

Cautilli GP, Wehbe MA (1991) Scapholunate distance and cortical ring sign. J Hand Surg 16A:501–504

Cerezal L, Del Pinal F, Abascal F, Garcia-Valtuille R, Pereda T, Canga A (2002) Imaging findings in ulnar-sided wrist impaction syndromes. Radiographics 22:105–121

Chamay A et al (1983) Radiolunate arthrodesis: factor of stability for the rheumatoid wrist. Ann Chir Main 2:5–17

Crittenden JJ, Jones DM, Santarelli AG (1970) Bilateral rotational dislocation of carpal navicular. Radiology 94:629–630

Cudlip SA, Howe FA, Clifton A et al (2002) Magnetic resonance neurography studies of the median nerve before and after carpal tunnel decompression. J Neurosurg 96:1046–1051

Czitrom AA et al (1987) Ulnar variance in carpal instability. J Hand Surg 12A:205–212

DeSchepper J, Roggen I, Van Biervliet S, Robberecht E, Gies I, De Waele K, De Wachter E, Malfroot A, De Baets F, Toye K, Goemaere S, Louis O (2012) Comparative bone status assessment by dual energy X-ray absorptiometry, peripheral quantitative computed tomography and quantitative ultrasound in adolescents and young adults with cystic fibrosis. J Cyst Fibros 11:119–124

DiBenedetto MR et al (1991) Quantification of error in measurements of radial inclination and radial-carpal distance. J Hand Surg 16A:399–400

Drozdzowska B, Pluskiewicz W (2003) Skeletal status in males aged 7–80 years assessed by quantitative ultrasound at the hand phalanges. Osteoporos Int 14(4):295–300. Epub 2003 Apr 18

Feipel V, Rooze M (1998) The capsular ligaments of the wrist : morphology, morphometry and clinical applications. Surg Radiol Anat 21:175–180

Friberg S, Lundstrom B (1976) Radiographic measurements of radio-carpal joint in normal adults. Acta Radiol Diagn 17:249–256

Gabl M, Rangger C, Lutz M, Fink C, Rudisch A, Pechlaner S (1998) Disruption of the finger flexor pulley system in elite rock climbers. Am J Sports Med 26(5):651–655

Garcia-Ellis M (1987) Dorsal fractures of the triquetrum – avulsion or compression fractures ? J Hand Surg 12A:266–268

Gelberman RH, Salaman PB, Jurist JM, Posch JL (1975) Ulnar variance in Kienbock's disease. J Bone Joint Surg 57A:674–676

Gilula LA, Weeks PM (1978) Post-traumatic ligament instabilities of the wrist. Radiology 129:641–651

Goldfarb CA, Yin Y, Gilula LA, Fisher AJ, Boyer MI (2001) Wrist fractures :what the clinician wants to know. Radiology 219:11–28

Ham SJ, Konings JG, Wolf RF, Mooyaart EL (1993) Functional anatomy of the soft tissues of the hand and wrist: in vivo excursion measurement of the flexor pollicis longus-tendon using MRI. Magn Reson Imaging 11(2):163–167

Harper HAS et al (1974) The carpal angle in American populations. Investig Radiol 9:217–221

Hudson TM, Caragal WJ, Kaye JJ (1976) Isolated rotatory subluxation of the carpal navicular. Am J Roentgenol 126:601–611

Jedlinski A, Kauer JMG, Jonsson K (1995) X-ray evaluation of the true neutral position of the wrist : the groove for extensor carpi ulnaris as a landmark. J Hand Surg [Am] 20:511–512

Jung JM, Baek GH, Kim JH, Lee YH, Chung MS (2001) Changes in ulnar variance in relation to forearm rotation and grip. J Bone Joint Surg (Br) 83:1029–1033

Kaawach W, Ecklund K, DiCanzio J, Zurakowski D, Waters PM (2001) Normal ranges of scopholunate distance in children 6-14 years old. J Pediatr Orthop 21(4):464–467

Kamolz LP, Schrogendorfer KF, Rab M, Girsch W, Gruber H, Frey M (2001) The precision of ultrasound imaging and its relevance for carpal tunnel syndrome. Surg Radiol Anat 23(2):117–121

Kapandji AI, Kapandji TG (1993) Nouvelles données radiologiques sur la trapézométacarpienne. Résultats sur 330 dossiers. Ann Chir Main 4:263–274

Kichouh M, De Maesener M, Jager T, Marcelis S, Van Hedent E, Van Roy P, de Mey J (2011) Ultrasound findings in injuries of dorsal extensor hood: correlation with MR and followup findings. Eur J Radiol 77:249–253

Kim HK, Ryu J, Han, JS, Yang SB, Kish V (1994) A new cross-sectional area measurement technique for

intrinsic and extrinsic human wrist ligaments: in situ MRI study. Proceedings of the SIROT Inter-meeting

Kindynis P, Resnick D, Kang HS, Haller J, Sartoris DJ (1990) Demonstration of the scapholunate space with radiography. Radiology 175:278–280

Klauser A, Frauscher F, Bodner G, Halpern EJ, Schocke MF, Springer P, Gabl M, Judmaier W, Nedden DZ (2002) Finger pulley injuries in extreme rock climbers:depiction with dynamic US. Radiology 222(3):755–761

Klauser AS, Halpern EJ, De Zordo T, Feuchtner GM, Arora R, Gruber J, Martinoli C, Loscher WN (2009) Carpal tunnel assessment with US: value of additional cross-sectional area measurements of the median nerve in patients versus healthy volunteers. Radiology 250(1):171–177

Kristensen SS et al (1986) Ulnar variance determination. J Hand Surg 11B:255–257

Larsen CF, Mathiesen FK, Lindequist S (1991a) Measurements of carpal bone angles on lateral wrist radiographs. J Hand Surg 16A:888–893

Larsen CF, Stigsby B, Lindequist S, Bellstrom T, Mathiesen FK, Ipsen T (1991b) Observer variability in measurements of carpal bone angles on lateral wrist radiographs. J Hand Surg [Am] 16:893–898

Lee JC, Healy JC (2005) Normal sonographic anatomy of the wrist and hand. Radiographics 25(6):1577–1590

Leicht P, Mikkelsen B, Larsen CF (1996) Scapholunate distance in children. Acta Radiol 37(5):625–626

Levy M, Fischel RE, Stern GM, Goldberg I (1979) Chip fractures of the os triquetrum. The mechanism of injury. J Bone Joint Surg 7:355–357

Linscheid RL (1986) Kinematic considerations of the wrist. Clin Orthop 202:27–39

Linscheid RL et al (1972) Traumatic carpal instability of the wrist: diagnosis, classification, and pathomechanics. J Bone Joint Surg 54A:1612–1632

Mann FA, Wilson AJ, Gilula LA (1992a) Radiographic evaluation of the wrist :what does the hand surgeon want to know? Radiology 184:15–24

Mann FA et al (1992b) The influence of age and gender on radial height. J Hand Surg 18A:711–713

Mann FA et al (1992c) Normal palmar tilt: is dorsal tilting really normal? J Hand Surg 17B:315–317

Matsushita K et al (1992) X-ray evaluation of radial shortening for Kienböck's disease. J Hand Surg 17A:450–455

McMurtry RY, Youm Y, Platt AE, Gillespie TE (1978) Kinematics of the wrist II. Clinical applications. J Bone Joint Surg 60-A:955–961

Meade TD, Schneider LH, Cherry K (1990) Radiographic analysis of selective ligament sectioning at the carpal scaphoid : a cadaveric study. J Hand Surg 15A:855–862

Mirabello SC et al (1987) Correlation of clinical and radiographic findings in Kienböck's disease. J Hand Surg 12A:1049–1054

Moneim MS (1981) The tangential posteroanterior radiograph to demonstrate scapholunate dissociation. J Bone Joint Surg Am 63A:1324–1326

Nakamura R et al (1989) Method of measurement and evaluation of carpal bone angles. J Hand Surg 14A:412–416

Nakamura R et al (1991) The influence of age and sex on ulnar variance. J Hand Surg 16B:84–88

Natrass GR, King GJ, Mcmurty RY, Brant RF (1994) An alternate method for determination of the carpal height ratio. J Bone Joint Surg Am 76:88–94

Obermann WR (1991) Radiology of carpal instability. A clinical and anatomical study. Thesis, University of Leiden, Holland

Orset G, Lebreton E, Assouline A, Giordano P, Denis F, Pomel G (1991) Axial orientation of the phalanges following closing of the fingers. Ann Chir Main 17:101–107

Palmer AK et al (1982) Ulnar variance determination. J Hand Surg 7A:376–379

Pfirrmann CW, Theumann NH, Chung CB, Trudell DJ, Resnick D (2002) The hamatolunate facet: characterization and association with cartilage lesions–magnetic resonance arthrography and anatomic correlation in cadaveric wrists. Skelet Radiol 31(8):451–456. Epub 2002 Jun 20

Pirela-Cruz MA et al (1993) Ulnar translation of the carpus in rheumatoid arthritis: an analysis of five determination methods. J Hand Surg 18A:299–306

Pliefke J, Stengel D, Rademacher G, Mutze S, Ekkernkamp A, Eisenschenk A (2008) Diagnostic accuracy of plain radiographs and cineradiography in diagnosing scapholunate dissociation. Skel Radiol 37:139–145

Pluskiewicz W, Adamczyk P, Drozdzowska B, Pyrkosz A, Halaba Z (2006) Quantitative ultrasound and peripheral bone densitometry in patients with genetic disorders. Ultrasound Med Biol 32(4):523–528

Poznanski AK (1974) The hand in radiologic diagnosis. WB Saunders, Philadelphia

Poznanski AK (1991) Useful measurements in the evaluation of hand radiographs. Hand Clin 7:21–36

Reagan DS et al (1984) Lunotriquetral sprains. J Hand Surg 9A:502–513

Sarrafian SK, Melamed JL, Goshgarian GM (1977) Study of wrist motion in flexion and extension. Clin Orthop 126:153–159

Scheck RJ, Kubitzek C, Hierner R, Szeimies U, Pfluger T, Wilhelm K, Hahn K (1997) The scapholunate interosseous ligament in MR arthrography of the wrist: correlation with non-enhanced MRI and wrist arthrography. Skeletal Radio 26:263–271

Schimmerl-Metz SM, Metz VM, Totterman SM, Mann FA, Gilula LA (1999) Radiologic measurement of the scapholunate joint: implications of biologic variations in scapholunate morphology. J Hand Surg [Am] 24:1237–1244

Schuind FA, Linscheid RL, An KA, Chao EYS (1992) A normal data base of posteroanterior roentgenographic measurements of the wrist. J Bone Joint Surg 74-A:1418–1428

Smith DK (1993a) Dorsal carpal ligaments of the wrist: normal appearances on multiplanar reconstructions of

three-dimensional Fourier transform MR imaging. Am J Roentgenol 161:119–125

Smith DK (1993b) Volar carpal ligaments of the wrist: normal appearances on multiplanar reconstructions of three-dimensional Fourier transform MR imaging. Am J Roentgenol 161:353–357

Solgaard S (1992) Distal radius fracture (dissertation). University of Copenhagen, Copenhagen, pp 1–16

Stahelin A et al (1989) Determining carpal collapse. J Bone Joint Surg 71A:1400–1405

Stahl F (1947) On lunatomalacia (Kienböck's disease): clinical and roentgenological study, especially on its pathogenesis and late results of immobilization treatment. Acta Chir Scand (Suppl) 95

Steyers CM, Blair WF (1989) Measuring ulnar variance: a comparatison of techniques. J Hand Surg Am 14:607–612

Theumann NH, Pfirrmann CW, Drape JL, Trudell DJ, Resnick D (2002a) MR imaging of the metacarpophalangeal joints of the fingers: part I. Conventional MR imaging and MR arthrographic findings in cadavers. Radiology 222(2):437–445

Theumann NH, Pfirrmann CW, Chung CB, Antonio GE, Trudell DJ, Resnick D (2002b) Ligamentous and tendinous anatomy of the intermetacarpal and common carpometacarpal joints: evaluation with MR imaging and MR arthrography. J Comput Assist Tomogr 26(1):145–152

Theumann NH, Pfirrmann CW, Chung CB, Antonio GE, Trudell DJ, Resnick D (2002c) Pisotriquetral joint: assessment with MR imaging and MR arthrography. Radiology 222(3):763–770

Theumann NH, Pfirrman CW, Antonio GE, Chung CB, Gilula LA, Trudell DJ, Resnick D (2003) Extrinsic carpal ligaments :normal MR arthrographic appearances in cadavers. Radiology 226:171–179

Tomiano MM (2000) The importance of the pronated grip x-ray view in evaluating ulnar variance. J Hand Surg [Am] 25:352–357

Topper SM, Wood MB, Ruby LK (1997) Ulnar styloid impaction syndrome. J Hand Surg [Am] 22: 699–704

Tornvall AH et al (1986) Radiological examination and measurements of the wrist and distal radioulnar joint. Acta Radiol Diagn 27:581–588

Uchiyama S, Itsubo T, Yasutomi T, Nakagawa H, Kamimura M, Kato H (2005) Quantitative MRI of the wrist and nerve conduction studies in patients with idiopathic carpal tunnel syndrome. J Neurol Neurosurg Psychiatry 76:1103–1108

Warwick D et al (1993) Radiological measurements of radial shortening in Colles' fracture. J Hand Surg 18B:50–52

Watson H, Ottoni E, Pitts EC, Handal AG (1993) Rotatory subluxation of the scaphoid : a spectrum of instability. J Hand Surg 18B:62–64

Yamada J (1988) A cineradiographic study of normal wrist motion. J Jap Orthop Assoc 62:1043–1054

Yang Z, Mann FA, Gilula LA, Haerr C, Larsen CF (1997) Scaphopisocapitate alignment: criterion to establish a neutral lateral view of the wrist. Radiology 205:720–727

Yao L, Gai N (2009) Median nerve cross-sectional area and MRI diffusion characteristics: normative values at the carpal tunnel. Skelet Radiol 38(4):355–356

Youm Y et al (1978) Kinematics of the wrist I: an experimental study of radial-ulnar deviation and flexion-extension. J Bone Joint Surg 60A:423–431

Pelvis/Hip Paediatric

11

Prudencia N. M. Tyrrell, Apostolos H. Karantanas,
and Victor N. Cassar-Pullicino

Contents

P. N. M. Tyrrell, F.R.C.R. (✉)
The Robert Jones and Agnes Hunt Orthopaedic
Hospital, Oswestry, Shropshire, UK
e-mail: prudencia.tyrrell@rjah.nhs.uk

A. H. Karantanas, M.D., Ph.D.
University Hospital,
Stavrakia, Heraklion 711 10, Crete, Greece

V. N. Cassar-Pullicino, F.R.C.R.
Department of Radiology, Robert Jones and Agnes
Hunt Orthopaedic Hospital NHS Foundation Trust,
Oswestry, UK
e-mail: Victor.Pullicino@rjah.nhs.uk

11.1 Introduction

At birth the acetabulum is partly cartilaginous with the epiphyseal plate composed of the triradiate cartilage with contributions from the unossified portions of the ilium, ischium and pubis. The hip joint at this stage consists of an entirely cartilaginous femoral capital epiphysis lying within the acetabulum formed by the triradiate cartilage. Continued growth, development and ossification result in eventual fusion of the bones of the acetabulum. The ossific nucleus of the femoral head appears in the early weeks after birth. It is visible earlier on ultrasound than on the radiograph. Its position within the cartilaginous femoral head may be more posterior than usual if there is developmental dysplasia present.

In early infancy much of the hip joint is cartilaginous, and the bone which is present is still developing, growing and maturing. As a result difficulty can be experienced in identifying the correct bony landmarks from which to make measurements on the radiograph. This can lead to great variability in attempted reproducibility of some measurements. Interobserver measurements are more likely to differ significantly than intraobserver measurements, and this is particularly important in the paediatric population. When performing measurements in the paediatric age group, particularly because of continued expected interval growth, it is not the value of a single measurement that should be interpreted as being important and whether it is normal or abnormal, but rather the evolving trend that is seen when measurements are repeated at regular intervals. The ideal situation would be that measurements are also repeated by the same observer as far as is possible and even if not, ensuring that exactly the same landmarks are used to make the measurement. Variability in reproducibility of some measurements may be because of difficulty in determining, for example, what represents the lateral margin of the acetabulum. This in itself may be indistinct due to the underlying pathological process for which the measurement is required, for example, developmental dysplasia of the hip (DDH). Kim specifically addressed this point in a study to evaluate the most accurate

marking point on a plain radiograph when measuring the acetabular index and the centre-edge angle (Kim et al. 2000). The position of the hips for a particular measurement is important, and there must be clarity as to whether the measurement is being made with the hips in the neutral position or in a frog lateral position.

Measurements about the pelvis in the paediatric population require close attention to positioning of the pelvis ensuring that it is neither rotated nor inclined. Even a minor degree of obliquity can result in great variability of a measurement. Pelvic symmetry needs to be assessed before declaring that the radiograph is suitable to embark on obtaining the required measurements. As will be discussed later in this chapter, the transverse diameter of the obturator foramina bilaterally is used to confirm a true anteroposterior position. The ratio obtained by dividing the right obturator measurement by the left one should be 1 with the patient in the neutral position. It is still acceptable if it is in the range of **1.8–0.56** as the measurements will only differ by a maximum of 2° (Fig. 11.1). The degree of pelvic inclination can also introduce errors in the measured angles. The ratio between the vertical distance between the symphysis pubis and Hilgenreiner's line divided by the vertical obturator diameter should be in the range of **1.2 and 0.75** to ensure reliable accuracy of the measurements (Ball and Kommenda
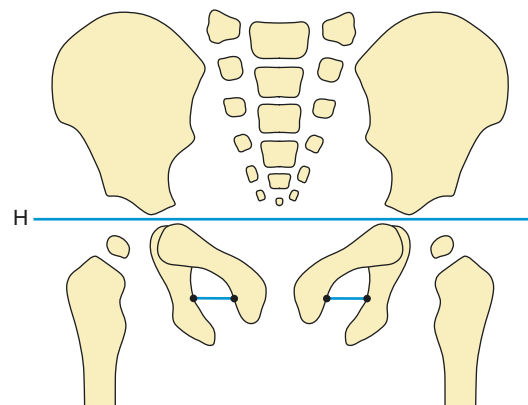
Fig. 11.1 Hilgenreiner's line. This is a horizontal line which passes through the centre of the triradiate cartilages. The obturator index is the ratio between the right and left obturator foraminal distance which is one in a neutrally positioned AP pelvis
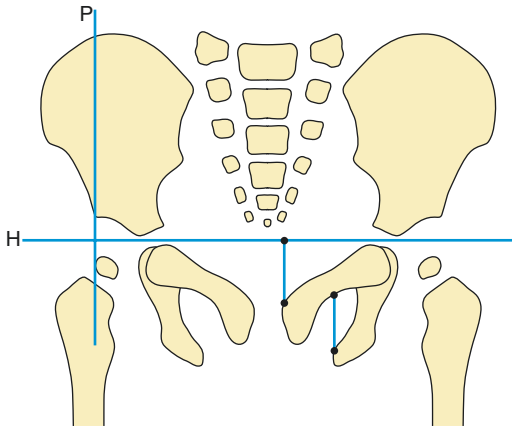
Fig. 11.2 Perkins' line. This is a vertical line drawn perpendicular to Hilgenreiner's line which passes through the lateral margin of the bony acetabulum. The ratio between the vertical obturator diameter and the vertical distance between the pubic bone and Hilgenreiner's line should be between 1.2 and 0.75 indicating an acceptable pelvic inclination range for reliable measurements

1968) (Fig. 11.2). Others have drawn lines from bony landmarks and then allowed for a conversion factor to ensure adequacy of position (Tönnis 1976). This is dealt with further in the pelvic inclination formula/pelvic symmetry sections.

Certain measurements are best made at a particular stage or age of development, for example, the acetabular index is best measured, while the triradiate cartilage is still open. This is because the measurement depends on Hilgenreiner's line which passes through the triradiate cartilage. The acetabular angle however is best measured when the triradiate cartilage is closed although it is often used in the older child when the cartilage is still open. For this measurement the teardrop needs to be visible, and this in itself only appears at 6–24 months of age and older in cases where the hip is dislocated. The centre-edge angle of Wiberg is best used after the age of 5 years. This is because it can be difficult to ascertain the centre of the femoral head when much of the head is cartilage and still relatively immature.

Most of the commonly used measurements will be made from a well-positioned anteroposterior (AP) radiograph. Radiographs are readily available and cheap. The time taken for the examination is brief, and usually an adequate and diag-

nostic radiograph can be obtained. Computed tomography (CT) and magnetic resonance imaging (MRI) have been used for some measurements, and there are anecdotal reports in the literature concerning these. Such modalities however are expensive and are not always readily available. Radiation dose is relatively high with CT, and keeping the child still for the duration of an MRI scan can be difficult without resort to use of some form of sedation. CT and MRI certainly have a role in the diagnosis and management of some conditions but would not be advocated for routine measurement of parameters which can be achieved otherwise by radiographs or by ultrasound.

The introduction of ultrasound (US) in the late 1970s and the work by Graf revolutionised how we assess and monitor the paediatric hip particularly in developmental dysplasia. The particular advantages of ultrasound in the paediatric population include no irradiation and assessment of cartilaginous structures not visible on radiographs, and it is dynamic and allows multiplanar evaluation. There is no sedation required (as compared with arthrography, CT, etc.), but it is operator dependent (Wientroub and Grill 2000). Measurement of Graf's alpha and beta US angles and assessment of femoral head coverage are routinely performed. Dynamic ultrasound is considered even more important than static evaluation and allows for assessment of the stability of the hip (Harcke and Grissom 1990). The literature reports variability in the degree of reproducibility of measurements but again emphasises the importance of serial measurements and evaluation of trend. Measurements alone are not everything, and any finding needs to be assessed in a clinical context.

There are a wide number of measurements referred to in the literature which have not been referred to here. Some of these are new measurements, and others are suggested variations of already established parameters. Reference here has only been made to the more common and generally accepted measurements, notwithstanding acknowledgement of other measurements used in other practices. The important aspect about any measurement and particularly so in the paediatric age group where normal growth (or

lack of) can be a confounding variable is that the significance of a single measurement can be difficult to interpret and therefore it is valuable to obtain serial measurements using standardised methods, that the measurer is or has been trained how to do it and finally that consistent measurers are employed as far as possible. In the child, the importance of measuring the contralateral side cannot be overemphasised (Song et al. 2008). There is a need to be wary however in that bilateral pathology can occur and to be mindful of this in evaluating the measurements together.

Certain lines drawn on the radiograph, between fixed points, act as reference lines relative to anatomical structures. Displacement of such structures can therefore be ascertained, and a radiographic diagnosis made. Interpretation of the radiograph is potentially more difficult prior to appearance of the femoral ossification centre. The ossification centres are not fixed in the time of their appearance. A very early ossification centre may be visible on ultrasound (prior to its visualisation on the radiograph) as early as 3–4 weeks after birth. However, it may not be radiographically apparent for several months. The position of the ossification centre within the femoral capital epiphysis is also variable. Although in the entirely normal child, it usually occurs centrally within the epiphysis, it often appears in the more posterior aspect of the epiphysis particularly in those with a history of developmental dysplasia. Shenton's line, Hilgenreiner's line, Perkins'

line and Z line are all common references on the radiograph and are detailed below.

The sourcil is a curved area of dense bone on the superior weight-bearing surface of the acetabulum. In a normal hip, the sourcil is uniformly thick and semilunar in shape with a horizontal or downward orientation. In the dysplastic hip, the sourcil is directed upwards (Kim et al. 2000). In childhood the sourcil may be difficult to appreciate due to much of the acetabulum being cartilaginous. If the pelvis is in any way rotated and in any event in hip dysplasia, the lateral bony margin and the sourcil may be difficult to define due to overlapping shadows and poor definition of the lateral bony margin of the acetabulum.

Not all measurements of the paediatric hip are related to developmental dysplasia. Most measurements however are related in some way to bony development. The acetabular angle and the alpha and beta angles are clearly related to developmental dysplasia. The iliac angle and iliac index are related to the shape of the ilium, alteration of which may be associated with some conditions such as Down's syndrome. Certain anatomical features are clearly associated with certain conditions, such as teardrop distance and Perthes disease. Although such measurements are not made routinely, when an abnormality has been identified, measurement of such a feature is a useful way of following the condition and evaluating development following appropriate treatment.

11.2   Lines in Paediatric Hip Measurement

The acetabulum is composed of the ilium, the ischium and the pubis. The junction of the three bones in the floor of the acetabulum is cartilaginous and known as the triradiate cartilage. The ossification centre of the femoral head becomes visible on radiographs between the second and eighth months of life. A number of lines have been identified about the pelvis and hips to assist with evaluation of the location of the unossified femoral head and also to assess the degree of acetabular coverage. These lines are drawn on the AP view of the pelvis and include the following.

Hilgenreiner's Line

Is a horizontal line which passes through the centre of the triradiate cartilages (Hilgenreiner 1925) (Fig. 11.1).

Perkins' Line

Is a vertical line drawn perpendicular to Hilgenreiner's line and is drawn at the lateral margin of the bony acetabulum (Perkins 1928) (Fig. 11.2). The intersection of Hilgenreiner's and Perkins' lines divides the hip into four quadrants. The femoral ossific nucleus, if present, or if not, the medial margin of the metaphysis, should lie within the inner lower quadrant if the hip is normal. The typical dislocated hip will lie in the upper outer quadrant.
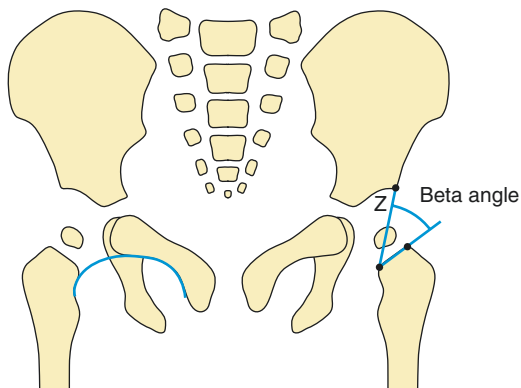
Fig. 11.3 Shenton's line. An arc drawn between the medial border of the right femoral neck and the superior margin of the obturator foramen should normally be smooth and continuous. The **Z line** should normally pass through the ossification centre of the femoral epiphysis (Z) and forms the **beta angle** with a line running along the femoral metaphysis

Shenton's Line

Is an arc drawn between the medial border of the femoral neck and the superior margin of the obturator foramen (Shenton 1911) (Fig. 11.3). In the normal hip, this is a smooth continuous uninterrupted line. In the dislocated hip with superior migration of the femoral head, the line is interrupted.

Z Line

Is an oblique line drawn across the hip joint connecting the lateral edge of the acetabular rim to the metaphyseal beak of the proximal femoral

metaphysis medially. The line should pass through the centre of the ossified portion of the femoral epiphysis (Fig. 11.3).

Beta Angle of Zsernaviczky and Turk

Is formed between the femoral metaphysis and the edge of the acetabulum. A line is drawn along the proximal metaphysis of the femur and allowed to intersect the Z line (connecting the lateral edge of the acetabulum and the medial edge of the femoral metaphysis) (Figs. 11.3 and 11.4) (Zsernaviczky and Turk 1975).

Normal angle is 50–56° and abnormal is >56°.
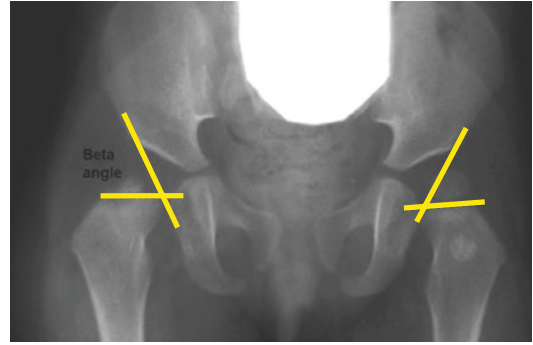
Fig. 11.4 Beta angle measured on AP radiograph

11.3   Pelvic Tilt, Inclination Formula and Pelvic Symmetry

Definition

Pelvic tilt (δ) is defined as the angle between a horizontal line and a line connecting the upper border of the symphysis with the sacral promontory (PS-SP line) (Fig. 11.5). A simple formula which is also used in adults is able to assess the pelvic tilt from AP radiographs.

Pelvic symmetry is the measurement to assess symmetry of the pelvis after proper radiographic positioning.

Indications

With increasing age the pelvis inclines posteriorly, whereas variations exist in the same subjects depending on the body position. When quantifying follow-up radiographs for any hip disorders, it is important to assess the pelvic inclination
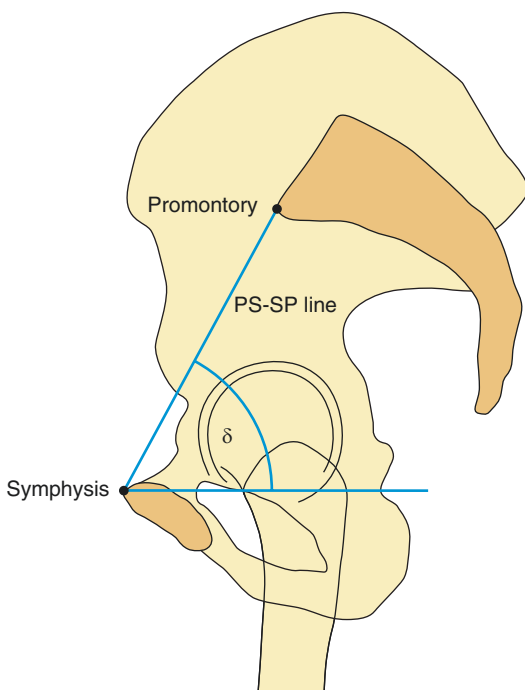
Fig. 11.5 The **PS-SP line** and pelvic tilt angle

which is measured on the lateral radiograph. Obtaining the measurement of inclination from AP radiographs reduces significantly the radiation burden.

The symmetry of the pelvis should be confirmed before performing follow-up evaluations.

Technique

Radiography: AP radiograph.

Full Description of Technique

Formula for Pelvic Inclination

A formula has been described to assess the pelvic tilt from AP radiographs.

The pelvic foramen distance (D) is defined as the distance between the midpoint of the inferior margins of the bilateral sacroiliac joints and the superior margin of the pubic symphysis on a lateral radiograph. The pelvic inclination angle (θ) is defined as the angle between a horizontal line and line D on a lateral radiograph. This allows conversion of the pelvic foramen height on AP radiographs to the pelvic inclination angle, using a mathematic formula (Kitajima et al. 2006).

The formula is $\theta = \arcsin$ (H/165 or H/157 for women and men, respectively) where θ is the inclination angle and H the distance between the midpoint of the line that connects the inferior margins of the bilateral sacroiliac joints and the superior margin of the pubic symphysis on an AP radiograph (Fig. 11.6).

Indicators of Pelvic Symmetry

Quotient of pelvic rotation (Tönnis' obturator foramen index). This measurement evaluates the pelvic position in the horizontal plane. It is the ratio of the maximum horizontal width of the obturator foramen of the right side and that of the left ('QR' and 'QL'). In neutral rotation the ratio is 1 but is considered to be acceptable when it is between **0.56** (pelvis turned to the right) and **1.8** (pelvis turned to the left). Within the range above, the measured angles do not differ by more than 2° (Fig. 11.7).
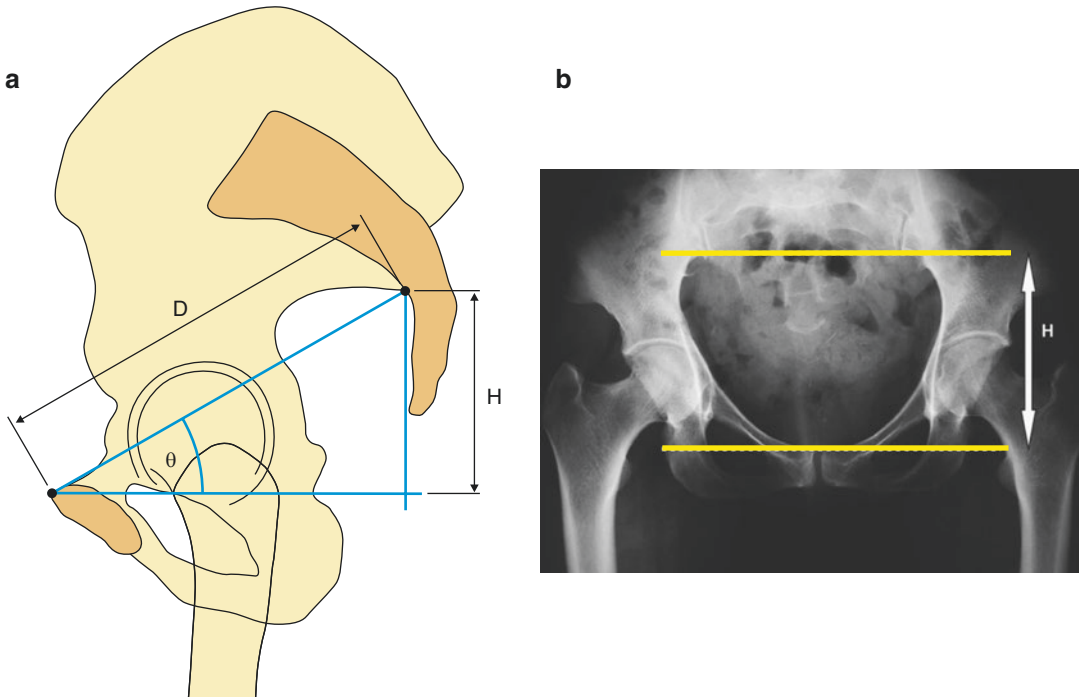
Fig. 11.6 Pelvic inclination formula to assess pelvic tilt from AP radiograph
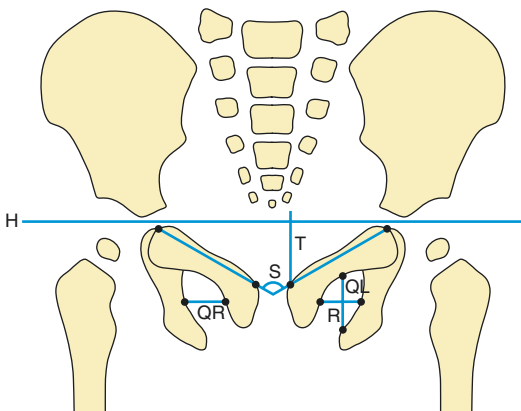
Fig. 11.7 Pelvic symmetry/tilt assessment utilising the **obturator index** (QR/QL), **symphysis-ischium angle** (S) and **pelvic tilt index** (R/T)

Symphysis-ischium angle. This evaluates the pelvic position in the sagittal plane and is formed by two lines which are tangential to the highest point on each ischium and which meet at the point of the symphysis that projects farthest into the pelvic aperture ('S') (Fig. 11.7). The range of normal values is from 90° to 135° and is related to the infant's age.

Pelvic tilt index. This also assesses the pelvic position in the sagittal plane and is the ratio between the vertical diameter of the obturator foramen and the distance between the upper brim of the symphysis pubis and Hilgenreiner's Y-line ('R' and 'T'). With the pelvis normally positioned, the ratio is between 0.75 and 1.2 (Fig. 11.7).

Reproducibility/Variation

The reliability of the obturator index increases with age. Quotient for pelvic rotation and pelvic tilt index is less accurate before the ossification appearance of the ischiopubic synchondrosis. High inter- and intraobserver variability exists for the pelvic inclination formula. The quotient of pelvic rotation becomes accurate after 7 months of age. The symphysis-ischium angle is useful up

to the second year of life, but after this the pelvic tilt index becomes more reliable.

Clinical Relevance/Implications

The pelvic position influences the anteroposterior ratio of acetabular coverage in both the paediatric and adult age groups (Katada and Ando 1984, Siebenrock et al. 2003). In the adult it is relevant in the development of coxarthrosis and the orientation of the acetabular component in total hip arthroplasty.

The pelvis tends to incline posteriorly with ageing, whereas significant changes occur in the orientation of the pelvis during daily activities. Therefore, the assessment of the pelvic inclination is important for comparing follow-up radiographs.

On the AP radiograph of the hip, the pelvis does not show excessive inclination in the sagittal plane, if the tip of the coccyx is centred over the pubic symphysis within a distance of 2 cm or less from the latter. If the distance is longer, then a correction for the pelvic inclination has to be done when evaluating various measurements in follow-up radiographs.

11.4 Acetabular Index (AI) Angle

Definition

This is the angle between an oblique line drawn from the most lateral edge of the bony acetabular roof to the centre point of the triradiate cartilage and Hilgenreiner's line (Fig. 11.8). The AI is used to evaluate the orientation of the acetabular roof in the coronal plane and the superior lateral coverage of the femoral head.

Normal values (male measurements 2° larger than female):

Newborn	27.5° (±4.9)
< 6 months	22.8° (±3.6)
1 year	20.8° (±3.9)
2 years	19.8° (±4.3)
2–3 years	18°
3–7 years	14.5°
7–15 years	10°

Abnormal > 35° suggests acetabular dysplasia.

Indication

It is used to follow the radiographic development of the acetabulum in children with developmental dysplasia of the hip (DDH) and to determine the need for subsequent surgery. Along with the beta angle measurement, the AI evaluates the need for pelvic osteotomies in those children with primary acetabular dysplasia or acetabular dysplasia resulting from a dislocated hip.
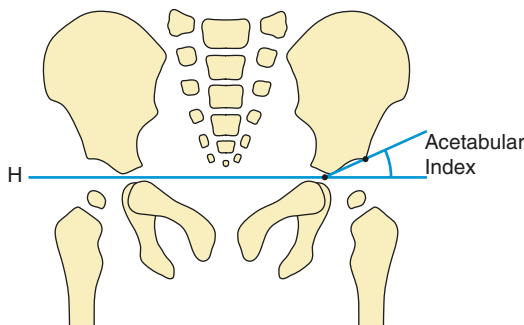
Technique

Radiography: AP radiograph of the pelvis centred 1 cm superior to the symphysis pubis.

Full Description of Technique

On an anteroposterior (AP) radiograph of the pelvis, a horizontal line is drawn between the centre of the two triradiate cartilages (Hilgenreiner's line). A line is drawn from the most lateral edge of the bony acetabular roof to the centre point of the triradiate cartilage. The acetabular index is formed at the intersection of these two lines.

Reproducibility/Variation

The AI is reproducible in all age groups. In children under 2 years of age, using a 95% confidence interval definition, a 4% change in AI is required before the observer can be certain that a true change has occurred in acetabular development. Other observers reported that a difference of less than 12° on successive radiographs should be interpreted with caution. Several studies have indicated that the AI is one of the most reliable and readily reproducible measurements related to assessment of developmental dysplasia in the child (Broughton et al. 1989; Kay et al. 1997; Spatz et al. 1997; Skaggs et al. 1998; Tan et al. 2001). Tan's study showed no significant interobserver or intraobserver difference between observers working in the same clinic.

Clinical Relevance/Implications

In the normal newborn, the AI averages 27.5° and decreases to approximately 20° by age 2 years (see normal values above). In the newborn with

Fig. 11.8 Acetabular index. The angle between a line drawn from the most lateral edge of the bony acetabular roof to the centre point of the triradiate cartilage, intersecting Hilgenreiner's line

clinical evidence of DDH, a normal radiograph does not exclude the presence of instability. The age at which the radiological diagnosis can be established is near the upper limit of the age for successful treatment of hip dysplasia using the Pavlik harness. In addition, the radiation exposure (about 20 **uGy**) is not negligible, particularly when radiographs have to be repeated. For all the above reasons, ultrasonography has replaced in general the AP radiograph for screening DDH.

Analysis/Validation of Reference Data

All of the above studies were performed in children as opposed to a mixed adult-child population as is often found in studies on developmental dysplasia. This in itself lends more weight to the validity of the reproducibility of data as difficulties can be encountered with some other measurements due to lack of ossification. Tan (2001) emphasises the importance of positioning of the child for the radiograph avoiding rotation, and this point is also addressed by Boniforti et al. (1997).

Conclusion

The AI is a readily reproducible and reliable measurement in assessment of the dysplastic hip and its response to treatment.

11.5 Acetabular Angle

Definition

The acetabular angle was first described by Sharp in 1961. Sharp's angle is defined between the teardrop line and a line to the lateral acetabulum. It measures the slope of the acetabulum and has classically been used when the triradiate cartilage is closed.

Normal		Abnormal	
<10 years	<45°	<10 years	>45°
>10 years	<40	>10 years	>40°

At puberty the normal acetabular angle is within 33–38° range.

The greater the abnormal angle, the more severe the dysplasia.

Indication

The acetabular angle is used in the follow-up of developmental dysplasia of the hip to assess treatment when the triradiate cartilage is closed (see "Adult Hip" section). It can also be used when the triradiate cartilage is open although difficulty may be experienced with the measurement (see below).

Techniques

Radiography: AP radiograph of pelvis centred approximately 1 cm above the symphysis pubis.

Full Description of Technique

On an AP radiograph, a horizontal line is drawn connecting the inferior most aspect of the teardrops on each side. A second line is then drawn on each side connecting the most lateral edge of the bony roof of the acetabulum to the inferior aspect of the teardrop figure. The acetabular angle is formed at the intersection of these two lines (Fig. 11.9).
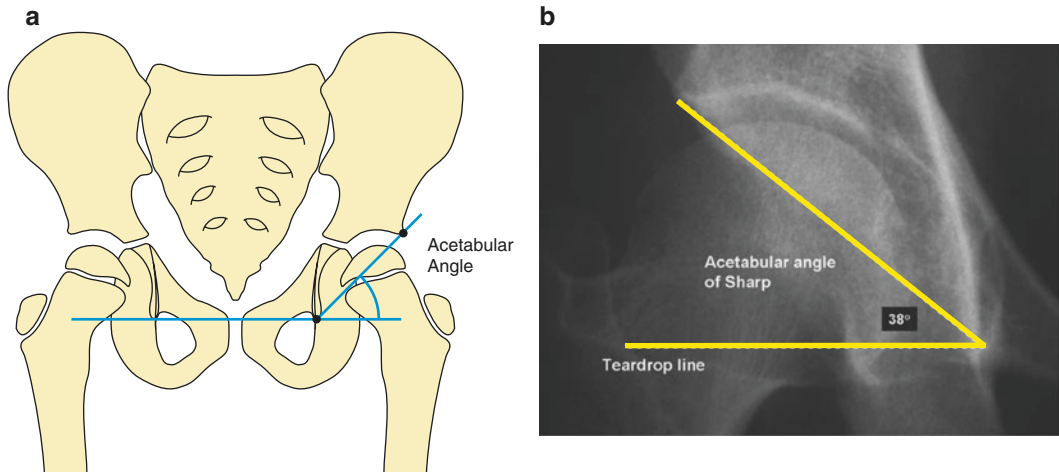
Fig. 11.9 **Acetabular angle**. This measures the slope of the acetabulum—diagram (**a**) and on radiograph (**b**). It is an uncommonly used measurement in the paediatric population

Reproducibility/Variation

Carney et al. (2005) indicates that few studies in the literature have addressed the reliability of the acetabular angle (in the child). Agus et al. (2002) analysed two methods. In the classic method, which was also used by Carney et al. (2005) the angle was measured from the inferior tip of the teardrop to the lateral edge of the bony acetabular roof. In the modified method, the angle was measured from the inferior tip of the teardrop to the most lateral portion of the subchondral bone condensation (the lateral aspect of the sourcil). In Carney's study the mean acetabular angle was in the abnormal range. They concluded that this was probably because normal acetabular angle values have been reported for patients with closed triradiate cartilages only, whereas their study was in children and hence with open triradiate cartilages. It is highly reproducible if applied after the age of 8. Carney et al. found that both the interobserver and intraobserver reliability of the measurement was good but would not recommend using it in preference to the acetabular index. Tan et al. (2001) found this angle reliable in intraobserver comparisons but not in interobserver comparisons.

Clinical Relevance/Implications

It has been put forward as another measurement in the assessment of developmental dysplasia and monitoring response to treatment but has not found universal acceptance in those with open triradiate cartilage often because of difficulty in readily identifying the inferior most tip of the teardrop on which an accurate measurement is dependent (Tan et al. 2001). It is also noteworthy that the teardrop does not appear on the radiograph until between 6 and 24 months and hence this measurement is difficult to perform in the very young.

Analysis/Validation of Reference Data

Little reference data on this measurement in the growing hip.

Conclusion

Uncommonly used measurement in the paediatric population.

11.6 The Iliac Angle and the Iliac Index

Definition

The iliac angle is a measure of the slope of the lateral margin of the iliac bone. The iliac index is the sum of both the AI and Iliac angles divided by two.

Normal iliac angle	55° (44–66)	Abnormal iliac angle	44° (30–56)
Normal index	> 78° (65–97)	Abnormal index	< 60° (49–78)
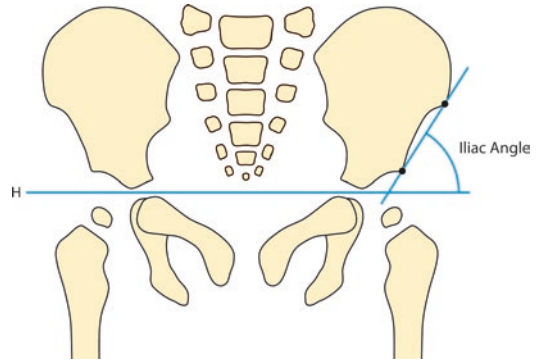
Fig. 11.10 Iliac angle. This a measure of the slope of the lateral margin of the iliac bone

Indication

It may be an indicator of underlying chromosomal abnormality (Caffey and Ross 1958; Astley 1963).

Techniques

Radiography: AP radiograph of pelvis.

Full Description of Technique

On the AP radiograph, the iliac angle is formed between Hilgenreiner's line and an oblique line joining two points of the ilium, that is, the most lateral point of the iliac wing above and the supero-lateral margin of the ossified acetabulum (Fig. 11.10).

The iliac index is a combination of the iliac angle and the acetabular angle of the growing hip (the acetabular angle of the growing hip being equivalent to the acetabular index). The
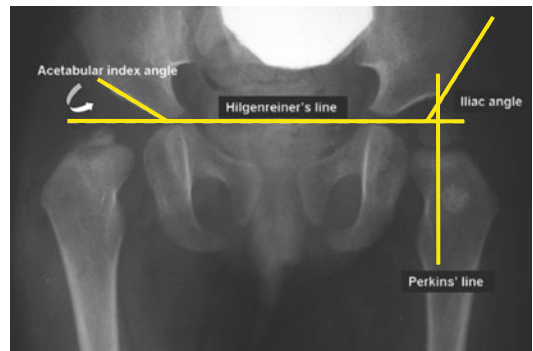
Fig. 11.11 AP pelvic radiograph. The **iliac index** is the sum of both the AI and iliac angles bilaterally divided by 2

iliac index is the sum of both the iliac angles and acetabular values bilaterally divided by 2 (Fig. 11.11).

Reproducibility/Variation

Few studies are available on reproducibility of this measurement.

Clinical Relevance/Implications

Astley studied 106 normal children from 0 to 8 years and 34 children in whom there was a clinical question of Down's syndrome. If the iliac index was less than 60, Down's syndrome was considered very possible. If the index measured more than 78, the child was probably normal.

With the advent of ultrasound and more sophisticated imaging methods, for assessment of Down's syndrome and other chromosomal disorders, and of course the advances in chromosomal analysis, the significance of this index has reduced.

Analysis/Validation of Reference Data

The iliac index, depending on its value, is potentially a contributory finding in chromosomal disorders, but no value is diagnostic.

Conclusion

Prenatal diagnosis of many chromosomal disorders can now be made, and postnatal chromosomal analysis obviates the need to use this index for assistance with diagnosis. However, it may be an additional observational finding in such conditions.

11.7 Alpha Angle (Graf US Angle)

The Graf angles are drawn relative to the iliac line, acetabular roof and labrum, in the true coronal plane.

Definition

The alpha angle is indicative of the slope of the bony acetabulum. This angle is a measure of the depth of the acetabulum and is an indicator of acetabular coverage as determined on ultrasound using the method of Graf (1980, 1984, 1987).

Normal	Abnormal
>60°	<50°

Indication

Evaluation of developmental hip dysplasia in newborns with clinical suspicion of instability. Most agree that in the presence of risk factors, US examination is best performed when an infant is 4–6 weeks old. Risk factors include mainly breech presentation, positive family history and oligohydramnios, talipes, arthrogryposis, spinal dysraphism, generalised ligamentous laxity, twins and postnatal saddling. The clinically unstable hip must be examined at 1–2 weeks of age. Infants with clinically stable hips presenting with a click should be examined at 2–4 weeks of age.

Techniques

Ultrasound: Coronal image of the hip.

Full Description of Technique

The high-frequency linear transducer should be placed on the lateral aspect of the hip joint while the infant is placed in the lateral decubitus position with the thigh flexed by 20° and slightly
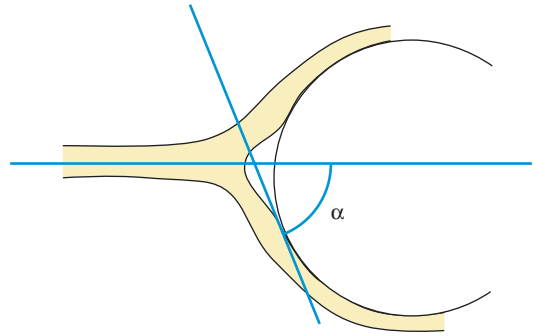
Fig. 11.12 The **alpha angle**, measured on ultrasound, is indicative of the slope of the bony acetabulum and is a measure of the depth of the acetabulum

internally rotated. A coronal image of the hip is obtained by scanning longitudinally from this lateral approach so that the line of the ilium is parallel to the transducer. The true coronal plane shows both the femoral head and the deepest portion of the acetabulum. The basic line is drawn parallel to the straight lateral margin of the ilium.

The alpha angle is the angle between a line extended from the lateral line of the ilium (the iliac line) and a line tangent to the bony acetabular roof (Fig. 11.12).

Reproducibility/Variation

Dias et al. (1993) evaluated interobserver and intraobserver agreement with respect to interpretation of static images and found that the alpha angle had only a fair degree of reproducibility in both inter- and intraobserver comparisons. The range of interobserver measurements of the beta angle was much wider than the intraobserver range. Cheng et al. (1994) found the alpha angle to be the most reliable of the static measurements. Bar-On et al. (1998) found intraobserver reproducibility to be good but interobserver agreement only moderate. Rosendahl et al. (1995) found high intraobserver agreement in morphology on a static scan, whereas interobserver agreement was moderate. However, there was moderate interobserver agreement in determining hip stability. It was found that

interobserver and intraobserver agreement in reproducing the scans was poorer than for interpreting them. They emphasise the need for substantial training and close attention to detail in order to obtain high interobserver agreement. Simon et al. (2004) found a high variability of the alpha and beta angles between observers for the same sonogram.

Clinical Relevance/Implications

US is the most widely used method for confirming a clinically suspected DDH and is the primary imaging technique for diagnosis and its follow-up. US alone cannot be considered a more reliable tool compared with physical examination. The surgical treatment rate did not decrease significantly in newborns screened with US compared to those who had clinical examination alone, but the non-surgical treatment rate was almost double in the US-screened group suggesting variable reliability.

The Graf classification is related to both the alpha and the beta angle. The alpha angle should be 60° or more. An angle <50° implies deficient development of the acetabulum at any age. A shallow acetabulum (between 50° and 60°) in a baby less than 3 months may simply reflect physiological immaturity (Graf type IIa) (Graf 1984; Millis and Share 1992; Gerscovich 1997a, b) but needs to be followed up to ensure normal development. A persistently shallow acetabulum after 3 months of age is abnormal. Quantitative measurements at one point in time are clearly important, but equally or even more important are the serial changes over time. Calculation of the alpha (or beta) angle cannot be made if the femoral head is dislocated anteriorly or posteriorly as the femoral head and the standard plane of the acetabulum are not visualised together (Fig. 11.13).

Analysis/Validation of Reference Data

There is wide variability in the degree of interobserver and to a degree of intraobserver reproducibility. Of the studies reviewed, no major misdiagnoses were made, and the important thing is that trends were identified correctly even if there was variability in actual figures measured. The diagnostic accuracy of US imaging for DDH in the screening population has not been investigated thoroughly (Roposch et al 2006). There is not sufficient evidence to support or reject a general US screening of newborns for DDH.
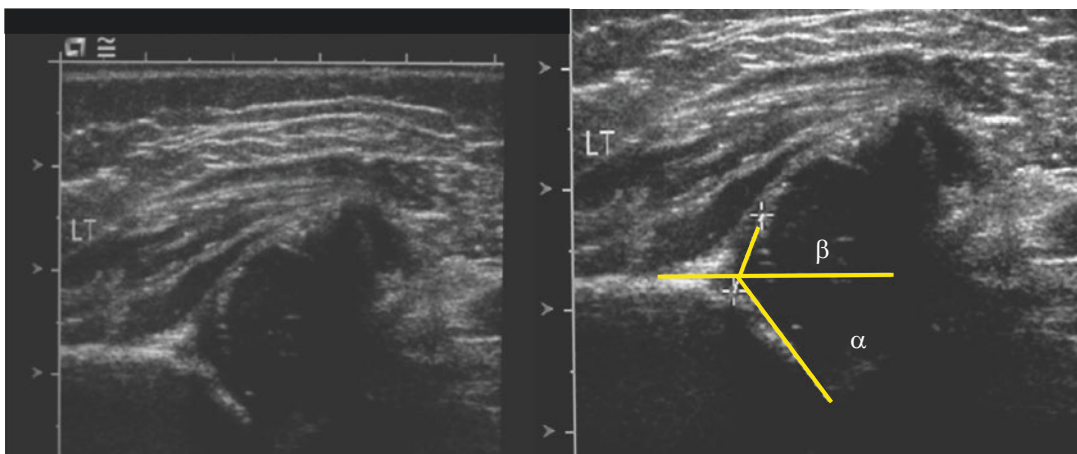
Fig. 11.13 US images done in the true coronal plane for calculating Graf's alpha and beta angles

Conclusion

Ultrasound is a satisfactory method for the diagnostic evaluation of hip dysplasia and is especially valuable if done on a serial basis to monitor improvement and response to treatment. Close attention to detail is necessary together with a good basic training in the application and frequent use to maintain skills. It is not yet clear if DDH detected by screening US is clinically relevant. Further studies on the best strategy for US screening are needed.

11.8   Beta Angle (Graf US)

Definition

The beta angle is the angle formed between a line drawn tangent to the lateral aspect of the femoral head and the iliac line (Fig. 11.14). It is indicative of the degree of fibrocartilaginous roof coverage through the labrum.

Normal	Immature	Abnormal
<55°	55°–77°	>77°

An increased beta angle indicates superior femoral head displacement and is used in sub-classifying the dysplasia.

Indication

Used in the assessment of developmental dysplasia of the hip.

Techniques

Ultrasound: Coronal image of the hip.

Full Description of Technique

A coronal image of the hip is obtained by scanning longitudinally from a lateral approach so that the line of the ilium is parallel to the trans-ducer. The true coronal plane shows the femoral head and the deepest portion of the acetabulum.

The beta angle is the angle between the iliac line and a line tangent to the lateral aspect of the femoral head. In practice, the beta angle is not as frequently used as the alpha angle and the percent coverage of the femoral head (Millis and Share 1992).

Reproducibility/Variation

See under Sect. 11.7.

Clinical Relevance/Implications

It is normal when <55°. An angle >77° is usually associated with subluxation and labral displacement. A value between 55°and 77° is associated with an immature hip. The beta angle together with the alpha angle contributes to the Graf classification of hip morphology and acetabular development (Graf 1984; Gerscovich 1997a, b).

Analysis/Validation of Reference Data

The beta angle is not as reproducible as the alpha angle. In the different studies, it is not used as much as the alpha angle.

Conclusion

The beta angle is not used to the same degree in analytical studies and during ultrasound assessment. It is probably more usual that the alpha angle or femoral head coverage will be measured. A full assessment will of course include this measurement.

Fig. 11.14   The **beta angle**, as measured on ultrasound, is indicative of the degree of cartilaginous roof coverage

11.9 Acetabular Coverage of the Femoral Head (US)

Definition

The relative percentage of coverage of the femoral head by the bony acetabulum (Morin et al. 1985).

Normal	Abnormal
50–58% coverage	<33% coverage

Indication

Assessment of developmental dysplasia of the hip.

Technique

Ultrasound: Coronal view—longitudinal scan from lateral approach.

Full Description of Technique

The US transducer is positioned on the lateral aspect of the flexed hip with the plane parallel to the long axis of the body and parallel to the line of the ilium. A coronal image of the hip is obtained by scanning longitudinally from a lateral approach so that the line of the ilium is parallel to the transducer. The true coronal plane shows the femoral head and the deepest portion of the acetabulum. The sonographic acetabular coverage of the femoral head is expressed as the percentage of femoral head coverage which is the depth between the iliac line and the medial aspect of the femoral head divided by the maximum diameter of the femoral head × 100 (Morin et al. 1985) (Fig. 11.15). The technique was introduced by Morin and further developed by Terjeson et al. (1989). It is based on the same principle as the radiographic migration percentage (MP) (Gerscovich 1997a, b). Values are not related to the patient's age.

$$\frac{d}{D} \times 100\% = \text{Femoral head coverage}$$
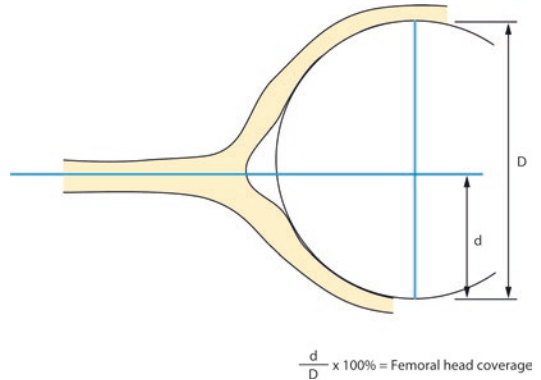
Fig. 11.15 The **acetabular coverage** of the femoral head as measured on ultrasound is the relative percentage of coverage of the femoral head by the bony acetabulum

Reproducibility/Variation

A study in 1994 (Holen et al. 1994) demonstrated moderate interobserver variation in evaluation of the femoral head coverage. The 95% confidence limit (±2 SDs) was ±8%. A study by Falliner in 2006 to determine the reproducibility of ultrasound measurements using the methods of Graf and Terjesen was done. This showed a mean alpha angle of 62.4° and mean femoral head coverage (FHC) of 55.4%. Statistical analysis showed almost equal reproducibility for alpha angle and FHC in the interobserver test but better repeatability for Graf's method (alpha angle) in the intraobserver test.

Clinical Relevance/Implications

There is varied opinion about what is normal. Holen et al. (1994) suggested that femoral head coverage of more than 50% should be considered normal. This is in agreement with Millis and Share (1992). However, Morin et al. (1985) suggested 58% or more femoral head coverage to be normal, while 33% is an absolute indicator of dysplasia. Terjesen (1996) also found this to be a rapid and reliable technique for the evaluation of hips in children under 2 years.

Analysis/Validation of Reference Data

Morin devised this method of assessment as an alternative method to the Graf technique as some people may find it easier.

Conclusion

Reproducible and considered by some easier to use than alpha and beta measurements in the assessment of developmental dysplasia of the hip.

11.10 Femoral Head Displacement in DDH (Yamamuro's Distances and Smith's Ratios)

Definition

Measurements of the lateral and superior displacement of the femoral head.

Indications

Developmental dysplasia of the hip.

Technique

Radiography: AP radiograph.

Full Description of Technique

A series of measurements produce the **Yamamuro's distances and Smith's ratios** to assess displacement (Yamamuro and Chene 1975, Smith et al 1968)**.**

Linear Measurements of Superior Femoral Displacement

Normal Values
Yamamuro-A distance. This is the distance in mm between the middle point of the proximal femoral metaphysis and the Hilgenreiner's or Y-Y line. The range of normal values for infants of **1 month to 4 years of age is 7–14 mm.**

Hilgenreiner-H distance. This is the distance between the highest point of the proximal femoral metaphysis and the Y-Y line. The normal value is **8–10 mm**.

h/b ratio. This is the ratio of the distance between the highest point of the femoral metaphysis and the Y-line and the distance between Perkins' line and a parallel line passing through the centre of the sacrum. The normal value for infants of **2–5 years of age is 0.10–0.20.**

Abnormal Values
h/b ratio: 0 to − 7.

Linear Measurements of Lateral Femoral Displacement

Normal Values
Yamamuro-B distance. This is the distance in mm between the middle point of the proximal femoral metaphysis and a line, perpendicular to the Y-line, which passes through the lateral edge of the ischium. The normal value for children of **1 month to 4 years of age is 5–12 mm.**

Hilgenreiner-D distance. This is the distance in mm between the inferior bony margin of the ilium and the projection on the Y-line of the high-
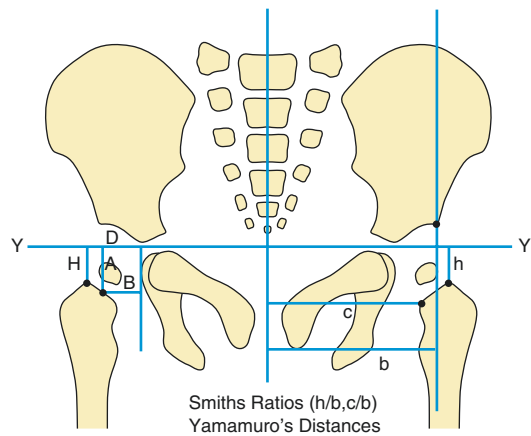
Fig. 11.16 Yamamuro's distances and **Smith's** ratio for linear (superior/lateral) displacement of the femoral head

est point of the proximal femoral metaphysis. Normal value is **14–16 mm**.

c/b ratio. This is the ratio of the distance between the medial beak of the proximal femoral metaphysis and the centre line and the distance between Perkins' line and the centre line. The normal value for infants of **2–5 years of age is 0.60–0.85.**

Abnormal Values
c/b ratio > 0.9.

Reproducibility/Variation

Yamamuro's measurements for linear displacement of the femoral head are accurate and less influenced by femoral rotation.

Smith's ratios are reliable. The use of a ratio reduces the effects of magnification.

Clinical Relevance/Implications

The measurements are useful to follow patients with DDH during treatment for normal development of the acetabulum (Fig. 11.16).

Conclusion

The measurements are a reliable indicator with an accurate performance rating between different observers.

11.11 Migration Percentage (MP) (Reimer's Index)

Definition

This was introduced by Mercer Rang in 1975 (Reimers 1980, Gerscovich 1997a, b). This indicates the percentage of the femoral head that is located lateral to the lateral edge of the acetabulum, i.e. lateral to Perkins' line. It is based on the same principle as the acetabular coverage of the femoral head as measured with ultrasound but essentially is measured as the percentage 'uncovered' femoral head. The remaining percentage represents the percentage femoral head coverage.

Normal	< 3 years	0%
	3–14 years	12% (0–20%)
Subluxation		33–100%

Indication

Reimer's index is used to determine the extent of subluxation of the hip in children with spasticity. It measures the degree of lateral acetabular deficiency. The migration percentage is also used in the assessment of subluxation/lateralisation in developmental dysplasia.

Techniques

Radiography: AP radiograph.

Full Description of Technique

On an AP radiograph, the migration percentage is defined by $d/D \times 100\%$, where d is the distance from the lateral aspect of the femoral head to Perkins' line divided by D, the diameter of the
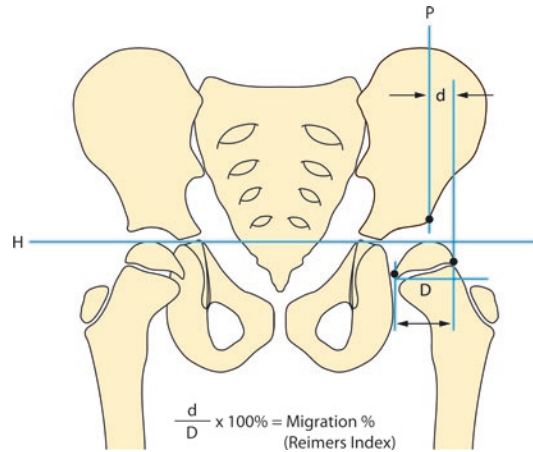
Fig. 11.17 The **migration percentage** (Reimer's index) indicates the percentage of the femoral head that is located lateral to the lateral edge of the acetabulum

femoral head parallel to Hilgenreiner's line (Gerscovich 1997a, b) (Fig. 11.17).

Reproducibility

Faraj et al. (2004) reporting on inter- and intra-measurer error in the assessment of Reimer's (1980) hip migration percentage found no statistical difference between the intra-sessional median absolute differences but found inter-measurer errors which may be clinically unacceptable. The two measurers however only had 6 months paediatric orthopaedic experience which may have contributed to the relatively suboptimal results.

Clinical Relevance

A migration index of more than 20% is considered to be abnormal (Moberg et al. 1999). Gerscovich states that normal values for children

less than 3 years old should be zero and for older children 12% (range 0–22%) (1997a, b).

Analysis/Validity of References

Parrott et al. (2002) believed that the results are acceptable in clinical practice provided treatment decisions are based on a series of radiographs taken at 6 month intervals, methods and training are standardised and consistent raters are used.

Conclusion

A valuable and useful measurement in follow-up of patients both pre- and postsurgical intervention.

11.12 Femoral Head Coverage

Definition

This is determined by calculating the percentage of the femoral head medial to Perkins' line in relation to the width of the femoral head parallel to Hilgenreiner's line (Wiig 2002) (Fig. 11.18). It was described by Heyman and Herndon in 1950 as the acetabulum-head quotient. It is based on the same principle as the acetabular coverage of the femoral head as measured with ultrasound.

Normal	Abnormal
70–80%	<70%

Indication

It is useful in the assessment of the hip in Perthes disease and also in the assessment of femoral head coverage in hip dysplasia.

Technique

Radiography: AP radiograph.

Full Description of Technique

On an AP radiograph, the femoral head coverage is the width of the femoral head medial to Perkins' line divided by the width of the femoral head × 100 (Fig. 11.18).

Reproducibility

Femoral head coverage radiographically shows small interobserver variability, and there is even less variability when examiners are experienced.
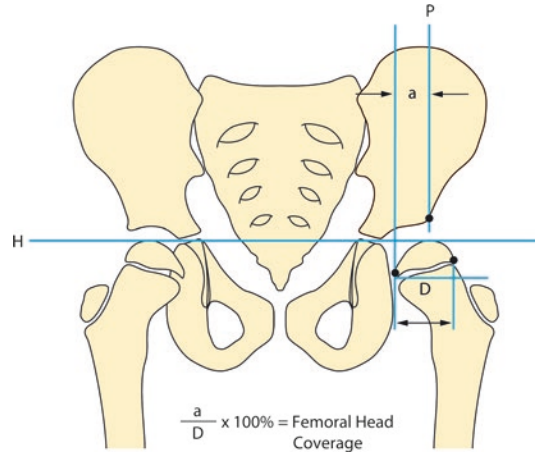
Fig. 11.18 The femoral head coverage as measured on a radiograph

It is probably more reliable than the centre-edge angle for inexperienced examiners (Wiig 2002).

Clinical Relevance

The lower normal limit of femoral head coverage is 80% as shown by Wiig (2002), but Heyman and Herndon (1950) reported 70% in normal hips.

Validity of References

A relatively reliable and reproducible measurement for assessing femoral head coverage and containment.

Conclusion

Some assessors find this to be an easier measurement to perform than the centre-edge angle.

11.13   The Centre-Edge Angle (Wiberg's Angle)

Definition

The centre-edge angle of Wiberg (1939) is the angle between a line drawn from the centre of the femoral head to the supero-lateral ossified margin of the acetabulum and a line drawn from the centre of the femoral head perpendicular to Hilgenreiner's line joining the triradiate cartilages of the acetabula (Fig. 11.19).

Normal	< 5 years	Unreliable
	5–8 years	> 20°
	9–12 years	> 25°
	13–16 years	26°–30°

Indication

Assessment of developmental dysplasia of the hip and other situations where knowledge of acetabular depth is required.

Technique

Radiography: AP radiograph of pelvis.
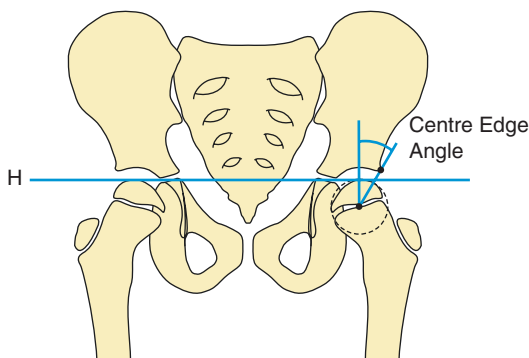
Fig. 11.19   The **centre-edge angle** of Wiberg

Full Description of Technique

On a well-positioned pelvic radiograph, Hilgenreiner's line (a horizontal line joining the triradiate cartilages of both acetabula) is drawn. The centre of the femoral head is determined, and from this two lines are drawn—one to the lateral bony edge of the acetabulum and one perpendicular to Hilgenreiner's line. The angle formed between these two lines is the centre-edge angle.

Reproducibility/Variation

In Tan's study (2001) which looked at 30 pelvic x-rays of 15 patients with an age range of 3–36 months (mean 26 months), there was no significant difference according to intraobserver reliability analysis. However, analysis of interobserver reliability showed significant differences. Differences in interobserver reliability in the very young may be due to difficulty in identifying the centre point of the unossified femoral head. Finding the centre point even in the stage of early ossification of the femoral head can be difficult (Tan et al. 2001) due to an eccentrically located ossific nucleus. Scoles et al. (1987) recommended that this angle should only be used after the age of 4 years, and Broughton suggested after 5 years (1989). Wiig et al. (2002) showed a low interobserver agreement for both normal hips and those affected by Perthes disease. They found better agreement between more experienced examiners when measuring the CE angle in patients over the age of 5 years than under it.

Clinical Relevance/Implications

Useful in older children in evaluating cases of minor dysplasia. At 5–8 years, the lowest normal limit is 19°; from 9 to 12 years the lowest limit is 25°, at 13–16 years 26–30° and

17–20 years 26–30° (Tönnis 1976). If the C-E angle is low, this may indicate dysplasia. If it is abnormally high, this may indicate protrusio acetabuli.

Analysis/Validation of Reference Data

It has been suggested that the centre-edge angle should be measured from the lateral most point of sclerosis in the roof of the acetabulum in this young age group rather than following the original method of Wiberg (Ogata et al. 1990). Kim et al. evaluated the lateral edge of the acetabulum to locate the most accurate marking point on a plain radiograph when measuring both the centre-edge angle and the acetabular index (Kim et al. 2000). They found that the most lateral bony margin of the acetabular roof on plain radiographs represents the anterolateral portion of the acetabulum, whereas the lateral end of the sourcil indicates the lateral margin of the superior portion of the acetabulum. In order to reduce the margin of intraobserver and interobserver error, it is important to indicate clearly which of the measuring points has been used and to remain constant in this when making and comparing measurements in individual patients, as there is quite a marked difference between the two depending on which point has been taken as the lateral marker.

Milani et al. (2000) described a technique for measuring Wiberg's angle in infants under the age of 3 months using sonographic images of their hips. Sonographic images were transferred to a computer where the images were analysed, and software provided the acetabular cartilaginous roof coverage angle (CRCA) which corresponds to the CEA angle in adults.

Conclusion

An appropriate measure for assessing femoral head coverage but only when measured by experienced examiners (Wiig 2002) due to difficulty in identifying the centre of the femoral head when it is incompletely ossified.

11.14   The Teardrop Distance

Definition

This is the distance from the lateral margin of the teardrop to the medial border of the proximal femoral metaphysis (Fig. 11.20).

Normal	Abnormal
<11 mm	>11 mm
Or >2 mm than contralateral side	

Indication

An indicator of hip joint disease and useful particularly in the early detection of Perthes disease. One of the earliest signs of Perthes disease is a widening of the teardrop distance (TDD).

Technique

Radiography: AP pelvis.

Full Description of Technique

AP radiograph. It is important that the femora/hips are not rotated internally or externally >30°, flexed more than 30° or abducted >15°. This is the distance from the lateral margin of the teardrop to the medial border of the proximal femoral metaphysis.
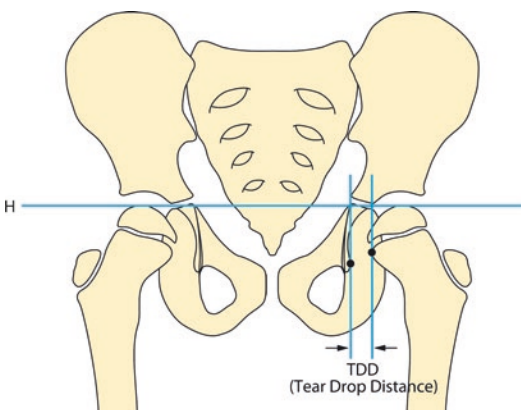
Fig. 11.20   The **teardrop** distance

Reproducibility/Variation

Eyring measured the teardrop distance on radiographs of 1070 normal hips of persons from 1 to 11 years old. He found the measurements were reproducible within 1 mm and were independent of the age of the patient (Eyring et al. 1965).

The teardrop distance is effectively measuring the medial joint space. Kaniklides and Dimopoulos (1996) suggested that the medial margin of the metaphysis and the medial boundary of the acetabulum as landmarks were not reliable measuring points for estimating subluxation in Perthes disease as they may be affected and deformed due to the disease and they may alter due to femoral or pelvic rotation. Katz (1969) however found that neither flexion nor extension of the pelvis significantly altered the teardrop figure, although pelvic rotation caused it to broaden.

Clinical Relevance/Implications

If the teardrop distance is >11 mm or more than 2 mm greater than that of the opposite hip, this is a sensitive indicator of hip joint disease, e.g. Perthes in the growing hip. It can also be indicative of the presence of a joint effusion.

Analysis/Validation of Reference Data

The teardrop does not appear until between 6 and 24 months of age in a normal hip and later in a dislocated hip. It is variable as regards its configuration in normals and can be dependent on a neutral position without rotation or inclination.

Conclusion

Based on Eyring's findings in 1070 children, it can be a sensitive indicator of early Perthes disease.

11.15 Medial Hip Joint Space

Definition

This is the distance from the medial aspect of the ossification centre of the femoral head at its widest portion, or from the medial aspect of the metaphysis when the femoral head is not ossified, to the adjacent acetabular wall (Gerscovic 1997) (Fig. 11.21).

Normal	Abnormal
5–12 mm	>12 mm
<1.5 mm between Rt and Lt	>1.5 mm between Rt and Lt

Indication

It evaluates for lateral displacement of the femoral head. Abnormality may indicate underlying hip pathology: if narrow, arthropathy, and if widened, possible effusion in children or early sign of Perthes disease.

Technique

Radiography: Measured on the frog lateral view (hips abducted and internally rotated).

Full Description of Technique

Radiography. Well-positioned frog lateral projection of the hips. Utilising Hilgenreiner's line, drop a perpendicular through the medial aspect/margin of the femoral head and through the lateral border of the teardrop. The distance between is the medial hip joint space measurement (equivalent to the teardrop distance of Eyring et al. 1965).

Reproducibility/Variation

Normal values are age independent and range from 5 to 12 mm. The difference between the right
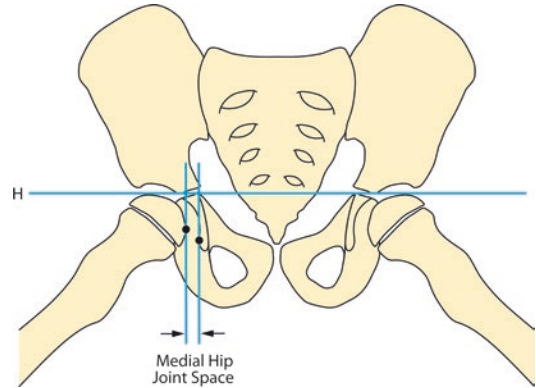
Fig. 11.21 The medial hip joint space

and left sides should not be more than 1.5 mm (Eyring et al. 1965). Kaniklides and Dimopoulos (1996) looked at AP radiographs and arthrograms of both hips on the same film with the legs in neutral position. The migration percentage (MP) was expressed as the fraction of the width of the femoral head extending beyond the acetabular edge. Kaniklides measured the medial joint space (MJS) from the medial border of the bony femoral head or femoral head cartilage on the arthrogram to the lateral border of the acetabular teardrop. This contrasted with Eyring. Kaniklides stated that the medial aspect of the metaphysis could become distorted due to underlying pathological processes and distort the metaphyseal beak leading to inaccurate measurement.

Kaniklides found a high interobserver agreement for both the medial joint Space (MJS) and the migration percentage (MP). He looked at 166 normals and 37 affected hips of patients with unilateral Perthes and 37 contralateral hips and therefore 240 in total. The lateral margin of the teardrop can be poorly defined in the dysplastic hip (Broughton et al. 1989) which may lead to difficulties in measurement.

Clinical Relevance/Implications

An abnormal medial hip joint space may indicate underlying joint disease or insult to the femoral head.

Analysis/Validation of Reference Data

This can be a difficult measurement to reproduce in some disease processes. In some situations, such as Perthes disease, to assess containment, the migration percentage may be more valuable.

Conclusion

May be valuable. If the joint space is widened and no obvious evidence of Perthes may indicate an effusion and suggest further assessment with ultrasound to confirm or further imaging, for example, with magnetic resonance imaging.

## 11.16	Symphysis Pubis Width

Definition

The width of the symphysis pubis.

Normal	Abnormal
<10 mm	>10 mm

Indication

To identify if abnormally widened. A number of conditions are associated with widening of or defective ossification of the symphysis pubis.

Due to bone growth and ossification of cartilage, the interpubic distance varies with age.

Technique

Radiography: An abdominal or pelvic radiograph can be used. Patel and Chapman (1993) found that there was no difference in the measurement whether one used a centring point at the level of the iliac crests or one 5 cm above the symphysis pubis as used in a pelvic radiograph.

The transverse width of the symphysis is measured to the nearest millimetre at its narrowest point (Fig. 11.22).

Reproducibility

Patel and Chapman (1993) examined 888 radiographs over an age range of birth to 16 years. Their findings were in broad agreement with the findings of Muecke and Currarino (1968). Ten mm as the upper limit of normal agreed with data from Heyman and Lundquist (1931). The mean width at 16 years is similar to that of Vix and Ryu (1971) in their study of 400 adults.

Clinical Relevance

Separation of the symphysis may be an important clue to an underlying condition in the paediatric age group. This may be divided into congenital and acquired conditions. Congenital disorders may be due to defective ossification or with normal ossification.

Analysis of Reference data

No significant areas of conflict.

Conclusion

A simple to perform measurement which, if widened, is a useful finding in relation to making an underlying diagnosis.

Fig. 11.22 The **symphysis pubis** distance. This is the transverse width of the symphysis measured to the nearest millimetre at its narrowest point

11.17   Klein's Line

Definition

This is a line drawn along the superior surface of the femoral neck. The epiphysis should normally project superior to it (Fig. 11.23), and the line laterally cuts off about 15% of the femoral epiphysis (Klein et al. 1951).

Indication

It is used in assessment of early slipped upper femoral epiphysis. In early slipped upper femoral epiphysis (SUFE), the epiphysis lies flush or level with the line. As slip continues, the epiphysis moves posterior and inferior to it.

Techniques

Radiography: AP radiograph of the pelvis centred approximately 1 cm above the symphysis pubis. The projection must be produced accurately, and the patella should face forward exactly parallel to the x-ray table. If this is not possible clinically on the affected side, the pelvis should be elevated on the affected side.
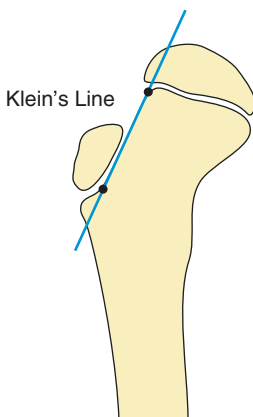
Fig. 11.23   Klein's line should pass through the femoral epiphysis laterally. A difference of 2 mm with the contralateral side indicates a slip

Full Description of Technique

On an AP radiograph, a line is drawn along the superior surface of the femoral neck. In the normal situation, this will extend through the superior aspect of the epiphysis (the epiphysis should normally project superior to it).

Reproducibility/Variation

Green et al. (2009) measured the head-shaft angle of Southwick and the Wilson percent epiphyseal displacement and evaluated the interobserver and intraobserver reliability and efficacy of these methods and also compared with Klein's line. They found that on the basis of the classical definition of Klein's line, only 40.3% of slips were identified. However, by modifying Klein's line such that they measured the width of epiphysis lateral to Klein's line, they improved sensitivity to 79% if a difference of 2 mm between hips indicated a slip.

Clinical Relevance/Implications

If the epiphysis lies level or inferior to Klein's line, there has been epiphyseal slip.

Analysis/Validation of Reference Data

Early or mild degrees of slip may be difficult and can be overlooked. Clinically if a slipped upper femoral epiphysis (SUFE) is suspected and Klein's line appears normal, the head-shaft angle of both hips should be measured to better evaluate for possible SUFE.

Conclusion

Application of Klein's line can be difficult in mild cases of slipped upper femoral epiphysis.

11.18 Femoral Neck-Shaft Angle

Definition

The angle formed between a line drawn parallel to the femoral neck and one drawn parallel to the long axis of the femoral shaft (Fig. 11.24).

Normal	3 years 145°	Coxa vara	< 125°
Adult	128° (125–135)	Coxa valga	> 135°

Indication

The amount of a varus deformity can be measured.

Technique

Radiography: AP radiograph.

Full Description of Technique

On an AP radiograph of the pelvis with the hips in neutral position, a line is drawn along and parallel with the femoral neck passing through the centre of the femoral head. A second line is drawn along and parallel to the femoral shaft. The femoral neck-shaft angle is the angle subtended between these two lines (Fig. 11.24).

Reproducibility/Variation

There is broad individual variation with a wide standard deviation in this angle (Tönnis 1976; Broughton et al. 1989).

Clinical Relevance/Implications

This normally measures 145° at 3 years of age, decreasing to between 125°and 135°in the adult with an average value of 128°.

Analysis/Validation of Reference Data

There is an intrinsic variability of the measurement between individuals.

Conclusion

Useful and straightforward measurement in the evaluation of varus deformity.
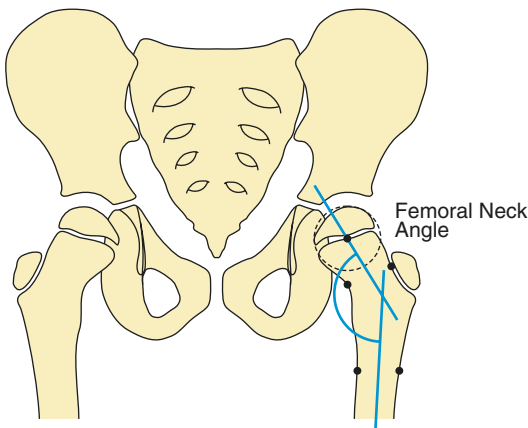
Fig. 11.24 The **femoral neck-shaft** angle

11.19 Epiphyseal-Shaft Angle of Southwick

Definition

This is the angle subtended between a perpendicular line to the epiphyseal line drawn along the femoral neck and one drawn along the femoral shaft. It is measured for both sides, and the difference between the two is the magnitude of slip severity.

Indication

This is used to describe the radiographic magnitude of epiphyseal slip severity in cases of slipped upper femoral epiphysis (SUFE).

Technique

Radiography: The angle is measured on the frog lateral radiograph of the pelvis.

Full Description of Technique

The angle is measured on the frog lateral radiograph of the pelvis. A line is drawn between the anterior and posterior tips of the epiphysis at the physeal plate level. A perpendicular line is drawn to this epiphyseal line through the femoral neck.

A line is then drawn along the mid femoral shaft.

The epiphyseal-shaft angle is the angle formed by the intersection of the perpendicular line and the femoral shaft line (Fig. 11.25). It is measured for both hips, and the magnitude of slip displacement is the angle of the involved hip minus the angle of a contralateral normal hip (Southwick 1967).
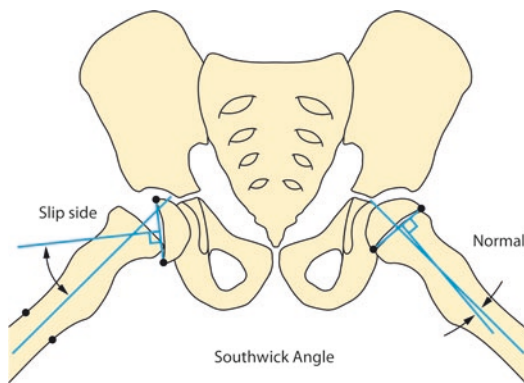
Fig. 11.25 The **epiphyseal-shaft angle** of Southwick

Reproducibility/Variation

In a study by Green et al. (2009), five separate observers on two separate occasions evaluated 30 AP and 30 frog lateral radiographs of patients with unilateral slipped capital femoral epiphysis (SCFE) for head-shaft angle, percent epiphyseal displacement and width of epiphysis lateral to Klein's line. Head-shaft angle and percent epiphyseal displacement were found to provide a reliable means of SCFE diagnosis.

Clinical Relevance/Implications

Normally the femoral neck axis is at 90° angle to the base of the epiphysis dividing into two equal halves. In the frog lateral projection, the base of the epiphysis is also normally perpendicular to the longitudinal femoral neck axis. The femoral head-shaft angle is used to identify the severity of slip in cases of slipped upper femoral epiphysis (SUFE). Using the measurement of this angle, a slipped upper femoral epiphysis is classified as mild if it less than 30°, moderate if it is between 30 and 50° and severe if it is more than 50°. If there is bilateral slipped upper femoral epiphysis, then 12° can be used as the control angle (Loder et al. 1999).

Analysis/Validation of Reference Data

Early or mild degrees of slip may be difficult and can be overlooked. Clinically if a slipped upper femoral epiphysis (SUFE) is suspected and Klein's line appears normal, the epiphyseal-shaft angle of both hips should be measured to better evaluate for possible SUFE.

Conclusion

The head-shaft angle of Southwick is valuable in evaluating the degree/severity of epiphyseal slip. Although it takes a bit longer to perform than the lateral slip angle of Wilson, its results are more reliable and reproducible.

11.20 Articulo-Trochanteric Distance (ATD)

Definition

The distance between the proximal femoral head and the greater trochanters.

Indications

Monitoring patients with Perthes disease.

Technique

Radiography: AP Radiograph

Full Description of Technique

The articulo-trochanteric distance (ATD) is measured between two lines perpendicular to Perkins' line: the line through the proximal tip of the greater trochanter and that through the most proximal point of the femoral head (Fig. 11.26).

Reproducibility/Variation

The level of interobserver agreement is high.
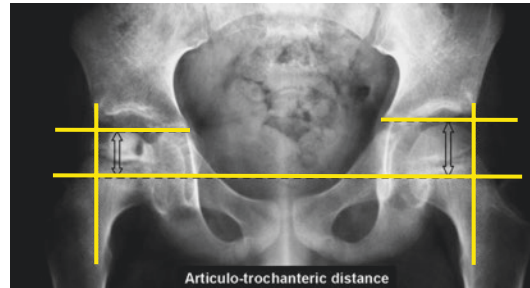
Fig. 11.26 Articulo-trochanteric distance is reduced on the right due to ischaemic necrosis

Clinical Relevance/Implications

The measurement is also applied for assessing the proper position of implants in various surgical procedures.

Analysis/Validation of Reference Data

Although the data is limited, the ATD showed good interobserver agreement with few interobserver differences.

Conclusion

The ATD is probably best utilised as a radiological measurement criterion in combination with other measurements in the follow-up assessment of Perthes disease such as CE angle and femoral head coverage.

References

Agus H, Bicimoglu A, Omeroglu H et al (2002) How should the acetabular angle of Sharp be measured on a pelvic radiograph? J Pediatr Orthop 22:228–231

Astley B (1963) Chromosomal abnormalities in childhood, with particular reference to Turner's syndrome and mongolism. Br J Radiol 36:2

Ball F, Kommenda K (1968) Sources of error in the roentgen evaluation of the hip in infancy. Ann Radiol (French) 11:299–301

Bar-On E, Meyer S, Harari G, Porat S (1998) Ultrasonography of the hip in developmental hip dysplasia. J Bone Joint Surg 80B(2):321–324

Boniforti FG, Fujii G, Anfliss RD, Benson MKD (1997) The reliability of measurements of pelvic radiographs in infants. J Bone Joint Surg (Br) 79-B:570–575

Broughton NS, Brougham DI, Cole WG, Menelaus MB (1989) Reliability of radiologic measurement in the assessment of the child's hip. J Bone Joint Surg 71-B:6–8

Caffey J, Ross S (1958) Pelvic bones in infantile mongolism. AJR Am J Roentgenol 80:458

Carney BT, Rogers M, Minter CL (2005) Reliability of acetabular measures in developmental dysplasia of the hip. J Surg Orthop Adv 14:73–76

Cheng JCY, Chan YL, Hui PW, Shen WY, Metreweli C (1994) Ultrasonographic hips morphometry in infants. J Pediatr Orthop 14:24–28

Dias JJ, Thomas IH, Lamont AC, Mody BS, Thompson JR (1993) The reliability of ultrasonographic assessment of neonatal hips. J Bone Joint Surg (Br) 75B(3):479–482

Edgren W (1965) Coxa plana. A clinical and radiological investigation with particular reference to the importance of the metaphyseal changes for the final shape of the proximal part of the femur. Acta Orthop Scand Suppl 84:1–129

Eyring EJ, Bjornson DR, Peterson CA (1965) Early diagnostic and prognostic signs in Legg-Calvé-Perthes disease. Am J Roentgenol Radium Ther Nucl Med 93:382–387

Falliner A, Schwinzer D, Hahne HJ, Hedderich J, Hassenpflug J (2006) Comparing ultrasound measurements of neonatal hips using the methods of Graf and Terjesen. J Bone Joint Surg (Br) 88B:104–106

Faraj S, Atherton WG, Stott NS (2004) Inter- and intra-measurer error in the measurement of Reimers hip migration percentage. J Bone Joint Surg (Br) 86:434–437

Gerscovich EO (1997a) A radiologist's guide to the imaging in the diagnosis and treatment of developmental dysplasia of the hip. I. Skelet Radiol 26:386–397

Gerscovich EO (1997b) A radiologist's guide to the imaging in the diagnosis and treatment of developmental dysplasia of the hip. II. Ultrasonography. Skelet Radiol 26:447–456

Graf R (1980) The diagnosis of congenital hip joint dislocation by the ultrasonic compound treatment. Arch Orthop Traum Surg 97:117–133

Graf R (1984) Classification of hip joint dysplasia by means of sonography. Arch Orthop Trauma Surg 102:248–255

Graf R (1987) Guide to sonography of the infant hip. Thieme, New York

Green DW, Mogekwu N, Scher DM (2009) A modification of Klein's line to improve sensitivity in slipped capital femoral epiphysis. J Pediatr Orthop 29:449–453

Harcke HT, Grissom LE (1990) Performing dynamic sonography of the infant hip. AJR Am J Roentgenol 155:837–844

Heyman CH, Herndon CH (1950) Legg-Perthes disease. J Bone Joint Surg Am 32:767–778

Heyman J, Lundquist A (1931) Symphysis pubis in pregnancy and parturition. Acta Obstetr Gynecol Scand 12:191–226

Hilgenreiner H (1925) Zur fruhdiagnose und fruhbehandlung der angeborenen Huftgelenkverrenkung. Med Klin 21:1385

Holen KJ, Terjesen T, Tegnander A et al (1994) Ultrasound screening for hip dysplasia in newborns. J Pediatr Orthop 14:667–673

Kaniklides C, Dimopoulos P (1996) Radiological measurement of femoral head position in Legg-Calvé-Perthes disease. Acta Radiol 37:863–869

Katada S, Ando K (1984) A roentgenographic evaluation of the indices for hip dysplasia in children influenced by pelvic tilt. In: Ueno R, Akamatsu N, Itami Y, Tagawa H, Yoshino S (eds) The hip: clinical studies and basic research. Elsevier Science, Amsterdam, pp 137–140

Katz JF (1969) Identification of the teardrop figure and acetabular margins on the roentgenogram. Clin Orthop 62:232

Kay RM, Watts HG, Dorey F (1997) Variability in the assessment of acetabular index. J Pediatr Orthop 17:170–173

Kim HT, Kim J II, Yoo C II (2000) Diagnosing childhood acetabular dysplasia using the lateral margin of the Sourcil. J Pediatr Orthop 20(6):709–717

Kitajima M, Mawatari M, Aita K et al (2006) A simple method to determine the pelvic inclination angle based on anteroposterior radiographs. J Orthop Sci 11:342–346

Klein A, Joplin RJ, Reidy JA et al (1951) Roentgenographic features of slipped capital femoral epiphysis. AJR Am J Roentgenol 66:361–374

Loder RT, Blakemore LC, Farley FA, Laidlaw AT (1999) Measurement variability of slipped upper femoral epiphysis. J Orthop Surg 7:33–42

Milani C, Ishida A, Filho JL, Dobashi ET (2000) A new methodology for the measurement of the Wiberg angle in infants under 3 months. J Pediatr Orthop 9:108–113

Millis MB, Share JC (1992) Use of ultrasonography in dysplasia of the immature hip. Clin Orthop Relat Res 274:160–171

Moberg A, Hansson G, Kaniklides C (1999) Acetabulum-head index in children with normal hips.: a radiographic study of 154 hips. J Pediatr Orthop 8:268–270

Morin C, Harcke HT, MacEwen GD (1985) The infant hip: real time US assessment of acetabular development. Radiology 157:673–677

Muecke EC, Currarino G (1968) Congenital widening of the symphysis pubis. Associated clinical disorders and roentgen anatomy of affected bony pelves. AJR Am J Roentgenol 103:179–185

Ogata S, Moriya H, Tsuchia T, Kamegaya M, Someya M (1990) Acetabular cover in congenital dislocation of the hip. J Bone Joint Surg 72-B:190–196

Parrott J, Boyd RN, Dobson F et al (2002) Hip displacement in spastic cerebral palsy: repeatability of radiologic measurement. J Pediatr Orthop 22:660–667

Patel K, Chapman S (1993) Normal Symphysis pubis width in children. Clin Radiol 27:56–57

Perkins G (1928) Signs by which to diagnose congenital dislocation of the hip. Lancet 1:648

Reimers J (1980) The stability of the hip in children. A radiological study of the results of muscle surgery in cerebral palsy. Acta Orthop Scand Suppl 184:1–100

Roposch A, Moreau NM, Uleryk E, Doria AS (2006) Developmental dysplasia of the hip: quality of reporting of diagnostic accuracy for US. Radiology 241:854–860

Rosendahl K, Aslaksen A, Lie RT, Markestad T (1995) Reliability of ultrasound in the early diagnosis of developmental dysplasia of the hip. Pediatr Radiol 25:219–224

Scoles PV, Boyd A, Jones PK (1987) Roentgenographic parameters of the normal infant hip. J Pediatr Orthop 7:656–663

Sharp I (1961) Acetabular dysplasia. The acetabular angle. J Bone Joint Surg 43B:268–272

Shenton EWH (1911) Disease in bone and its detection by the X-rays. Macmillan, London, pp 40–43

Siebenrock KA, Kalbermatten DF, Ganz R (2003) Effect of pelvic tilt on acetabular retroversion: a study of pelves from cadavers. Clin Orthop Relat Res 407:241–248

Simon EA, Saur F, Buerge M et al (2004) Inter-observer agreement of ultrasonographic measurements of alpha and beta angles and the final type classification based on the Graf method. Swiss Med Wkly 134:671–677

Skaggs DL, Karminsky C, Tolo VT, Kay RM, Reynolds RAK (1998) Variability in measurement of acetabular index in normal and dysplastic hips, before and after reduction. J Pediatr Orthop 18:799–801

Smith WS, Badgley CE, Orwig JB, Harper JM (1968) Correlation of postreduction roentgenograms and thirty-one-year follow-up in congenital dislocation of the hip. J Bone Joint Surg Am 50-A:1081–1098

Song FS, McCarthy JJ, MacEwen GD, Fuchs KE, Dulka SE (2008) The incidence of occult dysplasia of the contralateral hip in children with unilateral hip dysplasia. J Pediatr Orthop 28:173–176

Southwick WO (1967) Osteotomy through the lesser trochanter for slipped capital femoral epiphysis. J Bone Joint Surg Am 49:807–835

Spatz DK, Reiger M, Klaumann FM, Stanton RP, Lipton GE (1997) Measurement of acetabular index intra-observer and inter-observer variation. J Pediatr Orthop 17:174–175

Tan L, Aktas S, Copuroglu C, Ozcan M, Ture M (2001) Reliability of radiological parameters measured on anteroposterior pelvis radiographs of patients with developmental dysplasia of the hip. Acta Orthop Belg 67:374–379

Terjesen T (1996) Ultrasound as the primary imaging method in the diagnosis of hip dysplasia in children aged < 2 years. J Pediatr Orthop B 5:123–128

Terjeson T, Bredland T, Berg V (1989) Ultrasound for hip assessment in the newborn. J Bone Joint Surg (Br) 71-B:767–773

Tönnis D (1976) Normal values of the hip joint for the evaluation of X-rays in children and adults. Clin Orthop Relat Res 119:39–47

Vix VA, Ryu CY (1971) The adult symphysis pubis: normal and abnormal. AJR Am J Roentgenol 112:517–525

Wiberg G (1939) Studies on dysplastic acetabula and congenital subluxation of the hip joint. With special reference to the complication of osteoarthritis. Acta Chirurgica Scandinavica, Suppl. 58

Wientroub S, Grill F (2000) Ultrasonography in developmental dysplasia of the hip. Curr Conc Rev J Bone Joint Surg 82(B):1004

Wiig O, Terjesen T, Svenningsen S (2002) Inter-observer reliability of radiographic classifications and measurements in the assessment of Perthes disease. Acta Orthop Scand 73:523–530

Yamamuro T, Chene SH (1975) A radiological study on the development of the hip joint in normal infants. J Jap Orthop Assoc 49:421–439

Zsernaviczky J, Turk G (1975) The beta-angle. A diagnostic sign for the early diagnosis of congenital hip dysplasia. Rofo 123:131–133

Pelvis/Hip: Adult

12

Apostolos Karantanas

Contents

A. Karantanas, M.D., Ph.D.
Department of Medical Imaging, Department of Radiology, University Hospital, University of Crete, Heraklion, 711 10 Crete, Greece
e-mail: karantanas@uoc.gr

12.1   Introduction

The requirement for objective measurements of the mature pelvis and hip is primarily dictated by three major aetiologies: prior events in the paediatric age group (acetabular dysplasia, Perthes disease, SUFE), developmental conditions that present in the young adult (acetabular over- or under-coverage, femoroacetabular impingement—FAI) and acquired adult hip disorders (post-traumatic, avascular necrosis, osteoarthritis).

Hip dysplasia is a collective term which refers to a developmental abnormality of the acetabulum, femoral head or both regardless of aetiology. In acetabular dysplasia, most of the measurements utilised in the paediatric age group become unreliable and inappropriate after fusion of the epiphysis, although some (acetabular angle, centre-edge angle) are still useful, reliable and helpful. An array of measurements exists in assessing the adult dysplastic hip, and the more useful and practical ones are presented in this chapter. Most are based on radiographic assessment from the AP view utilising important reproducible and reliable landmarks. The centre-edge angle is important in assessing the superior and lateral femoral head coverage by the acetabulum, while the HTE angle assesses the roof orientation and coverage as well. The percentage of femoral head coverage assesses the congruity of the head in the acetabulum, while the acetabular depth-to-width index declares the acetabular depth. Evidence of dysplasia using these angle measurements on the AP view then requires further assessment of the acetabulum by the faux profile view which allows assessment of the anterior acetabular coverage using the VCA angle or by axial CT assessment which provides sector angles of both the anterior and posterior acetabular coverage.

FAI is described as being of two types: morphological acetabular abnormalities (coxa profunda, protrusio acetabuli, acetabular retroversion) that predispose to a pincer impingement and femoral head asphericity (focal or generalised) leading to cam impingement. However, measurements of the entire hip joint are required as both types are known to coexist in up to 86% of cases. Although measurements for assessing the underlying morphological characteristics of FAI have been established, it is important at the outset that one appreciates the importance of validating that the correct radiographic technique has been used as an essential prerequisite.

Measurements of the hip are also required in assessing the degree of morphological change related to a variety of acquired conditions that involve the hip, namely, the joint space. Trauma to the acetabulum or femoral head, avascular necrosis and primary osteoarthritis are the main conditions that lead to joint changes.

As most of the radiographic techniques are obtained in the supine position, it is important to remember that measurement values based on these projections do not necessarily represent the same acetabular-femoral relationships on dynamic weight-bearing positions. Accuracy and reliability factors apply not just to measurements based on conventional radiographic appearances but also to those based on cross-sectional imaging, namely, CT and MRI. Pelvic symmetry is important to minimise radiographic error rates, but it is also important to realise that the pelvic tilt introduces errors in the measurements not only on conventional radiographs but also in the 2D axial images generated by CT and MRI. Software dedicated to incorporate the pelvic inclination has been developed to reduce this source of error, as well as resorting to carrying out the required measurement parameters from 3D reformatted images. Although CT and MRI are as a rule deemed superior to radiography in providing some measurements, there are still residual unresolved areas of disagreement in the literature. Controversy exists on a number of fronts, ranging from the best modality deemed to be most reliable, the degree of abnormality related to symptom production and the way the measurements are used in clinical/surgical management.

12.2 Lines and Landmarks in Adult Pelvic/Hip Measurements

The majority of the tried and tested measurements are made with reference to the radiographic appearances on the AP and cross-lateral views. In the assessment of the adult dysplastic hip, the AP view of the pelvis is obtained with the patient supine, with 15–20° internal rotation of the lower limbs to correct the natural femoral anteversion, an FFD of 120 cm, with the central beam perpendicular to the table centred midway between the superior outline of the symphysis pubis and a line joining the ASIS's. Criteria for acceptable standards for pelvic radiography are applied to cover correct exposure, symmetric appearance of the pelvis and a true AP appearance of the femoral necks. Radiographs must meet proper validation criteria before they are used for measurement estimation: coccygeal alignment with the mid-symphysis and a distance between the sacrococcygeal joint and the symphysis less than 32 mm in men and 47 mm in women. Anatomical pelvic and hip landmarks act as fixed points allowing reference lines to be made from which distances and subtended angles can be calculated. On the AP radiograph, the following radiographic lines and landmarks are utilised (Fig. 12.1).

1. **Acetabular sourcil**. Appearing as a curved eyebrow-shaped dense area of subchondral bone, the **sourcil cotyloidien** is readily identified on the superior weight-bearing articular surface of the acetabulum.
2. Drifting laterally along the sourcil outline and starting from the lateral rim of the acetabulum edge (**E** point), two lines can be traced following the anterior and posterior acetabular rims. The **anterior acetabular rim** is less conspicuous and normally lies superior and medial to the easily defined **posterior acetabular rim**, which is more vertically orientated lying lateral and inferior to the anterior rim. As the acetabulum normally becomes more anteverted from a cranial to a caudal direction, the lines should diverge from their superolateral starting point as they course inferomedially. Along the femoral neck axis from the centre of the femoral head, the lines should be about 1.5 cm apart.
3. The **centre of the femoral head** (**C** point) is easily defined due to the femoral head's spherical shape. Normally the centre of the femoral head is along the same horizontal level as the superior tip of the ipsilateral greater trochanter. The posterior acetabular rim outline normally runs through the centre of the femoral head. A line joining the centre of both femoral heads, the **C-C line,** is the reference line as the horizontal
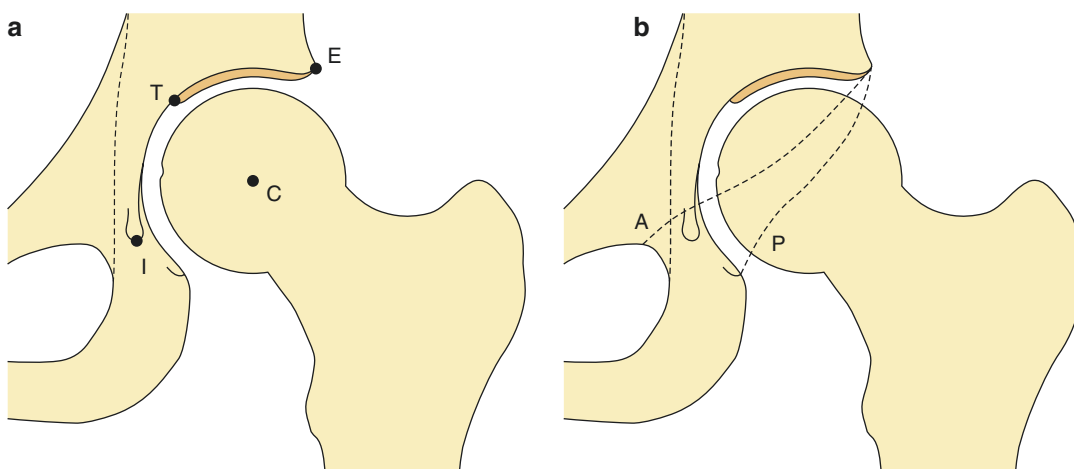
Fig. 12.1 (**a**, **b**) Acetabular and femoral head landmarks used in hip measurements. The anterior acetabular outline (*A*) normally lies superiorly and medial to the posterior (*P*) acetabular outline 1.5 cm apart at the level of the centre of the femoral head. Note that the ilioischial line normally lies medial to the medial wall of the acetabulum and teardrop

to which other oblique lines intersect. A reference line parallel to the C-C line can be used instead drawn between the inferior points of the teardrops—**horizontal teardrop line**—when measuring some angles such as sharp's angle.

4. Drifting medially towards the medial limit of the weight-bearing sourcil (T point), one can identify the outline of the nonarticulating false acetabulum. The floor of the false acetabulum depicts the **acetabular fossa** and the most medial rim of the acetabulum.

5. The lower end of the medial acetabular rim inferiorly becomes contiguous with Kohler's teardrop. The teardrop's lateral outline represents the wall of the acetabular fossa and is referred to as the **acetabular line**, while its medial outline is the anteroinferior margin of the quadrilateral surface. The inferiormost point of the acetabulum is the lower limit of the teardrop (**I** point). The teardrop is seen just above and lateral to the superolateral outline of the obturator foramen. On radiographs the teardrop is lateral to the ilioischial line. The wall of the acetabular fossa (which represents the medial acetabular floor inferiorly and is seen as the acetabular line) forms the lateral border of the teardrop which is continuous with the medial border of the tear drop which represents the cortex of the ischioilial pelvic wall. The acetabular fossa therefore normally lies lateral to the ilioischial line, and the medial acetabular rim denotes the limits of the medial joint space which should not be confused with the ilioischial line.

6. The **ilioischial line**. The ilioischial line is actually formed by that portion of the quadrilateral plate which is tangential to the central beam projected as a line. It extends cranially towards the medial outline of the ilium of the pelvic brim, while caudally it merges with the medial outline of the ischium (Fig. 12.1). The acetabular line lies lateral to the ilioischial line in men by an average of 2 mm, while in women the acetabular line is an average of 1 mm medial to the ilioischial line. The acetabular line, which is the medial wall of the acetabulum, and the ilioischial line, which is a portion of the quadrilateral plate, are centrally located structures. Being centrally located, their interrelationship is not significantly affected by minimal degrees

of rotation. It is this relationship that is measured in assessing their relative positions to establish the diagnosis of coxa profunda (deep acetabulum) and protrusio acetabuli. Estimating the medial acetabular wall thickness from AP radiographs for reaming capacity at hip arthroplasty is unreliable. For this purpose, CT is needed to measure the *smallest* quadrilateral plate acetabular distance (QPAD) which has a mean thickness **normally of 1.1 mm,** increasing directly proportionally with degree of severity up to **8 mm in dysplastic hips**.

7. **Hip centre**. The hip centre position is determined by the position of the medial aspect of the femoral head relative to the ilioischial line. The centre is lateralised if this distance is greater than 10 mm and not lateralised if its less than 10 mm. Lateralised femoral heads are considered to be a sign of structural instability or dysplasia.

8. **Skinner's line**. On an AP view of the pelvis, a line is drawn through and parallel to the femoral shaft axis. A second line (Skinner's) is then drawn tangentially from the tip of the greater trochanter perpendicular to the shaft axis. The fovea capitis should normally lie at the level or above this line (Fig. 12.2). If the fovea lies below this line, then this indicates that the femur is displaced superiorly in relation to the head which is due to a fracture or other causes of coxa vara.
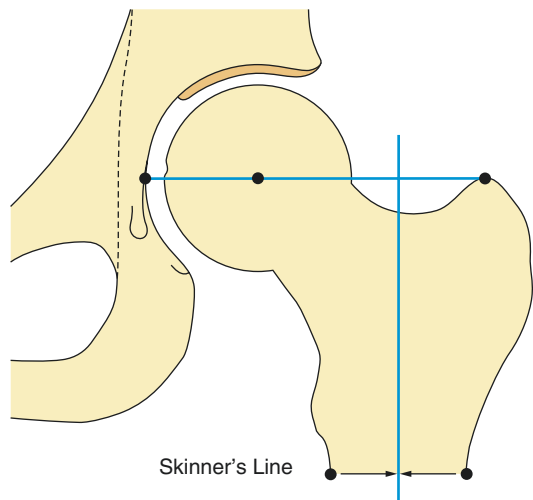
Fig. 12.2 Skinner's line

12.3   Joint Space Width (JSW): Teardrop Distance

Definition

The joint space width (JSW) is the distance from the most proximal surface of the femoral head to the opposing articular surface of the acetabulum. The teardrop distance is defined as the distance from the lateral margin of the pelvic teardrop to the most medial aspect of the femoral head.

Indications

The hip joint space width is used for diagnosis and monitoring of osteoarthritis.

The teardrop distance is used for depicting joint fluid and early Perthes disease as discussed in the paediatric chapter.

Technique

AP radiography (Fig. 12.3).

Full Description of Technique

For follow-up measurement in the same individual, more than one joint space value is selected.

SJ: Super joint space is the distance from the femoral head subchondral outline to the acetabular sourcil line at 90° from the C-C horizontal line.

AJ: Axial joint space is the corresponding distance just lateral to the acetabular fossa (medial border of sourcil bony condensation).

MJ: Medial joint space is the distance along the C-C horizontal line through the centre of the femoral heads.

Normal JSW		
SJS	**>40 years**	**4 mm (2–7 mm)**
	<40 years	**4 mm (3–6 mm)**
AJS	**<40 years**	**4 mm (3–7 mm)**
	>40 years	**4 mm (2–7 mm)**
MJS	**<40 years**	**8 mm (4–12 mm)**
	>40 years	**8 mm (4–14 mm)**
Abnormal JSW		

Hip OA is defined according to minimum joint spaces of **<2.5 mm** ("probable" OA) and **<1.5 mm** ("definite" OA)
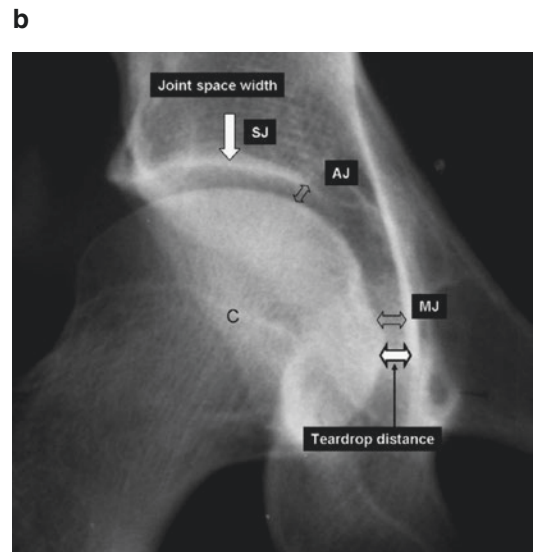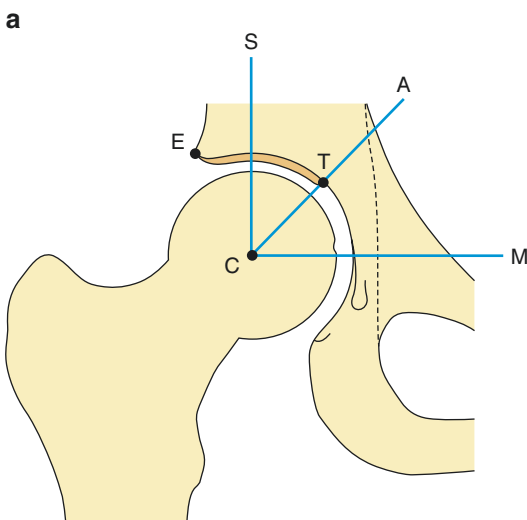
Fig. 12.3 (**a**, **b**) Joint space width—teardrop distance

The teardrop distance is defined as the distance from the lateral margin of the pelvic teardrop to the most medial aspect of the femoral head on an AP pelvic radiograph. Measurements of the teardrop distance are not influenced by age and positioning provided that there is no more than 30° internal or external rotation of the femur. A teardrop distance widening of **11 mm or more** or the presence of a teardrop **asymmetry of 2 mm or more**, in the absence of degenerative joint disease, is consistent with joint fluid in adults. In the paediatric age group, a distance widening of 2 mm or more is an early indicator of Legg-Calve-Perthes disease.

Reproducibility/Variation

The SD for a joint space of 4 mm is less than 1 mm. There are no significant conflicting measurements in the literature within this range. The inter- and intraobserver variation is less than 4%.The supine position is employed routinely to obtain an AP pelvic radiograph. Comparative JSW studies in the same patients did not reveal any significant measurement differences in the supine and weight-bearing positions.

Clinical Relevance/Implications

Conventional radiographs have been used as the primary diagnostic method for hip OA for many decades. Asymmetric joint space narrowing is a highly reliable sign of OA.

It is a very important parameter in the assessment of hips with femoroacetabular impingement. The presence and degree of associated chondral damage carries a significant prognostic significance. A preoperative hip joint space equal or less than 2 mm was found to be predictive of a poor clinical outcome in arthroscopic treatment of FAI with patients subsequently requiring total hip arthroplasty.

Analysis/Validation of Reference Data

Various studies have challenged the application of absolute measurements since a wide JSW variation exists in the normal values described above, ranging from 3 to 8 mm and from 2 to 6 mm at the superolateral and superomedial sites, respectively, with an associated right/left asymmetry in about 6% of subjects.

In addition, a JSW variability exists because of changes induced by the way patients hold their legs when the joint is painful. Finally, the JSW appears to be related to acetabular anatomy, regardless of the presence of OA, and is larger in *dysplasia* (negative correlation with CE angle) and smaller in *coxa profunda* (positive correlation with HTE angle). Technically optimised acquisition of the X-rays is therefore important.

Conclusion

The limited ability of the plain radiograph to detect osteoarthritis at its early stage limits the usefulness of JSW as a diagnostic tool. However, joint space narrowing can be considered the most reliable marker in the evaluation of the progression of OA.

12.4   Pelvic Inclination Formula/ Pelvic Symmetry

These important considerations need to be re-emphasised, and the readers are recommended to familiarise themselves with the coverage found in the preceding chapter. Some further expansion on the effect of pelvic tilt in the adult measurements will be included in the individual measurements presented in this section with coverage of both radiographic and axial imaging (CT/MRI).

Using the AP view of the pelvis, one can work out whether the degree of pelvic inclination is acceptable by measuring the distance from the **superior border of the symphysis pubis to the tip of the coccyx which normally should be between 1 and 3 cm.**

This method is preferred to that proposed by Siebenrock et al. who provided measurement values for acceptable pelvic inclination in men and women by measuring the distance from the superior border of the symphysis pubis to the junction of the sacrococcygeal joint. The latter landmark is not always easy to identify.

Normal symphysis pubis–sacrococcygeal junction distance	
Men	32.3 mm
Women	47.3 mm

12.5 Acetabular Version

Definition

The acetabulum is anteverted when the orientation of its opening is medial to the sagittal plane and retroverted when lateral to the sagittal plane.

Indications

Patients with hip pain and/or early osteoarthritis. Preoperative planning for surgical correction of the dysplastic hip.

Techniques

Radiography.
CT.
MRI.

Full Description of Technique

The acetabulum is normally anteverted. Acetabular anteversion can be first evaluated on the AP radiograph. The AP radiograph for this purpose needs to be obtained in a standard manner. The patient is supine with the legs internally rotated by about 15–20° to adjust for the natural femoral anteversion. In this position, only the tip of the lesser trochanter is seen to project beyond the outline of the medial femoral cortex. The centring of the beam is *crucial* and is different from the one employed in obtaining an AP radiograph for preoperative planning for a total hip replacement which requires a lower centring point. The employment of the lines and landmarks previously introduced in the assessment of acetabular morphology for this purpose is based on this AP radiograph and not on focal AP views of the individual hip. The hip view is obtained with a different centring point which is not useful or reliable in assessing acetabular anatomical status. In addition the horizontal C-C line and teardrop line cannot be drawn from this hip view. Comparative studies have shown that the relationship of the acetabular rim line configuration alters on the hip view. The hip view

produces an increase in the anteversion of the anterior wall of the acetabulum. This means that the anterior and posterior acetabular lines can appear normally related to each other on this view masking the presence of abnormal acetabular morphology. In addition it also falsely increases the apparent depth of the acetabulum. Lastly an altered FFD can also result in a false apparent relationship of the anterior and posterior rim outlines as well.

It is also essential to know the pelvic tilt for reliable interpretation of the hip and acetabular parameters. Pelvic tilt can have a profound effect on the measurements from this AP radiograph. In an acceptable AP radiograph, the tip of the coccyx should point to the middle of the symphysis pubis. Neutral pelvic tilt around the horizontal can be broadly defined if the distance between the superior borders of the symphysis pubis to the sacrococcygeal junction is 3.2 cm in men and 4.7 cm in women. Measurement accuracy however relies on factoring in of the pelvic tilt as previously described in the paediatric section. A shoot-through true lateral pelvic radiograph determines the pelvic tilt which normally should reveal a 60° pelvic inclination angle between the horizontal line and the oblique line joining the symphysis pubis superiorly to the sacral promontory. Increased pelvic tilt is seen on the AP view as an increased distance between the symphysis pubis and the sacrococcygeal joint. This leads to an apparent retroversion of the acetabular rim on both sides with crossover of the anterior and posterior acetabular lines.

On this AP view, the anterior and posterior acetabular rim margins are normally approximately 1.5 cm apart as measured from the centre of the head in a plane vertical to the anterior aspect of the acetabular rim (Fig. 12.4). The distance shown in the figure is lower than the normal range. The acetabulum is anteverted if the line of the anterior aspect of the rim does not cross the line of the posterior aspect of the rim before reaching the lateral aspect of the sourcil. Conversely it is deemed retroverted if the line of the anterior rim does cross the line of the posterior rim before reaching the lateral edge of the sourcil. If the posterior rim line runs lateral to the femoral head centre, there is posterior acetabular wall over-coverage. In acetabular retroversion,
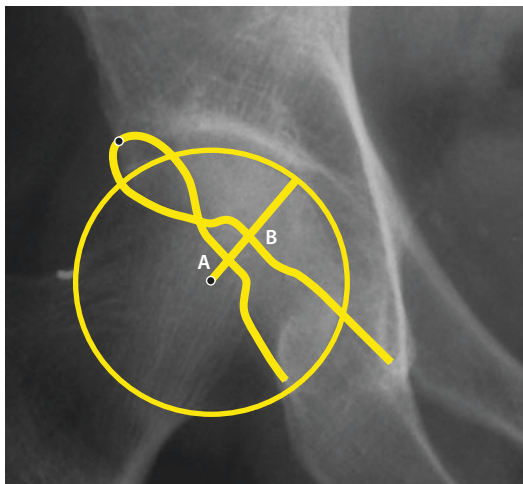
Fig. 12.4 Crossover of the anterior and posterior acetabular outlines in acetabular retroversion. A line drawn from the centre of the femoral head along the femoral neck axis intersects the posterior rim at *A* and the anterior rim outline at *B*. The *A*–*B* distance is less than normal which should be 1.5 cm

Fig. 12.5 Axial CT images through the cranial aspect of the hip showing anteversion and retroversion
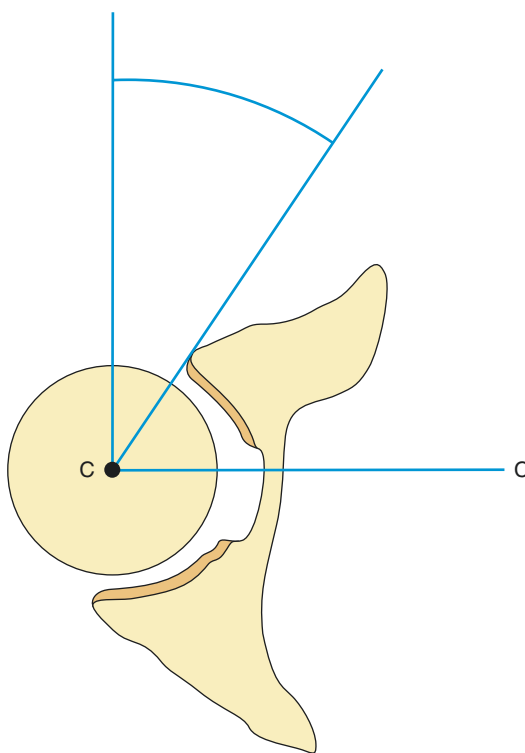
Fig. 12.6 Assessment of acetabular anteversion angle on cross-sectional imaging

Males	18.5 ± 4.5°
Females	21.5 ± 5°

there is anterior acetabular wall over-coverage which results in an approximation of both the acetabular lines with eventual crossover producing a figure-of-eight configuration. True acetabular retroversion has a deficient posterior wall which is highlighted by the centre of the femoral head lying lateral to the posterior aspect of the hip. In anterior over-coverage, the hip also exhibits a crossover sign, but there is no associated posterior wall deficiency.

CT and MRI scans are suitable to draw the lines used to measure acetabular version. A line is drawn midway between the two halves of the pelvis to define the sagittal plane because the scan often cuts the hemipelves at different levels or the body is not perfectly horizontal. On each side, a parallel line is drawn in the sagittal plane, beginning at the posterior margin of the acetabulum. The angle of acetabular anteversion is measured between the line corresponding to the sagittal plane and a line drawn tangential to the anterior and posterior acetabular margins (Fig. 12.5). The normal values for acetabular anteversion are 15–20°.

Anda et al. suggested that the axial CT slice at the femoral head centre is sufficient for measuring acetabular version, but they did not refer this to a gold standard (Fig. 12.6). Using this method, they objectively calculated the acetabular version in males and females as follows:

Other authors suggest using the most cranial axial slice through the femoral head claiming that this is more clinically significant and accurate. The cranial slice however not uncommonly has the drawback of a poorly defined anterior edge of the acetabulum promoting inconsistency in measurements (Fig. 12.5).

Reproducibility/Variation

Although there has been controversy on the accuracy and reproducibility of the methods used in measuring acetabular version, most agree with favouring CT over radiography. CT is highly reproducible if the technique is standardised. CT allows objective assessment of the degree of acetabular retroversion as specific measurements can be made. Two critical issues need to be agreed to optimise CT—a standard axial level for the measurement and the effect of pelvic tilt. The accuracy of CT measurements to a large part relates to the points on the acetabulum from which these measurements are made. This is complicated by the anatomical fact that the acetabulum normally becomes more anteverted as one extends from a cranial to caudal plane, so that the level at which the measurements are made significantly affects the resultant values. There is still no universal agreement on the axial level at which acetabular version is measured.

As explained above, pelvic tilt does alter the measurements. Radiographically the relationship of the acetabular walls to each other including the presence/absence of the crossover sign can be greatly affected by the degree of pelvic tilt. CT analysis is also affected by the degree of pelvic tilt which means that establishing a measurement in relation to a fixed anatomical landmark is beneficial. Anterior pelvic tilt reduces the acetabular anteversion, whereas posterior pelvic tilt (an upright pelvic position) increases it. A neutral position of the pelvis may be obtained by placing the patients in the prone position, with the anterior tips of the iliac crests and the symphysis pubis resting on the table. Care should be taken for scanning the pelvis at exactly the same height at both sides.

In a comparative study, 2D CT measurements were done at two different axial levels—cranially at the level of the top of the femoral head and caudally at the equator of the femoral head. The measurements were then repeated after pelvic tilt correction.

The mean version results were as follows:

Cranial slice	9.3° (SD 6.5)	Before pelvic tilt correction
	15.7° (SD 8.0)	After pelvic tilt correction
Caudal slice	16.4° (SD 4.2)	Before pelvic tilt correction
	19.0° (SD 5.0)	After pelvic tilt correction

In a further comparative study between the above 2D CT measurements and a method using 3D CT measurements which automatically corrects for pelvic tilt, the cranial measurements after pelvic tilt correction had the best intraclass correlation coefficient.

Clinical Relevance/Implications

On cross-sectional imaging (CT or MR), retroversion can be identified if the anterior rim of the acetabulum is lateral to the posterior rim on the first axial image that includes the femoral head.

Analysis/Validation of Reference Data

A number of CT-based studies have shown that the acetabular version increases caudally in both normal and dysplastic hips. Traditionally, DDH was thought to be associated with anteversion of the acetabulum. Recently, an association between DDH and acetabular retroversion has been shown. Therefore, the quantification of the retroversion is important for treatment planning. In addition, various disorders have been associated with retroversion, and therefore quantification of retroversion is important in patients with nonspecific hip pain.

Conclusion

Proper assessment of the standard AP radiograph may reliably suggest the presence of a normally anteverted acetabulum or the presence of acetabular retroversion, but CT is required to provide specific objective measurements. The 2D CT axial methods give variable results for acetabular version depending on whether pelvic tilt has been accounted for and the axial level chosen. Acetabular retroversion is a form of acetabular dysplasia and is commonly found in patients with osteoarthritis, DDH and Legg-Calve-Perthes disease. This condition may result from a traumatically induced premature closure of the triradiate cartilage in childhood or may be idiopathic. Clinically, it can be associated with hip and groin pain, clicking and clunking.

12.6   Acetabular or Sharp's Angle

This angle is used before and after skeletal maturity and is covered in the previous chapter.

12.7   Centre-Edge or Wiberg's Angle

Definition

The centre-edge (CE) angle is formed from the centre of the femoral head and two lines: a vertical one through the centre of the femoral head parallel to the long axis of the body and the other to the superolateral rim of the acetabulum.

Indications

This important angle is the starting point for assessing the dysplastic hip because an abnormal value is diagnostic. The CE angle, originally described by Wiberg, evaluates the degree of superior and lateral acetabular coverage of the femoral head in the frontal plane, in patients with suspected DDH, and assesses the outcome after reduction.

Technique

AP radiography (Fig. 12.7).

Full Description of Technique

The CE angle is formed by a vertical line through the centre of the femoral head and parallel to the longitudinal body axis and the line connecting the centre of the femoral head with the most lateral point (**E**) of the acetabular sourcil. The vertical line through the centre of the femoral head should be perpendicular to the **C-C** line joining the centres of the femoral heads.

Normal	>25°
Dysplasia	<20°
Borderline	20–25°
Coxa profunda	39–44°
Protrusio acetabuli	>44°

It is important to carefully study the radiographic anatomy of the lateral acetabular margin before drawing the oblique line. If the sourcil and lateral acetabular rim are conjoined laterally (with or without a beak), then the E point is easily defined. If there is a gap between the lateral limit of the sourcil and lateral edge of the lateral acetabular rim, then the oblique line needs to pass through the lateral limit of the sourcil and not the E point. The CE angle is a more reliable measure of head cover when the lateral limit of the sourcil (**E2**) is chosen as the reference point rather than the lateral edge of the acetabulum (**E1**) when
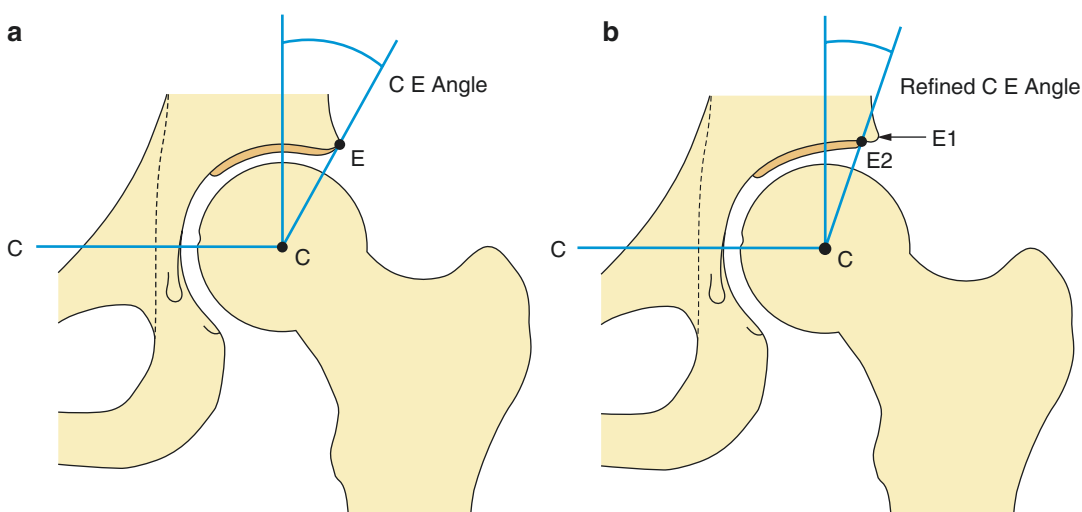
Fig. 12.7   Centre-edge angle drawn in classic mode (**a**) and in refined mode (**b**)

these two points do not overlap. This is referred to as the **refined CE angle or Ogata's angle**. When there is an interval separating the lateral sourcil limit from the lateral edge of the acetabulum, the most lateral point of the acetabular roof on AP radiographs is actually anterior and lateral to the most superior part of the acetabulum. It is imperative to distinguish between these two lateral acetabular points of reference in these circumstances, as the most lateral classical reference point (**E1**) will overestimate the head coverage (Fig. 12.8).

Reproducibility/Variation

Highly reproducible if applied after the age of 6. In descriptive statistics comparing measurements in asymptomatic men and women, significant differences were observed. The mean CE angle for all patients was 36.3°, with a measurement of 37.7° (95% CI, 26.9–48.5°) in men and 34.9° (95% CI, 23.5–43°) in women.

Clinical Relevance/Implications

The CE angle quantifies the subluxation of the femoral head which leads to reduced weight-bearing area and focal concentration of compressive stress resulting to accelerated degeneration of the articular cartilage and osteoarthritis.

Normal values for CE angles are more than 20° for ages 3–17 years and more than 25° in adults. Values below 20° in adults and below 15° in children and adolescents are considered abnormal. Hips with CE angles between 20° and 25° in adults and between 15° and 20° in children and adolescents are "uncertain" for dysplasia hips. The CE angle is associated with the pelvic inclination; a decrease of the CE angle of 2–4° is expected if the pelvis tilts about 15° posteriorly.

Values between 39° and 44° correspond to a *deep acetabulum* (*coxa profunda*), whereas values over 44° correspond to *protrusio acetabuli*.

Analysis/Validation of Reference Data

Ogata et al. observed that a poor acetabular cover may develop in some hips which originally had a normal CE angle. In these hips, the lateral border of bony condensation (E2) did not reach the lateral rim of the acetabular roof (E1). The classic CE angle measurements thus may overestimate the femoral head coverage, particularly in children between 3 and 8 years of age.

Conclusion

The CE angle is one of the most easy and widely performed measurements on hip radiographs.
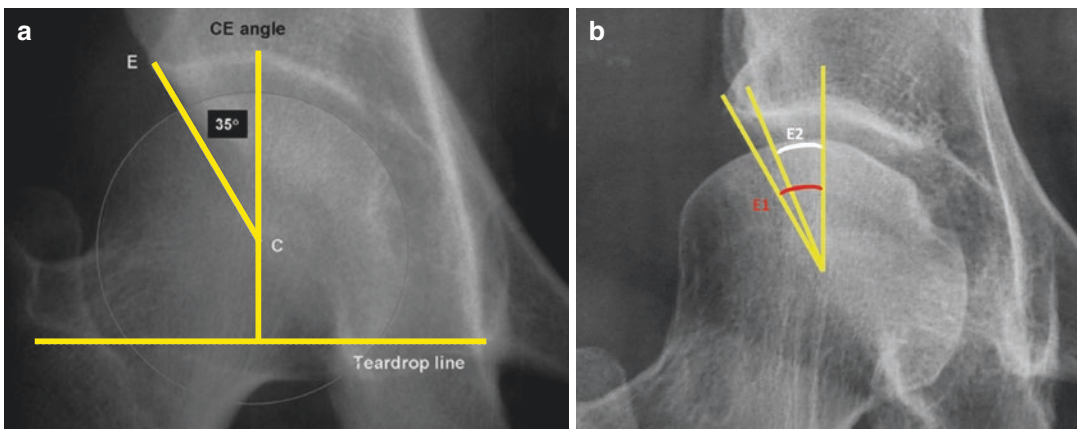
Fig. 12.8 Radiographic measurements of the classic CE angle (**a**) and refined CE angle (**b**)

12.8   Horizontal Toit Externe (HTE) or Tonnis Angle

Definition

The horizontal toit externe (HTE) angle assesses acetabular inclination and is formed by the horizontal line and the weight-bearing surface of the acetabulum. It is also known as the *Bombelli's angle of weight-bearing zone*.

Indications

The HTE angle is used to evaluate the slope and orientation of the acetabular roof in the coronal plane, providing information about the superolateral coverage of the femoral head by the bony acetabulum.

Techniques

AP radiography (Fig. 12.9).

Full Description of Technique

The HTE angle is measured between a line parallel to the horizontal **C-C** line joining the centres of the femoral heads and an oblique line extending from the most medial point of the weight-bearing acetabulum (**T**), to the lateral acetabular margin (**E**). The weight-bearing portion of the acetabulum (sourcil) is demonstrated as a sclerotic and arched appearance.

Normal	0 to <10°
Abnormal	
Dysplasia	>10°
Pincer type FAI	<0°
Coxa profunda	−5°

Reproducibility/Variation

Highly reproducible.

Clinical Relevance/Implications

The HTE angle supports further evidence on the possible underlying acetabular dysplasia. Its normal value should be under 10°.

Values over 12° correspond to *dysplasia*, whereas values less than −5° to a *deep acetabulum*.

a

b
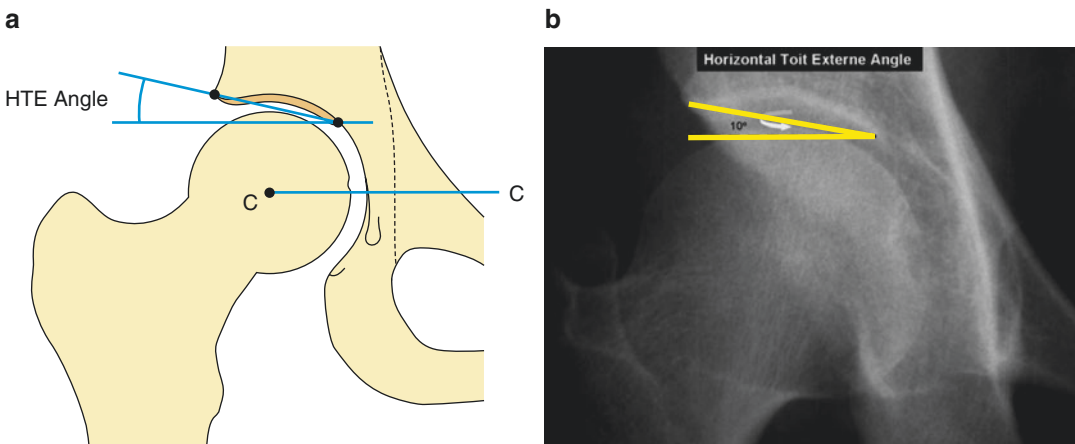
Fig. 12.9 (**a**, **b**) HTE angle

12.9 ACM Angle (Idelberger-Frank Acetabular Angle)

Definition

The ACM angle measures the depth of the acetabulum.

Indication

Acetabular dysplasia.

Normal	45° (±3°)
Abnormal	>50°

Technique

AP radiography (Fig. 12.10).

Full Description of Technique

The ACM angle is formed by the AC line and the MC line. The lettering designations of the radiographic landmarks are specific for this measurement and are as follows: A is the most lateral edge of the acetabulum, B is the lowest point of the acetabular margin, M represents the midpoint between A and B, and C is the point on the bony acetabulum intersected by a perpendicular from point M. In young children, the point C can be at the cartilaginous part. If the value of ACM is 45°, the acetabulum can be considered as a hemisphere. The sphericity of the acetabulum decreases with increasing ACM values. In the original description, the normal values range between 42° and 50°. Others showed that in the first 6 years of life, values above 45° can be considered normal. For newborns, this value can even be as high as 60°. Beyond 8 years of age though, the data of various age groups lies between 40° and 45°.
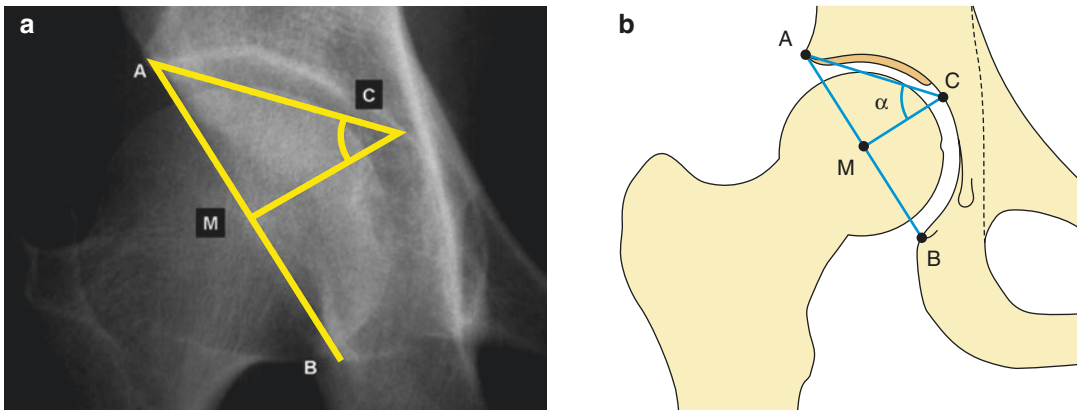
Fig. 12.10 (**a**, **b**) ACM angle

Reproducibility/Variation

Moderately reproducible because of the poor definition of the depth of the acetabulum and to a lesser degree of the inferior margin of the acetabulum. More reliable and consistent after puberty as landmarks are more readily definable.

Clinical Relevance/Implications

One of the advantages of this measurement method is that the value of this angle is less sensitive to the position of the pelvis.

Analysis/Validation of Reference Data

Limited data regarding validation in the value of this measurement in its application before and after puberty.

Conclusion

Useful particularly in the mature pelvis but not used widely.

## 12.10	Acetabular Depth and Acetabular Depth-to-Width Index

Definition

Acetabular depth is the measurement of the deepest diameter of the acetabulum coverage.

Indications

Acetabular dysplasia.

Technique

AP radiography (Fig. 12.11).

Normal	> 9mm
Abnormal	< 9mm

Full Description of Technique

Acetabular depth is defined as the greatest perpendicular distance from the acetabular roof to a line joining the lateral margin of the acetabular roof and the upper corner of the symphysis pubis on the same side. An acetabular depth of <9 mm suggests acetabular dysplasia.

The depth of the acetabulum can be also evaluated by the **acetabular depth-to-width index** which is estimated by dividing the width (measured from the lateral acetabular rim to the teardrop-apex) by the depth (measured at the most medial point of the weight-bearing acetabulum). The width line (**W**) of the acetabulum is measured between the **E** and the **I** points. Acetabular depth (**d**) is the length of the line from point **T** (the medial end of the sourcil) perpendicular to the constructed line depicting **W** (Fig. 12.12).

Fig. 12.11 Acetabular depth
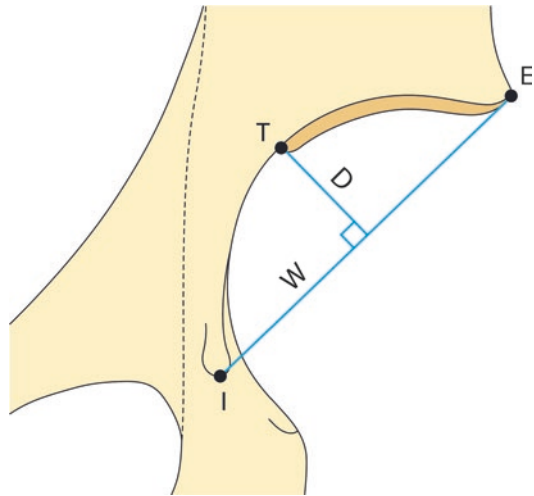
Fig. 12.12 Acetabular depth-to-width index

Fig. 12.13 Acetabular depth-to-width radiographic index
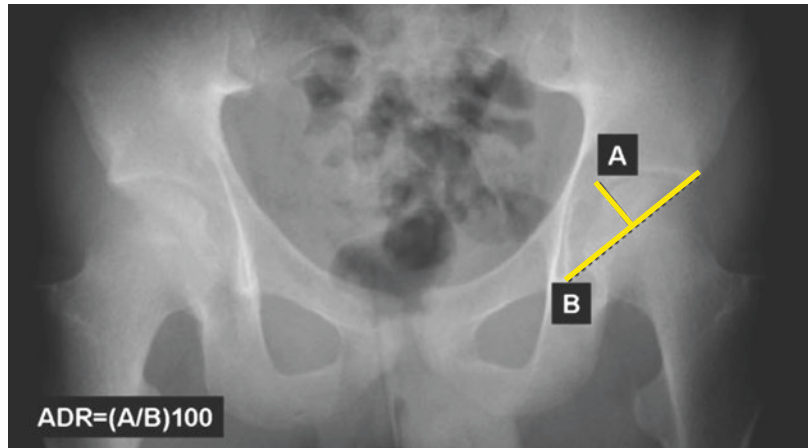
The depth-to-width index is calculated by the ratio of depth to width (d/W) multiplied by 100 (Fig. 12.13). Values of the ratio (d/W) × 100 in vivo have been found to be around 60 in adults. In Murphy et al.'s study comparing normal and dysplastic hips with secondary OA, all of the dysplastic hips had an index lower than 39.

Normal index	>39 (Average 60)
Abnormal (dysplasia) index	<39

Reproducibility/Variation

Moderate reproducibility.

Clinical Relevance/Implications

Although clinically relevant when <9 mm, the acetabular depth measurement has no upper normal limits. Indeed, a high value may be found in abnormal cases, such as coxa profunda and protrusio acetabuli.

Analysis/Validation of Reference Data

In a comparative study between normal and dysplastic hips with osteoarthritis, all normal hips were shown to have acetabular index values over 38°.

Conclusion

Reliable discriminator.

12.11 Anterior Centre-Edge or VCA (Vertical-Centre-Anterior) Angle of Lequesne and De Seze

Definition

The VCA angle measured from the false-profile (FP) view is formed by the vertical line through the centre of the femoral head and the line connecting the centre of the femoral head to the most anterior aspect of the acetabulum.

Indications

When an abnormality of the acetabulum seen on the AP radiograph signals a deficiency of acetabular roof coverage (abnormal CE angle), a false-profile view of the pelvis which allows the measurement of the VCA angle will evaluate the anterior coverage of the acetabulum.

Normal	>25°	Abnormal	<20°

Technique

Radiography—false-profile view (Fig. 12.14).

Full Description of Technique

The **anterior centre-edge angle**, or *VCA* angle, is measured on oblique radiographs of the pelvis (false-profile view). The view in essence represents a true lateral view of the abnormal hip. Patients are in the standing position with the pelvis rotated at an angle of 25° relative to the X-ray
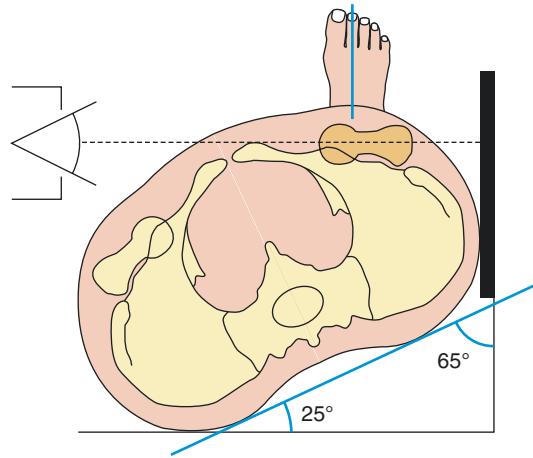
Fig. 12.14 Radiographic technique used in acquiring the false-profile view

beam and 65° to the X-ray film cassette. The foot closest to the bucky stand is parallel to the X-ray film cassette plane (Fig. 12.14). The side to be examined is positioned next to the film cassette and the central beam centred on its femoral head. This radiograph is technically correct if the distance between the two femoral heads is approximately the size of one femoral head.

The VCA angle is formed by the vertical line (**V**) through the centre of the femoral head and the line connecting the centre of the femoral head (**C**) to the most anterior aspect of the acetabular sourcil margin (**A**). VCA angle values of 25° or more are normal, whereas 20–25° is borderline and less than 20° abnormal (Fig. 12.15).

Reproducibility/Variation

Highly reproducible if the radiographic view is technically correct.

a **b**
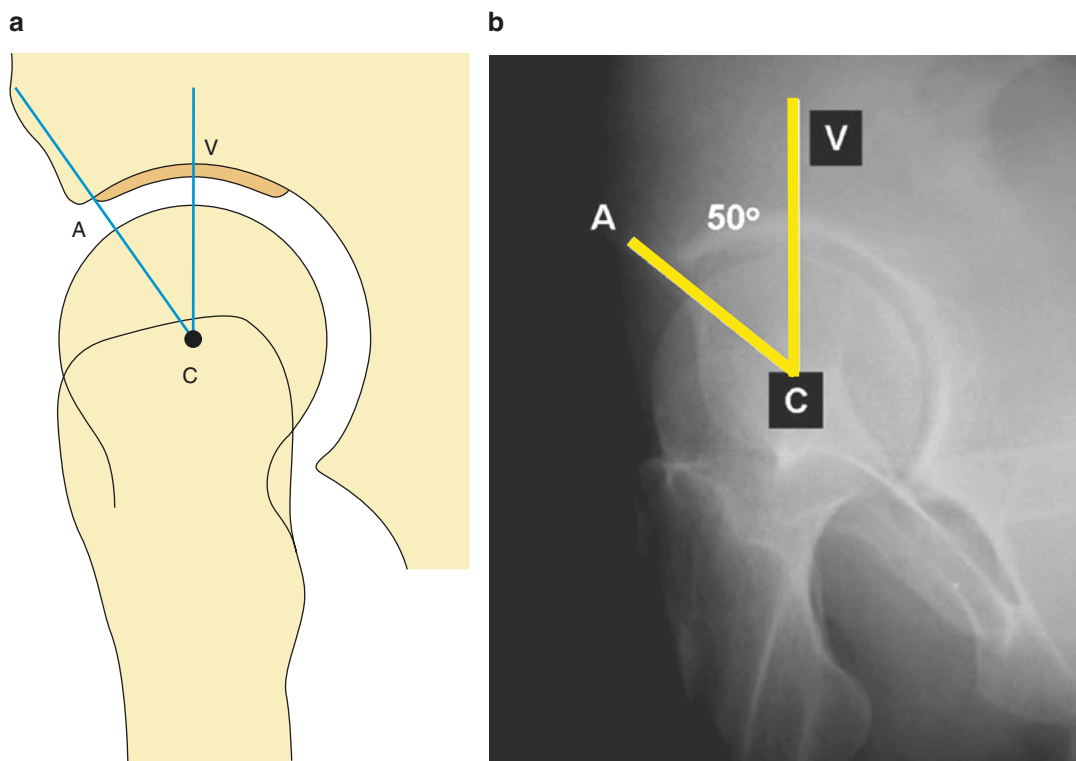
Fig. 12.15 (**a**, **b**) VCA angle

Clinical Relevance/Implications

The false-profile view corresponds to a true lateral view of the hip and allows measurement of the anterior/superior coverage by the acetabulum. This view is able to demonstrate early degenerative changes which commonly tend to begin at the anterior aspect of the joint.

Analysis/Validation of Reference Data

As indicated previously, values less than 20° correspond to **dysplasia.** Values between 39° and 44° correspond to a **coxa profunda** and more than 44° suggest **protrusio acetabuli**.

Conclusion

Requires good technique to ensure consistently reliable measurements. The VCA angle measured on the FP view is not identical to the AASA as measured on CT which will be discussed in the next section. The VCA is measured in the sagittal plane demonstrating the anterior/superior coverage by the acetabulum, while the AASA is measured in the horizontal plane demonstrating anterior coverage only.

12.12　AASA-PASA-HASA

Definition

The **anterior acetabular sector angle** (AASA), the **posterior acetabular sector angle** (PASA) and the **horizontal acetabular sector angle** (HASA) describe the anterior, posterior and global coverage of the femoral head by the acetabulum.

Indications

Acetabular dysplasia. Hip dysplasia is usually associated with hypoplasia of the anterior acetabulum and reduced femoral head coverage. Once an acetabular morphological abnormality has been established (abnormal CE angle, etc.) on the AP radiograph, further information concerning acetabular coverage is required. The VCA angle as described above is a radiographic option to provide anterior coverage information using the false-profile view. CT lends itself as a helpful modality to assess the acetabular morphology.

Normal values	AASA	Males	$63 \pm 6°$
		Females	$64 \pm 6°$
	PASA	Males	$102 \pm 8°$
		Females	$105 \pm 8°$
	HASA	Males	$167 \pm 11°$
		Females	$169 \pm 10°$

Technique

CT (Fig. 12.16).

Full Description of Technique

Anda et al. described a standardised CT technique for this purpose. First a scout view of the pelvis is obtained. Then axial scans are obtained through the centre of both femoral heads. An optimal axial section through the centre of the femoral heads should be used for measurements. The anterior coverage is evaluated by the AASA, the posterior coverage by the PASA and the global acetabular coverage by the HASA. The HASA value is the sum of AASA and PASA.
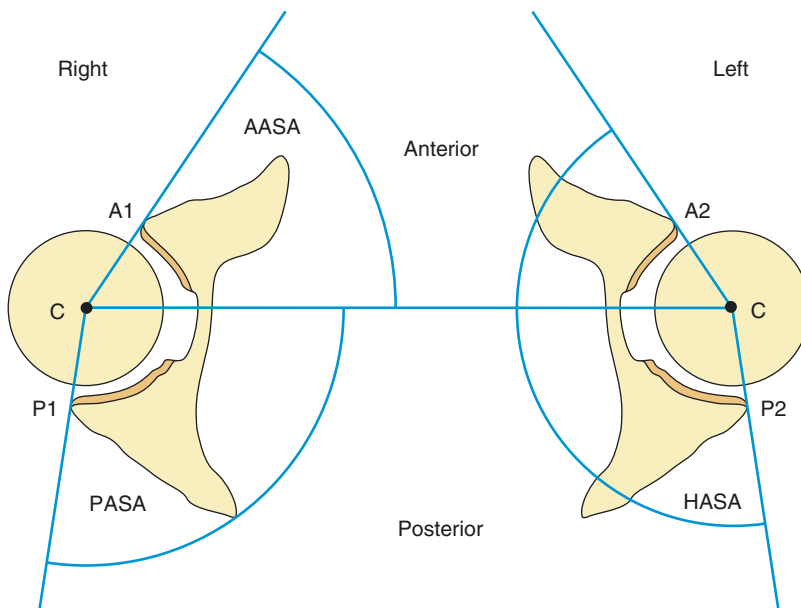
Fig. 12.16 AASA-PASA-HASA determinants on cross-sectional imaging
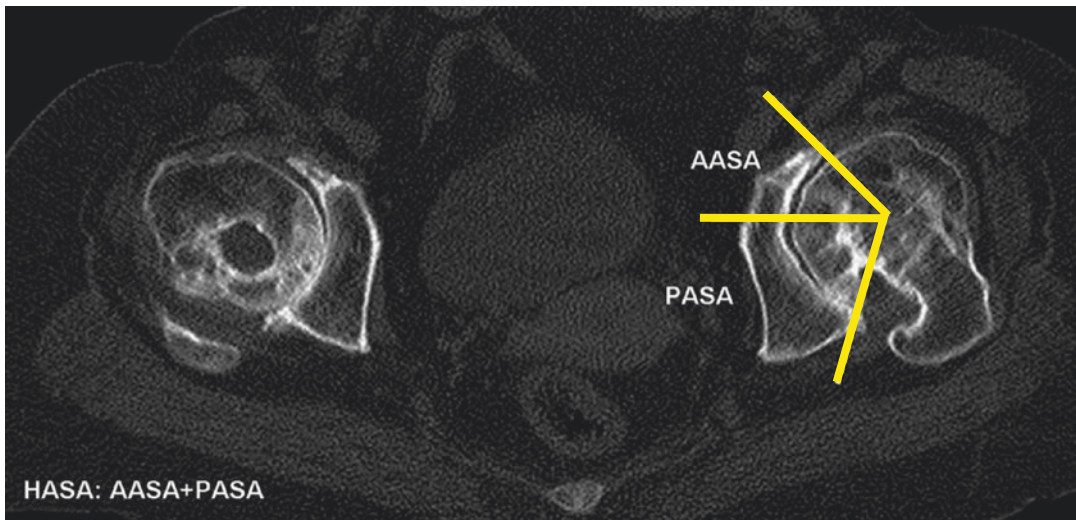
Fig. 12.17   AASA and PASA assessment on CT axial image

The angles are drawn from a horizontal C-C line through the centre of the femoral heads and two oblique lines from the centre of each of the heads to the most anterior and posterior point of the acetabulum, respectively, of each hip. The mean normal values are 63° in men and 64° in women for the AASA and around 105° for the PASA in both sexes (see normal value range above). These values are decreased in patients with hip dysplasia (Fig. 12.17).

Reproducibility/Variation

Highly reproducible.

Clinical Relevance/Implications

Developmental dysplasia results in a decreased acetabular support and this is better appreciated with CT.

Analysis/Validation of Reference Data

Accepted technique with a well-described standard using reliable fixed points and producing reproducible values.

Conclusion

A deficiency of the anterior coverage is commonly found in patients with hip dysplasia. Measurement of the PASA is important in neuromuscular dysplasia and in cerebral palsy, where a significant number of hips show a severely deficient posterior acetabulum. The PASA is also needed when a Salter osteotomy is planned.

12.13 M-Z Distance

Definition

It is the distance in mm between the centre of the acetabulum and the centre of the femoral head.

Indications

Developmental dysplasia.

Technique

AP radiography (Fig. 12.18).
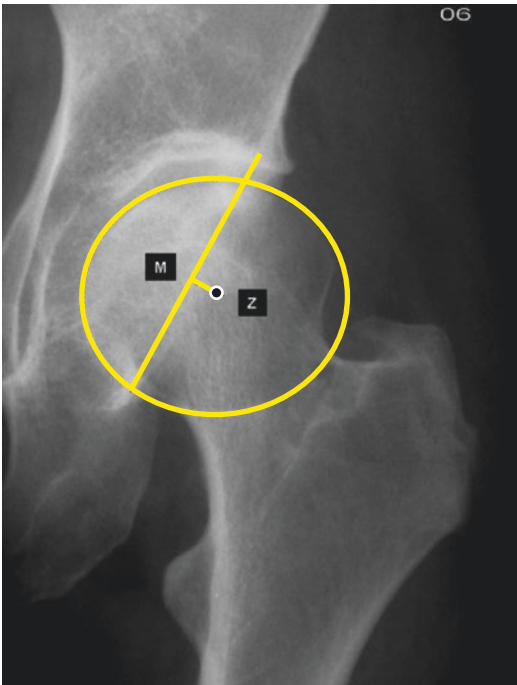
Fig. 12.18 M-Z distance

Full Description of Technique

MZ is the distance (in mm) between points M (centre of acetabulum) and Z (centre of femoral head). The critical point for MZ between normal and dysplastic hip joints was found to be **6–8 mm.**

Reproducibility/Variation

In children younger than 5 years of age, it is difficult to define point Z accurately.

Intraobserver and interobserver variations of MZ measurement were reported to be 3.3 and 3.1 mm, respectively, in children and adolescents and 3.8 and 5.7 mm, respectively, in adults.

Poor reproducibility is the result of the difficulty in defining both the inferior border of the acetabulum and the lateral end (lateral rim or lateral border of bony condensation).

Clinical Relevance/Implications

The MZ distance has been described to evaluate the lack of concentricity between the femoral head and acetabulum, but is not widely used.

Analysis/Validation of Reference Data

Limited data renders validation difficult

Conclusion

Easy to perform if landmarks are well delineated.

12.14   Acetabular Head Index (AHI): Femoral Head Extrusion Index (FHEI)

Definition

The acetabular head index (AHI) refers to the proportion of the femoral head covered by the acetabulum.

Similarly, the femoral head extrusion index (FHEI) refers to the proportion of the uncovered femoral head.

Indications

Acetabular dysplasia.
Degree of containment in Perthes disease.

Technique

AP radiography (Fig. 12.19).

Full Description of Technique

The hip joint **congruence** is defined as the % of the femoral head that is covered by the acetabulum. Three vertical lines are required drawn perpendicular to the horizontal C-C line. Line 1 is through the most medial part of the joint space,

line 2 passes through the lateral edge of the acetabulum the E point, while line 3 passes as a tangent through the lateral outline of the femoral head. Two horizontal measurements are made between these vertical lines. The horizontal distance A (between lines 1 and 2) is divided by B (the horizontal distance between lines 1 and 3). The ratio A/B is then multiplied by 100 producing the AHI. Normal values of femoral head coverage are above 75%. The smaller the index, the more dysplastic the hip is (Fig. 12.20).
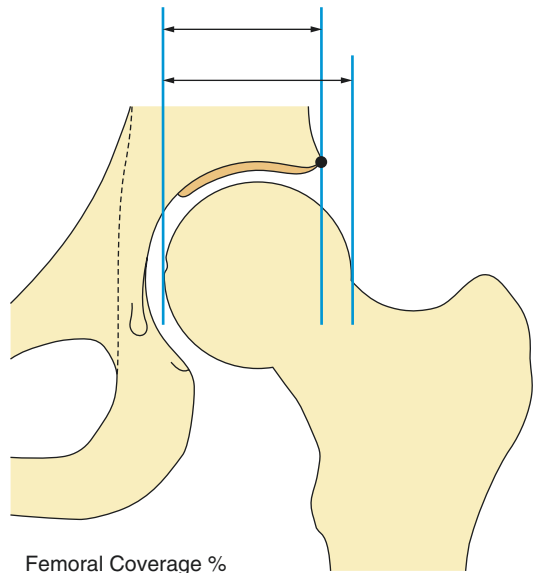
Femoral Coverage %

Fig. 12.19   Femoral head coverage
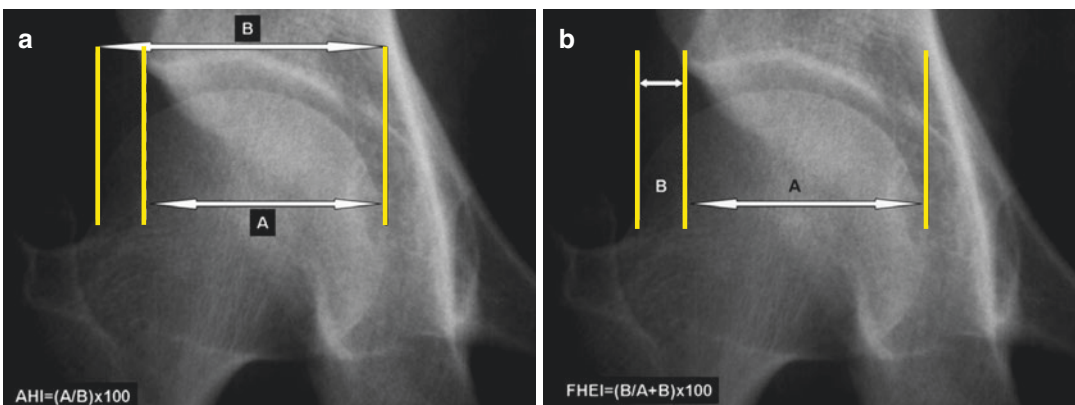
Fig. 12.20   Acetabular head index (**a**) and femoral head extrusion index (**b**)

Normal AHI	>75%	Normal FHEI	<25%
Dysplasia	<75%	Dysplasia	>25%

The FHEI quantifies similarly the degree of the femoral head uncovered by the acetabulum expressed in percentage. Values of more than 25% are frequent in acetabular dysplasia.

Reproducibility/Variation

The AHI and FHEI are highly reproducible and not significantly affected by pelvic rotation.

Clinical Relevance/Implications

This is a useful measurement in the follow-up assessment of the changes with growth in the femoroacetabular relationship. It is particularly suited in Perthes disease, acetabular dysplasia and outcome assessment following corrective surgery.

Analysis/Validation of Reference Data

CT evaluation to assess congruity can also be performed to study the acetabular coverage. There is no specific CT measurement to assess reliably the femoral head shape/position.

Conclusion

Both measurements are reliable in producing the required congruency assessment.

12.15   Acetabular Depth in Coxa Profunda

Definition

Acetabular morphological abnormality producing a deep-seated acetabulum with generalised over-coverage of the femoral head. It is highlighted on the AP view by the medial location of the floor of the acetabular fossa which touches or medially overlaps the ilioischial line.

Indications

Hip pain in the young adult could be due to an underlying impingement arising from a focal or generalised acetabular over-coverage. In coxa profunda, the generalised over-coverage is associated with abnormal measurements of previously described angles, namely:

CE angle	>39°
Acetabular index	0 or <0 (−value)

Technique (Fig. 12.21)

An AP radiograph of the pelvis depicts the altered acetabular morphology.

Full Description of Technique

The standard radiographic technique described earlier in this chapter to assess acetabular version is required. A supine position with legs internally rotated by 15–20° is employed with the central beam focused midway between the ASIS distance at an FFD of 1.2 m. Pelvic symmetry is essential. It is stressed once again that a focal radiographic view of the hip is contraindicated as it is produces a false assessment of the lines and landmarks. This is a well-described pitfall as a beam centred on the hip instead of the pelvis produces pseudo-coxa profunda features
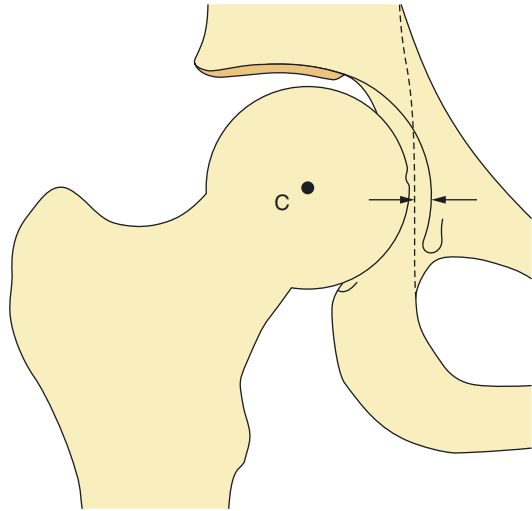
Fig. 12.21 Coxa profunda. In coxa profunda, the head is more medial with the acetabular fossa being at or medial to the ilioischial line. The measured distance (*arrowed*) is given a negative connotation

and increases the anteversion of the anterior wall of the acetabulum.

On this pelvic view, normal acetabular relationships are highlighted with the ilioischial line lying medial to the outline of the acetabular fossa. The medial acetabular rim inferiorly is continuous with the teardrop forming its lateral wall.

Both the medial and lateral outlines of the teardrop normally lie lateral to the ilioischial line (Fig. 12.21). The distance between the ilioischial line and the medial acetabular rim is measured where the two lines cross the horizontal C-C line joining the centres of the femoral heads. The distance is designated positive when the ilioischial line is normally located medially and negative when it is abnormally located laterally which is what is seen in coxa profunda (and protrusio acetabuli—see later).

Coxa profunda diagnostic criteria for the distance (negative value) between the medial acetabular rim and the ilioischial line vary in adult men and women:

Men	<−3 mm
Women	<−6 mm
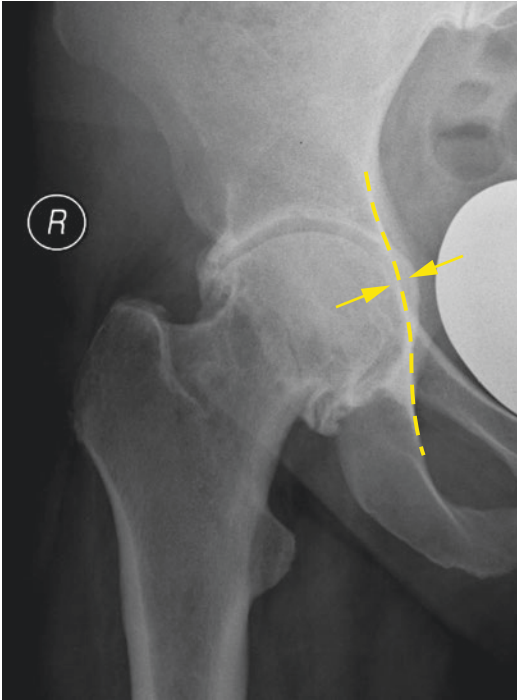
Fig. 12.22 Coxa profunda and osteoarthritis

The radiographic outline of the femoral head despite its generalised acetabular over-coverage still lies lateral to the ilioischial line (Fig. 12.22).

Reproducibility/Variation

Accuracy and reproducibility are good but depend on proper radiographic technique and clear measurement landmark instructions. The measurement criteria in children are different with a cut-off of -0.8 mm for boys and -2.7 mm for girls (mean $= 2 \times$ SD).

Clinical Relevance/Implications

Coxa profunda is one of the underlying causes of the acetabular pincer type of femoroacetabular impingement from generalised over-coverage.

Analysis/Validation of Reference Data

Moderate data supporting validation

Conclusion

Useful and reliable if based on measurements applied on good radiographic technique.

12.16 Protrusio Acetabuli Distance

Definition

Protrusion distance is the measurement of the intrapelvic protrusion of the acetabulum. Protrusio acetabuli is present if on the AP view the medial aspect of the femoral head lies medial to the ilioischial line.

Indications

Measuring the progression of the protrusio acetabuli observed in association with various disorders. This is associated with underlying hormonal disorders, usually occurs in females, but is often idiopathic and bilateral. Although similar to coxa profunda in causing a generalised acetabular over-coverage and predisposing to the acetabular pincer type of FAI, it is different being progressive and associated with the femoral head outline extending medially to cross the ilioischial line.

Technique

AP radiography of the pelvis as described previously in the coxa profunda section (Fig. 12.23).
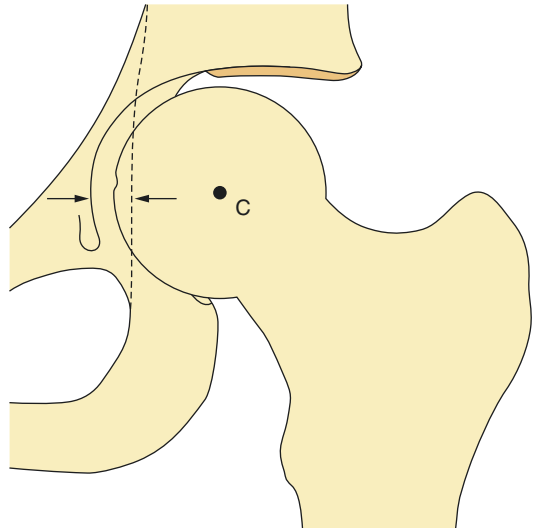
Fig. 12.23 Protrusio acetabuli. In protrusio, the femoral head is medial to the ilioischial line with the centre of the femoral head migrating medial to both the posterior and anterior acetabular outlines and intersected by the ilioischial line

Full Description of Technique

The essential evaluation exercise and diagnostic criteria are similar to coxa profunda. The ilioischial **Kohler line** begins on the pelvic border of the ilium and ends on the medial border of the body of the ischium, abutting with the dome of

the acetabulum on its way. If the outline of the acetabular dome passes medial to Kohler's line, a protrusion exists and the magnitude is reflected by the distance between the medial acetabulum and the ilioischial line.

Protrusio is considered to be present if the medial wall of the acetabulum extends medial to the ilioischial line by 3 mm in males or 6 mm in females.

Reproducibility/Variation

This method is highly reproducible but is applicable to serial radiographs of individual patients and is not suitable for comparing patients.

Clinical Relevance/Implications

Protrusio acetabuli, also known as *arthrokatadysis* (*Greek words arthro = joint and katadysis = diving*), has been defined as a condition in which the head of the femur lies further in the pelvis than normal (Fig. 12.24).

Analysis/Validation of Reference Data

Reliable indicator of progression of protrusio acetabuli with time as long as the same
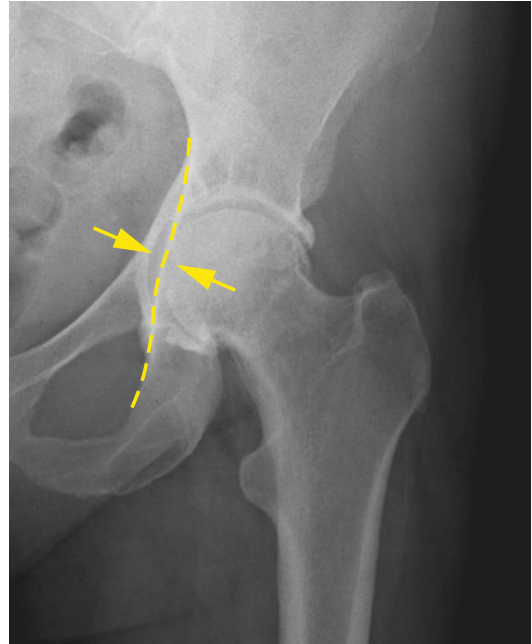
Fig. 12.24 Protrusio acetabuli and osteoarthritis

radiographic technique is used in follow-up radiographs.

Conclusion

Measurement diagnostic and differentiates it from coxa profunda.

12.17   Acetabular Depth in Pincer-Type Femoroacetabular Impingement

Definition

Measurement of the deeply situated femoral head.

Indications

Patients who demonstrate on plain radiographs acetabular over-coverage (centre-edge angle of greater than 40° or abnormal VCA angle) and/or acetabular retroversion (crossover sign). This applies to coxa profunda and protrusio acetabuli as well.

Technique

CT.
MRI.

Full Description of Technique

The acetabular depth should be measured on the axial oblique image obtained from the coronal images, on the image through the centre of the femoral neck. The depth of the acetabulum is defined as the distance between the centre of the femoral head and the line connecting the anterior acetabular rim to the posterior acetabular rim. In pincer-type impingement, the value is negative since the centre of the femoral head lies medial to the line connecting the acetabular rim (Fig. 12.25).

Reproducibility/Variation

One study showed that in pincer impingement, the acetabular depth is about 5 mm.
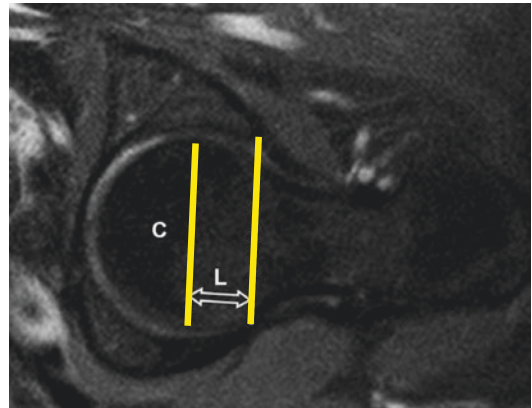
Fig. 12.25   Acetabular depth using axial MR assessment

Clinical Relevance/Implications

Femoroacetabular impingement results from an abnormal contact between the femur and the acetabular rim and has been recently recognised as a cause of hip pain in all age groups, possibly resulting in the development of early osteoarthritis. In pure pincer-type impingement, the predominant abnormality is with the morphology of the acetabulum resulting in over-coverage, with a relatively normal contour of the proximal femur. The acetabular over-coverage can be global, as in a patient with protrusio acetabuli, or localised, as in a patient with acetabular retroversion.

Analysis/Validation of Reference Data

Limited data does not allow satisfactory validation.

Conclusion

Good indicator of the presence of impingement.

12.18 Femoral Head Asphericity in Cam-Type Femoroacetabular Impingement: α-Angle/Anterior Offset/AO Ratio Measurements

Definition

Confirmation and quantification of femoral head asphericity has four possible measurable parameters: the alpha angle, femoral offset or offset ratio and triangular index.

The **alpha (α) angle** is a parameter used to quantify the degree of femoral deformity and reflects the insufficient anterolateral head-neck offset and femoral head asphericity. It is formed between the femoral neck axis and a line connecting the head centre with the point of commencement of the asphericity of the head/neck contour (Fig. 12.26). The method also evaluates the degree of femoral head-neck offset abnormality allowing the estimation of the offset ratio as well.

The **anterior femoral head-neck offset** is defined as the difference between the radius of the femoral head (R) and the widest part of the

femoral neck anteriorly at its junction with the head (r) (Fig. 12.27). The **offset ratio** is defined as the ratio between the anterior offset and the diameter of the femoral head.

The **triangular index** will be dealt separately in the next section.

Indications

The term "pistol grip" or "tilt" deformity describes a flattened head/neck junction laterally by a bone bump seen on the standard AP radiographs of the hip. The degree of this deformity cannot be assessed optimally on the AP view which usually underestimates it as there is a sagittal component to the abnormality anterosuperiorly, which is not possible to detect/quantify on the AP view. Quantification of the degree of "pistol grip" deformity in the proximal femur suggestive of impingement, assessed previously on AP radiographs, is therefore needed. A lateral radiograph can be used to assess the anatomical relationship between the femoral head and neck anteriorly. MRI is increasingly being used for this purpose as it has a number of advantages.
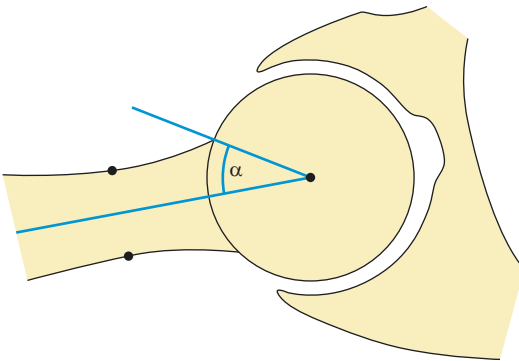
Fig. 12.26 α-angle—normal
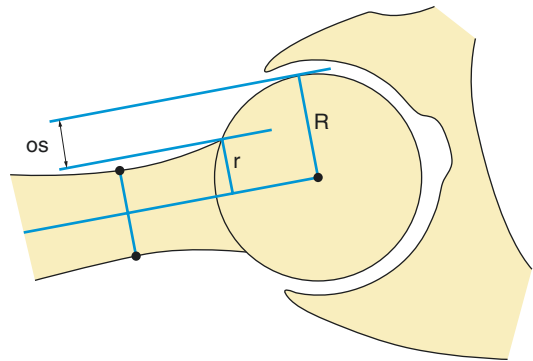
Fig. 12.27 Anterior femoral head offset—normal

Normal	**<55°**
Abnormal	**>55° (cam impingement)**

As discussed later on, the alpha angle threshold signalling, a head-neck deformity may in fact be even lower at about 42°.

Techniques

Radiography—If radiography is the chosen modality, it is imperative to assess femoral head asphericity on both the AP and lateral radiographs because the head can appear spherical on the AP view but be aspherical on the lateral view. MRI

Full Description of Technique
(Fig. 12.26)

Radiography. Mose's concentric circular templates can be used as a quick initial assessment of the femoral head status whereby asphericity is present if the femoral epiphysis is seen to extend beyond the margins of the best-fit reference circle by more than 2 mm. If the femoral epiphysis extends beyond the margins of the reference circle by less than 2 mm, the head is likely to be spherical.

A radiograph can be employed to determine the alpha angle and offset ratio. There are however a number of possible radiographic techniques that can be used. In a comparative study on femoral specimens (11 aspherical heads and 10 spherical heads) using six radiographic projections to assess femoral head/neck asphericity, Meyer et al. found that the measured alpha angle varied with the projections. The Dunn view in 45° or 90° flexion of the hip, neutral rotation and 20° abduction or the crosstable projection in 15° internal rotation were found to be the best projections. These projections minimise the false-negative results. Crosstable lateral radiographs with external rotation in particular should not be used. The problem is that patients with cam impingement have diminished range of hip joint movement especially internal rotation

(<20°) as one of the clinical features, which does introduce practical difficulties in obtaining optimally positioned radiographic projections.

The Dunn view can be obtained by flexing the symptomatic hip in 45° or 90° with the patient in the supine position. The hip is abducted by 20°, but there is neutral rotation. With an FFD of 120 cm, the beam is centred midway between the ASIS and symphysis pubis.

The crosstable lateral view requires the patient to lie supine with the contralateral hip and knee flexed beyond 80°. The symptomatic limb is internally rotated by 15°, and the X-ray beam is directed parallel to the tabletop orientated 45° to the symptomatic limb centred on the femoral head.

The frog lateral view is obtained with the patient supine and the affected limb flexed at the knee by 30–40° and the hip abducted by 45°. The heel of the affected limb rests against the medial aspect of the contralateral knee. Using an FFD of 102 cm, the X-ray beam is centred midway between the ASIS and symphysis pubis. Despite initial enthusiasm in some quarters, the frog lateral view is not regarded as a reliable predictor of the alpha angle in FAI.

MRI 1) Oblique angle assessment—The α-angle is measured on 2–3-mm-thick oblique axial gradient-echo, fat-suppressed PD or T1-W MR arthrographic images, planned on the coronal MR images. The oblique axial plane is acquired parallel to the axis of the femoral neck and passing through the centre of the femoral head. This plane, which is individual to the patient and chosen on the basis of the coronal scout view, corresponds to a lateral radiograph with the film cassette parallel to the femoral neck (Figs. 12.26 and 12.28).

MRI 2) Multiple radial assessment—The maximal α-angle value from multiple radial images can be used as an alternative MR method. The radial images are obtained using the centre of the femoral neck as the axis of rotation. Patients with clinically suspected FAI can have an underestimated or missed cam abnormality if only the oblique axial plane is the basis of assessment. In Rakhra et al.'s comparative study, 54% of subjects had an α-angle less than 55° on the conventional oblique axial plane image, but 55° or more on the radial plane images.
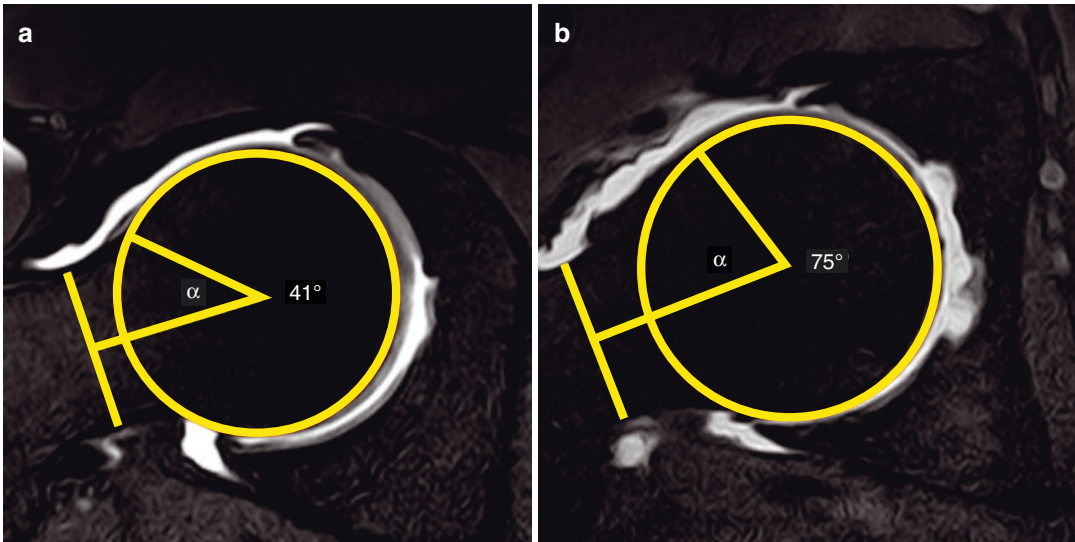
Fig. 12.28 MRI assessment of α-angle using oblique 2.5 mm fat-suppressed T1-wt TSE axial images. (**a**) Normal hip configuration. (**b**) A 42-year-old male patient with clinical indication of cam-type femoroacetabular impingement

A 3D isotropic T1-wt spoiled gradient-echo (MPRAGE/Turbo-Flash) sequence with water excitation (1 mm slice thickness, 25 cm FOV, 256×256 matrix) is obtained, from which 2-mm-thick oblique sagittal MPR images are produced perpendicular to the long axis of the femoral neck. Using the latter plane, 2-mm-thick radial MPR images are generated at 15° interval using the centre of the femoral head as the centre of rotation. The generated images are all orthogonal to the head-neck junction. Then a clockface nomenclature is employed designating the anterior-most head-neck junction as the 3 o'clock position, with the 12 o'clock position representing the superior-most junction. Selected radial specific images, four in all, are chosen to evaluate the anterosuperior quadrant of the head-neck junction corresponding to the 12, 1, 2 and 3 o'clock positions (Fig. 12.29).

For the **α-angle**, a best-fit circle is drawn around the contour of the femoral head. A line is drawn from the centre of the circle outlining the femoral head to the point at which the femoral head or neck protrudes beyond the confines of the circle anteriorly. A second line is constructed along the long axis of the femoral neck starting from the centre of the femoral head extending laterally to the midpoint of the neck at its narrowest point. In the MR radial method, the α-angle value varies with the clockface position, and the maximal angle is recorded. It is worth noting that the radial value at the 3 o'clock position is equivalent to the value obtained from the image through the middle of the femoral neck using the oblique MR image method, and usually in a cam deformity, the radial values are higher at the 2 o'clock vector. An alpha angle greater than 50° is abnormal although using a threshold of 55° may be more specific to cam impingement (Fig. 12.29).

To determine the **anterior femoral head-neck offset**, the endpoints used in determining the alpha angle are used. Lines are drawn parallel to the longitudinal axis of the femoral neck from both anterior points on the femoral head and femoral neck, respectively (Fig. 12.30). The difference between the perpendicular distances between these lines and the femoral neck axis creates the anterior head-neck offset (Fig. 12.31).

Normal asymptomatic anterior offset	11.6 ± 0.7 mm
Cam impingement anterior offset	7.2 ± 0.7 mm
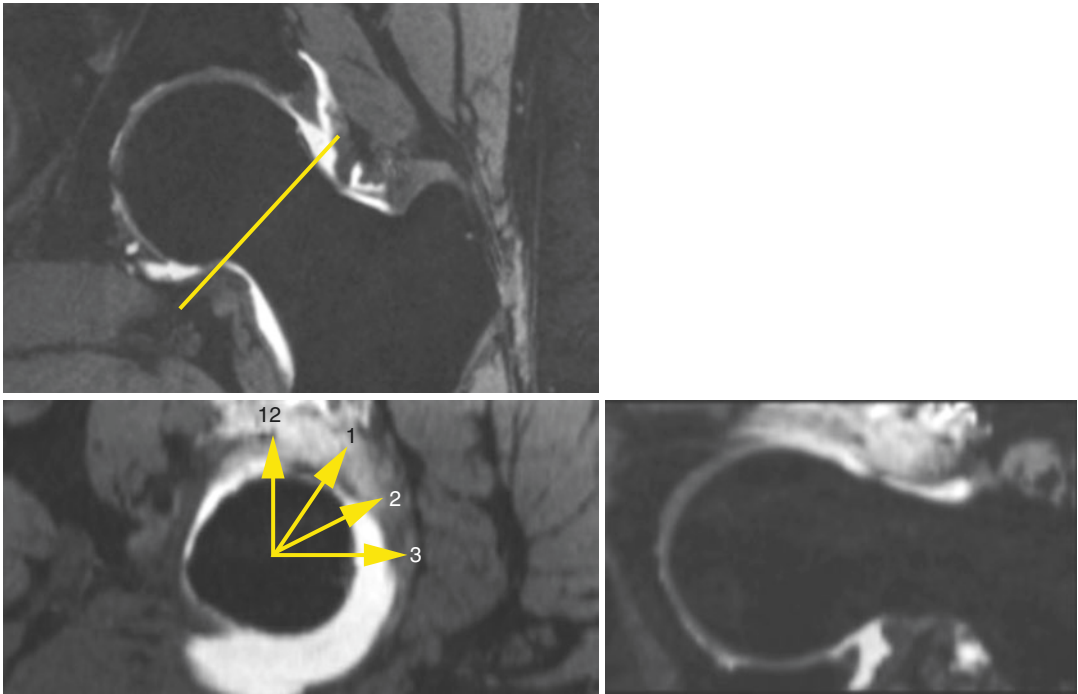
Fig. 12.29 α-angle assessment using multiple MR radial images
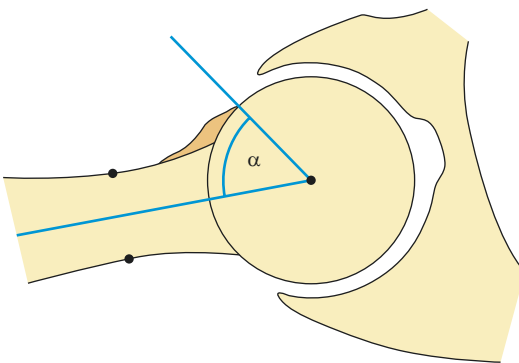
Fig. 12.30 CAM effect—abnormal α-angle
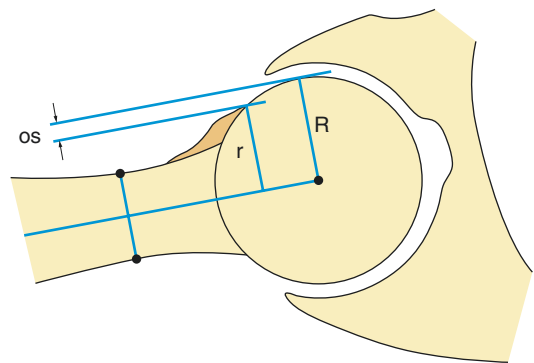
Fig. 12.31 Cam effect—abnormal anterior femoral offset

The **anterior offset ratio** can then be calculated between the anterior offset divided by the diameter of the femoral head.

Normal asymptomatic anterior offset	0.21 ± 0.03 mm
Cam impingement anterior offset	0.13 ± 0.0 mm

Reproducibility/Variation

The α-angle can be underestimated on the radiographic projection if rotation is not controlled.

The α-angle measured on oblique MR images exhibits a high degree of intra- and interobserver agreement. However, values reporting average alpha angles in patients with FAI are higher in

some studies (69.7° and 74.0°) compared with others that have found the abnormal threshold to be 55°. This could reflect the variability in location used to make the measurements.

The oblique axial plane optimally images the anterior contour of the femoral head-neck junction. More specifically however, it has been shown that the most pronounced femoral head offset is seen in the anterosuperior quadrant. For these reasons, there has been a move towards recommending MR radial images to evaluate the head-neck junction over its full circumference as opposed to just anteriorly using the oblique axial image method. Indeed rates of up to 54% false-negative values in FAI have been published when using the popular oblique axial plane protocol. As a result, the multiple radial plane protocol for its measurement was recently introduced as described above.

Clinical Relevance/Implications

Studies have shown that an elevated α-angle is associated with symptomatic impingement. Cam impingement refers to a "pistol grip" deformity in the contour of the anterior/superior femoral head-neck junction with the acetabulum being normal. Various methods have been described to measure the asphericity of the femoral head as well as the abnormal offset. These include measurement of the α-angle, the epiphyseal extension and the amount of femoral head-neck offset. The α-angle estimation is the easiest to measure and exhibits a high degree of intra- and interobserver agreement.

Impingement by the cam effect from femoral asphericity on the anterior acetabular rim induces cartilage injury predisposing to early osteoarthritis. Stulberg et al. proposed that the "pistol grip" deformity is seen in 40% of hip osteoarthritis.

Analysis/Validation of Reference Data

The α-angle was originally described as a measurement obtained from the oblique axial MR image through the centre of the femoral head. It is increasingly applied to conventional radiogra-

phy, but it is not known if applying these definitions across imaging modalities is valid or not. In practice most patients with cam impingement have alpha angles in excess of 63°. Although the crosstable lateral radiograph in 15° internal rotation is the recommended view for assessing the alpha angle and AOR radiographically, there are no robust quantitative definitions of normal and abnormal anatomy based on this projection. Despite this, the measurements from this technique are employed in routine clinical use, and the user needs to be aware that a recent UK study with validation, good repeatability and measurement reproducibility has shown a wider reference interval in normal hips than previously thought. These reference intervals indicate that clinically and radiographically normal hips may have alpha angles and AORs that would be considered abnormal if the threshold value of 55° is employed. The values on normal asymptomatic hips from both genders were combined in Pollard et al.'s study, to derive 95% confidence intervals for the studied population as follows:

Normal values		
Alpha angle mean	6–49°	(95% reference interval 32–62)
Anterior offset ratio	0.18–0.20	(95% reference interval 0.14–0.24)

Based on but extrapolating from this data of a sample from the general population, patients presenting with symptomatic FAI and an **α-angle of 63°** or **more, or an AOR below 0.14**, have proximal femoral anatomy beyond the reference interval.

As the proximal femur has greater offset anteromedially than anterolaterally, the α-angle increases and the AOR decreases with progressive internal rotation. The measurements from the crosstable lateral radiograph in 15° internal rotation have been validated (best reliability/reproducibility) for the purpose of quantifying the morphology and cam deformity of the proximal femur. In Notzli's article, there was a high degree of intra- and interobserver agreement using the oblique axial MR method. Divergence of observational assessment occurred only in

those hips with the largest alpha angles, but these were all clearly placed in the abnormal range. α-angle threshold values for cam deformities are still not fully agreed ranging between 50° and 55°.

Given the elliptical shape of the femoral neck, it is quite obvious that the oblique axial plane images will result in significantly lower α-angle measurements than the radial plane images. Rakhra et al.'s comparative study showed that the radial MR method is more sensitive to the presence, location and size of the anatomic deformity than the oblique axial method which had a false-negative rate of 56%.

For the mean AOR in normal asymptomatic hips, the values are quite consistent in the literature ranging between means of 0.15 and 0.19.

Conclusion

α-angle measurement is a reliable means of defining femoral head sphericity, is a good predictor for the risk of anterior FAI and is significantly correlated with the extent of cartilage hip defects. α-angle assessment using MRI is a fast and reliable measure to assess femoral asphericity.

12.19 Femoral Head Asphericity in Cam-Type Femoroacetabular Impingement: Triangular Index

Definition

The triangular index is a comparative measure between the natural radius of the femoral head (r) and the geometric resultant radius (R) calculated at the neck-head junction.

Indications

Hip pain in young adult to exclude underlying cam impingement.

Technique

AP radiograph (Fig. 12.32).

Full Description of Technique

This measurement technique requires a simple geometric calculation using Pythagoras theorem for right-angled triangles ($a^2 + b^2 = C^2$). Firstly the centre of the femoral head is located using Mose's circular templates. Then the longitudinal axis of the femoral neck is identified by connecting the femoral head centre to the midpoint of the narrowest dimensions of the femoral neck. The length of the natural radius of the femoral head (r) is then marked laterally along the constructed longitudinal axis of the femoral neck. Along this line, a point corresponding to the midpoint (i.e. halfway) of the natural radius is marked, and from this point, the perpendicular height (H) to the superior border of the head/neck junction is measured. Using this height (H), the corresponding radius (R) is calculated using Pythagoras theorem for right-angled triangles described above. If the resultant radius (R) at the point $0.5r$ along the axis of the femoral neck, at the head/neck junction, exceeds the natural
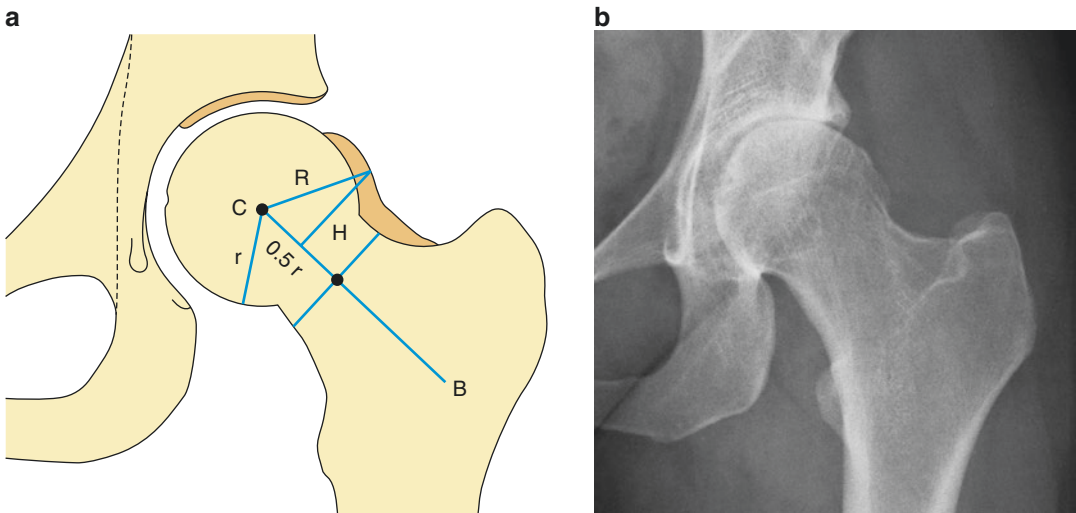
Fig. 12.32 Cam effect—triangular index measurement technique (**a**) with radiographic depiction of the bony bump on the AP view (**b**)

radius (r) of the femoral head by 2 mm on a radiograph with 1.2 magnification, then a hump malformation is present indicating the presence of head asphericity.

$R > r + 2$ mm

Reproducibility/Variation

This method produces a reliable and accurate assessment of femoral head asphericity which can be applied to both AP and lateral radiographs.

Clinical Relevance/Implications

It provides a simple and accurate description of the bony hump deformity causing the femoral head asphericity. The greater R is at the femoral head/neck junction compared with the natural head radius r, the more severe the hump morphology.

Analysis/Validation of Reference Data

The triangular index is purely geometric in its calculation and is based on measurements from fixed reference points. It has been found to be more reliable than the radiographic estimation of the α-angle. Probably this is because the exact point at which the radius of the aspherical femoral head deviates from the natural radius and increases laterally on a curved surface is not easy to define accurately.

Importantly the triangular index is not affected by rotation. In a comparative study with α-angle measurements on femoral specimens radiographed at different degrees of rotations, the triangular index result did not change unlike the alpha angle measurement.

Conclusion

More reliable in assessing the presence and magnitude of femoral head asphericity from conventional radiographs.

12.20 3D MDCT Quantitative Assessment of Cam Deformity

The angular measurements that are available to detect the cam deformity in femoroacetabular impingement currently focus on defining a contour abnormality of the femoral head. These techniques do not provide a quantifiable estimate of the deformity (extent, height and spatial orientation/location) which is increasingly becoming relevant as a preoperative map for minimally invasive surgical techniques.

Harnessing 3D volumetric-based multidetector CT technology to acquire the 3D dataset holds great promise in quantifying the bony abnormality accurately. In a large study on 102 dry cadaveric femora, this technique identified 49 instances of a bony prominence at the head-neck junction anterolaterally. The capabilities of this method are reflected in the average measured values which were:

Average surface area	326 mm² (SD 172 mm²)
Average height	3.23 mm (SD 0.74 mm)
Computed alpha angle of normal femora	47.65° (38.67–59.81)
Computed alpha angle of cam-type femora	67.72° (53.04–88.02)

In addition using this method, the 3D alpha angle can be calculated using the MR methods described previously. Limited studies have shown that when acquired accurately using 3D through automated computational analysis, the alpha angle correlates significantly with the 3D MDCT morphological detection method. Importantly there is also an acceptable correlation between the computed alpha angle and the multiple radial plane estimation but not the oblique axial plane estimation of the alpha angle. The technique has had to date only limited exploration in vivo and in vitro, but due to its potential, it is briefly included.

The rate of insufficient alpha angle corrections after corrective arthroscopic osteochondroplasty surgery in impingement patients is still in the order of 24%. This is despite using CT-based navigational systems which have an inherent accuracy of less than 1 mm. The CT-based protocol used in previous studies had major weaknesses which included the inability to display the amount of bone which needed to be resected. Without this information, it is not possible despite a very accurate navigational system to improve surgical accuracy and outcomes.

12.21 Femoroacetabular Impingement: Beta Angle

Definition

The (β) angle measures the angle between the head-neck junction and the acetabular rim with the hip in 90° flexion. It is useful in patients with FAI irrespective of the underlying FAI type.

Indication

FAI independent of aetiology. The increased α-angle (>55°) gives information about the severity of the femoral head-neck pathology, while the increased centre-edge angle (>40°) describes acetabular over-coverage, but neither are able to quantify the status during the impingement process.

Technique (Fig. 12.33)

The β-angle is an additional technique allowing measurement of the distance between the femoral head-neck junction and the acetabular rim with the hip in a position promoting impingement.
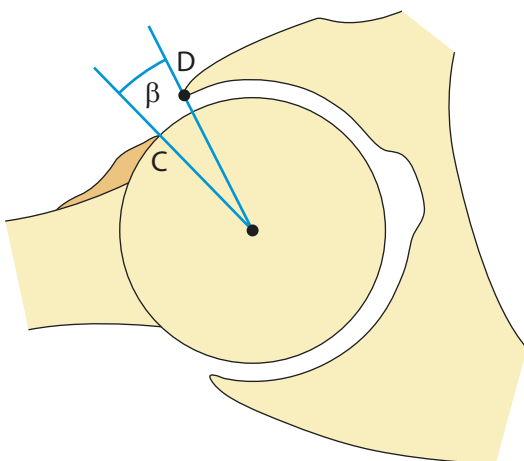
Fig. 12.33 β-angle combining femoral (C) and acetabular (D) components of femoral acetabular impingement

This assessment can be measured on images produced by a special radiographic technique or positioning in an open MR scanner.

Radiography. Beta view radiographs are obtained with the patient sitting in a chair, with the hip in 90° flexion and the femur in 20° abduction and 0° rotation. The femur needs to be horizontal, and this is checked by ensuring that the plane between the greater trochanter and lateral condyle is parallel to the ground. The beam is angled 15° in the AP direction rendering it tangential to the acetabular plane. It is centred on the femoral shaft about 6 cm lateral to the ASIS using 84 kV. On the resulting radiograph, the head-neck junction lies superiorly, with the femoral neck perpendicular to the acetabular plane.

MRI. An open MRI system is required for a positional study to show the space between the anterior femoral neck and the acetabular rim with the hip in 90° flexion. When the hip is in 90° flexion, the anterior femoral neck faces cephalad. The MRI plane needs to be in the orientation that allows measurement of the minimum space between the neck and rim at the site of potential FAI. As this space can be measured as an angle in the plane of motion, it is comparable with the clinically measured internal rotation. The patient is placed supine, and with the help of a support, the hip is placed in 90° of flexion and in neutral rotation in the sagittal plane before a flexible radiofrequency coil is positioned around the hip.

A coronal scout view passing through the centre of the hip is used with the hip in 90° flexion to determine the plane of acetabular anteversion. Then anteroposterior sections through the acetabulum are obtained tilted 90° to the acetabular opening. On this basis, 4-mm-thick sections are obtained. Using this technique, Wyss et al. found that the available space between the rim and femoral neck was consistently smallest in the section 4 mm anterior to the hip centre. The neck-rim relationship is then measured from this scan.

Using the MR image, the anterior limit of head congruency can be defined as the point where the distance from the centre of the head first exceeds the true radius of the cartilage-covered head. The lateral bony margin of the

acetabulum is then identified, and lines are drawn from the centre of the femoral head to the previously identified points. The angle formed by these lines is called the beta angle. It represents the arc of congruent internal rotation available with the hip in 90° flexion.

| Normal asymptomatic individuals | 30 ± 9° |
| FAI patients | 5 ± 9° |

Full Description of Technique

To measure the β-angle from the obtained radiograph, the method is similar to the one described above on the MR image. Briefly three points are defined: firstly the centre of the femoral head, secondly the point representing the anterior limit of head-neck congruency from where the distance from the bone to the head centre first exceeds the radius of the femoral head and thirdly the point which is at the superolateral rim of the acetabulum. The β-angle is subtended by the lines from the head centre to these points, respectively (Fig. 12.33).

| Normal beta angle | 38.7° (95% confidence interval 36.5–41.0) |
| FAI beta angle | 15.6° (95% confidence interval 13.3–17.7) |

Reproducibility/Variation

There are no significant differences in the measured β-angle values between men and women in either normal or FAI patients.

Excellent inter- and intraobserver correlation with a high reliability and reproducibility in both normal and FAI patients. This is seen using both radiographic and MRI techniques.

Clinical Relevance/Implication

A radiographically measured beta angle >30° is normal and in keeping with symptomatic FAI if <29°.

Using both radiographic and MRI-based measurements, the β-angle when compared with clinical examination showed significant correlation with range of internal rotation but not degree of flexion.

The β-angle can also be used postoperatively, and studies have shown improvement in the measurements following arthroscopic osteochondroplasty of the head-neck junction. This also correlated with clinical improvement of internal rotation.

Analysis/Validation of Reference Data

The mean β-angle in FAI measured radiographically is 15.6° compared with a mean β-angle measurement on MRI of 4°. This could be due to the inclusion of cartilaginous components of the bony bump visualised by MR not seen radiographically. However, it is also possible that it is not always possible to extrapolate measurements done using two different imaging techniques.

Conclusion

As the measurement is done with the hip at 90° flexion, any deformity impinging on joint motion is assessed whether it originates from the femoral, acetabular or both sides of the hip joint. It also shows that the physical examination with specific reference to internal rotation is reliable in indicating the presence of FAI. It provides additional objective dynamic dimension in FAI patients both preoperatively and postoperatively.

12.22   Femoral Anteversion and McKibbin Instability Index

Definition

Femoral anteversion is the angle between the transverse axis of the knee joint and the transverse axis of the femoral neck.

Indications

Diagnosis and selection of patients for derotational osteotomies.

Techniques

CT.
MRI.
The subject is covered further in the chapter on Long Bone Measurements.

Full Description of Technique

Femoral anteversion is the angle between the transverse axis of the knee joint, which is best indicated by a line drawn tangential to the maximum posterior convexity of both femoral condyles, and the transverse axis of the femoral neck. The latter line is drawn through the centre of the femoral head and along the central axis of the femoral neck.

The transverse axis of the knee joint has been a topic for discussion. Instead of the posterior tangential line, some propose the *transcondylar axis*. The latter is determined by first drawing tangents to the anterior and posterior aspects of the femoral condyles, and then a line drawn bisecting the angle between the two lines represents the *transcondylar axis*.

The *diacondylar plane* proposed by others connects two points at the widest flare of the condyles.

Since the femoral neck cannot be visualised in the transverse plane because of its anterior and
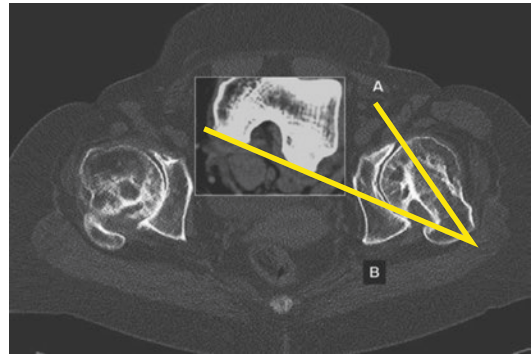
Fig. 12.34 Femoral anteversion and McKibbin instability index

cephalad orientation, images made at different levels can be superimposed to create a summation image (Fig. 12.34).

Alternatively, the angles of the femoral neck and femoral condyles formed with respect to the transverse plane are subtracted. However, if the femoral condyles are internally rotated on the images, the angle of rotation must be added to the angle of anteversion.

Normal values	15–20°
Dysplasia	>20°

Reproducibility/Variation

Highly reproducible in adults.

Clinical Relevance/Implications

Precise measurement of femoral anteversion is important in the selection of patients for preoperative planning of derotational osteotomy of the femur.

The *McKibbin instability index* is based on the assumption that the effects of femoral and acetabular anteversion may be additive or may offset each other. The McKibbin instability index is calculated as the sum of the angles of femoral and acetabular anteversion, with an index of 60 denoting severe instability. The normal range for the McKibbin instability index is 30–40°. Abnormal values are associated with hip pain and osteoarthritis.

Normal McKibbin index	30–40°
Abnormal McKibbin index	>40°

Analysis/Validation of Reference Data

Decreased femoral anteversion is seen in association with slipped capital femoral epiphysis, coxa vara, deep acetabulum, dysplasia of the hip and pistol grip deformity, after derotational varus osteotomy in children (when the femoral anteversion, which has been reduced to 0°, does not remodel), and in patients with previous fractures of the femoral shaft. Increased femoral anteversion is seen in developmental dysplasia of the hip, Legg-Calve-Perthes disease, intoeing gait and cerebral palsy.

The measurement on a single image of the proximal neck has been reported to underestimate anteversion by about 10° in normal patients. This error is greater for images through the proximal part and less for images that were taken in the distal part of the femoral neck. This inaccuracy may be explained by the fact that a single section through the femoral neck often fails to indicate the direction of the axis of the femoral neck. The most proximal portion of the inferior neck with no head portion on the CT axial slice provides the most accurate estimate of the neck axis.

Conclusion

It is unclear whether isolated anteversion of the femur can be considered a form of hip dysplasia. Even though increased anteversion is commonly found in hip dysplasia, no relationship has been established with the acetabular development.

12.23   Femoral Neck Shaft Angle (NSA) or Centrum-Collum-Diaphyseal (CCD) Angle of Muller

Definition

The NSA is the angle formed by lines drawn along the long axis of the femoral shaft and along the axis of the femoral neck passing through the centre of the femoral head. It is also known as *centrum-collum-diaphyseal (CCD) angle of Muller.*

Indications

Along with the angle of femoral anteversion, the NSA is required prior to surgery for correcting the dysplastic hip. A coxa valga deformity is the usual abnormality in hip dysplasia patients. Further indications include detection and preoperative planning of femoral fractures and developmental coxa vara.

Technique (Fig. 12.35)

AP radiography. The appearance of the femoral neck radiographically is significantly affected by femoral anteversion. To counteract this, the NSA is most accurately measured with the legs in 20° internal rotation which is the standard in obtaining this radiograph.

Full Description of Technique

The patient is placed flat on the back with the feet pointing medially. The central ray passes through a point 1 in. below the centre of the inguinal ligament perpendicular to the plane of the film. An angle is formed by the long axes of the femoral shaft and neck (see below).

The most reliable method of constructing the respective femoral shaft and femoral neck axis needs to be employed (Fig. 12.35). Firstly the femoral shaft axis is determined by joining two
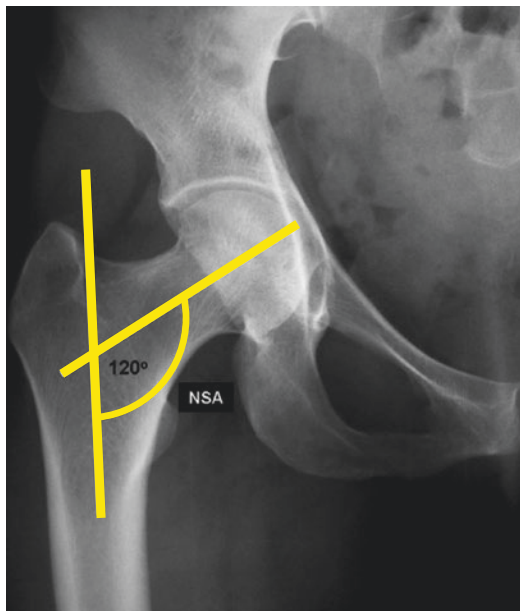
Fig. 12.35 Radiographic measurement of femoral neck shaft angle

points obtained by bisecting two transverse diameters of the proximal subtrochanteric femoral diaphysis. Secondly the centre of the femoral neck is determined. To do this, a circle is first drawn around the femoral head outline and the centre of the femoral head is located. This circular arc intersects the femoral neck at two points on the superior and inferior femoral neck outlines, respectively. A line is then drawn joining these two points, and a bisector is created to this line. The line joining this line's midpoint to the centre of the femoral head is the femoral neck. (Please refer to the Paediatric section for diagram details.)

Normal values	125–135°
Abnormal values	Coxa vara, <125°
	Coxa valga, >140°

Reproducibility/Variation

Highly reproducible if applied after the age of 6.

Clinical Relevance/Implications

Apart from surgical planning, the study of NSA is important to study osteoarthritis in an individual patient. In addition, the use of a combination of femoral BMD and NSA may improve hip fracture risk prediction as the latter is significantly higher in patients with hip fractures.

Analysis/Validation of Reference Data

Using this radiographic method, the NSA measurement is a close approximation of the true NSA. The measurement is significantly affected by femoral neck anteversion, and attention to the correct interpretation of the measurements is vital prior to surgical planning. If corrective surgery is being planned, an exact value must be obtained using charts (not included) taking into account the degree of femoral anteversion.

In congenital coxa vara, the medial contour of the femoral neck is often deficient. Alternatively the inferior point of femoral neck intersection with the circular arc is replaced by obtaining a point where a perpendicular to the femoral shaft axis intersects the highest point on the inferomedial outline of the femoral neck to define the centre of the femoral neck.

Conclusion

As femoral anteversion significantly affects the radiographic projection of the neck shaft angle, accurate positioning is a mandatory prerequisite. Both angles are required prior to carrying out any planning for corrective surgery.

12.24   Stem Anteversion

Definition

This is the angle between the transverse axis of the stem and the transverse axis of the knee joint.

Indications

To assess postoperatively the stem anteversion in patients with total hip replacements and hip pain.

Technique (Fig. 12.36)

CT

Full Description of Technique

The femoral stem axis is defined as the line along the anterior and posterior borders of the implant. The stem anteversion is evaluated as an angle between the posterior condylar axis and the axis of the femoral stem at the most proximal portion of the inferior neck with no head portion included in the image.

Reproducibility/Variation

Highly reproducible.

Clinical Relevance/Implications

An excess or deficit in the value of stem anteversion may influence the range of motion because of impingement effects and may be the cause of loosening.

Analysis/Validation of Reference Data

The surgeon's intraoperative intention using visual assessment in placing the stem in an anteversion of 10–20° is imprecise especially in the cementless femoral stem.

Conclusion

This measurement often indicates that the stem is often not within the intended range of anteversion.

Fig. 12.36 Stem anteversion angle on cross-sectional imaging with superimposition of the femoral stem axis on the transcondylar axis of the distal femur (S denotes the presence of the stem implant in the proximal femur)

12.25 Femoral Head: Index of Necrotic Extent

Definition

The measurement of the extent of the avascular necrotic process in the femoral head.

Indications

Quantification of avascular necrosis of the femoral head.

Techniques

MRI.

Full Description of Technique

A is the necrotic arc angle in the coronal plane, and *B* is the necrotic arc angle in the sagittal plane. The index of necrotic extent ($[A/180] \times [B/180]) \times 100$ is derived from the size of subchondral involvement at the midcoronal and midsagittal planes, and the modified index of necrotic extent is derived from the maximum size of subchondral involvement in both planes (Fig. 12.37).

Reproducibility/Variation

Highly reproducible.

Clinical Relevance/Implications

The size of the necrotic lesion is important in determining whether a subchondral fracture will occur.

Analysis/Validation of Reference Data

There are numerous methods for quantifying the extent of osteonecrosis of the femoral head, some quite complicated requiring advanced software analysis.

Conclusion

There is no consensus regarding which method is the most reliable.
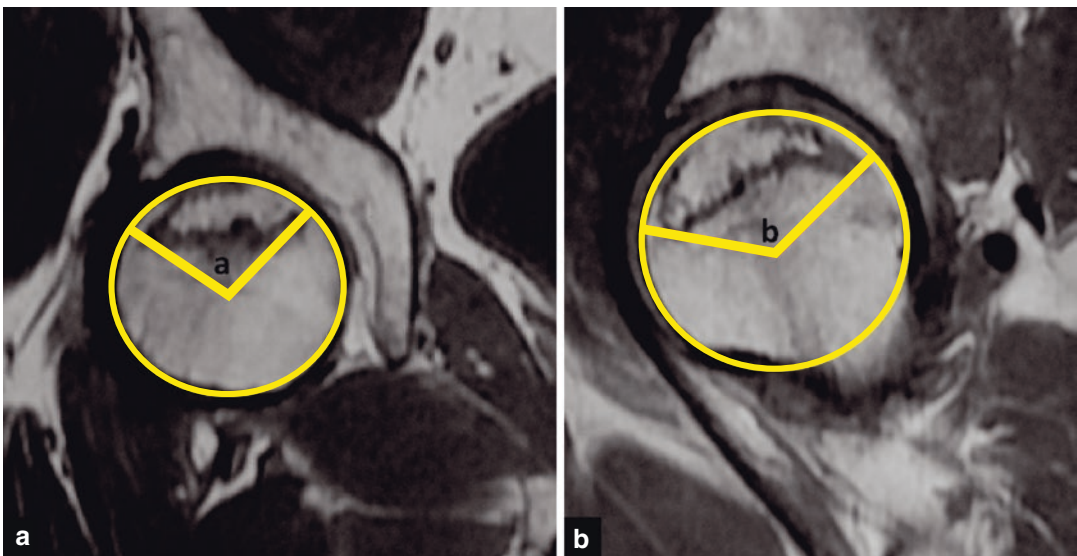
Fig. 12.37 Coronal (**a**) and sagittal (**b**) T1-wt MR images used in determining the necrotic extent index of the femoral head

12.26   Pelvic Instability: Symphysis Pubis Excursion on Flamingo Radiographs

Definition

Translation of the symphysis pubis is the total excursion measured at the symphysis pubis on alternating single-leg-stance radiographs.

Indications

Pelvic pain due to instability from anatomical, hormonal, biomechanical, metabolic and endocrine causes.

Technique

AP radiography of the pelvis to assess symphysis pubis (Fig. 12.38).

Full Description of Technique

Three AP radiographs are required at an FFD of 0.6 m with the patient standing: dual stance, single-leg-stance on the right and single-leg-stance on the left. The dual stance film acts as the control. In every case, the high pubic ramus changed from right to left coinciding with the change of stance leg.

A vertical reference line is drawn to pass through the spinous process of L4 and L5 and the tip of the coccyx. Two lines are then drawn perpendicular to this line to the most superior aspect of the pubic symphysis on the right and left. The distance between these lines is equal to the translation, and the degree of motion can be compared with the baseline dual-leg-stance film. The sum of the translation from baseline is then added to give a total translation in centimetre. Under normal conditions, there is a difference in the magnitude of the translation between men and women and nulliparous and multiparous women.

Standing	Weight bearing right	Weight bearing left
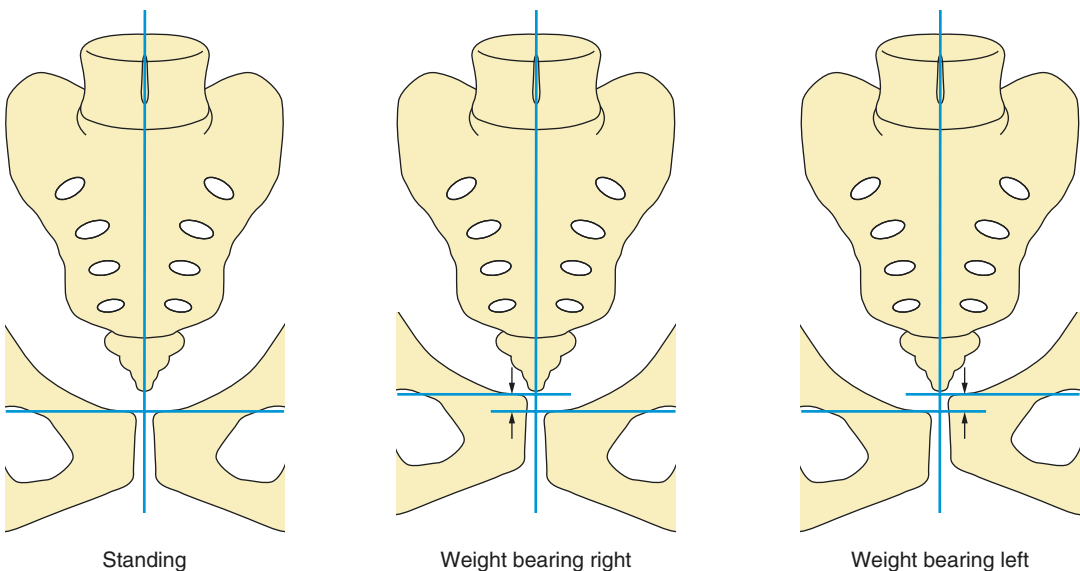
Fig. 12.38 Symphysis pubis excursion with the patient standing on both legs, standing on the right leg and then standing on the left leg

Normal Physiological Translation of Mean Translation at Symphysis Pubis in mm + SD

Men	1.4 ± 1.0 mm	Women	
		Nulliparous	1.6 ± 0.8 mm
		Multiparous	3.1 ± 1.5 mm

The increased normal translation in multiparous women is also directly proportional to the number of pregnancies.

Abnormal translation in keeping with pelvic instability is defined as >0.5 cm of change in alignment between the views.

Reproducibility/Variation

There is excellent interobserver correlation highlighting the repeatability of this method of measurement.

Clinical Relevance/Implications

During single-leg-stance, strong shearing forces act on the symphysis pubis in two opposite vertical directions simultaneously and create the shift seen in pelvic relaxation. The diagnosis of pelvic instability is made on the basis of the difference in the heights of the symphyseal bodies on the two AP single-leg-stance radiographs. The measurements are made from the top of the symphyseal bodies with respect to the perpendicular plumbline from the sacrum. The vertical difference in height between the two points is measured in centimetre, and the values from both radiographs are added together to provide a total translation value.

Analysis/Validation of Reference Data

Previously Chamberlain had concluded that the upper limit of normal physiological range is 2 mm.

Conclusion

Normally up to 0.5 cm of physiological motion can take place at the symphysis pubis in asymptomatic individuals as seen on alternating single-leg-stance AP radiographs.

12.27   MRI Pelvimetry

Definition

Pelvimetry is the evaluation of the relative sizes of the fetal head (Fig. 12.39) and the maternal pelvis.

A positive cephalopelvic disproportion index is present if the narrowest pelvic diameter (either the sagittal diameter of the inlet or the transverse diameter of the midpelvis) is less than 9 mm wider than the fetal biparietal diameter.
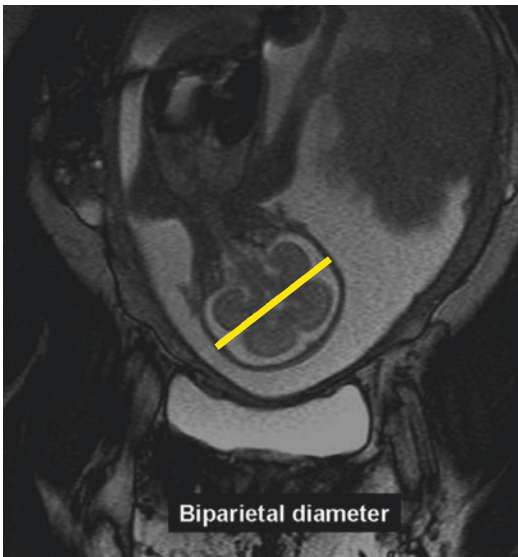
Fig. 12.39 MR pelvimetry—biparietal diameter

Indications

To select women with potential difficulties in vaginal delivery.

Technique

MRI.

Full Description of Technique

MRI pelvimetry has replaced radiographic and CT pelvimetry due to the ability for multiplanar imaging and the lack of ionising radiation. MRI pelvimetry is applied on midsagittal, transverse and oblique sections of the pelvis.

Axial Image

Interspinous (*bispinous*, *midpelvic*) *diameter*: This is the most important measurement as it is usually the narrowest point of the midpelvis, where obstructive labour most often occurs. The measurement is made at the level where the ischial spines are best visualised. This level is usually within 1–2 cm of the femoral head fovea (Fig. 12.40).

Intertuberous diameter: This is the widest distance between the ischial tuberosities (Fig. 12.41).

Midsagittal Image

Anterior-posterior inlet diameter (*obstetric conjugate*): This measurement is the distance
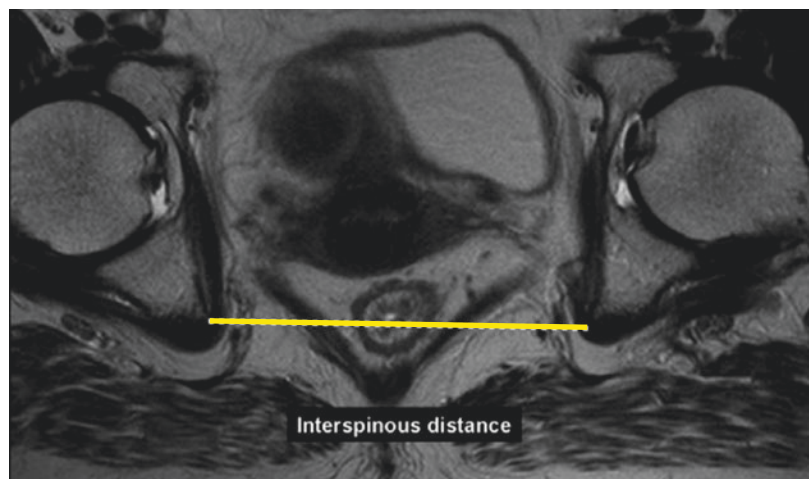
Fig. 12.40 MR pelvimetry—interspinous distance

Fig. 12.41 MR pelvimetry—intertuberous distance
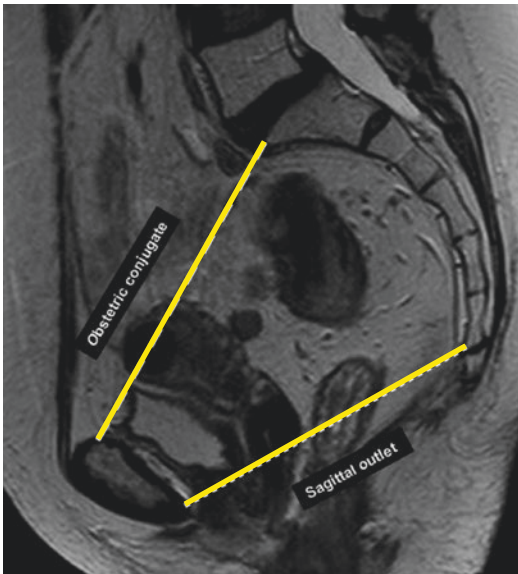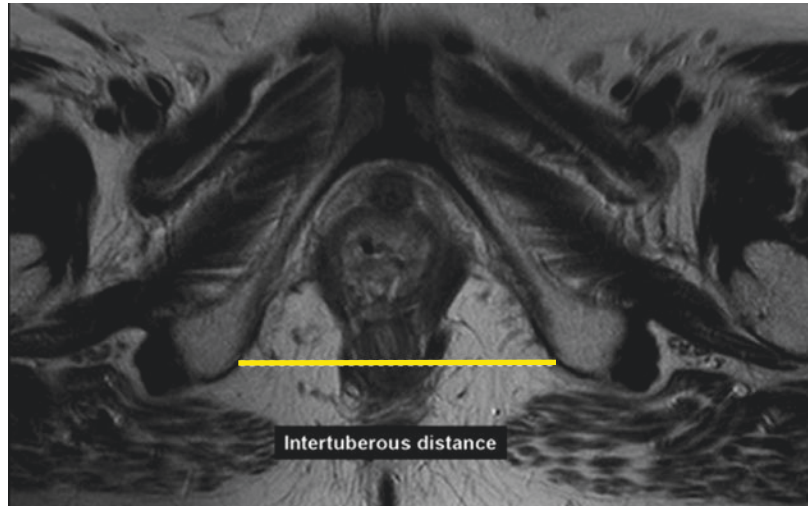
Fig. 12.42 MR pelvimetry—sagittal outlet/obstetric conjugate distances

Fig. 12.43 MR pelvimetry transverse diameter

from the posterior-superior aspect of the pubic symphysis to the most anterior aspect of the first sacral vertebral body (sacral promontory).

Sagittal outlet: This is the distance from the bottom of the inner cortex of the symphysis to the end of the sacrum (Fig. 12.42).

Oblique Coronal Image

The oblique section is performed in a plane through the superior pubic symphysis and the promontorium. The *transverse inlet diameter* is the largest transverse distance of the pelvis. A line is drawn through the widest area of the pelvis between the arcuate lines of the iliac bones (Fig. 12.43).

Reproducibility/Variation

The *intertuberous diameter* is the most difficult to define. Moderate difficulty in definition demonstrates the *sagittal outlet.* All other parameters are highly reproducible.

Clinical Relevance/Implications

A small maternal pelvis is a contraindication for vaginal delivery of a fetus in breech presentation because of the potential difficulty in delivering the fetal head.

A pelvis too small for safe vaginal delivery has been defined as one measuring less than 12 cm in the widest *transverse inlet diameter*, 11 cm in the *anterior-posterior inlet diameter* or 10 cm in the *interspinous diameter*.

Analysis/Validation of Reference Data

While most investigators agree that pelvimetry will not alter the conduct of labour in a vertex presentation, it may reveal small-sized pelvis in breech presentation which if associated with hyperextension of the fetal head may result in increased risk of cervical cord damage and is an indication for caesarean section. MRI implies no radiation but does not show a significant improvement over previously described pelvimetric techniques.

Conclusion

MRI is the modality of choice for assessing the maternal pelvis.

12.28 Ischiofemoral Space: Quadratus Femoris Space

Definition

The ischiofemoral space (IFs) lies between the ischial tuberosity and the lesser trochanter.

The quadratus femoris space (QFs) contains the quadratus femoris muscle (QFm), and it lies between the hamstring tendons and the lesser trochanter.

Indications

The abnormally narrowed IFs and QFs are related to the ischiofemoral impingement syndrome (IFIs) which is clinically demonstrated with hip pain. The QFm shows on MRI abnormal morphology and/or signal intensity.

Techniques

CT/MRI.
Axial images.
Axial T1-wt images.

Full Description of Technique

The following spaces should be assessed on thin section axial images whether with CT or MRI. MRI should be performed with high-field scanners (1.5–3.0 T) and a phased array coil.

Ischiofemoral space (IFs): The smallest distance between the lateral cortex of the ischial tuberosity and the medial cortex of the lesser trochanter.

Quadratus femoris space (QFs): The smallest space for passage of the quadratus femoris muscle (QFm) bordered by the superolateral surface of the hamstring tendons and the posteromedial surface of the iliopsoas tendon or lesser trochanter (Fig. 12.44). Axial T1-W MR images are the preferred ones for measurements (Fig. 12.45).
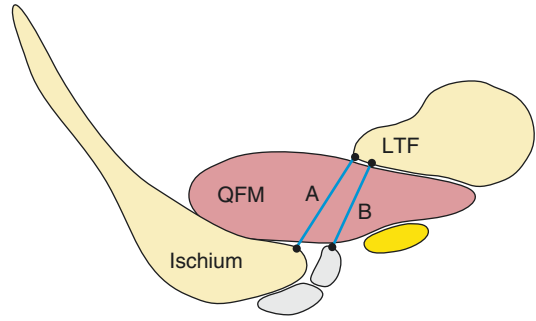
Fig. 12.44 Diagram depicting measurement points for IFs and QFs estimation

Reproducibility/Variation

No currently available data exist on the reproducibility of the above measurements.

In one cadaveric study, the mean IFs was 23.5 ± 4.7 mm and the mean QFs 20.4 ± 5.6 mm. In the same study, 52% of the hips showed abnormalities within the QF muscle.

In a MRI study, the IFs was found 23 ± 8 mm in controls vs 13 ± 5 mm in patients. The QFs was, respectively, found 12 ± 4 mm vs 7 ± 3 mm (lower leg in internal rotation).

In another MRI study of symptomatic patients examined with the lower leg in neutral position, IFs was found 12.9 mm and the QFs 6.7 mm on the average.

Clinical Relevance/Implications

Patients with IFIs present with chronic pain in the groin or buttock. The pain may radiate to the lower extremity due to the proximity of the QFm to the sciatic nerve. The symptomatic patients with narrowed IFs and QFs show on MRI oedema, partial tear and fatty infiltration of the QFm and oedema and partial tears of the hamstring tendons. CT scanning can show the narrowed space but is not capable of depicting the QFm abnormalities.

Normal IFs	>20 mm
Abnormal IFs	<20 mm
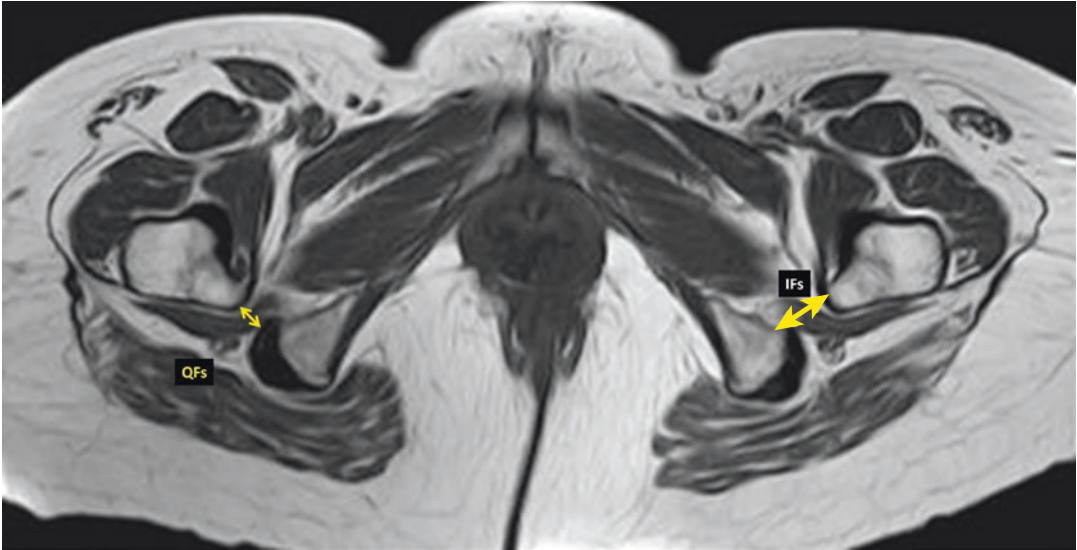
Fig. 12.45 MRI T1 axial image showing IFs and QFs distances

References

Abitbol MM, Taylor UB, Castillo I, Rochelson BL (1991) The cephalopelvic disproportion index: combined fetal sonography and x-ray pelvimetry for early detection of cephalopelvic disproportion. J Reprod Med 36:369–373

Anda S, Terjesen T, Kvistad KA, Svenningsen S (1991a) Acetabular angles and femoral anteversion in dysplastic hips in adults: CT investigation. J Comput Assist Tomogr 15:115–120

Anda S, Terjesen T, Kvistad KA (1991b) Computed tomography measurements of th acetabulum in adult dysplastic hips: which level is appropriate? Skeletal Radiol 20(4):267–271

Armbuster RG, Guerra J, Resnick D, Goergen TG, Feingold ML, Niwayama G, Danzig L (1978) The adult hip: an anatomic study, part 1: the bony landmarks. Radiology 128:1–10

Audenaert E, Baelde N, Huysse W, Vigneron L, Pattyn C (2011) Development of a three-dimensional detection method of cam deformities in femoroacetabular impingement. Skeletal Radiol 40:921–927

Beaule PE, Zaragoza E, Motamedi K, Copelan N, Dorey FJ (2005) Three-dimensional computed tomography of the hip in the assessment of femoroacetabular impingement. J Orthop Res 23(6):1286–1292

Boniforti FG, Fujii G, Anfliss RD, Benson MKD (1997) The reliability of measurements of pelvic radiographs in infants. J Bone Joint Surg Br 79-B:570–575

BruckI R, Hepp WR, Tonnis D (1974) Eine abgrenzung normaler und dysplastischerjugendlicher huftgelenke durch den huftwert. Arch Orthop Unfallchir 74: 13–32

Brunner A, Hamers AT, Fitze M, Herzog RF (2010) The plain Beta-angle measured on radiographs in the assessment of femoroacetabular impingement. J Bone Joint Surg Br 92-B:1203–1208

Buckley SL, Sponseller PD, Magid D (1991) The acetabulum in congenital and neuromuscular hip instability. J Pediatr Orthop 11:498–501

Busse J, Gasteiger W, Tonnis D (1972) A new method for roentgenologic evaluation of the hip joint-the hip factor. Arch Orthop Unfallchir 72:1–9

Cherian SF, Laorr A, Saleh KJ, Kuskowski MA, Bailey RF, Cheng EY (2003) Quantifying the extent of femoral head involvement in osteonecrosis. J Bone Joint Surg Am 85:309–315

Cibere J (2006) Do we need radiographs to diagnose osteoarthritis? Best Pract Res Clin Rheumatol 20:27–38

Clohisy JC, Carlisle JC, Beaule PE, Kim YJ, Trousdale RT, Sierra RJ, Leunig M, Schoenecker PL, Millis MB (2008) A systematic approach to the plain radiographic evaluation of the young adult hip. J Bone Joint Surg Am 90(Suppl 4):47–66

Cooperman DR, Wallensten R, Stulberg SD (1983) Acetabular dysplasia in the adult. Clin Orthop 175:79–85

Dandachli W, Islam SU, Liu M, Richards R, Hall-Craggs M, Witt J (2009) J Bone Joint Surg Br 91(8):1031–1036

Dandachli W, Islam SU, Tippett R, Hall-Craggs M, Witt J (2011) Analysis of acetabular version in the native hip: comparison between 2D axial and 3D CT measurements. Skeletal Radiol 40:877–883

Delaunay S, Dussault RG, Kaplan PA, Alford BA (1997) Radiographic measurements of dysplastic adult hips. Skeletal Radiol 26:75–81

Dorr LD, Wan Z, Malik A, Zhu J, Dastane M, Deshmane P (2009) A comparison of surgeon estimation and computed tomographic measurement of femoral component anteversion in cementless total hip arthroplasty. J Bone Joint Surg 91:2598–2604

Eijer H, Leunig M, Mahomed MN, Ganz R (2001) Crosstable lateral radiograph for screening of anterior femoral head-neck offset in patients with femoroacetabular impingement. Hip Int 11:37–41

Eyring EJ, Bjornson DR, Peterson CA (1965) Early diagnostic and prognostic signs in Legg-Calve-Perthes disease. Am J Roentgenol 93:382–387

Ezoe M, Naito M, Inoue T (2006) The Prevalence of acetabular retroversion among various disorders of the hip. J Bone Joint Surg Am 88:372–379

Fowkes LA, Petridou E, Zagorski C, Karuppiah A, Toms AP (2011) Defining a reference range of acetabular inclination and centre-edge angle of the hip in asymptomatic individuals. Skeletal Radiol 40:1427–1434

Fredensborg N (1976) The CE angle of normal hips. Acta Orthop Scand 47:403–405

Ganz R, Parvizi J, Beck M, Leunig M, Notzli H, Siebenrock KA (2003) Femoroacetabular impingement: a cause for osteoarthritis of the hip. Clin Orthop 417:112–120

Garras DN, Carothers JJ, Olson SA (2008) Single-leg-stance (Flamingo) radiographs to assess pelvic instability. How much motion is normal? J Bone Joint Surg Am 90:2114–2118

Gimovsky ML, Willard K, Neglio M, Howard T, Zeme S (1985) X-ray pelvimetry in a breech protocol: a comparison of digital radiography and conventional methods. Am J Obstet Gynecol 153:887–888

Giori NJ, Trousdale RT (2003) Acetabular retroversion is associated with osteoarthritis of the hip. Clin Orthop Relat Res 417:263–269

Gnudi S, Ripamonti C, Gualtieri G, Manavolta N (1999) Geometry of proximal fêmur in the prediction of hip fracture in osteoporotic women. Br J Radiol 72: 729–733

Gosvig KK, Jacobsen S, Palm H, Sonne-Holm S, Magnusson E (2007) A new radiological index for assessing asphericity of the femoral head in Cam Impingement. J Bone Joint Surg 89-B:1309–1316

Gusis SE, Babini JC, Garay SM, García Morteo O, Maldonado Cocco JA (1990) Evaluation of the measurement methods for protrusio acetabuli in normal children. Skeletal Radiol 19(4):279–282

Herrlin K, Pettersson H, Selvik G, Lidgren L (1988) Femoral anteversion and restricted range of motion in total hip prostheses. Acta Radiol 29:551–553

Heyman CH, Herndon CH (1950) Legg-Perthes Disease: a method for the assessment of the roentgenographic result. J Bone Joint Surg Am 32A:767–778

Hoiseth A, Reikeras O, Fonstelien E (1989) Lack of correlation between femoral neck anteversion and acetabular orientation. Acta Orthop Scand 60:93–96

Hubbard MJS (1969) The measurement of progression in protrusion acetabuli. Am J Roentgenol 106:506–508

Idelberger K, Frank A (1952) Uber eine neue methode zur bestimmung des pfannendachwinkels bei jugendlichen und erwachsenen. Z Orthop 82:571578

Ito K, Minka MA 2nd, Leunig M, Werlen S, Ganz R (2001) Femoroacetabular impingement and the cam-effect: an MRI-based quantitative anatomical study of the femoral head-neck offset. J Bone Joint Surg Br 83:171–176

Keller TM, Rake A, Michel SC, Seifert B, Efe G, Treiber K, Huch R, Marincek B, Kubik-Huch RA (2003) Obstetric MR pelvimetry: reference values and evaluation of inter- and intraobserver error and intraindividual variability. Radiology 227:37–43

Kim YM, Ahn JH, Kang HS, Kim HJ (1998) Estimation of the extent of osteonecrosis of the femoral head using MRI. J Bone Joint Surg Br 80:954–958

Kim SS, Frick SL, Wenger DR (1999) Anteversion of the acetabulum in developmental dysplasia of the hip: analysis with computed tomography. J Pediatr Orthop 19(4):438–442

Kleemann RU, Heller MO, Stoeckle U, Taylor WR, Duda GN (2003) THA loading arising from increased femoral anteversion and offset may lead to critical cement stresses. J Orthop Res 21:767–774

Konan S, Rayan F, Haddad FS (2010) Is the frog lateral plain radiograph a reliable predictor of the alpha angle on femoroacetabular impingement? J Bone Joint Surg Br 92-B:47–50

Koo K-H, Kim R (1995) Quantifying the extent of osteonecrosis of the femoral head. A new method using MRI. J Bone Joint Surg Br 77:875–880

Lequesne M (1963a) Mesure des angles fondamentaux de la hanche radiographique de l'adulte par un rapporteur combine. Rev Rheum 30:479–485

Lequesne M (1963b) Coxometrie. Mesure des angles fondamentaux de la hanche radiographique de l'adulte par un rapporteur combiné. Rev Rhum 30:479–485

Lequesne M, deSeze S (1961) Le faux profil du bassin: Nouvelle incidence radiographique pour l'edude de la hanche: Son utilite dans les dysplasies et les differentes coxpathies. Rev Rhum Mal Osteoartic 28:643–652

Lequesne M, Laredo JD (1998) The faux profil (oblique view) of the hip in the standing position. Contribution to the evaluation of osteoarthritis of the adult hip. Ann Rhum Dis 57:676–681

Lequesne M, Lemoine A, Massare C (1964) Le "complet" radiographique coxofemoral. Depistage et bilan préopératoire des vices architecturaux de la hanche. J Radiol Electrol 1(2):27–44

Lequesne M, Malghem J, Dion E (2004) The normal hip joint space: variations in width, shape, and architecture on 223 pelvic radiographs. Ann Rheum Dis 63:1145–1151

McBride MT, Muldoon MP, Santore RF, Trousdale RT, Wegner DR (2001) Protrusio acetabuli: diagnosis and treatment. J Am Acad Orthop Surg 9:79–88

Meyer DC, Beck M, Ellis T, Ganz R, Leunig M (2006) Comparison of six radiographic projections to assess head/neck asphericity. Clin Othop Rel Res 445:181–185

Moore RJ, Fazzalari NL, Manthey BA, Vernon-Roberts B (1994) The relationship between head-neck-shaft angle, calcar width, articular cartilage thickness and bone volume in arthrosis of the hip. Br J Rheumatol 33:432–436

Murphy SB, Kijewski PK, Wilkinson RH, Griscom NT (1987) Femoral anteversion. J Bone Joint Surg Am 69:1169–1176

Murphy S, Ganz R, Muller M (1995) The prognosis of untreated dysplasia of the hip. J Bone Joint Surg 77-A:986–989

Murray RO (1965) The aetiology of primary osteoarthritis of the hip. Br J Radiol 38:810–824

Nelitz M, Guenther KP, Gunkel S, Puhl W (1999) Reliability of radiological measurements in the assessment of hip dysplasia in adults. Br J Radiol 72:331–334

Nötzli HP, Wyss TF, Stoecklin CH, Schmid MR, Treiber K, Hodler J (2002) The contour of the femoral head-neck junction as a predictor for the risk of anterior impingement. J Bone Joint Surg Br 84:556–560

Ogata S, Moriya H, Tsuchiya K, Akita T, Kamegaya M, Someya M (1990) Acetabular cover in congenital dislocation of the hip. J Bone Joint Surg Br 72:190–196

Omeroglu H, Bicimoglu A, Agus H, Tumer Y (2002) Measurement of center-edge angle in developmental dysplasia of the hip: a comparison of two methods in patients under 20 years of age. Skeletal Radiol 31:25–29

Ozcelik A, Omeroglu H (2003) Two alternative methods for the measurement of MZ distance on a hip radiograph. Arc Orthop Trauma Surg 123:215–218

Pessis E, Chevrot A, Drape JL, Leveque C, Sarazin L, Minoui A, Le Blevec G, Chemla N, Dupont AM, Godefroy D (1999) Study of the joint space of the hip on supine and weight-bearing digital radiographs. Clin Rad 54:528–532

Pfirrmann CW, Mengiardi B, Dora C, Kalberer F, Zanetti M, Hodler J (2006) Cam and pincer femoroacetabular impingement: characteristic MR arthrographic findings in 50 patients. Radiology 240:778–785

Philippon MJ, Briggs KK, Yen YN, Kuppersmith DA (2009) Outcomes for hip arthroscopy for femoroacetabular impingement associated with chondrolabral dysfunction: minimum two year follow-up. J Bone Joint Surg Br 91:16–23

Pollard TCB, Villar RN, Norton MR, Fern ED, Williams MR, Simpson DJ, Murray DW, Carr AJ (2010) Femoroacetabular impingement and classification of the cam deformity: the reference interval in normal hips. Acta Orthop 81(1):134–141

Rakhra KS, Sheikh AM, Allen D, Beale PE (2009) Comparison of MRI alpha angle measurement planes in femoroacetabular impingement. Clin Orthop Rel Res 467(3):660–665

Reynolds D, Lucas J, Klaue K (1999) Retroversion of the acetabulum. A cause of hip pain. J Bone Joint Surg Br 81:281–288

Ruby L, Mital MA, O'Connor J, Patel U (1979) Anteversion of the femoral neck: comparison of methods of measurement in patients. J Bone Joint Surg Am 61:46–51

Ryder CT, Crane L (1953) Measuring femoral anteversion: the problem and a method. Bone Joint Surg Am 35:321–328

Siebenrock KA, Kalbermatten DF, Ganz R (2003) Effect of pelvic tilt on acetabular retroversion: a study of pelves from cadavers. Clin Orthop Relat Res 407:241–248

Siebenrock KA, Wahab KH, Werlen S, Kalhor M, Leunig M, Ganz R (2004) Abnormal extension of the femoral head epiphysis as a cause of cam impingement. Clin Orthop 418:54–60

Siegel J, Templeman DC, Tornetta P III (2008) Single-leg-stance radiograph in the diagnosis of pelvic instability. J Bone Joint Surg Am 90:2119–2125

Stark DD, McCarthy SM, Filly RA, Parer JT, Hricak H, Callen PW (1985) Pelvimetry by magnetic resonance imaging. Am J Roentgenol 144:947–950

Steinberg ME, Bands RE, Parry S, Hoffman E, Chan T, Hartman KM (1999) Does lesion size affect the outcome in avascular necrosis? Clin Orthop 367:262–271

Stulberg SD, Cordell LD, Harris WH, Ramsey PL, MacEwen GD (1975) Unrecognised childhood hip disease: a major cause of idiopathic osteoarthritis of the hip. In: The hip. Proc of the third meeting of the Hip Society. CV Mosby Co., St Louis, pp 212–228

Sugano N, Noble PC, Kamaric E (1998) A Comparison of alternative methods of measuring femoral anteversion. J Comput Assist Tomogr 22:610–614

Suh KT, Kang JH, Roh HL, Moon KP, Kim HJ (2006) True femoral anteversion during primary total hip arthroplasty: use of postoperative computed tomography-based sections. J Arthroplasty 21:599–605

Sussman WI, Han E, Schuenke MD (2013) Quantitative assessment of the ischiofemoral space and evidence of degenerative changes in the quadratus femoris muscle. Surg Radiol Anat 35:273–281

Sweeney JP, Helms CA, Minagi H, Louie KW (1987) The widened teardrop distance: a plain film indicator of hip joint effusion in adults. Am J Roentgenol 149:117–119

Taneja AK, Bredella MA, Torriani M (2013) Ischiofemoral impingement. Magn Reson Imaging Clin N Am 21:65–73

Tannast M, Siebenrock KA, Anderson SE (2007) Femoroacetabular impingement: radiographic diagnosis—what the radiologist should know. Am J Roentgenol 188:1540–1552

Terjesen T, Benum P, Anda S, Svenningsen S (1982) Increased femoral anteversion and osteoarthritis of the hip. Acta Orthop Scand 53:571–575

Than P, Sillinger T, Kranicz J, Bellyei A (2004) Radiographic parameters of the hip joint from birth to adolescence. Pediatr Radiol 34:237–244

Tönnis D (1976) Normal values of the hip joint for the evaluation of X-rays in children and adults. Clin Orthop 119:39–47

Tonnis D, Heinicke A (1999) Acetabular and femoral anteversion: relationship with osteoarthritis of the hip. J Bone Joint Surg Am 81:1747–1779

Torriani M, Souto SC, Thomas BJ et al (2009) Ischiofemoral impingement syndrome: an entity with hip pain and abnormalities of the quadratus femoris muscle. Am J Roentgenol 193:186–190

Tosun O, Algin O, Yalcin N et al (2012) Ischiofemoral impingement: evaluation with new MRI parameters and assessment of their reliability. Skeletal Radiol 41:575–587

Visser JD, Jonkers A, Hillen B (1982) Hip joint measurements with computerized tomography. J Pediatr Orthop 2:143–146

Werner CML, Copeland CE, Ruckstuhl T, Stromberg J, Turen CH, Bouaicha S (2011) Relationship between Wiberg's lateral centre edge angle. Lequesne's acetabular index, and medial acetabular bone stock. Skeletal Radiol 40:1435–1439

Wiberg G (1939) Studies on dysplastic acetabuli and congenital subluxation of the hip joint : with special reference to the complication of osteoarthritis. Acta Chir Can 58(S):7–38

Wiberg G (1953) Shelf operation in congenital dysplasia of the acetabulum and in subluxation and dislocation of the hip joint. J Bone Joint Surg Am 35:65–80

Wyss TF, Clark JM, Weishaupt D, Notzli HP (2007) Correlation between internal rotation and bony anatomy in the hip. Clin Orthop 460:152–158

Zaretsky MV, Alexander JM, McIntire DD et al (2005) Magnetic resonance imaging pelvimetry and the prediction of labor dystocia. Obstet Gynecol 106:919–926

Knee

13

C. Miller*, K. Johnson*, S. Mohan*, and R. Botchu**

Contents

---

*Paediatric - Miller C, Johnson K, Mohan S
**Adult - Botchu R

C. Miller • K. Johnson • S. Mohan
Birmingham Children's Hospital, Birmingham, UK
e-mail: Claire.Miller@bch.nhs.uk;
karl.johnson@bch.nhs.uk; shyam.mohan@bch.nhs.uk

R. Botchu (✉)
Department of Musculoskeletal Radiology,
The Royal Orthopaedic Hospital, Bristol Road South,
Northfield, Birmingham, UK
e-mail: Rajesh.botchu@nhs.net

13.1   Introduction

The knee is a pivot condylar joint (trocho-ginglymus) formed by the articulation of the distal femur and proximal tibia. The tibiofemoral joint is divided into medial and lateral tibiofemoral joints. It is an essential joint involved in gait. In this chapter paediatric aspects are emphasised first separate from adult considerations. The ossification centres of the distal femur and proximal tibial physis are usually present at birth, but in some cases the latter can appear within the first 2 months. The proximal tibial physis fuses with the tibial shaft at 18 years. An accessory physis forms the tibial tuberosity.

In newborns and children <1 year of age, there is normally a pronounced varus angulation. This usu-ally corrects at 18–24 months of age usually after walking for about 6 months. Then by the age of 2–3, a pronounced normal valgus angulation is seen (10–15°) which diminishes with age ending with a mild valgus (7–8°) by the age of 7 which is the adult knee position (Figs. 13.1 and 13.2). There should not be a varus angulation >2 years of age which occurs in Blount's disease (tibia vara). The femorotibial angle confirms the varus position of the knee. The metaphyseal-diaphyseal angle (MDA) is however more reliable and accurate (Fig. 13.3). It is the angle between the line drawn parallel to the top of the proximal tibial metaphysis and the line drawn perpendicular to the tibial shaft long axis. Six month follow up radiographs are needed to differentiate physiological bowing -9° +- 3.9° from Blount's disease which usually has an MDA angle >11°.
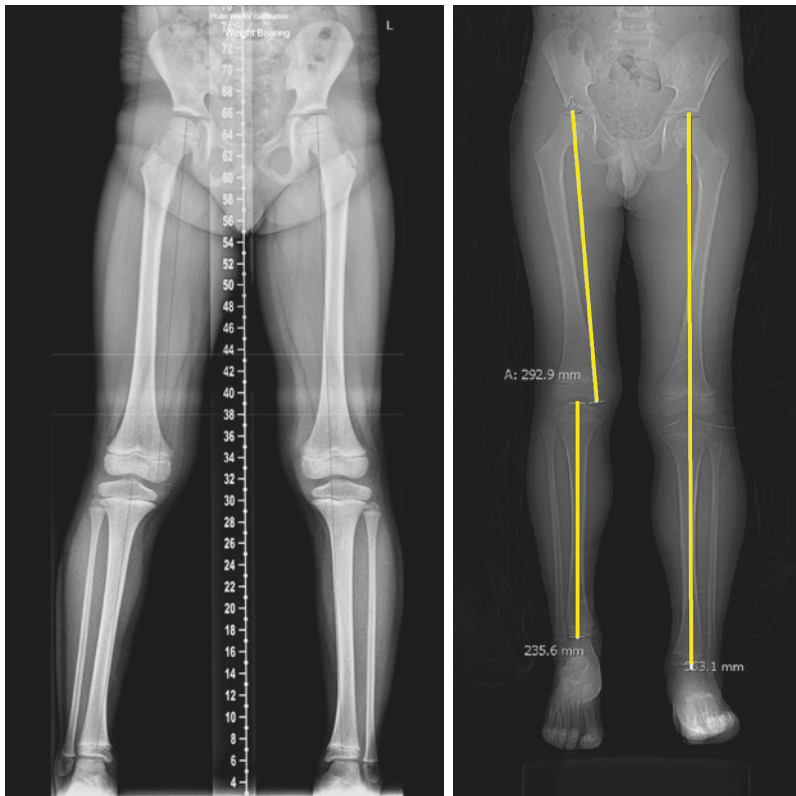
Fig. 13.1 AP CT scanogram of a child with hemihypertrophy and overgrowth of the left lower limb. Individual long bone measurements are demonstrated on the right lower limb and whole lower limb measurements on the left side. Both measurements are performed on both sides and compared to identify the difference in limb lengths and the segment of most significant length discrepancy. The whole limb measurement line is also used for assessing the mechanical axis deviation

Fig. 13.2 Femorotibial
angle. Angle between the
anatomical axis of the
femur and tibia (**a**), and the
angle between the
anatomical and mechanical
axis of femur and tibia (**b**)
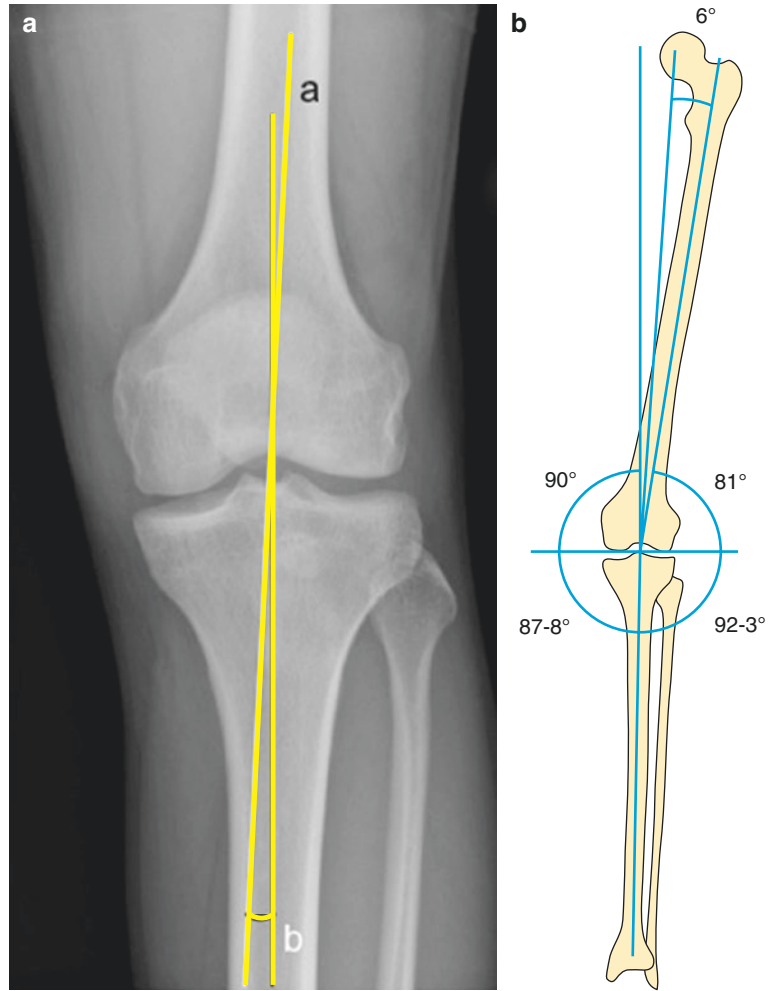
The knee joint has static and dynamic stabilisers. Static stabilisers include the geometry of the tibiofemoral joint, capsule, cruciate ligaments and collateral ligaments. The muscles and tendon are the dynamic stabilisers of the knee joint (Kakarlapudi and Bickerstaff 2000).

After paediatric considerations, we describe the normal radiological measurements of the tibiofemoral joints and the soft tissues of the tibiofemoral joint in an adult. An understanding of the normal tibiofemoral measurements and alignment is essential to identify an abnormality.
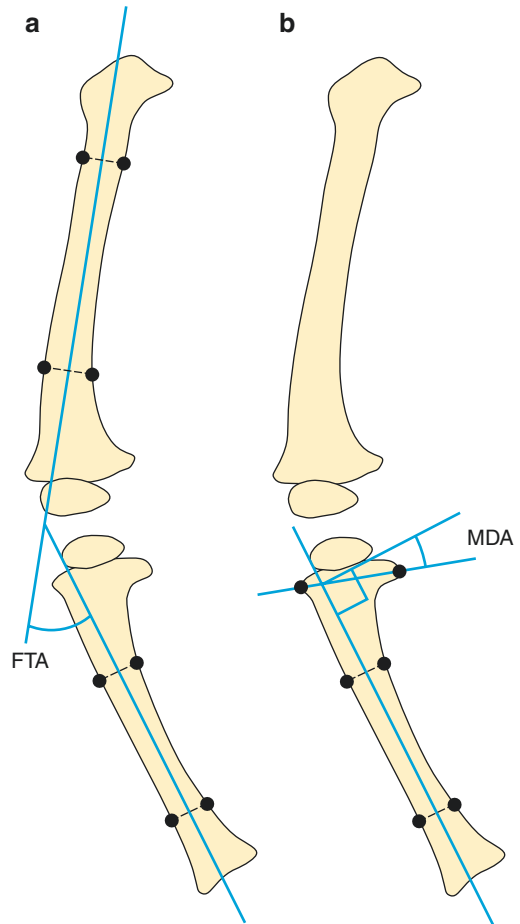
Fig. 13.3 Femorotibial angle (FTA) (**a**). Angle between the anatomical axis of femur and tibia. Metaphyseal-diaphyseal angle (MDA) (**b**). On an AP standing radiograph of the leg centred over the knees. A line is drawn perpendicular to the longitudinal axis of the tibia. Another line is drawn through the two beaks of the metaphysis to determine the transverse axis of the tibial metaphysis. The meta-diaphyseal angle is the angle bisected by these two lines

13.2 Leg Length Measurement

Definition

Limb length discrepancy is defined as a significant difference between lengths of the lower limbs. This can be caused by a number of factors, some of which causes a functional shortening and others a structural shortening.

Indications

Assessment of degree of shortening of lower limbs to consider surgical correction.

Techniques

Radiography and CT.

Full Description of Technique(s)

Limb length discrepancy is commonly assessed by standing radiographs or supine CT scanogram technique. In the former, an AP projection of the whole lower limb is obtained centring the beam at the patella. If there is a marked discrepancy between the limb lengths, a block can be placed under the shorter limb to avoid marked pelvic tilt. The entire length of the lower limb can then be measured from the highest point of the femoral head to the lowest point on the distal tibial articular surface. A difference of more than 1 cm is considered significant. This line can also be used to assess the mechanical axis of the lower limb. In normal children, the mechanical axis should pass through the middle of the knee joint or just medial to the midline. If there is significant deviation from this position, this can imply abnormal loading forces which are significant if surgical correction is being considered. If there is significant limb length discrepancy, then individual bone lengths can be measured to identify the segment where the discrepancy is most marked. The femur is measured from the top of the femoral head to the distal most point on the medial femoral condyle. The tibia is measured from the highest point on the proximal articular surface to the distal tibial articular surface.

CT scanogram technique requires the patient to lie supine on the gantry table with feet parallel. An AP scout view is obtained. A lateral scout can be used if there is significant angulation or bowing of the limb in the sagittal plane. Measurements are similar to those described with the AP radiographic method.

Reproducibility/Variation

Huurman et al. demonstrated with in vitro specimens that the accuracy and interobserver variability of measuring limb lengths with both techniques were very similar with less than 3 mm difference in lengths from the actual specimen compared to both techniques. However, if the limbs were angled in the vertical plane, there was a significantly lower accuracy with the radiographic technique. Hence the CT scanogram may be a preferable technique if there is significant flexion or extension deformity. In addition, Porat et al. showed that there can be a significant ionising radiation dose reduction with the CT scanogram technique compared to standing radiographs.

Clinical Relevance/Implications

Limb length discrepancy can cause significant abnormalities of posture and gait. Assessment of limb length discrepancy can be done with clinical measurements, but they have been shown to have poor reliability and reproducibility. Radiographic or CT scanogram techniques are now standard in the assessment of limb length discrepancy (Fig. 13.1).

13.3   Metaphyseal-Diaphyseal Angle

Definition

This represents the angle between the proximal tibial metaphysis and the tibial shaft.

Indications

This measurement is used in the assessment of genu varum. An angle greater than 11° is indicative of, but not diagnostic of tibia vara (Blount's disease).

Technique

Radiography.

Full Description of Technique

AP standing radiographs are performed of the leg with centering over the knees. A line is drawn through the transverse plane of the proximal tibial metaphysis (between the distal most ossified peaks of the medial and lateral beaks of the tibial metaphysis). A second line is drawn perpendicular to the long axis of the tibia. The angle created between these two lines is the metaphyseal-diaphyseal angle (Fig. 13.3).

Reproducibility/Variation

107 patients were analysed in the study. Patients with congenital or traumatic causes of bowing were excluded. A total of 48 patients were followed up over a 36-month period. No changes were found between the use of supine or standing radiographs. Patients were classified as having physiological bowing if after 18 months there was >10° of varus bowing. Tibia vara was diagnosed on the basis of lucency, sclerosis or fragmentation of the medial proximal tibial metaphysis.

Clinical Relevance/Implications

An angle of more than 11° was associated with later development of tibia vara on radiographs. The average angle for those with physiological bowing was 5.1°, whereas this figure was 16.4° for those with tibia vara. The determination of this angle can therefore be helpful in early diagnosis of bow leg deformity and stratify the need for surgical intervention (Fig. 13.3).

13.4 Tibial Torsion

Definition

It was first described by Le Damany in 1903 as twisting of the tibia about its longitudinal axis resulting in a change of alignment of the planes of motion of the proximal (knee) and distal (ankle) articulations. There are normal stages of torsion described during development. In utero there is medial torsion secondary to restricted movement, which becomes neutral after birth due to derotation. Over the next few years as walking develops, there is gradual external torsion.

Normal measurements for tibial torsion for the different modalities range from a mean of 40.5° in children to 41.7° in adults. A positive angle denotes external rotation and a negative value denotes internal rotation.

Indications

To select patients for derotation osteotomy

Technique

CT and MRI

The same imaging planes and techniques can be used for both modalities.

The patient lies supine with the legs extended along the *z*-axis of the scanner. Imaging is taken in the axial, unangled plane. Slices are acquired just below the knee and above the ankle. Two lines of reference are drawn: one proximal and one distal. The method described by Jend et al. is used (Schneider and Laubenberger 1997). The proximal line is drawn at a slice just above the fibula head at a tangent dorsal to the tibial ridges. The distal line is taken at a slice just above the ankle. A circle is drawn to include the fibular notch but exclude the medial malleolus. The centre of the fibular notch is determined, and a line through this point and the centre of the circle is drawn. The tibial torsion angle is the angle between these two lines.

Clinical Relevance

It has been shown that there is an increased prevalence of knee osteoarthritis and arthropathies associated with abnormal torsion. Measuring torsion is also important in surgical planning in such cases as chondromalacia patellae and equinovarus (Schneider and Laubenberger 1997).

Reproducibility/Variation

Studies have shown statistically significant relationship between anatomical and ultrasound measurements (on dry bone). The planes used for measurements in US and CT/MRI differ, and therefore the range of normal values varies between these modalities (Schneider and Laubenberger 1997; Joseph et al. 1987; Krishna et al. 1991; Jend and Heller 1981). For this reason ultrasound has gone out of favour as an imaging modality.

MRI measurements have been shown to be analogous to CT measurements but are influenced by the imaging plane chosen. The CT method will generally produce smaller angles to the bicondylar plane than the angle of the poste-

rior tibial surface. Further detailed coverage is found in Chap. 17.

The tibial torsion will vary with growth. In the article by Kristiansen et al 2001 at 4 years of age it averages 28° (range 20-37°), increasing by one degree per year up to the age of 10 when the torsion will normally be around 34°. After 10 years of age to skeletal maturity the range would be expected to be 34-38°. However other earlier articles Staheli et al 1972 and Ritter et al 1976 have shown lesser normal values with growth as follows:

Birth - 1 year 4-7°; 2-8 years 9-11°; and 9-13 years 12-14° (Staheli et al).

Birth 4° +/- 5; 6 months 6° +/- 2; 1 year 10° +/- 2; 2 years 11° +/- 3.

Analysis/Validation of Reference Data

The CT method will generally produce smaller angles to the bicondylar plane than the angle of the posterior tibial surface.

Conclusion

The use of non-ionising forms of radiation rather than CT is favoured in the paediatric population and MRI has been shown to be a suitable method.

13.5   Tibiofemoral Angle

Definition

The angle subtended between the longitudinal axis of the femur and tibia (Fig. 13.3).

Indications

To assess genu valgum and genu varum.

Technique

AP standing radiography.

Full Description of Technique

AP standing radiographs are performed of the leg with centring over the knees. A line is drawn along the longitudinal axis of the femur and tibia midway between the femoral and tibial diaphysis respectively. The angle between these two lines at the knee joint forms the tibiofemoral angle.

Reproducibility/Variation

A study from Finland performed 1480 examinations of the tibiofemoral angle both clinically and radiologically. The clinical findings correlated directly with those of the radiographic analysis. Determining the longitudinal axis of the femur in infants however can be difficult and best estimates can be made. This does not present a problem in older children.

Clinical Relevance/Implications

The terms genu valgum and varum describe the relationship of the tibia with respect to the femur. Genu valgum indicates abduction of the tibia at the knee joint and varum, adduction. From birth and through childhood, alignment progresses from a position of varum to valgum and returns to neutral in adolescence. At 3 years of age when the child is walking, the average angle of valgus is 11° which reduces to 6° by age of 13. In adults a mild varus is normally seen (Salenius and Vannkka 1975).

Conclusion

Knowledge of the normal developmental variations in the tibiofemoral angle avoids unnecessary treatment and helps to identify those who require further management.

13.6   Anatomical Landmarks

The medial and lateral femoral condyles articulate with the medial and lateral tibial condyles, respectively, to form the medial and lateral tibiofemoral joint. These can be evaluated on radiographs (AP, lateral, notch view), MRI and CT. The measurement of the medial and lateral femoral condyles is variable depending on the ethnicity and gender; however, there is no statistically significant difference between right and left in the same individual. The bicondylar width of distal femur is larger in males (8.8 cm, approx.) than females (7.8 cm, approx.). The depth of the medial femoral condyle is 6.1 cm and that of the lateral femoral condyle is 5.8 cm. These are slightly shallower in females than males, measuring 5.5 and 6.1 cm. The mean intercondylar width is 2.2 cm in males and 1.8 cm in females. The depth of the notch is 2.6 cm (approx.) (Terzidis et al. 2012). Patellofemoral landmarks are not included in the assessment of knee as they are fully dealt with in Chap. 14.

13.7 The Alignment: Mechanical and Anatomical Axis

The alignment can be assessed on a frontal knee radiograph or full-length frontal radiograph view of the lower limb. It has been shown that the measurements from these two radiographs are comparable. The radiograph is obtained in a weight-bearing position with the feet in mild external rotation. The angle between the feet is approximately 15°. The cassette is in intimate contact with the posterior aspect of the extended knee with the radiograph source centred an inch inferior to the lower pole of patella. The mechanical femoral axis is measured by marking a centre point between the tibial spines and measuring the angle between the centre point to the femoral head and centre point to the midpoint between the medial and lateral cortices of the distal tibia at the level of ankle joint (tibial plafond) (Figs. 13.1, 13.2 and 13.3).

The femoral anatomical axis can be assessed by several methods: Moreland, Paley and Coventry's method. Moreland's method involves bisecting the proximal and distal shaft of the femur extending to join the midpoint of the distal femur 10 cm proximal to the knee joint. Paley's method involves extending the line formed by joining the midpoints of the proximal and distal diaphysis of the femora (Paley 2002). This is further expanded in Chap. 17.

The tibial anatomical axis is formed by joining the midpoint of the tibial plateau and the midpoint of the diaphysis 20 cm distally. This can also be formed by joining the midpoints of the proximal and distal diaphysis. These axes are formed on an AP radiograph. Tibial angle (beta) is formed between the tibial anatomical axis and the tangential line to the tibial articular surface.

The tibial and anatomical axis can also be measured on the lateral radiographs. Lateral tibial axis can be formed by several methods. These include anterior proximal tibial cortex, posterior tibial cortex and proximal tibial anatomical axis. These are measured 5–15 cm distal to the knee. This can also be formed by joining the midpoints of the shaft of the tibia 10 cm distal to the knee and 10 cm proximal to the ankle joint.

The femoral anatomical axis on the lateral radiograph is formed by joining the midpoint of the shaft 5 and 10 cm proximal to the knee joint.

The normal tibiofemoral angle is 180° with a variation of approximately 5°. Genu varum has a tibiofemoral angle of less than 180°, and if the angle is more than 180°, it is genu valgum (Paley 2002; Colebatch et al. 2009). The mechanical axis (load bearing axis) is formed by joining the centre of the femoral head to the midpoint of the tibial plafond. The condylar plateau angle is the angle between the articular surface of the distal femur and the articular surface of the proximal tibia. The angle is formed medially in genu valgum and laterally in genu varum. The condylar hip angle is between the tangential line to the distal femoral condyles and the mechanical axis of the femur. Plateau ankle angle is between the tibial mechanical axis and the tangent to the articular surface of the tibia (Fig. 13.3). The femoral shaft axis is formed by drawing a line through the centre of the femoral shaft. The midpoint of the femoral condyle notch forms the point for assessment of the femoral axis and midpoint of the tibial spine is used for the tibial axis (Cooke et al. 2007). The angle between the mechanical axis of the femur and tangential line to the distal aspect of medial and lateral femoral condyle is 81°, and the angle between the tangent of the distal femur and the mechanical axis is 90°.

There should not be more than 5 mm of tibial condyle lateral to line drawn vertically from the lateral edge of the lateral femoral condyle (Fig. 13.4). If there is more than 5 mm of tibial condyle lateral to the vertical line along the lateral edge of the lateral femoral condyle, one should suspect a tibial plateau fracture that results in lateral bowing/displacement of the lateral cortex of the lateral femoral condyle.

The normal tibial joint angle is 3° of varus and normal femoral joint angle is 3° of valgus. The angle between the femoral anatomical axis and mechanical axis of femur is approximately 6°. The normal values of the other angles are listed below (Fig. 13.2).

Medial proximal tibial angle—angle between the tibial anatomical axis and tangent to the articular surface of tibia—is 88°. Lateral distal femoral

Fig. 13.4 Tibial offset. The distance between the vertical line along the lateral edge of the lateral femoral condyle (a) and lateral tibial condyle (b)

Fig. 13.5 Whiteside line (WL) is drawn joining the deepest part of the trochlea to the centre of intercondylar notch. EP is the epicondylar line. PC—line drawn along the posterior point of lateral and medial femoral condyles. WEP—Whiteside-epicondylar angle. WPC—Whiteside posterior condylar angle. PCA—Posterior condylar angle between the condylar line and epicondylar axis

angle—angle between the femoral mechanical axis and tangent to distal condyle of the femur—is 88°.

Whiteside-condylar angle is the angle between the Whiteside line and a line drawn tangential to the posterior edge of medial and lateral femoral condyles. The average measurement is 95°.

Whiteside line is formed by joining the deepest part of the trochlea to the centre of the posterior intercondylar notch. Transepicondylar line is formed by joining the most prominent points of the lateral and medial femoral condyles. The angle between this and Whiteside line is Whiteside-epicondylar angle. The mean angle is 90° (Fig. 13.5).

Clinically this is essential to preserve during a total knee replacement. There is a significant difference between the left and right side of Whiteside-epicondylar and Whiteside-condylar angles. There is also slight variation based on ethnicity. These measurements have been shown to be reproducible by several studies including Paley (2002).

13.8   Joint Space Width Measurement

Definition/Technique

This is measured on weight-bearing radiographs on AP and lateral views. This is the distance between the tangential lines to the articular surface of the distal femoral condyle and proximal tibia (Ravaud et al. 1996). A detailed method of assessing this is described. A tangential line is drawn along the articular surfaces of the medial and lateral femoral condyles. Further lines are drawn tangential to the deepest part of the articular surface of medial and lateral tibial articular surfaces. The deepest point of the intercondylar notch is identified. Lines are drawn perpendicular to the tibial and femoral tangential lines from the deepest point of the intercondylar notch. The distance between the femoral and tibial lines at this level is measured, and this is shown to be a reliable method in measuring joint space width (Bing-chen et al. 2011). The joint space width on radiographs has been shown to have good correlation with sum of the articular cartilage of the femoral condyle and tibial condyles (Buckland-Wright et al. 1995).

Clinical Relevance

This is helpful in evaluation of the degree of degenerative change and also in planning for total knee replacement. Average joint space width of the knee is 4.6 mm (Bing-chen et al. 2011). The average medial joint space width is **4 mm** and that for the lateral joint is **6 mm**. There is an average joint space loss of 0.13 mm per year. Measurement of the joint space width is a reliable and cost-effective method of assessing the grade of degenerative change. Rytter classified the degeneration into grade 0 (normal), grade 1 (25% decreased), grade 2 (50% decrease) and grade 3 (severe narrowing) (Rytter et al. 2009).

Reproducibility

This is affected by position of the knee, rotation of the foot, weight bearing, non-weight bearing and X-ray source inclination. Weight-bearing radiographs are more accurate in assessing the joint space width in contrast to non-weight-bearing radiographs. Rosberg and colleagues had suggested performing weight-bearing anteroposterior radiographs of the knee in 45° of flexion to accurately measure the joint space width in comparison to extension anteroposterior radiographs. Kotani and coworkers had shown better assessment of joint width with 20° of flexion (Kotani et al. 2005). Bing-chen et al. had shown a reliable method of measuring joint space width with 35° of flexion (Bing-chen et al. 2011). Buckland and colleagues had shown that the joint space width in the centre of the joint on weight-bearing radiograph is smaller than the sum of the articular cartilages (Buckland-Wright et al. 1995). Evaluation of joint space width of medial tibiofemoral joint on radiographs is more reliable than the lateral tibiofemoral joint space.

This can also be measured on coronal and sagittal MR images. This can also be measured on ultrasound. The joint space width can be assessed on weight-bearing radiographs, which has been shown to be reproducible. This can also be assessed on fluoroscopy with comparable results. This is measured as the distance between the bony margin of the femoral condyle and corresponding tibial condyle. This is measured at the midpoint of the distance between the tibial spine and edge of the tibial condyle (Fig. 13.6).
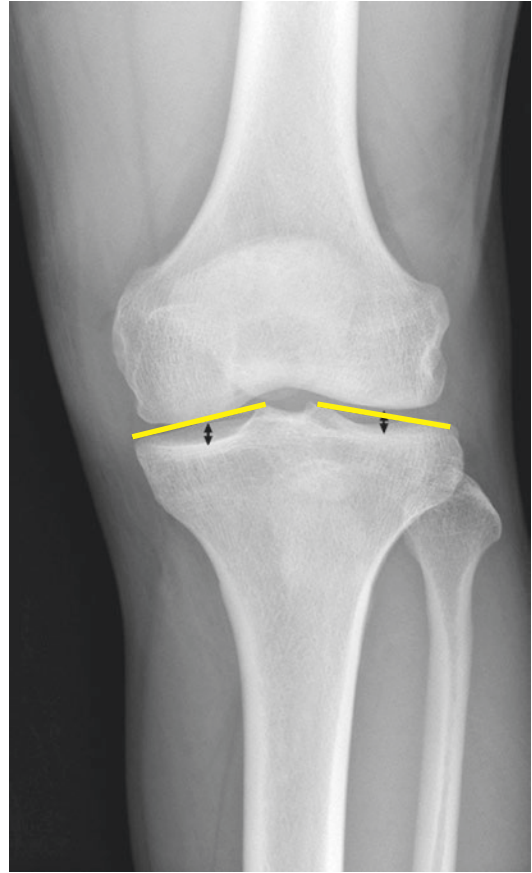
Fig. 13.6 Joint width. Measured at centre point between the tibial spine and edge of the tibial condyles

13.9   Articular Cartilage

The normal cartilage thickness is **2.2 mm**. The mean cartilage thickness of the medial femoral condyle is 2.1–2.4 mm, and for the lateral femoral condylar articular cartilage, it is 1.9–2.3 mm (Ravaud et al. 1996; Beattie et al. 2008; Anas et al. 2013). The cartilage thickness on the right is slightly thicker than the left (2.1–2.4 mm vs. 1.9–2.1 mm for lateral femoral condyle, 1.9−2.3 mm vs. 2.1 mm for medial femoral condyle) (Kilic et al. 2014). The average medial joint space width is 4 mm and that for the lateral joint is 6 mm. The average cartilage thickness of the femoral condyles ranges from 1.6 to 2.6 mm. The articular cartilage of the proximal tibia is thinner (1.5–2.5 mm) in the area, which is covered by meniscus that on the area which not covered by meniscus (2–2.9 mm). These values have been based on cadaveric studies with similar results on ultrasound and MRI.

Technique

This is measured on coronal and sagittal MR images as well as on high-resolution ultrasound.

Clinical Relevance

The articular cartilage can be reliably measured with good intra-class correlation with high-resolution ultrasound as demonstrated on a cadaveric study (Naredo et al. 2009). Cartilage is thicker in boys than girls and decreases with age (Spannow 2010). Measurement of articular cartilage thickness enables one to assess the degree of degeneration and aids in management of the patient especially in surgical planning.

Reproducibility

The measurement of articular cartilage is reliably measured on ultrasound and MRI (Kilic et al. 2014; Naredo et al. 2009; Spannow 2010). Measurement on MRI is most accurate with an error of approximately 10% in comparison to direct measurement (Shepherd and Seedhom 1999).

13.10   Intercondylar Notch

The intercondylar notch is narrow distally and widens proximally being widest in its midportion. It measures 1.8 cm and is wider in its midportion measuring 2.3 cm (Koukoubis et al. 1997). Morphoanatomy of the notch is dependent of age, sex, height and weight (Botchu et al. 2013).

Technique

Notch index can be measured on MRI and radiographs (Fig. 13.7). The measurement on MRI is superior to radiographs. Intercondylar notch ratio is the ratio between the width of the notch and intercondylar width. Normal ratio is less than **0.27** (Botchu et al. 2013; Herzog et al. 1994; Al-Saeed et al. 2013).

Clinical Relevance

Women have a smaller notch (18 mm) than men (21 mm) (Koukoubis et al. 1997; Stijak et al. 2009; Murshed et al. 2005). A narrow notch is defined as ratio less than 0.26 (Al-Saeed et al. 2013). Narrow notch is associated with a smaller ACL (Dienst et al. 2007). Narrow notch, i.e. notch index of less than 0.2, has been shown to be associated with ACL rupture. Patients with a narrow intercondylar notch have increased incidence
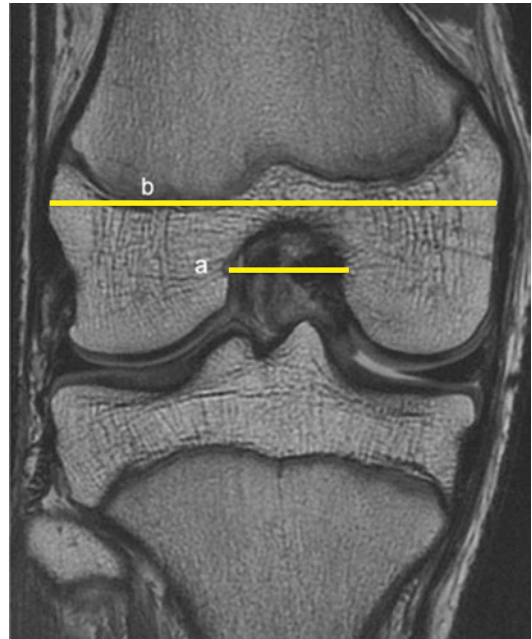
Fig. 13.7 Notch index. Ratio between the width of the notch (a) to the intercondylar width of distal femur (b)

of cyclops lesions in patients with post-ACL reconstruction (Fujii et al. 2014).

Reproducibility

Evaluation of notch index on radiographs depends on the technique and projection of the radiograph. Intercondylar notch and notch index can be reliably measured on MRI (Botchu et al. 2013).

13.11   Lateral Femoral Sulcus

Definition

The lateral femoral sulcus is a normal anatomical coronal oblique smooth groove on the femoral articular surface lateral to the most anterior aspect of the intercondylar notch (Cobby and Schweitzer 1992; Sanders and Folio 2007).

Technique

Measurements are taken from a lateral knee radiograph. A line is drawn at a tangent to the junction of the sulcal depression with the lateral femoral condyle. The depth is taken as the perpendicular line between the base of the sulcus and this tangent (Fig. 13.8).

Clinical Relevance

A depth of **1.5 mm** represents measurement of three standard deviations above the mean, and a sulcus depth greater than this is usually associated with ligamentous injuries especially rupture of the ACL. This is usually smooth; however, an irregular sulcus with depth of greater than 2 mm is defined as a deep lateral femoral sulcus. The deep femoral sulcus corresponds to impaction of the lateral femoral condyle against the posterolateral aspect of the proximal tibia (Cobby and Schweitzer 1992; Sanders and Folio 2007).

Reproducibility

This might be a challenge to identify on a lateral radiograph. On MR sagittal images, this can be quite easy to identify. In the group of patients with confirmed normal ACL ($n = 62$), the mean depth of the sulcus was 0.45 mm. In those with confirmed ACL tears, the mean depth was 0.89 mm ($n = 41$) (Cobby and Schweitzer 1992). Where the sulcus is shallow, this method of measurement can be inaccurate as the depth itself is obscured by the lines drawn.

Fig. 13.8 Lateral femoral sulcus is measured by drawing a tangential line along the articular surface of the lateral femoral condyle and measuring the perpendicular distance to the deepest point of the sulcus

13.12 Posterior Tibial Slope

This is normal anatomical posterior inclination of the proximal tibia. This is variable depending on the ethnicity.

Technique

It can be measured on sagittal MR images or on lateral radiographs and ranges from 0 to 18°. It is measured between the proximal tibial anatomical axis and articular surface of the proximal tibia. It can also be measured reliably between the tibial shaft anatomical axis or posterior tibial cortex and articular surface of the proximal tibia. The normal posterior tibial slope is **5–6**° (Haddad et al. 2012) (Fig. 13.9).

Clinical Relevance

The tibial slope is similar between the medial and lateral tibial slopes. The posterior tibial slope is higher in females (6°) to males (5°). It is an essential component in planning of total knee replacement (Haddad et al. 2012) (Fig. 13.10).

Reproducibility

It can be more accurately measured on MR than radiographs, but there is relatively good correlation in the measurements using both modalities. Kindly refer to Chap. 17 for further detailed analysis.
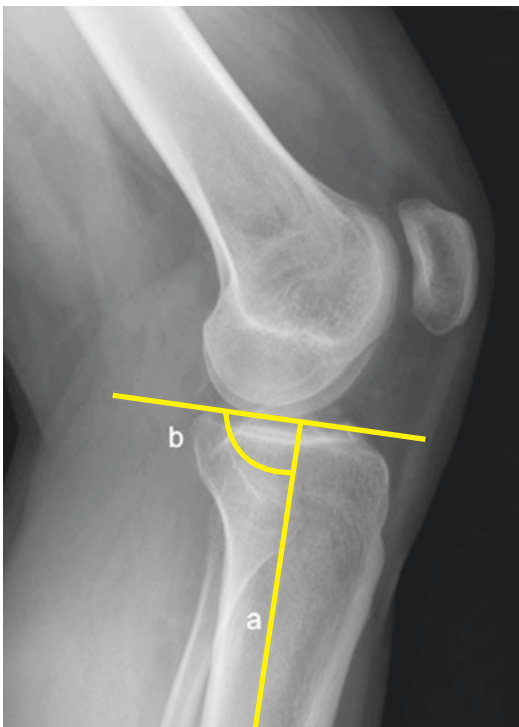
Fig. 13.9 Posterior tibial slope. Angle between the tibial anatomical axis (a) and horizontal line along the tibial plateau (b)
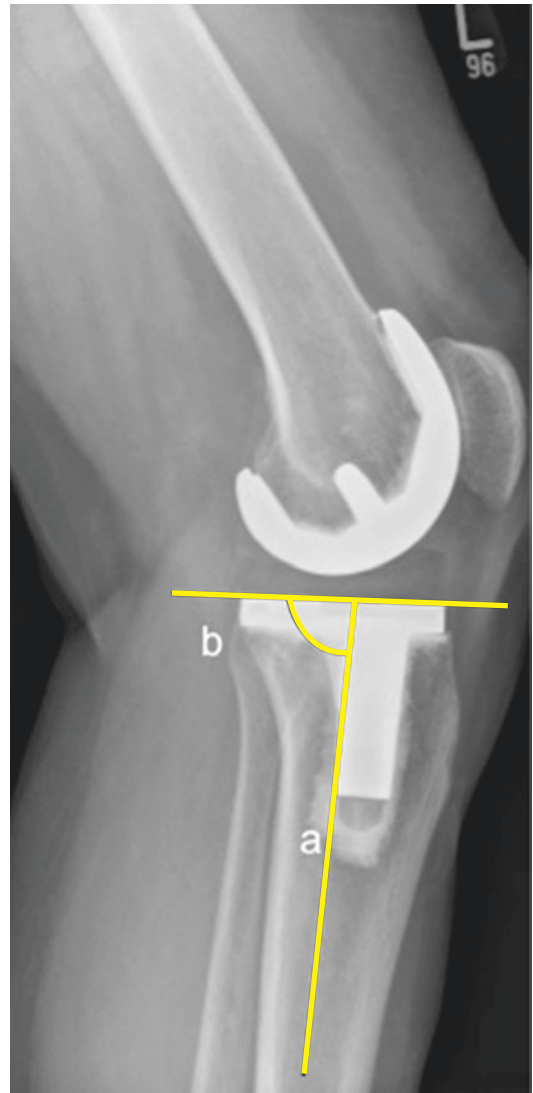
Fig. 13.10 Posterior tibial slope. Angle between the tibial anatomical axis (a) and horizontal line along the tibial component (b)

13.13 Posterior Condylar Offset Ratio (PCOR)

Definition

The posterior condylar offset (PCO) is defined by Bellemans et al. (2002) as the maximal thickness of the posterior condyle projecting posteriorly to the tangent of the posterior cortex of the distal femoral shaft on a true lateral radiograph. The mean PCO is **29.01 mm** (SD 2.04 mm) for males and **27.19 mm** (SD 2.15 mm) for females. This concept was introduced as a variable which could have an important role in function and range of knee flexion following total knee arthroplasty with PCL retention. To avoid variation due to magnification, the concept of a ratio was used in Bellemans et al.'s measurements, by using the diameter of the femoral diaphysis 10 cm proximal to the femoral articular surface. It is the ratio between the diameter of the femoral diaphysis and the distance between the posterior cortex of the femur and posterior condyle of the distal femur.

A new posterior condylar offset ratio was recently proposed by Johal et al. (2012) defined as the 'maximal thickness of the posterior condyle projecting posteriorly to a straight line drawn as the extension of the posterior femoral shaft cortex, divided by the maximal thickness of the posterior condyle projecting posterior to a straight line drawn as the extension of the anterior femoral shaft cortex on a true lateral radiograph of the distal quarter of the femur'. Normal PCOR is **0.44**, which is reproducible. PCOR is 0.47 in TKR (Johal et al. 2012).

The ratio measurements preoperatively do not take into account the articular cartilage thickness of the distal femur which is 2–3 mm thick which makes it difficult to compare with ratio measurements postoperatively. This is why the PCOR on preoperative radiographs is 0.44 and on postoperative radiographs it is 0.47. If the preoperative ratio measurements are adjusted to include the cartilage thickness, the ratio would approximate 0.47.

Bellemans et al. showed that for every millimetre lost in PCO following total knee arthro-plasty compared with preoperative values, 6.1° of knee flexion was lost. A reduction of 3 mm or more of PCO had around 30° less flexion postoperatively.

Technique

This can be reliably measured on true lateral radiographs or sagittal MR images using either Bellemans et al. or Johal et al.'s method. The transverse diameter of the femoral diaphysis and the maximum diameter of the distal femur at the level of femoral condyle are measured. PCO is the ratio between these two diameters (Figs. 13.11 and 13.12).
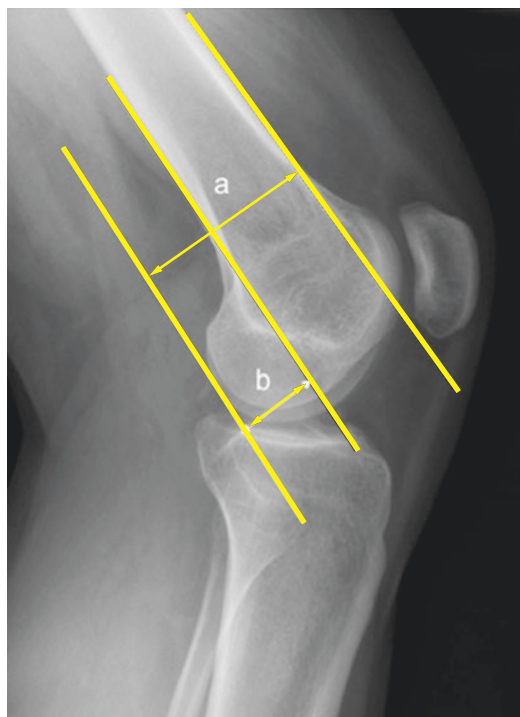
Fig. 13.11 Posterior femoral condylar offset. Ratio between the distance between the vertical line along the posterior aspect of the femoral cortex and vertical line along the posterior femoral condyle (b) to the distance between the anterior femoral cortex and posterior condylar line (a)
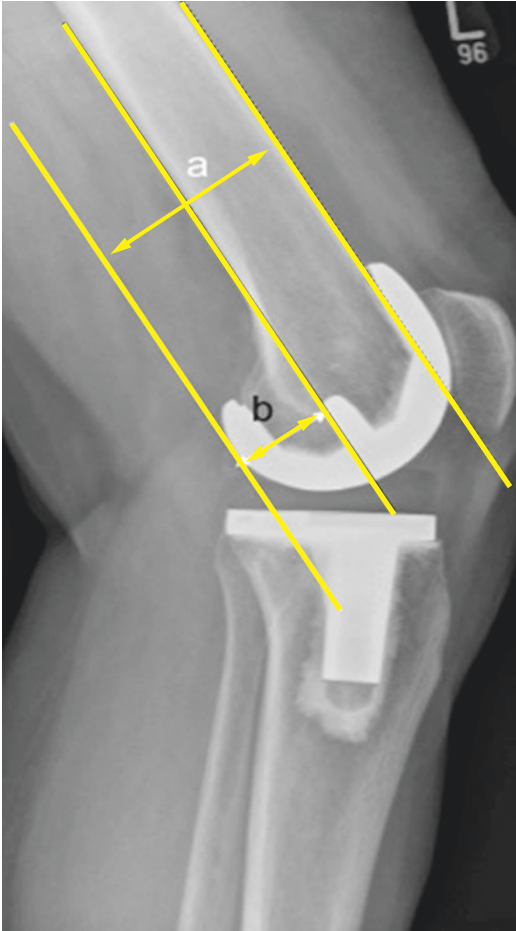
Fig. 13.12 Posterior femoral condylar offset. Ratio between the distance between the vertical line along the posterior aspect of the femoral cortex and vertical line along the posterior femoral component (b) to the distance between the anterior femoral cortex and posterior condylar line (a)

Clinical Relevance

Restoration of posterior condylar offset is important in TKR providing a good range of movement and flexion stability. This is useful objective criteria for assessment of TKR. It's important to restore this especially in PCL retaining TKR. There is 12° decrease in flexion for every 2 mm decrease in posterior condylar offset (Johal et al. 2012).

Reproducibility

Clement and colleagues had shown good intra- and interobserver reliability in measurement of PCO on radiographs with kappa ranging from 0.84 to 0.94 (Clement et al. 2014).

13.14 Tibial Translation

Definition

This is defined as anterior translation of tibia with respect to femur in patients with ACL rupture and is analogous to anterior drawer sign.

Technique

This can be measured on lateral radiographs or sagittal MR sequences. On sagittal MRI images, this is assessed at the level of mid-lateral femoral condyle. Vertical lines are drawn along the posterior aspect of femoral condyle and posterior proximal tibia. The normal distance between the two lines is less than **5 mm** (Fig. 13.13). The line drawn along the posterior edge of posterior aspect of proximal tibia on sagittal MR images does not intersect the posterior horn of lateral meniscus (Beldame et al. 2011) (Fig. 13.14).

Clinical Relevance

In patients with ACL rupture, there is anterior translation of the tibia in relation to femur of more than 7 mm, and the vertical line along the posterior edge of the proximal tibia on the sagittal MRI intersects the posterior horn of lateral meniscus.

Reproducibility

This can be reliably measured on radiographs or sagittal MR image. Beldame et al. had reported an intra-class correlation of 0.96 with an error of 0.19 mm (Beldame et al. 2011).
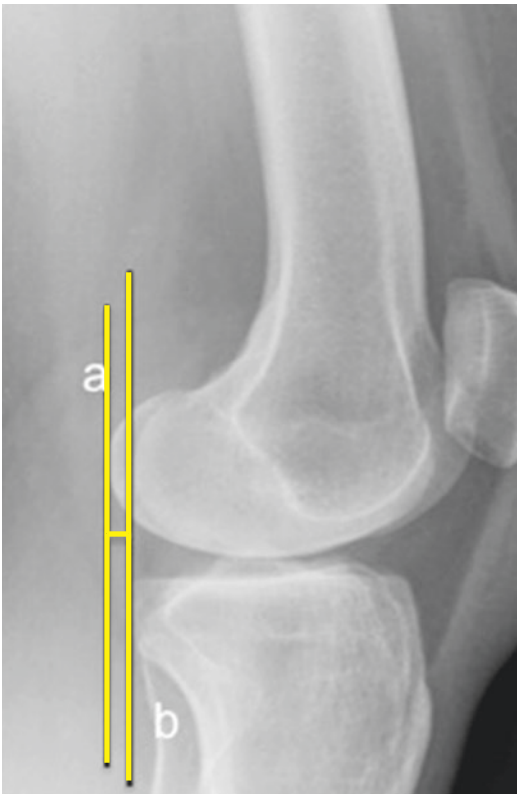
Fig. 13.13 Tibial translation. Distance between the vertical line drawn along the posterior aspect of the proximal tibia (a) and posterior aspect of the distal femur (b)
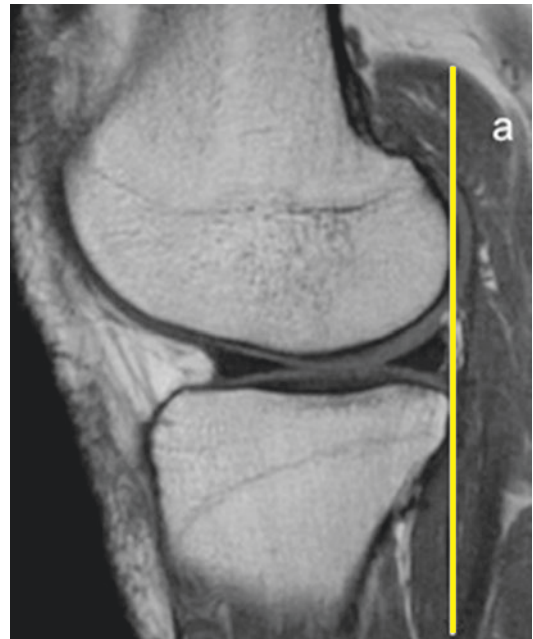
Fig. 13.14 Lateral meniscal coverage. Vertical line drawn along the posterior edge of the proximal tibia does not intersect the posterior horn of lateral meniscus

13.15   Menisci

There are two C-shaped menisci (medial menis-cus and lateral meniscus) in the medial and lateral tibiofemoral joint, respectively, which deepen the articular surface and act as a static stabiliser. The width and thickness of the menisci are measured on coronal and sagittal MR sequences (Fig. 13.15). The posterior horn of medial meniscus is thickest (6.9 mm) with the mid-body measuring 5.2 mm and the anterior horn 6.3 mm. The body and posterior horns of the lateral meniscus are thicker measuring 6.4 and 7 mm, whereas the anterior horn measures 4.8 mm. The lateral meniscus is wider in anterior (10 mm) and posterior (13 mm) parts than the body (7 mm). The width of medial meniscus is 10, 7.8 and 13 mm in anterior, body and posterior horn (Dhananjaya 2014).

The height and width of medial meniscus is 5.3 and 7.7 mm at the anterior horn, 5 and 7.3 mm in the body and 5.5 and 11.7 mm in the posterior horn. The width and height of lateral meniscus is 8.8 and 4.3 mm in the anterior horn, 8.3 and 4.9 mm in the body and 9.7 and 5.3 mm in the posterior horn (Erbagci et al. 2004). The medial
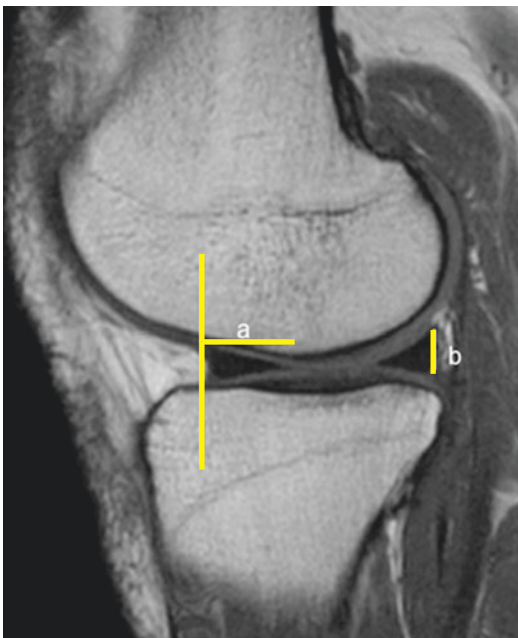
Fig. 13.15 Sagittal MR showing measurement of the width (a) and height (b) of the meniscus

meniscus covers 50% of the tibial plateau, and the lateral meniscus covers 70% of the lateral tibial plateau.

Technique

This is measured on MR images. A ratio of the width and thickness of the medial and lateral meniscus can be measured. A ratio of 0.32 of the lateral meniscus helps one to diagnose complete and incomplete discoid meniscus and ratio of 0.40 for medial meniscus (Choi et al. 2013). The volume of the meniscus can be assessed by MRI (Araki et al. 1994).

Clinical Relevance

The thickness and width of the menisci are vari-able and is influenced by ethnic origin (Dhananjaya 2014). The thicker portion of menis-cus is prone to injuries, which is attributed to the relative increased exposure to forces by the fem-oral and tibial condyles.

The morphology and measurement of the meniscus enables one to predict the areas that are more prone to tears. Assessing the volume of the meniscus on MRI helps one to assess for menis-cal tears and degeneration (Araki et al. 1994). This has also shown to assist in planning of arthroscopic surgeries.

If the lateral meniscal tissue is 15 mm wide, i.e. seen on three consecutive 5 mm slices, it is considered to be discoid. In discoid meniscus, one can see meniscal tissue within the intercon-dylar notch. Discoid meniscus is further classi-fied into complete, incomplete and Wrisberg type. A ring type of discoid meniscus has also been described which has a normal posterior tibial attachment (Monllau et al. 1998). One needs to identify this, and this is associated with an increased incidence of meniscal tears (Fox 2007). Discoid meniscus is associated with other anomalies, which include hypoplasia of lateral femoral condyle, fibular anomalies, muscular anomalies and abnormal shape of lateral malleolus.

Reproducibility

The meniscal morphology and measurements are comparable on MRI in comparison to cadaveric studies. Measurements on MRI have been shown to be reliable (Prodromos et al. 2007). The meniscal measurements are similar on both sides, and this has been utilised in meniscal transplantation (Prodromos et al. 2007). The interobserver variability in the measurement of meniscal size on MRI has been shown to be within acceptable limits (Siorpaes et al. 2012). Discoid meniscus can be identified on MRI and high-resolution ultrasound. On ultrasound, there is absence of triangular configuration of meniscus, and meniscus is thickened in discoid meniscus. Meniscal size is dependent on the BMI, height and sex. Women have a smaller meniscus than men; larger menisci are seen in people with high BMI (Stone et al. 2007).

13.16   Meniscal Extrusion

Definition

The edge of the meniscus is normally along the edge of tibial condyle. If the meniscus extends beyond the edge of the tibial condyle, it is considered to be extruded. A medial meniscal displacement of more than 3 mm is defined as major meniscal extrusion, and displacement of less than 3 mm is minor meniscal extrusion (Costa et al. 2004; Rennie and Finlay 2006). A displacement of the lateral meniscus of 1 mm beyond the lateral edge of the tibial condyle is considered a meniscal extrusion (Fox 2007).

Technique

This is measured on coronal images and is the distance between vertical lines along the edge of tibial condyle and the edge of the meniscus.

Clinical Relevance

Costa et al. had shown significant association of major meniscal extrusion with meniscal degeneration, complex tears as well as tears of the root of the meniscus (Costa et al. 2004). The degree and extent of tears is significantly associated with type of meniscal extrusion, i.e. major or minor meniscal extrusion. This can also be associated with ACL tear (Rennie and Finlay 2006).

Reproducibility

This has been shown to be reproducible with low interobserver variation in a study by Siorpaes et al. (2012). The variation can be reduced further by measuring meniscus extrusion on the central five coronal slices across the tibial surface.

13.17   Medial Collateral Ligament

MCL is a static stabiliser and consists of a superficial and deep component extending from the medial femoral condyle to medial tibial condyle (Phisitkul et al. 2006). The average distance of the superficial MCL from its femoral origin to joint line is 3.2 cm and from the joint line to the tibial attachment is 6.2 cm with the total length being 10 cm. It is thicker in the central portion (17 mm) and of equal size in its proximal and distal parts measuring 10 mm. The deep portion of MCL has two components, meniscofemoral and meniscotibial ligament. The meniscofemoral ligament measures 20 mm and the meniscotibial 7 mm. MCL is almost vertical at its femoral attachment making an angle of 1° with the femoral axis and courses posteriorly making an angle of 18° within the tibial axis (Liu et al. 2010; Otake et al. 2007).

Technique

This is measured on coronal and sagittal MR images.

Clinical Relevance

An understanding of the anatomy is essential to enable appropriate treatment of MCL injury and in surgical planning of MCL reconstruction.

Reproducibility

The measurements of the MCL on MRI are comparable to the measurement on cadavers (Lai et al. 2011).

13.18   Lateral Collateral Ligament

LCL extends from the lateral epicondyle of the femur inserting onto the fibular head. The LCL is 11 mm thick, 4.1 mm wide and 5.3 cm long and is a static stabiliser. The angle between the LCL and femoral axis is 18°, and the angle between the fibular attachment and the posterior tibial axis is 11°. The angle between the LCL and popliteus is 41° (Otake et al. 2007).

Technique

This is measured on coronal and sagittal MR images. It can also be measured by high-resolution ultrasound (Lai et al. 2011).

Clinical Relevance

This is useful in surgical planning of reconstruction of lateral collateral ligament (Costa et al. 2004; Rui-shan 2011).

Reproducibility

LCL measurements can be reliably measured on MRI and ultrasound (Otake et al. 2007; Lai et al. 2011). The measurements are comparable between cadavers, MRI and ultrasound. The measurements are dependent on person's BMI. The thickness of the LCL decreases with varus stress.

13.19   ACL

Definition

ACL is a static stabiliser extending from the anterior part of the proximal tibia inserting to the medial aspect of the lateral femoral condyle. It is 38 mm in length and has a width of 11 mm. ACL has two bands, anteromedial measuring 7 mm in width and the posterolateral band measures 6 mm. It is parallel to Blumensaat's line. The length of the anteromedial band in the sagittal plane is 37 mm and a width of 5 mm on coronal and sagittal plane. The length of posterolateral band is 20 mm on sagittal images, width of 4.5 mm on sagittal and 3.8 mm on coronal images (Cohen et al. 2009). The angle between the ACL and Blumensaat's line is 1.6°. The angle between the ACL and the proximal tibia is 55° in sagittal images and 62° on coronal view in an adult (Kweon et al. 2013).

Technique

A line is drawn through the ACL. The intersecting angle between this and Blumensaat line and the intersection between the ACL and proximal tibial articular surface are measured (Fig. 13.16).

Clinical Relevance

These angles enable one to assess ACL. ACL is thickened with loss of normal orientation and disruption of normal angle in ACL injuries. The anatomical measurements also enable one to identify damage to one or both bundles of ACL (Cohen et al. 2009).
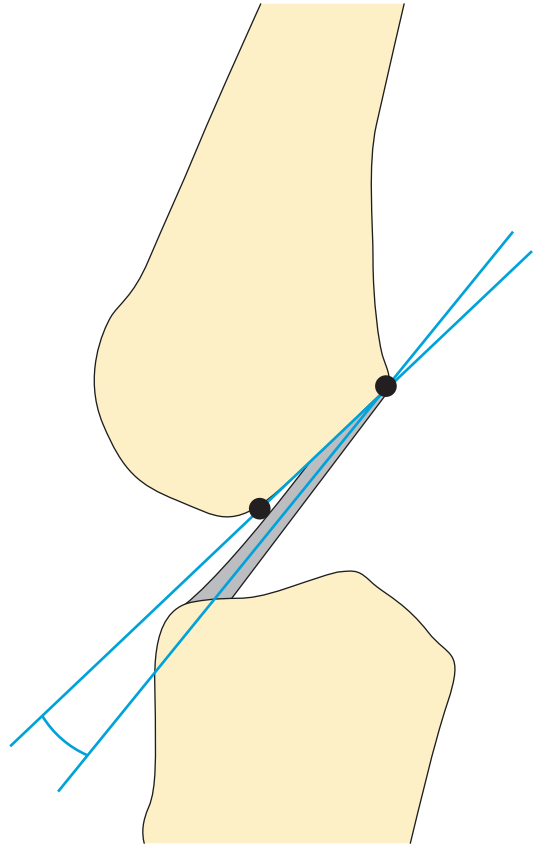
Fig. 13.16 Blumensaat's angle. The intersecting angle between the ACL and Blumensaat line

Reproducibility

The ACL angles are variable and are dependent on the age and sex. These change significantly with age (Kim et al. 2008). The measurement of ACL on MRI has been shown to be reliable with interobserver variability of 0.75–0.85 on sagittal sequences (Cohen et al. 2009).

ACL Angle

Definition

This is the angle between the tangent to the anterior aspect of the distal portion of the ACL and the tangent to the anterior aspect of the intercondylar eminence (Fig. 13.17). ACL has an average cross-sectional area of 54 mm^2 at the site of intersection with the PCL. The cross-sectional area of ACL and ACL notch index is smaller in females than males. ACL notch index is the ratio of the cross-sectional area of the notch to the cross-sectional area of the ACL (Dienst et al. 2007; Harmon and Ireland 2000).

Technique

The intersection of the tangential lines described above is drawn on a midsagittal MR image of the knee. The cross-sectional area of ACL is calculated on MRI (Fig. 13.17).
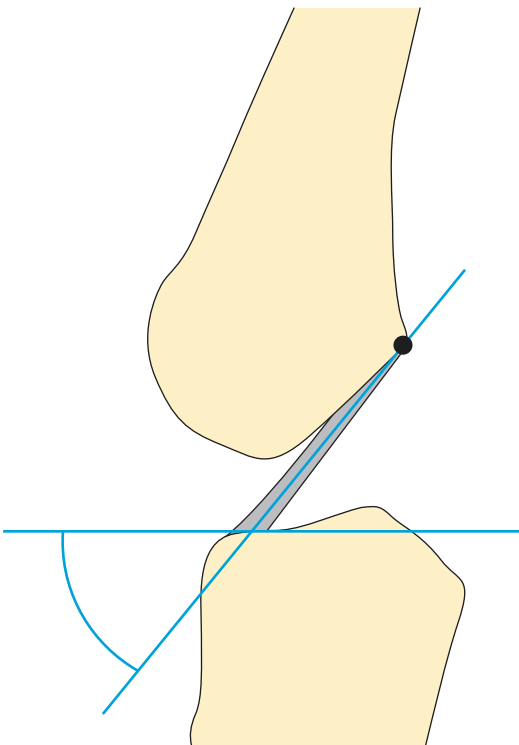
Fig. 13.17 ACL angle. The intersecting angle between the ACL and proximal tibial articular surface

Clinical Relevance

There is minimal overlap between the normal and abnormal values; hence the ACL angle can be a useful quantitative measure when assessing for ACL integrity (Gentili and Seeger 1994; Mellado et al. 2004; Murao et al. 1998).

Reproducibility

A recent study showed a 100% sensitivity and 100% specificity when a threshold value of **45°** was used. Previous studies showed a slightly reduced sensitivity and specificity with this cut-off, but these were still above 90%.

Blumensaat's Angle

This is the angle between the tangent to the anterior aspect of the distal portion of the ACL and the tangent to the intercondylar roof (Gentili and Seeger 1994; Mellado et al. 2004) (Fig. 13.16).

Technique

The intersection of the tangential lines described above is drawn on a midsagittal MRI image of the knee. A hand held goniometer can be used to measure the angle. Normal value is **<15°**.

Clinical Relevance

The Blumensaat angle is usually a negative value with increasing values above zero in abnormal instances. There is more overlap between the normal and abnormal values than with the ACL angle and is therefore a slightly less useful measure when assessing for ACL tears (Murao et al. 1998).

Reproducibility

Recent study showed a 90% sensitivity and 98% specificity when a threshold value of 0° was used. Previous studies have used a different cut-off value of 9°. In the paediatric population, a cut-off value of 10° yielded a sensitivity of 94% and sensitivity of 96% (Murao et al. 1998).

13.20 PCL

Definition

The posterior cruciate ligament extends from the posterior aspect of proximal tibia to the lateral aspect of the medial femoral condyle and has a posteromedial and anterolateral band. It is 38 mm in length and 18 mm wide. The PCL angle formed between the femoral and tibial parts of the PCL is **123°** (Fig. 13.18). This is decreased (less than 106°) in pathological conditions (Kweon et al. 2013).

Technique

A line drawn through the posterior cruciate ligament should touch/traverse the distal femur (Fig. 13.19). In ACL rupture there is abnormal contour of the PCL (buckling), and the line doesn't intersect the distal femur.

Clinical Relevance

When the ACL is not well demonstrated on standard imaging, then the use of the PCL index as one of the indirect signs of ACL rupture is recommended. This angle is decreased in ACL rupture.

Reproducibility

This has been shown to be reliable indicator in ACL rupture (Manaster et al. 2013).

PCL Index

PCL index is an objective indicator of the arc/orientation of the PCL.

Technique

Position the knee in a knee coil with full extension and 15° of external rotation. Measurements are performed from sagittal sequences. The shortest distance between the femoral and tibial attachment of the PCL is identified as *x*, and maximum distance between this and PCL is *y*. Ratio of these two lines, i.e. *x* and *y*, is PCL index (Liu and Osti 1994; Siwinski 1998) (Fig. 13.20).
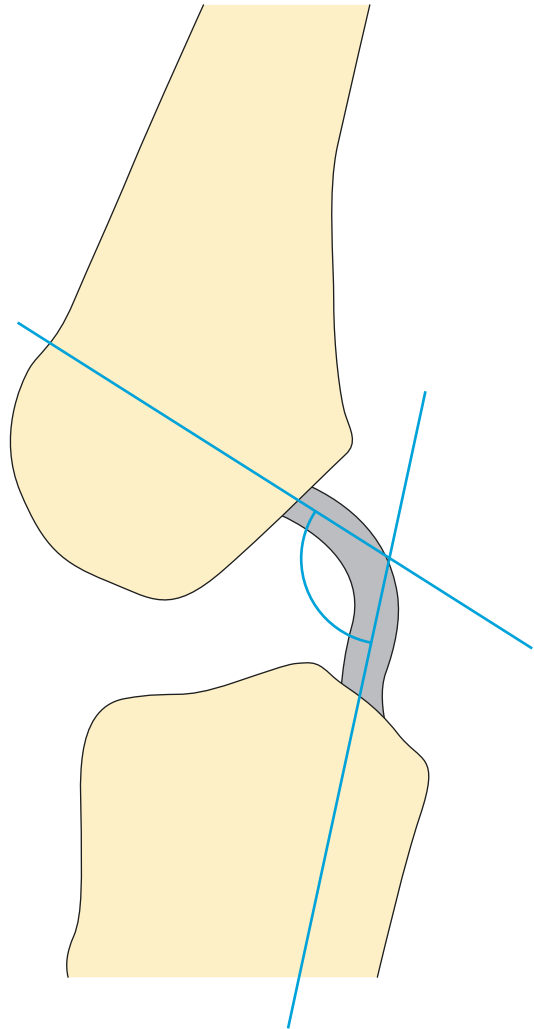
Fig. 13.18 PCL angle. Angle between the tibial and femoral component of PCL

Clinical Relevance

When the ACL is not well demonstrated on standard imaging, then the use of the PCL index as one of the indirect signs of ACL rupture is recommended.

Reproducibility

The PCL index is reduced in cases of ACL injury. PCL index of **5** is normal. An index value of around 2.8 is seen in full-thickness tear of the ACL and PCL index of 3.1 in partial thickness tear of the ACL. These have been shown to have a specificity of 90% and sensitivity of 94% (Liu and Osti 1994; Siwinski 1998).

Fig. 13.19 PCL orientation. Line drawn along the tibial component of the PCL should intersect the distal femur
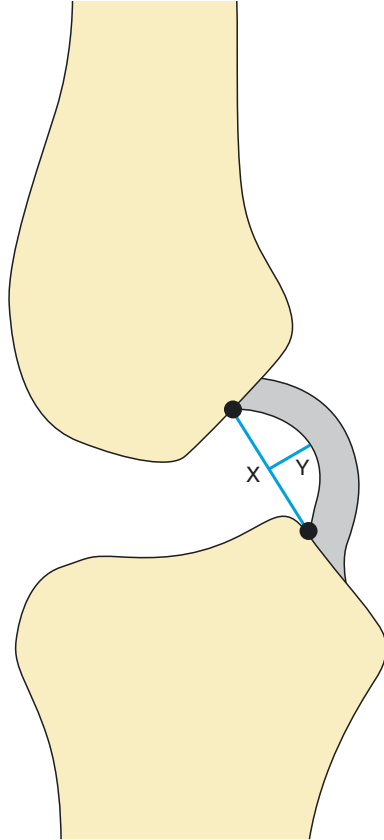
Fig. 13.20 PCL index. Ratio of the *x* (shortest distance of PCL) and *y* (distance between *x* and PCL)

13.21 Nerves

Technique

The cross-sectional area of the sciatic nerve can be assessed on MR axial images (Fig. 13.21). The coronal and sagittal images help one to analyse the sciatic nerve as well. The mean width of the sciatic nerve at the lower border of the piriformis is 19 mm (Brooks et al. 2011). The average cross-sectional area of the sciatic nerve in the distal thigh is 52.6 mm^2, common peroneal nerve in the popliteal fossa is 11.7 mm^2 and tibial nerve has a cross-sectional area of 35 mm^2 (Cartwright et al. 2008, 2013).

Clinical Relevance

The cross-sectional area of sciatic nerve is increased in chronic inflammatory demyelinating polyneuropathy (67 mm^2) and slightly increased in inherited neuropathy (46.5 mm^2) (Sinclair et al. 2011).

Reproducibility

It has been shown that cross-sectional area of the sciatic nerve can be reliably assessed on ultrasound and MR. There is side to side variation in the cross-sectional area of 9–18 mm^2 of the sciatic, tibial and common peroneal nerves. These have been shown to be directly proportional to the weight and BMI. However, the cross-sectional area is not significantly affected by height or age (Cartwright et al. 2008, 2013).
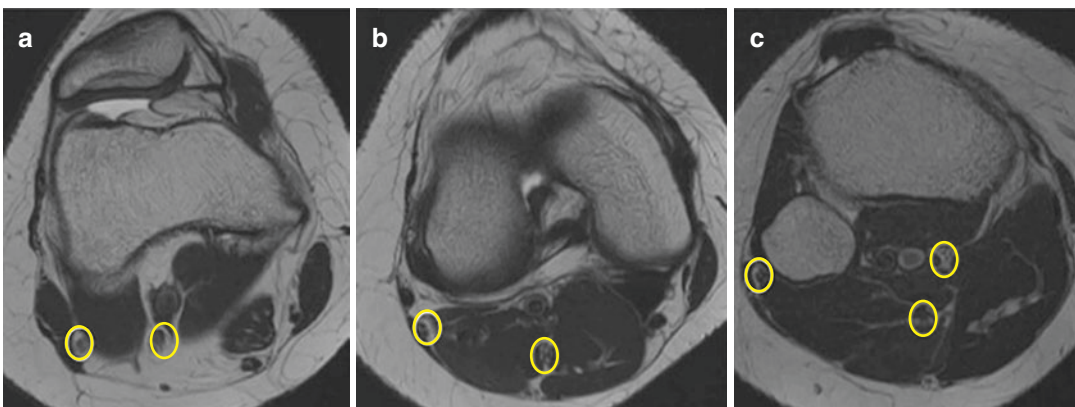
Fig. 13.21 (**a**–**c**) Nerves of knee. Axial images of the knee showing the branches of the sciatic nerve

13.22 TKR Measurements

As in the native knee, anatomical alignment can be assessed on frontal knee radiographs.

Technique

The alpha angle is the angle between the anatomical axis of femur and a line drawn perpendicular to the femoral condyle. The beta angle is the angle between the tibial component and the tibial anatomical axis. The neo-joint space is the vertical height measured between the proximal tibial component and the cranial margin of the tibial tubercle or the tip of the head of the fibula. Rotation of the tibial component is measured between the posterior edges of the tibial component to the posterior tibial axis. Femoral component rotation is assessed by calculating the angle between the posterior aspect of the femoral component and the axis of the femoral condyle. Posterior condyle offset is measured between the line drawn along the posterior femoral cortex and posterior aspect of the femoral component on lateral radiograph (Paley 2002; Sarmah et al. 2012) (Figs. 13.10, 13.12, 13.22).

Clinical Relevance

This is variable depending on the type of implant (Sarmah et al. 2012). This in conjunction with posterior tibial slope effects the range of movement of the TKR.

Reproducibility

The measurements of axis and angles of the knee mentioned above can be measured reliably on radiographs (Paley 2002).
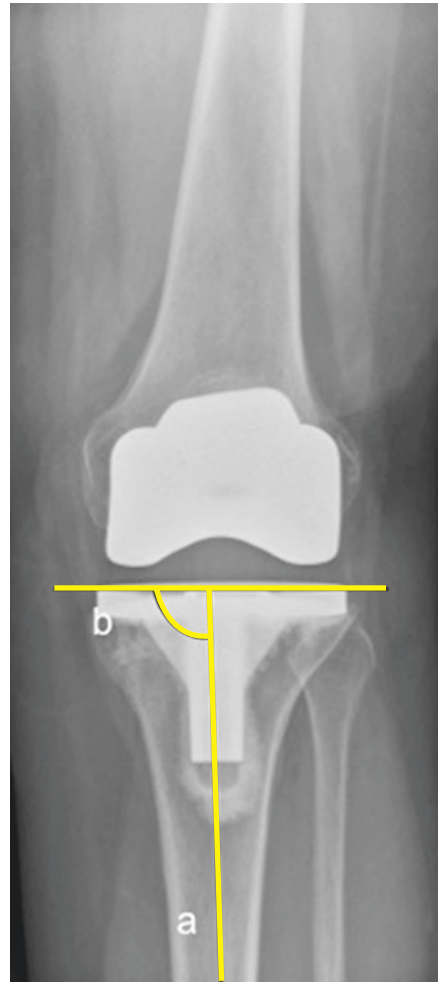
Fig. 13.22 Tibial plateau angle. Angle is the intersection between the tibial anatomical axis and the horizontal line parallel to the tibial component of the TKR

References

Al-Saeed O, Brown M, Athyal R, Sheikh M (2013) Association of femoral intercondylar notch morphology, width index and the risk of anterior cruciate ligament injury. Knee Surg Sports Traumatol Arthrosc 21(3):678–682

Anas I, Musa TA, Kabiru I, Yisau AA, Kazaure IS, Abba SM, Kabir SM (2013) Digital radiographic measurement of normal knee joint space in adults at Kano, Nigeria, Egypt. J Radiol Nucl Med 44(2):253–258

Araki Y, Yamamoto H, Nakamura H, Tsukaguchi I (1994) MR diagnosis of discoid lateral menisci of the knee. Eur J Radiol 18(2):92–95

Beattie KA, Duryea J, Pui M, O'Neill J, Boulos P, Webber CE, Eckstein F, Adachi JD (2008) Minimum joint space width and tibial cartilage morphology in the knees of healthy individuals: a cross-sectional study. BMC Musculoskelet Disord 9:119

Beldame J, Bertiaux S, Roussignol X, Lefebvre B, Adam JM, Mouilhade F, Dujardin F (2011) Laxity measurements using stress radiography to assess anterior cruciate ligament tears. Orthop Traumatol Surg Res 97(1):34–43

Bellemans J, Banks S, Victor J, Vandenneucker H, Moemans A (2002) Fluoroscopic analysis of the kinematics of deep flexion in total knee arthroplasty: influence of posterior condyle offset. J Bone Joint Surg [Br] 84-B:50–53

Bing-chen AN, Wang You FK, Yi-Ming Z, Ke-Rong D (2011) New variables for measuring joint space width to evaluate knee osteoarthritis. Chin Med J 124(23):3886–3890

Botchu R, Obaid H, Rennie WJ (2013) Correlation between trochlear dysplasia and the notch index. J Orthop Surg (Hong Kong) 21(3):290–293

Brooks JBB, Silva CAC, Soares SA, Kai MR, Cabral RH, Fragoso YD (2011) Anatomical variations of the sciatic nerve in a group of Brazilian cadavers. Rev Dor São Paulo 12(4):332–336

Buckland-Wright JC, Macfarlane DG, Lynch JA, Jasani MK, Bradshaw CR (1995) Joint space width measures cartilage thickness in osteoarthritis of the knee: high resolution plain film and double contrast macroradiographic investigation. Ann Rheu Dis 54:262–268

Cartwright MS, Passmore LV, Yoon JS, Brown ME, Caress JB, Walker FO (2008) Cross-sectional area reference values for nerve ultrasonography. Muscle Nerve 37(5):566–571. https://doi.org/10.1002/mus.21009

Cartwright MS, Mayans DR, Gillson NA, Griffin LP, Walker FO (2013) Nerve cross-sectional area in extremes of age. Muscle Nerve 47(6):890–893

Choi SH, Shin KE, Chang MJ, Woo SY, Lee SH (2013) Diagnostic criterion to distinguish between incomplete and complete discoid lateral meniscus on MRI. J Magn Reson Imaging 38(2):417–421

Clement ND, Hamilton DF, Burnett R (2014) A technique of predicting radiographic joint line and posterior femoral condylar offset of the knee. Arthritis 2014:121069. https://doi.org/10.1155/2014/121069

Cobby M, Schweitzer ME, Resnick D (1992) The deep lateral femoral notch: an indirect sign of a torn anterior cruciate ligament. Radiology 184:855–858

Cohen SB, van Beek C, Starman JS, Armfield D, Irrgang JJ, Fu FH. MRI measurement of the 2 bundles of the normal anterior cruciate ligament. Orthopedics. 2009;32(9). pii: orthosupersite.com/view.asp?rID=42856. https://doi.org/10.3928/01477447-20090728-35

Colebatch AN, Hart DJ, Zhai G, Williams FM, Spector TD, Arden NK (2009) Effective measurement of knee alignment using AP knee radiographs. Knee 16(1):42–45

Cooke TD, Sled EA, Scudamore RA (2007) Frontal plane knee alignment: a call for standardized measurement. J Rheumatol 34(9):1796–1801

Costa CR, Morrison WB, Carrino JA (2004) Medial meniscus extrusion on knee MRI: is extent associated with severity of degeneration or type of tear? AJR Am J Roentgenol 183(1):17–23

Dhananjaya KV, Murlimanju BV, Poornima V, Ullal S, Mitra P, Dinesh KV, Saralaya VV, Prabhu LV, Prashanth KU (2014) In vivo morphometry of menisci of the knee in south Indians: a preliminary study. Biomed J 37(1):14–17. https://doi.org/10.4103/2319-4170.117889

Dienst M, Schneider G, Altmeyer K, Voelkering K, Georg T, Kramann B, Kohn D (2007) Correlation of intercondylar notch cross sections to the ACL size: a high resolution MR tomographic in vivo analysis. Arch Orthop Trauma Surg 127(4):253–260

Erbagci H, Gumusburun E, Bayram M, Karakurum G, Sirikci A (2004) The normal menisci: in vivo MRI measurements. Surg Radiol Anat 26(1):28–32

Fox MG (2007) MR imaging of the meniscus: review, current trends, and clinical implications. Radiol Clin N Am 45(6):1033–1053

Fujii M, Furumatsu T, Miyazawa S, Okada Y, Tanaka T, Ozaki T, Abe N (2014) Intercondylar notch size influences cyclops formation after anterior cruciate ligament reconstruction. Knee Surg Sports Traumatol Arthrosc 23(4):1092–1099

Gentili AG, Seeger LL, Yao L et al (1994) Anterior cruciate ligament tear: indirect signs at MR imaging. Radiology 193:835–840

Haddad B, Konan S, Mannan K, Scott G (2012) Evaluation of the posterior tibial slope on MR images in different population groups using the tibial proximal anatomical axis. Acta Orthop Belg 78(6):757–763

Harmon KG, Ireland ML (2000) Gender differences in noncontact anterior cruciate ligament injuries. Clin Sports Med 19(2):287–302

Herzog RJ, Silliman JF, Hutton K, Rodkey WG, Steadman JR (1994) Measurements of the intercondylar notch by plain film radiography and magnetic resonance imaging. Am J Sports Med 22(2):204–210

Jend HH, Heller M, Dallek M et al (1981) Measurement of tibial torsion by computer tomography. Acta Radiol Diagn 22(3A):271–276

Johal P, Hassaballa MA, Eldridge JD, Porteous AJ (2012) The posterior condylar offset ratio. Knee 19(6):843–845

Joseph B, Carver R, Bell MJ et al (1987) Measurement of tibial torsion by ultrasound. J Pediatr Orthop 7(3):317–323

Kakarlapudi TK, Bickerstaff DR (2000) Knee instability: isolated and complex. Br J Sports Med 34(5):395–400

Kilic G, Kilic E, Akgul O, Ozgocmen S (2014) Ultrasonographic assessment of diurnal variation in the femoral condylar articular cartilage thickness in healthy young adults. Am J Phys Med Rehabil 94(4):297–303

Kim HK, Laor T, Shire NJ, Bean JA, Dardzinski BJ (2008) Anterior and posterior cruciate ligaments at different patient ages: MR imaging findings. Radiology 247(3):826–835. https://doi.org/10.1148/radiol.2473071097

Kotani H, Ishisaka N, Furu M, Miki T, Ueo T (2005) A new plain radiography method using the optimal angle of knee flexion for assessing early degeneration of the knee joint. J Arthroplast 20:614–617

Koukoubis TD, Glisson RR, Bolognesi M, Vail TP (1997) Dimensions of the intercondylar notch of the knee. Am J Knee Surg 10(2):83–87

Krishna M, Evans R, Sprigg A et al (1991) Tibial torsion measured by ultrasound in children with talipes equinovarus. J Bone Joint Surg 73-B:207–210

Kweon C, Lederman ES, Chhabra A (2013) Chapter 2. Anatomy and biomechanics of the cruciate ligaments and their surgical implications. In: Fanelli GC (ed) The multiple ligament injured knee. A practical guide to management. Springer, New York, p XVII

Lai MH, Chang ST, Chou YC, Chang CH, Wang TY, Huang HC, Li TY (2011) Real-time ultrasonographic characteristics of the lateral collateral ligament of the knee in cross-leg position with varus stress maneuver. J Med Sci 31(4):153–159

Liu S, Osti L, Dorey F et al (1994) Anterior Cruciate Ligament tear a new diagnostic index on magnetic resonance imaging. Clin Orthop Relat Res 302:147–150

Liu F, Yue B, Gadikota HR, Kozanek M, Liu W, Gill TJ, Rubash HE, Li G (2010) Morphology of the medial collateral ligament of the knee. J Orthop Surg Res 5:69. https://doi.org/10.1186/1749-799X-5-69

Manaster BJ, May DA, Disler DG (2013) Knees 2: soft tissues. Musculoskeletal imaging. The requisites, 4th edn. Elsevier, Mosby, p 203

Mellado JM, Calmet J, Olona M et al (2004) Magnetic resonance imaging of anterior cruciate ligament tears: re-evaluation of quantitative parameters and imaging findings including a simplified method for measuring the anterior cruciate ligament angle. Knee Surg Sports Traumatol Arthrosc 12:217–224

Monllau JC, León A, Cugat R, Ballester J (1998) Ring-shaped lateral meniscus. Arthroscopy 14(5):502–504

Murao H, Morishita S, Nakajima M et al (1998) Magnetic resonance imaging of anterior cruciate (ACL) tears: diagnostic value of ACL-tibial plateau angle. J Orthop Sci 3:10–17

Murshed KA, Çiçekcibaşi AE, Karabacakoğlu A, Seker M, Ziylan T (2005) Distal femur morphometry: a gender and bilateral comparative study using magnetic resonance imaging. Surg Radiol Anat 27(2):108–112

Naredo E, Acebes C, Möller I, Canillas F, de Agustín JJ, de Miguel E, Filippucci E, Iagnocco A, Moragues C, Tuneu R, Uson J, Garrido J, Delgado-Baeza E, Sáenz-Navarro I (2009) Ultrasound validity in the measurement of knee cartilage thickness. Ann Rheum Dis 68(8):1322–1327

Otake N, Chen H, Yao X, Shoumura S (2007) Morphologic study of the lateral and medial collateral ligaments of the human knee. Okajimas Folia Anat Jpn 83(4):115–122

Paley D (2002) Chapter 1. Normal lower limb alignment and joint orientation. Textbook-principles of deformity correction. Springer, Berlin

Phisitkul P, James SL, Wolf BR, Amendola A (2006) MCL injuries of the knee: current concepts review. Iowa Orthop J 26:77–90

Prodromos CC, Joyce BT, Keller BL, Murphy BJ, Shi K (2007) Magnetic resonance imaging measurement of the contralateral normal meniscus is a more accurate method of determining meniscal allograft size than radiographic measurement of the recipient tibial plateau. Arthroscopy 23(11):1174–1179.e1

Ravaud P, Chastang C, Auleley GR, Giraudeau B, Royant V, Amor B, Genant HK, Dougados M (1996) Assessment of joint space width in patients with osteoarthritis of the knee: a comparison of 4 measuring instruments. J Rheumatol 23(10):1749–1755

Rennie WJ, Finlay DB (2006) Meniscal extrusion in young athletes: associated knee joint abnormalities. Am J Roentgenol 186(3):791–794

Rui-Shan D (2011) Anatomy and clinical significance of fibular collateral ligament of knee. Acta Anatomica Sinica 42(4):513–516

Rytter S, Egund N, Jensen LK, Bonde JP (2009) Occupational kneeling and radiographic tibiofemoral and patellofemoral osteoarthritis. J Occup Med Toxicol 4:19. https://doi.org/10.1186/1745-6673-4-19

Sanders TG, Folio LR (2007) The deep lateral femoral notch: a sign of anterior cruciate ligament disruption. Mil Med 172(6):viii–viix

Sarmah SS, Patel S, Hossain FS, Haddad FS (2012) The radiological assessment of total and unicompartmental knee replacements. J Bone Joint Surg Br 94(10):1321–1329

Schneider B, Laubenberger J, Jemlich S et al (1997) Measurement of femoral antetorsion and tibial torsion by magnetic resonance imaging. Br J Radiol 70:575–579

Shepherd DET, Seedhom BB (1999) Thickness of human articular cartilage in joints of the lower limbs. Ann Rheum Dis 58:27–34

Sinclair CD, Miranda MA, Cowley P, Morrow JM, Davagnanam I, Mehta H, Hanna MG, Koltzenburg M, Reilly MM, Yousry TA, Thornton JS (2011) MRI shows increased sciatic nerve cross sectional area in inherited and inflammatory neuropathies. J Neurol Neurosurg Psychiatry 82(11):1283–1286

Siorpaes K, Wenger A, Bloecker K, Wirth W, Hudelmaier M, Eckstein F (2012) Interobservor reproducibility of quantitative meniscus analysis using coronal multiplanar DESS and IWTSE MR imaging. Magn Reson Med 67(5):1419–1426

Siwinski D, Ziemianski A (1998) Value of posterior cruciate ligament index in the diagnosis of anterior cruciate ligament injuries. Arch Orthop Trauma Surg 118:116–118

Spannow AH, Pfeiffer-Jensen M, Andersen NT, Herlin T, Stenbog E (2010) Ultrasonographic measurements of joint cartilage thickness in healthy children: age and sex related standard reference values. J Rhematol 37(12):2595–2601

Stijak L, Nikolić V, Blagojević Z, Radonjić V, Malobabić S (2009) Morphometric parameters of the intercondylar notch, gender and age differences. Acta Chir Iugosl 56(1):53–59. [Article in Serbian]

Stone KR, Freyer A, Turek T, Walgenbach AW, Wadhwa S, Crues J (2007) Meniscal sizing based on gender, height, and weight. Arthroscopy 23(5):503–508

Terzidis I, Totlis T, Papathanasiou E, Sideridis A, Vlasis K, Natsis K (2012) Gender and side-to-side differences of femoral condyles morphology: osteometric data from 360 Caucasian dried femori. Anat Res Int 2012:679658. https://doi.org/10.1155/2012/679658

Patellofemoral Joint

14

David A. Elias

Contents

14.1 Anatomical/Functional Considerations

Introduction

Patellofemoral pain syndrome is a common complaint which comprises a group of pathologies relating to the patellofemoral joint. It is the leading cause of knee pain in patients younger than 45 years. This group includes patients with patellofemoral instability in which the static or dynamic relationship between the patella and femoral trochlea is abnormal resulting in patella subluxation or dislocation. The radiological evaluation of patellofemoral instability has received considerable attention in the scientific literature, and this will be the focus of this chapter. However, it should be recognised that the correlation between imaging findings and symptoms is often variable (MacIntyre et al. 2006), and patients with patellofemoral symptoms may be found to have radiological measurements

D. A. Elias
Department of Diagnostic Imaging,
King's College Hospital, Denmark Hill, London, UK
e-mail: david.elias@nhs.net

within normal ranges, whilst asymptomatic subjects may sometimes be shown to have abnormal measurements of patellofemoral relationships (Elias and White 2004).

This may in part be due to the fact that imaging of patellofemoral relationships is commonly performed in the supine resting knee, whilst failure occurs in the weightbearing active knee. Thus dynamic imaging techniques which allow the measurement of patellofemoral relationships during weightbearing are increasingly advocated. However, this discrepancy between symptoms and measurements may also reflect the fact that patients with patellofemoral pain syndrome form a heterogeneous group, some of whom undoubtedly have abnormalities of patellofemoral relationships, whilst others may have a variety of poorly understood pain-generating mechanisms, not necessarily manifesting in patellofemoral malalignment. Interpretation of the scientific literature is hindered by the common use of patient groups with patellofemoral pain syndrome with little focus on differentiation between those with a true instability and those without. This is partly because of a lack of a consensus definition of patellar instability, but the implicit assumption that all patients with patellofemoral pain syndrome have underlying patellofemoral instability to a greater or lesser degree is now being challenged (Wilson 2007).

Patellofemoral alignment refers to the static relationship between the patella and the trochlear groove at a given degree of knee flexion. Patellofemoral tracking refers to the dynamic, varying patellofemoral alignment that occurs during knee motion. Malalignment and maltracking, therefore, describe abnormalities in static or dynamic patellofemoral relationships, respectively, which may result in cartilage wear, ligamentous strain or patellar dislocation, and there may be associated pain, apprehension or giving way.

Determinants of Patellofemoral Alignment

Patellofemoral articular surface anatomy is one determinant of patellofemoral alignment. The patella is a sesamoid bone, and its articular cartilage is the thickest in the body measuring **4–6 mm** in young healthy adults. The superior 75% of the retropatellar surface articulates with the femoral trochlear sulcus. Furthermore, the retropatellar articular surface consists of a wide concave lateral facet and a narrower convex medial facet, which are separated by a central ridge or keel. A small odd facet is variably present at the medial margin. A hypoplastic medial facet has been shown to be associated with patellar maltracking disorders. The patella articulates with the trochlear groove which is formed of the anterior femoral condyles. The lateral femoral condyle has a greater AP dimension than the medial condyle which helps to counter lateral translation of the patella. At full knee extension, the patella lies superior to the trochlear cartilage. As the knee flexes to around 30, the patella begins to engage with the trochlea. Between 30 and 90 degrees of flexion, the inferior and then superior patellar cartilage articulate with the trochlea. Beyond 120 of flexion, contact between the articular surfaces reduces.

During normal weightbearing activity, patellar position is determined by a complex, dynamic interplay of various passive and active patellar stabilisers. The depth of the trochlear groove is important in maintaining patellofemoral alignment, at mid range of motion of the knee; other structures become more important particularly towards full extension. The *Q* angle is measured clinically as the angle between a line joining the anterior superior iliac spine to the centre of the patella and a line joining the centre of the patella to the tibial tuberosity. This provides an indirect measurement of the valgus translational stress on the patella during quadriceps contraction, and an increased *Q* angle has been associated with patellofemoral pain (Insall et al. 1976). Some authors have disputed this association (Fairbank et al. 1984), possibly because unstable patellae may be laterally displaced in the supine resting knee, thus artificially reducing the *Q* angle. Therefore the *Q* angle may be better measured at 30 degrees of knee flexion at which point the patella and trochlea are engaged preventing lateral displacement (Fithian et al. 1995). In any case, the *Q* angle is affected by hip anteversion, knee valgus

and the relative positions of the trochlea and tibial tuberosity, reflecting the effects of overall lower limb bony alignment on patellofemoral relationships (Sanfridsson et al. 2001; Lin et al. 2008).

A number of soft tissue structures also maintain patellofemoral alignment. The passive stabilisers include the patellar ligament and the medial and lateral patellar retinacula.

The patellofemoral ligament is a fascial thickening of the deep layer of the medial patellar retinaculum which has been shown to be the major passive restraint preventing medial patellar dislocation (Conlan et al. 1993). It originates from the medial femur between the medial epicondyle and the adductor tubercle and runs just deep to the inferior fibres of vastus medialis to insert on the superior two thirds of the medial patellar margin. The active stabilisers of the patella consist of the four quadriceps muscles. The inferior portions of vastus medialis and lateralis form discrete muscles known as vastus medialis obliquus and vastus lateralis obliquus, respectively. These have horizontally orientated fibres which function as active medial and lateral patellar restraints.

Factors Affecting Measurements of Patellofemoral Tracking

Measurement Technique

Patellar motion is complex but can be described as translational motion along three perpendicular axes and rotation about three perpendicular axes (Bull et al. 2002) (Fig. 14.1). Katchburian et al., following an extensive review of the literature, advocate that ideal description of patellar position should be relative to the femoral long axis and to the centre of the femoral groove (Katchburian et al. 2003) although these may not be practicably dependent on the measurement system. In general, the use of the posterior femoral condyles as a reference line on axial imaging is preferable to the use of the anterior condyles, as the shape and position of the anterior condyles are much more variable especially in trochlear dysplasia. However, different authors have used the anterior condyles (Kujala et al. 1989a), poste-

rior condyles (Brossmann et al. 1993; Powers et al. 1998), whole femur (Nagamine et al. 1995; Sakai et al. 1996) or even tibia (Stein et al. 1993) as a reference point, complicating comparison between different studies.

Clearly the accuracy and reproducibility of a measurement technique are also of importance in determining its value. The significance of this is affected by the expected size of a clinically relevant change in measurement. Small changes in many of the measurements described below may have significant effects on loading of the patellofemoral joint and therefore on knee pain and cartilage wear. As an example, CT measurement of tibial tuberosity-trochlear groove distance (TT-TG) has been shown to vary by a mean of 3.2 mm (range 0–13 mm) in consecutive studies on the same patient (Lustig et al. 2007). In the same study, tibial tubercle transfer, which is commonly used in the treatment of patellofemoral maltracking, was shown to medialise the tubercle by 8.6 mm on average, a value which lies within the 95% confidence intervals for the variability of the measurement.

A number of authors have questioned the value of using quantitative measurements of patellar alignment at all, particularly for kinematic magnetic resonance imaging (MRI) studies in which only relatively low-resolution images are usually available because of the limited time available for acquisition of each image (O'Donnell et al. 2005). Instead a subjective assessment of patellofemoral tilt and displacement can be made, preferably using a set of images combined as a cine loop, from a dynamic study of knee flexion/extension. This approach has obvious advantages in speed of study evaluation and also obviates the common difficulty in quantitative studies that specific bony landmarks required for a particular measurement may often not be identifiable on a single image.

Type of Motion

Irrespective of the type of measurement system used, the approach of measuring patellofemoral relationships at a fixed degree of static knee flexion clearly has limited relevance to the ambulant situation, even where several static measurements are performed at various knee flexion
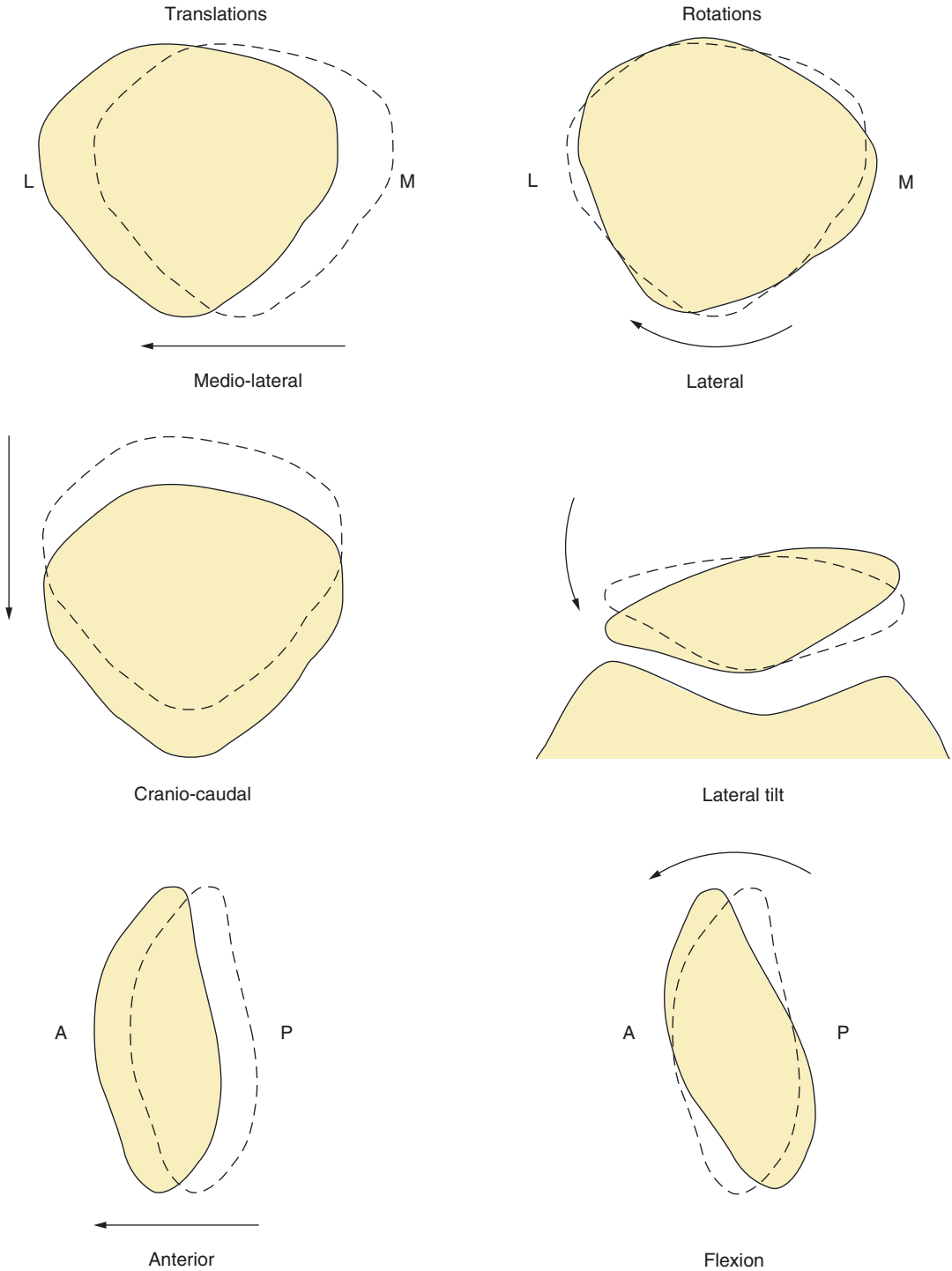
Fig. 14.1 Directions of motion which may be used to describe patellar tracking (Adapted from Katchburian et al. 2003)

angles. The patella position in the relaxed supine knee at a given knee flexion angle may be an unreliable estimate of its position at the same flexion angle during walking. This is because of the effect of weightbearing and quadriceps contraction on patellar position. Quadriceps loading

has been advocated in supine or prone studies to better replicate the ambulant situation, but a static load will have very different effects on the nature of quadriceps activity to the changing loads during walking. In particular, vastus medialis activity, critical for dynamic control of patellar tracking, may vary or even be inhibited in symptomatic knees. Additionally, femorotibial rotational alignment, which affects the *Q* angle and therefore the lateral pull on the patella, will vary between the supine resting knee and the ambulatory knee. Therefore, although practicality has dictated that many studies are performed on the supine or prone resting knee, the applicability of findings to the weightbearing ambulatory state should always be questioned. Some have considered arthroscopic studies of patellar tracking to be a gold standard, but the absence of weightbearing and quadriceps activation in arthroscopic studies means that similar concerns apply (Brossmann et al. 1994). Additionally, measurements of patellar tilt and lateral displacement have been shown to be affected by the presence of a knee effusion, further questioning the reliability of arthroscopic assessment (Brossmann et al. 1996).

Imaging Techniques

Conventional Radiography

The standard radiographic series for assessment of patellofemoral relationships includes an AP, a lateral and an axial view. The AP view of the knee is of limited value in the assessment of the patellofemoral joint, the lateral view is particularly useful in determining the vertical position of the patella, whilst the axial view is especially useful as it provides details of the patellofemoral relationships and morphology in the horizontal plane. Dysplasia of the femoral trochlea is readily appreciated in the axial plane, although severe trochlear dysplasia does produce the "lateral trochlear sign" on the lateral projection. On the lateral view, the subchondral outline of the normal trochlea is seen as a dense white line parallel and congruous with the subchondral outline of the lateral femoral condyle. It is continuous with

Blumensaat's intercondylar line posteriorly and merges with the anterior cortex of the distal femur above the level of the trochlea. The intersection or "crossing over" of these two lines indicates severe trochlear dysplasia and is quantitatively expressed by measuring the ventral prominence or trochlear bump (Dejour et al. 1994). The measurement of ventral prominence reflects the depth insufficiency of the trochlear groove and is related to patellar instability (Fig. 14.2).

A variety of methods of performing the axial view have been described (Fig. 14.3). Most commonly the axial view is performed with the patient supine with 30–45 degrees of knee flexion (Davies et al. 2004). In order to produce a more physiological assessment, a standing axial view has been advocated, but this requires a specially designed knee support (Egund and Ryd 2002). Stress axial views have been advocated in which a device is used to apply a constant lateral or medial displacing force on the patella, whilst the radiograph is performed (Teige et al. 1996). The axial radiograph has limited value however in the assessment of patellofemoral alignment as it generally requires knee flexion of at least 30 degrees, and therefore alignment during the critical early part of knee flexion cannot be studied (Fig. 14.4) (Walker et al. 1993). A further limitation of the axial radiograph, with respect to measurement of patellofemoral alignment, is that the posterior femoral condyles, which generally provide the most reliable reference plane for many measurements, are not visualised.

Ultrasound

Ultrasound has been used for the assessment of patellar alignment in children (Nietosvaara and Aalto 1993).

Transverse images allow assessment of the trochlear groove and patellofemoral relationships, whilst sagittal images allow measurement of patellar height. However, even when assessed by experienced musculoskeletal radiologists, there is poor reliability and validity compared with MRI and CT in patellar instability cohorts

Fig. 14.2 Ventral prominence. (**a**) Normal parallel relationship of the anterior aspect of the lateral condyle (*C*) and subchondral outline of the trochlea (*T*) which is continuous with Blumensaat's line (*B*). (**b**) Crossover sign highlighting the intersection of the two lines along the anterior condylar contour producing a ventral prominence
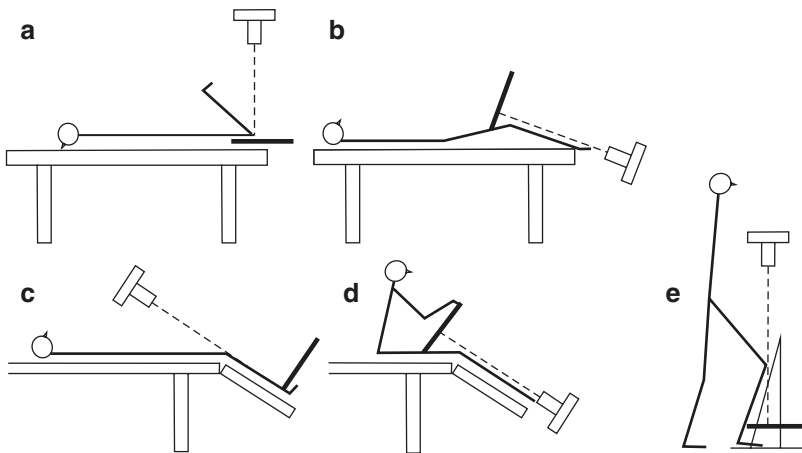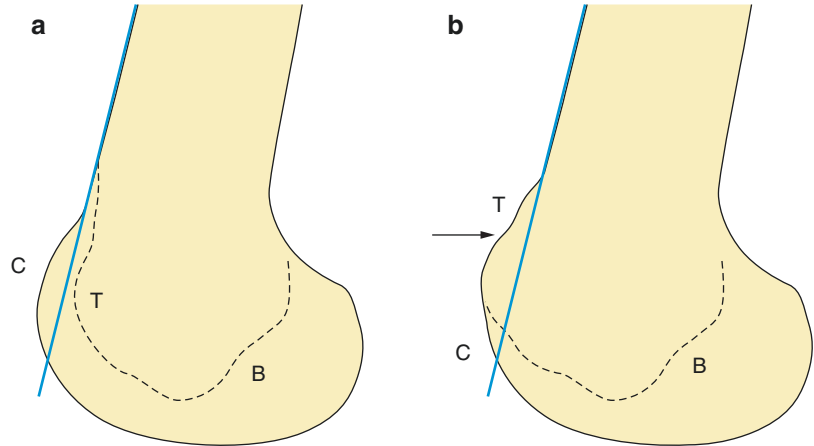
Fig. 14.3 Radiographic techniques for the axial radiograph of the patella. Prone axial radiographs (**a**) are performed with knee flexion 90 and therefore are insensitive for subluxation in most patients with maltracking, where subluxation tends to occur in the early part of flexion. Supine axial radiographs may be performed with the knee flexed at 20 (**b**) (Laurin et al. 1979) or flexed at 45 (**c**)

(Merchant et al. 1974). The Merchant technique may be performed with the beam direction reversed (**d**), eliminating the need for a special cassette holder. A weightbearing axial view (**e**) has been described which requires a specially designed knee support, but this may provide a more physiological assessment (Egund and Ryd 2002) (Figure reproduced from Elias and White (2004))

(Toms et al. 2009). This is probably related to the small field of view provided by ultrasound probes resulting in difficulties in reliably orientating the patella to the bony femoral condylar landmarks.

Computed Tomography

Studies have demonstrated that in many patients with patellofemoral maltracking and pain, patellar subluxation occurs in the extended knee but resolves by around 30 degrees of flexion as the patellar begins to engage with the trochlear groove, and therefore cross-sectional examina-

tion of patellofemoral alignment has advantages over axial radiography since early flexion can be readily examined (Walker et al. 1993; Inoue et al. 1988; Kujala et al. 1989a). Conversely asymptomatic subjects often show some patellar subluxation or tilt in full extension. Therefore imaging at between 5 and 30 degrees of flexion is of most value in distinguishing between normal and abnormal alignment and tracking (Fig. 14.4). A passive supine CT examination may be performed with the knee at 0, 10, 20 and 30 degrees of flexion. For a patient with an equal leg and
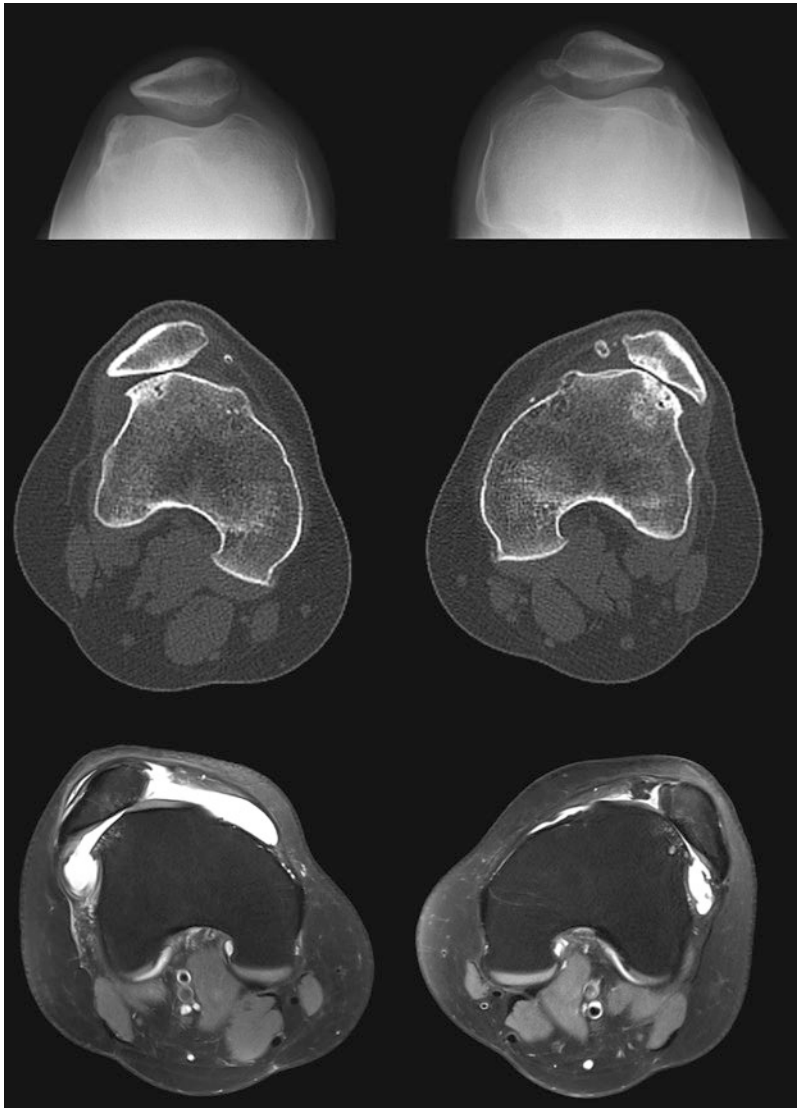
Fig. 14.4 Conventional axial radiographs (*top*) show seemingly well-located patellae as the radiographs are obtained at a minimum of 30 degrees of flexion. In reality there is severe patellar instability which is unmasked when CT (*middle*) or MRI (*bottom*) axial imaging is obtained at 5 degrees of flexion. Note the associated severe osteoarthrosis and also the bilateral fragments avulsed from the medial patellar margin related to previous lateral patellar dislocations

thigh length of 450 mm, this requires raising the knee by 0, 40, 80 and 115 mm from the table top (Whitehouse 2002). This can be achieved with a balloon placed under the knee and inflated to each level. Alternatively, devices are available which allow passive placement of the knee in various fixed flexion angles. At each position axial images are performed through the patellofemoral joints.

Rapid techniques capable of capturing CT images during active knee motion have been developed in order to evaluate patellofemoral relationships more physiologically. This was originally performed with electron beam imaging (Stanford et al. 1988). More recently, helical CT has been used to perform a continuous 10 s exposure with a stationary table (Dupuy et al. 1997; Muhle et al. 1999a, b). Repeated mid-trochlear

axial images are acquired during active knee flexion and extension with the thigh strapped to the table. A weighted boot may be used to increase quadriceps loading.

Evaluation of subluxation and tilt on axial static and dynamic CT imaging may be performed qualitatively preferably with the use of a cine loop for dynamic studies. Alternatively quantitative measures described below may be applied at various degrees of knee flexion.

Magnetic Resonance Imaging

MRI examinations may be performed supine or prone. Prone examinations require appropriate padding with a hole for the patella or a table cut out such that the patella will not be artificially displaced by the table. The use of a restraining device which prevents femoral displacement and rotation whilst allowing free patellar and tibial motion is ideal. Generally the body coil rather than a dedicated knee coil is used so that both knees may be examined together and to allow as much knee flexion as possible within the bore of a closed magnet. Fast imaging sequences such as spoiled gradient recalled acquisition in the steady state (GRASS) have been used to perform axial images through the mid-trochlea during active motion (Shellock et al. 1992). Imaging may be triggered manually or with motion sensitive detectors (Muhle et al. 1995). Supine MRI studies comparing measures of patellofemoral alignment in patients with and without clinical patellar instability have shown accentuated differences between study groups where knee flexion and extension are active and continuous, as compared with images taken at different degrees of static knee flexion (Brossmann et al. 1993; Muhle et al. 1995). In prone studies, a special quadriceps loading device has been shown to accentuate differences in patellofemoral tracking between symptomatic and asymptomatic knees (Shellock et al. 1993). This may be because of the importance of quadriceps dysfunction in patellofemoral maltracking, a factor excluded in passive studies.

A simple, inexpensive technique for performing active supine loaded dynamic MRI patellar tracking studies has been described (McNally 2001). The knees are supported on a foam cushion which allows approximately 30 degrees of flexion. The knees are loosely constrained by strapping them together, and an inflated ball is placed between the patient's ankles and the upper wall of the magnet bore. When the active study begins, the ball valve is released allowing the ball to deflate, and the patient is asked to slowly extend against the resistance of the deflating ball.

Recently open MRI has been used to evaluate patellofemoral tracking during active flexion and extension with subjects nearly fully weightbearing and almost erect but only supported by a backrest to stabilise the subject within the scanner (Draper et al. 2008). This system was successfully used to measure lateral displacement and axial plane tilt of the patella, and this technique therefore shows promise as a method for quantitative evaluation of patellofemoral tracking in a near physiological setting.

14.2 Trochlear Anatomy: Sulcus Angle (Trochlear Angle)

Definition

The angle between the medial and lateral femoral trochlear facets
Normal <145°
Abnormal >145°

Indications

Patellofemoral maltracking
Trochlear dysplasia

Techniques

Axial knee radiograph
Transverse image of the mid-trochlear groove—US
Transverse image of the mid-trochlear groove—CT
Transverse image of the mid-trochlear groove—MRI
MRI is proven to be better than axial radiography in characterising trochlear sulcus morphology as the measurement on a skyline radiograph only assesses the lower part of the trochlear sulcus which is not truly a representative of trochlear anatomy.

Full Description of Technique

On the axial knee radiograph, the angle is measured between a line joining the deepest point of the intercondylar sulcus and the summit of the
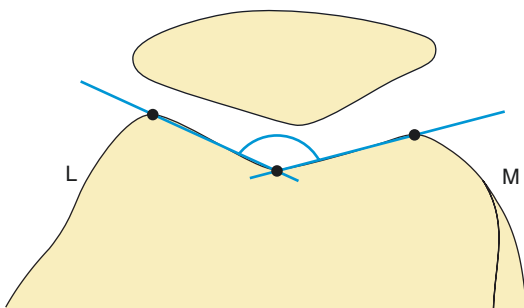
Fig. 14.5 Measurement of sulcus angle on an axial radiograph of the knee

lateral femoral condyle and a line joining the deepest point of the intercondylar sulcus and the summit of the medial femoral condyle (Fig. 14.5).

On CT and MRI, measurement techniques have varied. The sulcus angle is most commonly measured at 10–20 of knee flexion. Axial slice thickness varies on different CT and MRI studies, and there is a lack of clarity in the literature as to which axial slice should be chosen for sulcus angle measurement. With thinner axial sections, the trochlear morphology is seen to vary from the proximal to the distal slices.

Recent articles have described the use of the image showing "the best anatomic representation of the trochlear groove" (Alemparte et al. 2007), "the proximal" or "distal" trochlea (Fucentese et al. 2007) and the level where the femoral epicondyles were most widely separated on the medial to lateral axis (Toms et al. 2009), whilst earlier studies have not described how a slice was chosen (Davies et al. 2000; Kujala et al. 1989b). Walker et al. (1993) performed 4-mm-thick CT slices through the knees at 10 of flexion. The authors comment that with consecutive axial slices progressing inferiorly through the trochlea, the trochlea deepens and then the bony cortices begin to blur and broaden as the anterior surface passes backwards towards the condyles. They chose the most inferior image on which the anterior cortices remain sharp (i.e. vertically orientated) to measure the sulcus angle. This technique is logical but may be more difficult to apply with modern multislice scanners with often submillimetre resolution. Studies have also varied on whether landmarks are defined from the subchondral bone or the overlying cartilage surface (Toms et al. 2009). Whilst the subchondral bone may be more reliably identified, the cartilage surface may be of greater clinical relevance in determining patellofemoral instability.

On ultrasound the sulcus angle has been measured in children with the knee in 10 of flexion on a transverse scan just below the level of the patellar apex (Nietosvaara and Aalto 1993).

Reproducibility/Variation

Axial radiographic measurement of the sulcus angle has been shown to have a good reliability with intra- and interobserver intraclass correlation

coefficients of 0.94 and 0.92, respectively (Davies et al. 2000). However others have argued that measurement may not be so reproducible where the lateral trochlea has a rounded anterior tip, resulting in difficulty in placing measurement lines (Walker et al. 1993). For cross-sectional imaging techniques, some studies have reported reasonable intra- and interobserver variabilities (Kujala et al. 1989b; Toms et al. 2009), whilst others have suggested measurement is unreliable because of variability of trochlear shape with axial slice (Koskiken et al. 1993). In one CT study, intra- and interobserver variabilities were poor for measurement of the sulcus angle in 0 of knee flexion, whilst inter- and intraobserver correlations were above 80% for measurement of the sulcus angle at 20 of knee flexion (Delgado-Martinez et al. 2000). A more recent study has suggested good reliability of CT, US and MRI measurements of the sulcus angle using the subchondral bone surface for landmarks (Toms et al. 2009). Where the cartilage surface is used for landmarks, CT and MR measurements were reliable, but US measurements were not.

Normal values for the sulcus angle as measured on axial radiographs are given as 138 (SD 6) (Merchant et al. 1974) or 140.4 (SD 5.2) (Davies et al. 2000). Merchant et al. (1974) found no significant change in trochlear shape through a range of beam to femur angles of 15–75.

Clinical Relevance/Implications

Trochlear dysplasia, as defined by an abnormally increased sulcus angle, has been shown to correlate with other features of extensor mechanism dysplasia. In one study of 137 knees with pain and instability, a normal sulcus angle was shown to be predictive of normal patellar alignment as measured by other radiographic parameters (Davies et al. 2000). The authors suggest, therefore, that the sulcus angle could represent a good initial screening tool, which, if abnormal, should be supplemented by assessment of other parameters of patellofemoral tracking.

The sulcus angle measured with low-field MRI was found to be the strongest discriminator of several indices of patellofemoral alignment between female patients with recurrent patellar dislocation and controls (Kujala et al. 1989b). Increasing sulcus angle has also been shown to correlate with increasing pain and functional impairment, as well as with increased areas of cartilage loss and bone marrow lesions in the patellofemoral joint (Kalichman et al. 2007b).

Analysis/Validation of Reference Data

Variation exists as to the values of this angle depending on the imaging technique employed, with a lack of reliable reference database limiting the evidence for appropriate validation.

Conclusion

The sulcus angle is a useful correlate of patellofemoral dysfunction and may be measured on axial views and with cross-sectional imaging techniques. However because of variation in trochlear shape along its superoinferior extent, there is a lack of reproducibility of the measurement with CT and MRI and a lack of consensus in the literature on the ideal measurement technique. It may be more reliably measured on CT studies at 20 of knee flexion, rather than at 0 of knee flexion.

14.3   Trochlear Anatomy: Lateral Trochlear Inclination

Definition

The angle between a line along the lateral trochlear facet and a line joining the posterior borders of the medial and lateral femoral condyles
Normal >11°
Abnormal <11°

Indications

Patellofemoral maltracking
Trochlear dysplasia

Techniques

Axial image through trochlea utilising CT or MRI

Full Description of Technique

On MRI, the most superior axial image demonstrating a cartilaginous trochlea is chosen for measurement (Fig. 14.6). A line is drawn on this image tangential to the subchondral bone of the lateral trochlea facet, and the angle is measured between this and a line tangential to the subchondral bone of the posterior aspect of the femoral condyles (Carrillon et al. 2000).

Reproducibility/Variation

Using the MRI technique defined above, good interobserver variability was reported for this measurement (Carrillon et al. 2000).

Clinical Relevance/Implications

The use of a threshold of 11 resulted in a sensitivity of 93% and a specificity of 87% for the identification of patients with previous patella dislocation as compared to controls (Carrillon et al. 2000).
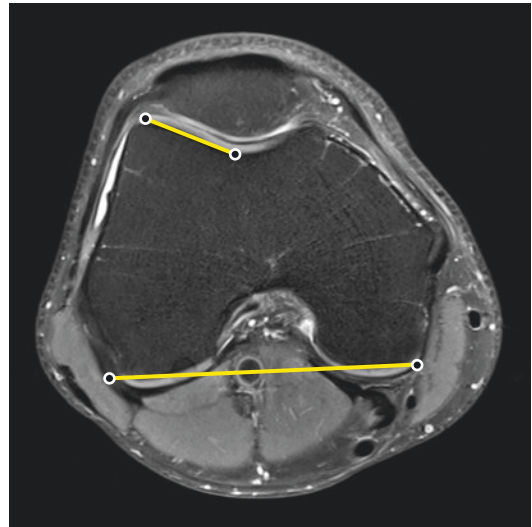
Fig. 14.6 Measurement of lateral trochlear inclination on an axial MR image of the knee at the most superior level that demonstrates trochlear cartilage

Analysis/Validation of Reference Data

By comparison with the sulcus angle, measurement of lateral patellar inclination has the advantage of using the posterior condyles as a reference line for the measurement, and this is likely to show less variability in dysplastic knees than the medial trochlear facet. Additionally, performance of the measurement at the most proximal axial slice with a trochlear cartilage covering allows assessment of the critical superior trochlear groove which is likely to be most sensitive for dysplasia and patellar instability. However, the use of the posterior condylar reference line prevents this measurement from being used on axial radiographs as the posterior condyles are not visualised.

Conclusion

Lateral trochlear inclination may be a preferable measurement to sulcus angle for use in MRI studies.

14.4   Trochlear Anatomy: Trochlear Groove Depth

Definition

This is the perpendicular distance in the antero-posterior plane from the deepest point of the femoral trochlea to the plane defining the most anterior limit of the femoral condyles.

Normal value >5 mm
Hypoplasia 3–5 mm
Dysplasia <3 mm

Indications

Patellofemoral maltracking
Trochlear dysplasia

Techniques

True lateral radiograph
Axial CT image through the trochlea—CT
Axial MR image through the trochlea—MRI

Full Description of Techniques

On a true lateral radiograph of the knee (Fig. 14.7), trochlear groove depth is measured 1 cm distal to its upper limit by measuring the AP distance from the anterior summit of the anterior-most femoral condyle to the trochlear floor at this level (Murray et al. 1999).

A variety of methods for measuring trochlear depth have been proposed on cross-sectional studies (Pfirrmann et al. 2000; Martinez et al. 1983; Kujala et al. 1989a, b; Walker et al. 1993; Delgado-Martinez et al. 2000). Pfirrmann et al. (2000) compared measurements at different trochlear levels on axial MRI and found that trochlear depth measured on the axial image 3 cm above the femorotibial joint line was most discriminatory between patients with and without trochlear dysplasia. They advocate measuring all distances relative to and perpendicular to a line joining the posterior femoral condyles. The trochlear depth is calculated as (height of lateral femoral condylar summit + height of medial femoral condylar summit)/2 − (height of deepest point of trochlear groove). This measurement is applicable to CT and MRI (Fig. 14.8).

An alternative method for measurement of trochlear depth involves drawing a reference line between the tips of anterior femoral condyles. The perpendicular distance from this line to the depth of the trochlear groove is measured (Endo et al. 2007, Walker et al. 1993). This measurement is applicable to axial radiographs as well as CT, MRI and US. Since this method relies on the position of the anterior tip of the medial femoral condyle for the reference line, it may be less reliable than methods using the posterior condyles.

Fig. 14.7 Measurement of trochlear groove depth on the lateral radiograph of the knee
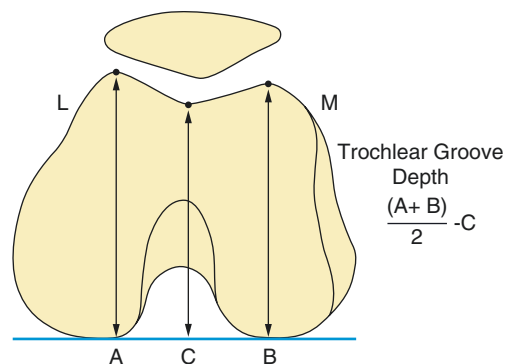
Fig. 14.8 Measurement of trochlear groove depth on CT or MRI. Measurements are taken on an axial image 3 cm above the femorotibial joint. Trochlear groove depth is calculated as $(A + B)/2 − C$

Reproducibility/Variation

Measurement of the trochlear depth on a lateral radiograph is very sensitive to slight rotation from the true lateral. A study of cadaveric femora showed that as little as 5 of rotation could produce a false-positive or false-negative diagnosis of trochlear dysplasia (Koeter et al. 2006). Ideally, therefore, fluoroscopy should be used to ensure that the posterior borders of the femoral condyles precisely overlap, for this measurement to be performed reliably. Trochlear measurements can vary due to size differences, the proximal extent of the trochlear cartilage and if the trochlear cartilage versus bone is referenced for measurements.

It is important to use bony landmarks to avoid the variation introduced by cartilage thickness (Van Huyssteen et al. 2006).

Clinical Relevance/Implications

The trochlear depth at the proximal trochlea is a potentially important anatomical determinant of patellofemoral instability.

In one study, lateral femoral condyle wedge osteotomy performed in patients with patellar instability and trochlear dysplasia identified on lateral radiographs had no postoperative instability with improved pain and function scores confirming the importance of trochlear depth (Koeter et al. 2007a, b).

In one MR study, femoral sulcus depth index (calculated as twice the trochlear depth described by Pfirrmann et al. above) was found to be the most discriminatory of multiple measurements in distinguishing between knees with previous dislocation and controls (Kujala et al. 1989a, b). Pfirrmann et al. reported a sensitivity of 100% and specificity of 96% in diagnosing trochlear dysplasia if the trochlear sulcus measures 3 mm or less at 3 cm above the tibiofemoral joint.

Analysis/Validation of Reference Data

As limited data in the literature is available, it is not possible to conclusively validate the various methods that can be employed in its assessment. Very importantly, the method using measurements made from lateral radiographs is the most problematic.

Conclusion

The depth of the proximal trochlea is a potentially important correlate of patellar stability. The usefulness of this measurement on lateral radiographs is however limited by its potential sensitivity to slight rotation, and fluoroscopy should be used to avoid this. Trochlear depth measurement on MRI seems to correlate well with instability, but there is little data on reproducibility.

14.5 Trochlear Anatomy: Lateral: Medial Trochlea Facet Ratio

Definition

The ratio of the width of the lateral trochlear facet to the width of the medial trochlear facet
Normal <1.7
Abnormal >1.7

Indications

Patellofemoral maltracking
Techniques
Axial radiograph of the knee
Axial image of the trochlea—CT
Axial image of the trochlea—MRI

Full Description of Technique

On an axial radiograph of the knee, the ratio between the widths of the lateral and medial trochlear facets is measured (Beaconsfield et al. 1994). A ratio of 1.7 (lateral/medial facet width) is considered dysplastic (Fig. 14.9).

In one MRI study, the authors recommend measuring this parameter on an axial image 3 cm above the femorotibial joint line (Pfirrmann et al. 2000). At this level, a threshold ratio of 0.4 (medial/lateral facet width) was found to have a sensitivity of 100% and a specificity of 96% for the diagnosis of trochlear dysplasia compared with controls, with dysplastic knees having a relatively smaller medial facet.

Reproducibility/Variation

Note that in some articles, the ratio is presented differently as medial/lateral instead of lateral/medial which can cause some confusion.
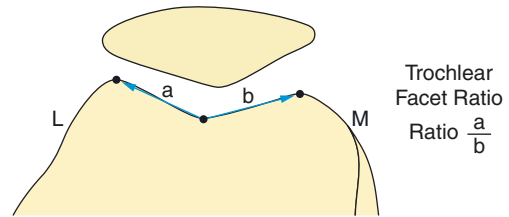
Fig. 14.9 Measurement of lateral/medial trochlear facet ratio on an axial radiograph of the knee. Ratio is *a/b* sensitivity of 100% and a specificity of 96% for the diagnosis of trochlear dysplasia compared with controls, with dysplastic knees having a relatively smaller medial facet

Clinical Relevance/Implications

As discussed in previous measurements in this section concerning the effects and associations of trochlear dysplasia to patellar instability and anterior knee pain

Analysis/Validation of Reference Data

There is insufficient reference data to provide a validation assessment.

Conclusion

Lateral/medial trochlear facet ratio is a recognised measure of trochlear dysplasia, but little data is available regarding its reproducibility and clinical utility.

14.6 Axial Plane Patellar Displacement: Congruence Angle

Definition

The angle between the bisected sulcus angle (see above) and the central ridge (keel) of the patella
Normal −6 (SD 11)
Abnormal >+16

Indications

Patellofemoral maltracking

Techniques

Axial knee radiograph
Axial CT section through the mid-patella and trochlea
Axial MRI section through the mid-patella and trochlea

Full Description of Techniques

The sulcus angle (see above) is measured and bisected through the deepest point of the inter-condylar sulcus to produce a reference line. The congruence angle is the angle between the reference line and a line joining the deepest point of the intercondylar sulcus with the lowest point on the articular ridge of the patella (keel) which divides the medial and lateral facets (Merchant et al. 1974). If the patellar articular ridge lies lateral to the reference line, the congruence angle is designated positive. Where the patellar ridge lies medial to the reference line, the congruence angle is negative.

The congruence angle may be measured on axial radiographs of the knee (Fig. 14.10). The angle may similarly be measured at varying degrees of flexion on CT or MRI, with or without quadriceps contraction. On CT and MRI, the mid-patella is often not visualised on the same axial image as the deepest point of the trochlear groove, particularly when the knee is relatively extended. In this situation, the sulcus
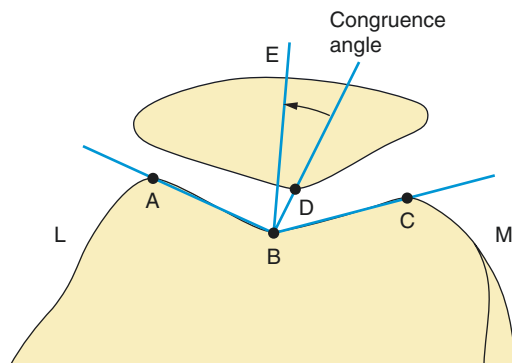
Fig. 14.10 Measurement of the congruence angle on an axial radiograph of the knee. First, the sulcus angle is measured (AB/BC) and bisected to form a reference line (BE). The line BD is drawn from the deepest point of the interarticular sulcus of the trochlea to the deepest point of the interarticular ridge of the patella. The congruence angle is measured between BD and BE

angle will need to be measured on the image where the trochlear groove is deepest and, either by superimposition of images or preferably by copying of measurements between different images on a workstation, the measured sulcus angle will need to be transferred to the mid-patella image.

Reproducibility/Variation

In Merchant's original description of the congruence angle, the authors found a mean angle in normals of −6 (SD 11) and a mean angle of +23 in patients with recurrent patellar dislocation (Merchant et al. 1974). However, in studies of patients with patellar tracking disorders, but not necessarily recurrent patellar dislocations, the sensitivity of the congruence angle measured on axial radiographs has been questioned for patients who have lesser degrees of instability (Inoue et al. 1988; Aglietti et al. 1983).

In a CT study of normal knees at 15 of flexion with relaxed quadriceps, the authors found a very wide range of congruence angle measurements (mean = +5; range −28 to +38) (Alemparte et al. 2007). Another CT study of normal knees in full extension also showed a wide range of positive congruence angle measurements (27–43) (Reikeras and Hoiseth 1990).

In a CT study, between 0 and 20 of knee flexion, moderate interobserver reliability was found in congruence angle measurements, but in around 5% of cases, it could not be measured due to uncertain reference points, and the authors concluded that it was "not reliable" (Delgado-Martinez et al. 2000). Other authors have commented that identification of the deepest point of the intercondylar groove on CT studies of patients with significant subluxation may be problematic (Inoue et al. 1988). In an MRI study of patients with recurrent dislocation, the mean congruence angle fell in both patients and controls as knee flexion increased from 0 to 30 degrees (Kujala et al. 1989a, b). However, at each level of flexion up to 30 degrees, patella dislocators showed a higher mean congruence angle.

Clinical Relevance/Implications

Similar relevance and implications addressed previously concerning patellar instability and anterior knee pain

Analysis/Validation of Reference Data

There is a wide variation using different imaging techniques in the normal/abnormal values found in the literature which results in weak validation support.

Conclusion

The congruence angle has been well described as a measure of patellofemoral shift and may be used with axial radiographs, CT and MRI. However, it has a wide variability in normal knees, especially near to full extension, and studies have increasingly questioned the reliability of this technique.

14.7 Axial Plane Patellar Displacement: Lateral Patellar Displacement

Definition

Lateral displacement of the patella relative to the trochlea
Normal <2 mm
Abnormal >2 mm

Indications

Patellofemoral maltracking

Techniques

Axial radiograph/CT/MRI

Full Description of Techniques

On an axial radiograph, lateral patellar displacement is measured by drawing a tangential line joining the anterior summits of the medial and lateral femoral condyles and dropping a perpendicular to this at the level of the summit of the medial condyle (Fig. 14.11). The distance from this line to the medial margin of the patella is measured and given a positive value when the medial patella border lies lateral to the medial femoral condylar summit (Laurin et al. 1979).

Axial linear patellar displacement can also be measured on axial radiographs using perpendicular reference points. The method was devised as

Fig. 14.12 The reference tangent line joining the anterior condylar summits is intersected by two perpendicular lines from the depth of the sulcus and patellar ridge. The intervening space is the required measurement

the replacement method for the conventional congruence angle estimation when difficulties were encountered in its measurement on digital radiographs due to angle superimposition (Urch et al. 2009). The linear displacement is obtained by first drawing a reference line tangential to the most anterior summits of the medial and lateral trochlear facets. A second line is drawn from the depth of the sulcus and passed perpendicularly through the reference line. A third line is then drawn from the keel of the patella perpendicular to the reference line. The distance between the two perpendicular lines' intersections on the reference line is the linear displacement measurement (Fig. 14.12).

On CT and MR imaging, lateral patellar displacement may be measured using a trochlear reference line through the most anterior point of the medial femoral condyle and running perpendicular to a line joining the posterior femoral condyles (Muhle et al. 1999b). Lateral patellar displacement is measured as the distance from the trochlear reference line to the medial border of the patella (Fig. 14.13). The authors do not specify how to choose the axial image on which measurements should be made. This measurement has also been used for quantification in kinematic studies (Brossmann et al. 1993).
Normal value <2 mm
Mild 2–5 mm
Moderate 5–10 mm
Severe >10 mm

Fig. 14.11 Measurement of lateral patellar displacement on the axial radiograph of the knee
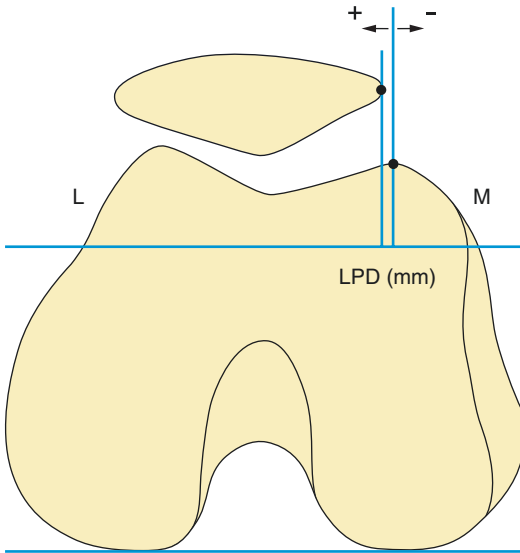
Fig. 14.13 Measurement of lateral patellar displacement on CT or MR imaging measured relative to the summit of the medial femoral condyle

Fig. 14.14 Measurement of lateral patellar displacement on CT or MR imaging measured relative to the trochlea apex

In a more recently described method using CT and MRI, lateral patellar displacement can be measured relative to the trochlear apex as follows (Wittstein et al. 2006): the axial slice with the greatest AP diameter of the femoral condyles is chosen, and on this image, a line is drawn joining the posterior cortex of the femoral condyles (posterior condylar line). A reference line perpendicular to this is drawn through the apex of the femoral trochlea on the same image. These lines are then copied to the axial image which contains the widest transverse diameter of the patella. Lateral patellar displacement is measured as the distance from the patellar apex to the transferred reference line through the trochlear apex (Fig. 14.14).

In a fourth technique, the axial image is chosen with the widest transverse patella diameter (Grelsamer et al. 1998). Two reference lines are drawn, one through the medial and one through the lateral trochlear summits, both perpendicular to the posterior condylar line. The distance is then measured from the medial reference line to the medial patellar border and from the lateral reference line to the lateral patellar border. For each measurement, a positive value is assigned where the patellar border lies lateral to the trochlear reference line (Fig. 14.15). The mean value

Fig. 14.15 Measurement of lateral patellar displacement on CT or MR imaging measured relative to the summits of both the medial and lateral femoral condyles. All lines are drawn perpendicular to the posterior condylar line (Y). M_1 and L_1 are reference lines through the summits of the medial and lateral femoral condyles, respectively, whilst M_2 and L_2 are drawn through the medial and lateral patellar margins, respectively. The distances M_2–M_1 and L_2–L_1 are calculated such that a positive value is given where the patellar line is lateral to its corresponding trochlear reference line. The lateral patellar displacement is taken as the mean of the two measurements (0 mm in this example)

of the two measurements is termed the medial or lateral displacement (MLD).

In a more sophisticated approach, one group has used high-resolution MR images of the knee to generate a coordinate system from subject-specific bone models of the patella, femur and tibia (MacIntyre et al. 2006). The models were used to register bony landmarks on low-resolution MR images performed at different supine loaded knee flexion angles in patients with and without patellofemoral pain and clinical malalignment. The authors found widely overlapping measurements for all planes of rotational and translational motion of the patella, with only lateral translation at 19 degrees of knee flexion found to be marginally significantly increased in patients with patellofemoral pain and clinical malalignment compared with controls.

A preliminary study has evaluated US measurement of lateral displacement (Herrington et al. 2006). The measurement is performed with the knee flexed at 20. In the axial plane, the transducer is aligned with the lateral edge of the superior border of the patella, and the distance between the bony margin of the lateral patella and the anterior margin of the lateral femoral condyle is measured.

Reproducibility/Variation

The primary disadvantage of measurement of lateral patellar displacement on the axial radiograph is that displacement is measured at flexion angles at which lateral displacement may be abolished in all but the most unstable knees.

A further disadvantage of linear displacement measurements, obtained on axial radiographs, is the magnification effect on the measurement, which means that unlike the congruence angle measurement (which is unaffected by magnification), they are not true values. They require to be compared clinically with the noninjured knee. The intraobserver reliability, however, is usually high and above $r^2 = 0.90$ (Urch et al. 2009) for all measurements.

In cross-sectional imaging evaluation, lateral patellar displacement may have advantages over congruence angle as a measure of mediolateral patellar shift because it does not require prior measurement of the sulcus angle which may not be present on the mid-patellar slice. This may be a particular advantage in kinematic studies, where relatively low-resolution images, with few slices only, are available at each flexion angle. In such studies, accurate measurement of the sulcus angle may be unrealistic.

Clinical Relevance/Implications

As previously discussed, the displacement is an indication and a measure of patellar instability and related to patellofemoral symptoms. It should be remembered that the presence of a joint effusion in itself can cause and enhance patellar subluxation.

Analysis/Validation of Reference Data

Each of the various techniques given for cross-sectional imaging evaluation of lateral patellar displacement has strengths and weaknesses. Methods using a single axial image on which all measurement lines are drawn may be more straightforward to perform but present difficulties in extended knees, particularly in the presence of patella alta, when the patella may lie well superior to the trochlear landmarks.

Techniques using the central ridge (keel) of the patella as a landmark suffer from the fact that the central ridge may appear broad and therefore difficult to define in some patellar types and also the cartilage surface over the central ridge may not silhouette the bony contour leading to potential inaccuracy (Grelsamer et al. 1998). Additionally, the central ridge may be difficult to precisely identify on low-resolution images available from some kinematic MR techniques. On the other hand, techniques using the medial or lateral borders of the patella as landmarks may be difficult to apply where those borders are irregular, perhaps because of osteochondral injury following a previous patellar dislocation.

Conclusion

Lateral patellar displacement is a valuable measure of mediolateral patellar position and has been successfully applied to axial radiographs and cross-sectional imaging for both static and kinematic studies. A variety of different methods for measuring lateral displacement on cross-sectional studies are described.

14.8 Axial Plane Patellar Displacement: Bisect Offset

Definition

The percentage of the patellar width which lies lateral to the apex of the trochlear sulcus

Indications

Patellofemoral maltracking

Techniques

Axial image through the mid-patella—CT
Axial image through the mid-patella—MRI

Full Description of Technique

A line is drawn along the posterior femoral condyles, and a perpendicular reference line is dropped through this at the level of the deepest point of the trochlear sulcus. A line is drawn across the widest mediolateral width of the patella. The bisect offset is the percentage of the
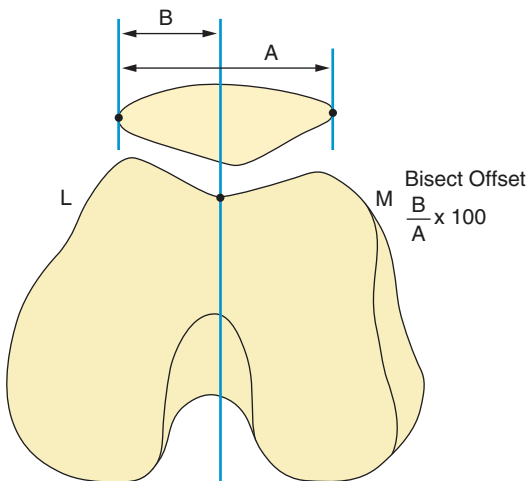
Fig. 14.16 Bisect offset as measured on axial CT or MR images of the knee. A reference line, perpendicular to the posterior intercondylar line, is drawn through the deepest point of the trochlear sulcus, and the distance from the reference line to the lateral margin of the patella (B) is expressed as a percentage of the maximum mediolateral patella width (A). Bisect Offset = $B/A \times 100$

patellar width line which lies lateral to the mid-trochlear reference line (Fig. 14.16).

An alternative method for measuring a similar parameter is to draw a line joining the anterior summits of the femoral condyles and, from this, to drop a perpendicular reference line from the summit of the lateral condyle. The reference line crosses a line drawn along the widest width of the patella. The "lateral shift" is calculated as the percentage of the patellar width line which lies lateral to the reference line (Delgado-Martinez et al. 1996).

Reproducibility/Variation

The bisect offset provides an alternative method of measuring mediolateral patellar position in CT and MRI studies. This technique has been used particularly in kinematic studies, with both non-weightbearing supine (Muhle et al. 1999b; Brossmann et al. 1993; Dupuy et al. 1997) and erect weightbearing systems (Draper et al. 2008). One recent study has found good intra- and interobserver reliabilities for bisect offset measurement on static knee MRI with extended knees (Kalichman et al. 2007b).

The effect of quadriceps contraction and degree of knee flexion on bisect offset was recently assessed in subjects without patellofemoral pathology (Laugharne et al 2016). The authors demonstrated that quadriceps activation in extended knees produced a statistically significantly increased, and abnormal bisect offset, but this normalised at 30 degrees knee flexion. Quadriceps activation can sometimes occur involuntarily in anxious patients, and the authors found that 30 degree knee flexion prevented quadriceps activation having an effect on the bisect offset measurement.

Clinical Relevance/Implications

In an MRI study of patients with knee osteoarthritis, increasing bisect offset was shown to be correlated with increasing cartilage loss and bone marrow lesions in the lateral patellofemoral compartment (Kalichman et al. 2007a, b). In a recent

study, bisect offset measured in erect weightbearing knees using an open MRI system showed significantly increased lateral patellar translation in patients with patellofemoral pain compared with controls and a reduction in lateral patellar translation whilst wearing a patellar brace or sleeve (Draper et al. 2008).

Analysis/Validation of Reference Data

The bisect offset is an alternative method for measuring mediolateral patellar position. This technique has been particularly favoured in kinematic studies. This is probably because image resolution tends to be low and the use of lateral patellar displacement requires the measurement of very small distances unless the patella is very far displaced. For the bisect offset, measurement lines have a reasonable length even for normal patellar positions, and, in theory, the bisect offset may be expected to have a relatively better reproducibility for near-normal patellar positions.

Conclusion

Bisect offset is a useful method for measuring mediolateral patellar position and is probably especially useful in relatively low-resolution kinematic studies.

14.9 Axial Plane Rotation of the Patella: Lateral Patellofemoral Angle

Definition

Axial plane rotation of the lateral patella facet defines lateral patellar tilt.
Normal PFA >8° opening laterally
Abnormal PFA <8° or angle opening medially

Indications

Patellofemoral maltracking. Abnormal patellar tilt is more frequently symptomatic than isolated lateralisation. Abnormal tilt without lateral translation is known as excessive lateral pressure syndrome (ELPS). In cases of severe ELPS, the patella may indeed be medially subluxed due to the tightness of the lateral retinaculum.

Techniques

Axial radiograph of the knee
Axial image through the mid-patella—CT
Axial image through the mid-patella—MRI

Full Description of Techniques

The lateral patellofemoral angle measurement was originally described on axial knee radiographs at 20 of knee flexion (Laurin et al. 1978). This was defined as the angle between a line drawn tangential to the lateral patellar facet and a line joining the anterior summits of the medial and lateral femoral condyles (Fig. 14.17).

On CT and MRI studies, the lateral patellofemoral angle may be measured similarly to Laurin's description, with reference to a line across the anterior summits of the femoral condyles, or alternatively it may be measured with reference to a line across the posterior condyles (Schutzer et al. 1986; Wittstein et al. 2006). It is measured at the level of the patellar midpoint as referenced on sagittal imaging (Fig. 14.18).

Reproducibility/Variation

The originators of the lateral patellofemoral angle measurement found that on axial radiographs, the lateral patellofemoral angle opened laterally in 97% of normal knees (Fig. 14.19) and was parallel in 3%,
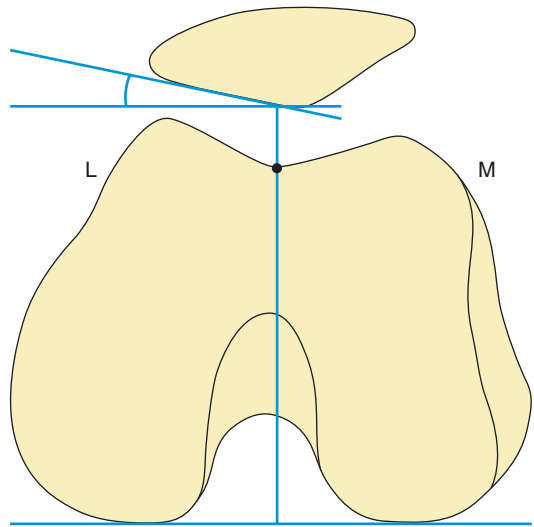
Fig. 14.18 Measurement of the lateral patellofemoral angle on axial CT or MR imaging of the knee
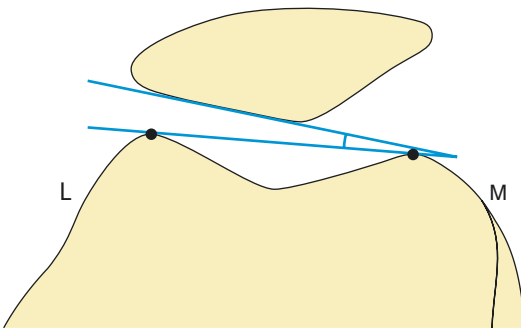
Fig. 14.17 Measurement of the lateral patellofemoral angle on the axial knee radiograph
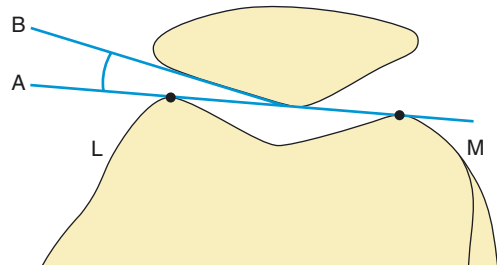
Fig. 14.19 Normal patellofemoral angle opening laterally

whilst in patients with recurrent patellar subluxation, the angle was parallel in 80% and opened medially in 20% (Laurin et al. 1979) (Fig. 14.20). By contrast in a study of 137 knees with symptoms of anterior pain or instability, 97% of knees had a lateral patellofemoral angle which opened laterally (normal) on axial radiographs taken at 25 of knee flexion (Davies et al. 2000). This discrepancy may relate to the different patient groups. In Laurin's study, the patients had recurrent patellar subluxations and therefore may be significantly more likely to have a gross tracking abnormality than in Davies' study in patients with "symptoms of knee pain or instability". In a more recent study of 30 asymptomatic volunteers, the 95% confidence interval for the lateral patellofemoral angle measured on axial knee radiographs at 30° of knee flexion was 8–25° (Alemparte et al. 2007).

In a CT study of lateral patellofemoral angle measured relative to the posterior femoral condyles, the authors found a lateral tilt of <7 degrees to be abnormal (Schutzer et al. 1986). In a different CT study of 43 normal adults in supine extension, the normal range for the lateral patellofemoral angle was found to be 11–26° (Reikeras and Hoiseth 1990). In a more recent study of CT scans of 30 normal volunteers at 15° of knee flexion without loading, the 95% confidence interval for the lateral patellofemoral angle was −6 to +23° where the tips of the anterior femoral condyles were used as a reference line and +1 to +29° where the posterior condyles were used as a reference
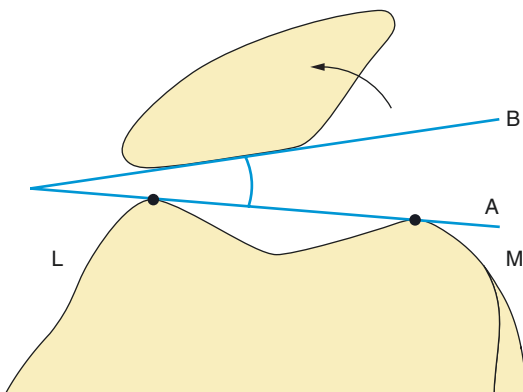
line (Alemparte et al. 2007). The authors found good interobserver reliability for both measurements, but commend the use of posterior condyles as a reference as this gives a likely threshold of approximately 0° between normal and abnormal.

In a CT study of multiple parameters of patellofemoral alignment and trochlear dysplasia, the lateral patellofemoral angle, using the anterior summits of the femoral condyles as the reference line, was found to be the most reliable overall in terms of inter- and intraobserver correlation (Delgado-Martinez et al. 2000). Interobserver correlation was slightly poorer when using the posterior condyles as a reference line.

However the authors do not state how images were chosen for measurement, and it may be that all measurements were done on a single axial slice, which may have included the mid-patella but may not have shown the posterior condyles well. Results for this parameter could potentially be improved therefore, if the image with the largest condylar AP width is used to place the posterior condylar line, and this line is then transferred (on a workstation) to the appropriate mid-patellar image for identifying the lateral facet.

Clinical Relevance/Implications

Lateral patellofemoral angle with respect to the posterior femoral condyles has also been used successfully in kinematic MRI studies to demonstrate differences in patellar tracking in patients with clinical patellar instability versus controls (Brossmann et al. 1993; Muhle et al. 1999b). Measurement of the lateral patellofemoral angle, relative to the posterior femoral condyles, on supine motion that triggered dynamic MRI studies has been shown to correlate well with a semiquantitative assessment of patellar tilt on arthroscopic examination (Brossmann et al. 1994). A static MRI study of knees in relaxed extension used the anterior condyles as a reference line and showed a decreased lateral patellofemoral angle in patients with anterior knee pain clinically suspected to be due to malalignment compared with controls (Wittstein et al. 2006).

Fig. 14.20 Abnormal patellofemoral angle opening medially

An MRI study of knee osteoarthritis showed that decreasing lateral patellofemoral angle was correlated with increasing lateral patellofemoral compartment cartilage loss and bone marrow lesions (Kalichman et al. 2007b).

Analysis/Validation of Reference Data

A potential drawback to the use of the lateral patellofemoral angle is its dependence on the shape of the lateral patellar facet which may vary, especially in patients with maltracking. Furthermore, unlike the patellar tilt angle (below),

it does not directly correlate with the clinical evaluation of tilt which identifies the position of the whole bone. Additionally, the measurement is somewhat counterintuitive in that the value of the lateral patellofemoral angle reduces as clinical tilt increases.

Conclusion

The lateral patellofemoral angle has been shown to be a useful measure of axial plane patellar rotation for both axial radiographs and cross-sectional imaging.

14.10 Axial Plane Rotation of the Patella: Patellar Tilt Angle

Definition

The angle between a line drawn along the widest mediolateral equatorial width of the patella and the reference line passing along the anterior summits of the femoral condyles
Normal 2 degrees +/– 2 degrees
Abnormal >5°

Indications

Patellofemoral maltracking

Techniques

Axial radiograph
Axial mid-patella image—CT
Axial mid-patella image—MRI

Full Description of Technique

The patellar tilt angle, measured on the axial radiograph of the knee, is defined as the angle between a line drawn along the widest mediolateral width of the patella and a reference line. The reference line may be taken as the horizontal (provided that the film is taken with the foot in the anatomical parasagittal plane and the film cassette is parallel to the floor) (Grelsamer et al. 1993). The reference line may alternatively be taken as a line joining the anterior summits of the femoral condyles (Fig. 14.21).

On CT and MRI studies, the patellar tilt may be measured similarly with reference to a line across the anterior summits of the femoral condyles (Sasaki and Yagi 1986), or alternatively it may be measured with reference to a line across the posterior condyles (Fig. 14.22) (Fulkerson et al. 1987; Grelsamer et al. 2008).

Reproducibility/Variation

For axial radiographic evaluation, the use of the horizontal, as a reference line, avoids the use of the anterior femoral condyles which may be dys-
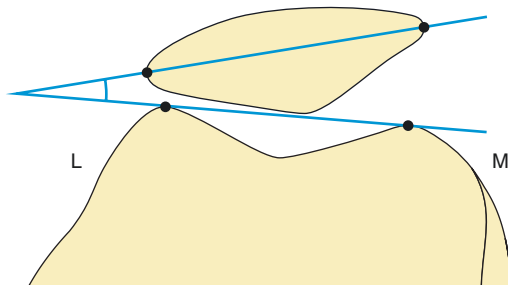
Fig. 14.21 Measurement of the patellar tilt angle on the axial radiograph of the knee
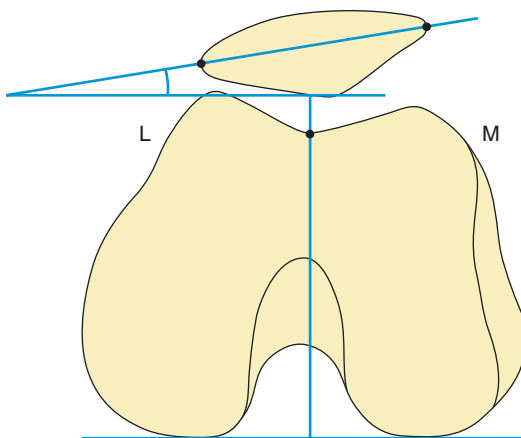
Fig. 14.22 Measurement of the lateral patellofemoral angle on axial CT or MR imaging of the knee

plastic in unstable knees but potentially introduces significant measurement error if the radiographic technique is not optimal.

In a CT study, patellar tilt angle, measured with respect to a reference line between the anterior summits of the femoral condyles, showed good intra- and interobserver correlations, although it did not perform quite as well as the lateral patellofemoral angle (Delgado-Martinez et al. 2000). More recently, a CT study of 30 normal volunteers, in 15 of knee flexion without loading, showed good interobserver reliability for measurement of the tilt angle using the posterior condyles as the reference line (Alemparte et al. 2007). The authors found the 95% confidence interval for a normal measurement of patellar tilt to be −22° to −1° (where a negative angle implies medial opening). In a CT study of patients with patellofemoral pain, measurements of patellar tilt using three different reference lines

were correlated with measurements of femoral and tibial rotation (Lin et al. 2008). The authors found that measurements of patellar tilt using the horizontal plane (as per Grelsamer et al. 1993) or using the posterior femoral condyles (as per Fulkerson et al. 1987) varied with femoral and tibial rotation. Where a line across the anterior femoral condyles was used (as per Sasaki and Yagi 1986), the patella tilt measurement was independent of femoral or tibial rotation measurements.

Clinical Relevance/Implications

In a recent study, MRI which measured the patellar tilt angle, with the posterior femoral condyles as a reference line, was found to correlate well with clinically measured patellar tilt, and the authors recommended using an MR tilt angle of 10 degrees as the upper limit of normal (Grelsamer et al. 2008). A surgical study has shown that medial patellofemoral ligament reconstruction significantly improved both clinical symptoms and patellar tilt in patients with previous patellar dislocation (Schottle et al. 2005). In a recent study utilising an erect weightbearing open MRI system, patients with patellofemoral pain were

shown to have an increased patellar tilt angle compared with controls, and the tilt reduced with the use of a brace (Draper et al. 2008).

Analysis/Validation of Reference Data

The patellar tilt angle has some potential advantages over the lateral patellofemoral angle as a measure of axial plane patellar rotation. First, it does not rely on the morphology of the lateral patellar facet which may be dysplastic in patients with patellar instability. Second, it is akin to the measure of clinical tilt, and its value increases with increasing clinical tilt.

A potential drawback is that identification of the medial and lateral patellar borders may be problematic particularly in patients who may have had retinacular injury at the patellar attachment or in patients with medial patellar impaction defects due to previous patellar dislocation.

Conclusion

The patellar tilt angle is a useful measure of axial plane patellar rotation and has been used in passive and dynamic studies.

14.11   Superoinferior Displacement of the Patella: Patellar Height: Patellotibial Measurements

Patella alta is a frequent finding on examination of patients with patellar instability. There are four main patellotibial measurements which indirectly assess the patellofemoral relationships and biomechanics (Philips et al. 2010): *the Insall-Salvati ratio*, *Caton-Deschamps index*, *Grelsamer-Meadows* (*modified Insall-Salvati*) *index* and *Blackburne-Peel index*.

Definitions

Insall-Salvati ratio. The ratio of patellar ligament length to maximal diagonal patellar length

Caton-Deschamps index. The ratio of the distance between the inferior margin of the articular surface of the patella and the anterosuperior angle of the tibia and the length of the patellar articular surface

Grelsamer-Meadows index. The ratio of the distance between the inferior margin of the patellar articular surface to the tibial tubercle and the length of the patellar articular surface

Blackburne-Peel index. The ratio of the distance between the inferior margin of the patellar articular surface and the anterior extension of the tibial plateau line and the length of the patellar articular surface

Indications

Patellofemoral maltracking/anterior knee pain

Techniques

Lateral radiograph of the knee
Sagittal MR image through the patellar ligament and patella

Full Description of Techniques

Insall-Salvati Ratio
On a lateral radiograph performed with the knee in semiflexion, the patellar ligament is measured along its posterior margin from its
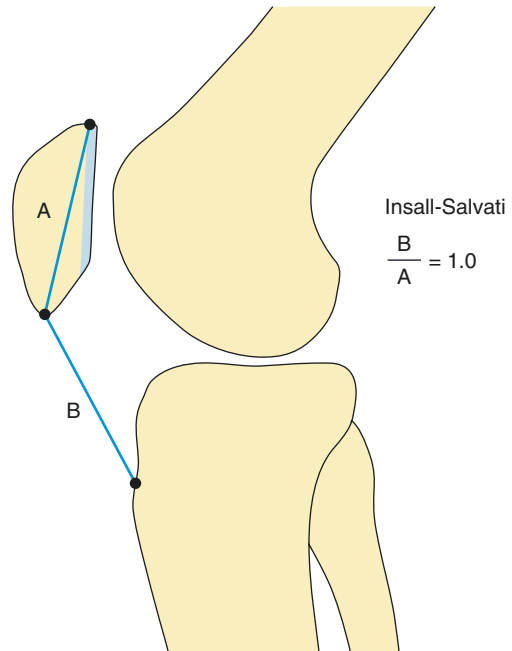
Fig. 14.23 The Insall-Salvati ratio

origin at the inferior patellar pole to its insertion at the tibial tubercle (Fig. 14.23). There is usually a clearly defined notch at the tibial tuberosity representing the insertion point which may be used. The patellar length is then measured as the longest diagonal length of the patella on the lateral view. The Insall-Salvati ratio is defined as the ratio of the patellar ligament length to the patella length (Insall and Salvati 1971). Traditionally, two standard deviations above or below normal lead to a diagnosis of patella alta or baja, respectively.

Normal radiographic range 1.02 ± 0.13
Patella alta >1.2
Patella baja <0.8

On MRI, the Insall-Salvati ratio may be measured using a mid-sagittal plane image through the patellar ligament and (if necessary a different) mid-sagittal plane image through the patella (Miller et al. 1996). The patella ligament length is measured as the distance from posterior margin of the patellar attachment of the patellar ligament to the inferior patellar pole to the proximal margin of the ligament insertion onto the tibia. A straight line measurement is used even where the ligament is bowed or wavy. The patellar length is

measured as the maximal oblique diameter of the patella in its mid-sagittal plane. The ratio of patellar ligament to patellar length gives the MRI equivalent of the Insall-Salvati ratio.

Caton-Deschamps Index

Since the Insall-Salvati index may be falsely reduced in patients who have a long non-articulating inferior patellar facet, whilst it is really the height of the articular surface of the patellar which is of concern, other indices have been developed to avoid this problem. The most popular of these, the Caton-Deschamps index, is defined as the distance from the anterosuperior angle of the tibia to the inferior margin of the patellar articular surface, divided by the length of the retropatellar articular surface (Fig. 14.24) (Caton et al. 1982).

Normal 0.6–1.3
Patella alta >1.2
Patella baja <0.6

Grelsamer-Meadows Index

As an alternative to this, the Grelsamer-Meadows index, also known as the modified Insall-Salvati index has been described to
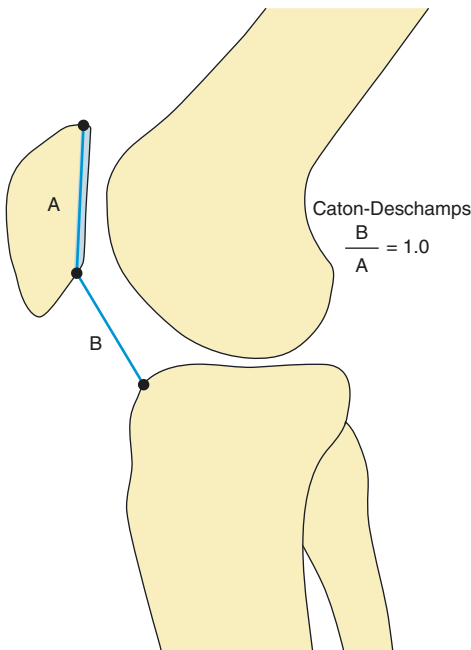
Fig. 14.24 The Caton-Deschamps index
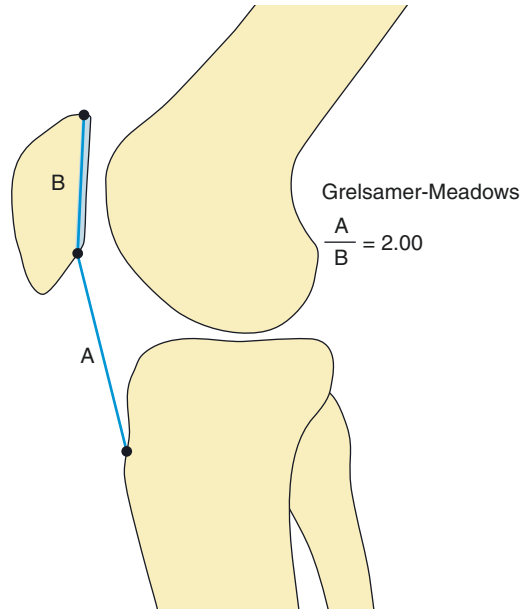
Fig. 14.25 The Grelsamer-Meadows (modified Insall-Salvati) index

diminish the potential errors that arise from morphological patellar variations (Fig. 14.25). This index is the ratio between the distance from the inferior margin of the patellar articular surface to the distal insertion of the patellar ligament at the tibial tuberosity, divided by the length of the patellar articular surface (Grelsamer and Meadows 1992).

This is similar to the Caton-Deschamps index but avoids the use of the anterosuperior angle of the tibia which may be absent in some 10% of cases.

Normal <2
Patella alta >2

Blackburne-Peel Index

In this measurement, the length of the patellar articular surface is used again for the ratio denominator, but the tibial tubercle is exchanged with the tibial plateau as the tibial reference point (Blackburne and Peel 1977). The tibial plateau line runs parallel to the plateau joining the anterior and posterior margins of the concave medial tibial plateau (Fig. 14.26).

Normal 0.8–1.0
Patella alta >1.0
Patella baja <0.8
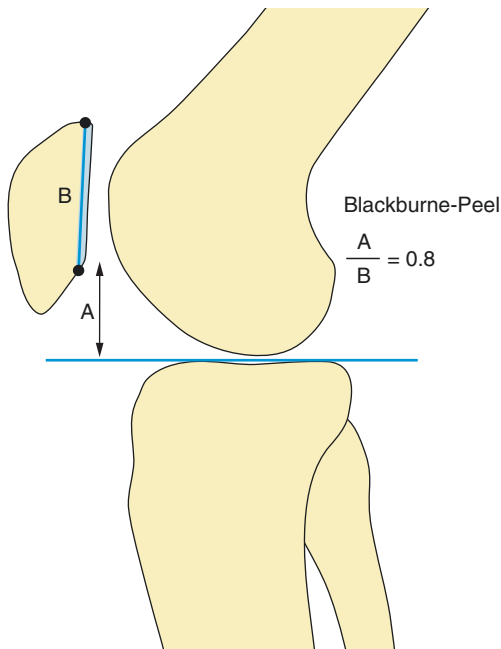
Fig. 14.26 The Blackburne-Peel index

Reproducibility/Variation

The upper limit of normal for the Insall-Salvati ratio has been given as 1.2 (Insall and Salvati 1971), 1.25 (Grelsamer and Meadows 1992) or 1.33 (Alemparte et al. 2007). In one report, a higher upper limit of normal was found for asymptomatic females (1.37) compared with males (1.25) (Alemparte et al. 2007). Low interobserver variability has been shown for the Insall-Salvati ratio (Seil et al. 2000), and it does not appear to be sensitive to the angle of knee flexion. In the paediatric age group, the Insall-Salvati index and the Grelsamer-Meadows index can be spuriously increased producing a pseudopatella alta due to incomplete ossification of the patella and tibial tuberosity (Figs. 14.27 and 14.28).

The Caton-Deschamps ratio has a similar upper limit of normal given as 1.2 or 1.24 (Alemparte et al. 2007). The Grelsamer-Meadows index has an upper limit of normal of 2, with 97% of asymptomatic controls found to have a ratio below this level (Grelsamer and Meadows 1992).

The MRI measurement of the Insall-Salvati ratio has an upper limit of 1.3 (Miller et al. 1996). Shabshin et al. (2004) have suggested that the upper and lower limits of normal are 1.5 and 0.74 (1.52 females and 1.32 for males).

Fig. 14.27 Measurement of the Insall-Salvati ratio on the lateral radiograph of the knee. The ratio is calculated as the ratio of the patella ligament length to the patellar length

Fig. 14.28 Measurement of the modified Insall-Salvati ratio (Grelsamer and Meadows) on the lateral radiograph of the knee. The ratio is calculated as the distance from the inferior margin of the patellar articular surface to the distal insertion of the patellar ligament at the tibial tuberosity, divided by the length of the patellar articular surface

Clinical Relevance/Implications

In a study of 160 patients with patellofemoral pathology and 140 without, the modified Insall-Salvati index as measured on lateral radiographs was found to be higher in knees with patellofemoral pathology than in those without (Grelsamer and Meadows 1992).

In a recent supine weightbearing MRI study of subjects with and without patella alta as defined by an MRI measurement of the Insall-Salvati index of greater or less than 1.2, the authors found that patients with patella alta had significantly greater lateral patella tilt and displacement at 0 of knee flexion and had significantly lower patellofemoral cartilage contact areas at all degrees of knee flexion (Ward et al. 2007). In a different study of patients with anterior knee pain clinically suspected to be due to patellofemoral maltracking, MRI measured patella alta was found to be more common in patients compared to asymptomatic controls (Wittstein et al. 2006).

An MRI study of patients with knee osteoarthritis found that increasing MRI measured patella ligament/patella length ratio was associated with increasing areas of cartilage loss and bone marrow lesions in the patellofemoral joint (Kalichman et al. 2007a, b). The authors point out that with increasing patellar ligament length, the mechanical advantage afforded by the patella to the functional lever arm of the extensor mechanism would diminish, and this would result in increased patellofemoral contact pressures, which in turn would be expected to predispose to osteoarthritis.

Analysis/Validation of Reference Data

In all of the methods described above, care needs to be given to accurately defining the bony landmarks as they are not always easy to identify. The inferior margin of the patellar articular surface is not easily identifiable, and the interobserver variation of methods using this denominator is higher than the Insall-Salvati ratio. In addition to this problem, the size of the patella can vary, and pathological bony overgrowth (e.g. osteoarthritis) can distort the native anatomy. The methods which use the tibial tubercle as one of the bony landmarks also assume it lies at a constant distance inferior to the tibial plateau.

Overgrowth of the tibial tubercle from Osgood-Schlatters disease will also create difficulties in defining the point of measurement. These issues can lead to both inter- and intraobserver errors. The improved soft tissue definition of digital radiography allows accurate depiction of the patellar ligament which helps to reduce the problem. In addition, radiographic Insall-Salvati measurements have been shown to have a high correlation with absolute anatomical measurements in cadaveric studies (Schlenzka and Schwesinger 1990). Furthermore, despite the known difficulties in the accurate depiction of landmarks, Berg et al. (1996) found the Caton-Deschamps index to be very reproducible and accurate but closely behind the Blackburne-Peel index with reference to the interobserver error. Recently, a study has assessed discrimination validity of the measurement methods for patellar height (Smith et al. 2011). The radiographic methods of Caton-Deschamps, Blackburne-Peel, Insall-Salvati and MRI method of Insall-Salvati have shown good discrimination validity with a statistically significant difference between the healthy control and patellar instability cohorts ($p<0.0001$) (Smith et al. 2011).

Conclusion

Increased patellar height is an important correlate of patellofemoral pathology and of maltracking disorders in particular. Patellotibial measurements have been the most widely accepted measurements of patellar sagittal position, both because of the use of readily identifiable osseous landmarks and because of the value of surgical techniques for tibial tuberosity distalization. The Insall-Salvati ratio is the most popular of the described measurements. It has been shown to be a reliable measure and may be relatively insensitive to the degree of knee flexion, and it has been successfully applied to MRI as well as lateral radiographs. Of the other, more recently described indices, the modified Insall-Salvati index (Grelsamer and Meadows 1992) shows most promise in that, like the Insall-Salvati index, it uses reliable bony landmarks but avoids inclusion of the inferior non-articulating facet of the patella which may confound the measurement. However, the reliability and reproducibility of the Caton-Deschamps and Blackburne-Peel indices have been more extensively studied in the literature.

14.12 Superoinferior Displacement of the Patella: Patellar Height: Patellofemoral Measurements

Patellofemoral (rather than patellotibial) biomechanics holds the key in explaining anterior knee pain. These measurements are deemed direct measurements as they refer to the patellofemoral rather than the patellotibial measurements which are regarded as the indirect measurements. Some direct methods employ the intercondylar notch as a reference line (Blumensaat's line), but as this does not have a fixed angle with the femoral axis, it is not a reliable landmark. Other measurements have been proposed using femoral condylar landmarks, but once again, this is prone to error due to normal size variations. MRI techniques have also been tried using chondral rather than bony landmarks.

Definitions

Patellotrochlear Index. The length of trochlear articular surface which overlaps the patellar articular surface is measured on the sagittal MR image through the thickest patellar cartilage/longest patellar length. This is divided by the length of the patellar articular surface (Biedert and Albrecht 2006).

Patellar Articular Overlap. Measurements as per patellotrochlear index (above) but instead of measuring a ratio, the absolute length of trochlear cartilage overlapping the patellar is taken (Munch et al. 2016).

Sagittal Patellofemoral Engagement. The length of the patellar articular surface is measured on the sagittal MR image with the longest patellar cartilage. This measurement line is transferred onto the sagittal MR image with the most proximally extending trochlear cartilage, and the length of trochlear articular surface overlapping the patellar cartilage measurement line is recorded. The ratio of the trochlear overlap measurement to the patellar cartilage length measurement gives the sagittal patellofemoral engagement (Dejour et al. 2013) (Fig. 14.29).

Fig. 14.29 Measurement of the patellotrochlear index and patellar articular overlap. Intermediate weighted sagittal MR image of the knee. The image is chosen with the longest sagittal length of patellar articular cartilage and this length is measured (P). Parallel to this line, the length of overlapping cartilage is measured (T). Patellar articular overlap is measured as the length T in mm. Patellotrochlear index is measured as the ratio T/P

Indications

Patellofemoral maltracking/anterior knee pain.

Technique

Sagittal MRI of the knee.

Full Description of Techniques

Patellotrochlear Index: This is described as measured on sagittal knee MR performed in 0° flexion with the foot in 15° external rotation and the

quadriceps consciously relaxed. Parameters are measured on the single midline sagittal section through the patellar which shows the thickest patellar articular cartilage and longest patellar bone.

The superoinferior length of the patellar cartilage is measured. On the same MR image, measured parallel to the patellar articular cartilage length measurement, the trochlear overlap is measured as the distance from the superior margin of the trochlear cartilage to the level of the inferior margin of the patellar articular cartilage. The ratio of trochlear overlap to the patellar cartilage length is calculated.

Normal values not yet determined. Suggested **normal >12.5 %; abnormal <12.5 %**.

Patellar Articular Overlap: This is described as measured on sagittal knee MR performed at rest in standard knee coils. The measurement is made on the midline sagittal section through the patella which shows the thickest patellar articular cartilage and longest patellar bone.

The length of overlap between trochlear cartilage and patellar cartilage is measured on this single slice, using a measurement line parallel to the patellar subchondral surface.

Normal ≥6 mm
Abnormal <6 mm

Sagittal Patellofemoral Engagement: This is described as measured on standard non-weight-bearing MRI with the knee close to full extension, and 2-mm sagittal images.

The length of the patellar articular cartilage is first measured on the sagittal MR image, where the patella shows the longest articular cartilage. This measurement line is then transferred to the
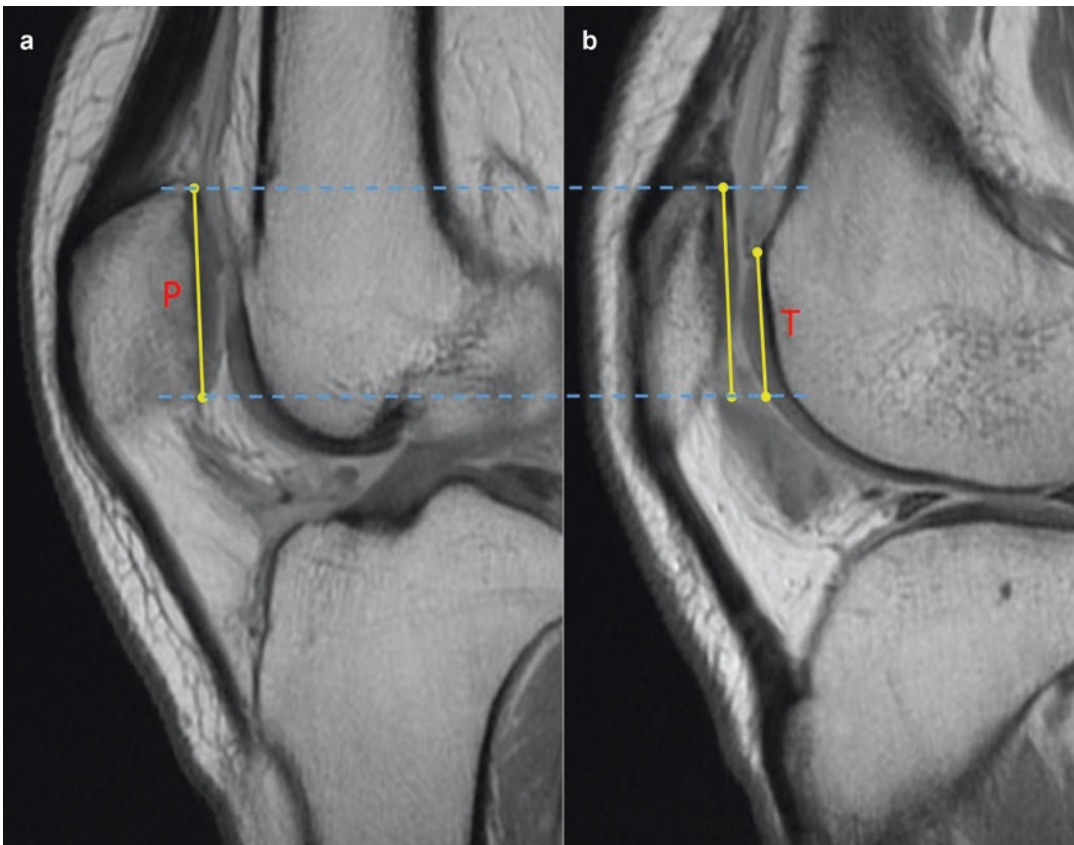
Fig. 14.30 Measurement of sagittal patellofemoral engagement. Intermediate weighted sagittal MRI of the knee. The image (**a**) with the longest sagittal length of patellar articular cartilage is chosen and this length is measured (P). The line P is then transferred to the sagittal image (**b**) on which the femoral trochlear cartilage is seen to extend most proximally. Measuring parallel to line P, the length of overlapping trochlear cartilage is measured (T). Sagittal patellofemoral engagement is calculated as the ratio T/P

sagittal MR image on which the femoral trochlear cartilage is seen to extend most proximally. On this second image, measuring parallel to the patellar cartilage measurement line, the trochlear overlap is measured as the distance from the superior margin of the trochlear cartilage to the inferior margin of the patellar cartilage length measurement. The ratio of trochlear overlap to patellar cartilage length is calculated (Fig. 14.30). **Normal >0.45**
Abnormal <0.45

Reproducibility/Variation

Measurement of the patellotrochlear index showed a good interobserver reliability in patients without patellofemoral pathology (Biedert and Albrecht 2006), and good inter- and intra-observer reliability in patients with patellofemoral dysplasia (Barnett et al. 2009). The patellar articular overlap showed interobserver reliability of >0.9 in patients with and without patellar instability (Munch et al. 2016). Inter-/intra-observer reliability was not assessed for sagittal patellofemoral engagement (Dejour et al. 2013).

Clinical Relevance/Implications

The patellotrochlear index and patellar articular overlap differ from sagittal patellofemoral engagement in that the former two measures utilise a single sagittal MR image for all measurement lines whilst in the latter the patellar measurement must be transferred to a separate image for the trochlear measurement. Whilst the former two measures have the advantage of practicality, requiring no special software tools, the latter accounts for the fact that in knees with a subluxed patella the longest trochlear and patellar cartilage may be seen on widely separated sagittal images.

The described MRI methods for assessing sagittal plane patellar position with reference to patellar and trochlear chondral landmarks have the potential for greater clinical relevance than patellotibial measurements, as patellotrochlear

chondral engagement is so critical for patellar tracking. The lack of correlation between patellotibial and patellofemoral measures of sagittal patellar position has been reported (Barnett et al. 2009; Dejour et al. 2013). In their study, Dejour et al. (2013) reported a group of patients with known previous patellar dislocation and found that some who had patella alta according to standard patellotibial measures had a normal sagittal patellofemoral engagement, possibly suggesting that tibial tuberosity distalization in such patients may be unnecessary. Equally, some known dislocators without patella alta on patellotibial measures showed a reduced sagittal patellofemoral engagement, possibly suggesting that tibial tuberosity distalization may have a role. The authors acknowledge that there may be important effects on measurements depending on the degree of knee flexion and quadriceps activation, and this certainly needs further study to validate the use of such measures more widely.

Analysis/Validation of Reference Data

Patellotrochlear index and patellar articular overlap have shown good inter- and intra-observer reliability but reliability of sagittal patellofemoral engagement requires further study at the present time. Although suggested normal ranges have been provided above, these are based on relatively limited samples in the original papers and further studies are needed to better define appropriate cut-off values for use in clinical practice.

Conclusion

Patellofemoral MR imaging measurements of sagittal plane patellar position hold the promise of greater clinical relevance than standard patellotibial measurements because of the direct measurement of patellofemoral chondral engagement which is critical to patellar stability. These measures require further validation to confirm their reliability and clinical utility, but are increasingly used as an adjunct to the more standard patellotibial measures.

14.13 Superoinferior Displacement of the Patella: Paediatric Measurements

Up until 1986, there was no acknowledgement that adult patellar height ratios cannot be applied accurately to the paediatric age group due to incomplete ossification. Micheli et al. (1986) were the first to investigate the effects of the growth spurt on the development of patella alta. They performed single AP serial radiographs at 6–12 month intervals over a 10 year period. The length of the patellar ligament was calculated as the distance between the inferior pole of the patella and the tibial plateau. A value greater than zero denoted patella alta, and all their 19 patients had a positive value. The error due to incomplete ossification explained in part the findings. Subsequent studies confirmed that all young children have a high Insall-Salvati ratio, which decreased with age assuming adult values at adolescence at around 10 in girls and 12 in boys with full ossification being reached at 15 and 17, respectively (Walker et al. 1998). To eliminate the error that results from incomplete ossification, Koshino and Sugimoto (1989) used the midpoints of the femoral and tibial physes to calculate the ratio between the patellotibial distance and the tibiofemoral distance (Fig. 14.31). The method is not affected by knee flexion in the range of 30–90 degrees. When compared with the Insall-Salvati measurement calculated on the same patients, the authors also indicated that 67% would have erroneously been classified as patella alta. In this novel method, lines are first very carefully drawn on a lateral radiograph through the distal femoral and proximal tibial physes and their midpoints determined. The longest diagonal line of the patella is then drawn and its midpoint determined. The ratio of the distance between the patellar line midpoint to the tibial physeal line midpoint and the line connecting the femorotibial physeal midpoints is then calculated (Fig. 14.32).

Normal 0.99–1.20
Patella alta >1.20
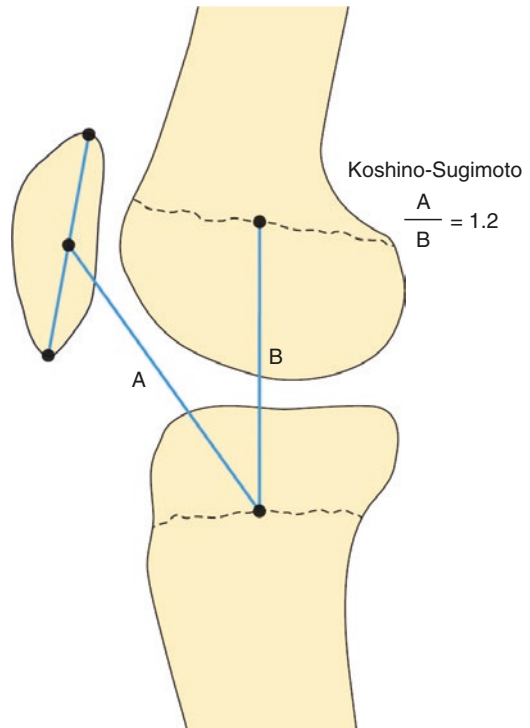
Fig. 14.31 Koshino-Sugimoto (1989) ratio. The measurement of the line *A* joining the midpoint of the patella to the midpoint of the tibial physes is divided by the interphyseal distance *B* calculated by joining the midpoints of the femoral and tibial physes
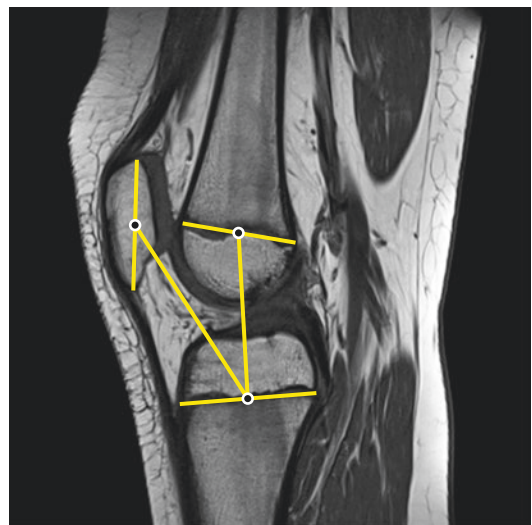
Fig. 14.32 Koshino-Sugimoto ratio measured on sagittal MR image

14.14 Tibial Tubercle-Trochlear Groove Distance

Definition

The axial plane distance between the deepest point of the trochlea and the apex of the tibial tubercle measured parallel to a posterior condylar reference line

Indications

Patellofemoral maltracking
Normal TT-TG distance <15 mm
Abnormal TT-TG distance >20 mm
Borderline TT-TG distance 15–20 mm

Techniques

Axial CT sections through the trochlea and tibial tubercle
Axial MRI sections through the trochlea and tibial tubercle

Full Description of Techniques

Axial CT or MR images are chosen through the deepest point of the trochlea groove and through the apex of the tibial tubercle (Dejour et al. 1994). The two images are superimposed, and a line joining the posterior margins of the posterior femoral condyles is drawn as a reference line. Two perpendiculars are then dropped from this reference line, one through the deepest point of the trochlear groove and the second through the most anterior point of the tibial tubercle. The shortest distance between these two perpendiculars is measured as the trochlea-tubercle distance (Fig. 14.33).

For MRI studies, there is a controversy regarding which axial image is best chosen for trochlear measurement (Schottle 2007). In one study, the image with the greatest AP width of the femoral condyles was chosen (Wittstein et al. 2006). Elsewhere the most superior image on which cartilage covers the trochlear surface has been used, on the basis that the instability tends to be most pro-
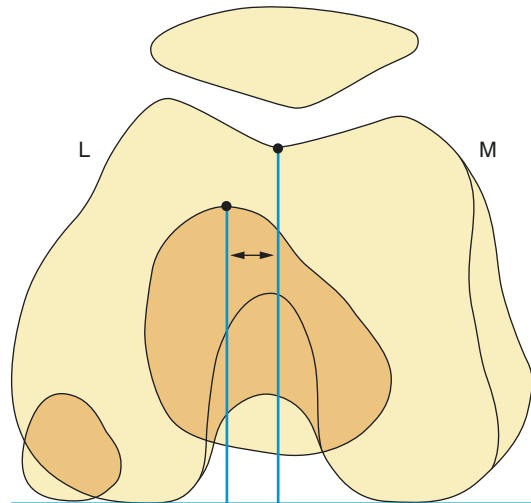
Fig. 14.33 Measurement of the trochlea-tubercle distance on axial CT or MR imaging of the knee. Axial images of the trochlear groove and the tibial tuberosity are superimposed. Perpendiculars are dropped from the posterior intercondylar line through the deepest point of the trochlear groove and the apex of the tibial tuberosity, and the distance between the two lines is measured

nounced near full extension, when the patella lies superiorly relative to the trochlear (Schottle et al. 2006).

A slight modification of the technique which has been shown to have better interobserver reliability is performed without superimposition of images (Koeter et al. 2007b). In this technique, the posterior condylar reference line and its perpendicular through the deepest point of the trochlear are drawn on the appropriate axial image, and, on a workstation, the lines are copied to the image through the tibial tubercle for the measurement to be completed. The avoidance of overlapping images reduces the potential error in placing measurement lines.

A modification of the technique has been suggested in which cartilaginous and patellar ligament rather than bony landmarks are used (Schottle et al. 2006). For this measurement, the most superior axial image on which cartilage covers the medial and lateral trochlea is chosen, and the deepest point of the overlying cartilage is taken as the trochlear landmark. For the tibial tubercle landmark, the image is

chosen which shows a complete attachment of the patellar ligament to the tubercle, and the landmark is taken as the midpoint of the tendon at this level. The authors term this the "functional" tibial tuberosity-trochlear groove distance and suggest that this may be measured on both CT and MRI.

Reproducibility/Variation

Dejour et al. (1994) used 20 mm as the upper limit of normal for the trochlear-tubercle distance, as 56% of patients with patellar instability but only 3% of controls had a measurement >20 mm. Thus a threshold of 20 mm produces a specific but poorly sensitive test for patellar instability. Wittstein et al. (2006) found that patients with anterior knee pain had a significantly greater trochlear-tubercle offset of 12.6 ± 1.1 mm compared with controls (9.4 ± 0.6 mm) on MRI. They suggested an upper limit of normal of 10 mm for the measurement. In a recent study of knee MRI in patients without anterior knee symptoms, the normal offset in males and females was measured at 10 ± 1 mm (Pandit et al. 2011). Given this somewhat conflicting literature, a cut-off of 15 mm is often chosen for the measurement as a compromise between sensitivity and specificity.

In a study of patients with patellar instability, 36 patients underwent CT examination on two separate occasions, and trochlea-tubercle distances were measured (Lustig et al. 2007). A mean difference between the two measurements of 3.2 mm (range 0–13 mm) was found. The authors suggest a number of possible sources of error. First, the choice of axial image through the deepest part of the trochlea and through the tibial tubercle was prone to some variation. For the tibial tubercle, the authors advocate choosing the first image on which there is no fat between the tibial tubercle and the patellar ligament. Second, some of the patients had markedly dysplastic trochlea grooves, making identification of the deepest point difficult. In a comparison of trochlea-tubercle distance mea-

surement between CT and MRI, 12 knees underwent both imaging modalities (Schottle et al. 2006). The authors found an excellent correlation between the two modalities and between different observers for both Koeter's technique and for the "functional" measurement (see above). More recently, one study (Camp et al. 2013) found that MR measurements were on average 2 mm less than CT measures of trochlear-tubercle distance.

The degree of knee flexion may also have a significant effect on the trochlear-tubercle distance. Tanaka et al. (2015) found that trochlear-tubercle distance reduced by almost 1 mm for every 5 degrees of increased knee flexion.

Clinical Relevance/Implications

The trochlea-tubercle distance provides a measure of the lateral pull on the patella, which, if not counteracted by the vastus medialis obliquus, will tend to result in lateral subluxation of the patella. Surgical correction of excessive tubercle lateralisation forms a part of common procedures for patellar instability, and this has been shown to reduce the trochlea-tubercle distance into the normal range (Lustig et al. 2007).

Analysis/Validation of Reference Data

The TT-TG distance is important in the full assessment of suspected patellofemoral derangement secondary to lateralisation or transposition of the tibial tubercle. It is essential in patients being considered for tibial tubercle osteotomy and refixation. Care should be addressed to the possibility that there may be other underlying contributing factors for increased TT-TG distance prior to surgery which includes femoral neck anteversion, external tibial torsion and subtalar pronation.

Conclusion

The trochlea-tubercle distance is an important measure of the lateral pull on the patellar and may be measured on CT and MRI studies.

14.15 Soft Tissue Injury: Vastus Medialis Obliquus (VMO) Insertion Level

Definition

A measurement of the level of the most distal insertion point of the VMO muscle

Indications

Patellofemoral maltracking

Techniques

Axial, coronal or sagittal MR images dependent on technique

Full Description of Technique

On axial MR images, the superior border of the patella is considered to be the reference level, and the number of axial images below this, on which the most distal fibres of the VMO muscle are seen, gives a measure of the insertion level (Koskinen and Kujala 1992).

Other measurements of this parameter have been used which evaluate the insertion level relative to the medial femoral condyle rather than the patella (Elias et al. 2002; Sanders et al. 2001). On sagittal images, the shortest distance between the cortex of the medial femoral condyle and the VMO muscle is measured. Alternatively, the vertical distance from the adductor tubercle to the inferior margin of the VMO muscle along the plane of the adductor tendon may be used (Fig. 14.34).

Reproducibility/Variation

Little data is available on the reproducibility of this measurement. Relative to the superior border of the patella, the insertion level of the VMO was measured as 2–2.5 cm in control subjects and 0.5–2.5 cm in patients with previous patellar dislocation (Koskinen and Kujala 1992).

Relative to the medial femoral condyle, the shortest distance between the VMO and medial femoral condylar cortex was 0.05 cm (range

Fig. 14.34 Measurement of elevation of the vastus medialis obliquus (VMO) muscle on sagittal MR imaging of the knee. The shortest distance (*a*) between the cortex of the medial femoral condyle and the VMO muscle may be measured. Alternatively, the vertical distance from the adductor tubercle to the inferior margin of the VMO muscle (*b*) along the plane of the adductor tendon may be used

0.00–1.00 cm) in normal knees and 0.5 cm (range 0.0–3.1 cm) in patients with patellar dislocation.

VMO elevation vertically along the coronal plane of the adductor magnus tendon was 0.90 cm (range 0.10–2.50 cm) in normal knees compared with 2.2 cm (range 0.6–4.5 cm) in patients with patellar dislocation. For both measurements, the difference between dislocators and controls was significant (Elias et al. 2002).

Clinical Relevance/Implications

Patellar dislocation may be associated with injury to the medial patellofemoral ligament and stripping of the VMO muscle from its distal attachment to the adductor tubercle and medial retinaculum. Advancement of the VMO insertion has been used as part of the surgical realignment procedure for patients with recurrent patellar dislocation.

Measurements made relative to the superior patella rather than the medial femoral condyle may

have the disadvantage of being artificially increased in patients with a superior patella bony spur or patella alta. Conversely, a disadvantage of the measurements relative to the femoral condyle is that the VMO may insert onto the adductor magnus tendon and not the adductor tubercle in some normal knees; therefore, an origin lying proximal to the adductor tubercle may not necessarily be evidence of avulsion (Conlan et al. 1993). Also, muscle atrophy with increasing age may cause VMO elevation in the absence of prior lateral patellar dislocation. The additional presence of fluid or oedema between the VMO and the adductor tubercle may be firmer evidence of disruption.

Analysis/Validation of Reference Data

There is insufficient reference data to allow a reasonable assessment of measurement validation.

Conclusion

This may be a potentially useful parameter of VMO dysfunction in patients who have had previous patellar dislocation, but several different measurements have been proposed and the supporting literature for each is scant.

Summary

A large number of potential measurements have been used for patients with patellofemoral dysfunction. Measurements relating to cartilage pathology are discussed elsewhere. Measurements relating to patellofemoral instability are broadly divided into the following categories:

1. Lower limb alignment
   Hip anteversion
   Knee varus/valgus
   Q angle (clinical measurement)
   Trochlea-tubercle distance

2. Trochlear anatomy
   Sulcus angle
   Lateral trochlear inclination
   Trochlear groove depth
   Lateral/medial trochlear facet ratio

3. Measurements of patellar position
   (a) Mediolateral patella displacement
       Congruence angle
       Lateral patella displacement
       Bisect offset
   (b) Axial plane rotation of the patella
       Lateral patellofemoral angle
       Patella tilt angle
   (c) Superoinferior displacement of the patella
       Insall-Salvati ratio
       Caton-Deschamps index
       Grelsamer-Meadows index (modified Insall-Salvati)
       Blackburne-Peel index
       Patellotrochlear Index
       Patellar Articular Overlap
       Sagittal Patellofemoral Engagement

4. Soft tissue injury
   VMO insertion level

These measurements have been performed with conventional radiographs, CT and MRI, and some have been described with US. Measurements of patellar position are described in static studies in various degrees of flexion or dynamic studies involving continuous motion. Studies have been performed supine, prone or standing and with or without weightbearing. Additionally, studies have been performed on patients with a history of patellar dislocation or with patellofemoral pain syndrome which may or may not have a component of patellofemoral instability. As a result the literature on these measurements is often inconsistent. Nevertheless, many of the above described measurements are helpful in the assessment of patellofemoral instability.

References

Aglietti P, Insall JN, Cerulli G (1983) Patellar pain and incongruence I: measurements of incongruence. Clin Orthop Relat Res 176:217–224

Alemparte J, Ekdahl M, Burnier L (2007) Patellofemoral evaluation with radiographs and computed tomography scans in 60 knees of asymptomatic subjects. Arthroscopy 23:170–177

Barnett AJ, Prentice M, Mandalia V, Wakeley CJ, Eldridge JD (2009) Patellar height measurement in trochlear dysplasia. Knee Surg Sports Traumatol Arthrosc 17(12):1412–1415

Beaconsfield T, Pintore E, Maffuli N (1994) Radiological measurements in patellofemoral disorders. Clin Orthop Relat Res 308:18–28

Berg EE, Mason SL, Lucas MJ (1996) Patellar height ratios: a comparison of four measurement methods. Am J Sports Med 24:218–221

Biedert RM, Albrecht S (2006) The patellotrochlear index: a new index for assessing patellar height. Knee Surg Sports Traumatol Arthrosc 14(8):707–712

Blackburne JS, Peel TE (1977) A new method of measuring patellar height. J Bone Joint Surg Br 59(2):241–242

Brossmann J, Muhle C, Schroder C (1993) Patellar tracking patterns during active and passive knee extension: evaluation with motion triggered cine MR imaging. Radiology 187:205–212

Brossmann J, Muhle C, Bull CC (1994) Evaluation of patellar tracking in patients with suspected patellar malalignment: cine MR imaging vs arthroscopy. Am J Roentgenol 162:361–367

Brossmann J, Koch S, Schwarzenberg H (1996) Effect of intraarticular pressure on patellar position: computed tomography study in cadaveric specimens. Investig Radiol 31:67–71

Bull AMJ, Katchburian MV, Shih YF (2002) Standardisation of the description of patellofemoral motion and comparison between different techniques. Knee Surg Sports Traumatol Arthrosc 10:184–193

Camp CL, Stuart MJ, Krych AJ, Levy BA, Bond JR, Collins MS, Dahm DL (2013) CT and MRI measurements of tibial tubercle–trochlear groove distances are not equivalent in patients with patellar instability. Am J Sports Med 41:1835–1840

Carrillon Y, Abidi H, Dejour D (2000) Patellar instability: assessment on MR images by measuring the lateral trochlear inclination-initial experience. Radiology 216:582–585

Caton J, Deschamps G, Chambat P (1982) Les rotules basses—a propos de 128 observations. Rev Chir Orthop 68:317

Conlan T, Garth WPJ, Lemons JE (1993) Evaluation of the medial soft tissue restraints of the extensor mechanism of the knee. J Bone Joint Surg Am 75:682–693

Davies AP, Costa L, Donnell ST (2000) The sulcus angle and malalignment of the extensor mechanism of the knee. J Bone Joint Surg Br 82B:1162–1166

Davies AP, Bayer J, Owen Johnson S (2004) The optimum knee flexion angle for skyline radiography is thirty degrees. Clin Orthop Relat Res 423:166–171

Dejour H, Walch G, Nove-Josserand L, Guier CH (1994) Factors of patellar instability: an anatomic—radiographic study. Knee Surg Sports Traumatol Arthrosc 2:19–26

Dejour D, Ferrua P, Ntagiopoulos PG, Radier C, Hulet C, Rémy F, Chouteau J, Chotel F, Boisrenoult P, Sebilo A, Guilbert S, Bertin D, Ehkirch FP, Chassaing V, French Arthroscopy Society (2013) The introduction of a new MRI index to evaluate sagittal patellofemoral engagement. Orthop Traumatol Surg Res 99(8 Suppl):S391–S398

Delgado-Martinez AD, Estrada C, Rodriguez-Merchant EC (1996) CT scanning of the patellofemoral joint. The quadriceps relaxed or contracted? Int Orthop 20:159–162

Delgado-Martinez AD, Rodriguez-Merchan EC, Ballesteros R (2000) Reproducibility of patellofemoral CT scan measurements. Int Orthop 24:5–8

Draper C, Besier TF, Santos JM (2008) Using real-time MRI to quantify altered joint kinematics in subjects with patellofemoral pain and to evaluate the effects of a patellar brace or sleeve on joint motion. J Orthop Res 12:1–7

Dupuy D, Hangen DH, Zachazewski JE (1997) Kinematic CT of the patellofemoral joint. Am J Roentgenol 169:211–215

Egund N, Ryd L (2002) Patellar and quadriceps mechanism [book section]. In: Davies AM, Cassar-Pullicino VN (eds) Imaging of the knee, 1st edn. Springer, Berlin

Elias DA, White LM (2004) Imaging of patellofemoral disorders. Clin Radiol 59:543–557

Elias DA, White LM, Fithian DC (2002) Acute lateral patellar dislocation at MR imaging: injury patterns of medial patellar soft tissue restraints and osteochondral injuries of the inferomedial patella. Am J Roentgenol 225:736–743

Endo Y, Schweitzer ME, Bordalo-Rodrigues M (2007) MRI quantitative morphologic analysis of patellofemoral region: lack of correlation with chondromalacia patellae at surgery. Am J Roentgenol 189:1165–1168

Fairbank JC et al (1984) Mechanical factors in the incidence of knee pain in adolescents and young adults. J Bone Joint Surg Br 66:685–693

Fithian DC, Mishra DK, Balen PF (1995) Instrumented measurement of patellar mobility. Am J Sports Med 23:607–615

Fucentese SF, Schottle PB, Pfirrmann CW (2007) CT changes after trochleoplasty for symptomatic trochlear dysplasia. Knee Surg Sports Traumatol Arthrosc 15:168–174

Fulkerson JP, Schutzer SF, Ramsby GR (1987) Computerised tomography of the patellofemoral joint before and after lateral release or realignment. Arthroscopy 3:19–24

Grelsamer RP, Meadows S (1992) The modified Insall-Salvati ratio for assessment of patellar height. Clin Orthop Relat Res 282:170–176

Grelsamer RP, Bazos AN, Proctor CS (1993) Radiographic analysis of patellar tilt. J Bone Joint Surg Br 75B:822–824

Grelsamer RP, Newton PM, Staron RB (1998) The medial-lateral position of the patella on routine magnetic resonance imaging: when is normal not normal? Arthroscopy 14:23–28

Grelsamer RP, Weinstein CH, Gould J (2008) Patellar tilt: the physical examination correlates with MR imaging. Knee 15:3–8

Herrington L, McEwan I, Thom J (2006) Quantification of patella position by ultrasound scanning and its criterion validity. Ultrasound Med Biol 32:1833–1836

Inoue M, Shino K, Hirosi H (1988) Subluxation of the patella. J Bone Joint Surg Am 9:1331–1337

Insall J, Salvati E (1971) Patella position in the normal knee joint. Radiology 101:101–104

Insall J, Falvo KA, Wise DW (1976) Chondromalacia patellae. A prospective study. J Bone Joint Surg Am 58:1–8

Kalichman L, Zhang Y, Niu J (2007a) The association between patellar alignment and patellofemoral joint osteoarthritis features-an MRI study. Rheumatology 46:1303–1308

Kalichman L, Zhu Y, Zhang Y (2007b) The association between patellar alignment and knee pain and function: an MRI study in persons with symptomatic knee osteoarthritis. Osteoarthritis Cartilage 15:1235–1240

Katchburian MV, Bull AMJ, Shih YF (2003) Measurement of patellar tracking: assessment and analysis of the literature. Clin Orthop Relat Res 412:241–259

Koeter S, Bongers EM, de Rooij J (2006) Minimal rotation aberrations cause radiographic misdiagnosis of trochlear dysplasia. Knee Surg Sports Traumatol Arthrosc 14:713–717

Koeter S, Horstmann WG, Wagenaar FCBM (2007a) A new CT scan method for measuring tibial tubercle trochlear groove distance in patellar instability. Knee 14:128–132

Koeter S, Pakvis D, van Loon CJ (2007b) Trochlear osteotomy from patellar instability: satisfactory minimum 2-year results in patients with dysplasia of the trochlea. Knee Surg Sports Traumatol Arthrosc 15:228–232

Koshino T, Sugimoto K (1989) New measurement of patellar height in the knees of children using the epiphyseal line midpoint. J Pediatr Orthop 9:216–218

Koskiken SK, Taimela S, Nelkimarkka O (1993) Magnetic resonance imaging of patellofemoral relationships. Skelet Radiol 2:403–410

Koskinen S, Kujala UM (1992) Patellofemoral relationships and distal insertion of the vastus medialis muscle: a magnetic resonance imaging study in nonsymptomatic subjects and in patients with patellar dislocation. Arthroscopy 8:465–468

Kujala UM, Osterman K, Kormanao M et al (1989a) Patellar motion analysed by magnetic resonance imaging. Acta Orthop Scand 60:13–16

Kujala UM, Osterman K, Kormano M (1989b) Patellofemoral relationships in recurrent patellar dislocation. J Bone Joint Surg 71B:788–792

Laugharne E, Bali N, Purushothamdas S, Almallah F, Kundra R (2016) Variability of measurement of patellofemoral indices with knee flexion and quadriceps contraction: an MRI-based anatomical study. Knee Surg Relat Res 28(4):297–301

Laurin CA, Levesque HP, Dussault R (1978) The abnormal lateral patellofemoral angle. J Bone Joint Surg Am 60A:55–60

Laurin CA, Dussault R, Levesque HP (1979) The tangential X-ray investigation of the patellofemoral joint: X-ray technique, diagnostic criteria and their interpretation. Clin Orthop 144:16–26

Lin YF, Jan MH, Lin DH (2008) Different effects of femoral and tibial rotation on the different measurements of patellar tilting: an axial computed tomographic study. J Orthop Surg Res 3:5

Lustig S, Servien E, Selmi AS (2007) Factors affecting reliability of TT-TG measurements before and after medialization: a CT scan study. Rev Chir Orthop 92:429–436

MacIntyre NJ, Hill NA, Fellows RA (2006) Patellofemoral joint kinematics in individuals with and without patellofemoral pain syndrome. J Bone Joint Surg Am 88A:2596–2605

Martinez S, Korobkin M, Fondren FB (1983) Diagnosis of patellofemoral malalignment by computed tomography. J Comput Assist Tomogr 7:1050–1053

McNally EG (2001) Imaging assessment of anterior knee pain and patellar maltracking. Skelet Radiol 30:484–495

Merchant AC, Mercer RL, Jacobsen RH (1974) Roentgenographic analysis of patellofemoral congruence. J Bone Joint Surg Am 56A:1391–1396

Micheli LJ, Slater JA, Woods E, Gerbino PG (1986) Patella alta and the adolescent growth spurt. Clin Orthop 213:159–162

Miller TT, Staron RB, Feldman F (1996) Patellar height on sagittal MR imaging of the knee. Am J Roentgenol 167:339–341

Muhle C, Brossmann J, Melchert UH (1995) Functional MRI of the patellofemoral joint: comparison of ultrafast MRI, motion triggered cine MRI and static MRI. Eur Radiol 5:371–378

Muhle C, Brinkmann G, Skaf A (1999a) Effect of a patellar realignment brace on patients with patellar subluxation and dislocation: evaluation with kinematic magnetic resonance imaging. Am J Sports Med 27:350–353

Muhle C, Brossmann J, Heller M (1999b) Kinematic CT and MR imaging of the patellofemoral joint. Eur Radiol 9:508–518

Munch JL, Sullivan JP, Nguyen JT, Mintz D, Green DW, Shubin Stein BE, Strickland S (2016) Patellar articular overlap on MRI is a simple alternative to conventional measurements of patellar height. Orthop J Sports Med 8:4(7)

Murray TF, Dupont JY, Fulkerson JP (1999) Axial and lateral radiographs in evaluating patellofemoral malalignment. Am J Sports Med 27:580–584

Nagamine R, Otani T, White SE et al (1995) Patellar tracking measurement in the normal knee. J Orthop Res 13:115–122

Nietosvaara AY, Aalto KA (1993) Ultrasonographic evaluation of patellar tracking in children. Clin Orthop Relat Res 297:62–64

O'Donnell P, Johnstone C, Watson M (2005) Evaluation of patellar tracking in symptomatic and asymptomatic individuals by magnetic resonance imaging. Skelet Radiol 34:130–135

Pandit S, Frampton C, Stoddart J, Lynskey T (2011) Magnetic resonance imaging assessment of tibial tuberosity–trochlear groove distance: normal values for males and females. Int Orthop 35:1799–1803

Pfirrmann C, Zanetti M, Romero J (2000) Femoral trochlear dysplasia: MR findings. Radiology 216:858–864

Philips CL, Silver DAT, Schranz PJ, Mandalia V (2010) The measurement of patellar height. A review of the methods of imaging. J Bone Joint Surg Br 92-B:1045–1053

Powers CM, Shellock FG, Pfaff M (1998) Quantification of patellar tracking using kinematic MRI. J Magn Reson Imaging 8:724–732

Reikeras O, Hoiseth A (1990) Patellofemoral relationships in normal subjects determined by computed tomography. Skelet Radiol 19:591–592

Sakai N, Luo ZP, Rand JA et al (1996) Quadriceps forces and patellar motion in the anatomical model of the patellofemoral joint. Knee 3:1–7

Sanders TG, Morrison WB, Singleton BA (2001) Medial patellofemoral ligament injury following acute transient dislocation of the patella: MR findings with surgical correlation in 14 patients. J Comput Assist Tomogr 25:957–962

Sanfridsson J et al (2001) Femorotibial rotation and the Q-angle related to the dislocating patella. Acta Radiol 42:218–224

Sasaki T, Yagi T (1986) Subluxation of the patella: investigation by computerised tomography. Int Orthop 10:115–120

Schlenzka D, Schwesinger G (1990) The height of the patella: an anatomical study. Eur J Radiol 11:19–21

Schottle PB (2007) Comment on Wittstein JR et al. Magnetic resonance imaging evaluation of patellofemoral alignment. Arthroscopy 23:333–334

Schottle PB, Fucentese SF, Romero J (2005) Clinical and radiological outcome of medial patellofemoral ligament reconstruction with a semitendinosus autograft for patella instability. Knee Surg Sports Traumatol Arthrosc 13:516–521

Schottle PB, Zanetti M, Seifert B (2006) The tibial tuberosity-trochlear groove distance; a comparative study between CT and MRI scanning. Knee 13:26–31

Schutzer SF, Ramsby GR, Fulkerson JP (1986) The evaluation of patellofemoral pain using computerized tomography. A preliminary study. Clin Orthop 204:286–293

Seil R, Muller B, Georg T (2000) Reliability and interobserver variability in radiological patellar height ratios. Knee Surg Sports Traumatol Arthrosc 8:231–236

Shabshin N, Schweitzer ME, Morrison WB (2004) MRI criteria for patella alta and baja. Skelet Radiol 33:445–450

Shellock FG, Mink JH, Deutsch AL et al (1992) Kinematic MR imaging of the patellofemoral joint: comparison of passive positioning and active movement techniques. Radiology 184:574–577

Shellock FG, Mink JH, Deutsch AL (1993) Patellofemoral joint: identification of abnormalities with active-movement, unloaded versus loaded kinematic MR imaging techniques. Radiology 188:575–578

Smith TO, Davies L, Toms AP, Hing CB, Donell ST (2011) The reliability and validity of radiological assessment for patellar instability. A systematic review and met-analysis. Skelet Radiol 40:399–414

Stanford W, Phelan J, Kathol MH et al (1988) Patellofemoral joint motion: evaluation by ultra-fast computed tomography. Skelet Radiol 17:487–492

Stein LA, Endicott AN, Sampalis JS et al (1993) Motion of the patella during walking: a video digital fluoroscopy study in healthy volunteers. Am J Roentgenol 161:617–620

Tanaka MJ, Elias JJ, Williams AA, Carrino JA, Cosgarea AJ (2015) Correlation between changes in tibial tuberosity-trochlear groove distance and patellar position during active knee extension on dynamic kinematic computed tomographic imaging. Arthroscopy 31(9):1748–1755

Teige RA, Faerbe W, Des Madryl P (1996) Stress radiographs of the patellofemoral joint. J Bone Joint Surg Am 78A:193–203

Toms AP, Cahir J, Swift L, Donell ST (2009) Imaging the femoral sulcus with ultrasound, CT and MRI: reliability and generalisability in patients with patellar instability. Skelet Radiol 38:329–338

Urch SE, Tritle BA, Shelbourne D, Gray T (2009) Axial linear patellar displacement—a new measurement of patellofemoral congruence. Am J Sports Med 37:970–973

Van Huyssteen AL, Hendrix MRG, Barnett AJ, Wakeley CJ, Eldridge JDJ (2006) Cartilage-bone mismatch in the dysplastic trochlea: an MRI study. J Bone Joint Surg Br 88-B:688–691

Walker C, Cassar-Pullicino VN, Vaisha R (1993) The patello-femoral joint—a critical appraisal of its geometric assessment utilizing conventional axial radiography and computed arthro-tomography. Br J Radiol 66:755–761

Walker P, Harris I, Leicester A (1998) Patellar tendon-to-patella ratio in children. J Pediatr Orthop 18:129–131

Ward SR, Terk MR, Powers CM (2007) Patella alta: association with patellofemoral alignment and changes in contact area during weight-bearing. J Bone Joint Surg Am 89A:1749–1755

Whitehouse RW (2002) Computed tomography (CT) and CT arthrography [book section]. In: Davies AM, Cassar-Pullicino VN (eds) Imaging of the knee, 1st edn. Springer, Berlin

Wilson T (2007) The measurement of patellar alignment in patellofemoral pain syndrome: are we confusing assumptions with evidence? J Orthop Sports Phys Ther 37:330–341

Wittstein JR, Bartlett EC, Easterbrook J (2006) Magnetic resonance imaging evaluation of patellofemoral malalignment. Arthroscopy 22:643–649

Foot and Ankle: Paediatric Measurements

15

Andrew Roberts

Contents

A. Roberts
Children's Unit Robert Jones and Agnes Hunt
Orthopaedic Hospital, Oswestry, UK
e-mail: andrew.roberts@rjah.nhs.uk

15.1 Introduction

This is a difficult, complex and often confusing topic to the uninitiated for a variety of reasons. These range from a lack of knowledge of the congenital and neuromuscular disorders associated with foot deformities, inexperience in analysing paediatric foot radiographs and lack of understanding of the descriptive terms used to document the abnormalities. Most of the measurements are based on the dorsoplantar (AP) and lateral radiographic views. Importantly the views are frequently obtained on weight bearing or simulated weight bearing (in infants or non-ambulatory patients, weight bearing can be simulated by dorsiflexion stress). The function of the foot is to transmit load, adapt to varying surface conditions and act as a lever for progression with effects at the knee and the hip. Adaptation requires flexibility, and only during weight bearing or simulated weight bearing will the configuration of the bony skeleton allowed by the constraints of the ligamentous structures become apparent.

The dorsoplantar view is obtained with the patient standing, the tibia perpendicular to the cassette and the central ray angled 15° posteriorly to avoid overlap of the leg onto the posterior aspect of the foot. Similarly the lateral view is obtained with a standing patient and the tibia perpendicular to the film cassette (Fig. 15.1).

Fig. 15.1 Position for lateral and AP standing radiograph

15.2   Anatomical Considerations and Terminology

The foot is divided into three compartments—hindfoot (talus, calcaneum), midfoot (cuboid, navicular, cuneiforms) and the forefoot (metatarsals, phalanges and sesamoids). The inherent flexibility of the portions of the foot is affected during growth by normal and abnormal biomechanical forces and by a host of developmental and neuromuscular disorders including cerebral palsy, spinal dysraphism, arthrogryposis, etc. As the talus is the only bone in the foot without a direct muscle attachment, it follows that foot malalignment as a result of these clinical syndromes affects the talus indirectly. The orientation of the talus changes during normal growth so that the AP weight-bearing angle between the talus and calcaneus varies with age being 30–50° in infancy and 20–40° after 5 years of age (Vanderwilde et al. 1988). In pathological neuromuscular states, this growth effect is altered producing foot deformity. Radiographic alignment

assessment needs to be organised and sequential, starting with the relationship of the tibia to the hindfoot, then the hindfoot/midfoot relationship followed by the midfoot/forefoot relationship (Ritchie and Keim 1964; Templeton et al. 1965).

There must be two orthogonal views (AP and lateral; see Fig. 15.2) to complete this analysis. On the AP view two lines are drawn: the midcalcaneal line parallel to the lateral cortex of the calcaneum which usually intersects the base of the fourth metatarsal and the midtalar line drawn parallel to the medial cortex of the talus which usually passes through the base of the first metatarsal. It is important to stress that what is important in these two lines is their relationships to the base of the metatarsals and not their shafts. The navicular bone should normally align with the talus, and hindfoot malalignment often results in talonavicular subluxation. On the lateral view, the calcaneus is normally dorsiflexed relative to the ground forming the posterior part of the medial plantar arch, and a line can be drawn either as a tangent along its inferior surface or in the newborn, paral-
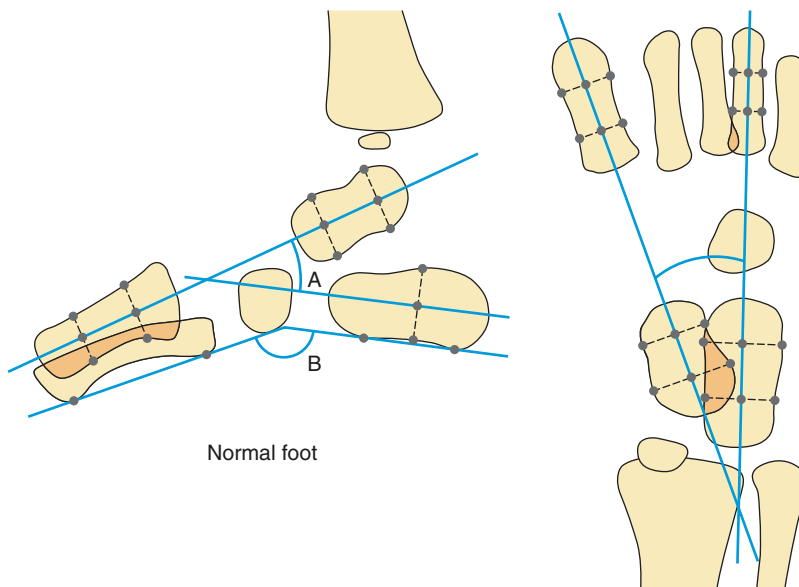
Fig. 15.2   Lateral and AP relationships in the normal foot

lel to it through the middle of the calcaneus. The midtalar line is then drawn across the middle of the talus. Incomplete ossification of the tarsal bones does not affect the drawing and relationship of these two lines. In hindfoot deformity leading to a more plantarflexed and vertically orientated talus, there is usually loss of the relationship between the midtalar line and the first metatarsal (Fig. 15.3). In the hindfoot the AP view is best at evaluating valgus and varus deformities. Valgus deformity results in increasing the angle between the midtalar and midcalcaneal lines, while varus deformities decrease the angle. Valgus deformities are usually associated with an external rotation of the midcalcaneal line, while varus deformities are associated with internal rotation of the midcalcaneal line. The relationship between varus/valgus and internal/external rotation is imposed by the oblique axis of the subtalar complex (Elftman and Manter 1935). The term *equinus* position refers to a plantarflexed posture of the hindfoot relative to its usual position with the term *calcaneus* position referring to the reverse of the equinus position with dorsiflexion of the calcaneus relative to its normal position. The term *cavus* refers to an elevated medial longitudinal arch resulting in an increase in the depth of the plantar arch which is formed by the metatarsals and calcaneus. Equinus, calcaneus and cavus positions are all best assessed on the lateral view.

The term *congenital talipes equinovarus (CTEV)* originates from talus and pes along with descriptions of the lateral and AP deformities. The term clubfoot should only be used when strictly referring to congenital talipes equinovarus and is synonymous with this term.

In hindfoot valgus, the talo-calcaneal angle on the AP view is increased because the calcaneum is abducted and externally rotated beneath the talus. The talus appears to be medially deviated as the midtalar line traverses medial to the base of the first metatarsal. This is only apparent, as the talus is positioned where it should be and the rest of the foot under and distal to the talus has become abducted and externally rotated. In a planovalgus foot the navicular subluxes laterally following the cuboid and calcaneum. On the lateral view, the talus becomes more vertically orientated as it loses the support of the sustentaculum tali and spring ligament, and the midtalar line passes in a plantarflexed orientation relative the line of the first metatarsal. In hindfoot varus, the talocalcaneal angle is reduced on the AP view as the calcaneum is adducted and internally rotated under the talus such that the axis of the two bones becomes more parallel. The rest of the foot is also internally rotated, and the midtalar line passes lateral to the base of the first metatarsal, while the navicular subluxes medially. Overlapping of the bases of the metatarsals is a readily appreciated feature of varus hindfoot posture on the AP view when significant forefoot pronation is also present. On the lateral view, the adducted calcaneum elevates the anterior talus reducing the talocalcaneal angle as the two axes become parallel to one another. When hindfoot varus coexists with cavus deformity producing a cavovarus deformity, the forefoot is markedly plantarflexed relative to the hindfoot, and the calcaneum frequently exhibits increased dorsiflexion relative to the tibia during weight bearing.
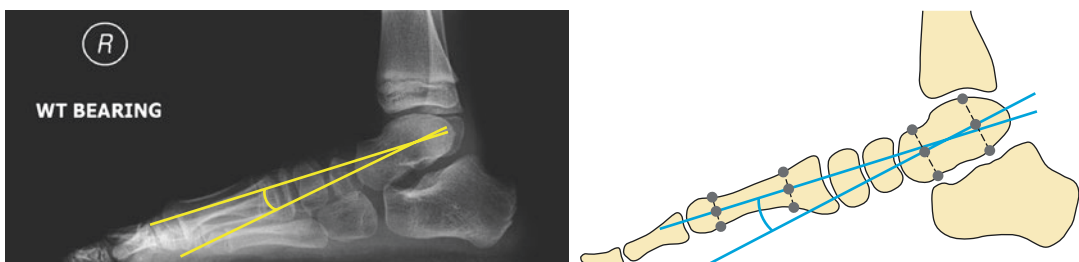
Fig. 15.3 Lateral weight bearing talo first metatarsal angle

In congenital talipes equinovarus, the radiographs show hindfoot equinus, hindfoot varus, midfoot cavus and adduction or inversion of the forefoot, while the posture of the foot as a whole is plantarflexed in equinus. The first ray is plantarflexed relative to the axis of the talus and requires elevation as a first step to manipulative reduction prior to drawing the forefoot and navicular into external rotation around the head of the talus when using the Ponseti technique of manipulative reduction. Hindfoot equinus has plantarflexion of the calcaneum as the radiographic hallmark, which means that the tibiocalcaneal angle is greater than 90° (normal angle 60–90°). The hindfoot varus is recognised on the lateral view by a very clear view through the middle talo-calcaneal facet. A reduced talo-calcaneal angle (Radler et al. 2007) is seen as the two bones assume a more parallel orientation (Radler et al. 2010). On the AP view the talo-calcaneal angle is reduced (Radler et al. 2007), as the bones overlap more than normal (Radler et al. 2010) and the midtalar line passes lateral to the base of the first metatarsal (Table 15.1).

Doubts have been raised concerning the validity of the AP talo-calcaneal angle (Kite's) in the monitoring of CTEV. Howard and Benson warned that the ossification centre of the talus lies primarily in the talar head and neck, normally forming an angle with the cartilaginous anlage of the body of the talus (Howard and Benson 1992). This angle becomes wider in clubfoot as there is marked angulation of the neck of the talus introducing an error in calculating the true AP talo-calcaneal relationship. Ippolito et al. in a comparative radiographic study with 3D CT showed that in 75% of treated CTEV cases, there was a statistically significant error (mean 15°) from the radiographic AP talo-calcaneal angle estimation when compared with CT (Ippolito et al. 2004).

Ippolito et al. concluded that this was due to the radiographic projection of the neck of the talus which was markedly angulated medially giving the

Table 15.1 Values for common angles in normality and CTEV

Angle	Normal	CTEV
AP talo-calcaneal	15–40°	<15°
AP talus first metatarsal	0–20°	<0°
Lateral talo-calcaneal	25–45°	<25°
Lateral tibio-calcaneal	60–90°	>90°

false impression of a divergence on the AP view between the calcaneus and talus. As a result they felt that AP radiographic talo-calcaneal angle estimation was not a valid outcome parameter for CTEV treatment. In the neonatal hindfoot, only the talus and calcaneus are ossified, and MRI could be potentially useful in revealing the position of the navicular as this is the last to ossify normally at the age of 2–3 years. Ultrasound can reliably also provide reproducible and objective assessment of the interosseous relationships. Various reproducible sonographic views are obtained with distances and angles around the navicular bone being particularly helpful (Wallander 2010).

The Ponseti method of treatment employing serial manipulation and casting has revolutionised the conservative treatment of clubfoot with good results in over 95% of cases. The early commencement of treatment in the first month of life is associated with a better outcome.

Flatfoot is normal in infants and young children. In flexible flatfoot, the arch is normal, while the subject is standing on their toes and flattened on the lateral weight-bearing view. A significant proportion of asymptomatic adults will exhibit flexible flatfoot (Harris and Beath 1947). Rigid flatfoot is associated with a flattened arch in a weight-bearing view and unchanging in shape when the subject rises up on their toes. The identification of rigidity/flexibility in the paediatric foot is based on clinical rather than radiological examination. Rigid flatfeet usually have associated underlying pathology and generally become symptomatic.

15.3 Lateral/AP Talo-calcaneal Angle: MRI

Definition

MRI measurement of surgically treated clubfoot.

Indications

Assessment of foot development following treatment for clubfoot allowing assessment of cartilaginous and bony anatomy.

Technique

MRI.

Full Description of Technique

Standard anatomical sagittal, transverse and coronal plane reconstruction. Imaging is performed under sedation with T1 and T2 sequences. 3–4 mm slice thickness is obtained with the best slice demonstrating anatomy chosen for measurement.

Lateral Talo-calcaneal Angle (L TCA)

The longitudinal axes of the cartilaginous talus and calcaneum are identified in the sagittal projection. The acute angle of intersection is the lateral talo-calcaneal angle (L TCA) (Fig. 15.4).

AP Talo-calcaneal Angle (AP TCA)

The inter-malleolar axis is identified on a transverse section and assumed to represent the axis of movement of the tibio-talar articulation and to lie
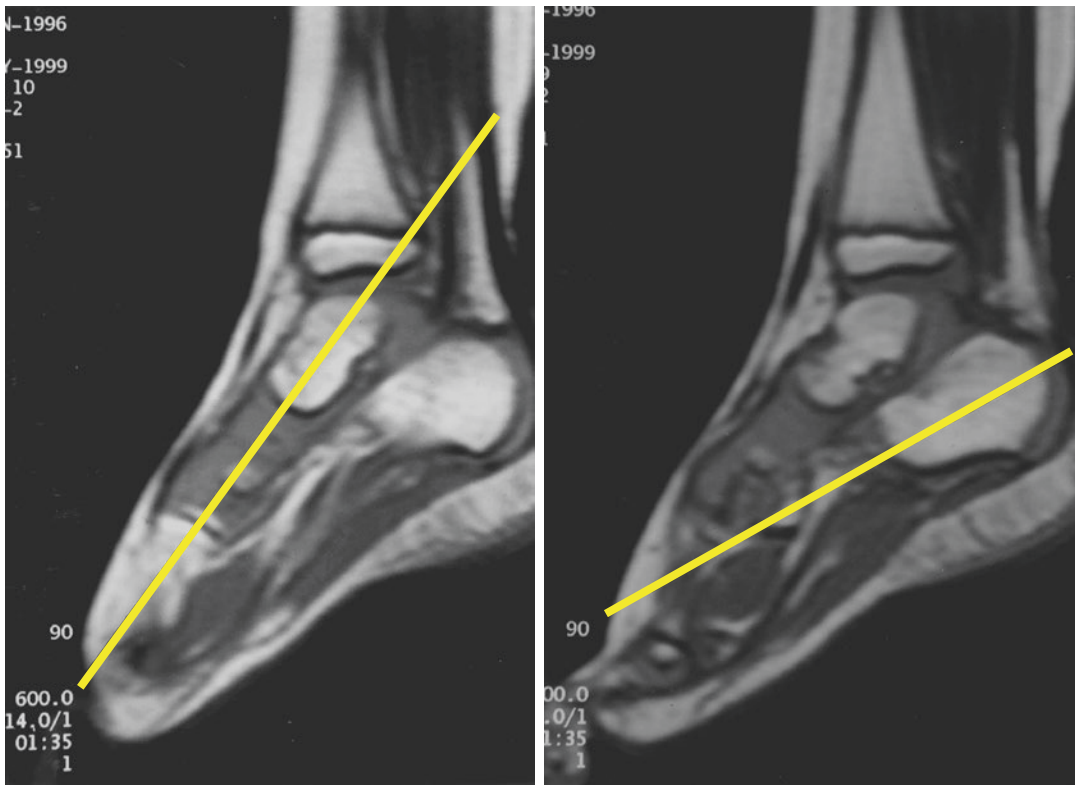
Fig. 15.4 Lateral MRI talo-calcaneal angle
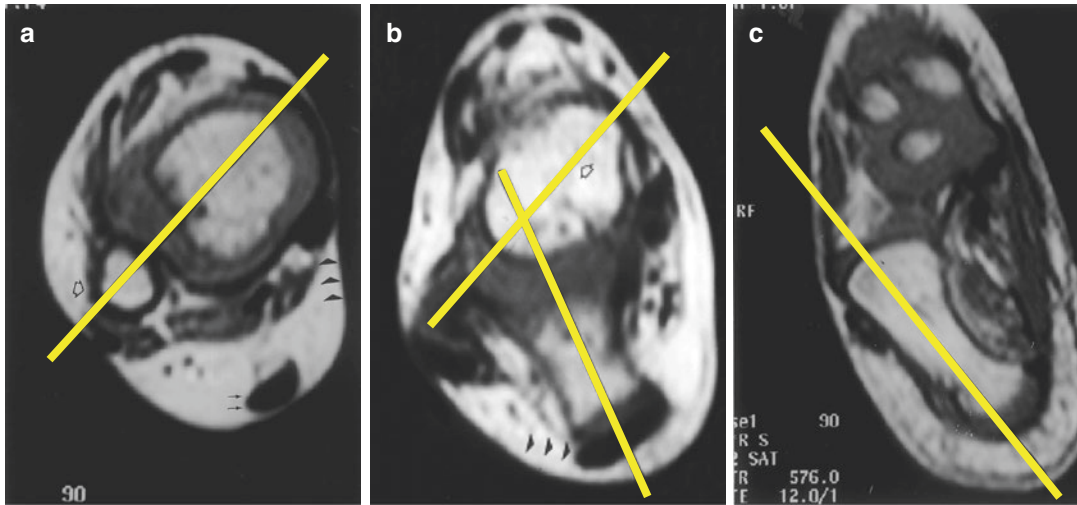
Fig. 15.5 AP MRI talo-calcaneal angle from Pekindil (2001)

perpendicular to the axis of the body of the talus. A perpendicular is drawn from the midpoint of the inter-malleolar axis and a common reference frame used to enable its intersection with the axis of the calcaneum (Fig. 15.5).

Reproducibility/Variation

Data on reproducibility is not available.

Clinical Relevance/Implications

MRI optimally identifies cartilaginous anatomy making this modality potentially useful in immature feet. Subluxation of the calcaneocuboid and talonavicular joints can be identified. The need for sedation coupled with difficulties of positioning makes the technique unattractive for routine clinical use. Cross-sectional imaging can reveal features such as deformity within the talar neck which can be a feature of CTEV.

The Normal Foot

Pekindil et al. examined seven children with talipes equinovarus (who had five unaffected feet) aged 4–11 years (Pekindil et al. 2001):

1. Mean L TCA 36°
2. Mean AP TCA 10.1° of internal rotation of the calcaneum relative to the talar body

Downey et al. examined seven unaffected feet in ten infants with talipes equinovarus between the age of 4 and 15 months (Downey et al. 1992):

1. Mean L TCA 28°±6°

CTEV

Pekindil et al. examined seven children with talipes equinovarus (who had nine affected feet) aged 4–11 years (Pekindil et al. 2001):

1. Mean L TCA 31.46°
2. Mean AP TCA 22.8° of internal rotation of the calcaneum relative to the talar body

Downey et al. examined seven unaffected feet in ten infants with talipes equinovarus between the age of 4 and 15 months (Downey et al. 1992):

1. Mean L TCA 5°±9°

Analysis/Validation of Reference Data

This measurement is not well validated with normal data varying considerably from one study to another. It may be useful to assess correction at the midfoot and importantly identify overcorrection.

Conclusion

Probably not useful for routine evaluation.

15.4   Lateral Talo-calcaneal Angle/ Lateral Tibio-calcaneal Angle in Maximum Dorsiflexion

Definition

Lateral radiographs of the foot to demonstrate the relationship between the talus and calcaneum and between the tibia and calcaneus with the foot held in a position of maximum dorsiflexion.

Indications

Diagnosis and evaluation of infant foot deformity including congenital vertical talus and talipes equinovarus.

Technique

Radiographic lateral view with the foot in maximum dorsiflexion.

Full Description of Technique

A lateral radiograph of the foot is taken in maximum dorsiflexion. The lateral border of the foot, the lateral malleolus and the lateral aspect of the leg are in contact with the cassette. Maximum dorsiflexion can either be achieved by means of pressure through a block placed on the plantar aspect of the foot with pressure applied to cause maximum ankle dorsiflexion or by strapping. A comparison of strapping versus block methods of dorsiflexion did not reveal a clinically significant difference in the measures of talo-calcaneal angle (Yeung et al. 2005).

Lateral Talo-calcaneal Angle in Maximum Dorsiflexion

Measurement is performed by drawing a line through the long axis of the talus extending towards the metatarsals and originally a line through the long axis of the calcaneum (Davis and Hatt 1955; Ritchie and Keim 1964). Most recent studies have utilised the plantar aspect of the calcaneum to define the axis of the calcaneum (Vanderwilde et al. 1988) (Table 15.2). It should be noted that the measurement technique detailed by Simons was performed intraoperatively with the child anaesthetised and thus a degree of control over posture exists that would not necessarily be obtained in the radiology department (Simons 1977) (Fig. 15.6).

Table 15.2 Change in lateral talo-calcaneal angle in maximum dorsiflexion during growth according to Vanderwilde

Years	Mean	+2SD	−2SD
0	45.7	56.2	34.5
1	44.8	55.0	33.8
2	43.7	54.1	33.5
3	43.0	53.4	32.9
4	42.5	52.7	32.6
5	42.1	52.0	32.1
6	41.3	51.8	31.7
7	41.4	51.9	31.0
8	40.8	51.4	30.7
9	40.3	51.4	30.4
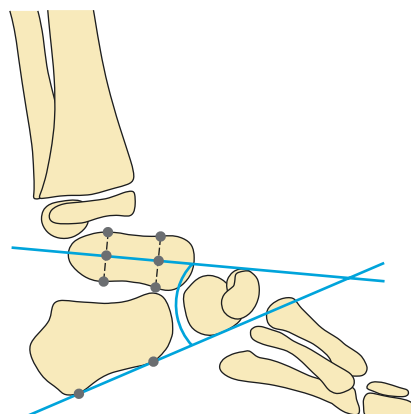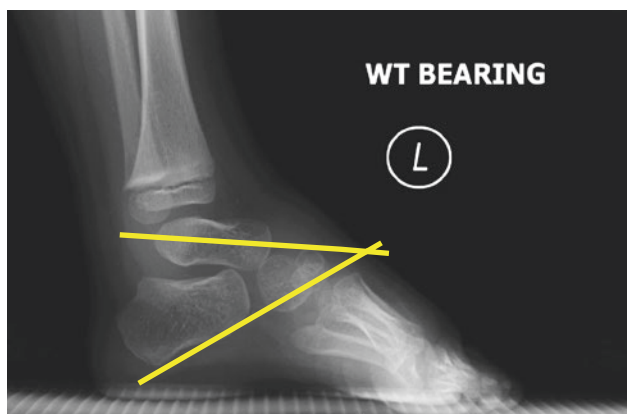
Fig. 15.6   Lateral weight-bearing talo-calcaneal angle

Lateral Tibio-calcaneal Angle in Maximum Dorsiflexion

With the foot positioned in maximum dorsiflexion, the mid-lateral line of the tibia is extended across the hindfoot, and the angle subtended anterior to this line by a line passing either along the inferior margin of the calcaneum or parallel to it through the midsubstance of the calcaneum is measured (Table 15.3) (Fig. 15.7).

Reproducibility/Variation

Although accurate positioning of the foot relative to the film is necessary to give reliable results, minor errors of positioning do not give clinically significant measurement errors (Simons 1977). The ability to identify the axes of the talus and

the calcaneum is considered to be an important source of potential variability of this measure. Radler et al. hypothesised that this would lead to low interobserver reliability particularly in the infant foot (Radler et al. 2010). Interclass reliability increased from 0.826 in infants to 0.862 in toddlers and 0.909 in children over the age of 3 suggesting that even in children under the age of 3 months, reliability is generally acceptable although their maximum difference observed in radiographs under 3 months of age was 30°.

Clinical Relevance/Implications

The obliquity of the subtalar axis leads to a reduction in the lateral TCA with increasing degrees of hindfoot varus. An increase in the lateral TCA is thus indicative of correction in talipes equinovarus whether achieved surgically or by Ponseti manipulation.

Normal

In typically developing children, the mean angle of the lateral tibio-calcaneal angle decreases from approximately 75° to 70° with angles measured after the age of 2 with the child weight bearing (Vanderwilde et al. 1988). The lateral talo-calcaneal angle remains relatively constant during childhood (Table 15.4).

Table 15.3 Change in lateral tibio-calcaneal angle in maximum dorsiflexion during growth according to Vanderwilde

Years	Mean	+2SD	−2SD
0	41.3	59.8	24.8
1	45.4	65.9	25.7
2	48.0	69.2	27.6
3	49.7	72.3	28.9
4	51.7	73.6	30.3
5	52.6	73.4	32.6
6	52.8	71.9	34.6
7	52.2	70.4	36.2
8	51.4	66.5	38.8
9	50.3	61.1	41.3
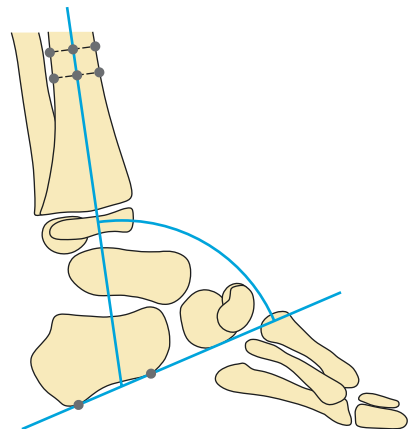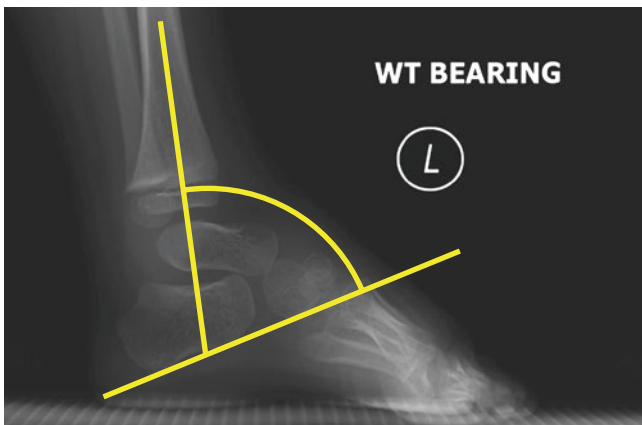
Fig. 15.7 Radiograph of the tibio-calcaneal lateral weight bearing angle

Table 15.4 Literature angles for lateral talo-calcaneal angle in maximum dorsiflexion

Author	Subjects	Feet	Mean	SD
Yeung et al. (2005)	14 children with CTEV strapping method	18	22	
Yeung et al. (2005)	14 children with CTEV block method	18	21	
de Gheldere and Docquier (2008)	CTEV	21	20.1	
Abulsaad and Abdelgaber (2008)	CTEV	70	21.4	6.64
Abulsaad and Abdelgaber (2008)	Normal	38	39.8	6.71
Radler et al. (2007)	CTEV	65	34.9	15.25
Radler et al. (2010)	Unaffected <3 months	111	47.3	9.2
Radler et al. (2010)	Unaffected 3–12 months	56	48.1	6.96
Vanderwilde et al. (1988)	Normal 12 months	24	39.6	
Radler et al. (2010)	Unaffected 12 months to <3 years	20	47.88	7.96
Vanderwilde et al. (1988)	Normal 24 months	24	41.6	
Radler et al. (2010)	Unaffected 3 years to <7 years	12	45.33	8.23
Vanderwilde et al. (1988)	Normal 48 months	10	33.1	
Radler et al. (2010)	Unaffected 7 years to <14 years	6	44.33	7.66
Vanderwilde et al. (1988)	Normal 8 years	6	32.8	

Table 15.5 Interobserver variation lateral TCA maximum dorsiflexion (Radler et al. 2010)

Age group	Mean difference	Standard deviation	Range of difference	Observations
Birth to <3 months	4.52	3.64	0–19	111
3 months to <12 months	3.39	2.85	0–16	56
12 months to <3 years	3.3	2.89	0–50	20

CTEV

With a varus hindfoot, the calcaneum is fore-shortened making its plantar aspect steeper. The talus becomes more parallel with the superior aspect of the calcaneum.

Analysis/Validation of Reference Data

Interobserver variation of lateral talo-calcaneal angle in maximum dorsiflexion in the unaffected foot of children with unilateral clubfoot was evaluated by Radler et al. (2010) (Table 15.5).

Conclusion

The lateral talo-calcaneal angle in maximum dorsiflexion is a technical measure of outcome following correction of talipes equinovarus in infants who have not started to walk.

15.5 Hallux Valgus Angle (HVA)

Definition

The orientation of the axis of the proximal phalanx of the great toe relative to the axis of the first metatarsal as seen in the AP weight bearing view.

Indications

Assessment of juvenile and adolescent hallux valgus.

Technique

AP radiograph of the weight-bearing foot.

Full Description of Technique

Patient stands on a level surface immediately above the plate (Fig. 15.8).

Reproducibility/Variation

The intra-observer reliability interclass correlation coefficient varies in the literature between 1.0 (McCluney and Tinley 2006) and 0.98 (Davids et al. 2007).

Clinical Relevance/Implications

A hallux valgus angle of greater than 15° is considered to be pathological. A survey of 18 typically developing children showed an HVA of 8° with a standard deviation of ±3° (McCluney and Tinley 2006).

The Normal Foot
The normal hallux valgus angle is approximately 8°±3°.

Adolescent Hallux Valgus
Any value greater than 15° of hallux valgus angle is consistent with a diagnosis of hallux valgus.

Analysis/Validation of Reference Data

No repeatability data available.

Conclusion

This measurement is used to define thresholds for treatment and monitor technical outcome in adolescent hallux valgus.

Fig. 15.8 Hallux Valgus angle
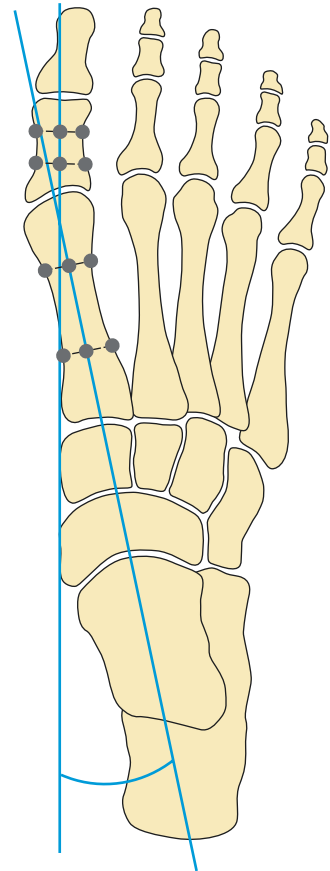
15.6   Metatarsus Adductus Angle

Definition

Orientation of the forefoot relative to the midfoot measured on an AP weight-bearing radiograph of the foot.

Indications

To assess metatarsus adductus.

Technique

AP weight-bearing radiograph.

Full Description of Technique

An AP radiograph of the weight-bearing foot is measured as follows: the axis of the second metatarsal is defined A-B (Fig. 15.9), and the midpoint in the lateral border of the cuboid between the articulation with the base of the fifth metatarsal and the articulation with the calcaneum is marked and the midpoint identified.

On the medial border of the foot, the midpoint between the medial aspect of the first metatarsal-cuneiform joint and the medial aspect of the talo-navicular articulation is marked. A line is drawn transversely between the two midpoints across the midfoot and a perpendicular constructed where this crosses the axis of the second metatarsal B-C (Fig. 15.9). The metatarsus adductus angle lies between the axis of the second metatarsal and the perpendicular A-B-C (Fig. 15.9).

Engel et al. have suggested using the longitudinal axis of the second cuneiform relative to the axis of the second metatarsal but do not offer inter- and intra-observer studies to compare reliability of their modification (Engel et al. 1983).

Reproducibility/Variation

Unknown.

Fig. 15.9 Schematic and radiograph showing metatarsal adductus angle
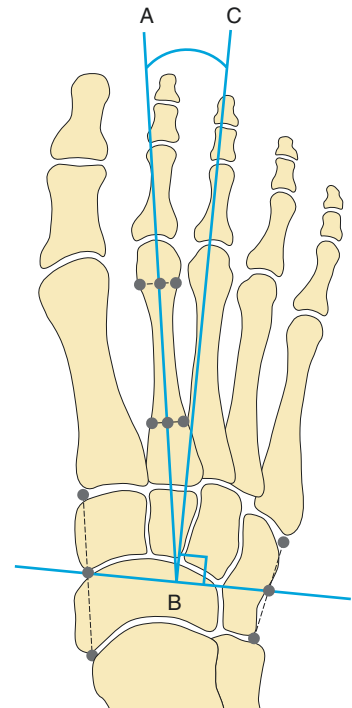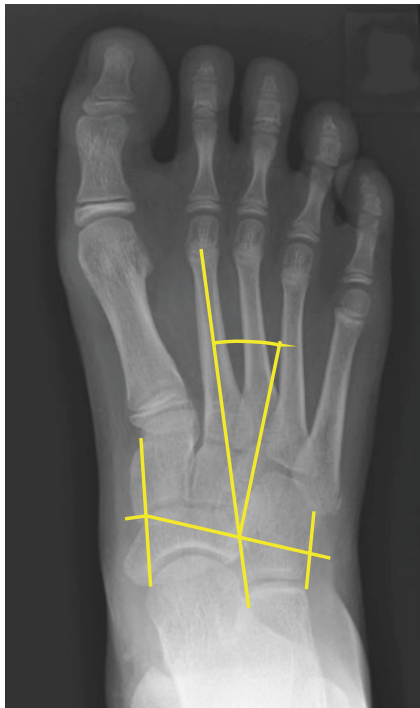
Clinical Relevance/Implications

This measure identifies deformity between the midfoot and the forefoot. Traditionally extensive surgical treatments either in the form of ligament release (Heymann and Herndon) or basal metatarsal osteotomies were performed for metatarsus adductus that was resistant to stretching treatment. Unfortunately the results were uniformly poor often leaving the patient with midfoot pain. The natural history of metatarsus adductus has been shown to be benign; thus measures of radiological deformity are of academic interest only (Farsetti et al. 1994).

The Normal Foot

The metatarsus adductus angle is normally between 10 and 20° using the measurement method shown in Fig. 15.9. The Engel measurement is reported as varying between 13 and 23°. Anything over the upper limit in either measure is considered suggestive of metatarsus adductus.

Conclusion

This measurement may be used to document natural resolution of isolated paediatric metatarsus adductus or to document forefoot deformity associated with talipes equinovarus.

15.7 Lateral Weight-Bearing Talo-calcaneal Angle

Definition

The acute angle subtended by axis of the talus and a line drawn along the inferior border of the calcaneum in a weight-bearing lateral view of the foot.

Indications

Evaluation of hindfoot alignment in children with planovalgus feet and after correction of talipes equinovarus.

Technique

Weight-bearing lateral radiograph of the foot (see Fig. 15.1).

Full Description of Technique

The child stands perpendicular to the X-ray beam with a plate supported between blocks between the ankles (Fig. 15.1). Significant degrees of midfoot adduction seen in treated clubfoot may lead to the hindfoot being externally rotated relative to the beam and may require internal rotation of the imaged foot to give a true lateral view of the hindfoot.

Reproducibility/Variation

Radler examined the interclass correlation coefficient for lateral weight-bearing talo-calcaneal measures in children between 3 and 7 years of age (0.75 (0.487–0.891)) and children aged 7 to under 14 (0.929 (0.851–0.971)) (Radler et al. 2010). This suggests that the measure is much more reliable in older children.

Clinical Relevance/Implications

Weight-bearing radiographs are more appropriate than maximum dorsiflexion views in children who have established walking.

The Normal Foot

The talo-calcaneal angle is shown in Fig. 15.2 as angle A. Normal values are in the region of 40° (Table 15.6).

CTEV

The varus posturing of the hindfoot beneath the talus produces a reduction in the lateral weight-bearing talo-calcaneal angle as shown in Fig. 15.10. Typical values in CTEV are in the region of 20° (Table 15.7).

The Valgus Foot

In pes planus, the head of the talus loses its support from the sustentaculum tali and spring ligament with an increase in the talo-calcaneal angle as shown schematically in Fig. 15.11.

Conclusion

Correlation of functional foot scores and lateral weight-bearing and AP weight-bearing talo-calcaneal angles is poor in treated clubfoot (Abulsaad and Abdelgaber 2008), but the measure may be of use in documenting pes planovalgus and the technical outcome of hindfoot correction in the weight-bearing child.

Table 15.6 Lateral weight-bearing talo-calcaneal angle and measures

Author	Subject group	Feet measured	Mean	SD
Abulsaad and Abdelgaber (2008)	CTEV	70	21.4	6.6
Abulsaad and Abdelgaber (2008)	Normal	38	39.8	6.7

Table 15.7 Lateral weight-bearing talo-calcaneal angle changes during growth according to Vanderwilde et al. (1988)

Years	Mean	+2SD	−2SD
0	38.8	55.5	23.0
1	41.2	55.5	27.1
2	43.3	56.4	29.6
3	44.4	56.9	31.6
4	45.0	56.7	32.9
5	45.3	56.1	33.5
6	44.4	55.6	33.5
7	43.7	54.8	32.5
8	42.1	53.6	30.5
9	39.7	51.4	28.4

Clubfoot
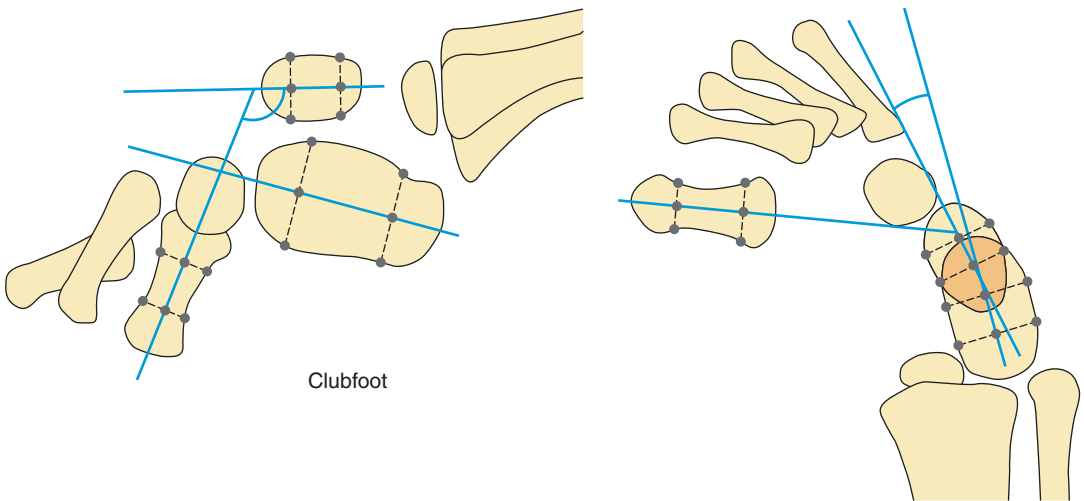
Fig. 15.10 Lateral and AP weight-bearing relationships in CTEV

Pes Planus
Increased talo-calcaneal angle
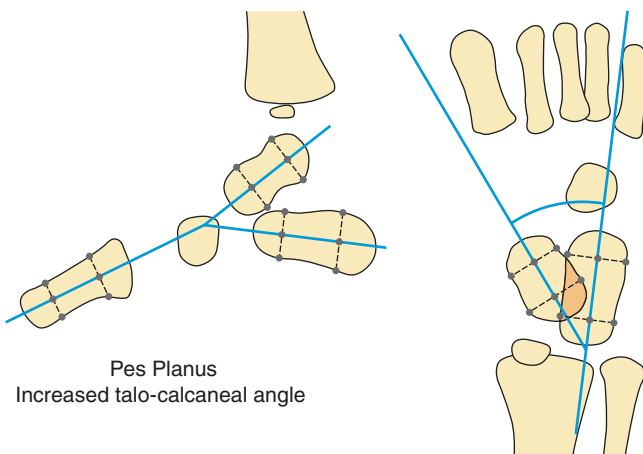
Fig. 15.11 Schematic representation of the relationships in pes planus

15.8 Lateral Weight-Bearing Tibio-calcaneal Angle

Definition

Defines the sagittal relationship between tibial axis and calcaneal axis (Fig. 15.7).

Indications

Evaluation of hindfoot alignment in children with planovalgus feet and after correction of talipes equinovarus.

Technique

Radiography.

Full Description of Technique

The child stands perpendicular to the X-ray beam with a plate supported between blocks between the ankles.

Reproducibility/Variation

Unknown (Table 15.8).

Table 15.8 Development of lateral weight-bearing tibio-calcaneal angle according to Vanderwilde

Years	Mean	+2SD	−2SD
0	77.9	96.1	59.2
1	74.3	91.2	57.9
2	71.7	87.3	56.4
3	69.5	83.5	56.3
4	67.7	80.1	56.3
5	66.8	77.8	57.1
6	66.6	76.5	58.1
7	67.1	75.1	59.7
8	67.9	74.1	61.7
9	69.3	74.1	64.7

Clinical Relevance/Implications

Children who have hindfoot deformity secondary to talipes equinovarus frequently develop secondary knee hyperextension. When standing, the hindfoot may align relatively normally, but the tibia is reclined giving an excessive tibio-calcaneal angle.

Conclusion

This measure is of use in identifying a combination of hindfoot equinus and knee hyperextension which may be seen in partially corrected clubfoot.

15.9 Lateral Weight-Bearing Talar First Metatarsal Angle

Definition

Defines the sagittal relationship between talar axis and first metatarsal axis. Positive values indicate that the talus is plantarflexed to a greater degree than the first ray (Fig. 15.3).

Indications

Evaluation of midfoot alignment in children with planovalgus, plantaris or cavus feet.

Technique

Weight-bearing lateral radiograph of the foot.

Full Description of Technique

The child stands perpendicular to the X-ray beam with a plate supported between the ankles.

Reproducibility/Variation

Radler investigated the interobserver differences in the weight-bearing talus first metatarsal angle (Table 15.9).

Table 15.9 Interobserver differences in measuring weight-bearing talus first metatarsal angle (Radler et al. 2010)

Age group	Mean difference	SD	Range
3 months to <12 months simulated weight bearing	4.15	3.45	0–13
12 months to <3 years weight bearing	3.67	2.67	0–8
3 to <7 years weight bearing	3.33	3.03	0–9
7 to <14 years weight bearing	3.49	2.52	0–12

Clinical Relevance/Implications

Positive angles denote a planovalgus posture with the axis of the talus lying in a more plantarflexed posture than the first ray. The natural development of a medial arch during childhood is shown in the data presented by Vanderwilde et al. (1988). The measure does not differentiate between a deformity within the midfoot (cavus) or in the tarsometatarsal joints (plantaris).

The Normal Foot
As the arch forms during childhood, the angle drops from 15° to approximately 10°.

CTEV and the Varus Foot
Increasing degrees of cavus lead to dorsiflexion of the talus and plantarflexion of the first ray. This reduces the talus first metatarsal angle until in extreme cases it can become negative (Fig. 15.12).

The Valgus Foot
Increasing plantarflexion of the talus coupled with dorsiflexion of the first ray as it comes to lie parallel to the ground leads to an increasing talus first metatarsal angle.

Reproducibility/Variation

Table 15.10 documents the development of this angle through childhood published by Vanderwilde et al. (1988).

Conclusion

Useful in the assessment of planovalgus and cavus foot deformity.

Fig. 15.12 Schematic diagram of a lateral radiograph of a cavus foot
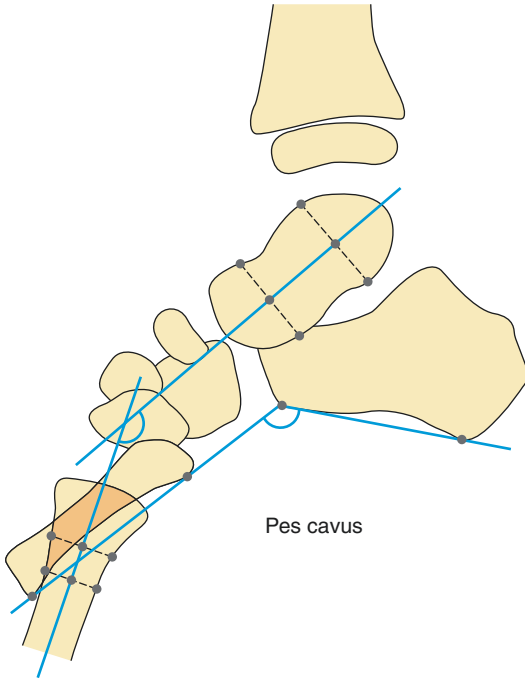
Table 15.10 Changes in the first metatarsal talar weight-bearing angle during growth according to Vanderwilde (1988)

Years	Mean	+2SD	−2SD
0	18.5	40.2	−2.4
1	15.7	34.2	−3.6
2	12.4	29.0	−3.7
3	10.1	24.3	−4.9
4	8.3	21.1	−5.4
5	6.9	19.8	−5.7
6	5.6	17.6	−6.3
7	5.6	17.2	−6.6
8	5.6	17.4	−6.4
9	5.2	18.9	−6.9

Pes cavus

15.10   Lateral Weight-Bearing Talo-horizontal Angle

Definition

Defines the sagittal relationship between the weight-bearing talar axis and the ground.

Indications

Evaluation of hindfoot alignment in children with planovalgus feet and after correction of talipes equinovarus.

Technique

Weight-bearing lateral radiograph of the foot.

Full Description of Technique

The child stands perpendicular to the X-ray beam with a plate supported between the ankles.

Reproducibility/Variation

Radler reports the following interobserver variability.

Clinical Relevance/Implications

Weight-bearing radiographs are more appropriate than maximum dorsiflexion views in children who have established walking. This measure is not regularly used in the assessment of childhood foot deformity (Table 15.11).

The Normal Foot

In the typically developing foot, this value varies during childhood gradually reducing with age (Tables 15.12 and 15.13).

Table 15.11 Reliability of lateral weight-bearing talar horizontal angle (Radler et al. 2010)

Age group	Mean difference	SD	Range
3 months to <12 months simulated weight bearing	3.26	2.65	0–9
12 months to <3 years weight bearing	3.67	2.53	0–7
3 to <7 years weight bearing	3.05	2.20	0–8
7 to <14 years weight bearing	2.55	1.85	0–7

Table 15.12 Weight-bearing talo-horizontal angle (Radler et al. 2010)

Age group	Mean angle	SD	Number of feet
3 months to <12 months simulated weight bearing	37.33	2.65	9
12 months to <3 years weight bearing	32.92	6.2	4
3 to <7 years weight bearing	30.24	6.83	14
7 to <14 years weight bearing	25.55	6.37	17

Table 15.13 Development of normal lateral talo-horizontal angle according to Vanderwilde

Years	Mean	+2SD	−2SD
0	35.1	55.7	13.5
1	33.0	49.9	15.7
2	32.1	46.1	17.9
3	31.1	42.6	19.4
4	30.0	39.1	19.7
5	28.9	37.6	19.9
6	28.1	36.4	19.4
7	26.9	35.6	17.2
8	26.1	35.6	15.7
9	25.3	36.0	13.9

CTEV and Varus Feet

The talus becomes relatively horizontal reducing the angle progressively towards zero.

The Valgus Foot

High levels of angle suggest an inappropriately vertical talus. The most extreme situation would be a congenital vertical talus where the angle may approach 90°.

Conclusion

This measure is not regularly used as a measure of hindfoot posture (Fig. 15.13).
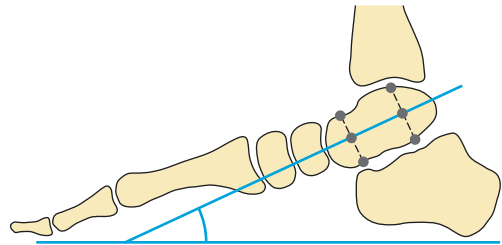
Fig. 15.13 Lateral talar horizontal Weight-bearing angle

15.11 Lateral Weight-Bearing Calcaneal Horizontal Angle

Definition

The angle between the tangent through the inferior outline of the calcaneus and the horizontal on a lateral weight-bearing radiograph.

Indications

Evaluation of pitch of hindfoot relative to the ground during weight bearing.

Technique

Radiography.

Full Description of Technique

The patient stands with the plate held between the ankles. The beam is directed from lateral to medial centred on the ankle.

Reproducibility/Variation

Unknown.

Clinical Relevance/Implications

This is the angle formed between the horizontal and a tangent on the plantar aspect of the calcaneum.

The Normal Foot
The normal weight-bearing calcaneal horizontal angle is between 20 and 30°.

CTEV
Angles greater than 30° are suggestive of midfoot cavus with greater deformity in the midfoot in proportion to the hindfoot and ankle. In extreme cases where the child is weight bearing on the forefoot only, the calcaneum may be in near normal alignment relative to the ground, but the hindfoot and heel are not in contact with the ground.

The Valgus Foot
In the planovalgus foot the calcaneal horizontal angle will be less than 20°.

The Calcaneus Foot
Where imbalance exists between the dorsiflexors and calf muscle, extreme deformities may develop. In spina bifida the preservation of L4 innervation in the absence of L5 and S1 will lead to a calcaneus deformity. In this instance the calcaneal horizontal angle is greatly increased (Fig. 15.14).

Fig. 15.14 Lateral weight-bearing radiograph of the calcaneus foot

15.12 Ultrasound Measurements of Infant Hindfoot

Definition

Standardised views of the relationship of the osteochondral structures of the neonatal hindfoot.

Indications

Evaluation of deformity in the neonatal foot—typically talipes equinovarus.

Technique

Ultrasound.

Full Description of Technique

Aurell et al. defined three sonographic projections and the measurements that could be obtained from those projections (Aurell et al. 2002). In addition to the static measure, the authors suggest that the forefoot may be adducted and abducted to assess the mobility of the navicular on the talar head in the medial projection. Four separate measures are described in Table 15.14 (See Figs. 15.1, 15.2 and 15.3 in Aurell et al. (2002)).

Reproducibility/Variation

Aurell et al. report the interobserver and intraobserver variability as interclass correlation coefficients for each age group for the four principal measures (Tables 15.15, 15.16, 15.17 and 15.18).

Because evaluation of the paediatric foot with ultrasound depends upon the position of the probe and the posture of the foot, significant variability should be expected. The data reported by Coley (Table 15.19) shows how various postures of the forefoot can change the relationship between the medial malleolus and the navicular tuberosity (Coley et al. 2007).

Clinical Relevance/Implications

After the diagnosis of clubfoot is made, dynamic sonographic assessment can evaluate the effect of positional therapeutic manoeuvres of the foot employed by the Ponseti technique. The severity of the midfoot deformity is assessed sonographically by measuring the medial malleolar-navicular distance in neutral foot abduction. The degree of equinus deformity is assessed by measuring the calcaneal-posterior tibial growth plate distance in maximum dorsiflexion and plantarflexion. Ultrasound is used in monitoring the efficacy of conservative treatment of paediatric foot deformity by this casting technique and defining the endpoint of treatment.

Table 15.14 Normal values for ultrasound evaluation of the infant foot (Aurell et al. 2002)

Age	Medial malleolus to navicular (*n*)	Calcaneus to cuboid (*n*)	Medial tissue distance (*n*)	Length of talus (*n*)
Birth	8.5 ± 1.1 (106)	1.16 ± 1.1 (106)	4.7 ± 0.7 (106)	17.7 ± 1.1 (92)
4 months	9.7 ± 1.3 (55)	2.1 ± 1.2 (55)	5.5 ± 1.0 (55)	21.0 ± 1.3 (38)
7 months	10.8 ± 1.3 (46)	3.0 ± 1.1 (46)	6.2 ± 1.3 (46)	23.1 ± 1.6 (34)
12 months	12.3 ± 1.3 (98)	2.8 ± 1.3 (98)	7.6 ± 1.0 (96)	–

Table 15.15 Correlation coefficients for mm-n (medial malleolus to navicular in mm) (Aurell et al. 2002)

Age group (months)	0	4	7	12
Intra-observer correlation (*r*)	0.86	0.87	0.85	0.85
Interobserver correlation (*r*)	0.77	0.65	0.66	0.81

Table 15.16 Correlation coefficients for calcaneus to cuboid distance (Aurell et al. 2002)

Age group (months)	0	4	7	12
Intra-observer correlation (*r*)	0.84	0.84	0.84	0.79
Interobserver correlation (*r*)	0.63	0.86	0.81	0.85

Table 15.17 Correlation coefficients for medial soft tissue thickness (Aurell et al. 2002)

Age group (months)	0	4	7	12
Intra-observer correlation (*r*)	0.68	0.94	0.92	0.90
Interobserver correlation (*r*)	0.55	0.89	0.93	0.82

Table 15.18 Correlation coefficients for length of talus (Aurell et al. 2002)

Age group (months)	0	4	7	12
Intra-observer correlation (*r*)	0.65	0.84	0.65	–
Interobserver correlation (*r*)	0.53	0.53	0.53	–

Table 15.19 Normal values for medial malleolus to navicular measurement in millimetres (Coley et al. 2007)

Group	In adduction	In neutral	In abduction
Normal	5.11	8.5	12.87
Unilateral unaffected	6.73	10.16	14
Unilateral CTEV	2.09	4.92	8.45
Bilateral CTEV	1.39	3.64	5.78

Conclusion

The noninvasive nature of this assessment may make it valuable in assessing the effectiveness of serial manipulation. Comparison with clinical scoring systems such as Pirani's or Dimeglio's has not yet been performed (Dimeglio et al. 1995; Pirani et al. 1999).

15.13 AP Weight-Bearing Talo-calcaneal Angle

Definition

Defines the alignment of the axis of the talus and calcaneum.

Indications

Assessment of hindfoot deformity.

Technique

Weight-bearing AP view of the foot.

Full Description of Technique
(Figs. 15.10 and 15.15)

With the child standing on the plate, the knee is flexed, and the X-ray beam is directed towards the head of the talus. Correct penetration of the image is essential to ensure that the axis of the calcaneum and talus can be identified. This may lead to a loss of image quality with respect to the forefoot.

Reproducibility/Variation

Note the warning proposed by Howard and Benson discussed above (Howard and Benson 1992).

Clinical Relevance/Implications

Increasingly varus posturing of the hindfoot produces a more parallel relationship between the talus and calcaneum.

The Varus Foot
Increasing degrees of varus posturing of the hindfoot causes the calcaneum to rotate internally

Table 15.20 Changes in AP weight-bearing talo-calcaneal angle during growth according to Vanderwilde

Years	Mean	+2SD	−2SD
0	41.9	56.4	27.4
1	40.1	52.9	27.1
2	37.7	49.9	26.0
3	35.7	46.8	25.4
4	33.6	44.2	24.0
5	31.7	41.3	22.2
6	29.5	39.6	19.5
7	27.1	37.0	17.5
8	24.7	35.3	14.8
9	21.6	33.4	11.2

beneath the talus producing a reduced angle. Typically values less than 20° are seen in the AP weight-bearing talo-calcaneal angle (Simons 1977) (Table 15.20).

The Valgus Foot
Progressive planovalgus leads to divergences of the axes of the talus and calcaneum. Eventually, once the head of the talus loses support from the sustentaculum tali and the plantar spring ligament stretches out, the talus plantarflexes and becomes foreshortened on the AP view. Typically the axes will diverge by greater than 45° in the presence of significant degrees of valgus in the hindfoot.

Conclusion

This measure is more prone to error because the axes of the calcaneum and talus may be unclear owing to underpenetration of the film and the AP axis of the calcaneum is less precisely defined than the nearly linear plantar aspect. If a lateral weight-bearing view is available, this should be utilised as the primary measure of subtalar alignment. Ippolito et al. cited a large number of papers that found no correlation between the AP weight-bearing talo-calcaneal angle and outcome and concluded that CT reconstructions in the older child are probably more useful (Ippolito et al. 2004).

Fig. 15.15 Use of windowing facility in PACS to reveal AP talo-calcaneal angle
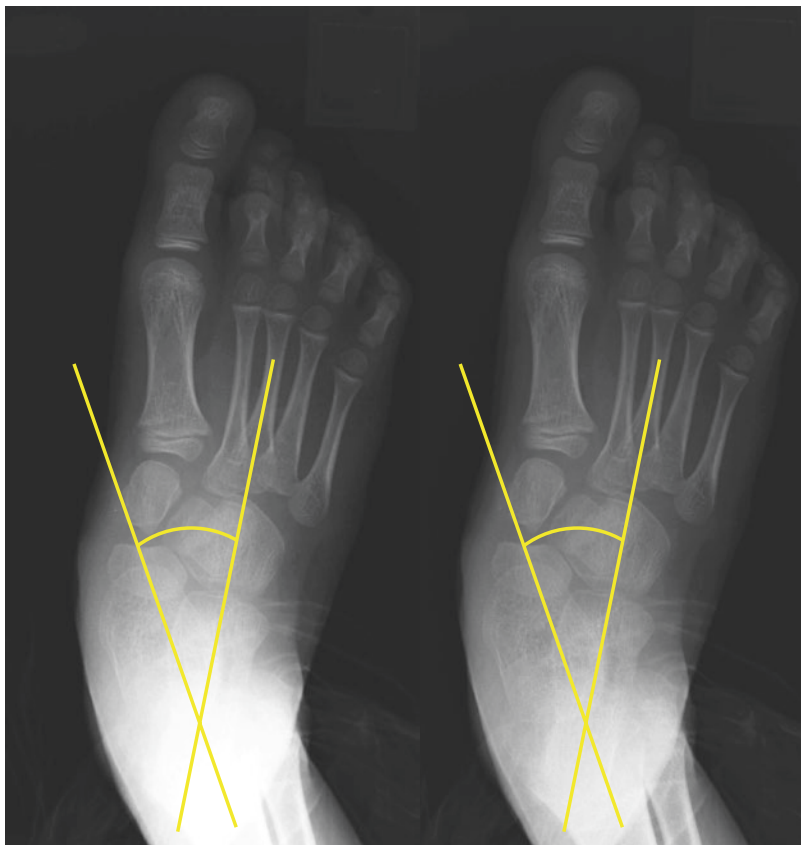
15.14   AP Weight-Bearing Talar First Metatarsal Angle

Definition

The angle between the axis of the talus and the first metatarsal as seen on an AP weight-bearing view. Positive angles are encountered where the distal projection of the axis of the first metatarsal is more medially directed than the talar axis (varus posturing of the forefoot).There is confusion in the literature as to what represents a positive angle. Simons refers to a varus posture of the first ray relative to the talus as positive (Simons 1977), whereas Vanderwilde gives a reference range in normal children varying from +20° at birth to approximately +8° by 8 years of age (Vanderwilde et al. 1988). Accordingly, caution is needed when referring to this angle in the literature.

Indications

Foot deformity

Technique

AP weight-bearing radiograph.

Full Description of Technique
(Fig. 15.16)

With the child standing on the plate, the knee is flexed, and the X-ray beam is directed towards the head of the talus.

Reproducibility/Variation

This measure has interobserver reliability data only for maximum dorsiflexion radiographs (Radler et al. 2010).

Clinical Relevance/Implications

The normal value of this is between zero and −20° (Simons 1977). In other words the first metatarsal is directed more laterally than the axis of the talus.

The Varus Foot
In the presence of hindfoot varus, the talus first metatarsal angle is typically greater than 15°. Abnormal angles relate the hindfoot to the forefoot but do not give explicit information on where in the midfoot the deformity is arising.
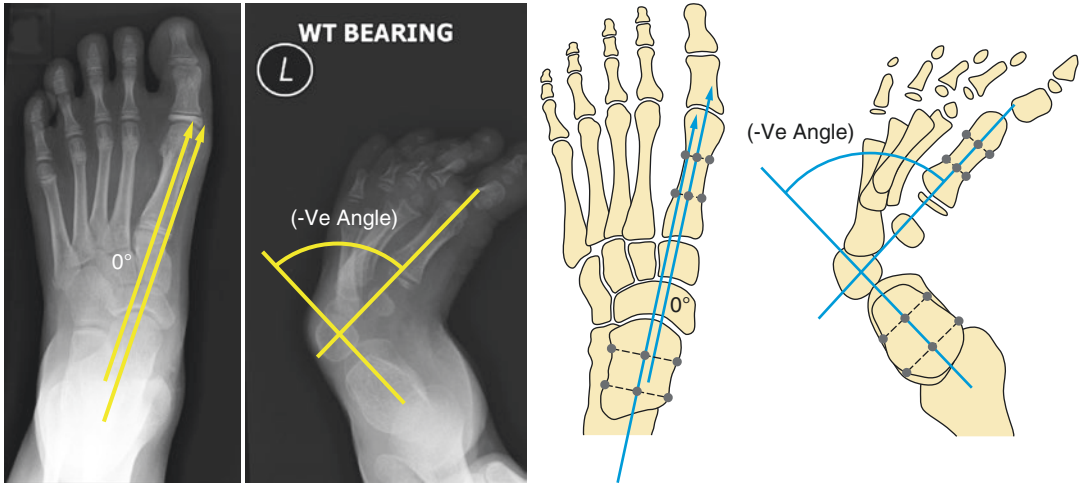
Fig. 15.16 Schematic and radiograph showing first metatarsal talar AP weight-bearing relationship

Table 15.21 Changes in the first metatarsal talar AP weight-bearing angle during growth according to Vanderwilde

Years	Mean	+2SD	−2SD
0	20.5	31.4	9.1
1	16.8	29.5	5.2
2	14.6	27.0	1.6
3	12.2	25.2	−0.9
4	10.4	23.8	−3.6
5	8.4	22.2	−5.7
6	6.6	20.7	−7.2
7	5.5	19.3	−8.1
8	3.9	18.3	−9.0
9	3.2	17.3	−9.7

15.15   AP Weight-Bearing Calcaneal Fifth Metatarsal Angle

Definition

The relationship between the axis of the fifth metatarsal and the calcaneum. Positive angles indicate that the distal projection of the fifth metatarsal is directed more laterally than the axis of the calcaneum.

Indications

The assessment of midfoot deformity, primarily metatarsus adductus.

Technique

AP weight-bearing radiograph.

Full Description of Technique

With the child standing on the plate, the knee is flexed, and the X-ray beam is directed towards the head of the talus.

Reproducibility/Variation

Unknown.

Clinical Relevance/Implications

Evaluation of the integrity of the lateral column of the foot.

The Normal Foot

Laaveg and Ponseti examined the group of adults following treatment for clubfoot identifying a mean value of $-12°\pm4°$ for the calcaneal fifth metatarsal angle (Laaveg and Ponseti 1980). Vanderwilde reported on normal values in children with average values close to 0 (Vanderwilde et al. 1988) (Table 15.22). As with the talus first metatarsal angle, caution should be exercised in ensuring that the angle is reported with its correct sign.

Conclusion

A measure of lateral column alignment disturbed in metatarsus adductus (Fig. 15.17).

Table 15.22 Changes in weight-bearing AP fifth metatarsal calcaneal angle with growth according to Vanderwilde

Years	Mean	+2SD	−2SD
0	2.4	14.6	−9.1
1	0.9	11.9	−9.9
2	−0.4	9.9	−10.0
3	−0.8	8.9	−10.2
4	−1.3	8.3	−10.2
5	−1.2	8.5	−10.1
6	−0.5	9.0	−9.9
7	0.3	10.5	−9.1
8	2.0	13.0	−8.8
9	3.8	15.1	−7.4

15.16 Bohler's Angle

Definition

Bohler's angle is the angle of intersection of lines drawn from the posterior superior corner of the calcaneal apophysis to the proximal edge of the posterior facet and a line drawn from the proximal edge of the posterior facet to the anterior superior aspect of the calcaneus at the calcaneo-cuboid joint (Bohler 1931).

Indications

Assessment of calcaneal fractures.

Technique

Lateral radiograph of the calcaneum, with the central beam over the malleoli.

Full Description of Technique
(Fig. 15.18)

Lateral weight-bearing radiograph of the ankle and hindfoot. Correct positioning requires radiographic superimposition of both malleoli.

Reproducibility/Variation

Clint et al. examined the interobserver and intra-observer reliability of Bohler's angle (Table 15.23) (Clint et al. 2010).

Clinical Relevance/Implications

A reduction of Bohler's angle suggests inadequate reduction of a fracture of the calcaneum with the potential for subtalar degeneration as a result of incongruence of the subtalar joint.

The Normal Foot

It has been claimed that variability of shape during growth prevents meaningful evaluation of Bohler's angle (Schmidt and Weiner 1982). Clint et al. examined the radiographs of a large number of children, producing a graph of angle versus age (Clint et al. 2010). Initial angles of the approximately 30° increase to about 40° at 6 years of age and then reduce a little to approximately 35° by 15 years of age.

Table 15.23 Agreement of measures for Bohler's angle (Clint et al. 2010)

| Intra-observer | 0.934 ± 0.012 |
| Interobserver | 0.903 ± 0.0215 |
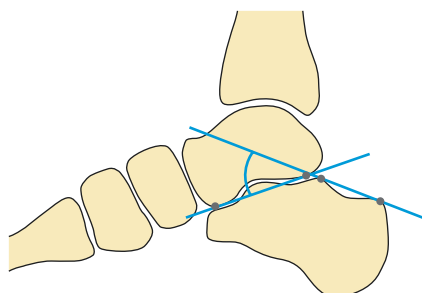
Fig. 15.18 Schematic and radiograph showing Bohler's angle

15.17   Gissane's Angle

Definition

Gissane's angle is the superiorly facing angle formed between the slope of the posterior facet and the middle facet (Fig. 15.19). It reveals the angular relationship of the calcaneal facets. Unlike Bohler's angle which may be misleading in the presence of combined extra-and intra-articular fractures, Gissane's angle is claimed to be more specific to assess intra-articular displacement.

Indications

Assessment of calcaneal fractures (Figs. 15.18 and 15.19) (Table 15.24).
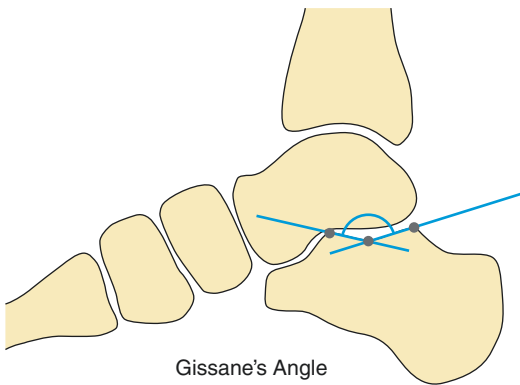
Fig. 15.19   Schematic demonstrating Gissane's angle

Table 15.24   Agreement of measures for Gissane's angle (Clint et al. 2010)

Intra-observer	0.566 ± 0.083
Interobserver	0.450 ± 0.096

Technique

Lateral radiograph of the calcaneum, with the central beam over the malleoli.

Full Description of Technique

Lateral weight bearing radiograph of the ankle and hindfoot. Correct positioning requires radiographic superimposition of both malleoli.

Reproducibility/Variation

Clint et al. examined the interobserver and intra-observer reliability of Gissane's angle.

Clinical Relevance/Implications

While Gissane's angle may be of relevance in the management of adult fractures, the intra-observer reliability is too poor to make it useful in children (Clint et al. 2010).

References

Abulsaad M, Abdelgaber N (2008) Correlation between clinical outcome of surgically treated clubfeet and different radiological parameters. Acta Orthop Belg 74(4):489–495

Aurell Y, Johansson A, Hansson G, Wallander H, Jonsson K (2002) Ultrasound anatomy in the normal neonatal and infant foot: an anatomic introduction to ultrasound assessment of foot deformities. Eur Radiol 12(9):2306–2312

Bohler L (1931) Diagnosis, pathology, and treatment of fractures of the os calcis. J Bone Joint Surg Am 13(1):75–89

Clint SA, Morris TP, Shaw OM, Oddy MJ, Rudge B, Barry M (2010) The reliability and variation of measurements of the os calcis angles in children. J Bone Joint Surg Br 92(4):571–575

Coley BD, Shiels WE, Kean J, Adler BH (2007) Age-dependent dynamic sonographic measurement of pediatric clubfoot. Pediatr Radiol 37(11):1125–1129

Davids JR, McBrayer D, Blackhurst DW (2007) Juvenile hallux valgus deformity: surgical management by lateral hemiepiphyseodesis of the great toe metatarsal. J Pediatr Orthop 27(7):826–830

Davis LA, Hatt WS (1955) Congenital abnormalities of the feet. Radiology 64(6):818–825

de Gheldere A, Docquier P-L (2008) Analytical radiography of clubfoot after tenotomy. J Pediatr Orthop 28(6):691–694

Dimeglio A, Bensahel H, Souchet P, Mazeau P, Bonnet F (1995) Classification of clubfoot. J Pediatr Orthop B 4(2):129–136

Downey DJ, Drennan JC, Garcia JF (1992) Magnetic resonance image findings in congenital talipes equinovarus. J Pediatr Orthop 12(2):224–228

Elftman H, Manter J (1935) The evolution of the human foot, with especial reference to the joints. J Anat 70(Pt 1):56–67

Engel E, Erlick N, Krems I (1983) A simplified metatarsus adductus angle. J Am Podiatry Assoc 73(12):620–628

Farsetti P, Weinstein SL, Ponseti IV (1994) The long-term functional and radiographic outcomes of untreated and non-operatively treated metatarsus adductus. J Bone Joint Surg Am 76(2):257–265

Harris R, Beath T (1947) Army foot survey. Report. National Research Council of Canada, Ottawa

Howard CB, Benson MK (1992) The ossific nuclei and the cartilage anlage of the talus and calcaneum. J Bone Joint Surg Br 74(4):620–623

Ippolito E, Fraracci L, Farsetti P, De Maio F (2004) Validity of the anteroposterior talocalcaneal angle to assess congenital clubfoot correction. AJR Am J Roentgenol 182(5):1279–1282

Laaveg SJ, Ponseti IV (1980) Long-term results of treatment of congenital club foot. J Bone Joint Surg Am 62(1):23–31

McCluney JG, Tinley P (2006) Radiographic measurements of patients with juvenile hallux valgus compared with age-matched controls: a cohort investigation. J Foot Ankle Surg 45(3):161–167

Pekindil G, Aktas S, Saridogan K, Pekindil Y (2001) Magnetic resonance imaging in follow-up of treated clubfoot during childhood. Eur J Radiol 37(2):123–129

Pirani S, Outerbridge HK, Sawatzky B (1999) A reliable method of clinically evaluating a virgin clubfoot evaluation. In Proceedings of the 21st SICOT World Congress. SICOT

Radler C, Manner HM, Suda R, Burghardt R, Herzenberg JE, Ganger R, Grill F (2007) Radiographic evaluation of idiopathic clubfeet undergoing ponseti treatment. J Bone Joint Surg Am 89(6):1177–1183

Radler C, Egermann M, Riedl K, Ganger R, Grill F (2010) Interobserver reliability of radiographic measurements of contralateral feet of pediatric patients with unilateral clubfoot. J Bone Joint Surg Am 92(14):2427–2435

Ritchie GW, Keim HA (1964) A radiographic analysis of major foot deformities. Can Med Assoc J 91:840–844

Schmidt TL, Weiner DS (1982) Calcaneal fractures in children. An evaluation of the nature of the injury in 56 children. Clin Orthop Relat Res 171:150–155

Simons GW (1977) Analytical radiography of club feet. J Bone Joint Surg Br 59-B(4):485–489

Templeton AW, McAlister WH, Zim ID (1965) Standardization of terminology and evaluation of osseous relationships in congenitally abnormal feet. Am J Roentgenol Radium Therapy, Nucl Med 93:374–381

Vanderwilde R, Staheli LT, Chew DE, Malagon V (1988) Measurements on radiographs of the foot in normal infants and children. J Bone Joint Surg Am 70(3):407–415

Wallander HM (2010) Congenital clubfoot. Aspects on epidemiology, residual deformity and patient reported outcome. Acta Orthop Suppl 81(339):1–25

Yeung EHK, Li YH, Ng ON, Chow W (2005) Radiographic assessment of congenital talipes equinovarus: strapping versus forced dorsiflexion. J Orthop Surg (Hong Kong) 13(3):253–258

The Adult Ankle and Foot

16

G. M. M. J. Kerkhoffs, R. R. van Rijn, P. A. A. Struijs,
C. M. Nusman, and M. Maas

Contents

G. M. M. J. Kerkhoffs, M.D., Ph.D.
Department of Orthopaedic Surgery, Suite G7-153,
Academic Medical Center Amsterdam,
PO Box 22660, 1100 DD Amsterdam,
The Netherlands
e-mail: g.m.kerkhoffs@amc.nl

R. R. van Rijn, M.D., Ph.D.
Department of Radiology, Suite C2-423.1, Academic
Medical Center Amsterdam, Meibergdreef 9,
1105 AZ Amsterdam, The Netherlands
e-mail: r.r.vanrijn@amc.uva.nl

P. A. A. Struijs, M.D., Ph.D.
Department of Orthopaedic Surgery, Suite G7-152,
Academic Medical Center Amsterdam,
PO Box 22660, 1100 DD Amsterdam,
The Netherlands
e-mail: p.a.struijs@amc.uva.nl

C. M. Nusman, M.Sc., Ph.D. • M. Maas, M.D., Ph.D. (✉)
Department of Radiology, Suite G1-211,
Academic Medical Center, Meibergdreef 9,
1105 AZ Amsterdam, The Netherlands
e-mail: m.nusman@amc.uva.nl; m.maas@amc.uva.nl

16.1   Anatomical Considerations, Lines and Landmarks

Measurements of osteoarticular relationships and their related soft tissue structures using multiple imaging modalities, play an important role in the diagnosis and management of traumatic and non-traumatic adult ankle and foot disorders. As in the paediatric foot, familiarity with anatomical landmarks/lines related to the adult standard radiographic projections is a necessary prerequisite before their clinical application. It is important to remember that the normal painless adult foot can have a wide range of bony relationships and measured values can indeed be in the abnormal range. Contralateral assessment and comparisons are very important in this respect (Steel et al. 1980).

In this chapter the large number of lines, angles and measurements are presented by grouping them under the heading of the standard radiographic view that allows their evaluation to be made. Weight-bearing films are essential as there are significant measurement differences from non-weight-bearing radiographic measurements. More detailed coverage of the main angles then follows. In particular special attention is given to the difficulties in evaluating the distal tibiofibular syndesmosis and the current roles that CT, MRI and US play in its evaluation in trauma and post-operative scenarios. Attention to the important soft tissue structures is then included emphasizing the role of US and MRI in evaluating the dimensions and morphological features of ligaments and tendons.

As highlighted in the previous chapter the talus is one of the most important bones of the adult ankle and foot articulating with the tibia, fibula, calcaneus and navicular. It forms three articulations, the *ankle* (talocrural), *distal tibiofibular* (syndesmosis) and the *subtalar* (talocalcaneal) joints. Although the osseous anatomy of the adult ankle joint renders it fairly stable with similarities to a mortise joint, there are two fundamental differences: the anterior width of the talar trochlea is wider (mean **28.5 mm**) than the

posterior width (mean **21.5 mm**), and the articular component of the lateral malleolus is longer than that of the medial malleolus. The planes of the concave tibial and convex fibular facets of the talus are not parallel. Ankle joint stability is therefore also reliant on its strong medial and lateral ligaments and the four strong ligaments of the syndesmosis.

Routine ankle radiographs include AP, mortise and lateral views. The mortise view done by internal rotation of about 20° brings the talus into a true AP projection with the malleoli equidistant from the cassette. The beam is centred on the joint space with the foot dorsiflexed to avoid superimposition of the lateral malleolus on the calcaneum. A number of lines, angles and "clear" spaces can be drawn and measured using these views. This is particularly relevant in trauma scenarios and should routinely form part of the radiographic review in the presence or absence of fractures. Different projections have different ranges of normal values (Sclafani 1985).

Lines and Angles on the Ankle AP View

The following lines and angles can be drawn and evaluated on this view (Fig. 16.1).

1. *Tibial shaft line*: through the mid-tibial shaft axis.
2. *Medial malleolus line*: tangential to the articular surface of medial malleolus.
3. *Lateral malleolus line*: tangential to the articular surface of the lateral malleolus.
4. *Talus line*: tangential to the articular surface of the talar dome.
5. *Talo-Tibial angle*: formed medially between the talus and medial malleolar lines, **Normal value 53° (range 45–65°)**
6. *Talo-Fibular angle*: formed laterally between the talus and lateral malleolar lines, **Normal value 52° (range 43–63°)**
7. *Medial talar edge angle* (MTEA): formed between the talus line and a second line to the medial talar surface facing the medial malleolus—**Normal value 110°** (a).
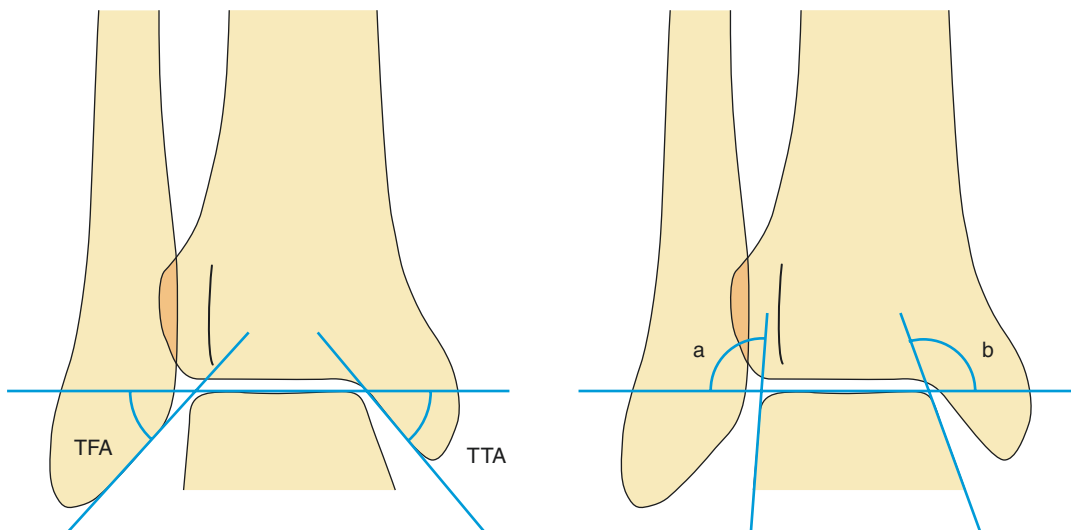
Fig. 16.1 Ankle anterior–posterior view. TFA = talo-fibular angle; TTA = talo-tibial angle; a = lateral talar edge angle, b = medial talar edge angle

8. *Lateral talar edge angle* (LTEA): formed between the talus line and the line through the lateral talar surface facing the lateral malleolus—**Normal value 91.8°** (b).

Measurements on the Ankle AP View

Several radiographic measurements can be used to assess the ankle and its distal tibiofibular syndesmosis (Fig. 16.2). Markers for integrity and stability include the tibiofibular overlap (Pettrone et al. 1983; Harper and Keller 1989), tibiofibular clear space (Leeds and Ehrich 1984; Sclafani 1985; Harper and Keller 1989) and the ratio of the medial and superior clear space (Beumer et al. 2004).

1. *Tibiofibular Clear Space (TFCS)*: is the lateral space between the lateral border of the posterior tibia and the medial border of the fibula measured 1 cm above the joint line from the tibial plafond (AB in Fig. 16.2).
   Normal value < 5 mm (on both AP and Mortise views).
   Abnormal value > 6 mm (in syndesmotic and deltoid ligament rupture).
   An increase by as little as 1 mm equates to a 42% reduction of the tibiotalar contact area

and therefore significant instability with a high risk of degenerative change.
2. *Tibiofibular overlap (TFO)*: is the space between the lateral border of the tibia and medial border of the fibula measured 1 cm above joint line from the tibial plafond. It should **normally be > 6 mm or 42%** of fibular width (CB in Fig. 16.2)**.**
3. *Ankle joint space* at the tibial plafond should normally be **3–4 mm.** The mean cartilage thickness of the talar dome is only **1.2–1.4 mm.** In general the thickness of the articular cartilage appears to be related to the congruence of the joint. The ankle joint has a high congruence ratio allowing compressive loads to be dissipated over a wide area.
4. *Medial clear space* should be **<3 mm** and equal to the *superior clear space.*
5. *Talar tilt*: **>2 mm** difference between medial and lateral joint space. **> 2° angulation** compared with contralateral side may indicate medial or lateral disruption.
6. *Varus and valgus stress views* of the ankle: Due to the normal variation resulting from normal joint laxity this can be controversial. A stress test is regarded as abnormal if:
   (a) the talar tilt is > or equal to 10° more than the contralateral normal side, or
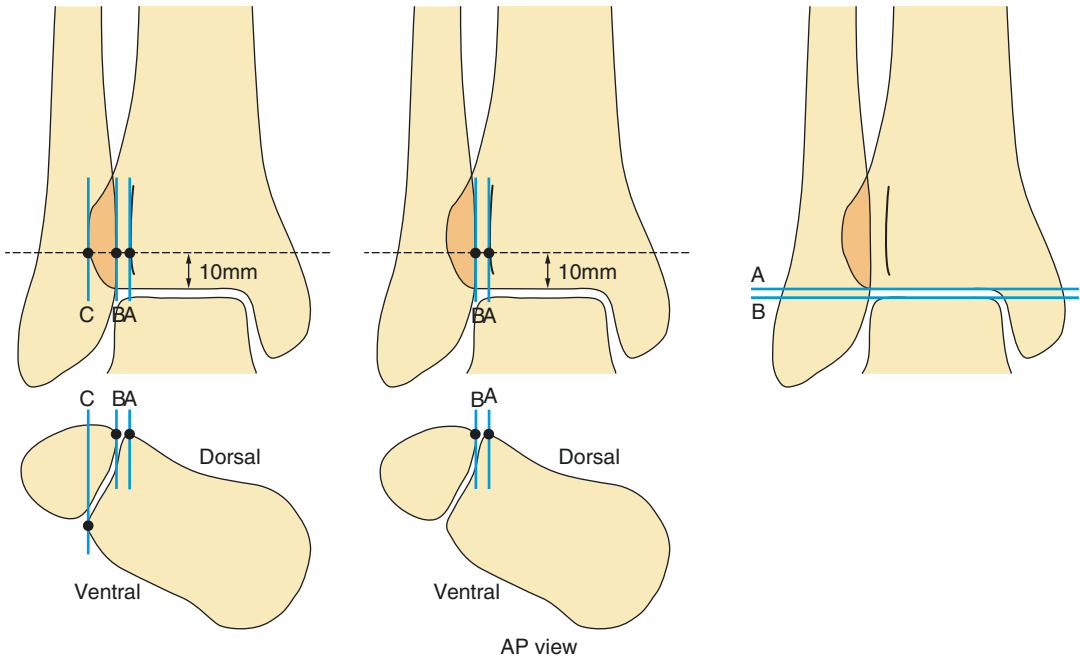
Fig. 16.2 Measurements on the ankle and the distal tibiofibular syndesmosis

(b) > or equal to 3 mm discrepancy in the opening of the lateral joint space distance between the injured and normal sides. This is measured from the most lateral aspect of the talar dome vertically to the tibial articular surface.

Varus stress is applied in plantar flexion to assess the integrity of the ATFL and CFL ligaments. Normal tilt angle between the talar dome and tibial vault lines opens laterally and is normally <5°. If tilt is >10° it is abnormal indicating lateral ligament failure.

Stable < 5° difference between injured and uninjured sides.
Unstable > 5°.

Valgus stress tests the deltoid ligament integrity. Park et al. (2006) indicated that stress views should be done with the ankle in dorsiflexion and in external rotation to assess the deltoid ligament integrity. Tears of the ligament produce a widening of the medial clear space to **5 mm or more**.

Measurements on the Mortise View

The following lines, angles and measurements can be made from the mortise view (Fig. 16.3).

1. *Medial clear space (MCS)*: between the medial tip of the talar dome and the lateral border of the medial malleolus measured 0.5 cm below the tibial plafond.

Normal value < 4 mm.
Abnormal value > 4 mm indicates lateral talar shift.

2. *Tibiofibular overlap (TFO)*: **normally > 1 mm**.
3. *Talocrural angle*: formed by a line joining both malleolar tips (Line 1) and the line paralleling the distal tibial articular surface (plafond) which is **normally 8–15°**. An alternative definition of this angle is the angle formed by the perpendicular drawn to the tibial plafond (Line 2) and the intermalleolar line (Line 3) which **normally is 75–87°** (Fig. 16.4). An angle >87° suggests syndesmotic injury.

4. *Talar tilt*: should be O° (range − 1.5–1.5°) as the lines drawn to the talar dome and distal tibial articular surface should be parallel.
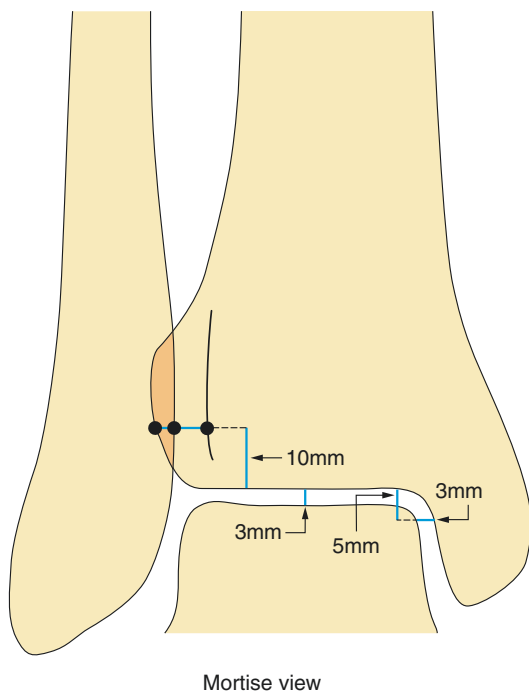
Mortise view

Fig. 16.3 Measurements on the ankle in mortise view
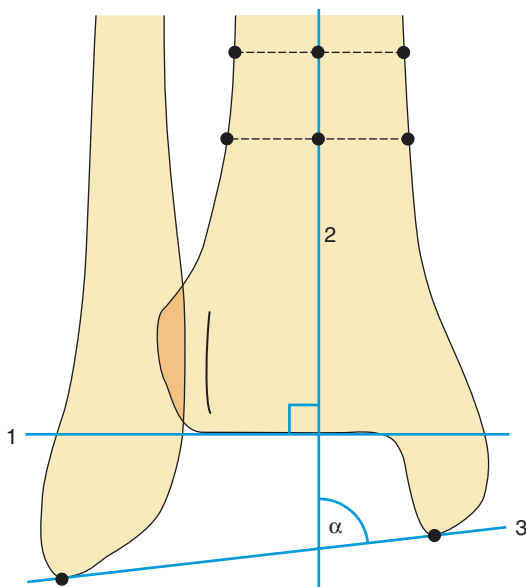
Fig. 16.4 Talocrural angle on the mortise view

Syndesmosis: MRI/CT/US

The distal tibiofibular syndesmosis is formed by two bones and four ligaments which include the distal anterior inferior tibiofibular ligament (AITFL), the distal posterior inferior tibiofibular (PITFL) ligament, the transverse tibiofibular ligament and the interosseous ligament (Fig. 16.5). It plays a crucial role in the stability of the talocrural joint (Miller et al. 2009). Syndesmotic injury refers to ligament injury and not just the syndesmosis as a fibrous joint in isolation, and it can occur in the presence or absence of a fracture. Disruption of at least two of the four lateral ligaments of the distal tibiofibular syndesmosis and injury to the deltoid ligament are required for a complete syndesmosis instability. Deltoid ligament disruption can rarely occur in isolation producing a widened medial clear space larger than the superior clear space but the syndesmosis is stable. Accurate measurements are vital because widening of the ankle mortise by 1 mm decreases the tibiotalar contact area by 42% promoting instability and premature osteoarthritis (Harris and Fallat 2004; Ramsey and Hamilton 1976). Using the classic radiographic criteria outlined above, earlier studies suggested that a diagnosis of syndesmosis disruption can be made reliably with no risk of false positives. A syndesmotic disruption produces a widened medial tibial clear space of >5 mm, a tibiofibular overlap of <10 mm on the AP view, and a tibiofibular overlap of <1 mm on the mortise view (Pettrone 1983).

The accuracy and reliability of these radiographic measurements as determinants of syndesmotic injury have however been questioned for a number of reasons. Firstly there is a wide normal anatomical variation of the degrees of tibial articular concavity and corresponding fibular convexity making up the articulation. As a result the concave incisura tibialis has a varying depth **(1.0–7.5 mm)** and shape with gender differences as well. Elgafy et al. (2010) showed that 67% of incisurae are crescent shaped compared with rectangular shape in the other 33% (Fig. 16.6). Secondly there is also normal variation in the size of both the anterior and posterior tibial tubercles which dictate the points of
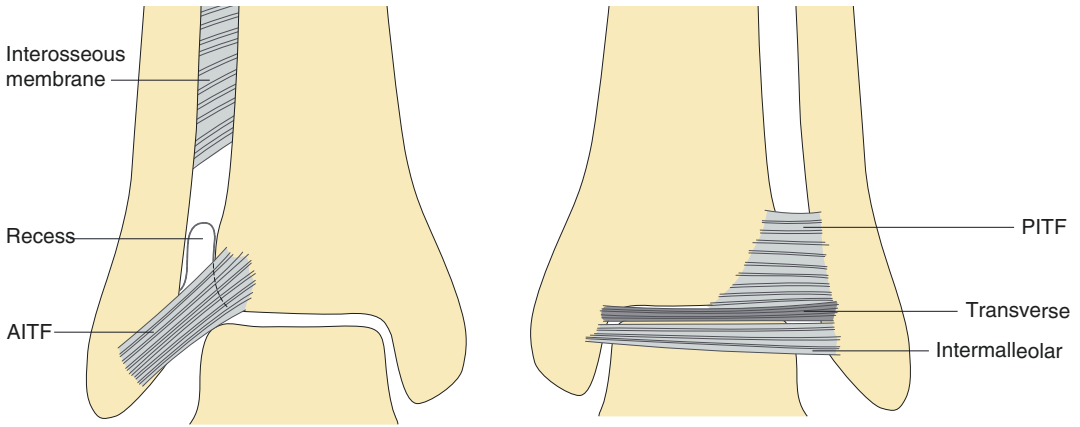
Fig. 16.5 Anatomy, ligaments and recess of the distal tibiofibular syndesmosis. AITF = anterior inferior tibiofibular ligament; PITF = posterior inferior tibiofibular ligament

Fig. 16.6 The anatomical variation of the tibial articular concavitiy (note iodinated contrast medium in the syndesmotic recess in c)
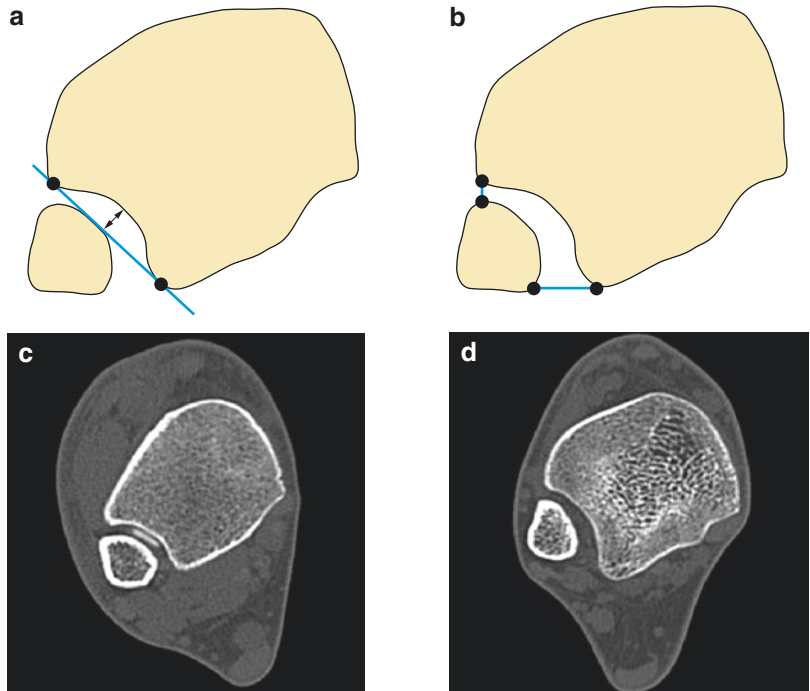
radiographic measurement done 1 cm above the level of the tibial plafond. Thirdly in a cadaver study by Beumer et al. (2004) using 12 rotational radiographic positions, it was concluded that there was no optimal radiographic parameter to assess the syndesmosis integrity. The presence and degree of talar shift will dictate the radiographic measurements and their perfor-mance in identifying syndesmosis injury. Tibiofibular overlap, medial clear space and superior clear space are the most useful because post-traumatic absence of tibiofibular overlap may indicate injury of the syndesmosis, and a medial clear space larger than the superior clear space is indicative of deltoid injury. More recently Shah et al. (2012) performed a large

study on 392 normal patients and found values for four of these measurements unreliable. They concluded that the previously reported classic radiographic criteria for syndesmotic injury were unreliable leading to either unnecessary treatment or failure to treat. Furthermore Takao et al. (2003) using arthroscopy as the gold standard showed that the AP and mortise measurements have different sensitivity, specificity and accuracy rates with 44.1%, 100% and 63.55% respectively for the AP view, and 58.3%, 100% and 71.2% for the mortise view compared with arthroscopy. The use of stress views is controversial as it carries a high false-negative rate in the acute setting (Hunt 2013).

Although the measurements have an overall low sensitivity for syndesmotic tears indicating that tears can be present without radiographic displacement, abnormal measurements should always be taken as indicative of injury until proven otherwise, and an MRI carried out of the distal tibiofibular ligaments in the oblique axial and coronal planes for optimal assessment. Nielson et al. (2005) found poor correlation between the MRI findings of syndesmotic injury and the tibiofibular clear space. A medial clear space measurement >4 mm correlated with disruption of the deltoid and the tibiofibular ligaments. It was also confirmed by Hermans et al. (2010, 2012) that radiographic measurements of the syndesmotic space, tibiofibular overlap and medial clear space did not correlate with evidence of ligamentous injury on concurrent MRI examinations. These studies clearly indicate that radiographic measurements are unreliable and imaging in the axial plane is required for optimal measurement assessment of the syndesmosis. Direct assessment of the ligaments is also required for full assessment.

Anatomical knowledge is therefore crucial to ensure that the measurements are carried out appropriately and in the appropriate imaging plane (Muhle et al. 1998). There is a small zone of tibiofibular contact with facets covered by hyaline cartilage (**0.5–1.0 mm** thick) extending superiorly from the tibial plafond and lateral malleolar cartilage respectively at the base of

the syndesmosis. On the tibial aspect this cartilage is 3–9 mm in length and only **2–5 mm** in height. The syndesmotic recess which extends vertically in the space from the ankle joint (Fig. 16.5), varies in size and also has an intrarticular synovial fat pad. The intra-articular fat pad ranges 0–7 mm, is attached to the fibula and the anterior aspect of the PITFL and functions like a meniscus. The syndesmosis recess's AP length has a 10–15 mm range, with a 2 mm width, and a 4.0–12 mm height range. The recess is limited cranially by the inferior edge of the interosseous ligament, posteriorly by the transverse ligament and PITFL, and anteriorly by the AITFL (Fig. 16.7). Morris et al. (1996) indicated that a recess of **>13 mm** in height on an MR study was indicative of syndesmotic rupture.

There are two ligaments anteriorly (Figs. 16.5 and 16.7). The *AITFL* is best seen in the coronal plane extending obliquely from its proximal medial tibial attachment (Tillaux-Chaput tubercle) about 5 mm above the articular surface to the distal lateral fibular attachment (Le Fort tubercle). Up to 20% of it is intra-articular. It makes an angle of 30–50° in the coronal plane to the tibial plafond, and posteriorly 65° in the sagittal plane. It is multifascicular with inherent fat interposed between the ligament tissue. There are 3 main anatomical components of the AITFL with the following anatomical measurements:

AITFL	Length	Width	Thickness
Superior	**6.0–8.9**	**4.0–4.9**	**1.8–3.0 mm**
Middle	**12.0–15.5**	**8.3–10.0**	**2.6–4.0 mm**
Inferior	**17.0–20.6**	**3.8–4.0**	**2.0–2.2 mm**

whereby the superior component is the shortest, the middle component the strongest and the inferior component the longest. It appears triangular on axial MRI with a multifascicular appearance separated by fat. As it runs obliquely, MRI in the axial plane can lead to it falsely appearing torn, and it is best assessed by an oblique axial sequence at 45° on the coronal scout. The *accessory antero-inferior tibiofibular ligament* is found in up to 94% of ankles lying in an intra-articular location inferior and parallel to the AITFL, coming into contact with the anterolateral
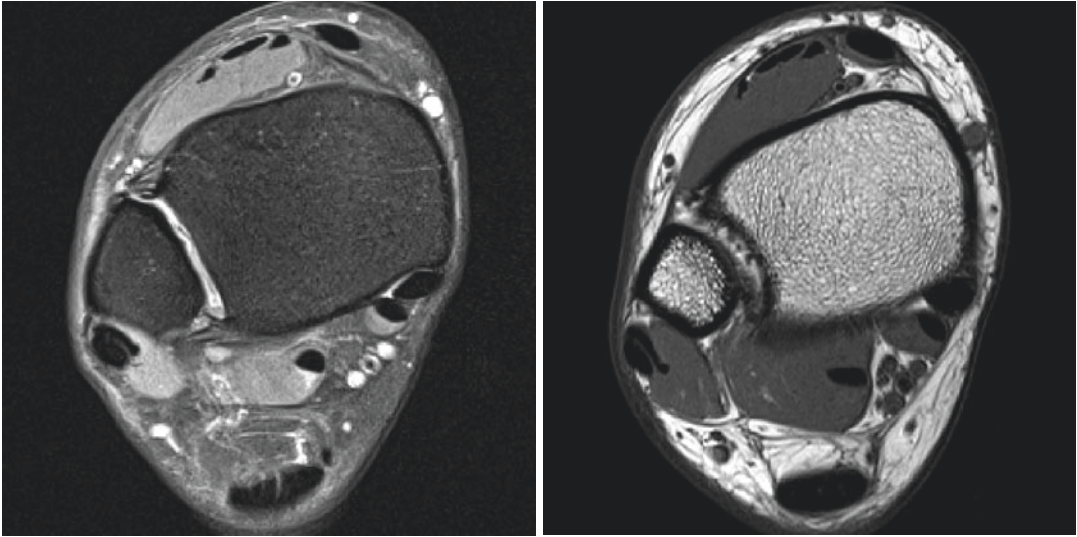
Fig. 16.7 Two axial MR images of the ankle, indicating ligaments and the recess of the syndesmosis. This recess is cranially limited by the inferior edge of the interosseous ligament, posteriorly by the transverse ligament and posterior inferior tibiofibular ligament and anteriorly by the anterior inferior tibiofibular ligament

aspect of the talar dome especially in dorsiflexion. It is 17–22 mm long, 3–5 mm wide and 1–2 mm thick (Subhas et al. 2008). This ligament, sometimes called Bassett's ligament can cause impingement after trauma if it becomes thickened as well as local synovitis and cartilage focal talar defects (Nikolopoulos et al. 2004).

Posteriorly the *PITFL* is a much stronger ligament running obliquely from the posterior aspect of the medial malleolus of the tibia proximal medial to the fibula distal lateral (Fig. 16.5). It makes an angle of 20–40° to the horizontal plane and 60–85° with the sagittal plane. It is more proximal and superficial to the transverse ligament. Its lower part is continuous with the transverse ligament as it runs horizontally, while cranially it is close to the interosseous ligament. It has a similar structure to the AITFL and shape appearing triangular with a broad tibial origin and multifascicular with interspersed fat. Its length varies due to the obliquety with the proximal portion shorter (9.7 +/−6.9 mm) than its distal portion (21.8 +/−7.5 mm). The mean width is 17.4 +/− 3.5 mm.

The *transverse tibiofibular ligament* runs horizontally with a length range of 22–43 mm (Fig. 16.5). It originates from the fibula posteromedially just above the fibular fossa and inserts on the dorsal tibial ridge along its entire medio-

lateral border. As it is attached to the posterior contour of the tibial articular surface it forms a true labrum seen on MRI embracing the posterior aspect of the talus. Some authors regard it as the deep component of the PITFL. When combined with the distal portion of the PITFL it forms the *intermalleolar ligament (IML)* which averages 3.7 mm wide and 2.8 mm thick with a length ranging from 22.0 to 39.7 mm depending on the imaging plane used. The IML is seen as a distinct ligament located between the PITFL and transverse ligament in over 80% of anatomical specimens but only 19% of MRI cases. Medially it exhibits a diverse origin from medial malleolus to the fibrous tunnels of the FHL tendon and extends as a thick ligament laterally to insert with the posterior talofibular ligament to the medial fossa of the lateral malleolus. This is why on sagittal images it has a scattered dot appearance medially and nodular laterally (Oh et al. 2006).

The *interosseous ligament* is the distal continuation of the interosseous membrane consisting of dense short fibres running obliquely upwards from the fibula forming the roof to the syndesmotic recess of the ankle joint. Its presence is variable, but it is prominent in cases of flattened tibial and fibular incisurae. It measures

3–6 mm in length, 2–4 mm in thickness, and 2–4 mm in width. It extends down to 2–3 cm above the tibiotalar joint (Figs. 16.5 and 16.7).

CT in the axial plane is sensitive to syndesmosis injury and is capable of identifying 2–3 mm diastasis not seen on routine radiography (Ebraheim et al. 1997). It also allows comparative assessment with the contralateral ankle and a difference of 2 mm or more indicates pathological displacement. However CT assessment is not done weight-bearing and will miss dynamic syndesmotic instability. Based on spiral CT assessment Taser et al. (2006a) showed that a 1 mm diastasis increased the volume of the syndesmosis by 43%, with an additional 20% increase for every further 1 mm. Elgafy et al. (2010) defined normal values for the syndesmosis using CT measurements taken 9–12 mm above the tibial plafond on bone windows. Two measurements were obtained, one anteriorly between the tip of the anterior tibial tubercle and the closest point to the fibula, and another posteriorly between the tip of the medial border of the fibula and the closest point on the tibial posterior tubercle (Fig. 16.6). The mean **anterior width was 2 mm** (range 1–3 mm), and the mean **posterior width was 4 mm** (range 3–6 mm) (Figs. 16.6 and 16.7). The anterior space is not identifiable on radiographs, while the posterior space is comparable to the tibiofibular clear space measured at the same reference points on an AP radiograph which normally is <5 mm (Taser et al. 2006b).

The syndesmosis can also be assessed in the axial plane using ultrasound. Mei-Dan et al. (2013) reported in a controlled study the role of dynamic stress US in assessing the syndesmosis, and provided normal values for the width of the anterior tibiofibular clear space measured at the level of the AITFL, 1 cm proximal to the joint line on over 100 normal individuals:

	Neutral	3.78 mm
Forced	Internal rotation	3.64 mm
Forced	External rotation	4.08 mm

It is important that all dynamic measurements are taken at the same level above the ankle joint**.** Differences between control and injured groups were statistically significant in a comparative study by Mei-Dan et al. (2009) using MRI as a gold standard.

A neutral position measurement **>5.06 mm** was assumed to indicate an abnormal finding (Mei-Dan et al. 2013).

Joint Effusion

An ankle joint effusion can be the only radiographic feature of ankle trauma as some fractures are occult. The radiographic size of the effusion is predictive of occult fracture whereby the larger the ankle joint effusion the increased likelihood of underlying fracture. Clark et al. (1995) showed that 33% of patients assessed within a 48 hour post-trauma period with an effusion measuring a **total** of 13 mm or more, had occult fractures detected by CT. In essence if the size of an effusion measured by the **sum** of the anterior and posterior capsular distension on a lateral radiograph is **>13 mm**, there is a positive predictive value of 82%, with a sensitivity of 82% and specificity of 91% for an underlying occult fracture (Fig. 16.8).
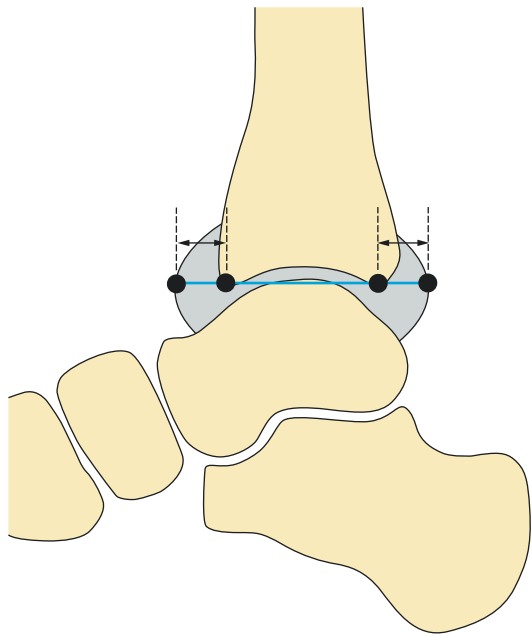
Fig. 16.8 Lateral view of the ankle indicating the locations which should be used to measure joint effusion

Axes/Angles on the Lateral View of the Ankle/Foot

There are a host of lines and angles that have evolved in the evaluation of foot and ankle disorders on standard lateral radiography of the ankle and foot.

Hindfoot dimensions. Baseline radiographic information is required when considering reconstruction, arthrodesis, osteotomy and total ankle replacement for hindfoot disorders. An appreciation of normal radiographic measurements has only relatively recently been addressed by Magerkurth et al. (2006). Parameters of joint configuration on lateral views were found to be reliable and include: the talar coverage by the tibia (tibiotalar sector), the angle of the distal tibial joint plane to the tibial axis (tilt), the AP width of the tibia, the talar height, ankle joint radius, and the offset of the centre of rotation from the tibial axis (Figs. 16.9, 16.10 and 16.11). A lateral radiograph must satisfy two quality criteria before deemed acceptable for measurement purposes: the distal fibula is superimposed on the posterior third of the tibia and both the medial and lateral joint lines are superimposed.

Several measurements can be done with respect to the hindfoot dimensions:

- anteroposterior position of talus
- tibia tilt angle, also known as sagittal antero-posterior distal tibial angle (sADTA)
- tibia articular surface width
- quotient of talar joint radius and relative height of the talus
- talar height
- tibiotalar sector
- ankle joint radius

The osseous configuration of joints has a bearing on joint stability best exemplified in studies of the ankle joint comparing normal from chronically unstable ankle joints. *Tibiotalar sector, the*
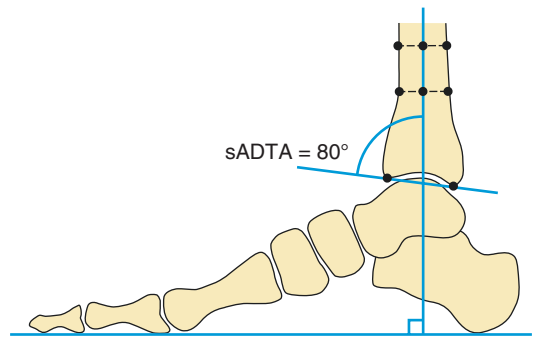
Fig. 16.10 Lateral view of the ankle, depicting the ankle joint radius. sADTA = anterior-to-posterior distal tibial angle

Fig. 16.9 Lateral view of the ankle, on which the tibiotalar sector (*left image*) and the A-P position of the talus highlighted by (•) relative to the tibial offset (*right image*), along with the talar radius (*r*) are depicted
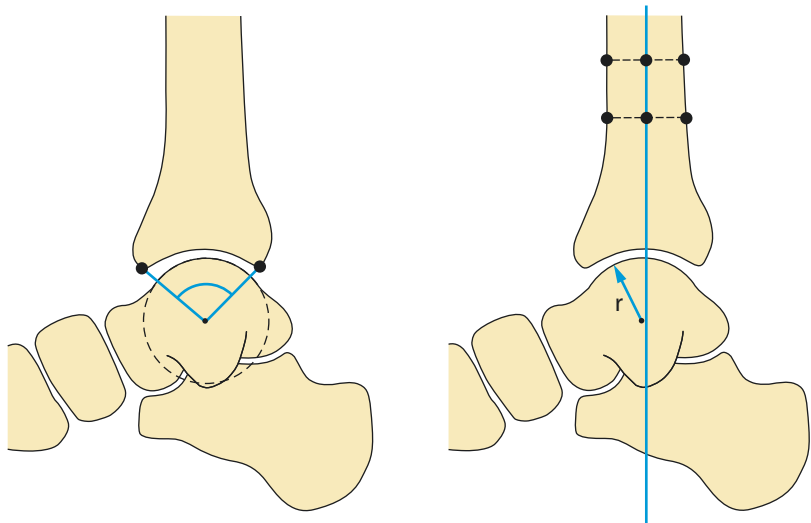
Fig. 16.11 Lateral view of the ankle, depicting the difference in radius of the talus and tibiotalar sectors between stable and unstable ankles

Stable   Unstable

Talar Declination Angle
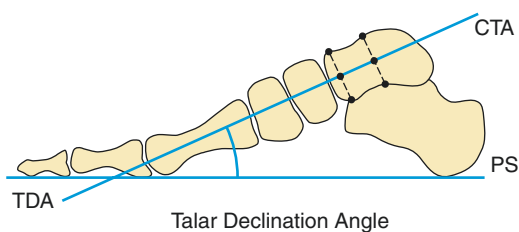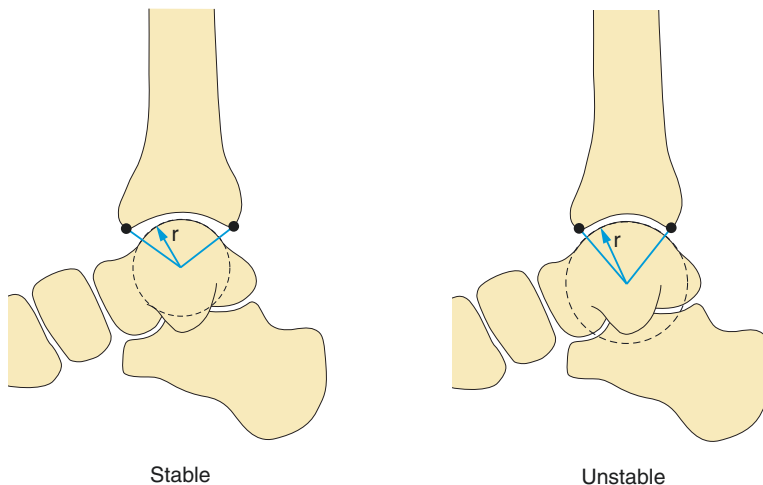
Fig. 16.12 Lateral view of the ankle, depicting the plane of support (PS), the collum tali axis (CTA) and the talar declination angle (TDA)

Lateral Tibio-Calcaneal Angle

Fig. 16.13 Lateral view of the ankle, depicting the lateral tibiocalcaneal angle

radius of the talus and the *talar height* have been found to be useful parameters in chronic deformities. Chronically unstable ankle joints for example have been shown by Frigg et al. (2007) to exhibit a larger radius of the talus 21.2 (2.4) mm and smaller tibiotalar sectors of 80° (5.1°), compared with control group measurements of 17.7 (1.9) mm and 88.4° (7.2°) respectively (Fig. 16.11).

There are many other radiographic lateral view weight-bearing axes and measurements. The ones used more commonly are briefly presented with their respective normal values and these include:

The *plane of support* (PS) is a horizontal reference line joining the most plantar point of the calcaneal tuberosity to the most plantar point of the fifth metatarsal (Fig. 16.12).

The *talar axis or collum tali axis* (CTA) passes through the midpoints of the head and neck of the talus (Fig. 16.12).

The *talar declination angle* (TDA) is the angle subtended between the PS and CTA (Fig. 16.12) and is normally about **21°**. (It should normally be the same as the first metatarsal declination angle).

The *lateral tibiocalcaneal angle* is measured between the axis of the tibia and the calcaneal axis (Fig. 16.13) with a **normal adult average of 70°** being typically **<65° in pes calcaneus**.

The *calcaneal inclination axis* (CA) is the line joining the most inferior point of the calcaneal tuberosity anteriorly to the most anterior point of the calcaneum at the inferior outline of the calcaneocuboid joint (Fig. 16.14).

The *lateral talocalcaneal angle* (LTCA) is the angle between the CA and the CTA which is

normally in the range of 30–50° with a mean of 35° (Fig. 16.14). It is **<30° in varus deformity** of the hindfoot and **>55° in valgus deformity** of the hindfoot.

*Calcaneal pitch angle (*CPA) normally between **10–20°**, is the angle between the PS or a horizontal reference line and the CA (Fig. 16.15) It is **<10° in pes planovalgus** (flatfoot) and **>20° in pes cavus.**

Boehler's Angle (**normal range 22–48°**) (Boehler 1931) is measured between a line tangent to the posterosuperior outline and a line tangent to the anterosuperior outline of the calcaneus (Fig. 16.16).

5th Metatarsal base height (**normal range 2.3–3.8 cm**). This assesses the longitudinal arch of the lateral column of the foot.

Philip-Fowler angle is a calcaneal angle drawn on the standing (Fowler and Philip 1945) lateral view between the line tangent to the inferior border of the calcaneus and the line tangent to the posterosuperior border of the calcaneus and the calcaneal tuberosity. It is **normally 44–69°** and angles **>75°** produce a prominent superior calcaneal tuberosity which promotes the production of the **Haglund deformity** (Fig. 16.17). The deformity is due to an abnormal prominence of the pos-terosuperior outline of the calcaneus, which can also be directly assessed using the *parallel pitch lines* described by Pavlov et al. (1982). The first line through the inferior border of the calcaneus is drawn, followed by a second parallel line to the first that passes through the posterior edge of the subtalar joint. Under normal conditions the posterosuperior border of the calcaneus is below the second line (negative), and it is deemed abnormal if it extends above it (positive) predisposing to the Haglund deformity (Fig. 16.18). However the relationship between symptomatic Haglund deformity and the two measuring methods described above was studied recently comparing symptomatic and controlled cohorts casting doubts on their value. The average Philip-Fowler angles in the control group and study group were 62.31 +/−7.79 and

Boehler's Angle

Fig. 16.16 Lateral view of the ankle, depicting the Boehler's angle

Lateral Talo-Calcaneal Angle
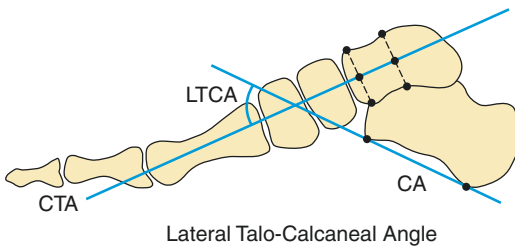
Fig. 16.14 Lateral view of the ankle, depicting the calcaneal inclination axis (CA), collum tali axis (CTA) and the lateral talocalcaneal angle (LTCA)

Calcaneal Pitch Angle
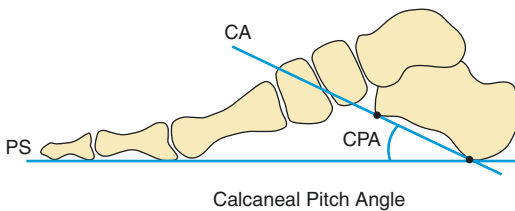
Fig. 16.15 Lateral view of the ankle, depicting the calcaneal pitch angle (CPA)

Philip-Fowler Angle
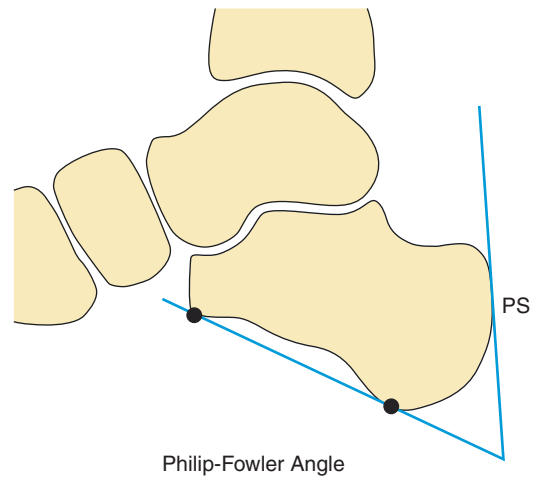
Fig. 16.17 Lateral view of the foot, depicting the Philip-Fowler angle

Haglund Deformity-Parallel Pitch Lines
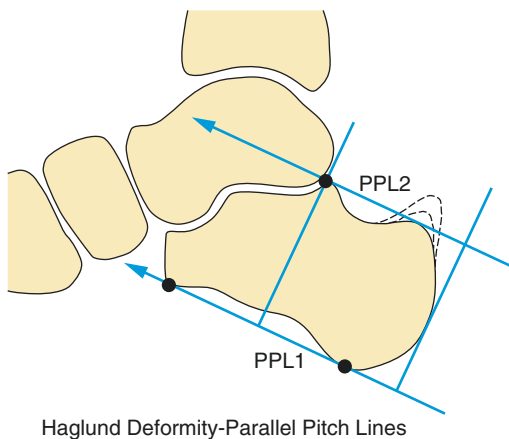
Fig. 16.18 Lateral view of the foot, depicting the Haglund deformity

60.14 +/− 7.01 respectively with no demonstrable statistical difference ($p = 0.490$) and a false negative rate of 94.6%. In addition there were 56.8% positive parallel pitch lines in the symptomatic group compared with 42.5% in the control group once again with no statistical difference ($p = 0.474$) with a false negative rate of 43.2% (Lu et al. 2007).

Axes/Angles on the AP View of the Foot

In the assessment of foot alignment as seen on a weight-bearing AP view of the foot one needs to appreciate that there are two often referred to longitudinal axis: the *anatomical axis* and the *mechanical axis*. The axis running from the centre of the second metatarsal head to the centre of the calcaneal tuberosity is the anatomical axis, while the axis from the centre of the first metatarsal head to the centre of the calcaneal tuberosity is the mechanical axis (Gentili et al. 1996).

The *longitudinal axis of the rearfoot* (LARF) or hindfoot reflects the axis of the calcaneus, but this is not easy to determine on an AP view of the hindfoot mainly due to radiographic superimposition of the tibia and fibula on the posterior aspect of the calcaneus. A tangent is therefore used as a reference line to the lateral calcaneal outline, ensuring that it is drawn to the distal portion of the lateral outline of the calcaneum so as to avoid the variable dimensions of the proximal contour of the calcaneum laterally which harbours the pero-

AP Talo-Calcaneal Angle

Fig. 16.19 Weight-bearing anterior–posterior view of the foot, depicting the longitudinal axis of the rearfoot (LARF), the collum tali axis (CTA) and the angle in between, which is the talocalcaneal angle (TCA)

neal trochlea (Fig. 16.19). Having established the tangential calcaneal line laterally, a parallel line is then drawn from the anteromedial corner of the calcaneus which should pass through the midpoint of the calcaneus posteriorly and usually also passes through the fourth metatarsal axis.

On the same AP view the *longitudinal talar axis* or *collum tali axis* (CTA) is determined by a line that joins the midpoints of the widest and narrowest points of the talar head and neck respectively. Normally this axis passes through the centre of the first metatarsal head, but it passes medial to it in the pronated foot and lateral to it in the supinated foot.
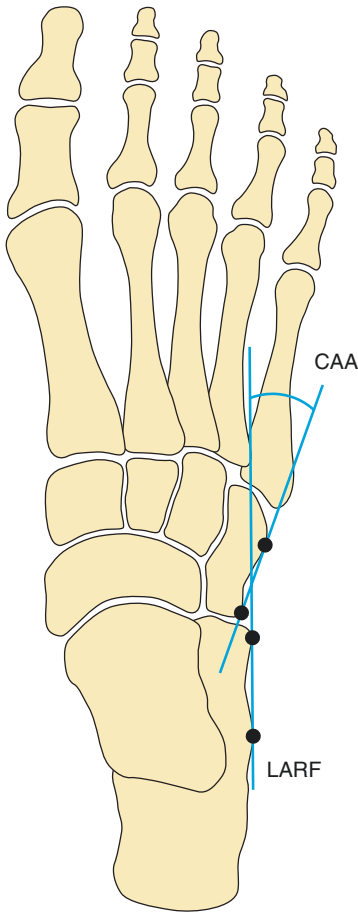
Cuboid Abduction Angle

Fig. 16.20 Weight-bearing anterior–posterior view of the foot, depicting the cuboid abduction angle (CAA). LARF = longitudinal axis of the rearfoot

The angle between the two lines described above (LARF and CTA) is the *AP talocalcaneal* (TCA or Kite) angle (Fig. 16.19). This angle is important in assessing paediatric disorders which has been covered separately in the previous chapter. On a weight-bearing AP radiograph of the adult foot, the AP talocalcaneal angle is created by drawing the long talar axis line which normally extends along the 1st metatarsal, and the line drawn along the lateral calcaneal surface as described above. As discussed earlier this view not uncommonly is underpenetrated which creates difficulties and potential measurement errors. In the adult foot the **normal range is 15–30°**, with **hindfoot valgus if > 30°** and **varus if < 15°**.
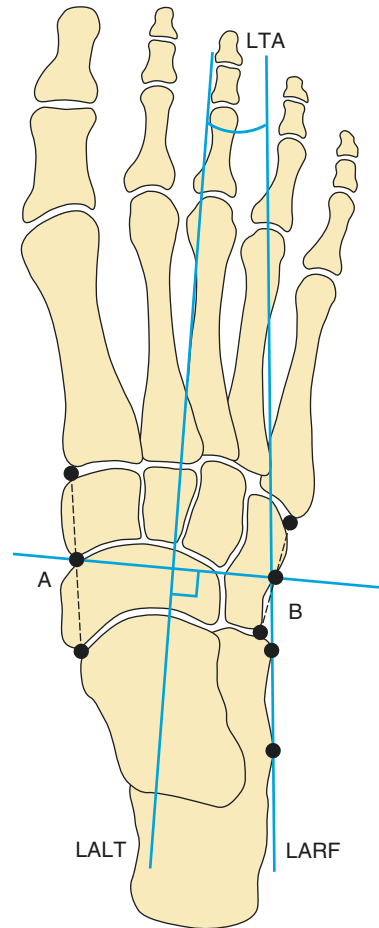
Lesser Tarsus Angle

Fig. 16.21 Weight-bearing anterior–posterior view of the foot, depicting the longitudinal axis of the lesser tarsus (LALT) and the lesser tarsus angle (LTA). LARF = longitudinal axis of the rearfoot

The *cuboid abduction angle* (CAA) is the angle subtended between the LARF and the line passing tangentially to the lateral surface of the cuboid with a **normal range of 0–5°** (Fig. 16.20).

The *longitudinal axis of the lesser tarsus* (LALT) is the line perpendicular to the lesser tarsus line (Fig. 16.21). The lesser tarsus line AB is determined by joining point A (which represents the midpoint between the medial aspect of the talonavicular joint and medial aspect of the first tarsometatarsal joint) to point B (which represents the midpoint between the lateral aspect of the calcaneocuboid joint and

the lateral aspect of the fifth tarsometatarsal joint).

The *lesser tarsus angle* (LTA) is the angle subtended between the LALT and the LARF (Fig. 16.21).

The *talonavicular angle* (TNA) is the angle subtended between the CTA and the lesser tarsus line AB (Fig. 16.22).

In addition on the AP weight-bearing view the *talonavicular coverage angle* is calculated between the lines drawn connecting the respective articular corners of the talus and navicular. **Normal values range from 1.8 to 19.3° in males**

and 6.7 to 21.7° in females. The degree of talar coverage by the navicular varies with deformity. In pes planus there is a lateral peritalar navicular subluxation, with a medial peritalar navicular subluxation in pes cavus. This is covered in greater detail in a separate section.

The *longitudinal axis of the metatarsus* (LAM) is the line that bisects the neck and proximal diaphysis of the second metatarsal.

The *forefoot adductus angle* (FAA) is the angle subtended between the LAM and the LARF with a **normal range of 4–12°** (Fig. 16.23).

Talonavicular Angle

Fig. 16.22 Weight-bearing anterior–posterior view of the foot, depicting the talonavicular angle (TNA). CTA = collum tali axis
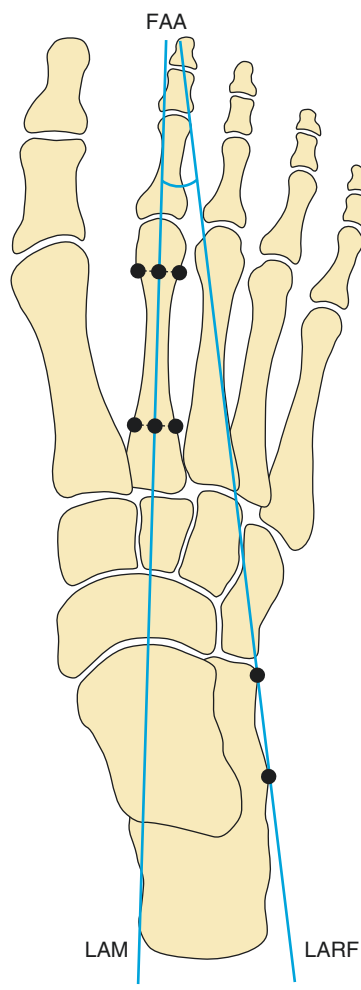
Forefoot Adductus Angle

Fig. 16.23 Weight-bearing anterior–posterior view of the foot, depicting the forefoot adductus angle (FAA) and the longitudinal axis of the metatarsus (LAM). LARF = longitudinal axis of the rearfoot

G. M. M. J. Kerkhoffs et al.

The *metatarsus adductus angle* (MAA) is the angle subtended between the LAM and the LALT and is **normally < 20° with a mean of 12.57 +/−0.22° (SD 5.18°)** (Fig. 16.24). It defines the angle between the five metatarsals and the lesser tarsus. The traditional Root method is time consuming as one has to bisect the lesser tarsus which features unreliable points of measurement. Laterally the halfway point between the calacaneocuboid-cuboid fifth joints is determined. Medially the halfway point between the talonavicular-medial cuneiform first metatarsal joints is then determined. A line joining the two points is then drawn transecting the lesser tarsus. The perpendicular to this line is the lesser tarsus longitudinal axis and its subtended angle with the longitudinal axis of the

second metatarsal is the metatarsus adductus angle. It has a normal range of 10–20° and a value >21° is abnormal indicating metatarsus adductus. In the simplified Engel et al. (1983) method this angle is created by the bisector of the middle cuneiform and its intersection with the second metatarsal axis. Using this method the angle is **normally < 24° with a mean of 17.91 +/− 0.22° (SD 5.20°).**

An assessment of the lengths of the metatarsals is valuable especially in deciding management of hallux valgus. The *metatarsal index* assessed on the weight-bearing AP radiograph defines the relationship of the first metatarsal to the other metatarsals (Fig. 16.25). An arc is first drawn joining the second to the fifth metatarsal heads, and then the position of

Fig. 16.24 Weight-bearing anterior–posterior view of the foot, depicting the metatarsus adductus angle (MAA), measured by means of the Root method (24a) and the Engel method (24b)
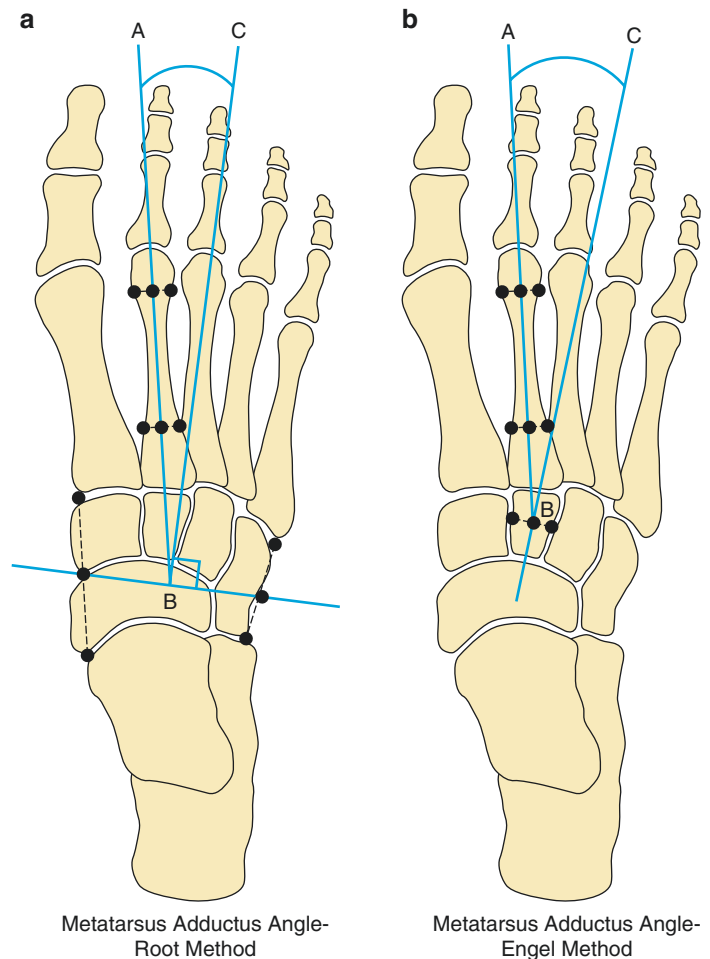
Metatarsus Adductus Angle-Root Method

Metatarsus Adductus Angle-Engel Method
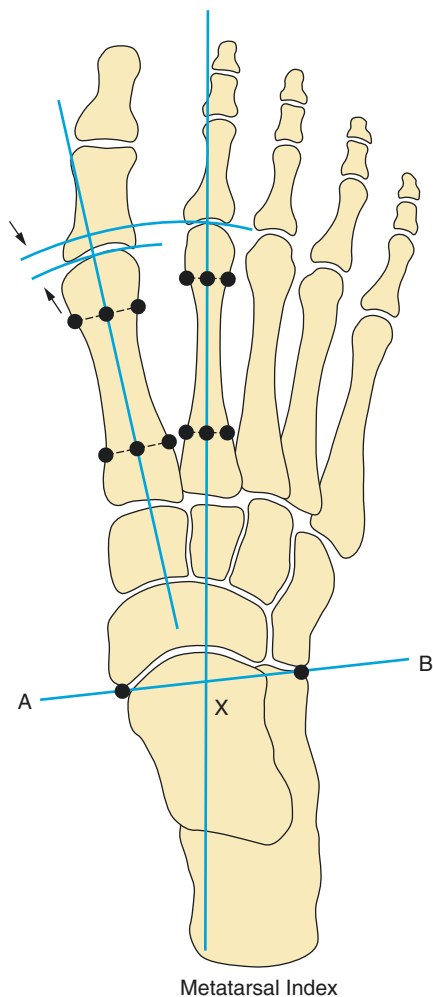
Metatarsal Index

Fig. 16.25 Weight-bearing anterior–posterior view of the foot, depicting the metatarsal index

the head of the first metatarsal head relative to the arc is determined. If the arc passes through the first metatarsal head this is deemed a neutral index, if it passes proximal to the first metatarsal head it is regarded as a plus index, and if it passes distal to the head a minus index. A minus index indicates a short first metatarsal which predisposes to hallux valgus, and a first metatarsal osteotomy is clearly contraindicated as a surgical therapeutic option. A simple geometric method devised by Hardy and Clapham is used in the relative assessment. Firstly a talar head centrepoint is deter-

mined on the AP radiograph by the intersection of the longitudinal axis of the second metatarsal and a line joining the proximal tip of the navicular medially to the calcaneocuboid joint laterally. Using this centrepoint two arcs are drawn through contours of the first and second metatarsal heads respectively, and the relative distance between the arcs is used to determine a plus or minus index using a 2 mm gap as the maximum allowable distance in each direction (Fig. 16.25).

The angle subtended by the longitudinal axes of the first and second metatarsals is called the *first–second intermetatarsal angle* (IMA) which is **normally < 10°** and **>10° in metatarsus primus varus**. This is important in surgical planning for hallux valgus deformity as it is increased as part of the deformity. As a rule abnormal IMA to 15° require a distal osteotomy while an IMA >15° requires a proximal osteotomy for correction.

On the AP weight-bearing radiograph other big toe measurements are calculated in surgical planning for hallux valgus surgery (Fig. 16.26).

The *hallux valgus angle* (HVA) is the angle between the longitudinal axis of the first metatarsal and first proximal phalanx and is **normally < 15–18°**; the *hallux interphalangeal angle* (HIA) is the angle between the longitudinal axes of the first proximal and distal phalanges and is **normally < 10°**; and the 1–2 intermetatarsal (IMA) angle is **normally < 10°** (Fig. 16.26).

The *proximal and distal articular set angles* (PASA and DASA) are also determined. PASA (**normal < 10°**) is the angle between the perpendicular to the articular surface of the first metatarsal head and the longitudinal axis of the first metatarsal, while DASA (**normal 0–6°**) is the angle between the perpendicular to the articular surface of the first proximal phalanx and its longitudinal axis (Fig. 16.27).

When a distal medial closing –wedge osteotomy is planned for hallux valgus correction, the *distal metatarsal articular angle* (DMAA) needs to be measured. This is a measure of the lateral slope of the articular surface of the first metatarsal head to its long axis and is **normally < 10°**. There is however a poor
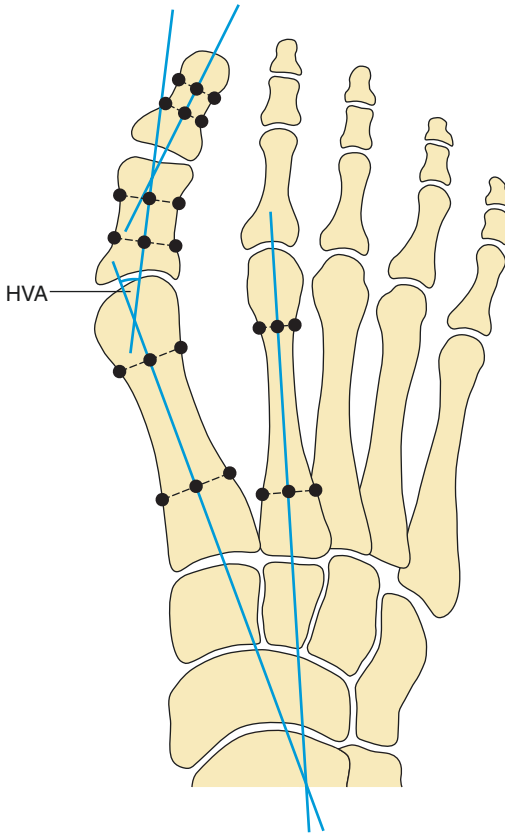
Fig. 16.26 Weight-bearing anterior–posterior view of the foot, depicting measurements required for evaluation of hallux valgus (HVA—hallux valgus angle, as well as the hallux interphalangeal angle - HIA, and the 1-2 intermetatarsal angle - IMA)

inter-observer reliability. If the DMAA is increased, the congruity of the first MTP joint needs to be assessed. This is because some hallux valgus cases with increased DMAA have congruent joints. The joint is declared congruent if lines drawn connecting the articular corners of the first proximal phalanx and the first metatarsal respectively are parallel. The majority of cases of hallux valgus have associated incongruent joints due to subluxation which requires articular surgical correction. If the angle at the incongruent first MTP joint is <20° it is deemed deviated, and if >20° it is designated as subluxed (Fig. 16.28). Congruency maintenance or restoration should be incorporated in the surgical management of hallux valgus.
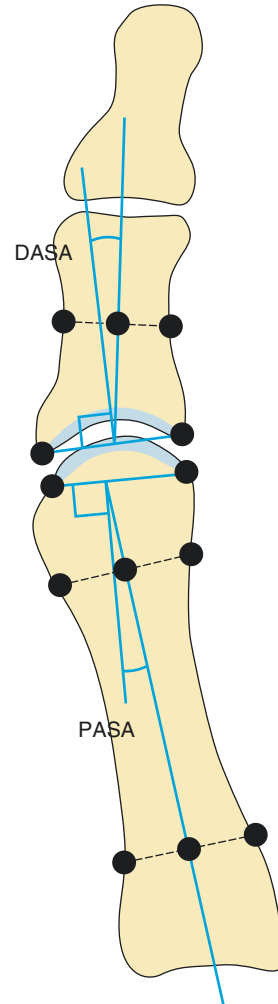
Fig. 16.27 Anterior–posterior view of the first metatarsal, depicting the proximal and distal articular set angles (PASA and DASA)

The Weight-Bearing Axis: Critical Overview

In the transverse plane the ankle axis is directed laterally, while in the coronal plane it is directed laterally and inferiorly. In the coronal plane the ankle axis at the tibial plafond lies at a mean of 93° to the vertical axis of the leg with a range of 88–100° SD +/− 2.7°.

On the AP view of the ankle the lateral distal tibial angle (LDTA) averages 89° between the middiaphyseal tibial axis and the talar dome. The
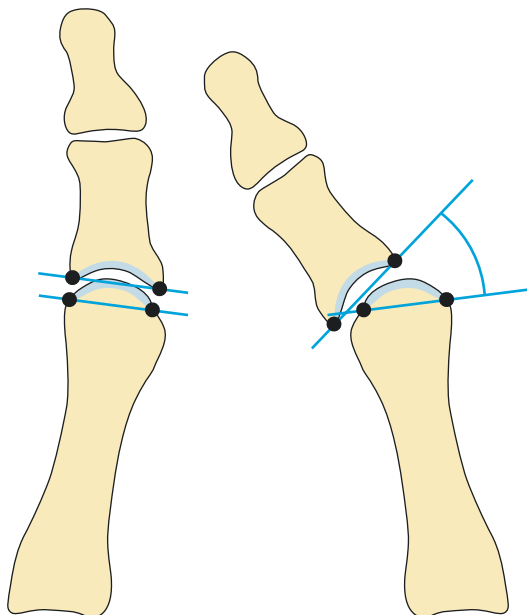
Fig. 16.28 Anterior–posterior view of the first metatarsal, depicting the distal metatarsal articular angle, which is normal at 0° (*left image*) and deviated or even subluxed when >0° (*right image*)

Fig. 16.29 Hindfoot alignement. Lat = lateral, med = medial

midtibial axis lies normally slightly medial to the centre of the talus. On the weight-bearing lateral ankle view the midaxis of the tibia normally passes through the lateral talar process, and the anterior-to-posterior distal tibial (sADTA) angle is 80°. The inclined subtalar axis passes from medial to lateral by about 23° in the transverse plane (range 4–47°), while from the horizontal plane it lies at an angle of about 42° (range 21–69°).

Hindfoot alignment is defined as the angular deviation in the frontal plane between the anatomical axis of the tibia and the longitudinal axis of the calcaneum (Fig. 16.29). Hindfoot alignment is best assessed radiographically, but care needs to be given to the optimal imaging method employed with strict attention to technique to minimize the risk of measurement errors. The original views proposed by Cobey were refined and replaced by the *hindfoot alignment view* and the *long axial view* radiographs. Technical factors are very important in their respective acquisition. The hindfoot alignment view requires the patient to stand on an elevated Plexiglas platform which has an inbuilt cassette holder in front of the feet

lying 20° to the vertical. The tube is placed posteriorly, centred on the ankle joint and angled 20° caudally to the horizontal perpendicular to the cassette. As foot rotation alters the measurement of the hindfoot alignment angle (HAA), it is important to always ensure that the long axis of the second metatarsal is perpendicular to the cassette when acquiring the Cobey view, and that the medial foot contour is parallel on the hindfoot and long axial views. On the hindfoot alignment view the midpoint of the calcaneal tuberosity normally lies slightly lateral to the midtibial axis producing a normal HAA of 0–5° valgus. Hindfoot valgus angles >10° are pathological and any degree of varus is abnormal. In the long axial view the patient stands on the film cassette and the posteriorly located tube is angled by 45° to the floor from the horizontal. The feet are placed 80 mm apart with the medial borders parallel to

each other by internal rotation so that the beam is parallel to the medial foot border.

In carrying out the hindfoot angular measurement there is universal agreement on how to define the midtibial axis, but varying methods have evolved in defining the longitudinal calcaneal axis. The midtibial longitudinal axis is defined by bisecting the tibia in the coronal plane 10 and 15 cm above the medial plafond. There is general agreement that a minimum distance between the two tibial points of 3 cm is required to maximize measurement reliability. To avoid the broad distal tibial metaphysis both points need to be at least 4 cm proximal to the ankle joint pace. Using Cobey's views Saltzman and El Khoury (1995) evaluated the alignment by measuring the horizontal distance between the tibial axis and the weight-bearing contact point of the calcaneum (Fig. 16.29). They reported that the weight-bearing midtibial axis fell within 8 mm from the lowest calcaneal point in 80% of asymptomatic adult subjects and within 15 mm in 95% with an inter-observer correlation coefficient of 0.97. The values were deemed positive if the tibial axis fell medial, and deemed negative if it fell lateral to the inferior calcaneal point. With the medial border of the feet aligned parallel to the X-ray beam the mean was −3.2 mm (SD = 7.2 mm).

These authors did not apply angular hindfoot measurement because of problems they encountered in measuring the calcaneal axis in pilot studies. Indeed the calcaneal axis on the hindfoot alignment view has never been defined (Buck et al. 2011). There is general agreement that two points are defined for this purpose. One is the midpoint between the lateral edge of the calcaneum at the level of the subtalar joint and the corner at the inferior aspect of the sustentaclum tali, and the other is the midpoint between the medial and lateral contours of the posterior calcaneal process. Defining the calcaneal axis can be challenging due to the inherent curved shape and variation of the calcaneum promoting unreliable measurements as shown by Saltzman et al. (1994). The main sources of inter-observer variation were in the intrinsic steps of measurement encompassing the landmarks selection, the draw-

ing of lines and the reading of the goniometer values. Buck et al. (2011) recommend that measurements on the hindfoot alignment view should not use the calcaneal axis as this is less reliable than the medial or lateral calcaneal contours. They indicated however that the calcaneal axis is reliable when used in measurements done on the long axial views. In addition there is a superior interreader reliability when the long axis view is used for measurements.

Normally the radiograph of an aligned hindfoot shows that the mid-diaphyseal tibial axis is virtualy parallel to the mid-diaphyseal calcaneal axis at 0°. The calcaneal axis is normally located 5–10 mm lateral to the tibial axis (Fig. 16.29). The long axial view has been found to be more reliable than the hindfoot alignment view (Reilingh et al. 2010) as indicated above. This could be related to the foreshortened view of the calcaneum on the hindfoot alignment view which is more prone to error as the distance between the points used in defining the calcaneal axis is smaller than on the long axial view. The inter-observer variability of the hindfoot alignment measurements can be significant and rotational malpositioning is a cause of measurement errors. 3-D measurements based on low-dose biplanar radiographs using phantom studies have shown that they are more accurate and reliable than the standard radiographic measurements (Sutter et al. 2013). Besides the increased precision of measurement from the 3-D biplanar radiographs, it is also the case that they are not dependent on the correct positioning of the foot which as indicated earlier is a significant potential cause of error.

Radiographs of the weight-bearing foot are used in the assessment of hindfoot varus and valgus deformities which include measurement indices from the lateral radiograph: calcaneal pitch angle, lateral talocalcaneal angle, tibiocalcaneal angle, lateral talus –first metatarsal angle, metatarsal stacking angle, naviculo-cuboid overlap and medial-lateral column ratio, and from the AP radiograph: talonavicular coverage angle and anteroposterior talus-first metatarsal angle. Reliability and validity studies have shown that the naviculo-cuboid overlap, the anteroposterior

talus-first metatarsal angle and the talonavicular coverage angle are acceptable in discriminating varus and valgus deformities (Lee et al. 2010).

Tendons, Ligaments and Nerves

The tendo-achilles is best assessed in the transverse and sagittal planes. In the axial plane the tendoachilles shows a normal concave anterior margin. The normal retrocalcaneal bursa on MRI measures <6 mm craniocaudally, 3 mm mediolaterally and 2 mm anteroposteriorly. The transverse oblique plane in MRI of the ankle produces a true cross-sectional evaluation of the ankle tendons.

The posterior tibialis tendon (PTT) is the commonest ruptured tendon in the hindfoot and often overlooked. Abnormal tendon size can be the only indicator of tendon dysfunction and the size of the PTT in axial MR images relative to the other tendons (FHL, FDL, AT and PT) at the level of the ankle is very useful. The PTT should be slightly smaller than the ATT and also slightly smaller than the summation of the PB and PL tendon measurements. It should normally be twice the size of either of the two adjacent tendons (FHL, FDL). Balen and Helms (2001) showed that abnormalities of the spring ligament are commonly associated with PTT injury in 92% of cases. PTT injury is also associated with plantar fasciitis on MRI.

The medial and lateral collateral ankle ligaments are well depicted by MRI and sonography. MRI allows differentiation of all the three components of the spring ligament complex. The superomedial CNL and the inferoplanter longidinal CNL components are consistently visualized while the medioplanter oblique CNL component is thinner, less clearly and consistently seen with its characteristic striated features. As highlighted by Boonthathip et al. (2010) and earlier when covering the measurements of the syndesmotic ligaments, care needs to be given to the oblique anatomical planes that some of these ligaments normally lie to the imaging plane which will affect the accuracy of measurement.

The tarsal tunnel is a fibrosseous space obliquely orientated as its roof the flexor retinaculum is connected obliquely between the medial malleolus and the medial calcaneal tubercle, which is referred to as the MMC axis. The posterior tibial nerve passes in the upper portion of the tunnel lying posterior to the tibialis posterior and flexor digitorum longus tendons and the posterior tibial vessels. The medial and inferior calcaneal nerves may arise proximal to, within or distal to the tarsal tunnel. Its bifurcation into the medial and lateral plantar nerves occurs in the tunnel in 88% of cases, proximally in 12% and rarely distally. Bilge et al.'s (2003) anatomical study measured the diameter of the posterior tibial nerve just before bifurcation as well as the diameters of the plantar nerves just after bifurcation:

Tibial nerve (mm)		LPN (mm)		MPN (mm)	
Rt	**Lt**	**Rt**	**Lt**	**Rt**	**Lt**
5.8 ± 0.8	6.03 ± 0.91	3.08 ± 0.6	3.01 ± 0.9	3.63 ± 0.7	3.64 ± 0.85

Bifurcation of the nerve occurs proximally at a higher level than that of the posterior tibial artery. The tibial nerve at its bifurcation commonly shows a distinct flattening appearing grooved as it lodges the artery.

16.2   Achilles Tendon Thickness: US

Definition

Achilles tendon anteroposterior thickness.

Indications

Measuring tendo-achilles thickness can mainly be helpful in diagnosing familial hypercholester-olaemia and Achilles tendon rupture.

Technique

Achilles tendon sonography.

Full Description of Technique

The patient lies prone with the feet dangling over the edge of the examination couch. The foot should be held at a 90° angle, to optimize the sur-face contact for imaging (Fig. 16.30).

The range of the transducer frequency varies from 5 to 12 MHz, although 7.5 MHz is mostly preferred. Thickness is measured at the level of the medial malleolus, mainly because it is an

obvious landmark. With the protocol mentioned above, the normal anterior–posterior thickness of the tendo-achilles should be within a small range, with variation between the different ethnicities (see below).

Authors	Population	Average thickness
Koivunen-Niemelä and Parkkola (1995)	Finnish	6.5 mm (± 0.8 SD)
Ying et al. (2003)	Chinese	5.23 mm (± 0.45 SD)
Mathieson et al. (1988)	North American	6.2 mm
Yuzawa et al. (1989)	Japanese women:	4.2 mm (± 0.5 SD)
	Men:	4.7 mm (± 0.4 SD)
Liem et al. (1992)	Dutch	6.2 mm (± 1.2 SD)

Reproducibility/Variation

Inter-observer variability is very low when observing a protocol and measuring at the same level. Influencing factors considering the Achilles tendon thickness are height, ethnicity, gender and age. The difference between men and women becomes significant in older age,
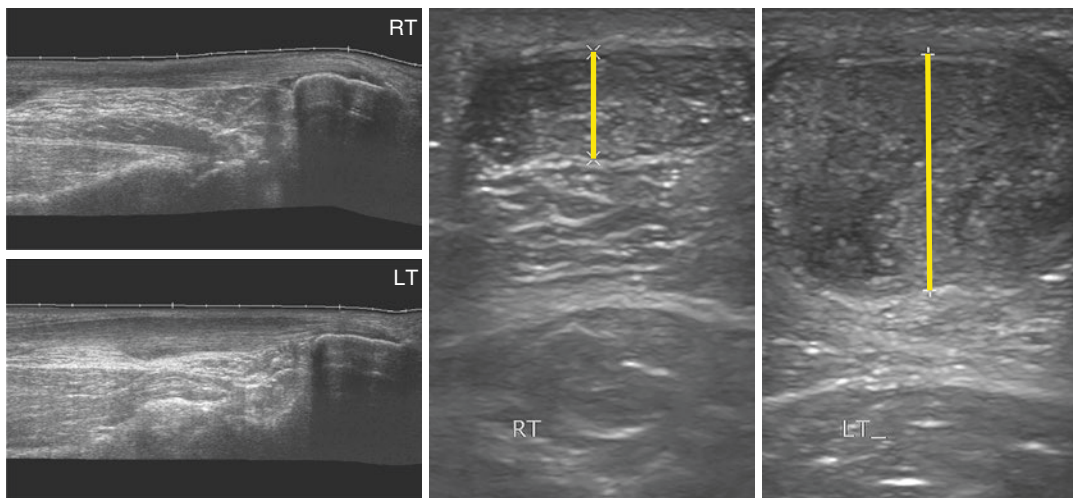
Fig. 16.30 Achilles tendon sonography, depicting a normal (RT) and thickened (LT) achilles tendon, visualized in two orientations

when mostly men's tendons are thicker. In the 30–80 normal age group Koivunen-Niemela (1995) found an average thickness of 6.7 +/− 0.8 mm in women and 7.1 +/− 1.2 mm in men. There is no significant difference between dominant and non-dominant ankles. In Ying et al.'s (2003) study the mean thickness of the achilles tendon varied between the frequent exercise group from the nonfrequent exercise group, measuring 5.43 (dominant) and 5.38 (nondominant) respectively in the exercise group, compared with 5.08 (dominant) and 5.04 (nondominant) in the nonexercise group.

Clinical Relevance/Implications

The measurement of achilles tendon thickness is useful for detecting and monitoring cholesterol accumulation (xanthomas) in familial hypercholesterolaemia. At the same time progressive thickness indicates beta-2-microglobulin accumulation in hemodialysis-related amyloidosis. The thickness is also positively correlated to achilles tendon rupture.

Analysis/Validation of Reference Data

Allowing for ethnic, age and gender differences the findings are consistent and reproducible (Mathieson et al. 1988; Liem et al. 1992; Yuzawa et al. 1989).

Conclusion

Sonographic measurement of the achilles tendon thickness is useful to indicate familial hypercholesterolaemia, beta-2-microglobulin accumulation in hemodialysis-related amyloidosis and tendon rupture. When following a protocol, interobserver variability is very low. Height, gender and age are factors to take into consideration because of the possible influence on the thickness.

16.3 Achilles Tendon Thickness: MRI

Definition

Achilles tendon anteroposterior thickness.

Indications

MRI of the achilles tendon provides a clear view of pathologic processes such as degeneration, ruptures and inflammations. MRI should be performed in addition to US mainly when US is not sufficient and more microscopic abnormalities have to be detected. With MRI it is also possible to evaluate the size of these lesions.

Technique

Achilles tendon T1 MRI sequences (Fig. 16.31).
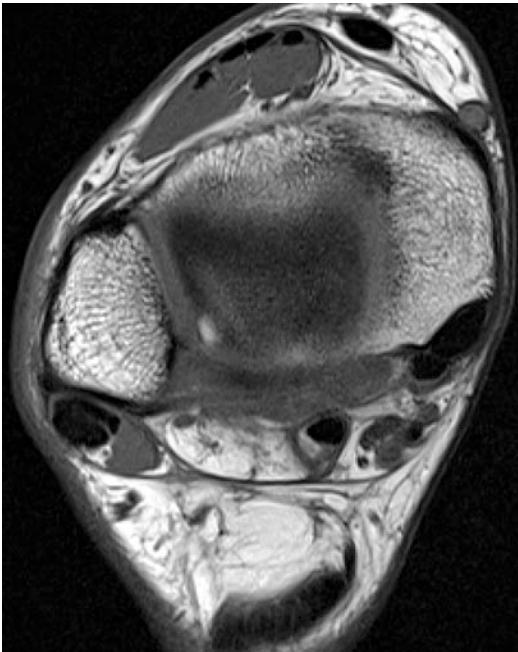
Fig. 16.31 Axial T1-weighted MR image of the foot/ankle, which clearly visualized the achilles tendon

Full Description of Technique

In order to measure anteroposterior achilles tendon thickness, both T1 sagittal and axial images should be obtained. Tendon thickness is measured at the thickest level below the soleus insertion. The normal average thickness of the achilles tendon is 6 mm.

Reproducibility/Variation

Height, male gender and age are positively related to the tendon thickness.

Clinical Relevance/Implications

MRI is performed when US remains unclear. Besides the ability to make a measurement with no statistically significant difference to US, MRI also enables the observer to define tendon degeneration and other intratendinous abnormalities, with tears at microscopic level, which may eventually lead to macroscopic tendon disorders (Neuhold et al. 1992; Schweitzer and Karasick, 2000).

Analysis/Validation of Reference Data

Although data not extensive there is overall good reproducibility (Haims et al. 2000; Koivumen-Niemela 1995).

Conclusion

Measuring the achilles tendon thickness with MRI is useful when the images obtained with US are unclear. MRI also allows the possibility to define microscopic intratendinous abnormalities, to predict or prevent tendinous degeneration and development of macroscopic lesions.

16.4   Anterior Talar Drawer

Definition

This is a measure of anteroposterior ankle laxity. Anterior talar drawer (mm) is measured as the shortest distance between the posterior lip of the distal tibial joint surface and the talar dome on a lateral ankle radiograph with the radiographic beam centred on the medial malleolus.

Indications

Indication for and evaluation of operative treatment for chronic lateral ankle laxity.

Technique

Stress Radiography (Kerkhoffs et al. 2002; Kerkhoffs 2007).

Fig. 16.32   Anterior drawer lateral radiograph

Full Description of Technique

Radiographs are taken in a standardized manner in a radiographic suite with standard equipment (Telos, Marburg, Germany) by 1 or 2 orthopaedic radiology technologists. Anterior talar drawer radiographs (Fig. 16.32) are taken with the patient lying on the respective lateral side with a flexed knee (30°). The fibular aspect of the foot is placed over a radiographic film, and the heel is fixed in the foot plate of the stress-testing device, allowing about 15° of ankle plantar flexion. Another pad of the apparatus supports the dorsal aspect of the middle lower leg. A posteriorly directed translating force of 15 kp is applied by a third pad, situated anteriorly above the inferior articular surface of the tibia.
Abnormal anterior translation: 5–10 mm or > 3 mm than contralateral side.

The mediolateral central beam is focused to the tuberosity of the medial malleolus.

Reproducibility/Variation

Based on the findings from this study, it can be concluded that measurement of the distance between the posterior lip of the distal tibia and the talar dome is the method of choice to characterize the position of the talus relative to the tibia in stress radiography. In order to standardize the radiographic evaluation of ankle injuries, this method should be the one employed to measure anterior talar translation. The ICC for intratester reliability is 0.95 for the anterior talar drawer test. The intertester anterior talar drawer ICC ranged from 0.73 to 0.87 (Beynnon et al. 2005).

Clinical Relevance/Implications

Stress radiography to measure anterior talar translation is an important research tool to evaluate the integrity of the ankle ligaments in studies of chronic ankle instability.

Analysis/Validation of Reference Data

Limited published data (Lohrer et al. 2008).

Conclusion

In conclusion, the results indicate that stress radiographs of the ankle joint can reliably be read if the proposed measurement techniques are applied. Further studies addressing the consistency and accuracy of different films that are repeatedly taken on the same subjects are needed to improve clinical relevance. Then, generally accepted normal values for the respective measures need to be established. Only measurement techniques with proven reliability should be used (Chandnani et al. 1994).

16.5   Boehler's Angle

Definition

The angle of the "tuber joint" as described initially by Boehler in 1931. This angle is formed by the intersection of a line drawn from the most cephalic point of the tuberosity to the highest point of the posterior facet, with a line from the highest point of posterior facet to the most cephalic part of anterior process of calcaneus.

Indications

Assessment of calcaneal fractures.

Technique

Ankle radiograph—standard lateral view (Fig. 16.16).

Full Description of Technique

Boehler's angle is drawn on a lateral radiograph of the ankle. The angle is composed of the intersection between:

1. Line between the peak of the anterior process to the peak of the posterior articular surface of the subtalar joint.
2. Line between the peak of the posterior articular surface of the subtalar joint to the peak of the tuberosity.

	Max	Min	Mean	Median	SD
Male	47.3°	21.1°	32.5°	33.0°	4.7
Female	45.3°	21.2°	32.0°	32.0°	5.3

There is no difference between the right and left foot (Thomas et al. 2006).

Reproducibility/Variation

Knight et al. (2006) showed that the interrater reliability of Boehler's angle is high with a low inter-observer variation.

Clinical Relevance/Implications

Boehler's angle can be used in assessing the presence of calcaneal fractures (Chen et al. 1991). A measurement <20° usually indicates a compression fracture of the superior aspect of the calcaneum/posterior facet of subtalar articulation. Its main use is in orthopaedic surgery where it is used to reconstruct the normal anatomy of the calcaneus after a fracture (Boehler 1931).

Analysis/Validation of Reference Data

Consistent reproduction of normal range in various studies.

Conclusion

A useful and reliable tool in the diagnosis and management of calcaneal fractures.

16.6 Calcaneal Pitch Angle

Definition

This is the angle between a line drawn from the plantar surface of the calcaneus to the inferior border of the calcaneo-cuboid interface, and a line from the plantar surface of the calcaneus to the inferior surface of the 5th metatarsal head.

Normal	10–20°
Decreased pitch	< 10° (pes planus)
Increased pitch	>20° (pes cavus)

Indications

Evaluation of flatfoot or cavus foot.

Technique

Lateral view of the foot (Fig. 16.15).

Full Description of Technique

Patient is supine. Turn patient toward affected side until the leg and foot are lateral. The lower leg should be parallel to the table. Keep the other leg behind to prevent over rotation. Ask the patient to dorsiflex their foot, if possible, so that the plantar surface is at 90° to the lower leg (This will best show the anterior pretalar fat pad).

Plantar surface of foot should be perpendicular to IR. Place the IR under the foot so that the midline is parallel with the long axis of the foot. Centre to the base of the metatarsals.

Reproducibility/Variation

Reliability of measurement of the CPA is high, with a reported inter-observer and intra-observer reliability of over 0.9 (1).

Clinical Relevance/Implications

The calcaneal pitch angle is an important measurement in deciding whether a patient has a flat foot or cavus foot. It can be used in assessment for orthotic devices and in preoperative planning for flatfoot or cavus foot surgery (Sensiba et al. 2010).

Analysis/Validation of Reference Data

Limited but suggest that measurement enjoys good reliability (Younger et al. 2005).

Conclusion

The calcaneal pitch angle is an important measurement, with high inter-observer and intra-observer reliability, in deciding whether a patient has a flat foot or cavus foot. It can be used in the assessment for orthotic devices and in preoperative planning for flatfoot or cavus foot surgery.

16.7   Distal Metatarsal Articular Angle (DMAA)

Definition

A line is drawn connecting two points placed at the most medial and most lateral extent of the 1st metatarsal head articular surface. A second line perpendicular to the long axis of the metatarsal is then drawn and this intersects the first at the DMAA with its apex lateral.

Normal angle < 10 ° (Average 7 °).

Indications

In preoperative planning of hallux valgus correction surgery, the DMAA is helpful in assessing the need for osteotomy if there is excessive valgus tilt of the articular surface.

Technique

DP view of the foot, weight-bearing (Fig. 16.28).

Full Description of Technique

Patient is weight-bearing in a supine position. Flex the knee of the affected leg. Place IR under foot parallel to its long axis. Place plantar surface of the foot flat to IR. Centre to the base of 3rd metatarsal. No rotation is evidenced by the joint between the medial and intermediate cuneiform is open (this is closed when the foot is rotated). First metatarsal shaft has equal concavity on both sides. Nearly equal spacing between 2nd to 5th metatar-

sals should be seen. There should be overlap of 2nd to 5th metatarsal bases. In the DP axial projection, the tarso-metatarsal and navicular-cuneiform joint spaces will be an open area.

Reproducibility/Variation

Reliability of measurement of the DMAA has been questioned by Coughlin and Freund (2001).

Clinical Relevance/Implications

The distal metatarsal articular angle is one of the important measurements needed to decide which surgical strategy should be applied to correct a hallux valgus deformity. In addition, it is a relevant parameter in assessment of clinical and radiological results of hallux valgus surgery (Pique-Vidal et al. 2006; Thomas et al. 2006).

Analysis/Validation of Reference Data

Limited studies (Deenik et al. 2008; McCluney and Tinley 2006).

Conclusion

The distal metatarsal articular angle is one of the important measurements needed to decide which surgical strategy should be applied to correct a hallux valgus deformity. In addition, it is a relevant parameter in assessment of clinical and radiological results of hallux valgus surgery. However, reliability in measurement is questioned.

16.8 Hallux Valgus Angle

Definition

The angle between the line from the center of the metatarsal base to the center of the first metatarsal head and the line connecting the midpoints of the proximal and distal articular surfaces of the proximal phalanx is the hallux abduction angle. Normal value is less than 15–18 °. Depending on the angle, different surgical techniques should be used to correct the deformity (Deenik et al. 2008; Thomas et al. 2006).

Normal value	<15°
Abnormal value	>15°

Indications

Preoperative planning of hallux valgus correction surgery.

Technique

DP view of the foot, weight-bearing (Fig. 16.33).

Full Description of Technique

Patient is weight-bearing in a supine position. Flex the knee of the affected leg. Place IR under foot parallel to its long axis. Place plantar surface of the foot flat to IR, centre to the base of 3rd metatarsal. There should be no rotation which is confirmed by seeing an open joint between the medial and intermediate cunei-forms (this is closed when the foot is rotated). First metatarsal shaft has equal concavity on both sides. Nearly equal spacing between 2nd to 5th metatarsals. There should be overlap of 2nd to 5th metatarsal bases. In the DP Axial projection, the tarso-metatarsal and navicular-cuneiform joint spaces will be an open area.

Reproducibility/Variation

Measurement of the hallux valgus angle or hallux abductus angle is very reliable, with interclass correlation coefficients of (nearly) 1.00 (McCluney and Tinley 2006).

Clinical Relevance/Implications

The hallux valgus angle is one of the important measurements needed to decide which surgical strategy should be applied to correct a hallux valgus deformity. In addition, it is a relevant parameter in assessment of clinical and radiological results of hallux valgus surgery.

Analysis/Validation of Reference Data

The angle has been shown to be reproducible and reliable.

Conclusion

Hallux valgus angle or hallux abductus angle is a reliable method for assessing, planning and evaluating hallux valgus pathology and surgery.

Fig. 16.33 Weight-bearing anterior–posterior view of the foot, depicting the hallux valgus angle (HVA, **a**) and the hallux interphalangeal angle (HIA, **b**)

Hallux Valgus Angle

Hallux Interphalangeal Angle
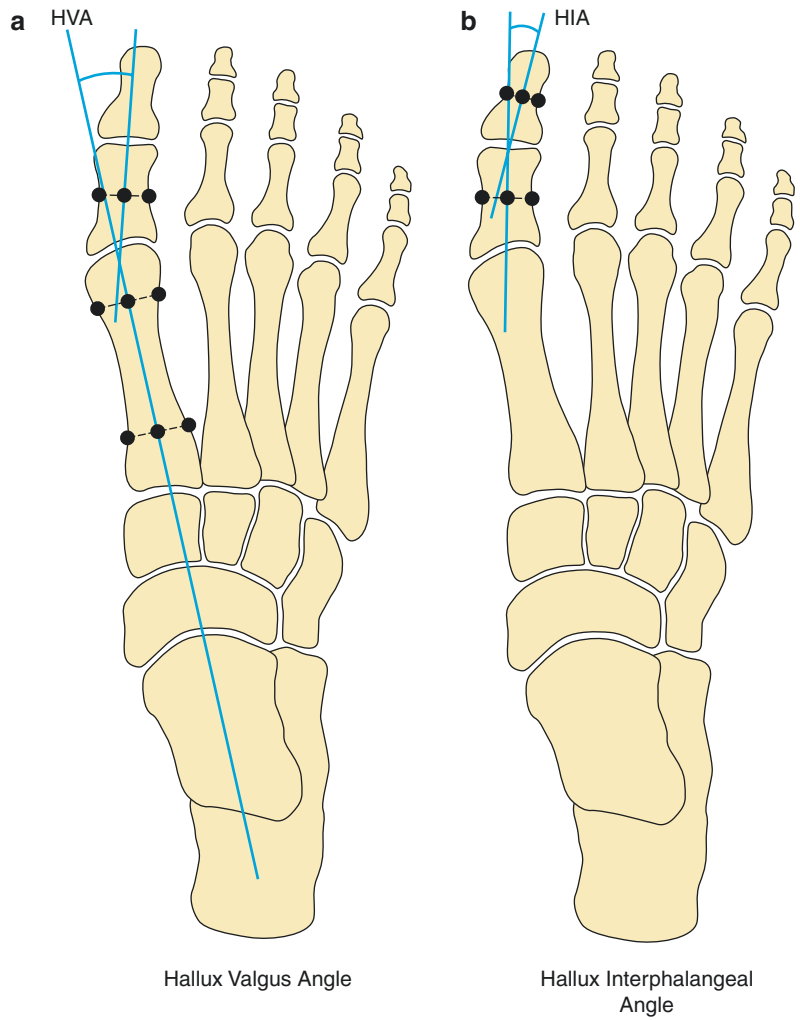
16.9 Hindfoot Dimensions

Definition

Hindfoot dimensions by conventional radiography. A critical overview has already addressed the pros and cons of the different radiographic methods in both the AP and lateral planes. This section will focus on the hindfoot alignment view measurements and the long axial view measurements.
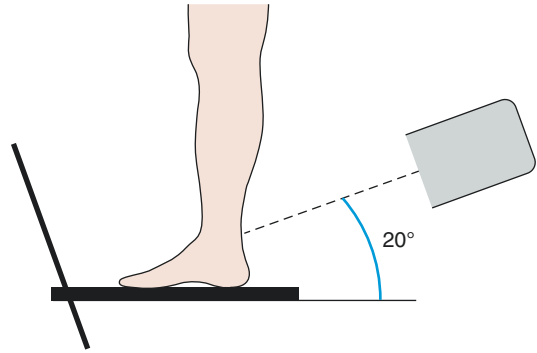
Indications

Reconstruction of complex hindfoot disorders need references for normal anatomical dimensions on standard radiography in order to perform successful reconstruction.

Technique

PA radiography.
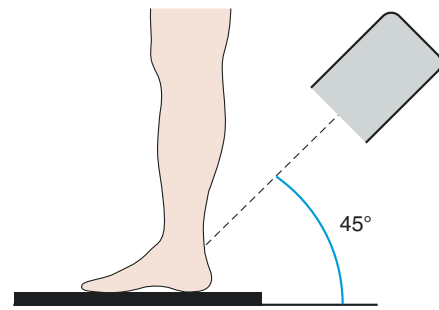
Full Description of Technique

Reilingh et al. (2010) compared the performance of two views. A *hindfoot alignment view* (Fig. 16.34) and a *long axial view* (Fig. 16.35) were acquired on 18 healthy volunteers in bilateral and unilateral weight-bearing stances. For the hindfoot alignment view, a cassette-holding box with a Plexiglas surface was used. The inclination angle of the beam was 20° to the floor. To record the long axial view, the film cassette was lying flat on the floor. The inclination angle of the beam was 45° to the floor. Volunteers stood on the cassette and were asked to hold their ankle in 10° of dorsal flexion, which was verified by a goniometer. The beam setting for the radiation source was 4 mAs and 50 kV, with a focus distance of 100 cm, with the beam pointed at the ankle joint.

Measurement method for the hindfoot alignment view. The mid-diaphyseal axis of the tibia is defined by bisecting the tibia into

Fig. 16.34 Hindfoot alignement view

Fig. 16.35 Long axial view

two mid-diaphyseal points (lines A and B) 30 mm apart and extending the line distally (line E). The mid-diaphyseal axis of the calcaneus is defined by a line through two points in the calcaneus. At a distance of 7 mm from the most distal part of the calcaneus, a horizontal line is drawn (line D). Line D is divided into a 40%:60% ratio, where the length of the 40% line is measured from the lateral side. A second line (line C) is drawn horizontally, 20 mm from the most distal part of the calcaneus. The calcaneus axis (line F) is drawn by connecting the 40% mark at line D and the bisected line C. The hindfoot angle (G) is the angle between lines E and F.

Measurement method for the long axial view (Fig. 16.36). The mid-diaphyseal axis of the tibia is defined by bisecting the tibia into two mid-diaphyseal points (lines A and B) 30 mm apart and extending the line distally
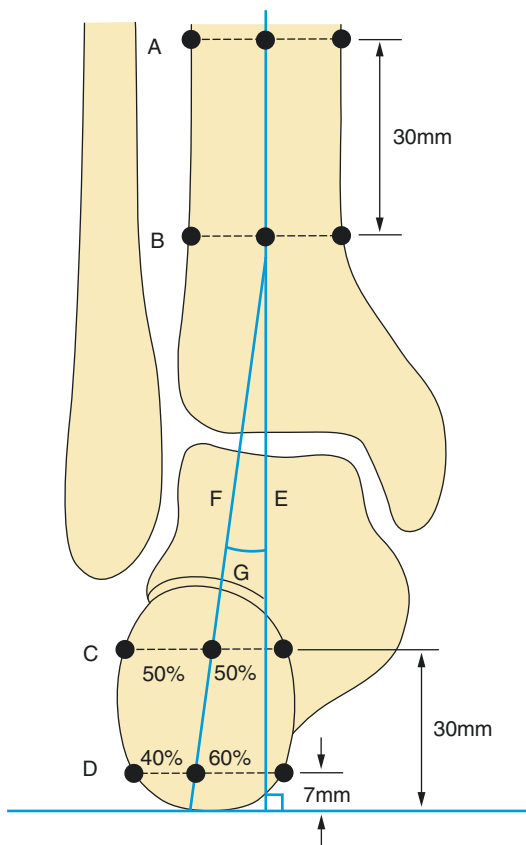
Fig. 16.36 Measurement method for the long axial view, with G representing the hindfoot angle

Reproducibility/Variation

The long axial view measurement values are reproducibly more reliable than those of the conventional hindfoot alignment view.

Clinical Relevance/Implications

It helps to identify physiological joint geometry if hindfoot pathology is suspected. Post-traumatic malalignment, reconstructive surgery, such as corrective osteotomy, ligament reconstruction and arthrodesis, can be planned according to the specified data. The ankle arthroplasty development and placement can be guided by these measurements.

Analysis/Validation of Reference Data

Nine orthopaedic surgeons measured each view. Measurements using the hindfoot alignment view gave respective intra- and interclass correlation coefficients of 0.72 and 0.58 for bilateral stance and 0.91 and 0.49 for unilateral weight-bearing stance. The long axial view showed respective intra- and inter-correlation coefficients of 0.93 and 0.79 for bilateral stance and 0.91 and 0.58 for unilateral weight-bearing stance. For both methods, the intra-observer ICCs were good and fair for both bilateral stance and unilateral weight-bearing stance. The inter-observer ICC was only good in the long axial view for bilateral stance. Supportive data of the increased accuracy of the long axial view compared with the hindfoot view.

(line E). The mid-diaphyseal axis of the calcaneus is defined by a line through two points in the calcaneus. At a distance of 7 mm from the most distal part of the calcaneus, a horizontal line is drawn (line D). Line D is divided into a 40%:60% ratio, where the length of the 40% line is measured from the lateral side. A second line (line C) is drawn horizontally, 30 mm from the most distal part of the calcaneus. The calcaneus axis (line F) is drawn by connecting the 40% mark at line D and the bisected line C. The hindfoot angle (G) is the angle between lines E and F.

Conclusion

The bilateral long axial view is more reliable than the hindfoot alignment view for measuring hindfoot alignment.

16.10   Intermetatarsal Angle

Definition

The intermetatarsal angle is the angle created by the lines bisecting the first and second metatarsals, measured on a dorsoplantar weight-bearing radiograph of the foot.

Indications

Determining the severity of hallux valgus deformity, metatarsus primus varus and post-operative evaluating of the surgical procedure.

Technique

DP weight-bearing radiographic view.

Full Description of Technique

Patient is in supine, weight-bearing position. The radiograph is obtained in a dorsoplantar projection, centred to the middle of the third metatarsal. The axes are drawn as depicted in Fig. 16.37. Alternately to create the first intermetatarsal longitudinal axis, a line connecting the centres of the first metatarsal head and the proximal articular surface of the first metatarsal can be employed. The angle of the intersection of the longitudinal axes of the first and second metatarsal is the intermetatarsal angle.

Normal value is **<8–11°**, with an average of 9.0–9.2°.

Normal value	<10°
Abnormal value	>10°

Reproducibility/Variation

When using the method as described above, inter-observer and intra-observer agreement was determined with a discrepancy of ≤2°, being the

1-2 Intermetatarsal Angle
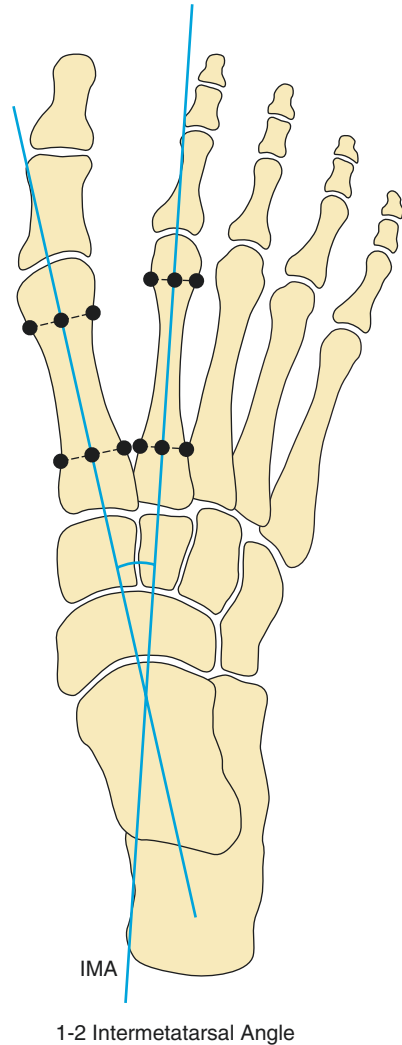
Fig. 16.37   Weight-bearing anterior–posterior view of the foot, depicting the intermetatarsal angle (IMA)

best of several other tested methods. This is based on Shima et al.'s (2009) findings.

Clinical Relevance/Implications

Radiographic measurement of the intermetatarsal angle is one of the most important parameters for assessing hallux valgus deformity and the extent of surgical correction needed. In addition this angle is useful in radiographic evaluating of the

results of the surgical treatment (Castro-Aragon et al. 2009).

Analysis/Validation of Reference Data

Limited data (Thomas et al. 2006).

Conclusion

Measurement of the intermetatarsal angle is a useful method for determining severity of hallux valgus deformity, before and after surgery.

16.11   Lateral Ankle Ligament Complex

Definition

On the lateral aspect of the ankle there is a complex of three ligaments (Muhle et al. 1999; Taser et al. 2006a). These three ligaments provide stability by attaching the lateral malleolus to the bones below the ankle joint (talus and calcaneus) (Fig. 16.38). They are the:

– anterior talo-fibular ligament (from the talus to the fibula) which is a flat quadrilateral ligament typically composed of two bands orientated at an angle of 25° (range 5–45°) to the horizontal plane and at a mean angle of 47° (range 45–56°) to the sagittal plane.
– calcaneo-fibular ligament (from the posterior surface of the lateral calcaneus to the fibula) makes a mean angle of 40° (range 30–58°) with the horizontal plane and a mean of 51° (range 32–60°) with the sagittal plane.
– posterior talo-fibular ligament (from the posterolateral talus to the fibula) orientated in the horizontal plane. The angle between the CFL and ATFL is around 132° (range 118–145°).

Indications

Ankle sprains are common injuries frequently associated with injuries to major supporting liga-ments. Lateral collateral ligaments are involved in 85% of ankle sprains with anterior talofibular ligament (ATFL) being the most frequently injured lateral ankle ligament. Knowledge of the anatomy of the major supportive ligaments, and their relationships to the osseous structures facilitates interpretation of the severity of ligamentous injury on conventional radiographs, and provides vital information for ligament reconstruction procedures. The length and width measurements of lateral ankle ligaments provide the estimation of ligament loss used during reconstruction procedures, while the origin and insertion locations help in restoration of the exact anatomy.

Technique

MRI.

Full Description of Technique

Several diagnostic studies are available for detecting acute injury to ankle ligaments such as arthrography, arthroscopy, stress radiographs, sonography and MRI. MRI is more sensitive in detecting the ligament injury than radiographs as images of ligaments are rendered, but its reliability varies with the position of the ankle, associated bony injury and presence of blood. In such difficult cases the angular orientation of ankle ligaments are required to obtain the MRI in the optimal spatial plane of the ligament.

Fig. 16.38   Three axial MR images depicting the three lateral ankle ligaments (*): anterior talo-fibular ligament (**a**), calcaneo-fibular ligament (**b**) and posterior talo-fibular ligament (**c**)

Muhle et al. (1998, 1999) described the optimal MRI planes for visualizing lateral ankle ligaments. ATFL is best seen on axial images, PTFL on axial and coronal images and CFL in 40°–50° plantar flexion axial images because the CFL is incompletely seen in the axial plane. They compared the lengths of ligaments measured on MRI images and direct anatomical measurements. They found discrepancies in the ligament length measurements between MRI images and direct anatomical measurements and recommended direct anatomical measurement as the best method for precise anatomy.

Reproducibility/Variation

In an anatomical study on cadaver based measurements Taser et al. (2006b) found mean values as follows:

ATFL length	**22.37 mm +/−2.50**	**ATFL width**	**10.77 mm +/−1.56**
CFL length	**31.94 mm +/−3.68**	**CFL width**	**4.68 mm +/−1.34**
PTFL length	**21.66 mm +/−4.84**	**PTFL width**	**5.55 mm +/− 1.25**

Clinical Relevance/Implications

The length and width measurements of lateral ankle ligaments provide both knowledge of nor-mal anatomy on MRI in order to detect discontinuity and oedema in the acute ligament ruptures, and estimation of ligament loss during reconstruction procedures and origin and insertion locations help in restoration of the exact anatomy.

Analysis/Validation of Reference Data

Limited data currently suggests that MRI has inherent difficulties in accurately measuring ligament dimensions compared with direct anatomical values taken at surgery.

Conclusion

The precise anatomical knowledge of the topographical anatomy of the ligaments is important for surgeons performing reconstructive surgeries. For "defining" the anatomical location of normal ligaments the knowledge of variations in anatomy is essential. A larger number of specimens may increase the incidence of variations in anatomy of ligaments. Secondly, correlation of cadaver anatomy with MRI anatomy of ankle ligaments could provide more information for the practicing surgeons. Further studies with larger sample size are required to define the normal anatomy of the vital lateral ankle ligaments.

16.12 Medial Collateral Ligament Complex

Definition

The medial collateral ligament (MCL) of the ankle, also known as the deltoid ligament, is composed of a deep and superficial layer. The MCL complex is a stabilizer against valgus forces, anterior and lateral talar excursion, and rotatory forces (Campbell et al. 2014).

Indications

These measurements can serve as a reference in cases of suspected ligamentous lesions. Data will also act as a guide to placement of repairs and deltoid ligament reconstruction.

Technique

MRI.

Full Description of Technique

The MCL arises from the medial malleolus and inserts in the talus, calcaneus and navicular bones. The MCL is composed of two anatomical layers, the *deep layer* which consists of anterior and posterior Tibiotalar Ligaments (TTLs) and the broad *superficial layer* consisting of the Tibionavicular Ligament (TNL), Tibiospring Ligament (TSL) and the Tibiocalcaneal Ligament (TCL) (Fig. 16.39). The layers are separated by a thin layer of fat. The deep ligaments have talar attachments and cross one joint, and the superficial ligaments cross two joints and have variable osseous attachments. Cadaveric studies have shown that the TNL, TSL and deep posterior TTLs are constant components and the deep posterior TTL is the largest band of the deltoid ligament. More recently Campbell et al. (2014) have also provided detailed cadaveric qualitative and quantitative data of each ligamentous band of the deltoid ligament comprising ligament band

length, footprint area of origin and insertion, as well as spatial orientation. In both MR imaging planes the differentiation of the deep from the superficial components is possible. The two deep layer TTLs are completely visualized on coronal images although the ATTL can be thin or absent.

Deep layer (Figs. 16.40 and 16.41):
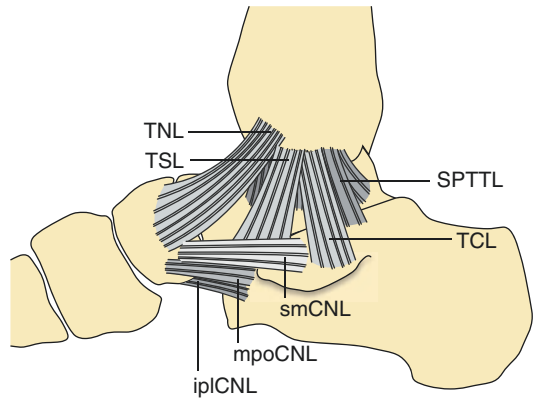
Fig. 16.39 Medial aspect of the ankle, depicting the medial collateral ligament complex, consisting of several individual ligaments. iplCNL = inferioplantar longitudinal calcaneonavicular ligament, mpoCNL = medioplantar oblique calcaneonavicular ligament, smCNL = superomedial calcaneonavicular ligament, SPTTL = superficial posterior tibiotalar ligament, TCL = tibiocalcaneal ligament, TNL = tibionavicular ligament, TSL = tibiospring ligament
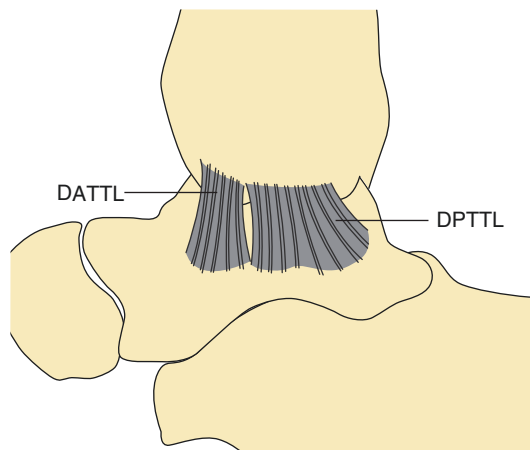
Fig. 16.40 Medial aspect of the ankle, depicting the deep anterior tibiotalar ligament (DATTL) and the deep posterior tibiotalar ligament (DPTTL)
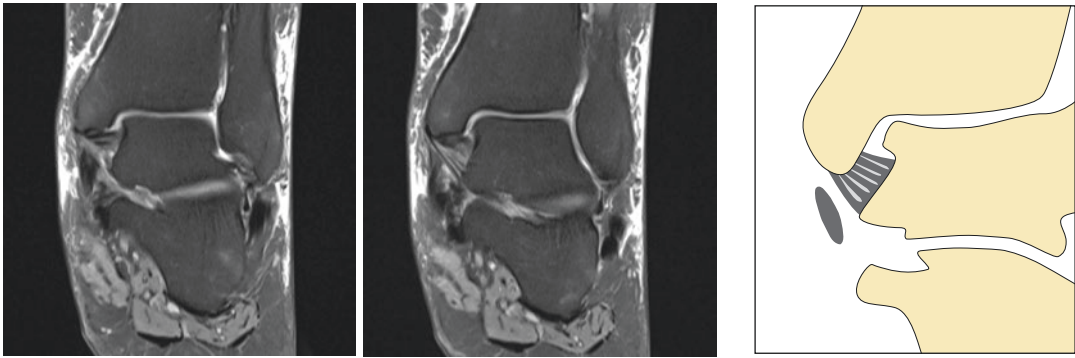
Fig. 16.41 Coronal MR images of the ankle, depicting the deep layers of the tibiotalar ligament (TTL)

1. Anterior TTL: originates from the anterior colliculus and the anterior part of the intercollicular groove of the medial malleolus and inserts on the medial surface of the talus just distal to the anterior part of the medial talar articular surface
2. Posterior TTL: originates from the upper segment of the posterior surface of the anterior colliculus, from the intercollicular groove, and of the anterior surface of the posterior colliculus of the medial malleolus. It inserts onto the medial surface of the talus under the tail of the articular facet.

Superficial layer (Fig. 16.42):

1. TNL: originates from the anterior border of the anterior colliculus of the medial malleolus and inserts onto the dorsomedial aspect of the navicular bone. This is best imaged in the axial and coronal planes.
2. TSL: originates from the anterior segment of the anterior colliculus of the medial malleolus. It inserts on the superior border of the superomedial part of the spring ligament complex. This is best imaged in the coronal plane.
3. TCL: originates from the medial aspect of the anterior colliculus of the medial malleolus and inserts on the medial border of the sustentaculum tali. This is best imaged in the coronal plane.
4. Superficial posterior tibiotalar ligament

Measurement parameters selected from Mengiardi et al.'s 2007 data are presented below.

	Deep layer	
	Anterior TTL	**Posterior TTL**
All	**1.5 (1–4) mm**	**8.2 (6–11) mm**
Female	**1.4 (1–2) mm**	**7.9 (6–10) mm**
Male	**1.7 (1–4) mm**	**8.6 (6–11) mm**
P-value	**0.31**	**0.014**

	Superficial layer		
	TNL	**TSL**	**TCL**
All	**1.6 (1–2) mm**	**2.0 (1–4) mm**	**1.2 (1–3) mm**
Female	**1.4 (1–2) mm**	**1.8 (1–3) mm**	**1.1 (1–2) mm**
Male	**1.9 (1–2) mm**	**2.2 (1–4) mm**	**1.3 (1–3) mm**
P-value	**0.001**	**0.003**	**0.46**

Reproducibility/Variation

Unknown.

Clinical Relevance/Implications

Injuries of the MCL complex are clinically relevant as they may, if not treated properly, lead to chronic pain and instability.
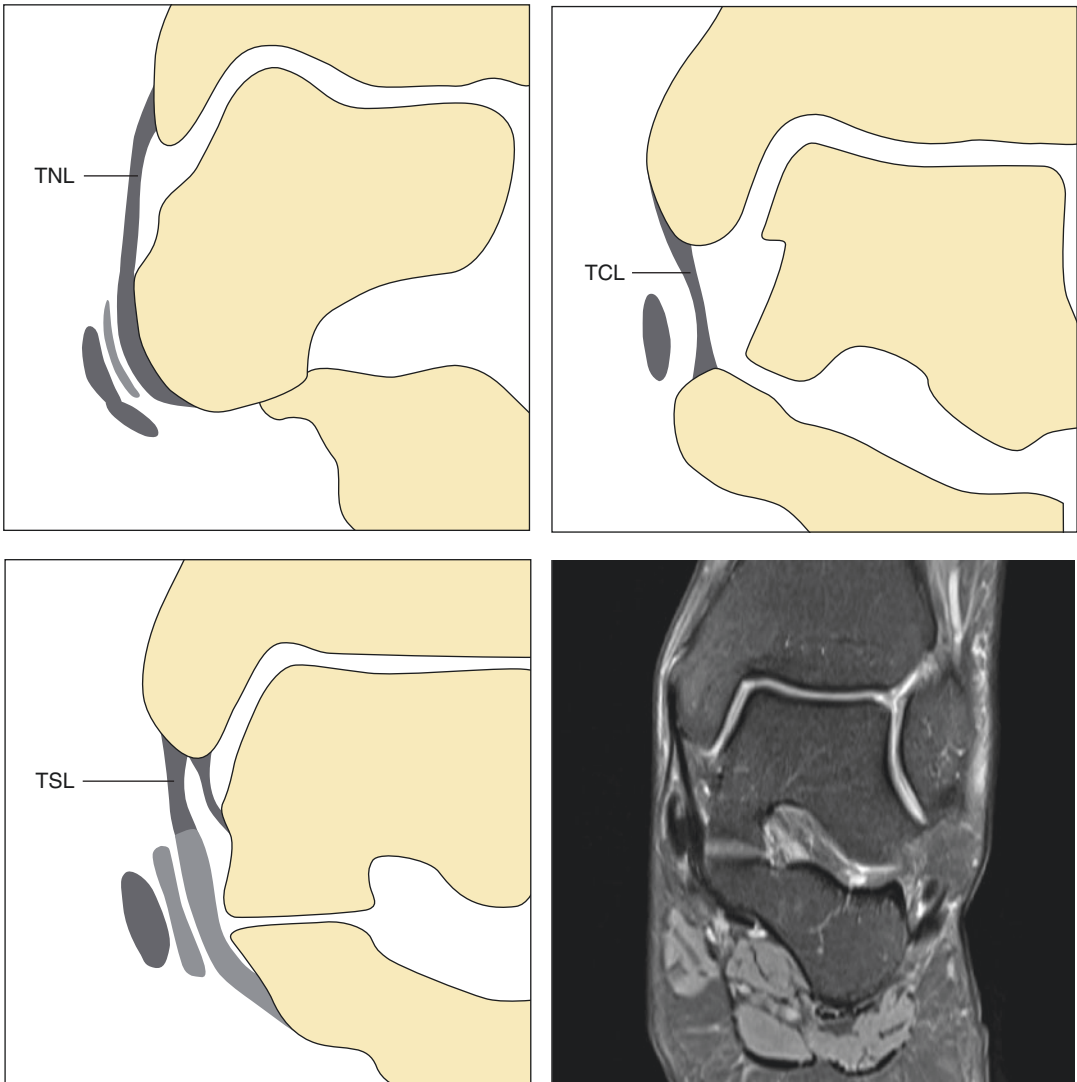
Fig. 16.42 Coronal views of the ankle, depicting the superficial layers of the tibiocalcaneal ligament (TCL), tibionavicular ligament (TNL) and the tibiospring ligament (TSL)

Analysis/Validation of Reference Data

Normal values were assessed in 56 healthy volunteers (29 female and 27 male; mean age 40.7 years (range, 23–60 years)) (Milner and Soames 1998a; Milner and Soames 1998b).

Conclusion

There are currently limited surgical options in reconstructive surgery, but the MCL ligamentous measurements, footprint data and spatial orientations would need to be taken into consideration for future development of therapeutic options.

16.13   Plantar Aponeurosis (Fascia)

Definition

Plantar fascia (central portion) at origin from medial calcaneus by direct measurement using US or MRI.

Indications

Plantar fasciitis, heel pain.

Technique

US (Fig. 16.43).
MRI.
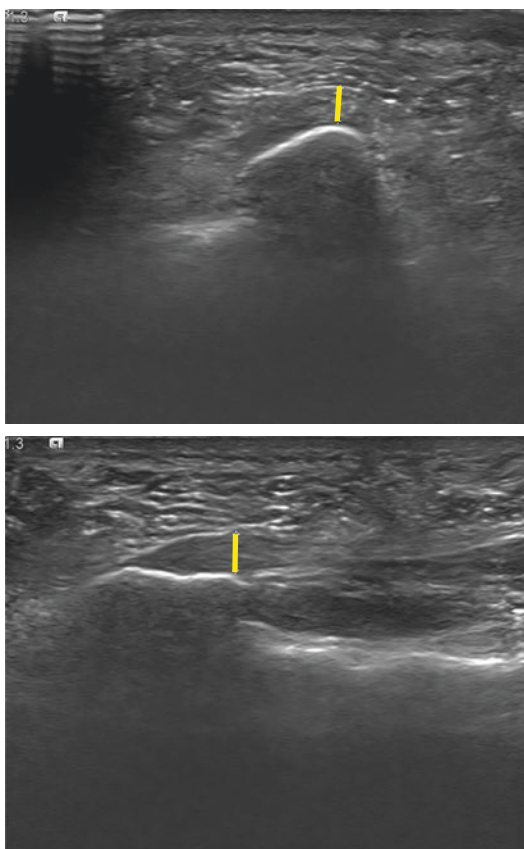
Fig. 16.43 Ultrasonography of the plantar fascia depicting plantar fasciitis

Full Description of Technique

Uzel et al. (2006) employed a 5–10 MHz linear array transducer. Sites of measurement were at the proximal insertion of fascia to medial calcaneal tubercle (Plantar fascia proximal (PFp) and 5 mm distal to this point (PFd).

Three groups were identified:

1. without Athletic Activity ($n = 50$),
2. minor activity ($n = 30$) and
3. >6 h of athletic activity ($n = 30$).

Statistics used: paired T Test.
Normal Measurements:

	PFp = 3.5 +/− 0.5 mm (range 2.6–4.8 mm) in group 1
	3.6+/− 0.6 mm (range 2.7–6.3 mm) in group 2
A	**3.8 +/− 10.5 mm (range 3.1–5.1 mm) in group 3**
B	**PFd = 3.0 +/− 0.5 mm (range 2.3–4.4 mm) in group 1**
	3.0 +/− 0.5 mm (range 2.2–4.2 mm) in group 2
	3.3 +/− 0.5 mm (range 2.5–4.9 mm) in group 3

Pascual Huerta and Alarcon Garcia (2007) used a 10 MHz linear array transducer. Measurements were obtained at four sites:

(a) 1 cm proximal to insertion in calcaneus,
(b) at insertion,
(c) 1 cm distal,
(d) 2 cm distal to insertion.

96 feet were included in study.
Normal Measurements:

(a) **1.99 +/− 0.65 mm (range 0.9–3.7 mm)**
(b) **3.33 +/− 0.69 mm (range 1.9–5.0 mm)**
(c) **2.7 +/− 0.69 mm (range 1.3–4.9 mm)**
(d) **2.64 +/− 0.69 mm (range 1.2–4.5 mm)**

No differences between (c) and (d). These sites are a good indicator for global thickness.

Gibbon and Long (1999) used a 5–10 MHz linear transducer. 96 adult heels were studied. Measurement was done at crossing of plantar

fascia with anterior inferior calcaneus. 20 males, 28 females, age range 21–67 years (mean 48 years).

Normal Measurements: 2.4–4.3 mm (mean 3.3 mm).

MRI in the sagittal (T1) and coronal (PD/T2) planes was used by Berkowitz et al. (1991) using a 1.5 T scanner and 3 mm section thickness. As in ultrasound the maximum thickness of the plantar fascia is measured proximally at its calcaneal insertion.

Normal Measurements.

Male	3.00 mm +/– 0.0 mm
Female	3.44 mm+/–0.53 mm

Reproducibility/Variation

In Uzel et al.'s (2006) study every distance was measured twice in millimeters to 1 decimal place; average of both measurements was taken.

In Pascal Huerta et al.'s (2007) study 95% confidence is given. However only 1 measurement was done and by 1 examiner.

In Gibbon's (1999) study three measurements were done and average recorded by (1999) 1 observer.

In Berkowitz's (1991) study two measurements were done in 9 asymptomatic feet.

Clinical Relevance/Implications

To differentiate between age and activity related normal values and diagnosis of plantar fasciitis. It is important to be aware of normal as well as age and activity related changes, not to be mistaken for pathology.

Analysis/Validation of Reference Data

Three different studies provide clear data on this measurement of plantar fascia. Reproducibility is tested with a similar normal value provided by MRI. Age, physical activity and gender differences exist.

Conclusion

Provided measurements are very helpful in daily practice.

16.14   Spring Ligament Complex

Definition

The spring ligament complex is composed of the ligaments between the calcaneus and the navicular bones at the superomedial and inferomedial aspect of the foot (Fig. 16.44). In combination with the plantar fascia, the plantar ligaments and the posterior tibialis tendon they form a stabilizing system for the longitudinal arch of the foot, which if dysfunctional promotes a flatfoot deformity.

Indications

These measurements can serve as a reference in cases of suspected ligamentous lesions.

Technique

US
MRI: Coronal—for smCNL and iplCNL. Transverse oblique—for smCNL and mpoCNL.
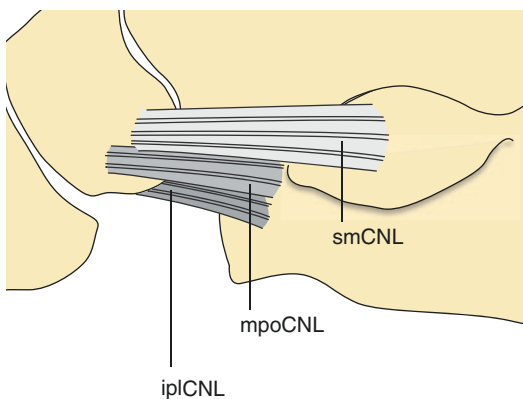
Fig. 16.44 The spring ligament complex consisting of three seperate ligaments. iplCNL = inferioplantar longitudinal calcaneonavicular ligament, mpoCNL = medioplantar oblique calcaneonavicular ligament, smCNL = superomedial calcaneonavicular ligament

Full Description of Technique

The spring ligament complex consists of three components:

1. *Superomedial Calcaneonavicular Ligament* (smCNL): the smCNL originates from the medial aspect of the sustentaculum tali and has a broad insertion on the superomedial aspect of the navicular bone. The tibiospring ligament, part of the superficial layer of the MCL complex described previously, always exhibits a broad attachment onto the smCNL.
2. *Medioplantar Oblique Calcaneonavicular Ligament* (mpoCNL): the mpoCNL originates from a region just anterior to the middle articular facet of the calcaneus and inserts at the medioplantar portion of the navicular bone.
3. *Inferioplantar Longitudinal Calcaneonavicular Ligament* (iplCNL): the iplCNL originates from the coronoid fossa of the calcaneus anteriorly and inserts at the inferior beak of the navicular bone.

Ultrasonography (Harish et al. 2007)
The transducer is aligned with one end of the probe at the sustentaculum tali and the other at the superomedial aspect of the navicular with slight dorsal angulation. The ligament is differentiated from its surrounding fat by its hyperechoic fibrillar echotexture.

On ultrasonography the mean dimension of the smCNL in healthy volunteers:
Normal value 3.0 mm (range 1.9–4.7 mm).

MRI (Yao et al. 1999)
Imaging protocol in the Mengiardi et al. (2005) study used a standard protocol for imaging ankles. Sagittal T1-weighted spin-echo MR images were obtained in the coronal (450/14, 4-mm section thickness, 16-cm field of view, matrix size of 256 _ 512, two acquisitions), transverse oblique (45° between the coronal and transverse planes, 435/ 14, 4-mm section thickness, 15-cm field of view, matrix size of 256 * 512, two acquisitions), and sagittal (450/14, 3-mm section thickness,

22-cm field of view, matrix size of 256 _ 512, one acquisition) planes.

Imaging planes: T2-weighted fast spin-echo MR images were obtained in the coronal (4000/91, 3-mm section thickness, 16-cm field of view, matrix size of 256 * 512, two acquisitions) and transverse (4000/ 86, 4-mm section thickness, 15-cm field of view, matrix size of 256 * 512, two acquisitions) planes. In addition, a fast spin-echo short-tau inversion-recovery sequence—short inversion time inversion recovery (4000/30/150 [repetition time msec/echo time msec/inversion time msec], 3-mm section thickness, 17-cm field of view, matrix size of 256 * 256, two acquisitions)—was performed in the sagittal plane.

Measurements on MRI are selected from Mengiardi et al.'s evaluation of the spring ligament complex. Coronal (smCNL and iplCNL) and transverse oblique (smCNL and mpoCNL) planes are best at imaging the ligament components.

smCNL	mpoCNL	iplCNL
3.2 (2–5 mm)	2.8 (1–5 mm)	4.0 (range 2–6 mm)

Reproducibility/Variation

The thickness is significantly correlated with age. In women the smCNL and iplCNL are significantly thinner compared to men. In Tanaguchi et al.'s anatomical study the mean thickness of the smCNL was 2.5 mm (range of 1.4–4.6 mm), while Yao et al.'s (1999) MRI study measured it as 4.7 mm at the same location. Inter-observer variation occurs at this site due to the difficulty in differentiating the PTT, the gliding layer separating it from the smCNL, and the smCNL which occurs in 86% of cases (Taniguchi et al. 2003).

Clinical Relevance/Implications

The spring ligament complex has two very important functions. Firstly it embraces and supports the medial and plantar parts of the talar head. Secondly it forms part of the stabilizing structures for the longitudinal arch of the foot. Coexisting lesions are often seen involving the PTT and the spring ligament in a high percentage of acquired flatfoot deformity. In patients with flatfeet the spring ligament complex is often involved. Given these normal values a **smCNL thickness of > 4 mm** can be considered abnormal.

Analysis/Validation of Reference Data

Ultrasonography
Four cadaveric feet and 40 asymptomatic adults.

MRI
Five cadaveric feet (2 left and 3 right) and 78 healthy volunteers (37 men and 41 women, mean age 48 years (range 23–83).

Difficulties have been encountered in all the MR studies in measuring the smCNL as it is not always easy in the majority (86%) to differentiate it as a distinct structure from the adjacent PTT. Mengiardi et al.'s measurements are the ones that closely correlate with anatomically based measurements.

Conclusion

Ultrasonography and MRI are both useful techniques in the evaluation of the spring ligament complex.

16.15   Talar Tilt

Definition

Talar tilt test is a subtalar laxity measurement. It is defined by ankle stress radiography in the frontal plane. The talar tilt test is used to examine the integrity of the calcaneofibular or the deltoid ligament. For talar tilt the talocrural angle is measured by drawing two tangent lines on an anteroposterior ankle radiograph, one to the inferior articular surface of the tibia and the other to the most proximal talar contour.

Indications

Indication for and evaluation of operative treatment for chronic lateral ankle laxity.

Technique

Stress Radiography.

Full Description of Technique

Radiographs are taken in a standardized manner in a radiographic suite with standard equipment (Telos, Marburg, Germany) by 1 or 2 orthopaedic radiology technologists. To obtain talar tilt radiographs (Fig. 16.45), the patient lies supine, and the respective knee is flexed to 20°. The heel is fixed in the freely rotating foot plate of the stress apparatus with the ankle in about 15° of plantar flexion and 20° of internal rotation. A lateral support is placed laterally and inferior to the fibular head. Proximal to the medial malleolus, a mediolateral directed force (15 kp) is administered through another pad of the device.

Reproducibility/Variation

The ICC for intratester reliability is 0.78 for the talar tilt stress radiography. Intertester reliability: ICC for talar tilt was 0.95 to 0.97 (Beynnon et al. 2005).

Fig. 16.45   Talar tilt radiography

Clinical Relevance/Implications

Stress radiography to measure talar tilt is an important research tool to evaluate the integrity of the ankle ligaments in studies of chronic ankle instability. This ability to objectively measure mechanical instability in a functionally unstable ankle is important in understanding the nature and cause of the instability (Chandnani et al. 1994; Lohrer et al. 2008)

Analysis/Validation of Reference Data

Limited studies which promote the importance of comparative assessment with the contralateral side.

Conclusion

In conclusion, our results indicate that stress radiographs of the ankle joint can reliably be read if the proposed measurement techniques are applied. Further studies addressing the consistency and accuracy of different films that are repeatedly taken on the same subjects are needed to improve clinical relevance. Then, generally accepted normal values for the respective measures need to be established. Only measurement techniques with proven reliability should be used.

16.16 Talonavicular Coverage Angle

Definition

The navicular axis is formed by a perpendicular to a line connecting the medial and lateral aspects of the navicular proximal articular surface. The talar axis is defined similarly as the perpendicular to the line joining the talar articular borders. The talonavicular coverage angle is formed by the talar and navicular axes. As forefoot abduction increases, the talonavicular coverage angle increases.

Indications

The indication for the measurement of the talonavicular coverage angle is to understand the relationship between radiographic measurements and

physical examination of a flatfoot deformity in the adult in comparison to a normal control group. With the understanding of this relationship goes the proposal of a new standard for the radiographic definition of a flatfoot deformity in adults. Standing anteroposterior radiograph of patients with posterior tibial tendon (PTT) dysfunction shows abnormal talonavicular coverage angle.

Technique

AP radiograph.

Full Description of Technique

Measurement technique of the AP talonavicular coverage angle (Fig. 16.46). On the AP weight-bearing radiograph, points are marked on the
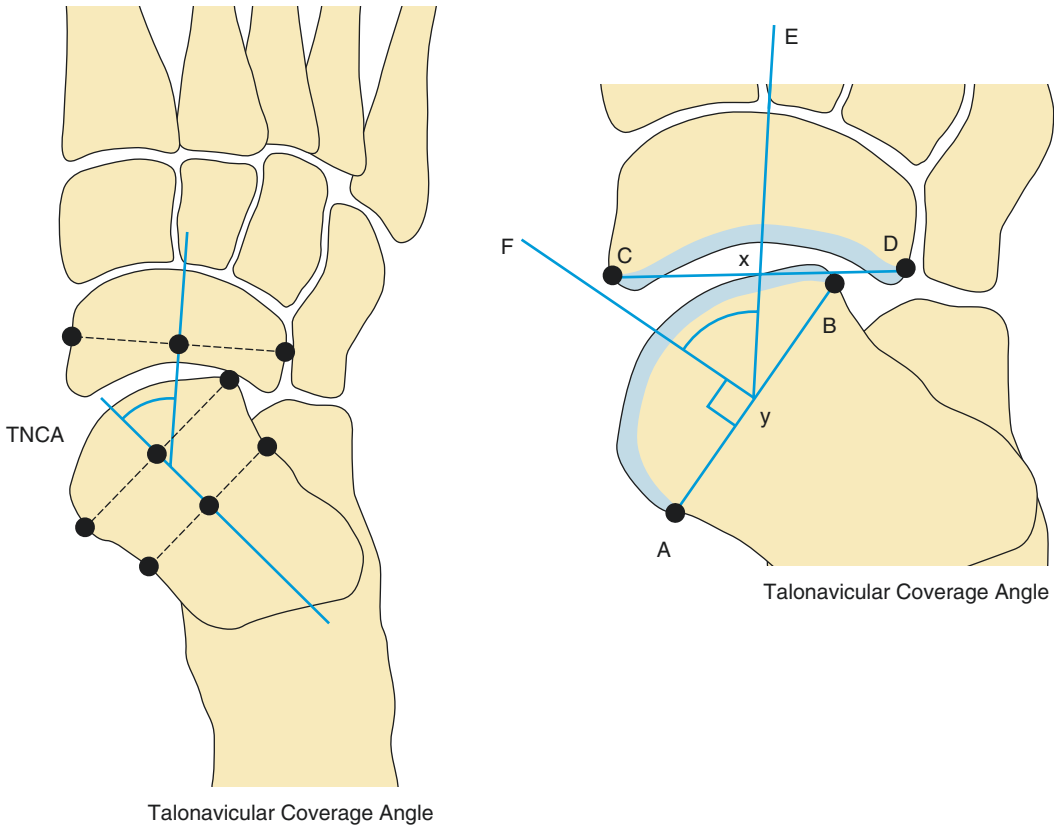
Fig. 16.46 Measurement of talonavicular coverage angle (TNCA, angle *y*) on a weight-bearing anterior–posterior radiograph of the foot

most medial (Point A) and lateral (Point B) margins of the articular surface of the talus, and a line is drawn connecting these two points (Line AB). Similar points are marked on the most medial (Point C) and lateral (Point D) margins of the articular surface on the navicular (line CD), and a line is drawn connecting these two points (Line CD). A perpendicular line is drawn from each of these lines, forming the AP Talonavicular Coverage Angle (Angle y).

Reproducibility/Variation

Younger et al. (2005) produced data on the correlation on the lateral radiograph showing intraobserver (0.01) and inter-observer (0.3) results of two readings done on two separate occasions of the talonavicular coverage angle (Younger et al. 2005).

Table 1   Radiographic measurement comparison

Measurement (SD) of AP talonavicular coverage angle		
Control group	Flatfoot group	Statistical significance
10.4° (4.2)	22.3° (6.7)	$t = -9.882, p < 0.01$

Clinical Relevance/Implications

There is no widely accepted definition of what constitutes a flatfoot in the adult. However, aspects of the deformity include collapse of the medial longitudinal arch, hindfoot valgus, eversion of the subtalar joint, and forefoot abduction.

Radiographs cannot define symptoms of a flatfoot, and the radiographic differences between a symptomatic adult flatfoot and an asymptomatic adult flatfoot are still to be determined (Table 1).

Analysis/Validation of Reference Data

A new validated value for the AP talonavicular coverage angle is **10° for normal feet and 22° for flatfeet** (Coughlin and Kaz 2009).

Conclusion

The talonavicular coverage angle is reaffirmed as a valid radiographic parameter of a flatfoot deformity.

References

Balen P, Helms C (2001) Association of posterior tibial tendon injury with spring ligament injury, sinus tarsi abnormality and plantar fasciitis on MR imaging. Am J Roentgenol 176:1137–1143

Berkowitz JF, Kier R, Rudicel S (1991) Plantar fasciitis: MR imaging. Radiology 179:665–667

Beumer A, Van Hemert WL, Niesing R, Entius CA, Ginai AZ, Mulder PG (2004) Radiographic measurement of the distal tibiofibular syndesmosis has limited use. Clin Orthop Rel Res 423:227–234

Beynnon BD, Webb G, Huber BM, Pappas CN, Renstrom P, Haugh LD (2005) Radiographic measurement of anterior talar translation in the ankle: determination of the most reliable method. Clin Biomech 20:301–306

Bilge O, Ozer MA, Govsa F (2003) Neurovascular branching in the tarsal tunnel. Neuroanatomy 2:39–41

Boehler L (1931) Diagnosis, pathology and treatment of fractures of the os calcis. J Bone Joint Surg 13:75–89

Boonthathip M, Chen L, Trudell DJ, Resnick DL (2010) Tibiofibular syndesmotic ligaments: MR arthrography in cadavers with anatomic correlation. Radiology 254:827–836

Buck FM, Hoffman A, Mamisch-Saupe N, Espinosa N, Resnick D, Hodler J (2011) Hindfoot alignment measurements: rotation-stability of measurement techniques on hindfoot alignment view and long axial view radiographs. AJR 197:578–582

Campbell KJ, Michalski MP, Wilson KJ, Goldsmith MT, Wijdicks CA, LaPrade RF, Clanton TO (2014) The ligament anatomy of the deltoid complex of the ankle: a qualitative and quantitative anatomical study. J Bone Joint Surg Am 96:e62

Castro-Aragon O, Vallurupalli S, Warner M, Panchbhavi V, Trevino S (2009) Ethnic radiographic foot differences. Foot Ankle Int 30(1):57–61

Chandnani VP, Harper MT, Ficke JR, Gagliardi JA, Rolling J, Christensen KP, Hansen MF (1994) Chronic ankle instability: evaluation with MR arthrography, MR imaging and stress radiography. Radiology 192(1):189–194

Chen MY, Bohrer SP, Kelley TF (1991) Boehler's angle: a reappraisal. Ann Emerg Med 20(2):122–124

Clark TW, Janzen DL, Ho K, Grunfeld A, Connel DG (1995) Detection of radiographically occult ankle fractues following acure trauma: positive predictive value of an ankle effusion. Am J Roentgen 164:1185–1189

Coughlin MJ, Freund E (2001) Roger A. Mann Award. The reliability of angular measurements in hallux valgus deformities. Foot Ankle Int 22(5):369–379

Coughlin MJ, Kaz A (2009) Correlation of Harris Mats, physical exam, pictures, and radiographic measurements in adult flatfoot deformity. Foot Ankle Int 30(4):604–610

Deenik AR, de Visser E, Louwerens JWK, de Waal Malefijt M, Draijer FF, de Bie RA (2008) Hallux val-gus angle as main predictor for correction of hallux valgus. BMC Musculoskelet Disord 9:70

Ebraheim NA, Lu J, Yang H (1997) Radiographic and CT evaluation of tibiofibular syndesmotic diastasis: a cadaver study. Foot Ankle Int 18:693–698

Elgafy H, Semaan HB, Blessinger B (2010) Computed tomography of normal distal tibiofibular syndesmosis. Skelet Radiol 39:559–564

Engel E, Erlick N, Krems I (1983) A simplified metatarsus adductus angle. J Am Podiat Assoc 73:62–628

Fowler A, Philip JF (1945) Abnormality of calcaneus as a cause of painful heel: its diagnosis and operative treatment. Br J Surg 32:494–498

Frigg A, Magerkurth O, Valderrabano V, Ledermann HP, Hintermann B (2007) The effect of osseous ankle configuration on chronic ankle instability. Br J Sports Med 41:420–424

Gentili A, Masih S, Yao L, Seeger LL (1996) Pictorial review : foot axes and angles. Br J Radiol 69:968–974

Gibbon WW, Long G (1999) Ultrasound of the plantar aponeurosis (fascia). Skelet Radiol 28:21–26

Haims AH, Schweitzer ME, Patel RS, Hecht P, Wapner KL (2000) MR imaging of the Achilles tendon: overlap of findings in symptomatic and asymptomatic individuals. Skelet Radiol 29(11):640–645

Harish S, Jan E, Finlay K, Petrisor B, Popowich T, Friedman L, Wainman B, Jurriaans E (2007) Sonography of the superomedial part of the spring ligament complex of the foot: a study of cadavers and asymptomatic volunteers. Skelet Radiol 36(3):221–228

Harper MC, Keller TS (1989) A radiographic evaluation of the tibiofibular syndesmosis. Foot Ankle 10: 156–160

Harris J, Fallat L (2004) Effects of isolated Weber B fibular fractures on the tibiofibular contact area. J Foot Ankle Surg 43:3–9

Hermans JJ, Beumer A, De Jong TAW, Kleinrensink GJ (2010) Anatomy of the distal tibiofibular syndesmosis in adults : a pictorial essay with a multimodality approach. J Anat 217:633–645

Hermans JJ, Wentink N, Beumer A, Hop WC, Heijboer MP, Moonen AF (2012) Correlation between radiological assessment of acute ankle fractures and syndesmotic injury on MRI. Skelet Radiol 41:787–801

Hunt K (2013) Syndesmosis injuries. Curr Rev Musculoskelet Med 6(4):304–312

Kerkhoffs GM, Blankevoort L, Schreurs AW, Jaspers JE, van Dijk CN (2002) An instrumented, dynamic test for anterior laxity of the ankle joint complex. J Biomech 35(12):1665–1670

Kerkhoffs GM, Blankevoort L, Kingma I, van Dijk CN (2007) Three-dimensional bone kinematics in an anterior laxity test of the ankle joint. Knee Surg Sports Traumatol Arthrosc 5(6):817–824

Knight JR, Gross EA, Bradley GH, Bay C, LoVecchio F (2006) Boehler's angle and the critical angle of Gissane are of limited use in diagnosing calcaneus fractures in the ED. Am J Emerg Med 24(4):423–427

Koivunen-Niemelä T, Parkkola K (1995) Anatomy of the Achilles tendon (tendo calcaneus) with respect to tendon thickness. Surg Radiol Anat 17(3):263–268

Lee KM, Chung CY, Park MS, Lee SH, Cho JH, Choi IH (2010) Reliability and validity of radiographic measurements in hindfoot varus and valgus. J Bone Joint Surg Am 92:2319–2327

Leeds HC, Ehrich MG (1984) Instability of the distal tibiofibular syndesmosis after bimalleolar and trimalleolar ankle fractures. J Bone Joint Surg Am 66:490–503

Liem MS, Leuven JA, Bloem JL, Schipper J (1992) Magnetic resonance imaging of achilles tendon xanthomas in familial hypercholesterolemia. Skelet Radiol 21(7):453–457

Lohrer H, Nauck T, Arentz S, Schöll J (2008) Observer reliability in ankle and Calcaneocuboid stress radiography. Am J Sports Med 36:1143–1149

Lu CC, Cheng YM, Fu YC, Tien YC, Chen SK, Huang PJ (2007) Angle analysis of Haglund syndrome and its relationship with osseous variations and Achilles tendon calcification. Foot Ankle Int 28(2):181–185

Magerkurth O, Knupp M, Ledermann H, Hintermann B (2006) Evaluation of hindfoot dimensions: a radiographic study. Foot Ankle Int 27:612–616

Mathieson JR, Connell DG, Cooperberg PL, Lloyd-Smith DR (1988) Sonography of the Achilles tendon and adjacent bursae. AJR Am J Roentgenol 151(1):127–131

McCluney JG, Tinley P (2006) Radiographic measurements of patients with juvenile hallux valgus compared with age-matched controls: a cohort investigation. J Foot Ankle Surg 45(3):161–167

Mei-Dan O, Kots E, Barchilon V, Massarwe S, Nyska M, Mann G (2009) A dynamic ultrasound examination for the diagnosis of ankle syndesmotic injury in professional athletes : a preliminary study. Am J Sports Med 37:1009–1016

Mei-Dan O, Carmont M, Laver L, Nyska M, Kammar H, Mann G, Clarck B, Kots E (2013) Standardisation of the functional syndesmosis widening by dynamic US examination. BMC Sports Sci Med Rehabil 5:9–11

Mengiardi B, Zanetti M, Schottle PB, Vienne P, Bode B, Hodler J, Pfirrmann CW (2005) Spring ligament complex: MR imaging-anatomic correlation and findings in asymptomatic subjects. Radiology 237(1):242–249

Mengiardi B, Pfirrmann CWA, Vienne P, Hodler J, Zanetti M (2007) Medial collateral ligament complex of the ankle: MR appearance in asymptomatic subjects. Radiology 242:817–824

Miller AN, Carroll EA, Parker RJ, Helfet DL, Lorich DG (2009) Posterior malleolar stabilization of syndesmotic injuries is equivalent to screw fixation. Clin Orthop Relat Res 468:1129–1135

Milner CE, Soames RW (1998a) Anatomy of the collateral ligaments of the human ankle joint. Foot Ankle Int 19:757–760

Milner CE, Soames RW (1998b) The medial collateral ligaments of the human ankle joint: anatomical variations. Foot Ankle Int 19:289–292

Morris JR, Lee J, Thordarson D, Terk MR, Brustein M (1996) Magnetic resonance imaging of acute Maisonneuve fractures. Foot Ankle Int 17:259–263

Muhle C, Frank LR, Rand T (1998) Tibiofibular syndesmosis : high resolution MRI using a local gradient coil. J Comput Assis Tomogr 22:938–944

Muhle C, Frank LR, Rand T et al. (1999) Collateral ligaments of the ankle: high-resolution MR imaging with a local gradient coil and anatomic correlation in cadavers. Radiographics 19(3):673–683

Neuhold A, Stiskal M, Kainberger F, Schwaighofer B (1992) Degenerative Achilles tendon disease: assessment by magnetic resonance and ultrasonography. Eur J Radiol 14(3):213–220

Nielson JH, Gardner MJ, Peterson MG (2005) Radiographic measurements do not predict syndesmotic injury in ankle fractures: an MRI study. Clin Orthop Relat Res:216–221

Nikolopoulos CE, Tsirikos AI, Sourmelis S, Papachristou G (2004) The accessory anteroinferior tibiofibular ligament as a cause of talar impingement : a cadaveric study. Am J Sports Med 32:389–395

Oh CS, Won HS, Hur MS, Chung IH, Kim S, Suh JS, Sung KS (2006) Anatomic variations and MRI of the intermalleolar ligament. Am J Roentgenol 186:943–947

Park SS, Kubiak EN, Egol KA, Kummer F, Koval KJ (2006) Stress radiographs after ankle fracture: the effect of ankle position and deltoid ligament status on medial clear space measurements. J Orthop Trauma 20:11–18

Pascual Huerta J, Alarcon Garcia JM (2007) Effect of gender age and anthropometric variables on plantar fascia thickness at different locations in asymptomatic subkects. Eur J Radiol 62(3):449–453

Pavlov H, Heneghan MA, Hersh A, Goldman AB, Vigorita V (1982) The Haglund syndrome: its initial and differential diagnosis. Radiology 144(1):83–88

Pettrone FA, Gail M, Pee D, Fitzpatrick T, Van Herpe LB (1983) Quantitative criteria for prediction of the results after displaced fracture of the ankle. J Bone Joint Surg Am 65:667–677

Pique-Vidal C, Maled-Garcýa I, Arabi-Moreno J, Vila J (2006) Radiographic angles in hallux valgus: differences between measurements made manually and with a computerized program. Foot Ankle Int 27(3):175–180

Ramsey PL, Hamilton W (1976) Changes in tibiotalar atea of contact caused by lateral talar shift. J Bone Joint Surg Am 58:356–357

Reilingh ML, Beimers L, Tuijthof GJM, Stufkens SAS, Maas M, Van Dijk CN (2010) Measuring hindfoot alignment radiographically : the long axial view is more reliable than the hindfoot alignment view. Skelet Radiol 39:1103–1108

Saltzman CL, El-Khoury GY (1995) The hindfoot alignment view. Foot Ankle Int 16:572–576

Saltzman CL, Brandser EA, Berbaum KS, DeGnore L, Holmes JR, Katcherian DA, Teasdall RD, Alexander

IJ (1994) Reliability of standard foot radiographic measurements. Foot Ankle Int 15:661–665

Schweitzer ME, Karasick D (2000) MR imaging of disorders of the Achilles tendon. AJR Am J Roentgenol 175(3):613–625

Sclafani SJA (1985) Ligamentous injury of the lower tibiofibular syndesmosis: radiographic evidence. Radiology 156(1):21–27

Sensiba PR, Coffey MJ, Williams NE, Mariscalco M, Laughlin RT (2010) Inter- and intraobserver reliability in the radiographic evaluation of adult flatfoot deformity. Foot Ankle Int 31(2):141–145

Shah AS, Kadakia AR, Tan GJ, Karadsheh MS, Wolter TD, Sabb B (2012) Radiographic evaluation of the distal tibiofibular syndesmosis. Foot Ankle Int 33:870–876

Shima H, Okuda R, Yasuda T, Jotoku T, Kitano N, Kinoshita M (2009) Radiographic measurements in patients with hallux valgus before and after proximal crescentic osteotomy. J Bone Joint Surg Am 91(6):1369–1376

Steel MW, Johnson KA, DeWitz MA, Ilstrup DM (1980) Radiographic measurements of the normal adult foot. Foot Ankle Int 1(3):151–158

Subhas N, Vinson EN, Cothran RL, Santangelo JR, Nunley JA II, Helms CA (2008) MRI appearances of surgically proven abnormal accessory antero-inferior tibiofibular ligament (Bassett's ligament). Skelet Radiol 37:27–33

Sutter R, Pfirrmann CWA, Espinosa N, Buck FM (2013) Three-dimensional hindfoot alignment measurements based on biplanar radiographs: comparison with standard radiographic meqsurements. Skeletal Radiol 42(4):493–498

Takao M, Ochi M, Oae K, Naito K, Uchio Y (2003) Diagnosis of a tear of the ibiofibular syndesmosis. The role of arthroscopy of the ankle. J Bone Joint Surg Br 85:324–329

Taniguchi A, Tanaka Y, Takakura Y, Kadono K, Maeda M, Yamamoto H (2003) Anatomy of the spring ligament. J Bone Joint Surg Am 85-A:2174–2178

Taser F, Shafiq Q, Ebraheim NA (2006a) Three-dimensional volume rendering of tibiofibular joint space and quantitative analysis of change in volume due to tibiofibular syndesmosis diastasis. Skelet Radiol 35:935–941

Taser F, Shafiq Q, Ebraheim NA (2006b) Anatomy of lateral ankle ligaments and their relationship to bony landmarks. Surg Radiol Anat 28:391–397

Thomas JL, Kunkel MW, Lopez R, Sparks D (2006) Radiographic values of the adult foot in a standardized population. J Foot Ankle Surg 45(1):3–12

Uzel M, Cetinus E, Ekerbicer C, Karaoguz A (2006) The influence of athletic activity on the plantar fascia in healthy young adults. J. Clin Ultrasound 34(1):17–21

Yao L, Gentili A, Cracchiolo A (1999) MR imaging findings in spring ligament insufficiency. Skelet Radiol 28:245–250

Ying M, Yeung E, Li B, Li W, Lui M, Tsoi CW (2003) Sonographic evaluation of the size of Achilles tendon: the effect of exercise and dominance of the ankle. Ultrasound Med Biol 29(5):637–642

Younger AS, Sawatzky B, Dryden P (2005) Radiographic assessment of adult flatfoot. Foot Ankle Int 26(10):820–825

Yuzawa K, Yamakawa K, Tohno E, Seki M, Akisada M, Yanagi H, Okafuji T, Yamanouchi Y, Hattori N, Kawai K et al. (1989) An ultrasonographic method for detection of Achilles tendon xanthomas in familial hypercholesterolemia. Atherosclerosis 75(2–3): 211–218

Long Bone Measurements

17

Jaspreet Singh, Prudencia N. M. Tyrrell,
and Victor N. Cassar-Pullicino

Contents

17.1   Introduction

Various radiological measurements have been described in the long bones of the upper and lower limbs. These help in the diagnosis of diseased states but are also important as a useful tool in planning surgical treatment and subsequent follow-up of such conditions. In certain conditions, radiological measurements are used to assess disease progression (e.g. infantile tibia vara vs. physiological bowing). These measurements may be related to an individual long bone or the alignment of the bones and joints in the entire limb. Within individual bones, there may be an abnormality in the length of the bone (e.g. ulnar variance), angular deformity in a sagittal or coronal plane at various levels (e.g. post-traumatic deformity) or an abnormality in the anatomical twist around the longitudinal axis (e.g. femoral and tibial torsion). Deformity in individual bones or the joint surfaces associated with soft tissue laxity may result in abnormal alignment of the entire limb. This results in

J. Singh (✉) • P. N. M. Tyrrell
Department of Radiology, Robert Jones & Agnes
Hunt Orthopaedic Hospital, Oswestry, UK
e-mail: jaspreet.singh2@nhs.net

V. N. Cassar-Pullicino
Department of Radiology, Robert Jones and Agnes
Hunt Orthopaedic Hospital NHS Foundation Trust,
Oswestry, UK
e-mail: Victor.Pullicino@rjah.nhs.uk

abnormal biomechanics and disproportionate transmission of load within the weight bearing joints. It is widely accepted that a malaligned state may lead to degenerative changes in the adjacent joints. Indeed the most important long-term consequence of a deformity in a long bone or malalignment in the entire limb is the early development of degenerative arthritis. Within the paediatric population, there is an increased potential of remodelling with growth, and this factor should be kept in mind whilst planning treatment. There may be spontaneous correction of angulation with growth and a larger angular deformity may be tolerated as compared to adults. In terms of length discrepancies, one should also keep in mind the predicted length at skeletal maturity. It is therefore important to be aware of the technique of performing these measurements and to have knowledge of the normal reference values.

17.2 Bicipital Groove

Bicipital groove dimension.

Medial wall angle	Normal	48–56°
	Abnormal	<30°
Sulcus depth	Normal	4.5 mm
	Abnormal	<3 mm

Indications

Biceps tendon subluxation/dislocation.

Techniques

Radiography
Bicipital groove view.

US
Transverse section at the level of the bicipital groove.

CT/MR
Axial sections at the level of the bicipital groove.

Full Description of Technique

The bicipital groove view is obtained with the patient supine and the arm in external rotation. The cassette is placed superior to the shoulder and perpendicular to the longitudinal axis of the humerus. The X-ray beam is directed cranially, parallel to the coronal axis of the humerus with a 15° medial angulation (Cone et al. 1983; Levinsohn and Santelli 1991), (Fig. 17.1a).
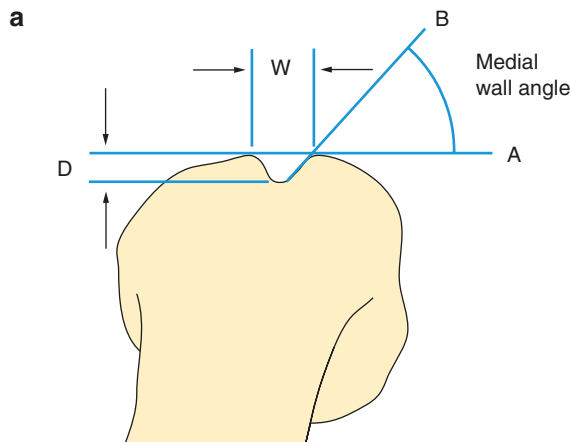
Fig. 17.1 (**a**) View of the bicipital groove. The width (*W*) and depth (*D*) of the groove have been depicted. The medial wall angle is measured between lines A and B as described in the text. (**b**) Transverse ultrasonographic view of the bicipital groove. (**c**) Axial CT section through the bicipital groove
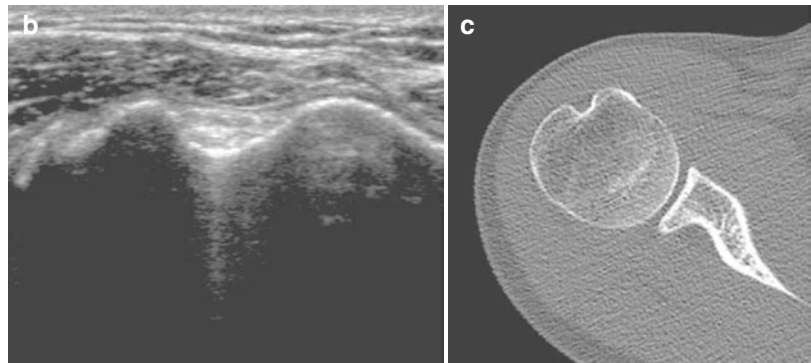
With ultrasound, the shoulder is scanned in seated position with humerus in a neutral position. The bicipital groove is examined with the transducer in a transverse position, strictly perpendicular to the groove over the anterior aspect of the shoulder (Fig. 17.1b).

CT and MRI can also be used to depict the bicipital groove. The bony anatomy is best appreciated on multi-slice CT (Fig. 17.1c) and three-dimensional reconstructions can be obtained.

Reproducibility/Variation

Following measurements have been made from the radiographs: width of the sulcus (*W*), depth of the sulcus (*D*) and medial wall angle. The medial wall angle is measured between a line tangent to the two tuberosities (line A) anteriorly and a line parallel to the medial wall of the sulcus (line B) (Fig. 17.1a).

Cone et al. (1983) studied 54 specimens and 100 patients. They found a wide variation in the medial wall angle with a mean value of 56° for the specimen group and 48° for the patient group. The mean width was 8.8 and 11 mm, and the mean depth was 4.3 and 4.6 mm respectively.

Farin and Jaroma (1996) evaluated the groove in 350 consecutive patients with ultrasound and radiography. They concluded that sonography was as accurate for evaluation of the dimensions of the bicipital groove as groove radiographs, but pathological changes of the walls of the groove could not be reliably evaluated with sonography.

Clinical Relevance/Implications

Cone et al. (1983) found that 90% of the patients had a sulcus depth greater than 3 mm and suggested that the tendon may have a tendency to subluxate/dislocate in individuals with a shallow groove ie less than 3 mm. Levinsohn and Santelli (1991) suggest that a medial wall angle of 30° or less may contribute to subluxation/dislocation.

Pfahler et al. (1999) studied the bicipital groove anatomy and tendon changes with mutual ultrasonography and radiography in 67 patients. They found a statistically significant correlation between groove anatomy and long head of biceps tendon disease.

17.3 Humerus: Baumann's Angle

Definition

Angle formed between the long axis of the humerus and physis of the capitellum.

Normal	70° (range 69–81°)
Abnormal	>81°

Indications

Supracondylar fracture humerus.

Technique

Radiography: Anteroposterior (AP) radiograph of the lower humerus.

Full Description of Technique

The film is placed posterior and parallel to the distal humerus and perpendicular to the X-ray beam. If the orientation of the X-ray beam is within a 10° arc, medial or lateral to the forearm, there is no distortion of the Baumann's angle (Worlock 1986). However, an orientation of the X-ray beam greater that 20° in the cranio caudal direction from the perpendicular invalidates the measurement (Webb and Sherman 1989). Baumann's angle is formed by the intersection of a line drawn along the long axis of the humerus and the growth plate of the capitellum (Fig. 17.2).

Reproducibility/Variation

Measurement of the Baumann's angle on AP radiographs has been shown to have a good reliability with intra-observer and inter-observer correlation coefficients of 0.80 and 0.78 respectively (Silva et al. 2009).
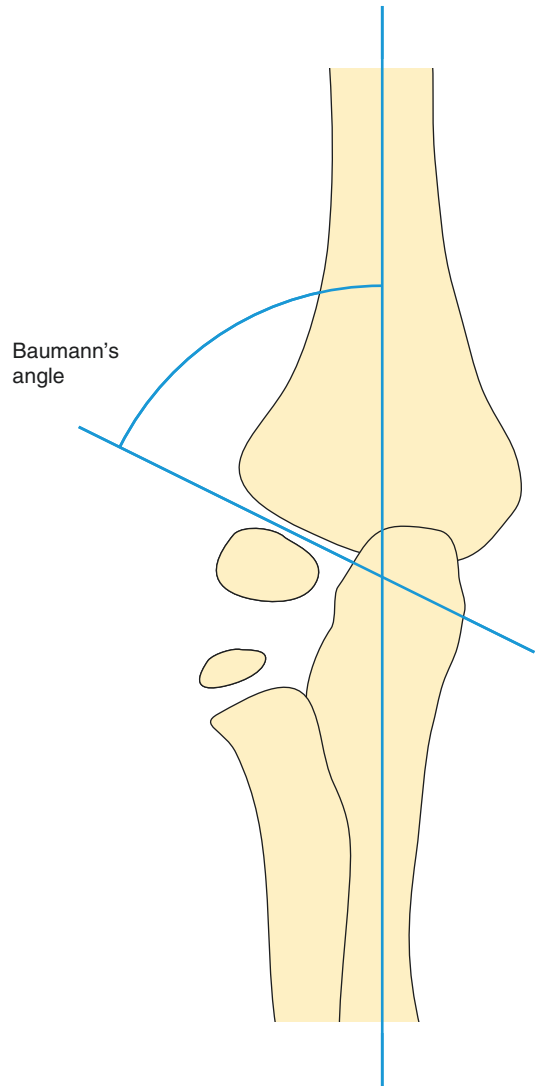
Fig. 17.2 Measurement of the Baumann's angle, formed by the intersection of a line drawn along the long axis of the humerus and the growth plate of the capitellum

Baumann's angle is reported to vary between 69 and 81°. A study looking at 577 elbow radiographs found no significant difference in measurements between boys and girls or between the right and left side (Keenan and Clegg 1996). The angle can be difficult to measure in children less than 2–3 years of age when there has not been enough ossification of the bony architecture, or in early adolescence when the metaphyseal border

becomes too irregular. In such instances, it may be difficult to trace a line along the capitellar physis, and therefore the measurement of the angle maybe inaccurate and may have poor reproducibilty.

Clinical Relevance/Implications

Baumann's angle is helpful in assessing adequacy of reduction of supracondylar fracture of the humerus. Comparison should be made between the injured and uninjured side as there is less than 2° of differ-ence (Dodge 1972). An increase in the Baumann's angle results in a cubitus varus deformity (decrease in carrying angle of the elbow). A 5° change in Baumann's angle causes an approximately 2° decrease in the carrying angle. A study of 27 chil-dren (Worlock 1986) revealed that the Baumann's angle after reduction of fracture could be used to pre-dict the final carrying angle. Also there was no sig-nificant difference between the Baumann's angle measured immediately after reduction and later at follow-up indicating that no significant growth dis-turbance occurred after the injury.

17.4 Humeral Torsion

Definition

Angle between the plane of the humeral head articular surface proximally and the transepicondylar axis distally.

Normal	17.9° (range 14.5–21.3°)
Abnormal	>22°

Indications

Prior to implanting a humeral head prosthesis, treatment of malunited fractures and severe arthritic deformity of the humerus, assessment of osseous adaptations in the "throwing" athletes (baseball pitchers, handball players, javelin throwers etc).

Technique

CT: Axial sections through the first 6 cm of the proximal part of the humerus and axial sections through the distal epiphysis.

Full Description of Technique

The humeral head axis is defined as a line perpendicular to the plane formed by the boundaries of the humeral head articular surface (line A). The boundaries of the articular surface of the humeral head can be identified by two different methods. A section passing through the centre of the head of the humerus is used. The first method uses the boundaries of the anatomical neck, which is indicated by a notch between the humeral head and lesser tuberosity anteriorly, and the humeral head and greater tuberosity posteriorly (Fig. 17.3a, b). The second method defines the articular surface using the limits of the subchondral bone (Boileau et al. 2008).

A line joining the most prominent medial and lateral extensions of the distal humerus defines the transepicondylar axis (line B) (Fig. 17.3c, d).

The angle between the humeral head axis and the transepicondylar axis is the angle of humeral torsion/humeral head retroversion (Fig. 17.3e, f).

Reproducibility/Variation

Humeral head retroversion has been measured using three methods—radiographic, CT scan and direct measurement in cadaveric specimens. CT scan methods measure humeral head retroversion more accurately as compared to radiographic methods. A study of 65 fresh humeri (Boileau et al. 2008) from 39 cadavers revealed a mean retroversion angle of 17.9° (95% confidence limit, 14.5–21.3). Hernigou et al. (2002) studied 120 cadaveric humeri and found the mean angle of retroversion to be 17.6 ± 12.3°. They found good interclass correlation coefficient (between 0.85 and 0.90) for measurements made in the distal part of the humeral head and the epicondylar axis. Despite a wide variation in the actual angle of torsion, there was little side to side variation in the same individual (mean difference of 2.1°).

Clinical Relevance/Implications

Determining humeral head retroversion using CT prior to operative intervention is more accurate than palpating epicondylar axis or using the forearm as a goniometer during surgery. CT is also useful in assessing rotational deformity of the humerus in fracture malunion or severe arthritis.

The landmarks in the proximal humerus can be difficult to identify in certain cases such as presence of large osteophytes, osteolysis or severely comminuted fractures. In such patients, the angle of retroversion can be extrapolated from measuring the contralateral normal humerus, as only little side-to-side differences have been found between the two normal humeri of the same individual (Hernigou et al. 2002).
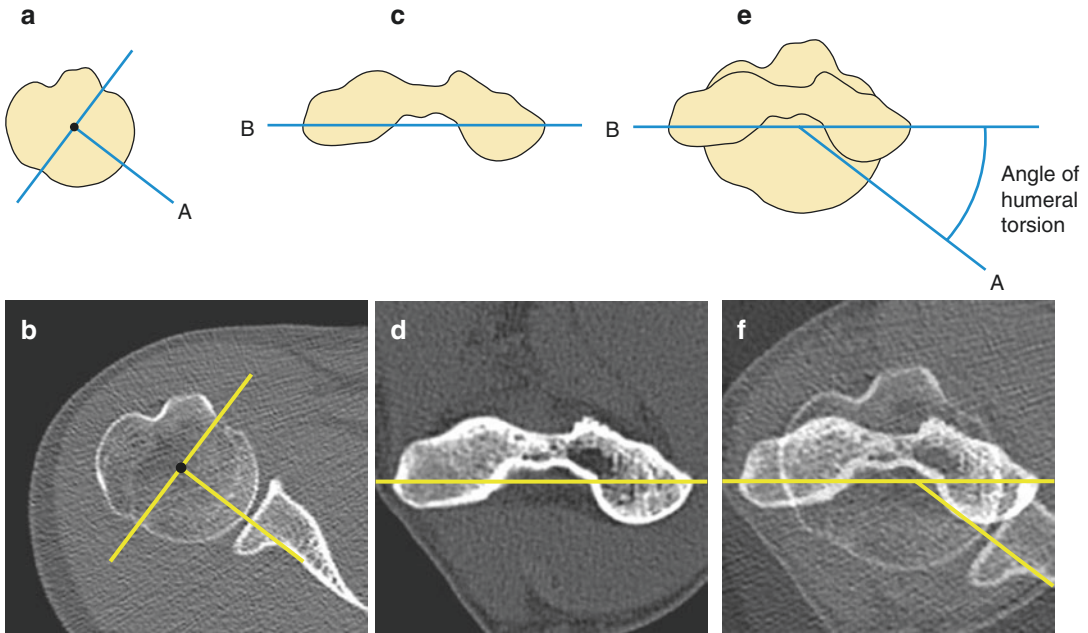
Fig. 17.3 (**a**, **b**) A section through the centre of the humeral head showing the boundaries of the humeral head articular surface and the humeral head axis (line A). (**c**, **d**) The transepicondylar axis (line B) is drawn by joining the most prominent medial and lateral extensions of the distal humerus. (**e**, **f**) The angle between the humeral head axis and the transepicondylar axis is the angle of humeral torsion/humeral head retroversion

Various studies have been performed to determine the role of humeral head retroversion in increased gleno humeral external rotation in professional throwing athletes (Crockett et al. 2002; Reagan et al. 2002; Osbahr et al. 2002). It has been found that in these athletes, in 90° of abduction, there is increased external rotation and decreased internal rotation in the dominant extremity and this correlates with an increase in the humeral retroversion. The total range of motion is same in both glenohumeral joints, implying that the arc of motion is further externally rotated or "spun back" on the dominant side (Crockett et al. 2002). Studies have shown that there is an increase in the humeral retroversion by 10–15° in the dominant arm of the throwing athletes. Interestingly, there is no difference in the non dominant shoulders of the throwing and non throwing athletes, suggesting

that increased retroversion is a developmental process which is likely secondary to remodelling of the proximal humerus during growth. It is postulated that this adaptive change is beneficial, as increased external rotation may help in generating greater velocity. It also appears to be protective in nature. Pieper (1998) studied 51 professional handball players. He noted that of the 38 athletes who were asymptomatic, there was a significant increase in humeral head retroversion by a mean of 14.4°. Amongst the other 13 athletes with chronic shoulder pain, there was no significant difference between the retroversion of the dominant and non dominant shoulders. He suggested that this osseus adaptation allowed increased external rotation without putting excessive strain on the anterior soft tissue structures, thus avoiding chronic pain and injury.

17.5   Ulnar Variance

Definition

Relative lengths of the distal articular surfaces of
the radius and ulna. It is positive if the ulna is
longer or negative if the ulna is shorter.

Normal	−0.9 mm (Range −4.2 mm to +2.3 mm)
Abnormal	< −4 mm, > + 2.4 mm

Indications

Ulnar impaction syndrome (positive variance),
avascular necrosis of the lunate/Keinbock's dis-
ease (negative variance, controversial).

Technique

Radiography–PA radiograph of the wrist.

Full Description of Technique

Ulnar variance is measured on a PA radiograph of
the wrist with forearm and wrist in neutral posi-
tion, elbow at 90° flexion and shoulder at 90° of
abduction. Three methods of measuring ulnar
variance have been described (Steyers and Blair
1989). These include

(a) "The project a line technique": a line is pro-
jected from the articular surface of the radius
towards the adjacent ulna. Distance between
this line and the carpal surface of the ulna is
the variance (Fig. 17.4a).
(b) Method of perpendiculars: A line is drawn
through the distal ulnar aspect of the radius,
which is perpendicular to the long axis of the
radius. Distance between this and the distal
aspect of the ulna is the variance (Fig. 17.4b)
(c) Concentric circle technique: A template of
concentric circles is superimposed on the
radiograph. The curve closest to the radial
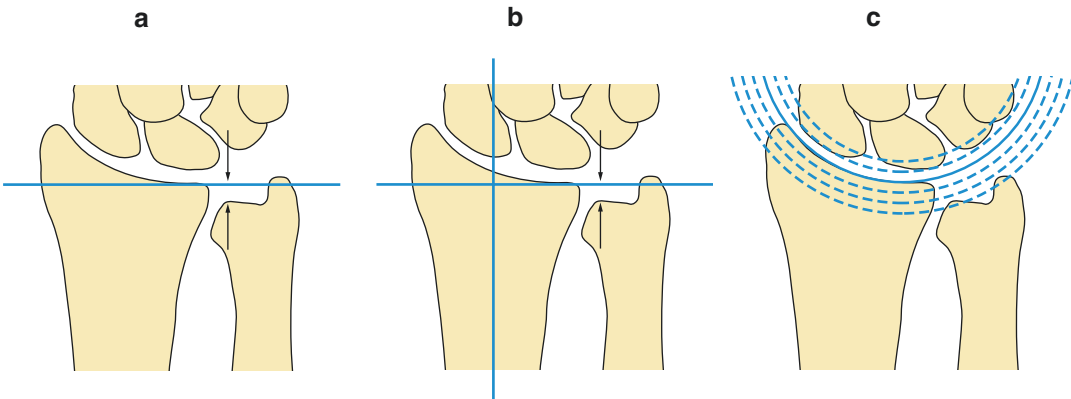
Fig. 17.4 Methods of measuring ulnar variance as described in the text. (**a**) "The project a line technique". (**b**) "The
method of perpendiculars". (**c**) "The concentric circle technique"

articular surface is chosen and the distance from this to the cortical outline of the ulna head is taken as the variance (Fig. 17.4c).

Reproducibility/Variation

Steyers and Blair (1989) compared the three commonly used methods of measuring ulnar variance. Their study showed that all three measurement methods have a high degree of intraobserver and interobserver reliability. The method of perpendiculars was most reliable for both inter-observer ($r = 0.9801$) and intra-observer ($r = 0.9719$) reliability, but the differences amongst the techniques were very small. They advocated that a clinician might choose a technique of their preference when measuring ulnar variance.

The mean ulnar variance is −0.9 mm with a normal range between −4.2 and 2.3 mm (Schuind et al. 1992).

Clinical Relevance/Implications

Variations in measurement may be developmental, post-surgical or post-traumatic.

Negative ulnar variance may be associated with avascular necrosis of the lunate/Keinbock's disease. A study performed on 44 patients with Keinbock's disease and 99 normal control subjects (Bonzar et al. 1998) confirmed an association between negative ulnar variance and Keinbock's disease even after correcting for age which was found to influence negative variance.

Positive ulnar variance is associated with ulnar impaction syndrome. Chronic impaction between the ulnar head and the carpus leads to degenerative triangular fibrocartilage tears, chondromalacia of the ulna, lunate and triquetrum and subsequently degernerative arthritis of the ulnocarpal and distal radioulnar articulations (Imaeda et al. 1996; Cerezal et al. 2002).

17.6 Leg Length Discrepancy

Definition

Difference in the total leg length as compared to the contralateral side.

Indication

Developmental anomalies, post-traumatic.

Techniques

Radiography—Orthoroentgenology.
CT—scanogram.

Full Description of Technique

In the past, evaluation of leg length has been made using orthoroentgenology. In this technique, three distinct exposures are made over the hip, knee and ankle in turn to minimise the magnification error. A single long film is used and a radio-opaque ruler is placed along side at about the height of the bone to avoid magnification (Green et al. 1946).

With the advent and now easy accessibility of CT, a CT scanogram is now the recommended method for measuring leg length. A full scout view of the lower limb is obtained from the hip joint down to the level of the ankle joint. The patient lies supine on the scanner table top. There is no significant magnification if the lower limb is placed in the centre of the gantry. The femur length is measured from the most superior aspect of the femoral head to the distal aspect of the medial femoral condyle. The tibial length is measured from the superior aspect of the medial tibial plateau to the tibial plafond (Helms and McCarthy 1984) (Fig. 17.5a, b).

Reproducibility/Variation

Various studies have revealed that a CT scanogram has excellent reliability and less gonadal radiation as compared to other methods utilising plain radiographs (Sabharwal and Kumar 2008). Aitken et al. (1985) compared CT scanogram versus conventional scanogram using plain radiography. All studies were reviewed by two radiologists independently and revealed high interobserver correlation ($r = 0.99$).

Clinical Relevance/Implications

Leg length inequality is associated with gait abnormalities and pelvic obliquity and may lead to degenerative arthritis of the lower extremity and the lumbar spine. Length discrepancies may arise due to congenital abnormalities or may be a consequence of trauma. Whilst planning treatment, it is important to be able to predict limb length at skeletal maturity.

Adults with a leg length discrepancy less than 2 cm are generally asymptomatic and only 10% required a shoe lift (Gross 1978). Most people agree that a discrepancy projected to be greater than 2.5 cm requires treatment, although clinical judgement must be weighed in individual cases.

Fig. 17.5 (**a**) Measurement of the femoral, tibial and total leg length. (**b**) CT scanogram depicting measurement of the femoral and tibial length in a case of malunited fracture shaft of left femur
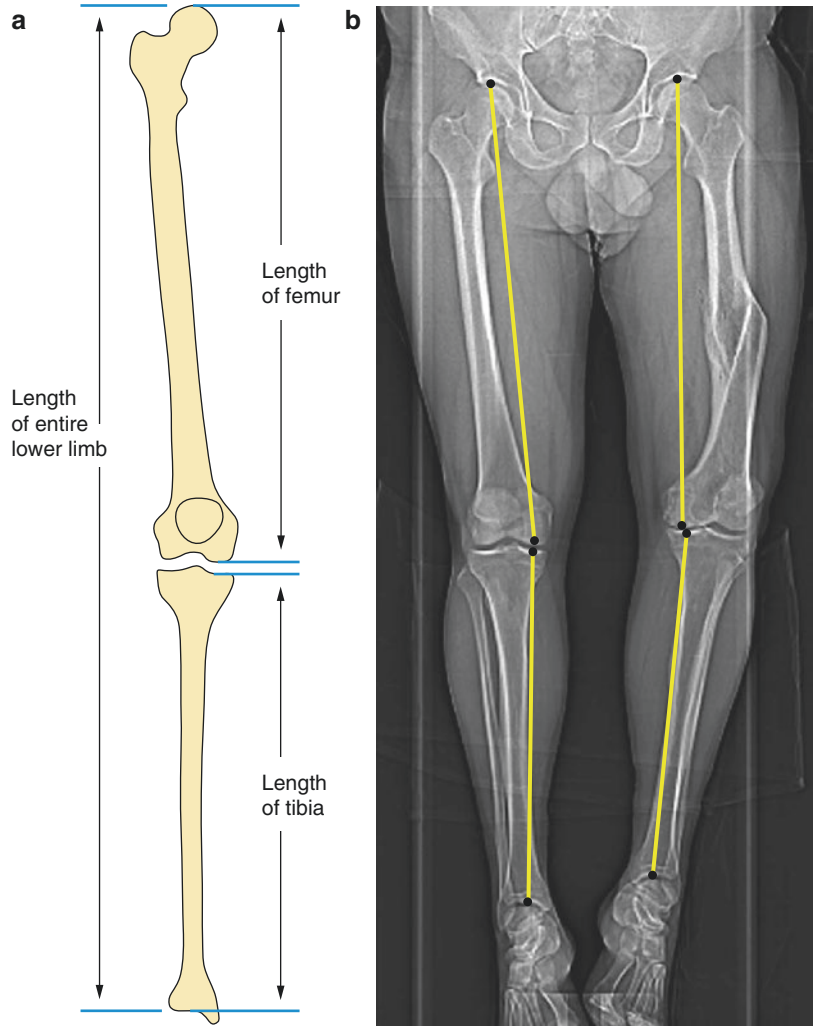
17.7 Femoral Neck Anteversion

Definition

Inclination of the axis of the femoral neck with reference to the transcondylar plane of the distal femur.

Normal adults	CT 22.2°, MRI 15.7°
Abnormal	Increased Anteversion CT > 28°, MRI > 20°
	Retroversion <0°

Indications

For assessment prior to derotation osteotomy.

Techniques

CT: Transverse image through the centre of femoral head, transverse image through the base of the femoral neck and transverse image through the distal femur at the level of the femoral condyles.
MRI: Oblique axial image along the axis of the femoral neck and axial image through the level of the femoral condyles.

Full Description of Technique

CT: To facilitate this examination, previous authors have described using a special footboard attached to the CT table for ensuring immobilisation, especially in children. No hip or knee flexion is allowed. Two blocks of transverse sections are obtained using the scout view as the localiser. The proximal sections should include the head of the femur, superior border of the greater trochanter and the base of the femoral neck. The distal sections are through the femoral condyles.

The femoral neck axis may be measured in one of two ways

(a) A single section that includes the head and neck (Fig. 17.6a) or the neck alone (Fig. 17.6b) (Hernandez et al. 1981). A line is drawn through the femoral neck that visually best describes the neck axis.
(b) A pair of sections through the centre of the head and the base of the neck. Murphy et al. (1987) showed that this method is more accurate than the first method. The centre of femoral head is plotted on the proximal section (Fig. 17.7a, d). The centre of the base of the femoral neck is plotted on the distal section (Fig. 17.7b, e). These two sections are then superimposed, and the femoral neck axis is formed by joining the two centre points (Fig. 17.7c, f). Although more accu-
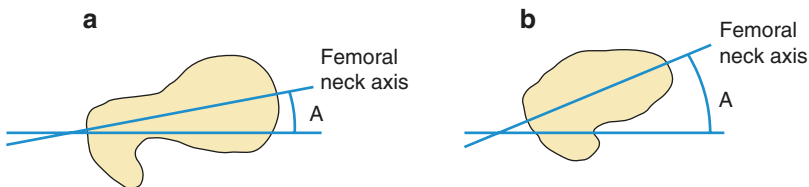
Fig. 17.6 Femoral neck axis measured on a single axial section. Measurement can be performed either through the proximal or the distal aspect of the femoral neck. (**a**) Proximal section through the head and neck of the femur. (**b**) Distal section through the neck of the femur alone

rate, this method can be more time-consuming. It is easier to perform if there is software available which makes it possible to superimpose multiple images.

The angle between the femoral neck axis and the CT table is measured (angle *A*). A line joining the most posterior aspects of the femoral condyles represents the transcondylar axis (Fig. 17.8a, b). The section with the maximum diameter of the condyles is chosen. The angle between the transcondylar axis and the CT table is measured (angle *B*). The difference between

these two angles is the angle of femoral neck anteversion (Fig. 17.9).

In anteversion the two angle measurements are added whilst in retroversion they are subtracted.

MR: A coronal scout view of the pelvis and hips is obtained. Oblique axial sections are obtained along the axis of the femoral neck (Fig. 17.10a). The inclination of the neck axis is measured on a single image showing the centres of the head and femoral neck (Fig. 17.10b). This is thought to be a more true representation of the femoral neck axis (Tomczak et al. 1997). A block of sections is
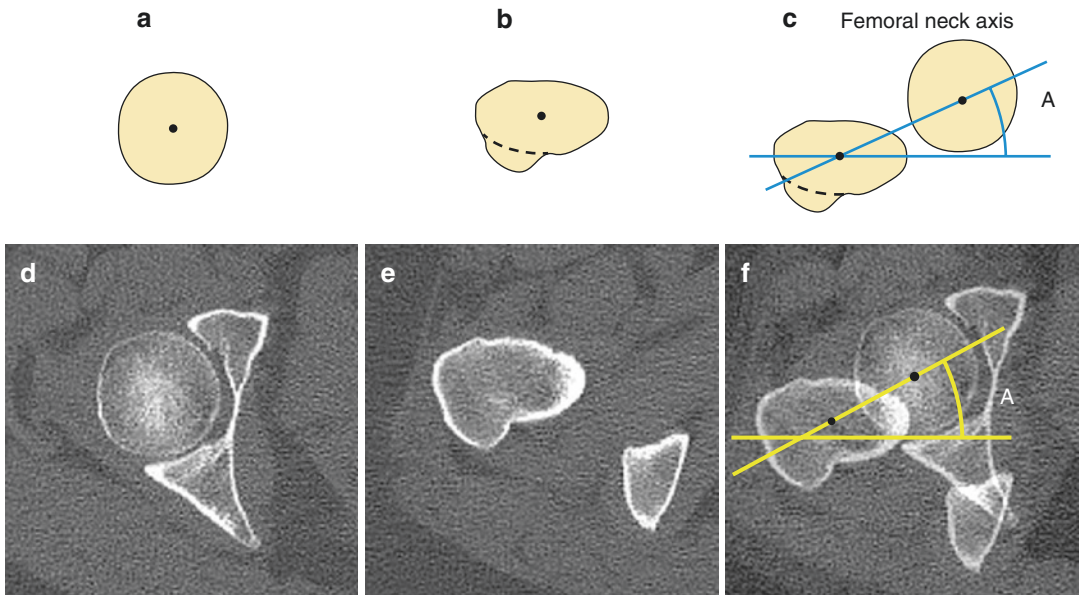
Fig. 17.7 Femoral neck axis measured on pair of sections through the centre of the head and the base of the neck. (**a**, **d**) Centre of the femoral head. (**b**, **e**) Centre of the base of the femoral neck. (**c**, **f**) Superimposition of the two images. A line joining the two centre points describes the femoral neck axis

Fig. 17.8 (**a**, **b**) Measurement of the transcondylar axis
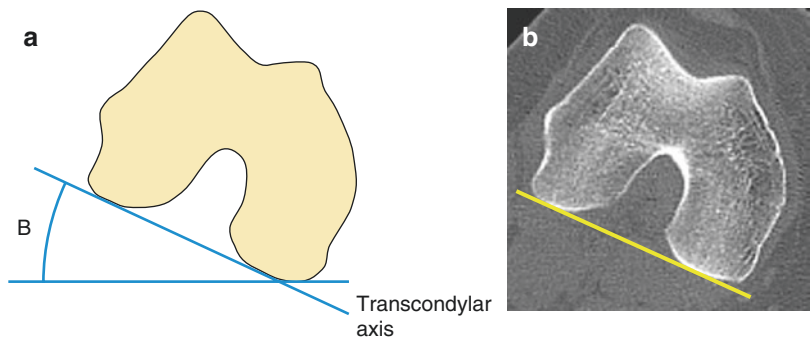
obtained through the level of the femoral condyles and the transcondylar axis obtained as described in the CT technique. Angles *A* and *B* are measured as described above, with subsequent calculation of the femoral neck anteversion.

Reproducibility/Variation

Various techniques for measuring femoral anteversion have been described in the literature. Normally, the femoral neck is anteriorly inclined as compared to the transcondylar axis and this is designated by a positive angle. When the femoral neck is posteriorly inclined, the term retroversion is used and the angle has a negative sign.
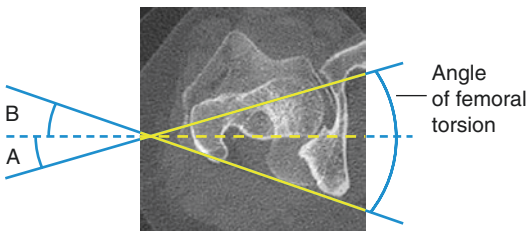
Fig. 17.9 A superimposed image showing the difference between the femoral neck axis and the transcondylar axis, which is the angle of anteversion. The summation of angles *A* + *B* calculates the angle of anteversion. The femoral neck axis has been determined on a single section through the femoral head and neck

The angle of anteversion may vary depending on the technique used. Normal range is accepted to be around 12–15° of anteversion in adults. Tomczak et al. (1997) found a mean value of angle of femoral torsion in adults to be 22.2° by CT imaging and 15.71° by MR imaging. Schneider et al. (1997) found the mean value of femoral antetorsion to be 10.4 ± 6.2°.

Hernandez et al. (1981) reported good reliability with low intraobserver and interobserver mean errors of 2° and 3° respectively. Schneider et al. (1997) reported an average difference of 2.4 ± 3.2° during repeat measurement by the same observer after more than 3 months.

Clinical Relevance/Implications

Abnormal measurements may be due to developmental causes such as femoral dysplasia, slipped capital femoral epiphysis, Perthe's disease or secondary to trauma. On average, femoral anteversion ranges from 30 to 40° at birth and decreases progressively throughout growth to about 15° at skeletal maturation. It is important to accurately measure the angle of anteversion and compare with the contralateral side prior to planning derotation osteotomy.
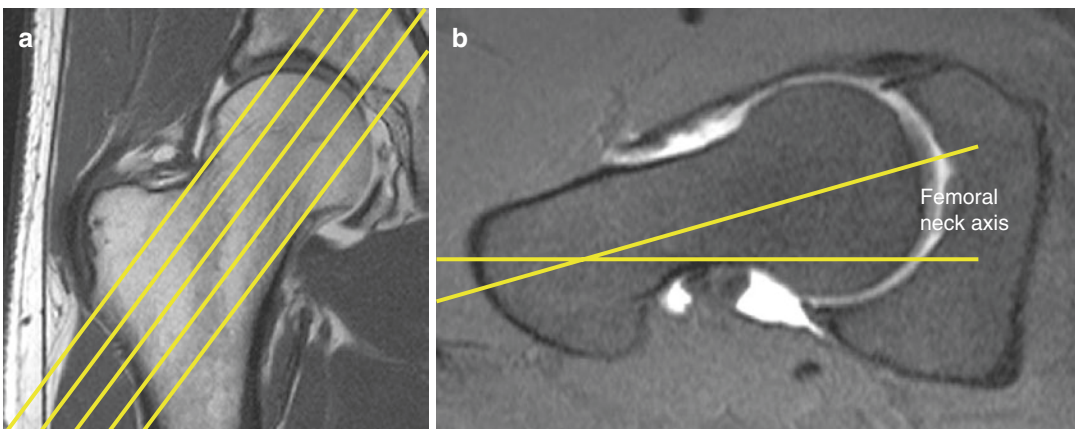
Fig. 17.10 MRI determination of the femoral neck axis. (**a**) A coronal scout view with the lines of reference running along the plane of the femoral neck. (**b**) An axial oblique image of the femoral neck showing the neck axis

17.8 Lower Limb Alignment

Definition

Alignment refers to the colinearity of the hip, knee and ankle. Orientation refers to the position of each articular surface relative to the axis of the individual bone (femur and tibia) (Tetsworth and Paley 1994).

Normal LDFA	85–90°
Normal MPTA	85–90°

Indications

Assessment and progression of osteoarthritis, preoperative planning, e.g. high tibial osteotomy, follow-up of knee implants.

Technique

Radiography—Weight-bearing full-length radiographs are the standard of reference for planning corrective lower limb surgery. Supine views are inappropriate as they significantly underestimate the extent of valgus malalignment in particular (Brouwer et al. 2003). A full-length, weight-bearing radiograph of the lower limb is mandatory. The X-ray beam is centred at the knee joint level and a graduated filter is placed in front of the beam to visualise the hip, knee and ankle with a uniform density. With the patients standing under full weight bearing, hips and knees are extended fully and positioned with the patella and the tibial tuberosity facing directly forward. This may require internal lower limb rotation to achieve correct positioning to ensure that the patella is facing forward. The patella needs to be radiographically located equidistant between the distal femoral condyles. Long leg radiographs are unreliable if the patella is rotated more than 10° to the frontal plane (Wright et al. 1991) (Fig. 17.11a).
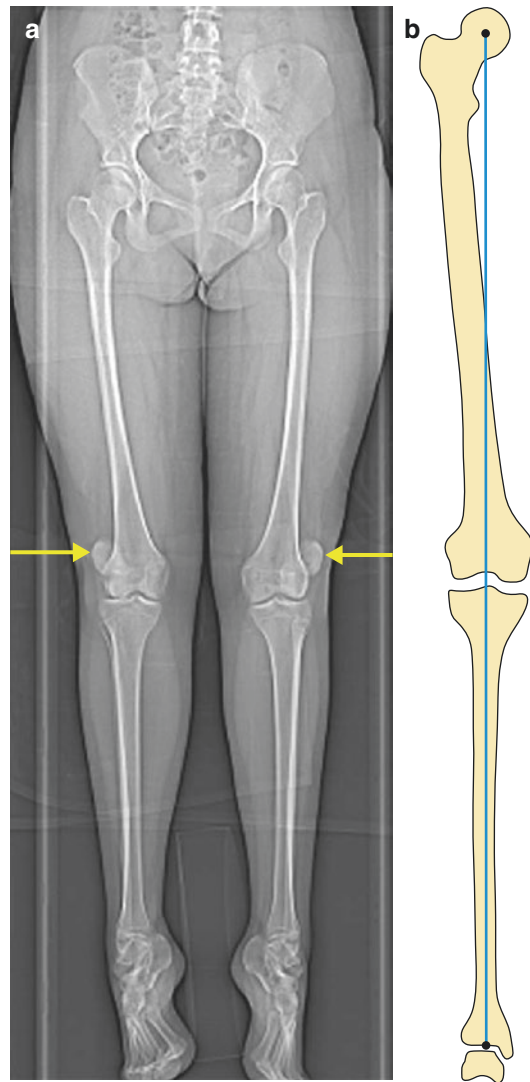
Fig. 17.11 (**a**) It is important to ensure that the patella and the tibial tuberosity are facing anteriorly before measurements relating to alignment are carried out. If the patella is rotated, as shown in this CT scanogram, then the measurements obtained will be unreliable. (**b**) Normal mechanical axis of the lower limb

Full Description of Technique

Alignment is determined by a line extending from the centre of the hip to the centre of the ankle, known as the mechanical axis of the limb.

This usually passes immediately medial to, or through the centre of the knee (Fig. 17.11b). Any deviation from this colinearity results in malalignment. A deviation of the mechanical axis by more than 1 cm from the centre of the knee joint suggests a deformity in the more proximal tibia or femur. The mechanical axis deviation (MAD) is measured by drawing a perpendicular segment from the axis to the centre of the knee (Fig. 17.12).

The mechanical axis of the femur is located as a line drawn from the centre of the femoral head to the centre of the knee. The mechanical axis of the tibia is a line drawn from the centre of the knee to the centre of the ankle joint. The angle between these two mechanical axes is the femoro-tibial angle (Fig. 17.12).

The anatomical axis of the femur is represented by a line drawn along the longitudinal axis of the femoral diaphysis, from the piriform fossa to the centre of the knee. The anatomic axis is approximately 6° of valgus from the mechanical axis (Fig. 17.13).

The centre of the femoral head is found by drawing a circle around the femoral head.

For determining the centre of the knee, five different points have been described in the literature. These are: centre of femoral notch, centre of tibial spine notch, centre of soft tissues, centre of tibia and centre of femoral condyles (Fig. 17.14). Moreland et al., in their measurements, used a visually selected midpoint of all these five points. For practical purposes, it is easiest to use the centre of the tibial spines or the femoral notch to mark the centre of the knee.

The centre of the ankle is a visually selected midpoint of the following three measured points: centre of soft tissues, centre of bones and centre of talus (Fig. 17.15). For practical purposes, the centre of the talus or the tibial plafond is easiest to use.

The line joining the distal most aspects of both femoral condyles in the frontal plane describes the knee joint orientation line of the distal femur. The angle between this line and the mechanical axis of the femur, as measured on the lateral aspect, defines the joint orientation of the distal femur and is known as the lateral distal femoral angle (LDFA) (Fig. 17.16).
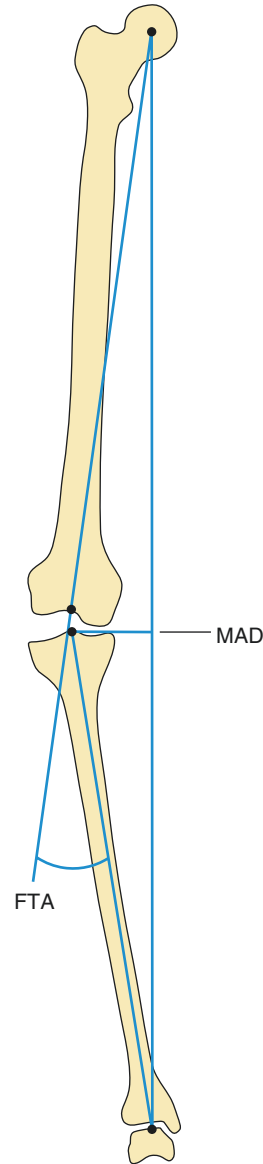
Fig. 17.12 Diagram showing varus deformity of the lower limb. The mechanical axis passes medial to the centre of the knee, and the mechanical axis deviation (MAD) is measured as described in the text. The angle between the mechanical axes of the femur and the tibia is the femoro-tibial angle (FTA)

A line drawn parallel to the proximal tibial articular surface describes the knee joint orientation line of the proximal tibia. The angle between this line and the mechanical axis of the tibia, as measured on the medial aspect, defines the joint orien-
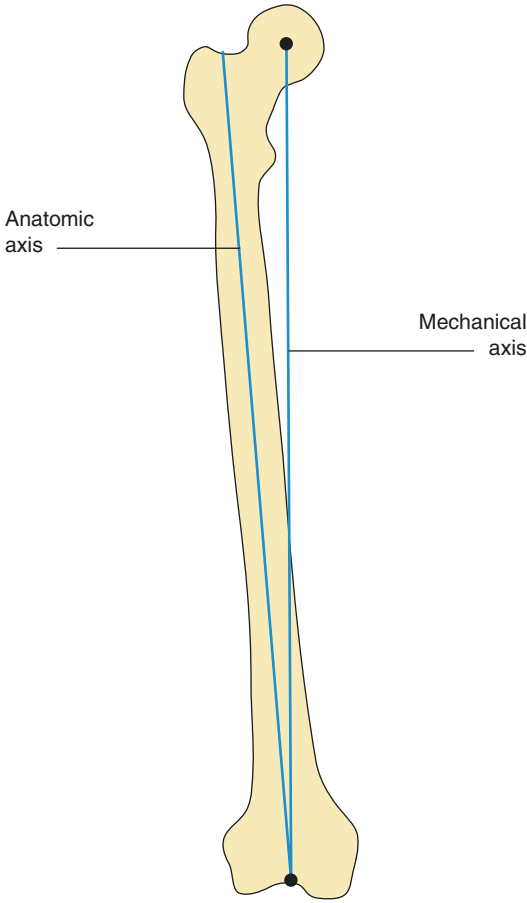
Fig. 17.13 Diagram showing the anatomical and mechanical axis of the femur. The anatomic axis is about 6° in valgus from the mechanical axis
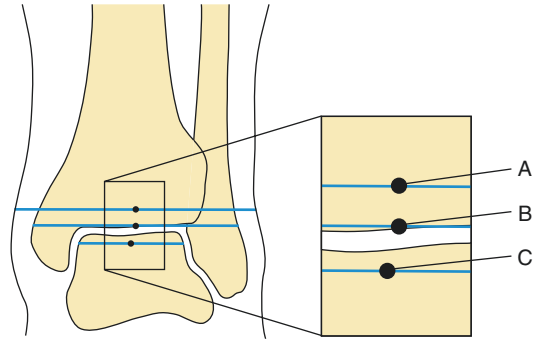
Fig. 17.15 Three different points described for determining the centre of the ankle: (A) centre of soft tissues, (B) centre of bones and (C) centre of talus
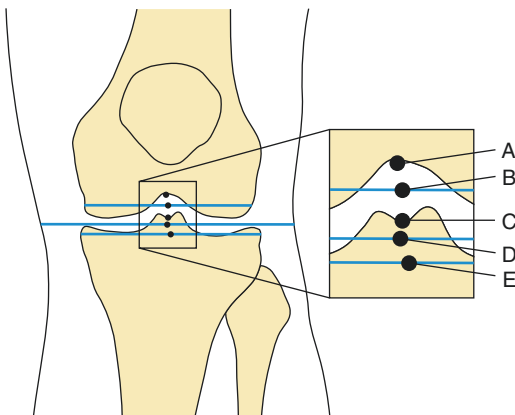
Fig. 17.14 Five different points described for determining the centre of the knee: (A) centre of femoral notch, (B) centre of femoral condyles, (C) centre of tibial spine notch, (D) centre of soft tissues and (E) centre of tibia
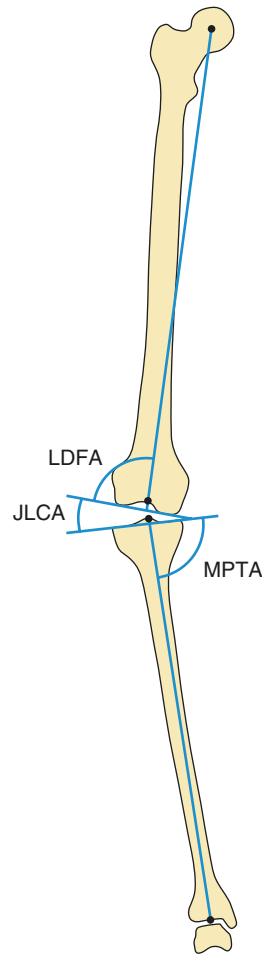
Fig. 17.16 Diagram showing the joint orientation line of the distal femur and the proximal tibia. The lateral distal femoral angle (LDFA), medial proximal tibial angle (MPTA) and the joint line convergence angle (JLCA) are measured as described in the text

tation of the proximal tibia and is known as the medial proximal tibial angle (MPTA) (Fig. 17.16).

The angle formed between the joint orientation lines of the distal femur and the proximal tibia is known as the joint line convergence angle (JLCA) (Fig. 17.16).

In isolated foot and ankle deformity it is still very important to determine the alignment of the whole of the lower limb with special reference to the tibia. On the AP view the mid-tibial diaphyseal anatomic axis forms an 89° angle (range 86–92°) with the talar dome (see hindfoot alignment view in ankle chapter). Normally the tibial longitiudinal axis is seen to pass just medial to the centre of the talus on the AP view. Incidentally normally the centre of the calcaneum is also lateral to the midaxis of the tibia. On the standing lateral view the tibial midaxis passes through the lateral talar process. With the foot in the plantigrade position the sagittal anterior distal tibial angle is formed on this view by the intersection of the midaxis of the tibia with the anterior-to-posterior tibial line which is normally 80°.

Reproducibiltiy/Variation

In a study of 25 normal male volunteers (Moreland et al. 1987), it was shown that the mechanical axis passes immediately medial to the centre of the knee. The angle between the femoral and tibial mechanical axis (FTA) measured $1.3 \pm 2°$. Hsu et al. reviewed weight bearing long leg radiographs in 120 subjects and also found that the mechanical axis passes just medial to the centre of the knee. They found the FTA to be $1.2 \pm 2.2°$.

The joint orientation line of the distal femur was measured in a study of 127 healthy volunteers (Chao et al. 1994). They found that the distal femoral articular surface is in a slight valgus alignment of $88.6 \pm 2.8°$. Other researchers have obtained similar values. McKie et al. found the distal femur valgus to be $87.8 \pm 1.6°$. Cooke et al. obtained full-length radiographs in 79 young adults and found the distal femur orientation to be in $86 \pm 1.2°$ of valgus. Based on these data, the normal orientation of the distal femoral joint line

is considered 87° valgus (Tetsworth and Paley 1994), with a normal LDFA between 85 and 90°.

The joint orientation line of the tibial articular surface is in slight varus as compared to the mechanical axis of the tibia. Chao et al. (1994), found the measurement to be $87 \pm 2.5°$. Cooke et al. (2007) found the proximal tibia in $87 \pm 1°$ of varus. McKie et al. and Moreland et al. (1987) confirmed these values and noted the measurement as $87.2 \pm 1.9°$ and $87.2 \pm 1.5°$ respectively. Based on these observations, the normal relationship of the proximal tibial joint orientation and the mechanical axis of the tibia is considered to be 87° varus, with a normal MPTA between 85 and 90°.

More recently, some studies have assessed anatomic alignment on short film radiographs centred at the knee (Fig. 17.17). These are easier to perform and are done in routine everyday practice. Local anatomical alignment is measured, rather than the
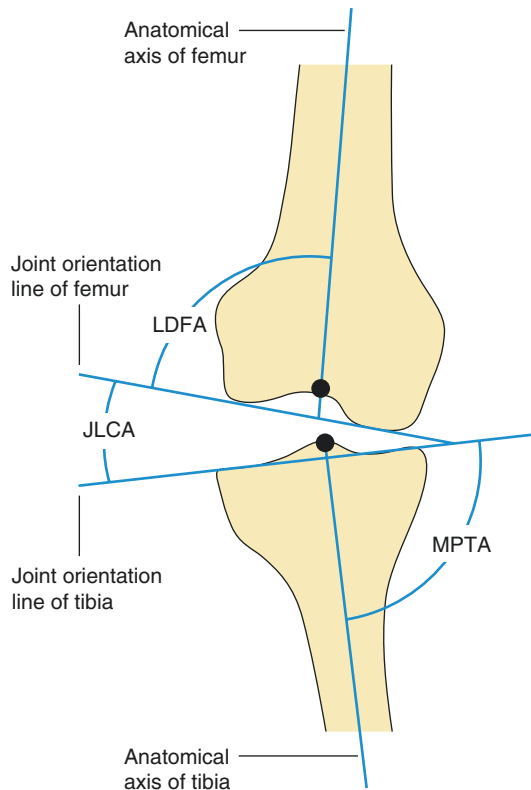
Fig. 17.17 Measurement of alignment parameters on a short film of the knee. The lateral distal femoral angle (LDFA), medial proximal tibial angle (MPTA) and the joint line convergence angle (JLCA) are shown

actual mechanical alignment. Strong correlation has been demonstrated between measurements obtained from long length films and those obtained from the anatomical axis in a short film (Kraus et al. 2005). It is recognised that these short films are more easily obtainable, but they do not capture proximal and distal anatomy where there may be an unrecognised deformity, and hence the full-length films with measurement of the mechanical axes remain the gold standard for evaluation of alignment in the lower limb (Hunter and Wilson 2009).

Clinical Relevance/Implications

Osteoarthritis is believed to be a result of local mechanical factors on the background of systemic susceptibility (Hunter and Wilson 2009). The mechanical axis represents the path of transmission of forces in the lower extremity. By definition, malalignment occurs when the centre of the knee does not lie close to this line. The goal of deformity correction is to not only restore normal alignment but also maintain or restore the normal orientation of each joint to the mechanical axis. One of the most important factors for long-term success after an osteotomy or joint replacement is to ensure an ideal lower extremity mechanical axis alignment. The knowledge of normal values helps in planning the osteotomy type, wedge angle and location and the precise placement of prosthetic components in joint replacements.

Valgus osteotomy of the proximal tibia is used in young patients with a progressively symptomatic varus knee and mild to moderate osteoarthritis. Ideal alignment following osteotomy produces a mechanical axis that passes through the mid third of the lateral compartment of the knee i.e. there should be a slight overcorrection of the mechanical axis (Fig. 17.18). The total amount of correction required is a combination of the angular deformity between the tibia and femur, joint line convergence angle and the overcorrection amount.
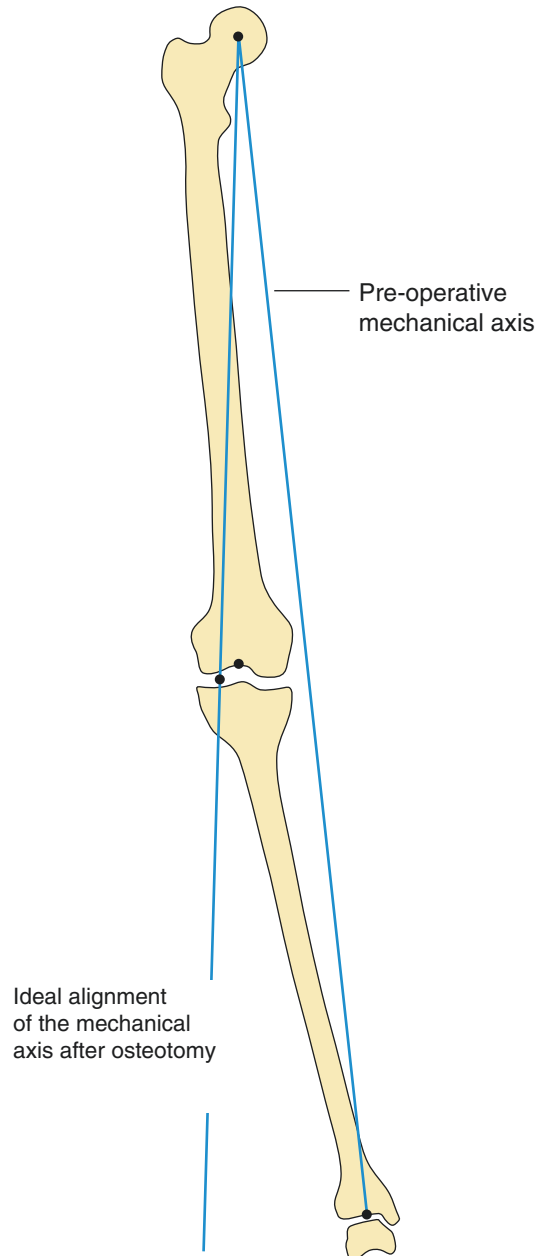
Fig. 17.18 The ideal alignment of the mechanical axis following high tibial osteotomy. After osteotomy the mechanical axis should pass through the mid third of the lateral compartment (deliberate overcorrection)
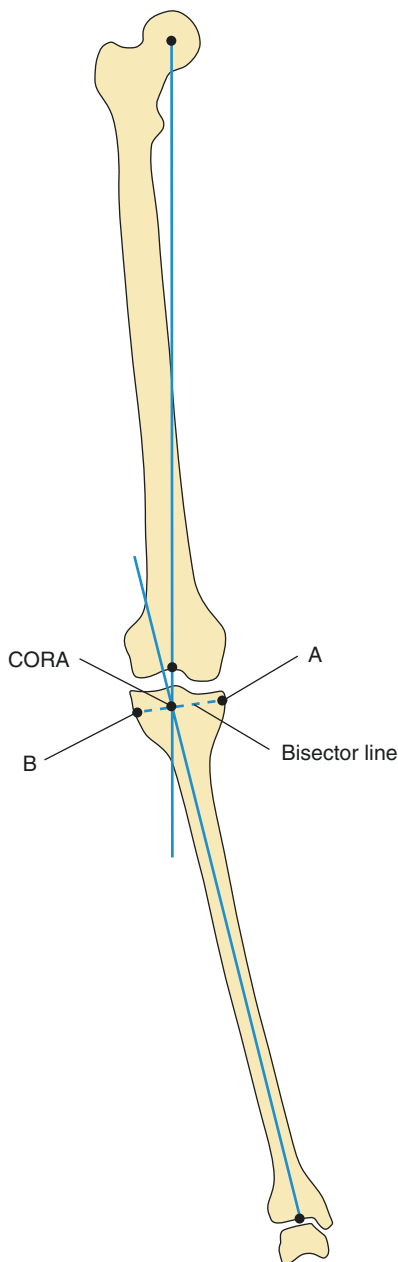
Fig. 17.19 Diagram showing the point of centre of rotation of angulation (CORA). This is the level where the osteotomy should be carried out. The bisector line through the CORA determines the apex points for either a closing (point A) or an opening (point B) wedge osteotomy. Further details are described in the text

The osteotomy should ideally be performed at the centre of rotation of angulation (CORA). This is the point of intersection of the proximal and distal mechanical axes (Fig. 17.19). If the LDFA is within normal limits, then extension of the mechanical axis of the femur can be used to describe the proximal axis of the tibia. The proximal and distal mechanical axes form a medial and lateral angle at the CORA. A transverse line is drawn through the CORA bisecting this angle. The points of intersection (A and B) on the medial and lateral cortex describe the apex points for a closing or opening osteotomy respectively (Fig. 17.19). The CORA in most genu varum conditions is at or near the knee joint. Angular corrections distal to this level results in a secondary deformity that requires lateral translation of the distal part (Paley et al. 1994).

The tibial osteotomy angle can be measured by a method described by Murphy (1994). This calculates the total amount of correction required to obtain a postoperative mechanical axis that passes through the mid third of the lateral compartment of the knee joint. The proposed postoperative mechanical axis is drawn and the projected postoperative position of the centre of the ankle is marked on this line (virtual ankle point, VA). Next two lines are drawn; firstly a line is drawn from the apex of the proposed osteotomy (point A for a closing wedge osteotomy) to the centre of the ankle. A second line is drawn from point A to the virtual ankle point. The angle between these two lines is the angle of correction (angle α) (Fig. 17.20a–c). The same process can be used for calculating the angle of correction for an opening wedge osteotomy. In this case the apex of the osteotomy is substituted by point B instead of point A (Fig. 17.21a, b). A closing osteotomy will result in a degree of shortening of the tibia, whereas an opening osteotomy maintains the original length of the convex cortex of the varus tibia.

Fig. 17.20 Magnitude of correction for a closing wedge osteotomy. (**a**) The proposed postoperative mechanical axis is shown with the projected position of the ankle joint (VA). A line is drawn from point A to the centre of the ankle, and a second line is drawn from point A to point VA. The angle between these two lines (angle α) is the angle of correction. (**b**) A wedge of bone of magnitude α is removed with apex at point A. (**c**) The final alignment after closure of osteotomy site. Note that the mechanical axis passes through the lateral compartment
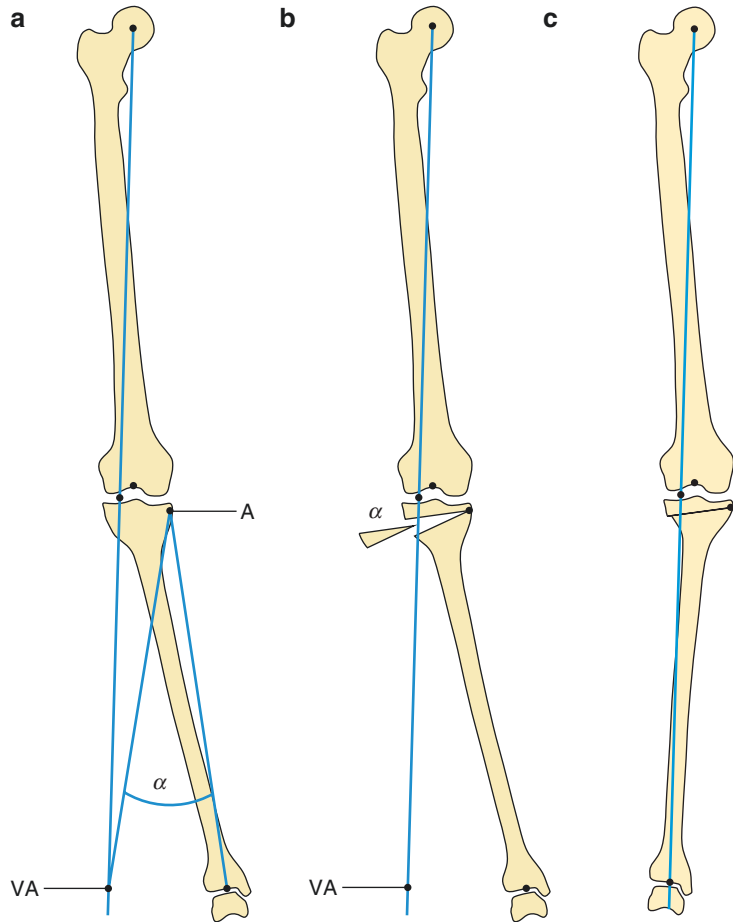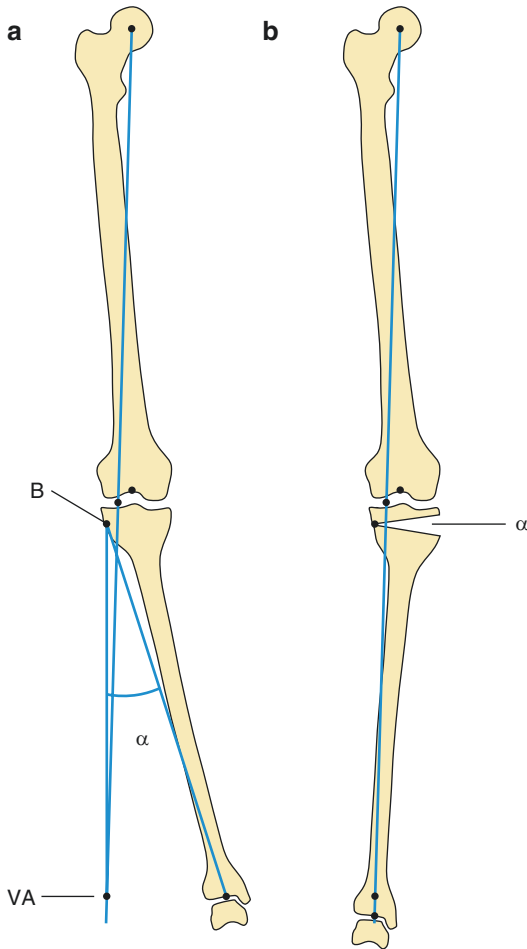
Fig. 17.21 Magnitude of correction for an opening wedge osteotomy. (**a**) The proposed postoperative mechanical axis is shown with the projected position of the ankle joint (VA). A line is drawn from point B to the centre of the ankle and a second line is drawn from point B to point VA. The angle between these two lines (angle α) is the angle of correction. (**b**) The final alignment after an opening osteotomy of magnitude α with the apex at point B. Note that the mechanical axis passes through the lateral compartment

17.9   Tibial Torsion

Definition

Anatomical twist of the proximal versus the distal articular axis of the tibial bone around the longitudinal axis.

Normal	20–30° (range 0–40°)
Abnormal	<0°, >40°

Indications

For assessment prior to derotation osteotomy.

Techniques

CT/MRI—Two blocks of axial images are required, one just below the level of the knee and the other just above the ankle joint.

Full Description of Technique

Tibial torsion is measured by drawing reference lines through the proximal aspect of the tibia and the distal tibio fibular articulation. The section of the proximal tibia is taken just above the fibular head. A tangent joining the dorsal ridges defines the reference line from this section (Jend et al. 1981; Schneider et al. 1997) (Fig. 17.22a, b). In the distal tibia, the section just above the ankle joint is chosen. Different methods of obtaining the reference line at this level have been described: a line joining the centre of a circle superimposed on the tibial pilon and the midpoint of the fibular notch (Jend et al. 1981) (Fig. 17.23a–d) or a line between the centres of the tibia and the fibula (Laasonen et al. 1984). A line passing through the medial and lateral malleolus (bimalleolar axis) has also been used to define the distal axis. The first method is considered to be the most accurate as it does not incorporate the fibula, the position of which can be variable.

The angle between the lines of reference and the horizontal is calculated and the torsion is calculated as the difference between the proximal angle (angle A) and the distal angle (angle *B*) (Fig. 17.24) which are added together. Lateral/external torsion is denoted as positive.

Reproducibility/Variation

A study of 98 patients using MRI (Schneider et al. 1997) found an average tibial torsion of 41.7° with standard deviation of 8.9°. This correlates well with CT based measurements made
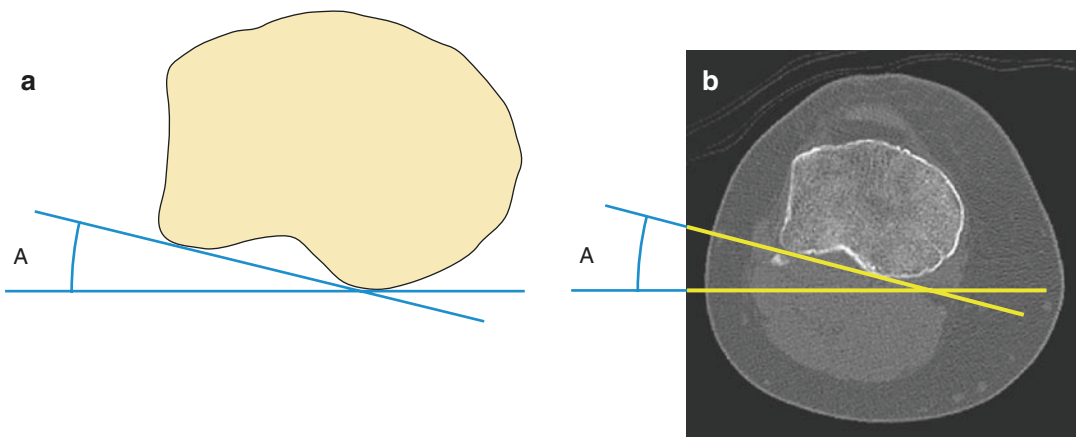
Fig. 17.22 (**a**, **b**) Tibial torsion assessment. Measurement of the proximal tibial axis of reference along the dorsal ridges of the proximal tibia
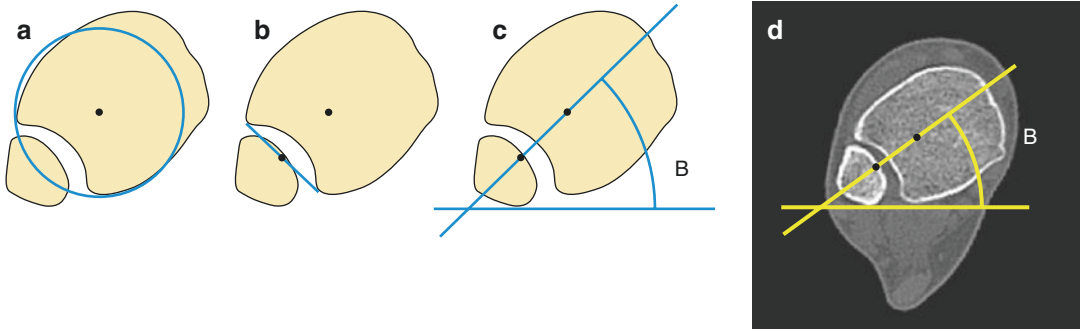
Fig. 17.23 Measurement of the distal tibial axis of reference for tibial torsion assessment. (**a**) Centre of the tibial pilon. (**b**) Centre of the fibular notch. (**c, d**) A line joining the two centre points describes the distal line of reference
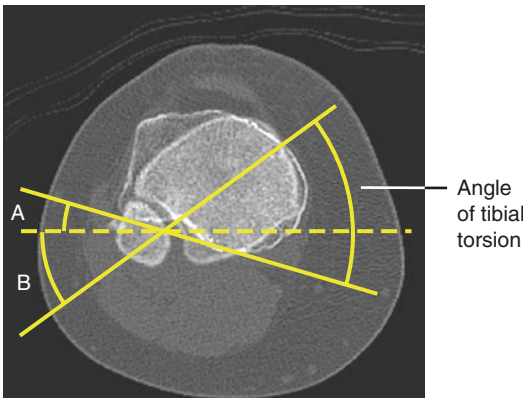
Fig. 17.24 Superimposed image showing the proximal and distal tibial axes of reference and subsequent calculation of the tibial torsion. Tibial torsion angle is *A + B*

by Jend et al. (1981), where they measured tibial torsion in 70 limbs and reported a value of 40° with a standard deviation of 9. Jakob et al. (1980) found a mean value of tibial torsion of 30° in 45 cadaveric tibiae.

Clinical Relevance/Implications

Rotational deformity of the tibia can be developmental or post-traumatic. Internal tibial torsion is the most common cause of intoeing in children and presents usually at about 2 years of age. Internal rotation decreases with growth and at maturity the tibia is normally laterally rotated. Hutter and Scott (1949) considered internal rotation (less than 0°) or severe external rotation (greater than 40°) to be abnormal. Staheli (1989) stated that operative correction is indicated if the torsion is greater than three standard deviations from the mean and indicated a value of $<-15°$ or $> +30°$.

17.10 Tibia: Metaphyseal–Diaphyseal Angle

Definition

Angle between the proximal tibial metaphysis and the tibial diaphysis.

Indications

Physiological bowing, infantile tibia vara (Blount's disease).

Further coverage in knee measurement section in Chap. 13.

Technique

Radiography: A standing AP radiograph of the lower extremity is obtained with the X-ray beam centred over the knee.

Full Description of Technique

A line is drawn connecting the medial and lateral beaks of the proximal tibial metaphysis (metaphyseal line, line A) (Fig. 17.25a). A second line (line B) is drawn perpendicular to the longitudinal axis of the tibia such that it intersects the metaphyseal line. A line along the lateral cortex or a line through the middle of the diaphysis can define the longitudinal axis of the tibia. The angle at the intersection of these two lines is the metaphyseal–diaphyseal angle (Fig. 17.25b) (Levine and Drennan 1982).

Reproducibility/Variation

Various studies have shown that MDA measurements are consistently reproducible with excellent interobserver and intraobserever reliability amongst reviewers. There is no significant vari-
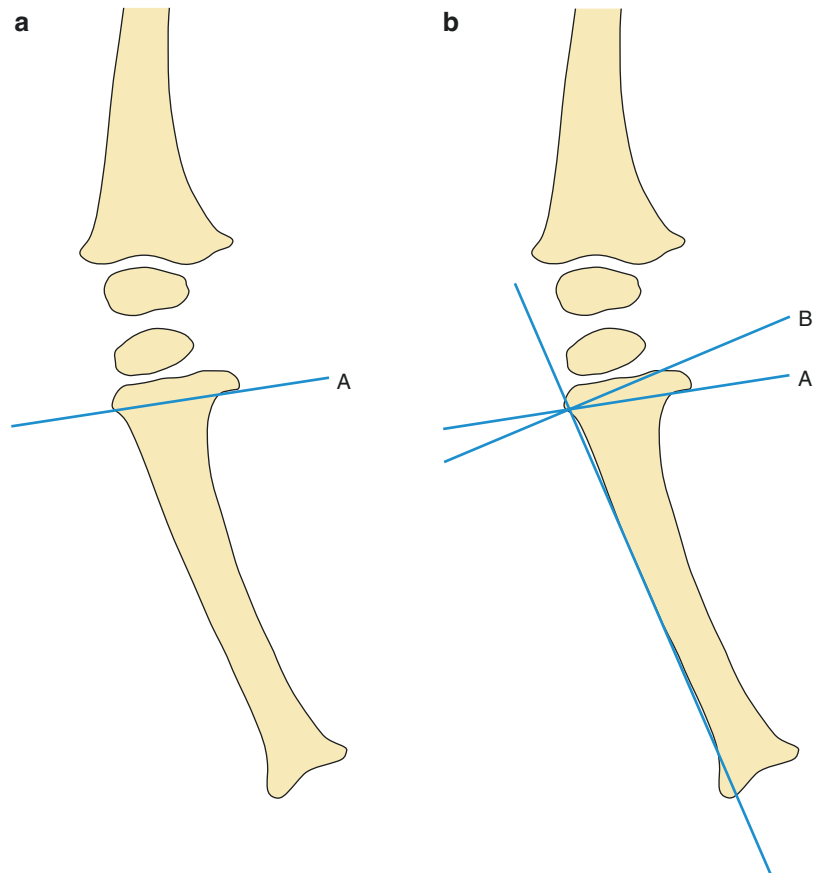
Fig. 17.25 Measurement of the metaphyseal–diaphyseal angle. (**a**) Metaphyseal line connects the medial and lateral beaks of the proximal tibial metaphysis (line A). (**b**) A line is drawn perpendicular to the longitudinal axis of the tibia (line B) such that it intersects the metaphyseal line. The angle between line A and B is the metaphyseal–diaphyseal angle

ability amongst the two methods used to designate the long axis of the tibia, i.e. lateral cortical line or central diaphyseal line (Auerbach et al. 2004; Lavelle et al. 2008; Foreman and Robertson 1985).

A cut-off of 11° has been suggested in literature to differentiate physiological bowing from Blount's disease (Levine and Drennan 1982). In this study, of the 30 affected extremities, 29 had an initial MDA of >11°. Three of the 58 extremities with an MDA angle of <11° developed any diagnostic changes of Blount's disease later.

Clinical Relevance/Implications

MDA is useful in the assessment of bow leg deformity and helps in differentiating physiological bowing from infantile tibia vara (Blount's disease). Feldman and Schoenecker (1993) compared 106 children (179 extremities) who had physiological bowing with 19 children (32 extremities) who had Blount's disease. When an MDA angle of 11° was used as a cut-off, they found a false positive error of 33% and a false negative error of 9%. If an MDA of <9° (physiological bowing) or >16° (Blount's disease) was used, then the error rate decreased to less than 5%. They suggested that if the angle is between 9 and 16°, then treatment with bracing should be considered only if there is instability on walking.

17.11 Tibia: Post-Traumatic Deformity Secondary to Malunion

Definition

Post-traumatic deformity of the tibia secondary to malunion.

Indications

Post-traumatic deformity of the tibia secondary to malunion.

Techniques

Radiography: Anteroposterior (AP), lateral and both oblique views of the tibia. Standing AP view of the entire lower limb for alignment.

CT: Scanogram and axial sections through the tibia with sagittal and coronal reformats.

Full Description of Technique

The AP standing radiograph is used to assess the alignment of the lower limb and measure mechanical axis deviation (MAD) as described in the "Lower limb alignment" section elsewhere in this chapter. Angular deformity is measured from the anatomic axis of each tibial segment. The junction of the proximal and distal axes is called the "centre of rotation of angulation" or CORA (the level at which an osteotomy should be performed), and the angle between these two axes is the angle of deformity (Fig. 17.26a–c). Leg length discrepancy and rotational deformity can be measured by CT scanogram and axial sections through the proximal and distal tibia respectively. These are described in detail in the relevant sections elsewhere in this chapter.
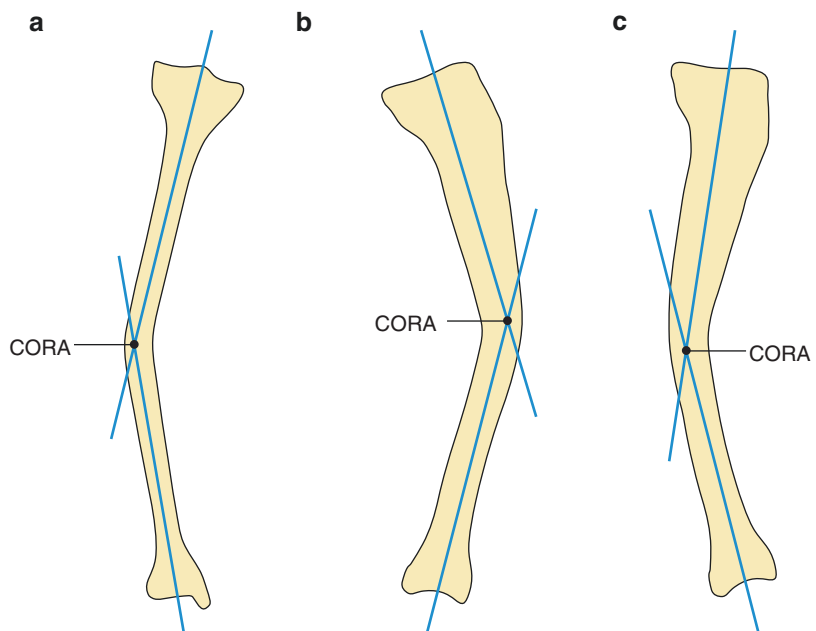
Fig. 17.26 Post-traumatic deformity of the tibia. (**a**) Angular deformity in the coronal plane. (**b**) Procurvatum deformity in the sagittal plane. (**c**) Recurvatum deformity in the sagittal plane

Clinical Relevance/Implications

Most clinicians believe that deformities of the tibial shaft result in alteration in the load distribution across the knee and ankle joints with consequent development of osteoarthritis. However, long-term follow-up clinical studies have not always supported this hypothesis. Merchant and Dietz (1989) reviewed 37 patients with isolated tibial fractures at an average of 29 years after injury. They found no correlation between the degree of deformity and the radiographic and clinical outcome. Van der Schoot et al. (1996) looked at 88 patients with isolated tibial shaft fractures with an average follow-up of 15 years after the injury. They evaluated the influence of angular malunion on the incidence of osteoarthritic changes in the adjacent joints, and found a statistically significant relationship between tibial malalignment and degenerative changes in the knee and ankle. Puno et al. (1991) retrospectively reviewed 28 patients with tibial fractures, at an average of 6–12 years after injury. They

were able to demonstrate a significant correlation between clinical outcome and ankle malorientation, but no similar correlation with knee malorientation.

The definition of what actually constitutes a tibial malunion has never been agreed upon and the maximum degree of acceptable angulation and shortening to avoid long term osteoarthritis remains controversial. It is important to remember that in addition to the angle of deformity, the level of deformity and the presence of translation also contribute to malalignment. The degree of acceptable deformity noted by various authors is extremely variable. Generally, patients can tolerate angulation of 5–8°, malrotation of up to 15–20° and shortening of 2 cm (Mechrefe et al. 2006). Disability from tibial malunion is produced mainly by varus and recurvatum deformities which are more poorly tolerated.

In children less than 9 years of age, deformity of axial alignment may correct spontaneously with growth, especially if it is near a joint and the epiphyseal growth plate has not been injured.

Clinical Relevance/Implications

The aforementioned angle is useful in determining the depression due to fracture of the tibial plateau. Based on this angle, Moore and Harvey also advocated a "tibial plateau view" where the X-ray beam is directed at an angle of 15° to the tibial crest, thereby providing a more accurate assessment of the amount of depression as the beam is parallel to the tibial articular surface.

17.13   Tibial Plateau Angle (Posterior Tibial Slope): MRI

The biomechanical importance of the tibial plateau angle (TPA) has been described abundantly in literature. The TPA is conventionally measured on a lateral radiograph, but this measurement has not been satisfactory. Various longitudinal axes have been defined (please refer to the previous section) with a wide variation in the reported values. Matsuda et al. (1999) described an MRI method for measuring the TPA that involved scanning the entire tibia from the tibial plateau to the ankle. Such a full-length scan is prone to plane-distortions, which can lead to a bowed appearance of the bone, therefore precluding accurate measurements (Doran et al. 2005). Three dimensional computed reconstructions are complex and time-consuming. Hudek et al. (2009) have described a technique based on a standard knee MRI, thereby circumventing the plane distortions. Both, medial and lateral TPA can be measured separately, with a good correlation and reproducilbilty.

The tibial plateau angle contributes to the anteroposterior stability of the knee and is also important factor in complications post knee arthroplasty, if not correctly restored. A separate measurement of medial and lateral TPA is important for corrective surgery after malunion of a tibial plateau fracture, reconstruction after tumor resection and in unicondylar knee arthroplasty. In such instances, the technique described below should be used.

Technique

The measurement of the tibial plateau angle (TPA) is done as follows.

A central sagittal image is chosen in which the intercondylar eminence and the attachment of the PCL are visualised. Subsequently, two circles are superimposed over the proximal tibia. The cranial circle should be in contact with the anterior, posterior and cranial tibial cortex. The caudal circle should be in contact with the anterior and posterior cortex, with the centre of the circle superimposed on the circumference of the cranial circle. The longitudinal axis is defined as the line joining the centres of these two circles (Fig. 17.28a).

Once the longitudinal axis has been defined, the sagittal images corresponding to the mid point of the medial and lateral tibial plateaus are chosen. The longitudinal axis defined above is then superimposed on these images and a reference line is drawn at a right angle to the longitudinal axis. The medial TPA is measured between the orthogonal reference line and a tangent connecting the uppermost anterior and posterior cortical edges of the medial tibial plateau. The lateral TPA is measured between the orthogonal reference
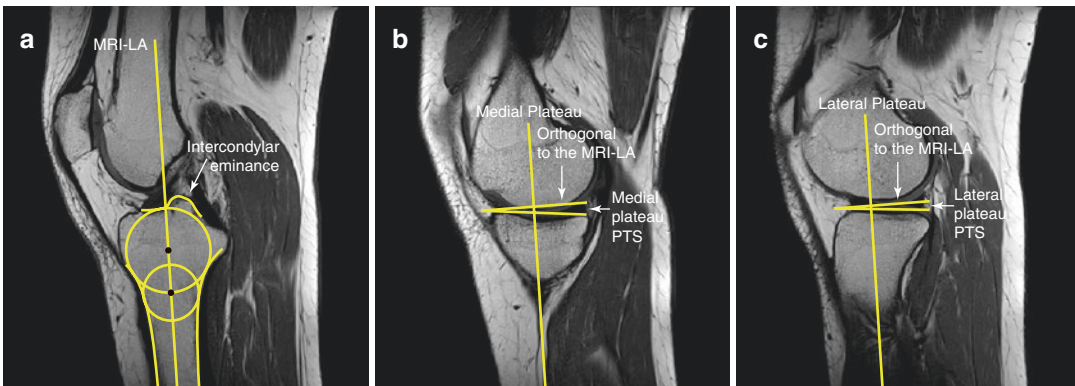
Fig. 17.28 Measurement of the tibial plateau angle using MRI technique. (**a**) Central sagittal slice showing the two superimposed circles and the longitudinal axis of the tibia. (**b**) Centre of the medial tibial plateau with depiction of the medial tibial plateau angle. (**c**) Centre of the lateral tibial plateau with depiction of the lateral tibial plateau angle

line and a tangent along the uppermost even part of the plateau (Fig. 17.28b, c).

Values/Reproducibility

The average medial TPA is 4.8° on MRI. Hudek et al. (2009) found that the angle was 3.4° smaller as compared to measurement on lateral radiographs. They computed a predictive equation relating the two measurements: lateral radiographs = MRI * 0.88 + 4.3. There was a good correlation between the two methods (ICC = 0.73). The reproducibility on lateral radiographs was better than for MRI, this was considered to be secondary to the fact that the radiographic method relies on a single image, whereas on MRI, several images are assessed. However, the typical error on MRI was only slightly higher. The mean difference between the medial and lateral TPA was $-0.43 \pm 3.7°$.

In 21 patients, a difference of greater that 5° was observed between the medial and lateral TPA.

Advantages/Disadvantages

In this method, only the proximal tibia is required for defining the longitudinal axis, therefore it can be performed on a routine standard MRI. It allows separate assessment of the tibial plateaus, which is difficult on a lateral radiograph. However, MRI determination of the TPA is more complex and time-consuming. It is not practical to perform this in all cases as a routine, but the technique can be used in patients who have a standard knee MRI for other clinical reasons and also in cases of corrective surgery after malunion of a tibial plateau fracture, reconstruction after tumour resection and in unicondylar knee arthroplasty.

17.14   Upright MRI in Lower Limb Measurements

Early applications of MRI technology to lower limb measurement were done in the supine position. Hinterwimmer et al. (2008) showed that this supine MRI method underestimates limb length and valgus alignment emphasising the requirement for weight bearing solutions. Upright MRI of the lower limb (Liodakis et al. 2011) holds significant promise as a new radiation-free technique for the measurement of the mechanical axis deviation (MAD), hip knee angles (HKA), leg length discrepancy and all the angles needed in frontal plane alignment (as described earlier by Paley) namely mLPFA, mLDFA, mMPTA, mLDTA and JLCA. Comparative studies with the standard full-length radiographs show that upright MRI of the frontal plane angles are precise, reliable and reproducible. There is very good correlation coefficients in the measured angles (except JLCA) along with a very high inter-observer and intra-observer agreement. However the leg length and MAD were significantly underestimated by MRI.

Technique

A whole body upright MRI scanner is required allowing full weight positioning. The scout views are obtained using coronal images of the pelvis/femur (six slices) with a 10 mm thickness. Then axial images of the femoral head and neck are obtained for femoral anteversion along with the knee/ankle torsion measurements based on axial images of the femur and tibia. As the centres of the femoral head, knee and ankle joints are not depicted on a single coronal MR image, multiple images are used and overlapped together using Adobe Photoshop software. In addition computer planning software is also required to calculate the mechanical axis and lower limb alignment.

Advantages/Disadvantages

The ionising radiation free upright MRI technique has the potential to replace both the standard full weight-bearing alignment radiographs and the CT studies currently used for torsion assessment of the long bones. The technique however takes about 30 min to complete with additional post-processing time. In addition the quality of the images is also dependent on the limb length with poor quality images beyond 85 cm. Overall the patient needs to be shorter than 1.75 m to ensure acceptable depiction of the femoral head. Currently this means that the technique is recommended in the paediatric population and those shorter than 1.75 m.

References

Aitken AG, Flodmark O, Newman DE, Kilcoyne RF, Shuman WP, Mack LA (1985) Leg length determination by CT digital radiography. AJR Am J Roentgenol 144(3):613–615

Auerbach JD, Radomisli TE, Simoncini J, Ulin RI (2004) Variability of the metaphyseal-diaphyseal angle in tibia vara: a comparison of two methods. J Pediatr Orthop 24(1):75–78

Boileau P, Bicknell RT, Mazzoleni N, Walch G, Urien JP (2008) CT scan method accurately assesses humeral head retroversion. Clin Orthop Relat Res 466(3):661–669

Bonzar M, Firrell JC, Hainer M, Mah ET, McCabe SJ (1998) Kienböck disease and negative ulnar variance. J Bone Joint Surg Am 80(8):1154–1157

Brouwer RW, Jakma TS, Bierma-Zeinstra SM, Ginai AZ, Verhaar JA (2003) The whole leg radiograph: standing versus supine for determining axial alignment. Acta Orthop Scand 74:565–568

Cerezal L, del Piñal F, Abascal F, García-Valtuille R, Pereda T, Canga A (2002) Imaging findings in ulnar-sided wrist impaction syndromes. Radiographics 22(1):105–121

Chao EY, Neluheni EV, Hsu RW, Paley D (1994) Biomechanics of malalignment. Orthop Clin North Am 25(3):379–386

Cone RO, Danzig L, Resnick D, Goldman AB (1983) The bicipital groove: radiographic, anatomic, and pathologic study. AJR Am J Roentgenol 141(4):781–788

Cooke TD, Sled EA, Scudamore RA (2007) Frontal plane knee alignment: a call for standardized measurement. J Rheumatol 34(9):1796–1801

Crockett HC, Gross LB, Wilk KE, Schwartz ML, Reed J, O'Mara J, Reilly MT, Dugas JR, Meister K, Lyman S, Andrews JR (2002) Osseous adaptation and range of motion at the glenohumeral joint in professional baseball pitchers. Am J Sports Med 30(1):20–26

Dejour H, Bonnin M (1994) Tibial translation after anterior cruciate ligament rupture. Two radiological tests compared. J Bone Joint Surg Br 76(5):745–749

Dodge HS (1972) Displaced supracondylar fractures of the humerus in children--treatment by Dunlop's traction. J Bone Joint Surg Am 54(7):1408–1418

Doran SJ, Charles-Edwards L, Reinsberg SA, Leach MO (2005) A complete distortion correction for MR images: I. Gradient warp correction. Phys Med Biol 50(7):1343–1361

Farin PU, Jaroma H (1996) The bicipital groove of the humerus: sonographic and radiographic correlation. Skelet Radiol 25(3):215–219

Feldman MD, Schoenecker PL (1993) Use of the metaphyseal-diaphyseal angle in the evaluation of bowed legs. J Bone Joint Surg Am 75(11):1602–1609

Foreman KA, Robertson WW Jr (1985) Radiographic measurement of infantile tibia vara. J Pediatr Orthop 5(4):452–455

Green WT, Wyatt GM, Anderson M (1946) Orthoroentgenography as a method of measuring the bones of the lower extremities. J Bone Joint Surg Am 28:60–65

Gross RH (1978) Leg length discrepancy: how much is too much? Orthopedics 1(4):307–310

Helms CA, McCarthy S (1984) CT scanograms for measuring leg length discrepancy. Radiology 151(3):802

Hernandez RJ, Tachdjian MO, Poznanski AK, Dias LS (1981) CT determination of femoral torsion. AJR Am J Roentgenol 137(1):97–101

Hernigou P, Duparc F, Hernigou A (2002) Determining humeral retroversion with computed tomography. J Bone Joint Surg Am 84-A(10):1753–1762

Hinterwimmer S, Graichen H, Vogl TJ, Abolmaali N (2008) An MRI-based technique for assessment of lower extremity deformities- reproducibility, accuracy and clinical applications. Eur Radiol 18:1497–1505

Hudek R, Schmutz S, Regenfelder F, Fuchs B, Koch PP (2009) Novel measurement technique of the tibial slope on conventional MRI. Clin Orthop Relat Res 467(8):2066–2072

Hunter DJ, Wilson DR (2009) Role of alignment and biomechanics in osteoarthritis and implications for imaging. Radiol Clin N Am 47(4):553–566

Hutter CG Jr, Scott W (1949) Tibial torsion. J Bone Joint Surg Am 31A(3):511–518

Imaeda T, Nakamura R, Shionoya K, Makino N (1996) Ulnar impaction syndrome: MR imaging findings. Radiology 201(2):495–500

Jakob RP, Haertel M, Stüssi E (1980) Tibial torsion calculated by computerised tomography and compared to other methods of measurement. J Bone Joint Surg Br 62-B(2):238–242

Jend HH, Heller M, Dallek M, Schoettle H (1981) Measurement of tibial torsion by computer tomography. Acta Radiol Diagn 22(3A):271–276

Keenan WN, Clegg J (1996) Variation of Baumann's angle with age, sex, and side: implications for its use in radiological monitoring of supracondylar fracture of the humerus in children. J Pediatr Orthop 16(1):97–98

Kraus VB, Vail TP, Worrell T, McDaniel G (2005) A comparative assessment of alignment angle of the knee by radiographic and physical examination methods. Arthritis Rheum 52(6):1730–1735

Laasonen EM, Jokio P, Lindholm TS (1984) Tibial torsion measured by computed tomography. Acta Radiol Diagn 25(4):325–329

Lavelle WF, Shovlin J, Drvaric DM (2008) Reliability of the metaphyseal-diaphyseal angle in tibia vara as measured on digital images by pediatric orthopaedic surgeons. J Pediatr Orthop 28(6):695–698

Levine AM, Drennan JC (1982) Physiological bowing and tibia vara. The metaphyseal-diaphyseal angle in the measurement of bowleg deformities. J Bone Joint Surg Am 64(8):1158–1163

Levinsohn EM, Santelli ED (1991) Bicipital groove dysplasia and medial dislocation of the biceps brachii tendon. Skelet Radiol 20(6):419–423

Liodakis E, Kenawey M, Doxastaki I, Krettek C, Haasper C, Hankemeier S (2011) Upright MRI measurement of mechanical axis and frontal plane alignment as a new technique: a comparative study with weight bearing full length radiographs. Skelet Radiol 40:885–889

Matsuda S, Miura H, Nagamine R, Urabe K, Ikenoue T, Okazaki K, Iwamoto Y (1999) Posterior tibial slope in the normal and varus knee. Am J Knee Surg 12(3):165–168

Mechrefe AP, Koh EY, Trafton PG, DiGiovanni CW (2006) Tibial malunion. Foot Ankle Clin 11(1):19–33

Merchant TC, Dietz FR (1989) Long-term follow-up after fractures of the tibial and fibular shafts. J Bone Joint Surg Am 71(4):599–606

Moore TM, Harvey JP Jr (1974) Roentgenographic measurement of tibial-plateau depression due to fracture. J Bone Joint Surg Am 56(1):155–160

Moreland JR, Bassett LW, Hanker GJ (1987) Radiographic analysis of the axial alignment of the lower extremity. J Bone Joint Surg Am 69(5):745–749

Murphy SB (1994) Tibial osteotomy for genu varum. Indications, preoperative planning, and technique. Orthop Clin North Am 25(3):477–482

Murphy SB, Simon SR, Kijewski PK, Wilkinson RH, Griscom NT (1987) Femoral anteversion. J Bone Joint Surg Am 69(8):1169–1176

Osbahr DC, Cannon DL, Speer KP (2002) Retroversion of the humerus in the throwing shoulder of college baseball pitchers. Am J Sports Med 30(3):347–353

Paley D, Maar DC, Herzenberg JE (1994) New concepts in high tibial osteotomy for medial compartment osteoarthritis. Orthop Clin North Am 25(3):483–498

Pfahler M, Branner S, Refior HJ (1999) The role of the bicipital groove in tendopathy of the long biceps tendon. J Shoulder Elb Surg 8(5):419–424

Pieper HG (1998) Humeral torsion in the throwing arm of handball players. Am J Sports Med 26(2):247–253

Puno RM, Vaughan JJ, Stetten ML, Johnson JR (1991) Long-term effects of tibial angular malunion on the knee and ankle joints. J Orthop Trauma 5(3):247–254

Reagan KM, Meister K, Horodyski MB, Werner DW, Carruthers C, Wilk K (2002) Humeral retroversion and its relationship to glenohumeral rotation in the shoulder of college baseball players. Am J Sports Med 30(3):354–360

Sabharwal S, Kumar A (2008) Methods for assessing leg length discrepancy. Clin Orthop Relat Res 466(12):2910–2922

Schneider B, Laubenberger J, Jemlich S, Groene K, Weber HM, Langer M (1997) Measurement of femoral antetorsion and tibial torsion by magnetic resonance imaging. Br J Radiol 70(834):575–579

Schuind FA, Linscheid RL, An KN, Chao EY (1992) A normal data base of posteroanterior roentgenographic measurements of the wrist. J Bone Joint Surg Am 74(9):1418–1429

Silva M, Pandarinath R, Farng E, Park S, Caneda C, Fong YJ, Penman A (2009) Inter- and intra-observer reliability of the Baumann angle of the humerus in children with supracondylar humeral fractures. Int Orthop. [Epub ahead of print]

Staheli LT (1989) Torsion—treatment indications. Clin Orthop Relat Res 247:61–66

Steyers CM, Blair WF (1989) Measuring ulnar variance: a comparison of techniques. J Hand Surg Am 14(4):607–612

Tetsworth K, Paley D (1994) Malalignment and degenerative arthropathy. Orthop Clin North Am 25(3):367–377

Tomczak RJ, Guenther KP, Rieber A, Mergo P, Ros PR, Brambs HJ (1997) MR imaging measurement of the femoral antetorsional angle as a new technique: comparison with CT in children and adults. AJR Am J Roentgenol 168(3):791–794

van der Schoot DK, Den Outer AJ, Bode PJ, Obermann WR, van Vugt AB (1996) Degenerative changes at the knee and ankle related to malunion of tibial fractures. 15-year follow-up of 88 patients. J Bone Joint Surg Br 78(5):722–725

Webb AJ, Sherman FC (1989) Supracondylar fractures of the humerus in children. J Pediatr Orthop 9(3):315–325

Worlock P (1986) Supracondylar fractures of the humerus. Assessment of cubitus varus by the Baumann angle. J Bone Joint Surg Br 68(5):755–757

Wright JG, Treble N, Feinstein AR (1991) Measurement of lower limb alignment using long radiographs. J Bone Joint Surg Br 73:721–723

Part III

Measurements in Disease States

Arthritis

18

Philip James O'Connor, J. Farrant,
Richard Hodgson, Kay-Geert A. Hermann,
Nathalie Boutry, Xavier Demondion, Chadi Khalil,
Anne Cotten, Anne Grethe Jurik,
Christian E. Althoff, Andrea Klauser,
Matthias Bollow, and Andrew J. Grainger

Contents

In this section the imaging modalities developed and validated for the diagnosis and assessment disease activity have been divided into three main sections: rheumatoid arthritis (1), ankylosing spondylitis (2) and osteoarthritis (3).

P. J. O'Connor (✉)
Leeds Teaching Hospitals Trust, The University of Leeds, Leeds, UK
e-mail: Philip.oconnor@nhs.net

J. Farrant
The Royal Free Hospital, London, UK

R. Hodgson
Centre for Imaging Sciences, University of Manchester, Manchester, UK

K.-G. A. Hermann
Musculoskeletal Radiology Section, Arthritis Imaging Research Group, Department of Radiology, Charité University Hospital—Campus Mitte, Berlin, Germany

N. Boutry • C. Khalil • A. Cotten
Department of Musculoskeletal Radiology, Centre Hospitalier Universitaire de Lille, Hôpital Roger Salengro, CHRU de Lille, Lille Cedex, France

X. Demondion
Department of Musculoskeletal Radiology, Centre Hospitalier Universitaire de Lille, Hôpital Roger Salengro, CHRU de Lille, Lille Cedex, France

Department of Anatomy, Faculty of Medicine, Centre Hospitalier Universitaire de Lille, Hôpital Roger Salengro, CHRU de Lille, Lille Cedex, France

A. G. Jurik
Department of Radiology, Aarhus University Hospital, Aarhus, Denmark

Department of Clinical Medicine, Aarhus University, Aarhus, Denmark

C. E. Althoff
Interventional Radiology Section, Charité University Hospital—Campus Mitte, Berlin, Germany

A. Klauser
Department of Radiology, Rheuma- und Sportbildgebung, Medical University Innsbruck, Innsbruck, Austria

M. Bollow
Department of Radiology, Augusta Hospital Bochum, Bochum, Germany

A. J. Grainger
Leeds Teaching Hospitals, Leeds, UK

18.1 Introduction

P. J. O'Connor, Chairman ESSR Arthritis Subcommittee

This section has been prepared by European Society of Musculoskeletal Radiology arthritis subcommittee. This group has extensive experience of arthritis imaging in clinical practice and clinical trials. This is reflected in the depth of practical knowledge in applying imaging scoring systems detailed in this text.

The use of scoring systems in arthritis has been an established part of practice for over 40 years. The oldest systems are based around radiography and have undergone much iteration over their years of development.

Recently there has been a revolution in arthritis therapy with the introduction of a new generation of biologic treatments. These are proving exceptionally effective and have become important in clinical practice. The development and assessment of these expensive therapies have led to increased interest in the scoring of disease

activity using imaging. This mainly applies to proof of concept trials, but as clinicians become increasingly aware of the degree of subclinical disease imaging can demonstrate, it is becoming part of clinical management. The main imaging modalities under development are magnetic resonance and ultrasound visualisation of synovial inflammation, bone marrow oedema and erosion; this section focuses down specifically on these areas.

We aim to describe the use and validity of scoring systems with reference to three main groups of conditions:

- Rheumatoid arthritis
- Spondyloarthropathy
- Osteoarthritis

This does not mean the use of these new imaging techniques is limited to these conditions but simply reflects the weight of published data to date. The group expects the use of these modalities to extend into new rheumatologic areas in time.

18.2 Rheumatoid Arthritis

Philip James O'Connor, J. Farrant, and Richard Hodgson

Rheumatoid arthritis (RA) is an autoimmune multisystem disorder of unknown aetiology. It has an incidence in the community of approximately 1% affecting women more frequently than men. In terms of health economics, it is an important cause of morbidity and mortality.

The defining pathological features of RA are synovitis, bone marrow oedema and bone erosion. Erosions are important in RA diagnosis and their presence is a key indicator of prognosis (Brower 1990). Erosions are common in RA patients (Pierre-Jerome et al. 1997), the majority developing during the first 2 years of the disease (van der Heijde et al. 1995).

MRI and ultrasound allow visualisation of synovitis and erosion with bone marrow oedema visible only on MRI. Radiography mainly assesses bone and joint space change.

Imaging Modalities

Imaging has potential value in the diagnosis of early rheumatoid arthritis.

A study of 50 patients with possible early RA underwent gadolinium (Gd-DTPA)-enhanced MR imaging of both hands. A third more patients were correctly diagnosed using MRI than using the classification tree of the American Rheumatism Association (Sugimoto et al. 2000).

Multiplanar imaging modalities such as ultrasound (US), computed tomography (CT) and MRI have been shown in several studies to demonstrate erosions with greater sensitivity than conventional radiography (CR), particularly in early RA (Wakefield et al. 2000; Alasaarela et al. 1998).

Erosions generally only become visible on conventional radiography (CR) after a substantial amount of bone is destroyed (Cimmino et al. 2000) with one study showing that erosions of the metacarpophalangeal (MCP) joints only became radiographically visible once MRI-estimated bone erosion volumes reached 20–30% of the metacarpal head.

OMERACT (Outcome Measures in Rheumatoid Arthritis Clinical Trials) is an international, multidisciplinary group set up with the aim of standardising techniques, joint pathology definitions and scoring systems for the use of imaging in RA (Conaghan et al. 2001). It determines the validity, reliability and feasibility of each imaging modality leading to a higher degree of international consensus. The group has developed an MRI scoring system for rheumatoid arthritis and is now turning its attention to other areas and disease entities. They are also starting to look at outcome measures using ultrasound. Anatomical coverage of the RA score is currently restricted to the wrists and hands but may provide a basis for a more comprehensive score (Conaghan et al. 2001).

Radiographic Scoring Systems

The traditional signs of RA seen using conventional radiography (CR) such as joint space loss, erosions and subluxations represent changes that occur at a late stage in the disease process by which time the joint is irreparably damaged.

The limitations of CR include its inability to directly visualise key structures such as synovium, cartilage, soft tissue and bone marrow. Furthermore a two-dimensional radiographic representation of three-dimensional (3D) structures obscures changes seen with other modalities (Lassere et al. 2001). CR is cheap and readily available, and although it is a useful tool in monitoring established disease progression, it remains a relatively blunt instrument in early disease. Radiographic scoring systems have been exhaustively assessed and are now have a unique position in imaging outcome measure in rheumatoid arthritis. They have FDA acceptance as an imaging outcome measure in phase three clinical trials and are considered a gold standard assessment for joint damage in long-term longitudinal studies.

Radiographic changes are specific but have low sensitivity to change compared to MR and ultrasound meaning studies need to run for longer periods with more patients to achieve significance. As a result there has been great interest in developing MR and ultrasound scoring systems

for proof of concept clinical trials where shorter study period and smaller patient recruitment time can be significant factor in bringing a product to market more quickly.

It is beyond the remit of this chapter to assess the literature and advantages and disadvantages of plain film scoring systems in detail and the reader is referred to established rheumatology texts and publications for this purpose.

In brief there are numerous approaches to radiographic scoring of disease activity.

Steinbrocker and Kellgren described global assessments of damage, i.e. these scores reflect change in the whole patient. There is general acceptance that there is a degree of heterogeneity in disease progression within rheumatoid. Joints may progress or respond to treatment differently within individual patient, as such a global assessment may not effectively reflect treatment change. As a result radiographic scoring system became more focused on individual joints.

Larsen, Sharp and the simple erosion narrowing score (SENS) described systems involving individual joint assessments.

This includes the Larsen and variants and the Sharp technique and variants ascribe scores for erosion and joint space narrowing separately as the key radiographic features of damage.

These more focused techniques are based on postero-anterior radiographs of the hands and wrists alone for the Sharp and Genant-Sharp scores and hands, wrist and feet for the Sharp-Van der Heidje, SENS and Larson and variants. All techniques are highly specific for RA disease change and demonstrate similar intra- and inter-reader reliability values of above 0.7 and sensitivity to change.

Reading can be performed in single order blinded to patient and sequence, paired but blinded to sequence and paired with known sequence. In the initial validation of scoring systems, it is important that as little bias as possible is introduced into the scoring system assessment, thus single order blinded to the patient, and sequence is required. Once this assessment has been performed, paired scoring can be introduced to improve reproducibility and sensitivity to change (Boini and Guillemin 2001).

Sharp Score and Variants

Original Sharp Score
In 1971 John Sharp proposed a scoring system for the hand and wrist (Sharp et al. 1971). This involved scoring joint space narrowing (JSN) and erosion separately with 29 erosion and 27 JSN sites assessed. Erosion was scored between 0 and 5 (max 290) and JSN 0–4 (max 216). This has undergone many modifications many of which are no longer in use. This section describes only major modifications of note.

Modified Sharp Score
A modification of the Sharp score was proposed in 1985; this is now considered the standard Sharp score (Sharp et al. 1985).

The score includes 17 areas for erosion (5 PIP, 5 MCP, 1st CMC and 6 wrist sites) and 18 areas for JSN.

Each erosion scores one point with a maximum of 5 for each site giving a maximum score of 170.

JSN is scored 1 for focal JSN, 2 for diffuse <50%, 3 for diffuse JSN >50% and 4 for fusion. The maximum JSN score is 144.

Van der Heidje Modified Sharp Score
In 1989 a modification including assessment of the MTP joints of the feet was described (Lassere et al. 1999). Sixteen joints in the hands and wrist and six joints in each foot (5 MTP and the 1st IP) were assessed for erosion and JSN. The scoring is semiquantitative with erosion scored on a 0–5 scale depending on the amount of joint surface involved (5 represents complete collapse). The maximum erosion scores are thus 160 for the hands and wrist and 120 for the feet. JSN is combined with a score for subluxation: 0 = normal, 1 = focal or borderline change, 2 = diffuse <50%, 3 = diffuse >50% or subluxation and 4 = ankylosis. The maximum JSN scores are 120 in the hands and wrists and 48 in the feet.

Genant Modified Sharp Score

In 1998 Genant and coworkers described a modification to the Sharp score (Genant et al. 1998). This changes the scoring increments for erosion and JSN to 0.5 and ascribes a definition for borderline/subtle changes. The areas assessed are unchanged from the modified Sharp.

For erosion 0 = normal, 0.5 = borderline change, 1 = mild definite erosion, 1.5 = mild worse, 2 = moderate, 2.5 = moderate worse, 3 = severe and 3.5 = severe worse. This gives a maximum erosion score of 98. JSN is scored on a 9-point scale: 0 = normal, 0.5 = questionable of subtle change, 1 = mild change, 1.5 = mild worse, 2 = moderate, 2.5 = moderate worse, 3 = severe, 3.5 = severe worse and 4 = ankylosis; the maximum JSN score is 104.

The scores for each hand are then summed and normalised to a 0–100 scale.

Simple Erosion Narrowing Score (SENS)

In 1999 Van der Heijde described the SENS method (van der Heijde et al. 1999). This is simplified method based on the Sharp-Van der Heijde score with the same joints scored. The system simply sums the number of affected joints for JSN and erosion. JSN and erosion are scored in each joint giving a maximum score for each joint of 2; this results in maximum total SENS score of 86.

Larson Scoring and Variants

Original and Modified Larson Scores

In 1974 a scoring system based on a standard film set of the hands, wrist and feet was developed. The film set represents six stages of disease progressing from normality to advanced rheumatoid damage with the reader matching the film being read to the film set.

The system has been modified several times; in the 1977 system, the grading was 0 = normal; 1 = periarticular soft tissue swelling, periarticular osteopaenia; 2 = definite early destruction (erosion, JSN); 3 = moderate destruction; 4 = severe destruction; and 5 = arthritis mutilans. The wrist is considered as one unit with the score weighted

by a factor of 5. Joints assessed that are in each upper limb are 5 DIPs, 4 PIPs, 5 MCPs, wrist and in each foot 5 MTP and the 1st IP. The score ranges from 0 to 250.

Because periarticular osteopaenia is difficult to quantify and highly observer dependant, it is generally excluded from Larson and Larson-based scoring systems.

Ultrasound Scoring Systems

Ultrasound is at an early stage of development as an imaging outcome measure in RA. Many of the studies quoted in the literature have been designed and undertaken by rheumatologists with differing levels of experience of imaging and ultrasound.

Technological developments will also be important in ultrasound of RA. The widespread introduction of 4D ultrasound with mechanical probe movement and eventually high-frequency matrix probes will have a substantial impact on reproducibility and reliability in ultrasound.

US is increasingly being considered to be an extension of the clinical examination and in many centres in Europe and North America is being undertaken by rheumatologists at the time of clinic appointment. This view of ultrasound as an extension of the clinical examination is unfounded. Ultrasound is an imaging modality; it should be treated as such and closely correlated with other imaging modalities and the clinical setting. One of the gravest dangers to the credibility of ultrasound as an assessment of rheumatological disease is failure to coordinate with other imaging modalities. Using ultrasound as a stand-alone technique is difficult; if rheumatology cannot provide this level of detailed correlation, then clinico-radiological conference review is advised in cases where other imaging has been undertaken.

There is little validity data in terms of comparing with histology and MRI, although these data are increasing. There is one concurrent pathology validation (Mcgonagle) though this study was somewhat limited by the small numbers of patients examined. There are several validation papers using MR as a comparator both for

synovitis and erosions. The degree of validation conferred by MR varies widely with a mix of high-field and low-field MR techniques employed. The majority of studies have single observer MR with either all or more often only a portion of the ultrasounded joints examined. The reader must be aware of the nature of the MR validation before accepting the quoted sensitivity and specificities. Reliability data is scarce particularly relating to intra-observer and interma-chine reliability. Longitudinal evidence is also scarce with few blinded studies assessing responsiveness to therapies. There is also little data available on the US appearance of normal joint structures (Wakefield et al. 2005).

Erosion

The OMERACT definition of erosion for US is an intraarticular discontinuity of the bone surface visible in at least two planes (Wakefield et al. 2005).

US scoring systems can be semiquantitative, measuring the number, joint and extent of erosions with a global score of 0–3 or 4. Quantitative assessment allows grading of erosions into grades 1–3 (1; less than 2 mm, 2; 2–4 mm and 3; greater than 4 mm).

US has been shown more sensitive than CR in detection of erosions (Wakefield et al. 2000; Weidekamm et al. 2003). A comparison of US and CR in the detection of erosions in MCP joints found that US detected sixfold more erosions than CR in early disease and 3.4-fold more in late disease (Wakefield et al. 2000). In this study all of the sonographic erosions not seen on radiography corresponded to MRI bone abnormalities, and the Cohen's kappa values for intra- and interobserver reliability of sonography were 0.75 and 0.76, respectively (Wakefield et al. 2000). Another study of 150 small joints and 2 observers (musculoskeletal radiologist and rheumatologist with limited US experience) reports inter-reader ICC value of 0.78 for erosion detection (grade 0–3) which was better than those for US detection of synovitis (Szkudlarek et al. 2003).

The ability of US and MRI to detect bone erosions in early-advanced rheumatoid arthritis has been compared where no erosion was evident on CR (Magnani et al. 2004). A significantly higher number of erosions were detected by US in MCP joints although no significant difference between US and MRI in detecting bone erosion was observed in wrist joints. Ten controls underwent examination of the same joints by US, and none showed bone erosions at US examination. The authors suggest that US is at least as sensitive as MRI in detecting bone erosions in MCP and wrist joints and that it is a useful diagnostic tool for early arthritis and may be utilised in the follow-up of patients with an established diagnosis of RA.

Synovitis

The OMERACT definition of synovitis for US is hypoechogenic thickened intraarticular tissue that is non-displaceable and poorly compressible that may exhibit Doppler signal (Wakefield et al. 2005).

It provides direct visualisation and assessment of synovitis, the primary site of disease in RA. Treatment response or disease activity can be assessed, and US can be used to guide therapy and therapeutic strategy. Real-time dynamic imaging, close clinical correlation and excellent spatial resolution allow symptom-based, anatomical and functional assessment. A good representation of the patient's disease can be achieved by multiple joint assessment during one session, an advantage US has over MRI particularly if contrast-enhanced MRI is to be used.

US can evaluate several features of both intra- and extraarticular disease. The US markers of intraarticular disease are effusion, synovial hypertrophy and vascularity, erosions and proliferative new bone formation. Extraarticular manifestations including tenosynovitis, enthesopathy, tendon rupture and bursae can also be assessed.

Normal synovium is not visualised sonographically. When thickened it appears as intraarticular tissue of variable echogenicity depending on the degree of synovial oedema. Oedematous synovium is of low echogenicity and can even be

anechoic making it difficult to differentiate from effusion. Two techniques can aid the diagnosis; compression will move the fluid but not the synovium, and using colour or power Doppler sonography (PDS) may detect vascular flow in synovitis that will not be seen in fluid.

Since accurate assessment of synovial volume is difficult using ultrasound, many studies have concentrated on the use of Doppler techniques to provide a measure of disease activity by assessing the vascularity of the inflamed synovium. PDS offers greater sensitivity than colour Doppler and has been shown to reliably assess synovial blood flow (Newman et al. 1994; Walther et al. 2001). PD ignores velocity signal but estimates the total strength of signal, it can demonstrate less flow in smaller vessels and there is no aliasing effect as is seen with colour flow. PDS can reliably depict soft tissue hyperaemia associated with tendons and bursae (Newman et al. 1994).

There are several potential pitfalls that the operator should be aware of when applying PDS. PDS findings are influenced by the examiner, the spatial and temporal resolution of the machine and the acoustical conditions involved in image processing. The probe must be used with minimal pressure to avoid compressing vessels, obliterating flow and thereby obtaining false negative results.

Edge artefact is related to strong specular reflectors and appears as steady colour along the rim of cortical bone or tendons. This can make adjustment of the gain setting difficult. The gain threshold should be set so that there is no observed signal in bone (Rubin 1999).

Flash artefact manifests as a colour signal caused by tissue motion. This motion is most commonly seen when there is surrounding hypoechoic effusion and is more of a problem when using PDS than with colour Doppler.

Artefacts may be distinguished from true flow by the stable location of the artefact and absence of pulsation.

PDS with contrast agent Levovist (Schering, Germany) has been shown to be concordant with MRI in all cases (Magarelli et al. 2001). With arthroscopy as reference, contrast-enhanced PDS (CEPDS) was found to be more accurate than

PDS in demonstrating increased synovial vascularity in knees (Fiocco et al. 2003). This study showed that CEPDS offered more reproducible PD signal scores as well as higher sensitivity (80% vs. 30%), but lower specificity (62% vs. 87%). While increasing the sensitivity of PDS, there are considerations such as additional costs, time and invasiveness.

Much of the available data in this field is preliminary, often with lack of consensus regarding standard examination technique or technical parameters. However there are studies that have attempted to quantify synovial inflammation from Doppler imaging. The objective quantification of PD (QPD) signal by counting pixels in a specific area of interest has been used to demonstrate a significant decrease in QPD post-intravenous steroid treatment (Teh et al. 2003).

Spectral Doppler resistive index (RI) aims to provide a more quantitative objective assessment of synovial vascularity although its reproducibility is unknown. The Doppler spectrum of three random synovial arteries was electronically traced in five wrists and the RI calculated. Following injection of intraarticular steroid, the RI increased in four patients consistent with decreased synovial blood flow (Terslev et al. 2003).

US has been compared to the gold standard of microscopic or macroscopic pathological evidence of synovitis (Walther et al. 2001; Fiocco et al. 1996; Schmidt et al. 2000), but studies exist for larger joints rather than smaller joints. Walther et al. (Walther et al. 2001, 2002) have found a close correlation between histological vascularity and semiquantitative grades of PD signal in the synovium in knee joints (*n* = 23) and hip joints (*n* = 24) in patients undergoing arthroplasty for either RA or OA. Both studies showed a highly significant correlation between power Doppler US findings and histopathological findings. B mode US-detected synovial thickness and arthroscopic grade of synovitis in knee joints also show significant correlation (Fiocco et al. 1996).

MRI has been used as a gold standard in many studies evaluating the use of US in synovial assessment as there is much evidence documenting agreement between pathologic and MRI

findings of synovitis (Gaffney et al. 1995; Ostergaard et al. 1997a, 1998; Ostendorf et al. 2001).

Studies comparing US and MRI in RA finger joints have shown a high level of agreement for synovitis, assessed by B mode (Fiocco et al. 1996; Szkudlarek et al. 2004) and particularly PDS (Terslev et al. 2003; Szkudlarek et al. 2001).

A prospective study of 60 patients showed that US was more sensitive than MRI in detecting synovitis, whereas MRI was more sensitive for detection of small erosions (Backhaus et al. 1999). PD signal and early MRI enhancement in rheumatoid MCP joints have been shown to be closely correlated; the sensitivity and specificity of PDS, with MRI as a reference, were 0.89 and 0.98, respectively (Szkudlarek et al. 2001). Both these studies however use only a binary score for assessment of synovitis (present or absent).

Szkudlarek et al. used a semiquantitative volume-based grading of MTP joint synovitis (grades 0–4) to compare B mode US and T1-weighted contrast-enhanced MRI. With MRI considered the reference method, the sensitivity, specificity and accuracy of B mode US for the detection of synovitis were 0.87, 0.74 and 0.79 (Ejbjerg et al. 2004). The authors suggest that the visualised inflammatory changes are similar or identical using both modalities (Szkudlarek et al. 2004).

However the results of the above studies must be treated with caution as few patients are involved in the studies (Szkudlarek et al. 2004, 2001) and there is only a single observer in each resulting in lack of intra-observer agreement values (Szkudlarek et al. 2004, 2001; Backhaus et al. 1999).

The use of US in longitudinal studies has demonstrated changes consistent with treatment response. PD signal and B mode synovial thickness decrease significantly when steroids (Teh et al. 2003; Terslev et al. 2003; Stone et al. 2001) or TNF antagonists (Terslev et al. 2003; Ribbens et al. 2003; Hau et al. 2002) are administered.

Again this evidence is based upon studies that contain relatively few patients and often one observer. One study relied upon subjective visual scale readings of one sonographer (Stone et al. 2001).

Generally weak correlation has demonstrated between US measures, clinical examinations and biochemical markers (Terslev et al. 2003; Ribbens et al. 2003; Hau et al. 2002).

No data regarding smallest detectable difference has been reported with US.

To detect change US must be reproducible, and it can be expected reproducibility will improve with technology developments in 4D ultrasound.

The problems with reproducibility are based on variations between results obtained by different observers and different US machines. The intra- and interobserver variations of US have not been widely tested (Szkudlarek et al. 2003; Ribbens et al. 2003), and the interscanner variation remains untested. Inter-scan variability poses a significant problem. Results for the same patient scanned at different time intervals using a different scanner may not be comparable.

Studies have shown good interobserver agreement on assessment of hand and foot joint synovitis. A four-grade semiquantitative evaluation of synovitis, joint effusion and power Doppler signal by two sonographers revealed ICCs of 0.81, 0.61 and 0.72, respectively, and unweighted kappa estimations of 0.63, 0.48 and 0.55, respectively, showing moderate to good correlation (Szkudlarek et al. 2003).

One study involving RA small joints included both reproducibility and longitudinal data. In this study intra- and interobserver variations on B mode US-determined synovial thickness in wrist, MCP and PIP joints of 11 patients were assessed with intra-observer coefficients of variation of 1.9–2.6% and interobserver coefficients of variation of 10.2–11.0% (Ribbens et al. 2003). Treatment with a TNF antagonist changed the synovial thickness more than the coefficient of variation in most joints, suggesting this measure is sensitive to change in clinically relevant situations (Ribbens et al. 2003).

There is only one study with data on the importance of US findings with respect to later radiographic or functional status (Taylor et al. 2004). This recent randomised controlled trial of TNF antagonist therapy in early RA showed that baseline US-determined synovial thickening and degree of vascularity in the MCP joints correlated with the radiographic joint damage in the following year in the placebo group, but not in the group receiving biological therapy.

The prognostic value of MRI regarding development of erosions is not directly transferable to US. Correlation between US and MRI findings of synovitis has been demonstrated, but several studies have shown that the strongest MRI predictor of future erosive damage is presence of bone marrow oedema (Ostergaard 1999; McGonagle et al. 1999; Conaghan et al. 2003a; McQueen et al. 2003a; Savnik et al. 2002a) not synovitis.

MRI Scoring Systems

Magnetic resonance imaging allows the direct visualisation of many bone and soft tissue changes in rheumatoid arthritis. Synovitis volume, bone marrow oedema and bone erosions are suitable for serial measurement. The OMERACT RAMRIS system is designed to allow straightforward, reproducible scoring of all these features. Alternatively, synovial volumes may be directly and quickly measured using semiautomated techniques. There is the potential for similar systems for measuring erosions. Dynamic contrast-enhanced MRI depends on the rate of enhancement of the synovium after intravenous contrast agent. Measurements depend on the underlying physiology of the inflamed synovium, in particular the vascularity and capillary permeability which are expected to closely mirror inflammatory activity in the joint. Measurements from MRI have been shown to correlate with clinical, laboratory, imaging and histological measures of inflammation, predict erosive progression and respond rapidly to various types of treatment. They are therefore expected to be good measures of disease activity, progression and response to therapy.

MRI has important implications for the diagnosis and correct management of patients with early unclassified polyarthritis. MRI studies of four groups of patients (established RA, early RA, other arthritis and arthralgias) have shown bone marrow oedema was found in 68% of patients with established RA and the number of bones with oedema was significantly higher than in any of the other patient groups (Savnik et al. 2001a). Twenty patients with recent onset knee effusion underwent MRI, and prominent perientheseal bone marrow oedema was a feature in

six out of ten spondyloarthropathy patients but was not found in the RA patients studied (McGonagle et al. 1998).

MRI scans performed at the first presentation of RA, often by the presence of bone marrow oedema or synovitis, can be used to diagnose and predict future radiographic damage, allowing DMARDS to be targeted to patients with aggressive disease (Ostergaard 1999, 2003a; McQueen et al. 2003a, 1998).

Scoring Systems

The Outcome Measures in Rheumatoid Arthritis Clinical Trials (OMERACT) group have devised and tested a rheumatoid arthritis MRI scoring system (RAMRIS) for the wrist and metacarpophalangeal (MCP) joints. This aims to provide a well-defined, reproducible measurement system applicable across different sites (McQueen et al. 2003b). Of the various measurements considered, bone erosions, bone marrow oedema and synovitis volume provided acceptable reproducibility (Lassere et al. 2003).

OMERACT defines a core set of MR sequences (Ostergaard et al. 2003b). T1-weighted images acquired before and after the administration of gadolinium-based, intravenous contrast are required to demonstrate enhancing synovitis. These images are also helpful for identifying cortical defects, a defining characteristic of bone erosions. Erosions must be visible in two planes to meet the RAMRIS criteria, so axial and coronal images are recommended. Small erosions need images from thin slices for reliable visualisation, and the OMERACT studies used slice thickness of 3 mm (Lassere et al. 2003; Conaghan et al. 2003b; Bird et al. 2003a). Bone marrow oedema is best assessed on pre-contrast T2-weighted images, typically in the coronal plane. Figure 18.1 shows examples of synovitis, erosions and marrow oedema on T1-weighted post-contrast and T2-weighted pre-contrast images. Studies looking at low-field (0.2 T) MR systems for OMERACT scoring have shown good correlation with standard field systems (1.5 T) for scoring synovitis and erosions but not marrow oedema (Schirmer et al. 2006; Ejbjerg et al. 2005a). Contrast dose

Fig. 18.1 T2 fat-suppressed axial images of the fingers showing failure of fat suppression in the index and ring fingers. This is characterised by increased signal in the bone marrow and subcutaneous fat that crosses anatomical boundaries

affects the synovitis scores (Eshed et al. 2006), so a standard dose of 0.1 mmol/kg is usually used (Lassere et al. 2003; Conaghan et al. 2003b; Bird et al. 2003a). There is some evidence to suggest that MRI of the feet may be more sensitive to early changes (Ostendorf et al. 2004).

The scores for each of synovitis, bone erosions and bone marrow oedema are made up from the sum of scores from individual joints. Synovitis is scored 0–3 in each of the distal radioulnar, radiocarpal, intercarpal-CMC and second to fifth MCP joints. Bone changes are scored in each of the carpal bones, distal radius, distal ulna and metacarpal bases. Erosions are scored 0–10 and oedema 0–3 as a fraction of the bone involved. Atlases have been produced to standardise scoring and facilitate inter-reader and inter-site comparisons (Conaghan et al. 2005; Ejbjerg et al. 2005b).

The EULAR (European League Against Rheumatism)-OMERACT RA MRI reference imaging atlas is an international reference set of images for bone erosions, bone oedema and synovitis aiming to standardise assessment of the disease and allowing semiquantitative scoring. Coronal and axial pre-contrast images were chosen to grade erosions from 0 to 10 according to the percentage of bone occupied by erosion. T2-weighted fat-saturated or STIR sequence images provided the most sensitive visualisation and scoring for bone oedema (Bird et al. 2005).

Erosions

There is no pathological correlation data available for MRI erosions in rheumatoid. MRI cannot be compared to the previous gold standard for bone erosions CR. CR is an ineffective gold standard as MRI has been found to be more sensitive in the detection of early rheumatoid erosions, and long-term follow-up is ineffective as all patient cohorts are subject to disease-modifying therapy. A study using miniarthroscopy of MCP joints has reported macroscopic evidence of erosive disease that correlated with MR erosions, but only surface areas of the lesions were visible (Ostendorf et al. 2001). Some reassurance comes from the fact that ultrasound (Wakefield et al. 2000) and CT (Perry et al. 2005) reveal the same erosive lesions as MRI.

Comparison with CT gives us some idea of their nature and to what extent they represent cortical and trabecular bone destruction (Alasaarela and McQueen). These studies show that there is 13–23% mismatch between MR erosion and lesions detected with CT. It is accepted that routine imaging using commercially available systems CT is a more reliable imaging modality to assess bone structure. CT is therefore more likely than MR to represent a gold standard in terms of assessing bone destruction in rheumatoid patients. These studies indicate that not all erosions seen at MR represent bone destruction; focal oedema in the cortex and underlying bone, partial voluming, observer error and even normal variation are all possible explanations for these findings.

Several studies have demonstrated superior sensitivity in depiction of erosions on MRI in early disease compared with CR (Foley-Nolan et al. 1991; Jorgensen et al. 1993; Ostergaard et al. 1995; Klarlund et al. 1999, 2000a; Lindegaard et al. 2001) (McQueen et al. 1998; Ostergaard et al. 1999). MRI has the ability to

visualise lesions 6–12 months before they appear on CR (McQueen et al. 1998, 2001). One study revealed carpal erosions on MRI in 45% of RA patients at 4 months from the onset of symptoms, whereas only 15% had erosions on CR (McQueen et al. 1998), rising to 74% at 1 year on MRI and 28.6% on CR (McQueen et al. 1999). Two studies showed that all radiographically detected erosions were present on MRI (Foley-Nolan et al. 1991; Jorgensen et al. 1993). However, this increased sensitivity may be at the cost of reduced specificity in erosion identification. The use of Gd-DTPA and multiplanar imaging to reduce partial volume artefact (McQueen et al. 1998) helps to avoid false positives. Occasionally erosions are detected one CR and not MRI (Klarlund et al. 2000a).

There is conflicting data regarding the progression of MRI-detected erosions to erosions detected by CR. One study shows that only one in four of the MRI erosions progressed to radiographic erosion during the first year of the disease (McQueen et al. 2001), possibly owing to healing or observer error, although radiographic identification of erosions at the wrist is notoriously difficult in early RA (Scott and Farr 1986), to the extent that many sites have been excluded from the van der Heidje modification of the Sharp score. This study also showed that patients with a high total MRI score, including erosion, bone oedema, synovitis and tendonitis scores, were more likely to develop erosions on CR at 2 years (McQueen et al. 2001).

Longitudinal studies demonstrate the persistence and progression of MRI erosions. These studies indicate that MRI erosions are not usually reversible and are present in 95% (McQueen et al. 1999) to 100% (Klarlund et al. 2000a) of those patients that had erosions at baseline. If MRI erosions were absent at baseline and the total MRI score was low, CR erosions were unlikely to develop 1 year later with negative predictive values of 0.91 and 0.92, respectively (McQueen et al. 1999).

The reliability of the OMERACT scoring system has been assessed in several studies. Intra-reader variation is low (interclass correlation coefficient >0.9) (Haavardsholm et al. 2005). The results for inter-reader correlation are less good with substantial variation between studies for synovitis (0.58–0.78), erosions (0.3–0.83) and oedema (0.32–0.95) (Lassere et al. 2003; Conaghan et al. 2003b; Haavardsholm et al. 2005; Ostergaard et al. 2001a). This variation may reflect the different characteristics of the patients groups studied (Conaghan et al. 2003b). There is also controversy over the relative reliability of wrist and MCP scores (Lassere et al. 2003; Conaghan et al. 2003b; Bird et al. 2005). Studies looking at changes in OMERACT scores have shown slightly poorer inter-reader correlation (Conaghan et al. 2003b; Haavardsholm et al. 2005). Smallest detectable differences have been estimated at less than 36% (Conaghan et al. 2003b; Haavardsholm et al. 2005; Ejbjerg et al. 2005c) for all measures, which has been compared favourably with clinical scores (Conaghan et al. 2003b). One should bear in mind though the %SDD quoted relates to the maximum score seen not the mean, this could give the reader a false impression of the modality performance in detecting changes in the average patient.

Several studies have applied the OMERACT scoring system to diagnosis, measurement of disease activity, prognosis and response to treatment. Low-grade changes have occasionally been seen in normal subjects (Ejbjerg et al. 2004). Higher scores for oedema in the MCP joints have been found in rheumatoid arthritis compared to other types of inflammatory arthritis (Solau-Gervais et al. 2006), suggesting a potential use in diagnosis. Synovitis and marrow oedema scores correlate with other measures of inflammation such as ESR, CRP and radiolabelled nanocolloid uptake, while erosion score correlates with ESR (Palosaari et al. 2004). OMERACT scores appear more sensitive to early erosions than plain X-rays (Ejbjerg et al. 2006), but not to long-term progression (Bird et al. 2004). Importantly, synovitis, oedema and erosion scores all predict erosive progression (Ostergaard et al. 2005; Palosaari et al. 2006). In patients receiving anti-TNFα therapy, there was a significant reduction in scores of synovitis (after 3 months) and marrow oedema (after 1 month) with significantly less erosive progression at 1 year (Tam et al. 2006; Quinn et al. 2005).

Bone Erosion Volume

Studies have measured the volume of erosions by expert manual outlining. Post-contrast, T1-weighted images are useful for highlighting defects in the cortical bone necessary to diagnose an erosion (Bird et al. 2003b). They may, however, be insensitive to erosions filled with fibrous tissue (Perry et al. 2005). Erosion volumes are usually measured in the coronal plane (Bird et al. 2003b; Ostrowitzki et al. 2004). Although thin slices are expected to improve accuracy, this has not been clearly demonstrated (Bird et al. 2003a).

Published work suggests reproducibility in the wrist is good, with intra-reader, inter-reader and inter-scan correlation coefficients over 0.9 and good correlation with OMERACT scores (Bird et al. 2005, 2003b). Both volume measurements and OMERACT scores are capable of detecting a similar (20%) change in erosions (Bird et al. 2003b). Interobserver agreement is poorer in the MCP joints, however (Bird et al. 2003a, 2005), with little evidence of benefit from training (Bird et al. 2005) or thinner slices (Bird et al. 2003a). This has been attributed to difficulty in estimating the proximal bone outline prior to erosion (Bird et al. 2005).

Erosion volume has been shown to correlate with the joint alignment and motion score (Bird et al. 2003a).

A semiautomated technique has allowed erosion volume to be calculated after manual outlining of the approximate joint area, using the combination of a T1-weighted spin echo and gradient echo image (Ostrowitzki et al. 2004; Carano et al. 2004). Results have been correlated with erosion scores. A fully automated method has been demonstrated in a rat model of inflammatory arthritis (Leung et al. 2006). The automated and semiautomated methods for determining erosion volume do not distinguish between oedema and erosions (Ostrowitzki et al. 2004; Leung et al. 2006). Little work has been published looking at the independent quantification of bone marrow oedema, despite evidence that this is important in predicting erosive progression (McQueen et al. 2003a; Palosaari et al. 2006).

Thus, there is little evidence of any improvement in accuracy by using volume measurements of erosions over OMERACT scoring, particularly in the MCP joints. Automated and semiautomated scores may, however, provide time-saving advantages and do offer the potential to objectively measures of bone volume loss in the future.

Bone Marrow Oedema

Bone marrow oedema is the term used to describe regions seen within the trabecular bone which have the imaging characteristics of fluid but where the cortex appears intact. It is a common but far from universal feature of rheumatoid arthritis and has been shown in 36–68% of patients with rheumatoid arthritis (McGonagle et al. 1999; McQueen et al. 2003a, 1998; Savnik et al. 2001a; Ostendorf et al. 2004). It appears with high signal intensity on T2-weighted fat-suppressed or STIR images and with low signal intensity on T1-weighted images. The fluidlike signal intensity led to the description of "oedema"; however, these lesions also enhance avidly following intravenous contrast, suggesting they are associated with increased vasculature, consistent with inflammation within the trabecular bone. This is supported by correlative studies with histology which suggest that the marrow oedema corresponds to regions of subchondral inflammation (McQueen and Ostendorf 2006; Jimenez-Boj et al. 2007; McQueen et al. 2007). There is also evidence that marrow oedema correlates with other measures of disease activity, including imaging measurements (MRI synovial volume, synovial vascularity, erosions and bone scintigraphy), clinical scoring (DAS, pain, Ritchie) and laboratory measurements (ESR, CRP, RF, anti-CCP, LLP3, IL6) (McQueen et al. 1998; Palosaari et al. 2004; Tamai et al. 2007, 2006).

RAMRIS includes a system for scoring bone marrow oedema in the wrist and MCP joints. OMERACT define bone marrow oedema as a lesion within the trabecular bone with signal characteristics of increased water content and

poorly defined margins. Such lesions may occur alone or around an erosion or other abnormality. Oedema is scored for each bone or bone area on a scale of 0–3 depending on the proportion of bone involved within 1 cm of the joint line (0: no oedema; 1: 1–33% bone oedematous; 2: 34–66% bone oedematous; 3: 67–100% bone oedematous).

The reliability of the RAMRIS scoring system for bone marrow oedema has been assessed in a number of studies. Intra-reader variation was good with ICCs of 0.82–0.98 (Haavardsholm et al. 2005; Durez et al. 2007). However inter-reader reproducibility was considerably more variable with ICCs of 0.32–0.95 (Lassere et al. 2003; Conaghan et al. 2003b; Haavardsholm et al. 2005; Ostergaard et al. 2001a; McQueen et al. 2007; Durez et al. 2007), perhaps reflecting the differences in the extent of oedema present in the different patient groups studied (Conaghan et al. 2003b). In contrast to other parameters, RAMRIS scoring of oedema appears to be markedly affected by the magnetic field strength, such that inter-reader ICCs are poorer at 0.2 T than 1 T (Bird et al. 2007; Conaghan et al. 2007) due to the poor sensitivity at low field (Ejbjerg et al. 2005a), although there seems little difference between 1.5 and 3 T (Wieners et al. 2007). The smallest detectable change has been estimated at 3.7–9.5 (Conaghan et al. 2003b; Haavardsholm et al. 2005).

There is now a convincing body of evidence that bone marrow oedema is linked to erosive progression on MRI and plain radiographs. Several studies have shown the presence of oedema is linked to the progression of erosive changes. A study of 40 patients with early and established RA showed the presence of bone marrow oedema in the wrist was the strongest predictor of erosive progression on MRI (Savnik et al. 2002a). Follow-up of 42 patients with early RA showed the presence of bone marrow oedema increased the risk of erosive progression on MRI (McQueen et al. 1999). RAMRIS scoring of bone marrow oedema has also been shown to predict bone erosion. A study of 84 patients with early RA was followed up with MRI and plain radiography over 1 year. A RAMRIS bone marrow oedema score of >2 was found to be an independent predictor of MRI or X-ray erosive progression (Haavardsholm et al. 2008). Twenty-seven patients with early RA were followed over 2 years. RAMRIS scoring of marrow oedema was the best predictor of erosive progression shown on MRI (Palosaari et al. 2006). In 31 patients, baseline RAMRIS oedema score was found to be predictive of radiographic erosions after 6 years (McQueen et al. 2003a).

Bone marrow oedema has also been shown to respond to TNF blocking treatment. A group of 20 patients with early RA showed a significant reduction in the RAMRIS oedema score after just 4 weeks of treatment with infliximab. A drop in the synovitis score was not seen until 3 months. A three-arm randomised trial of 44 patients with early RA compared methotrexate alone with methotrexate and intravenous corticosteroid with methotrexate with infliximab. Over 1 year there was a reduction in bone marrow oedema, such that scores were significantly lower in the infliximab group (Durez et al. 2007). A study of five patients receiving etanercept showed a substantial reduction in the bone marrow oedema score over 16 weeks, although this was not significant, most likely due to the small numbers of patients.

There are a number of problems with the RAMRIS system for scoring oedema. It depends on the fraction of bone involved, so the same amount of oedema may score differently depending on its location. Because the scoring system only measures the extent of bone involvement, it may be slow to respond to changes in disease activity. It can only be used in those patients in whom oedema is present. And finally, the scoring system is relatively coarse. A previous 10-scale score for marrow oedema was abandoned due to poor interobserver agreement (Lassere et al. 2003).

Despite these limitations, the RAMRIS system remains the best validated technique for scoring bone oedema and been shown to predict erosive outcome and respond rapidly to treatment.

It compares favourably with synovial volume as a marker for disease activity and has the added advantage of reflecting disease activity within the bone, at the site of erosion. It may therefore be expected to be a good predictor of the effect of treatment on erosive progression, although this has yet to be demonstrated.

Pitfalls in Scoring Erosions and Bone Marrow Oedema

Normal features can also cause confusion, for example, the interosseous ligaments at the wrist and the nutrient foramina of the carpal bones can simulate erosions (McQueen et al. 2005a). Small erosive-like lesions occur in around 2% of metacarpal and wrist bones in normal subjects (Ejbjerg et al. 2004).

Articular ligaments attaching to the MCP joint recesses and carpal ligamentous attachments with adjacent synovial inflammation can mimic erosive change or bone marrow oedema due to partial voluming (McQueen et al. 2005b).

For this reason slice thickness is an important consideration. A slice thickness of 3 mm or less is required to detect fine anatomical detail, but even then small erosions can be missed due to partial volume averaging. There is however a trade-off as thinner slices make reviewing the images more time consuming and the signal-to-noise ratio decreases (McQueen et al. 2005b).

Imaging erosion in joints that have been altered anatomically by the disease process can be difficult to interpret as you are essentially trying to image what is missing.

Patients with progressive disease but a decreasing erosion count is a potential pitfall. For example, a patient can have two erosions affecting a metacarpal head that enlarge and coalesce over the duration of a study. Despite disease progression the erosion count can decrease.

Healing erosions is also problematic in erosion scoring. Erosion visualisation relies on increased signal in adjacent tissues on T2 or T1 post-gadolinium scans to highlight the eroded cortex or subchondral plate. Anti-inflammatory therapy can reduce synovitis and bone oedema and thus decrease erosion conspicuity.

Failure of fat suppression is also a problematic artefact that can mimic bone marrow oedema; failure of the high signal to conform to normal anatomical boundaries is this key to identifying this artefact.

Synovitis

The OMERACT definition of synovitis on MRI is an area in the synovial compartment that shows above normal post-gadolinium enhancement of a thickness greater than the width of the normal synovium (Ostergaard et al. 2003a). Unfortunately no indication of the width of normal synovium is given for those wishing to apply this definition.

MRI plays an important role in the early detection of RA providing simultaneous assessment of osseous (including bone marrow) and soft tissue structures (both intra- and extraarticular) and can differentiate between synovium and cartilage. Thus, it is often considered to be the gold standard for synovial imaging (McQueen et al. 1998; McQueen 2000).

On T1 imaging the intraarticular synovial tissue is of intermediate signal and of high signal on T2 imaging. Pre- and post-intravenous Gd-DTPA T1-weighted imaging is excellent in assessing the synovium, and synovial enhancement allows distinction from fluid.

Inflamed synovium enhances immediately, and Gd-DTPA then diffuses rapidly to the adjacent joint fluid (Winalski et al. 1993; Peterfy et al. 1994a). This causes a blurring of the margins of the synovium which can lead to an overestimation of synovial volume. Early scanning after administering the gadolinium minimises this problem, but there is debate regarding optimal timing for quantification of synovial volume. One study suggests the first few seconds postinjection (Peterfy 2001) and another 5 min (Sugimoto et al. 2000), and a further study states that MR imaging should be performed within the initial 10 min and that small time variations are insignificant (Ostergaard and Klarlund 2001).

Volume of Synovial Proliferation

In an effort to improve on the reproducibility and sensitivity of scoring systems, various techniques have been put forward for the direct measurement of synovial volume (in mm^3).

As with OMERACT scoring, visualisation of the inflamed synovium for volume measurement requires intravenous contrast to reliably exclude other tissues (Savnik et al. 2001b). Higher doses improve synovial conspicuity and slightly increase the measured volume of enhancing tissue (Oliver et al. 1996). Strongly T1-weighted MR sequences optimise contrast between the enhancing synovitis and the surrounding tissues. While the precise protocol affects the delineation of the edges of the synovium, in particular the outer border, this is rarely important unless comparing images acquired with different imaging parameters. The delay between contrast administration and scanning is important as the volume of enhancing synovitis increases initially (see later) before stabilising after about 4 min. After approximately 10 min, contrast reaches the synovial fluid (Ostergaard et al. 2001b), obscuring the synovium/fluid interface. Imaging is therefore best performed between these times. Post-contrast images are the most important, but pre-contrast images (Savnik et al. 2001b; Ostergaard et al. 2001b) or subtraction images (Ostergaard et al. 1996a) can be helpful to confirm enhancement. In the absence of pre-contrast images, fat suppression may be useful (Tam et al. 2006). Images oriented in the axial plane are often the most useful for analysis (Savnik et al. 2001b; Ostergaard et al. 1996a) although coronal sections are sometimes used in the wrist and hand (Zikou et al. 2006). Thin slices are advantageous, particularly at the edges of the synovium, and this can be achieved using 3D sequences (Savnik et al. 2002a; Tan et al. 2003).

The most straightforward technique for measuring synovitis involves a skilled operator outlining the synovial tissue on each slice of a MR dataset. This has been reported in the knee, wrist and hand. Several studies have looked at the reproducibility of such measurements (Ostergaard et al. 1996a, b, 1997b). Intra-observer, interobserver and inter-scan errors were around 5% in the knee (Ostergaard et al. 1996a) and slightly higher in the wrist (Ostergaard et al. 1996b) with combined reproducibility errors of 18% (Ostergaard et al. 1996a). Changes of as little as 20% are detectable in the wrist (Bird et al. 2003b), better than achievable using OMERACT. Correlation between scoring and direct measurement ranged from moderate ($r = 0.7$) (Bird et al. 2003b) to good ($r = 0.88$) (Ostergaard et al. 1996b). In one study synovitis volume measurement was a better predictor of erosive progression than OMERACT score (Ostergaard et al. 1996b).

Outlining the synovitis manually can take 1–2 h per scan (Savnik et al. 2001b, 2002b; Ostergaard 1997). Thresholding in combination with rough manual outlining can substantially reduce analysis times, e.g. to 15 min (Ostergaard 1997). Image intensity thresholds are set as percentage enhancements (Ostergaard and Klarlund 2001; Ostergaard 1997; Creamer et al. 1997), relative to muscle (Tam et al. 2006; Lee et al. 2003) or interactively (Zikou et al. 2006; Argyropoulou et al. 2005). Other similarly enhancing tissues are excluded either by initial approximate outlining of the synovium (Ostergaard 1997; Lee et al. 2003) or removal after thresholding (Zikou et al. 2006; Argyropoulou et al. 2005). Reproducibility of such semiautomated measurements is poorer than manual outlining and is dependent on the threshold chosen, with an increase in overall reproducibility error of at least 6% compared to manual measurement (Ostergaard 1997). This has been attributed to partial volume effects and synovial fluid enhancement, both of which could be minimised with a suitable imaging protocol. Volumes are significantly lower than those measured manually, but correlation is good, particularly in the wrist. Automated identification using the technique of principle component analysis has also been successfully demonstrated (Klarlund et al. 2000b). An alternative approach to reducing imaging times by measuring the thickness of the synovium at four points, rather than the entire area of a slice (Savnik et al.

2002b), was less successful at reducing imaging times (45 min) and correlating with manual measures ($r = 0.7$). Semiautomated methods have been used to show correlations between synovial volume and clinical measures of disease activity (Tam et al. 2006; Zikou et al. 2006; Creamer et al. 1997; Argyropoulou et al. 2005; Palmer et al. 1995) as well as responses to treatment (Tam et al. 2006; Argyropoulou et al. 2005).

Several studies have shown interesting results using measurements of synovial volume. Significant differences have been shown between rheumatoid arthritis patients and normal controls (Ostergaard et al. 1994a) or arthralgia patients (Savnik et al. 2001a), although not between rheumatoid and other inflammatory arthritides (Savnik et al. 2001a). Correlations have been demonstrated with pain (Tam et al. 2006; Palmer et al. 1995), tenderness (Argyropoulou et al. 2005; Palmer et al. 1995), swelling (Zikou et al. 2006; Creamer et al. 1997; Argyropoulou et al. 2005; Palmer et al. 1995) and global clinical scores (Tam et al. 2006; Argyropoulou et al. 2005) as well as with ESR (Zikou et al. 2006) and FDG uptake (Palmer et al. 1995). A dependence on anatomical location has been observed (Tan et al. 2003). Comparison with histology in the knee has shown the volume of synovitis is related to disease activity with correlations with overall histological inflammation, specifically fibrin deposition and cellular infiltration (Ostergaard et al. 1997a). Evidence for synovial volume as a marker for disease progression comes from the correlation between synovial volume and erosive progression (Savnik et al. 2002a; Ostergaard et al. 1999, 2000). Synovial volume has also been shown to change in response to treatment. The decrease in synovial volume after synovectomy correlated with the duration of clinical remission (Ostergaard et al. 2001b). Reduction in the volume of enhancing synovitis has been demonstrated with DMARDS (Ostergaard et al. 2000) including methotrexate (Palmer et al. 1995; Polisson et al. 1995), oral steroids (Palmer et al. 1995) and anti-TNFα therapy (Tam et al. 2006; Argyropoulou et al. 2005). A rapid response has been demonstrated to intraarticular steroids, with a significant decrease in synovial volume after 1 day (Ostergaard et al. 1996a), with longer remission in patients with smaller pretreatment volumes.

Thus, measurements of synovial volume are relatively precise and reproducible and compares favourably with OMERACT scoring. Semiautomated techniques can be performed in acceptable times. Synovial volume correlates with histological markers of inflammation, rapidly demonstrates change with treatment and predicts erosive progression. It is therefore likely to represent a good marker for disease activity.

Dynamic Contrast-Enhanced MRI

Dynamic contrast-enhanced MRI (DCE-MRI) provides measurements which are sensitive to various underlying physiological parameters, including capillary permeability and synovial perfusion. As such it is expected to be a good marker for inflammation in rheumatoid arthritis and to be more responsive to changes in disease activity than simple static volume measurements.

In DCE-MRI, sequential images are acquired in rapid succession, every few seconds, while gadolinium-based contrast agent is administered intravenously. This allows the time course of the synovial enhancement to be determined. Figure 18.2 shows images obtained before and at increasing times after contrast injection, demonstrating rapid enhancement of the inflamed synovium.

Basic Principles
Gadolinium-based contrast agents move from the blood into the extravascular space where they reduce the T1 relaxation time of tissues, increasing the signal intensity on T1-weighted images. The enhancement of a tissue depends on the concentration of gadolinium and the pre-contrast T1. The contrast agent is unable to enter cells. It is initially in the synovial vessels; however, the capillaries in inflamed synovium are relatively permeable, so contrast moves from the plasma to the extravascular, extracellular fluid (ECF) of the synovitis. The net signal enhancement at any time in the synovium is therefore the weighted sum of the enhancement from the gadolinium in the plasma and that in the ECF. The rate at which plasma moves from the vessels to the ECF
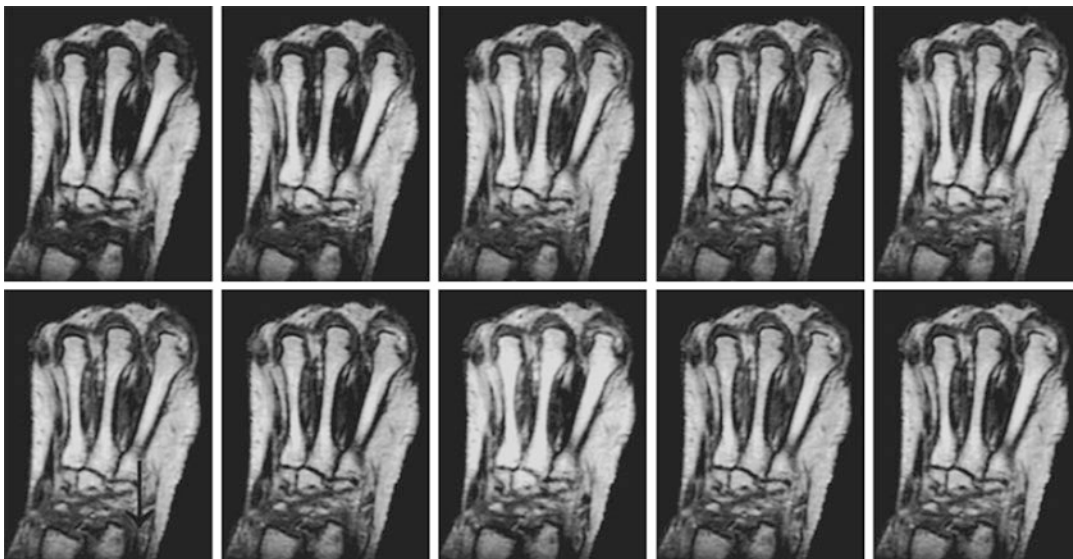
Fig. 18.2 Sections through 3D datasets acquired every 26 s, before during and after intravenous contrast administration

depends on the synovial vascularity (perfusion and capillary surface area) and the capillary permeability. These parameters are difficult to separate, but are expected to be good markers of inflammatory activity.

Typical signal intensity curves from DCE-MRI after IV administration of a bolus of contrast are shown in Fig. 18.3 for arterial plasma and synovium.

In the artery, the initial peak due to the bolus of gadolinium is followed by decay due to mixing, redistribution into the extracellular, extravascular fluid and excretion, with smaller recirculation peaks. In the inflamed synovium, there is an initial steep rise as the high concentration of gadolinium in the vessels. The initial shoulder represents the gadolinium peak in the plasma in the synovial vessels. This is usually relatively small as the synovial plasma volume is much smaller than the synovial ECF volume and in many cases, particularly when the temporal resolution is low, it may be impossible to distinguish. The concentration of gadolinium in the synovitis continues to rise until the fall in the plasma concentration means gadolinium starts to move in the opposite direction, from synovium into blood. Thus, the synovial gadolinium concentration, and hence the signal intensity, reaches a peak sometime after the
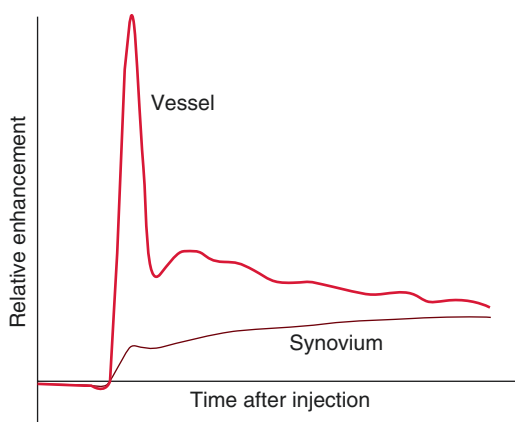
Fig. 18.3 Enhancement in signal intensity after intravenous contrast in vessel and synovium

arterial peak and then decreases slowly in the late phase.

Various measurements have been made from the enhancement curves. These depend to different extents on several underlying parameters, including the volume transfer constant (K^{trans}) which itself depends on the permeability of the capillary walls to gadolinium and the synovial vascularity, the proportion of the synovium occupied by plasma in vessels (v_p) and the proportion of the synovium occupied by ECF (v_e). They also depend to different extents on the bolus of contrast arriving at the synovium which, in turn is affected
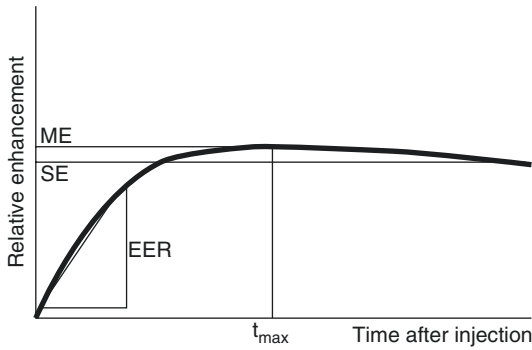
Fig. 18.4 Diagrammatic representation of the early enhancement rate (EER), static or late phase enhancement (SE), maximum enhancement (ME) and time to maximum enhancement (t_{max})

by the injection rate, the cardiac output and local blood flow.

In general, in active rheumatoid arthritis, synovial vascularity and capillary permeability are high. This leads to an increase in the ECF and the synovial volume. The early enhancement rate (EER) is frequently measured in rheumatoid arthritis (see Fig. 18.4). This is very sensitive to K^{trans}. The sensitivity to v_p and v_e depends on the duration the early enhancement rate is measured over; the shorter the time the stronger the dependence on v_p and the weaker the dependence on v_e.

The maximum enhancement of the synovitis depends on both K^{trans} and v_e, and to a lesser extent on v_p. It is also sensitive to the arterial contrast profile. The time to maximum enhancement is shortened by high values of K^{trans} and v_p but lengthened by v_e; it therefore tends to be erratic and is not expected to be a good measure of disease activity. The late phase or static phase enhancement corresponds to the enhancement measured using conventional (non-dynamic) contrast-enhanced MRI. This depends primarily on v_e, is less sensitive to K^{trans} and is insensitive to v_p. However it has the advantage of being insensitive to the arterial contrast profile and hence the injection rate of the gadolinium. Several studies have attempted pharmacokinetic modelling of the enhancement curves to explicitly determine the underlying parameters (Hodgson et al. 2007; Tofts et al. 2007; Workie and Dardzinski 2005;

Kirkhus et al. 2006; Workie et al. 2004; Zierhut et al. 2007).

Dynamic contrast-enhanced MRI is technically demanding, for several reasons. Because the synovium surrounds the joint, having a high surface area to volume ratio, segmentation is much more challenging than for an approximately spherical structure, such as a tumour. Accurate segmentation to separate the synovium from surrounding tissues therefore requires high spatial resolution in all three dimensions. In addition, high temporal resolution is also required to accurately define the initial rise in the early enhancement rate. These conflicting demands place significant technical demands on the imaging apparatus and protocols. In order to achieve strongly T1-weighted images with high spatial and temporal resolution, almost all studies have used gradient echo imaging sequences such as FLASH or SPGR. However, a wide range of imaging parameters have been used depending on system capabilities, the joint being imaged and the trade-off between spatial and temporal resolution. Despite the technical challenges, clinical studies have been performed at field strengths between 0.2 and 3 T (Palosaari et al. 2004; Hodgson et al. 2006; Cimmino et al. 2003). High field systems have the advantages of inherently better signal-to-noise ratios and improved T1 contrast. Several joints have been studied including the wrist (Cimmino et al. 2005; Huang et al. 2000; Lee et al. 1997), metacarpo-phalangeal joints (Szkudlarek et al. 2003, 2001; Tan et al. 2003), knee (Ostergaard et al. 1994b, 1996c; Reece et al. 2002) and shoulder (Hermann et al. 2003). Imaging of the knee has the advantage that larger volumes of synovitis are generally available for analysis. In the wrist synovial volumes are often smaller and the topology of the multiple joints is more irregular making segmentation more difficult. The resolution achievable depends on the joint being studied. In the majority of cases 2D multislice imaging sequences have been used in order to rapidly cover the joint. These have allowed images to be acquired with a temporal resolution as low as 6 s (Oliver et al. 1996; Tan et al. 2003; Kalden-Nemeth et al. 1997; Rhodes et al. 2004; Veale et al. 1999). Imaging of a single

slice allows rapid imaging which well characterises the enhancement curve (Rhodes et al. 2004; Veale et al. 1999), however consistent slice positioning is critical to obtaining reproducible results. Multislice imaging allows more extensive sampling of the synovitis, with a trade-off in temporal resolution (Palosaari et al. 2004; Gaffney et al. 1998). The spatial resolution achievable depends on the joint under investigation and slice thicknesses are typically around 5 mm in the knee (Ostergaard et al. 1998; Rhodes et al. 2004; Konig et al. 1990) and 2–3 mm in the hand and wrist (Szkudlarek et al. 2001; Palosaari et al. 2004; Huang et al. 2000) with in-plane resolutions of less than 1 mm². 3D imaging sequences give good T1 contrast and high resolutions in all three planes at the expense of longer imaging times (Palosaari et al. 2004; Palosaari et al. 2006). Recently, 3D FLASH sequences have been used to acquire images with resolutions of less than 1 mm in all three directions with a temporal resolution of 9–13 s (Hodgson et al. 2007; Tofts et al. 2007). Optimum imaging parameters (TR, TE and flip angle) vary according to the system capabilities, resolution and choice of imaging sequence. In general short echo times are advantageous for increasing signal and reducing T2 contrast which opposes the desired T1 contrast, with values used as low as 2 ms (Hodgson et al. 2007). The choice of repetition time is in theory a balance between better temporal resolution at short TR and higher signal-to-noise ratios at longer TR, but in practice is often as short as technically possible. TR values used range from 2 to 270 ms (Hodgson et al. 2007; Hermann et al. 2003), with most around 20–50 ms (Ostergaard et al. 1998, 1994b; Konig et al. 1990), shorter for 3D sequences (Hodgson et al. 2007). Optimum flip angle depends on the TR. Higher flip angles have the advantage of giving signal intensity which depends linearly on gadolinium concentration (Buckley and Parker 2003), however optimum contrast-to-noise is at lower flip angles (Dale et al. 2003). The EER depends linearly on the dose of gadolinium used at lower concentrations leading to improved accuracy at higher doses (Backhaus et al. 2002). However most studies have used standard doses of 0.1 mmol/kg.

Several studies have looked at the reproducibility of dynamic contrast-enhanced MRI data. Intra-reader variation has been measured at 3.9% (Cimmino et al. 2005) with ICC of 0.91–0.99 (Palosaari et al. 2004; Huang et al. 2000; Rhodes et al. 2004; Gaffney et al. 1998). Inter-reader variation of 2.8% (Cimmino et al. 2005) has been reported with ICCs of 0.95–0.96 (Rhodes et al. 2004). Inter-scan variations of 26% (Hodgson et al. 2007) and an ICC of 0.93 have been reported (Gaffney et al. 1998). Combined inter-scan and inter-reader median variation has been measured at 26% (Ostergaard et al. 1996c). These results compare favourably with other imaging measures (Table 18.1).

Dynamic contrast-enhanced MRI has been compared with a number of other markers of disease activity and outcome, including histological, laboratory, clinical and imaging measures.

Table 18.1 Radiological, histological, clinical and laboratory measures which have been shown to correlate with dynamic contrast-enhanced MRI

Correlation with dynamic contrast-enhanced MRI	References
Erosive progression	Palosaari et al. (2006), Huang et al. (2000)
Histological inflammation	Gaffney et al. (1995), Ostergaard et al. (1998), Gaffney et al. (1998), Konig et al. (1990), Tamai et al. (1994)
ESR/CRP	Ostergaard et al. (1998), Palosaari et al. (2004), Huang et al. (2000), Nagele et al. (1993)
Joint swelling	Ostergaard et al. (1994b)
Pain	Ostergaard et al. (1994b), Konig et al. (1990)
DAS, ACR, Paulus clinical scores	Cimmino et al. (2003), Lee et al. (1997), Kalden-Nemeth et al. (1997)
HAQ	Cimmino et al. (2003)
Static MRI	Palosaari et al. (2004), Huang et al. (2000), Hermann et al. (2003), Beckers et al. (2006)
Power Doppler ultrasound	Szkudlarek et al. (2003, 2001)
Scintigraphy	Palosaari et al. (2004)
PET	Beckers et al. (2006)

As previously discussed, erosive progression represents the imaging gold standard for disease progression in rheumatoid arthritis. Two studies have compared dynamic contrast-enhanced MRI of synovitis with erosive progression using the RAMRIS scoring system to assess erosions. One study looked at 42 patients over 1 year (Huang et al. 2000) and the other at 24 patients over 2 years (Palosaari et al. 2006). Both studies showed a correlation between the EER at the start of the study and the increase in RAMRIS score, indicating DCE-MRI of synovitis is a predictor of erosive progression.

Comparisons with histology have shown a link between DCE-MRI and histological measures of inflammation (Gaffney et al. 1995; Ostergaard et al. 1998). The EER correlates well with vascular area and vascular proliferation which is consistent with the expected strong dependence of the early enhancement rate on vascularity (Ostergaard et al. 1998; Gaffney et al. 1998; Konig et al. 1990; Tamai et al. 1994). Cellular infiltration, fibrin deposition and perivascular oedema are also correlated, which may be due to an increase in capillary permeability which would also be reflected in the EER (Ostergaard et al. 1998; Tamai et al. 1994). Fibrosis, however, does not appear to correlate (Ostergaard et al. 1998). These results are therefore consistent with the expected behaviour of the EER and suggest it is likely to be a good marker for acute inflammation and disease activity in rheumatoid arthritis.

Dynamic contrast-enhanced MRI has been linked to clinical pain and joint swelling as well as clinical assessment scores such as the Disease Activity Score (Cimmino et al. 2003), Paulus score (Kalden-Nemeth et al. 1997) and American College of Rheumatology Score (Lee et al. 1997) as well as global outcomes including the Health Assessment Questionnaire (Cimmino et al. 2003). It has also been correlated with joint swelling (Ostergaard et al. 1994b) and pain (Ostergaard et al. 1994b; Konig et al. 1990). Laboratory measures of inflammation including ESR have also been linked (Ostergaard et al. 1998; Palosaari et al. 2004; Huang et al. 2000; Nagele et al. 1993) although this is more contro-

versial (Gaffney et al. 1995; Ostergaard et al. 1996b; Kalden-Nemeth et al. 1997), perhaps suggesting a relatively weak link.

Early enhancement rates have been shown to correlate with other imaging measurements. Correlation with power Doppler ultrasound (Szkudlarek et al. 2003, 2001) and radiolabelled nanocolloid uptake (Palosaari et al. 2004) are consistent with the EER dependence on synovial blood flow and capillary permeability, although Doppler vascularity is limited to assessment of larger vessels than DCE-MRI. Correlations with MR measures of synovial volume (Huang et al. 2000; Beckers et al. 2006) may be due to a number of factors, including increased vascular volume and increased capillary permeability leading to increased extravascular fluid and cells. FDG PET activity also correlates with the RER (Beckers et al. 2006), suggesting a link between enhancement rate and metabolic activity.

Dynamic contrast-enhanced MRI has been used in a number of studies to show a response to various kinds of treatment including steroids, DMARDs and TNF blocking drugs. TNF blocking therapy has been the most extensively investigated. A study of 19 patients looked at the EER and maximum enhancement in the wrist after infliximab. There was a significant reduction after 14 weeks of treatment. The wrist or knee of 19 RA patients were imaged before and 1 month after starting infliximab. Again, a significant reduction in the EER was demonstrated. Two studies have used pharmacokinetic modelling to assess the response to TNF blocking drugs. A study of 12 patients showed a significant reduction in K^{PS} after TNF blocking treatment but not after methotrexate (Gardener et al. 2003). And a study of 11 patients showed reductions in K^{trans} and v_e 2 weeks after starting TNF blocking therapy (Hodgson et al. 2007). Other treatment regimes have also been investigated. A longitudinal study of 15 patients receiving intraarticular steroids looked at the change in EER from 1 day to 6 months after injection (Ostergaard et al. 1996c). This showed a reduction in the EER as soon as 1 week after treatment, the earliest response to therapy that has been demonstrated. A fall in the RER after 1 year of DMARD therapy

was shown in the wrists of 42 patients after 1 year (Huang et al. 2000). A randomised controlled trial of 34 patients with RA looked at the knee before and 4 months after starting treatment. Patients were randomised to receive either leflunomide or methotrexate. There was a significantly greater response in the RER to leflunomide (Reece et al. 2002). A study of a small group of patients showed a fall in enhancement rate 14 months after starting methotrexate and hydroxychloroquine (Lee et al. 1997).

The success of scoring of marrow oedema as a predictor of erosive progression has led to the use of DCE-MRI for assessing bone changes. A study of 25 patients with rheumatoid arthritis showed more extensive changes than were apparent using conventional MRI (Hodgson et al. 2008). It also demonstrated a response to TNFα blocking treatment before any change was apparent in OMERACT scores. This suggests DCE-MRI may have a role in assessing bone changes as well as synovitis.

Dynamic contrast-enhanced MRI has been successfully used in a number of situations that suggest it may make a good surrogate outcome measure. In particular is reproducible, correlates with erosive progression and histological measures of inflammation and responds to treatment. However there remains little information on whether changes in DCE-MRI parameters as a result of treatment accurately predict changes in clinical outcome. For example, it may be possible to reduce synovial inflammation without affecting erosive changes in the bone, although DCE-MRI of bone marrow may overcome this. Given the success of DCE-MRI as a research tool, it is tempting to apply it clinically. TNF blocking drugs are revolutionising the treatment of RA, successfully reducing disease activity in 50–70% of patients (Tam et al. 2006; Buch et al. 2005; Hyrich et al. 2006; van Riel et al. 2006). Many patients who do not respond may improve with another class of TNF blocker. There is therefore a clinical need to determine whether a patient is responding to a particular drug, so expensive, potentially harmful therapy can be discontinued if it is not working and an alternative treatment started. DCE-MRI has been proposed as a means of detecting an early response to treatment (Tam et al. 2006; Quinn et al. 2005; Hodgson et al. 2006). However, it remains to be demonstrated how soon DCE-MRI can show a response after starting therapy, whether the initial response predicts outcome in terms of erosive progression and whether significant responses can be demonstrated in individual patients. It is to be hoped that future studies will help to answer these questions, allowing DCE-MRI to improve the routine clinical care of patients.

In summary, DCE-MRI has been performed using a wide range of equipment. Measurements depend on synovial vascularity and are therefore expected to reflect inflammatory activity. This is supported by good correlation with histological measures of inflammatory activity. DCE-MRI has been shown to predict erosive progression and respond to treatment. It is therefore likely to be a good biomarker of disease activity in rheumatoid arthritis. Its use to date has been largely confined to clinical trials, and its utility in assessing the response of individual patients remains unproven.

Conclusion

MRI and ultrasound are well suited to providing quantitative measures in rheumatoid arthritis because of their ability to visualise bone and soft tissues in three dimensions. The MR OMERACT scoring systems has been well validated and allows straightforward quantitation of bone erosions, bone marrow oedema and synovial volume, all of which predict erosive progression. Synovial volume can be measured directly by manually outlining the inflamed synovium on MR scans, but such measurements are time consuming. Semiautomated techniques have been developed which allow measurement in acceptable times. Such measurements may be more reproducible and sensitive than OMERACT scoring, correlate with histological inflammation and respond quickly to treatment. Currently there is little convincing benefit to direct volume measurement of erosions, but automated techniques under development may allow fast, objective measurements

of bone loss. Finally, the use of dynamic contrast-enhanced MRI provides measurements which reflect the underlying pathophysiology of the inflamed synovium and may provide the most responsive measurements of disease activity. DCE-MRI measurements have also been shown to correlate well with other measures of acute inflammation, predict erosive progression and respond to treatment. However, the value of MRI measurements for defining remission, determining optimal treatment and predicting long-term response to therapy remains to be established.

18.3   Spinal Involvement in Ankylosing Spondylitis: Anatomy, Pathology, Pathogenesis and Imaging

Nathalie Boutry, Xavier Demondion, Chadi Khalil, and Anne Cotten

Introduction

Ankylosing spondylitis (AS) is a chronic inflammatory disease that principally affects the axial skeleton (i.e. the sacroiliac joints and the spine) and also the appendicular skeleton (i.e. the synovial and cartilaginous joints and the entheses) (Resnick and Niwayama 2002; Cotten 2005). Spinal involvement is responsible for chronic inflammatory back pain and stiffness. Typically, symptoms start in the lumbar spine and then spread to the thoracic and cervical regions. During the course of the disease (and ankylosis of the spine joints), clinical manifestations progressively decrease, but patients experience decreased spinal mobility, paravertebral muscle atrophy, accentuated thoracic kyphosis and reduced chest expansion (Resnick and Niwayama 2002).

Modified New York diagnostic criteria for AS (van der Linden et al. 1984) take into account the axial involvement and include clinical (i.e. low back pain lasting for 3 months, limitation of lumbar spine motion, decreased chest expansion) and radiographic (i.e. uni- or bilateral sacroiliitis) findings. Conventional radiography of the pelvis and the spine has been the mainstay for diagnosis of axial involvement, but this modality is insensitive to early bone and joint damage. Until recently, however, the absence of effective treatment to preserve structural integrity limited the need for more sensitive imaging modalities. This situation changed following the introduction of the anti-TNF-α agents that have shown great promise for alleviating inflammatory symptoms of AS and possibly preventing structural changes in the spine. The latter include miscellaneous abnormalities of the vertebrae, discs, posterior joints, ligamentous attachments, paraspinal musculature and atlantoaxial joint. Imaging can also

be useful in the management of patients with established AS, not only in monitoring disease activity but also in detecting complications related to spinal involvement.

Discovertebral Abnormalities

Early radiographic findings typically occur at the thoracolumbar and lumbosacral junctions (and coned views of these areas may be necessary to detect incipient lesions). With progression of the disease, spinal alterations extend to the rest of the thoracolumbar spine and eventually to the cervical spine. Discovertebral abnormalities include Romanus spondylitis, syndesmophytes, endplate erosion and destruction and discal calcifications and ossifications.

Romanus spondylitis—Also called "Romanus lesion", it is an early and distinctive feature of AS, corresponding to osseous erosions along the anterior aspect of the discovertebral junction, at the superior and inferior vertebral corners (Resnick and Niwayama 2002; Cotten 2005). On lateral views, this lesion is responsible for vertebral squaring (i.e. loss of the normal concavity of the anterior vertebral surface) (Fig. 18.5a). Romanus spondylitis (which has become rare nowadays) represents enthesitis at the insertion of the peripheral annulus fibrosus (Sharpey's fibres) (Fig. 18.5b). Reactive sclerosis and bone formation are secondarily responsible for increased radiodensity of the vertebral body corners ("shiny corner" sign) and irregularities of the anterior vertebral surface (Resnick and Niwayama 2002) (Fig. 18.5c). Magnetic resonance imaging (MRI) is superior to conventional radiography in depicting inflammatory changes associated with Romanus spondylitis. These exhibit low signal intensity on T1-weighted sequences and high signal intensity on T2-weighted and gadolinium-enhanced T1-weighted sequences (Jevtic et al. 2000; Levine et al. 2004; Maksymowych and Landewe 2006) (Fig. 18.6a–c). Enhancement is best detected by fat-suppressed gadolinium-enhanced T1-weighted MR images. Signal intensity changes are typically located within bone marrow of the anterior and, to a lesser extent, posterior vertebral body corners, but they may be more extensive (Jevtic et al. 2000; Maksymowych

Fig. 18.5 Romanus spondylitis. Lateral radiograph (**a**) reveals vertebral squaring. *Reprinted with permission from reference (*Cotten 2005*).* Photograph of the discovertebral junction (**b**) shows the peripheral annulus fibrosus *(arrows)* inserting at the vertebral body corners. *af* annulus fibrosus, *ap* annulus pulposus. Lateral radiograph (**c**) demonstrates vertebral squaring associated with sclerosis of the anterior vertebral corners. Note also the apophyseal joint ankylosis
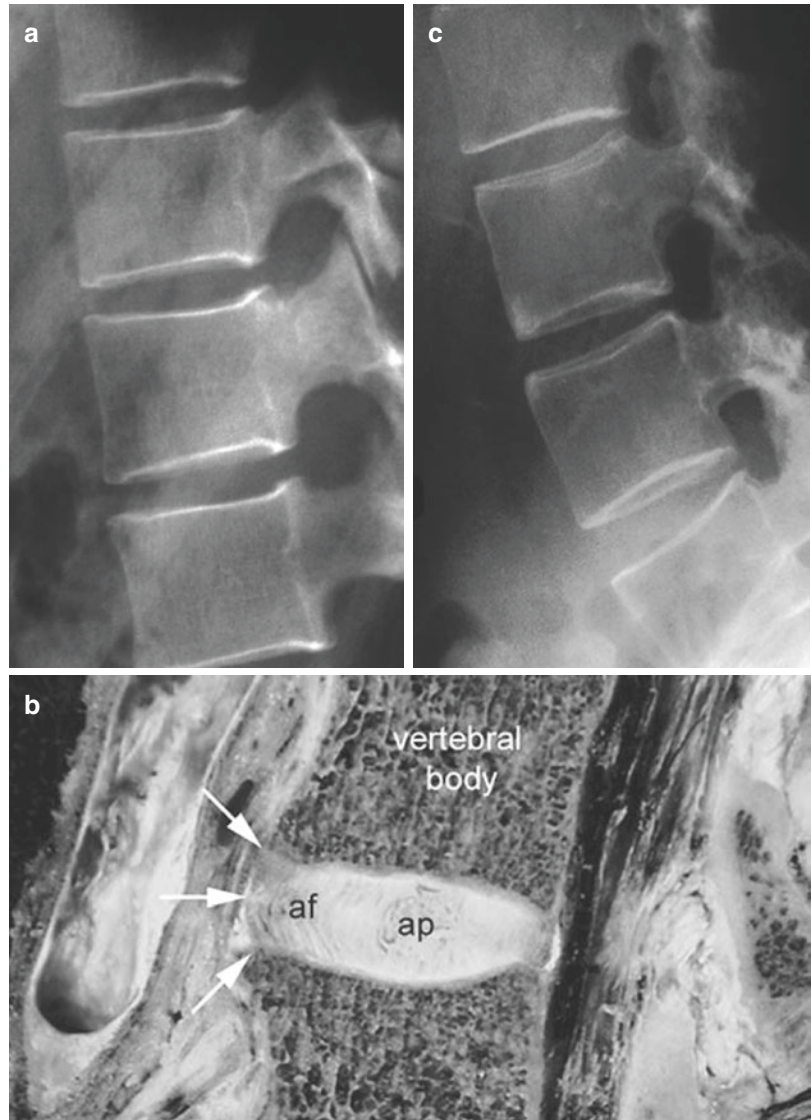
and Landewe 2006) (Fig. 18.6a–c). Histopathologically, such abnormalities reflect interstitial bone marrow oedema and cellular infiltration (Appel et al. 2006). Oedematous and inflammatory MR changes may also be observed in the vicinity of the peripheral annulus fibrosus, along the anterior longitudinal ligament and in the paravertebral connective tissue. These are best demonstrated on fat-suppressed T2-weighted and gadolinium-enhanced T1-weighted MR sequences. Regression of inflammation within vertebral body corners may lead to low signal intensity on all sequences (due to sclerosis) or high signal intensity on T1-weighted sequences (due to fat replacement) (Jevtic et al. 2000) (Fig. 18.7).

Syndesmophytes—They occur during the healing phase of enthesitis and represent gradual ossification of the peripheral annulus fibrosus. Radiographically, syndesmophytes appear as thin vertical outgrowths arising from the vertebral edges, predominantly in anterior and lateral aspects of the spine (Resnick and Niwayama 2002) (Fig. 18.8a, b). Their vertical nature is due
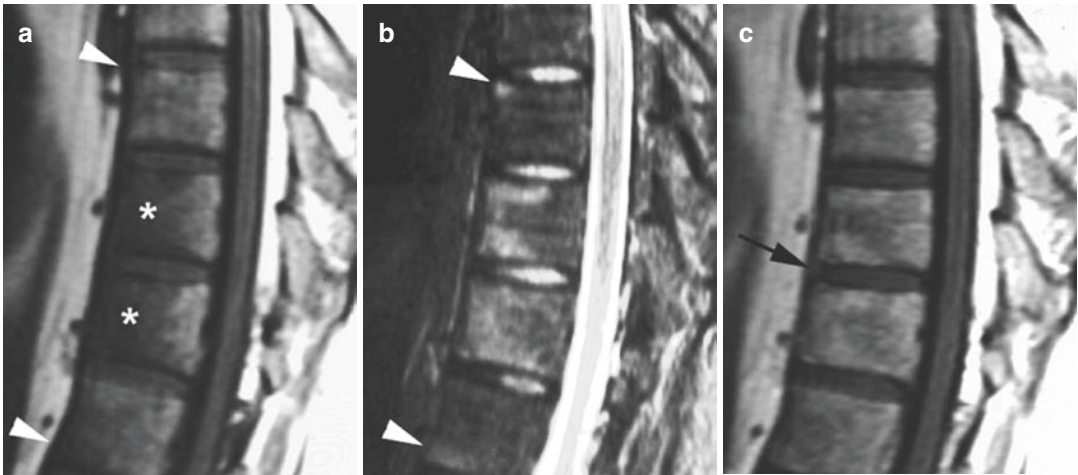
Fig. 18.6 Romanus spondylitis. Sagittal T1-weighted (**a**), fat-suppressed T2-weighted (**b**) and gadolinium-enhanced T1-weighted (**c**) spin echo MR images demonstrate signal intensity changes at the anterior vertebral corners *(arrowheads)* and, more extensively, within vertebral bodies *(asterisks)*. Note also the enhancement within peripheral annulus fibrosus *(arrow)*
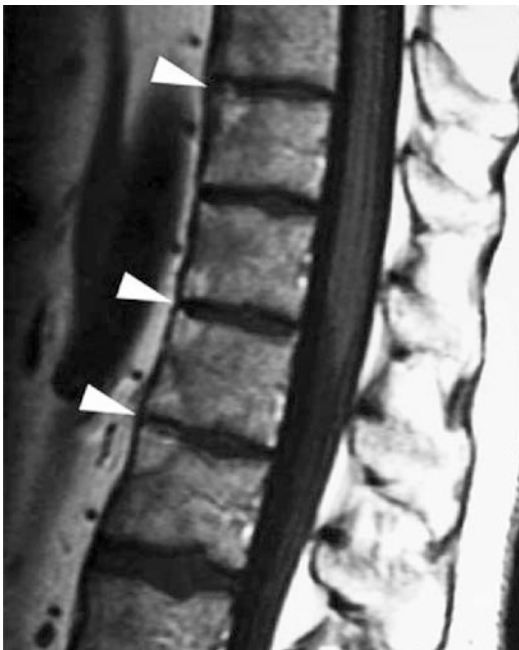
Fig. 18.7 Romanus spondylitis. Sagittal T1-weighted spin echo MR image shows fatty changes within bone marrow of the anterior vertebral body corners at several levels *(arrowheads)*

to apophyseal joint ankylosis that represents an early manifestation of AS (in contrast to paravertebral ossifications as seen in other seronegative spondyloarthropathies that may indicate less involvement of the apophyseal joints) (Resnick and Niwayama 2002). As they enlarge, syndesmophytes extend from one vertebral body to the next, eventually bridging the intervertebral disc space (Resnick and Niwayama 2002) (Fig. 18.8a, b). This may ultimately result in a virtually complete fusion of the thoracolumbar spine ("bamboo spine"). In the later stages of the disease, syndesmophytes may become thicker, extending into the anterior longitudinal ligament, the discs and the adjacent soft tissues. MRI is inferior to conventional radiography in depicting syndesmophytes (Maksymowych and Landewe 2006). It shows high signal intensity on T1-weighted sequences in the anterior part of the intervertebral discs (Jevtic et al. 2000; Levine et al. 2004) (Fig. 18.8c).

Discovertebral erosions and destruction— Also called "Andersson lesions", destructive abnormalities of the discovertebral junction may be seen in early and late phases of AS. Their pathogenesis remains debated (and it is unknown whether inflammatory or traumatic mechanisms contribute to these alterations) (Resnick and Niwayama 2002). Discovertebral lesions have been classified into three types (although other varieties of discovertebral lesions may be encountered in AS) (Resnick and Niwayama 2002;
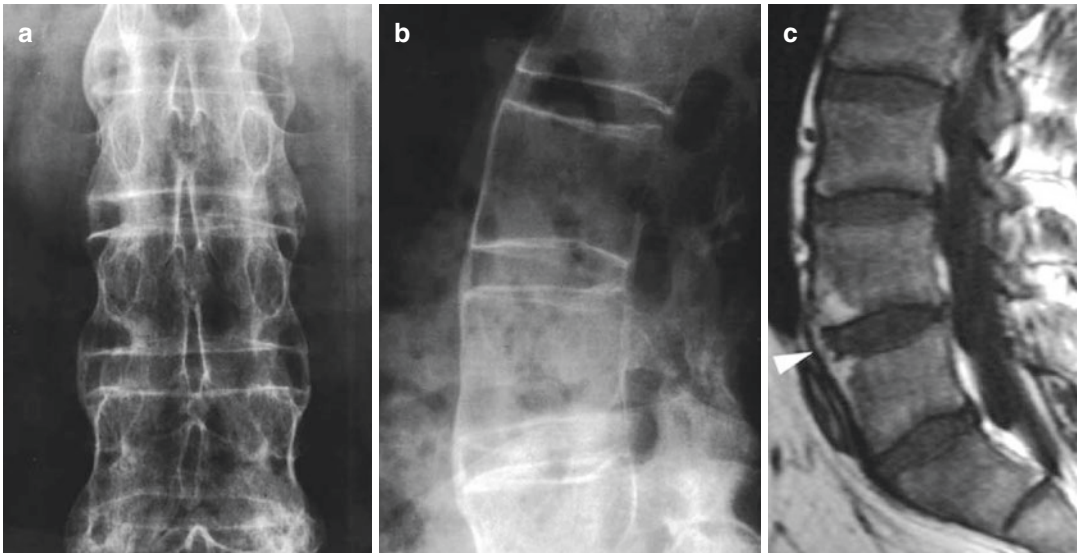
Fig. 18.8 Syndesmophytes. Anterior-posterior (**a**) and lateral (**b**) radiographs reveal typical syndesmophytes. Sagittal T1-weighted spin echo MR image (**c**) shows high signal intensity in the anterior part of the disc *(arrowhead)*. Note also the high signal intensity of the anterior vertebral corners

Cawley et al. 1972). Type I lesions involve the central portion of the discovertebral junction that is covered by the cartilaginous endplate. Such localised lesions reflect intraosseous displacement of disc material (i.e. Schmorl's node formation), presumably because of AS-related osteoporosis and/or repetitive injuries to the discovertebral junction secondary to apophyseal joint abnormalities (Resnick and Niwayama 2002). Radiographically, type I lesions appear as endplate irregularities or small radiolucent areas limited by reactive sclerosis and connected with the intervertebral disc. MRI shows intraosseous disc herniations through focal endplate disruptions (Levine et al. 2004) (Fig. 18.9a–c). Different patterns of signal intensity alterations may be seen within vertebral body marrow close to the endplates, reflecting oedematous, fatty or sclerotic changes (Levine et al. 2004) (Fig. 18.9a–c). Enhancement inside the Schmorl's nodes or the disc may be seen after gadolinium injection (Fig. 18.9c). Type II lesions involve the peripheral portion of the discovertebral junction that is not covered by the cartilaginous endplate. These localised lesions remain unexplained (secondary to enthesitis, Schmorl's node formation or kyphotic disc changes) (Resnick and Niwayama 2002). Radiographically, they appear as irregular anterior or posterior defects with surrounding sclerosis (Resnick and Niwayama 2002), and it may be difficult to differentiate on MRI marrow signal intensity changes associated with type II lesions with those associated with Romanus spondylitis. Type III lesions involve both the central and peripheral portions of the discovertebral junction. Such extensive lesions may be seen early in the disease process (associated with inflammation referred to as "spondylodiscitis") or much more frequently, late in the disease process (associated with improper fracture healing referred to as "pseudarthrosis") (Resnick and Niwayama 2002; Levine et al. 2004). Radiographically, type III lesions are characterised by extensive osseous resorption and sclerosis, whereas MRI shows diffuse endplate destruction, various degrees of oedematous, fatty or sclerotic changes within vertebral bone marrow, focal increased signal on T2-weighted images within intervertebral discs and no evidence of soft tissue mass (Resnick and Niwayama 2002; Levine et al. 2004; Maksymowych and Landewe 2006). In patients
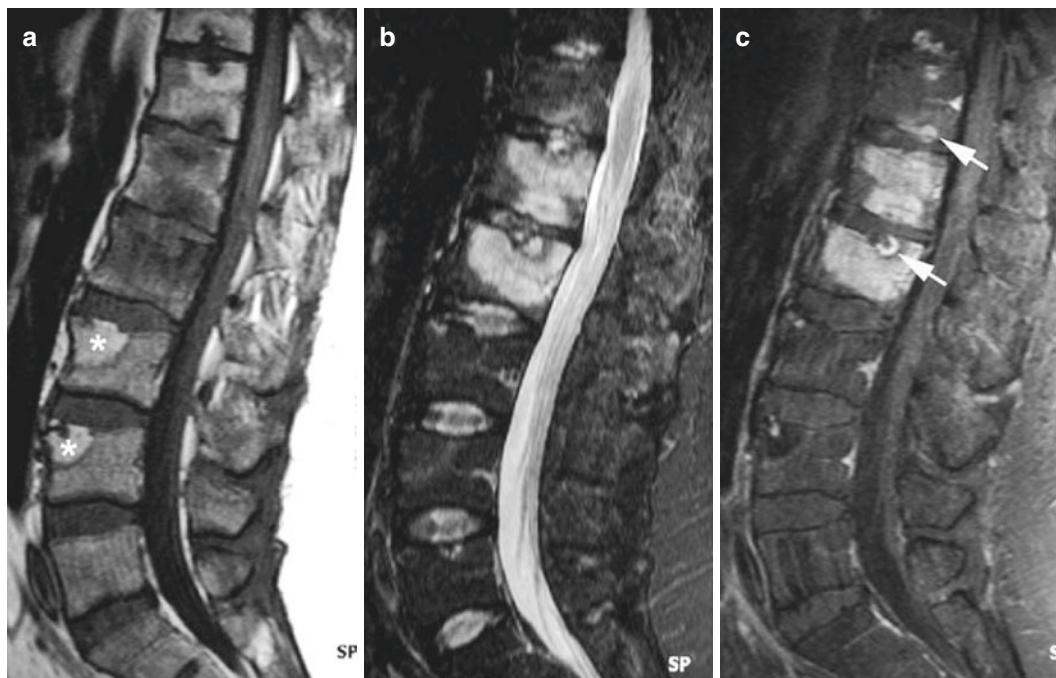
Fig. 18.9 Type I discovertebral lesions (Schmorl's node formation). Sagittal T1-weighted (**a**), fat-suppressed T2-weighted (**b**) and gadolinium-enhanced T1-weighted (**c**) spin echo MR images show signal intensity changes within bone marrow close to the endplates, focal high signal intensity in the disc spaces as well as enhancement inside Schmorl's nodes (*arrows*). Note also the high signal intensity of some anterior vertebral corners *(asterisks)* related to previous spondylitis

with advanced disease (especially with spinal ankylosis), type III lesions usually result from improper fracture healing through the fused posterior elements and the disc (Resnick and Niwayama 2002). In the absence of fracture, however, these alterations may result from abnormal motion in a mobile spinal segment separating two adjacent ankylosed regions (Resnick and Niwayama 2002). Compared to conventional radiography, computed tomography (CT) may be useful to better assess the extent of spinal alterations and the integrity (or not) of posterior elements (Fig. 18.10).

Discal calcifications and ossifications—Patients with ankylosed spine may develop calcifications and/or ossifications within intervertebral discs. On radiographs, these deposits (which are not specific of AS) may be central or eccentric, circular or linear (Resnick and Niwayama 2002). On MRI, calcifications may be observed as foci

Fig. 18.10 Type III discovertebral lesions. Sagittal CT reconstruction reveals extensive discovertebral erosions associated with bone sclerosis. *Reprinted with permission from reference (*Cotten 2005*)*

of low signal intensity on T2-weighted images, whereas ossifications appear as foci of high signal intensity on T1-weighted images (Fig. 18.11).

Fig. 18.12 Posterior joint abnormalities. Transverse CT scan reveals arthritic changes of the right costovertebral joint, ankylosis of the left costovertebral joint and bone sclerosis of the anterior vertebral body related to spondylitis. *Reprinted with permission from reference (*Cotten 2005*)*

Fig. 18.11 Discal ossifications. Sagittal T1-weighted spin echo MR image shows high signal intensity changes within intervertebral discs. Note also the spinal ankylosis. *Reprinted with permission from reference (*Cotten 2005*)*

Posterior Joint Abnormalities

Abnormalities of apophyseal, costovertebral and costotransverse joints are commonly observed in patients with AS. These include erosion of subchondral bone, sclerosis and partial or complete joint ankylosis (Resnick and Niwayama 2002). Inflammatory changes may be more frequent and more prominent in the first and lower costovertebral joints (because ribs articulate only with vertebral bodies and not with intervertebral discs, in contrast to other costovertebral joints) (Ellrodt

et al. 1986; Khanna and Keightley 2005). However, posterior joint abnormalities can be difficult to detect radiographically at the thoracolumbar spine and could require CT to precise bone and joint damage (Fig. 18.12). MRI demonstrates subchondral oedematous and inflammatory bone marrow changes, well-demonstrated on fat-suppressed T2-weighted and gadolinium-enhanced T1-weighted images (Fig. 18.13). Oedema and enhancement may extend to the pedicles and the posterior vertebral bodies (Fig. 18.13). In later stages, joint ankylosis is best seen on T1-weighted images (especially in the transverse plane) and appears as partial or complete obliteration of the articular space. In the thoracic spine, complete ankylosis at the costovertebral joints is responsible for reduced chest expansion, whereas in the cervical spine, similar abnormality of the apophyseal joints may be associated with osseous resorption of the anterior aspect of one or more vertebral bodies (Resnick and Niwayama 2002) (Fig. 18.14). The latter probably results from disuse (Resnick and

Fig. 18.13 Posterior joint abnormalities. Sagittal fat-suppressed gadolinium-enhanced T1-weighted spin echo MR image shows signal intensity changes within bone marrow of the apophyseal joints and adjacent soft tissues. Note also the high signal intensity changes within pedicles and posterior vertebral bodies related to costovertebral joint arthritis (not shown)

Fig. 18.14 Posterior joint abnormalities. Lateral radiograph reveals anterior osseous resorption in the lower cervical region *(arrowheads)*. Note the syndesmophyte formation at multiple levels and apophyseal joint ankylosis. *Reprinted with permission from reference (*Cotten 2005*)*

Niwayama 2002). Besides bone and joint involvement, ossification of the apophyseal joint capsules may also be encountered in patients with AS. When extensive, such ossification creates two lateral vertical radiodense lines on frontal radiographs of the thoracolumbar spine.

Posterior Ligamentous Abnormalities

Lesions of posterior spinal ligaments (i.e. the supraspinous and interspinous ligaments, the ligamenta flava and, to a lesser extent, the posterior longitudinal ligament) are prominent features of AS (Resnick and Niwayama 2002). Initially, MRI is the only modality capable of visualising oedema and inflammation at ligamentous attachments (i.e. enthesitis), especially on fat-suppressed T2-weighted and gadolinium-enhanced T1-weighted sequences (Fig. 18.15). In later stages, ligamentous calcification, ossification and spinous process erosions become evident on plain radiographs. Extensive ossification of supraspinous and interspinous ligaments creates a single central vertical radiodense line on frontal radiographs of the thoracolumbar spine ("dagger" sign). Together with ossification of the apophyseal joint capsules, it appears on frontal radiographs as three vertical radiodense lines ("trolley-back" sign) (Fig. 18.16). On MRI, ligamentous ossifications are visible as thickened ligaments with increased signal on T1-weighted images (which corresponds to bone marrow) (van der Linden et al. 1984). Spinous process erosions may also be encountered (especially in the lower cervical and upper thoracic regions), leading to tapering of spinous processes on lateral radiographs (Resnick and Niwayama 2002).

Fig. 18.15 Posterior ligamentous enthesitis. Sagittal fat-suppressed gadolinium-enhanced T1-weighted spin echo MR image shows inflammatory changes at posterior ligamentous attachments *(arrows)*. Note also the inflammatory changes of the anterior vertebral body corners of C4 and C5 *(arrowheads)*, suggestive of spondylitis

Fig. 18.16 Extensive ossification of posterior ligaments ("trolley-back" sign). The central radiodense line *(arrowheads)* is related to the ossification of supra- and interspinous ligaments ("dagger" sign), whereas the two lateral radiodense lines are related to the ossification of apophyseal joint capsules. *Reprinted with permission from reference (*Cotten 2005*)*

Paraspinal Musculature Involvement

Abnormalities of the paraspinal musculature have been described in patients with AS, contributing to stiffness and weakness (Gordon et al. 1984; Cooper et al. 1991). Atrophy is associated with extensive bony ankylosis of the spine (Gordon et al. 1984). Erector and multifidus spinae muscles are involved, and CT scans demonstrate gross atrophy with replacement of the normal muscle by fat (Gordon et al. 1984)

(Fig. 18.17). However, besides atrophy from disuse (that is observed in long-standing disease), paraspinal muscle fibrosis may be a specific pathological component of early AS (Cooper et al. 1991).

Fig. 18.17 Paraspinal musculature abnormalities. Transverse CT scan reveals replacement of paraspinal musculature by fat *(asterisk)*. Note for comparison the normal appearance of psoas muscles. In this patient with cauda equina syndrome, note also a scalloped erosion of the lamina related to thecal diverticulum *(arrow)*

Atlantoaxial Joint Arthropathy

Atlantoaxial joint arthropathy may also be observed in patients with AS. This finding, which occurs much more frequently in those with rheumatoid arthritis, is associated with inflammatory changes of the synovial and ligamentous structures surrounding the odontoid process (Resnick and Niwayama 2002; Jevtic et al. 2000). Atlantoaxial joint arthropathy results in erosions of the odontoid process, atlantoaxial subluxation and eventually atlantoaxial fusion (Jevtic et al. 2000). MRI may be useful in assessing the degree of periodontoid synovial proliferation (especially after gadolinium injection), delineating the extent of subluxation and detecting abnormalities of the spinal cord.

Complications of Spinal Involvement

Complications related to spinal involvement include vertebral fractures, spinal stenosis and cauda equina syndrome.

Vertebral fractures—Patients with AS are especially susceptible to vertebral fractures, as a consequence of spinal ankylosis and osteoporosis, and a history of trauma is not mandatory (Resnick and Niwayama 2002; Levine et al.

2004). The fracture may involve any segment of the vertebral column, but the lower cervical spine and, to a lesser extent, the thoracolumbar junction are frequently affected (Resnick and Niwayama 2002; Goldberg et al. 1993; Karasick et al. 1995). Cervical spinal fractures usually produce neurologic deficit, but thoracic and lumbar spinal fractures may be unrecognised clinically (and symptoms falsely attributed to AS). These vertebral fractures are unstable, as they involve all three columns of the spine. Radiographic diagnosis is often made difficult by extensive structural changes. However, evidence of type III discovertebral lesions (*see chapter dedicated to discovertebral abnormalities*) associated with adjacent spinal ankylosis may indicate improper fracture healing ("pseudarthrosis") (Fig. 18.18a). Such radiographic finding should incite the physician to perform CT (or MRI) to look for a fracture. In this regard, sagittal CT reconstructions are invaluable for assessing the fracture extent through the posterior elements and/or the vertebral body, whereas MRI is useful in detecting involvement of the disc and ligamentous structures and potential neurologic complications (van der Linden et al. 1984; Goldberg et al. 1993; Karasick et al. 1995; Peh et al. 1993) (Fig. 18.18b).

Spinal stenosis—It may result from ossification of the intervertebral discs, apophyseal joints and posterior ligaments (such as ligamenta flava) or, less frequently, from atlantoaxial subluxation related to joint arthropathy.

Cauda equina syndrome—This syndrome is a recognised although infrequent manifestation of AS. It occurs in patients with long-standing disease and marked spinal ankylosis and may produce insidious symptoms of sensory and/or motor impairment of the lower limbs, saddle anaesthesia and incontinence. Myelographic, CT and MRI findings include widening of the dural sac and multiple thecal diverticula eroding the posterior elements of the lumbosacral spine (Resnick and Niwayama 2002; Schroder et al. 1994; Grosman et al. 1983; Ginsburg et al. 1997; Charlesworth et al. 1996) (Fig. 18.17). Erosions of the posterior vertebral bodies have also been reported (Resnick and Niwayama 2002; Ginsburg et al. 1997). The cause of this cauda equina
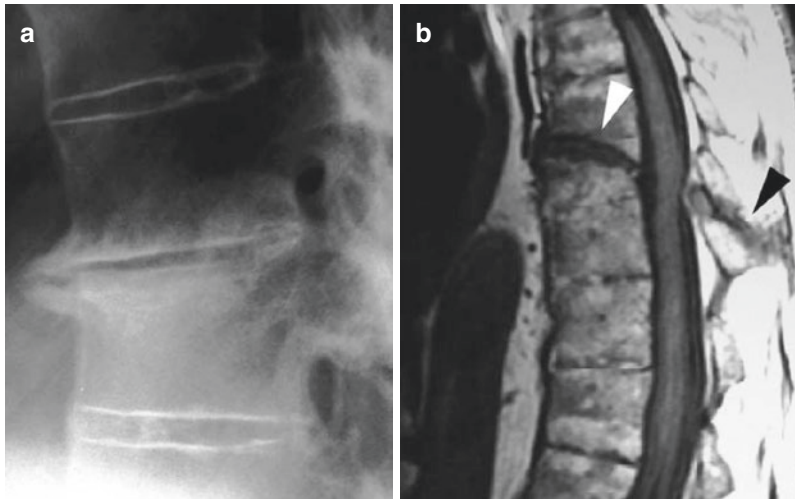
Fig. 18.18 Vertebral fracture. Lateral radiograph (**a**) demonstrates new bone formation indicative of abnormal motion between two ankylosed spinal segments. Six months earlier, a previous radiograph (not shown) showed a transdiscal fracture that had not been diagnosed. Sagittal

T1-weighted spin echo MR image in another patient (**b**) reveals evidence of a horizontal thoracic fracture *(arrow-heads)* through the posterior elements, the posterior vertebral body and the disc T8-T9. *Reprinted with permission from reference (*Cotten 2005*)*

syndrome is obscure but may be due to arachnoiditis (Charlesworth et al. 1996).

Technical Considerations

K.G. Hermann and P. O'Connor

Magnetic resonance imaging of the axial skeleton can be performed at 1.0 or 1.5 T. It is advantageous to use special spinal and body phased-array coils.

An established protocol for spinal imaging comprises a sagittal T1-weighted turbo spin echo sequence and a sagittal fat-saturated T2-weighted turbo spin echo sequence or STIR sequence with high spatial resolution (512 image matrix). STIR sequences and fat-saturated T2-weighted sequences sensitively detect minimal inflammatory increases in fluid. Administration of a paramagnetic contrast agent is helpful for assessing spinal involvement in rheumatoid disease when sagittal T1-weighted sequences with fat saturation and transverse T1-weighted imaging of specific segments are acquired. Coronal images are well suited to identify changes of the lateral edges of the vertebral

bodies, the facet and costotransverse joints and the spinal ligaments. Coronal sequences are not part of the standard MRI protocols because they are not required by any of the current MRI scoring systems.

Imaging in a semi-coronal plane along the long axis of the sacral bone has proven useful for assessing involvement of the sacroiliac joints. Semi-coronal imaging should be supplemented by a sequence in at least one other plane, e.g. a coronal, axial or oblique axial sequence (perpendicular to the oblique coronal plane).

The imaging protocol comprises at least a T1-weighted turbo spin echo sequence and a STIR sequence. This minimal protocol can be supplemented by opposed-phase T2*-weighted sequences, unenhanced T1-weighted sequences with fat saturation and/or contrast-enhanced T1-weighted, fat-saturated sequences. State-of-the-art 3D sequences with slice thicknesses of 1–2 mm improve the detection of erosions compared to conventional turbo spin echo sequences and are similar to computed tomography in the visualisation of erosions. Administration of a paramagnetic contrast medium is recommended for the detection of early sacroiliitis, but this recommendation remains to be corroborated by

studies. A contrast-enhanced dynamic study using a T1-weighted gradient echo sequence in opposed-phase technique provides information on the time course of signal enhancement and allows very sensitive detection of early inflammatory processes (Braun et al. 1994; Bollow et al. 1995, 1998). Dynamic MRI is rarely performed in the routine clinical setting because it is susceptible to false positive results due to inadequate placement of the regions of interest.

Scoring Systems of the Axial Skeleton

Conventional Radiography

Grading of Sacroiliitis
A. G. Jurik

Conventional radiography is an established method for detecting and quantifying the morphological changes of the sacroiliac joints (SIJs) induced by inflammation, but is only able to detect definite joint alterations (Fig. 18.19). It has been widely accepted that radiographic abnormalities of the SIJs are graded according to the New York criteria for sacroiliitis in five stages:

0. Normal
1. Suspicious changes
2. Minimal abnormality in the form of small areas of erosions or sclerosis without alteration in the joint width
3. Unequivocal abnormality—moderate or advanced sacroiliitis consisting of erosions, sclerosis, widening, narrowing and/or partial ankylosis
4. Severe abnormality in the form of total ankylosis (van der Linden et al. 1984)

The inter- and intra-observer variation is, however, considerably for slight changes (Hollingsworth et al. 1983), and training does not seem to improve the ability to analyse radiographs with regard to sacroiliitis (van Tubergen et al. 2003). The New York criteria have been elaborated to grade SIJ involvement in ankylosing spondylitis, but are also used in other forms of spondyloarthropathy although it does not include grading of asymmetrical or unilateral changes.

A grading system taking into account the occurrence of both unilateral and regressive changes has been proposed (Dale 1980), but it has not gained wide clinical acceptance.

Grading of Spinal Changes
K. G. Hermann; C. E. Althoff

Quantification of the radiologically visible changes of the sacroiliac joints is the basis for the diagnosis of AS (van der Linden et al. 1984). However, the changes of the SIJs do not allow sensitive monitoring of the course of the disease. Besides the SIJs, AS commonly involves the spine. Several scoring systems have been proposed for grading spinal manifestations.

Bath Ankylosing Spondylitis Radiological Index
The Bath Ankylosing Spondylitis Radiological Index (**BASRI**) (MacKay et al. 1998) comprises three components: radiographs of the sacroiliac joints that are graded according to the New York criteria (stages 2–4) (van der Linden et al. 1984) and anteroposterior and lateral views of the lumbar spine (score of 0–4) and cervical spine (score of 0–4), resulting in a total score of 2–12. The changes in each region are globally classified as normal, suspicious, moderate or severe (Table 18.2, Fig. 18.20). The BASRI for the spine can be combined with the index for the hip (BASRI-h, score of 0–4) to yield the combined BASRI-t (MacKay et al. 2000) (total score of 2–16).

Stokes Ankylosing Spondylitis Spine Score
The Stokes Ankylosing Spondylitis Spine Score (**SASSS**) is a more detailed scoring system that uses lateral views of the lumbar spine with evaluation of the anterior and posterior vertebral edges (Taylor et al. 1991; Averns et al. 1996). Each vertebral edge from the inferior endplate of T12 through L5 is evaluated for the presence of erosions, sclerosis, squaring, syndesmophytes and total bony bridging (score of 0–72) (Table 18.3).
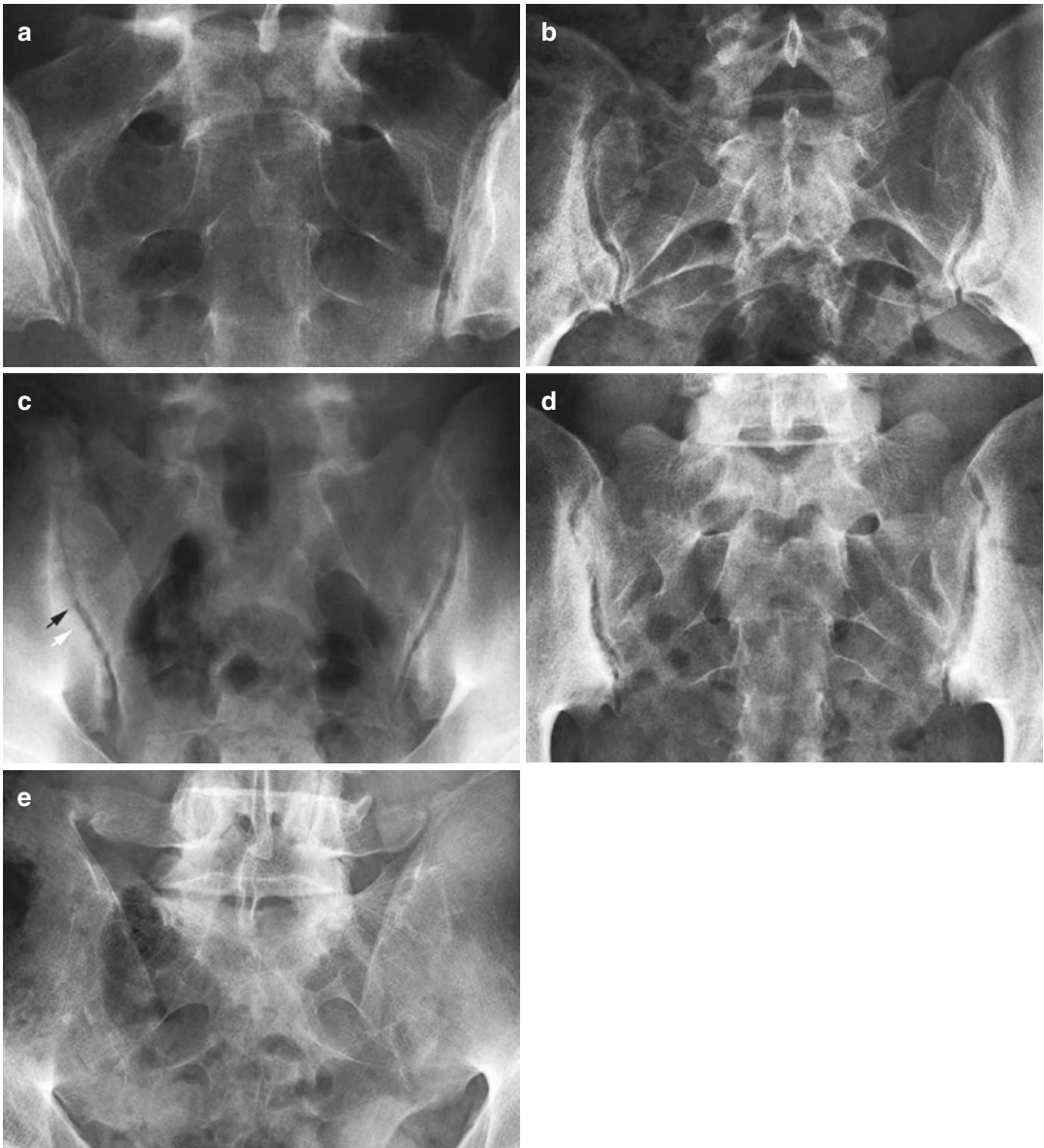
Fig. 18.19 The five grades of sacroiliitis according to New York criteria. (**a**) Grade 0 = normal joints; (**b**) grade 1, suspicious changes of the left SIJ in the form of slight irregularity of the joint facets (24-year-old man); (**c**) grade 2, minimal abnormality in the form of small areas of erosions (*black arrow*) and sclerosis (*white arrow*) without alteration in the joint width (28-year-old man); (**d**) grade 3 changes in the form of moderate erosion with subchondral sclerosis and focal joint space widening (25-year-old woman); and (**e**) grade 4 with homogeneous joint ankylosis including ankylosis corresponding to the ligamentous structures (48-year-old man)

Modified Stokes Ankylosing Spondylitis Spine Score

The modified SASSS (**mSASSS**) according to Creemers et al. (2005) also grades changes of the cervical spine (analysis extends from the inferior endplate of C2 to the superior endplate of T1) while excluding the posterior edges of the lumbar vertebral bodies (score of 0–72 as with the SASSS).

Discussion

The mSASSS seems to be most suitable for use in clinical trials. It is the most reliable of the three

Table 18.2 Bath Ankylosing Spondylitis Radiological Index (BASRI) for the spine

0	Normal	No lesions
1	Suspicious	No definite change
2	Mild	Any number of erosions, squaring or sclerosis, with or without syndesmophytes, on ≤2 vertebrae
3	Moderate	Syndesmophytes on ≥3 vertebrae, with or without fusion involving 2 vertebrae
4	Severe	Fusion involving ≥3 vertebrae

Adapted from (MacKay et al. 1998)
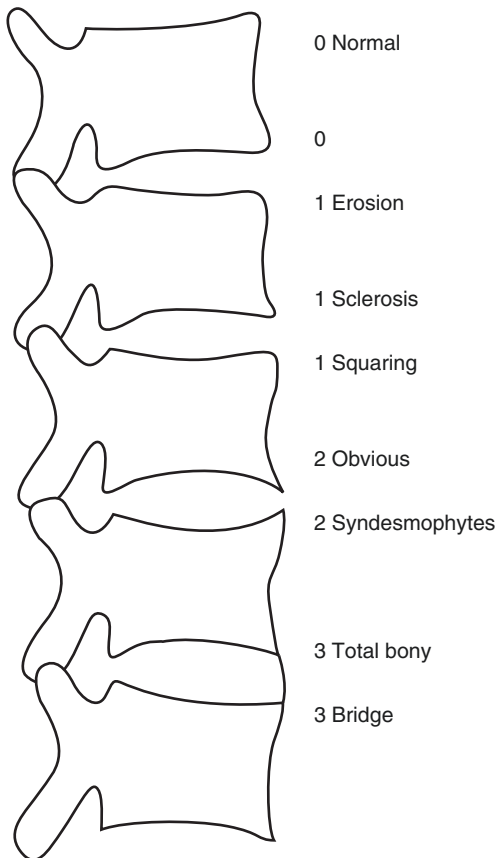
Fig. 18.20 Bath Ankylosing Spondylitis Radiological Index (BASRI). Schematic drawing of lateral lumbar X-ray scoring. Adapted from Taylor et al. (1991)

scoring systems and is most sensitive to changes (Wanders et al. 2004). The mSASSS includes the cervical and lumbar spine, while there is only little loss of information compared with the SASSS. The mSASSS shows significant changes

Table 18.3 Stokes Ankylosing Spondylitis Spine Score[a]

0	Normal
1	Erosions, sclerosis or squaring
2	Syndesmophyte
3	Total bony bridging

[a]Score assigned to each vertebral edge

already after 12 months, while the BASRI does not show changes until after 24 months (Wanders et al. 2004). However, assessment using the mSASSS takes much longer, which is a drawback under routine conditions. Grading of the sacroiliac joints and hips using the BASRI is not suitable to monitor the course of disease over time. There are many patients with severe disease without hip involvement. It is important to include the cervical and lumbar spine, as with the BASRI and mSASSS, since nearly 10% of patients have involvement of the cervical spine, while the lumbar spine is not affected. This is why the SASSS appears to be unsuitable. All currently available scoring systems exclude the thoracic spine due to technical limitations resulting from superimposition of the ribs. However, recent scientific evidence suggests that the thoracic spine is the most frequent site of spinal involvement. Therefore, it is desirable to develop suitable protocols using other imaging modalities such as MRI (Braun et al. 2004). The above-described radiological scoring systems have their place in the long-term follow-up of chronic changes and have mainly been used in studies. Further experience is necessary to precisely define their role in the routine clinical setting.

Magnetic Resonance Imaging

Introduction
K. G. Hermann

Various scoring systems have been proposed to quantify the typical acute and chronic MRI changes of the sacroiliac joints and spine and thus enable robust and sensitive monitoring of the course of disease under treatment. The ASAS group (ASAS Website 2007) and OMERACT conferences (OMERACT Website 2007) have started to evaluate the scores (van der Heijde

et al. 2005). Six scores have been proposed to grade acute inflammatory changes of the SIJs:

1. Leeds score (Marzo-Ortega et al. 2001)
2. MISS score (MR Imaging of Seronegative Spondyloarthropathies) (Marzo-Ortega et al. 2002)
3. Aarhus score (Puhakka et al. 2003)
4. Hermann/Bollow SIJ score (Hermann et al. 2004)
5. Rudwaleit/Sieper SIJ score (Rudwaleit et al. 2005)
6. SPARCC SIJ index (Spondyloarthritis Research Consortium of Canada) (Maksymowych et al. 2005a)

Four different scoring systems have been developed for classifying spinal changes:

1. Leeds score (Marzo-Ortega et al. 2001)
2. ASpiMRI score (Braun et al. 2003)
3. Berlin score (modification of the ASpiMRI) (Baraliakos et al. 2005a)
4. SPARCC MRI spinal inflammation index (Maksymowych et al. 2005b)

Some of these scores were not further advocated for use in studies after having been published. This applies to the Leeds score, the MISS score and the Rudwaleit/Sieper SIJ score. Briefly, the Leeds score only grades changes of the lumbar spine and sacroiliac joints but includes acute lesions of the posterior spinal elements and chronic SIJ lesions. Scores are assigned on the basis of lesion counts in the different regions. When the score is used for follow-up, MR images obtained at two different time points are compared in a pairwise fashion and the findings rated as follows: −3, resolution; −2, moderate improvement; −1, mild improvement; 0, no improvement; 1, mild deterioration; 2, moderate deterioration; and 3, severe deterioration (Marzo-Ortega et al. 2001). The MISS initiative created a new score for grading of sacroiliitis. To this end, each SIJ is divided into two halves, and the acute changes of each half are then given an extent score (0–3), an intensity score (0–2) and a global score (0–3). In addition, chronic changes of each half are graded on a scale of 0–4 in accordance with the modified New York criteria (Marzo-Ortega et al. 2002). The Rudwaleit/Sieper SIJ score also divides each joint into two halves. Each half is then graded according to the extent of active inflammatory changes: 0, no changes; 1, osteitis of up to 25% of the area; 2, osteitis of up to 50% of the area; and 3, osteitis of more than 50% of the area (Rudwaleit et al. 2005).

ASspiMRI and Berlin scores
K. G. Hermann

The **A**nkylosing **S**pondylitis **spi**nal **M**agnetic **R**esonance **I**maging (ASspiMRI) score with its modifications is currently the only MRI score that includes the entire spine. It consists of two parts, the ASspiMRI-a for grading acute spinal changes and the ASspiMRI-c for grading chronic spinal changes. Thus, it is also the only MRI scoring system that takes into account chronic changes. The spine is divided into 23 vertebral units (VUs) from C2 to S1, and each VU is assigned a 7-point score from 0 to 6 for acute changes and another for chronic changes (resulting in a total score of 0–138 for acute changes and a second for chronic changes). For the acute score, the size of bone marrow oedema (grades 1–3) and the extent of additional erosions (grades 4–6) are evaluated (Fig. 18.21). Both STIR sequences and contrast-enhanced sequences are used but only one of these is mandatory. Systematic comparison of both sequences has revealed only little differences (Baraliakos et al. 2005b; Hermann et al. 2005a). In addition, T1-weighted sagittal images are obtained for anatomical reference. The ASspiMRI-c score takes into account sclerosis, erosions, syndesmophytes, vertebral deformity (squaring, ton-shaped vertebrae), bridging and fusion (Table 18.4).

Grades 4–6 of the ASspiMRI-a score are assigned on the basis of the size of endplate erosions regardless of the size of surrounding bone marrow oedema. The oedema decreases in size under treatment, while erosions remain unchanged or even increase in size. This is why the score may not adequately reflect the situation

Bone edema

1 Vertebral unit   Grade 1   Grade 2   Grade 3

Erosion

Grade 4   Grade 5   Grade 6
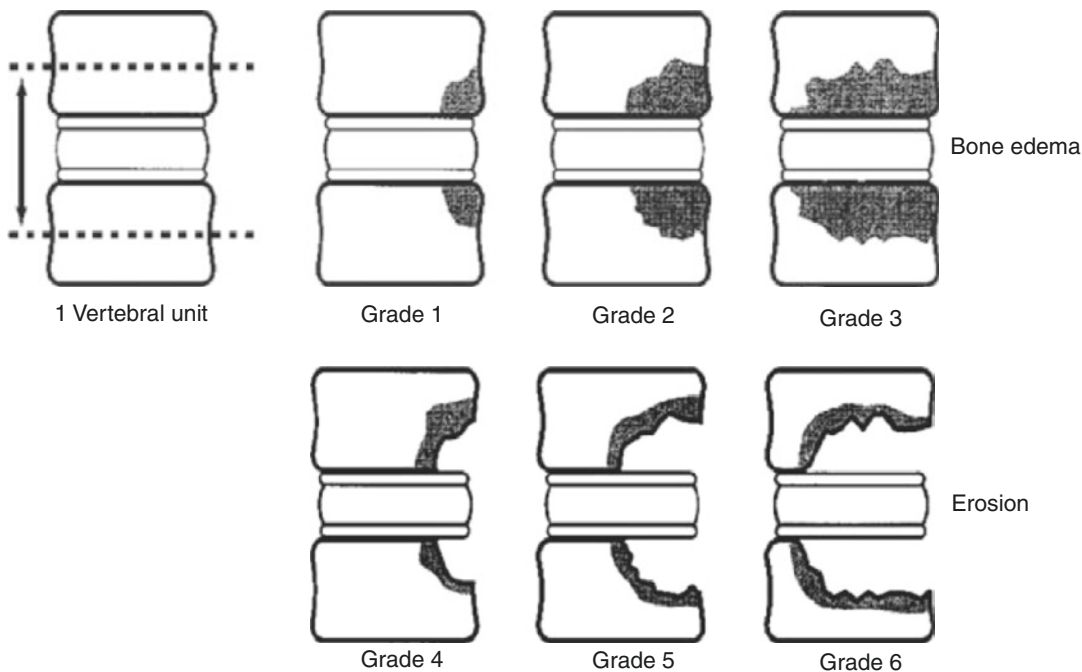
Fig. 18.21 ASspiMRI-a score. Schematic drawing of the vertebral unit and the Ankylosing Spondylitis Spinal Magnetic Resonance Imaging score for acute changes (ASspiMRI-a). With permission from Braun et al. (2003)

Table 18.4 Chronicity score (ASspiMRI-c)

0	Normal, no lesions
1	Minor sclerosis/suspicion of relevant changes
2	Sclerosis/vertebral squaring/ton-shaped vertebrae/possible syndesmophyte
3	1–2 syndesmophytes/minor erosion
4	More than two syndesmophytes/spondylodiscitis/severe erosions
5	Vertebral bridging (<50%)
6	Vertebral fusion (≥50%)

Adapted from (Braun et al. 2003)

in such cases and miss certain therapeutic effects. To overcome this limitation, a modification of the ASspiMRI-a was proposed, referred to as the Berlin score (Baraliakos et al. 2005a). The modified version only takes into account bone marrow oedema and assigns scores of 0–3 for each VU, resulting in a maximum score of 69. Preliminary studies show better inter-reader agreement for the Berlin score.

Lesions of the posterior elements are not taken into account by the two ASspiMRI scores or the Berlin modification of the ASspiMRI-a.

SPARCC Scores
A. Klauser

The scoring method of THE SPONDYLOAR-THRITIS RESEARCH CONSORTIUM OF CANADA (SPARCC) is based on the evaluation of abnormal increased signal on T2-weighted sequences with the use of fat suppression, representing increased concentration of "free water" referred to as "bone marrow oedema" in active inflammatory lesions in both spine and sacroiliac joints. The scoring method described below assumes that images have been acquired according to the MRI acquisition protocol described in this website (MRI of the Spine-SPARCC MRI methodology: http://www.altarheum.com/research.html), summarised as follows:

Imaging Parameters Spine
The total spine is imaged (two segments with slight overlap) including C1–S2 (must include). The protocol includes a T1 SE and short tau inversion recovery (STIR) using 15 slices, in case of scoliosis and to visualise medial aspects of

ribs, 4 mm thick, 10% gap and a FOV 380 mm, adjusted according to magnet specifications.

Imaging Parameters SI Joint

T1 SE and short tau inversion recovery (STIR) sequences are used with 12 slices, 4 mm thick, 10% gap and FOV 250 mm, adjusted according to magnet specifications. It is intentional that the 12-slice protocol does not cover the entire synovial and ligamentous compartments.

Scoring Methodology: Spine

The SPARCC scoring method for the spine is developed to require minimal scan time, no contrast administration, to evaluate the extent of lesions in three-dimensional planes and to limit the evaluation number of vertebral levels. The assessment of disease activity in two-dimensional planes in the spine was evaluated in recent studies and validated for a simplified scoring system (Braun et al. 2003). The SPARCC MRI index relies on scoring lesions in three dimensions, because inflammatory lesions within bone are often asymmetrical and therefore more precisely quantified with a method that systematically assesses lesions in several dimensions. This was assessed in a study of 24-week response of patients with AS randomised to infliximab versus placebo by evaluation of effect size and standardised response mean (Maksymowych et al. 2005b). The conclusion was that SPARCC MRI index has demonstrated to be a feasible, reproducible and responsive index for measuring spinal inflammation in AS. Furthermore it meets the standards of feasibility, truth and discrimination, which have proposed by Outcome Measures in Rheumatology Clinical Trials (OMERACT) (Boers et al. 1998).

Scoring:

1. The scores are dichotomous—present or absent.
2. For scoring purpose the SPARCC methodology uses the discovertebral unit (DVU) accordingly to a previously reported definition (Braun et al. 2003), which describes the DVU as the region between two virtual lines through the middle of each vertebra and includes the intervertebral disc and the adjacent vertebral endplates.
3. Six DVU only are selected for scoring. By using other scoring methods, evaluation of the

vertebral body of all 23 vertebral segments is mandatory necessitating the scoring of regions subject to artefact and/or limited anatomical resolution. However, the median number of affected vertebral segments was typically 5–6 in a severely affected cohort of patients that would be regarded as eligible for trials of anti-TNF therapies. Therefore a method has been proposed that scoring can be limited to a maximum of 6 of the most severely affected levels. The reason for that was a prior study, where the mean number of affected DVU per patient was 3.2 (95% CI, 1.2–5.2) (Maksymowych et al. 2005b). In patients with many affected levels, the less conspicuous lesions are often subtle, and therefore the scoring of these lesions is less responsive to therapy. Furthermore limiting the assessment to only the most severely affected levels improves feasibility in terms of less time necessary for evaluation than for the entire spine. While this approach may introduce measurement error, due to readers differing in their selection of levels for scoring, the alternative—assessment of the entire spine—is subject to further problems: Being forced to score the entire spine will result in the inclusion of less discernable lesions which may reduce sensitivity to change and forces the reader to score levels that are affected by signal artefact. This is not a minor issue as some degree of artefact can occur when scanning the entire spine with large fields of view. It is therefore not surprising that a comparison of the SPARCC scoring method for all 23 DVU versus only the 6 most severely affected DVU shows similar reliability but better responsiveness for the latter approach (Maksymowych et al. 2007).

4. Each DVU is divided into four quadrants, and each vertebral endplate is scored independently for BME: 1 upper anterior endplate, 2 upper posterior endplate, 3 lower anterior endplate and 4 lower posterior endplate. The presence of increased signal in each quadrant is recorded for each of the three sagittal slices. Maximum score is 12 per DVU. Maximum score for six levels = 72 (Fig. 18.22).

The levels are chosen as representing the six most abnormal levels on the STIR sequence.
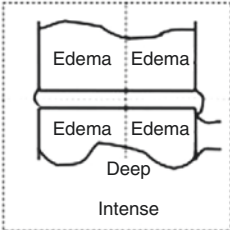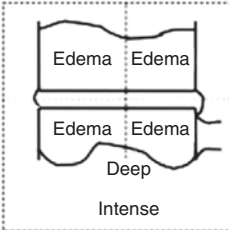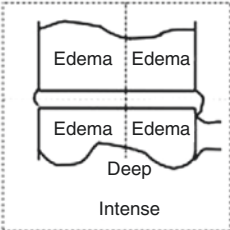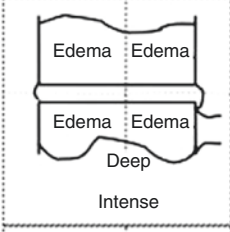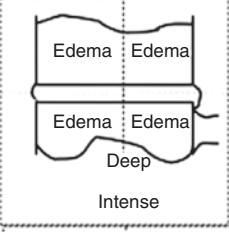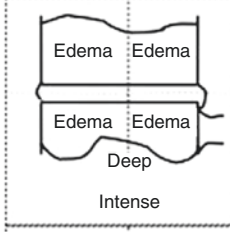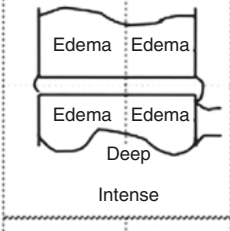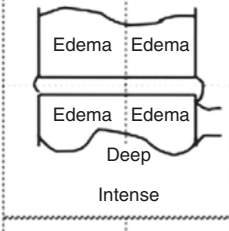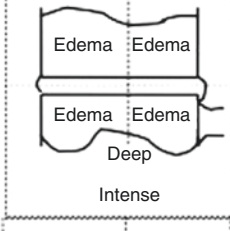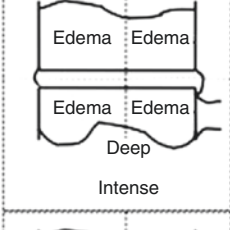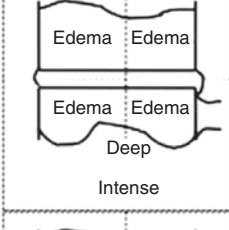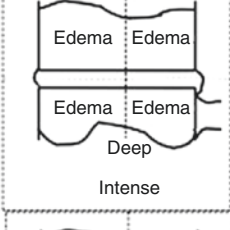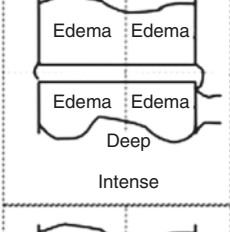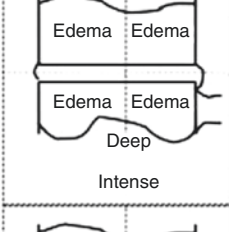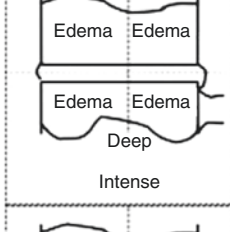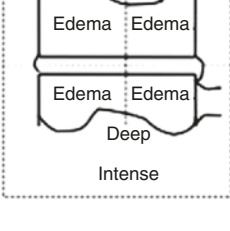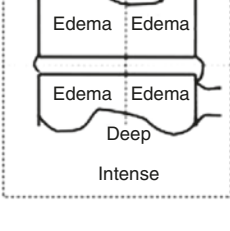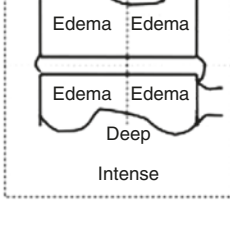
Fig. 18.22 SPARCC spine scoring sheet

Only abnormalities on the STIR sequence are scored. T1 SE images are included for anatomical reference only and are not scored.

5. Scoring of depth and intensity

After selecting levels for each DVU, three consecutive sagittal slices are chosen for scoring at each level representing the most abnormal slices for that level, which allows evaluation of the coronal extent of lesions as well as assessment in the sagittal plane.

On each slice, the presence of a lesion exhibiting intense signal in any quadrant is given an additional score of 1. Similarly, the presence of a lesion exhibiting depth 1 cm in any quadrant is given an additional score of 1. This leads to a maximum additional score of 6 for that level and brings the total score to 18 per DVU:

A score for "intense" may be assigned to each level on each slice. High signal from cerebrospinal fluid acts as a reference for assigning an "intense" reading score to a bone lesion. A score of 1 is assigned if "intense" signal is seen in any quadrant on a single slice, therefore maximum score per slice is 1, per level is 3 and for six levels = 18.

A score for "deep" may be assigned to each level on each slice. A lesion is graded as "deep" if there is homogeneous and unequivocal increase in signal extending over a depth of at least 1 cm from the surface of the endplate. A score of 1 is assigned if "deep" signal is seen in any quadrant on a single slice, therefore maximum score per slice is 1, per level is 3 and for six levels = 18.

In summary, a total maximum score of 108 can be obtained, based on the presence of "bone marrow oedema" (=72), the presence of "intense oedema" (=18) and the presence of "deep oedema" (=18).

6. Bone marrow signal in the centre of each vertebra constitutes the reference normal signal. If the entire vertebra is abnormal, closest normal level is used for reference.

7. Discal lesions are not scored because they are often abnormal in patients with mechanical low back pain and degenerative disc disease.

8. Levels scored at a second time point are the same as those on the first.

Scoring Methodology: Sacroiliac Joints

The development and validation of a simplified scoring system for the assessment of disease activity in two-dimensional planes in the sacroiliac joints has been validated by the SPARCC methodology, because there is no well-established method for evaluating pathological MRI findings of the SIJs (Maksymowych et al. 2005a).

1. All scores are dichotomous—present or absent.

2. Only six coronal slices are assessed. Slices 4–9 are usually selected as those representing the largest proportion of the synovial compartment of the SI joints. Scoring of the SI joints is confined to those coronal slices depicting the synovial portion of the joint. In a preliminary overview of MRI performed at the SIJ in other patients with AS, the synovial portion was consistently evident in six consecutive coronal slices. Of the 12 acquisitions from posterior to anterior, this was typically slices 4–9. Therefore six consecutive coronal slices from posterior to anterior are scored. All lesions within the iliac bone and within the sacrum up to the sacral foramina are included. Only abnormalities on the STIR sequence are scored. T1 SE images are used for anatomical reference only and are not scored.

3. Within the iliac bone all lesions are scored.

4. Within the sacrum, lesions medially as far as the lateral border of the sacral foramina are scored. Sacral interforaminal bone marrow signal is used as the reference for normal to determine a threshold for increased signal in periarticular bone. Increased signal within the sacroiliac joint space or in the ligamentous portion of the joint is not scored.

5. Scoring method. Each SI joint is divided into four quadrants: 1 upper iliac, 2 lower iliac, 3 upper sacrum and 4 lower sacrum. The presence of increased signal in each quadrant is recorded. Maximum score for two SI joints in each coronal slice is 8. Maximum score for six coronal slices = 48 (Fig. 18.23).

The presence of increased signal on STIR in each of these four quadrants is scored. The

Fig. 18.23 SPARCC sacroiliac joint scoring sheet

maximum score for abnormal signal in the two SI joints of one coronal slice is therefore 8.

6. Joints that included a lesion exhibiting intense signal are each given an additional score of 1 per slice that demonstrated this feature. Therefore a score of 1 is assigned in any quadrant of an SI joint on a single slice. High signal from slow flowing venous blood within presacral veins acts as a reference for assigning an "intense" reading score to a bone lesion. This results in a maximal score for a single coronal slice to 12.

7. Similarly, each joint that includes a lesion demonstrating continuous increased signal of depth is also given an additional score of 1 to each SI joint on each slice. A lesion is graded as "deep" if there is homogeneous and unequivocal increase in signal extending over a depth of at least 1 cm from the articular surface. Maximum score per slice is therefore 2 and for six slices = 12.

In summary, the score leads to a maximum sum of 72, resulting from the possible presence of "bone marrow oedema" (=48), the presence of "intense oedema" (=12) and the presence of "deep oedema" (=12).

8. Images scored at a second time point are selected to correspond as closely as possible to the first time point—normally 4–9, 3–8 or 5–10.

Discussion

Systematic examination of spinal lesions by MRI using another scoring method concurred with the observations that the majority of affected levels were located in the thoracic spine although revealed somewhat more lesions in the cervical spine (Baraliakos et al. 2005a).

Posterior segment of the spine, including the facet joints, processes and interspinous ligaments have not yet been systematically evaluated by MRI. Whether inclusion of these regions will improve MRI-based scoring systems needs

further studies. This could raise concerns that a scoring system limited to only the most severely affected DVU might not capture residual disease limiting its ability to record more effective treatment strategies. A similar discussion affects the scoring of the SI joints, because several slices even showing bone marrow oedema corresponding to osteitis and enthesitis will not be scored, and therefore activity, which might be responsive to treatment, will be missed (see example in Fig. 18.24).

Another discussion affects the use of contrast media in imaging inflammatory disease, because reproducibility and responsiveness was slightly improved by using contrast enhancement in the spine (Maksymowych et al. 2005b). Even for assessment of sacroiliitis, Muche et al. stress the value of contrast administration, because STIR sequences were less sensitive than contrast-enhanced sequences, in that it was not possible to show all relevant changes in 27% of patients (Muche et al. 2003).

The analyses of the SPARCC scoring method for the assessment of spinal inflammation by MRI showed that the limitation of scoring only the six most severely affected levels captures 62% of all affected DVU and 74% of the total DVU score is feasible (Maksymowych et al. 2007). Furthermore, interobserver reliability was excellent regardless of whether analysis was limited to only the most severely affected levels or included the entire spine, while responsiveness was optimal when scoring was limited to only the six most severely affected levels. These observations, together with improved feasibility, support the notion that during assessment of the entire spine in AS, scoring all affected DVU is unnecessary and may therefore facilitate acceptance of this approach for clinical research and in clinical trials.

This is not surprising, because scoring the entire spine, as opposed to only the more severely affected DVU, will include more subtle lesions that may be less responsive to change and more difficult to assess. If readers are permitted to select levels for scoring, some error in reading due to the presence of signal artefact may be eliminated as the reader has the choice of not selecting those levels that are clearly subject to phase encoding, partial volume or other artefacts. In addition, reliability of assessment is not as good in the cervical spine, and responsiveness to change in this region is poor.

In summary, SPARCC's primary purpose is to record change in inflammatory lesions for clinical and therapeutic trials research by limiting the analysis to a maximum of six most severely affected levels/slices. This results in excellent inter-reader reliability for both status and change scores, which could improve the feasibility in clinical trials and research.

Aarhus MRI Grading Methods
A. G. Jurik

Published Aarhus MRI Grading Method
A semiquantitative grading system has been elaborated and tested by Puhakka et al. (2003, 2004). It was based on the following sequences: STIR, T1, T2 high resolution and T1 FS before and after intravenous Gd contrast using both semi-coronal and semi-axial slice orientation. The MR images were analysed with regard to abnormalities in the cartilaginous and ligamentous joint portion separately for the following sign of activity: bone marrow oedema and Gd contrast enhancement in the bone marrow, cartilaginous and ligamentous joint space and at entheses outside the joint. Assessment of chronic structural joint changes included erosion, osseous sclerosis (low signal intensity at T1 and/or T1 FS), fat accumulation in the bone marrow, joint space alteration and new bone formation at entheses.

Only some of the abnormalities were used to obtain a quantitative value (grade) for disease severity. Entheseal changes were omitted from the scoring system due to a relative low frequency, and fatty marrow changes were excluded because the analysis was designed to compare chronic changes at MRI and CT. All included grading parameters (Table 18.4) were scored 0–3, where 0 = normal, 1 = minimal, 2 = moderate and 3 = severe. The analysis of osseous lesions included assessment at four anatomical sites of each SIJ, the sacral and iliac side of the cartilaginous and ligamentous portion of the joint (Fig. 18.25). The severity was calculated as
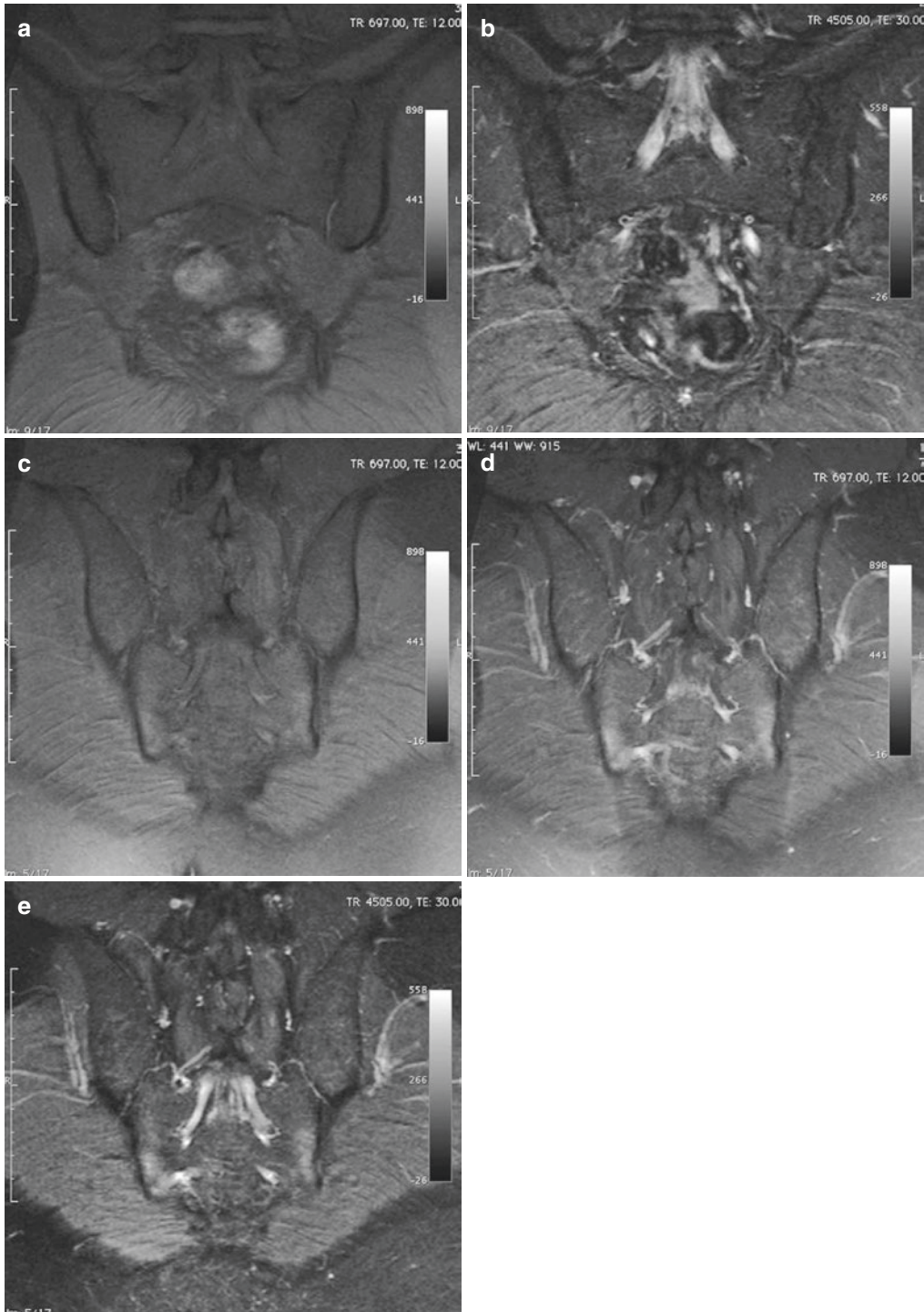
Fig. 18.24 Limitations of SPARCC scoring method. Patient with HLA-B27, signs of enthesitis and lower back pain. (**a**) Coronal spin echo T1 fat saturated and (**b**) short tau inversion recovery (STIR) showing no intraarticular pathologies. However, when para-articular slices are included, (**c**) spin echo T1 fat saturated, (**d**) STIR and (**e**) spin echo T1 fat saturated after contrast injection bone marrow oedema and enhancement can be seen bilaterally, consistent of inflammatory disease
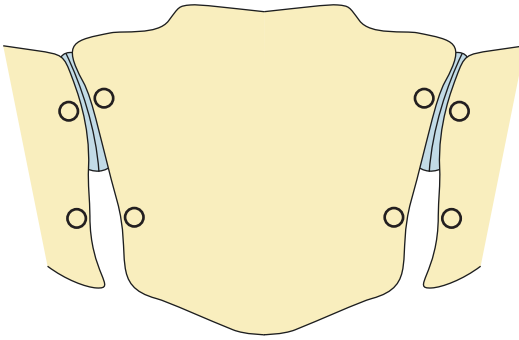
Fig. 18.25 Aarhus sacroiliac joint MRI grading method. Drawing showing the osseous positions evaluated, four in the cartilaginous and four in the ligamentous portion of the joints

Table 18.5 Scoring system for MRI abnormalities based on assessment at eight osseous position (the iliac and sacral side of the cartilaginous and ligamentous part of the joints, respectively) and four joint space positions (cartilaginous and ligamentous joint space) (Puhakka et al. 2003)

MRI abnormalities	An osseous joint position or a joint space Grade range	One SIJ: 4 osseous positions; two joint spaces Score range	A patient: 8 osseous positions; 4 joint spaces Score range
Bone marrow oedema	0–3	0–12	0–24
Bone marrow Gd enhancement	0–3	0–12	0–24
Joint space Gd enhancement	0–3	0–6	0–12
Overall activity score			0–60
Erosion	0–3	0–12	0–24
Sclerosis	0–3	0–12	0–24
Joint space width	0–3	0–6	0–12
Overall joint destruction activity score			0–60

Gd gadolinium contrast

a sum of the score for the abnormality in each position, the total maximal score for each abnormality being 12 per joint and 24 for a patient (Table 18.5). Similarly a total score for joint space width alteration and Gd contrast enhancement in the joint space was obtained with a total maximal score of 6 per joint and 12 for a patient. An overall MRI score for inflammatory activity was calculated as a sum of bone marrow oedema, Gd contrast enhancement in the bone marrow and in the joint space (maximal score 60 per patient) and a score for joint destruction as a sum of the scores for erosions, sclerosis and joint width alteration (maximal 60 per patient) (Table 18.5).

The detailed grading system was tested on 41 patients based on independent blinded image evaluation of two senior radiologists without preceding formal training within the new area for MRI (Puhakka et al. 2003). Parameters indicating disease activity were observed with a good intra-observer and relative good interobserver agreement, whereas grading of chronic structural changes, especially joint space narrowing but also osseous sclerosis, was less reliable (Table 18.6). MRI was found comparable to CT for detecting joint erosion and apparently also for detecting sclerosis although the evaluation of "sclerosis" by MRI may be difficult. MRI seemed inferior to CT with regard to assessment of new

bone formation at entheses and apparently also for evaluation of joint space alteration (Puhakka et al. 2003).

Despite not being optimal, the grading system has been shown to have sensitivity to change in a 1-year follow-up study being able to detect decreasing disease activity, but increasing chronic changes without concomitant clinical signs indicating this (Puhakka et al. 2004).

Reasons for Modification of the Aarhus Method
The previous published method has to be modified to obtain a reliable interobserver variation taking into account the results published in addition to the extended experience gained in the institution and the findings by others.

A new grading system for **disease activity** should give the possibility of using only STIR and also additional post-contrast sequence. The reported value of contrast enhancement has var-

Table 18.6 Inter- and intra-observer agreement for the most frequent disease parameters present at MRI based on 41 patients (82 SIJs) (Puhakka et al. 2003)

	Interobserver analysis		Intra-observer analysis	
	Agreement (%)	Kappa value	Agreement (%)	Kappa value
Oedema bone	73	0.49	95	0.89
Enhancement bone	73	0.47	98	0.94
Enh. joint space	82	0.64	98	0.94
Bone erosion	77	0.54	98	0.95
Osseous sclerosis	71	0.41	93	0.85
Fatty degeneration	84	0.67	93	0.84
Joint space alteration	59	0.18	95	0.90

ied, and it has not been proved that post-contrast sequences are unnecessary. In our previous analysis based on both STIR and post-contrast sequences, we observed a significant correlation between oedema at STIR and contrast enhancement in the bone marrow indicating that contrast enhancement may not be necessary (Puhakka et al. 2003). The finding of a significant relation between oedema and enhancement has been confirmed in another analysis where the use of a post-contrast sequence was found more sensitive than STIR (Bredella et al. 2006). Comparable reproducibility regarding subchondral oedema and enhancement has been demonstrated in cross-sectional analysis, but the reproducibility of change to scores seemed better with post-contrast images (Maksymowych et al. 2005a). This finding is not surprising as oedema may persist for some period after vascularised inflammation has vanished. STIR has been reported less sensitive than post-contrast sequences with regard to joint space inflammation (Muche et al. 2003). This is probably because it may be difficult to obtain a clear delineation of the joint space on STIR images. If the new scoring system should have the potential of being used based on STIR images, only joint space oedema and enhancement therefore has to be omitted.

The intensity and depth of inflammatory changes seems to influence the disease course (personal experience). These parameters therefore have to be included as part of the grading in accordance with the SPARCC system (Maksymowych et al. 2005a).

The evaluation of **chronic structural changes** has varied. Signs indicating sclerosis seem not to be reliable. The finding of lesions with reduced water content (low signal intensity at both T1 and T2/STIR) can be due to both fibrotic tissue and increased bony tissue (Bredella et al. 2006) and may occur together with signs of activity. In accordance with this, sclerosis verified at CT in our study was found to vary somewhat at MRI (Puhakka et al. 2003). Regions displaying significantly increased density at CT compatible with the definition of sclerosis did not always appear with low signal intensity at all MR sequences. They could contain regions with increased signal intensity at STIR and/or contrast enhancement as signs of inflammatory activity and could also display regions with increased signal intensity at T1 as sign of fat accumulation in bone marrow (Fig. 18.26). The interobserver agreement for joint space alteration at MRI was only 59%, indicating that it can be problematic to include this parameter in a SIJ scoring system. Another reason for not using this parameter is that the joint in ankylosing spondylitis initially shows widening followed by gradual narrowing until definite ankylosis has developed so a normal joint width may be pathological (Puhakka et al. 2003). The importance of fatty marrow degeneration as a sign of chronic changes has been observed in the form of a correlation to higher radiographic scores (Bredella et al. 2006).

An exclusion of joint space alteration and sclerosis, and inclusion of fatty marrow alteration in a new grading system, therefore seems justifiable.
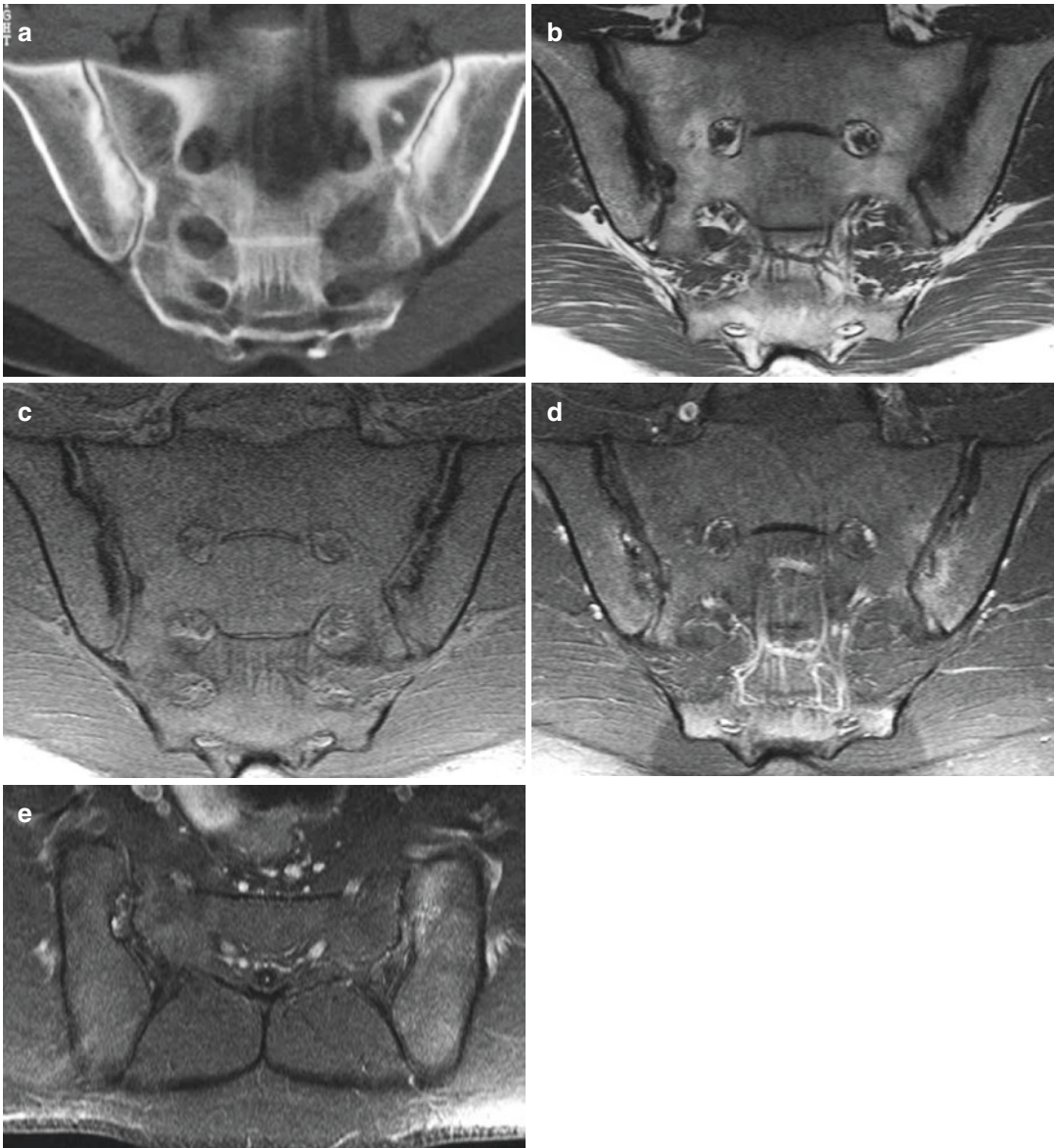
Fig. 18.26 Sacroiliitis with both active and chronic changes. (**a**) Semi-coronal CT slice showing bilateral joint space narrowing and erosion with subchondral sclerosis. MRI, (**b**) coronal T1, (**c**) T1 FS and (**d**) T1 FS post-contrast and (**e**) semi-axial T1 FS post-contrast. The sclerotic areas at CT appear with decreased signal intensity at T1 FS, but had irregular signal intensity at T1 and contained scattered enhancement. The semi-axial slice clearly show left-sided iliac bone enhancement in both the cartilaginous and ligamentous part of the joint

A relative good interobserver agreement has been observed for both signs of activity and chronic structural changes using a global joint score (Heuft-Dorenbosch et al. 2006). Thus, it may be advantageous to use a more simple grading system, but it will then be difficult to detect minor disease changes.

New Proposal for MRI Grading

The scoring for activity and chronic structural changes is based on all slices through the joint, including semi-coronal and semi-axial slices to differentiate between the cartilaginous and ligamentous joint portion. Signs of activity (subchondral oedema and/or contrast enhancement) and

Table 18.7 New proposal for MRI grading of sacroiliitis activity

Activity score			
MRI abnormalities		Max. score per position	Max. total patient score
Oedema	Extent	3	24
	Intensity	1	8
	Depth	1	8
Total activity (STIR)		5	40
Enhancement	Extent	3	24
	Intensity	1	8
	Depth	1	8
Total activity (post-Gd)		5	40
Total activity based on both STIR and post-Gd images		10/2 = 5	80/2 = 40

signs of chronic changes (fatty marrow degeneration and erosion or obliteration of the joint space) are evaluated and graded corresponding to eight anatomical joint portion—four cartilaginous and four ligamentous.

The activity score includes subchondral oedema and/or enhancement graded with regard to extent, intensity and depth as follows:

- *Extent:* Grade 0 = normal; grade 1 = slight: ≤25% of subchondral area; grade 2 = moderate: 25–≤50% and grade 3 = severe: >50% of the subchondral area.
- *Signal intensity:* Grade 0 = no, slight or moderate and grade 1 = pronounced (water level at STIR and great vessel level at post-contrast images) covering at least 1 cm^2 of the subchondral area.
- *Depth, maximal:* Grade 0: ≤1 cm and grade 1: >1 cm in some areas.

The total maximal score is 40 for STIR and post-contrast sequence, respectively, and if based on both likewise 40 (Table 18.7).

The chronic score includes fatty marrow degeneration and erosion or joint space alteration. Fatty marrow degeneration was graded for both extent and depth and erosion or joint space alteration for extent only. The subdivision for extent and depth was comparable with that for acute changes (*extent*: grade 0 = normal, grade 1 = slight ≤25%, grade 2 = moderate 25–≤50% and grade 3 = severe >50% of the subchondral area or joint facet. *Depth, maximal:* grade 0, ≤1 cm, and grade 1, >1 cm in some areas). The total maximal score is 56 (Table 18.8).

Table 18.8 New proposal for MRI grading of chronic structural sacroiliitis changes

Chronic score			
MRI abnormalities		Max. score per position	Max. total patient score
Fatty degeneration	Extent	3	24
	Depth	1	8
Erosion	Extent	3	24
Total max. chronic score		7	56

Hermann/Bollow Sacroiliitis Score
K. G. Hermann; M. Bollow

As early as in 1996, Bollow and Braun used an MRI scoring system for sacroiliitis to monitor the therapeutic effects of steroid injections into the sacroiliac joints (Bollow et al. 1996; Braun et al. 1996). The score grades chronic structural changes and acute inflammatory lesions. Various features including erosions and sclerosis as well as transarticular bridging, ankylosis and fat deposits in para-articular bone marrow were summarised in a so-called chronicity grade (Table 18.9, Figs. 18.27, 18.28, 18.29 and 18.30). The chronicity grade reflects the continuous progression of the disease and is based on histological insights (Bollow et al. 2000). It was developed in analogy to the grading of radiological changes (van der Linden et al. 1984). Each sacroiliac joint is evaluated as a unit, which is fast and allows use of the score in the routine clinical setting (Bollow et al. 2006). A limitation of the chronicity index is that it does not register short-term structural changes occurring in the course of disease.

The first version of the sacroiliitis score additionally comprised an activity index that was determined on the basis of dynamic T1-weighted

gradient echo images. However, when used under routine conditions, the index turned out to be susceptible to false positive results in morphologically normal sacroiliac joints. The most common reason for misinterpretation was placement of the region of interest in the retroarticular space, where the connective tissue contains numerous vessels which may mimic inflammation on contrast-enhanced images. Another reason why the method did not become widely used is that quantification

of the activity grade from a dynamic study using ROIs is too time consuming.

A modification that simplifies determination of disease activity has been proposed recently (Hermann et al. 2004). The modified semiquantitative grading system uses STIR images and/or static fat-saturated T1-weighted turbo spin echo images obtained after contrast administration (T1-TSE-FS post-CM). The sacroiliac joint is divided into four quadrants: iliac and sacral region and anterior and posterior halves (Fig. 18.31). For each of the four quadrants, increases in bone marrow signal intensity on STIR or T1-TSE-FS post-CM images are graded on a scale from 0 to 4 (e.g. in Fig. 18.32):

0 = unchanged signal intensity
1 = increased signal intensity confined to joint space, joint capsule or erosions (up to 10% of the joint area)
2 = mild changes (signal increase of 11–33% of the area)
3 = moderate changes (signal increase of 34–66% of the area)
4 = severe changes (signal increase of more than 66% of the area)

The changes must be present in at least two slices. The scores of the four quadrants are added up, resulting in a total score of 0–16 per joint (maximum score of 32 per patient). In case of discrepancy between the STIR and post-contrast images, the higher score is used. In general, it is assumed that both sequences have similar sensi-

Table 18.9 MRI grading of chronic changes in sacroiliitis. Modified from (Bollow et al. 1996)

Chronicity grades of sacroiliitis	
Grade 0	No chronic inflammatory changes
Grade I	Mild subchondral sclerosis without blurring of joint contours Fewer than two erosions per slice Normal width of joint cavity
Grade II	Moderate subchondral sclerosis with blurring of up to one third of joint cavity More than two erosions per slice without confluence Normal width of joint cavity
Grade III	Pronounced para-articular sclerosis obscuring more than one third of joint cavity And/or pseudodilatation of joint cavity by confluent erosions And/or circumscribed transarticular bone buds with narrowing of joint cavity
Grade IV	Definitive ankylosis of more than one fourth of joint cavity "Phantom joint" appearance of joint cavity, which is filled with fat marrow-like tissue

Fig. 18.27 Chronicity grade I. **a** Schematic drawing, (**b**) T2-weighted gradient echo sequence with fat saturation and (**c**) T1-weighted fast spin echo sequence of chronic sacroiliitis grade I. For further descriptions see Table 18.8. With permission from Bollow et al. (2006)
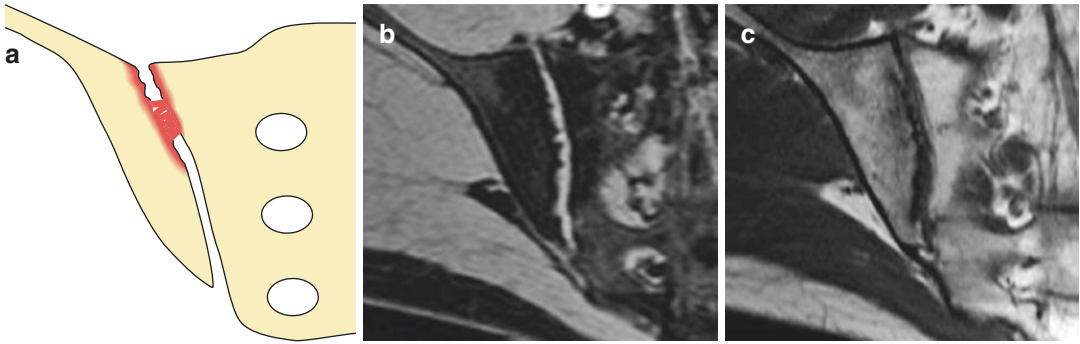
Fig. 18.28 Chronicity grade II. (**a**) Schematic drawing, (**b**) T2-weighted gradient echo sequence with fat saturation and (**c**) T1-weighted fast spin echo sequence of chronic sacroiliitis grade II. For further descriptions see Table 18.9. With permission from Bollow et al. (2006)
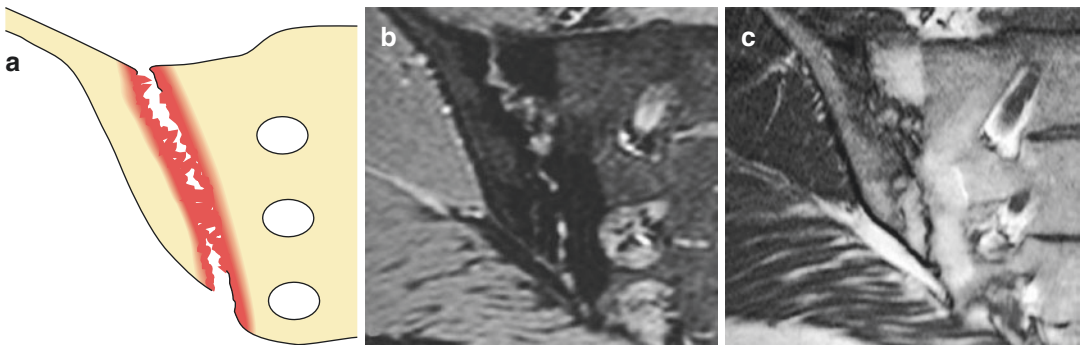
Fig. 18.29 Chronicity grade III. (**a**) Schematic drawing, (**b**) T2-weighted gradient echo sequence with fat saturation and (**c**) T1-weighted fast spin echo sequence of chronic sacroiliitis grade III. For further descriptions see Table 18.9. With permission from Bollow et al. (2006)
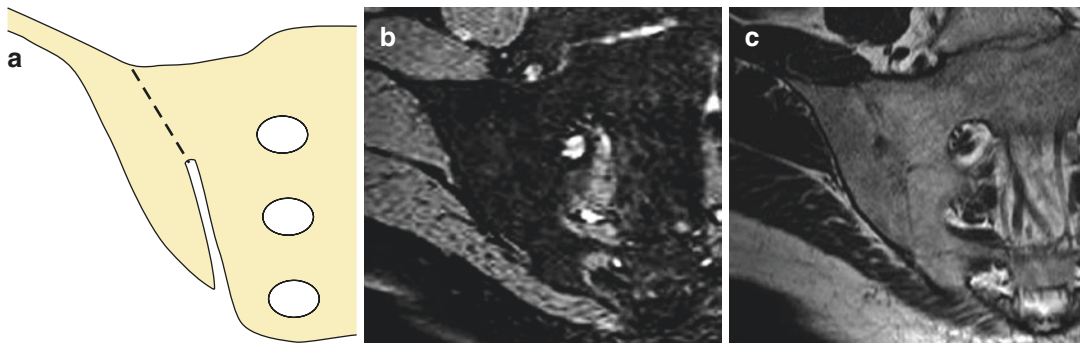
Fig. 18.30 Chronicity grade IV. (**a**) Schematic drawing, (**b**) T2-weighted gradient echo sequence with fat saturation and (**c**) T1-weighted fast spin echo sequence of chronic sacroiliitis grade IV. For further descriptions see Table 18.9. With permission from Bollow et al. (2006)

tivity and specificity with agreement around 90% (Muche et al. 2003 #190).

Classification of Spinal Changes in AS
K. G. Hermann
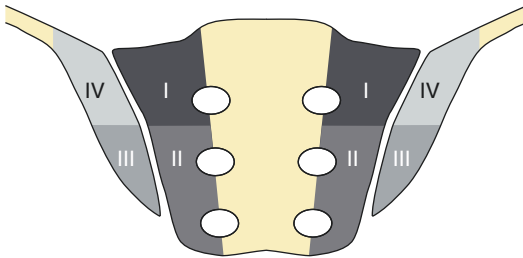
Fig. 18.31 Diagram of the quadrant method. The joint cleft divides each sacroiliac joint into two iliac and two sacral quadrants. A virtual horizontal line which usually touches the inferior border of the first sacral neural foramen divides the joint area into two halves and separates two anterior and two posterior quadrants. With permission from Bollow et al. (2006)

The changes of the discovertebral unit (Romanus spondylitis and Andersson lesions) have typical MRI appearances at different stages of AS. Three classes of lesions can be distinguished: acute inflammatory lesions, postinflammatory fatty bone marrow degeneration and ankylosis (Hermann and Bollow 2002; Hermann et al. 2005b). The MRI signal intensities are summarised in Table 18.10 and Fig. 18.33, which is meant as a guide to understanding the signal changes that occur in the course of disease.

The MRI grading system is based on the classification of degenerative disc disease proposed by Modic et al. (1988) and appears to facilitate the description and reporting of spinal changes in AS. This classification differs from the other scoring systems presented in this chapter in that it is not intended for use in clinical studies.
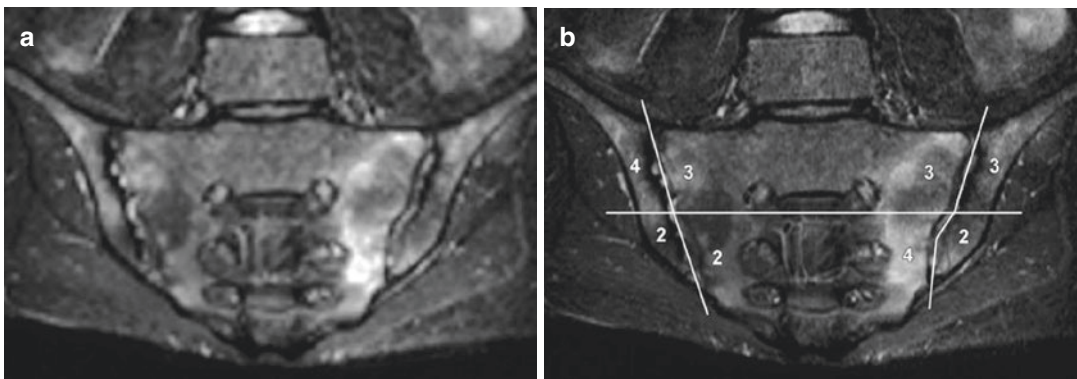
Fig. 18.32 Example of the quadrant method. (**a**) Short tau inversion recovery sequence (STIR) and (**b**) the same slice with the applied quadrant method and scores of active sacroiliitis in a 26-year-old male

Table 18.10 Classification of the spinal MRI changes in spondyloarthritis in relation to a discovertebral unit consisting of an intervertebral disc and the adjacent halves of the superior and inferior vertebrae

Class	T1-weighted sequence	T2-weighted/STIR sequence	Interpretation
0	Vertebra: intermediate Disc: low	Vertebra: low Disc: high	Normal findings
1	Vertebra: low Disc: low	Vertebra: high Disc: high	Florid inflammatory changes
2	Vertebra: high Disc: low	Vertebra: low Disc: high	Chronic postinflammatory fatty bone marrow degeneration
3	Vertebra: intermediate Disc: intermediate	Vertebra: low Disc: low	Partial or complete ankylosis
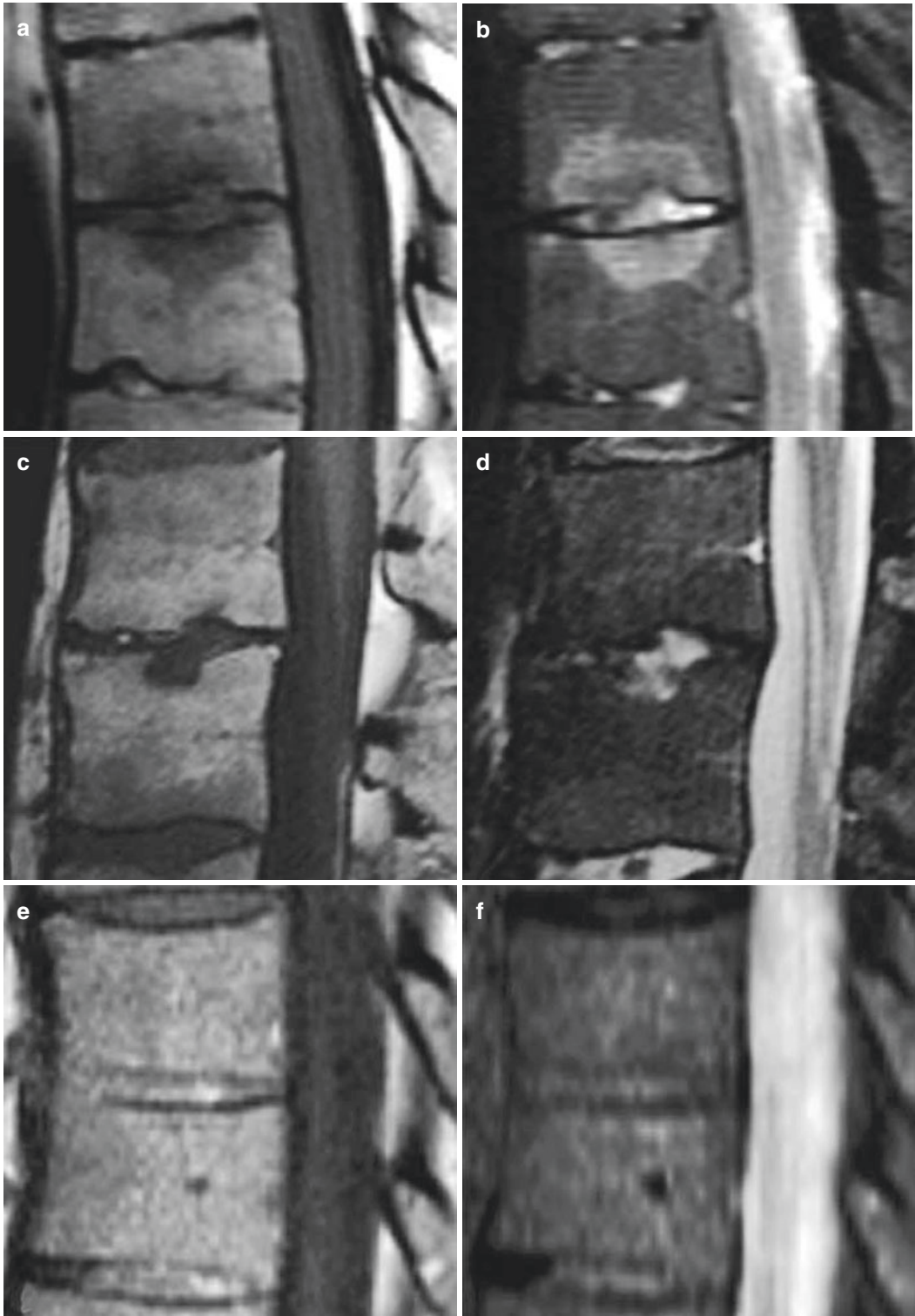
Fig. 18.33 Classification of spinal changes in AS. (**a**) T1-weighted fast spin echo sequence (T1-FSE) and (**b**) short tau inversion recovery sequence (STIR) of acute Andersson lesion (class I lesion); (**c**) T1-FSE and (**d**) STIR of chronic Andersson lesion with fatty degeneration (class II lesion); (**e**) T1-FSE and (**f**) STIR of a partially ankylosed spinal segment as last stage of Andersson lesion (class III lesion). For further descriptions see Table 18.10

Summary

K. G. Hermann and A. Klauser

Imaging and scoring should be as sensitive as possible since untreated AS seriously impairs quality of life. The natural history of SpA consists of acute episodes of enthesal and osseous inflammation. Therefore extending the analysis to all localisations of possible enthesitis, even the extraarticular ones such as the anterior and posterior iliac spines, the iliac crest and the posterior elements of the spine, may give a more accurate picture of the true extent of inflammation.

Conventional radiography remains an effective imaging method in the diagnosis, management and follow-up of spinal involvement in patients with AS. Radiographic grading of sacroiliitis according to the modified New York classification (van der Linden et al. 1984) has some weaknesses (van Tubergen et al. 2003) but continues to have an important role in diagnosing ankylosing spondylitis. The modified Stokes Ankylosing Spondylitis Spine Score is currently preferred for the follow-up of spinal changes (Wanders et al. 2004; van der Heijde and Landewe 2005).

MRI has opened up new horizons for the early detection of spinal inflammation as well as short-term and long-term follow-up. This deserves emphasis since effective new treatment (anti-TNF-α agents) might be able to prevent structural damage. While the OMERACT initiative has undertaken to develop a scoring system for grading the MRI changes of peripheral joints in rheumatoid arthritis (Ostergaard et al. 2003b), a number of scoring systems have been developed for spondyloarthritis by different research groups, and these were evaluated by the OMERACT initiative (van der Heijde et al. 2005; Lukas et al. 2007). There is an ongoing debate about the most suitable scoring method (Maksymowych and Lambert 2007), and different ones may be preferable in different situations. The SPARCC grading systems for the sacroiliac joints and spine yield robust results in short-term and mid-term clinical studies because they have low interobserver variation (Maksymowych et al. 2005a, b). Good interobserver agreement is due to the fact that these scores only take into account the six most severely inflamed discovertebral units or the six most relevant slices of the sacroiliac joints. Very small and potentially misleading lesions are thus excluded. To evaluate the natural course of AS, the Berlin score (a modification of the ASspiMRI-a method) (Baraliakos et al. 2005a) seems to be most suitable for acute changes and the ASspiMRI-c (Braun et al. 2003) for grading chronic changes. The roles of the Hermann/Bollow sacroiliitis score (Hermann et al. 2004) and the recent modification of the Aarhus MRI grading system (Puhakka et al. 2003) remain to be determined in clinical studies.

Newer imaging modalities such as ultrasound or whole-body MRI could further improve the assessment of enthesitis, which is the key feature of AS, but often results in only very distinct minor alterations detectable by MRI.

18.4   Imaging Assessment of Osteoarthritis

Andrew J. Grainger

Although osteoarthritis is recognised as being the most common joint disease and a major cause of disability, its pathogenesis remains poorly understood. The radiological changes of osteoarthritis are well described on both conventional radiography (CR) and using more modern imaging tools including MRI.

Much attention has centred on identifying a means to assess the severity of osteoarthritis using imaging and, increasingly, to monitor change in disease severity. The changes of OA on CR include joint space loss, osteophyte formation, subchondral bony attrition, cyst formation and sclerosis and, as the disease progresses, deformity. However one of the fundamental problems when considering assessment of OA using CR is that OA is essentially a disease of pain and disability, and the changes seen on radiographs correlate poorly with the clinical symptoms (Creamer 2000).

Conventional Radiography

Joint Space Measurement
Changes seen on CR remain the basis of the majority of studies using CR to assess OA severity and outcome. For many years cartilage loss has been considered fundamental to the OA disease process, and the prevention of cartilage loss has been considered as the primary aim of any therapeutic intervention. This has led to the use of joint space width (JSW), sometimes referred to as joint space narrowing (JSN) as a surrogate measure of cartilage loss. The majority of the work on this measure of osteoarthritis has been undertaken in the knee and the hip, although the technique has also been used in the ankle (Marijnissen et al. 2001) and the joints of the hand (Duryea et al. 2000). In both the knee and the hip, the measured joint space is highly dependent on the position of the joint and its radiographic alignment (Altman et al. 1996;

Buckland-Wright et al. 1995; Ravaud et al. 1996; Auleley et al. 2001; Goker et al. 2005). Although methods to improve the reliability of JSW measurements have been developed and validated, controversy remains over the techniques employed (Mazzuca and Brandt 2003; Conrozier et al. 2004; Buckland-Wright et al. 2004; Mazzuca et al. 2004).

Using scrupulous technique good reliability in joint space measurements can be achieved. However issues of validity exist with evidence that meniscal extrusion contributes to joint space loss in the knee and in early OA is the main cause indicating that JSW is not a valid marker for articular cartilage loss (Adams et al. 1999; Gale et al. 1999).

Raynauld et al. further called into question the validity of JSW as a measure of disease by showing its relative insensitivity to change. They found that despite a lack of change in JSW over a 2 year period, there was a significant change in articular cartilage volume as assessed by MRI (Raynauld et al. 2004).

Comprehensive Radiographic Scoring Techniques
Joint space is not the only feature of osteoarthritis that can be evaluated using CR, and a number of semiquantitative scoring systems have been developed for the diagnosis and monitoring of OA. The most well know of these is the Kellgren and Lawrence scoring system (Kellgren and Lawrence 1957). This has faced criticism on several fronts, including placing too much emphasis on osteophyte formation at the expense of other features of OA and being relatively insensitive to change. It is also criticised for inconsistencies between versions and attempting to apply the same criteria to different joints in the face of epidemiological studies which support joint specific radiographic scoring systems (Spector and Cooper 1993). Modifications have been proposed along with alternative systems (Spector and Cooper 1993; Altman et al. 1987; Kallman et al. 1989; Verbruggen and Veys 1996).

In 1989 Kallman et al. proposed a system for scoring OA in the hand using a 4 point (0–3) scale for osteophyte and joint space narrowing

along with scores for the presence or absence of sclerosis, cysts, deformity and cortical collapse. This was undertaken in 11 joints in the hand. An atlas was provided and inter-reader reliability was found to be good except scoring of cysts (Kallman et al. 1989).

Altman et al. have also developed scoring systems for OA in the hips and knees as well as the hands and in 1995 published an atlas which assessed multiple features of the disease using specifically tailored criteria for the hand, hip and knee (Altman et al. 1995). A revised atlas has recently been published (Altman and Gold 2007). The Altman scoring system probably represents the gold standard for radiographic scoring of osteoarthritis at this time.

A well-recognised problem with conventional radiographs for the assessment of disease progression is that radiographic changes correlate poorly with clinical criteria used to assess the disease such as pain and function (Pham et al. 2003). This means that clinical indices of disease state will continue to be important primary outcome measures for osteoarthritis in studies looking at treatment response. Nevertheless scoring systems for plain films are still in use and continue to be used to provide diagnostic inclusion criteria for clinical trials (Altman et al. 1991; Altman 1991a, b).

MRI Scoring Techniques

Articular Cartilage
MRI can directly image articular cartilage, and much of the work using MRI to assess osteoarthritis progression has concentrated on the assessment of articular cartilage through quantitative and semiquantitative methods.

The choice of MR sequence is critical to this process, and amongst the sequences commonly employed, authors have proposed fat-suppressed PD or T2-weighted imaging, T1-weighted spoiled gradient echo with fat suppression and water excitation imaging. Semiquantitative scoring systems have relied on grading the thickness of cartilage loss, but more recently attempts have been made to examine cartilage in the knee semiquantitatively

using a regionalized approach breaking down the articular surfaces and assigning a score to each (Kornaat et al. 2005; Peterfy et al. 2004). These systems score cartilage semiquantitatively as part of an overall assessment of knee OA assimilating scores for multiple features (see later). The 13-region scoring system employed in the whole-organ MRI scoring system (WORMS) devised by Peterfy et al. shows a high ICC between two trained readers (>0.98) (Buckland-Wright et al. 2004) and appears to translate well onto a lower field strength system using time-efficient sequence protocols (Roemer et al. 2005). However Conaghan et al. identified problems with this WORMS system and in particular suggested that scales for cartilage morphology and signal may need to be redeveloped (Conaghan et al. 2004).

There are studies utilising semiquantitative cartilage scores in longitudinal studies although these report varying results in terms of change in cartilage score over time and a clear picture has not yet emerged (Biswal et al. 2002; Wang et al. 2006; Zhai et al. 2005).

Quantitative measurement of articular cartilage on MRI eliminates the problem of intra- and inter-rater variation. Using a range of image analysis tools that have been developed, values such as cartilage volume, thickness and surface area can be produced. In addition measurements of the denuded subchondral bone can be made along with measures of focal cartilage lesions. Sophisticated techniques for analysing the data derived have been produced including thickness maps and measures of joint congruity. A formal nomenclature for such measures of articular cartilage has recently been proposed (Eckstein et al. 2006a). To derive these parameters, the image analysis process involves segmentation of the cartilage from the surrounding structures. To date fully automated segmentation procedures have been unsuccessful, and while semiautomated systems have been developed, most large-scale studies rely on manual outlining of the cartilage (Eckstein et al. 2006b). Although a variety of joints have been assessed in this way (Graichen et al. 2003, 2000; McGibbon et al. 2003; Peterfy et al. 1995), the thickness of the cartilage and the

relatively flat surfaces involved make cartilage morphometry in the knee technically easier, and the vast majority of the published work relates to the knee. Studies generally report a high degree of accuracy for quantitative cartilage measurements when compared with animal, cadaveric or surgical specimens (Eckstein et al. 2006b).

Comparisons between MR scanners also exist and have found small differences which has led Eckstein et al. to note that as long as the same scanner and sequence are used for baseline and follow-up studies at all sites, longitudinal multicentre studies are feasible (Eckstein et al. 2006b). Clearly the problem of variations between scanners is an issue that requires careful consideration when designing multicentre trials. Eckstein et al. also note the importance of precision in quantitative cartilage measurements. This equates to the degree of random variation in the measured parameter (reproducibility of the parameter with repeated measurements). This is rather more variable between studies and appears to be most significant in the knee on the highly curved femoral surfaces (Eckstein et al. 2006b).

It has been found that cartilage volume measures are more reproducible than cartilage thickness measures, partly because they are less susceptible to diurnal variation and not dependent on selecting a reproducible site for repeat measurements (Burgkart et al. 2001; Cicuttini et al. 1999; Graichen et al. 2004; Peterfy et al. 1994b; Pilch et al. 1994; Waterton et al. 2000). However cartilage volume measures raise other questions relating to validity and sensitivity to change (Teichtahl et al. 2006).

In addition to measuring the amount of cartilage present and degree of cartilage loss, it is also possible to obtain an assessment of cartilage make-up and change in quality using imaging techniques. Measurements of T2 and the parameter $T1_{rho}$ have been shown to vary with cartilage composition (Eckstein et al. 2006b; Duvvuri et al. 1997; Liess et al. 2002; Menezes et al. 2004; Regatte et al. 2002). However the evidence indicates that these are not affected by a single element of the cartilage composition and at the moment the role of these parameters and their

potential use remains at the experimental stage. The T1 of articular cartilage if measured after a time delay following IV gadolinium administration is found to vary according to the distribution of the gadolinium that has diffused into the cartilage. This technique of delayed gadolinium-enhanced MRI of cartilage (dGEMRIC) is based on the principle that gadolinium-DTPA (Gd-DTPA) is a negatively charged species and that will diffuse into cartilage with time, but will be distributed according to the ionic make-up of the cartilage. Since glycosaminoglycan (GAG) molecules, a component of proteoglycans, are also negatively charged, there will a relatively increased take up of Gd-DTPA in areas of GAG deficiency (Bashir et al. 1999).

Comprehensive Radiographic Scoring Techniques

Although OA has been traditionally assessed and characterised by articular cartilage loss, it is increasingly realised that it is more appropriate to view it as a multifactorial process which involves changes in the structure and function of multiple joint components (Martin and Buckwalter 2001). Many of these other changes are appreciated on MRI. These include changes in the subchondral bone, ligaments, fibrocartilage and synovium. Changes in the subchondral bone are variable and include cyst formation and marrow oedema-like changes. The amount of synovitis that can be demonstrated in osteoarthritis suggests a significant inflammatory element to the disease. An important question that has yet to be resolved is the degree to which these changes seen on MRI relate to the patients symptoms and to the progression of the disease. Studies have produced confusing data in this area (Felson 2005).

The complex relationships between the abnormalities seen on MRI and the clinical situation led Peterfy et al. to note that a "whole-organ evaluation is needed to evaluate properly the structural integrity of joints affected by OA" (Peterfy et al. 2004). This led to the development by Peterfy and coworkers of a whole-organ MRI score (WORMS) for evaluating OA in the knee (Peterfy et al. 2004). This uses semiquantitative

techniques to score a variety of features of knee OA on MRI including cartilage, marrow changes, osteophytes, menisci, ligaments and synovitis. The knee is subdivided into regions for assessment and a score assigned to each of the features for each region. This tool has been used in large-scale longitudinal studies and is certainly the most established whole-organ scoring tool in current use. It seems to show good reliability. However issues relating to its use have been identified in recent studies including questions relating to the scaling of items, particularly in patients with "early" OA where only the lowest points on the scales are used. There are also issues relating to the combination of several constructs in a single score as is seen in the semiquantitative scoring of cartilage used in the WORMS tool (Conaghan et al. 2006; Hunter et al. 2006).

Two novel OA whole-organ scoring systems have now been reported with evidence of good inter- and intra-reader reliability (Kornaat et al. 2005; Hunter et al. 2007). The Boston-Leeds Osteoarthritis Knee Score (BLOKS) has been more widely used and has been compared with WORMS (Lynch et al. 2010; Felson et al. 2010; Hunter et al. 2010). This found strengths and weaknesses in both scoring systems and has led to the recent publication of a new iteratively developed scoring system designed to address the weaknesses while keeping the strengths of the existing systems (Hunter et al. 2011). This has been called the MRI osteoarthritis knee score (MOAKS) and has been tested for reliability which has proved good or excellent for the majority of features scored. As yet no large-scale studies to validate this scoring system or to assess its responsiveness to change have been undertaken.

It is likely that further refinements will be made in the future, and it is to be hoped that one system will be adopted as a standard tool for future OA studies. A remaining issue is that all these tools are still only designed for use in knee OA, a relatively easy joint to study. MRI is increasingly being applied to OA changes in other joints, and it will have to be determined whether these existing scoring systems will be applicable to other joints and what further modifications will be required.

References

Adams JG, McAlindon T, Dimasi M, Carey J, Eustace S (1999) Contribution of meniscal extrusion and cartilage loss to joint space narrowing in osteoarthritis. Clin Radiol 54(8):502–506

Alasaarela E, Suramo I, Tervonen O et al (1998) Evaluation of humeral head erosions in rheumatoid arthritis: a comparison of ultrasonography, magnetic resonance imaging, computed tomography and plain radiography. Br J Rheumatol 37(11):1152–1156

Altman RD (1991a) Classification of disease: osteoarthritis. Semin Arthritis Rheum 20(6 Suppl 2):40–47

Altman RD (1991b) Criteria for classification of clinical osteoarthritis. J Rheumatol Suppl 27:10–12

Altman RD, Gold GE (2007) Atlas of individual radiographic features in osteoarthritis, revised. Osteoarthritis Cartilage 15(Suppl A):A1–56

Altman RD, Fries JF, Bloch DA, Carstens J, Cooke TD, Genant H et al (1987) Radiographic assessment of progression in osteoarthritis. Arthritis Rheum 30(11):1214–1225

Altman R, Alarcon G, Appelrouth D, Bloch D, Borenstein D, Brandt K et al (1991) The American College of Rheumatology criteria for the classification and reporting of osteoarthritis of the hip. Arthritis Rheum 34(5):505–514

Altman RD, Hochberg M, Murphy WA Jr, Wolfe F, Lequesne M (1995) Atlas of individual radiographic features in osteoarthritis. Osteoarthritis Cartilage 3(Suppl A):3–70

Altman R, Brandt K, Hochberg M, Moskowitz R, Bellamy N, Bloch DA et al (1996 Dec) Design and conduct of clinical trials in patients with osteoarthritis: recommendations from a task force of the Osteoarthritis Research Society. Results from a workshop. Osteoarthritis Cartilage 4(4):217–243

Appel H, Loddenkemper C, Grozdanovic Z et al (2006) Correlation of histopathological findings and magnetic resonance imaging in the spine of patients with ankylosing spondylitis. Arthritis Res Ther 8:R143

Argyropoulou MI, Glatzouni A, Voulgari PV et al (2005) Magnetic resonance imaging quantification of hand synovitis in patients with rheumatoid arthritis treated with infliximab. Joint Bone Spine 72(6):557–561

ASAS Website (2007) http://www.asasgroup.org. Last accessed 26 Oct 2007

Auleley GR, Duche A, Drape JL, Dougados M, Ravaud P (2001) Measurement of joint space width in hip osteoarthritis: influence of joint positioning and radiographic procedure. Rheumatology (Oxford, England) 40(4):414–419

Averns HL, Oxtoby J, Taylor HG, Jones PW, Dziedzic K, Dawes PT (1996) Radiological outcome in ankylosing spondylitis: use of the Stoke Ankylosing Spondylitis Spine Score (SASSS). Br J Rheumatol 35:373–376

Backhaus M, Kamradt T, Sandrock D et al (1999) Arthritis of the finger joints: a comprehensive approach comparing conventional radiography, scintigraphy, ultra-

sound, and contrast-enhanced magnetic resonance imaging. Arthritis Rheum 42(6):1232–1245

Backhaus M, Burmester GR, Sandrock D et al (2002) Prospective two year follow up study comparing novel and conventional imaging procedures in patients with arthritic finger joints. Ann Rheum Dis 61(10):895–904

Baraliakos X, Rudwaleit M, Listing J et al (2005a) Magnetic resonance imaging in ankylosing spondylitis—a detailed analysis. Ann Rheum Dis 64(Suppl 3):1059

Baraliakos X, Hermann KG, Landewe R et al (2005b) Assessment of acute spinal inflammation in patients with ankylosing spondylitis by magnetic resonance imaging: a comparison between contrast enhanced T1 and short tau inversion recovery (STIR) sequences. Ann Rheum Dis 64:1141–1144

Bashir A, Gray ML, Hartke J, Burstein D (1999) Nondestructive imaging of human cartilage glycosaminoglycan concentration by MRI. Magn Reson Med 41(5):857–865

Beckers C, Jeukens X, Ribbens C et al (2006) (18)F-FDG PET imaging of rheumatoid knee synovitis correlates with dynamic magnetic resonance and sonographic assessments as well as with the serum level of metalloproteinase-3. Eur J Nucl Med Mol Imaging 33(3):275–280

Bird P, Ejbjerg B, McQueen F et al (2003a) OMERACT rheumatoid arthritis magnetic resonance imaging studies. Exercise 5: an international multicenter reliability study using computerized MRI erosion volume measurements. J Rheumatol 30(6):1380–1384

Bird P, Lassere M, Shnier R et al (2003b) Computerized measurement of magnetic resonance imaging erosion volumes in patients with rheumatoid arthritis: a comparison with existing magnetic resonance imaging scoring systems and standard clinical outcome measures. Arthritis Rheum 48(3):614–624

Bird P, Kirkham B, Portek I et al (2004) Documenting damage progression in a two-year longitudinal study of rheumatoid arthritis patients with established disease (the DAMAGE study cohort): is there an advantage in the use of magnetic resonance imaging as compared with plain radiography? Arthritis Rheum 50(5):1383–1389

Bird P, Joshua F, Lassere M et al (2005) Training and calibration improve inter-reader reliability of joint damage assessment using magnetic resonance image scoring and computerized erosion volume measurement. J Rheumatol 32(8):1452–1458

Bird P, Ejbjerg B, Lassere M et al (2007) A multireader reliability study comparing conventional high-field magnetic resonance imaging with extremity low-field MRI in rheumatoid arthritis. J Rheumatol 34(4):854–856

Biswal S, Hastie T, Andriacchi TP, Bergman GA, Dillingham MF, Lang P (2002 Nov) Risk factors for progressive cartilage loss in the knee: a longitudinal magnetic resonance imaging study in forty-three patients. Arthritis Rheum 46(11):2884–2892

Boers M, Brooks P, Strand CV, Tugwell P (1998) The OMERACT filter for outcome measures in rheumatology. J Rheumatol 25:198–199

Boini S, Guillemin F (2001) Radiographic scoring methods as outcome measures in rheumatoid arthritis: properties and advantages. Ann Rheum Dis 60(9):817–827

Bollow M, Braun J, Hamm B et al (1995) Early sacroiliitis in patients with spondyloarthropathy: evaluation with dynamic gadolinium-enhanced MR imaging. Radiology 194:529–536

Bollow M, Braun J, Taupitz M et al (1996) CT-guided intraarticular corticosteroid injection into the sacroiliac joints in patients with spondyloarthropathy: indication and follow-up with contrast-enhanced MRI. J Comput Assist Tomogr 20:512–521

Bollow M, Biedermann T, Kannenberg J et al (1998) Use of dynamic magnetic resonance imaging to detect sacroiliitis in HLA-B27 positive and negative children with juvenile arthritides. J Rheumatol 25:556–564

Bollow M, Fischer T, Reisshauer H et al (2000) Quantitative analyses of sacroiliac biopsies in spondyloarthropathies: T cells and macrophages predominate in early and active sacroiliitis-cellularity correlates with the degree of enhancement detected by magnetic resonance imaging. Ann Rheum Dis 59:135–140

Bollow M, Braun J, Hermann KG (2006) Sakroiliakalgelenk (mit Exkurs: Spinale Entzündungsmuster rheumatischer Erkrankungen). In: Vahlensieck M, Reiser M (eds) Magnetresonanztomographie des muskuloskelettalen Systems. Thieme, Stuttgart

Braun J, Bollow M, Eggens U, König H, Distler A, Sieper J (1994) Use of dynamic magnetic resonance imaging with fast imaging in the detection of early and advanced sacroiliitis in spondylarthropathy patients. Arthritis Rheum 37:1039–1045

Braun J, Bollow M, Seyrekbasan F et al (1996) Computed tomography guided corticosteroid injection of the sacroiliac joint in patients with spondyloarthropathy with sacroiliitis: clinical outcome and follow up by dynamic magnetic resonance imaging. J Rheumatol 23:659–664

Braun J, Baraliakos X, Golder W et al (2003) Magnetic resonance imaging examinations of the spine in patients with ankylosing spondylitis, before and after successful therapy with infliximab: evaluation of a new scoring system. Arthritis Rheum 48:1126–1136

Braun J, Baraliakos X, Golder W et al (2004) Analysing chronic spinal changes in ankylosing spondylitis: a systematic comparison of conventional x rays with magnetic resonance imaging using established and new scoring systems. Ann Rheum Dis 63:1046–1055

Bredella MA, Steinbach LS, Morgan S, Ward M, Davis JC (2006) MRI of the sacroiliac joints in patients with moderate to severe ankylosing spondylitis. AJR Am J Roentgenol 187:1420–1426

Brower AC (1990) Use of the radiograph to measure the course of rheumatoid arthritis. The gold standard versus fool's gold. Arthritis Rheum 33(3):316–324

Buch MH, Seto Y, Bingham SJ et al (2005) C-reactive protein as a predictor of infliximab treatment outcome in patients with rheumatoid arthritis: defining subtypes of nonresponse and subsequent response to etanercept. Arthritis Rheum 52(1):42–48

Buckland-Wright JC, Macfarlane DG, Williams SA, Ward RJ (1995 Nov) Accuracy and precision of joint space width measurements in standard and macro-radiographs of osteoarthritic knees. Ann Rheum Dis 54(11):872–880

Buckland-Wright JC, Ward RJ, Peterfy C, Mojcik CF, Leff RL (2004) Reproducibility of the semiflexed (metatarsophalangeal) radiographic knee position and automated measurements of medial tibiofemoral joint space width in a multicenter clinical trial of knee osteoarthritis. J Rheumatol 31(8):1588–1597

Buckley DL, Parker GJM (2003) Measuring contrast agent concentration in T1-weighted dynamic contrast-enhanced MRI. In: Jackson A, Parker DL, Geoffrey JM (eds) Dynamic contrast enhanced magnetic resonance imaging in oncology. Springer, Berlin, pp 69–79

Burgkart R, Glaser C, Hyhlik-Durr A, Englmeier KH, Reiser M, Eckstein F (2001) Magnetic resonance imaging-based assessment of cartilage loss in severe osteoarthritis: accuracy, precision, and diagnostic value. Arthritis Rheum 44(9):2072–2077

Carano RA, Lynch JA, Redei J et al (2004) Multispectral analysis of bone lesions in the hands of patients with rheumatoid arthritis. Magn Reson Imaging 22(4):505–514

Cawley MI, Chalmers TM, Kellgren JH, Ball J (1972) Destructive lesions of vertebral bodies in ankylosing spondylitis. Ann Rheum Dis 31:345–358

Charlesworth CH, Savy LE, Stevens J, Twomey B, Mitchell R (1996) MRI demonstration of arachnoiditis in cauda equina syndrome of ankylosing spondylitis. Neuroradiology 38:462–465

Cicuttini F, Forbes A, Morris K, Darling S, Bailey M, Stuckey S (1999) Gender differences in knee cartilage volume as measured by magnetic resonance imaging. Osteoarthritis Cartilage 7(3):265–271

Cimmino MA, Bountis C, Silvestri E et al (2000) An appraisal of magnetic resonance imaging of the wrist in rheumatoid arthritis. Semin Arthritis Rheum 30(3):180–195

Cimmino MA, Innocenti S, Livrone F et al (2003) Dynamic gadolinium-enhanced magnetic resonance imaging of the wrist in patients with rheumatoid arthritis can discriminate active from inactive disease. Arthritis Rheum 48(5):1207–1213

Cimmino MA, Parodi M, Innocenti S et al (2005) Dynamic magnetic resonance of the wrist in psoriatic arthritis reveals imaging patterns similar to those of rheumatoid arthritis. Arthritis Res Ther 7(4):R725–R731

Conaghan P, Edmonds J, Emery P et al (2001) Magnetic resonance imaging in rheumatoid arthritis: summary of OMERACT activities, current status, and plans. J Rheumatol 28(5):1158–1162

Conaghan PG, O'Connor P, McGonagle D et al (2003a) Elucidation of the relationship between synovitis and bone damage: a randomized magnetic resonance imaging study of individual joints in patients with early rheumatoid arthritis. Arthritis Rheum 48(1):64–71

Conaghan P, Lassere M, Ostergaard M et al (2003b) OMERACT rheumatoid arthritis magnetic resonance imaging studies. Exercise 4: an international multi-center longitudinal study using the RA-MRI score. J Rheumatol 30(6):1376–1379

Conaghan P, Hunter DJ, Tennant A, Amin S, Clancy M, Guermazi A et al (2004) Evaluation of an MRI scoring system for osteoarthritis of the knee using modern psychometric approaches. Osteoarthritis Cartilage 12(Suppl B):S118

Conaghan P, Bird P, Ejbjerg B et al (2005) The EULAR-OMERACT rheumatoid arthritis MRI reference image atlas: the metacarpophalangeal joints. Ann Rheum Dis 64(Suppl 1):i11–i21

Conaghan P, Tennant A, Peterfy C, Woodworth T, Stevens R, Guermazi A et al (2006) Examining a whole-organ magnetic resonance imaging scoring system for osteoarthritis of the knee using Rasch analysis. Osteoarthritis Cartilage 14(Suppl 1):116–121

Conaghan PG, Ejbjerg B, Lassere M et al (2007) A multicenter reliability study of extremity-magnetic resonance imaging in the longitudinal evaluation of rheumatoid arthritis. J Rheumatol 34(4):857–858

Conrozier T, Mathieu P, Piperno M, Provvedini D, Taccoen A, Colson F et al (2004) Lyon Schuss radiographic view of the knee. Utility of fluoroscopy for the quality of tibial plateau alignment. J Rheumatol 31(3):584–590

Cooper RG, Freemont AJ, Fitzmaurice R, Alani SM, Jayson MI (1991) Paraspinal muscle fibrosis: a specific pathological component in ankylosing spondylitis. Ann Rheum Dis 50:755–759

Cotten A (2005) Rhumatismes inflammatoires chroniques. In: Imagerie musculosquelettique—pathologies générales. Masson, Paris, pp 3–44

Creamer P (2000 Sep) Osteoarthritis pain and its treatment. Curr Opin Rheumatol 12(5):450–455

Creamer P, Keen M, Zananiri F et al (1997) Quantitative magnetic resonance imaging of the knee: a method of measuring response to intra-articular treatments. Ann Rheum Dis 56(6):378–381

Creemers MC, Franssen MJ, van't Hof MA, Gribnau FW, van de Putte LB, van Riel PL (2005) Assessment of outcome in ankylosing spondylitis: an extended radiographic scoring system. Ann Rheum Dis 64:127–129

Dale K (1980) Radiographic grading of sacroiliitis in Bechterew's syndrome and allied disorders. Scand J Rheumatol 32(Suppl):92–97

Dale BM, Jesberger JA, Lewin JS et al (2003) Determining and optimizing the precision of quantitative measurements of perfusion from dynamic contrast enhanced MRI. J Magn Reson Imaging 18(5):575–584

Durez P, Malghem J, Toukap AN et al (2007) Treatment of early rheumatoid arthritis: a randomized magnetic resonance imaging study comparing the effects of methotrexate alone, methotrexate in combination with infliximab, and methotrexate in combination with intravenous pulse methylprednisolone. Arthritis Rheum 56(12):3919–3927

Duryea J, Jiang Y, Zakharevich M, Genant HK (2000 May) Neural network based algorithm to quantify joint space width in joints of the hand for arthritis assessment. Med Phys 27(5):1185–1194

Duvvuri U, Reddy R, Patel SD, Kaufman JH, Kneeland JB, Leigh JS (1997) T1rho-relaxation in articular cartilage: effects of enzymatic degradation. Magn Reson Med 38(6):863–867

Eckstein F, Ateshian G, Burgkart R, Burstein D, Cicuttini F, Dardzinski B et al (2006a) Proposal for a nomenclature for magnetic resonance imaging based measures of articular cartilage in osteoarthritis. Osteoarthritis Cartilage 14(10):974–983

Eckstein F, Burstein D, Link TM (2006b) Quantitative MRI of cartilage and bone: degenerative changes in osteoarthritis. NMR Biomed 19(7):822–854

Ejbjerg B, Narvestad E, Rostrup E et al (2004) Magnetic resonance imaging of wrist and finger joints in healthy subjects occasionally shows changes resembling erosions and synovitis as seen in rheumatoid arthritis. Arthritis Rheum 50(4):1097–1106

Ejbjerg BJ, Narvestad E, Jacobsen S et al (2005a) Optimised, low cost, low field dedicated extremity MRI is highly specific and sensitive for synovitis and bone erosions in rheumatoid arthritis wrist and finger joints: comparison with conventional high field MRI and radiography. Ann Rheum Dis 64(9):1280–1287

Ejbjerg B, McQueen F, Lassere M et al (2005b) The EULAR-OMERACT rheumatoid arthritis MRI reference image atlas: the wrist joint. Ann Rheum Dis 64(Suppl 1):i23–i47

Ejbjerg BJ, Vestergaard A, Jacobsen S et al (2005c) The smallest detectable difference and sensitivity to change of magnetic resonance imaging and radiographic scoring of structural joint damage in rheumatoid arthritis finger, wrist, and toe joints: a comparison of the OMERACT rheumatoid arthritis magnetic resonance imaging score applied to different joint combinations and the Sharp/van der Heijde radiographic score. Arthritis Rheum 52(8):2300–2306

Ejbjerg BJ, Vestergaard A, Jacobsen S et al (2006) Conventional radiography requires a MRI-estimated bone volume loss of 20% to 30% to allow certain detection of bone erosions in rheumatoid arthritis metacarpophalangeal joints. Arthritis Res Ther 8(3):R59

Ellrodt A, Goldberg D, Oberlin F, Huchet B, Cayla J (1986) Erosive arthritis of the costovertebral joint in seronegative spondyloarthropathy. J Rheumatol 13:452–454

Eshed I, Althoff CE, Schink T et al (2006) Low-field MRI for assessing synovitis in patients with rheumatoid arthritis. Impact of Gd-DTPA dose on synovitis scoring. Scand J Rheumatol 35(4):277–282

Felson DT (2005) The sources of pain in knee osteoarthritis. Curr Opin Rheumatol 17(5):624–628

Felson DT, Lynch J, Guermazi A, Roemer FW, Niu J, McAlindon T et al (2010) Comparison of BLOKS and WORMS scoring systems part II. Longitudinal assessment of knee MRIs for osteoarthritis and suggested approach based on their performance: data from the Osteoarthritis Initiative. Osteoarthritis Cartilage 18(11):1402–1407

Fiocco U, Cozzi L, Rubaltelli L et al (1996) Long-term sonographic follow-up of rheumatoid and psoriatic proliferative knee joint synovitis. Br J Rheumatol 35(2):155–163

Fiocco U, Ferro F, Cozzi L et al (2003) Contrast medium in power Doppler ultrasound for assessment of synovial vascularity: comparison with arthroscopy. J Rheumatol 30(10):2170–2176

Foley-Nolan D, Stack JP, Ryan M et al (1991) Magnetic resonance imaging in the assessment of rheumatoid arthritis—a comparison with plain film radiographs. Br J Rheumatol 30(2):101–106

Gaffney K, Cookson J, Blake D et al (1995) Quantification of rheumatoid synovitis by magnetic resonance imaging. Arthritis Rheum 38(11):1610–1617

Gaffney K, Cookson J, Blades S et al (1998) Quantitative assessment of the rheumatoid synovial microvascular bed by gadolinium-DTPA enhanced magnetic resonance imaging. Ann Rheum Dis 57(3):152–157

Gale DR, Chaisson CE, Totterman SM, Schwartz RK, Gale ME, Felson D (1999) Meniscal subluxation: association with osteoarthritis and joint space narrowing. Osteoarthritis Cartilage 7(6):526–532

Gardener JC, Aierhut ML, Gardner GC et al (2003) Vascularity in the RA wrist at 1–2 months following initiation of anti-TNFalpha and methotrexate therapy. Rheumatology (Oxford) 47(suppl):S131

Genant HK, Jiang Y, Peterfy C et al (1998) Assessment of rheumatoid arthritis using a modified scoring method on digitized and original radiographs. Arthritis Rheum 41(9):1583–1590

Ginsburg WW, Cohen MD, Miller GM, Bartleson JD (1997) Posterior vertebral body erosion by arachnoid diverticula in cauda equina syndrome: an unusual manifestation of ankylosing spondylitis. J Rheumatol 24:1417–1420

Goker B, Sancak A, Haznedaroglu S, Arac M, Block JA (2005) The effects of minor hip flexion, abduction or adduction and x-ray beam angle on the radiographic joint space width of the hip. Osteoarthritis Cartilage 13(5):379–386

Goldberg AL, Keaton NL, Rothfus WE, Daffner RH (1993) Ankylosing spondylitis complicated by trauma: MR findings correlated with plain radiographs and CT. Skelet Radiol 22:333–336

Gordon TP, Sage MR, Bertouch JV, Brooks PM (1984) Computed tomography of paraspinal musculature in ankylosing spondylitis. J Rheumatol 11:794–797

Graichen H, Springer V, Flaman T, Stammberger T, Glaser C, Englmeier KH et al (2000) Validation of high-resolution water-excitation magnetic resonance imaging for quantitative assessment of thin cartilage layers. Osteoarthritis Cartilage 8(2):106–114

Graichen H, Jakob J, von Eisenhart-Rothe R, Englmeier KH, Reiser M, Eckstein F (2003) Validation of cartilage volume and thickness measurements in the human shoulder with quantitative magnetic resonance imaging. Osteoarthritis Cartilage 11(7):475–482

Graichen H, von Eisenhart-Rothe R, Vogl T, Englmeier KH, Eckstein F (2004) Quantitative assessment of car-

tilage status in osteoarthritis by quantitative magnetic resonance imaging: technical validation for use in analysis of cartilage volume and further morphologic parameters. Arthritis Rheum 50(3):811–816

Grosman H, Gray R, St Louis EL (1983) CT of long-standing ankylosing spondylitis with cauda equina syndrome. AJNR Am J Neuroradiol 4:1077–1080

Haavardsholm EA, Ostergaard M, Ejbjerg BJ et al (2005) Reliability and sensitivity to change of the OMERACT rheumatoid arthritis magnetic resonance imaging score in a multireader, longitudinal setting. Arthritis Rheum 52(12):3860–3867

Haavardsholm EA, Boyesen P, Ostergaard M et al (2008) MRI findings in 84 early rheumatoid arthritis patients: bone marrow edema predicts erosive progression. Ann Rheum Dis 67(6):794–800

Hau M, Kneitz C, Tony HP et al (2002) High resolution ultrasound detects a decrease in pannus vascularisation of small finger joints in patients with rheumatoid arthritis receiving treatment with soluble tumour necrosis factor alpha receptor (etanercept). Ann Rheum Dis 61(1):55–58

Hermann KGA, Bollow M (2002) Magnetic resonance tomography in spondylarthropathies. Akt Rheumatol 27:323–331

Hermann KG, Backhaus M, Schneider U et al (2003) Rheumatoid arthritis of the shoulder joint: comparison of conventional radiography, ultrasound, and dynamic contrast-enhanced magnetic resonance imaging. Arthritis Rheum 48(12):3338–3349

Hermann KG, Braun J, Fischer T, Reisshauer H, Bollow M (2004) Magnetic resonance imaging of sacroiliitis: anatomy, histological pathology, MR-morphology, and grading. Radiologe 44:217–228

Hermann KG, Landewe RB, Braun J, van der Heijde D (2005a) Magnetic resonance imaging of inflammatory lesions in the spine in ankylosing spondylitis clinical trials: is paramagnetic contrast medium necessary? J Rheumatol 32:2056–2060

Hermann KG, Althoff CE, Schneider U et al (2005b) Magnetic resonance imaging of spinal changes in patients with spondyloarthritis and correlation with conventional radiography. Radiographics 25:559–570

Heuft-Dorenbosch L, Weijers R, Landewe R, van der Linden S, van der Heijde D (2006) Magnetic resonance imaging changes of sacroiliac joints in patients with recent-onset inflammatory back pain: inter-reader reliability and prevalence of abnormalities. Arthritis Res Ther 8:R11

Hodgson R, Barnes T, Connolly S et al (2006) Dynamic contrast enhanced MRI of the wrist demonstrates early response to antiTNFalpha therapy in rheumatoid arthritis. In American College of Rheumatology annual scientific meeting. American College of Rheumatology, Washington, DC

Hodgson RJ, Connolly S, Barnes T et al (2007) Pharmacokinetic modeling of dynamic contrast-enhanced MRI of the hand and wrist in rheumatoid arthritis and the response to anti-tumor necrosis factor-alpha therapy. Magn Reson Med 58(3):482–489

Hodgson R, Grainger A, O'Connor P et al (2008) Dynamic contrast enhanced MRI of bone marrow oedema in rheumatoid arthritis. Ann Rheum Dis 67(2):270–272

Hollingsworth PN, Cheah PS, Dawkins RL, Owen ET, Calin A, Wood PH (1983) Observer variation in grading sacroiliac radiographs in HLA-B27 positive individuals. J Rheumatol 10:247–254

Huang J, Stewart N, Crabbe J et al (2000) A 1-year follow-up study of dynamic magnetic resonance imaging in early rheumatoid arthritis reveals synovitis to be increased in shared epitope-positive patients and predictive of erosions at 1 year. Rheumatology (Oxford) 39(4):407–416

Hunter DJ, Conaghan P, Peterfy C, Bloch D, Guermazi A, Woodworth T et al (2006) Responsiveness, effect size, and smallest detectable difference of magnetic resonance imaging in knee osteoarthritis. Osteoarthritis Cartilage 14(Suppl 1):112–115

Hunter DJ, Lo GH, Gale D, Grainger AJ, Guermazi A, Conaghan PG (2007) The development and reliability of a new scoring system for knee osteoarthritis MRI: BLOKS (Boston Leeds Osteoarthritis Knee Score). Ann Rheum Dis 67(2):206–211

Hunter DJ, Zaim S, Mosher TJ (2010) What semi-quantitative scoring instrument for knee OA MRI should you use? Osteoarthritis Cartilage 18(11):1363–1364

Hunter DJ, Guermazi A, Lo GH, Grainger AJ, Conaghan PG, Boudreau RM et al (2011) Evolution of semi-quantitative whole joint assessment of knee OA: MOAKS (MRI Osteoarthritis Knee Score). Osteoarthritis Cartilage 19(8):990–1002

Hyrich KL, Watson KD, Silman AJ et al (2006) Predictors of response to anti-TNF-alpha therapy among patients with rheumatoid arthritis: results from the British Society for Rheumatology Biologics Register. Rheumatology (Oxford) 45(12):1558–1565

Jevtic V, Kos-Golja M, Rozman B, McCall I (2000) Marginal erosive discovertebral "Romanus" lesions in ankylosing spondylitis demonstrated by contrast enhanced Gd-DTPA magnetic resonance imaging. Skelet Radiol 29:27–33

Jimenez-Boj E, Nobauer-Huhmann I, Hanslik-Schnabel B et al (2007) Bone erosions and bone marrow edema as defined by magnetic resonance imaging reflect true bone marrow inflammation in rheumatoid arthritis. Arthritis Rheum 56(4):1118–1124

Jorgensen C, Cyteval C, Anaya JM et al (1993) Sensitivity of magnetic resonance imaging of the wrist in very early rheumatoid arthritis. Clin Exp Rheumatol 11(2):163–168

Kalden-Nemeth D, Grebmeier J, Antoni C et al (1997) NMR monitoring of rheumatoid arthritis patients receiving anti-TNF-alpha monoclonal antibody therapy. Rheumatol Int 16(6):249–255

Kallman DA, Wigley FM, Scott WW Jr, Hochberg MC, Tobin JD (1989) New radiographic grading scales for osteoarthritis of the hand. Reliability for determining prevalence and progression. Arthritis Rheum 32(12):1584–1591

Maksymowych WP, Dhillon SS, Park R, Salonen D, Inman RD, Lambert RG (2007) Validation of the spondyloarthritis research consortium of Canada magnetic resonance imaging spinal inflammation index: is it necessary to score the entire spine? Arthritis Rheum 57:501–507

Marijnissen AC, Vincken KL, Viergever MA, van Roy HL, Van Roermund PM, Lafeber FP et al (2001 Apr) Ankle images digital analysis (AIDA): digital measurement of joint space width and subchondral sclerosis on standard radiographs. Osteoarthritis Cartilage 9(3):264–272

Martin JA, Buckwalter JA (2001) Roles of articular cartilage aging and chondrocyte senescence in the pathogenesis of osteoarthritis. Iowa Orthop J 21:1–7

Marzo-Ortega H, McGonagle D, O'Connor P, Emery P (2001) Efficacy of etanercept in the treatment of the entheseal pathology in resistant spondylarthropathy: a clinical and magnetic resonance imaging study. Arthritis Rheum 44:2112–2117

Marzo-Ortega H, Braun J, Maksymowych WP et al (2002) Interreader agreement in the assessment of magnetic resonance imaging of the sacroiliac joints in spondyloarthropathy—the 1st MISS study [abstract]. Arthritis Rheum 46(Suppl):S428

Mazzuca SA, Brandt KD (2003) Is knee radiography useful for studying the efficacy of a disease-modifying osteoarthritis drug in humans? Rheum Dis Clin N Am 29(4):819–830

Mazzuca SA, Brandt KD, Buckwalter KA, Lequesne M (2004) Pitfalls in the accurate measurement of joint space narrowing in semiflexed, anteroposterior radiographic imaging of the knee. Arthritis Rheum 50(8):2508–2515

McGibbon CA, Bencardino J, Yeh ED, Palmer WE (2003) Accuracy of cartilage and subchondral bone spatial thickness distribution from MRI. J Magn Reson Imaging 17(6):703–715

McGonagle D, Gibbon W, Emery P (1998) Classification of inflammatory arthritis by enthesitis. Lancet 352(9134):1137–1140

McGonagle D, Conaghan PG, O'Connor P et al (1999) The relationship between synovitis and bone changes in early untreated rheumatoid arthritis: a controlled magnetic resonance imaging study. Arthritis Rheum 42(8):1706–1711

McQueen FM (2000) Magnetic resonance imaging in early inflammatory arthritis: what is its role? Rheumatology (Oxford) 39(7):700–706

McQueen FM, Ostendorf B (2006) What is MRI bone oedema in rheumatoid arthritis and why does it matter? Arthritis Res Ther 8(6):222

McQueen FM, Stewart N, Crabbe J et al (1998) Magnetic resonance imaging of the wrist in early rheumatoid arthritis reveals a high prevalence of erosions at four months after symptom onset. Ann Rheum Dis 57(6):350–356

McQueen FM, Stewart N, Crabbe J et al (1999) Magnetic resonance imaging of the wrist in early rheumatoid arthritis reveals progression of erosions despite clinical improvement. Ann Rheum Dis 58(3):156–163

McQueen FM, Benton N, Crabbe J et al (2001) What is the fate of erosions in early rheumatoid arthritis? Tracking individual lesions using x rays and magnetic resonance imaging over the first two years of disease. Ann Rheum Dis 60(9):859–868

McQueen FM, Benton N, Perry D et al (2003a) Bone edema scored on magnetic resonance imaging scans of the dominant carpus at presentation predicts radiographic joint damage of the hands and feet six years later in patients with rheumatoid arthritis. Arthritis Rheum 48(7):1814–1827

McQueen F, Lassere M, Edmonds J et al (2003b) OMERACT rheumatoid arthritis magnetic resonance imaging studies. Summary of OMERACT 6 MR imaging module. J Rheumatol 30(6):1387–1392

McQueen F, Ostergaard M, Peterfy C et al (2005a) Pitfalls in scoring MR images of rheumatoid arthritis wrist and metacarpophalangeal joints. Ann Rheum Dis 64(Suppl 1):i48–i55

McQueen F, Beckley V, Crabbe J et al (2005b) Magnetic resonance imaging evidence of tendinopathy in early rheumatoid arthritis predicts tendon rupture at six years. Arthritis Rheum 52(3):744–751

McQueen FM, Gao A, Ostergaard M et al (2007) High-grade MRI bone oedema is common within the surgical field in rheumatoid arthritis patients undergoing joint replacement and is associated with osteitis in subchondral bone. Ann Rheum Dis 66(12):1581–1587

Menezes NM, Gray ML, Hartke JR, Burstein D (2004) T2 and T1rho MRI in articular cartilage systems. Magn Reson Med 51(3):503–509

Modic MT, Steinberg PM, Ross JS, Masaryk TJ, Carter JR (1988) Degenerative disk disease: assessment of changes in vertebral body marrow with MR imaging. Radiology 166:193–199

Muche B, Bollow M, Francois RJ, Sieper J, Hamm B, Braun J (2003) Anatomic structures involved in early- and late-stage sacroiliitis in spondylarthritis: a detailed analysis by contrast-enhanced magnetic resonance imaging. Arthritis Rheum 48:1374–1384

Nagele M, Kunze V, Koch W et al (1993) Rheumatoid arthritis of the wrist. Dynamic Gd-DTPA enhanced MRT. Rofo 158(2):141–146

Newman JS, Adler RS, Bude RO et al (1994) Detection of soft-tissue hyperemia: value of power Doppler sonography. AJR Am J Roentgenol 163(2):385–389

Oliver C, Speake S, Watt I et al (1996) Advantages of an increased dose of MRI contrast agent for enhancing inflammatory synovium. Clin Radiol 51(7):487–493

OMERACT Website (2007) http://www.omeract.org. Last accessed 26 Oct 2007

Ostendorf B, Peters R, Dann P et al (2001) Magnetic resonance imaging and miniarthroscopy of metacarpophalangeal joints: sensitive detection of morphologic changes in rheumatoid arthritis. Arthritis Rheum 44(11):2492–2502

Ostendorf B, Scherer A, Modder U et al (2004) Diagnostic value of magnetic resonance imaging of the forefeet in early rheumatoid arthritis when findings on imaging

of the metacarpophalangeal joints of the hands remain normal. Arthritis Rheum 50(7):2094–2102

Ostergaard M (1997) Different approaches to synovial membrane volume determination by magnetic resonance imaging: manual versus automated segmentation. Br J Rheumatol 36(11):1166–1177

Ostergaard M (1999) Magnetic resonance imaging in rheumatoid arthritis. Quantitative methods for assessment of the inflammatory process in peripheral joints. Dan Med Bull 46(4):313–344

Ostergaard M, Klarlund M (2001) Importance of timing of post-contrast MRI in rheumatoid arthritis: what happens during the first 60 minutes after IV gadolinium-DTPA? Ann Rheum Dis 60(11):1050–1054

Ostergaard M, Gideon P, Henriksen O et al (1994a) Synovial volume—a marker of disease severity in rheumatoid arthritis? Quantification by MRI. Scand J Rheumatol 23(4):197–202

Ostergaard M, Lorenzen I, Henriksen O (1994b) Dynamic gadolinium-enhanced MR imaging in active and inactive immunoinflammatory gonarthritis. Acta Radiol 35(3):275–281

Ostergaard M, Gideon P, Sorensen K et al (1995) Scoring of synovial membrane hypertrophy and bone erosions by MR imaging in clinically active and inactive rheumatoid arthritis of the wrist. Scand J Rheumatol 24(4):212–218

Ostergaard M, Stoltenberg M, Gideon P et al (1996a) Changes in synovial membrane and joint effusion volumes after intraarticular methylprednisolone. Quantitative assessment of inflammatory and destructive changes in arthritis by MRI. J Rheumatol 23(7):1151–1161

Ostergaard M, Hansen M, Stoltenberg M et al (1996b) Quantitative assessment of the synovial membrane in the rheumatoid wrist: an easily obtained MRI score reflects the synovial volume. Br J Rheumatol 35(10):965–971

Ostergaard M, Stoltenberg M, Henriksen O et al (1996c) Quantitative assessment of synovial inflammation by dynamic gadolinium-enhanced magnetic resonance imaging. A study of the effect of intra-articular methylprednisolone on the rate of early synovial enhancement. Br J Rheumatol 35(1):50–59

Ostergaard M, Stoltenberg M, Lovgreen-Nielsen P et al (1997a) Magnetic resonance imaging-determined synovial membrane and joint effusion volumes in rheumatoid arthritis and osteoarthritis: comparison with the macroscopic and microscopic appearance of the synovium. Arthritis Rheum 40(10):1856–1867

Ostergaard M, Gideon P, Stoltenberg MB et al (1997b) Volumes of synovial membrane and joint effusion determined by MR imaging. Markers of severity and/or activity in rheumatoid arthritis? Ugeskr Laeger 159(25):3956–3961

Ostergaard M, Stoltenberg M, Lovgreen-Nielsen P et al (1998) Quantification of synovitis by MRI: correlation between dynamic and static gadolinium-enhanced magnetic resonance imaging and microscopic and macroscopic signs of synovial inflammation. Magn Reson Imaging 16(7):743–754

Ostergaard M, Hansen M, Stoltenberg M et al (1999) Magnetic resonance imaging-determined synovial membrane volume as a marker of disease activity and a predictor of progressive joint destruction in the wrists of patients with rheumatoid arthritis. Arthritis Rheum 42(5):918–929

Ostergaard M, Hansen MS, Stoltenberg MB et al (2000) Magnetic resonance imaging as a marker of inflammation, destruction and prognosis in rheumatoid arthritis wrists. Ugeskr Laeger 162(31):4145–4149

Ostergaard M, Klarlund M, Lassere M et al (2001a) Interreader agreement in the assessment of magnetic resonance images of rheumatoid arthritis wrist and finger joints – an international multicenter study. J Rheumatol 28(5):1143–1150

Ostergaard M, Ejbjerg B, Stoltenberg M et al (2001b) Quantitative magnetic resonance imaging as marker of synovial membrane regeneration and recurrence of synovitis after arthroscopic knee joint synovectomy: a one year follow up study. Ann Rheum Dis 60(3):233–236

Ostergaard M, Hansen M, Stoltenberg M et al (2003a) New radiographic bone erosions in the wrists of patients with rheumatoid arthritis are detectable with magnetic resonance imaging a median of two years earlier. Arthritis Rheum 48(8):2128–2131

Ostergaard M, Peterfy C, Conaghan P et al (2003b) OMERACT rheumatoid arthritis magnetic resonance imaging studies. Core set of MRI acquisitions, joint pathology definitions, and the OMERACT RA-MRI scoring system. J Rheumatol 30(6):1385–1386

Ostergaard M, Duer A, Nielsen H et al (2005) Magnetic resonance imaging for accelerated assessment of drug effect and prediction of subsequent radiographic progression in rheumatoid arthritis: a study of patients receiving combined anakinra and methotrexate treatment. Ann Rheum Dis 64(10):1503–1506

Ostrowitzki S, Redei J, Lynch JA et al (2004) Use of multispectral magnetic resonance imaging analysis to quantify erosive changes in the hands of patients with rheumatoid arthritis: short-term and long-term longitudinal studies. Arthritis Rheum 50(3):716–724

Palmer WE, Rosenthal DI, Schoenberg OI et al (1995) Quantification of inflammation in the wrist with gadolinium-enhanced MR imaging and PET with 2-[F-18]-fluoro-2-deoxy-D-glucose. Radiology 196(3):647–655

Palosaari K, Vuotila J, Takalo R et al (2004) Contrast-enhanced dynamic and static MRI correlates with quantitative 99Tcm-labelled nanocolloid scintigraphy. Study of early rheumatoid arthritis patients. Rheumatology (Oxford) 43(11):1364–1373

Palosaari K, Vuotila J, Takalo R et al (2006) Bone oedema predicts erosive progression on wrist MRI in early RA—a 2-yr observational MRI and NC scintigraphy study. Rheumatology (Oxford) 45(12):1542–1548

Peh WC, Ho TK, Chan FL (1993) Case report: pseudoarthrosis complicating ankylosing spondylitis—appearances on magnetic imaging. Clin Radiol 47:359–361

Perry D, Stewart N, Benton N et al (2005) Detection of erosions in the rheumatoid hand; a comparative study of multidetector computerized tomography versus magnetic resonance scanning. J Rheumatol 32(2):256–267

Peterfy CG (2001) Magnetic resonance imaging in rheumatoid arthritis: current status and future directions. J Rheumatol 28(5):1134–1142

Peterfy CG, Majumdar S, Lang P et al (1994a) MR imaging of the arthritic knee: improved discrimination of cartilage, synovium, and effusion with pulsed saturation transfer and fat-suppressed T1-weighted sequences. Radiology 191(2):413–419

Peterfy CG, van Dijke CF, Janzen DL, Gluer CC, Namba R, Majumdar S et al (1994b) Quantification of articular cartilage in the knee with pulsed saturation transfer subtraction and fat-suppressed MR imaging: optimization and validation. Radiology 192(2):485–491

Peterfy CG, van Dijke CF, Lu Y, Nguyen A, Connick TJ, Kneeland JB et al (1995) Quantification of the volume of articular cartilage in the metacarpophalangeal joints of the hand: accuracy and precision of three-dimensional MR imaging. AJR 165(2):371–375

Peterfy CG, Guermazi A, Zaim S, Tirman PF, Miaux Y, White D et al (2004) Whole-Organ Magnetic Resonance Imaging Score (WORMS) of the knee in osteoarthritis. Osteoarthritis Cartilage 12(3):177–190

Pham T, Van Der Heijde D, Lassere M, Altman RD, Anderson JJ, Bellamy N et al (2003) Outcome variables for osteoarthritis clinical trials: the OMERACT-OARSI set of responder criteria. J Rheumatol 30(7):1648–1654

Pierre-Jerome C, Bekkelund SI, Mellgren SI et al (1997) The rheumatoid wrist: bilateral MR analysis of the distribution of rheumatoid lesions in axial plan in a female population. Clin Rheumatol 16(1):80–86

Pilch L, Stewart C, Gordon D, Inman R, Parsons K, Pataki I et al (1994) Assessment of cartilage volume in the femorotibial joint with magnetic resonance imaging and 3D computer reconstruction. J Rheumatol 21(12):2307–2321

Polisson RP, Schoenberg OI, Fischman A et al (1995) Use of magnetic resonance imaging and positron emission tomography in the assessment of synovial volume and glucose metabolism in patients with rheumatoid arthritis. Arthritis Rheum 38(6):819–825

Puhakka KB, Jurik AG, Egund N et al (2003) Imaging of sacroiliitis in early seronegative spondylarthropathy. Assessment of abnormalities by MR in comparison with radiography and CT. Acta Radiol 44:218–229

Puhakka KB, Jurik AG, Schiottz-Christensen B et al (2004) MRI abnormalities of sacroiliac joints in early spondylarthropathy: a 1-year follow-up study. Scand J Rheumatol 33:332–338

Quinn MA, Conaghan PG, O'Connor PJ et al (2005) Very early treatment with infliximab in addition to methotrexate in early, poor-prognosis rheumatoid arthritis reduces magnetic resonance imaging evidence of synovitis and damage, with sustained benefit after infliximab withdrawal: results from a twelve-month

randomized, double-blind, placebo-controlled trial. Arthritis Rheum 52(1):27–35

Ravaud P, Auleley GR, Chastang C, Rousselin B, Paolozzi L, Amor B et al (1996 Aug) Knee joint space width measurement: an experimental study of the influence of radiographic procedure and joint positioning. Br J Rheumatol 35(8):761–766

Raynauld JP, Martel-Pelletier J, Berthiaume MJ, Labonte F, Beaudoin G, de Guise JA et al (2004) Quantitative magnetic resonance imaging evaluation of knee osteoarthritis progression over two years and correlation with clinical symptoms and radiologic changes. Arthritis Rheum 50(2):476–487

Reece RJ, Kraan MC, Radjenovic A et al (2002) Comparative assessment of leflunomide and methotrexate for the treatment of rheumatoid arthritis, by dynamic enhanced magnetic resonance imaging. Arthritis Rheum 46(2):366–372

Regatte RR, Akella SV, Borthakur A, Kneeland JB, Reddy R (2002) Proteoglycan depletion-induced changes in transverse relaxation maps of cartilage: comparison of T2 and T1rho. Acad Radiol 9(12):1388–1394

Resnick D, Niwayama G (2002) Ankylosing spondylitis. In: Resnick D, Niwayama G (eds) Diagnosis of bone and joint disorders, 4th edn. Saunders WB, Philadelphia, pp 1023–1081

Rhodes LA, Tan AL, Tanner SF et al (2004) Regional variation and differential response to therapy for knee synovitis adjacent to the cartilage-pannus junction and suprapatellar pouch in inflammatory arthritis: implications for pathogenesis and treatment. Arthritis Rheum 50(8):2428–2432

Ribbens C, Andre B, Marcelis S et al (2003) Rheumatoid hand joint synovitis: gray-scale and power Doppler US quantifications following anti-tumor necrosis factor-alpha treatment: pilot study. Radiology 229(2):562–569

Roemer FW, Guermazi A, Lynch JA, Peterfy CG, Nevitt MC, Webb N et al (2005) Short tau inversion recovery and proton density-weighted fat suppressed sequences for the evaluation of osteoarthritis of the knee with a 1.0 T dedicated extremity MRI: development of a time-efficient sequence protocol. Eur Radiol 15(5):978–987

Rubin JM (1999) Musculoskeletal power doppler. Eur Radiol 9(Suppl 3):S403–S406

Rudwaleit M, Baraliakos X, Listing J, Brandt J, Sieper J, Braun J (2005) Magnetic resonance imaging of the spine and the sacroiliac joints in ankylosing spondylitis and undifferentiated spondyloarthritis during treatment with etanercept. Ann Rheum Dis 64:1305–1310

Savnik A, Malmskov H, Thomsen HS et al (2001a) Magnetic resonance imaging of the wrist and finger joints in patients with inflammatory joint diseases. J Rheumatol 28(10):2193–2200

Savnik A, Malmskov H, Thomsen HS et al (2001b) MRI of the arthritic small joints: comparison of extremity MRI (0.2 T) vs high-field MRI (1.5 T). Eur Radiol 11(6):1030–1038

Savnik A, Malmskov H, Thomsen HS et al (2002a) MRI of the wrist and finger joints in inflammatory joint dis-

eases at 1-year interval: MRI features to predict bone erosions. Eur Radiol 12(5):1203–1210

Savnik A, Bliddal H, Nyengaard JR et al (2002b) MRI of the arthritic finger joints: synovial membrane volume determination, a manual vs a stereologic method. Eur Radiol 12(1):94–98

Schirmer C, Scheel AK, Althoff CE et al (2006) Diagnostic quality and scoring of synovitis, tenosynovitis and erosions in low-field MRI of patients with rheumatoid arthritis: a comparison with conventional MRI. Ann Rheum Dis 66(4):522–529

Schmidt WA, Volker L, Zacher J et al (2000) Colour Doppler ultrasonography to detect pannus in knee joint synovitis. Clin Exp Rheumatol 18(4):439–444

Schroder R, Urbach H, Zierz S (1994) Cauda equina syndrome with multiple lumbar diverticula complicating long-standing ankylosing spondylitis. Clin Investig 72:1056–1059

Scott DL, Farr M (1986) Assessing the progression of joint damage in rheumatoid arthritis. Drugs 32(Suppl 1):63–70

Sharp JT, Lidsky MD, Collins LC et al (1971) Methods of scoring the progression of radiologic changes in rheumatoid arthritis. Correlation of radiologic, clinical and laboratory abnormalities. Arthritis Rheum 14(6):706–720

Sharp JT, Young DY, Bluhm GB et al (1985) How many joints in the hands and wrists should be included in a score of radiologic abnormalities used to assess rheumatoid arthritis? Arthritis Rheum 28(12):1326–1335

Solau-Gervais E, Legrand JL, Cortet B et al (2006) Magnetic resonance imaging of the hand for the diagnosis of rheumatoid arthritis in the absence of anti-cyclic citrullinated peptide antibodies: a prospective study. J Rheumatol 33(9):1760–1765

Spector TD, Cooper C (1993) Radiographic assessment of osteoarthritis in population studies: whither Kellgren and Lawrence? Osteoarthritis Cartilage 1(4):203–206

Stone M, Bergin D, Whelan B et al (2001) Power Doppler ultrasound assessment of rheumatoid hand synovitis. J Rheumatol 28(9):1979–1982

Sugimoto H, Takeda A, Hyodoh K (2000) Early-stage rheumatoid arthritis: prospective study of the effectiveness of MR imaging for diagnosis. Radiology 216(2):569–575

Szkudlarek M, Court-Payen M, Strandberg C et al (2001) Power Doppler ultrasonography for assessment of synovitis in the metacarpophalangeal joints of patients with rheumatoid arthritis: a comparison with dynamic magnetic resonance imaging. Arthritis Rheum 44(9):2018–2023

Szkudlarek M, Court-Payen M, Strandberg C et al (2003) Contrast-enhanced power Doppler ultrasonography of the metacarpophalangeal joints in rheumatoid arthritis. Eur Radiol 13(1):163–168

Szkudlarek M, Narvestad E, Klarlund M et al (2004) Ultrasonography of the metatarsophalangeal joints in rheumatoid arthritis: comparison with magnetic resonance imaging, conventional radiography, and clinical examination. Arthritis Rheum 50(7):2103–2112

Tam LS, Griffith JF, Yu AB et al (2006) Rapid improvement in rheumatoid arthritis patients on combination of methotrexate and infliximab: clinical and magnetic resonance imaging evaluation. Clin Rheumatol 26(6):941–946

Tamai K, Yamato M, Yamaguchi T et al (1994) Dynamic magnetic resonance imaging for the evaluation of synovitis in patients with rheumatoid arthritis. Arthritis Rheum 37(8):1151–1157

Tamai M, Kawakami A, Uetani M et al (2006) The presence of anti-cyclic citrullinated peptide antibody is associated with magnetic resonance imaging detection of bone marrow oedema in early stage rheumatoid arthritis. Ann Rheum Dis 65(1):133–134

Tamai M, Kawakami A, Uetani M et al (2007) Bone edema determined by magnetic resonance imaging reflects severe disease status in patients with early-stage rheumatoid arthritis. J Rheumatol 34(11):2154–2157

Tan AL, Tanner SF, Conaghan PG et al (2003) Role of metacarpophalangeal joint anatomic factors in the distribution of synovitis and bone erosion in early rheumatoid arthritis. Arthritis Rheum 48(5):1214–1222

Taylor HG, Wardle T, Beswick EJ, Dawes PT (1991) The relationship of clinical and laboratory measurements to radiological change in ankylosing spondylitis. Br J Rheumatol 30:330–335

Taylor PC, Steuer A, Gruber J et al (2004) Comparison of ultrasonographic assessment of synovitis and joint vascularity with radiographic evaluation in a randomized, placebo-controlled study of infliximab therapy in early rheumatoid arthritis. Arthritis Rheum 50(4):1107–1116

Teh J, Stevens K, Williamson L et al (2003) Power Doppler ultrasound of rheumatoid synovitis: quantification of therapeutic response. Br J Radiol 76(912):875–879

Teichtahl AJ, Cicuttini FM, Wluka AE (2006) Imaging modalities in the outcome assessment of knee osteoarthritis. Curr Rheumatol Rev 2:131–136

Terslev L, Torp-Pedersen S, Savnik A et al (2003) Doppler ultrasound and magnetic resonance imaging of synovial inflammation of the hand in rheumatoid arthritis: a comparative study. Arthritis Rheum 48(9):2434–2441

Tofts PK, Leung KK, McLeish K et al (2007) Nonlinear modelling of dynamic contrast enhanced Gd imaging data in rheumatoid arthritis: extraction of ktrans. In Joint annual meeting ISMRM-ESMRMB. ISMRM, Berlin, Germany

van der Heijde D, Landewe R (2005) Selection of a method for scoring radiographs for ankylosing spondylitis clinical trials, by the assessment in Ankylosing Spondylitis Working Group and OMERACT. J Rheumatol 32:2048–2049

van der Heijde DM, van Leeuwen MA, van Riel PL et al (1995) Radiographic progression on radiographs of hands and feet during the first 3 years of rheumatoid arthritis measured according to Sharp's method (van der Heijde modification). J Rheumatol 22(9):1792–1796

van der Heijde D, Dankert T, Nieman F et al (1999) Reliability and sensitivity to change of a simplifica-

tion of the Sharp/van der Heijde radiological assessment in rheumatoid arthritis. Rheumatology (Oxford) 38(10):941–947

van der Heijde D, Landewe RB, Hermann KG et al (2005) Application of the OMERACT filter to scoring methods for magnetic resonance imaging of the sacroiliac joints and the spine. Recommendations for a research agenda at OMERACT 7. J Rheumatol 32:2042–2047

van der Linden S, Valkenburg HA, Cats A (1984) Evaluation of diagnostic criteria for ankylosing spondylitis. A proposal for modification of the New York criteria. Arthritis Rheum 27:361–368

van Riel PL, Taggart AJ, Sany J et al (2006) Efficacy and safety of combination etanercept and methotrexate versus etanercept alone in patients with rheumatoid arthritis with an inadequate response to methotrexate: the ADORE study. Ann Rheum Dis 65(11):1478–1483

van Tubergen A, Heuft-Dorenbosch L, Schulpen G et al (2003) Radiographic assessment of sacroiliitis by radiologists and rheumatologists: does training improve quality? Ann Rheum Dis 62:519–525

Veale DJ, Reece RJ, Parsons W et al (1999) Intra-articular primatised anti-CD4: efficacy in resistant rheumatoid knees. A study of combined arthroscopy, magnetic resonance imaging, and histology. Ann Rheum Dis 58(6):342–349

Verbruggen G, Veys EM (1996) Numerical scoring systems for the anatomic evolution of osteoarthritis of the finger joints. Arthritis Rheum 39(2):308–320

Wakefield RJ, Gibbon WW, Conaghan PG et al (2000) The value of sonography in the detection of bone erosions in patients with rheumatoid arthritis: a comparison with conventional radiography. Arthritis Rheum 43(12):2762–2770

Wakefield RJ, Balint PV, Szkudlarek M et al (2005) Musculoskeletal ultrasound including definitions for ultrasonographic pathology. J Rheumatol 32(12):2485–2487

Walther M, Harms H, Krenn V et al (2001) Correlation of power Doppler sonography with vascularity of the synovial tissue of the knee joint in patients with osteoarthritis and rheumatoid arthritis. Arthritis Rheum 44(2):331–338

Walther M, Harms H, Krenn V et al (2002) Synovial tissue of the hip at power Doppler US: correlation between vascularity and power Doppler US signal. Radiology 225(1):225–231

Wanders AJ, Landewe RB, Spoorenberg A et al (2004) What is the most appropriate radiologic scoring method for ankylosing spondylitis? A comparison of the available methods based on the Outcome Measures in Rheumatology Clinical Trials filter. Arthritis Rheum 50:2622–2632

Wang Y, Ding C, Wluka AE, Davis S, Ebeling PR, Jones G et al (2006) Factors affecting progression of knee cartilage defects in normal subjects over 2 years. Rheumatology (Oxford, England) 45(1):79–84

Waterton JC, Solloway S, Foster JE, Keen MC, Gandy S, Middleton BJ et al (2000) Diurnal variation in the femoral articular cartilage of the knee in young adult humans. Magn Reson Med 43(1):126–132

Weidekamm C, Koller M, Weber M et al (2003) Diagnostic value of high-resolution B-mode and doppler sonography for imaging of hand and finger joints in rheumatoid arthritis. Arthritis Rheum 48(2):325–333

Wieners G, Detert J, Streitparth F et al (2007) High-resolution MRI of the wrist and finger joints in patients with rheumatoid arthritis: comparison of 1.5 Tesla and 3.0 Tesla. Eur Radiol 17(8):2176–2182

Winalski CS, Aliabadi P, Wright RJ et al (1993) Enhancement of joint fluid with intravenously administered gadopentetate dimeglumine: technique, rationale, and implications. Radiology 187(1):179–185

Workie DW, Dardzinski BJ (2005) Quantifying dynamic contrast-enhanced MRI of the knee in children with juvenile rheumatoid arthritis using an arterial input function (AIF) extracted from popliteal artery enhancement, and the effect of the choice of the AIF on the kinetic parameters. Magn Reson Med 54(3):560–568

Workie DW, Dardzinski BJ, Graham TB et al (2004) Quantification of dynamic contrast-enhanced MR imaging of the knee in children with juvenile rheumatoid arthritis based on pharmacokinetic modeling. Magn Reson Imaging 22(9):1201–1210

Zhai G, Ding C, Stankovich J, Cicuttini F, Jones G (2005) The genetic contribution to longitudinal changes in knee structure and muscle strength: a sibpair study. Arthritis Rheum 52(9):2830–2834

Zierhut ML, Gardner JC, Spilker ME et al (2007) Kinetic modeling of contrast-enhanced MRI: an automated technique for assessing inflammation in the rheumatoid arthritis wrist. Ann Biomed Eng 35(5):781–795

Zikou AK, Argyropoulou MI, Voulgari PV et al (2006) Magnetic resonance imaging quantification of hand synovitis in patients with rheumatoid arthritis treated with adalimumab. J Rheumatol 33(2):219–223

Metabolic Bone Disease

19

Thomas M. Link

Contents

19.1 Introduction

Osteoporosis is the most important metabolic bone disease, and measurements of bone mineral density (BMD) to diagnose osteoporosis are of substantial importance. In fact according to the WHO criteria, BMD measurements using dual X-ray absorptiometry (DXA) are used to define osteoporosis and osteopenia in postmenopausal Caucasian women (WHO 1994). In 2000 the NIH consensus development conference (NIH Consensus Development Panel on Osteoporosis Prevention D, and Therapy 2001; Online NCS 2000) defined osteoporosis as a skeletal disorder characterized by compromised bone strength predisposing to an increased risk of fracture. Bone strength reflects the integration of two main features: bone density and bone quality. Bone density is expressed as grams of mineral per area or volume and, in any given individual, is determined by peak bone mass and amount of bone loss. Bone quality refers to architecture, turnover, damage accumulation (e.g., microfractures), and mineralization. To develop quantitative measures

T. M. Link, M.D.
Department of Radiology and Biomedical Imaging,
University of California, San Francisco,
400 Parnassus Avenue, A-367, Box 0628,
San Francisco, CA 94143, USA
e-mail: thomas.link@ucsf.edu

for these latter entities is the subject of current research, and specifically bone architecture imaging is an interesting field for radiology.

Measurements in osteoporosis are also required to diagnose and quantify vertebral fractures, and since previous publications showed that these fractures were frequently missed by radiologists (Gehlbach et al. 2000; Mueller et al. 2004, 2008), there is currently substantial interest in better diagnosing these fractures. Vertebral fractures occur with a higher incidence earlier in life than all other types of osteoporotic fractures (Meunier et al. 1999). Also they are associated with a worse disease prognosis, but it is difficult to determine the exact number of fractures that occur annually as a substantial proportion are clinically undetected (Link et al. 2005; Riggs and Melton 1995).

BMD measurements are not only used in osteoporosis but also other metabolic diseases that cause bone loss, including hyperthyroidism, hyperparathyroidism, Cushing's disease, and osteomalacia. BMD may be useful for longitudinal measurement to monitor disease. Diabetes mellitus also induces increased fracture risk, yet BMD measurements are not useful to measure fracture risk as BMD is increased in diabetic patients (Schwartz 2003).

19.2 Bone Mineral Density Measurements

The best-established diagnostic techniques to measure osteoporosis are currently those focusing on BMD, i.e., DXA (dual-energy X-ray absorptiometry) and QCT (quantitative computed tomography). A number of newer emerging techniques are QUS (quantitative ultrasound) and high-resolution tomographic techniques analyzing bone structure such as high-resolution magnetic resonance imaging (MRI) and computed tomography (CT).

Since BMD is the parameter which can be determined best in vivo, has a high precision, and correlates well with the biomechanically determined bone strength (it explains approximately 70% of bone strength (NIH Consensus Development Panel on Osteoporosis Prevention D, and Therapy 2001; Online NCS 2000)), the WHO defined osteoporosis on the basis of bone mineral density (WHO 1994). A bone mineral density (BMD) which is more than 2.5 standard deviations below that of a Caucasian, young, healthy female adult reference population (*T*-score) is defined as osteoporosis. A BMD which is 1–2.5 standard deviations below that of the young and healthy reference population is defined as osteopenia (Table 19.1). This definition, however, was originally only established for BMD of the proximal femur and later for BMD of the posterior-anterior lumbar spine determined using DXA, but has been applied to define diagnostic thresholds at other skeletal sites and for other technologies. Because of the difficulty in accurate measurement and standardization between instruments and sites, controversy exists among experts regarding the continued use of this diagnostic criterion (NIH Consensus Development Panel on Osteoporosis Prevention D, and Therapy 2001; Online NCS 2000). It is also not clear how to apply this diagnostic criterion across ethnic groups as well as to children and men.

BMD can be measured with a variety of different techniques. Photo-densitometry was one of the first quantitative techniques that was used to determine bone mass of the calcaneus, metacarpals, and phalanges (Heuck and Schmidt 1960). The so-called digital X-ray radiogrammetry (DXR) is a newer method, which automatically identifies regions in the radius, ulna, and three middle metacarpals and measures bone density (Rosholm et al. 2001). This method has a high precision and reliability and may be used in standard radiographs of the forearm to predict hip, vertebral, and wrist fracture risk (Bouxsein et al. 2002).

Single-photon absorptiometry (SPA) is another technique for measuring peripheral BMD, which uses a highly collimated photon beam from a radionuclide source (such as iodine-125) to measure photon attenuation (Vogel 1987). This technique measures BMD of the distal radius and the calcaneus; since SPA is a single energy technique, a standardized water bath is required. SPA has a high precision and low exposure dose, but the use of a radionuclide source is a limitation of this technique. The same applies to dual-photon absorptiometry (DPA), which may be used for the spine, hip, and total body due to the dual-energy technique (typically gadolinium-153 with energies of 44 and 100 keV), which reduces the soft tissue contribution substantially (Mazess and Wahner 1988). Again this technique has a high precision and a low exposure dose but the scanning time is relatively long. Due to isotope source changes, both, SPA and DPA, are at present of limited clinical significance and have been replaced by DXA, which uses an X-ray tube instead of a radionuclide source.

Table 19.1 WHO definition of osteoporosis according to the *T-score*

T-score ≤ -1	Normal
$-2.5 \leq$ *T-score* < 1	Osteopenia
T-score < -2.5	Osteoporosis
T-score ≤ -2.5 and fractures	Severe osteoporosis

Please note that this classification is only established for DXA (lumbar spine, proximal femur, and to some extent for the distal radius) in Caucasian postmenopausal women. *T-score* is defined as the standard deviation of the individual's BMD compared to a young normal reference population

Dual X-ray Absorptiometry (DXA)

As in DPA, the principle of DXA is a dual-energy measurement, which is based on the fact that radiation of distinct energies is attenuated by tissues to different extents. In both soft tissue and bone, a low-energy beam is attenuated to a greater degree than a high-energy beam. Contrast in attenuation between bone and soft tissue is greater for the low-energy beam than for the high-energy beam, such that the attenuation profile of bone may be determined by subtracting both the low- and high-energy attenuation profiles. Compared to DPA, DXA, however, has a number of advantages including an increased precision, a shorter examination time, a finer collimation with a better spatial resolution, and the lack of radionuclide source decay (Pacifici et al. 1988; Mazess and Barden 1988).

DXA scanners provide either pencil or fan beam techniques. Currently, most available scanners apply fan beam techniques, which have substantially faster examination times. Precision of DXA is high and radiation exposure is low (Table 19.2). Using DXA BMD is most frequently determined at the spine (posterior-anterior (pa) or lateral) (Fig. 19.1) and at the proximal femur (Fig. 19.2). Whole body measurements as well as measurements at the distal radius and the calcaneus may also be obtained. The pa examination of the lumbar spine is a standard procedure with a precision in vivo of 1%, a radiation exposure resp. effective dose of 1−50 μSv (the higher dose is required for digital high-resolution images), and a fairly high accuracy (4–10%) (Pacifici et al. 1988; Glüer et al. 1990; Mazess et al. 1989) (Table 19.2). For monitoring BMD, the precision alone, however, is not the only parameter required to assess the diagnostic performance of a technique. We also need to know the annual rate of BMD loss in normal patients using this technique as well as the least significant change between two measurements, which are 0.5–2% resp. 3% for the pa lumbar spine (Table 19.3).

Using an automated software areal BMD (g/cm^2) is determined usually in L1–L4. These projection images, however, have a number limitations: (1) vertebrae with a larger size have a

Table 19.2 Accuracy, precision, and radiation dose for osteodensitometric techniques

Technique	Measurement site	Accuracy (%)	Precision error (%)	Radiation exposure: effective dose (microSv)
1. *Older techniques*				
Photodensitometry	Finger	10	5	< 5
SPA/DPA	Lumbar spine	2–11	2–3	5
	Proximal femur	2–11	2–5	3
SXA	Radius/calcaneus	4–6	1–2	<1
Dual-energy QCT	Lumbar spine	3–6	4–6	~500[a]
2. *Standard techniques: axial skeleton*				
DXA	Lumbar spine			
	–PA	4–10	1	1–50[b]
	–Lateral	5–15	2–6	3–50[b]
	Proximal femur	6	1.5–3	~1–2[c]
	Whole body	3	1	~3[c]
QCT	Lumbar spine	5–15	1.5–4	60–500[d]
3. *Standard techniques: peripheral skeleton*				
DXA	Radius	4–6	1	< 1
pQCT	Radius	2–8	1–2	~ 1

[a]125 kVp/85 kVp and 410 mAs
[b]Low values apply for pencil beam scanners; using fan beam scanners, the effective dose is three to fivefold higher; depending on the image quality, radiation dose may increase substantially
[c]For pencil beam scanners
[d]60 μSv are obtained using a low-dose protocol (80 kV, 125 mAs)
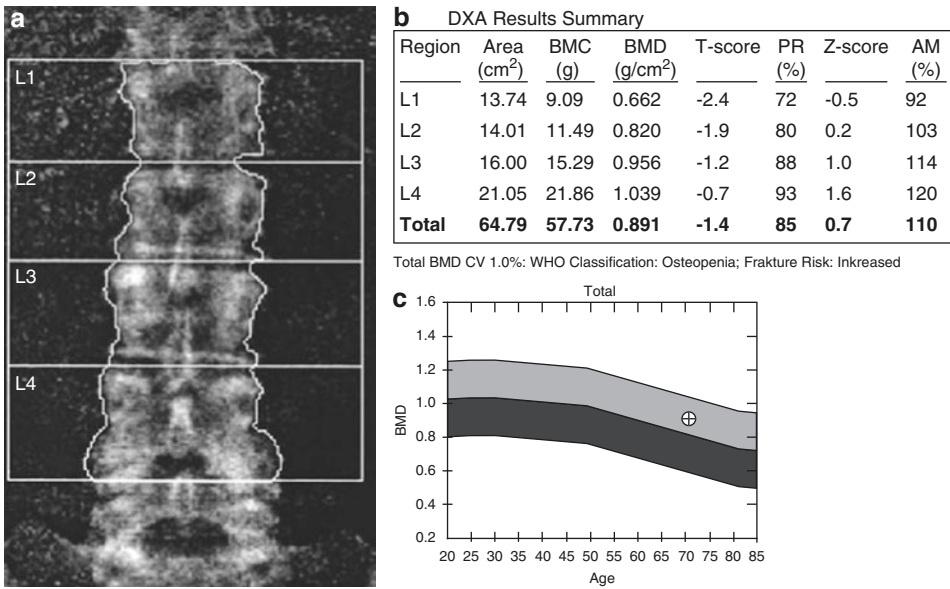
Fig. 19.1 (**a**–**c**) DXA of the lumbar spine, pa. Digital image (**a**) and bone mineral density analysis (**b**, **c**). The DXA result summary (**b**) lists the data for the individual and all vertebrae. This includes the area of the vertebrae, the bone mineral content (*BMC*) in g, and the areal BMD in g/cm². In addition, *T-score* and *Z*-score are listed. The Z-score is defined as the standard deviation compared to an age-matched normal reference population. Also percentages are given comparing data to a young and age-matched, normal reference population. (**c**) Shows the BMD data of the patient in relation to patient age and the normal BMD ranges for age and race
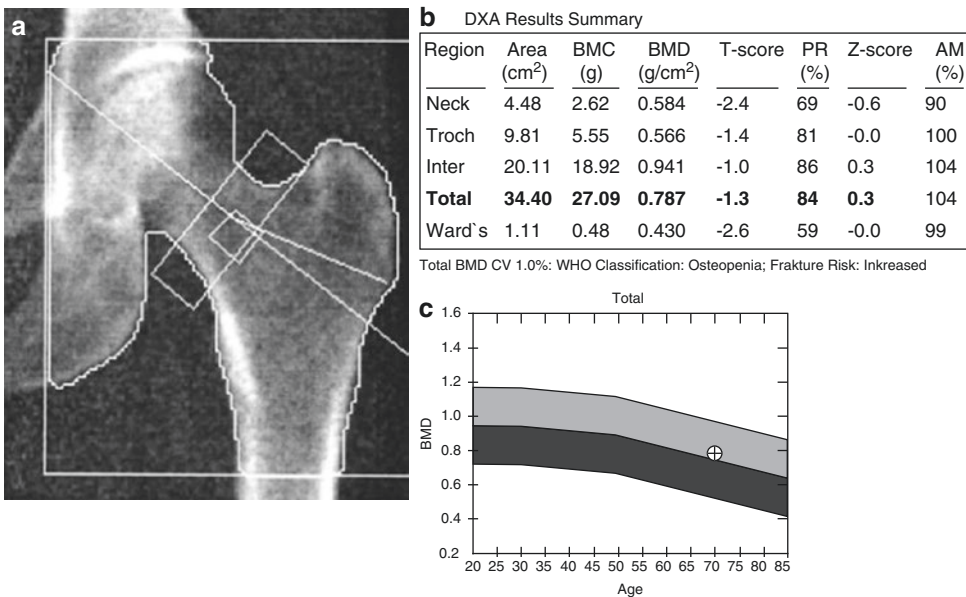
Fig. 19.2 (**a**–**c**) DXA of the proximal femur. Digital image with all ROIs (**a**) and bone mineral density analysis (**b**, **c**). The DXA result summary (**b**) lists the data for the neck, trochanteric, intertrochanteric, and Ward's ROIs. The total ROI consists of neck, trochanteric, and intertrochanteric ROIs. Ward's ROI is clinically not of significance. The area of the ROIs, bone mineral content (*BMC*) in g, and areal BMD in g/cm² are listed. In addition, *T*-score and *Z*-score are presented. (**c**) Shows the BMD data of the patient in relation to patient age and the normal BMD ranges for age and race

Table 19.3 Least significant change (LSC, defined as the smallest change in bone mineral density that can be diagnosed with statistical significance; this is calculated based on the precision error (CV, coefficient of variation) for longitudinal measurements using the equation: $LSC = 1.96\sqrt{2}\,CV$) and rate of bone loss for DXA and QCT (Prevrhal S, Genant HK (1999) Quantitative Computertomographie; Radiologe 39:194–202)

	LSC in %	Annual bone loss (%/year)
QCT	6–11	2–4
pQCT	3	1
DXA, pa lumbar spine	3–4	1–2
DXA, proximal femur	4–8	0.5–1

Fig. 19.3 DXA of the lumbar spine. Digital image shows degenerative changes of the facet joints along with mild right convex curvature, thus falsely increasing areal BMD: while at *L1*, a *T*-score of −2.0 is calculated (osteopenic) and a *T*-score of −0.4 is measured at *L4* (normal)

higher BMD, (2) aortic calcification and all other soft tissue calcifications in the ROIs increase BMD, and (3) degenerative changes of the spine including osteophytes, facet sclerosis, and degenerative disk disease may also falsely increase BMD (Fig. 19.3). In elderly patients with substantial degenerative changes of the lumbar spine, pa DXA of the lumbar spine therefore may not be a suitable technique. Lateral DXA is less influenced by these changes since it assesses only the vertebral bodies and thus focuses more on trabecular bone. However, drawbacks of this technique are a lower precision, a higher radiation exposure, and a superimposition of the pelvis and the ribs, which may limit analysis of the lumbar spine to L3 (Larnach et al. 1992; Rupich et al. 1990, 1992). So far, pa DXA is still the standard DXA procedure to assess the lumbar spine.

Analyzing DXA scans, a number of pitfalls have to be considered which may be operator dependent such as mislabeled vertebrae, misplaced disk space markers, wrong sized ROIs, and opaque artifacts in the analysis region. These analysis errors are of greater magnitude than the machine's intrinsic precision errors (Staron et al. 1999).

DXA of the proximal femur is a particularly important examination since it is currently one of the best techniques to assess fracture risk of the hip. The examination of the hip, however, is more demanding than that of the spine (Engelke et al. 1995). The proximal femur has to be positioned in a standardized fashion and a number of ROIs

have to be placed correctly. The correct location of these ROIs varies according to the manufacturer. Standard ROIs are the neck region, the trochanteric region, as well as the intertrochanteric region. The ROI, which is used most frequently, is the total femur and neck region. The diagnosis of osteoporosis and osteopenia at the hip should only be based on these two regions according to ISCD guidelines. The total femur ROI consists of the neck region, the trochanteric region, and the intertrochanteric region. Ward's triangle has an inferior precision compared to other ROIs and is currently not used as a standard ROI. The precision for hip BMD and the annual rate of loss are lower compared to pa lumbar spine, and the least significant change is higher (Tables 19.2 and 19.3).

As in DXA of the lumbar spine, a number of operator-dependent errors may occur in the proximal femur and should be detected by the radiologist (Staron et al. 1999; Theodorou and Theodorou 2002). Most of these errors are due to improper positioning of the patient and the ROIs. Correct

positioning of the patient includes internal rotation of the hip with a straight femoral shaft (the lesser trochanter should not or just barely be visualized). Correct positioning and size of the ROIs, in particular the neck box, may vary according to the manufacturer (e.g., Lunar/GE systems have a standardized size of the neck box which is placed automatically in the region of the neck with the smallest diameter). Osteoarthritis, Paget's disease, fracture, vascular calcifications, calcific tendinitis, enostosis, and avascular necrosis of the hip are also potential sources of error. Conventional radiographs may be required, if an atypical density profile is shown. If these lesions are too large or developmental dysplasia of the hip is found, BMD has to be determined at a different site.

An upper neck region has been introduced, which is supposed to predict the risk of femur neck fractures better than the complete neck ROI (Duboeuf et al. 1997; Boehm et al. 2005). Both the thickness and porosity in the upper neck region are believed to be critical to maintaining femoral strength. Also the upper neck region demonstrates a more rapid age-related decline than the standard femoral neck region (Crabtree et al. 2000). Dual femur measurements are recommended to reduce precision error and facilitate the evaluation of skeletal response at the femur (Faulkner et al. 1995; Bonnick et al. 1996).

According to the guidelines of the International Society of Clinical Densitometry (ISCD) (Baim et al. 2008), more than one vertebral body should be measured for a meaningful lumbar spine BMD examination; in other words, if three vertebral bodies have to be excluded from the analysis, this measurement should not be used for the classification of the patient according to WHO criteria. If DXA measurements at the lumbar spine and hip result in different classifications, the lowest T-score will be used to make the diagnosis. At the proximal femur, the lowest of the total femur and neck ROI T-score will be used to classify the patient according to WHO criteria.

In men older than 50 years, a diagnosis of osteoporosis can be made based on a T-score of <−2.5. In men younger than 50 years, Z-scores are preferred, and a diagnosis of osteoporosis should not be based on densitometric data alone (Baim et al. 2008). If a male under the age of 50 has a Z-score of <−2.0, terminology such as "BMD is below the expected range for age" should be used. The same applies for premenopausal females.

In children T-scores are not used to make a diagnosis of osteoporosis; instead, Z-scores are used. The Z-score is defined as the standard deviation of the individual patient in comparison to an age-matched normal reference population. If the Z-score is lower than −2.0, a diagnosis of "low density for chronological age" is made (Baim et al. 2008). A diagnosis of osteoporosis should not be made based on densitometric data alone. Also please note that Z-scores can only be used in patients with normal size and skeletal development. Adjustments for altered skeletal development may be made on the basis of bone age, which may derived from hand radiographs, but currently no standard recommendations for these adjustments are available.

Peripheral DXA

Peripheral DXA techniques include those analyzing the distal radius and the calcaneus. These techniques have a high precision and a low radiation exposure, but annual BMD loss at these sites is low, which is a potential limitation for monitoring BMD. Dedicated devices have been developed which are portable and inexpensive and have shorter scan times (Fordham et al. 2000). It has been shown that these techniques may be useful in assessing osteoporosis and fracture risk (Sweeney et al. 2002). In comparison with spine and hip DXA measurements, however, the peripheral BMD measurements are less suited to predict fracture risk of the spine and of the proximal femur. But they may be useful in reducing the cost of detection of osteoporosis and provide a greater opportunity for identification of women at risk of fracture (Fordham et al. 2000).

Figure 19.4 shows a DXA image of the distal radius. While a number of ROIs have been identified at the distal radius according to ISCD guidelines, the most relevant ROI is the one third radius (33% radius) ROI on the nondominant forearm

a

Radius	Area (cm^2)	BMC (g)	BMD (g/cm^2)	T-score	PR (%)	Z-score	AM (%)
UD	6.25	3.74	0.598	-2.4	64	-1.0	81
MID	14.25	6.07	0.426	-2.8	55	-2.1	61
1/3	25.46	20.32	0.798	-2.2	67	-1.3	77
TOTAL	**45.96**	**30.13**	**0.656**	**-2.5**	**63**	**-1.6**	**74**

Total BMD CV 1.0%: WHO Classification: Osteopenia; Fracture Risk: Increased
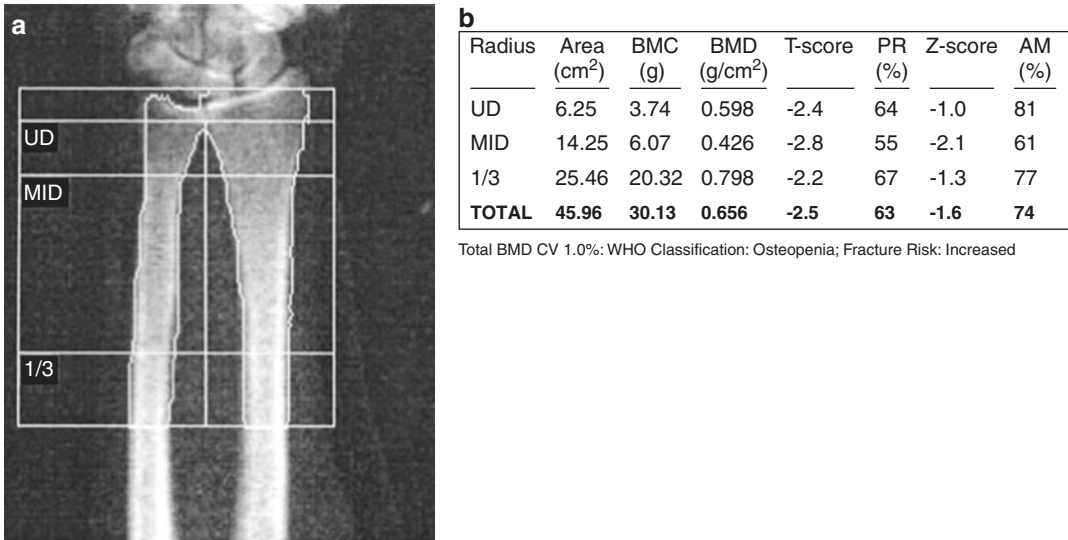
Fig. 19.4 (**a**, **b**) DXA of the distal radius. Digital image with all ROIs (**a**) and bone mineral density analysis (**b**). The DXA result summary (**b**) lists the BMD data for the ultradistal radius (*UD*) ROI, the midradius (*MD*) ROI, and the one third region (33%). The 33% ROI is the most important ROI and used for the diagnosis of osteoporosis. The area of the ROIs, bone mineral content (*BMC*) in g, and areal BMD in g/cm^2 are listed. In addition, *T*-score and *Z*-score are presented

(Baim et al. 2008). Only this ROI should be used to define osteoporosis or osteopenia in an individual patient according to WHO criteria. Peripheral DXA may be advisable if lumbar spine and proximal femur cannot be used, in patients with hyperparathyroidism and in very obese patients.

Geometric Measurements Derived from DXA Images

A number of geometric measurements have been identified at the hip, which may improve fracture risk prediction. Among these, the automated hip axis length measurement is probably the most significant as it is supposed to improve the prediction of proximal femur fracture (Reid et al. 1994; Peacock et al. 1995; Glüer et al. 1994; Faulkner et al. 1994) (Fig. 19.5). A 10% increase (1 cm) in hip axis length increases fracture risk by 50–80%. In addition, a previous study showed that the femur strength index calculated from DXA images may be an independent parameter of bone strength (Faulkner et al. 2006). Beck et al. developed measurements based on DXA images to calculate hip strength, which have been used in a number of previous studies (Beck et al. 1996, 1990; Nurzenski et al. 2007). None of these measurements, however, has been established for routine use.

Quantitative Computed Tomography (QCT)

Currently, 2D and 3D measurements are used for QCT. While 2D measurement is only used for the lumbar spine, 3D measurements may also be performed at the proximal femur (Fig. 19.6). Usually at the lumbar spine, the first to third lumbar vertebrae are analyzed. In contrast to DXA, QCT allows a true densitometric, volumetric, measurement (in mg/ml) of trabecular bone, while DXA gives an areal BMD (in mg/cm^2), which includes trabecular and cortical bone. Since trabecular bone has a substantially higher metabolic turnover, it is more sensitive to changes in BMD (annual rate of bone loss in QCT 2–4% versus 1% in pa DXA of the lumbar spine). A big advantage of QCT is that it is not as susceptible to
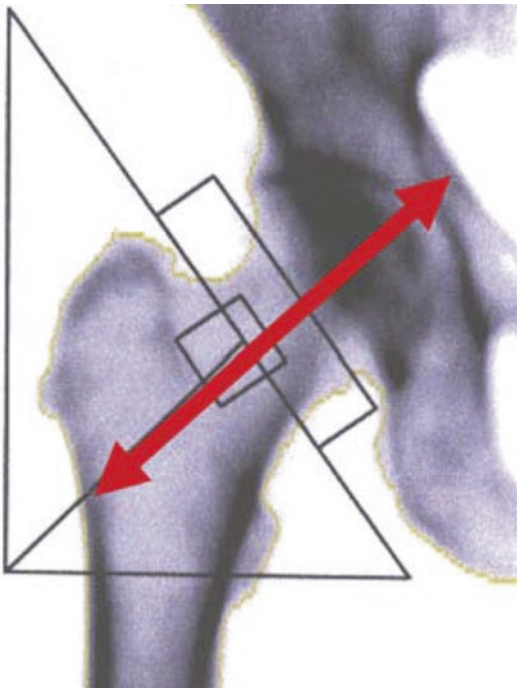
Fig. 19.5 Hip axis length measurement derived from DXA image

degenerative changes of the spine as DXA. Osteophytes and facet joint degeneration as well as soft tissue calcifications (in particular of aortic calcification) do not falsely increase BMD in QCT (Diederichs et al. 2011). As in DXA, however, fractured or deformed vertebrae must not be used for BMD assessment since these vertebrae usually have an increased BMD.

QCT may be performed at any CT system; however, a calibration phantom is usually used and dedicated software improves the precision of the examination. The patient is examined supine, lying on the phantom usually with a water or gel-filled cushion in between to avoid artifacts due to air gaps. Calibration phantoms are required to transform the attenuation measured in HU (Hounsfield units) into BMD (mg/ml). The patient and the phantom are examined at the same time, which is defined as simultaneous calibration. The Cann-Genant phantom with five cylindrical channels filled with K_2HPO_4 solutions (of known concentrations) was the first

phantom in clinical use (Genant et al. 1983; Cann and Genant 1980). However, due to the limited long-term stability of these solutions, solid-state phantoms with densities expressed in mg calcium hydroxyapatite/ml were developed, which do not change with time and are more resistant to damage. Two of the most frequently used phantoms include (1) the solid-state "Cann-Genant" phantom (Arnold 1989) (Fig. 19.6c) and (2) the phantom developed by Kalender et al. (Kalender et al. 1987; Kalender and Süss 1987) (Fig. 19.6b). The latter phantom has a small cross section and is constituted of only two density phases: a 200 mg/ml calcium hydroxy-apatite phase and a water equivalent phase.

2D QCT

Single mid-vertebral slice positions of L1–L3 parallel to the vertebral endplates are selected in the lateral digital radiograph resp. scout view (Fig. 19.6a). An automated software, selecting the mid-vertebral planes, may be useful to reduce the precision error (Kalender et al. 1988). Usually a slice thickness of 8–10 mm is used. A low-energy, low-dose protocol (e.g., 80 kVp and 120 mAs) is recommended to minimize radiation exposure (down to an effective dose of 50–60 μSv, including the digital radiograph) (Engelke et al. 2008). Bone marrow fat increases with age and may falsely decrease BMD. Thus, the actual BMD may be underestimated by 15–20%. Due to age-matched databases, however, the clinical relevance of this fat error is small (Glüer and Genant 1989). A dual-energy QCT technique was described to reduce the fat error. However, since this technique has an increased radiation exposure and a decreased precision, its use is limited to research purposes (Genant and Boyd 1977; Felsenberg and Gowin 1999).

A number of ROIs have been used to determine the BMD in the axial sections of the vertebral bodies. Manually placed elliptical ROIs and automated image evaluation with elliptical and peeled ROIs (Fig. 19.6b) have been described (Kalender et al. 1987; Steiger et al. 1990). The
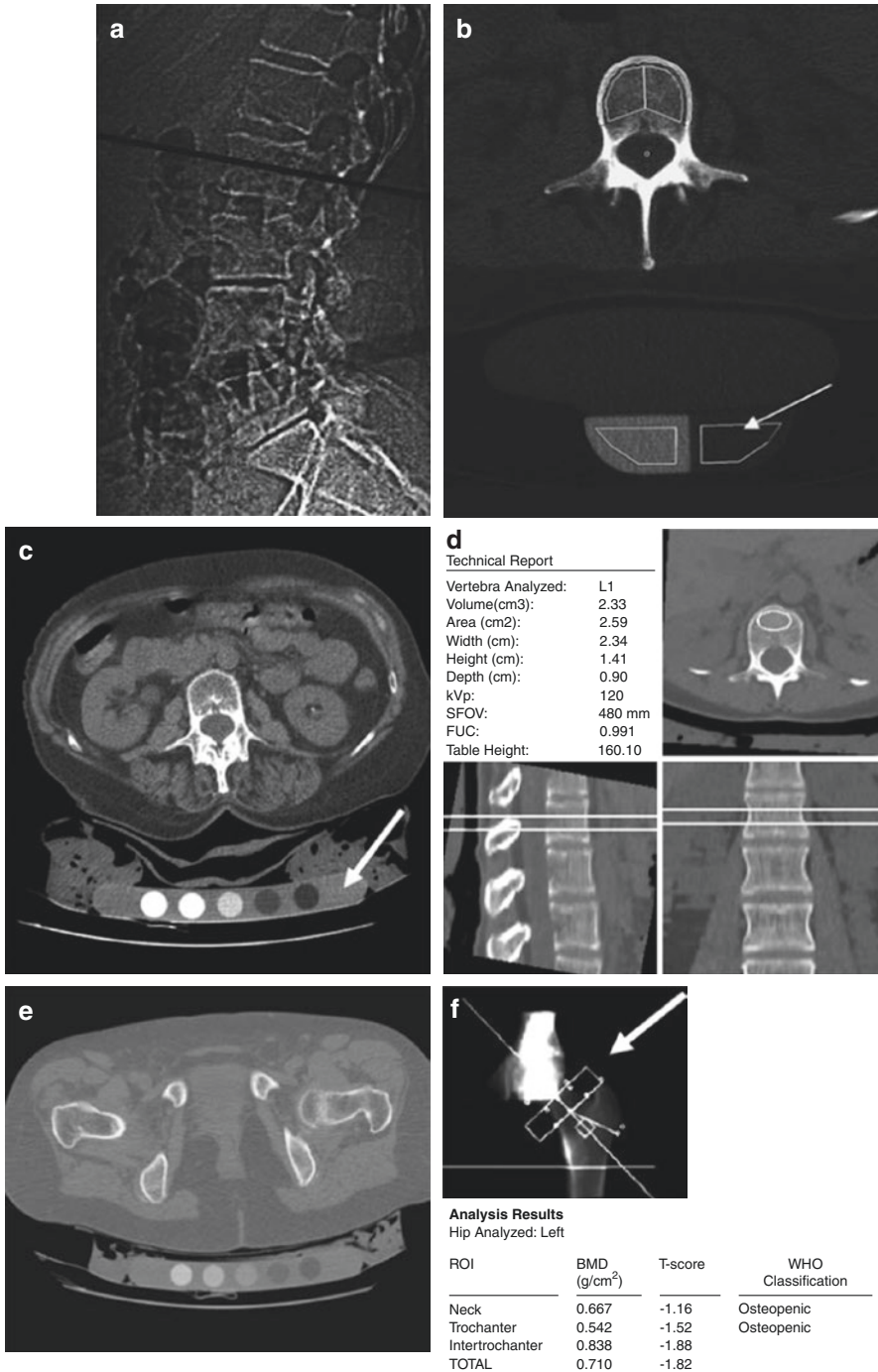
Fig. 19.6 (**a–f**) 2D QCT of the lumbar spine (**a**, **b**) and 3D QCT of the lumbar spine (**c**, **d**) and the proximal femur (**e**, **f**). In (**a**) a lateral digital radiograph of the lumbar spine is shown indicating a mid-vertebral slice position at L2 where (**b**) was obtained. In the single section of L2 (**b**), automated software is used to generate ROIs of the trabecular and cortical bone and the two element calibration phantom (*arrow*). Using the calibration phantom ROI densities, BMD is calculated for cortical and trabecular bone in L2. In (**c**) a section obtained from a volumetric QCT lumbar spine dataset is shown with a five-element calibration phantom (*arrow*). (**d**) Depicts the volumetric analysis of L1 BMD using an automated oval-shaped ROI. In (**e**) a section obtained from a volumetric QCT proximal femur dataset is shown with a five-element calibration phantom. (**f**) Depicts the BMD analysis of the proximal femur: from the volumetric dataset, a 2D image (*arrow*) is generated similar to a DXA image, and in this image, the same ROIs as in DXA are identified and BMD is measured. Since DXA- and QCT-derived measures are highly correlated, *T*-scores are used for this measurement

ROI developed by Kalender et al. uses an automatic contour tracking of the cortical shell to determine an ROI analyzing trabecular and cortical (as visualized by CT) BMD separately (Kalender et al. 1987). The use of automated ROIs improves the precision of BMD measurements (Kalender and Süss 1987; Sandor et al. 1985). Steiger et al. have shown that elliptical and peeled ROIs yield similar results and have an extremely high correlation ($r = 0.99$) (Steiger et al. 1990).

BMD data obtained by QCT are compared to an age-, sex-, and race-matched database (Kalender et al. 1989; Block et al. 1989). T-scores used for the assessment of osteoporosis according to the WHO definition have been established for DXA but not for QCT, though they may be given by the software of the manufacturers (Engelke et al. 2008). If these T-scores are used to diagnose osteoporosis, a substantially higher number of individuals compared to DXA will be diagnosed as osteoporotic, since BMD measured with QCT shows a faster decrease with age than DXA. Researchers have therefore advocated to use BMD measurements analogous to the WHO definition but with thresholds corresponding to lower T-scores (Felsenberg and Gowin 1999). According to the American College of Radiology Guidelines for the performance of QCT (2008), BMD values have been classified analogous to WHO criteria: 120–80 mg/ml are defined as osteopenic, while BMD values below 80 mg/ml are defined as osteoporotic, which corresponds to a T-score of approximately -3.0.

The big disadvantage of 2D QCT is its lower precision compared to that of DXA (1.5–4% versus 1%), and therefore significant longitudinal changes have to be substantially larger (6–11% versus 3%). However, since the metabolic activity of trabecular bone is higher, a lower precision is sufficient for QCT to monitor the same changes in longitudinal examinations as in DXA.

3D QCT

With spiral and multislice CT acquisition of larger bone volumes, such as entire vertebrae and the proximal femur, is feasible within a few seconds. These data sets can be used to obtain 3D images, which provide geometrical and volumetric density information. A drawback of these techniques, however, is a relatively high exposure dose, which has been estimated to be as high as 350 μSv for the spine and 1200 μSv for the hip using the software developed by Kalender et al. (1999). The primary advantage of volumetric QCT of the spine is an improved precision for trabecular BMD measurements, which was 1.3% as determined in an vivo study (Lang et al. 1999).

Algorithms to process volumetric CT images of the proximal femur and to measure bone mineral density in the femoral neck, the total femur, and the trochanteric regions are also available (Lang et al. 1997). Proximal femur 3D QCT has a high precision of 0.6–1.1% for trabecular bone and may also be used to determine geometric measures such as the cross-sectional area of the femur neck and the hip axis length. These measurements may be useful in optimizing fracture prediction of the proximal femur.

While WHO criteria are not applicable to volumetric QCT measurements of the lumbar spine, the American College of Radiology Guidelines for the performance of QCT (2008) are also used for 3D QCT as outlined above. One of the manufacturers also provided BMD ranges to quantify increase in fracture risk: a BMD of 110–80 mg/cc indicates a mild increase in fracture risk, BMD values of 50–80 mg/cc indicate a moderate increase in fracture risk, and a BMD lower than 50 mg/cc indicates a severe increase in fracture risk.

For the proximal femur, 3D datasets may be used to derive a projectional 2D image of the proximal femur, and in this image, standard DXA-equivalent ROIs may be placed (Fig. 19.6f). BMD values are determined in g/cm². Since the correlations between these calculated BMD values of the proximal femur and those obtained by DXA are extremely high, the WHO classification may be applied to those BMD values in postmenopausal, Caucasian females, but not to those of males. Thus a T-score <-2.5 derived from those datasets indicates osteoporotic BMD.

Peripheral QCT

Dedicated peripheral QCT (pQCT) scanners have been developed to assess the BMD of the distal radius (Butz et al. 1994). These scanners have a low radiation dose and a high precision with a short examination time but have the same limitations as peripheral DXA in the monitoring of patients with osteoporosis. While this technique is potentially suited to predict fracture risk, studies have shown the limitations of this technique in predicting spine fractures and proximal hip fractures compared to other bone densitometry techniques (Augat et al. 1998a, b; Grampp et al. 1997). More recently, high-resolution peripheral QCT scanners have been used to assess peripheral BMD and bone structure at the distal radius and tibia (Boutroy et al. 2005; Burghardt et al. 2010a, b).

19.3   Other Measurements to Quantify Bone Mineral

Radiographic Measurements

A number of radiographic measurement techniques for osteoporosis and other metabolic bone diseases have been used to better quantify bone mineral. This includes the Barnett-Nordin (Barnett and Nordin 1960) and metacarpal index (Nielsen 2001) at the hand, the Singh index at the proximal femur (Singh et al. 1970), and the Saville index as well as biconcavity index according to Nordin at the spine (Hermanutz et al. 1977). Most of these measurements only have a very limited role in the assessment of osteoporosis and are hampered by poor reproducibility (Singh index) as well as poor correlation with BMD measurements (Saville index).

The metacarpal index derived from radiographs has been used both clinically and in research studies. The metacarpal index may be determined in an automated fashion or manually (Dey et al. 2000). The measurements are performed at the second metacarpal of the diameter of the right hand. The outer and inner diameter of the metacarpal are measured at the midpoint of the metacarpal (Fig. 19.7), and the index is calculated using the following equation:

$$MCI = \frac{Outer - Inner\ Diameter}{Outer\ Diameter}$$

An MCI lower than 0.44 is considered as pathological. Previous studies have shown that this measurement is associated with risk factors of osteoporosis and that it predicts the risk of hip fractures (Haara et al. 2006). Another study found it comparable to peripheral assessment of skeletal status by forearm densitometry and a cheap and widely available noninvasive technique to assess skeletal status (Dey et al. 2000).

Mandibular measurements obtained from panoramic radiography of the maxilla and mandibula have also been used to semiquantitatively assess bone mineral status. Indices and scores have been developed that were used in a number of scientific studies with varying results (Devlin and Horner 2002; Halling et al. 2005). The Klemetti
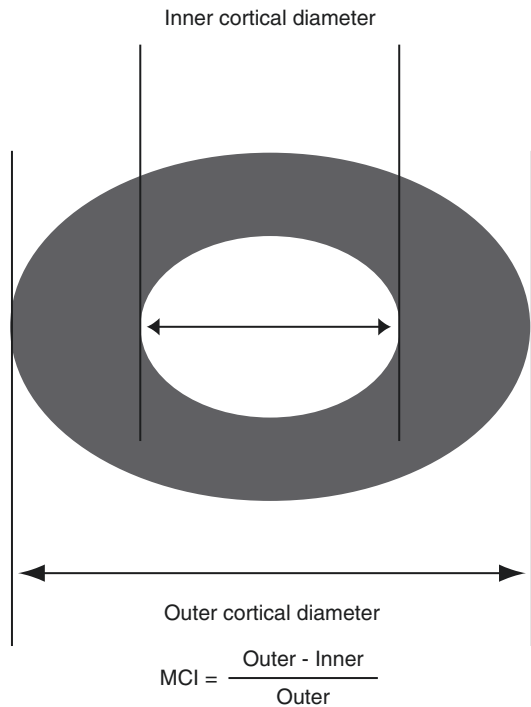
Fig. 19.7 Metacarpal index measurement obtained from hand radiographs at the second metacarpal of the right hand

index scores mandibular radiographs according to three grades: "0," normal (even and sharp endosteal margin of the mandibula); "1," moderately eroded (evidence of lacunar resorption or endosteal cortical residues); and "2," severely eroded (unequivocal porosity). In a previous study, this score was found useful in predicting reduced bone mineral density (Halling et al. 2005).

Quantitative Ultrasound

Quantitative ultrasound (QUS) techniques have been proposed for the assessment of osteoporosis, in particular at peripheral skeletal sites such as the calcaneus, tibia, and phalanges (Guglielmi et al. 2003; Hans et al. 1998, 1999; Njeh et al. 1997, 2001). The underlying basis of this method is based on the attenuation of sound waves as they pass through bone and the time taken for a sound wave to propagate through bone. A transducer is placed close to an easily accessible bone,

with very little soft tissue overlying it, and as the signal travels through the bone, it is attenuated. The attenuation increases with frequency, and the rate of attenuation over a given frequency range is measured and provides a measure of broadband ultrasonic attenuation or BUA. The speed of sound or SOS is also measured by many commercial ultrasound devices, and this measure provides the time it takes the sound waves to travel between two transducers.

The attenuation of the sound waves is reduced when the number of attenuating elements, in case of bone, and the number of trabeculae are reduced. The speed of sound is higher in normal bone than in osteoporotic bone. Given the fact that these parameters are not only affected by bone mass but also by the distribution of trabeculae within the bone, it has been suggested that this measurement also provides information on bone architecture. Ultrasound methods are attractive for the assessment of osteoporosis, as the cost of the equipment is low; there is no ionizing radiation and the equipment is portable. Initial scanners required the foot be immersed in a water bath; however, the newer systems are dry and employ an ultrasound gel for contact.

There have been large retrospective and prospective studies (Gluer et al. 2004) that have shown that QUS measures provide results comparable to BMD measures concerning prediction of hip fractures (Boonen and Nicholson 1998) and vertebral fractures (Knapp et al. 2001). The clinical issues associated with the reliability and reproducibility of the ultrasound measures include reproducible placement of the transducers and temperature variations of the foot. In order to improve the performance of this technique, rigorous quality assurance is required.

However, it should be considered that at present, quantitative ultrasonography is still no substitute for the gold standard test, DXA (Krieg et al. 2008). It cannot be used to diagnose osteoporosis or to monitor the effects of medications on BMD. A thorough understanding of the utility and limitations of this test is necessary for using it effectively in clinical practice (Krieg et al. 2008). As more data become available, however, it may play a larger role (Guglielmi et al. 2009).

Measurements of Bone Structure

Though still not part of the clinical workup, techniques to visualize trabecular bone architecture noninvasively have been developed to better understand bone strength. It is well known that bone strength is not only measured with bone mass or BMD but that also measurements of bone quality are required to better predict fracture risk (NIH Consensus Development Panel on Osteoporosis Prevention D, and Therapy 2001). Several high-resolution imaging modalities have been optimized to assess bone structure including MRI, multislice CT, and peripheral high-resolution pQCT (extreme CT). Investigators have also used conventional radiographs to better quantify trabecular bone architecture.

Radiographic Assessment

One of the early studies used lateral radiographs of the lumbar spine and determined Fourier transform and fractal analysis-based texture measures (Caligiuri et al. 1993, 1994). These investigators found that the texture measurements appeared more successful than BMD obtained with DXA in predicting the presence or absence of fractures elsewhere in the spine. Buckland-Wright et al. (1994) analyzed magnification radiographs of lumbar vertebrae in an experimental and clinical study using fractal signature analysis (FSA). Similar analysis by Link et al. (1996) using morphometric texture parameters and direct magnification radiographs has shown that texture measures may have some relevance in predicting biomechanical properties. In the study by Veenland et al. (1997) on direct magnification radiography of human cadaveric vertebrae, texture parameters based on mathematical morphology were assessed. Multivariate regression of fracture stress (FS) versus BMD and the textural parameters showed that, for the female vertebrae, a combination of one texture parameter and BMD gave a better prediction of fracture stress than BMD alone.

Several authors used calcaneus radiographs to analyze bone structure with fractal dimension. Lespessailles et al. (1993, 1998a; b) performed in vitro and in vivo studies and compared fractal dimension derived from a fractional Brownian

motion model with biomechanical stability, bone histomorphometry, and osteoporotic status. The authors found a significant correlation between this texture measure and biomechanical strength; however, BMD performed substantially better. Trabecular bone architecture was partially reflected by fractal dimension. The histomorphometry measures—trabecular spacing and trabecular number—correlated best with fractal dimension. In an in vivo study, Pothuaud et al. (1998) used the same technique and found significant differences between patients with osteoporotic spine fracture and age-matched controls. ROC analysis showed higher diagnostic performance in differentiating fracture and non-fracture patients for texture measures compared to BMD of the proximal femur (DXA).

Assessment from Three-Dimensional Tomographic Images

MRI: With the advent of higher field strength, phased array coils, and improved software and hardware, it has been possible to push the frontiers of magnetic resonance imaging. The three-dimensional imaging capability, along with the fact that MR is a nonionizing modality, makes it potentially very attractive as a tool for imaging trabecular bone structure. The marrow surrounding the trabecular bone network, if imaged at high resolution, reveals the trabecular network as seen in the representative image (Fig. 19.8).

The skeletal sites most commonly imaged with MRI are the radius (Link et al. 2002; Majumdar et al. 1996; Newitt et al. 2005, 2002; Wehrli et al. 1998) and calcaneus (Link et al. 2002, 1998; Lin et al. 1998; Majumdar et al. 1993). The distal radius is a site with a large quantity of trabecular bone and a common site for osteoporotic fractures. It is easily accessible with localized surface (detection) coils, and subjects are able to comfortably tolerate immobilization for the period required for high-resolution imaging. Calcaneus, although not a typical site for osteoporotic fractures, has been used with success to predict fracture at other sites, and this skeletal site is well adapted to high-resolution MR imaging. The phalanges have recently been of increased interest as a site for bone density
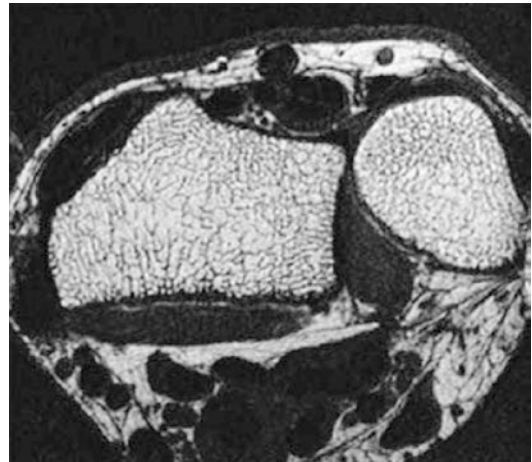
Fig. 19.8 High-resolution MRI of the distal radius used to calculate structure measurements of trabecular bone architecture

measurement (Jara et al. 1993; Kuehn et al. 1997) and can also be imaged by high-resolution MR imaging. Recent studies also focused on MR imaging of tibial bone architecture (Wehrli et al. 2004), and feasibility studies at the proximal femur have been performed (Krug et al. 2005).

CT: New multislice CT (MS-CT) scanners are now clinically available that provide higher spatial resolutions and thus allow better depiction of the trabecular bone structure in vivo. Initial clinical studies have been performed, and Ito et al. showed that vertebral microarchitecture can be visualized by MS-CT, and microstructure parameters obtained by MS-CT, together with volumetric BMD, provided better diagnostic performance for assessing fracture risk than DXA measurement (Ito et al. 2005).

For dedicated assessment of trabecular and cortical bone architecture in the distal tibia and radius in vivo, a new high-resolution peripheral CT scanner is now available with isotropic spatial resolution and a voxel size of 82 μm^3. Using this system, the first published study found that postmenopausal women had lower density, trabecular number, and cortical thickness than premenopausal women ($P < 0.001$) at both radius and tibia (Boutroy et al. 2005). Furthermore, it was found, although spine and hip BMD were similar, that fractured osteopenic women had lower trabecular density and more heterogeneous trabecular distri-

bution ($P < 0.02$) at the radius compared with unfractured osteopenic women. The authors concluded that clinical, peripheral microCT is a promising technique to assess microarchitecture at peripheral sites providing insight in age- and disease-related changes. The precision of these measurements was 2.5–4.4% for trabecular architecture parameters (Boutroy et al. 2005). Representative images of the distal tibia obtained with this device are shown in Fig. 19.9.

One of the main issues associated with extending the CT technology to image trabecular bone structure in vivo in humans lies in the trade-off

between radiation exposure and spatial resolution. The higher the spatial resolution of images required, the greater the exposure to radiation. However, despite this need to balance these two factors, the peripheral prototypes were successful in achieving excellent visualization of the trabecular structure (Boutroy et al. 2005). Clinical MS-CT imaging of more central areas of the skeleton such as the spine and the proximal femur, however, may be more challenging.

Bone Structure Analysis Algorithms

Multiple different image processing and image analysis algorithms have been developed to measure bone structure in high-resolution MRI or CT datasets. The goal of all of these is to quantify the trabecular bone structure in two or three dimensions. The measures that have been derived so far are many; some of them are synonymous with the histomorphometric measures such as trabecular bone volume fraction (BV/TV), trabecular thickness (Tb.Th), trabecular spacing (Tb.Sp), and trabecular number (Tb.N); and others include connectivity or Euler number, fractal dimension, tubularity, and maximal entropy.
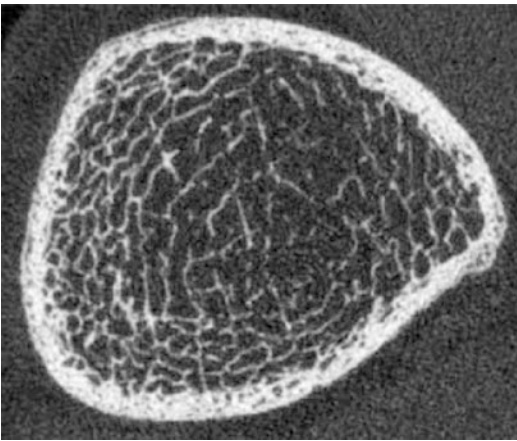
Fig. 19.9 High-resolution peripheral QCT of the distal tibia in a postmenopausal patient. From these datasets, measurements of 3D trabecular and cortical bone structure are calculated

19.4   Measurements of Fracture and Deformity at the Spine

Osteoporosis-related vertebral fractures have important health consequences for older women, including disability and increased mortality (Ensrud et al. 2000). Because these, fractures can be prevented with appropriate medications, and recognition and treatment of high-risk patients are warranted. In a cross-sectional survey, Gehlbach et al. (2000) analyzed 934 women aged 60 years and older who were hospitalized and had a chest radiograph obtained. Moderate or severe vertebral fractures were identified for 132 (14.1%) study subjects. But only 50% of the contemporaneous radiology reports identified a fracture as present, and only 17 (1.8%) of the 934 participants had a discharge diagnosis of vertebral fracture. Relatively few hospitalized older women with radiographically demonstrated vertebral fractures were thus identified or treated by clinicians. The results of this study should increase the awareness of the radiologist in diagnosing vertebral fractures. The presence of one vertebral fracture increases the risk of any subsequent vertebral fracture fivefold (Melton et al. 1999), and 20% of the women that had a recent diagnosis of a fracture will sustain a new fracture within the next 12 months (Lindsay et al. 2001).

Since most vertebral fractures do not come to clinical attention, the radiographic diagnosis is particularly important. Unfortunately, there is no universal definition of what constitutes an osteoporotic fracture in a radiograph of the lumbar or thoracic spine. Usually, the anterior or central part of the vertebral body is affected and shows deformation; if the posterior part is affected, a malignant cause of fracture should always be considered first. Assessing the deformity, it has to be considered that there are frequently differences in height between the anterior and posterior part of vertebral body of approximately 1–3 mm at the thoracic spine, less pronounced at the lumbar spine. Therefore, a difference in height of 4 mm between posterior versus central and anterior part of the vertebra is suspicious for a fracture deformity. Based on a large number of osteoporosis studies, Genant et al. (1993) defined an osteoporotic fracture as a deformity of more than 20%. According to their semiquantitative (SQ) score, the severity of vertebral fractures may be visually determined from radiographs (Genant et al. 1993) (Fig. 19.10). In this score 4 grades are differentiated: grade 0, no fracture; grade 1, mild fracture (reduction in vertebral height 20–25%, compared to adjacent normal vertebrae); grade 2, moderate fracture (reduction in height 25–40%); and grade 3, severe fracture (reduction in height more than 40%). The

Fig. 19.10 SQ score for osteoporotic vertebral deformities according to Genant et al. (1993). An osteoporotic fracture is defined as a deformity >20% of the anterior, central, or posterior part of the vertebra. Please note, however, that the first differential diagnosis in posterior deformities is metastatic bone disease

T4–L4 vertebrae are analyzed and 0.5, 1.5, and 2.5 scores are also possible. A definite fracture is defined as a score ≥1. Figure 19.11 shows examples of different grades of osteoporotic fractures in the thoracic and lumbar spine in postmenopausal patients.

A number of other scores have been developed such as the "spine deformity index" and the "radiological vertebral index" (Leidig-Bruckner et al. 1994; Minne et al. 1988; Meunier et al. 1978), but these scores are less frequently used:

1. Spine Deformity Index (Leidig-Bruckner et al. 1994; Minne et al. 1988): This technique uses the anterior, central, and posterior height of T4 as a standard since this vertebral body is rarely affected by osteoporotic fractures. The heights measured at T5–L5 are divided by the corresponding heights of T4 and summarized for all vertebrae. This measurement constitutes "vertebral deformity index."
2. Radiological Vertebral Index (Meunier et al. 1978): The T3–L4 vertebral bodies are analyzed, and each vertebral body is scored as (1) normal vertebral shape, (2) biconcave shape, and (3) wedge-shaped vertebral body with more pronounced deformity. The individual scores are summarized and divided by the number of vertebral bodies. In this score, the severity of the fracture is not assessed.
3. Barnett-Nordin Index (Barnett and Nordin 1960): This score is derived from the central and anterior height of L3 and L4. However, given the fact that only two vertebral bodies are assessed, this score has limited significance.

Conventional radiographs of the spine are not suited to quantify bone loss in the early diagnosis of osteoporosis since it takes a bone loss of more than 20–40% before an osteoporosis is visualized in the radiographs (Lachmann and Whelan 1936). Morphological signs described on spine radiographs such as a coarse trabecular structure and a frame-like appearance of the vertebrae are also not very reliable (Doyle et al. 1967) and are not clinically used any more.

Conventional radiographs, however, are important in the differential diagnosis of osteoporosis since a number of other diseases may present with bone loss and fractures (Link et al. 2005). In rare cases, osteoporosis may present with a coarse trabecular structure with thick ver-

Fig. 19.11 (**a**, **b**) Radiographs of the thoracic (**a**) and the lumbar spine (**b**) with osteoporotic fractures. T9 is fractured (wedge-shaped deformity) in (**a**) and the L1–L4 vertebrae show central height loss in (**b**)
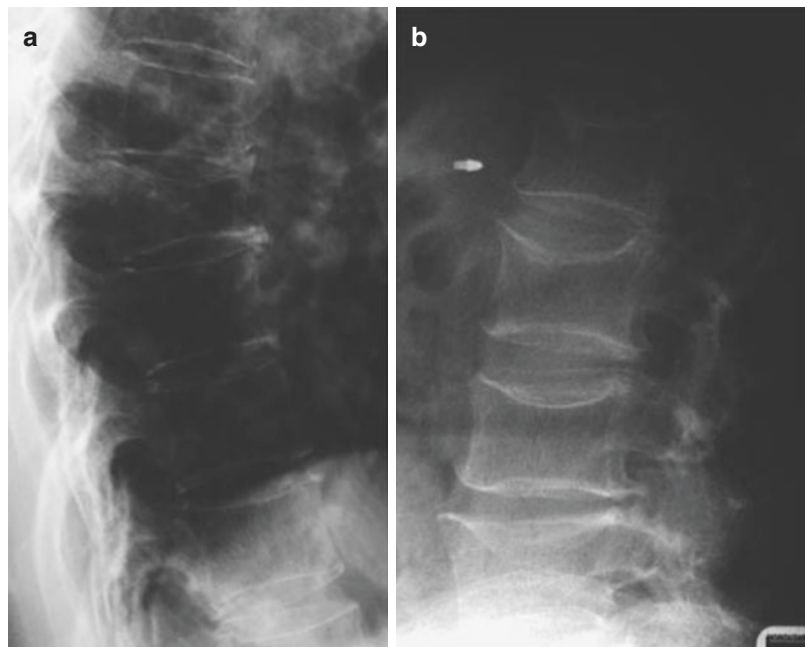
tical trabeculae suggestive of vertebral hemangioma. This so-called hypertrophic atrophy, however, is generalized, and the trabecular bone structure appears more coarser than in hemangioma. Important differential diagnoses in osteoporosis are osteomalacia, hyperparathyroidism, renal osteopathia, and of course malignant bone marrow disorders such as multiple myeloma and diffuse metastatic disease. Vertebral deformities are found in Scheuermann's disease as well as due to traumatic fractures and malignant lesions. Degenerative disease can also be characterized by mild wedge-shaped deformities of the vertebral bodies, but usually these deformities are less than 20%.

Conclusion

Measurements in osteoporosis and metabolic diseases are of significant impact for diagnosis and monitoring of disease stage. Standard measurements are performed by means of DXA at the proximal femur and spine; other sites and techniques are not standardly used but may have specific indications. Low-cost measurement techniques that may be used if DXA is not available include hand radiographs and ultrasound. Radiographs of the lumbar spine are useful to quantify/measure osteoporosis, but the presence of an osteoporotic fracture may be used for the diagnosis of the disease. Different definitions of what constitutes an osteoporotic fracture are available as well as the grading of its severity. The most established definition to diagnose an osteoporotic fracture uses a deformity of ≥20% as a threshold. It should be noted that the radiologist has a crucial role in identifying and monitoring patients with osteoporosis and therefore needs to be familiar with quantitative and semi-quantitative measurements of bone mass and strength (Link and Adams 2009).

References

Arnold B (1989) Solid phantom for QCT bone mineral analysis. Proceedings of the seventh international workshop on bone densitometry, Palm Springs, California, 17–21 Sep 1989

Augat P, Fan B, Lane N, Lang T, LeHir P, Lu Y et al (1998a) Assessment of bone mineral at appendicular sites in females with fractures of the proximal femur. Bone 22:395–402

Augat P, Fuerst T, Genant H (1998b) Quantitative bone mineral assessment at the forearm: a review. Osteoporos Int 8:299–310

Baim S, Binkley N, Bilezikian JP, Kendler DL, Hans DB, Lewiecki EM et al (2008) Official positions of the International Society for clinical densitometry and executive summary of the 2007 ISCD Position Development Conference. J Clin Densitom 11(1):75–91

Barnett E, Nordin B (1960) The radiological diagnosis of osteoporosis: a new approach. Clin Radiol 11:166–174

Beck TJ, Ruff CB, Warden KE, Scott WW Jr, Rao GU (1990) Predicting femoral neck strength from bone mineral data. A structural approach. Investig Radiol 25(1):6–18

Beck TJ, Ruff CB, Mourtada FA, Shaffer RA, Maxwell-Williams K, Kao GL et al (1996) Dual-energy X-ray absorptiometry derived structural geometry for stress fracture prediction in male U.S. Marine Corps recruits. J Bone Miner Res 11(5):645–653

Block J, Smith R, Glüer CC, Steiger P, Ettinger B, Genant HK (1989) Models of spinal trabecular bone loss as determined by quantitative computed tomography. J Bone Miner Res 4:249–257

Boehm HF, Eckstein F, Wunderer C, Kuhn V, Lochmueller EM, Schreiber K et al (2005) Improved performance of hip DXA using a novel region of interest in the upper part of the femoral neck: in vitro study using bone strength as a standard of reference. J Clin Densitom 8(4):488–494

Bonnick S, Nichols D, Sanborn C, Payne S, Moen S, Heiss C (1996) Right and left proximal femur analyses: is there a need to do both? Calcif Tissue Int 58:307–310

Boonen S, Nicholson P (1998) Assessment of femoral bone fragility and fracture risk by ultrasonic measurements at the calcaneus. Age Ageing 27(2):231–237

Boutroy S, Bouxsein ML, Munoz F, Delmas PD (2005) In vivo assessment of trabecular bone microarchitecture by high-resolution peripheral quantitative computed tomography. J Clin Endocrinol Metab 90(12):6508–6515

Bouxsein M, Palermo L, Yeung C, Black D (2002) Digital X-ray radiogrammetry predicts hip, wrist and vertebral fracture risk in elderly women: a prospective analysis from the study of osteoporotic fractures. Osteoporos Int 13:358–365

Buckland-Wright JC, Lynch J, Rymer J, Fogelman I (1994) Fractal signature analysis of macroradiographs measures trabecular organization in lumbar vertebrae of postmenopausal women. Calcif Tissue Int 54:106–112

Burghardt AJ, Buie HR, Laib A, Majumdar S, Boyd SK (2010a) Reproducibility of direct quantitative measures of cortical bone microarchitecture of the distal radius and tibia by HR-pQCT. Bone 47(3):519–528

Burghardt AJ, Issever AS, Schwartz AV, Davis KA, Masharani U, Majumdar S et al (2010b) High-resolution peripheral quantitative computed tomographic imaging of cortical and trabecular bone microarchitecture in patients with type 2 diabetes mellitus. J Clin Endocrinol Metab 95(11):5045–5055

Butz S, Wüster C, Scheidt-Nave C, Götz M, Ziegler R (1994) Forearm BMD as measured by peripheral quantitative computed tomography (pQCT) in a German reference population. Osteoporos Int 4:179–184

Caligiuri P, Giger M, Favus M, Jia H, Doi K, Dixon L (1993) Computerized radiographic analysis of osteoporosis: preliminary evaluation. Radiology 186(2):471–474

Caligiuri P, Giger ML, Favus M (1994) Multifractal radiographic analysis of osteoporosis. Med Phys 21(4):503–508

Cann C, Genant H (1980) Precise measurement of vertebral mineral content using computed tomography. J Comput Assist Tomogr 4:493–500

Crabtree N, Lunt M, Holt G, Kroger H, Burger H, Grazio S et al (2000) Hip geometry, bone mineral distribution, and bone strength in European men and women: the EPOS study. Bone 27:151–159

Devlin H, Horner K (2002) Mandibular radiomorphometric indices in the diagnosis of reduced skeletal bone mineral density. Osteoporos Int 13(5):373–378

Dey A, McCloskey EV, Taube T, Cox R, Pande KC, Ashford RU et al (2000) Metacarpal morphometry using a semi-automated technique in the assessment of osteoporosis and vertebral fracture risk. Osteoporos Int 11(11):953–958

Diederichs G, Engelken F, Marshall LM, Peters K, Black DM, Issever AS et al (2011) Diffuse idiopathic skeletal hyperostosis (DISH): relation to vertebral fractures and bone density. Osteoporos Int 22(6):1789–1797

Doyle F, Gutteridge D, Joplin G, Fraser R (1967) An assessment of radiologic criteria used in the study of spinal osteoporosis. Br J Radiol 40:241–250

Duboeuf F, Hans D, Schott A, Kotzki P, Favier F, Marcelli C et al (1997) Different morphometric and densitometric parameters predict cervical and trochanteric hip fracture: the EPIDOS Study. J Bone Miner Res 12:1895–1902

Engelke K, Glüer CC, Genant HK (1995) Factors influencing short-term precision of dual x-ray bone absorptiometry (DXA) of spine and femur. Calcif Tissue Int 56:19–25

Engelke K, Adams JE, Armbrecht G, Augat P, Bogado CE, Bouxsein ML et al (2008) Clinical use of quantitative computed tomography and peripheral quantitative computed tomography in the management of osteoporosis in adults: the 2007 ISCD Official Positions. J Clin Densitom 11(1):123–162

Ensrud K, Thompson D, Cauley J, Nevitt M, Kado D, Hochberg M et al (2000) Prevalent vertebral deformities predict mortality and hospitalization in older

women with low bone mass. Fracture Intervention Trial Research Group. J Am Geriatr Soc 48(3):241–249

Faulkner KG, McClung M, Cummings SR (1994) Automated evaluation of hip axis length for predicting hip fracture. J Bone Miner Res 9(7):1065–1070

Faulkner K, Genant H, McClung M (1995) Bilateral comparison of femoral bone density and hip axis length from single and fan beam DXA scans. Calcif Tissue Int 56:26–31

Faulkner KG, Wacker WK, Barden HS, Simonelli C, Burke PK, Ragi S et al (2006) Femur strength index predicts hip fracture independent of bone density and hip axis length. Osteoporos Int 17(4):593–599

Felsenberg D, Gowin W (1999) Knochendichtemessung mit Zwei-Spektren-Methoden. Radiologe 39:186–193

Fordham J, Chinn D, Kumar N (2000) Identification of women with reduced bone density at the lumbar spine and femoral neck using BMD at the os calcis. Osteoporos Int 11:797–802

Gehlbach S, Bigelow C, Heimisdottir M, May S, Walker M, Kirkwood J (2000) Recognition of vertebral fracture in a clinical setting. Osteoporos Int 11:577–582

Genant HK, Boyd DP (1977) Quantitative bone mineral analysis using dual energy computed tomography. Investig Radiol 12:545–551

Genant HK, Cann CE, Pozzi-Mucelli RS, Kanter AS (1983) Vertebral mineral determination by quantitative computed tomography: clinical feasibility and normative data. J Comput Assist Tomogr 7:554

Genant HK, Wu CY, van Kuijk C, Nevitt MC (1993) Vertebral fracture assessment using a semiquantitative technique. J Bone Miner Res 8:1137–1148

Glüer C, Genant H (1989) Impact of marrow fat in accuracy of quantitative CT. J Comput Assist Tomogr 13:1023–1035

Glüer CC, Steiger P, Selvidge R, Elliesen-Kliefoth K, Hayashi C, Genant HK (1990) Comparative assessment of dual-photon-absorptiometry and dual-energy-radiography. Radiology 174:223–228

Glüer CC, Cummings SR, Pressman A, Li J, Glüer K, Faulkner KG et al (1994) Prediction of hip fractures from pelvic radiographs: the study of osteoporotic fractures. J Bone Miner Res 9(5):671–677

Gluer CC, Eastell R, Reid DM, Felsenberg D, Roux C, Barkmann R et al (2004) Association of five quantitative ultrasound devices and bone densitometry with osteoporotic vertebral fractures in a population-based sample: the OPUS Study. J Bone Miner Res 19(5):782–793

Grampp S, Genant H, Mathur A, Lang P, Jergas M, Takada M et al (1997) Comparisons of noninvasive bone mineral measurements in assessing age-related loss, fracture discrimination, and diagnostic classification. J Bone Miner Res 12:697–711

Guglielmi G, Njeh CF, de Terlizzi F, De Serio DA, Scillitani A, Cammisa M et al (2003) Palangeal quantitative ultrasound, phalangeal morphometric variables, and vertebral fracture discrimination. Calcif Tissue Int 72(4):469–477

Guglielmi G, Adams J, Link TM (2009) Quantitative ultrasound in the assessment of skeletal status. Eur Radiol 19(8):1837–1848

Haara M, Heliovaara M, Impivaara O, Arokoski JP, Manninen P, Knekt P et al (2006) Low metacarpal index predicts hip fracture: a prospective population study of 3,561 subjects with 15 years of follow-up. Acta Orthop 77(1):9–14

Halling A, Persson GR, Berglund J, Johansson O, Renvert S (2005) Comparison between the Klemetti index and heel DXA BMD measurements in the diagnosis of reduced skeletal bone mineral density in the elderly. Osteoporos Int 16(8):999–1003

Hans D, Njeh CF, Genant HK, Meunier PJ (1998) Quantitative ultrasound in bone status assessment. Rev Rhum Engl Ed 65(7-9):489–498

Hans D, Srivastav SK, Singal C, Barkmann R, Njeh CF, Kantorovich E et al (1999) Does combining the results from multiple bone sites measured by a new quantitative ultrasound device improve discrimination of hip fracture? J Bone Miner Res 14(4):644–651

Hermanutz KD, Beck KJ, Franken T (1977) Radiological observations on bone changes in women after bilateral ovariectomy with and without oestrogen prophylaxis (author's transl). Rofo 126(6):546–550

Heuck F, Schmidt E (1960) Die quantitative Bestimmung des Mineralgehalts des Knochens aus dem Röntgenbild. Fortschr Röntgenstr 93:523–554

Ito M, Ikeda K, Nishiguchi M, Shindo H, Uetani M, Hosoi T et al (2005) Multi-detector row CT imaging of vertebral microstructure for evaluation of fracture risk. J Bone Miner Res 20(10):1828–1836

Jara H, Wehrli F, Chung H, Ford J (1993) High-resolution variable fliple angle 3D MR imaging of trabecular microstructure in vivo. Magn Reson Med 29:528–539

Kalender WA, Süss C (1987) A new calibration phantom for quantitative computed tomography. Med Phys 9:816–819

Kalender WA, Klotz E, Süss C (1987) Vertebral bone mineral analysis: an integrated approach. Radiology 164:419–423

Kalender W, Brestowsky H, Felsenberg D (1988) Bone mineral measurements: automated determination of the mitvertebral CT section. Radiology 168:219–221

Kalender W, Felsenberg D, Louis O, Lopez P, Klotz E, Osteaux M et al (1989) Reference values for trabecular and cortical vertebral bone density in single and dual-energy quantitative computed tomography. Euro J Radiol 9:75–80

Kalender W, Schmidt B, Zankl M, Schmidt M (1999) A PC program for estimating organ dose and effective dose values in computed tomography. Eur Radiol 9:555–562

Knapp KM, Blake GM, Spector TD, Fogelman I (2001) Multisite quantitative ultrasound: precision, age- and menopause-related changes, fracture discrimination, and T-score equivalence with dual-energy X-ray absorptiometry. Osteoporos Int 12(6):456–464

Krieg MA, Barkmann R, Gonnelli S, Stewart A, Bauer DC, Del Rio BL et al (2008) Quantitative ultrasound in the management of osteoporosis: the 2007 ISCD Official Positions. J Clin Densitom 11(1):163–187

Krug R, Banerjee S, Han ET, Newitt DC, Link TM, Majumdar S (2005) Feasibility of in vivo structural anal-

ysis of high-resolution magnetic resonance images of the proximal femur. Osteoporos Int 16(11):1307–1314

Kuehn B, Stampa B, Heller M, Glueer C (1997) In vivo assessment of trabecular bone structure of the human phalanges using high resolution magnetic resonance imaging. Osteoporos Int 7:291

Lachmann E, Whelan M (1936) The roentgen diagnosis of osteoporosis and its limitations. Radiology 26:165–177

Lang T, Keyak J, Heitz M, Augat P, Lu Y, Mathur A et al (1997) Volumetric quantitative computed tomography of the proximal femur: precision and relation to bone strength. Bone 21:101–108

Lang T, Li J, Harris S, Genant H (1999) Assessment of vertebral bone mineral density using volumetric quantitative CT. J Comput Assist Tomogr 23:130–137

Larnach TA, Boyd SJ, Smart RC, Butler SP, Rohl PG, Diamond TH (1992) Reproducibility of lateral spine scans using dual energy x-ray absorptiometry. Calcif Tissue Int 51:255–258

Leidig-Bruckner G, Genant HK, Minne HW, Storm T, Thamsborg G, Bruckner T et al (1994) Comparison of a semiquantitative and a quantitative method for assessing vertebral fractures in osteoporosis. Bone 15(4):437–442

Lespessailes E, Benhamou C, Touliere D (1993) Fractal evaluation of trabecular bone microarchitecture of calcaneus: study of reproducibility. J Bone Miner Res 8:264

Lespessailles E, Jullien A, Eynard E, Harba R, Jacquet G, Ildefonse J et al (1998a) Biomechanical properties of human os calcanei: relationships with bone density and fractal evaluation of bone microarchitecture. J Biomech 31:817–824

Lespessailles E, Roux J, Benhamou C, Arlot M, Eynard E, Harba R et al (1998b) Fractal analysis of bone texture on os calcis radiographs compared with trabecular microarchitecture analyzed by histomorphometry. Calcif Tissue Int 63:121–125

Lin JC, Amling M, Newitt DC, Selby K, Srivastav SK, Delling G et al (1998) Heterogeneity of trabecular bone structure in the calcaneus using magnetic resonance imaging. Osteoporos Int 8(1):16–24

Lindsay R, Silverman S, Cooper C, Hanley D, Barton I, Broy S et al (2001) Risk of new vertebral fracture in the year following a fracture. JAMA 285:320–323

Link TM, Adams JE (2009) The radiologist's important roles and responsibilities in osteoporosis. Eur J Radiol 71(3):385–387

Link T, Majumdar S, Lin J, Newitt D, Konermann W, Meier N et al (1996) Texture analysis of magnification radiographs in correlation with compressive strength of human vertebrae and bone mineral density. J Bone Miner Res 11(S1):S475

Link TM, Majumdar S, Augat P, Lin JC, Newitt D, Lu Y et al (1998) In vivo high resolution MRI of the calcaneus: differences in trabecular structure in osteoporosis patients. J Bone Miner Res 13(7):1175–1182

Link TM, Vieth V, Matheis J, Newitt D, Lu Y, Rummeny EJ et al (2002) Bone structure of the distal radius

and the calcaneus vs BMD of the spine and proximal femur in the prediction of osteoporotic spine fractures. Eur Radiol 12(2):401–408

Link TM, Guglielmi G, van Kuijk C, Adams JE (2005) Radiologic assessment of osteoporotic vertebral fractures: diagnostic and prognostic implications. Eur Radiol 15(8):1521–1532

Majumdar S, Genant H, Gies A, Guglielmi G (1993) Regional variations in trabecular structure in the calcaneus assessed using high resolution magnetic resonance images and quantitative image analysis. J Bone Miner Res 8S:351

Majumdar S, Newitt D, Mathur A, Osman D, Gies A, Chiu E et al (1996) Magnetic resonance imaging of trabecular bone structure in the distal radius: relationship with X-ray tomographic microscopy and biomechanics. Osteoporos Int 6(5):376–385

Mazess RB, Barden HS (1988) Measurement of bone by dual-photon absorptiometry (DPA) and dual-energy x-ray absorptiometry (DEXA). Ann Chir Gyn 77:197–203

Mazess RB, Wahner HM (1988) Nuclear medicine and densitometry. In: Riggs BL, Melton LJI (eds) Osteoporosis: etiology, diagnosis, and management. Raven Press, New York, pp 251–295

Mazess RB, Collick B, Trempe J, Barden H, Hanson J (1989) Performance evaluation of a dual energy x-ray bone densitometer. Calcif Tissue Int 44:228–232

Melton LR, Atkinson E, Cooper C, O'Fallon W, Riggs B (1999) Vertebral fractures predict subsequent fractures. Osteoporos Int 10:214–221

Meunier P, Bressot C, Vignon E, Edouard C, Alexandre C, Coupron P et al (1978) Radiological and histological evolution of post-menopausal osteoporosis treated with sodium fluoride-vitamin D-calcium. Preliminary results. Hans Huber Publishers, Bern

Meunier P, Delmas P, Eastell R, McClung M, Papapoulos S, Rizzoli R et al (1999) Diagnosis and management of osteoporosis in postmenopausal women: clinical guidelines. International Committee for Osteoporosis Clinical Guidelines. Clin Ther 21:1025–1044

Minne H, Leidig G, Wüster C, Siromachkostov L, Baldauf G, Bickel R et al (1988) A newly developed spine deformity index (SDI) to quantitate vertebral crush fractures in patients with osteoporosis. Bone Miner 3:335–349

Mueller D, Isbary M, Boehm H, Bauer J, Rummeny E, Link T (2004) Recognition of osteoporosis-related vertebral fractures on chest radiographs in postmenopausal women. RSNA Nov 28 to Dec 04 2004. Chicago. p 305

Muller D, Bauer JS, Zeile M, Rummeny EJ, Link TM (2008) Significance of sagittal reformations in routine thoracic and abdominal multislice CT studies for detecting osteoporotic fractures and other spine abnormalities. Eur Radiol 18(8):1696–1702

Newitt DC, van Rietbergen B, Majumdar S (2002) Processing and analysis of in vivo high-resolution MR images of trabecular bone for longitudinal stud-

ies: reproducibility of structural measures and micro-finite element analysis derived mechanical properties. Osteoporos Int 13(4):278–287

Newitt DC, Hyun B, Black DM, Rosen CJ, Majumdar M (2005) Use of MRI of the distal radius to assess qualitative and quantitative aspects of cortical bone in postmenopausal women. J Bone Miner Res 20(Suppl 1):S119

Nielsen SP (2001) The metacarpal index revisited: a brief overview. J Clin Densitom 4(3):199–207

NIH Consensus Development Panel on Osteoporosis Prevention D, and Therapy (2001) Osteoporosis prevention, diagnosis, and therapy. JAMA 285: 785–795

Njeh CF, Boivin CM, Langton CM (1997) The role of ultrasound in the assessment of osteoporosis: a review. Osteoporos Int 7(1):7–22

Njeh CF, Chen MB, Fan B, Grigorian M, Shepherd JA, Saeed I et al (2001) Evaluation of a gel-coupled quantitative ultrasound device for bone status assessment. J Ultrasound Med 20(11):1219–1228

Nurzenski MK, Briffa NK, Price RI, Khoo BC, Devine A, Beck TJ et al (2007) Geometric indices of bone strength are associated with physical activity and dietary calcium intake in healthy older women. J Bone Miner Res 22(3):416–424

Online NCS (2000) Osteoporosis prevention, diagnosis, and therapy. JAMA 17(1):1–36

Pacifici R, Rupich R, Vered I, Fischer KC, Griffin M, Susman N et al (1988) Dual energy radiography (DER): a preliminary comparative study. Calcif Tissue Int 43:189–191

Peacock M, Turner C, Liu G, Manatunga A, Timmerman L, Johnston CJ (1995) Better discrimination of hip fracture using bone density, geometry and architecture. Osteoporos Int 5:167–173

Pothuaud L, Lespessailles E, Harba R, Jennane R, Royant V, Eynard E et al (1998) Fractal analysis of trabecular bone texture on radiographs: discriminant value in post menopausal osteoporosis. Osteoporos Int 8:618–625

Reid I, Chin K, Evans M, Jones J (1994) Relation between increase in length of hip axis in older women between 1950s and 1990s and increase in age specific rates of hip fracture. BMJ 309:508–509

Riggs B, Melton LR (1995) The worldwide problem of osteoporosis: insights afforded by epidemiology. Bone 17:505S–511S

Rosholm A, Hyldstrup L, Backsgaard L, Grunkin M, Thodberg H (2001) Estimation of bone mineral density by digital X-ray radiogrammetry: theoretical background and clinical testing. Osteoporos Int 12:961–969

Rupich R, Pacifici R, Griffin M, Vered I, Susman N, Avioli LV (1990) Lateral dual energy radiography: a new method for measuring vertebral bone den-sity: a preliminary study. J Clin Endocrinol Metab 70(6):1768–1770

Rupich RC, Griffin MG, Pacifici R, Avioli LV, Susman N (1992) Lateral dual-energy radiography: artifact error from rib and pelvic bone. J Bone Miner Res 7(1):97–101

Sandor T, Kalender WA, Hanlon WB, Weissman BN, Rumbaugh C (1985) Spinal bone mineral determination using automated contour detection: application to single and dual—energy CT. SPIE Med Imaging Instrum 555:188–194

Schwartz AV (2003) Diabetes mellitus: does it affect bone? Calcif Tissue Int 73(6):515–519

Singh YM, Nagrath AR, Maini PS (1970) Changes in trabecular pattern of the upper end of the femur as an index of osteoporosis. J Bone Joint Surg 52-A(3):457–467

Staron R, Greenspan R, Miller T, Bilezikian J, Shane E, Haramati N (1999) Computerized bone densitometric analysis: operator-dependent errors. Radiology 211:467–470

Steiger P, Block J, Steiger S (1990) Spinal bone mineral density measured with quantitative CT: effect of region of interest, vertebral level and techniques. Radiology 175:537–543

Sweeney A, Malabanan A, Blake M, Weinberg J, Turner A, Ray P et al (2002) Bone mineral density assessment: comparison of dual-energy X-ray absorptiometry measurements at the calcaneus, spine, and hip. J Clin Densitom 5:57–62

Theodorou D, Theodorou S (2002) Dual-energy X-ray absorptiometry in clinical practice: application and interpretation of scans beyond the numbers. Clin Imaging 26:43–49

Veenland J, Link T, Konermann W, Meier N, Grashuis J, Gelsema E (1997) Unraveling the role of structure and density in determining vertebral bone strength. Calcif Tissue Int 61:474–479

Vogel JM (1987) Application principles and technical considerations in SPA. In: Genant HK (ed) Osteoporosis update 1987. Radiology Research and Education Foundation, San Francisco, pp 219–231

Wehrli F, Hwang S, Ma J, Song H, Ford J, Haddad J (1998) Cancellous bone volume and structure in the forearm: noninvasive assessment with MR micro-imaging and image processing. Radiology 206: 347–357

Wehrli FW, Leonard MB, Saha PK, Gomberg BR (2004) Quantitative high-resolution magnetic resonance imaging reveals structural implications of renal osteo-dystrophy on trabecular and cortical bone. J Magn Reson Imaging 20(1):83–89

WHO (1994) Technical report: assessment of fracture risk and its application to screening for postmenopausal osteoporosis: a report of a WHO study group. World Health Organization, Geneva, Switzerland

Bone Marrow Disease

20

Andrea Baur-Melnyk and Tobias Geith

Contents

A. Baur-Melnyk, M.D. (✉) • T. Geith, M.D. (✉)
Department of Radiology, University Hospital,
LMU Munich, Germany
e-mail: andrea.baur@med.uni-muenchen.de;
tobias.geith@med.uni-muenchen.de

Abstract

The bone marrow consists of active red marrow and inactive fatty marrow which is mainly situated in the extremities. Red marrow can be replaced by various conditions. Focal disease is easy to perceive; however, diffuse disease is often hard to detect. Gadolinium application can help for quantification of contrast enhancement. Based on the results of a control cohort, the enhancement of normal bone marrow showed great variations between 3% and 40%, mean 17% (in adults age >40 years). In patients with multiple myeloma, mean enhancement is significantly higher >40 Vol.%. Other diseases with stimulation of red marrow can simulate diffuse disease and also lead to an increase of contrast enhancement. Therefore the clinical background is of great importance when interpreting such exams. Quantitative whole-body MRI with ADC analysis might be a feasible diagnostic tool to assess the short-term treatment response in myeloma patients.

Measurements have also been performed for therapy control in patients with Gaucher's disease. Gaucher's disease is a disease of the reticuloendothelial system. The reduction of the fat cell content, which reflects the severity of the disease, can be measured quantitatively by the chemical shift method. A semiquantitative method is the BMB score, which is a combination of scoring systems of the peripheral skeleton and the axial bone marrow component in

patients with Gaucher's disease. It incorporates both the visual interpretation of the signal intensities and the geographic location of the disease on conventional MR images of the spine and femur.

Dynamic contrast-enhanced MRI (DCE-MRI) has the potential to noninvasively assess the microvascular structure of bone marrow. In patients with acute myeloid leukemia in complete remission, K_{ep} (efflux rate constant) measured with tracer kinetic modeling represents the contrast exchange between blood plasma and extravascular extracellular space. It is thought that bone marrow vessels and their endothelium should be normalized with reduced vessel wall permeability in complete remission, and therefore show low values of K_{ep}. Increased values for K_{ep} may indicate a high risk of relapse and were associated with shorter overall survival and relapse-free survival, as could be shown in an initial study.

A sometimes challenging question is the differentiation of acute osteoporotic and malignant vertebral fractures. In uncertain cases, quantitative diffusion-weighted imaging and chemical shift imaging can provide additional features to overcome the diagnostic limitations of morphologic signs in MRI.

20.1 Introduction

Magnetic resonance imaging (MRI) allows for a visualization of bone marrow components concerning fat and water-bound protons. In adults hematopoietically active "red marrow" is located in the central skeleton (spine, pelvis, proximal femur and humeri, thoracic cage, and the skull), while inactive fatty "yellow marrow" is located in the distal parts of the extremities and the epi- and apophysis. Normal red marrow has intermediate to high signal intensity on T1-w SE images, high signal intensity on T2-w TSE images, and low signal intensity on fat-suppressed images (e.g., STIR). This is consistent with the composition of red bone marrow by ~40% fat and ~40% water. Yellow marrow is predominantly composed by fat cells and collagen fibers and shows strongly high signal intensity on T1-w SE, T2-w TSE images and low signal intensity on fat-suppressed images.

Bone marrow can be replaced or infiltrated by various benign and malignant disease states (Plecha 2000). This can happen in a focal or a diffuse fashion. Focal disease is shown by focal low signal intensity on T1-w SE and usually high signal intensity on T2-w SE and fat-suppressed images. Neoplastic focal marrow infiltration can be due to metastases, myeloma, lymphoma, and primary malignant bone tumors. Benign focal marrow replacement can be due to hemangiomas (typical/atypical), focal fat islands or hematopoietic islands without fatty components within red marrow or in the periphery of the skeleton (Vande Berg et al. 2005). Focal disease is easy to perceive due to the high contrast to normal marrow. Measurements are usually not necessary.

It is much harder to detect diffuse marrow alterations. Diffuse neoplastic infiltration can be due to metastases, myeloma, lymphoma, leukemia, chronic myeloproliferative disease, and myelodysplastic syndrome. Benign diffuse signal alterations can be due to stimulated marrow: increased need for erythrocytes in, e.g., hemolytic anemia and chronic bleeding; increased need of leukocytes, e.g., in sepsis or chronic inflammations; or stimulated marrow due to drugs (e.g., erythropoietin, granulocytic growth factor, early status post chemotherapy). Since MRI cannot differentiate between water-bound protons in neoplastic cells or hematopoietic cells, MRI is unspecific and should only be interpreted in conjunction with exact clinical information (Nobauer and Uffmann 2005).

20.2   Myeloma

Since diffuse marrow infiltration is sometimes hard to detect, measurements concerning gadolinium enhancements have been performed. Multiple myeloma is a disease which shows diffuse infiltration in about 30–40% of cases. According to the amount of marrow replacement, the signal on T1-w SE images is reduced. In cases of high-grade diffuse involvement (>50 Vol.% in bone marrow biopsy), the signal intensity is nearly equal to the signal intensity of the intervertebral disc or muscle on T1-weighted SE images due to the increase of water and decrease of fatty components. In cases of intermediate grade of involvement in biopsy (20–50 Vol.%), the signal reduction is only moderate and often hard to diagnose.

Based on the results of a control cohort, the enhancement of normal bone marrow showed great variations between 3% and 40%, mean 17% (in adults age >40 years) (Baur et al. 1997) (Fig. 20.1). This is explained mainly by the variations of the fat cell content in normal marrow interindividually and the changes that occur during aging with an increase of fat. Patients with lower fat content, mainly younger patients, show a stronger gadolinium enhancement than individuals with a higher fat cell content. In another study gadolinium enhancement was correlated to

Fig. 20.1 Contrast enhancement in percentage. Interindividual variability of percentage of contrast enhancement in bone marrow in 87 healthy subjects

the grading of diffuse infiltration, neovascularization of bone marrow, and the fat/hematopoietic cell content in myeloma (Baur et al. 2004). In myeloma patients with an intermediate- or high-grade diffuse infiltration of the bone marrow, mean enhancement was significantly higher than in normal bone marrow ($p < 0.0001$). Also in patients with low-grade diffuse infiltration, gadolinium enhancement was significantly higher than in normal bone marrow ($p < 0.01$) but showed a strong overlap with normal bone marrow (Table 20.1). As a simple rule it can be stated that if the percentage increase of signal exceeds the limit of 40% in patient older than 40 years, this can be considered as pathologic. The reasons for increased enhancement in diffuse infiltration by myeloma were an increased microvessel density, increased cellularity, and a decreased fat cell content (Vacca et al. 1994; Aguayo et al. 2000; Rajkumar et al. 2000; Baur et al. 2004). The fluent transitions of the plasma cell content, the fat cell content and the microvessel density, as well as the fact that all three parameters contribute to contrast enhancement explain that no definite cutoff values can be found for contrast uptake in diffuse infiltrating multiple myeloma. In addition, the percentage signal increase after gadolinium administration does not reflect an absolute value of perfusion, since the contrast media diffuses quickly into the extracellular space.

To measure the gadolinium enhancement of the bone marrow, the MRI examination protocol should include sagittal T1-weighted SE sequences without fat saturation before and after intravenous gadopentetate dimeglumine (Gd-DTPA) administration (0.1 mmol/kg body weight, 0.2 ml/kg). The contrast medium should be given as a bolus injection followed by a saline flush. Scan parameters on the pre- and post-contrast T1-weighted SE sequences have to be identical; the values for receiver and transmitter adjustments have to be kept constant.
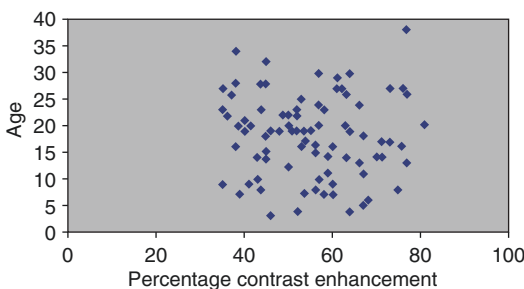
Table 20.1 Gadolinium enhancement in normal bone marrow and diffuse myeloma infiltration

Gadolinium enhancement	Normal marrow (%)	Low (%)	Intermediate (%)	High grade (%)
Mean enhancement	18	25	49	90
Standard deviation	8	10	19	30
Range	3–38	10–44	19–94	62–165

SI measurements should be made with circular region of interests placed in three vertebral bodies of the lumbar spine. The mean value should be calculated from the three measurements to compensate for SI differences within the bone marrow depending on changes in the ROI's position. Avoid placing the ROI's in midsagittal slices with basivertebral veins. The ROIs have to be placed in identical positions of the vertebral body on T1-weighted images before and after injection of contrast material (Fig. 20.2). The percentage SI increase is calculated as follows:

$$\text{Volume} = 4/3\pi \left(d/2\right)^3$$

Previous studies in patients with lymphoproliferative disease demonstrated that *dynamic gadolinium-enhanced MRI* can distinguish malignant from normal bone marrow. In the study of Moulopoulos, focal infiltration of the bone marrow in various malignancies was examined (Moulopoulos et al. 2003). Mean wash-in and washout rates and the ratio between wash in and time to maximum slope were significantly higher in areas with focal infiltration than in controls. The study population of Rahmouni et al. comprised a mixture of 31 patients with multiple myeloma and Non-Hodgkin's and Hodgkin's lymphoma (Rahmouni et al. 2003). Maximum enhancement, slope, and washout on dynamic turbo fast low-angle shot sequences were significantly different for patients with bone marrow involvement versus controls. Time to maximum enhancement did not differ significantly. The enhancement time curve values increased with increasing bone marrow involvement grades.

With the introduction of anti-angiogenetic therapy contrast enhancement may play a role in monitoring disease status. First results of a clinical histological study in patients with multiple myeloma showed that the mean microvessel density was significantly lower in patients after chemotherapy in responders as opposed to non-responders. The progression-free survival was significantly longer than in patients without a decrease in microvessel density (Sezer et al. 2001).

Horger et al. examined the feasibility of whole-body diffusion-weighted MRI in the short-term evaluation of response to treatment in multiple myeloma patients using a single-shot EPI sequence in 12 patients using *b*-values of 50, 400, and 800 s/mm^2. Eleven patients were classified as responders and one as non-responder. DWI results accurately (100%) correlated with disease course according to standard clinical and laboratory criteria. At baseline, all lesions showed restricted diffusion; in responders ADC values had an increase of 63.9% (range -8.7–211.3%), while the non-responder had a decrease of 7.8% during therapy. In parallel, M-gradient measurement showed a mean decrease of 45.1% (range, 19.6–88.8%) in responders and an increase of 21.8% in the non-responder. Amplitude of response measured by the course of ADC values proved higher in the appendicular skeleton (99.8%) compared with the axial skeleton (54.3%) ($p = 0.037$). These initial results show that quantitative whole-body MRI with ADC analysis might be a feasible diagnostic tool to assess the short-term treatment response in myeloma patients (Horger et al. 2011).
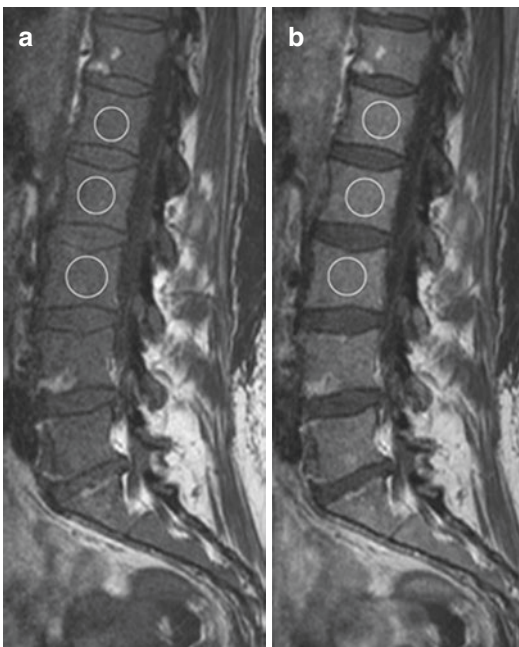
Fig. 20.2 T1-w SE image (TR/TE 572 ms/15 ms) pre- and post-contrast in a patient with diffuse infiltration by myeloma. The regions have to be placed in identical positions in lumbar vertebral bodies. Mean signal intensity increase can be calculated. An increase of more than 40% in adults (>40 years) is indicative of diffuse infiltration

20.3 Infectious Spondylitis

The typical pattern of infectious spondylitis is a hyperintense signal on T2-w images of the intervertebral disc, an early destruction of the adjacent vertebral endplates, and a vertebral bone marrow edema. Paravertebral and epidural extension, abscesses, and enhancement of the intervertebral disc, bone marrow, and surrounding granulation tissue may be associated. A study in patients with infectious spondylitis showed that systemic reactive marrow changes can simulate diffuse neoplastic infiltration similar to myeloma or chronic myeloproliferative diseases (Stabler et al. 2000). Due to a stimulation of leucopoiesis, the fat cell content in the bone marrow of the spine above and below the level of spondylitis is consecutively reduced. This leads to a decrease in signal on T1-w SE images, an increase on STIR images. Patients with infectious spondylitis showed a significantly higher mean enhancement of 28.2% (SD 12.2) when compared to a control group (mean enhancement 17.5%, SD 7.9, $p < 0.001$). This reactive bone marrow stimulation with increased gadolinium uptake occurred in 27% of patients with infectious spondylitis. Measurements were performed in the same way as described in patients with myeloma.

Another approach is the use of quantitative diffusion-weighted imaging. Pui et al. showed, that the mean ADC values of the bone marrow of 69 tuberculous ($1.15 \pm 0.39 \times 10^{-3}$ mm^2/s), 9 pyogenic ($1.30 \pm 0.45 \times 10^{-3}$ mm^2/s), and 50 malignant (1.02×10^{-3} mm^2/s) vertebral fractures were significantly higher, compared to normal vertebral marrow. Malignant bone marrow showed significantly lower ADC values than the ADCs of pyogenic infection or tuberculosis. No significant difference could be shown between adult ($1.15 \pm 0.42 \times 10^{-3}$ mm^2/s) and pediatric ($1.14 \pm 0.36 \times 10^{-3}$ mm^2/s) tuberculous lesions or between tuberculosis and pyogenic infection. For distinguishing infection from malignancy, they showed quite a low sensitivity, specificity, and accuracy of 60.26%, 66.00%, and 62.50%, using the cutoff ADC of $\geq 1.02 \times 10^{-3}$ mm^2/s. The overlap between ADC values for malignancy (probably due to different content of cells, protein, calcifications, or cytoplasm) and inflammation (probably due to different content of cells, mucoid protein, necrotic tissue, microorganisms, and pus) limited the usefulness of diffusion MRI in differential diagnosis, which was not able to obviate biopsy. But the sensitivity, specificity, and accuracy increased to 94.12%, 82.35%, and 90.20%, respectively, when there were associated soft tissue lesions with a cutoff ADC of $\geq 1.17 \times 10^{-3}$ mm^2/s (Pui et al. 2005).

20.4   Gaucher's Disease

Measurements have also been performed for therapy control in patients with Gaucher's disease. Gaucher's disease is a disease of the reticuloendothelial systems with a lack of the enzyme glucocerebrosidase. Glucocerebrosides accumulate in the reticuloendothelial system (bone marrow, liver, spleen, and lymph nodes). The infiltration of the bone marrow with Gaucher's cells leads to cell necrosis, fibrous proliferation, and resorption of bony trabeculae. The fat content of red marrow is reduced. In x-rays osteonecrosis and diffuse osteopenia can be found. In MRI the signal is diffusely reduced on T1-w SE images. In contrast to myeloma or leukemia, the signal is not increased on fat-suppressed images. The epi- and apophysis remain excluded of the process.

Quantitative Measurements Using the Chemical Shift Method

The reduction of the fat cell content, which reflects the severity of the disease, can be measured quantitatively by the chemical shift method. Dixon described a method to quantify the fat signal fraction by separating the individual signals from water and fat, F_f, hence Dixon quantitative chemical shift imaging (Dixon QCSI) (Dixon 1984). The QCSI technique has been explored in Gaucher's disease (Akkerman and Maas 1995; Hollak et al. 2001). The measured mean values in the lumbar spine (L3–L5) in healthy volunteers ranged from 0.27 to 0.55 (mean 0,37). In Gaucher's patients, the mean values ranged from 0.08 to 0.40 (mean 0.20). Bone complications, like bone crisis, fractures, and osteonecrosis, occur more often in patients with low fat fractions (<0.20), reflecting advanced disease (Maas et al. 2002).

A coronal measurement slice (if necessary slightly tilted to transversal) is set out on a sagittal localizer image, such that the posterior parts of the vertebrae of interest are optimally visualized (Fig. 20.3). The measurement is acquired using a surface coil. Two sets of acquisitions are performed, one of which the water signal (W) and the fat signal (F) are "in-phase" ($I = W + F$). In the second acquisition, fat and water have opposed phases ($O = |W - F|$). In order to separate the water and fat signals, the phase difference between the two acquisitions helps to sort out regions with water-dominant signal and regions with fat-dominant signal. With the help of the sign image, water and fat images are obtained by simple algebraic manipulations. For the water image (W), we have $W = I + S \cdot O$ and for the fat image (F) we have $F = I - S \cdot O$. The fat fraction is described on a color-coded scale range from 0 (no fat) to 1 (all fat). The mean value of the vertebral bodies L3, L4, and L5 is the final fat fraction (Fig. 20.4).

Semiquantitative Measurements with the Bone Marrow Burden Score (BMB)

The BMB score is a combination of scoring systems of the peripheral skeleton and the axial bone marrow component (Maas et al. 2003). It incorporates both the visual interpretation of the signal
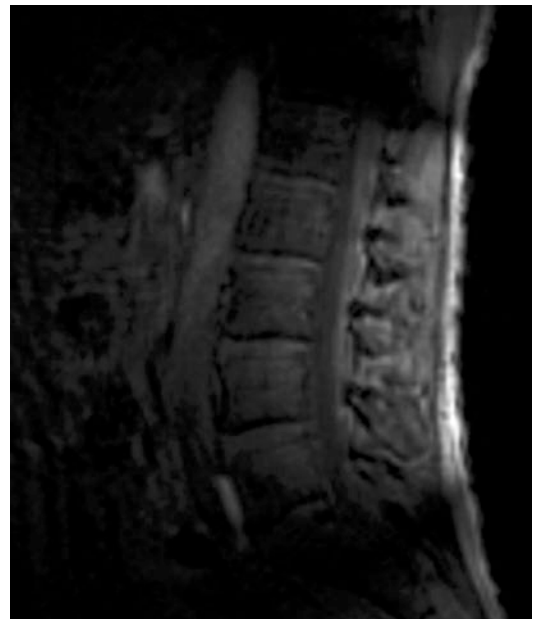
Fig. 20.3 Quantitative chemical shift imaging in a patient with Gaucher's disease. Placement of the localizer

L3	0,196	0,430	0,381	0,590
L4	0,250	0,439	0,525	0,600
L5	0,284	0,440	0,536	0,566
av.	0,24	0,44	0,48	0,59
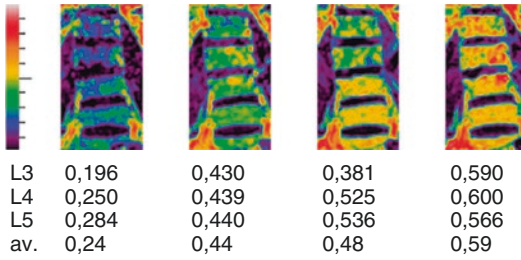
Fig. 20.4 Coronal color-coded display of fat fraction measurement in the lumbar spine, ranging from 0 (*purple*) to 1 (*red*). Patient with Gaucher's disease is measured pre- (*left image*) and subsequently three times (annually) during/after enzyme replacement therapy. Due to therapy success, the fat fraction is increased, which can be measured by chemical shift imaging. Low fat content is shown in blue to violet; high fat content is shown in *yellow* to *red*. With permission from Maas et al. (2003)

intensities and the geographic location of the disease on conventional MR images of the spine and femur. In the lumbar spine, the SI of the marrow on T1-weighted SE sequences is compared to signal intensity of a healthy intervertebral disc. The bone marrow SI on T2-weighted SE sequences was evaluated with the presacral fat as a normal isoin-

tense reference. In addition the infiltration pattern (patchy versus diffuse) of the disease within the vertebral bodies is graded. The patchy infiltration pattern in Gaucher's disease consists of localized areas of abnormal marrow (low signal intensity on T1- and T2-weighted SE images) on a background of normal bone marrow (high signal intensity and T1- and T2-weighted SE images). In the diffuse pattern, the bone marrow is completely replaced. The diffuse pattern is considered to reflect a more advanced stage of the disease. Furthermore, the absence of fat in the basivertebral vein region was added as a score, in a binominal fashion (present/absent). The disappearance of fat surrounding the basivertebral plexus was included in the BMB. In the femurs the marrow signal intensities on T1-weighted and T2-weighted images were graded compared to the signal intensity of subcutaneous fat. The intensities were scored as hyperintense, slightly hyperintense, isointense, slightly hypointense, and hypointense. The femurs were divided in three sites of involvement, proximal epiphysis/apophysis, meta-diaphysis, and distal epiphysis.

20.5 Assessment of Outcome and Survival in Patients with Acute Myeloid Leukemia in Complete Remission

Many parameters such as age, karyotype, and performance status are known to be prognostic factors in patients with acute myeloid leukemia (AML) before they receive chemotherapy (Ferrara et al. 2008). If complete remission (CR) is maintained for more than 3 years, the likelihood of relapse is less than 10% (de Lima et al. 1997). To improve the duration of remission, patients at high risk of relapse should be detected as early as possible. DCE-MRI has the potential to noninvasively assess the microvascular structure of bone marrow. Chen et al. examined 51 patients with acute myeloid leukemia in complete remission with DCE-MRI. Semiquantitative parameters (peak and slope) as well as quantitative parameters (amplitude, K_{ep} [efflux rate constant], and K_{el} [elimination constant]) were calculated. It could be shown that high values of

peak (≥ 0.41), slope (≥ 0.0235), amplitude (≥ 0.03), and K_{ep} (≥ 0.0082) were associated with shorter overall survival ($p = 0.004$, 0.01, 0.034, and 0.026, respectively). A high value of K_{ep} was also associated with shorter relapse-free survival ($p = 0.008$). After multivariate Cox proportional hazards analysis, only K_{ep} revealed as an independent factor for overall survival (relative risk, 30.305; $p = 0.21$) and relapse-free survival (relative risk, 6.477; $p = 0.009$). K_{ep} (efflux rate constant) measured with tracer kinetic modeling represents the contrast exchange between blood plasma and extravascular extracellular space. It is thought that bone marrow vessels and their endothelium should be normalized with reduced vessel wall permeability in complete remission and therefore show low values of K_{ep}. Increased values for K_{ep} may indicate not adequately normalized vessel permeability and therefore may indicate a high risk of relapse. K_{ep} might serve as a guide for the selection of personalized treatment plans in patients with AML and complete remission (Chen et al. 2011).

20.6 Differentiation of Benign and Malignant Vertebral Fractures

The differentiation of benign and malignant vertebral fractures is a common clinical problem, if there is no adequate trauma anamnesis. Although there exist morphologic MRI criteria in the differentiation of both entities (Frager et al. 1988; An et al. 1995; Cuenod et al. 1996; Shih et al. 1999; Baur et al. 2002; Jung et al. 2003), especially in the first 8–12 weeks after the vertebral fracture, similar appearance of benign and malignant vertebral fractures on T1-w, T2-w, and STIR images due to edema and hemorrhage can mimic malignant findings in a benign osteoporotic vertebral fracture (Moulopoulos et al. 1996). To overcome this diagnostic impairment, quantitative diffusion-weighted imaging and quantitative chemical shift imaging promise to be additional features in determining the nature of an acute vertebral fracture.

Quantitative Diffusion-Weighted Imaging

The apparent diffusion coefficient (ADC) is calculated using two or more images with different diffusion weightings (*b*-values). Acute osteoporotic fractures show an increased diffusion with high values on ADC maps, which is explained by the disruption of the trabecular structure and bone marrow edema in the diseased vertebrae. Pathologic fractures are associated with restricted diffusion, i.e., lower values on ADC maps. In spinal tumors with vertebral body compression fractures, increased tumor cell packing leads to a smaller and more restricted extracellular space, resulting in increased signal from restricted water protons, as has been observed in lytic metastases (Baur et al. 2003). Although the results showed somewhat variable results, the majority of the studies revealed typical ADC ranges associated with normal and pathological bone marrow. Normal bone marrow shows ADCs of 0.2 to 0.5×10^{-3} mm²/s. Metastases or malignant fractures range from ~0.7 to 1.0×10^{-3} mm²/s

(Fig. 20.5), osteoporotic or traumatic fractures show ADCs of ~1.0 to 2.0×10^{-3} mm²/s (Fig. 20.6) (Dietrich et al. 2009).

Biffar et al. examined 24 osteoporotic vertebral fractures and 20 malignant vertebral fractures and showed that DW-ssTSE (*b*-values 100, 250, 400, 600 s/mm²) could significantly discriminate between both entities showing a sensitivity of 65% and specificity of 88% at an ADC of 1.49×10^{-3} mm²/s as a cutoff value. DW-EPI showed no statistical differences due to an underestimated signal attenuation and gross geometrical image distortions caused by susceptibility heterogeneities (Biffar et al. 2010).

Karchevsky et al. performed a meta-analysis and reviewed four studies assessing the ADC values of benign and malignant vertebral fractures. They could show that mean ADC values in benign fractures were significantly higher than malignant fractures with a standardized mean difference (SMD) of 2.8 and a 95% confidence interval for the SMD of 2.1–3.5. Mean ADCs of pathologic fractures and malignant lesions were in the range from 0.19 to 0.853×10^{-3} mm²/s, benign fractures showed ADCs from 0.32 to 1.94×10^{-3} mm²/s (Karchevsky et al. 2008).

Although quantitative diffusion-weighted imaging shows significant differences between benign and malignant vertebral fractures, its specificity is limited due to a remarkable overlap. Although the ADC value itself should be independent from sequence type and sequence parameters, the measured values are influenced by sequence-specific artifacts, range of used *b*-values, application of fat saturation, noise, and perfusion effects. DWI of bone marrow requires considerably more robust imaging techniques than typical MRI of the brain, and therefore it is still a technique on very active research.

Quantitative Chemical Shift (In-/Opposed-Phase) Imaging

Chemical shift imaging uses the different precession frequencies of water and fat protons due to the differences in their molecular environment. The greater the signal intensity loss on
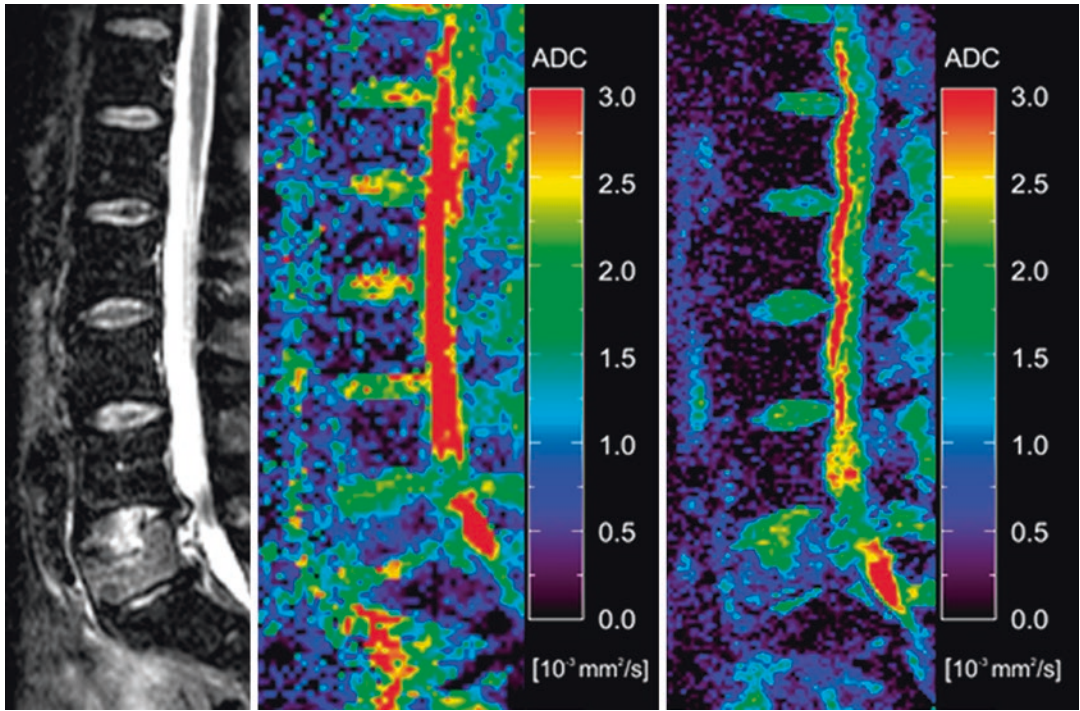
Fig. 20.5 Malignant fracture due to hypopharyngeal cancer: (**a**) STIR image showing edema in the whole vertebral body. Corresponding ADC maps acquired with (**b**) DW-HASTE (mean ADC 0.64) and (**c**) DW-EPI (mean ADC 0.73) showing relatively low values due to high cell packing
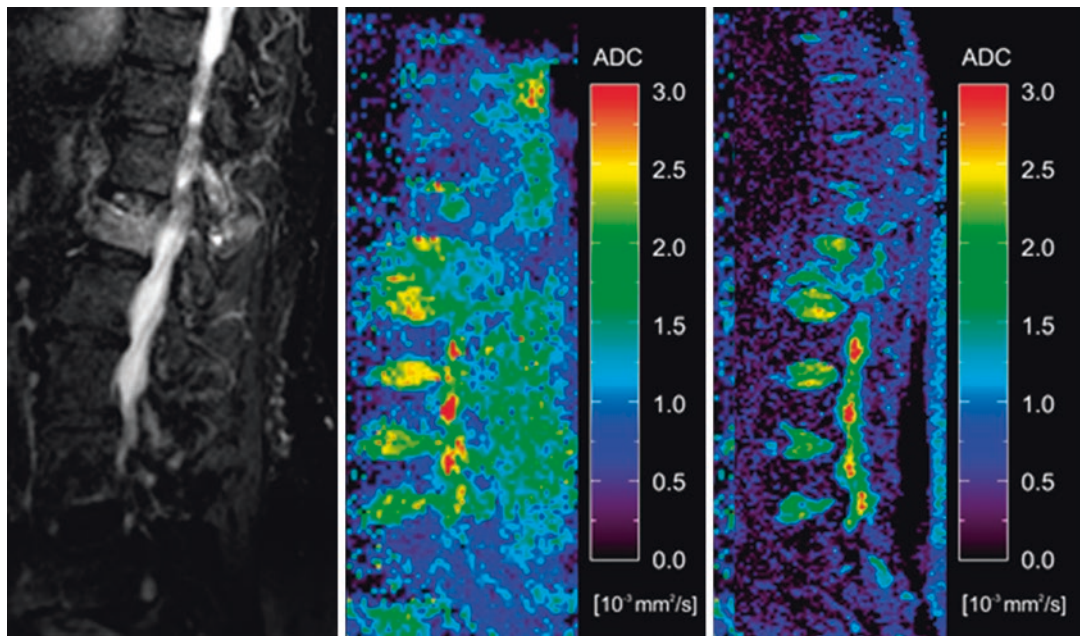
Fig. 20.6 Osteoporotic fracture: (**a**) STIR image showing edema in the whole vertebral body. Corresponding ADC maps acquired with (**b**) DW-HASTE (mean ADC 1.59) and (**c**) DW-EPI (mean ADC 1.41) showing relatively high values due to edema

opposed-phase images compared to in-phase images is, the greater is the fat content in the vertebral bone marrow. If tumor has infiltrated the vertebral bone marrow, the fatty marrow is expected to be displaced, resulting in a lower content of fat, and therefore higher signal inten-

sity on opposed-phase images (Fig. 20.7). In osteoporotic vertebral fractures, mostly normal fatty marrow should be detected, without significant changes in the fat content, resulting in a signal intensity drop, nearly equal to normal bone marrow (Fig. 20.8). The relative signal intensity
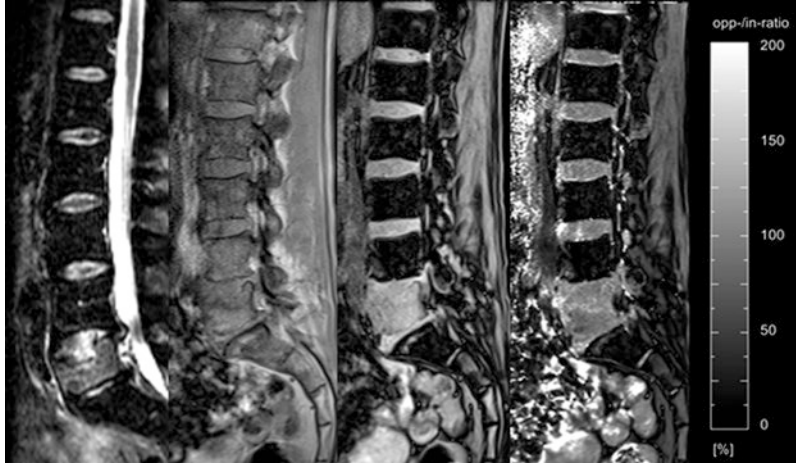
Fig. 20.7 Malignant fracture due to hypopharyngeal cancer: (**a**) STIR image showing edema in the whole vertebral body. Corresponding (**b**) inphase image showing high signal intensity and (**c**) opposed-phase image also showing high signal intensity in comparison with normal vertebral

bone marrow. The opp-/in-ratio is 99%, which means that there is only a slight signal drop of −1% on opposed-phase images compared to inphase images. Note that normal vertebral bone marrow has a much lower opp/in-ratio, corresponding to a higher signal drop on opposed-phase images

Fig. 20.8 Osteoporotic fracture: (**a**) STIR image showing edema in the whole vertebral body. Corresponding (**b**) inphase image showing high signal intensity and (**c**) opposed-phase image showing a low signal intensity, as also shown in normal vertebral bone marrow. The opp-/

in-ratio is 69%, which means that there is a high signal drop of −31% on opposed-phase images compared to inphase images, as can also be noted in normal vertebral bone marrow

ratio (signal intensity$_{OP}$/signal intensity$_{IP}$) (Eito et al. 2004; Erly et al. 2006) can be calculated for quantitative measurement.

Studies at 1.5 T revealed mean signal intensity ratios of 0.46 ± 0.14 (SD) for normal vertebral bone marrow (Eito et al. 2004), whereas nonneoplastic fractured vertebrae showed mean intensity ratios of 0.63 ± 0.21 SD (Eito et al. 2004) to 0.58 ± 0.02 SD (Erly et al. 2006), while malignant compression fractures had higher mean signal intensity ratios of 1.02 ± 0.11 SD (Eito et al. 2004) to 0.98 ± 0.095 SD (Erly et al. 2006).

Performing ROC-analysis, a signal intensity ratio of >0.8 indicating malignancy showed best discrimination of benign and malignant vertebral fractures with a sensitivity of 95% and a specificity of 89% (Erly et al. 2006).

Chemical shift imaging is a reliable supportive tool for the differentiation of benign and malignant vertebral fractures. However, if strong edema and reduced fat content are present, the signal intensities can also be high on opposed-phase images in osteoporotic fractures. Care should be taken to acquire the same sequence type with the appropriate sequence parameters, since a slight shift, e.g., in TE and flip angle can cause a significant shift in contrast.

References

Aguayo A, Kantarjian H et al (2000) Angiogenesis in acute and chronic leukemias and myelodysplastic syndromes. Blood 96(6):2240–2245

Akkerman EM, Maas M (1995) A region-growing algorithm to simultaneously remove dephasing influences and separate fat and water in two-point Dixon imaging. Proceedings of the Society for Magnetic Resonance in Medicine and the European Society for Magnetic Resonance in Medicine and Biology

An HS, Andreshak TG et al (1995) Can we distinguish between benign versus malignant compression fractures of the spine by magnetic resonance imaging? Spine (Phila Pa 1976) 20(16):1776–1782

Baur A, Bartl R et al (2004) Neovascularization of bone marrow in patients with diffuse multiple myeloma: a correlative study of magnetic resonance imaging and histopathologic findings. Cancer 101(11): 2599–2604

Baur A, Dietrich O et al (2003) Diffusion-weighted imaging of bone marrow: current status. Eur Radiol 13(7):1699–1708

Baur A, Stabler A et al (2002) Acute osteoporotic and neoplastic vertebral compression fractures: fluid sign at MR imaging. Radiology 225(3):730–735

Baur A, Stabler A et al (1997) MRI gadolinium enhancement of bone marrow: age-related changes in normals and in diffuse neoplastic infiltration. Skelet Radiol 26(7):414–418

Biffar A, Baur-Melnyk A et al (2010) Multiparameter MRI assessment of normal-appearing and diseased vertebral bone marrow. Eur Radiol 20(11): 2679–2689

Chen BB, Hsu CY et al (2011) Dynamic contrast-enhanced MR imaging measurement of vertebral bone marrow perfusion may be indicator of outcome of acute myeloid leukemia patients in remission. Radiology 258(3):821–831

Cuenod CA, Laredo JD et al (1996) Acute vertebral collapse due to osteoporosis or malignancy: appearance on unenhanced and gadolinium-enhanced MR images. Radiology 199(2):541–549

de Lima M, Strom SS et al (1997) Implications of potential cure in acute myelogenous leukemia: development of subsequent cancer and return to work. Blood 90(12):4719–4724

Dietrich O, Biffar A et al (2009) Diffusion-weighted imaging of bone marrow. Semin Musculoskelet Radiol 13(2):134–144

Dixon WT (1984) Simple proton spectroscopic imaging. Radiology 153(1):189–194

Eito K, Waka S et al (2004) Vertebral neoplastic compression fractures: assessment by dual-phase chemical shift imaging. J Magn Reson Imaging 20(6):1020–1024

Erly WK, Oh ES et al (2006) The utility of in-phase/opposed-phase imaging in differentiating malignancy from acute benign compression fractures of the spine. AJNR Am J Neuroradiol 27(6):1183–1188

Ferrara F, Palmieri S et al (2008) Clinically useful prognostic factors in acute myeloid leukemia. Crit Rev Oncol Hematol 66(3):181–193

Frager D, Elkin C et al (1988) Subacute osteoporotic compression fracture: misleading magnetic resonance appearance. Skelet Radiol 17(2):123–126

Hollak C, Maas M et al (2001) Dixon quantitative chemical shift imaging is a sensitive tool for the evaluation of bone marrow responses to individualized doses of enzyme supplementation therapy in type 1 Gaucher disease. Blood Cells Mol Dis 27(6):1005–1012

Horger M, Weisel K et al (2011) Whole-body diffusion-weighted MRI with apparent diffusion coefficient mapping for early response monitoring in multiple myeloma: preliminary results. Am J Roentgenol 196(6):W790–W795

Jung HS, Jee WH et al (2003) Discrimination of metastatic from acute osteoporotic compression spinal fractures with MR imaging. Radiographics 23(1):179–187

Karchevsky M, Babb JS et al (2008) Can diffusion-weighted imaging be used to differentiate benign from pathologic fractures? A meta-analysis. Skelet Radiol 37(9):791–795

Maas M, Hollak CE et al (2002) Quantification of skeletal involvement in adults with type I Gaucher's disease: fat fraction measured by Dixon quantitative chemical shift imaging as a valid parameter. AJR Am J Roentgenol 179(4):961–965

Maas M, van Kuijk C et al (2003) Quantification of bone involvement in Gaucher disease: MR imaging bone marrow burden score as an alternative to Dixon quantitative chemical shift MR imaging—initial experience. Radiology 229(2): 554–561

Moulopoulos LA, Maris TG et al (2003) Detection of malignant bone marrow involvement with dynamic contrast-enhanced magnetic resonance imaging. Ann Oncol 14(1):152–158

Moulopoulos LA, Yoshimitsu K et al (1996) MR prediction of benign and malignant vertebral compression fractures. J Magn Reson Imaging 6(4):667–674

Nobauer I, Uffmann M (2005) Differential diagnosis of focal and diffuse neoplastic diseases of bone marrow in MRI. Eur J Radiol 55(1):2–32

Plecha DM (2000) Imaging of bone marrow disease in the spine. Semin Musculoskelet Radiol 4(3):321–327

Pui MH, Mitha A et al (2005) Diffusion-weighted magnetic resonance imaging of spinal infection and malignancy. J Neuroimaging 15(2):164–170

Rahmouni A, Montazel JL et al (2003) Bone marrow with diffuse tumor infiltration in patients with lymphoproliferative diseases: dynamic gadolinium-enhanced MR imaging. Radiology 229(3):710–717

Rajkumar SV, Leong T et al (2000) Prognostic value of bone marrow angiogenesis in multiple myeloma. Clin Cancer Res 6(8):3111–3116

Sezer O, Niemoller K et al (2001) Decrease of bone marrow angiogenesis in myeloma patients achieving a remission after chemotherapy. Eur J Haematol 66(4):238–244

Shih TT, Huang KM et al (1999) Solitary vertebral collapse: distinction between benign and malignant causes using MR patterns. J Magn Reson Imaging 9(5):635–642

Stabler A, Doma AB et al (2000) Reactive bone marrow changes in infectious spondylitis: quantitative assessment with MR imaging. Radiology 217(3):863–868

Vacca A, Ribatti D et al (1994) Bone marrow angiogenesis and progression in multiple myeloma. Br J Haematol 87(3):503–508

Vande Berg BC, Lecouvet FE (2005) Normal variants and frequent marrow alterations that simulate bone marrow lesions at MR imaging. Radiol Clin N Am 43(4):761–770. ix

Bone and Soft Tissue Tumours

21

Hassan Douis and A. Mark Davies

Contents

21.1 Introduction

Much of the use of imaging in the detection, diagnosis and management of bone and soft tissue tumours relies on evaluation of morphological changes. There are, however, a number of situations where particular measurements derived from different imaging techniques can be of considerable value in predicting fracture risk, planning surgery and assessing response to treatment. The purpose of this chapter is to review these different applications.

H. Douis (✉)
University Hospital Birmingham,
Birmingham, B15 2TH, UK
e-mail: douis.hassan@hotmail.co.uk

A. M. Davies
Department of Radiology, Royal Orthopaedic
Hospital NHS Foundation Trust, Birmingham, UK

21.2 Prediction of Fracture Risk

Long Bones

In the adult, the bone is the third most common site of metastatic disease after the lung and liver. Pathological fractures are a common complication of metastases from breast, prostate, thyroid, lung and renal primaries. It is generally accepted that prediction of a pathological fracture before the actual fracture event, thereby allowing surgical intervention, subsequently significantly reduces patient morbidity (Ward et al. 2000; Damron and Ward 2003). A recent study by Mavrogenis et al., for example, demonstrated that patients presenting with impending fractures from femoral metastases have a better survival rate when compared to patients presenting with actual fractures from femoral metastases (Mavrogenis et al. 2011). Not unexpectedly, osteolytic lesions are more likely to fracture than osteoblastic metastases, and weight-bearing bones are most commonly affected, i.e. lower limb long bones (Ashford et al. 2006). An early study noted that almost 60% of pathological fractures through breast metastases in the femur occurred when a well-defined lytic lesion of 2.5 cm diameter or larger involved the cortex (Snell and Beals 1964). Later studies suggested that prophylactic internal fixation of metastases should be considered if 50% of the diameter of the bone was involved (Parrish and Murray 1970; Fidler 1973). Subsequently, Fidler measured the size of the metastasis on radiographs in 100 consecutive pathological fractures in long bones and expressed this as a percentage of the diameter of the bone (Fidler 1981). He showed that fractures were unlikely (<2.5%) when less than 50% of the cortex was destroyed, likely (60%) when 50% of

the cortex was destroyed, and most likely (80%) when 75% of the cortex was destroyed. Harrington concluded that the main risk factors that should prompt consideration of prophylactic stabilisation are (1) cortical bone destruction >50%, (2) a lesion >2.5 cm in maximum diameter in the femur and (3) persistent pain on weight-bearing despite local radiotherapy (Harrington 1982). In an attempt to quantify the most significant risk factors, Mirels proposed a scoring system based on lesion size, site, radiographic nature and degree of pain (Table 21.1) (Mirels 1989).

In this study, lesion size was measured independently by three orthopaedic surgeons and recorded as <1/3, 1/3 to 2/3 or >2/3 of the diameter of the bone. Eighty-one percent of fractures occurred in lesions measuring more than two-thirds of the diameter of the bone. When applying the scoring system, a total score≥9 indicates an impending fracture (Table 21.1). However, it is not clear from this paper how precisely the measurements were obtained from the radiographs. Was it from a single radiograph (anteroposterior or lateral) or the sum of measurements from two radiographs obtained at right angles (anteroposterior and lateral)? Despite this query, this classification has the advantage of being relatively simple, reproducible and valid across physicians of differing levels of experience with a sensitivity of 91% and specificity of 35% (Damron and Ward 2003; Damron et al. 2003). CT has been used in an attempt to increase specificity of pathological fracture prediction (Hipp et al. 1995; Dijkstra et al. 1997). The most accurate measurements with the most precise description of methodology was provided by a Dutch study analysing risk factors for pathological fracture with femoral metastases using radiographs and, in an unspecified number of cases, CT (van der Linden et al. 2003).

Table 21.1 Mirels' rating system for prediction of pathological fracture risk in long bones (from Mirels 1989)

Score	Site	Nature	Size[a]	Pain
1	Upper extremity	Blastic	<1/3	Mild
2	Lower extremity[b]	Mixed[c]	1/3 to 2/3	Moderate
3	Peritrochanteric	Lytic	>2/3	Functional

[a]Relative proportion of bone width involved with tumour
[b]Non-peritrochanteric lower extremity
[c]Mixed lytic and blastic

The measurements obtained in millimetres from radiographs are illustrated in Fig. 21.1.

The terminology might be a little confusing to many radiologists as it refers to the "largest axial length" and "largest axial cortical involvement" meaning the longitudinal extent (i.e. in the long axis along the line of the bone) rather than the conventional understanding of axial as meaning the transverse plane (Fig. 21.1). The main conclusion of this study was that only the axial cortical involvement >30 mm ($p = 0.01$) and the circumferential cortical involvement >50% ($p = 0.03$) were predictive of fracture.

Pathological fractures in children may result from a wide variety of both intrinsic and extrinsic processes. Intrinsic processes include conditions such as osteogenesis imperfecta and bone tumours, whereas extrinsic processes include previous surgical intervention (biopsy, fixation, etc.) and radiotherapy. Pathological fractures may be further classified as being due to pathology which is solitary, multifocal (polyostotic), generalised to the whole skeletal system or a generalised condition with skeletal involvement (Saraph and Linhart 2005). Most paediatric pathological frac-tures through isolated bone lesions tend to be due to tumours or tumour-like lesions. A three-centre study identified a total of 88 cases collected over a period of 5 years. The commonest cause of fracture was a simple bone cyst (40%) followed by nonossifying fibroma (19%), fibrous dysplasia (16%), osteosarcoma (15%) and aneurysmal bone cyst (10%) (Ortiz et al. 2005). In a series of 75 children with simple bone cysts who had sustained 52 pathological fractures, Ahn and Park reported that the percentage of bone occupied by the cyst in the transverse plane on both anteroposterior and lateral radiographs was >85% in every case of fracture (Ahn and Park 1994). A more complex method of measurement to calculate a "cyst index" has been proposed by Kaelin and MacEwen (1989). This cyst index gives the proportion between the radiographic area of the cyst and the size of the involved bone, measured as the diameter of the diaphysis squared. The areas involved are shown in Fig. 21.2.

The size of the bone, the distance from the growth plate, the length of the cyst and the radiodensity that depends on the radiographic technique are not factors in this evaluation. The
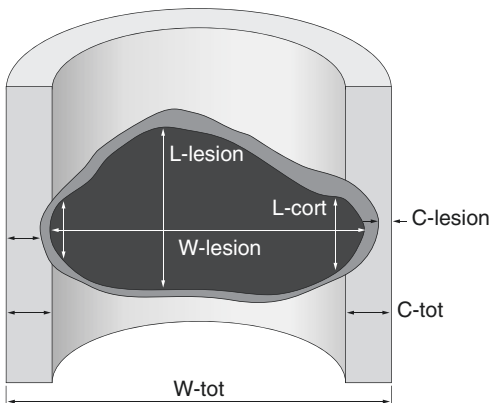
Fig. 21.1 Diagram showing measurement of metastatic lesions in the femur in millimetres for assessing fracture risk (based on van der Linden et al. 2004). L-lesion, largest axial (longitudinal) length of the entire lesion. W-lesion, largest transverse extension of the lesion. W-tot, largest transverse width of the bone. C-tot, maximal thickness of cortex without lesional involvement. C-lesion, minimum thickness of cortex with lesional involvement. Axial (longitudinal) cortical involvement >30 mm and circumferential cortical involvement >50% are both predictive of pathological fracture
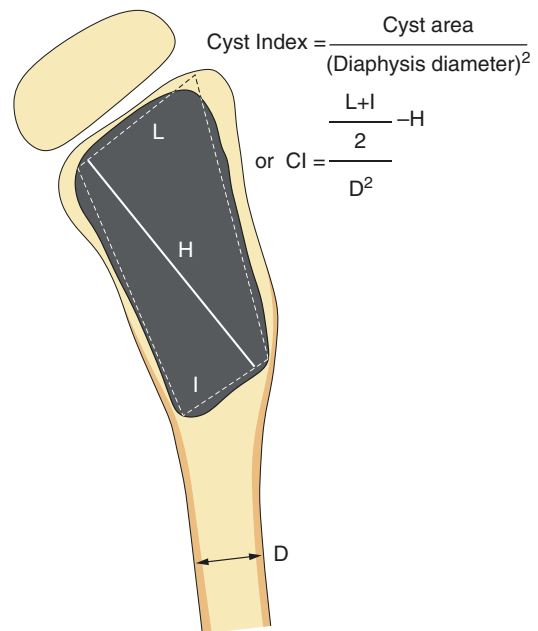
Fig. 21.2 Diagram showing measurements and formula for calculation of cyst index in the assessment of fracture risk in simple bone cyst (based on Kaelin and MacEwen 1989)

area of the cyst is measured by its largest dimension be it on the anteroposterior or lateral radiographs. The shape of the cyst may be oval or trapezoidal, and the area can be calculated by drawing one or two trapezoids around the borders of the cyst. The diameter of the cyst is measured in its tubular diaphyseal portion. The average cyst index in humeral fractures was 6.12 (SD = 1.8) and in femoral fractures 4.74 (SD = 1.19). The authors calculated that the lowest cyst index for a pathological fracture through the proximal humerus is 4 and 3.5 for the proximal femur (Kaelin and MacEwen 1989). Large nonossifying fibromas can also present with a pathological fracture. Arata and coworkers reported that if a nonossifying fibroma involves more than 50% of the transverse diameter of the bone or measures >33 mm in length, there is an increased risk of pathological fracture (Arata et al. 1981). A more recent series, however, showed that 59% cases of nonossifying fibromas exceeded these threshold measurements without fracturing (Easley and Kneisl 1997). Recently, quantitative computed tomography-based structural analysis has been used to predict the fracture risk in children with benign skeletal lesions. This technique uses computed tomography to quantify the resistance of a bone to axial, bending or twisting forces. In a prospective study, Leong et al. evaluated the specificity of quantitative computed tomography-based structural analysis in predicting the fracture risk in children with benign appendicular skeletal lesions and compared it with the specificity of plain radiographs in predicting pathological fractures in this patient cohort. They found that quantitative computed tomography-based rigidity analysis had a specificity of 97% and was therefore more specific in predicting the risk of pathologic fractures when compared to conventional criteria based on plain radiographs which demonstrated a specificity of only 12%. Structural rigidity analysis however requires in-depth knowledge of image-analysis software, the interpretation of the results requires knowledge of structural mechanics and computed tomography is less readily available than conventional radiography. Furthermore, this technique exposes the child to relatively large radiation doses. It is therefore doubtful if quantitative computed tomography-based structural analysis will be used in routine clinical practise (Leong et al. 2010).

Spine

Assessment of bone mineral density in the spine and consequent risk of vertebral fracture is well recognised in osteoporosis and is covered in chapter "Measurements in Metabolic Bone Disease". This section reviews the role of imaging in the prediction of pathological fractures of the spine. As elsewhere in the skeleton, early intervention to prevent vertebral fractures in patients with tumours, particularly metastases, can reduce morbidity (Dewald et al. 1985. McAfee and Zdeblick 1989). Unfortunately, the complex anatomy and loading of the spine, unlike the long bones, do not lend itself readily to simple estimates of the proportion of the bone involved with tumour as an indicator of fracture risk (i.e. vertebral collapse). Not surprisingly tumour size and pedicle destruction on radiographs elevate fracture risk but do not yield parameters to establish a clear threshold for fractures (Taneichi et al. 1997). Recent studies have concentrated on biomechanically based models utilising data derived from CT including tumour volume expressed as a percentage of total vertebral volume, bone mineral density measurements, etc. (Roth et al. 2004) and parametric analysis of three-dimensional poroelastic finite-element models (Whyne et al. 2003). These are complex techniques that, as yet, have not crossed over into routine clinical practise.

MR imaging is very sensitive in detecting marrow changes particularly in the spine. Clearly, the greater the proportion of tumour infiltration of a vertebral body, the greater the risk of vertebral collapse, but no clear threshold parameters for assessing fracture risk on MR imaging exist (Lecouvet et al. 1997, 1998). One study has reported promising initial results in the assessment of vertebral fracture risk in patients with multiple myeloma using dynamic contrast-enhanced MR imaging (Scherer et al. 2002). A cut-off level of 25 arbitrary units was shown to discriminate between vertebrae that fractured during 6-month follow-up and those that did not.

21.3   Tumour Diagnosis

Bone Tumours

The imaging investigation of a suspected bone tumour should always commence with radiographs obtained at right angles (Morrison et al. 2005). The features that enable a differential diagnosis to be generated are generally identifiable on the radiograph, namely, pattern of bone destruction, periosteal new bone formation and matrix mineralisation. Skeletal scintigraphy is of limited importance in the diagnostic workup of solitary lesions but can be helpful in identifying multifocal/polyostotic disease, e.g. fibrous dysplasia. There is really no role for diagnostic ultrasound in primary bone tumours although it may be used as an alternative to fluoroscopy for image-guided biopsy (Saifuddin et al. 1998). CT is used to obtain "radiographic" information over and above that of conventional radiographs particularly in areas of complex anatomy (e.g. spine, pelvis) or superimposition of structures (e.g. scapula) (Woertler 2003). It is also useful in revealing subtle features such as early cortical destruction, faint matrix mineralisation and small osteoid osteomas. Direct measurement of the thickness of the cap of a peripheral cartilage tumour with CT, ultrasound or MR imaging can help differentiate an osteochondroma from a peripheral chondrosarcoma (Kenney et al. 1981; Woertler et al. 2000). The association of cartilage cap thickness and malignancy is well described. A cap thickness of <2 cm when measured perpendicular to the osteochondroma is likely to be benign. A cap thickness > 2 cm is associated with an increased likelihood of malignancy. Although the cartilage cap is easily measured if the cartilage cap is small and uniform, it is difficult to obtain accurate and reliable measurements of the cartilage cap if the cap is convoluted or irregular. Until recently, there has been no standardised measuring technique for the assessment of the thickness of irregular and convoluted cartilage caps. Bernard and coworkers retrospectively evaluated cartilage cap thickness on CT and MRI in 67 histologically proven osteochondromas and 34 histologically proven exostotic chondrosarco-

mas and correlated the cartilage cap thickness on CT and MRI with the gross pathologic findings in 32 cases (26 osteochondromas, 6 chondrosarcomas). In their study they proposed the following technique for the measurement of cartilage cap thickness. The cartilage cap thickness is measured by identification of the tidemark of low-signal-intensity mineralisation which serves as a boundary between the medullary cavity and the overlying cartilage. A connecting line is then drawn between adjacent peaks in the tidemark undulations. Crevasses of the cartilage between tidemark undulations are subsequently excluded. The thickest portion of the cartilage thickness is then measured perpendicular to the tidemark (Fig. 21.3).

Using this measurement technique for cartilage cap thickness, they found measurement variances of 3 mm or less when correlating the cartilage cap thickness on imaging with the cartilage cap thickness on gross pathologic specimens. Furthermore, Bernard et al. found that a
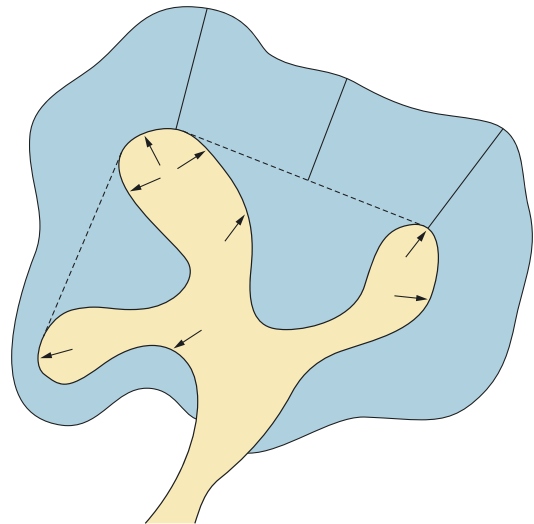
Fig. 21.3 Diagram (based on and adapted from Bernard et al. 2010) demonstrating how to measure the cartilage cap in a convoluted osteochondroma. First, the tidemark (*arrows*) which represents the boundary between the medullary space of the osteochondroma and the cartilage cap is identified. Adjacent peaks of the tidemarks are connected through a line (*dotted lines*), and the cartilage crevasses are subsequently excluded in the measurement of the cartilage cap thickness. The thickest portion of the cartilage cap (*solid lines*) which is perpendicular to the tidemarks represents the cartilage cap thickness

cutoff value for the cartilage cap thickness of 2 cm in the differentiation of osteochondromas from chondrosarcomas led to 100% sensitivity, 98% specificity on MRI and 100% sensitivity and 95% specificity on CT. This study therefore provides a standardised, reliable technique for the measurement of convoluted cartilage caps and confirms a cutoff value of 2 cm for cartilage cap thickness in the distinction of osteochondromas from chondrosarcoma (Bernard et al. 2010).

MR imaging is less specific than radiographs in the differential diagnosis of primary bone tumours in the majority of cases (Berquist 1993). In some cases MR imaging can contribute to diagnosis by virtue of morphological information, relative signal intensities on different pulse sequences and patterns of contrast enhancement. Subjective assessment of relative signal intensities is preferred to absolute measurements on unenhanced or static contrast-enhanced MR imaging because of the numerous variables such as pulse sequence parameters, surface coils and magnet strength. One quantifiable technique that has been extensively evaluated in the musculoskeletal system over the past 20 years is dynamic contrast-enhanced MR imaging (DCEMRI). It can be applied in the diagnosis as well as for assessing tumour response to medical treatments (see Sect. 21.5) and detection of local recurrence following surgery. The following section gives a brief overview of DCEMRI that applies equally well to the following sections in this chapter.

Static contrast-enhanced MR imaging refers to standard pulse sequences performed after an intravenous injection of a gadolinium chelate. As these sequences typically take several minutes to acquire, the tissues are in an equilibrium state with the contrast agent distributed between the blood and interstitial space (Verstraete et al. 1994a). DCEMRI is a sequence commencing shortly before a rapid bolus injection (approximately 5 ml/s) of a gadolinium chelate and continuing during and for approximately 3 min after the injection. Repeated slices through the same section(s) are obtained using a gradient echo sequence. A temporal resolution of 3 s per slice is achieved by employing a very short repetition and echo time (<10 ms) by the use of a reduced flip angle (<90°) radiofrequency pulse with rapid reversal of the readout gradient (Verstraete et al. 1994b, 1995). Temporal resolution is more important than spatial resolution so that only one average per acquisition should be used. Representative slice(s) have to be chosen from the pre-contrast sequences on the assumption that this section will be typical of the contrast enhancement pattern of the entire lesion. Variations in enhancement patterns, however, have been reported between different regions within musculoskeletal lesions (Mirowitz et al. 1992). Ideally, an artery should be included within the imaging plane as it enables accurate measurement of the time of onset of enhancement in the lesion as compared with the time of arrival of the bolus. If repeated examinations are required, e.g. for monitoring the effect of chemotherapy, a standardised technique should be applied to ensure accurate reproducibility. This should include the site of intravenous access and the injection rate of the gadolinium chelate. Once the sequence has been completed, the images can be assessed qualitatively and/or quantitatively in one of several ways. An easy method is with subtraction in which the first image pre-contrast medium injection is subtracted from the subsequent images (de Baere et al. 1992). Early enhancing areas are readily identified and any high signal from fat and subacute haemorrhage nullified.

The easiest quantitative method is to identify regions of interest (ROIs) on the image and plot time-signal intensity curves (TSIC) using software routinely available on all magnet manufacturers' consoles (Erlemann et al. 1989, 1990; Fletcher et al. 1992). The TSIC can be displayed as a graph and the early pharmacokinetics of the contrast medium assessed either subjectively by looking at the shape of the curve or objectively by measuring the rate of enhancement from the slope during the first pass of the contrast medium through the tumour (Fig. 21.4) (Verstraete et al. 1995).

During this first pass, approximately 50% of the contrast medium enters the interstitial

Fig. 21.4 Time-signal intensity curves derived from a dynamic contrast-enhanced MR imaging sequence (based on Verstraete et al. 1995). T start is the time of onset of enhancement. SI prior and SI end represent the start and finish signal intensities of the first pass
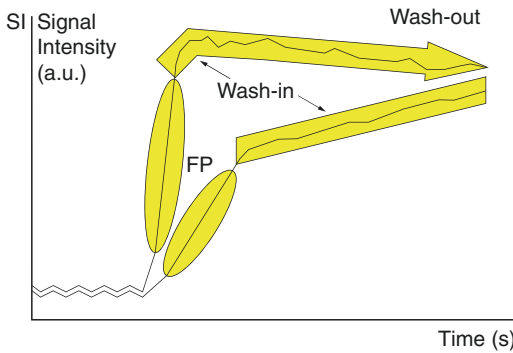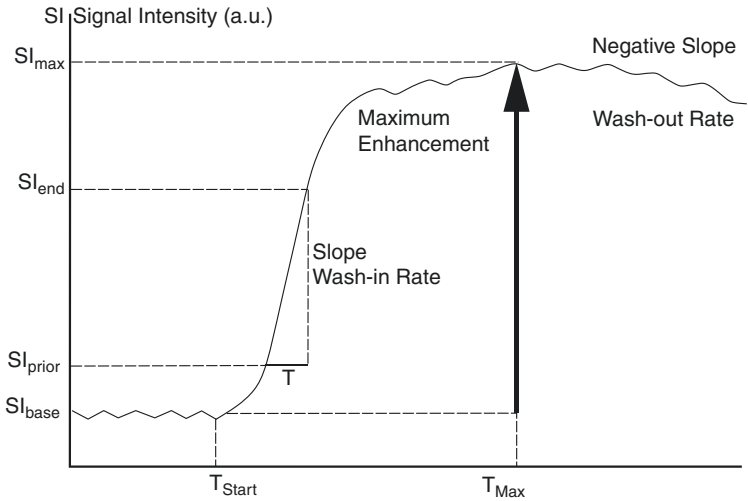
Fig. 21.5 Time-signal intensity curves derived from a dynamic contrast-enhanced MR imaging sequence showing two different patterns (based on Verstraete et al. 1995). The first with a very rapid first pass, washin and then slow washout. The second with a slower but progressive first pass, washin and washout

space—a greater percentage may be seen in pathological tissues. The concentration gradient and diffusion rate of the contrast medium then drop, and changes in signal intensity are determined by capillary permeability and composition of the interstitial space. In tissues with a small interstitial space, washout of the contrast medium may occur with a gradual decrease in the signal intensity, whereas in tissues with a larger interstitial space, a progressive washin will occur (Fig. 21.5).

The main disadvantage of using the ROI method is that it relies initially on the subjective judgement of the operator as to where to place the individual ROIs. A less operator-dependent method is first-pass imaging which calculates the first-pass slope value on a pixel-by-pixel basis according to the following equation (Fig. 21.6) (Verstraete et al. 1994a, 1994b, 1995):

$$\text{Steepest slope} = \frac{\left(\text{SI end} - \text{SI prior}\right)}{\left(\text{SI baseline} \times T\right)} \times 100$$

SI baseline represents the mean signal intensity (SI) in a pixel before contrast enhancement; T is the time interval between two consecutive images with the largest change in SI in a pixel and reflects the temporal resolution of the sequence. The operator-dependent selection of different ROIs is avoided. This technique produces parametric images that correlate with tissue microvascularisation and perfusion but does not give a TSIC. A development of the first-pass imaging post-processing is spatial mapping of instantaneous enhancement rates that applies an exponential fitting algorithm on a pixel-by-pixel basis to allow estimation of the initial slope of the curve in order to produce parametric slope images (Lang et al. 1995). Other post-processing techniques for evaluating DCEMRI are factor analysis of medical image sequences (FAMIS) (Bonnerot et al. 1992) and discrete signal processing of dynamic contrast-enhanced MR images

Fig. 21.6 Post-processing procedure to produce first-pass images derived from a dynamic contrast-enhanced MR imaging sequence (based on Verstraete et al. 1994a, 1994b, 1995). The change in signal intensity (SI) is evaluated on a pixel-by-pixel basis and a new image produced
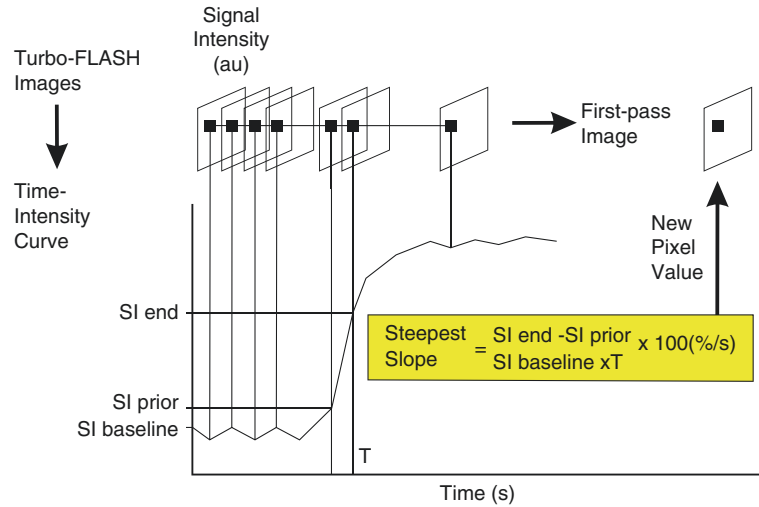
(Reddick et al. 1994). Both techniques would appear to remain largely confined to research units and not be used in routine daily practise.

DCEMRI has been used to try and distinguish between benign and malignant musculoskeletal lesions of both the bone and soft tissue (Erlemann et al. 1989, 1992; Woude et al. 1998b; van der Woude et al. 1998b). All the studies have shown trends with malignant lesions tending to exhibit more rapid tissue vascularisation and perfusion but with overlap in the slope values of highly vascular benign lesions as compared with malignant lesions. DCEMRI, therefore, cannot reliably differentiate benign from malignant bone tumours in most cases. It should be used in conjunction with routine MR imaging sequences to help narrow down a differential diagnosis rather than make the diagnosis. Examples where DCEMRI may be helpful include osteoid osteoma where a rapid washin/washout distinguishes the tumour from a cortical abscess (Liu et al. 2003; Woertler 2003). There can frequently be diagnostic difficulties in differentiating enchondroma from a low-grade central chondrosarcoma. DCEMRI is said to show more rapid enhancement in chondrosarcoma than enchondroma (Giernaerdt et al. 2000, de Coninck et al. 2013), but it should be noted that tumour vascularity is not a criterion used histologically to differentiate benign from malignant cartilage tumours. In addition, the gold standard for the diagnosis of enchondroma ver-

sus low-grade chondrosarcoma is questionable as a study showed that pathologists frequently find this distinction equally challenging (Sliced Study Group 2007).

Diffusion-weighted MR imaging has been shown to be helpful in differentiating benign versus pathological vertebral compression fractures (Baur et al. 1998). Although the original paper shows a quantitative method of assessment, most will use a qualitative technique whereby benign fractures show isointense or low signal intensity compared with the surrounding normal bone marrow, whereas metastatic vertebral compression fractures show relatively high signal intensity (Baur and Reiser 2000). In contrast to vertebral compression fractures, there is little evidence on the role of DWI in the characterisation of primary bone tumours. Hayashida et al., for example, found that the mean ADC value for chondrosarcomas was intermediate between that of simple bone cysts and fibrous dysplasia (Hayashida). In contrast, Yakushiji et al. found that showed that the minimum ADC values of chondroblastic osteosarcomas were lower than the minimum ADC values of conventional chondrosarcomas but higher than the minimum ADC values of other osteosarcomas (Yakushiji et al. 2009). Furthermore, a study performed by Douis et al. which evaluated the role of DWI in the differentiation of enchondromas from chondrosarcomas found that there was no statistically

significant difference in the minimum and mean ADC values of enchondromas, grade 1 chondrosarcomas, grade 2 chondrosarcomas or grade 3 chondrosarcomas. The authors only found a statistical difference in the minimum and mean ADC values in the dedifferentiated chondrosarcoma group which was due to the high-grade sarcoma component of the lesion. The diagnostic challenge however does not lie in the differentiation of an enchondroma from a high-grade chondrosarcoma or dedifferentiated chondrosarcoma but in the distinction of enchondromas from low-grade chondrosarcomas. Based on this study, there is therefore no role for DWI in the differentiation of enchondromas from low-grade chondrosarcomas (Douis et al. 2014).

Soft Tissue Tumours

Soft tissue masses will only be demonstrable on radiographs if particularly large, if there are significant density differences from surrounding muscle (i.e. calcification or fat) or if there is secondary involvement of the underlying bone. CT shows similar features with increased soft tissue contrast resolution particularly if intravenous iodinated contrast medium is administered. Ultrasound can be helpful in the detection of a soft tissue mass and in distinguishing solid from cystic lesions. Analysis using Doppler ultrasound of the vascularity of soft tissue tumours has been shown to be of limited value when differentiating benign from malignant tumours (Griffith et al. 2004). The excellent contrast resolution of MR imaging is such that it reliably detects all soft tissue masses

and routine studies together with static contrast-enhanced sequences will indicate the correct diagnosis in approximately 50% cases (Berquist et al. 1990; Ma et al. 1995; Moulton et al. 1995). A prospective non-quantified analysis of various MR parameters reported differentiation of malignant from benign lesions with a sensitivity of 93%, specificity of 82%, negative predictive value of 98%, positive predictive value of 60% and an accuracy of 85% (Gielen et al. 2004). Early studies using DCEMRI on both bone and soft tissue tumours indicated that there was a significant overlap of the slope values of highly vascularised benign soft tissue tumours and many malignancies (Erlemann et al. 1989; Verstraete et al. 1995). A prospective study concluded that static and DCEMRI, when added to non-enhanced MR imaging, improved differentiation between benign and malignant soft tissue masses (van Rijswijk et al. 2004). The quantifiable component of this study was the production of a TSIC from the dynamic data that was then subjectively classified according to the shape of the curve (Fig. 21.7).

Contrast-enhanced MR imaging parameters which favoured malignancy in this study were liquefaction, early dynamic enhancement (<6 s after arterial enhancement), peripheral or inhomogeneous dynamic enhancement and rapid initial enhancement followed by a plateau or washout phase (i.e. TSIC shapes Types III and IV in Fig. 21.7) (van Rijswijk et al. 2004).

The role of DWI in the differentiation of benign from malignant soft tissue lesions has been evaluated in multiple studies with rather mixed results. Whilst Maeda et al. (2007) and Einarsdóttir et al. (2004) found no statistically significant difference
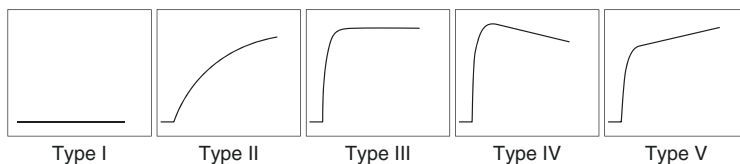
Fig. 21.7 Classification of subjective assessment of TSICs (based on van Rijswijk et al. 2004). Type I—no enhancement. Type II—gradual increase in enhancement. Type III—rapid initial enhancement followed by a plateau phase. Type IV—rapid initial enhancement followed by a washout phase. Type V—rapid initial enhancement followed by progressive late enhancement

in the ADC values of benign from malignant soft tissue tumours, other authors have demonstrated a difference in ADC values of benign and malignant soft tissue lesions. Oka et al., for example, found that the mean ADC of desmoid tumours was significantly higher than that of malignant soft tissue tumours (Oka et al. 2011). Similarly, Razek et al. reported that the mean ADC values of malignant tumours were lower than the mean ADC values of benign lesions. The authors stated that a threshold ADC value of 1.34×10^{-3} mm^2/s resulted sensitivity of 94%, a specificity of 88% and a diagnostic accuracy of 91%. The authors also found a statistically significant difference in the ADC value between well- and poorly differentiated soft tissue lesions (Razek et al. 2012). Furthermore, Subhawong et al. found that the mean and minimum ADC values of cysts were higher than those of soft tissue sarcomas. According to the authors, a threshold mean ADC value of 2.5×10^{-3} mm^2/s resulted in a sensitivity of 80% and a specificity of 100% (Subhawong et al. 2013). These findings are however hampered by the fact that in our experience certain benign soft tissue lesions such as abscesses or haematomas can demonstrate marked restricted diffusion. The role of DWI in the characterisation of soft tissue lesions therefore remains uncertain.

21.4　Tumour Staging

Bone Tumours

Surgical staging of a suspected bone sarcoma should ideally be performed prior to biopsy as oedema and haemorrhage caused by the procedure may exaggerate the extent of the tumour. In addition, MR imaging, particularly if DCEMRI is performed, may show the most vascularised component of the lesion and thereby indicate the most appropriate site to biopsy. Routine staging studies include an MRI of the presumed primary lesion with at least one large field-of-view sequence to exclude skip metastases, a CT scan of the chest and whole-body bone scintigraphy (or alternatively whole-body MRI) to exclude further bony lesions. Review of the MRI scan should record the extent of the tumour in the bone and soft tissue and the relationship with surrounding important structures, namely, muscle compartments, the adjacent joint and neurovascular bundle. Not surprisingly MR imaging is superior to both bone scintigraphy and CT in demonstrating bone marrow involvement (Bloem et al. 1988; Gillespy et al. 1988; O'Flanagan et al. 1991; Onikul et al. 1996; van Trommel et al. 1997). Precise measurements of bone marrow involvement with an accuracy of <2 mm can be made from T1-weighted images using routine console software (Fig. 21.8).

STIR images may overestimate tumour extent, as perineoplastic oedema tends to merge with the margins of the true tumour (Onikul et al. 1996). DCEMRI can be used to distinguish the oedema from tumour tissue as it enhances slower than viable tumour (Lang et al. 1995). If there is any doubt as to the true intraosseous extent of the tumour repeat, MR imaging after adjuvant chemotherapy is useful, as perineoplastic oedema will tend to resolve, thereby revealing the true tumour margins. If anything, it is more prudent to overestimate the extent of the tumour within the bone. A more extensive

Fig. 21.8 (**a**) Antero-posterior digital radiographic image of the lower limbs in a child with an osteosarcoma of the left distal femoral metaphysis. Measurements obtained from this image are adequate for planning prosthetic replacement of the distal femur, but more precise measurements of the primary tumour are required from (**b**) the coronal T1-weighted MR image to ensure wide excision of the tumour and to exclude skip metastases
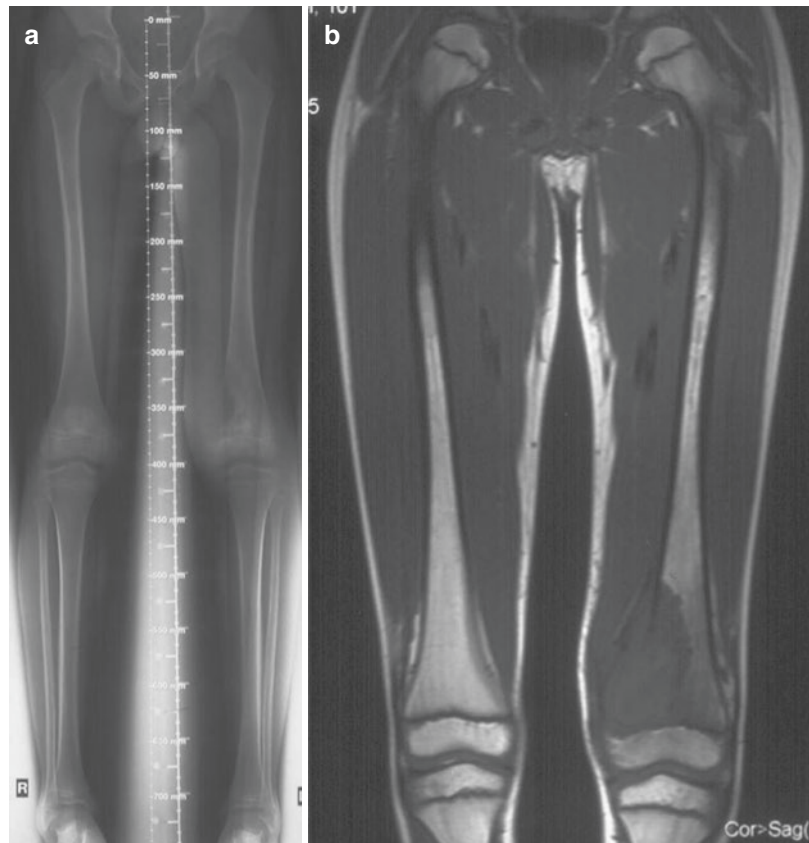
surgical resection with a slightly larger prosthesis or allograft rarely alters the surgical technique, but a contaminated margin due to an underestimation could adversely affect the long-term prognosis for the patient. There are two systems currently used for staging malignant primary bone tumours: the Musculoskeletal Tumour Society (MSTS) system (Enneking et al. 1980) and the American Joint Committee on Cancer (AJCC) system (Peabody et al. 1998). If using the latter system, it is necessary to measure the greatest dimension of the tumour as a relatively recent revision-designated tumours ≤8 cm in maximum diameter as T1 and those >8 cm as T2 (Greene et al. 2002a; Stacy et al. 2006). No particular advantage in the ability to predict prognosis for one staging system over the other staging systems has been shown (Heck et al. 2003). Further measurements may be required from the initial MR staging study depending on individual unit requirements and data collection for various chemotherapy trials. These include measuring the total length of the diseased bone to calculate the proportion of the bone involved with tumour and an estimate of the pre-chemotherapy tumour volume (see Sect. 21.5).

Most patients with a primary sarcoma of the appendicular skeleton will be suitable for limb salvage surgery. Before the advent of CT and more recently MR imaging, measurements of tumour extent were obtained somewhat crudely from conventional radiographs. Today these measurement radiographs are still obtained usually in digital form and the extent of surgery planned with reference to the MR study measurements (Fig. 21.8). Using the radiographs the surgeon will indicate to the biomedical engineer producing the custom-built prosthesis the precise resection levels proximal and distal to the tumour. With both anteroposterior and lateral measurement films, the biomedical engineer can assess the calibre of the medullary canal to produce the best fit for the proximal and distal stems of the prosthesis. If the patient is pre-skeletal fusion, then a radiograph of the left hand and wrist should be obtained to assess the patient's bone age and thereby estimate future growth potential as a growing/extendable prosthesis may be inserted. Primary sarcomas of the pelvis may be amenable to resection and insertion of a custom-built hemipelvic replacement. Because of the complex bony anatomy of the pelvis, measurement radiographs are insufficient for production of the prosthesis. For this purpose in the authors' unit, "life-size" CT images of the pelvis are provided to the biomedical engineer. If the images are provided on hardcopy film, then it is important to ensure that the scale on the images is true life-size. Alternatively if the data is provided in a digital format, the engineer will need to make the appropriate correction factor when viewing the images as well as recognising the cephalic-caudal distances involved.

Soft Tissue Tumours

Routine staging studies for a suspected soft tissue sarcoma include a MR scan of the primary lesion and a CT scan of the chest. The value of the latter is debatable if the tumour is shown to be histologically low grade or the patient is sufficiently elderly or infirm as to make the identification of small pulmonary metastases irrelevant to management of the primary tumour. Bone scintigraphy is rarely indicated but may be appropriate if the sarcoma subtype has a predilection to metastasise to the bone, e.g. rhabdomyosarcoma. Similarly, CT of the abdomen and pelvis may be appropriate if the primary lesion is a myxoid liposarcoma as this is recognised to metastasise to the abdomen. The most commonly applied staging system for soft tissue sarcoma is the American Joint Commission on Cancer (AJCC) system (Greene et al. 2002b). This is a variation on the similar AJCC system for bone sarcoma with the T stage defined as T1 if the tumour ≤5 cm and T2 if >5 cm in maximum diameter. Other soft tissue tumour staging systems which use 5 cm as a staging determinant are the Memorial Sloan-Kettering Cancer Centre and the Hajdu systems (Greer et al. 1992). The Musculoskeletal Tumor Society (MSTS) system can also be applied to soft tissue tumours but has been found to be less useful than the other systems (Wunder et al. 2000).

21.5 Assessment of Tumour Response to Medical Treatments

The improved disease-free survival rates for the commonest bone sarcomas, osteosarcoma and Ewing sarcoma can largely be attributed to the introduction of systemic multi-agent adjuvant chemotherapy. Its aim is to eradicate microscopic metastases and to improve local control of the primary tumour, thereby facilitating limb salvage surgery. Unenhanced MR sequences will show signal and morphological changes following chemotherapy, but these do not correlate well with the histopathological response (Teo and Peh 2004). A decrease in tumour volume correlates well with a good histological response in Ewing sarcoma and less well in osteosarcoma. This is because the soft tissue component in osteosarcoma can progressively mineralise and retain its volume and intratumoural haemorrhage due to progressive necrosis may show an increase in tumour volume despite a good histological response in both situations (van der Woude et al. 1998b). In contrast, initial tumour size as assessed on pretreatment MRI has been shown to predict histologic response and survival in patients with stage II osteosarcoma (Kim et al. 2008).

Tumour volumes can be calculated on unenhanced MR scans both prior to and following adjuvant chemotherapy. Change in tumour volume can be expressed as a ratio by dividing the tumour volume after chemotherapy by the initial tumour volume. A straightforward method of estimating tumour volume is to measure the maximum dimensions of the tumour in three planes and then calculate the volume either as a cylinder, if there is a little or no soft tissue component, or an ellipsoid, if there is a moderate soft tissue component (Fig. 21.9) (Sauer et al. 1987; Abudu et al. 1999; Shin et al. 2000).

This is simple to perform but does not apply well to complex anatomical areas such as the pelvis. An altogether more laborious and undoubtedly time-consuming method is three-dimensional volume measurement with MR imaging (Shin et al. 2000; van Rijswijk et al. 2003). This involves tracing around the margins of the tumour on every axial slice and calculating the volume by multiplying the surface area on each slice with the slice thickness (Fig. 21.10).
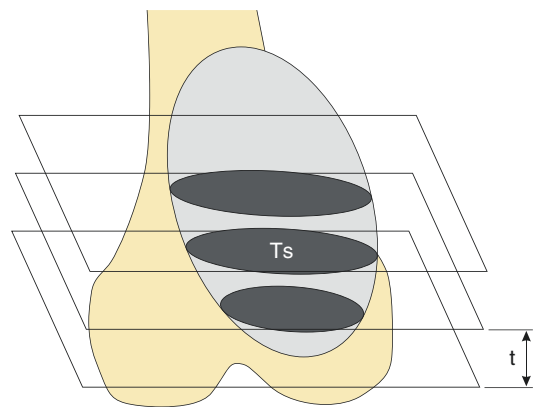
Fig. 21.10 Schematic diagram (based on Shin et al. 2000) showing the method of three-dimensional tumour measurements from MR imaging. The tumour volume (*T*) is calculated by measurement of each tumour surface area (Ts) multiplied by the scan thickness (*t*). It is important to add any interslice gap to the slice thickness before calculating tumour volume

Fig. 21.9 Diagram indicating tumour volume measurement in long bones if the tumour has little or no soft tissue component (i.e. cylindrical) or has a moderate to large soft tissue component (i.e. ellipsoid) (based on Abudu et al. 1999)

a = lengh
b = lateral diameter
c = anteposterior diameter

Volume = a x b x c x 0.735

Volume = a x b x c x 0.52
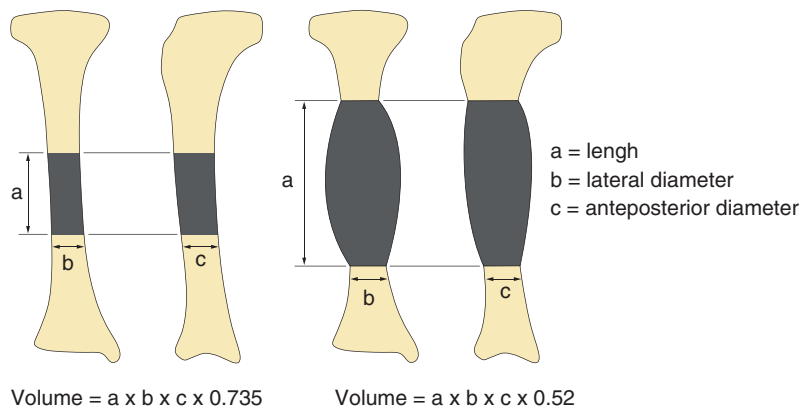
It is important that any interslice gap is included in the slice thickness estimation. The overall tumour volume can be calculated by adding together the separate volumes for each slice (+interslice gap). A standardised MR technique is mandatory if valid comparisons are to be made regarding tumour volume changes pre- and postchemotherapy. This also applies to the simpler calculations viewing the tumour as a cylinder or ellipsoid. Interestingly, one study claims that, based on interobserver and intraobserver variability for volumetric measurements, the three-dimensional was the most reproducible (Shin et al. 2000).

Static contrast-enhanced MR images cannot reliably differentiate between residual viable tumour, immature granulation tissue, neovascularity in necrotic areas and reactive hyperaemia (Erlemann et al. 1990; Fletcher 1991; Lawrence et al. 1993). Numerous studies have assessed the value of DCEMRI in monitoring the response to adjuvant chemotherapy in bone sarcomas (Erlemann et al. 1990; de Baere et al. 1992; Bonnerot et al. 1992; Hanna et al. 1992; Fletcher et al. 1992; Shapeero et al. 1992; Verstraete et al. 1994a, b; van der Woude et al. 1995; Dyke et al. 2003). All have shown the technique to be reliable in distinguishing good responders (>90% tumour necrosis) from poor responders (<90 tumour necrosis). It is important that a standardised technique is applied for both the pre-chemotherapy and post-chemotherapy scans. Post-processing can be performed as per the different techniques described in Sect. 21.3.1. The simplest method is to compare the TSICs from the two scans. If the enhancement slope on the second scan remains the same or only slightly less than on the original scan, then the tumour is a poor responder. If the slope has flattened (i.e. a slower rate of enhancement), then this suggests a good responder. It is important to recognise that responders cannot be distinguished from nonresponders after only one cycle of chemotherapy (Fletcher et al. 1992).

Nevertheless, a relatively recent study has identified DCEMRI as a prognostic factor for event-free survival and overall survival before commencement of treatment and showed that DCEMRI was indicative of a histologic response to neoadjuvant therapy (Guo et al. 2012).

Diffusion-weighted MRI has revealed promising results in monitoring the response to adjuvant chemotherapy in some malignant primary bone tumours. A few studies have demonstrated that differences in ADC values in osteosarcoma and Ewing sarcoma prior and after chemotherapy correlate with the degree of tumour necrosis and therefore can differentiate between responders and nonresponders (Hayashida et al. 2006b, Uhl et al. 2006). However a study by Oka et al. which assessed if mean and minimum ADC values could differentiate between responders and nonresponders to chemotherapy in osteosarcoma found that only the minimum ADC value in this patient cohort was able to differentiate between responders and nonresponders whilst the mean ADC value failed to show a statistically significant difference between the two groups (Oka et al. 2010). Similarly, Bajpai and coworkers who evaluated 31 patients with osteosarcoma revealed that mean ADC values did not correlate with tumour necrosis whilst the ADC value adjusted for tumour volume did correlate with histological response (Bajpai et al. 2011). Furthermore, Wang et al. found that the ADC values after neoadjuvant chemotherapy in good responders in osteosarcoma were higher than those of poor responders and that the ADC values between viable and necrotic tumour after chemotherapy were statistically significant (Wang et al. 2013). Diffusion-weighted MRI therefore seems to be a promising and powerful tool in the assessment of treatment response of osteosarcomas. Further research is however required on this topic to corroborate these findings.

Various scintigraphic techniques have been studied in assessing response to chemotherapy in patients with bone sarcoma including three-phase Tc99m-methylene diphosphonate (Bloem et al. 1988; Erlemann et al. 1990; Knop et al. 1990), gallium-67 scintigraphy (Estes et al. 1990) and thallium-201 scintigraphy (Ramanna et al. 1990). Although published results for these techniques were reasonable, the low spatial resolution and low specificity mean they have largely been superseded by DCEMRI (van der Woude et al. 1998a, b). The role of positron emission tomography (PET) in sarcoma management remains

uncertain. PET provides a non-invasive measure of metabolic changes in tumour tissue. Numerous authors have suggested that FDG PET correlates with poor response to chemotherapy, tumour necrosis (Kong et al. 2013, Cheon et al. 2009; Costelloe et al. 2009; Franzius et al. 2000; Hamada et al. 2009; Hawkins et al. 2002; Nair et al. 2000; Schulte et al. 1999) and survival in osteosarcoma (Costelloe et al. 2009). However, a study by Hawkins et al. suggested that FDG PET only partially correlates with histologic response to chemotherapy, whilst in their study, SUVmax after neoadjuvant chemotherapy was associated with improved progression-free survival (Hawkins et al. 2009). Similarly, the role of FDG PET in the assessment of treatment response in Ewing sarcoma has also been investigated. Hawkins et al. found that an SUVmax of less than 2.5 after neoadjuvant chemotherapy was associated with an improved 4-year progression-free survival of 72%. The same study demonstrated that SUVmax before and after chemotherapy was concordant with histologic response in 68% and 69%, respectively (Hawkins et al. 2005). The role of FDG PET in the evaluation of treatment response appears therefore promising; however, the validity of the studies published so far is hampered by the relatively small sample size, and therefore prospective studies with larger size patient samples are required to assess the role of FDG PET in the treatment response of osteosarcoma and Ewing sarcoma.

The value of neoadjuvant chemotherapy in the management of soft tissue sarcoma is less well defined than in bone sarcoma. Volume measurement changes and DCEMRI can both be used to assess response to chemotherapy in a similar manner to that described for bone sarcomas above (van Rijswijk et al. 2003). Similarly, few studies have reported that PET/CT may be able to predict histopathologic response after neoadjuvant chemotherapy in high-grade soft tissue sarcoma (Benz et al. 2009; Evilevitch et al. 2008), whilst a few studies also demonstrated that pretreatment SUVmax in soft tissue sarcoma predicts overall survival and progression-free survival (Lisle et al. 2009; Schwarzbach et al. 2005). The role of neoadjuvant chemotherapy in soft tissue sarcomas is however equivocal. Therefore, the utility of PET/CT in the management of soft tissue sarcomas appears to be of limited value.

References

Abudu A, Davies AM, Pynsent PB, Mangham DC, Tillman RM, Carter SR, Grimer RJ (1999) Tumour volume as a predictor of necrosis after chemotherapy in Ewing's sarcoma. J Bone Joint Surg Br 81B:317–322

Ahn JI, Park JS (1994) Pathological fractures secondary to unicameral bone cysts. Int Orthop 18:20–22

Arata MA, Peterson HA, Dahlin DC (1981) Pathological fractures through nonossifying fibromas. J Bone Joint Surg Am 63A:980–988

Ashford RU, Pendlebury S, Stalley PD (2006) Management of metastatic disease of the appendicular skeleton. Curr Orthop 20:299–315

de Baere T, Vanel D, Shapeero L, Charpentier A, Terrier P, di Paola M (1992) Osteosarcoma after chemotherapy: evaluation with contrast material enhanced subtraction MR imaging. Radiology 185:587–592

Bajpai J, Gamnagatti S, Kumar R, Sreenivas V, Sharma MC, Khan SA, Rastogi S, Malhotra A, Safaya R, Bakhshi S (2011) Role of MRI in osteosarcoma for evaluation and prediction of chemotherapy response: correlation with histological necrosis. Pediatr Radiol 41:441–450

Baur A, Stabler A, Bruning R, Bartl R, Krodel A, Reiser M, Deimling M (1998) Diffusion-weighted MR imaging of bone marrow: differentiation of benign versus pathologic compression fractures. Radiology 207:349–356

Baur A, Reiser MF (2000) Diffusion-weighted imaging of the musculoskeletal system in humans. Skelet Radiol 29:555–562

Benz MR, Czernin J, Allen-Auerbach MS, Tap WD, Dry SM, Elashoff D, Chow K, Evilevitch V, Eckardt JJ, Phelps ME, Weber WA, Eilber FC (2009) FDG-PET/CT imaging predicts histopathologic treatment responses after the initial cycle of neoadjuvant chemotherapy in high-grade soft-tissue sarcomas. Clin Cancer Res 15:2856–2863

Bernard SA, Murphey MD, Flemming DJ, Kransdorf MJ (2010) Improved differentiation of benign osteochondromas from secondary chondrosarcomas with standardized measurement of cartilage cap at CT and MR imaging. Radiology 255:857–865

Berquist TH, Ehman RL, King BF, Hodgman CH, Ilstrup DM (1990) Value of MR imaging in differentiating benign from malignant soft tissue masses: a study of 95 lesions. Am J Roentgenol 155:1251–1255

Berquist TH (1993) MR imaging of primary skeletal neoplasms. Radiol Clin N Am 31:411–424

Bloem JL, Taminiau AHM, Eulderink F, Hermans J, Pauwels EKJ (1988) Radiologic staging of primary bone sarcoma: MR imaging, scintigraphy, angiogra-

phy, and CT correlated with pathologic examination. Radiology 169:805–810

Bonnerot V, Charpentier A, Frouin F, Kalifa C, Vanel D, Di Paola R (1992) Factor analysis of dynamic MR imaging in predicting response of osteosarcoma to chemotherapy. Investig Radiol 27:847–855

Cheon GJ, Kim MS, Lee JA, Lee SY, Cho WH, Song WS, Koh JS, Yoo JY, Oh DH, Shin DS, Jeon DG (2009) Prediction model of chemotherapy response in osteosarcoma by 18F-FDG PET and MRI. J Nucl Med 50:1435–1440

Costelloe CM, Macapinlac HA, Madewell JE, Fitzgerald NE, Mawlawi OR, Rohren EM, Raymond AK, Lewis VO, Anderson PM, Bassett RL Jr, Harrell RK, Marom EM (2009) 18F-FDG PET/CT as an indicator of progression-free and overall survival in osteosarcoma. J Nucl Med 50:340–347

Damron TA, Morgan H, Prakash D, Grant W, Aronowitz J, Heiner J (2003) Critical evaluation of Mirels' rating system for impending pathologic fractures. Clin Orthop 415S:S201–S207

Damron TA, Ward WG (2003) Risk of pathologic fracture: assessment. Clin Orthop 415S:S208–S211

De Coninck T, Jans L, Sys G, Huysse W, Verstraeten T, Forsyth R, Poffyn B, Verstraete K (2013) Dynamic contrast-enhanced MR imaging for differentiation between enchondroma and chondrosarcoma. Eur Radiol 2013(23):3140–3152

Dijkstra PD, Oudkerk M, Wiggers T (1997) Prediction of pathological subtrochanteric fractures due to metastatic lesions. Arch Orthop Trauma Surg 116: 221–224

Douis H, Jeys L, Grimer R, Davies AM (2014) Is there a role for Diffusion-Weighted MRI (DWI) in the diagnosis of central cartilage tumours? Skelet Radiol 43:1347

Dyke JP, Panicek DM, Healey JH, Meyers PA, Huvos AG, Schwartz LH, Thaler HT, Tofts PS, Gorlick R, Koutcher JA, Ballon D (2003) Osteogenic and Ewing sarcomas: estimation of necrotic fraction during induction chemotherapy with dynamic contrast-enhanced MR imaging. Radiology 228:271–278

Easley ME, Kneisl JS (1997) Pathologic fractures through nonossifying fibromas: is prophylactic treatment warranted. J Pediatr Orthop 17:808–813

Einarsdóttir H, Karlsson M, Wejde J, Bauer HC (2004) Diffusion-weighted MRI of soft tissue tumours. Eur Radiol 14:959–963

Enneking WF, Spanier SS, Goodman MA (1980) A system for the surgical staging of musculoskeletal sarcoma. Clin Orthop (153):106–120

Erlemann R, Reiser M, Peters P, Vasallo P, Nommensen B, Kusnierz-Glaz CR, Ritter J, Roessner A (1989) Musculoskeletal neoplasms: static and dynamic Gd-DTPA enhanced MR imaging. Radiology 171:767–773

Erlemann R, Sciuk J, Bosse A et al (1990) Response of osteosarcoma and Ewing's sarcoma to preoperative chemotherapy: assessment with dynamic and static MR imaging and skeletal scintigraphy. Radiology 175:791–796

Erlemann R, Sciuk J, Wuisman P et al (1992) Dynamic MR tomography in diagnosis of inflammatory and tumourous space-occupying growths of the musculoskeletal system. Rofo 156:353–359

Estes DN, Magill HL, Thompson EI, Hayes FA (1990) Primary Ewing sarcoma; follow-up with Ga-67 scintigraphy. Radiology 177:449–453

Evilevitch V, Weber WA, Tap WD, Allen-Auerbach M, Chow K, Nelson SD, Eilber FR, Eckardt JJ, Elashoff RM, Phelps ME, Czernin J, Eilber FC (2008) Reduction of glucose metabolic activity is more accurate than change in size at predicting histopathologic response to neoadjuvant therapy in high-grade soft-tissue sarcomas. Clin Cancer Res 14:715–720

Fidler M (1973) Prophylactic internal fixation of secondary neoplastic deposits in long bones. Br Med J 1:341–343

Fidler M (1981) Incidence of fracture through metastases in long bones. Acta Orthop Scand 52:623–627

Fletcher BD (1991) Response of osteosarcoma and Ewing sarcoma to chemotherapy: imaging evaluation. Am J Roentgenol 157:825–833

Fletcher BD, Hanna SL, Fairclough DL, Gronmeyer SA (1992) Pediatric musculoskeletal tumors: use of dynamic contrast-enhanced MR imaging to monitor response to chemotherapy. Radiology 184:243–248

Franzius C, Sciuk J, Brinkschmidt C et al (2000) Evaluation of chemotherapy response in primary bone tumors with F-18 FDG positron emission tomography with histologically assessed tumor necrosis. Clin Nucl Med 25:874–881

Gielen JMLA, De Schepper AM, Vanhoenacker F, Parizel P, Wang XL, Sciot R, Weyler J (2004) Accuracy of MRI in characterization of soft tissue tumors and tumor-like lesions. A prospective study in 548 patients. Eur Radiol 14:2320–2330

Giernaerdt MJA, Hogendoorn PCW, Bloem JL, Taminiau AHM, van der Woude HJ (2000) Cartilaginous tumors: fast contrast-enhanced MR imaging. Radiology 214:539–546

Gillespy T, Manfrini M, Ruggieri P, Spanier SS, Pettersson H, Springfield DS (1988) Staging of intraosseous extent of osteosarcoma: correlation of preoperative CT with pathologic macroslides. Radiology 167:765–767

Greene FL, Page DL, Fleming ID (eds) (2002a) American joint committee on cancer. Bone, 6th edn. Springer-Verlag, New York, NY, pp 213–219

Greene FL, Page DL, Fleming ID (eds) (2002b) American Joint Committee on Cancer. Soft tissue, 6th edn. Springer-Verlag, New York, NY, pp 193–197

Greer RJ, Woodruff J, Casper ES et al (1992) Management of small soft tissue sarcoma of the extremity in adults. Arch Surg 127:1285–1289

Griffith JF, Chan DPN, Kumta SM, Chow LTC, Ahuja AT (2004) Does Doppler analysis of musculoskeletal soft tissue tumours help predict tumour malignancy? Clin Radiol 59:369–375

Guo J, Reddick WE, Glass JO, Ji Q, Billups CA, Wu J, Hoffer FA, Kaste SC, Jenkins JJ, Ortega Flores XC, Quintana J, Villarroel M, Daw NC (2012) Dynamic contrast-enhanced magnetic resonance imaging as a prognostic factor in predicting event-free and overall survival in pediatric patients with osteosarcoma. Cancer 118:3776–3885

Hamada K, Tomita Y, Inoue A, Fujimoto T, Hashimoto N, Myoui A, Yoshikawa H, Hatazawa J (2009) Evaluation of chemotherapy response in osteosarcoma with FDG-PET. Ann Nucl Med 23:89–95

Hanna SL, Parham DM, Fairclough DL, Meyer WH, Lee AH, Fletcher BD (1992) Assessment of osteosarcoma response to preoperative chemotherapy using dynamic FLASH gadolinium-DTPA-enhanced MR mapping. Investig Radiol 27:367–373

Harrington KD (1982) New trends in management of lower extremity metastases. Clin Orthop 169: 53–61

Hawkins DS, Rajendran YG, Conrad EU, Bruckner JD, Eary JF (2002) Evaluation of chemotherapy response in pediatric bone sarcomas by [F-18]-fluorodeoxy-D-glucose positron emission tomography. Cancer 94:3277–3284

Hawkins DS, Schuetze SM, Butrynski YE, Rajendran YG, Vernon CB, Conrad EU, Eary JF (2005) [F-18]-fluorodeoxy-D-glucose positron emission tomography predicts outcome for Ewing sarcoma family of tumors. J Clin Oncol 23:8828–8833

Hawkins DS, Conrad EU 3rd, Butrynski JE, Schuetze SM, Eary JF (2009) [F-18]-fluorodeoxy-D-glucose-positron emission tomography response is associated with outcome for extremity osteosarcoma in children and young adults. Cancer 115:3519–3525

Hayashida Y, Hirai T, Yakushiji T, Katahira K, Shimomura O, Imuta M, Nakaura T, Utsunomiya D, Awai K, Yamashita Y (2006a) Evaluation of diffusion-weighted imaging for the differential diagnosis of poorly contrast-enhanced and T2-prolonged bone masses: initial experience. J Magn Reson Imaging 23:377–382

Hayashida Y, Yakushiji T, Awai K, Katahira K, Nakayama Y, Shimomura O, Kitajima M, Hirai T, Yamashita Y, Mizuta H (2006b) Monitoring therapeutic responses of primary bone tumors by diffusion-weighted image: initial results. Eur Radiol 16:2637–2643

Heck RK, Stacy GS, Flaherty MJ, Montag AG, Peabody TD, Simon MA (2003) A comparison study of staging systems for bone sarcomas. Clin Orthop 415: 64–71

Hipp JA, Springfield DS, Hayes WC (1995) Predicting pathologic fracture risk in the management of metastatic bone defects. Clin Orthop 312:120–135

Kaelin AJ, MacEwen GD (1989) Unicameral bone cysts: natural history and the risk of fracture. Int Orthop 13:275–282

Kenney PJ, Gilula LA, Murphy WA (1981) The use of computed tomography to distinguish osteochondroma and chondrosarcoma. Radiology 139:129–137

Kim MS, Lee SY, Cho WH, Song WS, Koh JS, Lee JA, Yoo JY, Jeon DG (2008) Initial tumor size predicts histologic response and survival in localized osteosarcoma patients. J Surg Oncol 97:456–461

Knop J, Delling G, Heise U, Winkler K (1990) Scintigraphic evaluation of tumour regression during preoperative chemotherapy of osteosarcoma. Skelet Radiol 19:165–172

Kong CB, Byun BH, Lim I, Choi CW, Lim SM, Song WS, Cho WH, Jeon DG, Koh JS, Yoo JY, Lee SY (2013) ^{18}F-FDG PET SUVmax as an indicator of histopathologic response after neoadjuvant chemotherapy in extremity osteosarcoma. Eur J Nucl Med Mol Imaging 40:728–736

Lang P, Honda G, Roberts T, Vahlensieck M, Johnston JO, Rosenau W, Mathur A, Peterfy C, Gooding C, Genant HK (1995) Musculoskeletal neoplasm: perineoplastic edema versus tumor on dynamic postcontrast MR images with spatial mapping of instantaneous enhancement rates. Radiology 197:831–839

Lawrence JA, Babyn P, Chan HSL, Thorner PS, Pron GE, Krajbich IJ (1993) Extremity osteosarcoma in childhood: prognostic value of radiologic imaging. Radiology 189:43–47

Lecouvet FE, Malghem J, Michaux L, Michaux JL et al (1997) Vertebral compression fractures in multiple myeloma. Part II Assessment of fracture risk with MR imaging of spinal bone metastases. Radiology 204:201–205

Lecouvet FE, Vande Berg BC, Michaux L, Jamart J et al (1998) Development of vertebral fractures in patients with multiple myeloma: does MRI enable recognition of vertebrae that will collapse? J Comput Assist Tomogr 22:430–436

Van der Linden YM, Kroon HM, Dijkstra SP, Lok JJ, Noordijk EM, Leer JW, Marijnen CA, Dutch Bone Metastasis Study Group. Radiother Oncol. 2003 Oct;69(1):21–31. Simple radiographic parameter predicts fracturing in metastatic femoral bone lesions: results from a randomised trial

Van der Linden YM, Kroon HM, Dijkstra SP, Lok JJ, Noordijk EM, Leer JW, Marijnen CA, Dutch Bone Metastasis Study Group. Radiother Oncol. 2003;69(1):21–31. Simple radiographic parameter predicts fracturing in metastatic femoral bone lesions: results from a randomised trial.

Leong NL, Anderson ME, Gebhardt MC, Snyder BD (2010) Computed tomography-based structural analysis for predicting fracture risk in children with benign skeletal neoplasms: comparison of specificity with that of plain radiographs. J Bone Joint Surg Am 92:18277–11833

Lisle JW, Eary JF, O'Sullivan J, Conrad EU (2009) Risk assessment based on FDG-PET imaging in patients with synovial sarcoma. Clin Orthop Relat Res 467:1605–1611

Liu PT, Chivers FP, Roberts CC, Schultz CJ, Beauchamp CP (2003) Imaging of osteoid osteoma with dynamic gadolinium-enhanced MR imaging. Radiology 227:691–700

Ma LD, Frassica FJ, Scott WW Jr, Fishman EK, Zerhouni EA (1995) Differentiation of benign and malignant musculoskeletal tumors: potential pitfalls with MR imaging. Radiographics 15:349–366

Maeda M, Matsumine A, Kato H, Kusuzaki K, Maier SE, Uchida A, Takeda K (2007) Soft-tissue tumors evaluated by line-scan diffusion-weighted imaging: influence of myxoid matrix on the apparent diffusion coefficient. J Magn Reson Imaging 25:1199–1204

Mavrogenis AF, Pala E, Romantini M, Guerra G, Romagnoli C, Maccauro G, Ruggieri P (2011) Side effects in radiation in musculoskeletal oncology: clinical evaluation of radiation-induced fractures. Int J Immunopathol Pharmacol 24:29–37

McAfee PC, Zdeblick TA (1989) Tumors of the thoracic and lumbar spine: surgical treatment via the anterior approach. J Spinal Disord 2:145–154

Mirels H (1989) Metastatic disease in long bones: a proposed scoring system for diagnosing impending pathologic fractures. Clin Orthop 249:256–264

Mirowitz SA, Tooty WG, Lee JKT (1992) Characterization of musculoskeletal masses using dynamic Gd-DTPA enhanced spin-ecgo MRI. J Comput Assist Tomogr 16:120–125

Morrison WB, Dalinka MK, Daffner RH et al (2005) Bone tumors. In: ACR appropriateness criteria. American College of Radiology, Reston, VA, pp 1–5

Moulton JS, Blebea JS, Dunco DM, Braley SE, Bisset GS, Emery KH (1995) MR imaging of soft tissue masses: diagnostic efficacy and value of distinguishing between benign and malignant lesions. Am J Roentgenol 164:1191–1199

Nair N, Ali A, Green AA, Lamonica G, Alibazoglu H, Alibazoglu B, Hollinger EF, Ahmed K (2000) Response of osteosarcoma to chemotherapy. Evaluation with F-18 FDG-PET scans. Clin Positron Imaging 3:79–83

O'Flanagan SJ, Stack JP, McGee HM, Dervan P, Hurson B (1991) Imaging of intramedullary tumour spread in osteosarcoma. A comparison of techniques. J Bone Joint Surg Br 73B:998–1001

Oka K, Yakushiji T, Sato H, Hirai T, Yamashita Y, Mizuta H (2010) The value of diffusion-weighted imaging for monitoring the chemotherapeutic response of osteosarcoma: a comparison between average apparent diffusion coefficient and minimum apparent diffusion coefficient. Skelet Radiol 39:141–146

Oka K, Yakushiji T, Sato H, Fujimoto T, Hirai T, Yamashita Y, Mizuta H (2011) Usefulness of diffusion-weighted imaging for differentiating between desmoid tumors and malignant soft tissue tumors. J Magn Reson Imaging 33:189–193

Onikul E, Fletcher BD, Parham DM, Chen G (1996) Accuracy of MR imaging for estimating extent of osteosarcoma. Am J Roentgenol 167:1211–1215

Ortiz EJ, Isler MH, Navia JE, Canosa R (2005) Pathologic fractures in children. Clin Orthop 432:116–126

Parrish FF, Murray JA (1970) Surgical treatment for secondary neoplastic fractures. J Bone Joint Surg Am 52A:665–686

Peabody TD, Gibbs CP Jr, Simon MA (1998) Evaluation and staging of musculoskeletal neoplasms. J Bone Joint Surg Am 80A:1204–1218

Ramanna L, Waxman A, Binney G, Waxman S, Mirra J, Rosen G (1990) Thallium-201 scintigraphy in bone sarcoma: comparison with gallium-67 and technetium-MDP in the evaluation of chemotherapeutic response. J Nucl Med 31:567–572

Razek A, Nada N, Ghaniem M, Elkhamary S (2012) Assessment of soft tissue tumours of the extremities with diffusion echoplanar MR imaging. Radiol Med 117:96–101

Reddick W, Langston J, Meyer W et al (1994) Discrete signal processing of dynamic contrast-enhanced MR imaging: statistical validation and preliminary clinical application. J Magn Reson Imaging 4:397–404

van Rijswijk CSP, Geirnaerdt MJA, Hogendoorn PCW, Peterse JL, van Coevorden F, Taminiau AHM, Tollenaar RAEM, Kroon BBR, Bloem JL (2003) Dynamic contrast-enhanced MR imaging in monitoring response to isolated limb perfusion in high grade soft tissue sarcoma: initial results. Eur Radiol 13:1849–1858

van Rijswijk CSP, Geirnaerdt MJA, Hogendoorn PCW, Taminiau AHM, van Coevorden F, Zwinderman AH, Pope TL, Bloem JL (2004) Soft-tissue tumors: value of static and dynamic gadopentetate dimeglumine-enhanced MR imaging in prediction of malignancy. Radiology 233:493–502

Roth SE, Mousavi P, Finkelstein J, Chow E, Kreder H, Whyne CM (2004) Metastatic burst fracture risk prediction using biomechanically based equations. Clin Orthop 419:83–90

Saifuddin A, Burnett SJD, Mitchell R (1998) Pictorial review: ultrasonography of primary bone tumours. Clin Radiol 53:239–246

Saraph V, Linhart WE (2005) Modern treatment of pathological fractures in children. Injury 36(Suppl 1):A64–A74

Sauer R, Jürgens H, Burgers JM et al (1987) Prognostic factors in the treatment of Ewing's sarcoma: the Ewing's sarcoma study group of the German Society of Paediatric Oncology CESS 81. Radiother Oncol 10:101–110

Scherer A, Wittsack HJ, Strupp C et al (2002) Vertebral fractures in multiple myeloma: first results of assessment of fracture risk using dynamic contrast-enhanced MR imaging. Ann Hematol 81:517–521

Schulte M, Brecht-Krauss D, Werner M, Hartwig E, Sarkar MR, Keppler P, Kotzerke J, Guhlmann A, Delling G, Reske SN (1999) Evaluation of neoadjuvant therapy response of osteogenic sarcoma using FDG PET. J Nucl Med 40:1637–1643

Schwarzbach MH, Hinz U, Dimitrakopoulou-Strauss A, Willeke F, Cardona S, Mechtersheimer G, Lehnert T, Strauss LG, Herfarth C, Büchler MW (2005) Prognostic significance of preoperative [18-F] fluorodeoxyglucose (FDG) positron emission tomography (PET) imaging in patients with resectable soft tissue sarcomas. Ann Surg 241:286–294

Shapeero LG, Henry-Amar M, Vanel D (1992) Response of osteosarcoma and Ewing sarcoma to preoperative chemotherapy: assessment with dynamic and static MR imaging and skeletal scintigraphy. Investig Radiol 27:989–991

Shin KH, Moon SH, Suh JS, Yang WI (2000) Tumor volume change as a predictor of chemotherapeutic response in osteosarcoma. Clin Orthop 376:200–208

Skeletal Lesions Interobserver Correlation amongst Expert Diagnosticians (SLICED) Study Group (2007) Reliability of histopathologic and radiologic grading of cartilaginous neoplasms in long bones. J Bone Joint Surg Am 89:2113–2123

Snell WE, Beals RK (1964) Femoral metastases and fractures from breast cancer. Surg Gynecol Obstet 119:22–24

Stacy GS, Mahal RS, Peabody TD (2006) Staging of bone tumors: a review with illustrative examples. Am J Roentgenol 186:967–976

Subhawong TK, Durand DJ, Thawait GK, Jacobs MA, Fayad LM (2013) Characterization of soft tissue masses: can quantitative diffusion weighted imaging reliably distinguish cysts from solid masses? Skelet Radiol 42:1583–1592

Taneichi H, Kaneda K, Takeda N et al (1997) Risk factors and probability of vertebral body collapse in metastases of the thoracic and lumbar spine. Spine 22:239–245

Teo HEL, Peh WCG (2004) The role of imaging in the staging and treatment planning of primary malignant bone tumors in children. Eur Radiol 14:465–475

Uhl M, Saueressig U, Koehler G, Kontny U, Niemeyer C, Reichardt W, Ilyasof K, Bley T, Langer M (2006) Evaluation of tumour necrosis during chemotherapy with diffusion-weighted MR imaging: preliminary results in osteosarcomas. Pediatr Radiol 36:1306–1311

van Trommel MF, Kroon HM, Bloem JL, Hogendoorn PC, Taminiau AH (1997) MR imaging based strategies in limb salvage surgery for osteosarcoma of the distal femur. Skelet Radiol 26:636–641

Verstraete KL, De Deene Y, Roels H, Dierick A, Uyttendaele D, Kunnen M (1994a) Benign and malignant musculoskeletal lesions: dynamic contrast-enhanced MR imaging—parametric "first-pass" images depict tissue vascularization and perfusion. Radiology 192:835–843

Verstraete KL, Dierick A, De Deene Y et al (1994b) First-pass images of musculoskeletal lesions: a new and useful diagnostic application of dynamic contrast-enhanced MR imaging. Magn Reson Imaging 12:687–702

Verstraete KL, Vanzieleghem B, De Deene Y et al (1995) Static, dynamic and first-pass imaging of musculo-skeletal lesions by use of gadodiamide injection. Acta Radiol 36:27–36

Ward WG, Spang J, Howe D, Gordon S (2000) Femoral recon nails for metastatic disease: indications, technique and results. Am J Orthop 29:34–42

Whyne CM, Serena S, Lotz JC (2003) Burst fracture in the metastatically involved spine. Spine 28:652–660

Woertler K, Lindner N, Gosher G, Brinkschmidt C, Heindel W (2000) Osteochondroma: MR imaging of tumor-related complications. Eur Radiol 10:832–840

Wang CS, Du LJ, Si MJ, Yin QH, Chen L, Shu M, Yuan F, Fei XC, Ding XY (2013) Noninvasive assessment of response to neoadjuvant chemotherapy in osteosarcoma of long bones with diffusion-weighted imaging: an initial in vivo study. PLoS One 26(8):e72679

Woertler K (2003) Benign bone tumors and tumor-like lesions: value of cross-sectional imaging. Eur Radiol 13:1820–1835

Van der Woude HJ, Verstraete KL, Hogendoorn PCW, Taminiau AHM, Hermans J, Bloem JL (1998b) Musculoskeletal tumors: does fast dynamic contrast-enhanced subtraction MR imaging contribute to the characterization? Radiology 208:821–828

Van der Woude HJ, Bloem JL, Hogendoorn PCW (1998a) Postoperative evaluation and monitoring chemotherapy in patients with high-grade osteogenic and Ewing sarcoma: review of current imaging modalities. Skelet Radiol 27:57–71

Van der Woude HJ, Bloem JL, Verstraete KL et al (1995) Osteosarcoma and Ewing's sarcoma after neoadjuvant chemotherapy: value of dynamic MR imaging in detecting viable tumor before surgery. Am J Roentgenol 165:593–598

DeWald RL, Bridwell KH, Prodromas C et al (1985) Reconstructive spinal surgery as palliation for metastatic malignancies of the spine. Spine 10:21–26

Wunder JS, Healey JH, Davis AM, Brennan MF (2000) A comparison of staging systems for localized extremity soft tissue sarcoma. Cancer 88:2721–2730

Yakushiji T, Oka K, Sato H, Yorimitsu S, Fujimoto T, Yamashita Y, Mizuta H (2009) Characterization of chondroblastic osteosarcoma: gadolinium-enhanced versus diffusion-weighted MR imaging. J Magn Reson Imaging 29:895–900

Index

Index 859